A.I.M.P.A.

Commission internationale de physique des nuages

Communications à la VIII^{ème} conférence internationale sur la physique des nuages

Volume II

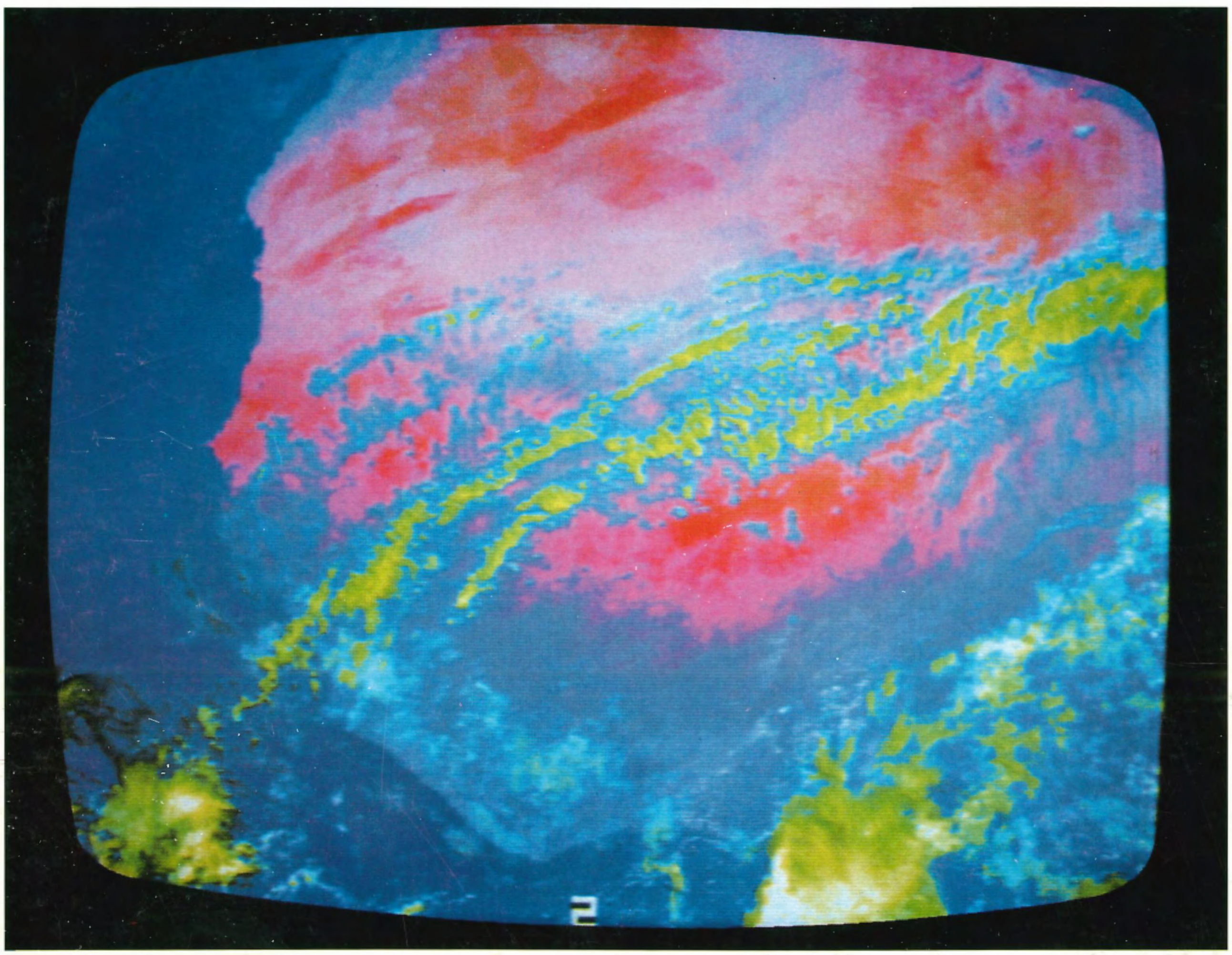

Clermont-Ferrand - France - 15-19 juillet 1980

VIIIEME CONFERENCE INTERNATIONALE SUR LA PHYSIQUE DES NUAGES

CLERMONT-FERRAND, 15-19 juillet 1980

Sous le haut patronage de :

MADAME LE MINISTRE ALICE SAUNIER-SEITE, MINISTRE DES UNIVERSITES

Sous le patronage international de :

LA COMMISSION INTERNATIONALE DE PHYSIQUE DES NUAGES

LA COMMISSION INTERNATIONALE DU RAYONNEMENT

L'ASSOCIATION INTERNATIONALE DE METEOROLOGIE ET PHYSIQUE DE L'ATMOSPHERE

L'ORGANISATION METEOROLOGIQUE MONDIALE

Et les patronages nationaux des organismes suivants :

CENTRE NATIONAL DE LA RECHERCHE SCIENTIFIQUE

DELEGATION GENERALE A LA RECHERCHE SCIENTIFIQUE ET TECHNIQUE

UNIVERSITE DE CLERMONT II

COMITE NATIONAL FRANCAIS DE GEODESIE ET GEOPHYSIQUE

SOCIETE AMERICAINE DE METEOROLOGIE

SOCIETE FRANCAISE DE METEOROLOGIE

Subventions ou aides

ASSOCIATION INTERNATIONALE DE METEOROLOGIE
ET PHYSIQUE DE L'ATMOSPHERE (AIMPA)

CENTRE NATIONAL DE LA RECHERCHE SCIENTIFIQUE (CNRS)

INSTITUT NATIONAL D'ASTRONOMIE ET DE GEOPHYSIQUE (INAG)

DIRECTION DES RECHERCHES ET ETUDES TECHNIQUES (DRET)

ETUDES ET RECHERCHES DE L'ELECTRICITE DE FRANCE (EDF)

DEPARTEMENT DU PUY-DE-DOME

VILLE DE CLERMONT-FERRAND

AIR INTER, UTA, AIR FRANCE

UNIVERSITE DE CLERMONT II

UNITE D'ENSEIGNEMENT ET DE RECHERCHE "SCIENCES"

ASSOCIATION POUR LE DEVELOPPEMENT DE L'ENSEIGNEMENT
ET DE LA RECHERCHE EN AUVERGNE

MINISTERE DE L'AGRICULTURE

MINISTERE DES UNIVERSITES

Comité International des Programmes

Pr R.G. SOULAGE (France), Président

Pr W.F. HITSCHFELD (Canada), Président de
la Commission Internationale de Physique des Nuages (CIPN)

Dr H.K. WEICKMANN (U.S.A.), Président honoraire
de CIPN

Dr E. MESZAROS (Hongrie), Secrétaire de CIPN

Dr A. GAGIN (Israël)

Pr R. LIST (Canada), Président de la IIIème Conférence Scientifique
de l'O.M.M. sur la Modification du Temps

Dr I.P. MAZIN (U.R.S.S.)

Dr S. MOSSOP (Australie)

Pr H.D. ORVILLE (U.S.A.)

Pr H.R. PRUPPACHER (U.S.A.)

Dr. P. RYDER (Grande-Bretagne)

Comité d'Organisation

R.G. SOULAGE (Président), C. BOUTIN, J. DESSENS, M. FOURNIER D'ALBE,
H. ISAKA, Y. POINTIN, R. ROSSET, R. SERPOLAY.

Cet ouvrage a été imprimé et composé par :

L'UNITE D'ENSEIGNEMENT ET DE RECHERCHE "SCIENCES"

DE L'UNIVERSITE DE CLERMONT II

et le

LABORATOIRE ASSOCIE DE METEOROLOGIE PHYSIQUE
(L.A. CNRS n° 267)
B.P. 45
63170 AUBIERE (France)

Tel. (73) 26 42 87
Telex : 990 805 F

Il est disponible à la même adresse

LEGENDE DE LA COUVERTURE

Composite couleur obtenu avec le dispositif DIVISET du L.M.D. par mélange des canaux visible et infrarouge d'une image prise au-dessus de l'Afrique de l'Ouest par le satellite Météosat (cliché L.M.D.).

Colour composite obtained on the DIVISET of the L.M.D. by superimposing visible and infra-red images taken over West Africa by Meteosat (photo L.M.D.).

TABLE DES MATIERES | TABLE OF CONTENTS

* Manuscript appears in the back of the book.
** See erratum in the back of the book.

Page

Page

*Manuscript appears in the back of the book.

Session III-2-3 : NUAGES CUMULIFORMES
CUMULIFORM CLOUDS

* Manuscript appears in the back of the book.

*Manuscript appears in the back of the book.

AUTHOR INDEX - INDEX DES AUTEURS

VOLUME 2

SESSION III : PROCESSUS THERMODYNAMIQUES, DYNAMIQUES, RADIATIFS ET INTERACTION AVEC LES PHENOMENES MICROPHYSIQUES. EVOLUTION DES DIFFERENTS TYPES DE NUAGES.

THERMODYNAMICAL, DYNAMICAL, RADIATIVE PROCESSES AND INTERACTION WITH MICROPHYSICAL PHENOMENA. EVOLUTION OF DIFFERENT TYPE OF CLOUDS.

SESSION IV : INTERACTIONS ENTRE ECHELLES.

SCALE INTERACTIONS.

SESSION V : INSTRUMENTATION.

INSTRUMENTATION.

<u>SESSION III</u> - PROCESSUS THERMODYNAMIQUES, DYNAMIQUES, RADIATIFS ET INTERACTION AVEC LES PHENOMENES MICROPHYSIQUES. EVOLUTION DES DIFFERENTS TYPES DE NUAGES

Thermodynamical, Dynamical, Radiative Processes and Interaction With Microphysical Phenomena. Evolution of Different Type of Clouds

III.1 - Nuages Stratiformes

Stratiform Clouds

SOME FIELD OBSERVATIONS OF RADIATION FOG AND THEIR INTERPRETATION

R. Brown

Meteorological Office, Bracknell, UK

1. Introduction

Since 1971 the UK Meteorological Office has been investigating the basic physics of radiation fog, both to understand the processes involved in its formation and dissipation and to assess the prospects for improved forecasting. Field observations have been made at Cardington, Bedford, UK (latitude 52° 06'N, longitude 0° 24'W), Roach et al (1976). In parallel with the development of the field project a numerical model of radiation fog has been constructed, Brown and Roach (1976). The first phase of the investigation, terminating in 1974 led to significant clarification of the principal constraints in the development of radiation fog. Radiative cooling was found to encourage fog formation whilst turbulence inhibited it. Gravitational settling of the fog droplets and the soil heat flux emerged as important factors. However the initial study was deficient in several respects. Measurements were made mainly from 16 m masts so that only the initial phase of fog development was comprehensively observed. Little microphysical data was gathered. The model simulated turbulent mixing using an exchange coefficient regime which was constant in time and so did not respond to the change in atmospheric stability brought about by a deep fog. A second phase of the project, designed to rectify these deficiencies, commenced in 1976. Some preliminary results from phase II are presented in this paper.

2. Instrumentation

Phase II involved a change from mast-based to tethered balloon-borne observations, partly to monitor the behaviour of the fog top and partly to realise the potential of greatly extended microphysical observations made possible by the acquisition of an Axially Scattering Spectrometer Probe (ASSP), manufactured by Particle Measuring Systems Inc., Colorado. Besides the ASSP, also mounted on the balloon were a Point Visibility Meter (Plessey Ltd., UK), two CSIRO pattern net radiometers, a pressure sensor to monitor the height of the instrument package, and a Cardington turbulence probe. The latter measured temperature, wind and humidity at low frequencies and also high frequency fluctuations in wind and temperature from which the turbulent fluxes of heat and momentum could be calculated.

The surface energy balance was determined from measurements of the soil heat flux, the surface net radiation and the surface moisture deposition (from a lysimeter). The behaviour of the nocturnal inversion was monitored using a monostatic acoustic sounder.

3. Results

Five coherent case studies have been obtained during the period 1976-78. These include a clear night when fog just failed to form, the steady growth of a deep fog, the dispersal of a shallow and deep fog by solar radiation and a fog dispersed by increasing gradient wind.

a. Microphysical Data

Although the mean drop size varied from fog to fog (in the range 3-10 μ m radius), certain other features were common to most of the profiles obtained through fog so far. The mean drop radius showed no trend with height or decreased with height and the maximum drop size decreased with height. Although the drop concentration underwent larger fluctuations than the mean radius it showed no trend with height. Thus the extinction coefficient was either constant or decreased with height. These observations are in contrast to those of Pinnick et al. (1978) who found that the concentration of larger drops and the extinction coefficient increased with height. However they point out that most earlier measurements in continental fogs showed these to decrease with height, which is in agreement with the observations reported here. Our observations are biased towards fogs which formed when the geostrophic windspeed approached the maximum for radiation fog formation ($7ms^{-1}$). This could have led to enhanced mixing at the fog top, as discussed later, and therefore to some evaporation of the drops in the upper part of the fog.

b. Temperature and Radiation Profiles

Only in phase II of the project has it been possible to obtain detailed observations through deep fogs. Figure 1 shows profiles of temperature, net radiation and radiative cooling through such a fog, approximately seven hours after its local formation. The lapse rate was wet adiabatic throughout most of the depth, indicating that the atmosphere within the fog was well mixed. This is believed to be due to a weak convective regime set up by radiative cooling beneath the fog top and warming at the surface. The latter sets in when the upward flux of heat from the soil exceeds the surface net radiative loss. It is hoped that the analysis of the turbulence data will confirm the convective nature of the turbulent motions.

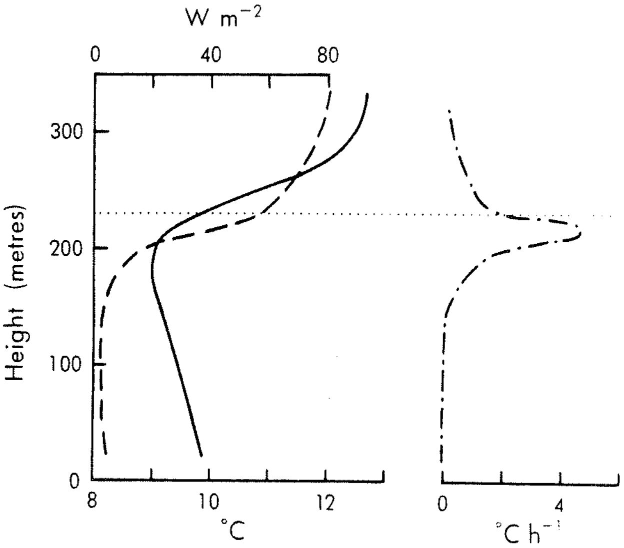

Figure 1. Profiles of temperature —— , net longwave radiation -----, and radiative cooling -.-.-. through the deep fog of 17/18 October 1977. ..... Fog top.

It can be seen from figure I that the pre-fog surface inversion had migrated to the fog top. The base of the inversion coincided with the fog top to within 20m. The acoustic sounder recieved echoes from the base of the elevated inversion and so identified the position of the fog top with a similar accuracy. The ability to detect the top of a mature fog (> 50m) has been demonstrated on several other nights. Thus acoustic sounding shows potential as an aid to forecasting fog clearance.

c. Wind Observations

A most interesting feature to emerge from the observations is that besides having a significant effect on the thermal structure of the boundary layer, a mature fog can also modify the windfield. Figure 2 shows a time-height cross-section of the windspeed on a radiation night when fog did not form. The geostrophic wind-speed was 5 - 5.5ms^{-1}. It can be seen that the maximum windshear was concentrated at the surface. Less pronounced elevated regions of shear were associated with the development of a nocturnal jet. Figure 3 shows a similar cross-section through the deep fog of 17/18 October 1977. The geostrophic windspeed on this night was 7ms^{-1}. It is evident that in this case the region of maximum windshear was not at the surface but close to the fog top and that it movedupwards with the fog top during the night. This was observed to occur in two other fogs for which detailed wind measurements were available and becomes noticeable once the fog has reached a depth of 40-50m. The weak convective regime which becomes established in a mature fog is believed

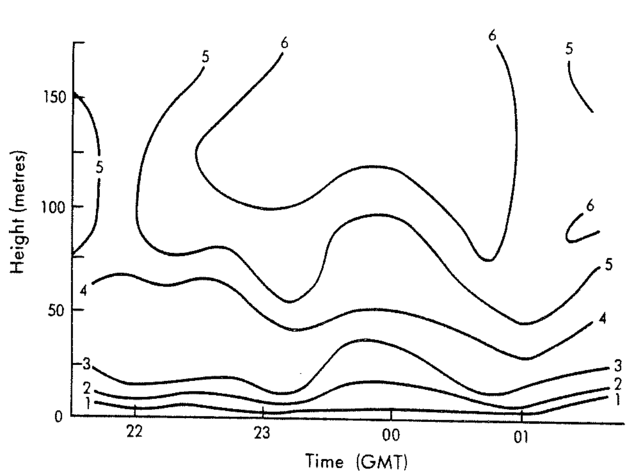

Figure 2. Cross-section of the windspeed (ms^{-1}) on a radiation night with no fog (3/4 November 1976).

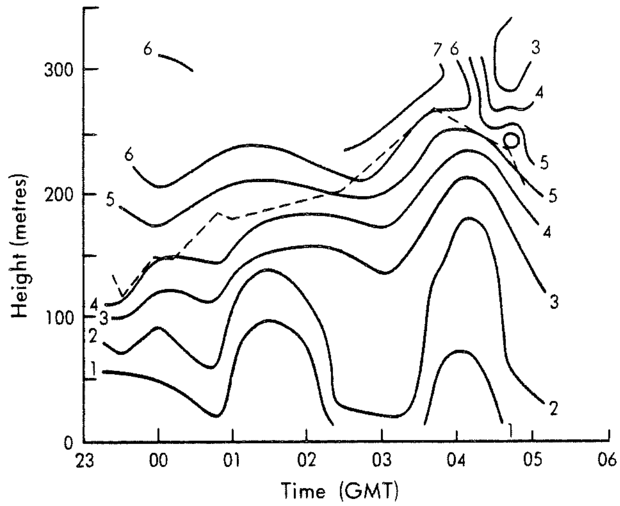

Figure 3. Cross-section of the windspeed (ms^{-1}) through the deep fog of 17/18 October 1977. --- Fog top.

to be responsible for this phenomenon. This enhances the turbulent transfer of momentum to the surface especially from higher levels where without fog the turbulence would be decaying after sunset. This leads to a momentum deficit beneath the fog top especially if the pre-fog inversion has caused the cessation of turbulent transport from levels above the fog top. Since this phenomenon does not appear to have been discussed in previous fog models, the model of Brown and Roach (1976) has been extended to include a prediction of the wind profile.

4. Numerical Fog Model

a. Description

The governing equations of the model are the 1-D continuity equations for heat, water vapour and liquid water. Longwave radiative transfer is incorporated using a simple two band scheme. When the air becomes supersaturated water is condensed and latent heat released until the air is just saturated. The radiative effects of the drops and droplet settling are parametrized in terms of liquid water content. The soil heat flux is calculated to a depth of 1m and the variation of the surface temperature with time is calculated from the surface energy balance. To this model have been added the following momentum equations:-

$$\frac{\partial u}{\partial t} = f v + \frac{\partial}{\partial z}\left(K_m \frac{\partial u}{\partial z}\right) \qquad (1)$$

$$\frac{\partial v}{\partial t} = f\left(U_g - u\right) + \frac{\partial}{\partial z}\left(K_m \frac{\partial v}{\partial z}\right) \qquad (2)$$

where u, v are orthogonal components of the wind parallel and perpendicular to the wind direction, f is the Coriolis parameter ($10^{-4}\ s^{-1}$) and Km an exchange coefficient for momentum. At the model top boundary at 900m $u = U_g$ and $v = 0$ where U_g is the geostrophic windspeed which is assumed to be constant with height. Below 2m a logarithmic velocity profile is assumed.

The exchange coefficients, held constant in the original model, have been made functions of the local gradient Richardson number (Ri) using the level 2 formulation of Mellor and Yamada (1974). This was found by them to agree closely with the second order closure model from which it was derived, when used to simulate the diurnal variation of the atmospheric boundary layer. The formulation predicts a critical Ri of 0.22 at which turbulence ceases. The model exchange coefficients are then set to values appropriate to molecular diffusion. The level 2 formulation requires the mixing length ℓ to be specified. This has been taken to be of the form:-

$$\frac{1}{\ell} = \frac{1}{kz} + \frac{1}{\ell_0} + \left[\frac{1}{k(z_\ell - z)},\ z > \frac{z_\ell}{2}\right] \qquad (3)$$

where ℓ_0 is an outer scale of turbulence set equal to the depth of the turbulent layer Z_f. The term in parentheses allows for the reduction in scale of mixing caused by the capping inversion.

The initial conditions simulated a convective boundary layer. The

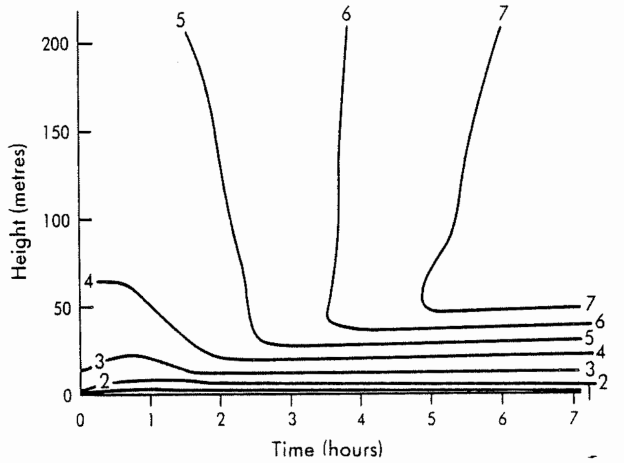

Figure 4. Cross-section of the model predicted windspeed (ms^{-1}) on a radiation night with no fog.

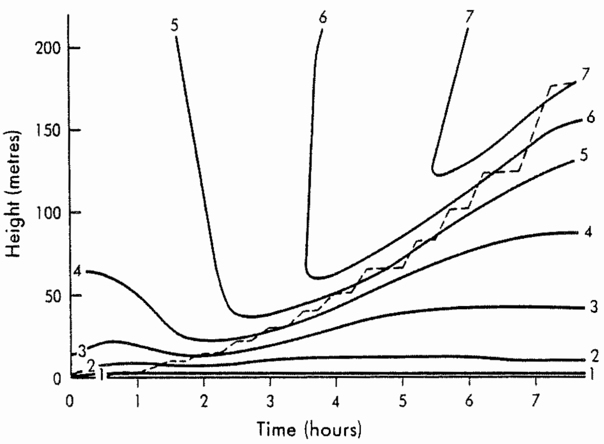

Figure 5. Cross-section of the model predicted windspeed (ms^{-1}) through a developing fog. --- Fog top.

temperature lapse rate was adiabatic from the surface to 300m and 0.09 °C m^{-1} from 300 to 900m. The initial wind profile was based upon the mean shape of the wind profile during convective conditions taken from ten years of routine boundary layer ascents.

b. Results

Figure 4 shows a time-height cross-section of the windspeed from the model ($U_g = 6ms^{-1}$) when fog formation was suppressed by the use of a low initial relative humidity (75%). Since solar radiation is omitted surface cooling sets in immediately due to a net radiative loss at the surface of $70wm^{-2}$. The atmosphere is initially turbulent ($R_i < 0.22$) to a depth of 300m but after an hour the turbulent boundary layer has collapsed to a depth of 10m. The cessation of turbulent transfer at higher levels causes the wind to undergo an inertial oscil-lation which leads to the development of a nocturnal jet with supergeostrophic windspeeds appearing after 4 hours integration. This leads to the deepening of the turbulent region to 30m after 7 hours integration. During the whole course of the integration the maximum windshear is concentrated at the surface.

Figure 5 shows the development of the windfield when fog is allowed to form by increasing the initial relative humidity to 95%. The stepped structure of the fog top (broken line) is an artifact of the grid point representation. It can be seen that a region of maximum shear is associated with the fog top as it grows upwards. This is noticeable from $3\frac{1}{2}$ hours when the fog is 40m deep. At this time the surface inversion has migrated towards the fog top and turbulence extends from the surface to just beneath the fog top. The model produces greater shear near the surface than is evident in figure 3 which could indicate that the exchange coefficient formulation underestimates the convective mixing within a fog.

5. Discussion

Both observations and model indicate that the development of radiation fog, besides altering the boundary layer temperature structure, also modifies the windfield. The important question which remains to be answered is whether the concentration of windshear at the fog top can enhance turbulent mixing across the interface. Experiments with a version of the model containing explicit microphysics have suggested that only mixing which extends through the fog top can reduce the mean drop size. Using the formulation of Mellor and Yamada there is no such mixing because the capping inversion increases R_i above 0.22despite the enhanced windshear. This critical value of R_i is implicit in the formulation and some features of the model suggest that it is too low e.g. small depth of the stable boundary layer. It is hoped that the turbulence probe data will indicate whether turbulence extends through the fog top and perhaps allow alternative estimates to be made of the relationship between turbulence and dynamic/thermodynamic structure.

REFERENCES

Brown,R. & Roach,W.T. 1976, The physics of radiation fog: II - a numerical study. Quart.J.R.Met.Soc.,102,No 432,pp 335-354.

Mellor,G.L. & Yamada,T. 1974, A hierarchy of turbulence closure models for planetary boundary layers. J.Atmos.Sci,31, No 10 pp 1791-1806.

Pinnick,R.G.,Hoihjelle,D.L.,Fernandez,G., Stenmark,E.B.,Lindberg,J.D. & Hoidale,G.B.,1978, Vertical structure in atmospheric fog and haze and its effects on visible and infrared extinction, J.Atmos.Sci., 35, No 10, pp 2020-2032.

Roach,W.T.,Brown,R.,Caughey,S.J.,Garland,J.A. & Readings,C.J., 1976, The physics of radiation fog: I - a field study, Quart. J.R.Met.Soc., 102, No 432, pp 313-333.

A MICROPHYSICAL MODEL OF RADIATION FOG

R Brown

Meteorological Office, Bracknell, UK

1. Introduction

Brown and Roach (1976) - hereafter referred to as I have described a model of radiation fog which gave results broadly in agreement with data obtained from a field study. Since the publication of I detailed information on the behaviour of the drop size distribution in fog has been obtained. However the original model does not contain an explicit description of the microphysics, necessitating parametrization of the radiative effects and gravitational settling of the fog droplets in terms of liquid water content. In fact these properties and the visibility are functions of the drop size distribution which in turn depends on such factors as the initial spectrum of the cloud condensation nuclei. It seemed desirable therefore to extend the model to include an explicit description of the microphysics. This paper describes the extended model and the initial results obtained from its use.

2. Theory

a. The governing equations of the model

The basic equations are essentially the 1-D continuity equations for heat and water vapour, as used in I, with additional equations for the time rate of change of supersaturation (σ), drop radius (r) and concentration. They are described fully in Brown (1980). The drop growth equation is of the form -

$$\frac{dr}{dt} = \left[\frac{\sigma}{r} - \frac{a_1}{r^2} + \frac{a_2 m}{r^4} - a_3 R\right]\left[A_1 + \beta_\beta A_2\right]^{-1} \quad (1)$$

where m is the nucleus mass and a_1, a_2, a_3, A1, A2 are temperature dependent coefficients. Besides the usual supersaturation, curvature and solute terms equation (1) contains an additional term due to Roach (1976) to allow for the net radiative loss (R) from the droplet. The factor β_β corrects for temperature and vapour density discontinuities within one molecular mean free path of the droplet surface, following Fukuta and Walter (1970). It is a function of the condensation coefficient (β) which is normally set equal to 0.033.

Within the model a cloud condensation nucleus (CCN) is so designated if it has an equilibrium radius > 0.3 μm at the ambient supersaturation. Nuclei are transported by turbulent diffusion but not by gravitational settling. They play no part in the model thermodynamic or radiative processes but merely act as a source of drops. Every time step those nuclei with an equilibrium radius > 0.3 μm are reclassified as drops. They then grow by condensation, release latent heat, settle under gravity and are subject to turbulent diffusion.

b. Solution of the droplet growth equation

It is not practical to integrate equation (1) directly because each drop eventually has a unique supersaturation history. To overcome this problem a bin technique is introduced based on the assumption that over a time step τ a fraction ΔN_i of the drops in bin i grow into bin i + 1, where ΔN_i is given by

$$\Delta N_i = \frac{N_i}{\Delta r_i}\left|\frac{dr_i}{dt}\right|\tau \qquad (2)$$

Δr_i is the bin width. The radius range 0.3 - 20 μm is covered by 55 bins. A disadvantage of the bin technique, when applied to equation (1), is that it is subject to numerical spreading because for an activated drop the solution is positive for all larger radii. The spreading has been reduced to an acceptable level by various techniques described by Brown (1980). The bin technique can then predict drop radius with an accuracy of 3% but numerical spreading limits the minimum dispersion (standard deviation/mean radius) of the predicted drop size distribution to 5%. The full model equation set produces dispersions of typically 40% which tests show are not numerically induced.

c. Model radiation scheme

The formulation of the equation for the radiative heating rate and the evaluation of the transmissivity of water vapour and carbon dioxide are described in I. In the original model by assuming that the droplet absorption efficiency factor for longwave radiation (Qa) was a linear function of r, it was possible to express the droplet transmissivity in terms of liquid water path. In the microphysical model it is possible to take some account of the radiative effect of the swelling nuclei before saturation is reached and also to use a more accurate expression for Qa. The droplet spectrum used in the radiative transfer equation is predicted by the model so that there is direct coupling between the microphysics and radiation. Droplet scattering has been omitted since it has a small (~ 10%) effect on the cooling rate.

d. Boundary and initial conditions

The model equations are solved from -1m to 200 m using 26 grid points. At 200 m the temperature, humidity mixing ratio, and drop and nucleus concentration are held constant. The variation of the surface temperature is calculated from the surface energy balance including the soil heat flux. The flux of nuclei and the drop concentration are taken to be zero at the surface. For all integrations the initial temperature is 5°C and the relative humidity 95%. The exchange coefficients are constant in time with $K_{max} = 10^{-2}\ m^2\ s^{-1}$ at 50 m.

3. Results

The model spectra are presented with droplets in the range 0 - 2 μm omitted. Their concentration varies from 10^3 to 10^4 cm^{-3} depending upon the spectrum of nuclei. They are also omitted from discussion of the predicted drop concentration and mean radii since most observational techniques do not detect them They are included in the calculation of the visibility.

A Junge type CCN distribution is assumed but with a plateau below 10^{-14}g. The basic spectrum (labelled B in figures 1 - 3) covered the mass range 6 x 10^{-13} to 3 x 10^{-15}g with 8 nucleus classes. The total concentration is 2323 cm^{-3} (40 μgm^{-3}). The nuclei are taken to be ammonium sulphate.

a. Basic features of the model fog

As described in I radiative cooling of the air to the colder ground produces saturation of the air below 2m after 1¼ hours. Figure 1 shows that the visibility has fallen to 1km after 1 hour, due to the growth of the nuclei. The supersaturation of the air causes several nucleus classes to be activated and the initial rapid growth of the droplets (due to their small radius) produces a sharp reduction in visibility to 200m, at a height of 2m, by 1¼ hours. As time proceeds the visibility declines more slowly because of reduction in the droplet growth rate with increasing radius and reduced supersaturation and radiative loss. Similar features are observed at higher levels but with a time delay.

Figure 2 (top) shows the droplet spectrum at 4 hours when the fog is 80m deep. The initial model drop concentrations of ~ 140cm^{-3} fall to 70cm^{-3} at 4 hours because of surface deposition. The mean drop size and dispersion show little variation with height except just beneath the fog top where the drops have been recently activated.

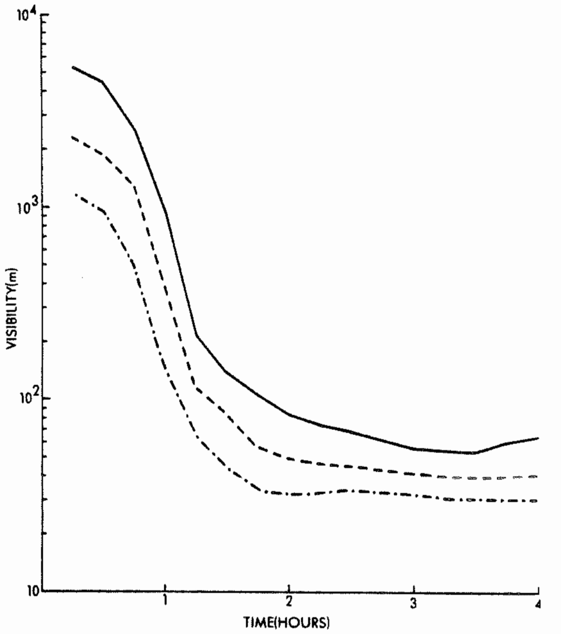

Figure 1. Visibility at 2m as a function of time from the start of the integration. Each curve represents a different nucleus concentration ——— spectrum B - - - spectrum D.-.-. spectrum E

The fog drop size distribution, visibility and liquid water content are found to be insensitive to variations in the width of the nucleus spectrum when the maximum nucleus mass is varied between 3 x 10^{-12} to 3 x 10^{-14}g. A high concentration of large nuclei (70cm^{-3} > 10^{-12}g) slows down the development of a dense fog but has little effect on the drop size distribution. This result encourages the hope that it may be possible to correlate the observed droplet spectra with parameters such as the turbulent mixing. This would be difficult if the size distribution of activated drops were sensitive to the spectrum of the larger nuclei since most CCN counters are inaccurate below 0.2% supersaturation.

b. Influence of the nucleus concentration

A series of integrations have been performed using a nucleus spectrum of constant shape but varying total concentration. Nucleus spectrum (B) has been described previously whilst those labelled (D) and (E) have concentrations 2½ and 5 times (B) respectively. As the nucleus concentration is increased the peak supersaturation is lowered, from 0.05% to 0.03% at 2m, and the visibility is reduced, Figure 1. It is found that the minimum visibility is proportional to $Nc^{-\frac{1}{3}}$ where Nc is the concentration of nuclei. The reduction in visibility is partly brought about by a reduction in mean drop size and partly by an increase in liquid water content (50% on average with nucleus spectrum E). As anticipated from published work on cumulus microphysics, increasing the nucleus concentration produces a drop size distribution with a smaller mean radius and higher drop concentration, Figure 2.

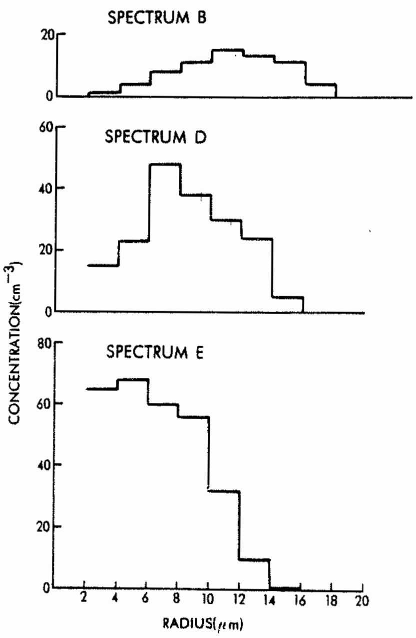

Figure 2. Drop size distribution at 2m after 4 hours integration as a function of nucleus concentration.

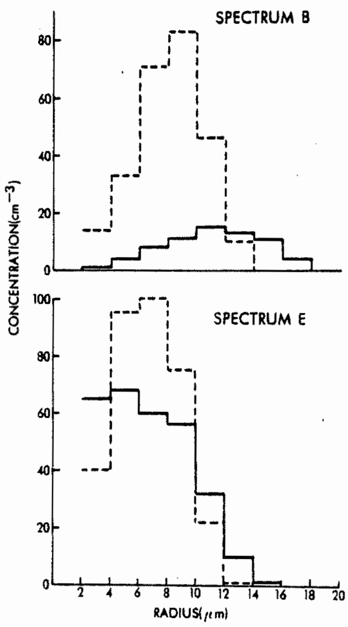

Figure 3. Drop size distribution at 2m after 4 hours integration —— with radiative term, - - - without radiative term in eq (1).

At the initial relative humidity of 95% radiative cooling by the unactivated droplets is neglible. When the relative humidity approaches 100% the droplet radiative cooling with nucleus spectrum E becomes comparable to the gaseous radiative cooling. Despite this the time of supersaturation of the air is delayed by 15 minutes compared to nucleus spectrum B. This indicates that the enhanced radiative cooling due to the high nucleus concentration is more than offset by additional removal of water vapour by the swelling nuclei. With spectrum E the maximum radiative cooling in the fog is doubled to $6^{\circ}Ch^{-1}$ compared to nucleus spectrum B. This doubles the liquid water content in the shallow fog but only increases it by 20% when the fog becomes optically thick.

c. The importance of net radiative loss from the drops

Roach (1976) has discussed the effect of longwave radiative exchange on the growth of fog drops. The microphysical model has been used to perform a more realistic examination of the importance of this effect than was possible by Roach. Two integrations have been performed with the radiative term removed from equation (1). The radiative cooling of the air by the drops is still included.

With nucleus spectrum B removal of the radiative term causes the mean drop radius to decrease by 30% and there is a similar increase in liquid water content. Figure (3) shows the effect on the drop spectrum. The drop concentration increases from $70cm^{-3}$ with radiative loss compared to $250cm^{-3}$ with no radiative loss. The extra drops are generated by the activation of additional nuclei caused by an increase in the maximum supersaturation with no radiative loss. Radiative exchange lowers the maximum supersaturation attained by lowering the critical supersaturation of the larger nuclei.

The radiative terms has little influence with a high nucleus concentration as can be seem from the lower drop spectra in Figure 3. This is because the drops only experience a radiative loss over a small distance beneath the fog top due to the high opacity of the fog.

d. Variation of the condensation coefficient

There is still some controversy over the value of β for pure water with estimates ranging from 0.022 to 1. When β is increased from 0.033 to 1 using nucleus spectrum B the maximum supersaturation is reduced from 0.057% to 0.037%, halving the concentration of nuclei activated. The minimum visibility is increased by 35% and the maximum liquid water content reduced by 22%. The mean drop radius at 4 hours is increased by 15%, Figure (4). This is surprisingly small compared to the increase in growth rate brought about by the increase in β. It may be accounted for by the increased supersaturation obtained with the lower value and by the decreasing influence of β as the drops grow larger.

Coating nuclei with long chain fatty acids or alcohols can considerably reduce their growth rate. This has been simulated in the model by reducing β to 3.3×10^{-3}, a conservative reduction compared to the minimum value reported experimentally of 3×10^{-5}. The

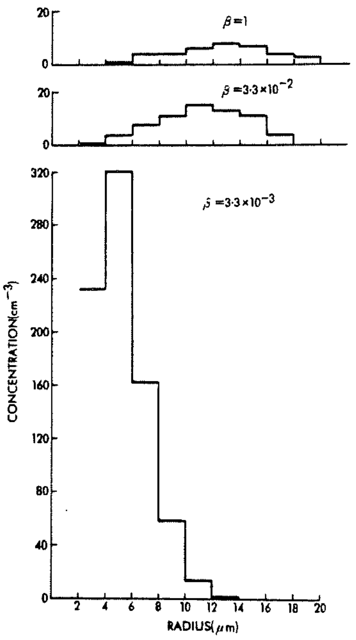

Figure 4. Drop size distribution at 2m after 4 hours integration as a function of β.

slower growth of the drops initially causes an increase in the maximum supersaturation which results in a much higher concentration of activated drops ($\sim$ 1000 cm^{-3}). Competition for available water then reduces the mean drop size at 4 hours by 50% compared to the case β = 3.3 x 10^{-2}, Figure 4. The minimum visibility is reduced by 65% to 19m, and the maximum liquid water content increased by 45%. These results indicate that the use of a surfactant to inhibit fog formation could instead lead to the formation of a dense fog.

4. Discussion

The microphysical model has shown the drop size distribution in radiation fog to be insensitive to the width of the nucleus spectrum but to depend on the concentration of nuclei and the value of β. When matching observed and model spectra it is difficult to obtain agreement of both the total concentration and mean radius. The latter can be matched by reducing β or increasing the nucleus concentration but then the drop concentrations are higher than those observed.

One explanation is that the exchange coefficients used here are only representative of the pre-fog stable conditions. Within a deep fog a weak convective regime is established, enhancing turbulent mixing. Preliminary experiments have indicated that enhanced mixing can reduce the mean drop size but only if it extends through the fog top so that fresh nuclei are mixed in from above.

References

Brown, R, 1980, A numerical model of radiation fog with an explicit formulation of the microphysics, Quart J R Met Soc., to be published.

Brown, R and Roach, W T, 1976, The physics of radiation fog: II - a numerical study, Quart. J.R.Met Soc., 102, No 432, pp 335 - 354.

Fukuta, N and Walter, L A 1970, Kinetics of hydrometeorgrowth from a vapour spherical model, J Atmos Sci, 27, No 8, pp 1160 - 1172.

Roach, W T 1976, On the effect of radiative exchange on the growth by condensation of a cloud or fog droplet, Quart J R Met Soc, 102, No 432, pp 361 - 372.

"SIMULTANEOUS MEASUREMENTS OF THE TURBULENT AND MICROPHYSICAL STRUCTURE OF NOCTURNAL STRATOCUMULUS CLOUDS"

S.J.Caughey, M.Kitchen and A.Slingo

Meteorological Office, Bracknell, Berks., UK

1. Introduction

The study of stratocumulus cloud is important in many respects. Firstly, it is a natural extension of the many investigations of the structure of cloud free atmospheric boundary layers. These studies have provided frameworks within which the statistics of boundary layer turbulence may be nondimensionalized and parametrised in terms of more readily measured quantities. Such schemes are not yet available for cloudy boundary layers and it would seem that the stratocumulus capped boundary layer would be a useful case for initial study. Stratocumulus may also turn out to be an important simplifying case in which to investigate the effect of entrainment of warm dry air on the cloud droplet spectrum and liquid water content, in seeking some justification for the inhomogeneous mixing model proposed by Latham and Reed (1977). The upper boundary of stratocumulus almost invariably marks an abrupt change to very much drier and warmer air aloft and hence one might expect the local microphysical consequences of entrainment to be particularly well marked.

This paper describes the results from two field studies of nocturnal stratocumulus carried out at RAF Cardington, Bedfordshire, on the 19/20 November 1976 and 26/27 October 1977. Observations of the cloud droplet population and the characteristics of turbulence in the cloud and inversion layers are discussed in some detail.

2. Instrumentation and experimental details

Measurements of the high frequency fluctuations of the longitudinal (u), lateral (v) and vertical (w) components of air motion and of temperature (T) were made using a turbulence probe attached to the tethering cable of a large (1300m^3) balloon (see Readings and Butler 1972). Signals were relayed to the ground by radio and sampled at 20 Hz prior to computer processing. Information on the cloud droplet field was obtained with a PMS ASSP-100 droplet spectrometer (10s data samples) whilst 2 net radiometers spaced by about 5m provided measurements of the net radiative flux profile through the boundary layer.

Two surface-based remote sensors were in operation, a microwave radiometer was used to provide estimates of the total liquid water path above the instrument (Slingo et al, 1980) and an acoustic sounder was used to monitor the general stability of the boundary layer (Caughey et al, 1980). Full details of the instrumentation can be found in the paper by Roach et al, (1980).

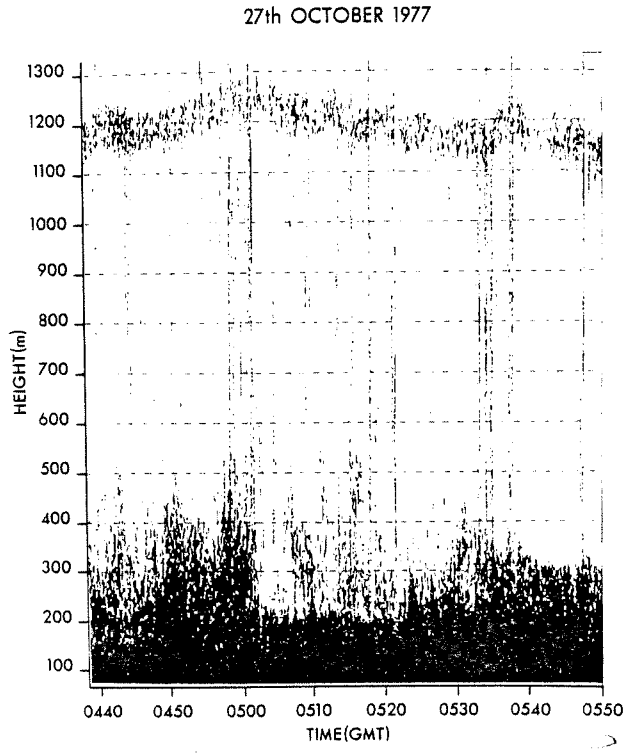

Figure 1. Acoustic sounder record taken during Case Study (2). The dark areas represent regions of strong echo and hence significant temperature fluctuations on a scale of one-half the acoustic wavelength.

The experimental strategy consisted of slowly raising and lowering the balloon-borne instruments through the sub-cloud, cloud and cloud top regions, with occasional periods at fixed heights to permit estimates of turbulent fluxes to be made.

3. General characteristics of the case studies

The essential difference between Case Study (1) (19/20 November 1976) and Case Study (2) (26/27 October 1977) is that during the former conditions were quasi steady-state whereas in the latter the cloud layer progressively lifted and thinned. This resulted from a less settled synoptic situation in which the mean wind speed in the cloud layer increased from 6 to 11 ms^{-1} during the observation period. Nevertheless the temperature and humidity profiles from both studies exhibited very similar features i.e. a near surface stable boundary layer (SBL) several hundred metres deep overlain by a deep adiabatic region which extended through the cloud to a sharp inversion layer immediately above cloud top. In both studies the cloud depth was substantially less than the overall boundary layer depth (taken as the height of the sharp capping inversion), being 400 m and 1100 m for Case Study (1) and 200 m and 1100 m for Case Study (2) respectively.

A section of the acoustic sounder record taken during Case Study (2) is given in Figure (1). The intense near surface echoes are from the SBL and indicate a layer of very variable depth occasionally extending up to $\sim$ 400 m. Above this the extensive echo free region reflects the presence of the deep adiabatic layer. Between 1100-1300 m an intense oscillatory layer echo is apparent and this is identified with the sharp capping inversion at cloud top . Since this is the region actively involved in entrainment we refer to it as the entrainment interfacial layer (EIL). It is important to note that there is no evidence in the acoustic records for entrained regions extending well down into the boundary layer which suggests a relatively small scale for the entrainment process. Examination of the turbulence probe observations suggest that the entrainment mechanism involved sporadic Kelvin-Helmholtz breakdown of the EIL and the entrainment scale was in the range 10-50 m .

4. Observations near cloud top

From transits with the instrument package through the cloud top and inversion detailed information on the temperature, wind velocity and liquid water content (LWC) variations were obtained. Figure (2) shows an example from Case Study (2) of a descent from the subsidence inversion layer (SIL) through the EIL into the cloud radiation layer (CRL i.e. the upper 5mb of cloud in which the bulk of the net radiative flux divergence occurs). The notable features here are the sharp and very large temperature step through the EIL and significant vertical velocity excursions (up to 1 ms^{-1}) in the cloud layer. Turbulence levels decrease rapidly towards the base of the EIL and fall to low levels in the SIL ($\sim$ 0.01 $m^2\ s^{-2}$). The LWC data suggest that on this occasion the cloud top extends up to the base of the EIL. Furthermore it would seem that, within the limit of measurement, the LWC rises immediately to the full in-cloud value. In contrast other transits showed deeper EIL's with irregular temperature steps and small regions in the CRL with temperature excesses over their surroundings of 1-2K. Similar features were observed in other transits from Case Study (1) and are identified with entrainment of warm air from the EIL/SIL into the cloud layer. The along-wind scale of the entrained volumes fell in the range 10-50 m. Some support for this interpretation comes from the change in character of the LWC profile into cloud on this occasion. With active entrainment this exhibits a much more gradual increase with distance into cloud, which is suggestive of evaporative loss.

Much attention has recently been paid to the inhomogeneous mixing model proposed by Latham and Reed (1977). In this the effect of entrained air on the cloud droplet field depends on the ratio τ_T/τ_r , where τ_T is a time scale for the diffusion of entrained air into the cloud and τ_r is that for the evaporation of a droplet of radius r . If $\tau_T/\tau_r \gg 1$ then the mixing process would be expected to proceed

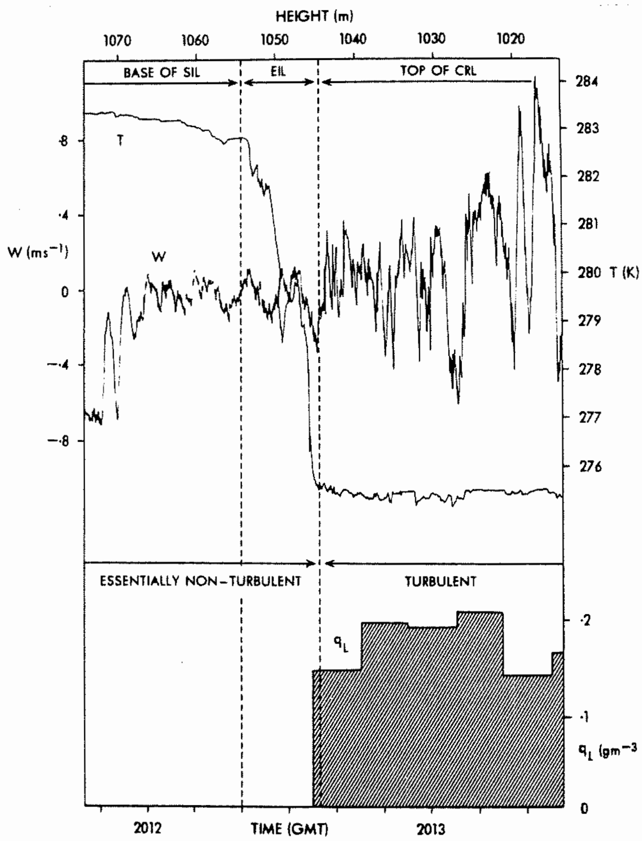

Figure 2. Time histories of the vertical velocity (W) temperature (T) and liquid water content (q_L) from a descent into the cloud top when the entrainment interfacial layer (EIL) was thin and relatively non-turbulent.

inhomogeneously whereas if the reverse were true homogeneous mixing would result. The time scale $\tau_T \sim (L^2/\varepsilon)^{1/3}$ (where L is the characteristic scale of entrainment features and ε is the rate of dissipation of turbulent kinetic energy in the cloudy air) may be estimated from the observations. Taking L $\sim$10 m and $\varepsilon \sim 10^{-3} m^2 s^{-3}$ (see Figure (5)) near cloud top we obtain $\tau_T \sim$ 50s. An estimate of the time scale for droplet evaporation may be made from the evaporation equation, ignoring the solute term i.e.

$$\frac{dr}{dt} = \frac{0.98\left(S_o - \frac{0.11}{r}\right)}{(r+\alpha)}$$

where

- S_o is the undersaturation of the entrained air
- r is the droplet radius
- α is the length associated with the condensation coefficient (taken as $\sim 5\,\mu m$)

This equation indicates that a 5 μm radius droplet will evaporate in $\sim$1s for a 20% undersaturation. In fact the air above the EIL was very dry indeed (RH$\sim$10%) so we may expect that this estimate is an upper limit to τ_r and hence the mixing should appear essentially inhomogeneous. Some support for this interpretation comes from an examination of the mean droplet spectrum in regions of high and low LWC. Figure (3) gives the spectra from regions in which the LWC was $<$ than 0.18 and $>$ than 0.27 gm^{-3} respectively. Clearly only minor changes in spectral shape have occured although the changes in droplet concentration are large. Mean profiles from all ascents/descents through cloud top show large reductions in droplet population as cloud top is approached but the maintenance

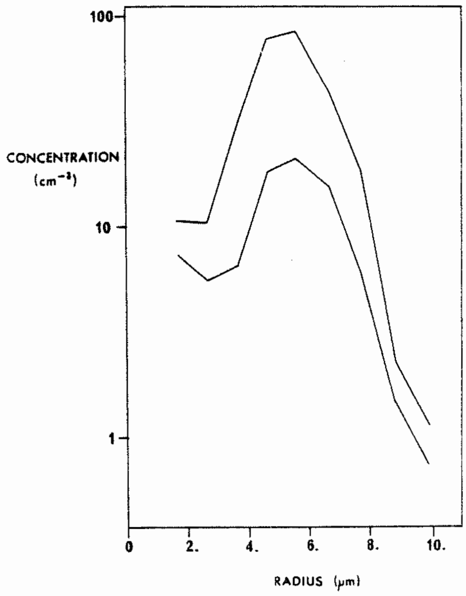

Figure 3. Average droplet spectra from the high ($>.27$ gm m^{-3}) and low ($<.18$ gm m^{-3}) regions on all traverses through the cloud top. The small change in spectral shape, although the droplet concentration is much less, suggests that the mixing is essentially inhomogeneous.

of a constant mean radius, as expected with an essentially inhomogeneous mixing process.

5. Convection with cloud

The turbulence probe data show a well defined convective field within cloud. An example of the fluctuation record for part of a run near cloud base ($z'/d \sim 0.3$, where z' is the height above cloud base and d is cloud depth) during Case Study (2) is given in Figure (4). The structure observed is essentially the same as that observed during Case Study (1) and indicates cooler regions associated with downdraughts. These 'plumes' appear to be responsible for most of the heat transfer and reflect the movement of radiatively cooled air away from the CRL.

Heat flux cospectra from level runs during Case Study (2) confirm the small negative heat flux in the near surface SBL ($\sim$ - 5Wm^{-2}) and the large positive fluxes generated in the cloud (30-40 Wm^{-2}) by radiative cooling. Above the EIL the heat flux is essentially zero. The well defined cospectra (-4/3 slopes at high frequency) are noteworthy and relate well to other heat flux cospectra from lower levels in the clear convective boundary layer (Caughey and Kaimal, 1977).

The behaviour of the characteristic wavelength for vertical velocity fluctuations, $(\lambda m)W$, and the dissipation rate of turbulence kinetic energy (ε) in the cloud layer are of some interest. These were deduced from vertical velocity power spectra using the relations

$$(\lambda_m)_W = \bar{u} / (n_m)_W$$

$$\varepsilon = 11.5 \left[n S_W(n) \right]^{3/2} (n/\bar{u})$$

where u is the mean wind speed, $(n_m)w$ is the frequency at which the power spectral maximum occurs and $S_w(n)$ is the power spectral density. The data for Case Studies (1) and (2) are shown in Figure (5). A sustained and nearly linear decrease in $(\lambda_m)_w$ from about 800 m near cloud base to $\sim$150-200 m is apparent and is related to the organisation and scale of convective elements. The dissipation rate data are rather more scattered and indicate values of roughly $10^{-3}m^2s^{-3}$ through the bulk of the cloud with a significant reduction near cloud top. The dashed line in Figure (5) indicates the dissipation rate expected if turbulence is generated through the buoyancy flux alone (see Caughey et al, 1980), i.e.

$$\varepsilon \sim g/\theta_v \, \overline{w'\theta_v'}$$

and the general agreement obtained suggests that the observed turbulence may be attributed to radiative cooling in the CRL since this is responsible for the buoyancy flux.

Concluding remarks

Single level turbulence probe studies of nocturnal stratocumulus indicate a very sharp and intermittently turbulent entrainment interfacial layer, with entrainment scales in the range 10-50 m. During entrainment episodes (identified with Kelvin-Helmholtz breakdown) the EIL thickens substantially and becomes fully turbulent. Within the cloud layer convective motions are clearly identifiable and these increase in scale away from cloud top. It is

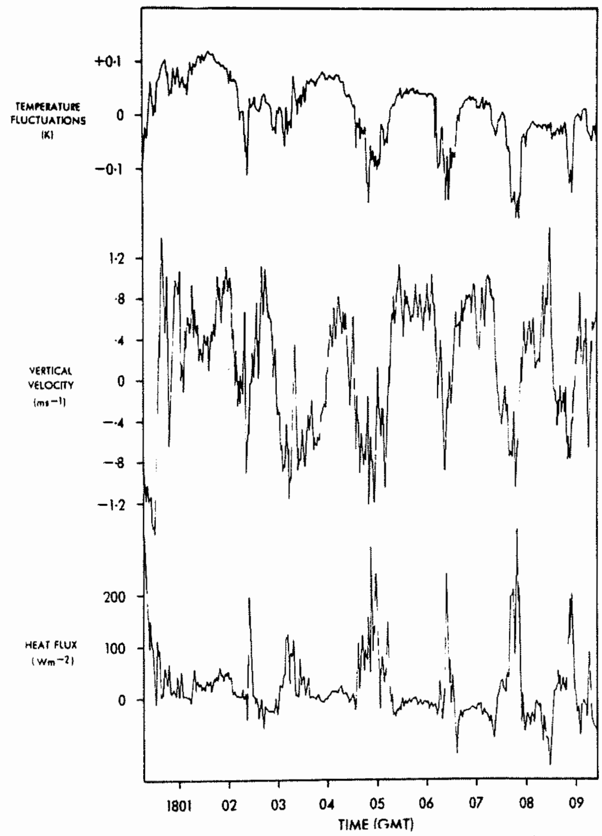

Figure 4. Time histories of vertical velocity, temperature and heat flux taken near cloud base ($z'/d \sim .3$)

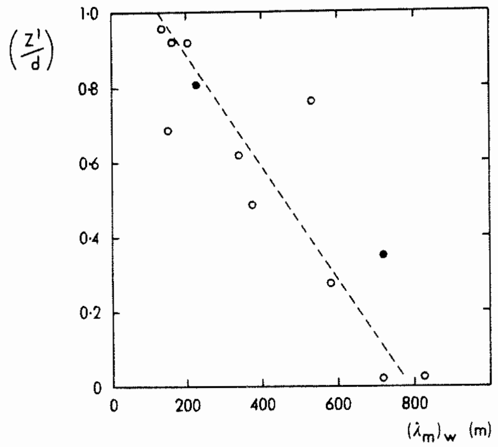

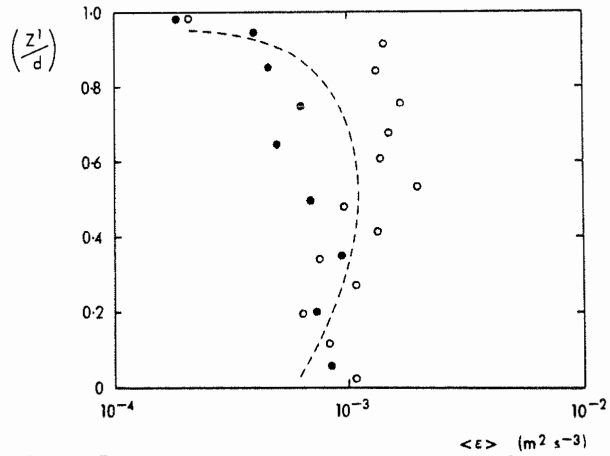

Figure 5. Distributions of the peak wavelength of the vertical velocity spectrum, $(\lambda_m)_w$, and the dissipation rate, ε, from Case Study 1 (o) and Case Study (2)(•). The dashed line in the lower figure corresponds to the ε profile deduced from the implied behaviour of the buoyancy flux (see Caughey et al, 1980).

considered that the turbulence field is driven by buoyancy fluctuations created by the large radiative cooling near cloud top. The observations suggest that the mixing should proceed essentially inhomogeneously and this is confirmed by the characteristics of the droplet field.

References

Caughey S.J., Crease B.A. and Roach W.T., 1980 "A Field Study of Nocturnal Stratocumulus: II Turbulence Structure and entrainment." Submitted for publication to Q.J.Roy Met Soc.

Caughey S.J., and Kaimal J.C., 1977. "Vertical heat flux in the convective boundary layer" Q.J.Roy.Met.Soc., 103, pp 811-815.

Crease B.A., Caughey S.J. and Tribble D.T., 1977 "Information on the thermal structure of the atmospheric boundary layer from acoustic sounding". Met.Mag., 106, 42-52.

Latham J., and Reed R.L., 1977. "Laboratory studies of the effects of mixing on the evolution of cloud droplet spectra" Q.J.Roy.Met.Soc., 103, 297-306.

Readings C.J. and Butler H.E, 1972. "The measurement of atmospheric turbulence from a captive balloon". Met.Mag., 101, 286-298.

Roach W.T., Brown R., Caughey S.J., Crease B.A., and Slingo A, 1980, "A Field Study of nocturnal stratocumulus I. Description and physical interpretation" Submitted for publication to Q.J.Roy.Met.Soc.

Slingo A., Brown R., and Wrench C.L., 1980, "A Field Study of Nocturnal stratocumulus III. High resolution radiative and microphysical observations". Submitted for publication to Q.J.Roy.Met.Soc.

CALCULATED OPTICAL PARAMETERS OF CLOUD

Hartmut Grassl and Madeleine Newiger

Max-Planck-Institut für Meteorologie
Hamburg, FRG

INTRODUCTION

Most clouds do not reach a magnitude allowing precipitation. Therefore these clouds mainly influence the optical characteristics of the atmosphere: They change, mainly increase, the short wave system albedo; shift the bulk absorption of solar radiation into the upper cloud layers, thus leading to enhanced solar heating rates of this part of the atmosphere; cause a greenhouse effect in the terrestrial spectral region by strong absorption of liquid water and ice within the only transparent region from 8-13 µm wavelength, thus leading to very strong cooling rates of the uppermost cloud layer. The magnitude of heating and cooling rates as well as the cloud albedo is besides the trivial dependence on vertical extent first of all a function of liquid water content (STEPHENS, 1978; GRASSL, 1978) and - especially for cloud albedo - of the droplet size. The latter dependence shows the possible influence of aerosol particle concentration changes on the optical parameters of a cloud via the dependence of cloud droplet numbers on the concentration of condensation nuclei.

This paper has three topics: 1) Comparison of reactions on an aerosol particle concentration and aerosol mass absorption coefficient change in both the solar and terrestrial part of the spectrum. Already used simple relations connecting total aerosol particle number to the optical depth of a cloud will be checked by measured size distributions from different geographical locations; 2) Determination of the influence of rain drops and aerosol particles on the absorption of solar radiation; 3) Influence of threedimensionality on flux inferred absorption of solar radiation.

INFLUENCE OF AEROSOL PARTICLES ON CLOUD MICROPHYSICS AND ON OPTICAL CLOUD PARAMETERS

In the solar spectral region from 0.3-4.0 µm wavelength estimates of the aerosol particles' influence on optical cloud parameters have already been given by TWOMEY (1978) and GRASSL (1975, 1978). A reappraisal by one of the present authors (see GRASSL, 1980) has shown that the formerly used bulk formula for the change of optical depth τ with aerosol particle number N_a within $\tau \sim N_a^{0.27}$ is only valid for rather narrow cloud drop size distributions as for instance DEIRMENDJIAN's C1, C2, C3, C6-clouds and measurements by RYAN et al. (1972) in continental and maritime cumulus clouds, however is not acceptable for size distributions measured in ground fogs (GARLAND, 1971). This may be due to the neglection of small droplets at a radius $r \leq 3$µm by many experiments.

Fig. 1 presents fractional absorption, netflux at the ground and albedo of a 500 m stratus cloud between 1000 and 1500 m height imbedded in a 45° latitude standard atmosphere for different droplet size distributions. Note the only slight changes in fractional absorption of solar radiation in contrast to the drastic changes in albedo and netflux at the ground. This clearly shows the potential for an albedo change by an aerosol particle concentration change, if one remembers the good agreement in mean radius and thus optical depth τ between C1 and a small continental cumulus as well as between C5 and a maritime stratus cloud (for details see GRASSL, 1980).

The accompanying variations in integral optical parameters for a C5 $\longrightarrow$ C1 transition (fig. 2) are caused by three different effects: Increasing droplet number and thus optical depth τ , slightly decreasing steepness of the phasefunction, possible additional absorption by continental aerosol particles. The total albedo change ΔA_w has two characteristics: a maximum positive value (10-12%) for thin clouds with $\tau_{C5} = 10$ corresponding to a vertical extent of approximately 350 m at a mean liquid water content of 0.2 gm^{-3} , and a switching to an albedo decrease at $\tau_{C5} = 40$. This crossover is strongly depending on the increase of aerosol particle absoprtion. In fig. 2 the imaginary part of the refractive index was chosen to be 0.02 for the continental cloud C1 while for C5 pure water droplets have been assumed. Adding the dashed and the dotted curve leads to the albedo change for no concurrent change in aerosol particle absorption.

The strong effects on integral parameters like albedo within the solar spectral region are not compensated by the terrestrial spectral region. Calculations of the long wave net flux (wavelength interval 4-200 µm) for the same size distributions have only shown net flux differences at the top of the atmosphere, at cloud top, and at the ground of 7.7, 9.0 and 11.0 W m^{-2} respectively for all distributions used. These values seem negligible if compared to corresponding changes within the solar part. A simple reasoning would lead to a reduction of longwave loss to space with increasing aerosol particle numbers, since an increased number of smaller droplets at fixed liquid water content increases optical depth and thus shifts the radiating layer upwards to lower temperatures. This effect is partly or totally compensated by a simultaneous decrease of the single scattering albedo, the ratio of the scattering to the extinction coefficient. Local effects however may be strong, since the cooling rates are shifted upwards as shown by fig. 3, which additionally includes heating rates due to absorption of solar radiation. Solar radiation absorption is highest in upper layers however with a maximum below the maximum cooling rates due to terrestrial radiation, the top layer of a cloud is strongly cooled even under noon conditions (as shown in fig. 3).

RAIN AND AEROSOL PARTICLES AS ABSORBERS OF SOLAR RADIATION IN A WATER CLOUD

The high 'measured' absorption of solar radiation in clouds (up to 35 or 40%), hitherto unexplained by the models of radiative transfer, lead us to the introduction of additional absorbers like aerosol particles and rain. Despite the assumption of extremely turbid conditions with strong absorbing particles and heavy rain still a discrepancy exists. Fig. 4 compares all our results to those given by STEPHENS et al. (1978) for different droplet size distributions (for details see NEWIGER and BÄHNKE, 1980). The lower own absorption values for pure water clouds are mainly due to a different atmosphere (STEPHENS et al. used a tropical atmosphere) and are slightly influenced by different water vapour absorption data.

POSSIBLE ERRORS OF THE ABSORPTION OF SOLAR RADIATION DERIVED FROM FLUX MEASUREMENTS

In a threedimensional radiative transfer model applying the δ -Eddington approximation as adopted by BÄHNKE (1979), following DAVIES (1978), one of us (M.N.) has shown, that the flux inferred absorption values can easily be explained by radiative fluxes going through the walls of a cubic cloud. A cloud with a vertical and horizontal extent of 4000 m still looses 22% to 30% of the incoming radiation through the walls, depending on the absorption by other components than the pure water droplets. The smaller the absorption within the cloud, the bigger the scattering through the walls, leading to only slight changes in flux inferred fractional absorption despite strongly different real absorption within the cloud: Measuring radiative flux below and above a 4000 m-cloud would lead to 38% (30 + 8) fractional absorption for pure water droplets and 38% (22 + 16) for a strongly absorbing aerosol component within the cloud, demonstrating the difficulty in determining fractional absorption and the impossibility to derive aerosol absorption from simple flux measurements.

A cloud with 8000 m horizontal extent and again 4000 m height would show 29 and 28% for the high and low absorption case respectively.

ESTIMATE OF GLOBAL ALBEDO CHANGE

Using results from the second section and assuming no additional absorption with an aerosol particle concentration increase, thus increasing cloud albedo for all clouds with growing aerosol particle numbers, we can as a first guess or upper limit derive changes in global albedo given a certain increase in aerosol particle density N_a . With a cloud cover N = 0.5, a global albedo of 30%, a mean albedo of 45% over cloudy areas, and using $d A_w / d\tau = 0.2/\tau$ as given by TWOMEY (1978) ΔA_w for $N_{a_2} / N_{a_1} = 2$ will be 3.38% for all thin clouds with $10 < \tau < 30$ and thus lead to $\Delta A_g = 1.7\%$ change in global albedo. Restricting changes to only 10% of the cloudy areas leaves only 0.17% change in global albedo.

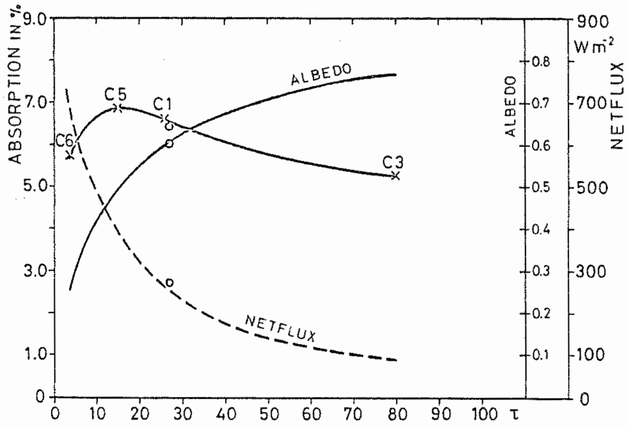

Fig. 1: Some optical parameters, integrated over the solar spectrum (0.3-3.7 μm) for an atmosphere containing a vertically inhomogeneous stratus cloud between 1000 and 1500 m height with a mean liquid water content of 0.2 gm^{-3} . The albedo of the atmosphere-cloud-ground system, fractional absorption within the cloud in percent, and net flux at the ground in W m^{-2} are shown for 4 analytical size distributions as a function of the optical depth of these distributions. The cosine of the sun's zenith angle is 0.9, surface albedo A_s = 0.2. The open circles stand for a measured stratus size distribution (see STEPHENS et al., 1978).

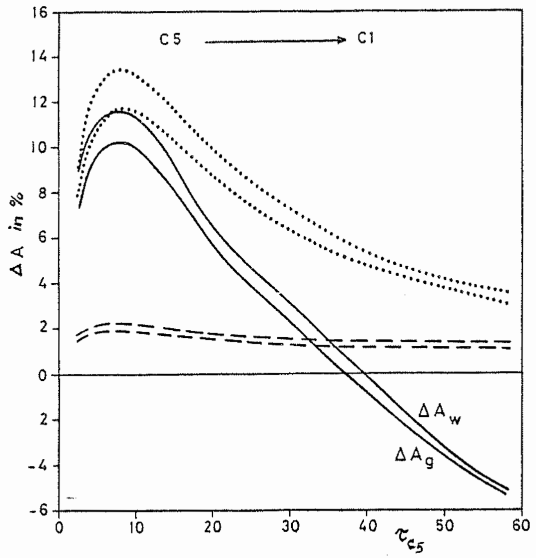

Fig. 2: Cloud albedo change ΔA_w and albedo change of the total system ΔA_g when switching from a C5 to a C1 size distribution as a function of the optical depth τ of a C5-cloud. The dashed curves stand for the contribution to ΔA_w and ΔA_g by a change of the phase funtion, the dotted curves show the effect of increased optical depth only disregarding an additional aerosol absorption.

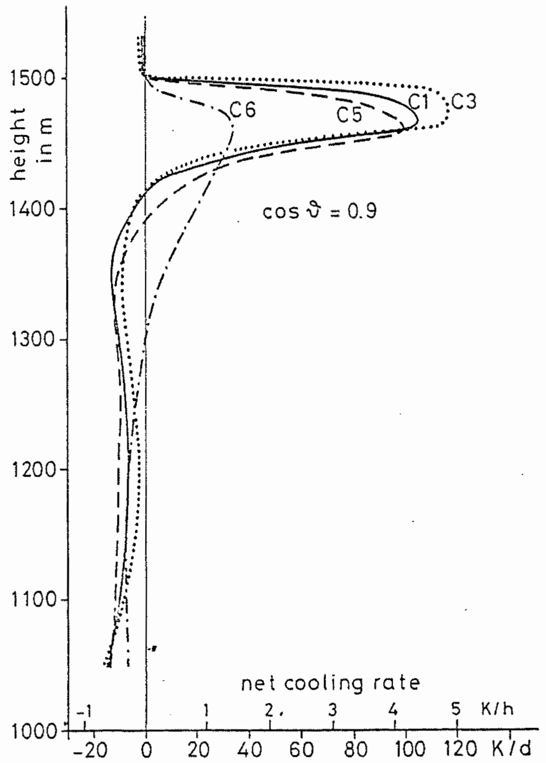

Fig. 3: Net cooling rates (solar + terrestrial radiation) in a stratus cloud for different drop size distributions and cos Θ = 0.9 with Θ sun's zenith angle.

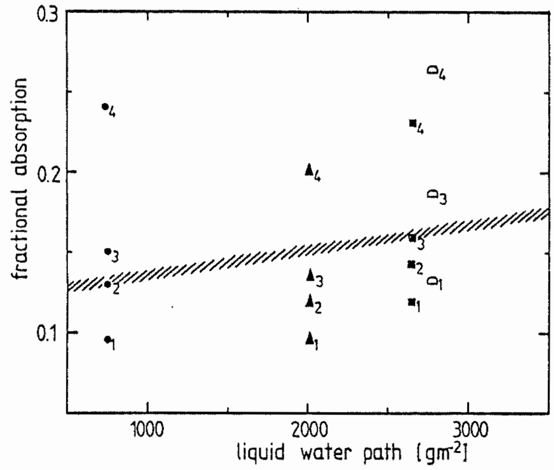

Fig. 4: Calculated fractional absorption of solar radiation as a function of liquid water path in g m^{-2} for different multicomponent clouds. ●(C1), ▲(C1 + Rain 10), ■ (Ns = C5 + C6 and Rain 10, vertically homogeneous), ▵ (Ns + Rain 10, vert. hom.). The indices stand for: (1) pure water, (2) Haze L (τ_a = 0.2) + pure water, (3) Haze L (K = 0.003 ≙ weak absorbing), and (4) Haze L (τ_a = 2.0 and K = 0.02 ≙ strong aerosol absorption). The hatched area shows STEPHENS et al. (1978) results for pure vertically inhomogeneous water clouds.

References:

BÄHNKE, K., 1979: Der Einfluß endlicher Geometrie auf die dreidimensionale Strahlungsübertragung in Wolken, thesis, University of Hamburg, 96 pages.

DAVIES, R., 1978: The effect of finite geometry on the three-dimensional transfer of solar irradiances in clouds; JAS 35, 1712-1725.

GARLAND, J.A., 1971: Some fog droplet size distributions obtained by an impaction method, QJRMS 97, 483-494.

GRASSL, H., 1975: Albedo reduction and radiative heating of clouds by absorbing aerosol particles, Contrib.Atmos.Physics 48, 199-210.

GRASSL, H., 1978: Strahlung in getrübten Atmosphären und in Wolken; Hamburger Geophysik. Einzelschriften, Reihe A, Heft 37, 136 pages.

GRASSL, H., 1979: Possible changes of planetary albedo due to aerosol particles; in Man's Impact on climate, Editors: Bach, Pankrath, Kellogg; Elsevier Amsterdam, 327 pages.

GRASSL, H., 1980: The influence of aerosol particles on optical cloud parameters; submitted to JGR.

NEWIGER, M. and BÄHNKE, K., 1980: Radiative transfer in precipitating clouds; submitted to Contrib. Atm. Phys.

RYAN, R.T.; BLAU, H.H.; VON THÜNA, P.C.; COHEN, M.L. and ROBERTS, G.D., 1972: Cloud microstructure as determined by an optical cloud particle spectrometer; JAM 11, 149-156.

STEPHENS, G.L.; PALTRIDGE, G.W. and PLATT, C.M., 1978: Radiation profiles in extended water clouds; Part III Observations; JAS 35, 2133-2141.

STEPHENS, G.L., 1978: Radiation profiles in extended water clouds, Part I and II, JAS 35, 2111-2132.

TWOMEY, S., 1978: Influence of the aerosol on optical properties of clouds; GARP Climate Dynamics Subprogramme, Report of JOC-Study Conference on Parameterization of extended cloudiness Appendix E, WMO, Geneva, October 1978.

EFFECTS OF HAZE DROPLETS IN FOGS AND CLOUDS ON THE PROPAGATION OF ELECTROMAGNETIC RADIATION

Edward E. Hindman II
Colorado State University
Fort Collins, Colorado 80523 USA
and
Richard E. Bird
Solar Energy Research Institute
Golden, Colorado 80401 USA

INTRODUCTION

Fog and cloud droplet sizes and concentrations were determined in the past using impactors (1,2). Consequently, the numbers of primarily submicron haze droplets were not measured because of the poor collection efficiency of the impactors. Recent measurements in fogs with electro-optic particle counters show the presence of high numbers of submicron haze droplets. These droplets contribute to the reduction in visibility (3). Recent measurements in stratus clouds with electro-optic particle counters also show the presence of high numbers of haze droplets (4). To our knowledge, data is lacking on the presence of haze drops in other types of clouds.

The commonly employed modified gamma droplet distributions (5) are augmented in this paper to account for the presence of haze droplets. The common and augmented distributions are used to calculate the volume extinction and backscatter coefficients of electromagnetic radiation as well as the meteorological range. It is shown that accounting for haze droplets for the fog investigated reduces the meteorological range by 27% and reduces the meteorological range by a lesser degree for the cloud investigated.

MEASUREMENTS

Measurements in fogs with electro-optic particle counters show that droplet populations contain variable concentrations of haze droplets in relation to the concentrations of fog droplets (here we define haze droplets as the unactivated droplets in the population and the fog droplets as the activated droplets). For example, Hudson (6) reports that a marine fog off the Oregon coast contained primarily fog droplets while a "post-Santa Ana" fog at San Diego, California, contained mostly haze droplets. He shows these differences relate to the concentrations of fog condensation nuclei (FCN) as determined with an isothermal haze chamber (7).

For calculations here, the droplet measurements obtained in coastal fog at Trinidad, California, (8) are used because of the high size resolution (Fig. 1). The droplet population in Fig. 1 is bimodal; a submicron mode (believed to be haze droplets) and a supermicron mode (believed to be fog droplets). To determine precisely the demarcation between the haze and fog droplets, a calculation must be performed, after that of Fitzgerald (9), utilizing FCN and cloud condensation nucleus measurements. Such a calculation is beyond the scope of this paper.

PROCEDURES

The volume extinction coefficient (β_e, m^{-1}) and volume backscatter coefficient ($\beta(\pi)$, m^{-1} $ster^{-1}$) as defined by Bird (10) were calculated for wavelengths (λ) of 0.55 and 10.5 μm using Mie light scattering theory. The droplet distribution from Trinidad, California, (Fig. 1) was differentiated to produce $\Delta n/\Delta r$ (cm^{-3} μm) versus r(μm) (Fig. 2). The portion of the distribution in Fig. 2 between 0.1 and 0.15 μm was fit by

$$n(r) = 2 \times 10^4 \qquad (1).$$

The portion of the distribution between 0.15 and 2 μm was fit satisfactorily with a Junge distribution of the form,

$$n(r) = 81.6\ r^{-2.9} \qquad (2)$$

The portion of the distribution between 2 and 10 μm was fit satisfactorily with the modified gamma distribution, after Deirmendjian,

$$n(r) = 32.36\ r^{5.75} e^{-2.3} \qquad (3)$$

The indices of refraction (m) of the droplets (assumed to be pure water) were as follows; at λ = 0.55 μm, m = 1.33 and at λ = 10.5 μm, m = 1.185-0.662i (11).

Two calculations were performed. The first employed the combined Junge and gamma distribution (Eqs. 1, 2, 3) at both wavelengths, and the second employed the gamma distribution (Eq. 3) over the size range $0.1 \leq r \leq 10$ μm. The meteorological range (V,m) was calculated using Koschmieder's expression $V = 3.912/\beta_e$. The results of the two calculations are given in the table.

Calculated Extinction (β_e) and Backscattering ($\beta(\pi)$) Coefficients and Meteorological Range (V) Using Trinidad Fog Droplet Data.

λ (μm)	β_e (m^{-1})		V (m)		$\beta(\pi)$ ($m^{-1}ster^{-1}$)	
	Calc. 1	Calc. 2	Calc. 1	Calc. 2	Calc. 1	Calc. 2
0.55	4.9×10^{-3}	3.6×10^{-3}	799	1087	2.4×10^{-4}	1.9×10^{-4}
10.5	1.2×10^{-3}	1.1×10^{-3}	-	-	2.7×10^{-6}	2.6×10^{-6}

RESULTS

Comparing the results in the table for the case with the submicron haze droplets included (Calculation 1) and for the case without the haze droplets (Calculation 2) it can be seen that the haze droplets have a greater effect on both the volume extinction coefficient (36% change) and the volume backscatter coefficient (26% change) at λ = 0.55 μm than at λ = 10.5 μm (9% change for the volume extinction coefficient, 4% change for the volume backscatter coefficient). Furthermore, the values for the meteorological range decreased 27% when the haze droplets were included in the calculations. This result indicates that haze droplets should be included in propagation calculations for fogs which contain high concentrations of haze droplets.

Clouds also can contain high concentrations of haze droplets as shown in Fig. 3. Comparing Figs. 2 and 3 reveals that the fog contained higher concentrations of submicron droplets in relation to the concentration of supermicron droplets. Consequently, the decrease in V in the cloud due to the presence of the haze drops is expected to be less than the 27% calculated for the fog.

CONCLUSIONS

Submicron haze droplets were shown to coexist with supermicron fog and cloud droplets in the fog and cloud investigated. Calculations showed that the haze droplets are deleterious to propagation at 0.55 μm and less so at 10.5 μm. Furthermore, the value for meteorological range in the fog decreased 27% when haze drops were included in the calculations. The reduction in the meteorological range for the cloud was deduced to be less than in the fog.

ACKNOWLEDGEMENTS

The work performed at CSU was funded by the Office of Naval Research, contract N00014-79-C-0793.

REFERENCES

1. Pilie', R.J., E.J. Mack, W.C. Kocmond, W.G. Eadie, and C.W. Rogers, 1975: The life cycle of valley fog. Part II: Fog microphysics. J. Appl. Meteor., 14, 364-374.

2. Mac Cready, P.B., Jr. and C.J. Todd, 1964: Continuous particle sampler. J. Appl. Meteor., 4, 450-460.

3. Hindman, E.E., II and O.E.R. Heimdahl, 1979: Calculated effects of haze droplets on visibility in natural and treated warm fogs. Optica Acta, 26, 671-678.

4. Pueschel, R.F., F.P. Parungo, E.W. Barrett, D.L. Wellman and H. Proux, 1979: Meteorological effects of oil refinery operations in Los Angeles. NOAA Technical Memorandum ERL APCL-22, 62 pp., Boulder, Colorado.

5. Deirmendjian, D., 1969: Electromagnetic Scattering on Spherical Polydispersions, American Elsevier Publishing Co., New York.

6. Hudson, J.G., 1978: Fog microphysical measurements on the West Coast. Ppts. Conf. on Cld. Phys. and Atmos. Elect., Am. Meteor. Soc., Boston, 121-128.

7. Hudson, J.G., 1980: Fog microstructure related to aerosol. J. Atmos. Sci., submitted.

8. Hindman, E.E., II, 1977: Aerosol particle workshop in a coastal environment. Bull. Am. Meteor. Soc., 58, 592-595.

9. Fitzgerald, J.W., 1978: A numerical model of the formation of droplet spectra in advection fogs at sea and its applicability to fogs off Nova Scotia. J. Atmos. Sci., 35, 1522-1535.

10. Bird, R.E., 1976: Extinction and backscattering by fog and smoke in the 0.33 - 12.0 micrometer wavelength region. Naval Weapons Center Technical Publication 5850, China Lake, California, 18 pp, unclassified.

11. Hale, G.M. and M.R. Querry, 1973: Optical constants of water in the 200 nm to 200 μm wavelength region. Applied Optics, 12, 555-563.

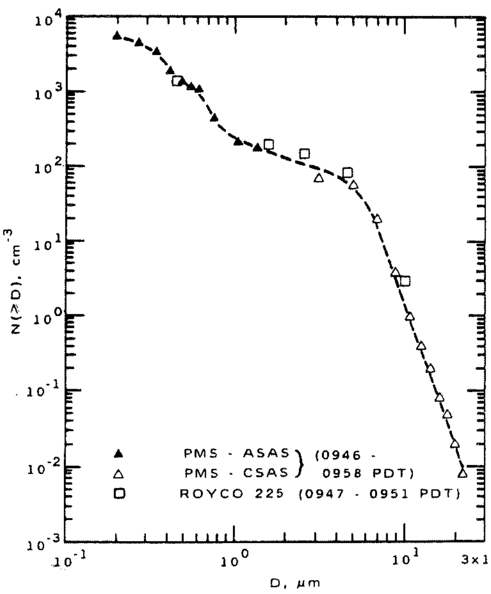

Fig. 1. Fog droplet size distributions determined from measurements with optical particle counters (ROYCO and Particle Measuring Systems) on 16 July 1976 at Trinidad, California.

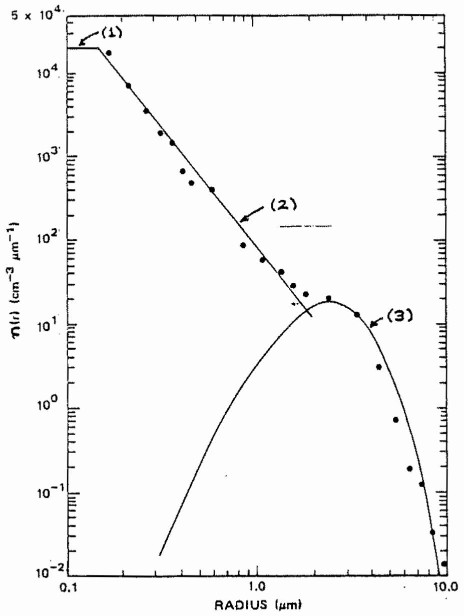

Fig. 2. Differentiation of Trinidad data from Fig. 1 (•) and analytic functions fit to the data (Equations 1, 2 and 3).

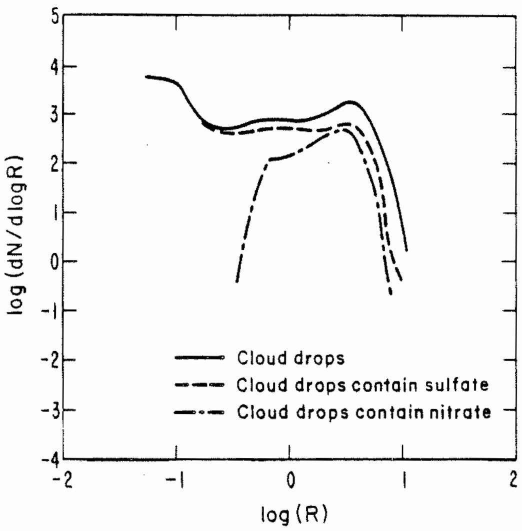

Fig. 3. Cloud droplet size distributions determined from measurements with a PMS ASASP-X and FSSP optical particle counters between 0730 and 0930 PDT on 20 October 1978 at Los Angeles, California; from (4).

RELATIONSHIPS BETWEEN IR EXTINCTION, ABSORPTION, BACKSCATTER AND LIQUID WATER CONTENT OF THE MAJOR CLOUD TYPES

S G Jennings — UMIST, Manchester ENGLAND

R G Pinnick — US Army Atmospheric Sciences Laboratory, NM 88002, U.S.A.

P Chýlek — M.I.T., Cambridge, Mass. 02139, U.S.A.

H J Auvermann & C V Ham — New Mexico State Univ., Las Cruces, NM 88003, U.S.A.

INTRODUCTION

Both fog and cloud have an important effect on radiative transfer in the atmosphere. Recently Chýlek (1978) and Pinnick et al (1979) have shown that in the case of atmospheric fog, at particular infrared wavelengths there do exist approximate linear relationships, that are independent of the form of the size distribution, between extinction, absorption and liquid water content (LWC). In this paper we extend these relationships between extinction, absorption and LWC to water droplet clouds which cover the major cloud categories.

We show that for visible and near-infrared wavelengths the cloud extinction coefficient $\sigma_e(km^{-1})$ is uniquely related to the backscatter coefficient $\sigma_{bs}(km^{-1}sr^{-1})$, independent of the form of the cloud drop size distribution. At the ruby laser wavelength $\lambda=0.694\mu m$ the relation is $\sigma_e=16\ \sigma_{bs}$. We also show however, that cloud liquid water content for clouds of unknown drop size distribution cannot be inferred from visible, infrared or nearmillimeter backscatter measurements alone.

EXTINCTION, ABSORPTION, BACKSCATTER AND LIQUID WATER CONTENT OF WATER CLOUDS

Consider a polydispersion of spherical droplets characterized by a size distribution n(r) and refractive index m. We want to investigate relationships between the cloud extinction and absorption coefficients σ_e and σ_a, the backscatter coefficient σ_{bs}, and the cloud liquid water content W given by

$$\sigma_e = \int \pi r^2 Q_e(m,x)n(r)dr \quad (1)$$

$$\sigma_a = \int \pi r^2 Q_a(m,x)n(r)dr \quad (2)$$

$$\sigma_{bs} = \frac{1}{4\pi}\int \pi r^2 G(m,x)n(r)dr \quad (3)$$

$$W = \rho\int \frac{4}{3}\pi r^3 n(r)dr \quad (4)$$

where ρ is the water droplet density, $Q_e(m,x)$, $Q_a(m,x)$ are the efficiency factors for extinction and absorption for a droplet with refractive index m and size parameter $x=2\pi r/\lambda$, and G(m,x) is the backscatter efficiency (or gain) defined as the ratio of the backscatter cross section to the geometric area.

The efficiency factors $Q_e(x)$ and $Q_a(x)$ for droplets having size parameter $x \leq x_m$ ($x_m = 2\pi r_m/\lambda$) can be approximated by linear functions of droplet size parameter $Q_e(x,\lambda) = c(\lambda)x$ and $Q_a(x,\lambda) = c'(\lambda)x$ as shown by Chýlek (1978) and Pinnick et al (1979).

The consequence of utilizing these simple linear approximations for the Mie efficiency factors in the expressions for the cloud extinction and absorption, given by Eqs.1,2 are far reaching. This is because these expressions now contain the integral $\int r^3 n(r)dr$ and thus the coefficients become proportional to cloud water content W and independent of the particle size distribution n(r):

$$\sigma_e = \frac{3\pi c}{2\lambda_0} W \quad (5)$$

$$\sigma_a = \frac{3\pi c'}{2\lambda_0} W \quad (6)$$

where $c(\lambda)$, $c'(\lambda)$ are the slopes of the straight lines approximating the Mie efficiency curves.

SELECTED CLOUD SIZE DISTRIBUTIONS

The cloud droplet size measurements used here we judge to be fairly reliable and were chosen to represent adequately the major cloud types ranging from cumulus, continental and maritime cumulus [Diem (1948), Battan & Reitan (1957), Squires (1958), Durbin (1959), Jiusto (1967), Warner (1969, 1973ab), Fitzgerald (1972), Fitzgerald & Spyers-Duran (1973), Ryan et al (1972) and Eagan et al (1974)], stratus and stratocumulus [Diem (1948), Singleton & Smith (1960), Jiusto (1967), Spyers-Duran (1972), Fitzgerald & Spyers-Duran (1973) Ryan et al (1972) and Eagan et al (1974)] orographic [Squires (1958)] and cumulus congestus, cumulonimbus [Diem (1948), aufm Kampe & Weickmann (1952)(1953) and Battan & Reitan (1957)]. The main sampling technique employed to obtain the cloud droplet size distributions was that of impaction onto coated slides or replicator whose collection efficiencies were corrected. The practical lower limit for detection of cloud droplets by the impaction technique is around 1.5μm radius. The sole cloud size determination by a light scattering counter (Ryan et al 1972) was calibrated by means of uniformly sized water droplets.

Altogether, 158 different size distributions were used in the analysis making use of the originally measured size categories which were digitised accordingly. Only non-precipitating clouds were used in the analysis and measurements which showed evidence of glaciation were excluded.

Using a Mie scattering programme and index of refraction of water as given by Hale & Querry (1973) and Ray (1972) we have calculated $\sigma_e, \sigma_a, \sigma_{bs}$ and W given by equs. (1) to (4) for the 158 cloud size distributions n(r) at wavelengths λ: 0.55, 0.694, 1.06, 3.8, 10.6, 1363, 2142.9 and 3191.5μm.

EXTINCTION, ABSORPTION AND LIQUID WATER CONTENT IN CLOUDS

The result for the volume extinction coefficient σ_e vs W at λ=10.6μm together with the approximation (5) is shown in Fig.1. At λ=10.6μm the Q_e=cx approximation is a good one (within a factor 2) for all size distributions except those with a large range of droplet size, such as cumulus congestus, cumulonimbus, and some layer clouds. This is in good agreement with the prediction of Chýlek (1978) and Pinnick et al (1979) that the Q_e=cx approximation is valid except for those size distributions which contain a large number of droplets with radii > 14μm. The numerical results at visible and near infrared wavelengths showed that no relation between extinction and LWC independent of size distribution exists - since the Q_e=cx approximation is valid only for water droplets $\lesssim$1.0μm in this wavelength region (Chýlek, 1978)

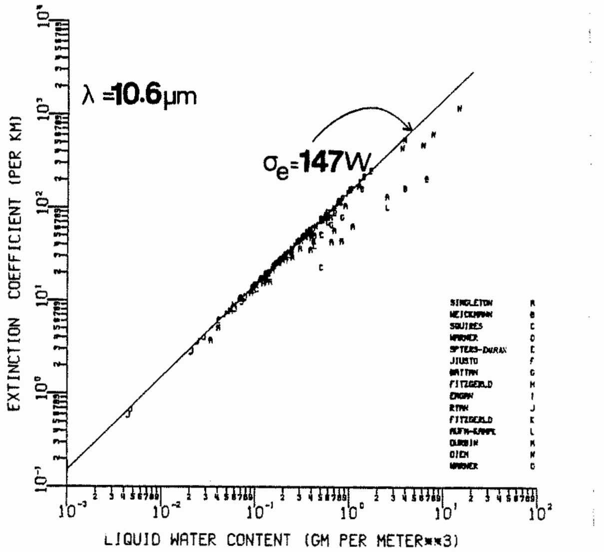

Fig.1 Variation of extinction coefficient with liquid water content in cloud for 158 size distribution measurements, covering all the major cloud types. In the infrared spectral region around λ=10.6μm, there exists a linear, size-distribution-independent relation between the volume extinction coefficient σ_e(km^{-1}) and the liquid water content W(g m^{-3}) of the form of Eq.(5), shown by the straight line.

A linear relation between cloud absorption and LWC according to (6) was found to be within a factor 2 for all cloud types at λ=3.8μm. This is in general accordance with the requirement that droplets with maximum radii of 14μm is adequate for the verification of Q_a=c'x for water droplets at λ=3.8μm (Pinnick et al 1979).

BACKSCATTER AND EXTINCTION IN CLOUD

For a realistic size distribution of cloud droplets we can expect to have a fairly uniform distribution of droplets throughout small ranges of drop sizes, let us say Δr≃1μm (corresponding to Δx=10 at λ=0.6943μm). Under this rather minor constraint we then average the exact Mie values G(x) over intervals Δx=10. These averaged values $\overline{G(x)}$ (Fig. 2) are nearly constant (except for the smallest drops) for all realistic cloud drop sizes. Thus to first order we can replace G(x) in Eq.3 by a constant value G(x,λ)=g(λ) that is independent of size parameter and depends only on the radiation wavelength λ: the extinction in cloud is dominated by droplets with radii 2μm$\lesssim$r$\lesssim$90μm and so the extinction efficiency in Eq.1 can justifiably be approximated by Q_e≅2. This approximation together with the approximation for backscatter gain G=g(λ) leads to the cloud extinction coefficient being linearly related to the backscatter coefficient

$$\sigma_e = \frac{8\pi}{g(\lambda)} \sigma_{bs} \qquad (7)$$

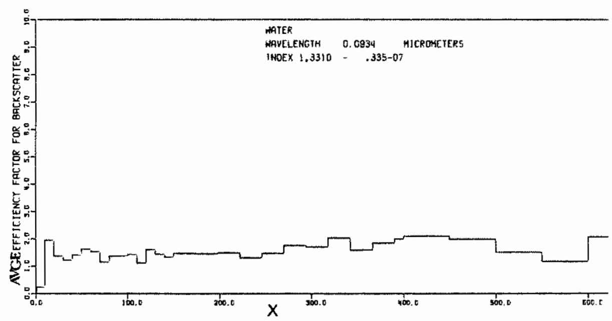

Fig.2 The averaged backscatter gain G(x,λ) for water droplets at a wavelength λ=0.694μm (refractive index m=1.331 - 3.35 x 10^{-8}i). $\overline{G(x,\lambda)}$ is averaged over size parameter Δx=10 (and intervals Δx =20 for x>150) and can be approximated by a constant value G(x,λ)=g(λ).

where g(λ) is determined by numerically averaging the values of $\overline{G(x)}$ as in Fig. 2. (The resulting averages are g(λ=0.694μm)=1.52, g(λ=1.06μm)=1.50).

To test the validity of the extinction-backscatter relation (7), we calculated using Mie theory the extincton coefficient according to Eq.1 and the backscatter coefficient according to Eq. 3 for the 158 different cloud droplet size distributions. Plotted in Fig.3 for each cloud size distribution are values of the extinction coefficient as a function of the backscatter coefficient at λ=0.694μm. The linear relation between extinction and backscatter coefficients, $\sigma_e=16\ \sigma_{bs}$, predicted using our size-distribution-independent relation (7) is also shown in Fig.3.

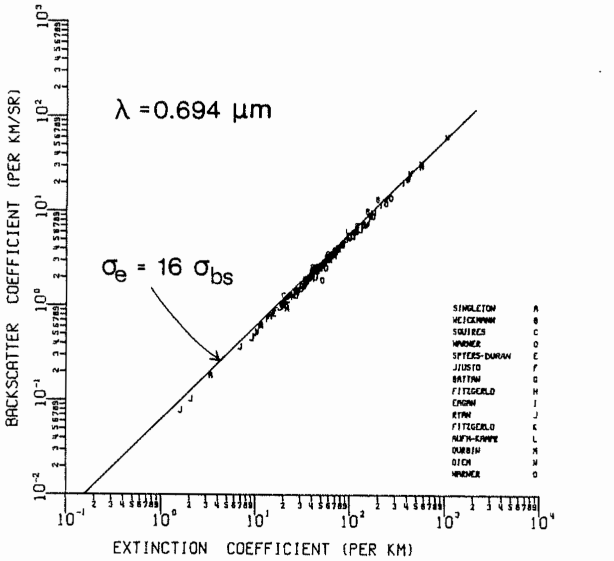

Fig.3 Volume backscatter coefficient vs volume extinction coefficient at wavelength $\lambda=0.694\mu m$ for 158 droplet size distributions measured in cumulus and stratus type clouds. The results are in good agreement with the size-distribution-independent prediction (7) shown by the straight line, relating extinction uniquely to backscatter.

For all considered cloud size distributions the relation (7) is within 30% of the numerical results. Thus if errors of this order are acceptable, cloud extinction coefficients can be inferred from measurement of the backscatter coefficient directly from Eq.7 without the need of knowing details of the cloud droplet size distribution.

The calculation of the extinction and backscatter coefficients for the 158 cloud size distributions at other laser wavelengths ($3.8\mu m$ and $10.6\mu m$) showed that no such relation exists. The results showed that for a particular extinction coefficient the backscatter coefficient varies by about an order of magnitude for different droplet size distributions. Therefore a lidar measurement could not be used (by itself) to deduce infrared extinction accurately in cloud. Neither can an unambiguous extinction-backscatter relation be expected to hold at near-millimeter wavelengths as can be seen from examining (1) and (3), knowing that the Rayleigh approximation holds with $G(x)\sim x^4$ and $Q_e(x)\sim x$.

BACKSCATTER AND LIQUID WATER CONTENT IN CLOUD

We extended our investigation to see if a relation might also exist between cloud liquid water content and backscatter coefficient. Perusal of Eqs.3 and 4 reveals that for liquid water content to be unambiguously related to the backscatter coefficient for arbitrary size distribution n(r) the backscatter gain needs to be approximated by a linear function of droplet radius $G(r) \propto r$(or equivalently $G(x) \propto x$).

We already know the backscatter gain (averaged over about $1\mu m$ radius intervals) at a wavelength $\lambda=0.694\mu m$ is nearly constant ($G(x)=g$) and not proportional to the particle size parameter (Fig.2). Hence there can be no size distribution-independent relation between LWC and backscatter coefficient at this wavelength as the ratio of these quantities contains the ratio of the third to second moments of the droplet size distribution. To obtain a quantitative measure of this size distribution dependence, we performed Mie calculations of the backscatter coefficient using Eq.3 and LWC using Eq.4 for the 158 cloud size distributions. The results of these calculations at $\lambda = 0.694\mu m$ are presented in Fig.4 and show that for a particular backscatter coefficient the cloud liquid water content can vary by as much as an order of magnitude with the droplet size distribution.

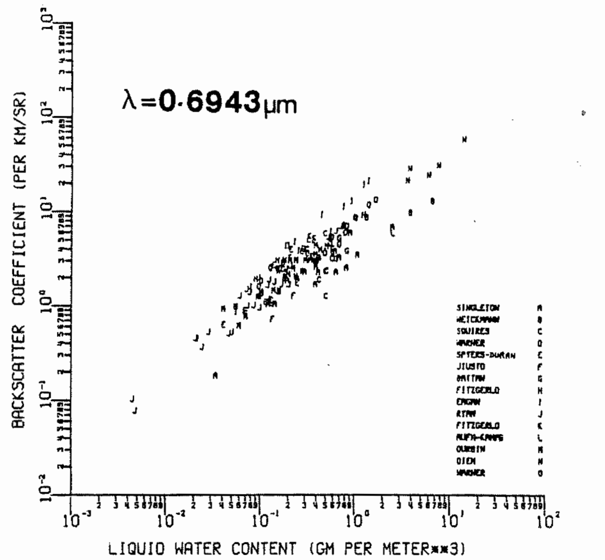

Fig.4 Volume backscatter coefficient at $\lambda=0.694\mu m$ versus cloud liquid water content for 158 measured droplet size distributions of cumulus and stratus type clouds. The results show that cloud liquid water content is not uniquely related to the backscatter coefficient.

Similar investigations of a possible relation between cloud LWC and backscatter coefficient at other infrared, visible, and nearmillimeter wavelengths ($\lambda=0.55\mu m$, $1.06\mu m$, $3.8\mu m$, $10.6\mu m$, $1364\mu m$ $2143\mu m$ and $3192\mu m$) show again that no unambiguous relations exist, and further that for a fixed backscatter coefficient at these other wavelengths the cloud liquid water content is generally an even more sensitive function of the droplet size distribution.

CONCLUSIONS

For all types of clouds consisting of spherical water droplets a linear relation between their extinction and backscatter coefficients at visible and near-infrared wavelengths has been derived, The relation is independent of the cloud size distribution. The relation should enable the determination of cloud extinction coefficient solely from a lidar return, providing the contribution of multiply-scattered photons to the lidar return can be neglected. However, no size-distribution-independent relation exists between cloud water content and backscatter coefficient at visible, infrared or nearmillimeter wavelengths.

The prediction of Chýlek (1978) of a linear relation, independent of the size distribution between extinction at λ around 10.6μm and liquid water content of cloud has been verified to within a factor 2 for all cloud size distributions, the exceptions being cloud types possessing a large range of drop sizes (cumulus congestus, cumulonimbus and some layer clouds). Integrated liquid water content along a path in cloud could be inferred from a CO_2 laser (λ=10.6μm) transmissometer measurement according to (5). A similar linear relation between cloud droplet absorption at λ=3.8μm and liquid water content has also been validated (within a factor 2) for all cloud types. The relation between cloud absorption and liquid water content can also be used, from a knowledge of cloud water content, to calculate cloud emissivity.

REFERENCES

aufm Kampe H J & Weickmann H K 1952 Trabert's formula and the determination of the water content in clouds. J.Met. 9, 167-171

Battan L J & Reitan C H 1957 Artificial stimulation of rain. Pergamon Press. 184-191

Chýlek P 1978 Extinction and liquid water content of fogs. J.Atmos.Sci., 35, 296-300

Diem M 1948 Messung der Gröse con Wolkenelementenll. Meteor.Rundschau 9/10 261-273

Durbin W G 1959 Droplet sampling in cumulus clouds. Quart.J.Roy.Met.Soc., 11, 202-215

Eagan R C, Hobbs P V & Radke L F 1974 Particle emissions from a larne kraft mill and their effects on the microstructure of warm clouds. J.Appl.Met. 13, 535-552

Fitzgerald J W 1972 A study of the initial phase of cloud droplet growth by condensation: comparison between theory and observation. PhD dissertation, Univ. Chicago. Illinois

Fitzgerald J W & Spyers-Duran P A 1973 Changes in cloud nucleus concentration and cloud droplet size distribution associated with pollution from St Louis J.Appl.Met.12, 511-516

Hale G M & Querry MR 1973 Optical constants of water in the 200nm to 20μm wavelength region. Appl.Opt., 12,555-563

Jiusto J E 1967 Aerosol and microphysics measurements in Hawaii. Tellus,19, 359-368

Pinnick R G, Jennings S G, Chýlek P and Auvermann H J 1979 Verification of a linear relation between IR extinction absorption and liquid water content of fogs. J.Atmos.Sci., 36, 1577-1586

Ray P S 1972 Broadband complex refractive indices of ice and water. Appl. Opt. 11, 1836-1844

Ryan R T, Blau H H, von Thüna P C and Cohen M L 1972 Cloud microstructure as determined by an optical cloud particle spectrometer. J.Appl.Met., 11, 149-156

Singleton F & Smith D J 1960 Some observations of drop size distributions in low layer clouds. Quart.J.Roy.Met.Soc. 86, 454-467

Spyers-Duran P A 1972 Systematic measurements of cloud particle spectra in middle level clouds. Tech.Note 43, Cloud Physics Lab., Univ. Chicago, Illinois

Squires P 1958 The microstructure and colloidal stability of warm clouds, I - the relation between structure and stability, Tellus, 10, 256-261

Warner J 1969 The microstructure of cumulus cloud I. General features of the droplet spectrum, J.Atmos.Sci.26,1049-59

Warner J 1973a The microstructure of cumulus cloud IV. The effect of the droplet spectrum of mixing between cloud and environment, J.Atmos.Sci.,30,256-261

1973b The microstructure of cumulus cloud V. Changes in droplet size distribution with cloud age. J.Atmos. Sci.30,1724-1726

Weickmann H K & aufm Kampe H J 1953 Physical properties of cumulus clouds J.Met.10,204-211

THERMODYNAMICS OF RADIATION FOG FORMATION AND DISSIPATION- A CASE STUDY

James E. Jiusto and G. Garland Lala
Atmospheric Sciences Research Center
State University of New York, Albany, New York, USA

1. Introduction

Fogs continue to plague air and ground transportation in various parts of the world. During the autumn season, radiation-type fogs commonly occur over extensive regions of the northeastern United States. Despite their known association with high pressure systems, clear skies, light winds and fairly moist air, it has proven extremely difficult to forecast fogs with satisfactory precision. This seems particularly true at inland stations where a subtle combination of ambient thermodynamic conditions must be met to produce fog.

Thus for several years a fog field program has been conducted at the municipal airport at Albany, New York (200 km north of New York City and ∿250 km from the Atlantic Ocean). By learning more about the physical processes during the evolution of radiation fog, it was felt that better subjective and numerical fog-forecasting techniques could be developed.

2. Measurement Program

Throughout evenings of anticipated haze and fog formation, the following detailed measurements are made:

a. visual range (AEG Telefunken scattered light meter)

b. temperature - 8 levels to 10 m (transistor temperature sensors)

c. wet bulb temperature (dewpoint) - 7 levels

d. horizontal and vertical winds - 1, 4 and 10 m (Gill anemometers)

e. net radiation (Swissteco, Funk type)

f. soil conditions - temperature and moisture, -0.1 and -0.5 m

g. dew rates - dew plates, 10 cm and 50 cm above ground (also Hiltner gauge)

h. aerosol characteristics - Royco 225 particle (droplet) detector; SUNY-ASRC CCN counter; T.S.I. electrical aerosol analyzer

i. drop size distributions - Royco counter and gelatin slides

j. fog water content - high volume filters

Most variables are continuously or periodically monitored with a computerized data-gathering system, allowing for rapid processing of the data.

Of the many fog and haze cases recorded, one particularly unique and complete fog data set was obtained on 29-30 September 1979. It revealed a number of interesting features pertaining to the dynamics and thermodynamics of radiation fog during the periods of formation, "steady-state" equilibrium, and ultimate dissipation.

3. Case Study Results

Figure 1 shows the continuous visual range (V.R.) trace for the 13 hour case extending from evening through early morning, while Figure 2 depicts the corresponding temperature traces for five selected levels (surface to 10 m). From the V.R. trace, we can define at least three periods of particular thermodynamic interest:

a. 2000-0230 EST; initial haze and light fog formation period with the V.R. typically between ∿1 and 8 km

b. 0230-0630 EST; dense fog (V.R. <500 m) formation of a persistent nature

c. 0630-0830 EST; fog dissipation after sunrise

As indicated during the initial period, and as we have invariably observed during haze and light fog situations, the variables such as temperatures, winds and visual range are highly oscillatory with time. The V.R. oscillations generally appear random and can be induced by changes in winds, temperature and/or net radiation; on occasion the oscillations are periodic (10-20 min. periods), as noted by Roach, 1976, and Lala et al., 1978, but such oscillations appear atypical. In this particular case the V.R. oscillations during the early period were often linked with changes in the Richardson number R_i:

$$R_i = \frac{g}{\theta} \frac{(d\theta/dz)}{(du/dz)^2}$$

In short, lower visibilities tended to be associated with a more stable boundary layer (R_i >0.5). Increases in winds and vertical mixing, at this stage, tended to warm the lower levels and weaken the light fog and haze (improve visibility).

Figure 2 shows that a strong inversion of as much as 5°C over the lowest 10 m prevailed during this period - classic low level radiation conditions. Note the abrupt change to quasi-isothermal conditions from 2230-2315 EST. This was primarily induced by a cloud bank passing overhead that reduced the outgoing net radiation from about 3.5 mW cm^{-2} to 0.5 mW cm^{-2}. Shortly thereafter, pronounced radiational cooling resumed as did variable oscillations. Over the period from 2000-0230 EST the number N of fog drops ≥0.5 μm diameter varied from about 20 to 100 cm^{-3} (∿30 cm^{-3} average), as shown in Figure 3. As would be expected V.R. varied inversely with N.

Dense fog (V.R. <0.5 km) set in at 0230 EST and persisted until about 0630 EST, shortly after sunrise. Several interesting events occurred during this "steady-state" period. The strong temperature inversion gave way to a low-level neutral to superadiabatic lapse rate as the level of maximum radiation shifted from the surface to the fog top (Figure 2). Somewhat surprisingly, horizontal wind speeds at all levels became much stronger (0.5 to 2 m sec^{-1}), in accordance with a near neutral boundary layer (R_i <<0.25). One customarily associates fogs with very light winds. Also the visibility - Richardson number relationship reversed during this period; low V.R. was associated with very low (less stable boundary layer) R_i values. We postulate that with cooling (and higher humidities) extending upward through a greater depth than earlier, that vertical mixing then had the more customary effect of coupling with radiational cooling to generate supersaturated conditions. Droplet concentrations exceeded 300 cm^{-3} and a pronounced increase in drop sizes occurred. For example, the number of drops larger than 10 μm diameter jumped by almost two orders of magnitude in 5 minutes time starting at 0230 EST.

After sunrise, the fog slowly dissipated. Note the increase in visibility to 5 km at 0800 EST (Figure 1), and the decrease in droplet concentration to 50 cm^{-3} (Figure 3). An historic question exists as to whether such fogs "burn off" because of direct adsorption of solar radiation by fog drops or by heating of the ground and warming from below. Undoubtedly both mechanisms contribute. In Figure 2, one can see a pronounced $2^{\circ}C$ increase at the surface from 0700-0800 EST. In this case at least, surface heating constituted a significant force for fog dissipation.

In summary, it can be said that the critical conditions for fog evolution are complex with transitions often occurring quite rapidly. As these and other figures will demonstrate, the microphysics measurements described frequently can help define the governing physical principles involved.

4. Acknowledgements

This research was supported by the Atmospheric Research Section of the National Science Foundation under Grant ATM7624048. We are grateful to Michael Meyer for his part in the field program and data analysis.

5. References

Lala, G., M. Meyer, and J. Jiusto, 1978: Preprints, Conf. on Cloud Physics and Atmos. Electricity, AMS, p. 233-235.

Roach, W.T., 1976: Quart. J. R. Met. Soc., 102, p. 355-359.

Silverman, B., and A. Weinstein, 1974: Fog. Weather and Climate Mod., Ed., W. Hess, J. Wiley and Sons, Chap. 9.

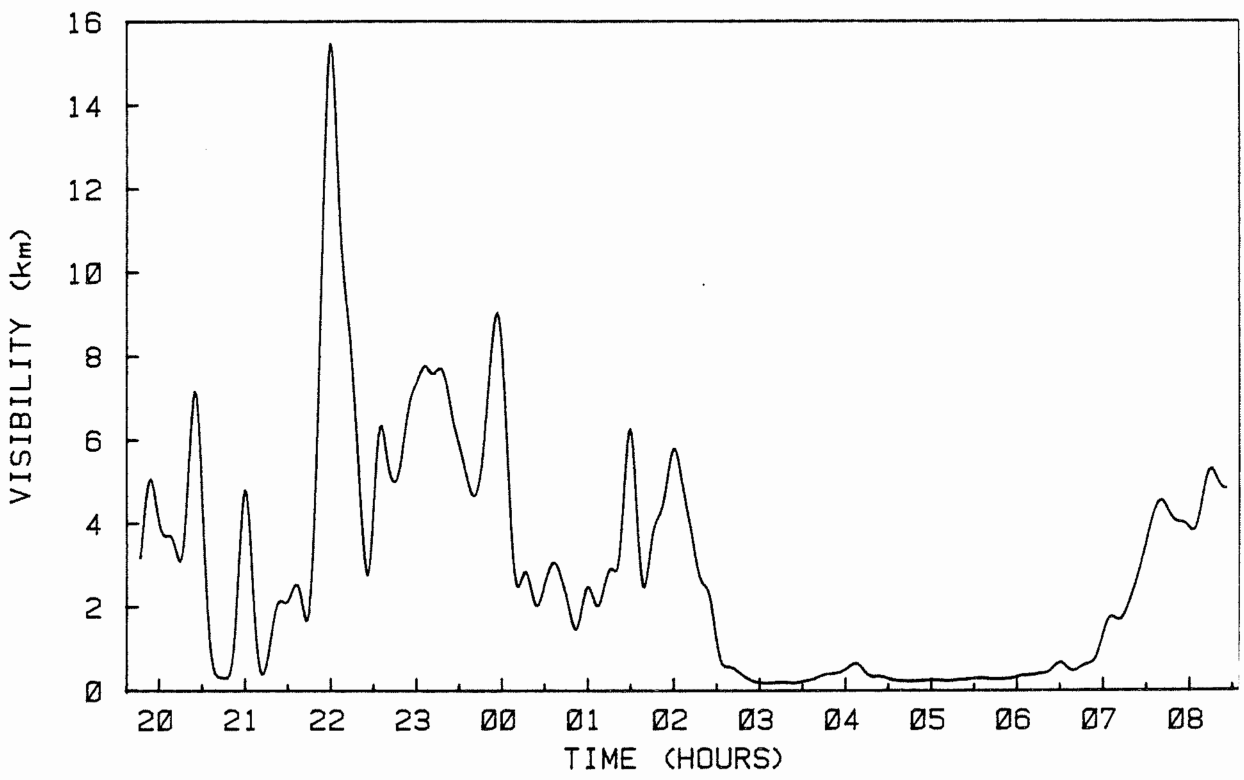

Figure 1. Visual Range vs. Time During Night of Fog Formation (29-30 September 1979)

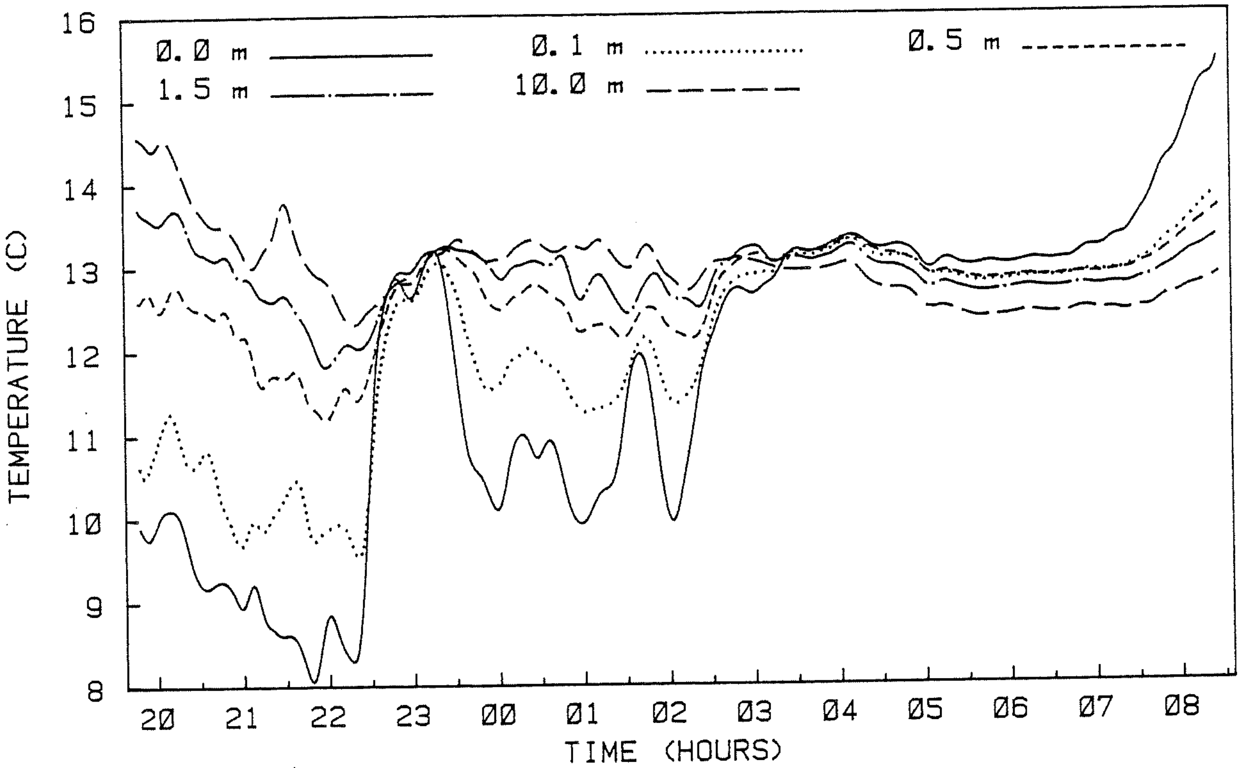

Figure 2. Temperatures vs. Time - surface to 10 m
(29-30 September 1979)

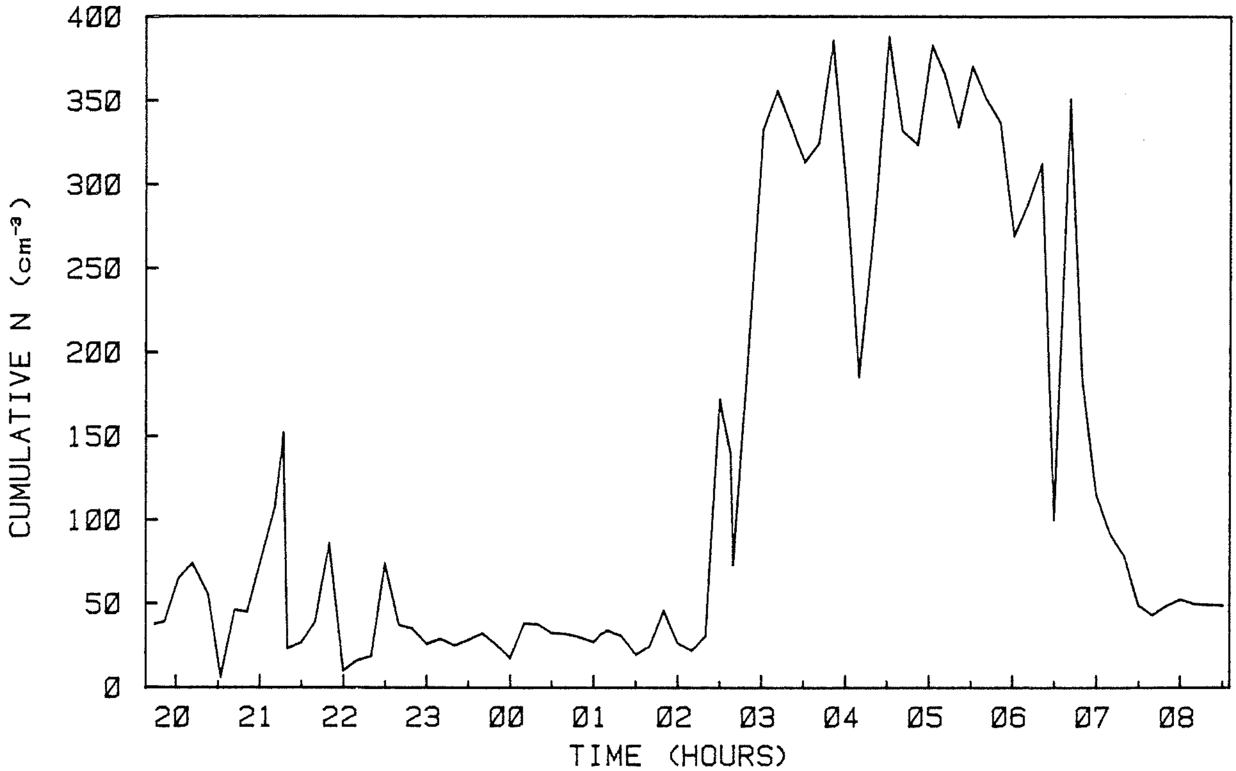

Figure 3. Total Concentration of Fog (Haze) Drops $\geq$0.5 μm Diameter vs. Time
(29-30 September 1979)

A LAGRANGIAN APPROACH TO THE SIMULATION OF THE CONDENSATION PROCESS

M Ouldridge
Meteorological Office, Bracknell, UK.

1. Introduction

During an attempt to explain some of the microphysical features of Stratocumulus cloud, it was observed that the modelled development of the droplet size distribution was heavily influenced by the conditions assumed at cloud base - particularly the updraught strength. This report discusses the details and implications of this sensitivity.

Several investigators have attempted to explain the evolution of the droplet size distribution in cumulus, and there is general agreement that simple parcel models are inadequate in retaining enough dispersion in the droplet sizes.

Warner (1969) and Bartlett and Jonas (1972) considered the effect of supersaturation fluctuations directly caused by a randomly - varying updraught, and concluded that these produced negligible dispersion. On the basis of Twomey's (1959) work, Warner (1969) also deduced that a measured spectrum of updraught strengths failed to produce the required degree of variability in droplet number density between parcels.

Clark (1974) and Manton (1979) have shown that the dispersion of droplet sizes is much more sensitive to fluctuations in supersaturation uncorrelated with updraught, i.e. occurring as a result of mixing.

With the exception of Warner, however, the above workers all made simplifying assumptions about the droplet size spectrum or the condensation growth rate expression such that their results are valid strictly for regions above cloud base after activation. Warner's work was more detailed microphysically, but his integrations were started at 100% relative humidity with the parcel instantaneously accelerated to the mean updraught velocity.

The present work returns to an adiabatic parcel model to study the activation process in detail.

2. Model

A closed parcel of air containing droplets and condensation nuclei is subjected to forced ascent with a prescribed velocity, and this is the only source of supersaturation. There is no turbulent exchange, nor fall-out of condensation products. All droplets and nuclei have identical histories: droplet radius at any time is a unique function of nucleus mass. The nucleus mass spectrum is constant throughout the integration, and is represented by a discrete distribution into 61 exponentially-spaced categories with a factor of $2^{1/3}$ between neighbours, and the smallest at 10^{-16}g.

The droplet growth rate expression is essentially that of Fukuta and Walter (1970), including effects of surface curvature, salt nucleus content (van 't Hoff factor = 2.2), and gas-kinetic effects at the surface (the thermal accommodation coefficient taken as unity and the condensation coefficient as 0.03).

Prohibitively small timesteps are avoided by allowing for a first-order change of humidity over a timestep, and by assuming that the factor accounting for surface curvature and nucleus mass is approximately locally linear in r^2, where r is the droplet radius. If all other factors are assumed constant over a timestep, the resulting approximate expression for the rate of change of r^2 can be integrated analytically. The negative feedback effect of droplet growth reducing ambient supersaturation is thus crudely modelled within the timestep.

The parcel thermodynamic variables are incremented by forward differencing every timestep.

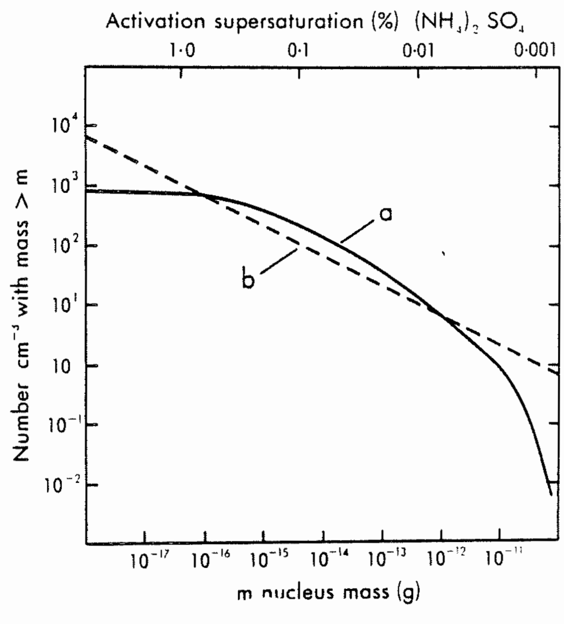

Figure 1. Salt nucleus mass spectra.

(a) Synthetic "continental" spectrum.

(b) Activation spectrum: k = 1.0

3. Nucleus Spectra

For the early integrations, performed specifically for comparison with experimental results, the nucleus spectrum shown in Fig.1(a) was used.

There exists considerable uncertainty in the measurement of condensation nucleus mass spectra.

Results are usually presented as activation spectra of the form

$$N = CS^k$$

where N is the number density of cloud condensation nuclei active at a supersaturation S(%), C is the number density active at 1%, and C and k are roughly constant.

Pruppacher and Klett (1978) have summarized results obtained by many workers, and the values of slope parameter k claimed for continental air alone range from 0.4 to 0.9. Hindman, Hobbs and Radke (1977) presented results in which the slope parameter k varied from 1.25 over western Washington to 2.10 over eastern Washington State, U.S.A.

The spectrum of Fig. 1(a) is artificial: it was designed to approximate that of continental air and has a slope parameter in the region corresponding to typical peak supersaturations (~ 0.1–0.3%) of k ~ 1, with few giant nuclei. The absolute number density was adjusted to give a realistic total droplet concentration in the range 1 μm to 20 μm radius when compared with experimental data.

For purposes of comparison with model results from other workers, a simpler form of the nucleus spectrum was used (Fig. 1(b)), with a constant k = 1.0, and N = 1000 cm^{-3} at S = 1%. Such a parametrization has been found (M. Kitchen, private communication) to fit quite adequately results obtained recently in urban air at the UK Meteorological Office over the range S = 0.2 to 1%.

4. Other Initial Conditions

Comparison is made here specifically between model results and measurements obtained in an extensive and persistent deck of Stratocumulus on the night of 19/20 November 1976 at the UK Meteorological Office Research Unit at Cardington, Bedfordshire. (See e.g. Roach et al (1980), Slingo, Brown & Wrench (1980)).

The observed cloud base temperature (+1.15°C) and pressure (945 mb) was used as a basis for a reverse - Normand construction to recover hypothetical values of temperature and humidity at 1000 mb. This was to ensure that the model, which is adiabatic, produced cloud in the correct place; the hypothetical 1000 mb temperature was close to the observed value (+6°C), but the real atmosphere was more humid.

The presence at Cardington of microwave and infra-red radiometers enabled cloud liquid-water content to be estimated quite accurately (Roach & Slingo, 1979), and so the droplet-sizing instrument, a PMS Axially Scattering Spectrometer Probe (ASSP) (Knollenberg, 1976) could be calibrated independently. Results presented in Slingo, Brown & Wrench (1980) show that, although there was considerable scatter, the droplet number density was 200–300 cm^{-3} throughout the cloud depth, (~40 mb). For the range of updraught strengths considered here, a total of 800 cm^{-3} ammonium sulphate nuclei, distributed as in Fig. 1(a), produced roughly the required number of droplets in the ASSP range.

The nuclei were assumed in equilibrium at the hypothetical 1000 mb humidity (~ 77%) and all parcels originated at 1000 mb.

5. Results and Discussion

The ASSP distributes droplets into bins according to diameter. As demonstrated in Slingo, Brown & Wrench (1980), the absolute total number density of droplets fluctuates widely, but the shape of the normalized distributions varies smoothly and slowly with height. Therefore, for easiest comparison, both the experimental data and model results are presented as they would appear to the ASSP, normalized to unit density over the ASSP range.

(a) Comparison with experiment.

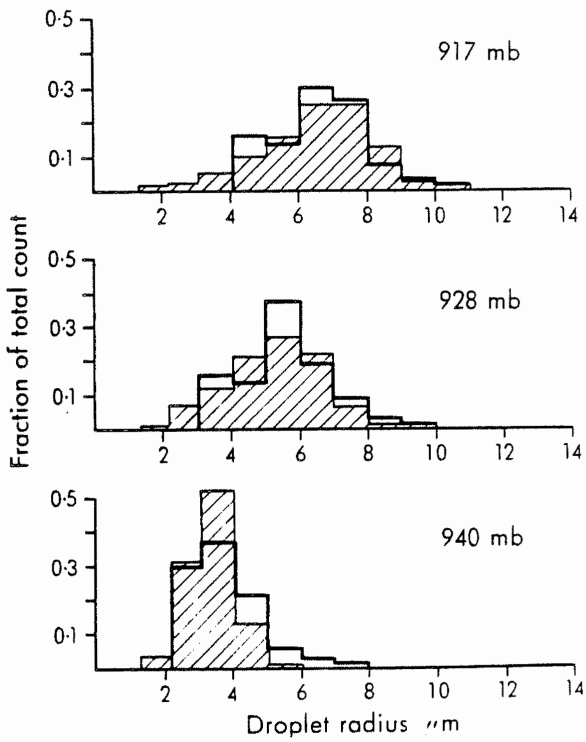

Figure 2. Full line: model results, distributed in ASSP channels. Parcel ascending at constant 15 cms^{-1}.

Hached background: ASSP data from Cardington, 19–20/11/76, profile 3.

Figure 2 demonstrates the ability of the model to simulate the evolution of the dropsize distribution in Stratocumulus. Experimental data are compared with the result of adiabatic ascent at a constant 15 cms^{-1}, when of the spectrum of Fig. 1(a), 270 cm^{-3} droplets grew to radii within the ASSP range.

Apart from the adjustments outlined above to ensure that the modelled condensation takes place in the correct part of the atmosphere and onto roughly the correct number of droplets, the input parameters for this comparison are nothing more than reasonable guesses. It is then surprising that the shape and variation with height of the observed droplet size distribution can be reproduced so well, particularly as the measured total number density fluctuates a great deal (Slingo, Brown & Wrench, 1980), with localized large departures from adiabatic liquid-water content.

Latham and Reed (1977) have argued that the turbulent mixing of different air parcels takes place inhomogeneously: localized regions of cloudy air are completely depleted of droplets in order to saturate the entrained air, whilst other regions are unaffected. The total number density of droplets should fluctuate in concert with the liquid water content, but the shape of the size distribution should be unaffected. The success of the present model in describing the shape of the experimental spectrum indicates that such a mechanism may be operating.

(b) Influence of updraught at cloud base.

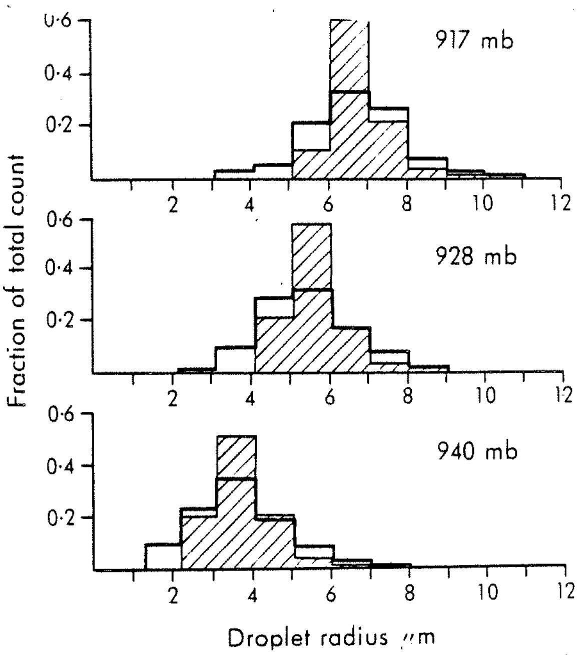

Figure 3. Model results, distributed in ASSP channels.

Full line: average of nine parcels subjected to fluctuating velocity: W_L = 15 cms^{-1}, W_E = 28 cms^{-1}.

Hached: model parcel under constant updraught of 28 cms^{-1}.

A strong updraught produces a high peak supersaturation, and large numbers of small nuclei are activated. This number of droplets competing for the available water results in a small mean radius. The small nuclei respond quickly, taking up the water and thus preventing the less responsive larger nuclei from growing. The result is a narrow distribution with many droplets at small radii. Conversely, a weak updraught produces a broader spectrum of fewer droplets at larger radii. It follows that, where a collection of parcels are subjected to a range of updraughts, the resulting average spectrum, taken over many parcels at a given height, will be broader than those of individual parcels.

Warner (1969) concluded differently. Using a result of Twomey (1959), which links the number of droplets, N, produced by an updraught W from a parent nucleus spectrum $\propto S^k$ in the relationship:

$$\ln N = (3k/(2k+4)) \ln W + \text{constant},$$

Warner deduced that a measured velocity spectrum could not produce a significant spread of N with "reasonable" values of k ($\sim$0.5).

Early results with the present model, using the nucleus spectrum of Fig.1(a), indicated that the dependence of N on W was stronger than Twomey's relationship would predict. A series of numerical experiments were therefore performed with a more directly comparable power-law nucleus spectrum, Fig. 1(b), with k set to unity.

Table I contains results of these model integrations, together with predictions from Twomey's relationship which, with k = 1, reduces to

$$N \propto W^{0.5}$$

Updraught strength cms^{-1}	Droplet concentrations cm^{-3}	
	Present work	Twomey (1959)
15	123	166
20	156	192
30	222	235

Table I. Concentrations of droplets, larger than largest unactivated droplet, predicted by present model, compared with results of Twomey's (1959) expression, for same nucleus activation spectrum.

Doubling the updraught strength in the present model almost doubles the number of "participating" droplets. (It should be noted that these are not all activated droplets: the largest nuclei respond so slowly that they do not activate however, in a closed parcel, a larger nucleus always means a larger droplet, regardless of activation).

The conclusion here is that Twomey's relationship underestimates the power of updaught variations to control the droplet number density.

The implications of this result were explored by subjecting a series of independent parcels to fluctuating updraughts. The velocities were generated using a Markov chain process as in the work of Bartlett & Jonas (1972) with a Lagrangian mean velocity W_L of 15 cms^{-1}, a variance of 400 cm^{2}s^{-2}.

Figure 3 shows the result of averaging over nine parcels treated as above. The mean parcel velocity at the point where the relative humidity first exceeded 100%, called the Eulerian mean W_E, was 28 cms^{-1}; the resultant droplet spectrum from a parcel subjected to a constant updraught of 28 cms^{-1} is also shown in Fig. 3. It is clear that the modest variability in updraught has broadened the resultant size distribution quite considerably.

The supersaturation in an ascending parcel grows quickly as long as there are few activated droplets present. It reaches a peak value when the bulk of the nuclei are activated, and thereafter its response to changes in updraught is subdued by the readiness of droplets to take on water. This feature is illustrated by model results with a fluctuating updraught in Fig. 4.

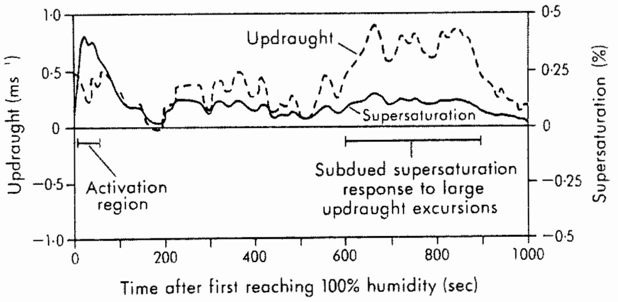

Figure 4. Trace of supersaturation for model parcel subjected to a fluctuating updraught.

There is therefore little chance of activation of fresh nuclei in the same parcel above cloud base, and so the number density of droplets throughout the cloud is essentially determined by the updraught experienced at the cloud base. The dispersion evident at 928 mb and 917 mb in Fig. 3 is almost entirely due to the spread in number activated at cloud base.

6. Conclusions

The development of the droplet size distribution in Stratocumulus cloud has been simulated with some success using a simple, adiabatic, Lagrangian model. That this was possible exclusive of the effects of mixing and entrainment lends support to the arguments of Latham & Reed (1977).

The model was then used to explore the sensitivity of the droplet size distribution to updraught structure, and it has been shown that the updraught experienced at cloud base can have a profound effect on subsequent development of the spectrum. This is largely a result of the correlation between updraught strength and droplet number density, which was shown to be stronger than that derived by Twomey (1959).

The present model has no claim to superiority over those of Clark (1976) and Manton (1979) in the region above cloud base where activation has ceased, but complements them in highlighting the essential variability introduced on activation before those models have become valid.

References

Bartlett J T & Jonas P R, 1972: "On the dispersion of the sizes of droplets growing by condensation in turbulent clouds". Quart. J. Roy. Met. Soc. 98, 150

Clark T L, 1974: "On modelling nucleation and condensation theory in Eulerian spatial domain". J. Atmos. Sci., 31, 2099.

Fukuta N & Walter, L A, 1970: "Kinetics of hydrometeor growth from a vapour-spherical model". J. Atmos. Sci. 27, 1160.

Hindman E E II, Hobbs P V & Radke L F, 1977: "Cloud condensation nucleus size distributions and their effects on cloud droplet size distributions". J. Atmos. Sci. 34, 951.

Knollenberg R G, 1976: "Three new instruments for cloud physics measurements". Preprint vol. Int. Conf. Cloud Physics, Boulder, Colorado, 554.

Latham J & Reed R L, 1977: "Laboratory studies of the effects of mixing on the evolution of cloud droplet spectra". Quart. J. Roy. Soc. 103, 297.

Manton M J, 1979: "On the broadening of a droplet distribution by turbulence near cloud base". Quart. J. Roy. Met. Soc. 105, 899.

Pruppacher H R & Klett J D, 1978: "Microphysics of clouds and precipitation". D Reidel Publishing Co., Dordrecht, Holland.

Roach W T, Brown R, Caughey S J, Crease B A, & Slingo A, 1980: "A field study of nocturnal stratocumulus. I. Observations and budgets". To appear in Quart. J. Roy. Met. Soc.

Roach W T & Slingo A, 1979: "A high-resolution infra-red radiative transfer scheme to study the interaction of radiation with cloud". Quart. J. Roy. Met. Soc. 105, 603.

Slingo A, Brown R and Wrench C L, 1980: "High resolution observations of stratocumulus clouds". To appear in Quart. J. Roy. Met. Soc.

Twomey S, 1959: "The nuclei of natural cloud formation. Part II: The supersaturation in natural clouds and the variation of cloud droplet concentration". Geofis. Pura. Appl. 43, 243.

Warner J, 1969: "The microstructure of cumulus clouds. Part II: The effect on droplet size distribution of the cloud nucleus spectrum and updraft velocity". J. Atmos. Sci. 26, 1272.

The Axially Scattering Spectrometer Probe is manufactured by Particle Measuring Systems, Inc., Boulder, Colorado, USA.

HEAT AND WATER BUDGETS OF NOCTURNAL STRATOCUMULUS: A FIELD STUDY

W T Roach, R Brown, S J Caughey, B A Crease, A Slingo

Meteorological Office, Bracknell, UK

1. Introduction

This paper describes and interprets observations of anticyclonic stratocumulus made with ground-based and balloon-borne equipment through the night of 19/20 November 1976 at Cardington, Bedford, UK (latitude 52°06'N, longitude 0°24'W) by the Cloud Physics and Boundary Layer Research Branches of the Meteorological Office, UK.

An account is given of the budgets of heat and water substance (vapour + liquid) in terms of the observed structure of the atmosphere from the ground to cloud top (referred to as the BL) with particular reference to the overall influence of anticyclonic subsidence. Other aspects of the interaction of turbulence, cloud top entrainment, microphysics and radiative transfer observed in this and other case studies appear in Slingo & Brown (1980) and Caughey et al (1980) which will be referred to as papers II and III respectively.

2. Instrumentation

a. Ground-based

Cardington is a regular Meteorological Office observing station, and standard observations of screen wet and dry-bulb temperature, wind, pressure and cloud were available. The surface energy balance was determined from measurements of the soil heat flux, surface evaporation using a Lysimeter, net radiative flux at 1 metre using a ventilated flux radiometer and profiles of mean windspeed and temperature to 16 metres.

A monostatic acoustic sounder, which generated 30 w of acoustic power from 64 vertically pointing horn loudspeakers, gave information on the variation of the height of the subsidence inversion base and on the structure of the cloud convection. A vertically pointing 95 GHz microwave radiometre was operated by the Appleton Laboratory and provided a continuous record of the total liquid water path through the cloud overhead at Cardington.

b. Balloon-borne

The balloon-borne instrument package comprised a drop sizing device, a turbulence probe, two net radiometers and a pressure sensor to monitor the height of the package. These were attached to the cable of a tethered balloon capable of lifting the equipment to a height of 1.5 km at speeds in the range 0.1–1 ms^{-1}. The equipment was powered by batteries and sensor outputs were telemetered to a ground receiving station.

Drops were sized by an axially scattering spectrometer probe manufactured by Particle Systems Inc, Colorado. This was modified for use on the balloon to work at sampling velocities of 7 ms^{-1}. The Cardington turbulence probe consists of a set of sensors mounted on a vane which is free to rotate about the balloon cable and keep the sensors pointing into the wind. Fine wire sensors are used to measure fluctuations in temperature and the three components of wind, while the mean wind vector is obtained from a sensitive cup anemometer and a magnetic flux measurement. Humidity is measured with a Vaisala 'Humicap' sensor. Two CSIRO pattern net radiometers were mounted on gimbals for attachment to the balloon cable. The domes were kept free of cloud droplets by guard rings and ventilated with dry air. The profiles of net radiative flux were used to obtain profiles of radiative heating through the cloud.

3. Synoptic Situation

An intense stationary anticyclone was centred over the Irish Sea, and maintained a northeast gradient of about 7 ms^{-1} over SE England. During most of the night of 19/20 November 1976, the UK was covered by a sheet of stratocumulus except for a persistent, quasi-stationary band of clear sky about 100 km wide over southern England (Fig 1). The northern edge of this clear band lay 30–60 km south of Cardington during the night, and geostrophic trajectory analysis indicated that air passing over Cardington crossed the cloud edge obliquely some 4 hours (100 km) downstream, having left the east coast near the Wash some 4 hours previously.

Surface temperatures and dewpoints in the cloudy areas away from the east coast were remarkably uniform in space and time. Upper air ascents indicated a subsidence inversion of 6–7°C at 900–920 mb in the NE flow over south England which contrasted with inversions of up to 13°C at much lower levels in the central region of the anticyclone.

4. Field Observations at Cardington

The principal feature was the remarkable steadiness of most of the principal parameters during the night.

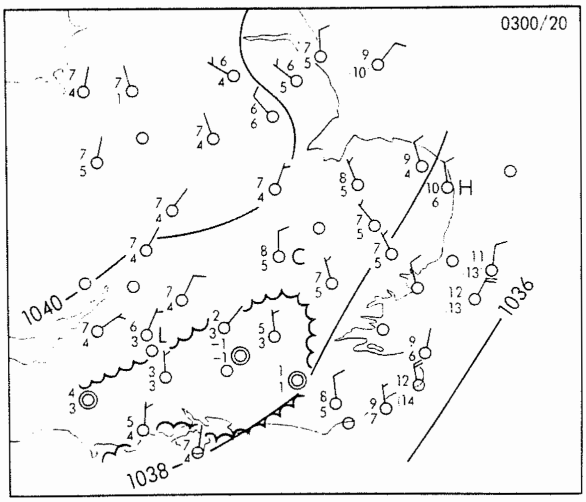

Figure 1 Conventional surface observations at 0300 20 November 1976

——— isobars (mb)   C – Cardington

cloud edge   L – Larkhill

a. <u>Surface Observations</u>

Screen temperatures varied little from 7.5°C through the night, while the dew-point decreased from about 6.5°C to 4.5°C during the night. The surface energy balance was mainly between a surface evaporation of 20 w m^{-2} and a downward eddy flux of sensible heat of similar magnitude (giving a Bowen ratio of order −1). Soil heat and net radiative fluxes contributed some 5–10 w m^{-2}.

The acoustic sounder indicated a subsidence inversion near 1.1 km throughout the night with a standard deviation of 15–20 m. Cloud base recorders within 100 km of Cardington indicate a base near 0.7-0.8 km with a standard deviation of 30–50 m. Thus the standard deviation in cloud thickness was 10–15%.

In contrast to the steadiness of most parameters the cloud water showed large fluctuations (but no long term trend) about a mean value of 56 g m^{-2}, standard deviation 14 g m^{-2}. Time spectral analysis of these fluctuations yielded peaks at 3 hours, 1 hour and 38 minutes, corresponding to advection distances of 75, 25 and 15 km respectively.

b. <u>Balloon Observations</u>

The balloon was operated partly in a profiling mode and partly in a constant height mode to obtain some measurements of turbulent flux (see (iii)).

Profiles of temperature, expressed in various ways, and of humidity mixing ratio are shown in Fig 2 and are characteristic of the whole period.

Principal features are the temperature step of about 5°C at cloud top and the very stable layer some 20 mb deep at the surface.

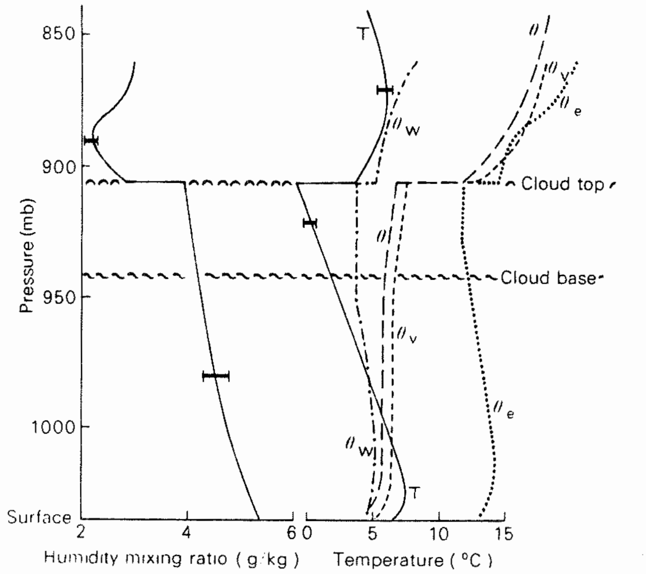

Figure 2 Representative profiles of the principal parameters. The approximate spread is indicated by horizontal bars.

T – dry bulb temperature

θ_w – wet bulb potential temperature

θ_e – equivalent potential temperature

θ_v – virtual potential temperature

The turbulence probe revealed the temperature step at cloud top to vary between 1 and 10 m in thickness and its base to coincide (within 1 m) with a very sharp cloud top. A steady lapse of humidity mixing ratio from group to cloud was capped by a humidity step of 1–1.5 g/Kg at cloud top.

Cloud liquid water content increased roughly linearly with height above cloud base at about $\frac{3}{4}$ the adiabatic value. The cloud droplet spectra are described in (ii).

Above the stable surface layer – which appears to correspond to the frictional boundary (Ekman) layer – the wind varied little from a speed of 6–7 ms^{-1} from 030°. Wind shear in the subsidence inversion was slight or non-existent throughout the period.

There is a net radiative loss at cloud top of about 75 W m^{-2} (see profile in Fig 3). Radiative cooling of 5–10 K hr^{-1} is concentrated in the top 3–5 mb of cloud, and a level of zero flux and flux divergence located about 15 mb below cloud top. A maximum radiative heating of 0.3 K hr^{-1} occurs at cloud base. Radiative cooling just above the temperature step at cloud top is 0.5–1 K hr^{-1}, while the net flux increases to about 85 W m^{-2} 20 mb above cloud top.

5. <u>Discussion</u>

It is considered that this case study is representative of a fairly commonly occurring situation, and insight into the physical and dynamical factors controlling this situation can be used to infer the behaviour of strato-cumulus with different boundary conditions.

a. Subsidence

It is likely that subsidence exerts a significant and perhaps controlling influence on the structure of the BL and its associated cloud layer. The nature of this influence is not well understood, but some estimate of the subsidence rate and its relationship to cloud top entrainment is required to estimate the heat and water budget of the BL. Subsidence rate is not yielded directly by the observations, but can be inferred indirectly from the following physical considerations.

(i) A radiative cooling rate of 0.5–1 K hr^{-1} just above the cloud top in the presence of a locally steady temperature must have been offset by subsidence heating. This balance is expressed by

$$w\left(\frac{\partial T}{\partial z}+\Gamma\right)=H_R \qquad (1)$$

where w = vertical velocity, $\frac{\partial T}{\partial z}$ = lapse rate of temperature, Γ = dry adiabatic lapse rate, H_R = radiative heating.

H_R was computed by applying a high resolution radiative transfer scheme (Roach and Slingo 1979) to the observed profiles of temperature, humidity mixing ratio and cloud droplet spectra and inserted in Eq 1 to obtain w. Surprisingly consistent estimates of about 0.5 cms^{-1} were obtained for subsidence rate.

(ii) The horizontal and vertical uniformity of the wind field throughout most of the BL suggests that subsidence continues more or less unchecked through cloud down to the stable surface layer within which the subsiding air is dispersed by frictionally induced divergence (Ekman suction). A rough quantitative estimate shows that the vorticity field of the low level winds could achieve this.

(iii) The constancy of cloud top height in the presence of a mean subsidence rate implies that entrainment of dry subsiding air must be taking place at a rate balancing the subsidence rate. This is supported by the observation of sub-adiabatic liquid water content, and by the maintenance of a near discontinuity of temperature at cloud top.

b. The Heat Budget

The inference of an entrainment rate of 0.5 cms^{-1} leads to an estimate of entrainment total heat flux of 15 W m^{-2} into the BL (consists of 30 W m^{-2} sensible heat gain and 15 W m^{-2} latent heat loss), which, when combined with a small surface heat flux only accounts for about one-quarter the radiative loss from cloud top. This can only be balanced by local cooling, or by horizontal advection or subsidence within the BL. Observations show that local cooling and subsidence are small and of opposite sign, and that horizontal advection must, by elimination, be the major term balancing radiative loss within the BL. This cannot be measured because of inadequate upper air data, but in any case will be small - amounting to a decrease in dewpoint of 0.8 K/100 km averaged throughout the BL if the energy loss is latent, or 0.5 K/100 km in temperature if the energy loss is sensible.

c. The Water Budget

In contrast to the heat budget, no one term appears to dominate the water budget. Surface evaporation and latent heat entrainment fluxes roughly balance, while the subsidence (vertical advection) term is also estimated to be about 20 W m^{-2} and has to be balanced by a horizontal advection term. This is about $\frac{1}{5}$ the total heat advection term. Thus we conclude that about half the cloud top radiative loss is compensated by horizontal advection of sensible heat (downstream cooling), about $\frac{1}{4}$ by horizontal advection of latent heat (downstream drying), and the remainder by local surface and entrainment heat fluxes. This is in contrast to the day-time convective boundary layer where the heat budget is balanced locally.

d. Flux Profiles

Although it was not practicable to make explicit observations of the eddy heat fluxes at several levels in the BL, the general form of the eddy flux profiles can be determined from the boundary conditions at the surface and cloud top, and the need to balance the radiative loss in the top part of the cloud by a maximum of upward convective heat flux of about 65 W m^{-2} in the interior of the cloud. This leads to a profile of the form shown in Fig 3, and which is similar in form to that deduced by Deardorff (1976) for nocturnal Sc.

e. Cloud Water Budget

Sub-adiabatic liquid water content is positive evidence of cloud top entrainment, but does not by itself give a quantitative estimate of the observed ratio ($\frac{3}{4}$) of liquid water content (q_l) to its adiabatic value (q_{ad}).

A simple quantitative theory is proposed in which it is suggested that the profile of q_l is determined by the difference between the saturated vapour pressure profile, and the profile of total water substance. The latter in turn is controlled by the requirement to balance the heat and water budgets by turbulent transfer, and leads to an expansion

$$\left(q_{ad}-q_l\right)_h=-\frac{C_p}{L}\int_0^h\frac{E_w}{H}\frac{\partial\theta_e}{\partial z}\,dz \qquad (2)$$

where the integral is performed from cloud base to height h above it.

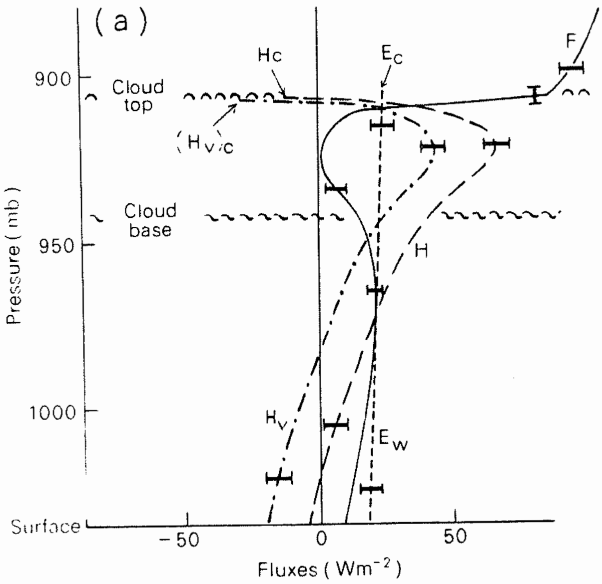

Figure 3 Flux profiles – upward directed fluxes positive

F – observed radiative net flux

H – inferred profile of total eddy heat flux

H_v – inferred profile of virtual heat flux

E_w – inferred profile of total water substance flux

H_c – total entrainment heat flux

$(H_v)_c$ – virtual entrainment heat flux

E_c – latent entrainment heat flux

$E_w = \rho L \overline{w'q'_w}$ = energy equivalent of eddy flux of total water substance

$H = \rho C_p \overline{w'\theta'_e}$ = total eddy heat flux

θ_e = equivalent potential temperature

$= \theta\left(1 + \frac{Lq}{C_p T}\right)$

Application of Eq 2 to profiles in Fig 3 shows that q_l/q_{ad} increases from about 0.7 at cloud base to about 0.8 near the base of the radiatively cooled layer of cloud, which is in substantial agreement with observation.

The large fluctuations in total cloud liquid water content (as observed by microwave radiometer) over periods of 1–3 hours is attributed to the fact that a change in total water substance is likely to appear entirely as a change in total cloud water since total vapour content in cloud is tied to the saturated vapour pressure curve along a steady state temperature profile. Thus a decrease of 1% in total water substance in one hour will induce a decrease of about 30% in total cloud water in the same period, and will require a heat input of about 10 W m^{-2}. This decrease can be achieved by a decrease in the supply of water vapour eddy flux into cloud base, or by an increase in the entrainment rate or of the dryness of air from above cloud. Superimposed on this will be a requirement to maintain air subsiding through cloud at saturation – the vertical advection term in the water budget.

It seems likely that an imbalance of about 10 W m^{-2} resulted in the dispersal of cloud some 100 km downstream of Cardington.

5. Conclusions

The locally steady conditions facilitated the inference of tentative relationships between subsidence rate, cloud top entrainment and the heat, water and cloud water budgets of the atmosphere from cloud top to ground.

Subsidence rate was indirectly inferred to be about 0.5 cm s^{-1} and to persist down to a shallow stable surface layer about 20 mb deep where it is dispersed by frictionally induced divergence (Ekman suction).

It appears that only about one-third of the radiative loss from cloud top was accounted for locally (ie by surface and cloud top entrainment fluxes), the balance being mainly accounted for by horizontal advection.

The observed ratio ($\frac{3}{4}$) of liquid water content to its adiabatic value is accounted for in terms of the ratio of eddy fluxes of total water substance and total heat. An account is also give of the observed large fluctuations of total cloud water and the downwind dispersal of cloud.

References

Caughey, S J, Kitchen, M and Slingo, A, 1980, "Simultaneous measurements of the turbulent and microphysical structure of nocturnal Stratocumulus clouds", Preprint Vol 8th Int Conf Cloud Physics.

Deardorff, J W, 1976, "Clear and cloud-capped mixed layers: their numerical simulation, structure, growth and parametrization", ECMWF Seminar, Reading 6–10 September 1976, pp 234–284.

Roach, W T and Slingo, A, 1979, "A high resolution infrared radiation transfer scheme to study the interaction of radiation with cloud", Quart J R Met Soc, 105, pp 603–614.

Slingo, A and Brown, R, 1980, "High resolution radiative and microphysical observations of nocturnal Stratocumulus", Preprint Vol 8th Int Conf Cloud Physics.

SENSITIVITY OF A LOW STRATIFORM CLOUD MODEL TO ITS MICROPHYSICAL PARAMETERS

R. Rosset (1), C. Fravalo (2) and Y. Fouquart (3)

(1) LAMP, Clermont-Ferrand, (2) LPARA, Brest, (3) LOA, Lille - FRANCE

It has long been recognized that extensive sheets of low clouds play a significant role in the energy budget at the earth's surface. These stratiform clouds maintain a delicate balance between thermodynamic, dynamic and radiative processes. In order to elucidate the relative importance of these different processes, we propose a comprehensive one-dimensional parametric stratiform cloud model designed with an equal stress put on all the processes. This requirement of equal stress has led us to a detailed formulation of the radiative fluxes, thus requiring emphasis to be put on the cloud microphysical characteristics.

I - Microphysics in a low stratiform cloud model

The intense mixing in a cloud-topped mixed layer of thickness H under an inversion results in a uniform vertical distribution of the moist static energy h and the total water content σ. This in turn implies a linear vertical variation for the following quantities : $F_h(z) + RL(z) + RS(z)$ and $F_\sigma(z)$, where RL(z) and RS(z) are the net long - and short - wave radiative fluxes and where FR(z) and $F_\sigma(z)$, the turbulent fluxes of h and σ at any level z are expressed as :

$$F_h(z) = F_{hs} - \frac{z}{H}(F_{hs} - F_{hH} + RS + RL) + RS - R(z) \qquad (1)$$

$$F_\sigma(z) = F_{\sigma s} - \frac{z}{H}(F_{\sigma s} - F_{\sigma H}) \qquad (2)$$

with $R(z) = RS(z) + RL(z)$, and the subscripts H and s respectively referring to the inversion and top of the surface layer levels.

Equations (1) gives the relationship between the turbulent $F_h(z)$ and radiative R(z) fluxes. Thus, within the cloud, due to R(z), $F_h(z)$ is non-linear with height as opposed to $F_\sigma(z)$ which is not directly affected to the radiative fluxes. This non-linearity mainly appears in the upper part of the cloud deck. There, the positive R(z) divergence implies $F_h(z)$ to be negatively divergent in order to satisfy equation (1). In consequence the vertical profile of the turbulent virtual static energy flux $F_{sv}(z)$:

$$F_{sv}(z) = \alpha F_h(z) - \varepsilon L\, F_\sigma(z) \qquad (3)$$

is non-linear in the cloud. Below the cloud base, $F_sv(z)$ turns out to be linear according to the relation :

$$F_{sv}(z) = F_h(z) - (1 - \delta\varepsilon)\, LF_\sigma(z) \qquad (4)$$

where the parameters :

$$\varepsilon = \frac{C_p T}{L} \; ; \; \alpha = \frac{1 + (1+\delta)\varepsilon\gamma}{(1+\gamma)} \; ; \; \gamma = \frac{L^2 q}{RvC_p T^2} ,$$

remain approximately constant with height - (T, absolute temperature ; q, water vapor mixing ratio ; L, latent heat of condensation; C_p, specific heat of the air at constant pressure ; Rv, the gas constant for water vapor ; $\delta = 0.61$).

Only Deardorff's 1976 model includes a radiative flux divergence layer of finite thickness and strenght (Kahn & Businger, 1979). In order to remedy this arbitrariness and in agreement with Paltridge's data (1971, 1974), we explicitly compute the radiative fluxes at any level in the mixed layer. In order to do so, we need to retain the microphysical characteristics of the cloud medium. More precisely, the mixed layer is divided into seven horizontally homogeneous sub-layers, six in the cloud and only one below. Within each sub-layer, the temperature, water vapor and liquid water ℓ mixing ratios are computed, this latter parameter defining in its turn the cloud spectrum.

We assume for the liquid water content $\ell(z)$ in the cloud a relationship of the form :

$$\ell(z) = \frac{g\beta}{L(1+\gamma)} A(z - z_c) \qquad (5)$$

where $\beta = \gamma - \frac{Lq}{\delta RvT}$, with g, acceleration of gravity ; z_c : cloud base height ; A is an empirical "diabatism" coefficient between 0 and 1 and is equal to the ratio of real ℓ to adiabatic ℓa liquid water contents.

In the framework of a simplified Mie theory, assuming a modified Γ distribution and on the basis of Paltridge's experimental results (1971, 1974) we represent the drop size distribution by its effective mean radius r_e (in μm), written as :

$$r_e = \frac{3}{2}(30\,\rho\ell + b) \qquad (6)$$

ρ being the air density (in g/l), ℓ in g/m^{-3} and b an adjustable parameter typically equal to 2 μm for maritime stratocumulus (Stephens, 1978).

A and r_e, together with $\ell(z)$ completely define the microphysical cloud properties in the radiation computations (Morcrette, 1978 ; Fouquart and Bonnel, 1979). Another original characteristics of our model is to be found in the formulation of the entrainment velocity w_e in terms of the turbulent as well as of the radiative fluxes (Fravalo et al., 1979).

II - Sensitivity tests

Our model is run on the basic data set described in Lilly (1968) and Deardorff (1976).

II.1 Coefficient A

For A between 0.02 and 0.8, the computed liquid water contents vary between 9.6×10^{-3} to 0.38 g/kg at the inversion level. In Fig. 1, 2 and 3 are reproduced as functions of A, the vertical profiles of RL(z) and RS_s - RS(z), F_h(z) and F_{sv}(z).

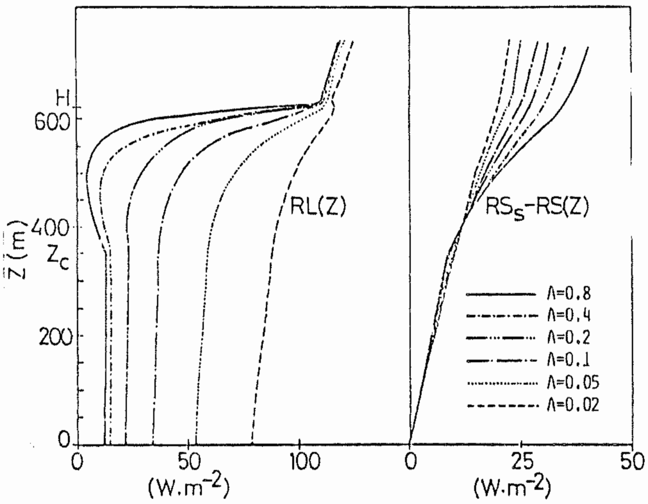

Figure 1 : *Evolution of the vertical profiles* RL(z) and RS_s - RS(z) *with the coefficient* A.

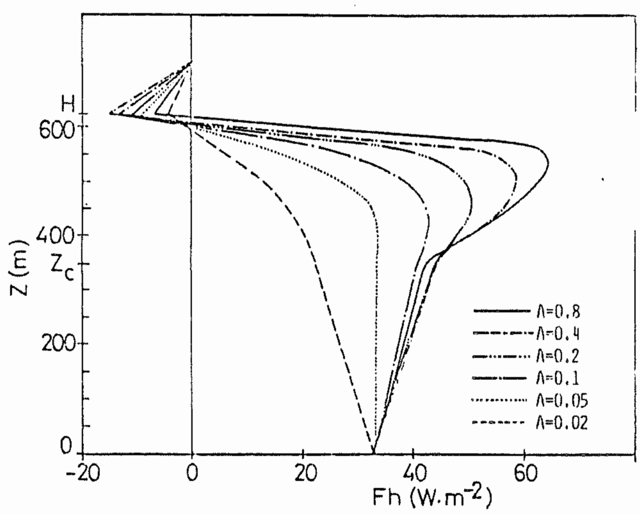

Figure 2 : *Evolution of the vertical profiles* F_h(z) *with* A.

Obviously, all the curves exhibit a strong dependence on A, particularly within the cloud. The second point to be noticed is in the existence of two domains separated by values of A between 0.1 and 0.2.

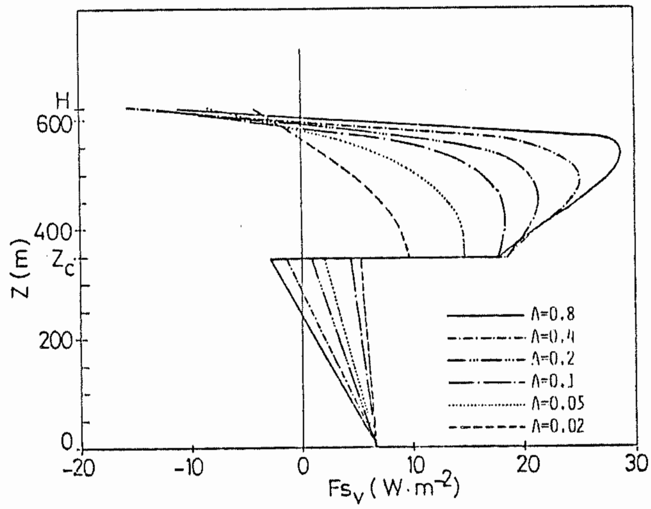

Figure 3 : *Evolution of the vertical profiles* F_{sv}(z) *with* A.

This is particularly clear on Fig. 4 which gives the variation of the entrainment velocity w_e as a function of A : w_e varies very rapidly with the cloud liquid water content for the lower values of this parameter. For A > 0.2, a kind of saturation effect can be observed on all the preceding figures, being more pronounced as A approaches unity.

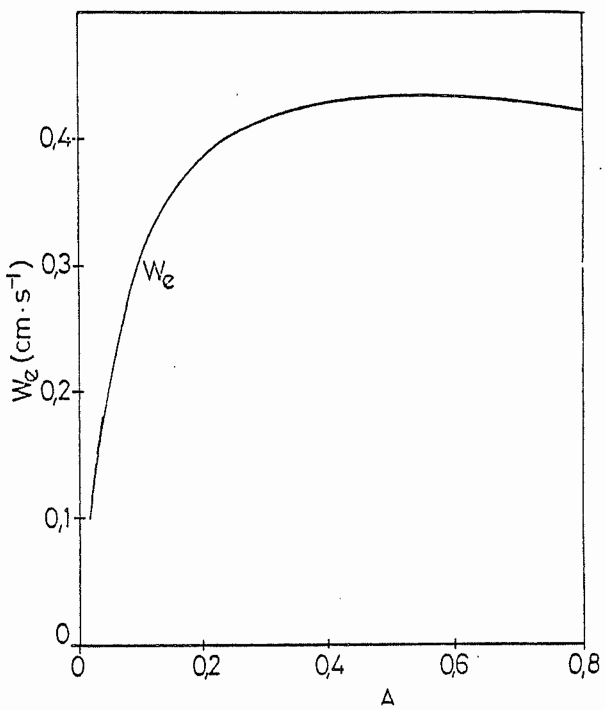

Figure 4 : *Evolution of the entrainment velocity* w_e *with* A.

II.2 Effective mean radius r_e

In the following, assuming a constant total precipitable liquid water content of 16 g/m^3 (with l_H = 0.096 g/kg and A = 0.2), we have varied the mean effective radius r_e from 5 µm to 14 µm. The first case corresponds to small droplets (b = 0.5 µm) and the second one to larger droplets (b = 6 µm) ; roughly approximating non-precipitating and precipitating clouds.

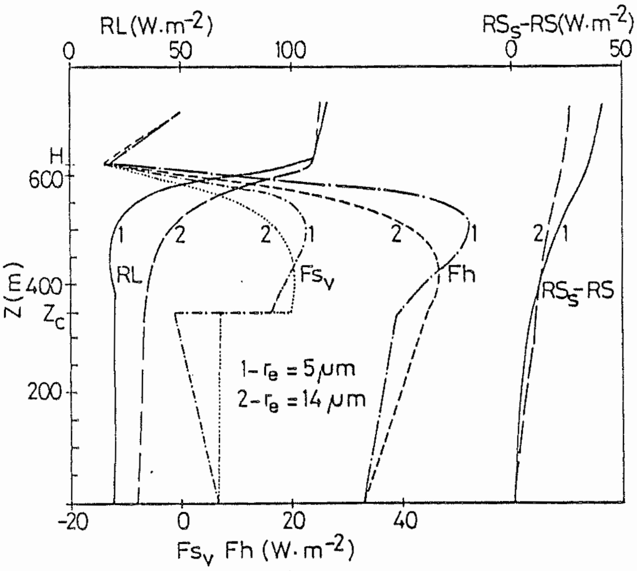

Figure 5 : Comparison of the vertical radiative and turbulent fluxes profiles for two different cloud microstructures but with the same liquid water content (ℓ_H = 0.096 g.kg^{-1}).

Our results show that the effective radius r_e modifies only slightly the vertical profiles of fluxes (Fig. 5) as well as the entrainment velocity w_e (Fig. 6).

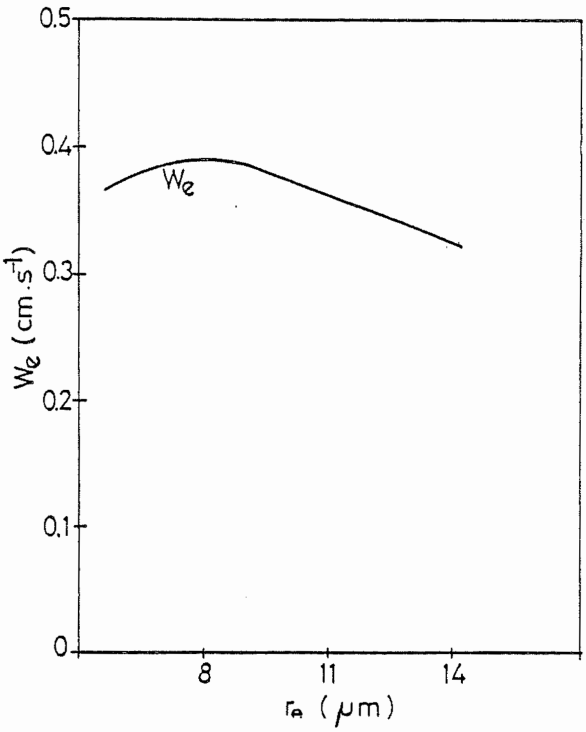

Figure 6 : Variation of the entrainment velocity w_e *with the effective mean radius* r_e.

III - Conclusions

The ultimate goal of the model is in the parameterization of the planetary boundary layer with stratiform clouds. Our present purpose here was to put the stress on its microphysical aspect, in connection with the turbulent and radiative fluxes. Our model has thus proved to be useful in specifying quantitative relationships between all these three types of terms. The main conclusion can be found in the great sensitivity of the results to the liquid water mixing ratio in the cloud deck, much greater than to the droplet spectra. The experimental implication is quite clear : the liquid water content in clouds must be measured with great care and accuracy when coupled with radiative measurements and computations. Preliminary measurements (not reported here) giving values of A smaller than 0.2 support this conclusion. The question remains about the factors which determine the values of A.

Acknowledgments

Thanks are due to Centre National de la Recherche Scientifique (RCP and ATP Pirdes) for its financial support.

References

Deardorff, J.W., 1976 : On the entrainement rate of a stratocumulus topped mixed layer. Quart. J. Roy. Meteor. Soc., 102, 563-582.

Fravalo, C., Fouquart Y. and R.Rosset, 1979 : A model of low stratiform clouds. Submitted to the J. Atmos. Sci.

Fouquart, Y. and Bonnel B., 1979 : Computations of solar heating of the earth's atmosphere : a new parameterization. To appear in Contrib. Atmos. Phys.

Kahn, P.H. and Businger J.A., 1979 : The effect of radiative flux divergence on entrainment of a saturated convective boundary. Quart. J. Roy. Meteor. Soc., 105, 303-306.

Lilly, D.K., 1968 : Models of cloud-topped mixed layers under a strong inversion. Quart. J. Roy. Meteor. Soc., 94, 292-309.

Morcrette, J.J., 1978 : Infrared fluxes in stratiform model clouds. Contrib. Atmos. Phys., 51, 338-351.

Paltridge, G.W., 1971 : Solar and thermal radiation flux measurements over the east coast of Australia. J. Geophys. Res., 76, 2857-2865.

Paltridge, G.W., 1974 : Infrared emissivity short wave-albedo and the microphysics of stratiform water clouds. J. Geophys. Res., 79, 4053-4058.

Stephens, G.L., 1978 : Radiation profiles in extended water clouds, I : theory. J. Atmos. Sci., 35, 2111-2122.

HIGH RESOLUTION RADIATIVE AND MICROPHYSICAL OBSERVATIONS OF NOCTURNAL STRATOCUMULUS

A.Slingo and R.Brown

Meteorological Office, Bracknell, U.K.

1 Introduction

This paper presents detailed observations of the radiative and microphysical structure of nocturnal Stratocumulus clouds on three occasions. It forms part of a comprehensive study of this type of cloud carried out by the U.K. Meteorological Office, using the tethered balloon facility at Cardington, Bedfordshire. Other aspects of this work are described by Roach et al. (1980), hereafter referred to as Paper I, and Caughey et al. (1980) (Paper II). The observations are relevant to the physics of radiative transfer and the mixing processes which occur in these clouds.

2 Instrumentation

A description of the balloon-borne instrumentation is given in Paper I. Dropsize data were obtained with a modified Axially Scattering Spectrometer Probe (ASSP), from which two estimates of the drop concentration were used to scale the drop-size distribution to produce two estimates of liquid water content. The first was obtained from only those drops which the processing electronics accepted for sizing, being within the so-called "Inner" sampling volume. As a check, a second estimate was derived from all the drops capable of producing a signal at the main photodetector above some threshold, but which were not necessarily accepted for sizing. These result from drops within the larger "Outer" volume.

Measurements were also made with a ground-based 95 GHz radiometer operated by the Appleton Laboratory. The contribution to the sky emission from the liquid water component was deduced and used to derive the integrated liquid water content of the column above the instrument. All three case studies show high frequency variability due to irregularities on a spatial scale of about 1 km, superimposed on longer period drifts due to mesoscale changes in the boundary layer structure.

The observed net infra-red radiative fluxes were corrected for the obscuration of the sky by the radiometer guard rings and by the balloon. The absolute accuracy of the corrected fluxes is estimated to be 10 per cent, although relative changes smaller than this can be identified. Theoretical fluxes from the high resolution infra-red radiation scheme of Roach and Slingo (1979) were obtained using the observed profiles of temperature, humidity mixing ratio, liquid water content and drop-size distribution as input data.

3 Results a) 19/20 November 1976

This case study is discussed in detail in Paper I. Figure I illustrates the cloud microphysical data obtained with the ASSP during the first balloon profile.

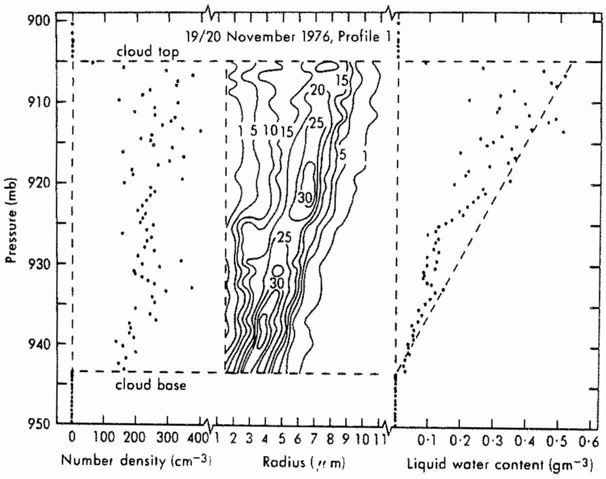

FIGURE 1.

The liquid water contents are the Inner volume estimates, scaled by a single factor so that the integrated liquid water path is equal to that measured by the microwave radiometer during the same period. The liquid water contents show considerable variability from point to point, but there is a systematic increase with height above cloud base at slightly less than the adiabatic rate, shown by the dashed line in Figure 1. In all three case studies the liquid water path inferred from the microwave radiometer data is smaller than the adiabatic value, the mean ratio being 0.75. There is some evidence for increased variability above 920 mb, the amplitude of which varies from profile to profile. Note the very sharply defined cloud top. The drop spectra are presented as contours of the percentage normalized spectral density, which allows the shape of the spectrum to be studied independently of the total liquid water content. The size distribution at any height may be reconstructed by noting that, for example, a value of 25 at 5.5 μm means that 25 per cent of the drops lie in the radius range 5-6 μm. The mode radius rises from about 3 μm at cloud base to about 8 μm at cloud top. The spectral dispersion, which is the ratio of the standard deviation to the mode, is roughly constant with height at about 25 per cent.

It is remarkable that, at any given height, the spectrum and mode radius are virtually unaffected by the liquid water content fluctuations. This means that the fluctuations are caused principally by variations in the total number of drops per unit volume. This is confirmed by the left hand diagram, which represents the drop total number density profile. The diagram also shows that the total number of drops per unit volume shows no systematic trend with height, so that the progressive increase of liquid water content with height is almost entirely provided by the increase in the mode radius.

The observed net radiative fluxes and the theoretical fluxes from the high resolution radiation scheme are compared in Figure 2.

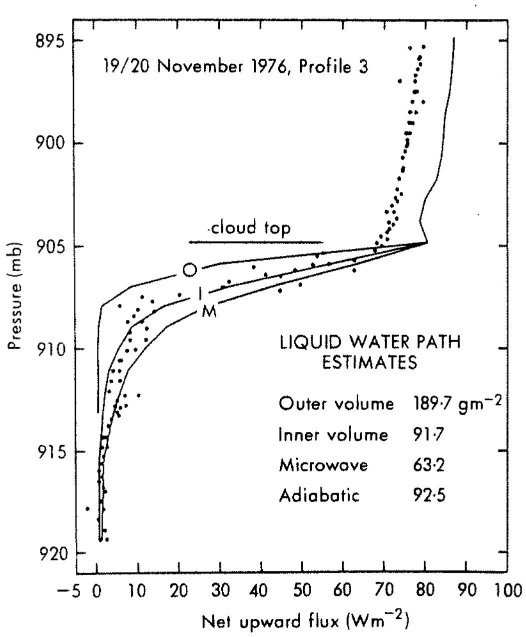

FIGURE 2.

Data from the initial balloon ascent below cloudbase have been merged with the third profile. The midnight radiosonde ascent from Hemsby (roughly 100 km upwind of Cardington) was used to complete the temperature and humidity profile above the balloon data. The radiation scheme was run with a surface temperature of 7.5°C and 1000 vertical levels, giving a resolution of about 1 mb. The solid curves indicate the theoretical profiles using the liquid water content estimates from the ASSP Inner (I) and Outer (O) volumes and also from the ASSP Inner volume estimate, scaled by the microwave radiometer (M). There is an uncertainty of about 0.5 mb in the positioning of the theoretical profiles owing to the 10 second sampling period and the resolution of the radiation scheme. The observed flux profile in the inversion shows a gradually increasing curvature as the cloud is approached due to the increasing contribution of the upward flux from the cooler cloud top. It is suggested in Paper I that the energy balance in this region is between radiative cooling and subsidence heating. The net fluxes show the expected rapid decrease as the cloud is entered, with the cloud becoming optically thick after about 10 mb, or 30 gm^{-2} liquid water path. The closeness of the theoretical curves makes it difficult to assess which is the best liquid water content estimate, but the Outer volume can be seen to be too high, while the Inner and Microwave values give closer agreement. The small ovestimate of the net flux above cloud top may be due to the radiosonde data being unrepresentative of the real profile, or to inaccuracies in the correction of the observed fluxes.

b) 26/27 October 1977

During the period of these observations Cardington lay in a southerly airstream on the edge of an anticyclone which was centred over northern Germany. The synoptic situation was less settled than in the previous case study and the cloud was thinner and more broken. Some problems were experienced with the ASSP on this occasion. The Inner volume particle counts were seriously underestimated and the Outer volume counts overestimated, in comparison with the microwave radiometer. It is believed that this was caused by low frequency oscillations of the signal baseline voltage. Laboratory simulations have shown that the derived drop-size distributions should not be affected by these counting errors. Despite these difficulties, there is good agreement between the observed and theoretical net fluxes when the liquid water path is corrected to the microwave radiometer value (Figure 3). All the corrected profiles underestimate the net flux towards cloud base, however, suggesting that the relative liquid water contents were overestimated here.

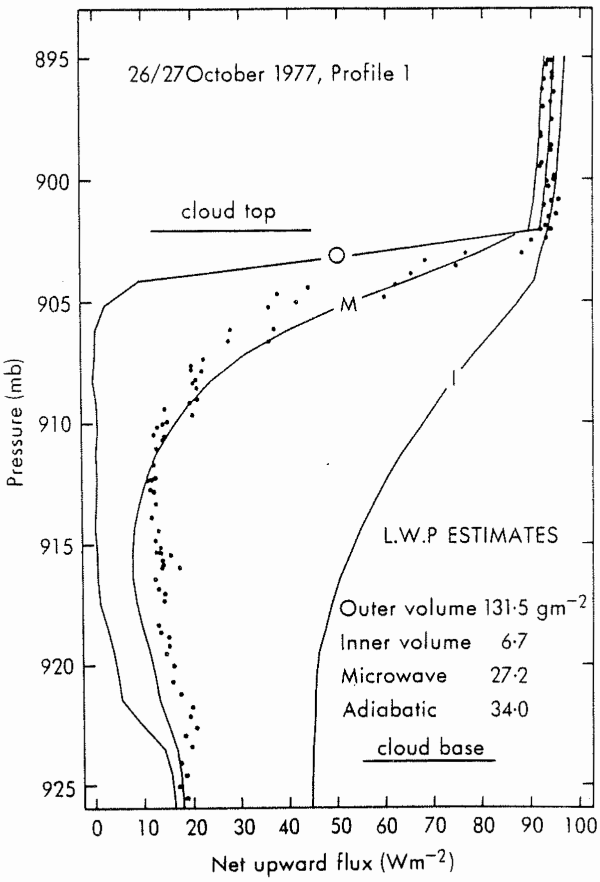

FIGURE 3.

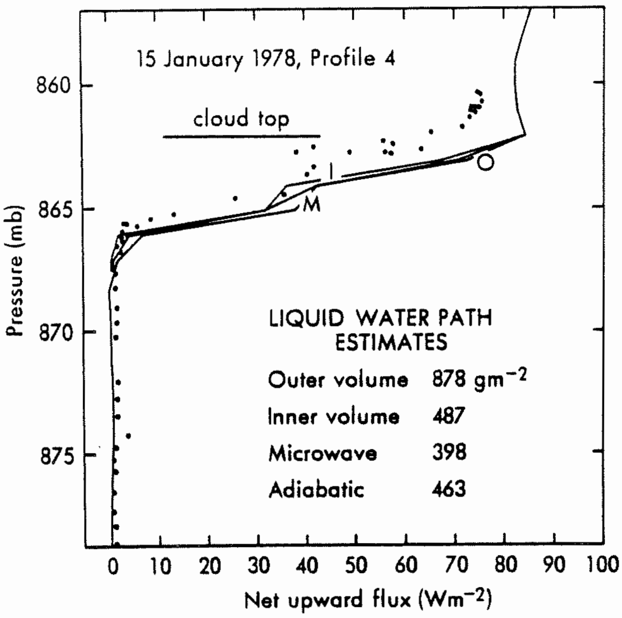

FIGURE 4.

c) 15 January 1978

On this occasion the British Isles were covered by a complex area of falling pressure between two anticyclones, centred over the North Atlantic and eastern Europe. Winds were light (1-3 ms^{-1}) and variable in direction between East and South, with a persistent and deep cloud layer variously reported as Stratus or Stratocumulus. The drop-size distributions showed little variability apart from a steady increase of mode radius from 4 μm at cloudbase to about 8 μm at cloud top, with a spectral dispersion of 22 ± 1 per cent throughout most of the cloud. Large fluctuations in liquid water content were observed which, as in the first case study, were related to variations in the total number density, rather than the shape of drop-size spectrum. The optical thickness of the cloud top was so large that all the liquid water content estimates lead to similar theoretical net flux profiles, which fall rapidly to near zero within the cloud (Figure 4). The observed fluxes show similar sharp gradients to the theoretical curves, the vertical displacement being within the expected error in positioning the theoretical fluxes.

4 Discussion

Latham and Reed (1977) have described Laboratory studies of the evolution of cloud drop spectra following the mixing of controlled amounts of saturated and under-saturated air. They found that changes in the total number of drops and in the liquid water content resulted, while the shape of the drop-size spectrum remained essentially unchanged. This result is inexplicable if the two air streams are mixed homogeneously, as this would lead to a significant reduction in the mean drop-size and an increase in the spectral dispersion as the drops evaporate in the now uniformly undersaturated air. If the mixing process is inhomogeneous, however, the new air mass consists of some regions where very little dry air has been mixed in and others where the proportion is much larger and has led to complete evaporation of all the drops. Inhomogeneous mixing therefore removes some drops of all sizes and results in changes in the total number density without affecting the spectrum. The present observations show similar behaviour and it seems possible that the inhomogeneous mixing process was operating in these clouds. The effect is most striking towards cloud top which suggests that the two streams being mixed are the cloudy air with the dry inversion air entrained at the cloud top. It is interesting that evidence for this process is apparent through a considerable fraction of the cloud depth. Further examples of inhomogeneous mixing are discussed in Paper II.

The shape of the net flux profiles and their position relative to the cloud top and inversion step are important in visualizing the cloud top entrainment process. It is clear that the bulk of the infra-red cooling occurs in the cloud itself and is due directly to the opacity of the cloud liquid water. The flux profiles are therefore constrained to follow the liquid water distribution, so that if the cloud top is deformed by turrets or gravity waves, the flux profiles will also deform to follow the liquid water. The amount of flux divergence available to initiate entrainment directly from above the cloud is therefore small and this supports the view that entrainment results indirectly from the motions induced within the cloud top by the radiative divergence. It is also important to note that since the majority of the infra-red cooling takes place within the cloud, this term must be included in the energy budget of the boundary layer, where it makes the dominant contribution (see Paper I).

5 References

Caughey S.J., Kitchen M. & Slingo A., (1980) "Simultaneous measurements of the turbulent and microphysical structure of nocturnal Stratocumulus clouds.", Preprint vol., 8th Int. Conf. Cloud Physics.

Latham J. & Reed R.L., (1977) "Laboratory studies of the effects of mixing on the evolution of cloud droplet spectra.", Quart. J. R. Met. Soc. 103, 297-306.

Roach W.T., Brown R., Caughey S.J., Crease B.A. & Slingo A., (1980) "A field study of nocturnal Stratocumulus.", Preprint vol. 8th Int. Conf. Cloud Physics.

Roach W.T. & Slingo A., (1979) "A high resolution infra-red radiative transfer scheme to study the interaction of radiation with cloud.", Quart. J. R. Met. Soc. 105, 603-614.

THE MODIFICATION OF DROP SPECTRA IN SEA STRATUS BY ENTRAINMENT

J.W. Telford, P.B. Wagner and S.K. Chai

Desert Research Institute
Reno, Nevada, USA

1. Introduction

One of the primary outstanding problems of cloud physics has been the need to provide an adequate explanation of how, large enough drops can form by condensation in cumulus clouds, to begin rain formation by coalescence. More directly it is neccessary to explain the observed drop size spectrum of cumulus clouds which show droplets of all radii up to a maximum, which far exceeds the sizes found by calculations of condensation growth in rising air parcels. Condensation growth leads to narrow radius distributions with smaller drops increasing proportionally in radius during condensation, faster than larger sizes. Various modifications to the process have changed this theoretical size distribution to various degrees but the changes so produced have never been large.

This paper shows how mixing of dry air in at cloud tops totally deactivates nuclei by completely evaporating them, and so removing them effectively from further action. Mixing between the evaporation-chilled parcels which are now dense enough to descend, and surrounding rising air, slowly increases the total water mixing ratio in the descending parcels, but the drops introduced at the higher levels completely evaporate as descent continues. This process broadens the spectra, all small drop sizes thus being formed while the large drops from undiluted updrafts are continually being added in by mixing. This process explains the broadening of the droplet spectrum.

The dilution process described above reduces the total water mixing ratio to less than adiabatic uplift from cloud base would allow, in effect it raises the lifting condensation level. The spectrum now contains droplets much larger than would be formed by lifting a fresh air parcel of the same mixing ratio up though the new lifting condensation level to the present level, although the largest drops are smaller than in the first original unmixed updraft.

However, now let us cycle this parcel upwards again. The number concentration of drops is far less than before, and we start off with large droplets, equivalent to the giant condensation nuclei of earlier studies. These largest drops now grow by condensation to sizes much exceeding the sizes attained in an original undiluted updraft at the same height.

This theoretical explanation was originally studied in order to explain observed drop spectra in cumulus clouds. However, the process should work equally well in marine stratus. Here, as in cumulus cloud, cloud top entrainment of dry air into cloud tops produces similar effects. However, in the stratus case the cloud has no edges to interface with the process so that a gradual descent through cloud gives a series of samples at different heights.

This paper presents a sample of the computed spectra and discusses data which shows that in a stratus cloud the process is even more efficient, producing drops 32 μm in diameter in clouds only a hundred meters or so deep.

2. The Theory

The growth of the droplets was calculated using regular condensation theory. The approximations necessary relate to grouping the drops present, into regular radii ranges. A further approximation relates to the nuclei released when the drops evaporate. No account has been kept of the modification of the nuclei spectrum in this way, and it has been assumed that the drops present always have removed the same number of the largest nuclei from the nuclei spectrum. This approximation will have an influence on the nuclei reactivated during later upward motion, but we do not believe this approximation will make a qualitative change to the results, and its correction requires a very substantial computational effort not justified until a better dynamical description becomes available.

This discreteness in radii also leads to irregularities in the histogram which would be smoothed out in a more extensive calculation, but once again the conclusions will not be affected.

In this study we take a parcel of air at cloud base and raise it 2000 m, add dry air until it just evaporates, return it to 1000 m, raise it to 2000m, return to 1500 m and raise it again to 2000 m, etc. In our earlier paper (Telford and Chai, 1979), the parcel cycling up and down mixes with the cloud air from the previous cycle at each 50 m level. In this paper, in order to check the effect on the droplet spectrum broadening of mixing at closer intervals, we did some calculations with mixing processes taking place at each 25 m.

The air first rises from cloud base to cloud top (2000 m) without mixing. The entrainment of dry air at cloud top evaporates all the drops. This droplet free air then sinks down to 1000 m, mixing with the original updraft at each 25 m level. The mixing rate chosen maintains a liquid water mixing ratio of 0.1 gm/kgm. After a 200 second dwell time at 1000 m, the air is then raised again to the cloud top, mixing with the previous downdraft at each 25 m interval. The mixing rate is 2.5% in volume at each such step.

Figure 1 shows the droplet spectrum at 1500 m during the second ascending cycle. Comparing with Figure 2, which is the case where the mixing processes take place at each 50 m interval. We can see that no major difference in the droplet spectra occurs from this change except that a more continuous spectrum can be found in Figure 1. In Figure 1, the droplet number density is 451 cm^{-3}, the liquid water mixing ratio is 0.73 gm/kgm, the water vapor mixing ratio is 5.82 gm/kgm and the supersaturation is 0.16 percent. In Figure 2, the droplet number density is 444 cm^{-3}, the liquid water mixing ratio is 0.81 gm/kgm, the water vapor mixing ratio is 5.83 gm/kgm and the supersaturation is 0.12 percent.

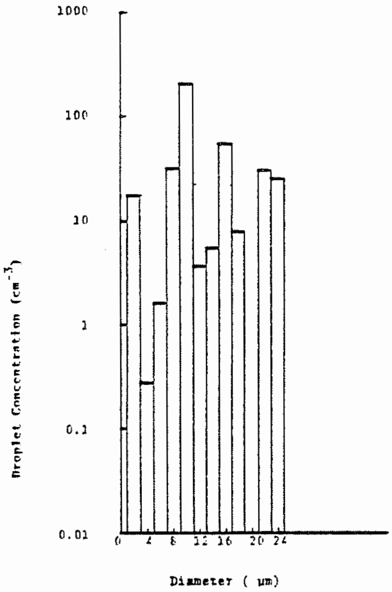

Figure 1. This histogram shows the cloud droplet spectrum at 1500 m in a parcel which first rose adiabatically to 2000 m and after mixing descended again to 1000 m with sufficient mixing with the adjacent cloud from the previous stage, at each 25 m level, to maintain a liquid water content of 0.1 gm/kgm. After a 200 seconds dwell time at 1000 m, the parcel rises again with mixing with the previously downdraft cloud, at each 25 m level, at a rate of 2.5% in volume.

Figure 3 is the droplet spectrum at 2000 m after the second updraft cycle, with mixing at each 25 m, and Figure 4 is that with mixing at each 50 m. Once again, the 25 m case gives a more continues spectrum than the 50 m case does, but no major difference in the two spectra can be found. In Figure 3, the droplet number density is 380 cm^{-3}, the liquid water mixing is 1.07 gm/kgm, the water vapor mixing is 4.92 gm/kgm and the supersaturation is 0.03 percent. In Figure 4, the droplet number density is 364 cm^{-3}, the liquid water mixing ratio is 1.31 gm/kgm, the water vapor mixing ratio is 4.97 gm/kgm and the supersaturation is 0.

From the figures we can conclude that mixing interval makes no difference on the droplet spectrum.

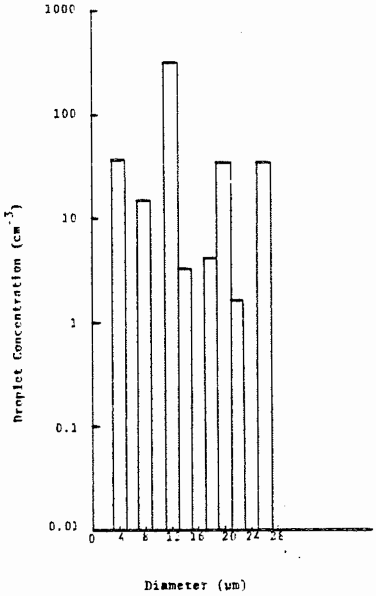

Figure 2. This histogram shows the cloud droplet spectrum at 1500 m in a parcel which experienced the same cycle as in Figure 1, but with mixing at each 50 m level.

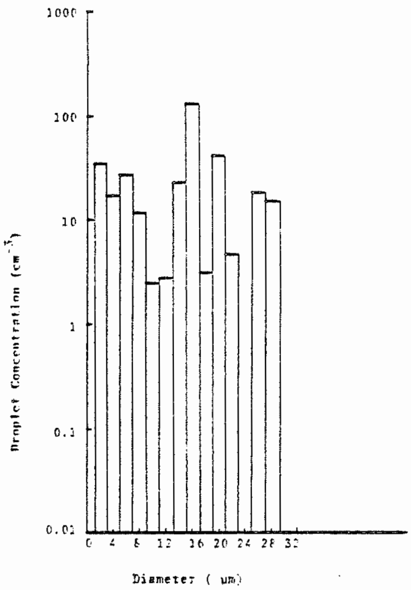

Figure 3. The cloud histogram of Figure 1 after rising to 2000 m.

Figure 5 shows the result of cycling the cloud between 2000- 1000- 2000- 1500- 2000- 1750- 2000 meter, with mixing at each 50 m level. The maximum drop diameter is 34 μm. Cycling this cloud parcel to 3000 m we get the spectrum as shown in Figure 6. We now have a significant number of 40 μm droplets in a cloud where the unmixed droplet spectrum would be all 19 μm droplets. This size is probably sufficent to start the coalescence growth of drops.

3. Stratus Cloud

The theoretical study establishes a procedure for speading the droplet spectrum and generating large drops. The mixing procedure we used was chosen deliberately to be extremely conservative. The observations seem to show however that much more extreme mixing procedures, diluting the cloud droplet concentration by more than a factor of ten, is common. In a thin stratus cloud where the original condensation produces droplet concentrations exceeding 600 drops cm^{-3}, we find parcels in the cloud containing concentrations of less than 100 drops cm^{-3}. The interesting point is that there is a strong correlation of the size of the largest drops with low droplet concentrations (Telford and Wagner, 1980).

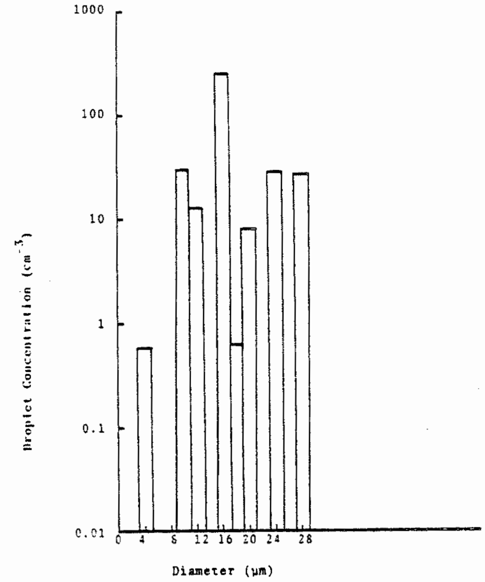

Figure 4. The cloud histogram of Figure 2 after rising to 2000 m.

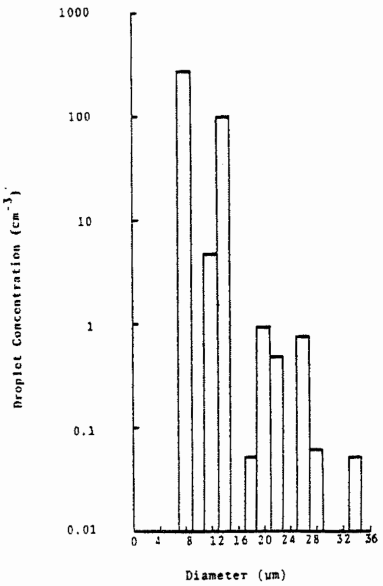

Figure 5. The cloud histogram of Figure 4 after a cycle of 2000-1500-2000-1750-2000 meters.

Figure 7 shows that only with 100 feet from the cloud base the peaks of liquid water content are close to the adiabatic values. The liquid water content is less than the adaibatic value everywhere above this level. Therefore, the newly formed cloud base parcels are wetter than average and must be unstable all the way to cloud top, and thus they might rise rather quickly through the cloud, even if some dilution does occur at each level.

At the cloud top, the droplet spectra is very uniform, from parcel to parcel, with large differences in droplet concentrations. The parcels always contain large numbers of small droplets. This tells us that the predominent mixing results from the penetrating downdrafts,

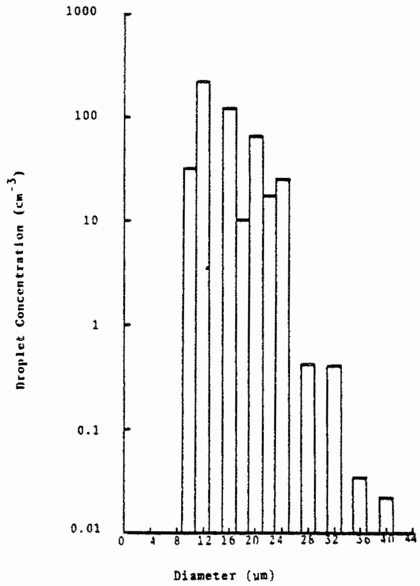

Figure 6. The cloud histogram of Figure 5 after cycling up over an additional 1000 m.

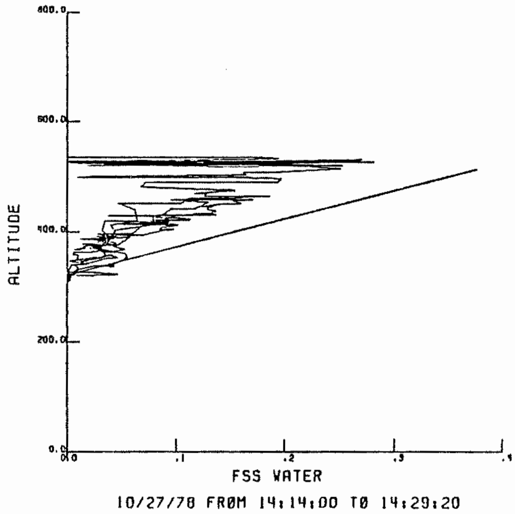

Figure 7. The liquid water mixing ratio derived from the drop spectrum as a function of altitude. The adiabatic liquid water mixing ratio based on the cloud base height has been added to the graph.

and that it is associated with drastically reduced liquid water contents, and actually results from a mixing process which has little effect on the droplet sizes. Evaporation totally removes drops until the intruding dry air is saturated and then the drops are separated further apart without changing sizes. However a very slight reduction in the size of the smaller drops also suggests that some mixing of a different type occurs which preferentially reduces smaller drops.

Figure 8 shows the 95 percentile liquid water diameter as a function of altitude. The largest drop is almost constant at 18 μm, from parcel to parcel, at cloud top. The liquid water mixing ratio and the droplet concentrations vary there by a factor of 10. Deeper in the cloud, the diameter of the largest drops varies greatly from parcel to parcel. The largest of these large drops increases from 18 μm to 32 μm at cloud base. This appears to be the result of vertical cycling in the mixing process, like our theoretical analysis depicts.

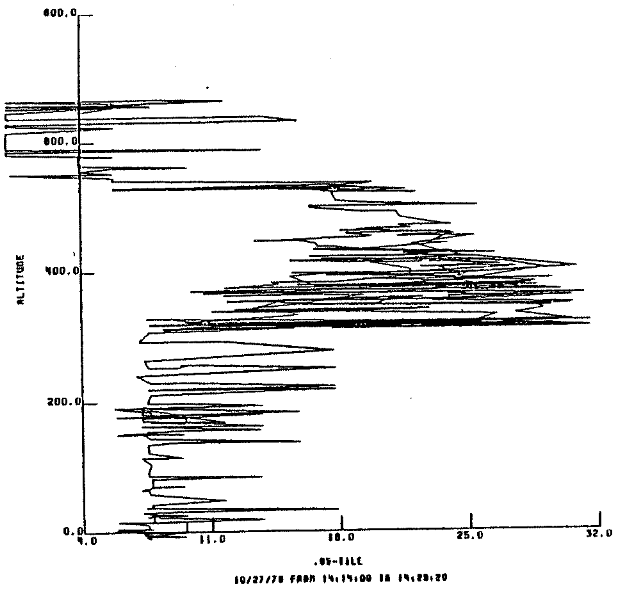

Figure 8. The diameter of the largest drops in micrometers (this is the 95% volume diameter) as a function of altitude. The regions below 320 m and above 530 m are outside the cloud region and are not significant because of the extremely small number of drops present.

There is a strong correlation of the size of the largest drops with low droplet concentrations deeper in the cloud. Given one parcel with smaller drops but high droplet concentration, the neighboring parcel may have larger big drops but low droplet concentration. The mixing between such parcels can be important in spectrum broadening.

We have measurements of the vertical air velocity. From this data we can note that the air is more turbulent deeper in the cloud, which supports the vertical cycling hypothesis.

Figure 9 shows the wide range in droplet concentrations at 18 μm which reflects the mixing near the cloud top. Joining those points in Figure 9 in sequence results in Figure 10. From this figure we can see that the points near 18 μm over a wide range of droplet concentration are in adjacent parcels (at cloud top), while in other adjacent samples deeper in the cloud are seen to include large drops and low concentrations near parcels contain small drops with high concentrations.

These observations show that the initial cloud nucleus spectrum has little effect on the mature cloud droplet spectra. There is evidence that the plume model for convective mixing in stratus clouds provides an explanation of some features of the droplet spectra. The generation of large cloud droplets has thus been shown to follow the mixing in of dry air at cloud tops and any suggestion that the cloud nuclei spectra play a dominant role in initiating coalescence processes appears to be extremely dubious.

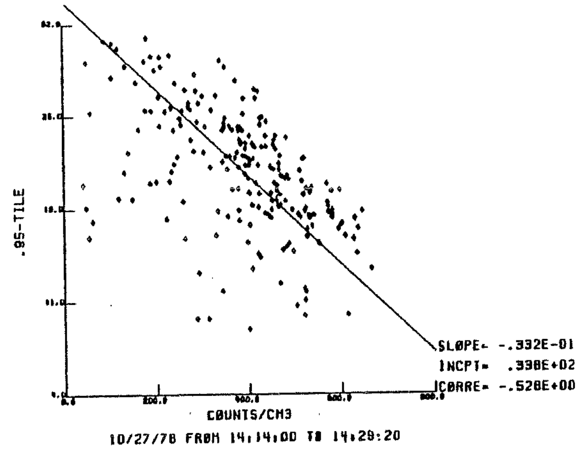

Figure 9. The diameter of the largest drops (the 95% volume diameter) vs. the droplet concentration in drops cm^{-3}. The line minimizes the squares of the perpendicular distance from the line to the points. The points corresponding to cloud top are those near 18 μm and ranging over large concentration changes of ten to one or more.

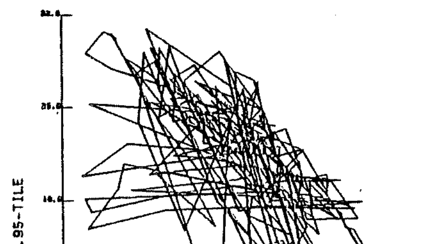

Figure 10. This figure shows the points in Figure 9 joined in the sequence they were observed.

References

Telford, J. W. and S. K. Chai, 1979: A New Aspect of Condensation Theory. Pure Appl. Geophys., in press.

Telford, J. W. and P. B. Wagner, 1980: Condensation Growth not Determined by Nuclei. Submitted for publication.

ON THE INTERACTION OF RADIATION AND CIRRUS CLOUDS

Peter Wendling

DFVLR, Institut für Physik der Atmosphäre, Wessling, Germany

1. Introduction

Clouds play a major role in the radiation balance of the earth-atmosphere system since they emit infrared radiation to space in proportion to cloud top temperature, absorb infrared radiation from below their level and because they reflect a significant fraction of the incoming solar radiation. The effect of cloud on atmospheric heating rates and surface temperature mainly depends on the value of the cloud albedo and on the degree of blackness of the cloud to infrared radiation from below. With regard to cirrus clouds their effects on the radiation budget of the earth atmosphere system are until now not well understood because of our incomplete knowledge of the scattering and absorption properties of non-spherical ice crystals. Furthermore as was shown by Barkstrom (1978) for water clouds the radiative flux divergence within the cloud itself may significantly affect the mass growth rate for reasonably large cloud elements. Since ice crystals are of importance in the initiation of precipitation in supercooled clouds it appears to be of interest to study the effects of radiative flux divergence on the mass growth rate of ice crystals.

The following work presents computations of the radiative flux divergence within cirrus clouds which are based on the single scattering and absorption properties of hexagonal ice crystals in the form of plates and columns. The computation of radiative transfer through the atmosphere is performed by applying the matrix operator method (Plass 1973) which considers multiple scattering. The results are applied to calculate the influence of radiative flux divergence on the mass growth rate of individual ice crystals.

2. Computation method and cloud model

To calculate the single scattering and absorption properties of hexagonal ice crystals we use the ray optics method which has been developed by Wendling et al. (1979). This method allows to determine the optical properties of finite sized hexagonal ice crystals. Radiative transfer calculations through cirrus clouds have been based until now upon the assumption that cirrus clouds consist either of ice spheres or of infinitely long cylinders with a circular or hexagonal cross section. The comparison of our results to previous calculations shows that the scattering of radiation by hexagonal ice crystals of finite size is characterized by a strong backscattering. Based on our method we computed the extinction and absorption coefficients for ice columns, plates and spheres. The results for ice spheres are based on Mie calculations. The matrix operator method is used to solve the radiative transfer equation and to calculate fluxes and cooling / heating rates. With this method clouds of very high optical thickness can be built up quickly once the initial operators for an infinitesimal layer of optical thickness $\Delta\tau$ are given. Internal sources such as the Planck black body radiation are included in our calculation. Our results mainly refer to the radiative cooling within the atmospheric 8 - 12 µm window region where the radiative flux divergence strongly affects the mass growth of cloud elements.

The assumed model atmosphere consists of the emitting ground and an emitting atmosphere below and above the cloud. The absorption and emission by the water vapour continuum is included in our final calculations. This is done by splitting into monochromatic problems by fitting the gaseous transmission function with a sum of exponentials. The cloud itself is assumed to be isothermal and to have an ice crystal size distribution uniformly distributed with height.

3. Results

We performed calculations of the 8 - 12 µm window cooling rate within cirrus clouds as function of crystal size and shape for different cloud height and thickness. The results given in Fig. 1 to Fig. 4 are for ice clouds consisting of plates (size: a = 50 µm, c = 10,8 µm, 2a = base diameter) or columns (a = 15 µm, c = 120 µm) with a concentration of 0.1 cm^{-3}. The computations are done for a cloud thickness of 100 m and 1000 m. The results until now do not include the water vapour continuum absorption. Our results show the well known behaviour of clouds, cooling near cloud top and warming near cloud base. As the cloud is placed higher in the atmosphere the difference between cloud and ground temperature increases and the cloud experiences a warming. When the cloud is thin we can have a warming at all cloud levels (Fig. 4). The highest cooling rate in the upper cloud part is about 0.5 °C/h.

With regard to the effect of crystal shape on cloud heating or cooling our results demonstrate that for plates with the same volume as columns heating at cloud base and cooling at cloud top is increased when compared to columns. The reason for this is that plates with the same volume have a larger cross section.

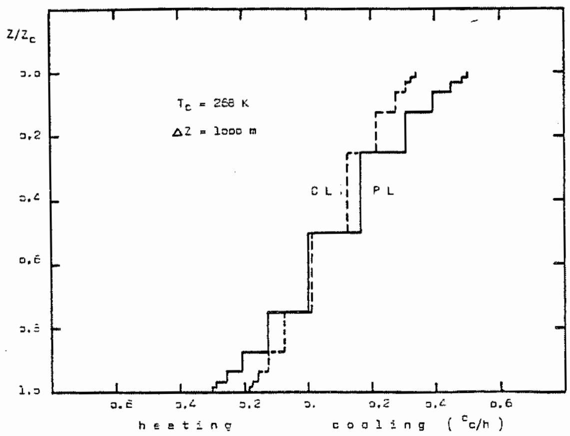

Fig. 1 Cooling rates in the cloud as function of cloud height (temperature: T_c) and crystal shape (CL: columns, PL: plates). Cloud level is given by Z/Z_c (cloud top: $Z/Z_c = 0$), cloud thickness by ΔZ. The ground temperature is assumed to be 300 °K, the temperature of the atmosphere above the cloud is 210 °K.

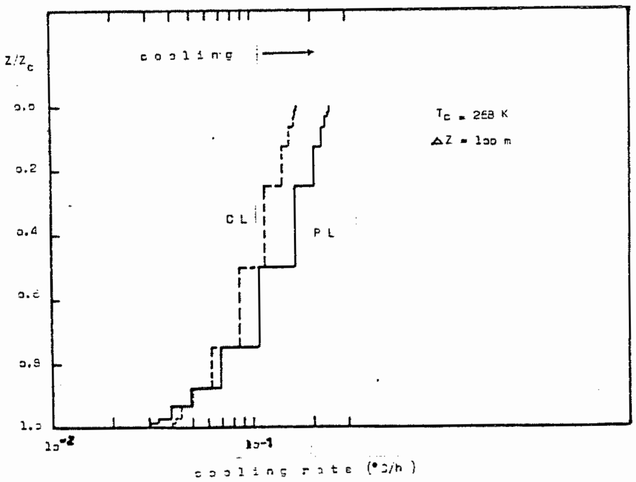

Fig. 2 same as Fig. 1 but ΔZ = 100 m

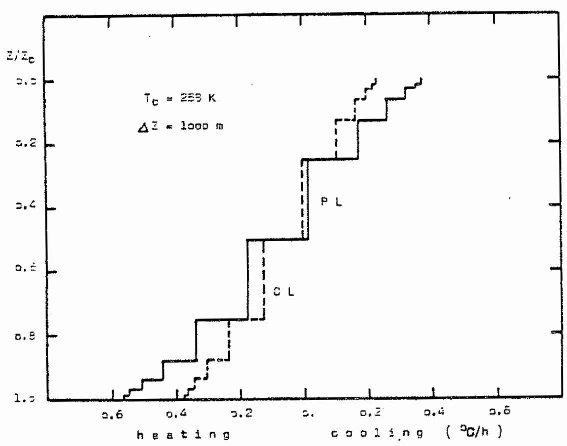

Fig. 3 same as Fig. 1 but T_c = 258 K

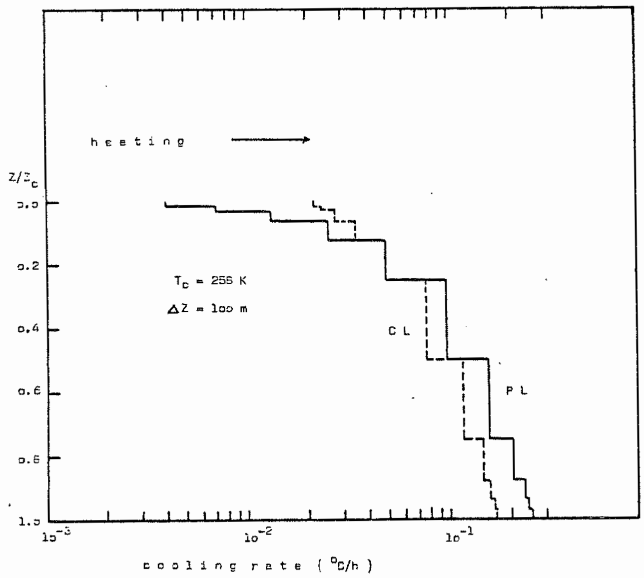

Fig. 4 same as Fig. 1 but ΔZ = 100 m and T_c = 258 K.

In order to estimate the effect of radiative cooling on the mass growth rate of individual ice crystals we calculated the mass growth rate according to

$$\frac{dM}{dt} = \frac{4\pi CK(S_i - 1) - L_s/R_w T^2}{L_s^2/R_w T^2 + KR_w T/De_i(T)}$$

where M denotes the crystal mass, D the diffusion coefficient, K the thermal conductivity, L_s the latent heat of sublimation, $e_i(T)$ the saturation vapor pressure with respect to ice. S_i refers to the ambient saturation ratio with respect to ice, C is a function of the size and shape of the ice particle. We neglected the effects of thermal accomodation and ventilation. With respect to the value of C ice columns are approximated by the formula for a prolate spheroid, plates by that of an oblate spheroid. The ambient cloud air is assumed to be water saturated. The results given in Table I refer to cloud top conditions. As is indicated the mass growth rate of ice crystals can be significantly increased by radiative cooling especially when the crystals become large and when the cloud top is placed lower in the atmosphere (Table I: T_c = 268 K). Plates with the same volume as columns grow faster than columns. The highest increase in mass growth found for plates is about 40%.

1000 m thick cloud

	$Tc = 268^{0}$ $\frac{dM}{dt}(\frac{g}{sec})$		$Tc = 258^{0}$ $\frac{dM}{dt}(\frac{g}{sec})$	
	without radiation	with radiation	without radiation	with radiation
Plates				
a = 50 µm c = 10,8 µm	0,934·E-9	1,088·E-9	1,532·E-9	1,538·E-9
a = 100 µm c = 21,6 µm	1,871·E-9	2,644·E-9	3,066·E-9	3,420·E-9
Columns				
a = 15 µm c = 120 µm	0,934·E-9	1,037·E-9	1,196·E-9	1,199·E-9
a = 30 µm c = 240 µm	1,451·E-9	2,019·E-9	2,379·E-9	2,634·E-9

Table I: Mass growth rate near cloud top as function of crystal shape and cloud temperature

4. References

Barkstrom, B.R., 1978: Some effects of 8-12 µm radiant energy transfer on the mass and heat budgets of cloud droplets. J. Atmos. Sci., 35, 665-673

Plass, G.N., G.M. Kattawar and F.E. Catchings, 1973: Matrix operator theory of radiative transfer. 1: Rayleigh scattering. Appl. Opt., 12, 314-329

Wendling, P., R. Wendling and H.K. Weickmann, 1979: Scattering of solar radiation by hexagonal ice crystals. Appl. Opt., 18, 2663-2671

III.2 - III.3 - Nuages Cumuliformes
Cumuliform Clouds

CALIBRATION OF A ONE-DIMENSIONAL MODEL OF TROPICAL CUMULUS CONVECTION

S. Achy* and R. Rösset**

*Faculté des Sciences, Université d'Abidjan, COTE D'IVOIRE
**L.A.M.P., Université de Clermont II, FRANCE

I - Introduction

Before its operational use, a convective cloud model necessitates to be calibrated. We propose here to calibrate the stationary and evolutionary versions of a parametric one-dimensional numerical model (1, 2) in the tropical atmosphere, on the basis of data collected in Ivory Coast during the October 1977 little rainy season (Moussafrica 77 (3)). Among these data, we mainly use the photogrammetry of clouds performed at Yamoussoukro, south of the ITCZ at this period of the year. As for the adjustment of the model parameters, we have concentrated upon the entrainment constant k defined as : $\mu = \frac{k}{r}$, where μ (in m^{-1}) is the classical entrainment coefficient and r the radius of the cloud cell.

II - Model adjustment as a function of the measured cloud top heights and vertical velocities

Table I displays the results of this adjustment for 2 particular days, october 26 and 27, 1977. In columns 2, 3 and 7, the photogrammetric data have been reported, respectively for cloud radii, cloud top heights as well as for the mean ascent rates of these latter. Column 4 gives the entrainment constants k tested in the model. On the same lines, have been reported in columns 5 and 6 for the evolutionary and stationary models, the corresponding calculated cloud top heights. Two points will be underlined here : firstly, the adjustment is realized for various k values in the 2 versions and secondly, according to the situations observed the optimal k values are different in a given version (0.22 on October 26 versus less than 0.15 on October 27). The optimal k values having thus been determined for the evolutionary model, columns 7 and 8 enable us to compare the measured and computed cloud top ascent rates : there is a good agreement between the two, especially on October 26. For the stationary model, further results have been displayed in Table II : we shall only insist here upon the wide range of the optimal k values, from 0.1 to 0.3.

III - Statistics on k

The variability in the optimal k values having been shown, we shall look now for statistical correlations between these values and cloud geometry, and/or the average properties of the ambient atmosphere (Fig. 1). For example, we observe in Fig. (1a) the rapid decrease of k as a function of the cloud anisotropy ratio between its thickness H and its radius r : this ratio H/r sketches the relative importance of the lateral entrained air versus the cloud base fluxes. In Fig. (1b), k is a function of $\overline{T}$, the average ambient temperature between the cloud base and top levels. Two distinct groups of points can be seen : a first group in which the top heights Z_M do not exceed 5500m (with a large dispersion in k) and a second group in which Z_M exceeds 15500 m (with $k \simeq 0.1$). In Fig. (1c) and (1d) are displayed large variations of k versus $(\overline{\frac{\partial T}{\partial Z}})$ and $(\overline{\frac{\partial X}{\partial Z}})$, respectively the average vertical gradients in environmental air temperatures and water vapour mixing ratios. As a matter of fact, the optimal k values most frequently observed for the thickest clouds lie near 0.1. As a result, the specification of k is not too crucial for the very deep convective clouds, as long as k lies near 0.1 ; this result doesn't apply to shallower clouds for which the values of k are much more dispersed.

IV - Cloud overshooting

The vertical velocity previously used in the adjustment procedure only referred to the ascent phase of the cloud top. At the end of this phase, the cloud tops temporarily overtake their equilibrium level by a height P (the overshoot distance). This height defines the minimum temperature reached, which, in its turn, determines the freezing probability of the cloudy air.

Saunders (4) distinguished two regimes of penetrative convection according to the value of (P/D) versus 0.6 (D being here the diameter of the convective element). As for us, after initialization of the stationary model with the radiosoundings released at Yamoussoukro during Moussafrica 77 and for various values of the initial cloud base radii between 0.5 and 4 km, we have reproduced in Fig. 2 the values of P computed as a function of the parameter $(\frac{W^2 D}{G})^{1/3}$, where G is the coefficient of atmospheric static stability above the equilibrium level, W the vertical velocity of the cloud when it first passes through this level and D the cloud diameter at that time.

In agreement with Saunders, Fig. 2 reveals a linear behaviour in P as a function of $\left(\frac{W^2 D}{G}\right)^{1/3}$. Nevertheless, in contrast with this latter author, the slope of our curve has a value of about 0.6 (versus 1.6 for Saunders). It is to be noted that among the 102 cases treated during Moussafrica 77, two cases only give $\left(\frac{P}{D}\right)$ ratios greater than 0.6 (deep penetrative convection) : the photogrammetric data (not reproduced here) confirm these results.

V - Conclusion

As a conclusion, we shall stress through an example the need of calibrating cloud numerical models such as ours by referring to a set of experimental data, previous to their operational use. For this purpose, we have drawn in Fig. 3 the vertical profiles of vertical velocities computed with the stationary model for the radiosoundings of 7.15, 10.52 and 17.02 on October 24, 1977 at Yamoussoukro. We observe that the maxima in vertical velocities as well as the corresponding cloud top heights are very variable as functions of the initial cloud base radii lying in the range 0.5 to 4 km. Fig. 3 brings also support to the concept of a critical cloud base radius in a given situation (between 2 and 2.5 km at 7.15 ; between 1.5 and 2 km at 10.52 and between 3.5 and 4 km at 17.02) beyond which the cloud thickness rapidly increases together with the rainfall probability occurrences at the ground. As a result, the operational use of our model requires the availability of basic pertinent measurements such as the effective cloud radii for the evaluation of which terrestrial photogrammetry offers a precious technique, however difficult to use everywhere.

Références

(1) WISNER C., H.D. ORVILLE, C. MYERS (1972) : A numerical model of a hail-bearing cloud, J.A.S., vol.29, pp. 1160-1181.

(2) ACHY A.S. (1979) : Qualification opérationnelle d'un modèle unidimensionnel de convection nuageuse tropicale, Thèse de Doctorat d'Etat, Université d'Abidjan, Mai 1979.

(3) Etude de la convection atmosphérique équatoriale : Résultats de la campagne Moussafrica 77, rapport n°3, L.A.M.P. et Universités de Clermont II et d'Abidjan, Décembre 1978.

(4) SAUNDERS P.M. (1962) : Penetrative convection in stably stratified fluids, Tellus, Vol.14, pp. 177-194.

Acknowledgments

We are grateful to the french and ivorian authorities involved in Moussafrica 77, particularly D.R.E.T. and the Ivorian Ministry of Education.

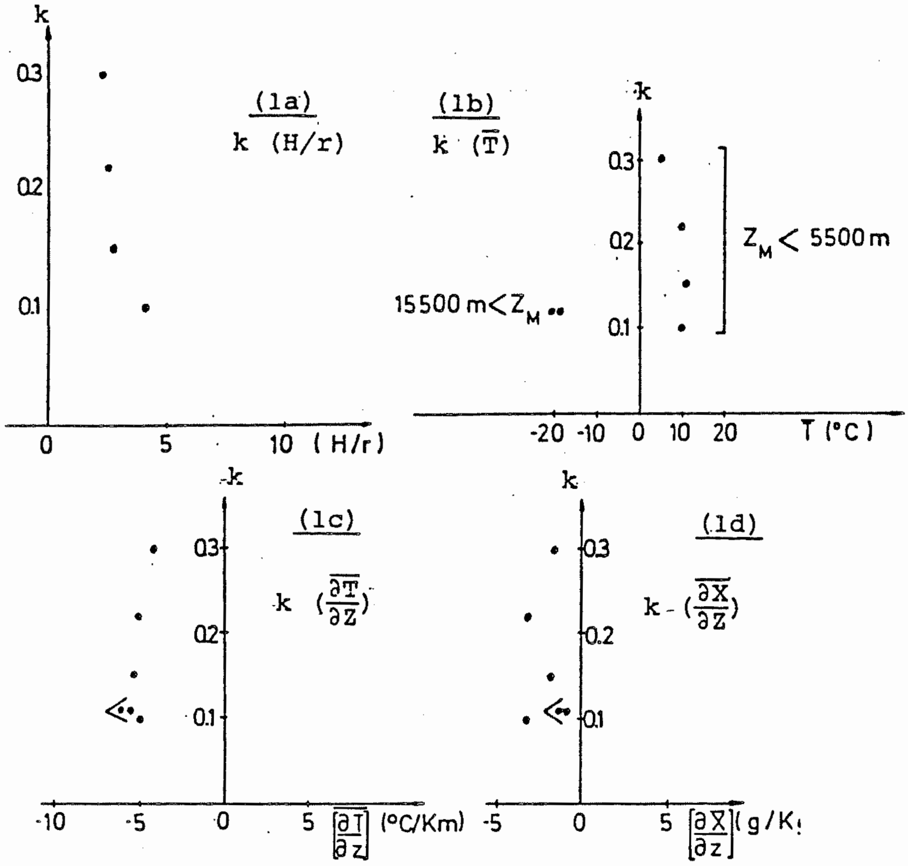

Figure 1 : *Statistics on k. (Note the 2 points obtained for $Z_M > 15500$ m).*

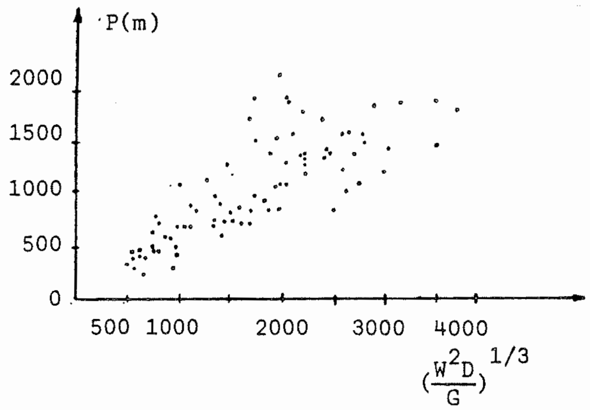

Figure 2 : *Correlations between the overshoot distance P and the parameter* $\left(\frac{W^2 D}{G}\right)^{1/3}$.

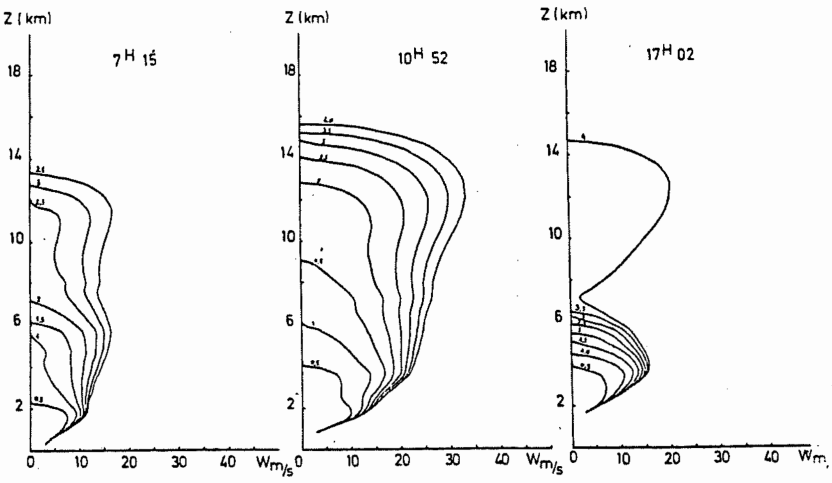

Figure 3 : *Computation of cloud developments on October 24, 1977 at Yamoussoukro. (Stationary model : initial cloud base radii from 0.5 to 4 km).*

DATE	Measured Radius (in km)	Cloud Top Heights (in m)				Mean Cloud Ascent Rates (in m/s)	
		Terrestrial Photogrammetry	K Entrainment Constant	Stationary Model	Evolutionary Model	Photogrammetry	Time-Dependent Model
			0.15	5400	4600		
			0.16	5200			
26/10/77	R = 1.62	4600	0.18	5000		2.71	2.69
			0.20	4800	3600		
			0.22	4600			
			0.25	4400			
			0.15	15300	15800		
27/10/77	R = 4.78	15800	0.16	15100		13.33	11.10
			0.18	14900		10.48	7.59
			0.20	14700	14600		

Table I : *Comparison between observed (photogrammetry) and computed results (October 26 and 27, 1977 at Yamoussoukro).*

DATE		Measured cloud Diameter (in km)	Cloud Top Maximal Height (in m)		Optimal value of K
			Terrestrial Photogrammetry	Stationary Model	
21/10/77	12 h 00 TU	6.60	15 690	15 450	0.11
	16 h 50 TU	2.88	4 880	6 400	0.30
24/10/77 17 h 00 TU		3.00	5 112	5 100	0.15
25/10/77 12 h 00 TU		3.60	6 660	5 500	0.10
26/10/77 12 h 00 TU		3.20	4 600	4 600	0.22
27/10/77 16 h 00 TU		9.60	15 800	15 700	0.11

Table II : *Determination of optimal values of k during Moussafrica 77.*

USE OF A ONE-DIMENSIONAL CUMULUS CLOUD MODEL AS A FORECASTING TOOL FOR PLUVIOMETRY IN THE TROPICS

S. Achy* and R. Rosset**

*University of Abidjan, IVORY COAST
**L.A.M.P., University of Clermont II, FRANCE

I - Introduction

There is no need to emphasize the interest of studies of the pluviometric regimes in the tropical and sahelian regions. In these regions, the pluviometric networks are generally not dense and the radiosounding stations too scarce. In this context, it appeared useful to elaborate a numerical one-dimensional model of cumulus convection (1) and to test its ability to forecast precipitation.

In other words, we have tried to relate through such a model the aerological data of the radiosoundings to the local pluviometric measurements. In spite of the limitations of this approach, limitations of which we are well aware, we hope to make a contribution in this domain which is so important for the tropical regions.

II - Procedures of study

The calibration of the model for the West-African tropical atmosphere being presented elsewhere (2), we shall not summarize here this part. Our present study can be divided into two distinct parts :

- firstly, we systematically apply our model to the region near Abidjan (Ivory Coast), for a six-month period (from January to June 1976) overlapping the dry and rainy seasons ;

- secondly, with the advantage of an additional radiosounding station at Yamoussoukro for a 15-day period, we apply the model to the two stations in order to retrace numerically meridional variations of rainfall inland from the coast of the Gulf of Guinea.

III - Comparison between observed rainfall and the computed cloud developments at Abidjan (Ivory Coast)

The selected period entends from January to June 1976. This period can be divided into three subperiods : usually, from January to about March 15, we are in the dry season, the rainy season being well established only by mid-May. Between these two seasons, we have a transition period with isolated convective rains. The dates above are subject to variations from year to year : these variations are of vital importance for agriculture. Our selected period overlaps the three subperiods.

For every day in this period, we fed into the stationary version of the model the daily radiosoundings at Abidjan. Then, for different initial cloud base radii, we computed the cloud characteristics, in particular the top heights, the vertical profiles of temperature and water content, together with the rain amount accumulated at the cloud base. Examples of application of this procedure are displayed here for four selected days : February 18 and March 3, 18 and 30, 1976. For these days, we reproduced in Fig. 1 the radiosoundings (T and T_d curves) together with the simulated clouds (base and top) as a function of their base radii (from 0.5 to 3 km with 0.5 km steps). Two cases are similar in the cloud developments : February 18 and March 18, with cloud tops over the 10 km level.

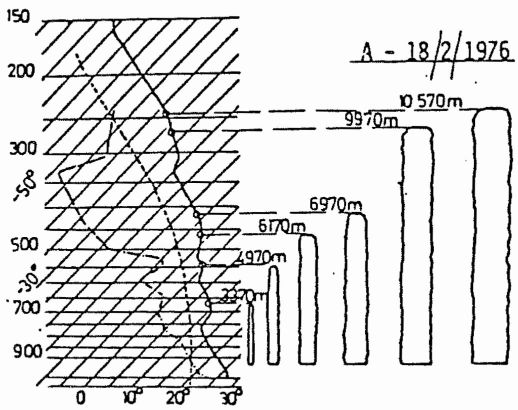

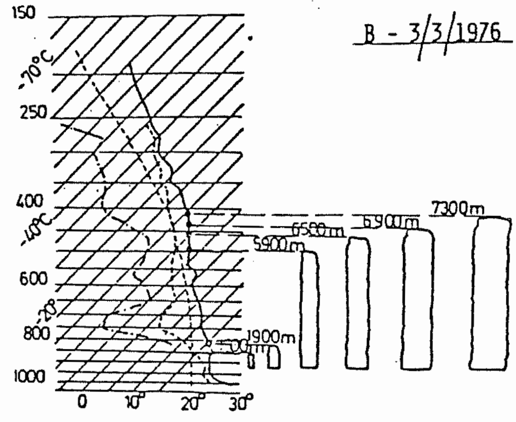

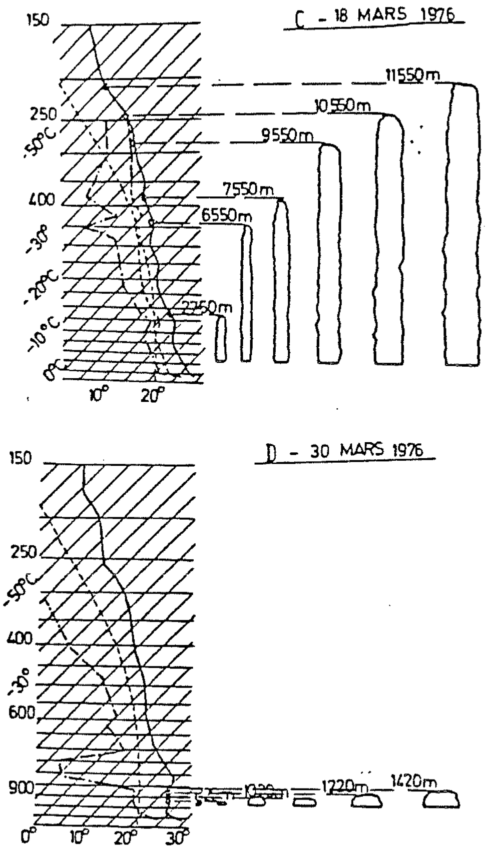

Figure 1 : The convective developments (on the right) together with the corresponding radio-soundings (on the left) for the 4 selected days (A to D) (cloud base radii from 0.5 to 3 km by 0.5 km steps).

For March 3 and 30, the cloud developments are more restricted, due to the very dry layers at the 800 mb - 900 mb levels. In addition, on March 30, development was further hampered by a very stable layer at 900 mb. Complementary results for these four days are reported in Table 1, with the radar echo top heights observed at Abidjan and the rain character (defined below).

Turning now to the pluviometric data, a map of the station network appears in Fig. 2. The sampling area lies within a circle 75 km in radius centered at Abidjan-Airport.

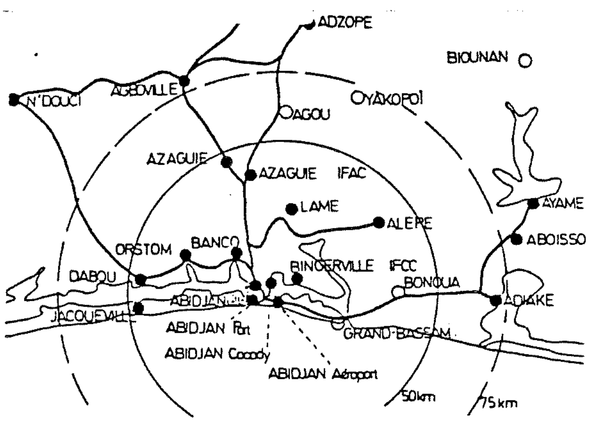

Figure 2 : Pluviometric network near Abidjan-Airport.

In this area, 18 stations have been retained. A binary classification has been adopted for the rainy sequences : "isolated rains" when no more than 2 stations have collected rain as opposed to the "generalized rains" otherwise.

Our results for the 6-month period have been grouped in Fig. 3. For each month, the ordinate indicates :

- the number of rainy days observed n_1 ;

- the number of days per month for which the model has given significant convective developments, i. e. cloud top heights over the 5 km level (0°C isotherm) for a 3 km-base radius (model less sensitive to the entrainment coefficient (2)) ;

- the number n_2 of days per month with observed rainfall at the ground together with significant convective developments.

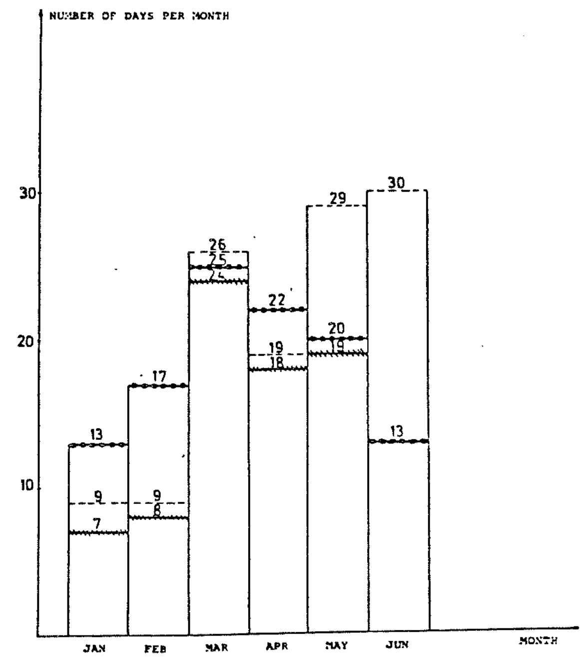

Figure 3 : Comparison on a monthly basis between :

- *the number of rainy days observed (---) ;*
- *the number of days for which the model indicated significant convective development (—•—•—) ;*
- *the number of days with observed rainfall at the ground together with significant convective development (wwwww).*

The main result to be noted from Fig. 3 is the good agreement between observations and computations in March (n_1 / n_2 = 0.92) and April (n_1 / n_2 = 0.95), during the transition period. This agreement decreases during the dry season (n_1 / n_2 = 0.78 in January and 0.89 in February) ; it is quite loose in the rainy season (n_1 / n_2 = 0.66 in May and 0.43 in June). These results can be easily interpreted : during the transition and even the dry seasons, rainfall is mainly due to isolated convective clouds for which the model is well suited. During the rainy season, on the contrary, the sky is overcast and rainfall is no longer of purely local origin (layer instability instead of particle instability as would be the case in our model).

IV - Comparative meridional study at two stations (Moussafrica 77)

This study only concerns a 15-day period in October 1977, during the little rainy season. The stationary model was fed with the daily (or more) radiosoundings at Abidjan (5° 15' N) and Yamoussoukro (6° 54' N), this latter station being situated at the limit between the forest and the savanna. The model results are displayed in Fig. 4, from October 18 to October 27, 1977 : for the 2 stations with radii from 0.5 to 4 km (0.5 km steps), we show the computed rainfall amounts accumulated at the cloud bases, together with the observed rainfall amounts (the small segments in Fig. 4). Two points must be noted in Fig. 4 : firstly, the modulation imposed upon the precipitations by the initial cloud radii and secondly, the variability of rainfall is greater at Yamoussoukro than at Abidjan, in fair agreement with current observations.

V - Conclusion

Our present study only aimed at checking the ability of the model previously calibrated in the tropical atmosphere, to simulate the spatial and temporal variations of rainfall over West Africa. We are well aware of the limitations inherent in this approach, namely the parametric treatment of rain in the model, the evaluation of the rainfall amount at the cloud base and the restricted spatial representativeness of the radiosoundings at a single station. Nevertheless, due to the scarcity of data, our study appeared to be worth while to be started. It is necessary now on the one hand to extend this study to longer periods and on the other hand, to complete it by stating more accurately the concept of "significant convective development" and by estimating the rain evaporation between the cloud base and the ground. These extensions are in progress : we think it could be useful for tropical and sahelian countries.

Acknowledgements

We are grateful to Professor R.G. Soulage for constant help and advices during the data collection and interpretation phases of this work. One of us (A.S. Achy) is very grateful to Professor H.D. Orville for having welcomed him in his group.

Our thanks go also to the Ministry of Scientific Research in Ivory Coast and to all the french and ivorian organizations cooperating during Moussafrica.

References

(1) A.S. Achy (1979) : Qualification opérationnelle de convection nuageuse tropicale. Thèse de Doctorat d'Etat, Université d'Abidjan, Mai 1979.

(2) A.S. Achy, R. Rosset (1980) : Calibration of a one-dimensional model of tropical cumulus convection. (This conference).

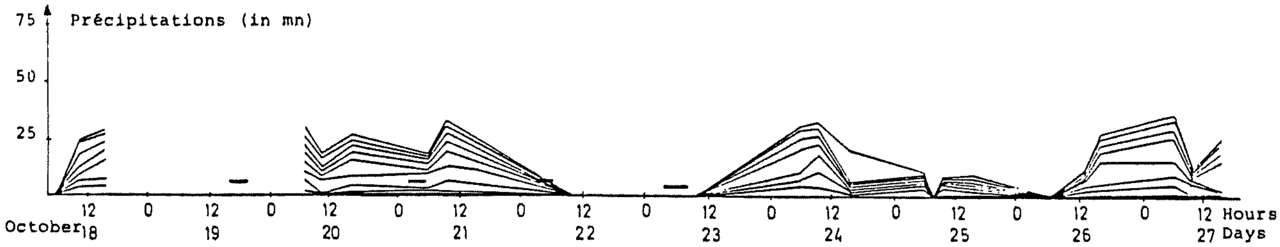

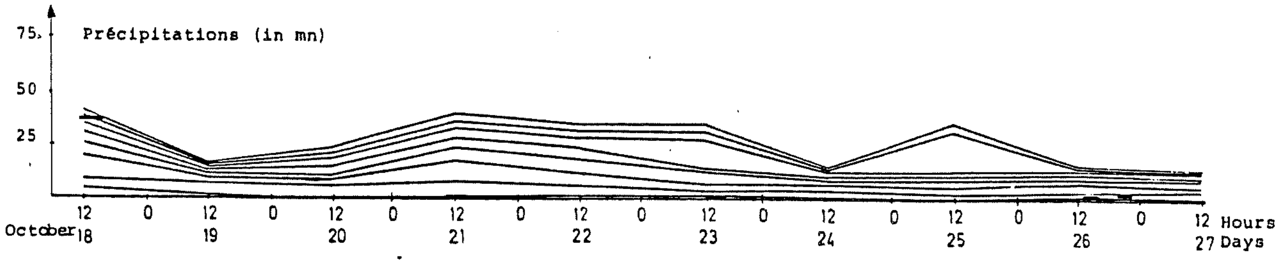

Figure 4 : *Accumulated precipitations (in mn) at the cloud base computed at Yamoussoukro (upper curves) and Abidjan (lower curves) (cloud base radii from 0.5 to 4 km by 0.5 km steps). The small segments give the observed rainfall at the ground. (Note the lack of model results for October 19).*

	Date	Cloud top height for different radii (m)						Radar echo top			Rainfall character	
		0.5	1.	1.5	2.	2.5	3. km	Height (m)	Time	site (°)	Isolated	Generalized
FEB	18	3379	4970	6170	6970	9970	10570	10000	14h30		+	
MAR	3	1500	1900	5900	6500	6900	7300	10500	19h00	4°		+
MAR	18	2750	6750	7950	9550	10550	11550	10000		3°		+
MAR	30	820	820	1020	1020	1220	1420					

Table 1 : *Observed (radar echoes and rainfall character) and computed (top heights characteristics for the 4 selected days.*

AGGREGATION OF SMALL CONVECTIVE RAIN CENTERS

Bernice Ackerman
Illinois State Water Survey
Urbana, Illinois, USA

Groups of small cumulus clouds frequently precede the development of convective rains in the Central U. S. This paper describes the evolution of a cloud field leading to rain and hail on 30 July 1979, as recorded by a high-powered 10-cm radar. The convection occurred over a densely-instrumented network over which the radar provided full volume surveillance every 4 minutes.

The area was under the influence of tropical maritime air mass providing afternoon temperatures of 30C and dewpoints of 25C and a very moist and unstable troposphere. The convection started around 1400 CDT as scattered, weak radar echoes which, with a few exceptions, were very short-lived. By 1530 the clouds were more numerous and a few became persistent. The evoluation of the echoes occurring over the northern half of the network is shown in Fig. 1. (The southern half was essentially cloud free.) Shown is the maximum 10-cm reflectivity measured in 1.5 km square columns reaching from the surface to the top of the volume scan.

Prior to 1515, only one cloud had any persistence or strength. By 1520 the numbers of small echoes had increased and two, A and F were larger, more persistent, and stronger than the others (Fig. 1a). These were the initial echoes of line formations which had different histories. Both first appeared at 1516, but A expanded and intensified much more rapidly than F. Within five minutes a second, B, had formed contiguous with A, while D formed to the west of F and echo E formed to the SE. With the development of echo C on the northwest side of A at 1527 (Fig. 1b) the main cloud area consisted of two approximately parallel lines of echoes, each composed of three distinctive echo "masses". The component cloud masses in these lines retained their identity but were usually multicellular, with the individual cells going through a history of growth and decay, to be followed by new cells coming up through the same general area. This multicellular structure is most evident in the composites in Fig. 1 in echo B but higher resolution analysis clearly show the same structure in the other echoes.

The echoes continued to form rapidly, with another cluster developing in the northeast by 1532. This cluster was dominated by echo L (Fig. 1c) which reached 52 dbz reflectivity within 4 min, whereas echoes J, K remained weak and not very tall. Two additional major echoes developed, cloud H at 1539 between lines CAB and DFE, and echo N at 1555 (Fig. 1e). The latter heralded the decline of DFE and the weaker echoes of the northeast cluster. The final complex, composed of line CAB, echoes H and N, and a new formation, O, south of B and H, intensified as it moved east, producing moderate to heavy rains and hail on the east edge of the network, as well as a small funnel cloud.

The evolution of the echo top and peak reflectivity, in echoes A and F (Fig. 2) are representative of the components in the lines. Both the intensity and height of echoes in Line CAB grew very rapidly, reaching 60 dbz within 10 or 15 min of formation. Following a minor decrease in height and intensity (coincidental with the beginning of light rain at the ground) the echo once more intensified with peak reflectivities remaining above 60 dbz for another hour. The early development of echoes in Line DFE was very slow, with maximum reflectivities remaining below 35 dbz and tops below 5 km for 15 min. Intensification followed, but slowly with reflectivities reaching peak values below 55 dbz. These reflectivities were maintained for less than 10 minutes.

Flight observations around the freezing level in convective clouds on days like 30 July have indicated high water contents, mostly in drops over 75 microns, and the existence of large water drops and/or ice pellets when cloud tops were well below -20C. In the early phases of echo A, when the reflectivities reached 60 dbz with echo top below -20C, and the high reflectivities confined to regions warmer than 0C, the intense cores may have been due to accumulation of large water drops, wetting of small ice pellets and/or slush. After 1525 the depth of high reflectivity extended into the -10C region. This coupled with the greater cloud heights suggest that the high reflectivities in the later cells may have been due to hail.

Acknowledgments. The contributions of Dr. Arthur Jameson and Miss Nancy Westcott who have participated in these analyses are much appreciated. This research was supported by the National Science Foundation under Grant ATM78-08865.

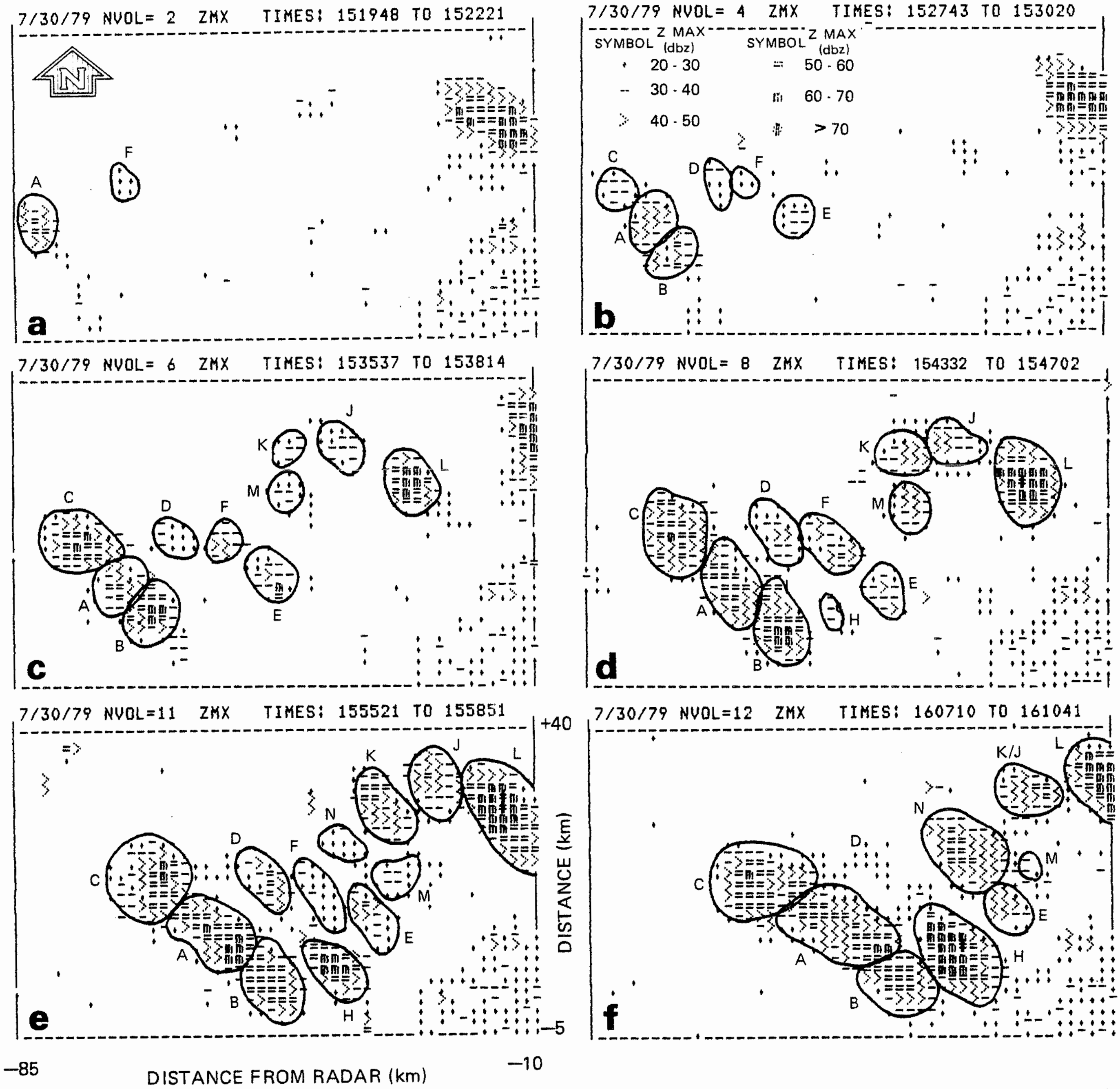

Figure 1. Map of maximum reflectivity in vertical columns of 1.5 km square cross-section. Sybmols explained in panel (b).

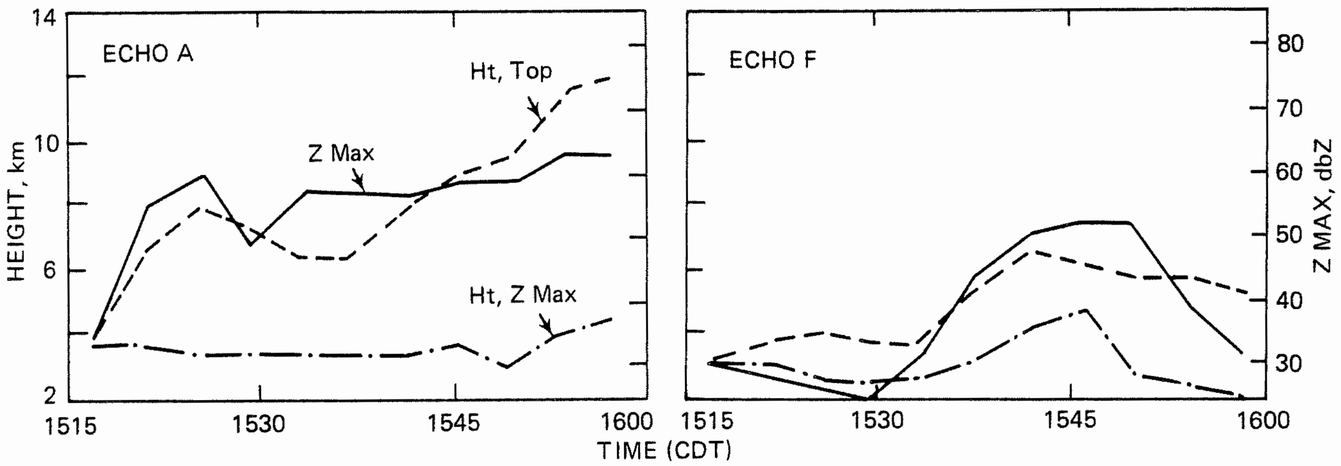

Figure 2. Temporal evolution of height of cloud top, maximum reflectivity, Z MAX, and height at which it occurred, for echo area A in line CAB, and F in line DFE.

A CUMULUS CLOUD MODELLING USING SUCCESSIVE ISOLATED THERMALS

V.M.Andreev, D.E.Syrakov, R.P.Mitseva

Sofia University, Faculty of Physics
Sofia BULGARIA

On the basis of experimental data and theoretical considerations (see, for example [1] - [4]) the convective cloud is assumed to consist of: a) nonactive cloud mass which expanses by the mechanism of turbulent diffusion and b) active part - a region of intensive upward motions. In the model the nonactive part consists of one or more diffusing thermals which have reached convection level. Active upward moving thermals pass through the nonactive part. Every consecutive thermal moves in an environment with constant profiles of the meteorological characteristics except in the nonactive cloud region. This region contains cloud droplets (liquid water content S_c) or/and cristals (S_{cf}), saturated vapour (Q_i) and temperature excess(ΔT). Thus, the nonactive cloud part is more favourable for the rising of the active consecutive thermals.

The basic structural element of the studied cloud is the model of isolated thermal. The changes of thermal's characteristics during the rise are described by one-dimentional steady-state numerical model [5] in which Kessler type parameterisation of precipitation processes is used (Fig.1).

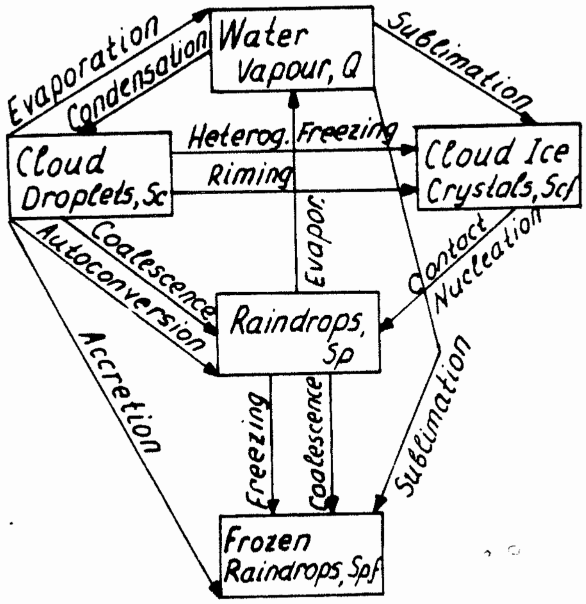

Fig.1. Scheme of the microphysical processes included in the isolated thermal model [5] .

The cloud model is realized in the following phases.

In the first phase it is assumed that every thermal which have reached convection level begins to diffuse isotropically as a spherical source of enthalpy, water vapour and cloud droplets (cristals). The constant diffusion coeffitient K is used. Evaporation process takes place simultaneously (Fig.2a). For the sake of conveniance the spherical nonactive part is transformed in a cylindrical layer of the same volume (Fig.2b).

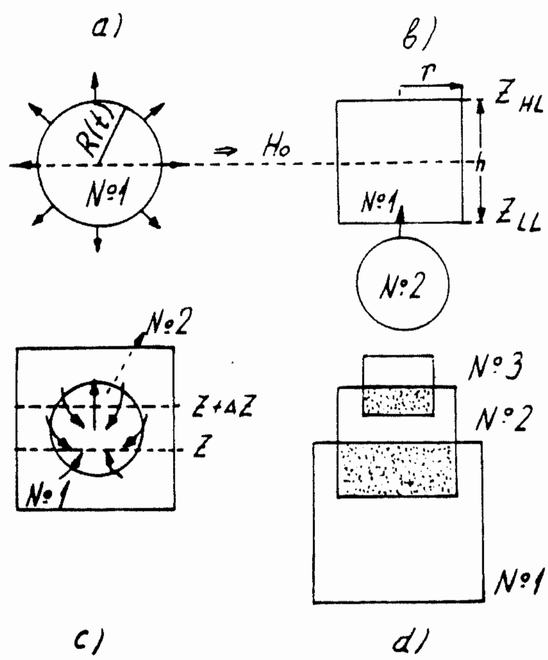

Fig.2. Phases of cloud modelling for three thermals in series

In the second phase the rising of a new active thermal through the nonactive cloud layer is considered. A part of the thermal's trajectory passes through the noncloud environment with constant conditions. In the cloud layer the thermal's lateral boundary conditions are those of the diffusing thermals, which vary in time (Fig.2c).

In the third phase the nonactive cloud part is modelled using the characteristics of some thermals which have reached convection level(Fig.2d)

As can be seen the parameters of the diffusing nonactive part of the cloud vary in time.On the other hand every next active thermal can be started by different time intervals with different initial properties. Therefore,such a model can describe the nonstationary variations of convective clouds including the dissipation stage.A similar modelling was made in [6,p.131] .

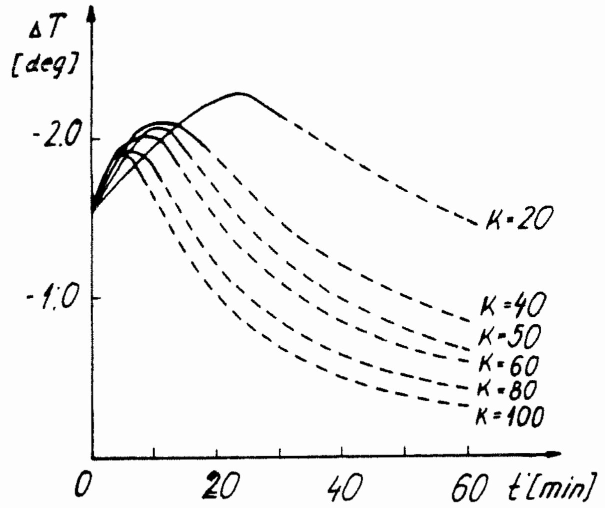

Fig.3. Time variations of temperature excess ΔT in the nonactive part formed by one thermal for different K = 20-100m^2/s

The first numerical experiments were *Cu hum* cloud modelling.One thermal is rising and having reached the convection level begins to change its parameters by the mechanism of turbulent diffusion and evaporation only.The time variations of ΔT and S_c at different K -values are shown in Fig.3 and Fig.4.The initial radius of the thermal is R = 1km. It can be seen that the cooling process of air in the thermal is still in progress in the initial phase.This is due to the predominating of the cloud droplets evaporation over the diffusion process of negative temperature excess.The duration of this stage increases with the increase of R and the decrease of K .The quantity ΔQ decreases all the time.The cloud water content S_c decreases very quickly with the time because both evaporation and diffusion lead to that(Fig.4).It can be seen from Fig.4 that if the life time of *Cu hum* or *Cu med* is in order of 15-30min the value of K should be in the interval 40-80 m^2/sec.The comparison of model results as shown in Fig.4 with natural experiment data will facilitate the estimation not only of the effective diffusion coefficient K but of its dependence on the scale of phenomenon as well.

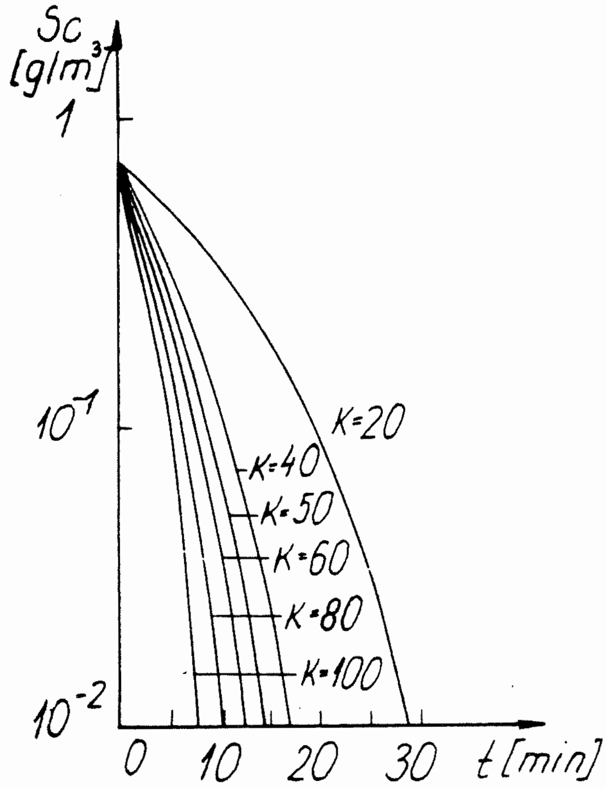

Fig.4. Same as Fig.3 for LWC - S_c

A part of the numerical experiments were made for ideal situation with constant relative humidity (f = 80%) and constant temperature lapse rate (γ = 7 deg/km). The following parameters were varied:initial thermal radius R ,diffusion coefficient K and starting time interval Δt between the successive thermals.In Fig.5 an example of time variation of relative humidity profile in the nonactive part of the cloud is shown.The moment of stopping of the first thermal is accepted as initial(t =0).The other results which are not shown here are to be published in Bulgarian J.of Geophysics.

In Fig.6 the comparison of a model results with natural experiment data [9] is shown.The model gives not only qualitative but good quantitative agreement as well.

Numerical experiments for convective cloud simulation (including *Cb*)in real atmosphere conditions are under investigation.

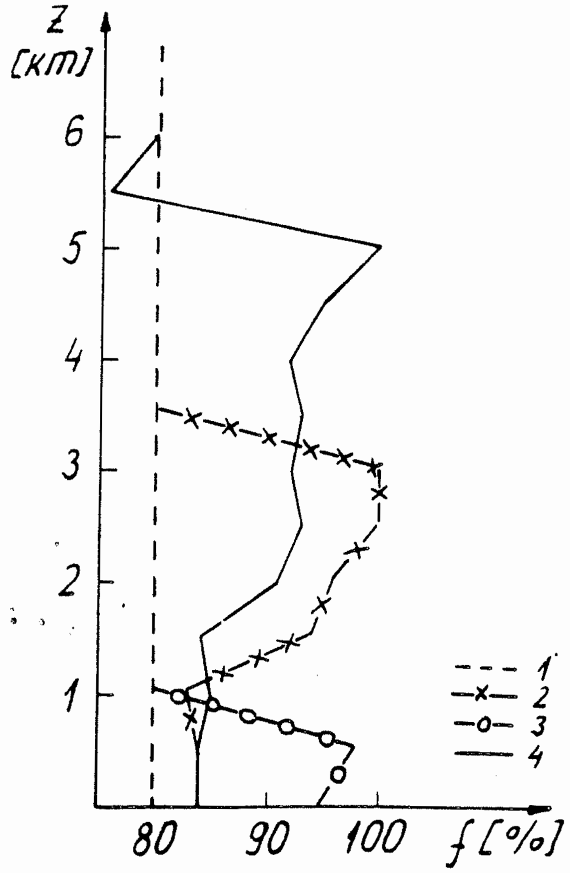

Fig.5. Relative humidity time variations in the nonactive cloud part. 1 - f =80%; 2 - 1 min after the first thermal stopping; 3 - after 36 min;four thermals are stopped;4 -after 77 min;twelve thermals are stopped.

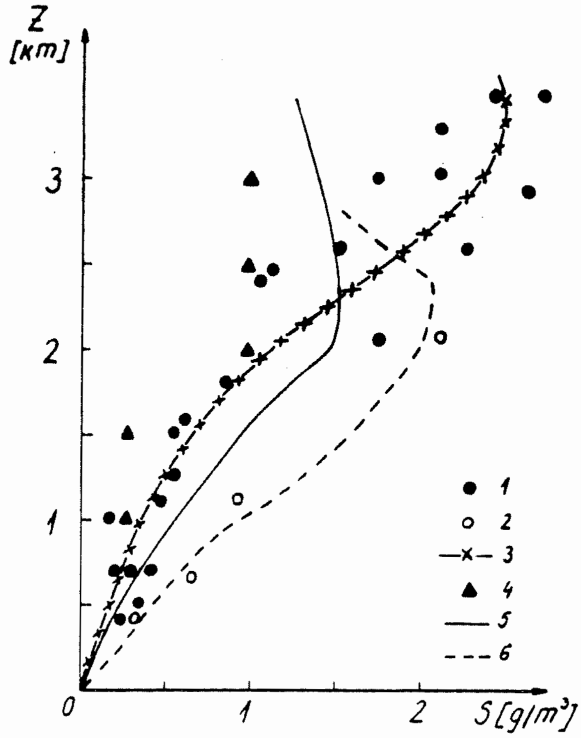

Fig.6. Comparison of model results with experimental data [9] 1 -mean experimental LWC on an individual fly-line; 2 - experimental LWC maxima from separate samples; 3 - mean experimental data line; 4 - mean LWC in a nonactive part when the model cloud is in stationary stage; 5 -mean model LWC in nonactive and active parts; 6 - LWC in the active part of stationary stage model cloud.

REFERENCES

1)Ludlam F.H.,R.S.Scorer,1953 Bubble Theory of Penetrative Convection,Q. J.Roy.Met.Soc.79,339. 2)Levine J. 1959 Spherical Vortex Theory of Bubble-like Motion Cumulus Clouds. J. Meteorol.16,6. 3)Borovikov A.M.et al 1961 Cloud Physics.Gidrometeoizdat 4)Schmeter S.M.1972 Convective Cloud Physics.Gidrometeoizdat 5)Andreev V. 1976 Microphysical Effects of a Dynamical Model of an Active Isolated Element of Convection,Bulgarian Geophysical J.2,4,p.17. 6)Andreev V., S.Panchev 1975 Dynamics of Atmospheric Thermals,Gidrometeoizdat. 7) Andreev V.,D.Syrakov,R.Mitseva,1979 Modelling of Convective Cloud Formation as Successively Arising Isolated Thermals,Bulg.Geophys.J.5,1,p.3. 8) Andreev V.,D.Syrakov,R.Mitseva,1979 Turbulent Diffusion of Stopped Nonactive Cloud Thermal - Numerical Experiment,Bulg.Geophys.J.5,3. 9)Voit F.I.,I.P.Mazin,1972 Cumulus Cloud Liquid Water Content,Izv.Akad.Nauk SSSR,Atmosph.Ocean.Phys.8,11,p.1166

THE INFLUENCE OF INHOMOGENEOUS MIXING ON CLOUD DROPLET EVOLUTION AND RAINFALL PRODUCTION

M B Baker*
Istituto di Fisica dell' Atmosfera (CNR)
Rome, ITALY

and

R G Corbin and J Latham
Physics Department, UMIST,
Manchester, ENGLAND

INTRODUCTION One of the central problems in cloud physics is the inadequacy of classical descriptions of the condensation stage of droplet spectral evolution. This manifests itself in several serious discrepancies between observations and theory. One is that the measured time required to produce raindrops in water clouds may be appreciably shorter than values calculated on the basis of classical theory for growth by condensation followed by stochastic coalescence. Another is that the predicted size distributions of cloud droplets within the condensational stage of growth are inconsistent with those observed in cumulus clouds. The major goal of this paper is to examine the hypothesis - emanating from experiments by Latham & Reed (1977) - that the inhomogeneous nature of the mixing between a cloud and undersaturated environmental air entrained into it produces fluctuations in supersaturation - not linked to fluctuations in vertical velocity - which cause spectral broadening and increased rates of droplet growth. The idea, which was developed by Baker & Latham (1979), is that when undersaturated environmental air is entrained into a growing cumulus some cloud droplets are greatly reduced in size, while others - at the same level, but more remote from the blobs or filaments of entrained air - are not directly influenced. This is clearly distinguished from the homogeneous description of entrainment employed by other workers, where it is assumed that the reduction in supersaturation produced by entrainment is, at any level, the same at all points.

If this idea has relevance to cloud physics it may be expected that adjacent regions would sometimes occur, within natural clouds, which possess closely similar droplet size distributions even when the values of liquid water content are very different. Confirmatory evidence for this prediction is provided by Blyth et al (1980) and others.

TIME CONSTANTS The extent to which the evaporation is inhomogeneous in a given situation will depend on certain rate processes associated with mixing within cumulus clouds. These are: turbulent diffusion of the entrained air into the cloud, molecular diffusion at the interface between a blob and the surrounding cloudy air, and the evaporation of a droplet of radius r in an undersaturated environment. The characteristic times governing these three processes are defined as τ_T, τ_D and τ_r respectively. If τ_T or τ_D is much less than τ_r, any inhomogeneities created by the mixing process will be substantially smoothed out before significant droplet evaporation can occur, and the mixing will approach the classical description employed by other workers. On the other hand, if $\tau_r << \tau_T, \tau_D$, the mixing process will approximate to the inhomogeneous description outlined here.

Taking X as the size of the blob, ϵ the rate of kinetic energy dissipation via turbulent mixing, D the molecular diffusion coefficient, S(%) the supersaturation, a the length associated with the condensation coefficient and characteristic values of the other parameters involved, we may write

$$\tau_T \sim (X^2/\epsilon)^{\frac{1}{3}}$$

$$\tau_r \sim 10^{-6}(\rho_w/\rho_\infty)((r+a)^2 - a^2)/DS$$

where r is in micrometres and ρ_w/ρ_∞ is the ratio of the densities of liquid water and saturated vapour. $\tau_T<\tau_D$ for all scales of interest. Calculations of the critical scale-length $X_c=\epsilon^{\frac{1}{2}}\tau_r^{3/2}$, for which $\tau_T/\tau_r = 1$ reveal that except for the highest levels of turbulence combined with low undersaturations the evaporation may be non-classical for scales in excess of about one metre.

LABORATORY EXPERIMENTS The validity of the foregoing arguments was examined by performing mixing experiments in a specially constructed vertical wind tunnel. A cloud of droplets was drawn up the tunnel, a flow of undersaturated air was introduced into it from a nozzle located on the axis, and the droplet characteristics, temperature and flow speed were measured at many radial and axial positions above the nozzle.

A spinning-top generator mounted axially in the vertical section of the tunnel, about 1m below the test section, was used to produce a unimodal droplet cloud covering the radius range 6 to 15μm. In acceptable conditions the droplet spectrum did not alter significantly with height or time during the course of an experiment (about 40 minutes) The drop sizes and concentrations were measured using an electrostatic disdrometer. Two mixing nozzles were used. The larger one was of diameter 10cm, and

*On leave from Civil Engineering Dept, University of Washington, Seattle, USA.

the other 3.8cm. The temperature in the mixing region was measured using a miniature bead thermistor. A hot wire anemometer was used to measure the wind velocity and turbulent characteristics.

Statistical examination of the measured time intervals between successive droplets arriving at the disdrometer was performed in order to reveal evidence of any structure that might be present in the cloud, especially in the mixing region. It illustrates the evolution from a random distribution prior to mixing, to a cloud with considerable structure shortly after mixing - this appears to correspond to pockets of original cloud intermixed with regions of zero or low droplet density - followed by gradual smoothing to an essentially homogeneous final state.

These experiments provide a test of the simple arguments, concerned with time constants, if - by utilizing both nozzles - the conditions $\tau_T/\tau_r<1$ and $\tau_T/\tau_r>1$ can be achieved. In the former case mixing will be rapid and the evaporation approach the classical description; in the latter case it will be distinctly inhomogeneous. Corbin(1979) deduced values of eddy diffusivity from the experimental results, and these led to values of τ_T~6s for the larger nozzle and τ_T~2s for the smaller. The values of τ_r for the conditions employed in the experiments were generally in the range 3 to 4s, so experiments with the two nozzles were expected to yield the required range of conditions. It was found that in all runs with the smaller nozzle the final mean radius of the droplets in the cloud was significantly lower, after entrainment, than the initial radius. On the other hand no significant change in mean size was found in nearly all of the runs with the larger nozzle although the liquid water content was substantially reduced. Thus we conclude that these experiments provide support for the arguments concerning the crucial role of the ratio τ_T/τ_r in affecting the droplet spectrum.

COMPUTATIONS OF SPECTRAL EVOLUTION In order to study the effects of inhomogeneous mixing of dry and moist cloudy air on droplet spectral evolution, we have modelled the process by a simple mechanism which represents a limiting case. In this model all air is entrained in identical blobs, or filaments, of given volume V_0 and relative humidity H. The nucleus spectrum in each is composed of NaCl particles in equilibrium at H. The parcels of dry air are entrained at a constant mean rate and the entrainment sites are distributed uniformly over the cloud volume V. Thus each droplet in the cloud has the same probability of encounter with the dry air. The mechanics of the encounter are not specified but the result is instantaneous total evaporation of sufficient numbers of droplets that the relative humidity in the original dry parcel rises to 100% and the dry particles grow by condensation to their equilibrium values at H=100%. Then the region affected by the blob mixes instantaneously with the surrounding cloudy air.

The evolution of the cloud through 1000 seconds was computed for: (1) Homogeneous entrainment (H) The classical model, in which environmental air and nuclei are entrained at a constant rate u; (2) Inhomogeneous entrainment (I) Dry air and nuclei are entrained in discrete blobs at a mean rate $\lambda(t)$.

In all the computations we assumed the environmental lapse rate Γ = -7.5°C/km. The updraught speed U was a constant and the cloud base temperature T_0 was prescribed. The initial NaCl nucleus spectrum and the number n of size classes included were based loosely on those employed by Warner (1969a), whose basic equations were used to calculate the evolution of the droplet spectrum. Runs were made for a wide range of values of U,H,T_0,n,u and droplet concentration N. In order to avoid complications in interpretation the CCN activity spectrum was truncated so that N remained constant during ascent.

Since the primary objective of these calculations was to establish whether this extreme model of inhomogeneous mixing (I, $\tau_r/\tau_T\to0$) provides a more accurate description of the effect of entrainment upon cloud droplet evolution than the classical, homogeneous model (H), which can be regarded the opposite extreme ($\tau_r/\tau_T\to\infty$), there was no justification for attempting to incorporate into our calculations a full treatment of the cloud dynamics. It appeared to us adequate to base our calculations upon the simple model of Warner and to ensure that the average entrainment rates were identical in the homogeneous and inhomogeneous models - from which it follows that the liquid water contents L at any level were the same on models H and I. This was found to be so.

It was found that on the inhomogeneous model, when blobs of air are entrained at high frequency (simulating a steady stream) the spectrum flattens and broadens and the dispersion γ increases, in the manner reported by Warner (1969b) to be characteristic of non-precipitating cumuli.

An example of a precise comparison of the predictions of the inhomogeneous model with observation is provided by

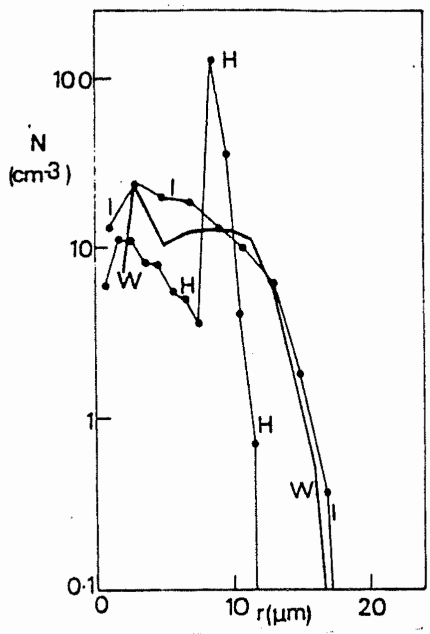

Figure 1. Size distribution in cumulus W, measured by Warner (1969b); H, calculated on the homogeneous model; I, on the inhomogeneous model. $N=200\text{cm}^{-3}$, $n=6$, $\lambda(0)^{-1}=10\text{s}$, $L=0.45\text{g m}^{-3}$, $U=1\text{m s}^{-1}$, $\mu=10^{-3}\text{m}^{-1}$.

Figure (1). The agreement between the curves W and I is seen to be excellent. On the other hand, curve (H), based on the homogeneous description of entrainment, is similar to those calculated by Warner (1973), but bears little resemblance to observation.

Another problem on which Warner has focused attention is the frequent occurrence of bimodal spectra in cumulus clouds. Spectra containing more than one mode, and resembling those observed by Warner (1969b), are predicted by the inhomogeneous model when the frequency of infiltration, λ, is low.

z(m)	100	300	600	1000
$R_H(\mu m)$	8.5	11.3	13.8	-
$R_I(\mu m)$	10.5	17.6	22.2	26.1
$N_T(l^{-1})$	58	2.6	0.53	0.15
$L_H(g\ m^{-3})$	0.10	0.39	0.72	-
$L_I(g\ m^{-3})$	0.06	0.41	0.71	1.00
$S_H(\%)$	0.37	0.17	0.14	-
$S_I(\%)$	1.12	0.42	0.39	0.34

Table 1. Calculated values, at various levels z, of liquid water content (L), supersaturation (S), maximum drop radius (R) and concentration of droplets of radius R, (N_T, inhomogeneous case only). The suffices H, I refer respectively to the homogeneous, and inhomogeneous models. $1/\lambda_0=10\text{s}$, $U=1\text{m s}^{-1}$, $N=200\text{cm}^{-3}$.

The results presented in Table (1) contain a striking prediction - that the largest droplets grow much faster through the condensational stage on the inhomogeneous than on the classical model. For example, about 200 seconds are required on the inhomogeneous model for the largest drops to achieve a radius of 15μm, while about 800 seconds are required on the homogeneous model. We see that on model I the largest droplets move through the condensational stage about three times as fast as is predicted classically. For larger values of $1/\lambda_0$ the rate of growth of the largest particles is not so great, but even for very large intervals between successive blobs (λ_0^{-1}=200,300s) the rate of growth is about twice the classical (homogeneous) value. Similar predictions have been made in a somewhat different treatment of this problem by Telford & Chai (1980). They appear to offer a solution to the long-standing question of the rate at which raindrops can be produced in cumulus. It is interesting to note that the values oof $N_T(\sim 1\ l^{-1})$ presented in Table (1) are of the right order of magnitude for raindrop concentrations.

The reason for the greatly enhanced growth-rates on the inhomogeneous model is apparent from the inspection of Table (1) - the values of supersaturation are much greater. This is because on the inhomogeneous model more droplets are completely evaporated and the newly activated ones that replace them cannot compete so effectively for the available water vapour. Thus the supersaturation rises above that for the homogeneous case, and those drops unaffected by the infiltrating blob will grow faster.

GENERAL MIXING CALCULATIONS During the mixing of cloudy and undersaturated air the local value $y(\underline{n},t)$ of each conserved variable y obeys a continuity equation of the form

$$\frac{\partial y}{\partial t} + \underline{\nabla}.(\underline{u}y) - D\nabla^2 y = R_y$$

where $\underline{u}$ is the local turbulent fluid velocity, and R_y is the local rate of change of y due to evaporation or condensation. We have performed crude numerical calculations of the turbulent mixing and concomitant phase changes by assuming that an equation of this form holds for each of the following variables: vapour density ρ_v, temperature T and population n(r) of droplets of radius r. The turbulent term has been replaced by diffusivity term $K\nabla^2 y$, we neglect buoyancy effects and the calculations were run for the case that a uniform sphere of radius λ containing undersaturated air is introduced at t=0 into an infinite cloud. During the calculations the diffusion proceeds for a time interval Δt during which there is no evaporation, and then all quantities remain fixed in space for a time interval Δt during which the phase change occurs. At the end of this period the time is marched forward through Δt and the cycle continued. The values of K, which were held constant for each run, were computed from ϵ and λ by the dimensional relationship $K=(\lambda^4\epsilon)^{\frac{1}{3}}$ for $\epsilon=10^{-3}, 10^{-2} m^2 s^{-3}$. We put $\Delta t=(\Delta\lambda)^2/6K$ for numerical stability of the diffusion algorithm, and we chose the spatial grid point separation $\Delta\lambda=0.1\lambda$. The initial values were $r<\lambda: T=277^oK$, $S=80\%$, $L\approx 3.6 \times 10^{-4} g\ m^{-3}$ $r>\lambda: T=278^oK$, $S=100\%$, $L=0.5 g\ m^{-3}$. The droplets inside and outside were assumed in equilibrium with their respective environments. All droplets were assumed to contain salt mass 5×10^{-13}g. The droplet concentration was everywhere 250 cm^{-3}.

As the calculations progressed all droplets with radii within each 0.1μm interval were compressed into a single size class whose number was chosen to conserve liquid water.

The results of these calculations show that for $\lambda=0.1$m, and for $\lambda=1$m, $\epsilon=10^{-2} m^2 s^{-3}$ the mixing is "classical" - that is, the phase changes are slow compared with the diffusion, and uniformity in S, L and T is achieved by the mixing with relatively little change in the droplet radii. In the case $\lambda=10$m, the phase changes occur on time-scales comparable with that of the diffusion, so that as the cloud begins to pour into the blob evaporation in that region brings S close to 100% and keeps the liquid water content there relatively low. The undersaturation is small, in subsequent stages of the mixing, and there is relatively little evaporation. Consequently, although the droplet spectra in the blob region contain some partially evaporated drops an increasing proportion are of basically the same sizes as those in the cloud.

These calculations, though crude, appear to be consistent with the field observations of Blyth et al (1980) and may provide a more realistic description of the mixing process.

REFERENCES

Blyth A M, Choularton T W, Fullarton G, Latham J, Mill C S, Smith M H and Stromberg I M 1980 The influence of entrainment on the evolution of cloud droplet spectra: II Field experiments at Great Dun Fell. (in press, Quart. J. Roy.Met.Soc.)

Baker M B and Latham J 1979 The evolution of droplet spectra and the rate of production of embryonic raindrops in small cumulus clouds. (J. Atmos. Sci. in press)

Latham J and Reed R L 1977 Laboratory studies of the effects of mixing on the evolution of cloud droplet spectra Quart.J.Roy.Met.Soc., 103, 297-306

Telford J T & Chai S 1980 A new aspect of condensation theory. Pageoph (in press)

Warner J 1969a The microstructure of cumulus cloud Pt II. The effect on droplet size distribution of the cloud nucleus spectrum and updraft velocity. J.Atmos.Sci., 26, 1272-1282

Warner J 1969b The microstructure of cumulus cloud. Pt I, General features of the droplet spectrum. J.Atmos.Sci 26, 1049-1059

Warner J 1973 The microstructure of cumulus cloud. Pt IV, the effect on the droplet spectrum of mixing between cloud and environment. J.Atmos.Sci., 30, 256-261

ACKNOWLEDGEMENTS The research described herein was supported by the National Science Foundation, the European Research Office, the Natural Environment Research Council and the US Office of Naval Research. Part of it was performed while one author (MBB) was in receipt of a Fulbright Scholarship.

MULTILEVEL TURBULENCE PROBE STUDIES OF THE STRUCTURE OF SMALL CUMULUS CLOUDS

S.J.Caughey and M.Kitchen

Meteorological Office, Bracknell, Berks., U.K.

1 Introduction

Previous observational studies of turbulence and mean airflow in and around cumulus clouds have in the main utilized aircraft to make one or more penetrations of selected clouds. In a comprehensive study of cumulus Warner (1970) made successive penetrations at 5 minute intervals but found no consistent pattern between levels, although some updrafts were observed to persist for 15-20 minutes. Other observations by MacPherson and Isaacs (1977) led them to the conclusion that the mean airflow within cloud was being masked by high levels of turbulence. It is also considered that turbulence plays a vital role in the entrainment of air into small cumulus and yet few detailed descriptions of the structure of the turbulence field within cloud are available. Warner (1977) recognised that a complete study of cumulus could not be based on aircraft sampling alone and the present study utilizes a tethered balloon system to investigate the structure of small cumulus. Amongst the advantages of this system are,

1. Simultaneous observations at more than one level may be obtained

2. There is little or no disturbance to the cloud

3. Since the clouds drift slowly through the instrumentation array a much longer, more representative, sample is obtained

4. It is relatively easy to resolve scales of motion down to $\sim \frac{1}{2} m$.

The disadvantages include the fact that significant cloud development may occur on the time scale of the observation and since it will take a fairly long time to collect data from a large number of clouds non-stationarity in boundary layer structure may be a problem.

2 Instrumentation and Experimental details

A large (1300 m^3) tethered balloon was used to support three turbulence probes (see Caughey 1977) and a PMS ASSP-100 droplet spectrometer. The highest probe and the ASSP were positioned a few metres apart and such that they intercepted the cumulus tops (up to 1400 m) whilst the other turbulence probes were positioned near cloud base (at ~ 1000 m) and within the convective

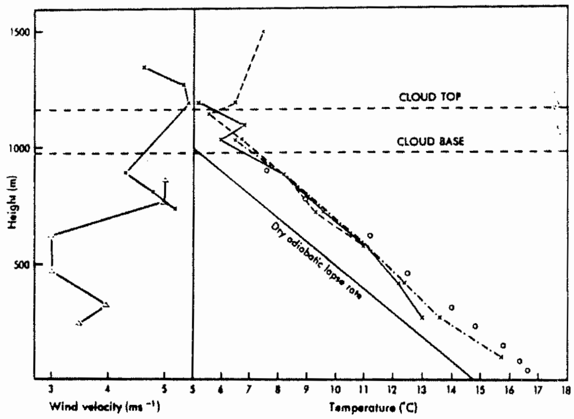

Figure 1. Wind velocity profiles from turbulence probe data (x) and tethered radiosonde (Δ). Temperature profiles are from the three probes, (x) descending in clear air at 1500 GMT and also from the tethered radiosonde ascent at 1440 GMT (o). A line with the slope of the dry adiabatic lapse rate is shown for comparison.

boundary layer (at ~ 800 m). Frequent cloud photographs were taken from the balloon tethering point and used to define cloud boundaries in the schematic figures presented later.

3 Broad scale structure of the boundary-layer

This paper discusses the observations made on the 1st June 1979 at RAF Cardington, Beds between 1045 and 1330 GMT. A light northeasterly airstream covered the area and shallow fair weather cumulus ($\frac{3}{8}$ cover) developed at the top of the convective boundary layer (CBL). Radiosonde ascents indicated a well mixed layer capped by an inversion (temperature step ~ 2K) with drier, stable air, aloft. The theoretical condensation level was 860 m and typical cloud base heights were in the range 1170 m to 950 m. Estimated cloud depths varied between 150 m and 300 m. Shown in Figure 1 are the mean wind and temperature profiles through the CBL and into the capping inversion, obtained from the turbulence probe data and an ascent at 1440 GMT by a tethered radiosonde. The presence of the broken and shallow cloud layer clearly has a negligible effect on the overall boundary layer structure.

Time histories of the vertical velocities for a section of the observation period and the associated temperature contours and cloud positions are given in Figure 2. (It should

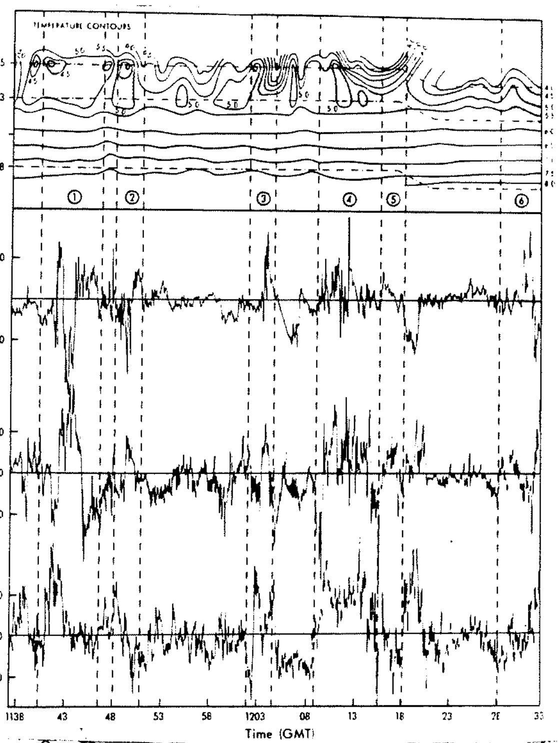

Figure 2. Vertical velocity time histories (w) for the three levels and temperature contours (0.5°C) plotted from the data at these levels (marked -.-.-). The clouds are marked by stipling and are identified by the numbers 1 to 6 . Two between cloud gaps are marked A and B.

be noted that the temperature measurement within cloud is affected by wetting of the resistance wire sensor and quantitative interpretation is therefore not possible, however the data are presented here to specify the capping inversion height and to assist discussion.) The turbulent up-and down-draughts (1-2 ms^{-1}) associated with the clouds are particularly prominant in the data and exhibit marked vertical coherence. Their position is also well correlated with the undulations of the capping inversion.

Turbulence statistics averaged over the whole run show similar behaviour to that observed in the higher regions of the cloud-free CBL (see Caughey and Palmer, 1979). Quantities such as the dissipation rate of turbulence kinetic energy, ε , and the vertical velocity variance, σ_W^2, decrease with height from $z/z_i \sim 0.6$ to 1.0 (where z_i is the CBL depth and z the observation height). The predominant scale for vertical motion also decreases as the capping inversion is approached.

3 Turbulence structure of individual clouds

Four clouds, in various stages of development, were selected for detailed study and the results for one are presented here. This cloud was considered to be at the 'mature' stage of the life cycle and contained a single updraught which reached $\sim$3 ms^{-1}. Gust vectors (5 s averaging period) were constructed for the vertical (see figure (3)) and horizontal planes and the cloud boundaries and suggested flow pattern added.

A high degree of vertical coherence is evident with a main inclined updraught which turns over at the CBL top in the direction of the mean shear, so that the overall circulation assumes a characteristic 'P' shape. Strong inflow at cloud base, which results in a local lifting of the base, is also evident. Theoretical studies by Bennetts and Gloster (1980) have indicated that 'P' type circulations should be a common occurrance and in certain circumstances may account for the observations of bimodal droplet spectra in large cumulus. Visual studies have also produced evidence for such flow patterns (Magono and Hozumi, 1975). The gust vectors in the horizontal plane show evidence for rotation of the flow about the updraught centre below cloud base. Other observations of rotating thermals have been discussed by Ludlam and Scorer (1953). The pattern of motion discussed above was observed in all clouds studied, including a weak dissolving cloud.

The distribution of the small scale turbulent fluctuations (ie scales from $\sim$ 1 m to $\sim$ 50 m) within and below cloud were also considered. The results showed that the up and downdraught regions contained the highest levels of turbulence. Vertical velocity power spectra averaged over the cloud duration sometimes showed evidence for a double peak structure, indicative of two predominant scales for vertical motion (see Figure (4)). The lower frequency peak (corresponding to a wavelength of $\sim$2 km) reflects motion on the scale of the main up and downdraught structure,

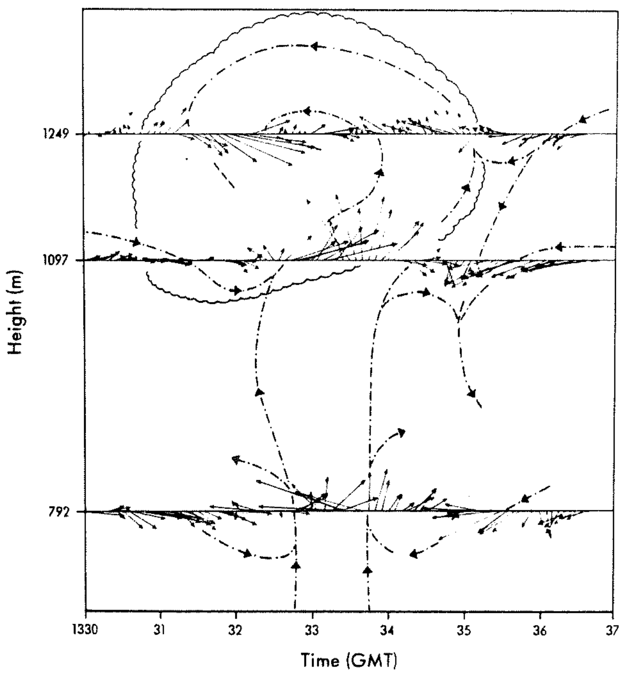

Figure 3. 5 second gust vectors plotted for cloud number 6 in the vertical plane. The cloud boundary is marked schematically together with the suggested flow pattern.

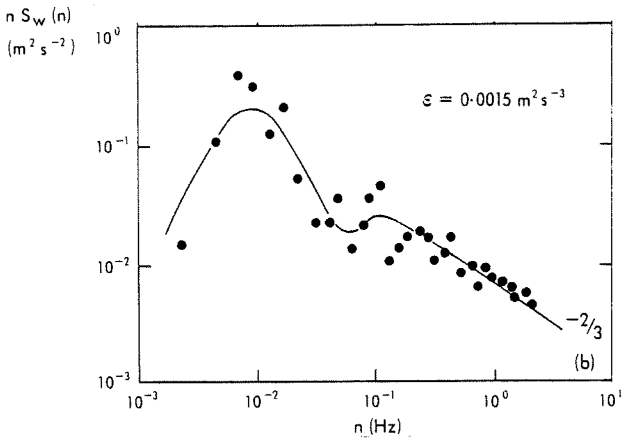

Figure 4. Vertical velocity spectra for cloud number 6 at 1097 .

whereas that at higher frequency (wavelength 50-100m) is characteristic of the embedded turbulent eddies. This is supported by the observation that the turbulence cascade, which forms the inertial subrange and produces a characteristic $-\frac{2}{3}$ spectral slope, begins at the higher frequency peak. These observations therefore lend some support for a separation of the main scales for convective and turbulent motion which is widely assumed in numerical studies of cumulus to allow a simpler treatment of the turbulence field.

Although the mean turbulent structure closely resembled that from the clear CBL it was found that the clouds strongly modulated the turbulence profiles. Typically turbulence dissipation rates increased with height and on occasions values at cloud top reached several times those in the clear CBL below. Maximum values were of order $3\ 10^{-3} m^2 s^{-3}$. Profiles of σ_W also serve to highlight the change in CBL structure (see Figure (5)). Passage of the clouds is invariably accompained by profile distortion and increased turbulence levels, the greatest effect being associated with the most visibly vigorous clouds. The gaps between clouds show a small decrease in σ_W with

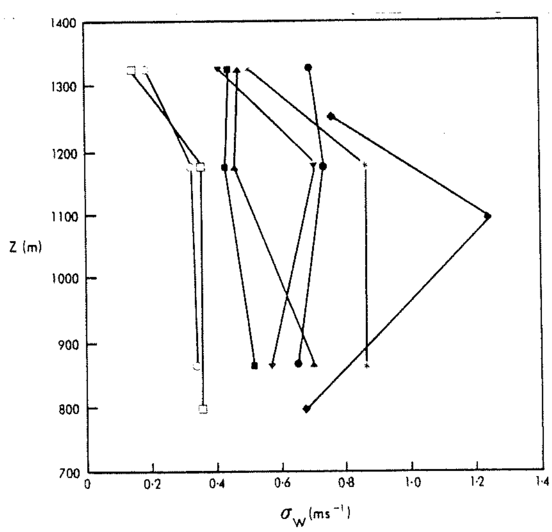

Figure 5. Profiles of σ_W for clouds 1(●), 2(■), 3(▲), 4(▼); 5(✱); 6(♦) and gaps A(○) and B(□).

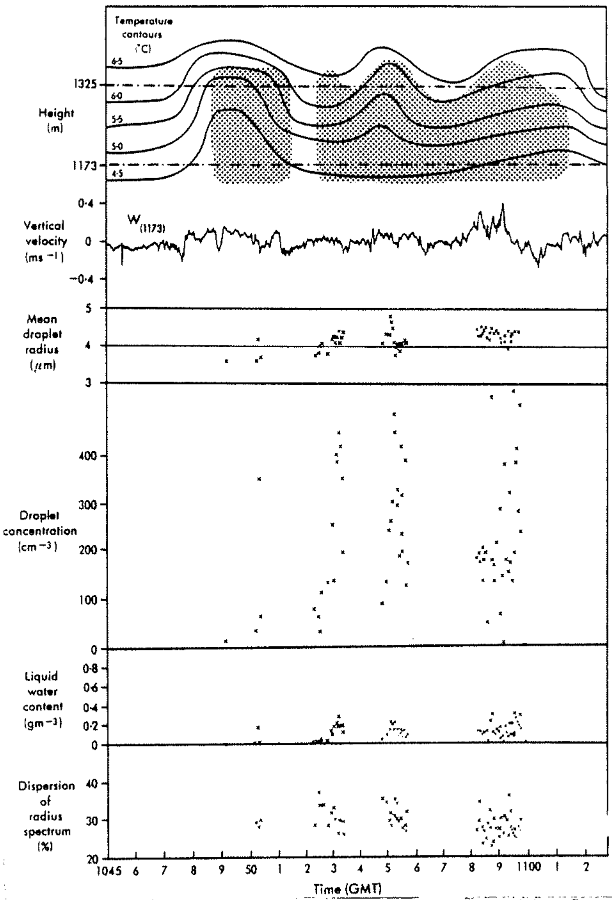

Figure 6. Temperature contours and vertical velocity time history from cloud base for two clouds, together with droplet data (Mean radius, concentration liquid water content and dispersion) from the ASSP-100.

height and much reduced turbulence levels.

4. Microphysical aspects

Information on the cloud droplet field from the ASSP-100 is presented in Figure (6) for two clouds, together with the vertical velocity time history near cloud base. The second cloud appears to have three turrets which were intercepted by the ASSP and this is also reflected in the undulations on the inversion and positions of the up-draughts. A striking point to emerge from the droplet data is that the large and rapid fluctuations in droplet concentration (between 0 and 500/cm^3 in distances of a few tens of metres) are accompanied by only very minor changes in the mean droplet radius ($\sim$10%). A comparison of droplet spectra from high and low ($>$.15gm^{-3} and $<$ 0.05gm^{-3} respectively) liquid water content regions is given in Figure (7) and confirms the small change in spectral shape occurring during evaporation. It would therefore seem that the mixing process in these clouds is proceeding essentially inhomogeneously, much as envisaged by Latham and Reed, 1977. Certainly it seems likely that with the measured turbulence levels in cloud the time scale for turbulent erosion of the entrained air was much longer than that for the evaporation of 4-5μm radius droplets.

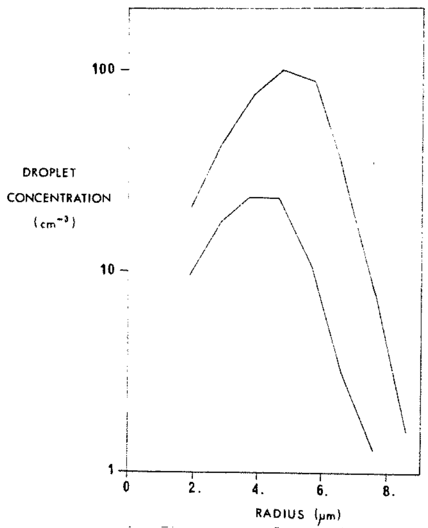

Figure 7. Mean droplet spectra for regions of high (> 0.15 gm^{-3}) and low (< 0.05 gm^{-3}) liquid water content.

5. Concluding remarks

The simultaneous multilevel observations presented above have identified the occurance of 'P' type circulations in shallow cumulus growing at the top of the CBL. Spectral analysis of the vertical air motion shows some evidence for two predominant length scales, the larger associated with the main convective elements and the smaller due to the associated turbulence field. The microphysical data point to a highly inhomogeneous cloud structure with large and rapid fluctuations in number density, but surprisingly constant mean droplet radius and spectral shape.

References

Bennets D.A. and Gloster J, 1980. "Bimodal size distributions within Cumulus Clouds" Proc. VIIIth. International Cloud Physics Conference, Clermont-Ferrand.

Caughey S.J., 1977. "The Cardington Turbulence Instrumentation" Met Office Turbulence and Diffusion Note No.82.

Caughey S.J. and Palmer S.G, 1979. "Some aspects of turbulence structure through the depth of the convective boundary layer". Q.J. Roy.Met.Soc. 105 pp 811-827.

Latham J. and Reed R.L., 1977. "Laboratory studies of the effects of mixing on the evolution of cloud droplet spectra" Q.J. Roy.Met.Soc. 103 pp 297-306.

Ludlam F.H. and Scorer R.S., 1953. "Reviews in modern meteorology 10. Convection in the atmosphere" Q.J. Roy.Met.Soc. 79 pp 317-341.

MacPherson J.I. and Isaacs G.A., 1977. "Turbulent Characteristics of some Canadian Cumulus Clouds" Jour.App.Met. 16, pp 81-90.

Magono C. and Hozumi K., 1975. "Rotating motion of cumulus clouds over the sea, as observed by time lapse movie" Tokyo (Met.Res.Inst), Management Comm.AMTEX, AMTEX Rep.No.8 (1975) pp 142-144.

Warner J., 1970. "The microstructure of cumulus clouds, Part III, The nature of the updraft" Journ.Atmos.Sci. 27 pp 682-688.

Warner J., 1977. "Time variation of updraft and water content in small cumulus clouds" Journ.Atmos.Sci. 34 pp 1306-1312.

ON MICRO-PHYSICAL PROCESSES IN MIDDLE-LEVEL PRECIPITATING CLOUD
—— MIXING OF FALLING PARTICLES ——

Y.Fujiyoshi and T.Takeda
Water Research Institute
Nagoya Univ., Nagoya, JAPAN

1. Introduction

The size distribution of precipitation particles originated from middle-level clouds has been calculated by many authors (for example, Srivastava,1978; Passarelli,1978), taking into account such growth processes of particles as ice crystal aggregation, raindrop coalescence, drop breakup, accretion of cloud droplets and vapor deposition. In their models precipitation particles are postulated to be originated only from a single cloud or generating cell. However, the mixing of precipitation particles originated from different clouds or generating cells was frequently observed by radar.

In our previous paper (Fujiyoshi et al., 1980) we reported on the basis of the observation of middle-level precipitating clouds using a vertically pointing radar, a field mill and an optical spectrometer with a charge detector that particles grew large when particles originated from different generating cells were mixed above the freezing level. The effect of the mixing among particles on their growth was supported by the measurement of the charges on raindrops on the ground. That is, we observed quite large charges of raindrops whose magnitude was as large as those of drops from thunderclouds when the mixing process occurred. This fact suggests that precipitation particles were charged through friction process.

In this paper we will show the RHI radar observation of the mixing process of particles falling from middle-level precipitating clouds. We will discuss what type of the mixing process is of great importance for the micro-physical processes in middle-level clouds.

2. Examples of the mixing process

The mixing process can be classified into the following types in accordance with the level where the process occurres —— above or below the freezing level —— and with the type of cloud from which precipitation particles are originated —— whether the clouds are convective or not.

(i) Mixing of precipitation particles from uniformly extended clouds.

Fig.1 shows an example of the vertical cross section of echo intensity in extended cloud. The movie of the radar display showed that the intensive echo layer fell into the weak echo layer above the freezing level, therefore suggested that the mixing process had occurred there (i-a). Precipitation particles are dispersed vertically during their falling, since the falling velocity is different among particles. The particles with large velocity would catch up with those with small velocity which fell earlier. It would be fully expected that the mixing process occurres below the freezing level, too (i-b).

It is found from our observations that rainfall intensity in this type of echoes was rather weak. The magnitude of surface electric field was weak and its time change was very little. The mixing of particles from uniformly extended clouds would cause a little enhancement of crystal aggregation or raindrop coalescence.

(ii) Mixing of particles originated from different generating cells.

Fig.2 shows an example of the vertical cross section of echo intensity in clouds containing generating cells. The cross section suggests the occurrence of the mixing process above the freezing level (ii-a). As shown in Fig.3, the mixing process did not occur in the streamer region, but it did near the generating cell when convective cells were deep and they existed closely (ii-b). Fig.4 shows that the mixing process occurred below the freezing level under shallow generating cells (ii-c).

Generally the magnitude of surface electric field was weak and it did not change so much in the types of (ii-a) and (ii-c). On the other hand, surface electric field changed very frequently with large amplitude and lightning discharge was observed even though the bright band appeared in radar scope in the type of (ii-b). The case reported in our previous paper (Fujiyoshi et al.,1980) belongs to the type of (ii-b). The mixing process would play an important role in micro-physical processes in the type of (ii-b).

(iii) Mixing between particles originated from uniformly extended cloud and those from convective cells.

The coexistence of uniformly extended middle-level cloud and convective cells around the freezing level was sometimes observed. Fig.5 shows an example of this type. The height of bright bands fluctuated following the passage of convective cells. It is interesting that the echo intensity of the convective cells was quite large though they were shallow. This fact suggests that particles grew large at the region where the mixing occurred. In this type of (iii), the growth process of particles in the region where the mixing occurres would be an interesting problem.

3. Concluding remarks

In this paper we described the various mixing of particles originated from middle-level clouds on the basis of radar observations. The mixing which was inferred to be very important for the growth of particles was observed,
(1) when the generating cells were deep and they existed closely, and
(2) when middle-level precipitating clouds which were uniformly extended were coexisted with convective cells which appeared around the freezing level.

Studying the change of echo intensity, we will discuss the growth process of particles for the types of mixing written above in detail.

References

Fujiyoshi,Y., T.Takasugi, Y.Gocho and T.Takeda, (1980) : Radar echo structure of middle-level precipitating clouds and the charge of raindrops. J.Meteor.Soc. Japan, to be published.

Srivastava,R.C., (1978) : Parameterization of raindrop size distributions. J.Atmos. Sci.,35,108-117.

Passarelli,R.E., (1978) : An approximate analytical model of the vapor deposition and aggregation growth of snowflakes. J.Atmos.Sci.,35,118-124.

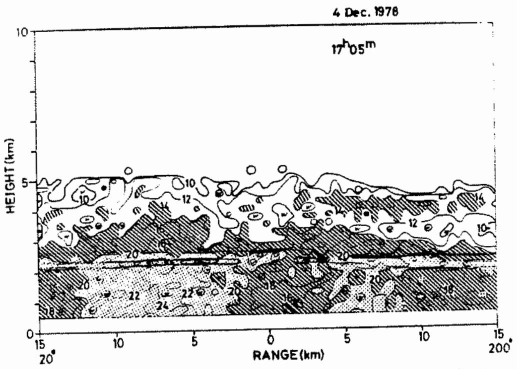

Fig.1 Vertical cross section of echo intensity. Contours are drawn every 2 dBZ. The bright band appeared at about 2.25 km.

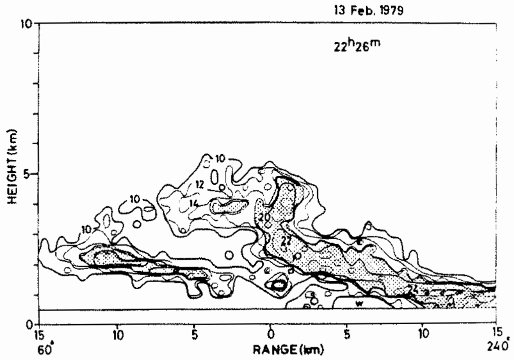

Fig.2 Vertical cross section of echo intensity. The bright band appeared at about 1 km.

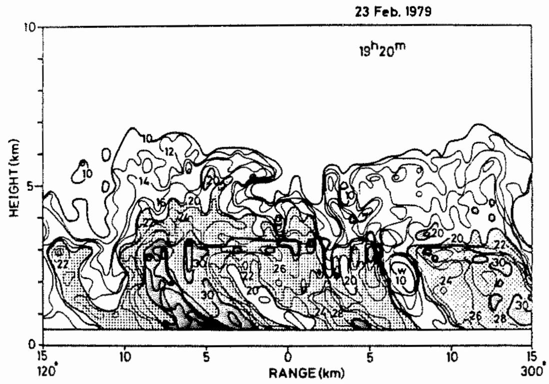

Fig.3 Vertical cross section of echo intensity. The bright band appeared at about 3 km.

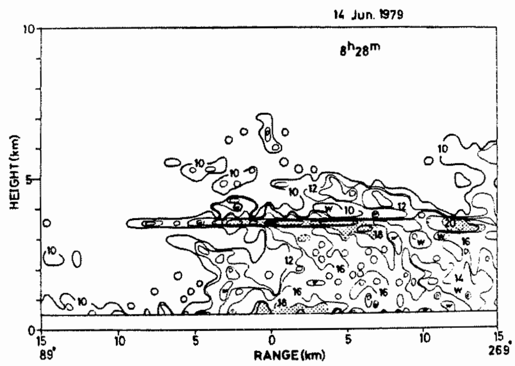

Fig.4 Vertical cross section of echo intensity. The bright band appeared at about 3.75 km.

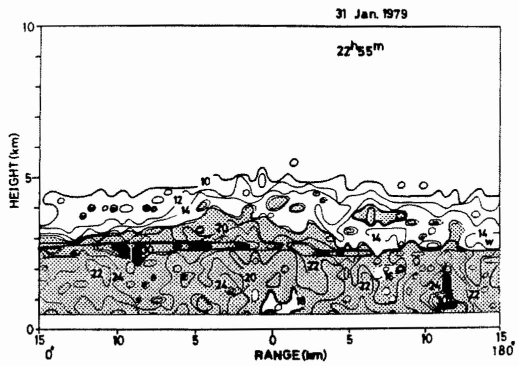

Fig.5 Vertical cross section of echo intensity. The bright band appeared at about 2.75 km.

THE RELATIONSHIP BETWEEN THE DEPTH OF CUMULIFORM CLOUDS AND THEIR RAINDROP CHARACTERISTICS

a. Winter Continental Cumuliform Clouds

A. Gagin
Department of Atmospheric Sciences
The Hebrew University of Jerusalem
Jerusalem, ISRAEL

1. Introduction

A computerized observation system consisting of a remotely located (50 km) C band volume scanning radar, x-band vertically pointing radar and groundbased distrometer, capable of providing the spacial distribution of the clouds, real time crosssections of clouds passing overhead together with their raindrop characteristics on the ground, was utilized to provide also data on cloud echo height and the vertical distribution of reflectivity together with the corresponding values of rain rates (or intensities), rain liquid water content, raindrops concentration and the raindrop mean volume diameters at a temporal resolution of 60 seconds.

The clouds studied were predominantly cumuliform clouds associated with cold fronts, post-frontal cloud bands and open Benard cell convective cloud clusters.

This study upgrades our previous studies on the relationship between the concentrations of ice crystals and graupel particles, in clouds of various depths and top temperatures, as performed by our research aircraft. Thus an attempt was made to add another link to the studies of the chain of events leading to the formation of precipitation particles, namely that of relating raindrop characteristics on the ground to the depth (or cloud top height since cloud base altitude is fairly uniform at approximately 2500 ft . m.s.l.) of such cumuliform clouds, for which our previous studies have established a relationship between the concentration of ice crystals and the embryomic graupel particles.

2. Results

The results outlined below are those obtained from a total number of 74 clouds for which the crosschecks of the two radars ensured that the ground based distrometer and the vertically pointing radar, located next to it, were both co-located under the main volume of the cloud under study. The reference for comparison was taken as the cloud top height. Rain drop size distributions and their derivatives such as rain rates, raindrop median volume diameters, rain liquid water contents and raindrop concentration were obtained for each cloud in two forms: maximum and mean values for cloud duration over the measuring site.

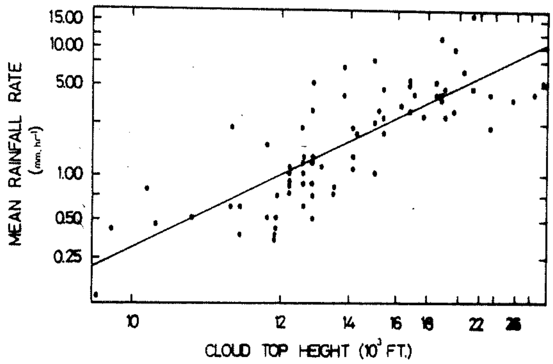

Figure 1. The dependence of mean rain rate on maximum cloud top height.

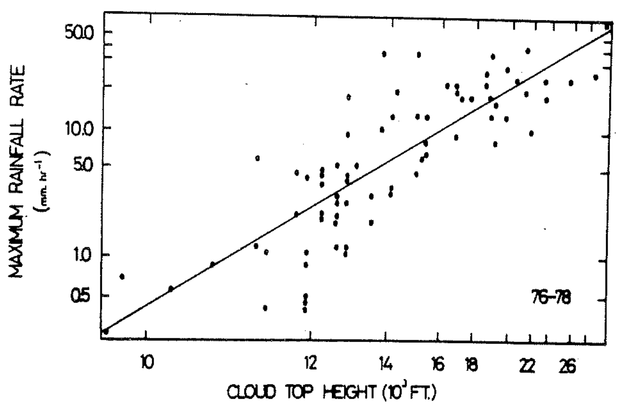

Figure 2. The dependence of maximum rain rate on maximum cloud top height.

Some of the major findings are listed below:

1. Both maximum and mean rain rates are shown to depend quite clearly on cloud top height. Correlation coefficients were found to be 0.84 and 0.81 respectively. See figures 1 and 2.

2. Clouds with tops lower than about 10,000 ft m.s.l. (cloud depth of about 3 km) rarely produce any rain which can be detected at the ground - about 200 m below cloud base.

3. Both mean liquid water content and raindrop mean volume diameter show similar positive correlation with cloud top. The corresponding values of the correlation coefficients are 0,77 and 0,73 respectively. See figures 3 and 4.

value of coefficient is significantly higher i.e. 0.75. See figures 5 and 6.

5. Raindrop concentrations (⩾ 0.6 mm) roughly correspond, on the average, to graupel concentrations at altitudes of 1000 ft. below cloud top, for clouds in the range of top heights of 11,000 to 20,000 ft or in the top temperature range -10 to -22^{o}c.

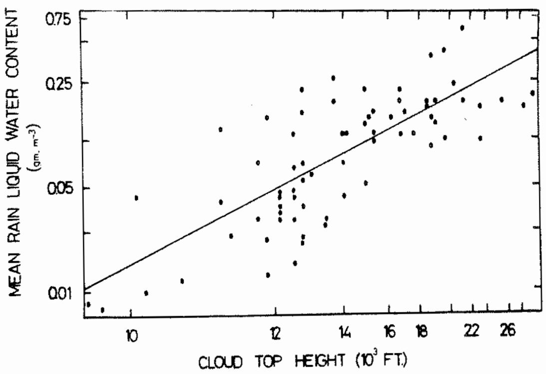

Figure 3. The dependence of mean rain liquid water content on maximum cloud top height.

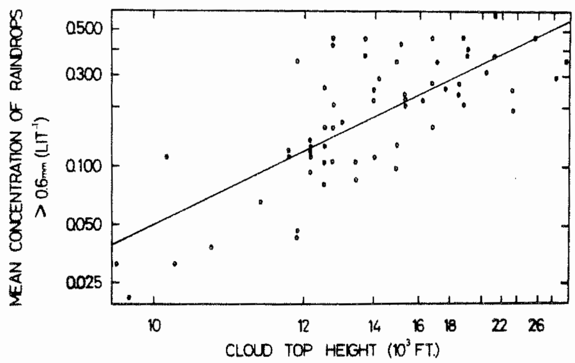

Figure 5. The dependence of mean raindrop concentrations, ⩾ 0.6 mm, on maximum cloud top height.

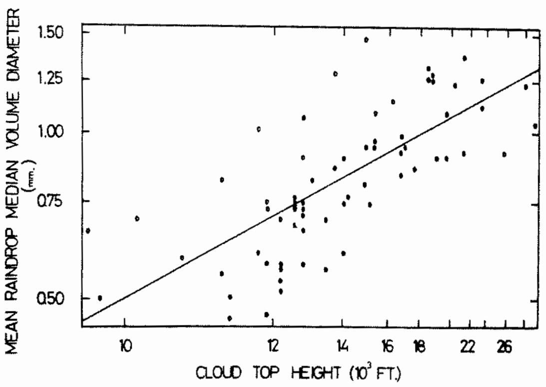

Figure 4. The dependence of mean raindrop mean volume diameter on maximum cloud top height.

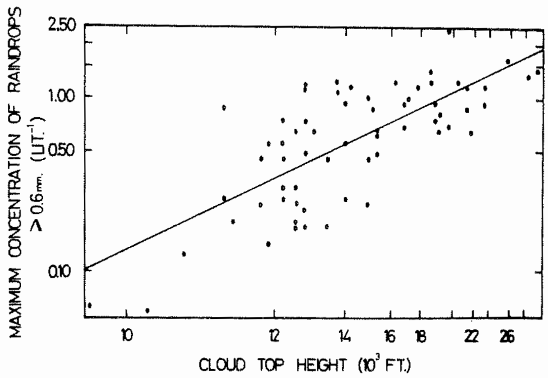

Figure 6. The dependence of maximum raindrop concentrations on maximum cloud top height.

4. The correlation of the concentration of raindrops larger than 100 um with cloud top height was found to be 0.55. However if one takes the corresponding correlation only for the concentration of raindrops ⩾ 0.6mm the

3. General conclusions

Tentative conclusions are drawn to suggest that:

a) In the winter continental cumuliform clouds of the Eastern Mediterranean the chain of events from ice crystals via graupel particles to raindrops on the ground can be described in a quantitative manner.

b) Comparisons of the observed raindrop distribution data with calculations obtained from a rather straightforward model of hydrometeor growth in clouds with a known vertical stratification of temperature, liquid water content, ice crystal concentrations and under some assumptions on the nature ofthe updraft vertical profiles, indicates a fair degree of agreement.

c) The highly correlated relationship between cloud depth and rain rates was used to determine, by comparisons with one dimensional model prediction of rainfall, the adequate autoconversion rates for such highly colloidal clouds. The best fit between the computed and observed rain rates was obtained for autoconversion rates of $K=10^{-4}$ and $a= 1.5$ as compared to those used for the Florida cumuli of $k = 10^{-3}$ and $a = 0.5$.

The later conclusion is taken to conclude that the local winter continental cumuliform clouds release their rainfall at relatively low precipitation efficiencies.

REFERENCES

1. Gagin A and I. Steinhorn, 1974: The role of solid precipitation elements in natural and artificial production of rain in Israel. J.Wea.Modif. 6, 216-228.

2. Gagin A., 1975: The ice phase in winter continental cumulus clouds. J. Atmos. Sci. 32, 1604-1614.

THE PARAMETERIZATION OF MICROPHYSICS IN DYNAMIC CLOUD MODELS

William D. HALL and Terry L. CLARK

National Center for Atmospheric Research*
Boulder, Colorado USA

Over the last few years considerable progress has been made in the numerical simulations of severe convection with the development of three-dimensional cloud models. Typically, microphysical treatments used in such multi-dimensional cloud models are crude and do not adequately describe the dominant microphysical processes controlling the development of precipitation. While detailed numerical treatments in more simplified frameworks have been established, computer storage requirements and central processing time limitations prohibit their direct application in three dimensions. The present goal of this work is to develop and test suitable parameterizations of microphysical processes that can be efficiently applied within three-dimensional cloud models.

The microphysical processes within clouds are generally classified into two types, warm cloud processes and cold cloud processes. Warm cloud processes include the nucleation, condensation, coalescence, and breakup which affect the spectral development of the liquid phases. The cold cloud processes include nucleation, diffusional, accretional, and aggregational growth of ice particles.

The most common applied warm rain parameterization is due to Kessler (1969). This scheme assumes that the total liquid water phase can be represented by two variables, cloud water and rain water mixing ratios. The scheme contains no information on the spectral distribution of cloud water and assumed that the rain is represented by a Marshal-Palmer type spectra. An auto-conversion concept is utilized in which cloud water is converted to rain water at a rate based upon the value of the cloud mixing ratio value. Clark (1976) attempted to improve the physical basis of the conversion of cloud water to rain water by proposing a microphysical parameterization that assumed the liquid phase spectra is represented by two log-normal distributions. After introducing this solution into the physical equations governing the condensation and coalescence processes moment tendency equations were constructed to form the basis of the parameterization. Although this method was successful and compared well with detailed calculations in a Lagrangian parcel framework, it was later discovered that problems with the sensitivity to the collection kernal and solution singularities associated with moment closure approximations could lead to physically inconsistent results.

Koenig and Murray (1976) extended the Kessler scheme to incorporate the ice phase. This scheme allowed two types of ice particles to occur depending upon whether the ice particle originated through sorption nucleation or by ice collisional contact nucleation with rain water. A significant improvement of the representation of the ice phase was made with this parameterization. They assumed that each ice species is represented by two variables - a number concentration and mixing ratio. This allows for the calculation of a characteristic particle size in which realistic growth rates and terminal velocities are directly applied.

In order to test any proposed parameterization scheme within an interacting dynamical framework, a detailed model within a two-dimensional slab symmetric dynamic framework was constructed (Hall, 1980). The detailed model assumes that the liquid water spectra is represented by 69 logarithmically-spaced discrete categories and the ice spectra is represented by 51 categories. The warm rain processes considered in the model are nucleation, condensation, coalescence, and breakup of water droplets. The ice phase processes considered include nucleation, diffusional and accretional growth. Figures A, B, C, and D show results for one run of the detailed model. The environmental sounding data employed for this run was taken on July 22, 1976 during the National Hail Research Experiment field program in northeastern Colorado. The cloud condensation activation spectra and ice nucleation characteristics applied represent average measured properties for this region. The vertical velocity structure, shown in Fig. A, at 27 minutes of integration time, illustrates two distinct maxima within the cloud. The primary maxima in vertical velocity at the top of the cloud has a value of 13.2 m/sec and the secondary maxima located near the side of the cloud is 5.1 m/sec at this time. Both maxima are associated with maximum downdraft velocities near the same levels just outside the cloud. This velocity configuration is due to the production of horizontal vorticity caused by strong horizontal gradients in bouyancy across the cloud boundary. In Fig. B the total liquid water mixing ratio field is shown and in Figs. C and D are shown the ice crystal concentrations of particles less than and greater than 400 nm diameter, respectively. This ice crystal concentration pattern is the result of ice particles being nucleated in the upper portions of the cloud and carried downward by vertical motions in the center and side of the cloud. The maximum concentration of the largest particles as found at this time is located within the updraft regions near the edges of the descending ice crystals. This result is due to transport and mixing of ice particles into larger liquid water content regions where

*The National Center for Atmospheric Research is sponsored by the National Science Foundation.

accretional growth is most rapid.

The detailed two-dimensional model will provide a basic framework for the testing of any proposed microphysical parameterization. Modification and testing of presently available parameterization schemes are currently in progress. It is hoped that through careful analysis of the detailed model a parameterization method will be constructed in which the dominant microphysical mechanisms controlling the development of precipitation will be adequately represented.

References

Clark, T. L., 1976: Use of log-normal distributions for numerical calculations of condensation and collection. *J. Atmos. Sci.*, *33*, 810-821.

Hall, W. D., 1980: A detailed model within a two-dimensional dynamic framework - model description and preliminary results, submitted to *J. Atmos. Sci.*

Kessler, E., 1969: On the distribution and continuity of water substance in atmospherica circulations. Meteor. Monogr., 10, No. 32, 84 pp.

Koenig, L. R. and F. W. Murray, 1976: Ice-bearing cumulus cloud evolution: Numerical simulation and general comparison against observations. *J. Appl. Meteor.*, *15*, 747-764.

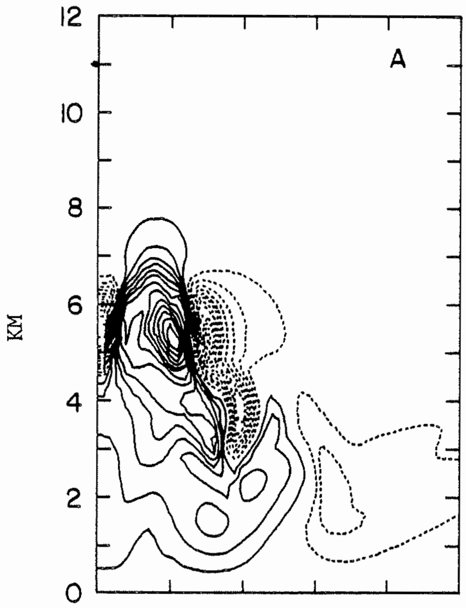

Figure A. Vertical velocity field, solid line positive, dashed line negative, contour interval is 1 m/sec.

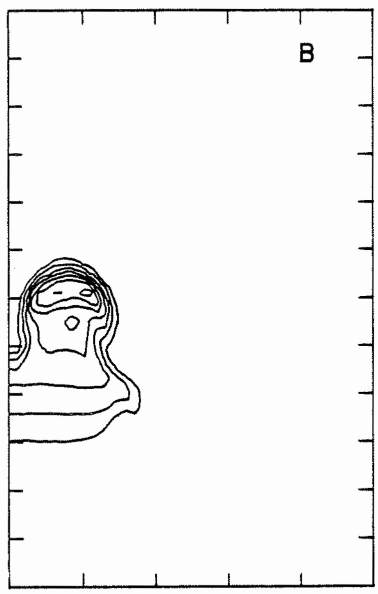

Figure B. Liquid water mixing ratio, contour interval is 1 gm/kg.

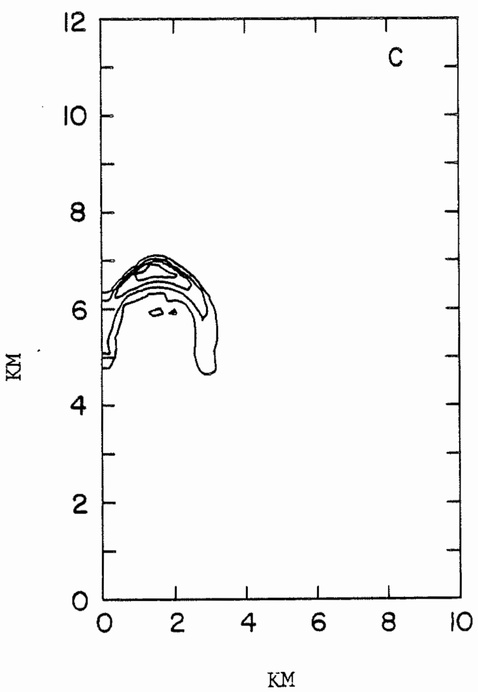

Figure C. Ice particle concentration of particles less than 400 μm diameter. Contour interval is 0.1 per liter.

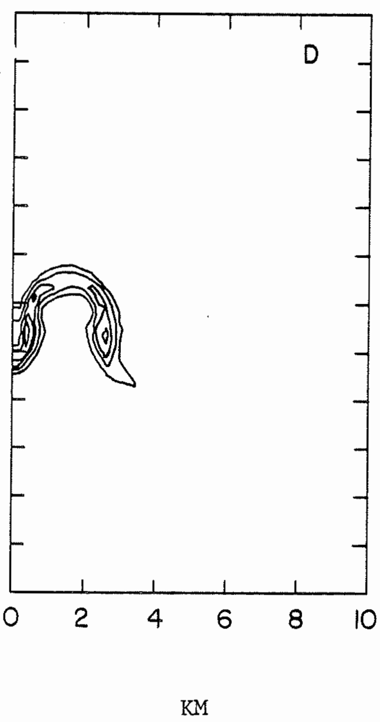

Figure D. Ice particle concentration of particles greater than 400 μm diameter. Contour interval is 0.01 per liter.

THE AUGMENTATION OF RAINFALL BY COOLING TOWER PLUMES

K.E.Haman and M.Niewiadomski

Institute of Geophysics,University of Warsaw
Warsaw,POLAND

1. Introduction

Augmentation of precipitation downwind from cooling towers of power plants has been announced allready in few papers - recently by Koenig (1978).Mechanism of this augmentation may be of microphysical character (since cooling towers emit drift droplets,which can act either directly as coalescence nuclei,or after evaporation may form giant condensation nuclei) or may have dynamical character (since in sufficiently unstable and humid weather developement of huge convective clouds can be triggered by cooling tower emission).

In this paper another mechanism of such augmentation is being tested.The cooling tower plume can penetrate Ns clouds or subfrontal cloud system increasing their thickness and water content,not only due to their initial water content,but also due to the humidity of environmental air entrained into the plume and forced to move upwards with it.The increased water content may be then washed out by precipitation falling from above,which in this way can increase its mass,or at least may reduce effects of evaporation in subcloud layer.It is worth of noting that Thor Bergeron have postulated such a mechanism for explaining the increased rainfall correlated with low hills (Bergeron 1965).The authors of this paper had observed a visibly thicker cloud deck in the wake of a great power plant,during a continous rainfall.This effect was detectable more than 15 km from the plant.

In the present paper,a semiquantitative analysis of this mechanism is made,aimed at approximative determination of the range and intensity of its effects and its dependence upon meteorological parameters.This analysis is performed by means of the one dimensional model of cooling tower plume,developed by the authors.

2.The plume model

The cooling tower plume in the model is considered to be a one dimensional steady jet with top hat profiles of all parameters in a plane perpendicular to its axis. The axis itself may be three dimensional curve.Horizontal velocity is assumed to be equal to the velocity of external wind at a given level.Vertical velocity of the plume is calculated from equation of motion,which takes into account the thermal buoyancy corrected for humidity and drag of condensed water,entrainment of environmental air,aerodynamic drag and internal circulation parametrized by virtual mass coefficient.Balances of enthalpy and total water with division into liquid water (LWC) and vapour take into account variations of pressure and entrainment.Washout by precipitation is introduced by means of rather rough parametrisation - physically consistent accounting for washout is very difficult in such a one dimensional plume model.The cross section of the plume is assumed elliptical - changes of semi-axes depend on deformation by by velocity gradients and entrainment of mass.THe entrainment hypothesis which closes tha balance of mass equation is basically a Taylor's type one - the rate of the mass flux inrease is directly proportional to the relative velocity of the plume withrespect to ambient air, and to the plume circumpherence/cross-section area ratio.It also takes into account the increase of entrainment with inclination of the plume and an extra term responsible for passive turbulent diffussion. The model allows for merging of plumes from various sources (also stacks) with relatively little distortion of the geometry of plumes. The input data consist of horizontally homogeneous pressure,temperature,humidity and wind sounding,heights,sizes and localizations of towers or stacks,as well as temperatures,water contents and outflowing air velocities at their outlets. The output consists of vertical and horizontal coordinates of the plume axis,pressure,temperature,humidity,LWC,velocity components of the plume and semi-axes of its perpendicular cross-section.Full description of the model is being prepared for publication. Among allready published models of cooling tower plumes,the improoved "Sauna" model (Junod et al.,1975) is probably the most similar one.

3.Basic idea of the numerical experiment

In the course of experiment,the changes of rainfall rates due to the coalescence with liquid water of clouds or plumes (continous coalescence model) as well as due to evaporation in cloud-free space are calculated.Computations are made for rainfall going through the plume and out of the plume.In the former case differences between trajectories of droplets of various sizes are taken into account,since the plume is horizontally inhomogenous.

THe following assumptions are made: the cloud has horizontally homogenous base height. Below the cloud base relative humidity is 97% - - above 100%. LWC in the cloud is height independent.The power plant has 6 cooling towers, 140 m high with diameters at the top 60m,arranged in two rows of three towers,300 m each from the other. The outflowing air has temperature

15 K higher than the ambient air, is saturated with water vapour, its LWC is 0.1 g/kg and vertical velocity is 5.5 m/s. This system corresponds to a power plant of about 5 GW. The rainfall starts at the 1.5 km level; it is divided into 5 size classes based on the Marshall-Palmer distribution.

The analysis of influence of the plume on the precipitation is based upon certain standard case (row 0 in Table 1). In the course of experiment, these parameters were varried according to the Table 1 in such a way, that in each run only one parameter (sometimes two) has been changed. The computations were made up to 10 or 25 km downwind from the plant and the rainfall rate increase (in %) with respect to the rainfall outside the plume on each kilometer has been found, as well as the rainfall integrated over the area under the plume. Table 2 gives the results obtained in certain selected runs. The first row (o) gives the rainfall increase in the standard case. The symbols of other runs indicate the row and column intersection in Table 1, which has been taken instead of the standard value.

4. Discussion of the results

The results presented in Tables 1 and 2, as well as certain other outprints concerning details of the geometry and thermodynamics of the plume, which cannot be presented because of the lack of space suggest the following conclusions:

i) It is obvious, that the main parameters which control the augmentation of rainfall are thickness of the plume and its LWC. However, their influence upon the rainfall rate is nonlinear and depends upon the dynamics and thermodynamics of the plume and environment in a rather complicated way.

ii) For stable stratification (lapse rate more than 1 K/km less than the wet adiabatic one) the rainfall augmentation is limited to about 10% in a range of about 10 km or less, except of the close neibourhood of the plant. Variations in wind, rainfall intensity, or temperature don't introduce essential changes into this picture. Characteristic feature of this situations are weak and damped Vaisala-Brunt oscillations, which may lead even to the loss of precipitation intensity in their troughs.

iii) For stratifications more close to the neutral one (lapse rate about 0.5 K/km less than the wet adiabate) the rainfall augmentation becomes very sensitive the changes of other parameters - particularily to the cloud base level. With low base (300 m), augmentation remains moderate but with higher base (500 m) essential relative increase of rainfall is observed at distances up to 25 km due both to the increased evapotation below the cloud (which decreases the reference rainfall), as well as to the slightly improoved conditions of plume rise at greater distances from the plant. For high base (800 m) the plume evaporates below the cloud base and its effect is reduced to the close vicinity of the plant.

iv) For stratification slightly unstable the augmentation of rainfall may increase very rapidly both in amount as in range, exceeding in certain points 100%, though the vertical velocity of the plume is kept well below 0.5 m/s. In such a case the augmentation of rainfall below the plume, only in the range up to 10 km, may exceed the total emission of water from the cooling towers.

5. Conclusions

Allthough the particular values of rainfall increase presented in Table 2 may result partly from the simplifying assumptions, the fact of possibility of strong augmentation of rainfall even up to 100%, in cases when within the Ns cloud stratification becomes close to the wet adiabtic one seems to be a real physical fact and systematic increase of rainfall in the lee of power plants can be explained by such effects. The snowfall might increse even more due to greater scavenging ability of snowflakes in comparison with raindrops.

References

Bergeron T., 1965. On the low level redistribution of atmospheric water caused by orography. Suppl.Proc.Int.Conf.on Cloud Phys. Tokyo, 1965.

Junod A., Hopkirk R.J., Schneiter D., Haschke D., 1975. Meteorological influences of atmospheric cooling systems as projected in Switzerland, Cooling Tower Environment 1974, Proc. of Symp., ERDA Techn.Inf.Center, Oak Ridge, Tenn. 1975, 239-264.

Koenig R.L., 1978. Self precipitation of snow from cooling towers, Proc.Cloud Phys.and Atmos.Electr., Issaquah, Wash. 1978, 426 - 429

Table 1

	1	2	3	4	5	6	7	8	9
	V	T	u	I	γ	γ_u	h	N	D
0	.2	15	6	1.5	4	0	3	a	a
1	.05	5	2	.75	4.5	7.5	5	b	b
2	.1	25	4	2.0	5	-	-	-	-
3	.3	-	8	-	0*	--	-	-	-

Table 2

run	x	2	4	6	8	10	15	20	25
0	%	27	24	15	8	8	5	2	-3
1.3	%	85	35	13	5	.5	-	-	-
3.3	%	20	16	18	11	6	-	-	-
1.4	%	16	21	17	11	13	10	4	0
1.5	%	29	30	27	16	13	-	-	-
2.5	%	30	38	47	40	32	-	-	-
1.7	%	5	25	23	18	22	-	-	-
2.7	%	8	19	8	.5	-.5	-	-	-
1.5/2.2	%	32	52	87	105	91	-	-	-
1.7/2.5	%	30	35	56	54	49	41	31	23

Legend: V - cloud LWC[g/kg]; T - surf.temp[°C]; u - surf.wind vel.[m/s]; I - rainfall [mm/h]; γ, γ_u - temper.and wind vel.lapse rates [K/km, m/s km]; N - number of cooling towers: a - 6 towers in two rows, b - 3 towers in one row; D - wind direction: a - along the rows of towers, b - across; h - cloud base height [hm]; x - distance down the plume [km]; % - relative increase of rainfall [%]; * - in cloud only.

A PARAMETERIZED EQUATION OF WARM RAIN FORMATION IN CUMULUS CLOUDS

by

Hu Zhi-jin

Academy of Meteorological Science, Central Meteorological Bureau, China

1. Introduction

Collision and coalescence have important influence not only on the process of precipitation formation (warm rain process) but also on the interaction between the microphysics and the dynamics of cloud. Kessler (1967), Berry (1968), Simpson (1969) and Cotton (1972) have developed the following parameterized equations, PAC(1)-(4) respectively, describing the autoconversion rate of cloud water to precipitation:

$$PAC(1) = K_1 (Qc-A),$$

$$\begin{cases} K_1 > 0 & \text{when } Qc > A, \\ K_1 = 0 & \text{when } Qc \leq A; \end{cases}$$

$$PAC(2) = \frac{Q_c}{T_1},$$

$$T_1 = \frac{60}{\rho Q_c}\left(2 + \frac{0.0266}{D_b}\frac{N_b}{\rho Q_c}\right);$$

$$PAC(3) = \frac{Q_c}{T_2},$$

$$T_2 = \frac{60}{\rho Q_c}\left(5 + \frac{0.0366}{D_b}\frac{N_b}{\rho Q_c}\right);$$

$$PAC(4) = \exp\left[k' - \frac{1}{4a'}(t-h')^2\right];$$

where Qc is the cloud water content ($g.kg^{-1}$); A is the threshold value; T_1, T_2 are the elapsed time for cloud droplet radius rg=40μ and 100μ respectively according to Berry's numerical experiments on cloud droplet collection; Db is the initial cloud droplet radius dispersion and Nb is the initial concentration (cm^{-3}); t is the time; k', a' and h' are functions of Db, Nb and liquid water content (LWC). Comparison of cloud model calculations with field observations in Hunan province of China indicates that the efficiency of rain formation are overestimated by equations PAC(1)-(3), and Weinstein and others (1968) made the same point. The possible explanation may be that according to the stationary equations PAC(1)-(3), raindrops are produced at the very beginning and grow rapidly due to the collection process. PAC(4) is a time dependent equation, but it has not been taken into consideration that LWC of a cloud parcel increases quickly in its early stage and LWC value at a given moment (t) is larger than the mean value over the time interval (o-t). The rate of rain formation is very sensitive to LWC, it will be overestimated if PAC(4) is employed directly, as shown by Silverman (1973).

2. A new parameterized equation of autoconversion

The conversion process of droplets into rain can be divided into two stages. In the preparatory stage the size spectrum of droplets expands, and yet there is no rain drops ($r \geq 100\mu$) at all. After that begins the conversion stage, and a stationary autoconversion rate is presumed, since the cloud model results are much less sensitive to the conversion rate (K_1) than to the threshold value (A), as shown by Weinstein (1970). Based on Berry's calculations, the elapsed time T_1 required for rg=40μ is chosen to mark off these two stages. During the time interval T_1 to T_2 nearly half of the cloud water is transformed into rain, partly due to autoconversion and partly due to collection of raindrops. Thus,

$$PAC(5)\begin{cases} = 0. \text{ when } t \leq \frac{60}{\rho Q_c}\left(2 + \frac{0.0266}{D_b}\frac{N_b}{\rho Q_c}\right), \\ = \frac{J_1 \cdot Q_c}{2(T_2 - T_1)} = \frac{J_1 \cdot \rho Q_c^2}{60}\left(6 + \frac{0.0200}{D_b}\frac{N_b}{\rho Q_c}\right)^{-1} \\ \quad \text{when } t > \frac{60}{\rho Q_c}\left(2 + \frac{0.0266}{D_b}\frac{N_b}{\rho Q_c}\right); \end{cases}$$

where J_1 is the portion of cloud water transformed due to autoconversion. Values of autoconversion rate calculated by PAC(1)-(5) for Db=0.25, Nb=300cm and LWC=2.5, 2.0, 1.5 m are shown in Fig.1. The threshold time of the beginning of autoconversion in PAC(5) corresponds to the time when PAC(4) attains $10^{-5}\ g.kg^{-1}\ s^{-1}$. If the coefficient J_1 in PAC(5) is presumed to be o.5, the value of PAC(5) is smaller than PAC(1)-(3), but somewhat larger than the maximum value of PAC(4). To study the evolution of LWC, a new concept "accumulative brewing process" is put forward. The portion of the accumulative brewing process completed within the time interval t-(t+dt) is taken to be $\frac{dt}{T_1}$. When $\int_0^t \frac{dt}{T_1} = 1$, the brewing process comes to an end, autoconversion begins. Thus,

$$PAC(5)\begin{cases} = 0 \text{ when } \int_0^t \frac{\rho Q_c}{60}\left(2 + \frac{0.0266}{D_b}\frac{N_b}{\rho Q_c}\right)^{-1} dt \leq 1, \\ = \frac{J_1 \cdot \rho Q_c^2}{60}\left(6 + \frac{0.0200}{D_b}\frac{N_b}{\rho Q_c}\right)^{-1} \\ \quad \text{when } \int_0^t \frac{\rho Q_c}{60}\left(2 + \frac{0.0266}{D_b}\frac{N_b}{\rho Q_c}\right)^{-1} dt > 1; \end{cases}$$

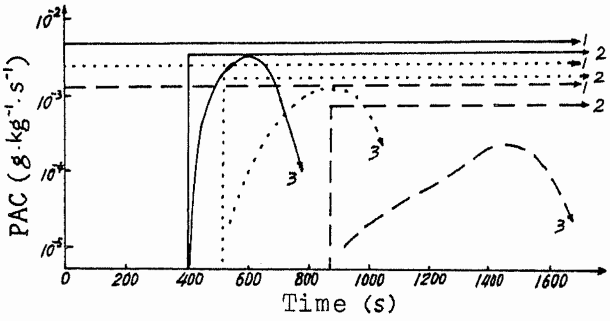

Fig.1. Comparison of autoconversion rates calculated from different equations: 1 -- PAC(3), 2 -- PAC(5), 3 -- PAC(4) for LWC=2.5(solid line), 2.0 (dotted line) and 1.5g.m^{-3} (dashed line)

3. Results of calculation

Several cases have been calculated, employing a one-dimensional stationary cloud model similar to that of Simpson (1969). Two autoconversion equations, PAC(3) and PAC(5), are used for comparison . For the stationary model PAC(5) is transformed into:

$$\mathrm{PAC}(5)\begin{cases} =0 & \text{when} \int_0^H \frac{dH}{J_2\cdot W\cdot T_1} \leqslant 1 , \\ =\frac{J_1\cdot\rho\cdot Q_c^2}{60}\left(6+\frac{0.0200}{D_b}\frac{N_b}{\rho Q_c}\right)^{-1} & \text{when} \int_0^H \frac{dH}{J_2\cdot W\cdot T_1} > 1 ; \end{cases}$$

where H is the height; W, vertical velocity. A coefficient J_2 is assumed, in view of the velocity calculated by Simpson's model is greater than the observed in Hunan province. The values of cloud top height, velocity, temperature and LWC calculated by PAC(5) and PAC(3) are in good agreement with each other, while the rain water and radar reflectivity differ significantly. The results for Sept.2,1974 are listed in Tab.1. The cloud base was 1.2km. The observed height of echo tops were 5.5-6.3km. Calculation by PAC(5) shows that: 1) for small cumulus (case 1) there are no rain water and radar echo, which is in agreement with field observations, 2) for medium cumulus with top height at 4.8km (case 2), rain water and radar reflectivity are much less than that calculated by PAC(3), and nearer to field observations, 3) the time and height of the first echo are 15-18min and 3.0-3.4 km respectively, which is much larger than the corresponding values from PAC(3) and closer to cloud model calculations with nonparameterized microphysics equations (Silverman 1973). The calculated height of the first echo from PAC(5) is in agreement with the medium value (3km above cloud base) observed by Koscielski and Dennis (1972).

4. Further application of the new equation

Several attempts are made to study the warm rain formation process with the new equation PAC(5) (1979): 1) The critical depth for the start of raining in cumulus with various growth speeds, cloud base temperatures and microstructures is calculated by PAC(5) on assumption that the LWC of cloud is equal to half of its adiabatic value. The calculated results agree fairly with the observed depth of cumulus with 50% probability of raining in 8 regions in the world. It is found that the rain formation depth of cumuli differ appreciably from one another and depend mainly upon the vertical growth rate and to a lesser degree upon the cloud microstructure. 2) The rain-enhancing efficiency of salt seeding in numerical simulation with PAC(1)-(4) is underestimated, while the natural rain formation efficiency is overestimated. Using PAC(5) and assuming that in the case of salt-seeding, some cloud water is converted into rain near the cloud base, the numerical simulation shows that the rain can be stimulated or enhanced and the height of first echo was lower, in accordance with the field observations in rain-enhancement experiments. 3) Assuming that in severe storms LWC approaches its adiabatic value, the rain-formation heights calculated by PAC(5) as a function of vertical velocity and cloud base temperature. The calculated heights are shown to be close to the first echo height of the multicell storm and to the upper boundary of the echo-free vault observed in 3 storms. Hence PAC(5) may be useful in severe storm models for the simulation of precipitation initiation and radar echo phenomena.

5. Acknowledgement

The author wishes to express sincere gratitude to Cai Li-dong of the Hunan Institute of Computation Technology for his assistance in computation.

6. References

Berry, E.X.(1968) Modification of the warm rain process, Proc. First Nat. Conf. on Wea. Mod. Amer. Met. Soc., Albany, New York, 81-85.

Silverman, B and Glass, M(1973) A numerical simulation of warm cumulus clouds: Part 1, J. Atm. Sci., 30, 1620-1637.

Simpon, J. and Wiggert, V. (1969) Models of precipitating cumulus towers, Mon. Wea. Rev., 97, 471-489.

Hu Zhi-jin and Cai Li-dong (1979) A parameterized numerical simulation of warm rain and salt-seeding in cumulus clouds, Scientia Atmospherica Sinica, 3, 4, 334-342.

Hu Zhi-jin (1979) On the conditions of warm rain formation in cumulus clouds, Acta Meteorologica Sinica, 37, 3, 72-79.

Cotton W. R., (1972) Numerical simulation of precipitation development in supercooled cumuli, part I, Mon. Wea. Rev., 100, 757-763.

Koscielski A. and Dennis A.S. (1972) Seeding effects in convective clouds in western South Dokata. Proc. Third Nat. Conf. on Wea. Mod. Amer. Meteo. Soc., Rapid City, 186-191.

Srivastava R.C. (1967) A study of the effect of precipitation on cumulus dynamics, J. Atoms. Sci., 24, 36-45.

Weinstein A.I. (1970) A numerical model of cumulus dynamics and microphysics. J. Atmos. Sci., 27, 246-255.

Table 1: Comparison between autoconversion equations

Case No.		1	2	3
Radii of updraughts (km)		0.5	1.0	2.0
Equations			PAC(5)/PAC(3)	
Depth of cloud (km)		2.8/2.8	3.6/3.6	5.0/4.8
Initiation of rain:	Time (min)	no/7	18/7	15/7
	Height* (km)	no/0.4	3.4/0.4	3.0/0.4
Max. rain water content ($g.m^{-3}$)		0/0.25	0.1/1.1	1.6/2.7
First echo:	Time (min)	no/9	18/11	15/10
	Height* (km)	no/1.2	3.4/1.0	3.0/1.0
Max. reflectivity (dBz)		no/34	30/56	60/64

* above cloud base

GEOGRAPHICAL AND CLIMATOLOGICAL VARIABILITY IN THE MICROPHYSICAL MECHANISMS OF PRECIPITATION DEVELOPMENT

David B. Johnson
State Water Survey Division
Illinois Institute of Natural Resources
Urbana, Illinois, USA

1. Introduction

In cloud physics research, as in many other areas of science, there is often a tendency to concentrate on increasingly detailed aspects of a particular problem, rather than to try to generalize the results. While individual studies of the many different physical processes involved in precipitation formation properly form the core of our discipline, we must examine these studies carefully in order to learn which factors are the most important in governing the microphysical mechanisms of precipitation development.

This study examines several aspects of precipitation development in an attempt to develop quantiative expressions which can illuminate the microphysical differences between clouds forming in different geographical or climatological areas.

2. The Coalescence Threshold and the Critical Cloud Depth Needed For The Onset Of Effective Coalescence

When a cloud first forms, the liquid water content is low and cloud droplets are small. Such conditions are not well suited for effective coalescence. As the cloud grows, however, the liquid water content increases and the cloud droplets grow bigger and bigger. Eventually a few large drops begin to grow by colliding and coalescing with the smaller, more numerous, cloud droplets. Johnson (1978; 1979) proposed a quantitative estimate for the minimum size of large drop that is capable of rapid coalescence growth for any specified water content and droplet concentration. Fig. 1 shows the variation of this minimum size of large drop, termed the coalescence threshold, with liquid water content and droplet concentration. When the liquid water content is low, no drops, regardless of their size, can grow effectively by coalescence. When the water content reaches some critical value, however, the coalescence threshold quickly decreases to the vicinity of 30-50 μm.

Recent aerosol measurements suggest that, even in continental areas, there is no shortage of natural particles which are capable of forming drops larger than the coalescence threshold, once liquid water contents exceed 1-2 g m^{-3} (see Johnson, 1978; 1979; 1980). This means that the sudden fall in the coalescence threshold can be used to partition a cloud into an initial incubation period, during which coalescence will not be effective, and a subsequent period in which coalescence is active. For a given droplet concentration, the critical liquid water content may be best defined by the "elbow" in the appropiate coalescence threshold curve shown in Fig. 1. If the total

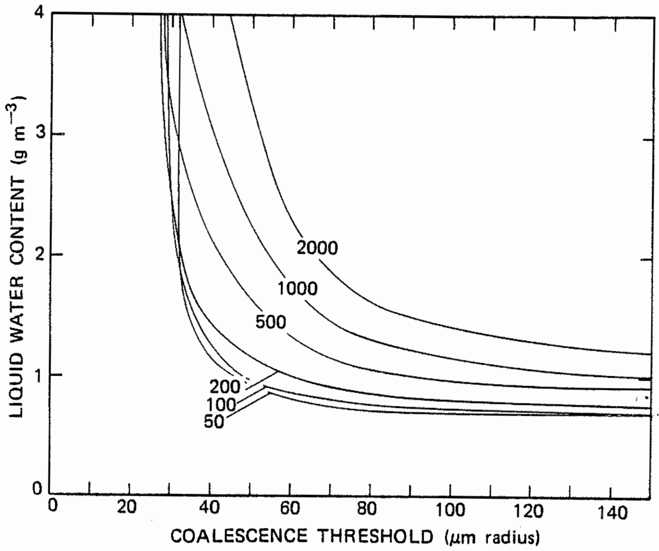

Figure 1. Minimum size drop capable of effective coalescence growth (coalescence threshold) as a function of liquid water content and droplet concentration (cm^{-3}).

concentration of cloud droplets, N, is specified in terms of the number per cubic centimeter, then the critical liquid water content, W_c (g m^{-3}), can be approximated by:

$$W_c = 1.0 + 0.02(N)^{0.5} \qquad (1)$$

Figure 2 shows the minimum cloud depth (km) required to reach W_c (assuming adiabatic water contents) for various cloud base temperatures and drop concentrations. Clouds smaller than the indicated cloud depth will not develop rain by the coalescence mechanism. Clouds that exceed this minimum depth are capable of producing coalescence rain, if the cloud survives long enough and does not first produce precipitation by other mechanisms. If the cloud base temperature is low enough, the liquid water content may never exceed W_c. In this case the cloud, regardless of its thickness, will not develop coalescence rain. For adiabatic water contents, however, this condition is restricted to the small and rather insignificant hatched area in the upper left corner of Fig. 2.

The dashed, or pecked, lines in Fig. 2 indicate the additional depth of cloud beyond the critical value, indicated by the solid lines, which is necessary to reach the -15C isotherm. The actual depth necessary for coalescence rain to develop depends rather critically on the cloud base temperature and updraft velocity. In this context, it is useful to review Ludlam's (1951) estimates of the minimum depth of cloud necessary for the production of showers by the coalescence mechanism. In general, however, we

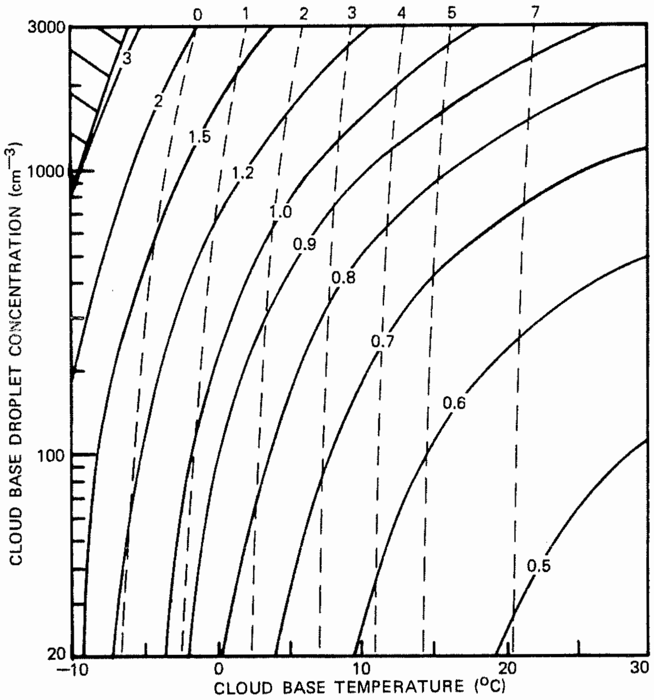

Figure 2. Minimum cloud depth (km) needed for the onset of effective coalescence (solid lines), and the additional height (km) required to reach the -15C isotherm for adiabatic water contents (dashed lines).

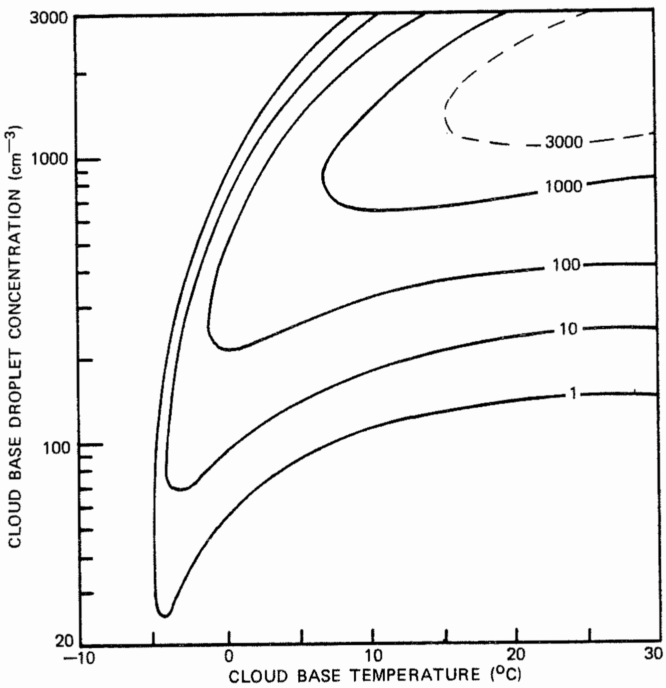

Figure 3. Relative efficiency of the Hallett-Mossop ice multiplication mechanism for adiabatic water contents.

may expect to find precipitation-sized particles produced by the coalescence mechanism within a few kilometers of the critical depth specified in Fig. 2.

If the cloud top extends into the sub-zero regions before coalescence rain develops, it is likely that ice processes will come into play. The nucleation of ice crystals is strongly temperature dependent, with the first ice crystals forming around -10 to -15C and increasing by about an order of magnitude in concentration for each additional decrease of five degrees. Once ice forms, however, ice multiplication processes can significantly increase the concentration of ice particles in the warmer regions of the cloud. Even if the upper regions of a cloud are completely glaciated, the ice particles can continue to grow by aggregation, forming large low-density aggregates which may be important in the formation of hail (see Heymsfield, 1980). It should be noted that this aggregation is not limited to temperatures near the melting level, but can occur at any temperature. Riming growth of single crystals, aggregates, or frozen drops requires appreciable amounts of supercooled water and will generally be confined to the regions between the 0C and the -15 or -20C isotherms (i.e. 3-4 km above the melting level).

3. Factors Governing Ice Particle Multiplication In Cumulus Clouds

In some clouds, many more ice crystals are observed at temperatures of -10C, or warmer, than can be accounted for by measured concentrations of ice nuclei. This has long been interpreted as evidence for some sort of ice multiplication mechanism. In a series of articles, Hallett and Mossop have reported on laboratory experiments supporting a possible "splintering" mechanism for the production of secondary ice crystals (Hallett and Mossop, 1974; Mossop and Hallett, 1974; Mossop, 1978a; Mossop and Wishart, 1978). Drops of 25 μm diameter and larger were found to be essential to this process. Mossop (1978b) used this fact to propose a "multiplication boundary" separating those cloud conditions in which multiplication takes place from those in which it it does not, in terms of the cloud base temperature and droplet concentration. In a separate paper, Mossop (1978a) suggested that the rate of production of secondary ice crystals is proportional to $N_l N_s^{0.93}$ where N_l is the number of large drops ($D > 24$ μm) swept up per second by a falling graupel particle at -5C, and N_s is the corresponding sweep-out rate of small ($D <$ 13 μm.

If we assume that N_l and N_s are proportional to the number concentration of large and small drops respectively, it is possible to convert Mossop's "multiplication boundary" to a contour plot of relative effectiveness of the Hallett-Mossop ice multiplication mechanism (Fig. 3). In this case, the cloud droplet distribution at -5C is assumed to be described by a gamma dis tribution with a relative dispersion (in radius) of 0.18. In this figure, as in Fig. 2, adiabatic water contents were assumed.

4. The Effect of Sub-Adiabatic Water Contents

Real clouds are seldom adiabatic. In cumuli just large enough to develop precipitation, in fact, the average liquid water content decreases from about half the adiabatic value near cloud base to about one-fifth the adiabatic value at

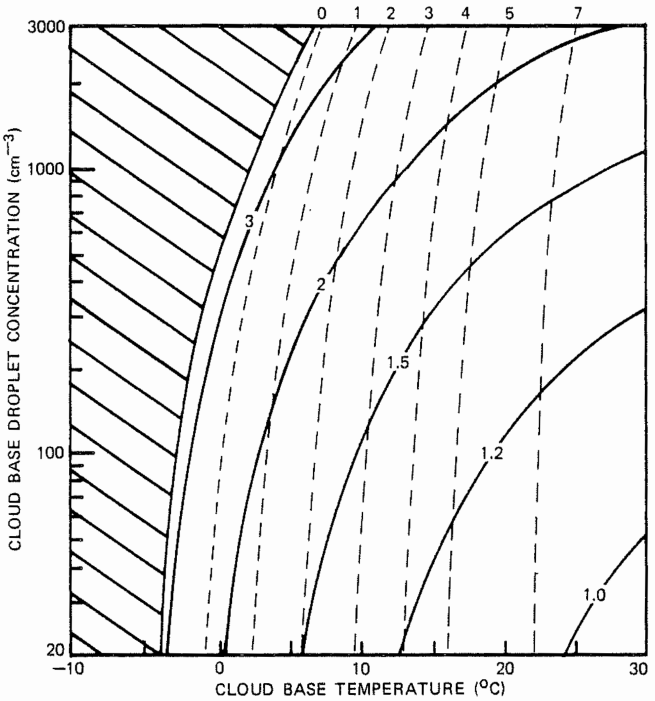

Figure 4. Minimum cloud depth (km) needed for the onset of effective coalescence (solid lines), and the additional height (km) required to reach the -15C isotherm for half adiabatic water contents (dashed lines).

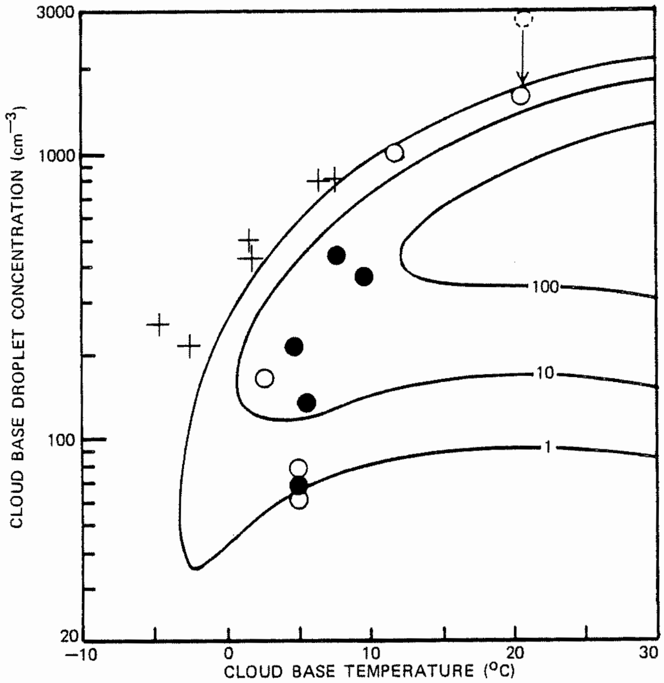

Figure 5. Relative efficiency of the Hallett-Mossop ice multiplication mechanism for water contents that are 20% of their adiabatic values.

2 km above cloud base (Warner, 1970). It is not always the average conditions, however, that are important in coalescence calculations. Even though small pockets of high water contents may dominate warm rain formation (see Twomey, 1976), clouds will not generally behave as if they were totally adiabatic. Figure 4 shows the effect of reducing the water content on the minimum depth of cloud necessary for effective coalescence growth to begin by arbitrarily reducing the liquid water content to half the adiabatic value. In this case the most noticeable changes from Fig. 2 are the increase in the critical cloud depth needed for coalescence onset, and a marked expansion of the area of which the liquid water content never gets large enough to allow effective coalescence.

While small areas of high water content can be disproportionally important in coalescence development, this is not the case with ice multiplication. Figure 5 illustrates the relative effectiveness of the Hallett-Mossop ice multiplication mechanism for liquid water contents which are reduced to 20% of their adiabatic values. This graph also includes Mossop's (1978b) compilation of ten observational studies that displayed ice multiplication (circles) and six cases in which multiplication did not take place (crosses). In one case (Flordia) I have indicated a probable overestimate of the droplet concentration with an arrow pointing toward a more reasonable number of droplets. The circles representing the five ice multiplication cases which showed the greatest amount of secondary ice production (as reflected in the observed ice crystal concentration) are completely filled in and, for the most part, congregate near the region of maximum predicted multiplication efficiency. Of the four additional Canadian data points discussed by Mossop (1979), only one showed any evidence of an active ice multiplication mechanism and it was located squarely in the middle of the predicted area of maximum multiplication.

5. Summary

Although simple theories of the type discussed in this paper are inherently limited to describing only the most general features of cloud evolution, these features are often the most important factors in explaining geographical or climatological differences in the microphysical mechanisms of precipitation development.

REFERENCES

Hallett, J., and S. C. Mossop, 1974: Production of secondary ice particles during the riming process. Nature, 249, 26-28.

Heymsfield, A. J., 1980: Precipitation and hail formation mechanisms in a Colorado storm. Preprints, VIII International Conf. on Cloud Physics, Clermont-Ferrand.

Johnson, D. B., 1978: Giant nuclei and warm rain initiation. Preprints, Conference on Cloud Physics and Atmospheric Electricity, Issaquah, American Meteorological Society, 31-34.

_____, 1979: The role of coalescence nuclei in warm rain initiation. Ph.D. Thesis, The University of Chicago, 119 pp.

_____, 1980: Hygroscopic seeding to initiate precipitation. Preprints, Third WMO Scientific Conference on Weather Modification, Clermont-Ferrand, W.M.O., Geneva.

Ludlum, F. H., 1951: The production of showers by the coalescence of cloud droplets. Quart. J. Roy. Meteor. Soc., 77, 402-417.

Mossop, S. C., 1978a: The influence of drop size distribution on the production of secondary ice particles during graupel growth. Quart. J. Roy. Meteor. Soc., 104, 323-330.

_____, 1978b: Some factors governing ice particle multiplication in cumulus clouds. J. Atmos. Sci., 35, 2033-2037.

_____, 1979: Reply to comments by Isaac and Schemenauer. J. Atmos. Sci., 36, 2273-2275.

_____, and J. Hallett, 1974: Ice crystal concentration in cumulus clouds: Influence of the drop spectrum. Science, 186, 632-634.

_____, and E. R. Wishart, 1978: The mechanism of splintering during rime growth. Geographical Res. Letters, 5, 1083-1085.

Twomey, S., 1976: The effects of fluctuations in liquid water content on the evolution of large drops by coalescence, J. Atmos. Sci., 33, 720-723.

Warner, J., 1970: On steady-state one-dimensional models of cumulus convection. J. Atmos. Sci., 27, 1035-1040.

LIQUID-PHASE MICROPHYSICAL INFLUENCES ON CLOUD DYNAMICS

L. Randall Koenig and Francis W. Murray

The Rand Corporation
Santa Monica, California, U.S.A.

1. INTRODUCTION

Numerical experiments using an axially symmetric field-of-flow cumulus cloud model revealed a strong, unexpected relationship between the rapidity of coarsening of the liquid-phase hydrometeors and the evolution of the cloud. The liquid-phase size spectrum exerted much more control on the dynamical properties of the cloud than did orders of magnitude changes in the number concentration of ice particles and the consequential differences in the rapidity of glaciation of the cloud (Koenig, 1977).

To investigate the origin of the sensitivity of the dynamical properties of the cloud to the liquid-phase microphysical processes, the temporal and spatial fields of the components of the force driving the circulations were analyzed.

2. EVIDENCE FOR CONTROL OF MICROPHYSICS ON DYNAMICS

Six experiments were run using the 1835 GMT sounding taken at St. Louis on 17 August 1973. For brevity, remarks will be confined to Cases 5 and 6. Case 5 may be thought of as depicting cloud growth in a CCN-sparse air mass in contrast to Case 6, which depicts growth in a CCN-abundant air mass. For a given water content, the conversion of suspended to precipitating water occurs much faster in the former case than in the latter, but in other respects the governing equations and input conditions are identical.

Figure 1 shows the draft structure on the axis of symmetry as a function of time for Cases 5 and 6. Comparing these shows that the cloud having the slower broadening of its drop distribution (Case 6) developed much more vigorous and transient circulation than did the cloud having the more rapid broadening. (Comparison with other runs would show this to be true regardless of the ice content of the simulated clouds.)

3. AN EXPLANATION

The components of the force driving the cloud circulations are shown at representative times in Figure 2. An analysis of these kinds of data shows that changes in the rate of coarsening of the liquid phase affects dynamics by changing the vertical distribution of the downward force caused by condensate. This causes a chain of events that brings about the collapse of one cloud but not the other.

Focusing attention on the early life of the cloud and components of force near the base, a comparison of Case 5 with 6 shows the former to have less net upward force due to the added force of the falling hydrometeors--a factor that is largely absent in the slowly coarsening case (6). In that case (6), condensate has low fallspeed, is carried upward, and tends to accumulate near the summit of the cloud. There the downward force due to condensate grows but, in the early period, is more than offset by the upward force of thermal buoyancy. Cloud base updrafts are relatively unretarded by condensate loading, and a vigorous circulation develops. With time, however, the accumulation of condensate near the summit causes negative downward forces to overcome the positive forces, and drafts rapidly decrease. The liquid condensate, no longer supported by strong drafts, falls, and in so doing brings negative forces that throughout the cloud overwhelm positive forces. The resulting negative acceleration soon causes the updraft to cease, and the cloud collapses.

The cause of the collapse in Case 6 stems from the growing downward force of condensate loading which in time exceeds positive forces, for they do not grow proportionally. In contrast, the forces in Case 5 remain more nearly in balance throughout the period of the calculation. Strong drafts do not occur, more drops fall out, and a strong downward condensate force does not develop near the cloud summit. (The oscillatory tendency in the upper half of the cloud is caused by the interplay between condensate accumulation and drafts, however.)

4. A CAUTION

In numerical models, the distribution of the forces driving the cloud depends on several factors, some physical, but others associated with the mathematical formulation of the model itself. Subgrid-scale (turbulent mixing) processes are poorly treated physically, but nevertheless they are accounted for. The net effect of these processes is to redistribute properties such as momentum and heat.

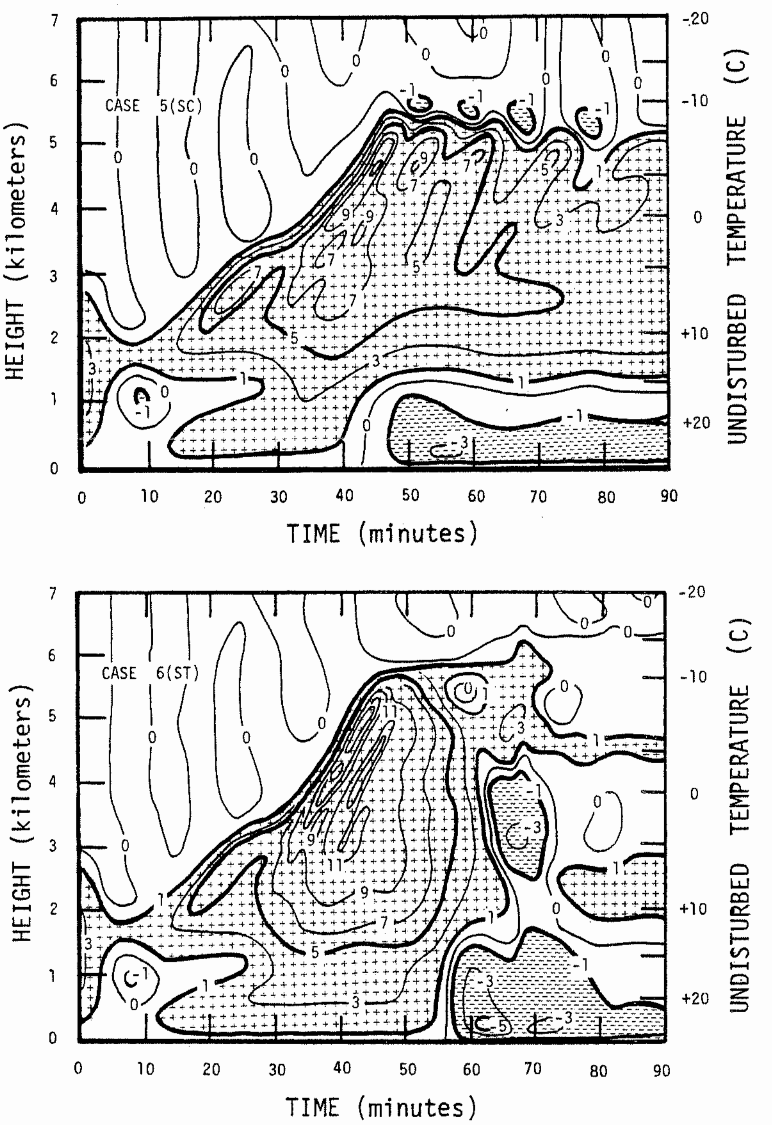

Figure 1. Time-height sections showing the evolution of the vertical draft velocity on the axis of Cases 5 and 6. Regions of greater than ± 1 m s^{-1} drafts are shaded; contours for drafts of ± 1 and ± 5 m s^{-1} are emphasized; contours of +11 m s^{-1} in Case 5 and +13 and +15 m s^{-1} in Case 6 are not labeled. The scale at the right indicates reference temperature as a function of height.

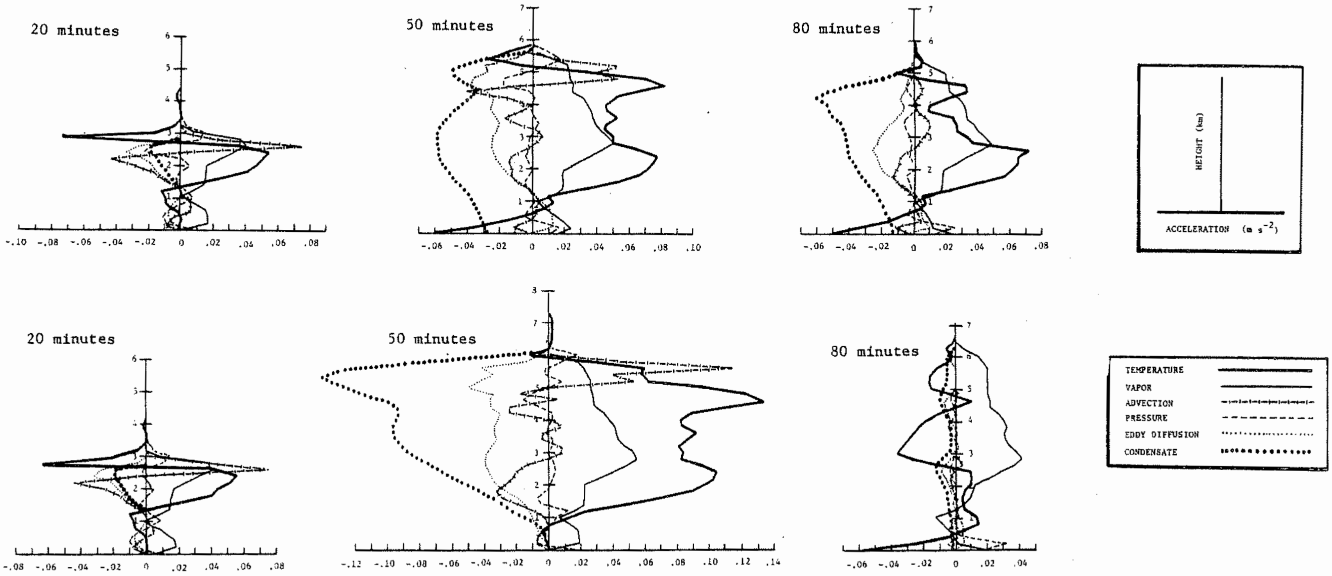

Figure 2. Components of the vertical acceleration on the central axis as functions of time and height for Cases 5 (upper) and 6 (lower).

Since these properties and their relation to the various forms of condensate control components of the force driving the cloud circulation, how the subgrid-scale processes are treated will determine to greater or lesser extent the net force acting on cloud elements. Recalling that the individual forces driving a cloud may be relatively large but the net force small, the influence of turbulent mixing may be disproportionately large.

REFERENCES

Koenig, L. R., 1977: "The Rime-Splintering Hypothesis of Cumulus Glaciation Examined Using a Field-of-Flow Cloud Model," Quart. J. Roy. Meteor. Soc. 103, 585-606.

Koenig, L. R., and F. W. Murray, 1979: Theoretical Experiments on Cumulus Dynamics and Glaciation, The Rand Corporation, R-2424-NSF, 116 pp.

Tag, P. M., F. W. Murray, and L. R. Koenig, 1979: "A Comparison of Several Forms of Eddy Viscosity Parameterization in a Two-Dimensional Cloud Model," J. Appl. Meteor. 18, 1429-1441.

INFLUENCE OF TURBULENCE AND CONDENSATION NUCLEI ON RAIN FORMATION IN CUMULUS CLOUDS: NUMERICAL EXPERIMENTS BASED ON THREE-DIMENSIONAL MODEL WITH DETAILED MICROPHYSICS

E.L.Kogan and I.P.Mazin
Central Aerological Observatory, Moscow, USSR

1. Introduction

In recent years many attempts have been made to assess the effect of turbulent mixing (TM) of cloud droplets on the evolving droplets distribution. But up to this time the role of TM in rain formation is not quite clear. This paper presents an attempt to solve the problem by a series of numerical experiments (NE) which may be considered as upper and lower estimates of the exact solution. The influence of TM between the cloud and its environment and the effect of CCN spectrum on rain formation are also studied.

2. Numerical model

The model was developed by Kogan /1978/, and includes equations for velocities $\vec{U}$, potential temperature T and water vapor mixing ratio q :

$$(1)\quad \frac{\partial \vec{U}}{\partial t}+(\vec{U}\cdot\vec{\nabla})\vec{U}=-\vec{\nabla}\pi'+\vec{g}\left(\theta'/\theta_o+0.61q'-Q\right)+\Delta'\vec{U}.$$

$$(2)\quad \frac{\partial \theta}{\partial t}+(\vec{U}\cdot\vec{\nabla})\theta=\frac{L}{C_p}\frac{\theta}{T}\frac{\delta M}{\delta t}+\Delta'\theta.$$

$$(3)\quad \frac{\partial q}{\partial t}+(\vec{U}\cdot\vec{\nabla})q=-\frac{\delta M}{\delta t}+\Delta' q.$$

π' represents perturbation of pressure,

$$(4)\quad \Delta'\equiv\frac{\partial}{\partial x}K\frac{\partial}{\partial x}+\frac{\partial}{\partial y}K\frac{\partial}{\partial y}+\frac{\partial}{\partial z}K\frac{\partial}{\partial z}.$$

describes TM with the eddy mixing coefficient K in the form:

$$(5)\quad K=cL_T^2\left[\sum_{i,j=1}^{3}\left(\frac{\partial u_i}{\partial x_j}\right)^2\right]^{1/2}.$$

$\frac{\delta M}{\delta t}$ is the change of q due to condensation-evaporation processes and is calculated taking into account the growth of both cloud droplets (CD) and CCN. The continuity equation has the form:

$$(6)\quad \vec{\nabla}\cdot\vec{U}=\sigma w\quad,\ \text{where } \sigma=-d\ln\rho_o(z)/dz.$$

takes into account air density changing with height. CD according to Berry are classified by size into 30 groups from 4 to 3250 μm; CCN - into 19 groups from 0.0076 to 7.6 μm.

Equations for density functions $f(m)$ and $n(z)$ are:

$$(7)\quad \frac{\partial f}{\partial t}+\vec{\nabla}\left[\vec{U}-\vec{v}_d(m)f\right]=\left[\frac{\partial f}{\partial t}\right]_{micro}+\Delta' f.$$

$$(8)\quad \frac{\partial n}{\partial t}+\vec{\nabla}\cdot(\vec{U}\cdot n)=-\left[\frac{\partial n}{\partial t}\right]_{nucl}+\Delta' n.$$

Term $[\partial f/\partial t]_{micro}$ represents the changes in $f(m)$ due to condensation, coagulation, breakup; $[\partial n/\partial t]_{nucl}$ represents CCN sink due to nucleation, Δ' and K are given above as (4) and (5).

The calculations are based on the accurate numerical methods, such as Lagrangian-Eulerian scheme for diffusional growth of droplets, Berry and Reinhardts method for coagulation and breakup, Marchook splitting method for calculating advection and turbulence, Klett and Davis data for coagulation kernel, Komabayashi and Srivastava data for breakup probabilities.

3. Influence of TM on cloud microstructure

3.1. Methodology

During the existence of turbulent mole, large drops ($r > 25$ μm) practically do not change their sizes and may be considered as a conservative substance. Droplets of smaller sizes grow rather fast and one cannot consider them conservative. The theory of stochastic condensation (i.e. droplet condensational growth in turbulent atmosphere) is being actively developed, but the equations of this theory are so complicated that up to now they have not been included into numerical models. The influence of this fact on the final result is not clear yet.

The analysis of equations for stochastic condensation shows that the refusal from them and using the above system of equations in certain conditions may give the narrowing of droplet size distribution, while in the other conditions-its broadening. Really, if droplets, at an average, grow with height, the neglecting of condensational growth and evaporation during their turbulent transport will lead to the fact that droplets, coming from below will be smaller than in reality, and vice versa.

Thus, the dispersion of droplet size distribution at the given level will grow.*/

We made two NE taking into account the abovesaid. In NE "A" term $\Delta' f$ in equation (7) was taken into account for all droplets, including small ones. (Small CD are also considered conservative). The result of this NE is considered as an upper estimate for the spectrum broadening. In NE "B" inside the cloud term $\Delta' f$ was taken into account only for drops $r > 25\ \mu m$. It is equivalent to the assumption that small droplets are not transported by TM. We think in this NE droplet size distribution must be narrower than real one, and the obtained result was regarded as a low estimate. In NE "C" term $\Delta' f$ for droplets $r < 25\ \mu m$ was not taken into consideration, i.e. both TM inside the cloud and the sink of these droplets due to mixing with environment were not taken into account.

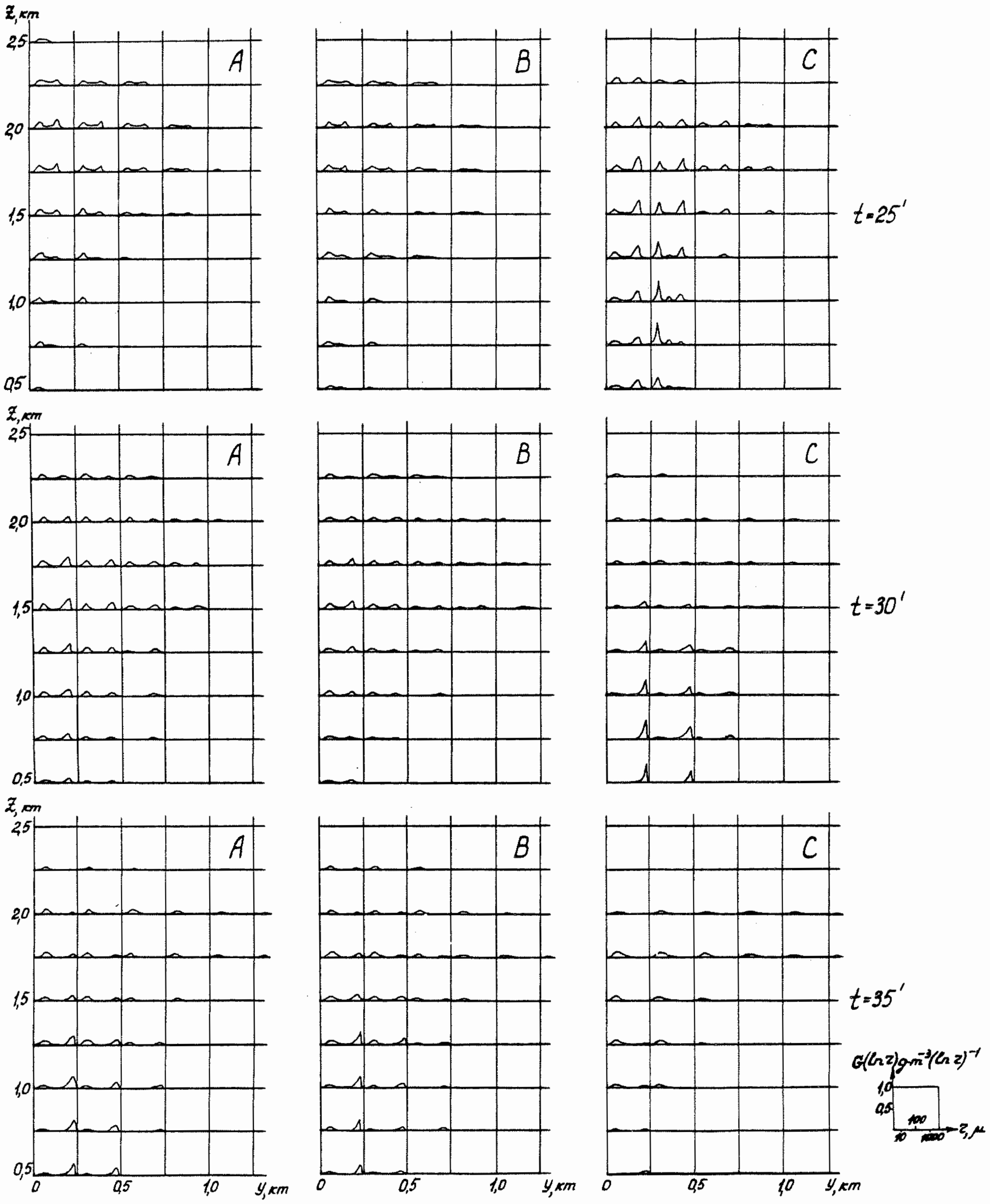

Fig.1. In each square the G-distribution is shown. $G(\ln r) = 3m^2 f(m)$

*/ V.M.Merkulovich (private communication) came to the conclusion that the assumption of CD conservativeness results in size distribution broadening, if LWC gradient $dQ/dz > 0.1$ gm^{-3} [100 m $^{-1}$]. In our experiments this condition was always valid for lower and middle parts of the cloud.

3.2. Results

Fig. 1 shows the changing of cloud microstructure with time in vertical section $x=0$ (level $z=0.5$ km corresponds to the cloud base). The results of experiments "A" and "B" are almost the same, but differ considerably from "C". One can see from Fig. 1 that in NE "C" large drops contain much more liquid water than in "A" (or "B") (LWC is proportional to the area under curve). Therefore rain in "C" starts and stops earlier. Thus, neglecting turbulent sink of small droplets near the cloud boundary ("C") distorts cloud microstructure, increasing sharply CD concentration and precipitation intensity. At the same time, the difference between maximum precipitation intensity in experiments "A" and "B" is about 20%.

From NE we may conclude that it is not expedient to use complicated equations of stochastic condensation in the numerical model of the convective cloud, because their account does not increased the accuracy of calculations on the whole. At the same time, the comparison between "B" and "C" shows that cloud microstructure may strongly depend on the quality of parameterization of turbulent exchange between the cloud and environment. This problem deserves serious attention.

precipitation up to t=45 min.

There are no considerable differences in cloud dynamics before precipitation starts. Note that in a maritime cloud horizontal gradients of vertical velocities may be 1.5 - 2 times less than in a continental one. It conforms to low bumpiness of aircraft in a maritime cloud (Kosarev and all, 1978).

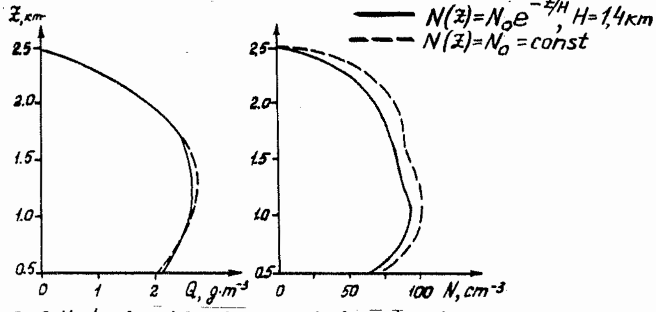

Fig. 3. Vertical profiles of LWC and cloud droplet concentration

The precipitation supresses updraft and leads to the cloud decay.

The comparison of NE 1 with 2, and 3 with 4 showed that if concentration of large CCN ($r > 0.2$ μm) increased by several orders, it did not cause any noticeable change even in the most sensitive characteristics. The results of NE 1 and 5 practically coincide (Fig. 3).

Consequently, only CCN concentration near the cloud base (or zone of entrainment) influences the development of a simulated cloud. CCN inflow into the middle and upper part of the cloud through lateral boundaries is not great and so their concentration at these levels practically does not influences cloud development.

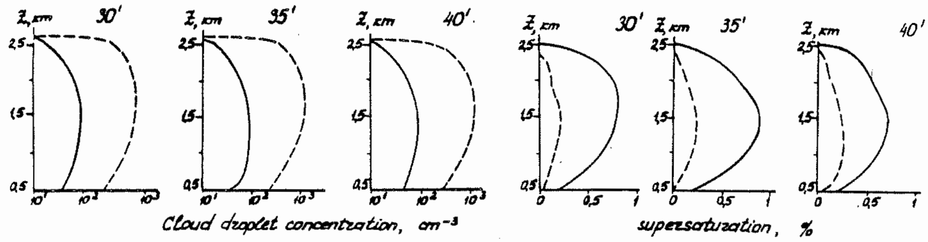

Fig.2
---- continent. CCN
—— maritime CCN

4. Role of condensation nuclei spectrum.

The series of 5 NE with different CCN distributions were performed. In the first NE maritime CCN spectrum is used, in the second - the same spectrum, but with greater concentration of large ($r > 0.2$ μm) nuclei. Analogical NE (Nos. 3,4) were made for continental spectrum. In all NE CCN concentration decreased exponentially with height, dropping twice when $\Delta z \approx 1.0$km. The 5th NE was the same as the first one with the exception that CCN concentration was constant in height.

One can see from Fig. 2, that the supersaturation in a continental cloud was about 0.1 ÷ 0.2%, in a maritime one - 0.3 ÷ 0.6%, with little changing with time. The droplet concentration in a maritime cloud practically did not exceed 10^2cm^{-3} and reached 10^3 cm^{-3} in a continental cloud. In a maritime cloud the droplets grew very fast and produced rain with I_{max} = 21 mm/h, but in a continental cloud there was no

References

Kogan E.L., 1978: Three-dimensional numerical model of a warm cumulus cloud with microphysical processes. Izv. Acad. Nauk USSR, Atmos. Ocean. Phys., 14, No. 8, 876-887.

Kosarev A.L., Mazin I.P., Nevzorov A.N., Potemkin V.G., Shugaev V.F., 1978: Intercomparison of some microphysical parameters of clouds in different geographical areas, Some Problems of Cloud Physics, Collected Papers. Borovikov memorial issue. Leningrad, 113-135.

THEORETICAL STUDY OF THE POWER SPECTRUM OF AIR MOTION IN CUMULUS CLOUDS

A J Lapworth

Meteorological Office, Bracknell, England

Introduction

Several workers - Ackerman (1967), Warner (1970), Beritashvili & Lominadze (1972), Macpherson & Isaac (1977) - have reported aircraft and photogrammetric measurements of air motions in and around cumulus clouds. The data are characterized by the presence of peaks in the gust power spectrum at wavelengths of 300 to 900 m separated by a 'spectral gap' of reduced power from peaks of 1-4 km corresponding to the cloud width. Warner has detected a systematic variation of the short wavelength peak with height with typical wavelengths of $\sim$300 m at the bottom of the cloud increasing to $\sim$700 m in the middle of the cloud and reducing to $\sim$200 m at the top. Ackerman, Warner, Lemone (1976) and Beritashvili & Lominadze have noted further peaks of small amplitude in the range 100-300 m that may be ascribed to turbulence. Other features of cumulus - a downdraught within the cloud, and oscillations at the top (Lee 1979) have been noted in instrumented aircraft flights and in numerical models of cumulus. The following simple linear analyses of cumulus dynamics has been performed to show that many of these features can be reproduced in such models and that some quantitative correlation can be identified.

The Models

The models use the two dimensional linearized equations for Boussinesq fluid within which there exist regions of saturated and unsaturated air divided by linear boundaries across which air, but no water, can flow. Movement of the boundaries can be shown to be of second order. Encouraged by the spectral gap found experimentally between the shortest wavelength, possibly turbulent motions and the larger scale convective motions, a simple eddy viscosity and diffusivity (ν_T) formulation is used. Values of ν_T between 1 and 100 m/s^2 have been suggested (see e.g. Krishnaumurti 1975) and several values in this range, with Prandtl number of one are used below.

Linear theory is very restricted in the types of boundary that can be studied analytically but two types of model have been tried. In the first, vertical boundaries are used to simulate the effect of the lateral cloud edges, while in the second the top of a growing cloud is simulated by the use of horizontal boundaries. In case (i) (see Fig(1)) the cloud is simulated by a region of saturated air with zero initial motion bounded by the ground beneath and a slippery lid inversion above, and laterally by two vertical edge boundaries of separation 2a. The environmental air is taken to be stable with respect to saturated motion, and the cloud is

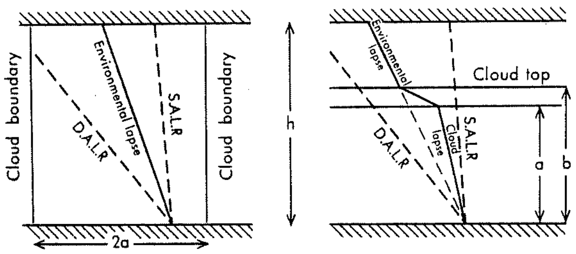

Model I – Cloud with lateral boundaries

Model II – Growing Cloud

Figure 1. Model diagrams with superimposed temperature lapses

assumed to be at the temperature of the environment. Although the initial mean motion is zero, it is tacitly assumed that subsequent motions will be related to those occurring in a developing cloud. In case (ii) the top of a cloud growing into environmental air stable to dry, but not saturated motions, is simulated by a saturated region of infinite horizontal extent under a layer of stable air. Between these two regions is a thin ($\sim$ 200 m) layer of saturated air across which a potential temperature drop of $\sim 1^\circ$C is assumed. The top and bottom boundaries are defined as in model (i), and an initial state of zero motion assumed.

The two dimensional linearized Navier-Stokes continuity and thermodynamic equations for saturated air, with no mean motion using the Boussinesq approximation can be reduced to the following well known sixth order differential equation for the vertical velocity w:

$$\left(\frac{\partial}{\partial t}-\nu_T\nabla^2\right)^2\nabla^2 \omega + g/\Theta_s\left(\frac{\partial\Theta_s}{\partial z}+\frac{\Theta_s L}{C_p T}\frac{\partial q_s}{\partial z}\right)\frac{\partial^2\omega}{\partial x^2}=0$$

where t is the time, Θ_s the potential temperature, T the absolute temperature, g the acceleration due to gravity, L the latent heat of vapourization of water, C_p the specific heat at constant pressure of air, q_s the saturated mixing ratio, z the vertical co-ordinate and x the horizontal co-ordinate. The second term in the equation can be expressed in terms of the saturated equivalent potential temperature $\Theta_{es}=\Theta_s(1-Lq_s/C_pT)$. The differential equation has solutions of the form $A\exp(kx+nz+\sigma t)$ for a given region where A,k,n and σ are all, in general, complex. We note immediately cloud liquid water $q_L=\frac{\omega}{\sigma}\partial q_s/\partial z$ giving the correlation between q_L and the cloud updraught noted experimentally in the middle of clouds by Warner (1970), the author and others. Numerical techniques are used to determine the values of σ as a function of cloud width in case (i), and of horizontal wavelength in case (ii). The fastest growing, and hence predominant modes are those with the largest positive real parts of σ while the imaginary part of σ gives the frequency of oscillatory modes. The form of these σ,a and σ,k curves for several cases and parameter values are discussed below. The boundary conditions given above and those applied at the interfaces between the regions: continuity of pressure, horizontal velocity, vertical velocity, stress, temperature and heat flux restrict the combinations of allowed solutions. After some manipulation non trivial solutions are found by requiring a complex determinant to be zero.

The main numerical problems are in deciding whether this determinant has passed through, or has merely passed near zero. This is because it has no absolute size and two dimensional freedom. A practical limit is set by machine truncation errors. Mapping the determinant in the neighbourhood of the zero has proved helpful. Thus a coarse search for minima in the determinant amplitude is first made by varying σ for fixed a or k. A high resolution search is then made in the vicinity of the minima and the numerical error in the determinant evaluated. Finally checks are made for equal or zero k(or n) values which give rise to trivial solutions.

Case (i)

In the first case described above the pure real positive values of σ are determined for cloud half widths varying from 0 to 2 kms(Fig 2). Calculations with zero viscosity and diffusivity show a growth rate that decreases monotonically with cloud width. (Davies 1979).

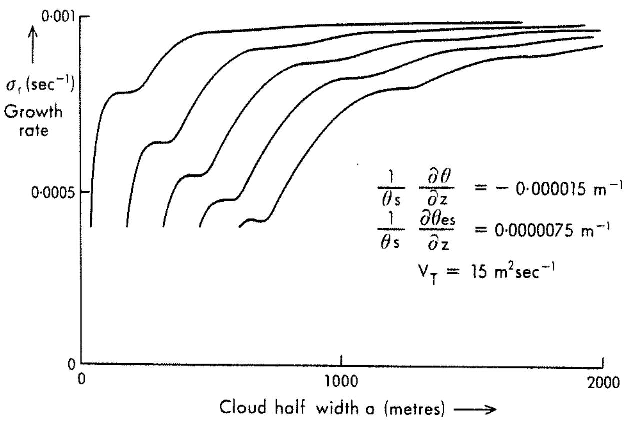

Figure 2. Growth rate of cloud versus width

However, in this viscous formulation with stable environment the growth rate increases from no growth at zero width to maximum growth at infinite width. The solutions of σ =f(a) are multivalued and the form of the updraught is studied for the branch giving the largest growth rate. For clouds of width 2a greater than ~4 km several branches merge together. The form of the main branch varies with saturated Rayleigh number $R_s = \frac{g\lambda^4}{\theta_s \nu^2}\frac{\partial\theta_{es}}{\partial z}$ reaching a maximum at smaller a for larger R_s. For an unstable environment, the curve tends to a finite value of σ at zero cloud width. The reduced σ at small width is due to viscosity, while the reason for maximum growth at infinite width is seen when the form of the updraught solutions for a particular branch is studied. Solutions for two widths are shown in Fig. 3

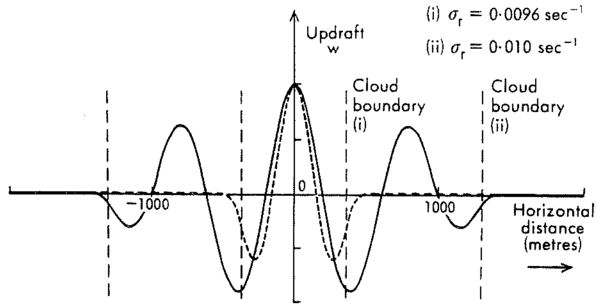

Figure 3. Updraft for clouds of width 740 and 2620 metres

and one of the main features is the edge downdraught which in general is localized at the cloud boundary and does not extend far into the environment. As a is increased the width of the updraught also increases up to a point when it splits into two updraughts with downdraughts between them and at the edges. At greater widths, several updraughts and downdraughts occur. Aircraft data in wide cumulus and cumulonimbus have shown internal downdraughts as strong as the updraughts. Thus there are peaks in the gust spectrum, which for the cloud parameters given in Fig 3 are at ~ 600 and ~1000 metres. These peaks do not vary greatly for cloud widths above a kilometer and are separated from any peak due to the cloud width itself. The multiple updraught solution appears to occur as a result of three factors. The cloudy air tries to grow at a minimum wavelength to reduce the horizontal accelerations in a vertically restricted region, but viscous forces oppose this resulting in an intermediate 'natural' growth wavelength. The growth mode is constrained to the cloud width up to a point by the boundary conditions but the tendency to revert to the natural wavelength causes two or more updraughts to form. All branches of σ = f(a) show multiple updraughts at large values of a. The breaking up of the updraught provides the reason the σ =f(a) curve does not decrease at large values of a. No long horizontal wavelength with its energetically unfavourable horizontal acceleration is formed.

Except in the case of small cloud widths the net updraught in the above solutions within the lateral cloud boundaries is small compared to the variance in w at wavelengths of less than a kilometre. The energy in the part of the spectrum attributable to the cloud width is negligible.

Two attempts have been made to determine whether evaporation at the cloud edge contributes significantly to the localisation of the edge downdraught on linear theory. In the first attempt the cloudy air is divided into three regions - a central region, and two edge regions in which evaporation was simulated by a decreased value of $\frac{\partial q_s}{\partial z}$. The edge downdraughts became shallower and less extended. In the second attempt the original cloud formulation is used but evaporation at the cloud boundary is allowed at a rate proportional to the local value of ω. The effect of this is small even at high evaporation rates. Thus in linear theory at least the observation of downdraughts at cloud edges is seen to be related to the difference in effective stability between the cloud interior and its environment rather than to local intense evaporation.

Oscillatory solutions have been investigated also. However these have low frequencies with decay rates high enough to make them experimentally unidentifiable.

Case (ii)

The cloud top model used in case (ii) involves linearizing about a basic state forced by a combination of non linear and condensation effects. As a basic state of zero motion is assumed this can be thought of as equivalent to a distribution of latent heat sources in the bulk cloud with an evaporation heat sink at the top. The (σ,k) curves for the three fastest growing branches of this model are shown in Fig 4. These all feature maxima which are

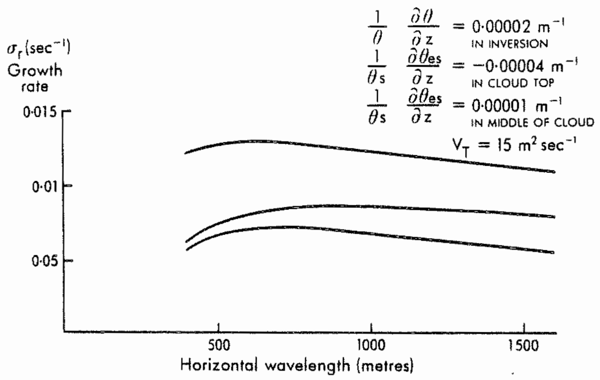

Figure 4. Growth rate of multilayer cloud versus horizontal wavelength

sensitive to the Rayleigh numbers in each layer as might be expected. The top branch maximises at a horizontal wavelength λmax $\sim$ 600 m and has maximum amplitude (Fig 5) in the thin unstable top layer which may account for the

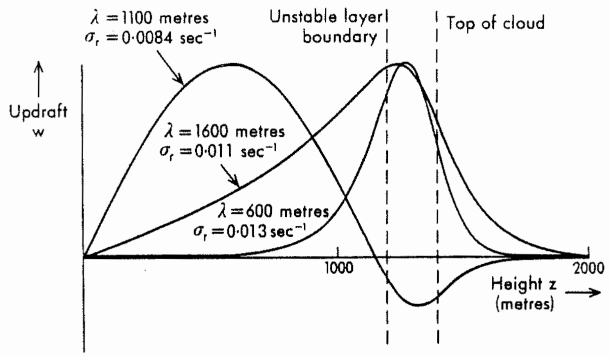

Figure 5. Updraft modes for cloud of height 1200 metres with top layer 200 metres thick

'bubbly' tops seen in growing cumulus. Its associated downdraughts could be a powerful entraining mechanism, and it is tempting to identify this mode with the narrow ($\sim$ 500 m) updraughts and downdraughts observed by MacPherson & Isaac (1977) in cloud tops and, by Warner (1970) although Warner observed much shorter wavelengths, of order 200 m. It may well be the case that the instability in the layer is much greater than assumed here in which case λ max would be shorter. These modes are strongly entraining at the cloud top and may provide the mechanism envisaged by Paluch (1979). At small wavelength this mode is rather localized in the vertical, but at greater λ it reaches further down into the bulk of the cloud below, and into the environmental air above, and may be identified with the long wavelength in the inversion noted by Kuo (1976). λ max varies slightly with the stability of the inversion above. Instability in the bulk cloud also increases the wavelength of the mode. The lack of penetration of the fastest growing mode into the bulk cloud means that the second fastest mode may be significant here.

This mode has a maximum updraught in the middle of the cloud combined with a downdraught in the unstable layer at the top, the connection being provided by turbulent viscosity. The growth rate maximises at a longer wavelength than the primary mode but the growth rate is about two thirds that of the primary. This mode can perhaps be identified with the longer wavelengths found by Warner there.

Oscillatory solutions are again investigated and none are found for positive real σ. However the solutions for a negative real part of σ only decay very slowly, having e-folding times greater than 30 minutes at long wavelengths. The frequencies are appropriate to the Brunt Vaisala frequency of the environmental air above the cloud, where the solution maximises (Fig 6) and have the form of a

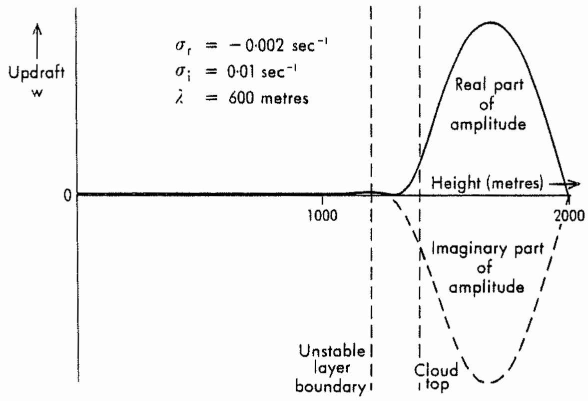

Figure 6. Oscillatory mode for cloud of height 1200 metres with top layer 200 metres thick

standing wave penetrating slightly into the cloud. Integrations of a full non-linear cloud model by the author indicate that in a cloud non-linear interactions are capable of initializing this mode significantly, which is the main mode in its layer despite its slightly negative growth rate. Oscillations of cloud tops have also been observed in the atmosphere (Lee, 1979). The variation of σ with k is similar to that found in the simpler case of a perturbed stable fluid bounded by a lid above and below.

The three level model has also been used to study a layer of stratocumulus above a convective boundary layer (CBL) and underneath a stable inversion. The forms of solutions obtained are related to those described above. In particular the rising solution in the CBL is connected to a downdraught in the cloud layer, and this, together with its different horizontal wavelength to the cloud layer mode, may be related to the fact that thermal updraughts in the CBL are often found not to be directly connected to updraughts in the stratocumulus above (e.g. Hackett 1976). However evaporation effects are probably at least partly responsible for this phenomenon.

Conclusion

Simple linear models have been used to study growth and oscillatory modes in clouds. Internal up and downdraughts and downdraughts localized at the cloud edges are seen to be a natural consequence of saturated motions in a region bounded by stable environmental air. Relatively short wavelength, strongly entraining motions are seen to be important at the tops of growing clouds, which can also induce oscillations in the overlying air. These results may provide a basis for the study of full non-linear initial value problem modes.

References

Ackerman B. 1967 The Nature of the Meteorological Fluctuations in Clouds J.App.Met 6 p.61.

Beritashvili B S and Lominadze V P 1972. On the Characteristic Dimensions of the elements of Convective clouds Izv., Atmospheric & Oceanic Physics 8 p.1310.

Davies H. Private Communication.

Hackett N. 1976 Sailplane & Gliding 27 p.244.

Kuo H L & Sun W Y 1976 Convection in the Lower Atmosphere and its effects J.A.S. 33 p.21

Krishnamurti R. 1975 On Cellular Cloud Patterns Part 3: Applicability of the Mathematical & Laboratory Models. J.A.S. 32 p.1373.

Lee J.T. Private communication.

Le Mone M.A. 1976 Modulation of Turbulence Energy by Longitudinal Roles in an Unstable Planetary Boundary Layer. J.A.S. 33 p.1308.

MacPherson J.I. & Isaac G.A. 1977 Turbulent Characteristics of some Canadian Cumulus Clouds J.App Met 16 p.81.

Paluch I.R. 1979 The Entrainment Mechanism in Colorado Cumuli J.A.S. 36 p.2467

Warner J. 1970 The Microstructure of Cumulus Cloud Part III: the Nature of the Updraught 27 p.682.

THE MICROESTRUCTURE OF CUMULUS CONGESTUS CLOUDS IN CUBA

Lubomir Levkov
Geophysical Institute
Academy of Sciences of Bulgaria
Sofia BULGARIA

Mario F. Valdes
Meteorological Institute
Academy of Sciences of Cuba
Havana CUBA

INTRODUCTION

The Academy of Sciences of Cuba and the Ministry of Agriculture sponsored a cloud seeding experiment project to future operational program to enhace precipitation on the east part of Cuba. In the frame work of this project cloud physics researchs have been made and some results obtained from droplet sampling and liquid water measurements of tropical cumulus clouds are presented in this paper.

The observations were made during two expeditions on the experimental area between May-August 1977 and August 1979. The cloud samples were made in isolated cumuli with depth 2 - 3,6 km, cloud top temperature above -2°C, using an IL-14 aircraft for afternoon fligths during days in which found good convective development asociated with cumulus activities but not in though synoptic situation. About 170 individual samples from nearly 100 traverses made at different levels through 80 clouds were analyzed. Cloud droplets were impacted on sooted glass slide in the sampling device described by Shmeter (1952). To found real diameter from the impression we used the calibration of Squires (1958) and for real concentration the K coefficient of Nevsorov and Shugaev (1974). Measurements of liquid water content have been made with Zaisev's equippment (Zaisev,1948) which use the size of coloured spot on the filter paper.

RESULTS AND CONCLUSIONS

General views of the microestructure of cloud and its vertical change were found dividing each cloud in three equal layers called: zone 1 (cloud base),zone 2 (middle cloud) and zone 3 (cloud top).

Summaries of the basic information available and from derived data are given in the table and are illustrated in the figures. Figures 1 and 2 show the droplet size distribution for all clouds and a representative particular case. Those curve have generally a single maximum with positive skew. In other way,the fluctuations obtained in the range 20 to 45 microns maybe connected with a secondary maximum. Both figures presents longer tailed spectrum in zone 3 than in zone 1. In the lowest few hundred meters of cloud the occurrence of 70 microns drops are very strange but at the top of them we could find even 150 microns.

The presents series of observations indicated a sistematic decrease in droplet concentration with increasing height.

The liquid water content (g/m^3) increased upward to within 200-400 m below cloud top. About 50 percent of the measurements are below 0,4 g/m^3. The greater part of the liquid water content belongs to the biggest droplets (Figures 3 and 4). The comparition of liquid water derived from the sum of droplet volumes and that from the paper tape-liquid meter shows value of the same order.

In the light of our data, we conclude:

1- Markedly tendency of the microestructural parameters to vary with height variations.

2- Cloud droplet concentration from our cumulus cloud compared with droplet concentration from maritime and continental cumuli (Battan and Reitan,1957) show intermediate concentration valeus. Because of that, the cumulus cloud that developed from 30 to 50 km from the seashore had strong maritime influence.

REFERENCES

Battan,L.J. and Reitan,C.H.(1957): Droplet size measurements in convective cloud. Artificial Stimulation of Rain Pergamon Press, London. 184-191

Nevsorov,A.N. and Shugaev,V.F.(1974): Caracteristicah y izmereni localnoii microstructurei oblakov. Trudi TzAO,106.

Shmeter,S.M.(1952): O soderjanie clora u vode oblakov u svazi ih microstructurei. Trudi. TzAO,9.

Squires,P (1958): The microstructure and colloidal stability of warm clouds. Tellus,10 . 256-271

Zaisev,V.A. (1948): Novi metod opredelenia vodnosti oblakov y tumanov. Trudi GGO 13

Characteristics	zone 1	zone 2	zone 3
Mean diameter(μ)	6,7	8,9	9,7
Mean vol.diam.(μ)	14,9	24,7	28,5
Mode diameter(μ)	5	5	5
Coef.dispersion	1,0	1,4	1,5
Mean. Concent.(cm^{-3})	186	55	47
Mean LWC (g/m^3)	0,4	0,5	0,8
Maximum LWC(g/m^3)	0,6	1,7	3,2
Predominant dia.(μ)	70	100	150
Mean concent. by LWC equippment	127	72	64
Mean LWC by droplet spectrum	0,3	0,4	0,6

Table. Microestructural parameters for zone 1 (cloud base), zone 2 (middle cloud) and zone 3 (cloud top).

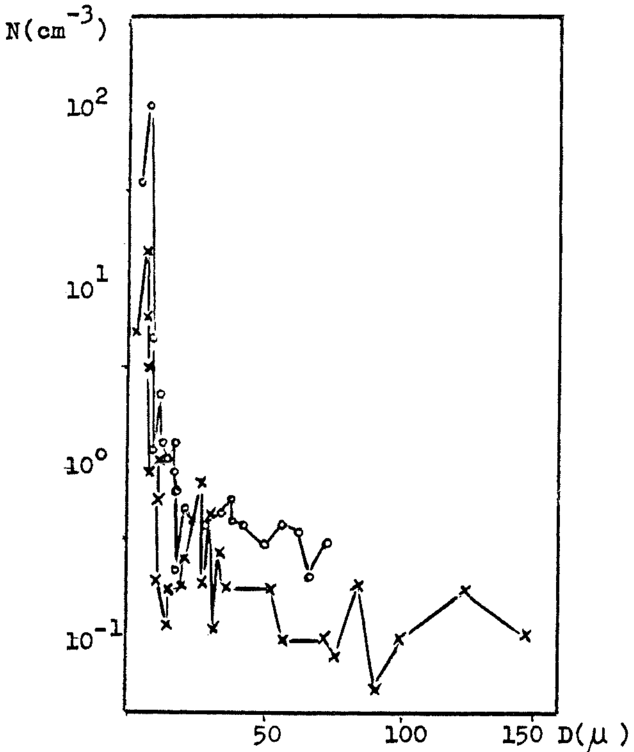

Figure 1- The average size distribution of all samples taken at zone 1 (0 —— 0) and zone 3 (✗ —— ✗).

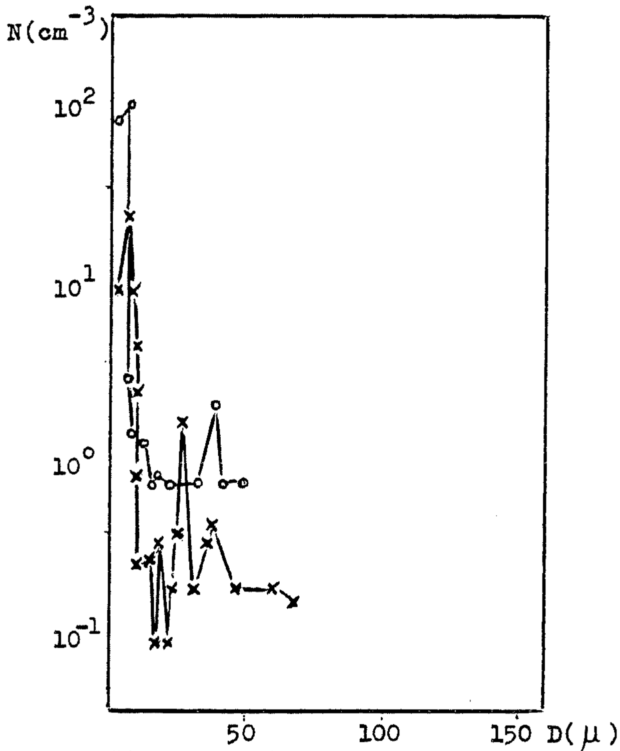

Figure 2- The size distribution of particular case on 22 August at zone 1 (0——0) and zone 3 (✗ —— ✗).

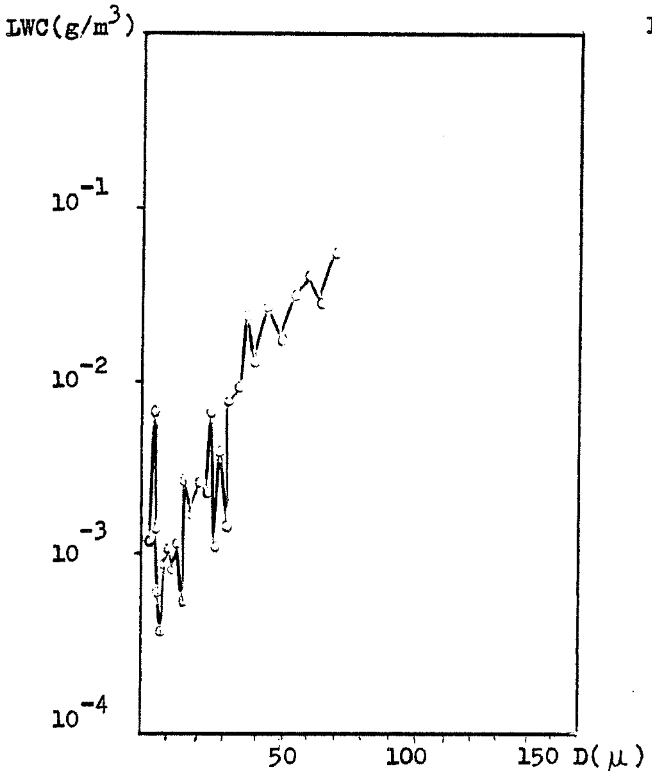

Figure 3. Liquid water content distributions for zone 1.

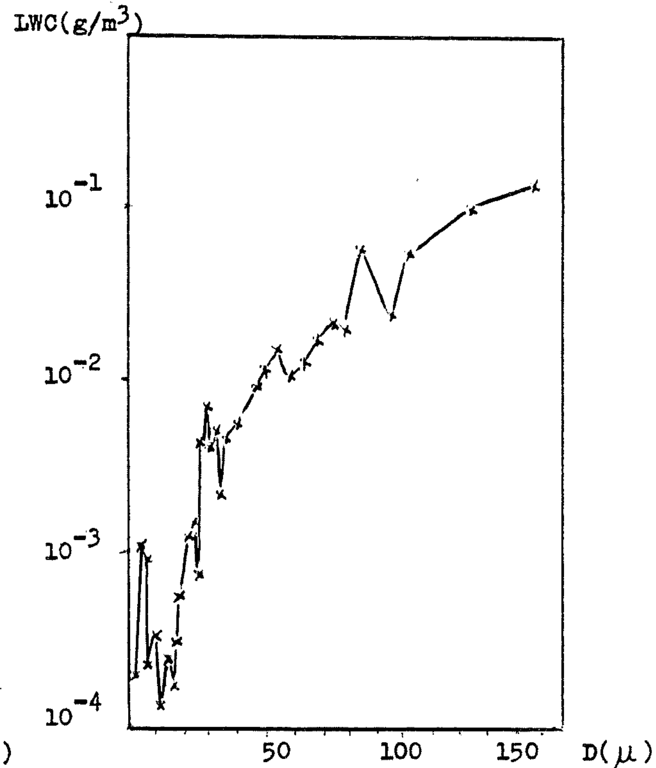

Figure 4. Liquid water content distributions for zone 3.

NUMERICAL RESULTS OF A MODEL OF A CUMULUS CLOUD

I.Nemešová , D.Řezačová

Institute of the Physics of the Atmosphere CAS
Prague CZECHOSLOVAKIA

1.Introduction

The original purpose of the proposed model of a Cu cloud was to formulate such a model in which attention is drawn to suitable simulation of the microstructural processes as a part of relationships for the macrostructural characteristics of the cloud.The fundamental ideas of one-dimensional steady-state models were used.The parametrization of the formation and fallout of precipitation was substituted by a system of equations which describes the processes taking place in a unit volume of cloud air.The description of the processes is a modification of Belyaev's approach for studying the processes of 0.01 to 10m scale by means of Lagrange's variables /1/.From the computed characteristics it is possible to go over to Euler's variables at the end of each time(or height) interval and to determine the quantities required for applying the operations associated with the dynamics of the cloud volume.In the original paper /2/ three model patterns were suggested -a one-stage model, without a fallout into the volume investigated and two others which contained an approximation of the fallout processes.The structure of all the versions was based on the principle of the alteration of micro- and macro-operations (Mi and Ma).Both operations were described in detail in /3,4, 5,6/.In the one-stage model both operations are combined in the computation diagram illustrated by Fig.1.In Fig.1 symbol $A(\tau_o)$ represents a set of quantities characterizing the initial conditions of the cloud volume in the cloud base;it contains the pressure,temperature,water vapour density and the characteristics of condensation nuclei and the spectrum of droplets.Besides $A(\tau_o)$ also sounding data, vertical velocity W_o and the radius of the upcurrent R_o enter the computations.On applying $Mi(\Delta\tau)$ operation to $A(\tau_o)$,we obtain the new set $A'(\tau_1)$ which represents the state of the volume at the end of interval $\Delta\tau$,during which the volume is being cooled at a constant rate. With the aid of $Ma(\tau_1)$ we then arrive at $A(\tau_1)$ and new vertical velocity W_1 and radius R_1.The block Tr represents the substitution of Lagrange's variables by Euler's.The set $A(\tau_1)$ and W_1 serves as the input set for the next step $Mi(\Delta\tau)$.The chain of operations ends at the time τ_i at which $W_i \leq 0$.As we can see the diagram cannot include the fallout of cloud elements.

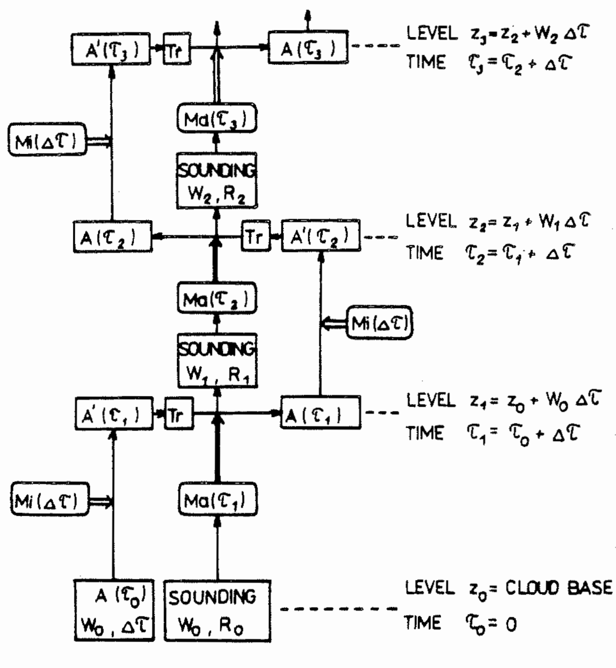

Fig.1. The computation diagram.

2.Input Data and Parameters

In this paper numerical testing of the model is limited to the liquid phase.All the variables are denoted by usual symbols.n(r) is the spectral function of droplets and the water content is denoted by Q.Indices e indicate the ambient atmosphere.

As the input external data we adopted the sounding data of July 5,1971 taken in Prague (Tab.1) for we got the heights of bases and tops of clouds.The weather situation was determined by a ridge of high pressure over Central Europe and by a NE flow.The macro-characteristics of the clouds corresponded roughly to the clouds in which Warner /7/ had made his droplet measurements.The bases were at an altitude of 1500m and the tops reached the level of up to 3000m.We identified our cloud base with the CCL at the level of 1410m.The set of cloud droplets in a unit volume in the cloud base was described by Khrgiyan-Mazin distribution where the maximum radius and numbers of droplets were determined from Warner's measurements.The characteristics of the spectrum and of the condensation nuclei were described previously.The input velocity W_o in turn assumed the values of 1,3 and 5 ms^{-1} for radii R_o 150, 350 and 500m.All the other input values are contained in Tab.2.

The fundamental input parameter is the time interval $\Delta\tau$.It determines the total time of integration of the system of equations in the Mi operation and the frequency of alternating of those operations.In addition, its choice affects the computation time substantially.The interval $\Delta\tau$ was in turn assumed to be 5, 10, 20, 25 and 30s.Numerical results show that the temperature excess and velocity are nearly independent of the choice of $\Delta\tau$ in the fixed range.The changes of the top level are within 30m. The water content and supersaturation react more sensitively to the changes of $\Delta\tau$. The water content is the higher, the shorter the chosen interval (up to 20%). The situation is the artificial consequence of linking up both operations. Shorter $\Delta\tau$ give higher output Mi values of supersaturation, which means the decreasing evaporation in the next Ma-operation. We had to choose the values of $\Delta\tau$ such that they represented steady-state water vapour values preserving simultaneously reasonable vertical "steps". Also short computation times spoke in favour of choosing larger $\Delta\tau$. In all program runs we put $\Delta\tau = 22$ s.

Tab.1. Sounding on July 5, 1971, 00 GMT, Prague. r_h is the relative humidity.

p/mbar/	z/m/	T/°K/	r_h/%/
960	470	289.2	82
900	1013	287.9	71
790	2100	278.5	87
674	3400	272.2	50
619	4070	271.0	23

Tab.2. Input values of the temperature, water vapour tension, virtual temperature and water content for selected values of the virtual temperature excesses at the cloud base.

$\Delta T_{v,0}$/°K/	T_0/°K/	u_0/mbar/	$T_{v,0}$/°K/	Q_0/gm^{-3}/
0.5	284.576	13.6408	286.29	0.38
1.0	285.022	14.0484	286.79	0.38

3. Numerical Results

The numerical results were obtained from the IBM 370 computer. The individual program runs require the CPU for 10 to 25 mins. We decided to illustrate the numerical results for the virtual temperature excess of 0.5°K (Figs. 2,3,4). The numerals from 1 to 8 denote possible combinations of W_0 and R_0, i.e. 1 to 3 ($W = 1\text{ms}^{-1}$), 4 to 6 ($W = 3\text{ms}^{-1}$), 7 to 8 ($W = 5\text{ms}^{-1}$) for R_0(150, 350, 500m), respectively. The case R_0=150, W_0=5 is omitted. The levels of the cloud tops are between 2532 and 3680m. Clearly, the larger the input radius and the larger the vertical velocity, the higher levels the computed cloud top attains. Fig.3 shows the dependence of the virtual temperature excesses of the ascending volume. The effect of the stratification of the atmosphere on the computed lifting forces is of principal importance as usual. Fig.4 contains the vertical dependence of supersaturation S (u/u_s-1) and of the water content. The supersaturation increases rapidly at the base, reaches a maximum value at the middle levels of the cloud and decreases to zero at its top. The maximum computed value of S is about 0.35%. The curves representing the water content for all the input combinations lie close to each other in the hatched area in Fig.4.

From the numerical results it is clear that the capability of the model to forecast the cloud top depends strongly on the choice of the initial values as it is the case with other one-dimensional models with entrainment. W_0 is usually taken 1 ms^{-1}. The value of a representative radius at the base is always problematic. Using Saunder's relation /8/ for the radius and identifying the base with emergence level, the estimated radius for the day is roughly 240m. The main characteristics for the chosen data are shown in Fig.5. We also added the computed spectra for 4 selected levels or at 4 individual times of ascent of the cloud volume. The spectra marked 1 and 4 correspond to the base and the top level, respectively. Fig.6 shows that between levels 1 and 2 (interval (0, τ_2)) the spectral curve is displaced

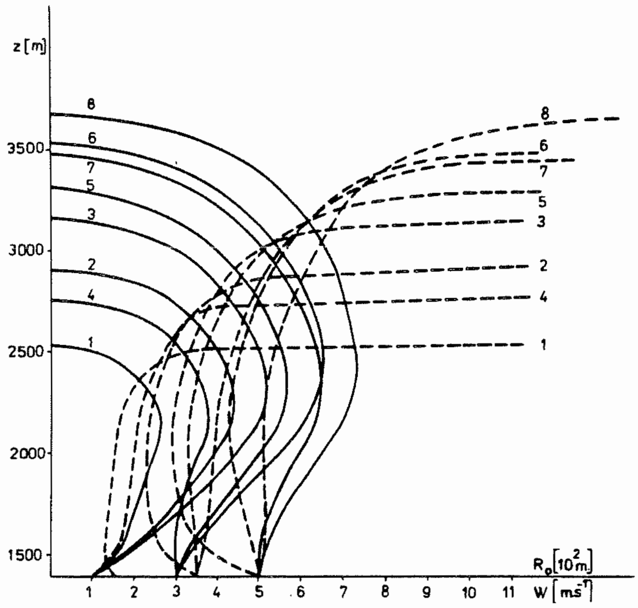

Fig.2. The vertical velocity W(full line) and the radius R(dashed line) as functions of the height. For symbols refer to the text.

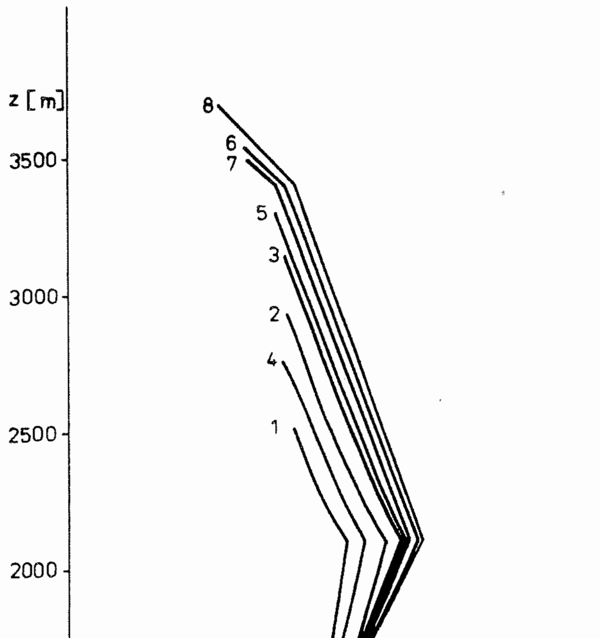

Fig.3. The virtual temperature excess as a function of the vertical coordinate. For curve symbols refer to the text.

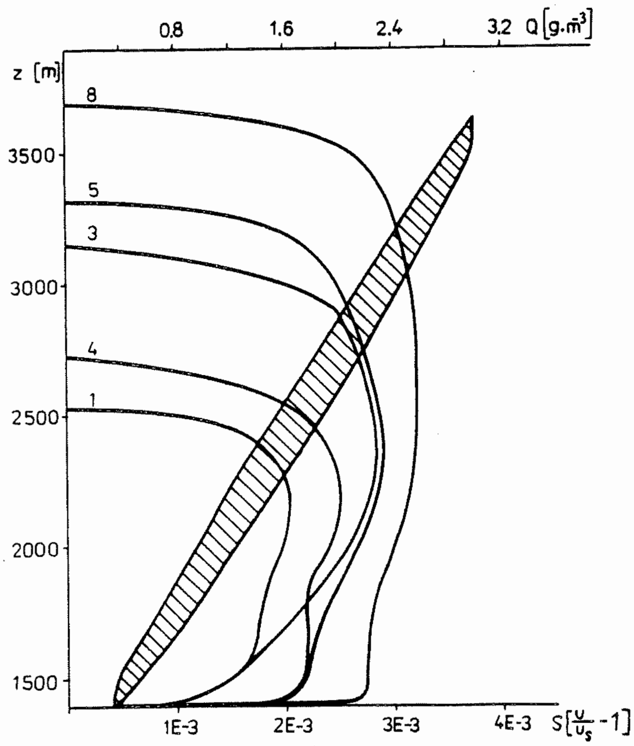

Fig.4. Vertical dependence of the supersaturation S and of the water content Q.The hatched area contains all the curves of the water content Q.

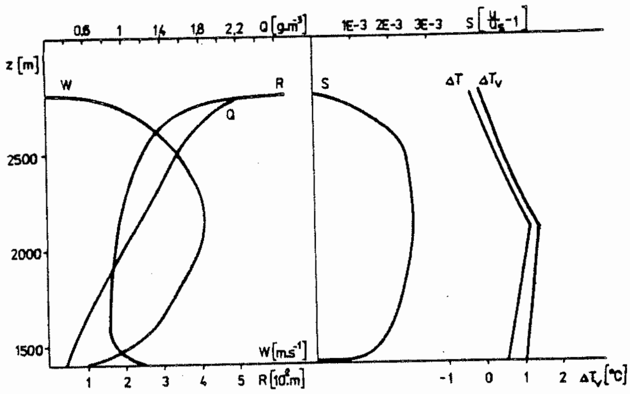

Fig.5. Vertical dependence of the vertical velocity W,the water content Q,radius R,supersaturation S and of the temperature excesses for W_0= 1ms^{-1}, R_0=240m.

toward higher values of thedroplet radius whereas at the level 3 the curve splits into two parts: the spectral function has zero value for cloud droplets whose radii are between 5 and 11 μm.At the top level the spectrum is again continuous. The development of the spectrum described is explained by a scheme of the droplet evaporation in the Ma operation: the droplets of the smallest radii evaporate first. Up to level 2, the increment of water droplets of small radii is nearly compensated for by evaporation and the resulting spectrum contains mainly the original droplets, the dimensions of which increased in the course of interval (0,τ_2).The spectrum at level 3 is composed of two parts.The first represents particularly the droplets generated on the condensation nuclei during

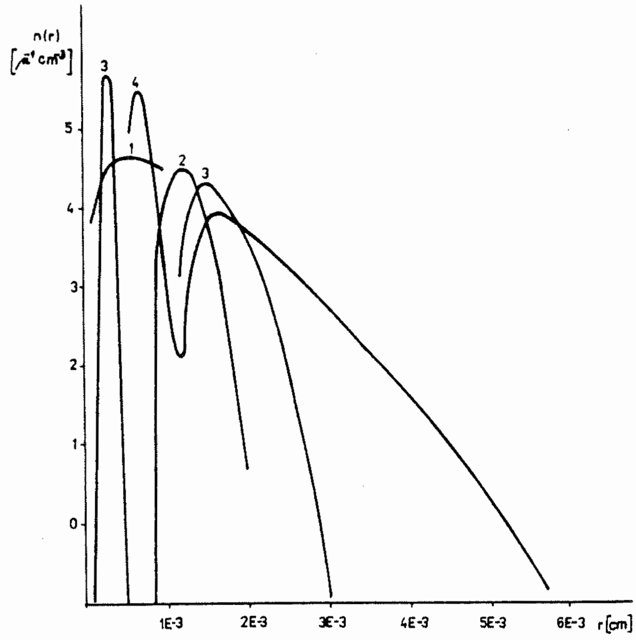

Fig.6.The spectral function at 4 selected levels,or 4 times. 1- base level (τ_1=0), 2 - 1950m level (τ_2 =220s),3 - 2466m level(τ_3 = 352s), level of the top 2810m(τ_4 =506 s).

the interval (τ_2,τ_3) and not evaporated in the course of the Ma-operations.The spectrum at the top is continuous within the radius interval of 6 μm to 56 μm.

4.Conclusions

The proposed model allows to follow the life history of an individual cloud volume which ascends from the cloud base and mixes with the ambient atmosphere.The time or vertical co-ordinate dependence of all macro-characteristics corresponds to the results of one-dimensional models, which also applies to the prognostic ability of the model.The computations produce droplet spectra and reproduce their bi-modality although the latter is the consequence of modelling the spectrum evaporation in the Ma-operations. The structure of alternating the Ma and Mi operations may be suitable for modelling the sequence of "lift" volumes,i.e. for a gradual "build-up" of a cloud. The originally proposed model in its general form /2/ represents a suitable basis for the contruction of a mixed cloud model where the dynamic equations are a modification of Kachurin´s approach.The numerical testing is expected to be completed in the next future.

References

/1/ Belyaev V.I.,1964: Metod Lagranzha v kinetike oblachnykh protsessov.Girdometeoizdat Leningrad.

/2/ Nemešová I.,D.Lakomá,1974: A steady-state Model of Cumulus Cloud Describing Phase Transitions by Kinetic Equations.I.Model Pattern. Studia geoph.et geod.,18,p.274

/3/Lakomá D.,1977:Numerical solution of Micro physical Equations in a Model of a Convective Cloud.I.Origin and Growth of Cloud Drops due to Condensation.Studia geoph.et Geod.,21, p.55

/4/ Lakomá D.,Motl V.,1977:Numerical Solution of Micro-physical Equations in a Model of a Convective Cloud.II.Condensation and Coagulation of Cloud Drops.Travaux Inst.Géoph. Tchécosl.Acad.Sci.No 497,Geofyzikální sborník,Academia,Praha (in press)

/5/ Nemešová I.,1976: Numerical Evaluation of the Description of Macrophysical Aspects in the Model of a Convective Cloud(Liquid Stage).Studia geoph.et geod.,20,p.81

/6/ Nemešová I.,1977:The Evaporation of Liquid Water in Describing the Dynamic Aspects in the Model of a Convective Cloud.Studia geoph.et geod.,21,p.179

/7/ Warner J.,1969: The Microstructure of Cumulus Cloud. Part I. General Features of the Droplet Spectrum. J.Atm.Sci, 26,p.1049

/8/ Saunders P.,1961: An Observational Study of Cumulus. J.Met.,18, p.451

RESULTATS PRELIMINAIRES DE SIMULATION NUMERIQUE A L'AIDE D'UN MODELE TRI-DIMENSIONNEL DE CONVECTION PRECIPITANTE

par

J.L. Redelsperger et G. Sommeria

Laboratoire de Météorologie Dynamique
CNRS, Paris

1) Introduction

Nous présentons ici une méthode originale de représentation de la turbulence et des précipitations pour un modèle tri-dimensionnel de convection atmosphérique. Cette méthode est développée et essayée sur le modèle de micro-échelle du Laboratoire de Météorologie Dynamique (Sommeria 1976), lui même dérivé du modèle de Deardorff (1972).

Le modèle de départ comprend quatre équations de base, l'équation de Navier-Stokes, l'équation thermodynamique, les équations d'évolution de la teneur en vapeur d'eau q et en eau liquide nuageuse q_c. Il couvre un domaine de 2 km de côté avec une maille cubique de 50 mètres dans une des versions utilisées pour les tests. Chaque modification est testée sur ce modèle de base afin de pouvoir en juger les effets avec des critères précis de comparaison ; l'objectif ultérieur est de les incorporer dans un modèle de convection profonde d'extension horizontale 40 x 40 km et d'extension verticale 16 km, en préparation au L.M.D.

2) Représentation de la turbulence d'échelle inférieure à la maille

Avant d'étendre le modèle au cas précipitant, il nous a semblé préférable de repenser le problème important de la turbulence à l'échelle inférieure à la maille. Ceci pour au moins deux raisons : nous voulions, d'une part, prendre en compte l'interaction de petite échelle entre les termes de condensation-évaporation et les autres variables du modèle ; d'autre part, nous voulions disposer d'un schéma mieux adapté pour l'introduction de la pluie. Nous avons donc modifié le schéma développé précédemment sur deux points principaux :

a) adjonction d'une équation pronostique pour l'énergie cinétique turbulente E

L'équation utilisée est écrite en approximation anélastique :

$$\partial \bar{E}/\partial t = -(1/\langle\rho\rangle)\partial/\partial x_j (\langle\rho\rangle\bar{u}_j\bar{E}) - \overline{u'_i u'_j}(\partial\bar{u}_i/\partial x_j) + (g/\langle\Theta_v\rangle)\overline{w'\Theta'_v} - c_2(\bar{E}^{3/2}/\Delta) + (1/\langle\rho\rangle)\ \partial/\partial x_j(\langle\rho\rangle c_1\Delta\bar{E}^{1/2}\ \partial\bar{E}/\partial x_j)$$

où u_i, Θ_v, ρ et Δ sont respectivement, le vecteur vitesse, la température potentielle virtuelle, la densité et la dimension de la maille.

Les termes de cisaillement et de flottabilité sont données directement par le schéma de paramétrisation de la turbulence ; le terme de dissipation turbulente est donné par une approximation de type coefficient de diffusion, le terme moléculaire par analyse dimensionnelle (c_1 et c_2 sont des constantes égales respectivement à 0.2 et 0.7).

Plusieurs simulations ont permis de montrer l'importance d'une équation pronostique pour E; en particulier le terme d'advection négligé jusqu'à présent accélère la formation des zones de turbulence et les intensifie.

b) utilisation de variables se conservant durant la condensation pour le calcul des flux à l'échelle inférieure à la maille

Le concept de variables se conservant durant la condensation a été introduit par Betts (1973). Leur utilisation pour le calcul des flux paramétrés permet de prendre directement en compte les interactions à l'échelle inférieure à la maille entre les termes de condensation-évaporation et les variables de base utilisées. Celà conduit à différencier les coefficients de diffusion (verticaux et horizontaux) pour le contenu en vapeur d'eau q et le contenu en eau liquide nuageuse q_c, ainsi qu'à prendre en compte le degré de saturation dans la paramétrisation de tous les flux. Les variables conservatives que nous avons utilisées pour notre paramétrisation sont la température potentielle d'eau liquide Θ_l et le contenu en eau totale q_w défini par :

$$\begin{cases} \Theta_l = \Theta - L\Theta q_c/TC_p \\ q_w = q + q_c \end{cases}$$

où θ est la température potentielle, L la chaleur latente de condensation de l'eau, C_p la chaleur massique à pression constante de l'air sec.

Les avantages de la méthode proposée (cas VAR CONS) ont été mis en évidence par comparaison avec le cas précédent utilisant des variables non conservatives (cas E PRO). Des différences importantes sont notées dans l'estimation des quantités turbulentes d'échelle inférieure à la maille, en particulier dans la couche nuageuse où on tient maintenant implicitement compte des processus de condensation aux échelles non résolues. La figure 1 montre l'exemple

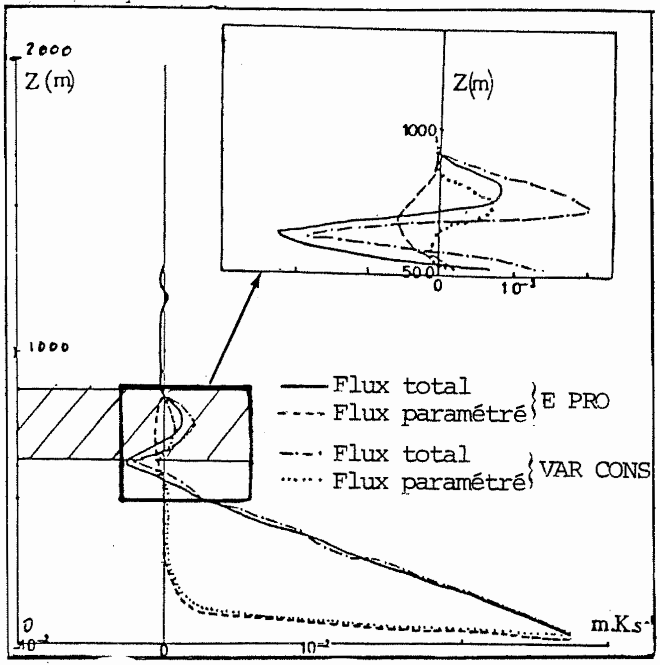

Fig. 1 : Flux totaux et paramétrés de Θ_v

du flux vertical de température potentielle virtuelle Θ_v. Dans la couche nuageuse, sa fraction paramétrée est positive dans VAR CONS et négative dans E PRO. Cette différence reflète l'effet de la flottabilité induite par la condensation à petite échelle qui, dans VAR CONS, rend similaires les flux paramétrés et calculés.

3) Représentation des précipitations

Pour représenter le phénomène de précipitation dans un modèle dynamique de nuage, on doit considérer la présence d'au moins deux classes d'eau liquide (Kessler 1969) : les gouttelettes de nuages, restant en suspension dans l'air, et les gouttes de pluie, tombant à une vitesse moyenne par rapport à l'air. La teneur spécifique en eau liquide q_l est alors la somme de q_r, teneur spécifique en eau précipitante, et de q_c, teneur spécifique en eau nuageuse. Une deuxième hypothèse (nécessaire pour exprimer les termes de production de pluie) est de se donner une distribution statistique de la taille des gouttes de pluie (par exemple, la distribution de Marshall-Palmer : $N = N_0 e^{-\lambda D}$).

Dans notre cas, l'équation d'évolution de la teneur spécifique en eau précipitante s'écrit alors :

$$\partial q_r/\partial t = -(1/\langle\rho\rangle)\,[\,\partial/\partial x_j\,(\langle\rho\rangle u_j q_r)\,] + (1/\langle\rho\rangle)\,[\,\partial/\partial z(\langle\rho\rangle v_t q_r)\,] + (\partial q_r/\partial t)_{AC} + (\partial q_r/\partial t)_A + (\partial q_r/\partial t)_{EV}$$

Dans cette équation, les trois derniers termes du membre de droite représentent les différents termes de production de pluie qui sont :
$(\partial q_r/\partial t)_{AC}$, le taux d'autoconversion d'eau précipitante, non nul dès que la teneur en eau nuageuse dépasse une valeur critique q_{cr},

$$(\partial q_r/\partial t)_{AC} = \begin{cases} D\,(q_c - q_{cr}) & \text{si } q_c \geqslant q_{cr} \\ 0 & \text{si } q_c \leqslant q_{cr} \end{cases}$$

$(\partial q_r/\partial t)_{EV}$, le taux d'évaporation des gouttes de pluie, lors de leur chute,

$$(\partial q_r/\partial t)_{EV} = c\,(q - q_s)\,q_r$$

$(\partial q_r/\partial t)_A$, le taux d'accrétion, représentant l'accroissement des gouttes en eau, lors de leur chute, $(\partial q_r/\partial t)_A = B\,q_c q_r$

D'autre part, $\langle\rho\rangle$ est la valeur moyenne horizontale de la densité, u_j la composante suivant l'axe j du vecteur vitesse, V_t la vitesse terminale moyenne des gouttes de pluie.

$$v_t = E\,q_r^{0.2} \quad \text{(E est de l'ordre de 5 m.s}^{-1}\text{)}$$

Le système d'équations d'évolution écrites pour u_j, q, q_l, q_r et Θ est ensuite moyenné sur le volume de chaque maille, ce qui fait apparaître les moments du second ordre. Ceux-ci sont obtenus grâce à une fermeture de leur équation d'évolution similaire à celle utilisée pour le cas sans pluie. Pour résoudre complètement le système, la connaissance des termes turbulents relatifs aux différents taux de production de pluie s'avère nécessaire.

On montre que ces termes s'écrivent de manière générale :

$$\overline{\text{PROD}\,A'} = K_\Theta \overline{A'\Theta'_l} + K_{q_w} \overline{A'q'_w} + K_{q_r} \overline{A'q'_r}$$

où PROD représente la somme des trois taux de production de pluie et A l'une des variables u_i, q_w, q_r, Θ_l.

K_Θ, K_{q_w} et K_{q_r} sont des fonctions des variables du champ moyen et des termes de production de pluie.

$$\overline{u'_h\Theta'_l} = -(2/3)\,(\Delta/c_l)\,\bar{E}^{1/2}\,(\partial\bar{\Theta}_l/\partial x_h)$$
$$\overline{u'_h q'_w} = -(2/3)\,(\Delta/c_h)\,\bar{E}^{1/2}\,(\partial\bar{q}_w/\partial x_h)$$
$$\overline{u'_h q'_r} = -(2/3)\,(\Delta/c_n)\,\bar{E}^{1/2}\,[1/(1 - K_{q_r}\,(\Delta/c_n\,\bar{E}^{1/2})\,]\,[\,(\partial\bar{q}_r/\partial x_h) + K_{\Theta_l}\,(\Delta/c_l\,\bar{E}^{1/2})\,(\partial\bar{\Theta}_l/\partial x_h) + K_{q_w}\,(\Delta/c_h\,\bar{E}^{1/2})\,(\partial q_w/\partial x_h)\,]$$

pour h = 1,2 (flux turbulents horizontaux),

et
$$\overline{w'\Theta'_l} = -(2/3)\,(\Delta/c_l)\,\bar{E}^{1/2}\,(\partial\bar{\Theta}_l/\partial z)\,\phi$$
$$\overline{w'q'_w} = -(2/3)\,(\Delta/c_h)\,\bar{E}^{1/2}\,(\partial\bar{q}_w/\partial z)\,\psi$$
$$\overline{w'q'_r} = -(2/3)\,(\Delta/c_n)\,\bar{E}^{1/2}\,(\partial\bar{q}_r/\partial z)\,\chi$$

pour les flux turbulents verticaux, où ϕ, ψ, χ, sont des fonctions compliquées du champ de variables moyennes (pour plus de détails voir Redelsperger 1980).

4) Exemples de résultats de simulation dans un cas précipitant

Les résultats suivants proviennent d'une simulation de 2 heures pour laquelle nous avons sélectionné l'heure 1.83, les quantités statistiques étant moyennées sur 200 sec.

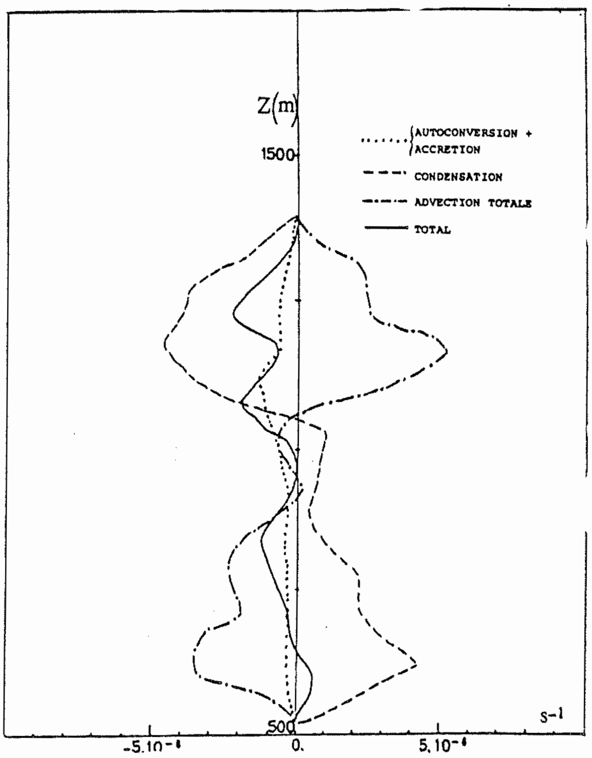

Fig. 2 : Bilan du contenu en eau liquide nuageuse q_c. Heure 1.83.

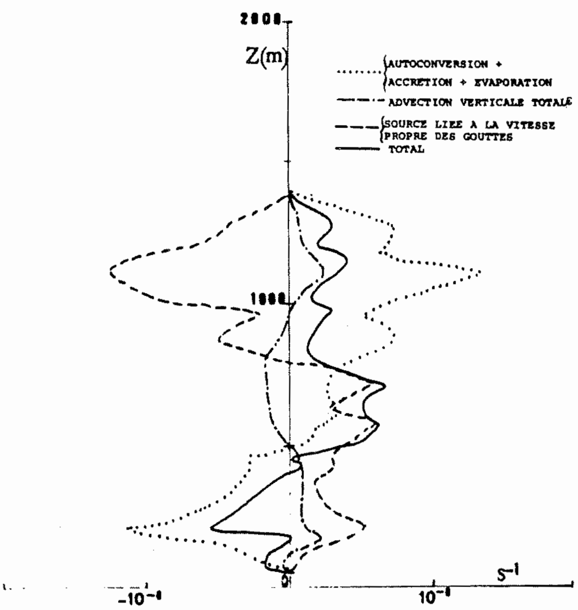

Fig. 3 : Bilan du contenu en eau liquide précipitante q_r. Heure 1.83.

Les figures 2 et 3 représentent respectivement les termes entrant dans le bilan de l'eau liquide nuageuse q_c et de l'eau précipitante q_r. La variation temporelle de q_c se subdivise en 3 termes, le terme d'advection verticale (calculée + paramétrée),

$$< \frac{1}{<\rho>} \frac{\partial}{\partial z} \overline{wq_c} >$$

le terme de condensation et le terme représentant la transformation de q_c en q_r. Le tiers supérieur de la couche nuageuse, entre 1000 et 1300 mètres est une région d'évaporation. Au contraire, la partie inférieure (500 à 1000 mètres) est une région de formation nuageuse, où le terme de condensation est prédominant. Le mécanisme de conversion en eau précipitante se passe essentiellement entre 1000 et 1200 mètres. La variation temporelle du contenu en eau liquide précipitante q_r se subdivise en trois termes, le terme d'advection verticale totale (calculée + paramétrée),

$$< \frac{1}{<\rho>} \frac{\partial}{\partial z} \overline{wq_r} >$$

le terme d'advection vertical dû à la vitesse propre des gouttes et le terme représentant soit les mécanismes d'accrétion et d'autoconversion, soit l'évaporation des gouttes. Nous constatons que q_r est en nette augmentation dans la couche nuageuse avec un maximum vers 700 mètres, bien que la plus grande partie du transfert de q_c en q_r se passe dans les 2/3 supérieurs des nuages avec un maximum vers 1100 mètres. Par contre q_r est en diminution dans toute la couche mélangée du fait de l'évaporation importante.

Nous présentons sur les figures suivantes

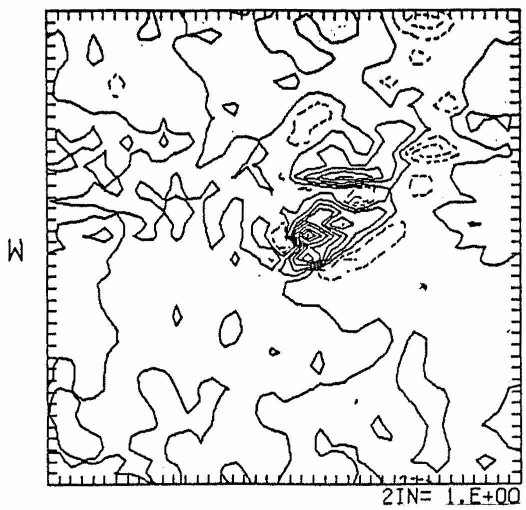

Fig. 4 : Coupe horizontale de la vitesse verticale w.

les coupes horizontales de $w, q, q_r, K_m (= \frac{\Delta}{15} E^{1/2})$ à l'altitude de 1025 mètres et à l'heure 1.83 (Figures 4 à 7). Sur ces figures les moyennes horizontales ont été soustraites sauf pour w et q_r ; les contours en trait plein et pointillé sont les isolignes correspondant respectivement aux valeurs supérieures et inférieures à la moyenne horizontale, l'intervalle entre les isolignes est noté IN en unité MKS sous chaque graphique.

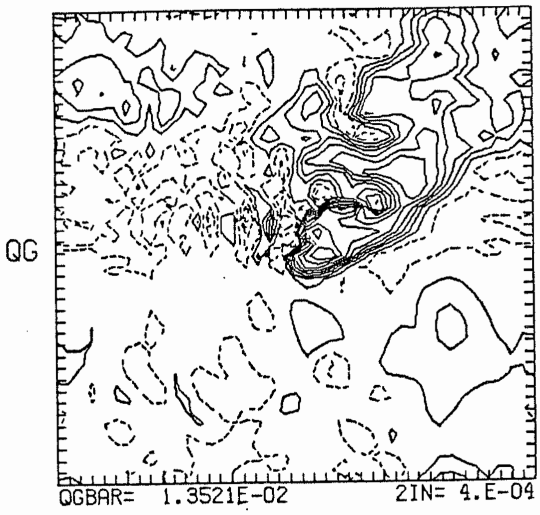

Fig. 5 : Coupe horizontale de l'humidité spécifique q.

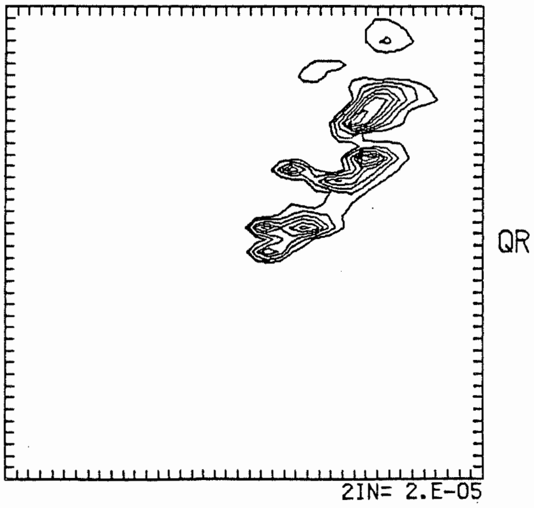

Fig. 6 : Coupe horizontale du contenu en eau liquide précipitante q_r.

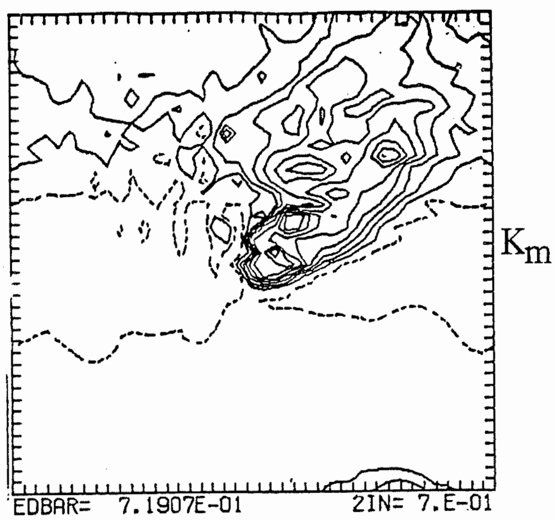

Fig. 7 : Coupe horizontale du coefficient de diffusion K_m.

Dans le cas présenté, la partie active est concentrée dans le quart supérieur droit du domaine où ont lieu les principaux échanges verticaux. On peut remarquer les corrélations positives entre les champs de w, q, q_r et K_m.

REFERENCES

1) A.K. BETTS (1973) : Non precipitating cumulus convection and its parameterization. Quart J.Roy.Met.Soc., Vol.99, p.178-196.

2) J.W. DEARDORFF (1972) : Numerical investigation of neutral and unstable planetary boundary layers. J.Atmos.Sci., 29, p.91-115.

3) E. KESSLER (1969) : On the distribution and continuity of water substance in atmospheric circulation. Meteor.Monogr., 10, n°32, 84 p.

4) J.L. REDELSPERGER (1980) : Traitement des phénomènes turbulents dans un modèle tri-dimensionnel de convection humide avec précipitations. Thèse de 3ème cycle, Université de Paris VI, 110 p.

5) G. SOMMERIA (1976) : Three-dimensional simulation of turbulent process in an undisturbed trade wind boundary layer. J.Atmos. Sci., 33, 216-241.

PROSPECTIVE CONSIDERATIONS ON THE LOCAL IMPACT OF A HEAT SOURCE

E. Richard, J. Pastre and R. Rosset

L.A.M.P., University of Clermont II, FRANCE

I. General considerations

The advent of power stations or power parks of increasing strength retains our attention on the local and regional effects of the release of large amounts of latent and sensible heat on the cloud cover. This problem has been tackled in its various aspects :

- a climatological aspect (possible modification of the atmosphere in some conditions leading to cloud formation and modification of the rainfall regimes in the vicinity of the stations) ;

- more localized aspects : modification of storms passing over power parks [1] and a possible destabilization of the atmosphere in some situations [2] . In any case, an analysis of these aspects requires the use of numerical models which enable us to modify at will the atmospheric situations and the heat source conditions. We have focused our study on the response of a given atmosphere in the form of cloud formation to a surface source of varying characteristics.

II. The model - Specification of the source : reference case

The model is a slab-symmetry two-dimensional model of cumulus convection in a vertical plane [3], [4]. We shall only sketch this model. There are 7 prognostic variables : η, the normal vorticity component, ϕ', the entropy of moist air and the 5 microphysical variables defining the respective mixing ratios for water vapour q_v, cloud droplets q_c, rain drops q_r, non-precipitating q_i and precipitating q_h ice particles.

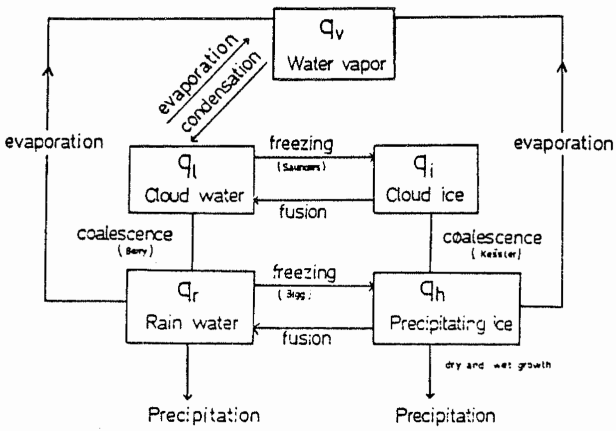

Figure 1 - Synoptic diagram of the microphysical processes.

Figure 1 displays the synoptic diagram of the microphysical processes. Our approach consists in choosing an atmospheric state (the warm humid sounding of Figure 2) and in varying the source characteristics.

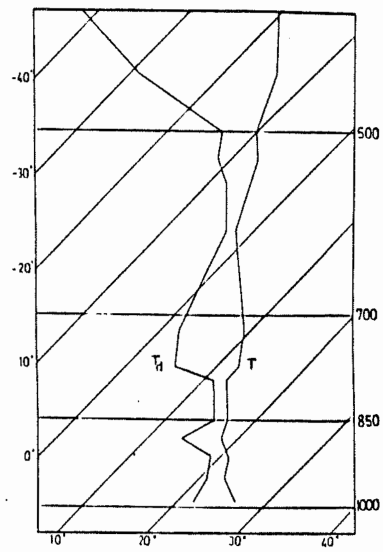

Figure 2 - The radiosounding in the reference case (T and Td curves).

We start our simulations with a reference case to which will be compared all the other cases obtained after modification of the source. In the reference case, the source is specified as follows : 2 point-sources 200m apart (1 grid distance) lie 200m above the lower boundary of the domain, at its centre. The time evolution in temperature and water vapour mixing ratios q_v at these 2 points are imposed according to the relations :

$$\frac{\partial T}{\partial t} = \frac{2\ \phi_S}{\rho C_p D_z} \qquad (1)$$

$$\frac{\partial q_v}{\partial t} = \frac{2\phi_L}{\rho L D_z} \qquad (2)$$

where ρ is the density of air, L the latent heat of condensation, C_p the specific heat of air under constant pressure, D_z a characteristic length (60m here), ϕ_S and ϕ_L are the respective sensible and latent heat flux intensities at the source (ϕ_S = 2.08kW/m^2 and ϕ_L = 3.14kW/m^2 as in [2]). So defined, the source appears as a black box, specified as a whole. Amongst all our results, we had to select only a few of them. For example, we have reproduced in Figure 3 for the reference case, the evolution of the maxi values, at every time in the domain, of the cloud water q_c and rain water q_r contents as well as the maxi horizontal (U) and vertical (W) velocities.

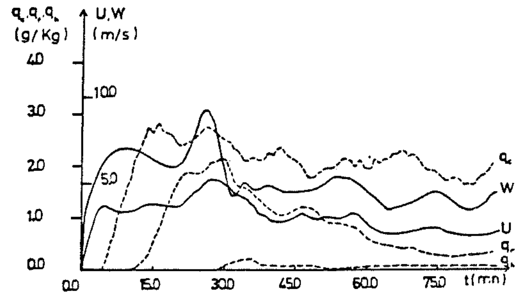

Figure 3 - Time variations of the maxi horizontal (U) and vertical (W) velocities and of the maxi cloud q_c, rain q_r and precipitating ice q_h contents (reference case)

This figure shows that after an initialization period of 20 to 30 mn, the model tends to stabilize with very small values for q_r and q_h. We have noted too (not reproduced here) the bubbling mode of convection in spite of the maintained fluxes at the source.

III. Modifications of the source characteristics

Various modifications have been brought to the source, while retaining the sounding of Figure 2.

a) Modification in the source strength :

The geometry of the source being kept unchanged, we have multiplied by a factor K (between 0.5 and 10) the fluxes ϕ_S and ϕ_L. We have reproduced in Figure 4 the initial rates of increase in the maxi q_c and q_r, U and W.

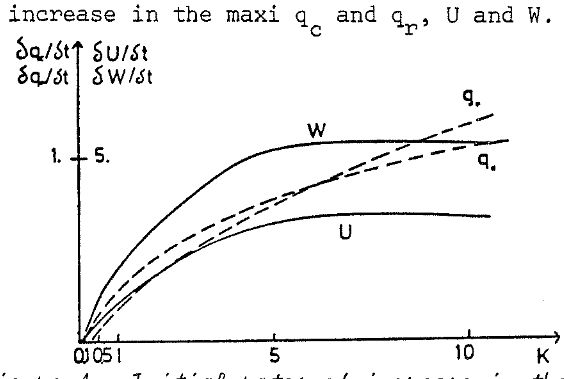

Figure 4 - Initial rates of increase in the maxi cloud q_c and rain q_r water contents and in the maxi horizontal U and vertical W velocities as functions of K.

The main conclusion to be drawn from this figure is the saturation effect appearing for K greater than about 5, particularly in the velocities. This would mean that beyond a certain energy input, the atmospheric response is no longer linear, but tends towards a limit depending upon the atmospheric stability and the source properties.

b) Dry cooling compared to wet cooling :

Keeping the source geometry and the total heat flux emitted unchanged when compared to the reference case, we have varied the ratio of sensible to latent + sensible heat fluxes from 0.8 to 0.4 and 0.2. Some of the results are displayed in Figure 5 for the maxi W velocities, and in Figures 6 and 7 for the maxi cloud q_c and rain q_r water contents. One can observe only small differences in q_c, in contrast to q_r. As for W (Figure 5), there is a secondary peak between 25 and 30mn, with a lag in time and a reduction in amplitude when passing from the dry to the wet cooling process.

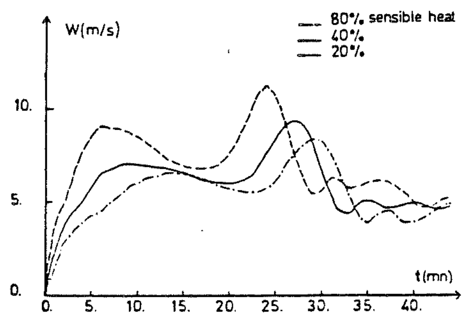

Figure 5 - Time evolution of the maxi vertical W velocities as a function of the ratio of sensible to (latent + sensible) heat fluxes of the source.

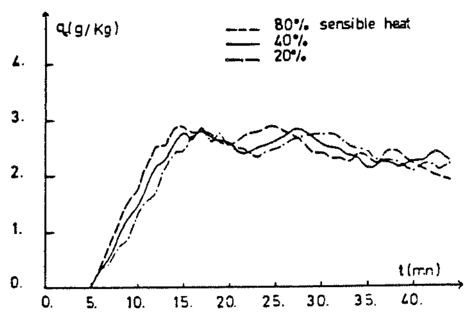

Figure 6 - Time evolution of the maxi cloud water content q_c as a function of the ratio of sensible to (latent + sensible) heat fluxes at the source.

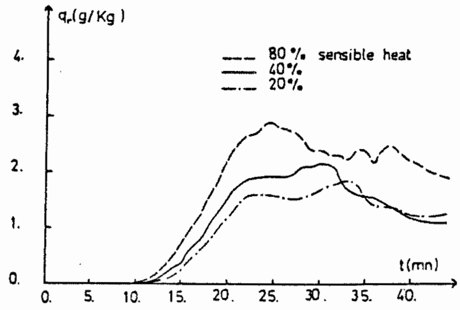

Figure 7 - Time evolution of the maxi rain water content q_r as a function of the ratio of sensible to (latent + sensible) heat fluxes at the source.

c) Increasing the distance between the point-sources :

Starting from the reference case, we have progressively increased the distance between the 2 point-sources in order to simulate well-separated cooling towers in a park. In Figure 8, are reproduced as functions of time the maxi cloud water content q_c for different spacings e between the sources.

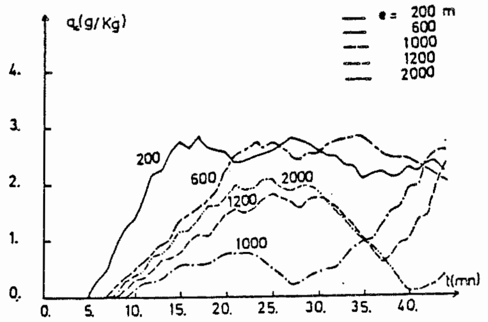

Figure 8 - Time variations of the maxi cloud water content q_c as a function of the spacing e between the 2 point-sources.

We observe a marked effect on the absolute values reached as well as on the shapes of the curves (e.g., compare the curves for 200m and 1200m). The paradoxical result for e = 1000m can be explained as follows : there is a lag in time between the maxima in W and in q_c, this lag increasing with e. When the first maximum in W has occurred and when this latter variable begins to decrease, the maxi q_c for 1000m has already been reached and thus q_c markedly decreases too. On the opposite, the time lag between W and q_c for e>1000m is such that the first maxi in q_c occurs when W is already decreasing, thus resulting in a reduced decrease in q_c.

d) Effect of a vertical wind shear :

In order to specify the effect of a vertical wind shear on the clouds forming over the station, we have displayed the evolutions in time of cloud water q_c (Figure 9) and rain water q_r contents (Figure 10). Three cases have been considered according to the wind shears : U'_o = 0, 0.714 and 2.14 m/s/km. The wind shear effect is noticeable for the rain process of figure 10 at this latter value of U'_o, thus emphasizing the inhibition of artificial convection by strong wind shears.

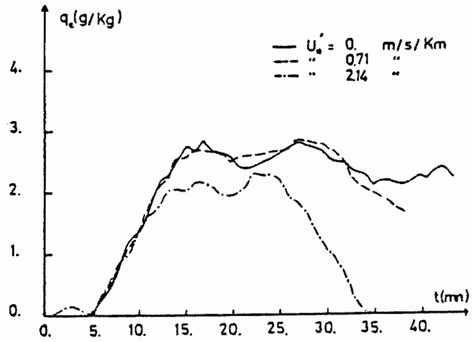

Figure 9 - Time variations of the maxi cloud water content q_c versus the vertical wind shear U'_o.

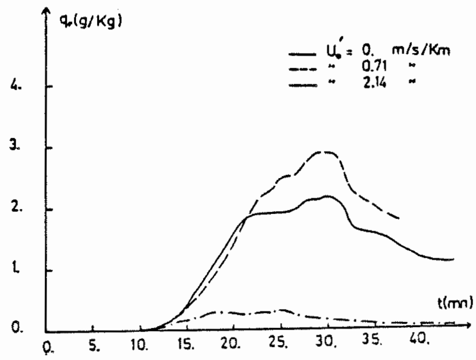

Figure 10 - Time variations of the maxi rain water content q_r versus the vertical wind shear U'_o.

IV. Conclusions

We have reproduced here only some of our computation results. The main interest of the present model as well as the others quoted in reference lies in the possibility of a systematic exploration of the atmospheric behaviour in response to its own properties and to the source characteristics. Our model is now being tested for extended periods of time.

V. Références

[1] Hane C.E. (1978) - "The application of 2-D convective cloud model to waste heat release from proposed nuclear energy centers" - Atmospheric Environment, Vol. 12, n° 9, pp. 1839-1848.

[2] Murray F.W., Koenig L.R. and Tag P.M.(1978) "Numerical simulation of an industriel cumulus and comparison with observations"- J.A.M., Vol. 17, n° 5, pp. 655-660.

[3] Pastre Jacqueline (1978) - "Un modèle bidimensionnel de convection atmosphérique : considérations énergétiques" - Thèse de 3ème Cycle, Université de Clermont.

[4] Richard Evelyne (1978) - "Considérations prospectives sur l'impact local d'un parc énergétique" - Rapport de D.E.A., Université de Clermont.

Acknowledgments

This work has been undertaken under a grant from Electricité de France (E.D.F.).

A THREE DIMENSIONAL NUMERICAL MODEL OF CONVECTIVE CLOUDS

A.E. Saab*, J.Y. Caneill*, T. Rasoamanana**, P. Sarthou**, B. Benech***

* Direction des Etudes et Recherches, E.D.F. - Chatou (FRANCE)

** Université Paul Sabatier - Toulouse (FRANCE)

*** Université de Clermont II - Lannemezan (FRANCE)

1. INTRODUCTION

It has been demonstrated that the dissipation of energy from a power generating facility can induce cumulus clouds that are quite different from ordinary plumes and that assume a full description of dynamic and microphysical processes.

Many attemps to model cumulus convection system have been made using one-dimensional [Weinstein (1970), Hanna (1976)] and two-dimensional models [Murray-Koenig (1979), Hane (1978), Bhumralkar (1976)]) ; but, due to computational difficulties, few three dimensional models have been essayed, for example Miller and Pearce (1974).

This paper describes a three dimensional numerical model designed to simulate hot plumes and industrial clouds, such as those generated by dry or wet cooling towers. This model is based on the equations of motion for a quasi-incompressible fluid, the first law of thermodynamics and the conservation of mass and it uses a cloud physic parametrization which computes explicitly the concentrations both of cloud water droplets and falling water drops.

The results of the model are compared with experimental results obtained during the "Cocagne" project [see Benech et al. (1980)] on the environmental impact of dumping waste dry heat in amounts of 1000 MW into the atmosphere from an oil-fired source.

2. DESCRIPTION OF THE MODEL

The variables of the problem are the three components of the wind speed $\vec{V}(u,v,w)$, the pressure p, the density ρ, the temperature T, the mixing ratios of water vapor C_v, cloud water droplets Q_c and precipitating drops Q_r.

The basic equations are the following :

- conservation of mass,
- conservation of momentum,
- conservation of energy
- conservation of species (water vapor, cloud droplets and precipitating drops),
- equation of state for the mixture air/water.

2.1 Parametrization of turbulence

The equations for the mean values contain the REYNOLDS stress $\overline{u_i u_j}$ and the velocity-temperature and velocity-concentration covariances : $\overline{u_i\theta}$, $\overline{u_i c_v}$, $\overline{u_i q_c}$ and $\overline{u_i q_r}$. To close those equations we use eddy viscosities and diffusivities ν_T and K_T :

$$\overline{u_i u_j} = -\nu_T\left(\frac{\partial \overline{V_i}}{\partial x_j} + \frac{\partial \overline{V_j}}{\partial x_i}\right)$$

$$\overline{u_i\theta} = -K_T\frac{\partial \overline{T^*}}{\partial x_i}$$

and similar equations for $\overline{u_i c_v}$, $\overline{u_i q_c}$ and $\overline{u_i q_r}$.

2.2 Microphysics

The microphysical processes included in the model are illustrated schematically in figure 1.

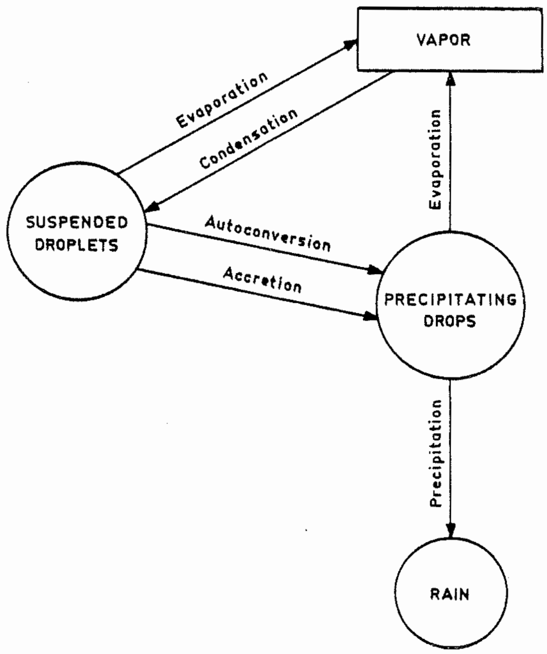

Suspended droplets are created by condensation. Precipitating drops are created by coalescence of suspended droplets among themselves, the process being called "autoconversion". The category of precipitating drops then grows in bulk mass density both by autoconversion and by accretion of suspended droplets.

The equations for Q_c and Q_r are the following :

$$\frac{\partial Q_c}{\partial t} + \frac{\partial}{\partial x_j}(U_j Q_c) = K_j, Q_c \frac{\partial^2 Q_c}{\partial x_j^2} + EC - AC - CC$$

$$\frac{\partial Q_r}{\partial t} + \frac{\partial}{\partial x_j}(U_j Q_r) = AC + CC - EV$$

(we neglect turbulent diffusion for precipitating drops) with :

- EC : Evaporation-Condensation,
- AC : Autoconversion,
- CC : Accretion,
- EV : Evaporation of precipitating drops.

For autoconversion and accretion, we use the KESSLER'S formulation :

$$AC = K_1 (Q_c - a)$$

$$a = 10^{-3} \text{ kg/kg}$$

$$K_1 = \begin{cases} 10^{-3} \text{ s}^{-1} & \text{if } Q_c > a \\ 0 & \text{if } Q_c \leqslant a \end{cases}$$

$$CC = K_2 . Q_c \, Q_h^{0,875} \text{ with } K_2 = 2,2$$

2.3 Method of solution

The procedure used is the "SMAC" method which was developed at Los Alamos and used in FRANCE by Gaillard (1978). It is explicit in time and implicit in pressure.

The spatial discretisation in momentum equations is a weighted mean of CDM2 (Centered momentum flux) and UDV (Upwind velocity flux).

The pressure/continuity treatment is based on a pressure correction formulation involving a simultaneous adjustement of velocities and pressures, in sequence :

- first we obtain a provisional velocity field from explicit momentum equations,
- then, we calculate velocity divergence at each cell and we use it to calculate a pressure change ΔP and an associated ΔV for obtaining continuity balance,
- we perform this treatment repeatedly until local balance prevails everywhere.

The model needs about 20 minutes of C.P.U. time to reach permanent conditions with $20 \times 9 \times 25$ grid points, on an I.B.M. 370/168.

3. SENSITIVITY TESTS AND COMPARISON WITH EXPERIMENTS

3.1 The "Cocagne" Project

The "Cocagne" project (Météotron) described in a previous report (EDF-IOPG 1979). As part of a program on artificially-induced convection related to the environmental effects of dry cooling towers, a sensible heat release of 1000 MW is produced by an oil-fired source. During each 30 minute experiment, a full description of the heat source, the ascending hot plume and the resulting cloud microphysical modifications is obtained using different experimental techniques :

- firstly, those which characterize the source : temperature sensors and three dimensional anemometers at 30 and 60 m above the heating area.
- secondly, those which characterize the ambiant atmosphere : radiosoundings and wind measurements with a radar,
- lastly, those which characterize the plume : aircraft, lidar, meteorological radar, infrared thermography...

Three campaigns have been carried out : June 19 to July 8, 1979 ; October 3 to 20, 1978 and May 27 to June 23, 1979.

The experiments were performed under a wide variety of background meteorological situations. We present, on this paper, the experiment of July 8, 1978 to illustrate the testing method in order to validate the numerical model.

3.2 Description of the Experiment of July 8, 1978

It is a case of formation of a cumulus in low wind speed conditions. The dry plume spreads vertically up to about 550 m, level of condensation. Above this height, we observed the formation of a cumulus, the top of which is at about 950 m. The atmospheric sounding is plotted in figure 2.

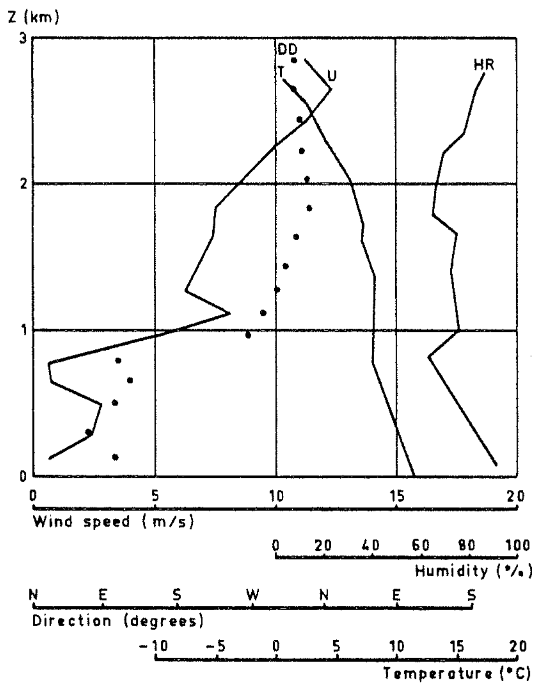

Figure 2 : Environmental temperature, humidity and wind speed soundings - July 8, 1978

3.3 Input of the Model

The characteristics of the heat source are the following :

- exit velocity : 4 m/s
- exit temperature : 21 °C
- exit relative humidity : 52 %

The finite difference mesh has the following dimensions :

- 20 grid points in the x-direction ($\Delta x = 60$ m)
- 9 grid points in the y-direction ($\Delta y = 45$ m)
- 25 grid points in the z-direction ($\Delta z = 60$ m)

Thus, the domain is 1200 m long by 400 m wide by 1500 m high.

The heating area is represented as a square of 180 m by 180 m at 60 m above the ground.

3.4 Simulation Results

The computed velocity field is shown in figure 3 and the evolution of the simulated cloud is shown in figure 4 (for $\nu_T = 40\ m^2/s$ and $K_T = 60\ m^2/s$).

Table 1 compares the dimension of the cloud observed during the experiment with those simulated by the model for different values of the coefficients of eddy viscosity and diffusivity.

Table 2 compares the vertical velocities computed, with those measured by the Aircraft.

We can observe, from dynamic and microphysical points of view, a good agreement between observed and computed values of cloud top, cloud base and water mixing ratio.

We also observe that the computed vertical velocities and the observed ones are of the same order of magnitude, bearing in mind that the observed values are instantaneous whereas the computed ones are averaged.

4. CONCLUSIONS

The results of the model were compared with those obtained on July 8, 1978 during the "Meteotron" experiments. The agreement between computed and observed values is quite satisfactory so long as the following parameters are considered : cloud top, cloud base, area of maximum liquid content, vertical velocities in the plume.

The validation of the model is now being achieved for other experiments of the three campaigns of 1978 and 1979.

In order to take into account the variations of the coefficients of eddy viscosity and diffusivity, we intend to use a parametrization of the same type as the one developed by TAG, MURRAY and KOENIG (1979).

We also intend to use this model to simulate a cloud observed by AUER (1976) over a refinery which emitted about 1000 MW of sensible and latent heat. Thus, we shall be able to compare the results of this model with those obtained by HANNA (1976) using a one dimensional model and by MURRAY-KOENIG (1979) using a two-dimensional convective model.

5. REFERENCES

AUER A. (1976)
Observation of an industrial cumulus.
J. of Appl. Met., Vol. 15, n° 4, pp. 406-413.

BENECH B. et al. (1980)
Thermodynamic and microphysical impact of a 1000 MW heat-released source into the atmospheric environment.
III^{ème} Scientific WMO Conference on Weather Modifications, Clermont-Ferrand.

BHUMRALKAR C. (1976)
Computer simulation of atmospheric effects of waste heat rejected from conceptual large power parks.
ASME, Paper n° 76, WA/HT-20, 8 pages.

EDF-IOPG (1979)
Programme convection artificielle.
EDF Report E32.79/03.

GAILLARD P. (1978)
Modélisation numérique des panaches d'aéroréfrigérants.
Université de LYON.

HANE C. (1978)
The application of a 2D convective cloud model to waste heat release from proposed nuclear energy centers.
Atm. Env., Vol. 12, n° 19, pp. 1839-1848.

HANNA S. (1976)
Comments on "Observation of an industrial cumulus".
J. of Appl. Met., Vol. 15, n° 11, pp. 793-799.

MILLER M., PEARCE R. (1974)
A three-dimensional primitive equation model of cumulonimbus convection.
Q.J.R.M.S., Vol. 100, n° 424, pp. 133-154.

MURRAY F., KOENIG L. (1979)
Simulation of convective cloudiness, rainfall, and associated phenomena caused by industrial heat released directly to the atmosphere.
R.2456 DOE. Rand Corporation.

TAG P., MURRAY F., KOENIG L. (1979)
A comparison of several forms of eddy viscosity parametrization in a 2D cloud model.
J. of Appl. Met., Vol. 18, n° 11, pp. 1429-1441.

WEINSTEIN A. (1970)
A numerical model of cumulus dynamics with microphysics.
J. of Atm. Sc., Vol. 27, n° 2, pp. 246-255.

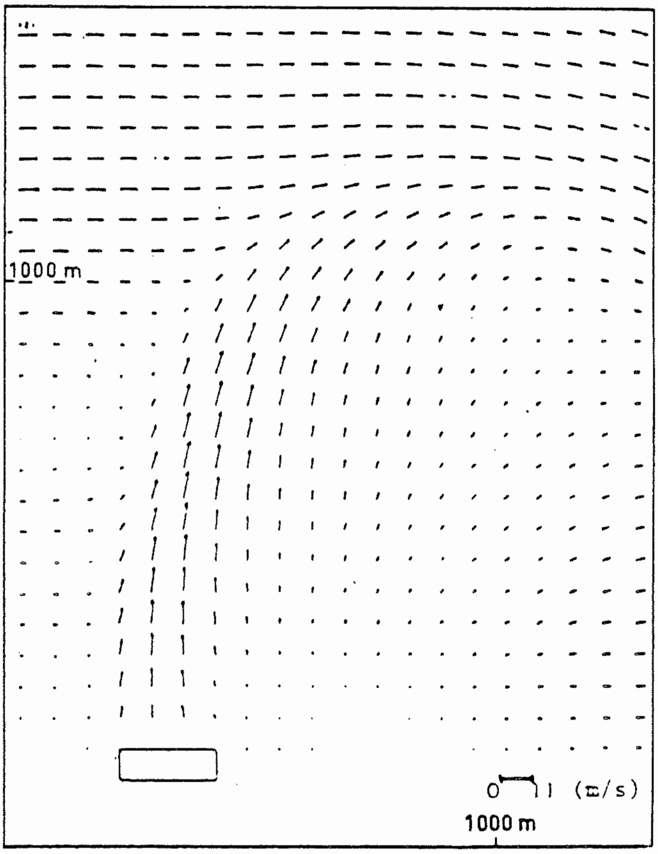

Figure 3 : Computed velocity field in the plane xOz.

	Predicted			Observed
$\nu_T(m^2/s)$ K_T	10 15	20 30	40 60	
Cloud base (m)	550	600	450	550
Cloud top (m)	1150	1150	1000	950
Max. Liquid content (g/kg)	0.76	0.84	0.51	0.2-0.3
at (m)	950-1050	900-1050	750-850	600-800

Table 1 : Cloud dimensions.

		Predicted			Observed
Height (m) \ $\nu_T(m^2/s)$ K_T		10 15	20 30	40 60	
300	W_{MAX} W_{MIN}	4. -0.2	4.9 -0.04	6.8 -1.2	7.6 -2.2
500	W_{MAX} W_{MIN}	4.3 -0.6	5.6 -0.3	8.3 -1.5	11.1 -2.6
700	W_{MAX} W_{MIN}	4.6 -1.2	5.7 -0.2	6.8 -0.7	3.8 -2.3
900	W_{MAX} W_{MIN}	4.4 -2.1	3. -0.7	3.8 -.5	4.1 -3.5

Table 2 : Vertical velocity inside the plume.

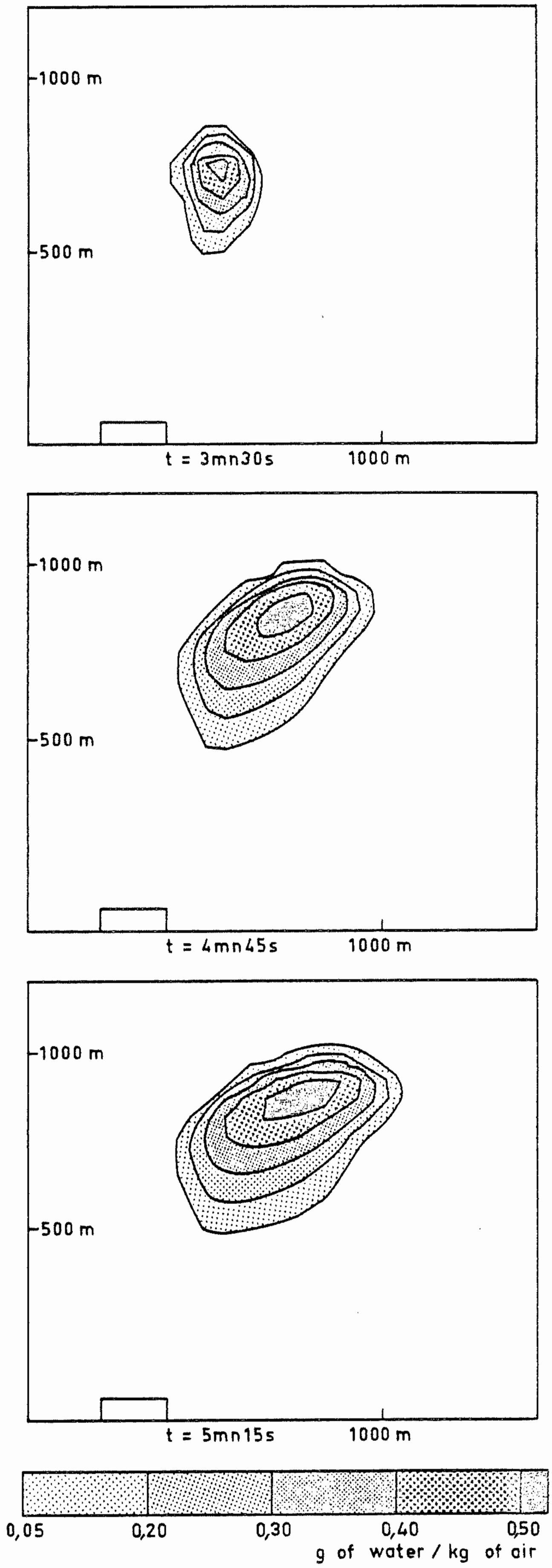

Figure 4 : Cloud water mixing ratio over the heating area.

HEAVY RAINFALL FROM VERY SHALLOW CONVECTIVE CLOUDS

H. Sakakibara
Meteorological Research Institute
Yatabe Ibaraki JAPAN

1. INTRODUCTION

Heavy rainfall usually results from deep convective clouds. In some cases, however, shallow clouds seem to have caused heavy rainfall, because large condensation rate and high precipitation efficiency were realized.

We analyzed a heavy rainfall from very shallow convective clouds over the coastal area of a mountainous region in Japan on 24-26 August 1977. Maxima of total and hourly rainfall amounts were 942 and 65 mm, respectively. The results of the analysis will be described and the causes of large condensation rate and high precipitation efficiency will be discussed.

2. DATA

Data of upper-air sounding, radar, rain gauge and surface observation at stations indicated in Fig.1 are used. As shown in Fig.1, roughly speaking, three mountain ranges stretching from north to south form a mesoscale mountainous region oriented from northeast to southwest in the Kii Peninsula.

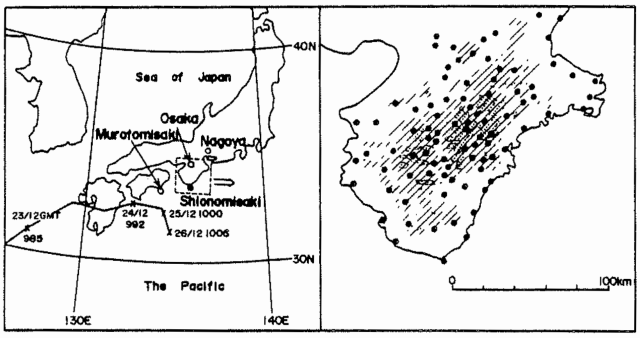

Fig.1 Map of analysis domain. The topography of the Kii Peninsula is shown in the right part. The stippled and hatched shadings represent land higher than 1000 m and 500 m above sea level, respectively. The path of severe tropical storm7707 is also shown by a solid line in the left part. Numerals associated with crosses indicate observation time and surface pressure at the center of the storm.

3. BRIEF DESCRIPTION OF THE RAINFALL AND SYNOPTIC SITUATIONS

Rainfall associated with a severe tropical storm began at about 01GMT, August 24 over the Kii Peninsula. Most of the rainfall was observed during the period 00GMT, August 24 to 00GMT, August 26. Total amount of rainfall from 00GMT, August 24 to 00GMT, August 27 is shown in Fig.2. Heavy rain occurred in a narrow zone of about 30 km wide along the southeastern coast line of the peninsula. There are two maxima of rainfall and the primary one is

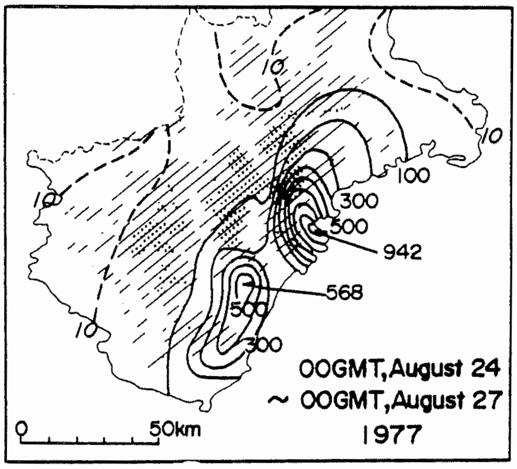

Fig.2 Total rainfall in mm (00GMT, August 24 to 00GMT, August 27, 1977) over the Kii Peninsula. The topography of the peninsula is also shown.

located over Owase. The distribution of rainfall amount seems to be strongly affected by topography. Analyses of 12 hours rainfall (not shown) indicate that when heavy precipitation occurred around Owase, precipitation was hardly observed over the leeward area of a mountain range to the west of Owase.

As seen in Fig.1, severe tropical storm 7707, Amy moved eastward slowly and it was almost stationary after 12GMT, August 24. Surface pressure at its center was increasing. Fig.3 shows that a large low pressure zone covers the southern part of Japan at 00GMT,

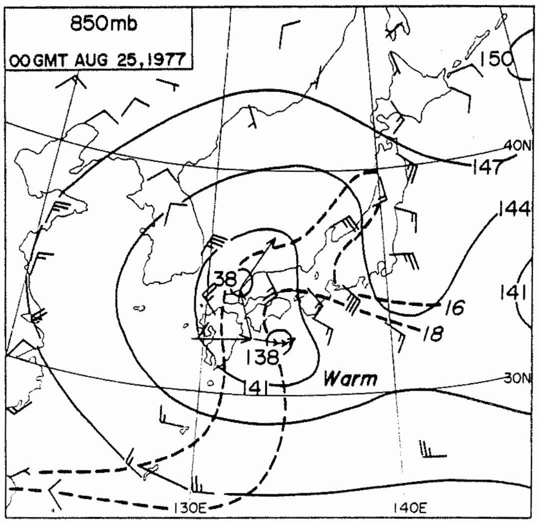

Fig.3 850-mb analysis for 00GMT, August 25, 1977. Arrows indicate the movement of low pressure systems in 12 hours. Solid lines represent geopotential height at 30 m intervals. Dashed lines are isotherms of 16 and 18 °C.

August 25. Anticyclone was to the east of Hokkaido. Around the Kii Peninsula the air was very warm and moist and winds had the component of easterly. A 500-mb chart (not shown) indicates that winds around the Kii Peninsula were westerly and that the air over southwestern Japan was very warm and dry, suggesting large-scale subsiding motion in the middle troposphere. It is very interesting that during the period of heavy rain very dry air was observed in the middle troposphere. Synoptic situations described above changed very slowly during the analyzed period.

Now we will study the vertical structure of the air mass by using upper-air sounding data at Shionomisaki. Fig.4 shows a time-height section of equivalent potential temperature and relative humidity. Inversion layers are also shown. It should be noted that there was always at least one inversion layer at about 600 mb after 12GMT, August 24 and that the air was very moist (nearly saturated) below the layer and very dry (relative humidity $<30\%$) above it. Air mass with high equivalent potential temperature ($\sim$352K) appeared in the lowest layer at about 00GMT, August 25. This corresponds to the incursion of warm and moist air in the eastern part of the severe tropical storm (see Fig.2). Stratification of the air mass was latently unstable as indicated in Fig.4.

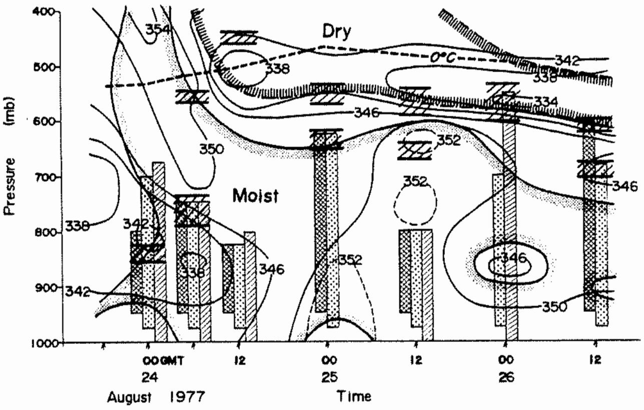

Fig.4 Time-height cross-section showing the thermodynamical structure of the air mass observed at Shionomisaki. The extent of dry air (relative humidity $<30\%$) is hatched and that of moist air (relative humidity $>95\%$) is stippled. Thin solid and dashed lines are isopleths of equivalent potential temperature (K). Thick double lines represent inversion layers. Hatched, stippled and cross-hatched columns indicate vertical extent of latent instability assuming for its lower boundary to be at 1000, 975 and 950 mb, respectively. The 0°C isotherm is also shown. Arrows at the bottom of the diagram denote the times of rawinsonde observation.

The time-height section of wind (not shown) indicates that the warm and moist air below the inversion layers was transported by easterly winds and the mean wind velocity had a large component normal to the direction of the mesoscale mountainous region, being almost perpendicular to the mountain range to the west of Owase (see Fig.1).

4. FEATURES OF THE RAIN

We will investigate the feature of the rain for various stations. Fig.5 shows time changes of the averaged rainfall intensity over 10 minutes observed at stations near the southeastern coast line of the peninsula. Rainfall intensity at each station shows a large time variation and it suggests that the rain had a convective nature. At stations along the coast line (Shionomisaki, Shingu and Kumano) the rainfall occurred intermittently. At stations on the windward side of the mesoscale mountainous region (Owase, Hachimantoge and Miyagawa) the rainfall was not intermittent. It is surprising that the average rainfall intensity attained about 100 mm hour^{-1} during the period 1850 to 1900GMT, August 24 at Owase (note that the ordinate for Owase is different from others). The rainfall at Hachimantoge seems to be more steady than the one at Owase. The time change of rainfall intensity at Miyagawa resembles the one at Owase, though its magnitude is much smaller. At stations on the leeward side of the heavy rain areas (Kawai and Hongu) the time changes of rainfall intensity are very similar each other. Convective rainfall was observed until 08GMT, August 24, but only a weak rain was observed afterward in contrast to heavy rain on the windward side. The rainfall at Odai was rather continuous and the long term variation of rainfall intensity is not similar to the one at Kawai or Hongu, but it seems to be similar to the one at Miyagawa or Owase. These features of the rainfall suggest that the heavy rain was strongly controlled by the mountainous topography.

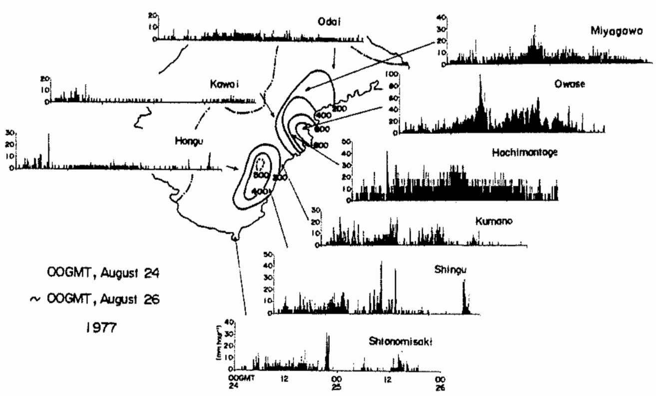

Fig.5 Time change of rainfall intensity averaged over 10 minutes for nine raingauge stations. Their locations are indicated by arrows on the map of the peninsula. The distribution of rainfall amount from 00GMT, August 24 to 00GMT, August 26 is also shown.

A fine structure of the heavy rain is shown by the detailed record of rainfall intensity at Owase (Fig.6). Heavy rains occurred frequently with a short period of 10 to 20 minutes. It will be suggested that precipitating cells passed over Owase successively.

5. STATIONARY ECHO BAND

As stated in the last section, the heavy rain around Owase is characterized by a rather continuous rainfall. Fig.7 shows the change of radar echoes observed at about 10 minutes

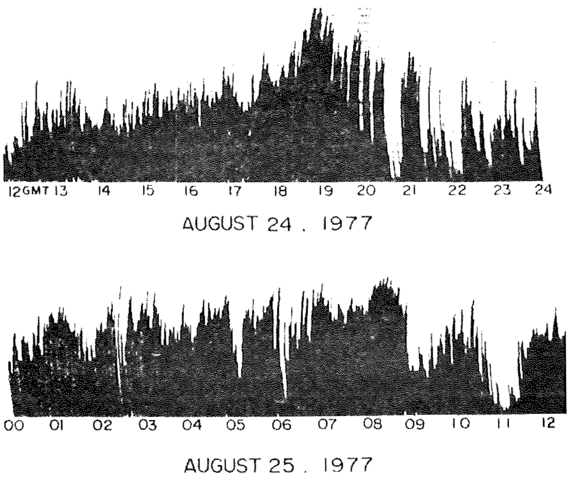

Fig.6 Time change of rainfall intensity observed every one minute at Owase.

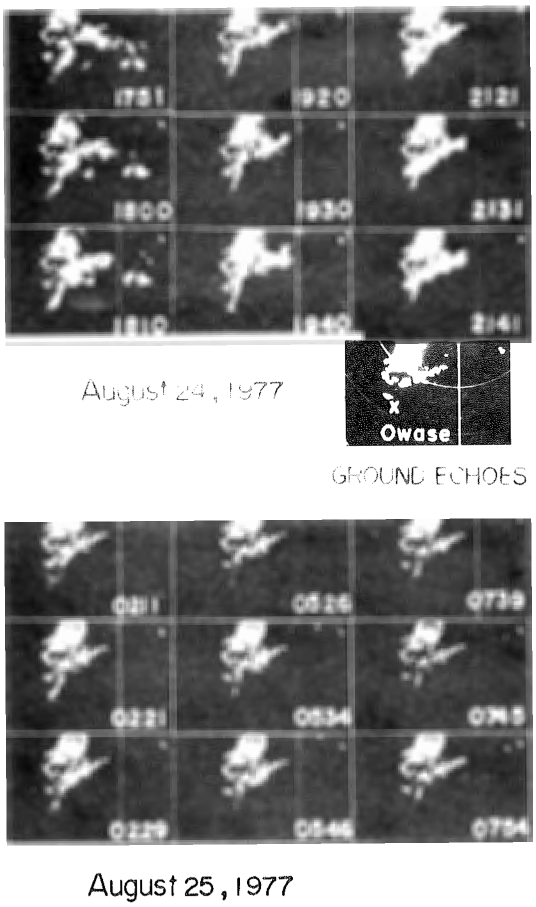

Fig.7 Photographs of radar echoes observed by the Nagoya radar. Observations were done at about 10 minutes intervals. The location of Owase is indicated by a cross symbol. Range marks are at 50 km intervals.

intervals by the Nagoya radar which is about 140 km distant from Owase. Narrow and straight echo bands were stretching from 10°~30° to 190°~210° along the coast line crossing over Owase. Since they frequently appeared over the same area, they had a feature of a stationary band in spite of easterly winds of about 10 m sec^{-1} in the lower troposphere. Echo bands had a convective nature and sometimes they were composed distinct convective cells. The height of echo top was about 3.5 km near Owase and it was always lower than 5 km after 12GMT, August 24. Since the height of freezing level was about 5.8 km, radar echoes were entirely below the level.

6. PRECIPITATION EFFICIENCY

Since synoptic situations changed slowly, we can obtain the time-averaged precipitation efficiency for the heavy rainfall area including Owase by using data of rainfall amount for 24 hours from 12GMT, August 24 to 12GMT, August 25 and upper-air soundings of every 12 hours at Shionomisaki. Time-averaged rainfall intensity over 24 hours is averaged horizontally in a band of 25 km wide and 50 km long oriented from 20° to 200° which almost includes the heavy rain area. The averaged rate of precipitation is about 250 mm day^{-1}. The mean condensation rate over the area is calculated on the assumption based on the results of foregoing analyses that the airflow below 900 mb was blocked by the mountain range to the west of Owase, of which the height is about 1000 m above sea level, and ascended penetratively through a two-dimensional cloud band up to 650 mb. The calculated condensation rate is 214 mm day^{-1} for a band of 25 km wide. Therefore, the precipitation efficiency was higher than unity. Although the estimate of the condensation rate may be somewhat uncertain because of infrequent soundings at the distant station Shionomisaki, it is certain that very high precipitation efficiency was realized over the heavy rain area.

Since radar echoes over the heavy rain area were entirely below freezing level, the condensation- coalescence process was responsible for the formation of the rain. Shallow convective clouds around the Kii Peninsula were suitable for the release of precipitation by the condensation- coalescence process, because they were formed in maritime subtropical air mass (see Fig.3).

In addition to the above-mentioned readiness for precipitation release, recycling of precipitation particles between them, which can cause precipitation efficiency higher, might take place in the present case. The time change of rainfall rate in Fig.6 suggests that the heavy rain resulted from crowded cumuli between which recycling of precipitation particles is expected. There was large wind shear during the heavy rain period. Takeda and Takase (1980) observed cells inclined windward in a staionary echo band near Owase in a similar situation to the present case. If we assume inclined cells in the present case, older cells may be able to seed new cells growing on the windward side of them with small precipitation particles coming out near the top of older cells.

Moist atmosphere favors the above-mentioned seeding because of reduced evaporation of small precipitation particles in the environmental air. It might also be favorable for the reduction of evaporation of cloud droplets due to entrainment. Therefore very moist air around the Kii Peninsula might also cause the precipitation efficiency higher.

7. SUMMARY

A heavy rainfall from very shallow convective clouds has been studied. We have paid attention to the causes of large condensation rate and of high precipitation efficiency which seem to be necessary for the occurrence of heavy rain from very shallow clouds.

In the lower troposphere, a weak tropical depression was nearly stationary over the southwest of the heavy rain areas. Warm and moist air was observed below inversion layers in the eastern part of the depression. Stratification in the lower troposphere was latently unstable. Distributions of rainfall amount seem to be strongly affected by mountain ranges. Narrow and straight echo bands which might be composed of crowded cumuli were frequently observed over the area on the windward side of a mountain range. Time-averaged precipitation efficiency for the heavy rain area including Owase was very high, if we assume from the results of the foregoing analyses that the airflow below 900 mb was blocked by the mountain range and ascended penetratively up to 650 mb. Crowded maritime cumuli and very moist air observed around Owase might be favorable for the high precipitation efficiency.

8. REFERENCE

Takeda, T., and K. Takase, 1980: Modification of rainfall system by orographic effects. (To be published.)

THE INFLUENCE OF THE UPDRAFT SHAPE ON GRAVITATIONAL COALESCENCE

P.K. Smolarkiewicz
Institute of Geophysics
University of Warsaw, Poland

1. Introduction

Till now there is no good method of experimental verification of validity of theoretical models of coalescence processes in natural clouds. During some measurements made by us inside a cooling tower, it was noticed that interior of the cooling tower can be treated as a kind of cloud chamber. The droplet spectra observed in cooling tower are determined mainly by two processes - coalescence and sedimentation. The theoretical model of these droplet spectra has been constructed in a way similar to that used in cloud physics. The results can be verified experimentally more easy than in natural clouds.

2. Abbreviated list of symbols

$g(\ln r) = 3\nu^2 n(\nu)$ - log-increment density function which is introduced for the purposes of displaying the results, $K(\nu,\nu')$ - collection kernel, LWC - liquid water content, $n(\nu,z,t)$ - droplets spectrum, N - concentration of droplets, r - radius of droplet, $R(z)$ - radius of cooling tower at level z, R_o, R_p, H, H_p - parameters of cooling tower geometry (fig.1), $S(z)$ - area of the cross section of flow, t - time, v_T - terminal velocity of droplets in still air, ν - volume of a droplet, $\bar{\nu}_o$ - average volume of spectrum $n_o(\nu)$, $w(z)$ - vertical velocity of updraft at level z, z - height coordinate, $\delta(z-z_o)$ - Dirac's symbol. ρ - distance from axis of symetry of flow, ↑ - "upwards", ↓ - "downwards", index " $_o$ " denotes values, which refer to the source.

3. Basic assumptions and equations

It is assumed that evolution of droplet spectra is going on within a steady and predetermined field of vertical velocity. At certain fixed level z_o (fig.1) a source of droplets steady and homogenous is installed. The effects of condensation or evaporation of droplets inside cooling tower can be neglected [Smolarkiewicz 1978]. The following variants of vertical velocity fields were considered: i) - horizontally homogenous and time independent velocity for hyperboloidal, conical and cylindrical tower (fig.1 - b,c); ii) - time independent; axialy symetric field in hyperboloidal tower; iii) - horizontally homogenous but time dependent flow for hyperboloidal tower. In the first variant it is assumed that at all levels droplets spectra are homogenous over cross section of updraft. This corresponds to the case of strong horizontal turbulent mixing. Basic equations can be written as follows:

$$\partial n/\partial t = -(1/S)\cdot\frac{\partial}{\partial z}[nS\cdot(w-v_T)] + \int_0^{\nu/2} K(\nu-\nu',\nu')n(\nu-\nu')n(\nu')d\nu' - \int_0^{\infty} K(\nu,\nu')n(\nu')n(\nu)d\nu' + n_o\cdot(w-v_T)\delta(z-z_o) \quad (1)$$

$$w\cdot S = \text{const.} \quad (2)$$

$$S \equiv S(z,R_o,R_p,H_p,H) \quad (3)$$

The first term on the r.h.s. of eq.(1) describes convective transport of droplets, the second and third term - coalescence, and the fourth one the effect of droplet production by the source. Eq.(2) express the continuity of air mass and equation (3) - geometry of the cooling tower.

Boundary and initial conditions for eq.(1) are:

$$[n\cdot(w-v_T)]^{\uparrow}_{z=0} = 0 \quad \text{if} \quad w-v_T \geq 0 \quad (4)$$

$$[n\cdot(w-v_T)]^{\downarrow}_{z=H} = 0 \quad \text{if} \quad w-v_T \leq 0 \quad (5)$$

$$n(\nu,z,t=0) = \begin{cases} n_o(\nu) & z=z_o \\ 0 & z\neq z_o \end{cases} \quad (6)$$

The conditions (4) and (5) express the assumption that no droplets come into the tower through the top and the base of it, and eq.(6) - that at the initial time the tower does not contain droplets.

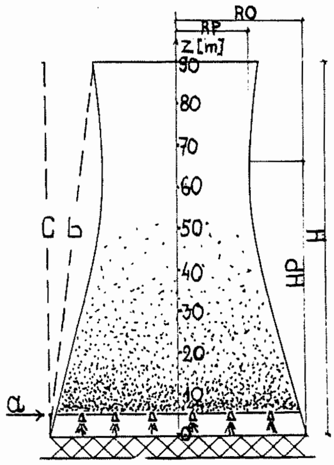

Fig.1 Scheme of cooling tower, a - source of droplets, dashed lines - shapes of conical (b) and cylindrical (c) tower

In the numerical experiments performed spectrum $n_o(\nu)$ was assumed to be given by the gamma distribution

$$n_o(\nu) = (LWC_o/\bar{\nu}_o)\exp(-(\nu/\bar{\nu}_o)) \quad (7)$$

[Scott 1968, Berry 1965], with $\bar{\nu}_o = \nu(r_o=100\mu m)$ and LWC = 1 or 3 g/m^3, what roughly corresponds to the conditions in cooling tower without eliminators.

4. Numerical model

Making use of (2) and (3), equation (1) can be solved numerically with conditions (4)-(7). The coalescence terms was evaluated by method of Berry(1965) for 55 classes of droplet volumes coverning range of radii from 5 to 2500 μm.

Collection kernel has form proposed by Long [1974]

$$K(\nu,\nu') = 9.44\cdot10^9(\nu^2 + \nu'^2) \quad \text{for } R<50\ \mu m$$
$$K(\nu,\nu') = 5.78\cdot10^3(\nu + \nu') \quad \text{for } R>50\ \mu m \qquad (8)$$

where R radius of the greater of two droplets (ν,ν' - in cubic centimeters). For evaluation of convective transport term in eq.(1) Lax scheme was used [Potter 1973] on twenty levels grid points. The terminal velocity of the droplet in still air is expressed by semiempirical formula of Beard [1977]. The final finite difference scheme becomes:

$$n_j^{k+1}(I) = (1/2S_j)(n_{j+1}^k(I)S_{j+1} + n_{j-1}^k(I)S_{j-1}) -$$
$$- (\Delta t/2\Delta z S_j)(n_{j+1}^k(I)w_{j+1}^{(I)}S_{j+1} - n_{j-1}^k(I)w_{j-1}^{(I)}S_{j-1}) +$$
$$+ (1/4S_j)(S_{j+1}\Omega_{j+1}^k(I) + 2\Omega_j^k(I)S_j + \Omega_{j-1}^k(I)S_{j-1})\cdot\Delta t +$$
$$+ n_o\delta_{j2} \qquad \text{for } 2<j<NH-1 \qquad (9)$$

$$(j=1\rightarrow z=0;\ j=2\rightarrow z=z_o;\ j=NH\rightarrow z=H; \quad w_j^{(I)} \equiv w_j - v_T(I))$$

where $\Omega_j^k(I)$ is coalescence term expressing the change of $n(I,(j-1)\Delta z,k\cdot\Delta t)$ due to coalescence, I - numerical parameter ($\nu=\nu_o 2^{(I-1)/2}$, ν_o size of the first class), δ_{j2} Kronecker's symbol. For first and last level forward and backward Euler's schemes were used. Weighted averaging of the coalescence term over three levels is applied for sake of stability. The computations were made with steps Δz=5m and Δt=0.6s. Steady state was achieved after 480 time steps (about 288 sec. physical time) what takes about one hour CPT of CDC 6600 computer.

5. The influence of updraft shape on the steady state solution

The computations were made for cooling towers with hyperboloidal, conical and cylindrical shapes what correspond to vertical velocity of updraft with one maximum (hyperboloid), monotonically increasing with height (cone), and independent on z (cylinder). Comparing the results (figures 2,3,4) it can be noticed that for updrafts without maximum of vertical velocity there is no strong second maximum in big-droplet end of the spectrum, which is present in the hyperbolic case. This result can be explained as follows. For the flow with hyperboloidal geometry a "trap" for big droplets forms above the level of maximum velocity of updraft. In this zone the droplets tend to accumulate at the levels where updraft compensate their free fall velocity, and they remain there untill they grow by coalescence to sizes large enough to fall down through the level of maximum velocity. In this way an accumulation zone with high LWC and better conditions for rapid coalescence appear above the level of maximum w (fig.5). The droplets which grow big enough to return and fall down, grow further by collisions with droplets going upwards, giving in steady state bimodal spectra at all levels (fig.2). For case of the cylindrical geometry of the flow, the vertical velocity remains constant. The big droplets appearing due to coalescence do not accumulate but rather start to fall downwards. In the "conical case" where velocity increases with height larger fraction of big droplets will be removed through the top. This process leads to spectra broader than the initial ones but the second maximum for large radii does not appear. The greater number of big droplets observed at low levels in "cylindrical case" than in the "conical" one, results from the fact that larger fraction of them is able to return downwards growing on the way. This results point out that the model of infinite updraft with height independent properties [Jonas and Mason 1974, Leighton and Rogers 1974, Young 1975] may be a strong oversimplification and cannot account for certain important mechanisms of forming bimodal or multimodal spectra.

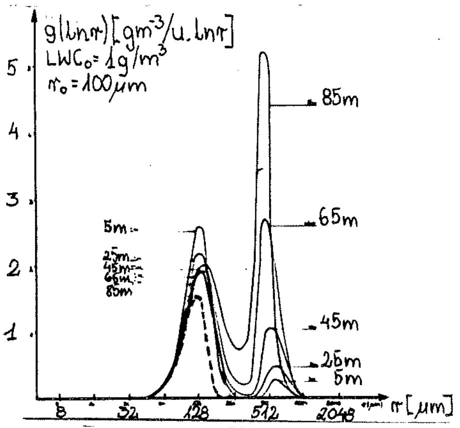

Fig.2 Steady state spectra for hyperboloidal geometry of flow, dashed line - spectrum of the source (the same in each experiment)

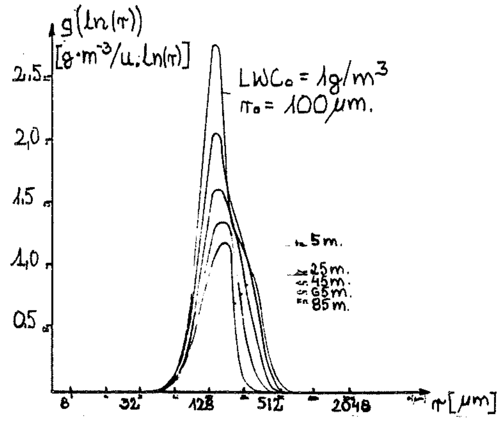

Fig.3 Steady state spectra for cylindrical geometry of flow

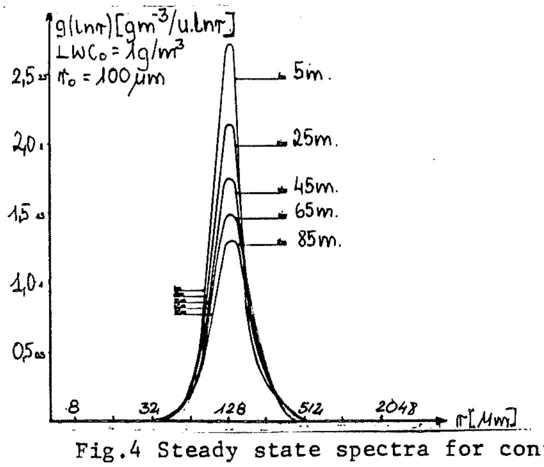

Fig.4 Steady state spectra for conical geometry of flow

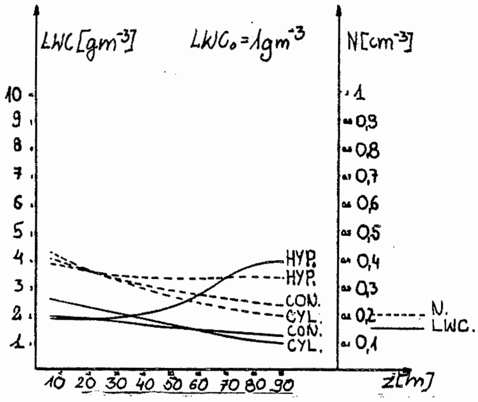

Fig.5 LWC and concentration distributions as a function of height for various geometries of flow

6. The influence of the horizontal turbulent mixing on the results in stationary state

In the variant ii) the velocity field has form

$$w(z,\rho) = w(z)\ f(\rho/R(z))$$

where function f has maximum for $\rho = 0$ (radial velocity component required by continuity equation should appear explicitly in transport terms of the kinetic equation), and assumption of horizontal homogenity is deleted. Nevertheless the onedimensional model can be retained along the axis of the flow. The kinetic equation becomes

$$\partial n/\partial t = -(w-v_T)\cdot(\partial n/\partial z) + \Omega + n_o\delta(z-z_o) \qquad (10)$$

where Ω coalescence term.

Change of the convective transport term with respect to the equation (1) express the fact that now there exist net horizontal transport of droplets with respect to the air. The results obtained for this variant are shown on figure 6. Comparing this with results of the variant i) (fig.2) one can see that in the variant ii) there are more big droplets at low levels. This can be explained by the horizontal convergence of droplets below the level of maximum w, and divergence above it due to inclination of droplets trajectories with respect to the streamlines of the air. Physically, variant i) corresponds to strongly turbulent flow with very effective horizontal mixing, variant ii) to laminar flow. Differences between these two variants suggest that assumption with respect to the horizontal structure of the air flow and droplets distribution may have very essential influence on the spectrum evolution in the model, and outline certain limits of applycability of onedimensional models in cloud microphysics.

7. The effect of the periodical pulsation of vertical velocity of an updraft

In variant iii) the vertical velocity of updraft, derived from eq.(2) and (3) was modified by periodic factor,

$$w(z,t) = w(z)(1 + 0.5\sin(2\pi t/T))$$

The experiments has been performed for two values of period T - 30 and 60 sec. Until the second maximum in spectrum appeared (about 200 time steps) the solution of equation (1) evolves in this case like that for time independent updraft. Afterwards approximatively periodic

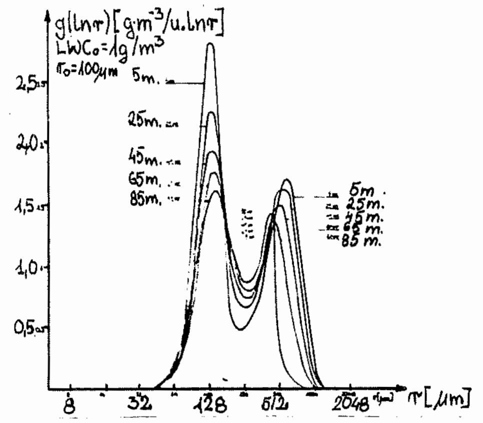

Fig.6 Steady state spectra for variant ii)

solutions with period 3-4 time T has been observed. At some instants this quasi-periodic solution passes through the form much alike to that observed in steady state of variant i).

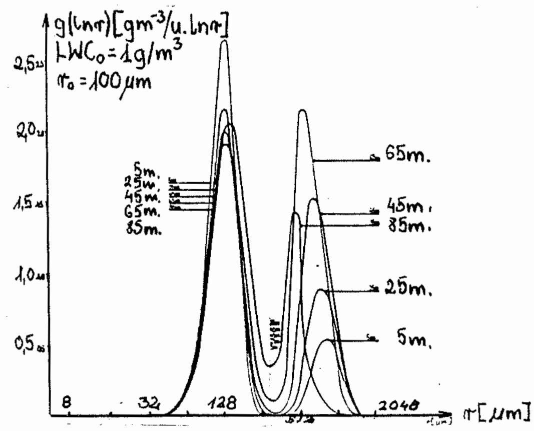

Fig.7 Example of solution for variant iii) with updraft velocity periodically variable in time ($2\pi t/T = \pi/2$)

Figure 7) shows the spectra corresponding to the moment just after maximum w(z,t) is attained. One can be see that variant iii) yields considerably broader instantaneous spectra than time independent variant i), at least below the level of maximum velocity. This result suggests that time pulsations of the updrafts present in natural clouds may also be responsible for faster broadening of the spectra.

8. Some additional remarks

In cours of the numerical experiments it was found that certain properties of the model, like conservation of the total water, are very sensitive to the numerical diffusion and production in the advective scheme. The adverse effect at these factors can be to high extent compensated by introduction of diffusion term with suitably chosen diffusivity. This effect must be taken into account when turbulent exchange coeficients beeing introduced into the models of coalescence in clouds.

References

Beard K.V.,1977:Terminal velocity adjustment for cloud and precipitation drops aloft, J.Atmos. Sci.,34,1293

Berry E.X.,1965:Cloud droplet growth by collection: a theoretical formulation and numerical calculation, Ph. D. dissertation, University of Nevada

Jonas P.R., B.J. Mason,1974:The evolution of droplet spectra by condensation and coalescence in cumulus clouds, Quart. J.R. Met. Soc., 100,286
Leighton H.G., R.R. Rogers,1974:Droplet growth by condensation and coalescence in strong updraft, J. Atmos. Sci.,31,271
Long A.B.,1974:Solutions to the droplet collection equation for polynomian kernels, J. Atmos. Sci.,31,1040
Potter D.,1973:Computational Physics, J.Wiley and Sons, London
Scott W.T.,1968:Analitic studyes of cloud droplet coalescence, J. Atmos. Sci.,25,54
Smolarkiewicz P.,1978:A simple method for estimation of drift droplet deposition from natural draft cooling tower, Act. Geoph. Pol., vol.XXVI,No 1,21
Young K.C.,1975: The evolution of drop spectra due to condensation, coalescence and breakup, J. Atmos. Sci.,32,965

CONSERVATION OF ENERGY IN A THREE-DIMENSIONAL WARM CLOUD MODEL

P.M. Tag

Naval Environmental Prediction Research Facility
Monterey, California 93940 USA

I. Introduction

A cloud simulation provides one of the more demanding tests of a model's ability to conserve energy because of the complexities involved during phase change. Unless water vapor changes phase, the conservation of energy related to water vapor is primarily related to the conservation of the water substance itself. However, the release of latent heat, as well as the transformation of water vapor to an alternate form, adds considerable complexity to the energy balance.

The purpose of this paper is to diagnose the transformations of energy which occur using an inviscid three-dimensional (3-D) numerical model of warm cloud formation. This diagnosis serves two purposes. First, we can assess the model's ability to conserve energy (and determine reasons for non-conservation). And second, we can observe the energy transformations with time for the purpose of better understanding the dynamic and thermodynamic changes resulting from a simple phase change.

In the following sections we first provide a brief description of the model. Second we describe the energy diagnosis package. And finally, we assess the energy diagnosis of a simple cloud simulation and its implications.

II. The Model

Our model is described in detail in Tag and Rosmond (1980). Briefly, the model is 3-D and anelastic, and the primary model equations (except for moisture) are derived in perturbation flux form. Coriolis force is neglected, there is no radiation, and the fluid is assumed to be inviscid (the energetics of a cloud simulation which includes subgrid turbulent mixing will be included in the paper's presentation.) In addition, although both vapor and liquid water can exist, precipitation is excluded. Although the momentum and thermodynamic equations are handled in the usual Eulerian fashion, phase changes and the advection of the moisture variables (mixing ratio of vapor and liquid) are handled in a Lagrangian manner. This latter procedure was developed by Murray (1970) for his two-dimensional (2-D) cloud simulations. Murray concluded that this approach was conceptually more straightforward for phase changes, which occur in a highly implicit way. To ensure water conservation, the water conservation scheme developed by Murray (1974) is used (see Tag and Rosmond, 1980). And finally, scheme C of Arakawa and Lamb (Chang, 1977) is used to define the grid staggering.

For the following cloud simulation we use a course 8x8x8 grid domain with periodic boundaries, with $\Delta x=\Delta y=600$ m and $\Delta z=50$ m. Because the purpose of this simulation is not to produce a detailed picture of a realistic cloud, the grid spacing is unimportant; in fact, all of the initial conditions to follow are quite artificial. It is our belief, however, that this artificiality will not adversely affect the important conservation aspects, or the validity of the relative energy comparisons, in this cloud simulation.

To initiate the cloud we chose a moisture perturbation distributed over four grid points (planar view), two by two, in the center of the domain. This perturbation is also two grid points in depth, with the lower point at grid point two (50 m). The surface temperature is set to 290 K; the lapse rate $\partial\bar{\theta}/\partial z$ is equal to 1.0 K km^{-1}. And to ensure cloud formation without immediate evaporation because of resolved mixing with the environment, relative humidity is set to 100.1% in the perturbation and to 95% elsewhere. We terminated the experiment at 25 min, at which time the updraft was approaching the upper boundary of the domain.

III. Energy Diagnosis

To assess energy conservation in the model domain, we compute the various forms of energy, as derived and defined by Murray and Koenig (1975a):

$$\text{Kinetic energy (KE)} = \bar{\rho}_D(1+\bar{r}_v)(u^2+v^2+w^2)/2$$
$$\text{Potential energy (PE)} = \rho_D(1+r_v+r_c)gz \qquad (1)$$

Thermal enthalpy, air (TEA) =

$$\rho_D C_p T$$

Thermal enthalpy, vapor (TEV) =

$$\rho_D r_v C_{pv} T \tag{1}$$

Thermal enthalpy, liquid (TEL) =

$$\rho_D r_c C_w T$$

Latent enthalpy (LE) = $\rho_D L' r_v$,

where ρ_D is the dry air density; r_v and r_c the respective mixing ratios of water vapor and liquid; C_p, C_{pv}, C_w the respective constant pressure specific heats of dry air, water vapor, and liquid water; the other symbols having their customary definitions. Murray and Koenig used $\bar{\rho}_D$ in place of ρ_D in TEA, TEV, TEL, and LE. Because variations in density can be of the same order as those for temperature, the change to actual dry air density was found to be necessary. In addition, Murray and Koenig used the latent heat of vaporization L in LE above. During the course of this experimentation, however, we discovered that the constant which is necessary to calculate latent enthalpy is not, in fact, the latent heat of vaporization. It is, instead, an alternate value (defined as L') which is approximately 27% larger than L. The reasoning behind, as well as a derivation supporting, this change can be found in Tag (1980). Murray and Koenig (1975b) used the energy formulations (1) in a realistic 2-D cloud simulation in which they emphasized the various fluxes of energy about the domain.

We perform a perturbation expansion of (1), where all variables are broken into a base state (f(z) only) and a perturbation quantity. Because the mean energy in the model domain is quite large, only an analysis of the total perturbation energy can accurately determine whether the model conserves energy.

Except for ρ'_D, all of the quantities in (1) are easily determined from the model equations. The diagnosis of ρ'_D requires considerable care to ensure a correct perturbation energy assessment. Two points are worthy of note: 1) it is not sufficient to logarithmically differentiate and linearize the equation of state to arrive at ρ'_D and 2) moisture must be included in determining ρ'_D. See Tag and Rosmond (1980) for a complete derivation.

IV. Cloud Simulation

In terms of energetics, the moisture perturbation described previously consists, approximately, of 85% LE' and 15% TEV', with a negligible contribution due to PE'. This combination contrasts with the mean atmospheric composition of 0.6% $\overline{\text{PE}}$, 87.7% $\overline{\text{TEA}}$, 1.7% $\overline{\text{TEV}}$, and 10.0% $\overline{\text{LE}}$ (both $\overline{\text{KE}}$ and $\overline{\text{TEL}}$ are zero). Not surprisingly, $\overline{\text{TEA}}$ is by far the dominant contributor in the mean atmosphere. Our perturbation adds only 0.01% to the total energy in the domain.[1]

The cloud and vertical velocities generated by the moisture perturbation are small, owing to the fairly stable environment and to the limitation of the domain's vertical extent. A maximum liquid water content (LWC) of 0.087 g kg^{-1} and a maximum vertical velocity (occurs in-cloud) of 0.22 m s^{-1} are achieved at 25 min. At this time the cloud is growing vigorously and produces a maximum temperature perturbation of 0.16 K due to condensation.

The conversion of LE' (85.22% of total) and TEV' (14.76% of total) into the other energy forms provides the stimulus for generating the model cloud. Note that there is no contribution due to KE' and TEL', and an insignificant contribution due to PE' at the start of the model run. Qualitatively, we might expect the following: 1) an increase in the sensible heat of the dry air (TEA') because of condensation, 2) creation of TEL' and a decrease in LE' as water condenses, 3) either an increase or decrease in TEV' because of the competing effects of vapor decrease and temperature increase, and 4) an increase in KE' from zero as circulations are produced within the domain.

All of the above changes are observed in the model simulation, with TEV' indicating a slight decrease

---

[1]Note that the absolute values (both mean and perturbation) of energy that we compute for TEA, TEV, and TEL are, in fact, fictitious. A correct determination of enthalpy should be based on an integration of the specific heat times the change in temperature from 0 K to the temperature in question. This integration is complicated because specific heats do not remain constant to absolute zero. For this reason a more realistic determination of enthalpy would be based on a temperature range $(T-T_o)$ through which the specific heats can realistically be assumed constant. For comparison and conservation purposes, however, this additional complexity is unnecessary. We will assume that T_o=0 K. Additional discussion is given in Tag (1980).

(14.76 to 12.19%). Since TEV' decreases only slightly, the energy conversions result mainly from LE' which decreases from its initial 85.22% of the total to 69.35% at 25 min. These decreases go mostly into warming the dry air (12.47% for TEA'), with a lesser amount going to TEL' (5.91%). PE' contains only 0.07% of the perturbation at time zero and decreases almost imperceptibly thereafter. KE' does, of course, increase from its initial zero value, but can claim a mere 0.02% of the total perturbation energy at 25 min. We see that much more energy lies unharnessed in other forms. A time plot of all perturbation energies is given in Fig. 1. Note the apparent cloud pulsation at 15 min, when some evaporation occurs prior to explosive cloud growth. Conservation of total perturbation energy in this experiment is good, with a maximum variation of 2.7% at the end of the 25 min run.

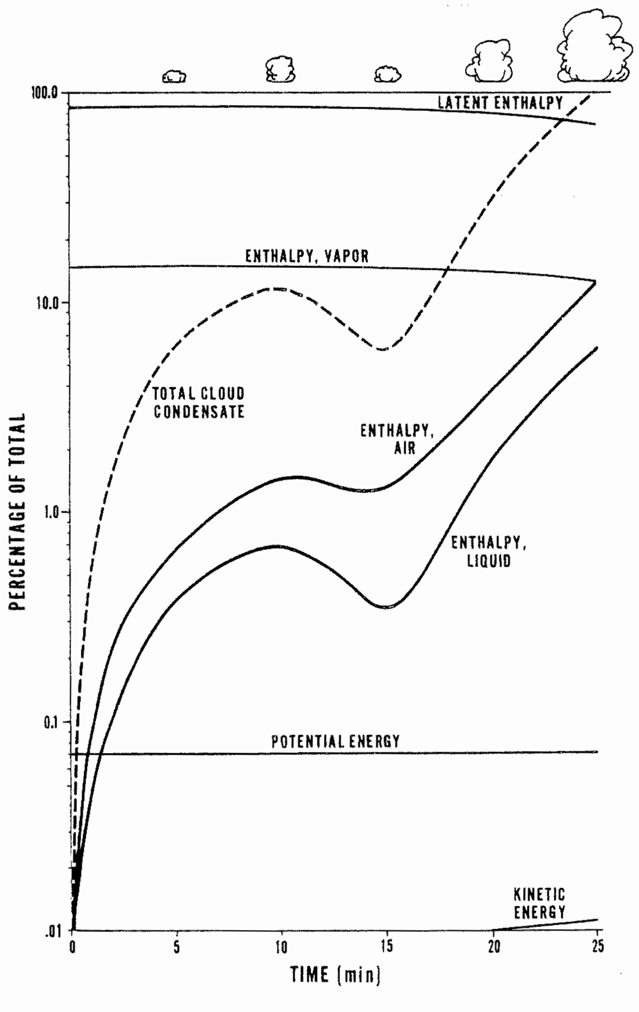

Fig. 1. Cloud simulation. Perturbation energy variation as a percentage of total perturbation energy. Dashed line represents percentage of cloud condensate (based on maximum value achieved at 25 min). Area inside schematic cloud illustration is proportional to amount of cloud condensate. Shape of schematic cloud does not represent model cloud.

Recall that a water conservation scheme was added to the model. To determine the effect of nonconservation, we switched off the conservation procedure in a second experiment. This modification changed an overall domain gain of 6.6 kg (with conservation) into a loss of 1.84×10^4 kg (without conservation). Although this latter figure appears exorbitant, it represents only 0.016% of the total water mass. In terms of total perturbation energy, this water loss translates into a 15% energy loss. However, KE' changes by only 0.33%, an insignificant variation. Practically, it is in the cloud liquid water that we do, in fact, see an important modification. Although the cloud has approximately the same physical size, total cloud condensate decreases by more than 10%. The point of this exercise is that a seemingly insignificant loss of water (0.016%) can produce a significant change in total perturbation energy (15%) and cloud condensate (10%).

V. Discussion

This simulation of the formation of a small nonprecipitating warm cloud has revealed several useful points regarding 1) the diagnosis of energy during phase change and 2) the relative magnitudes of energy forms resulting from a simple phase change.

Regarding the diagnosis of perturbation energy, we found that considerable care must be taken in assessing the perturbation quantities which result from a perturbation expansion of (1). The most crucial quantity was ρ'_D, the perturbation dry air density. We found that 1) a logarithmic differentiation, followed by linearization, of the equation of state is not nearly accurate enough to define ρ'_D and 2) the variation of moisture must be included.

Of the 85% LE' and 15% TEV' which resulted from the initiating moisture perturbation, approximately 18% was converted into other energy forms. Nearly all of it went into warming the air (TEA') and the generated cloud liquid water (TEL'). In comparison, the amount converted into kinetic energy (KE') was negligible. In a separate experiment which neglected the conservation of total water in the domain, a seemingly negligible (0.016%) loss of water resulted in a 15% loss in total perturbation energy and a 10% reduction in total cloud condensate.

This paper has addressed the energetics of cloud development generated only by condensation. The addition of ice with its differing specific heat, as well as the additional complication of the latent heat of fusion, would provide an obvious extention to this work.

VI. Acknowledgments. The author is grateful to Mr. Steven W. Payne of our facility for his constructive comments concerning various portions of this work.

VI. References

Chang, J., Editor, 1977: General circulation models of the atmosphere, vol. 17 of Methods in Computational Physics. Academic Press, New York, 337 pp.

Murray, F.W., 1970: Numerical models of a tropical cumulus cloud with bilateral and axial symmetry. Mon. Wea. Rev., 98, 14-28.

______, 1974: Conservation of mass of water substance in the RAND cloud model. Rand Working Note-8822-EPRF, Santa Monica, CA, 22 pp.

______, and L.R. Koenig, 1975a: Cumulus cloud energetics as revealed in a numerical model of cloud dynamics: Part I. Theoretical development. Pure appl. Geophys., 113, 909-923.

______, and ______, 1975b: Cumulus cloud energetics as revealed in a numerical model of cloud dynamics: Part II. Computational results. Pure appl. Geophys., 113, 925-947.

Tag, P.M., 1980: On the diagnosis and conservation of energy during condensation. Accepted for publication in J. Atmos. Sci.

______, and T.E. Rosmond, 1980: Accuracy and energy conservation in a three-dimensional anelastic model. Accepted for publication in J. Atmos. Sci.

ETUDE PRELIMINAIRE DE L'INTERACTION NUAGES-RAYONNEMENT DANS UN MODELE DE COUCHE LIMITE PLANETAIRE TRIDIMENSIONNEL

Ph. VEYRE

E.N.M., Météorologie Nationale, Paris.

G. SOMMERIA

Laboratoire de Météorologie Dynamique,
CNRS, Paris

1) Présentation du problème

Le problème de l'interaction entre les phénomènes dynamiques et radiatifs est un des aspects fondamentaux des mécanismes atmosphériques. Pour des échelles de temps suffisamment grandes, c'est à dire nettement supérieures à la journée, le rayonnement peut être considéré comme un facteur externe qui force l'état dynamique et thermodynamique de l'atmosphère. Au fur et à mesure que l'on descend dans l'échelle de temps le couplage entre le rayonnement et les autres processus devient plus complexe et se manifeste particulièrement par l'intermédiaire des nuages. Les effets radiatifs sur une masse nuageuse stationnaire ou horizontalement homogène sont calculables tout au moins en ordre de grandeur. Le problème devient beaucoup plus délicat quand il s'agit de nuages non stationnaires dont les fluctuations interagissent avec le champ radiatif. On tente d'aborder ici cette question par une simulation numérique tri-dimensionnelle dans le cas de petits cumulus.

Jusqu'à présent les études quantitatives sur l'interaction entre une couche de nuages et le champ radiatif ont été effectuées dans le cas de nuages stratiformes où l'hypothèse d'homogénéité horizontale peut être appliquée aussi bien aux processus dynamiques et microphysiques que radiatifs. C'est également dans ce cas que l'effet radiatif sur l'évolution du nuage est le plus important. Le rôle des flux radiatifs dans l'évolution d'une couche de stratus est mis en évidence dans un modèle simple par Lilly (1968). Il est discuté et approfondi par Deardorff (1976) et simulé en détail dans un modèle tri-dimensionnel par Deardorff (1980). D'autres modèles, uni-dimensionnels, mettent l'accent sur le rôle du refroidissement radiatif dans l'équilibre thermodynamique des nuages stratiformes ; on peut citer dans cet ordre d'idée le travail de Paltridge (1974) et de Fravalo et al. (1980).

Le rôle du refroidissement radiatif dans l'évolution des nuages cumuliformes a été pressenti par plusieurs auteurs, aussi bien aux petites échelles (initiation de la convection des petits cumulus, Sommeria 1976) qu'aux grandes échelles (initiation des perturbations tropicales, Albrecht et Cox 1975) mais n'a pas fait, jusqu'à présent, l'objet d'études quantitatives. Le travail présenté ici est un premier essai dans ce sens pour le cas de la convection nuageuse naissante. Une formulation schématique mais relativement complète des flux radiatifs infra-rouge est développée et associée à un modèle dynamique tri-dimensionnel. L'idée de base est de comparer sur un cas précis l'évolution de petits cumulus quand on tient compte ou non de l'effet des gouttelettes de nuage sur le champ radiatif. Le résultat trouvé ne correspond qu'à un cas particulier et à une période restreinte de comparaison mais donne une indication de l'importance de l'effet recherché.

2) Le modèle

Le modèle utilisé dans cette étude est une version légèrement améliorée de celui développé par Sommeria (1976) en collaboration avec J.W. Deardorff.

Dans le cas présent on a choisi des conditions typiques de couche limite tropicale non perturbée, conformément aux données d'une expérience faite en 1972 par le National Center for Atmospheric Research à Porto Rico (Pennell et LeMone 1974). Les caractéristiques dynamiques correspondant à ce cas d'étude font l'objet d'un article récent par Sommeria et LeMone (1978).

L'objectif était de réaliser un schéma de calcul des flux radiatifs qui prenne en compte de façon réaliste l'hétérogénéité du champ d'eau liquide. Pratiquement il s'agit aussi de maintenir le temps de calcul et l'encombrement de la mémoire de l'ordinateur dans des limites raisonnables. Ceci conduit à un certain nombre d'approximations dont la validité a été évaluée. On a négligé le rayonnement solaire par rapport au rayonnement infra-rouge et les échanges radiatifs latéraux par rapport aux échanges verticaux. Par souci d'économie de temps de calcul, on a choisi une formulation utilisant des émissivités intégrées sur tout le spectre (cf. Sasamori 1968), qui prennent en compte vapeur d'eau et gaz carbonique. On a modifié les formulations originales de Sasamori pour tenir compte de l'absorption par le continuum de la vapeur d'eau dans la bande 8-14 μ (d'après Roberts et coll. 1976). La figure 1 montre l'importance relative des différents types d'absorption dans l'expression du taux de refroidissement radiatif, pour les conditions de Porto Rico en absence de nuages (courbes 2-3-4). La courbe 1 correspond à un calcul de rayonnement simplifié (Sommeria 1976) avec, ici, prise en compte du gaz carbonique et de la vapeur d'eau. Les présents résultats ont été comparés à un modèle multispectral (Morcrette 1978) pour la validation.

Le but de ce travail est d'étudier l'influence sur la dynamique de la couche limite des inhomogénéités de champ de rayonnement, elles mêmes liées aux hétérogénéités du champ d'eau liquide. On utilise donc une méthode simplifiée qui consiste à négliger la présence du nuage en ce qui concerne les échanges radiatifs entre les différents niveaux de l'atmosphère et à la prendre en compte pour le calcul des termes prépondérants qui correspondent aux échanges avec le sol et l'espace. Le nuage est considéré comme un corps gris avec un coefficient d'absorption $K=120\ m^2 kg^{-1}$. Le modèle de rayonnement a été réalisé en collaboration avec Y. Fouquart de l'Université de Lille et ses caractéristiques sont exposées dans l'article Veyre et coll. (1980).

3) Essais de simulation

Le principe des essais de simulation est d'étudier, sur un cas particulier représentatif de la couche limite tropicale, la différence de comportement des petits nuages avec ou sans effet radiatif des gouttelettes d'eau nuageuse.

Nous avons fait deux simulations en parallèle, l'une ne prenant pas en compte l'eau liquide dans le calcul de rayonnement, l'autre la prenant en compte. Nous pouvons ainsi isoler le rôle du refroidissement radiatif des nuages sur la dynamique du système. Il doit jouer sur le terme de condensation (en modifiant le rapport de mélange saturant), sur la stabilité dans la couche nuageuse, et donc finalement sur la turbulence dans cette couche.

La comparaison a eu lieu sur un temps assez court (16 mn 40 s, soit 200 pas de temps), en partant d'une situation ou la convection n'est pas encore très développée (pas de temps 600) : nuages de faible extension verticale (de 600 à 1000 m) et se dissipant rapidement (durée de l'ordre de 5 minutes).

La figure 2 permet une comparaison des profils verticaux de contenu en eau liquide pour le pas de temps 801. La figure 3 permet d'apprécier l'évolution temporelle du contenu moyen en eau liquide dans le domaine d'intégration. On peut noter dans l'ensemble l'augmentation du contenu moyen en eau liquide quand on tient compte des nuages dans le calcul du rayonnement (la différence est de l'ordre de 10 % sur la période de comparaison et atteint 25 % au bout de 16 minutes). Dans ce dernier cas la montée du nuage et sa dissipation sont ralenties.

L'examen des quantités turbulentes montre que la plupart d'entre elles sont augmentées dans la couche nuageuse : variance des vitesses, et donc énergie cinétique turbulente (jusqu'à 25 % de différence), variance de la température potentielle (+ 10 %). Il ne semble pas y avoir de modification sensible du profil de la variance de l'humidité. On note des flux verticaux plus importants pour l'eau liquide et la vapeur d'eau (+ 15 % à la base des nuages) et pour la chaleur sensible virtuelle (+ 30 % à 900m), ce qui est encore lié à une activité plus intense de la turbulence dans la couche nuageuse. La figure 4 résume l'effet des nuages sur le terme de rayonnement, en moyenne horizontale. Le refroidissement radiatif est maximum vers 800 m, où il y a beaucoup de sommets de colonnes nuageuses et on a un effet d'écran sous les nuages (couche 0-600 m).

4) Conclusion

On a défini un modèle de rayonnement infrarouge prenant en compte tous les absorbants importants dans les basses couches (molécules et continuum), gaz carbonique, eau liquide.

Seul le champ d'eau liquide est pris en compte d'une manière détaillée, encore qu'il s'agisse d'une méthode très simplifiée. Un essai a été effectué pour des conditions météorologiques particulières. Dans notre cas, le refroidissement radiatif des nuages a favorisé leur développement, puisqu'on a constaté que la couverture nuageuse et le contenu en eau liquide ont été augmentés, que les nuages se sont maintenus plus longtemps. On a également noté une augmentation des variances, de l'énergie cinétique turbulente, ainsi que des flux verticaux turbulents d'eau et de chaleur sensible. On peut en conclure une augmentation de l'activité turbulente, qui tend à compenser les pertes et gains d'énergie par évaporation, condensation et rayonnement que ce soit au sommet ou à la base des nuages. A moyen terme, on devrait assister à une modification de la stabilité thermique moyenne dans la couche nuageuse. Il resterait à généraliser ce résultat pour des conditions variées et à eventuellement le paramétrer pour des modèles de prévision.

REFERENCES

(1) Albrecht B. et Cox S.K. (1975) : The large-scale response of the tropical atmosphere to cloud-modulated infrared heating. J.Atms.Sci., 32, 16-24.

(2) Deardorff J.W. (1976) : On the entrainment rate of a stratocumulus-topped mixed layer. Quart.J.Roy.Met.Soc., 102, 563-582.

(3) Deardorff J.W. (1980) : Stratocumulus-capped mixed layers derived from a three-dimensional model. Soumis au J.Atmos.Sci.

(4) Fravalo C., Y. Fouquart, R. Rosset (1980) A model of low stratiform clouds. Soumis au J.Atmos.Sci.

(5) Lilly D.K. (1968) : Models of cloud-topped mixed layers under a strond inversion. Quart.J.Roy.Met.Soc., 94, 292-309.

(6) Morcrette J.J. (1978) : Infrared fluxes in stratiform model clouds. Contrib. Atm. Phys., 51, 338-351.

(7) Sommeria G. (1976) : Three-dimensional simulation of a turbulent process in an undisturbed trade wind boundary layer. J.Atm.Sci., 33, 216-241.

(8) Sommeria G., M.A. LeMone (1978): Direct

testing of a three-dimensional model of the planetary boundary layer against experimental data. J.Atmos.Sci., 35, 25-39.

(9) Veyre Ph., G. Sommeria, Y. Fouquart (1980) : Modélisation de l'effet des hétérogénéités du champ radiatif infra-rouge sur la dynamique des nuages. Soumis au J.Rech.Atmos.

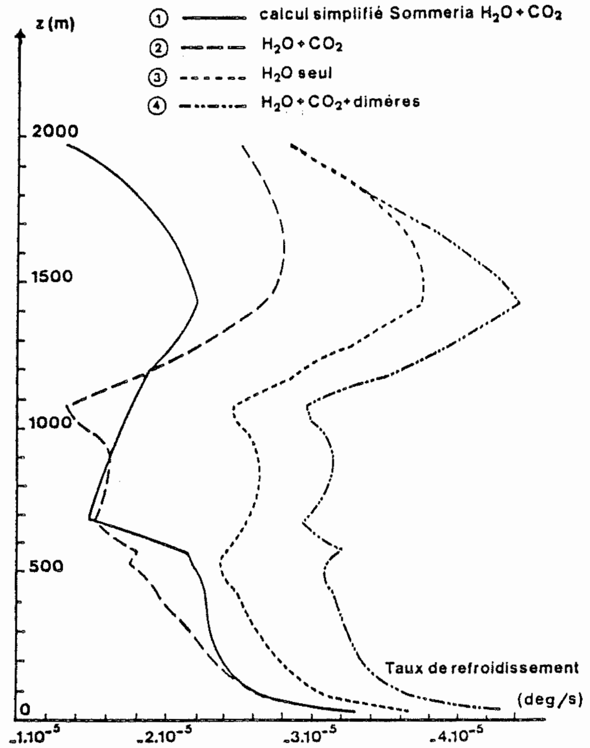

Fig. 1 : Taux de refroidissement radiatif en air clair.

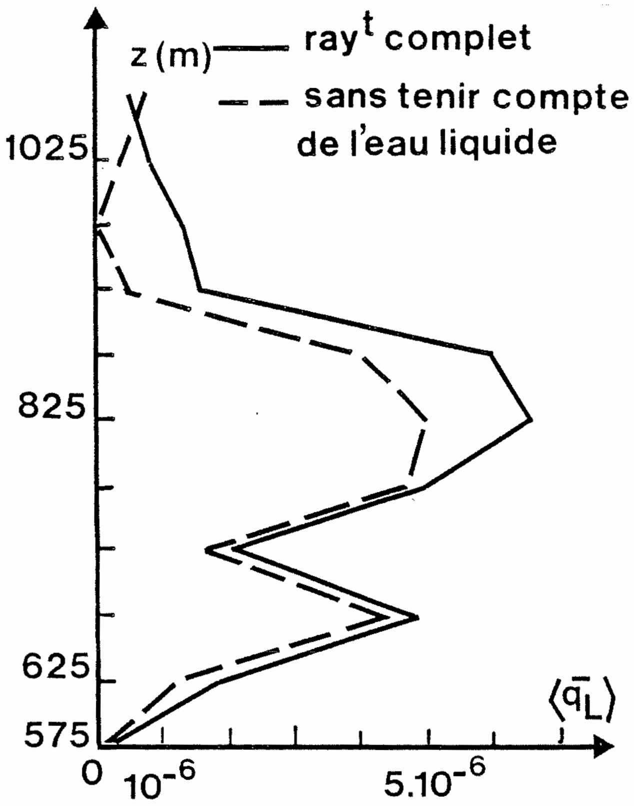

Fig. 2 : Moyenne par niveau du contenu spécifique en eau liquide au pas de temps 801.

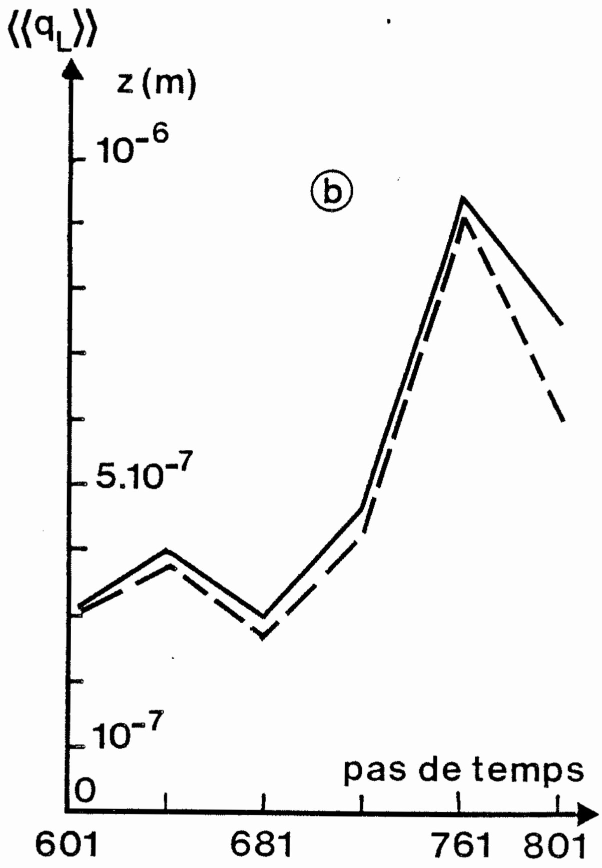

Fig. 3 : Evolution temporelle du contenu moyen en eau liquide dans le volume d'intégration (— et --- idem fig. 2).

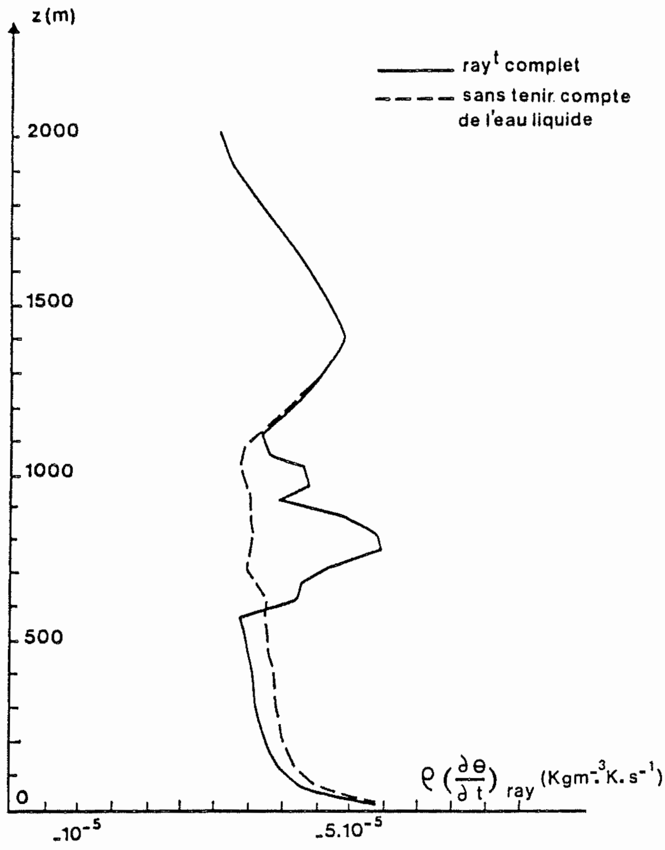

Fig. 4 : Moyenne par niveau et entre les pas de temps 761 et 801, du terme source de température par rayonnement.

A STUDY ON THE FORMATION OF THE PRECIPITATION IN CONVECTIVE CLOUD WITH CELLS

Xu Hua-ying, Li Gui-chen
Institute of Atmospheric Physics, Academia Sinica
Beijing, The People's Republic China

1. Introduction

Many observational facts show that the updraft in convective cloud is not uniform. Vulfson[1] pointed out that in convective cloud there are a great deal of cells of different sizes, the updraft in cells is almost larger than that outside the cells. The diameter of cells is about ten meters to several hundreds meters, the average is one hundred meters. The observations of Huang Mei-yuan[2] indicated that the liquid water content was fluctuated in cumulus as well as updraft, the larger liquid water content often corresponds to stronger updraft.

Therefore we could consider that the convective cloud consists of a great deal of cells in different scales, and that liquid water content and the speed of updraft in cloud cells are larger than those in their environment.

The formation of precipitation in convective clouds with cells has been studied by several authors, and the fluctuation of updraft in the cloud has been considered by Xu Hua-ying and Gu Zhen-chao[3,4] for calculating the formation of precipitation.

In this paper we investigate the formation of precipitation under the condition of simultaneous fluctuations of updraft and liquid water content.

2. The model

We suppose that the convective cloud consists of a great deal of cells of different scales, they distribute at random, the water content and speed of updraft in cloud cells are larger than that in their environment, and their values depend on the size of cell L. The cell moves upwards with the speed of the updraft in it. In the cloud outside the cells the liquid water content and updraft are uniform. During the cloud development the cells are forming continuously from cloud base and moving upwards in the cloud. The cloud gradually develops with the uprising of cells.

In the convective cloud the large drops or ice pellets grow up to form raindrops or hailstones through coalescence. Because a cloud consists of a great deal of cells of different intensity, the embryoes descending from a certain level in cloud meet several cells of various size at random. In spite of the embryoes of precipitation forming from the same height and the same size originally, the embryoes of precipitation will grow up to different size at cloud base, for they meet different numbers and various sizes of cells. Therefore we could obtain different size of raindrops or hailstones with certain density, some of which could grow even larger.

3. The equation

The increment of radius of particle by coalescence when getting through a cloud cell with size L is

$$\Delta R_L = \frac{E}{4\rho} q_L L \quad , \tag{1}$$

where E is an effective average value of collection efficiency for the droplet population, q is the liquid water content in the cloud cell with size L , ρ is the density of precipitation particles.

It can be seen from equation (1) that the increment of radius of particle passing through a cell with size L depends on the character of cell only, but it is independent of the size of particle falling into the cell. Consequently, the growth of particle which stochastically passed through several cells with different size can be easily expressed in mathematics.

In order to investigate the formation of precipitation, one must consider not only the growth rate of particles but also the path of particle in the cloud. Therefore, we discuss the displacement of particle in the cloud.

The distance needed for a particle passing through a cell of size L to gain a increment ΔR_L is

$$\Delta Z_L = \frac{4\rho}{E q_L} \left(\Delta R_L - W_L \int_R^{R+\Delta R_L} \frac{dR}{V(R)} \right) , \tag{2}$$

where W_L is the updraft in the cell with size L , and V(R) is the terminal fall speed of precipitation particles.

For the rest of the cloud, we have

$$\Delta Z = \frac{4\rho}{E q} \left(\Delta R - W \int_R^{R+\Delta R} \frac{dR}{V(R)} \right) , \tag{3}$$

where q and W are the average liquid water content and updraft in the rest of the cloud.

The relationship of the change of height for particle passing through the cloud inside and outside the cell with equal increment of particle radius ($\Delta R = \Delta R_L$) is

$$\Delta Z_L = \left(1 - \frac{W_L}{W}\right) L + \frac{W_L}{W} \cdot \frac{q}{q_L} \cdot \Delta Z \quad , \tag{4}$$

if $\frac{W_L}{W} = \frac{q_L}{q} = \beta_L$ and $\beta_L - 1 = \gamma L$,

then $\Delta Z_L = \Delta Z - (\beta_L - 1) L = \Delta Z - \gamma L^2 \; .$ (5)

Because the liquid water content and updraft in the cells are larger than those in the rest of the cloud, namely,

$$\beta_L > 1 \qquad \text{or} \qquad r > 0,$$

so that $\Delta Z_L < \Delta Z$.

Therefore the change of height for particle which passed through the cloud in the cell is small than which pessed through the cloud outside the cells, and the deviation depends on the character of cell only.

Hence, the relationship between the height H, from which a particle passing through a convective cell with size L, falls down to the cloud base and the displacement Z, required for same increment of the particle radius in cloud without cells is

$$Z = H + rL^2, \qquad (6)$$

we call Z the pseudo-height, it depends only on L. It can be seen from equation (6) that in the cloud with cells the height of cloud is increased.

We assume that the spectrum of cells with size L through which the particle swept is

$$N(L) = 2b^2 L^3 e^{-bL^2}. \qquad (7)$$

Therefore the spectrum of pseudo-height for the particle which passed through one cell is

$$g(Z) = N(L)\frac{dL}{dZ} = N(L)\ /\ 2rL\ . \qquad (8)$$

If $y = L^2$, then the spectrum of y is

$$f(y) = N(L)\frac{dL}{dy} = b^2\, y\, e^{-by}. \qquad (9)$$

The spectrum of y for the particle which passed through a cell is denoted by $f_1(y)$, it is equal to $f(y)$, $f_2(y)$ is the spectrum of y for the particle which passed through two cells and $f_n(y)$ is the spectrum of y for the particle which passed through n cells, which can be written as follows

$$f_2(y) = \int_0^y f_1(y-\xi)\, f_1(\xi)\, d\xi = \frac{1}{3!} b^4 y^3 e^{-by},$$

....

....

$$f_n(y) = \int_0^y f_{n-1}(y-\xi)\, f_1(\xi)\, d\xi = \frac{b^{2n}}{(2n-1)!}\, y^{(2n-1)} e^{-by}. \quad (10)$$

Therefore the spectrum of pseudo-height for the particle which passed through n cells is

$$g_n(Z) = f_n(y)\ /\ r$$

$$= \left(\frac{b}{r}\right)^{2n} \frac{1}{(2n-1)!} (Z-H)^{(2n-1)} e^{-\frac{b}{r}(Z-H)}. \quad (11)$$

The sweeping volume V_L of the particle fallen down to the cloud base from the height H is

$$V_L = \frac{\pi}{4}\, L^2\, (H + W_L t) = cL^2 + dL^3 \quad , \qquad (12)$$

where t is the average time for the particles passing from height H to the base of the cloud, hance the number of cells in unit volume of cloud is

$$m(L) = N(L)/\ V(L)\ . \qquad (13)$$

According to the spectrum of m(L) the parameter b could be expressed by the predominant diameter (L_n)

$$b = \frac{c}{2L_n^2\,(c + dL_n)}\ . \qquad (14)$$

The number of cells, through which the particle passed, can be expressed by Poisson distribution

$$P_n = \frac{\bar{N}^n}{n!}\, e^{-\bar{N}}\ , \qquad (15)$$

where $\bar{N}$ is the average number of cells swepted.

The probabitity of pseudo-height Z for the particle which passed through all of different number of cells

$$P(Z) = \sum_{n=1}^{\infty} P_n\ g_n\ (Z)\ . \qquad (16)$$

For a given pseudo-height the radius of particle on the cloud base can be obtain by calculation, it can be written as

$$G(R) = P(Z)\frac{dZ}{dR}\ , \qquad (17)$$

for the spectra of particles.

We assume that at the height H there are precipitation embryoes with the radius R_o, that the number of embryoes per unit volume is n_o, and that V_o is its terminal fall speed. On the cloud base these embryoes grow up by coalescence to form precipitation particle with terminal fall speed V(R), the spectrum of precipitation particles in a unit volume which descends from cloud base is

$$\psi(R) = G(R)\frac{n_o V_o}{V(R)}\ . \qquad (18)$$

4. The results of calculation

For the first we calculate the formation of rain. In that case the embryoes and the precipitation particles are water drops. In the calculation we assume the radius of the embryoes is 100 μm and its concentration is 100 m^{-3}. Its terminal velocities can be expressed as

$$V(R) = K_1 R \quad \text{for } 100\,\mu m \le R < 500\,\mu m,$$
$$V(R) = K_2 R^{1/2} \quad \text{for} \quad R \geq 500\,\mu m,$$

where $K_1 = 8000$, $K_2 = 200$ for M.G.S.

The liquid water content and updraft in the cloud outside the cells are 1 g/m^3 and 0.5 m/sec respectively, the thickness of cloud is 3.6 km and the character of the cells can be expressed by the concentration of cells $M = 10^{-6} m^{-3}$, the predominant size of cells L_n=70 m, and the liquid water content and updraft in cells are larger than that outside the cells, expressed by the parameter $r = 0.01\ m^{-1}$.

It found that the radius of precipitation particles have grown up to 1100-3000 μm on the cloud base, the predominant radius is 1800 μm and the concentration of all particles on the cloud base is $10m^{-3}$. This is in accord with the concentration of rain drops by field observations.

If the drops in the cloud without cells (in which the liquid water content and updraft are the same as the average value in cloud with cells) grow up to 1800 μm, it is necessary that the cloud thickness be 5.4 km. In this cloud only when the thickness is larger than 9.4 km the drops of 3000 μm could be produced and in the cloud with thickness 3.6 km the radius of drop grow up only to 1200 μm.

We calculated the spectra of rain drops for the embryoes descending from different height H, the results are drown in figure 1.

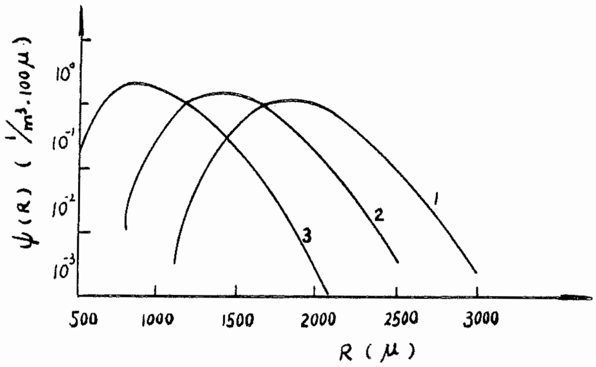

Fig.1. The raindrops spectra produced from the cloud with cells.
1 - H = 3000 m, 2 - 2000 m, 3 - 1000 m.

Next we calculate the formation of hailstones, in this cases the embryoes of hailstones are ice pellets . We assume that the radius of ice embryoes are 1 mm and its concentration is 10 m^{-3}. Its terminal falling speed can be written as

$$V(R) = \sqrt{\frac{8 \rho_i g R}{3 C_D \rho_a}} \qquad (22)$$

where ρ_i $(= 0.9\ 10^6\ g/m^3)$ is the density of hailstones, $C_D (=0.5)$ is the drag coefficient and ρ_a is the density of air, the liquid water content and updraft are 2 g/m^3 and 5 m/sec, the thickness of cloud is 4.5 km, the character of cell is the same as in the former. It can be shown that the radius of hailstones on the cloud base are grown up to 0.52-1.29 cm, the predominant radius is 0.85 cm, and the concentration of the hailstones on the cloud base is 0.1 m^{-3}. The hailstones spectrum is shown in figure 2.

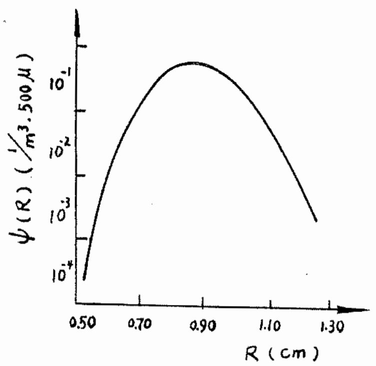

Fig.2. The hailstones spectrum produced from the cloud with cells.

If the ice pellets in the cloud without cells (in which the liquid water content and updraft is set equal to the average value in cloud with cells) grow up to 0.85 cm, it is necessary that a cloud thickness be 6.1 km, the hailstone of 1.29 cm could grow up only in cloud with thickness larger than 11 km.

Therefore in the shallow convective cloud with cells the precipitation particles and hailstones can occur larger than in clouds without cells if other things being equal.

5. The relationship between the formation of precipitation and characteristics of cloud cells

The characteristics of cells could be expressed by the intensity of fluctuation (r), the predominant size of cells (L_n) and the concentration of cells (m). In figure 3 and 4 express the influence of the fluctuation intensity (r) on the formation of precipitation.

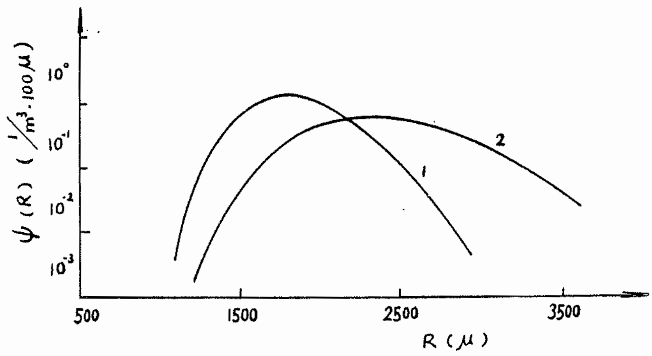

Fig.3. The influence of fluctuation intensity on spectrum of raindrops fallen out of the cloud base.
1 - r = 0.01, 2 - r = 0.02 .

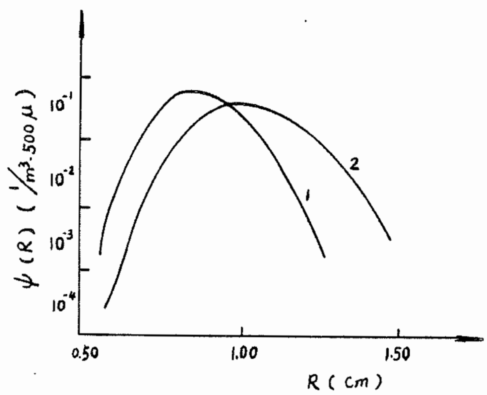

Fig.4. Some as Fig.3 except for hailstones.

In figure 5 and 6 the influence of the number of cells in unit volume (M) on precipitation is expressed.

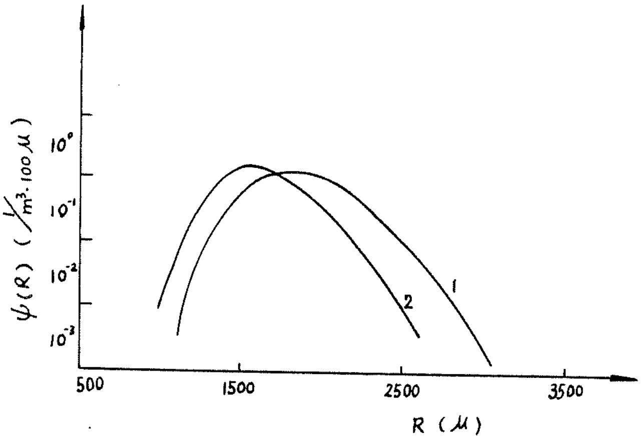

Fig.5. The influence of the concentration of cloud cells on spectrum of raindrops fallen out of the cloud base.
1 - $M = 10^{-6} m^{-3}$, 2 - $M = 0.7 \times 10^{-6} m^{-3}$.

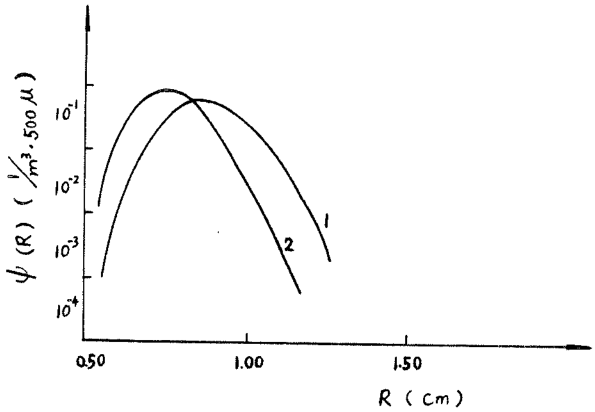

Fig.6. Some as Fig.5 except for hailstones.

In figure 7 the influence of the predominant size of cells (L_n) on precipitation is expressed.

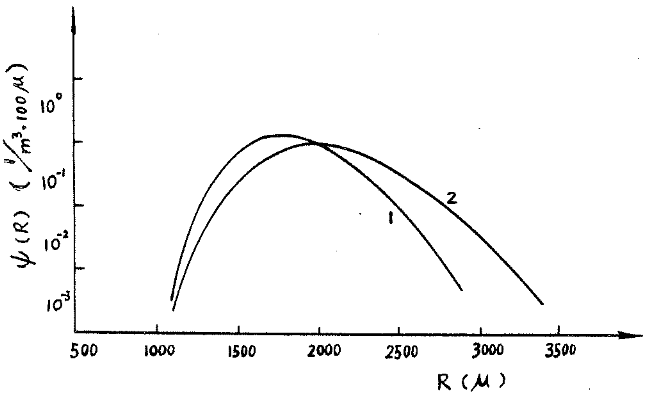

Fig.7. The influence of the dimension of cloud cells on spectrum of raindrops fallen out of the cloud base.
1 - $L_n = 70$ m , 2 - $L_n = 80$ m .

In a word the larger the values of r, M, L_n the more favourable the conditions for the formation of precipitation will be. This result is in good agreement with the field observation that intense precipitation is usually released from the convective cloud with stronger fluctuation or turbulence.

6. Summary

A model of particle growth in stochactic process in the cloud has been proposed based on the observed structure of convective cloud, the conclusion of calculation are as follows:

(1) The rainfall or hailfall could be produced in shallow cloud. The result also provides some basis for field work of artificial rainfall, for instance, rainfall could be expected after adequate quantity of larger waterdrops are sprayed to cloud with cells structure even if the cloud is not thick.

(2) The concentration of precipitation particles and hailstones obtained by these calculations in accordance with field observations. So that we found that our model in realistic.

References

(1) Vulfson. N., 1961: Studies of convective motions in the free atmosphere. Akad. SSSR Press, Moscow.
(2) Huang Mei-yuan, 1963: The microstructure of cumulus clouds. Izv. Akad. Nauk SSSR Ser. Geodiz. NO.2, 362-376.
(3) Xu Hua-ying and Gu Zhen-chao, 1963: On the formation of precipitation element in cloud with fluctuation. Acta Meteorologica Sinica, Vol.30, NO.1, 108-114.
(4) Xu Hua-ying and Gu Zhen-chao, 1966: On the formation of precipitation element in a shallow warm-cloud. Scientia Sinica, Vol.15, NO.1.

III.4 - Orages

Storms

DROP-SIZE DISTRIBUTIONS AND VERTICAL AIR MOTIONS IN A THUNDERSTORM AS INFERRED FROM DOPPLER RADAR OBSERVATIONS AT VERTICAL INCIDENCE

P. Amayenc and D. Hauser

Centre de Recherches en Physique de l'Environnement
Issy les Moulineaux FRANCE

1. INTRODUCTION

On July 18th 1978, the two C-band doppler radars of the RONSARD system (λ = 5.3 cm, peak power 250 kw, one way beamwidth 0.9°) were involved in an experiment aimed at studying convective storms near Zürich (Switzerland) and were situated 30 km apart. The present study deals with data gathered during about half an hour, between 1640 and 1810 UT, by means of the two radars in a moderately convective storm moving over radar R2, along the radars baseline from R2 towards R1. One of the radars (R2) operated vertical incidence soundings (VIS) sequences while the other one (R1) performed tilted scans within a space volume including the vertical sounding zone of the R2 radar. The nearest meteorological radiosounding at 14 UT (20 km away from the radars) indicates convective instability conditions between 2.5 and 8 km, with the 0°C isotherm level at 3.2 km and the -10°C isotherm level at 5 km. The R2 radar performed 7 successive VIS sequences of 135 s each which have been located within the general structure of the storm provided by the R1 radar data (Part 2). The purpose of this paper is to present some results concerning the drop-size distributions (for diameter greater than 100 μm) and the vertical air motions inferred from the VIS data by using a method described in part 3. The main features of their observed structures and these of the associated global parameters Ƶ (total reflectivity factor), M (rain water content) and R (rainfall rate) are presented and discussed in part 4, including a study of some classical relationships between Ƶ, M, R and the width of the DSD.

2. GENERAL STRUCTURE AND MOTION OF THE STORM

Data of radar R1 provide the general structure and motion of the storm. The precipitating zone extends horizontally over a space area of about 20 x 20 km and vertically up to about 8 km. The analysis of the horizontal motion of the reflectivity factor patterns indicates that the storm is advected at a velocity of about 20 m s^{-1} along the baseline of the radars. Figure 1 shows the Ƶ structure from R1 in the vertical plane including the radar baseline. A great variability is observed in the intensity and vertical extent of the structure of Ƶ, revealing the existence of different subcells. The successive parts of the storm which were observed during the seven VIS (T1 to T7) of the radar R2 are also indicated in that figure.

In figure 2 is shown the small scale structure of Ƶ in a height time representation for each of the seven VIS's corresponding to an analysis of the storm over an horizontal extent of about 2 km (taking into account the advection speed). A good agreement was found between the mean altitude profiles of Ƶ obtained from i) R1 data averaged over horizontal space in the zone relative to a given VIS ii) the time averaged R2 data corresponding to the same VIS. This indicates that the observed internal structure of the storm is advected without noticeable deformation.

3. VIS DATA ACQUISITION AND PROCESSING

The general characteristics of the RONSARD radars can be found elsewhere (NUTTEN et al., 1979). Those relative to VIS were : PRF = 732 HƵ, velocity span 19.6 m s^{-1}, velocity spectral resolution : 0.32 m s^{-1}, range gate length (spacing) 200 m (400 m), simultaneous data acquisition in 4 range gates within 88 ms. A unit scan covered the altitude range 0.8 km (minimum observation range) to 10.2 km or 1 km to 10.4 km, performing data acquisition in 24 range gates during 0.53 s. Each VIS sequence, operated during 135 s corresponding to 256 samples in each range gate. An off line program (see HAUSER and AMAYENC 1980, for details) was applied to the tape recorded complex time series (64 points) in order to determine the doppler spectra, and the doppler parameters Ƶ (total reflectivity factor), V_D (mean doppler velocity) and σ (doppler velocity standard deviation). Finally, in each range gate, the average values of these quantities were calculated, for stationary data, within 8 s periods (corresponding to a 25 % statistical fluctuation). Figure 3 illustrates the time-height structure of Ƶ, V_D and σ relative to the first VIS sequence. For this sequence as for the following ones, no bright band effect appears, which could reveal a clear partition between ice crystals and raindrops regions. The absence of large values of σ (> 2 m s^{-1}) excludes the presence of hail (no hail was observed at ground level) and indicates no strong effect of spectral broadening due to turbulence. In fact, the values of σ are typical of those of raindrops spectra (0.6 to 1.5 m s^{-1}). Local moderate turbulent broadening of the spectra is not excluded but has been neglected. Consequently, the doppler spectra were assumed to result essentially from the fall velocity spread of raindrops with a global shift due to the vertical air motion. The method used to infer the drop-size distributions (DSD) and the vertical air velocity w from the doppler spectra has been suggested by ATLAS et al (1973) but, as far as we know, it has never been used. It consists in determining the mean fall velocity V_T of raindrops by using an empirical V_T - Ƶ relationship proposed by JOSS and WALDVOGEL (1970) :

(1) $V_T = 2.6\ Ƶ^{0.107}$ (Ƶ in $mm^6\ m^{-3}$, V_T in $m\ s^{-1}$)

This relationship established from ground DSD's measurements can be extended to any altitude by using an appropriate correction for air density decrease (FOOTE and DU TOIT, 1969) and allows to determine w from V_D and Ƶ values :

(2) $w = V_D - V_T$ (all velocities negative upward)

The drop-size distribution N(D) in each diameter interval (D, D + dD) is then calculated classically from :

(3) $N(D) = D^{-6}\ z(v_T)\ dv_T/dD$ with $v_T = v_D - w$

where $z\ (v_T)\ dv_T$ is the measured reflectivity factor in the spectral velocity interval (v_T, $v_T + dv_T$) and v_D is the doppler velocity. In expression (3) the fall velocity-diameter dependance $v_T(D)$ at ground level has been taken from the analytical expression given by ATLAS et al (1973) representing the data of GUNN and KINZER (1948) within $\pm$ 2 %. This approach avoids any assumption on the form of the DSD which may widely vary in convective situations. However, each calculated DSD was characterized by determining the two classical N_o and λ parameters of the exponential distribution $N(D) = N_o \exp(-\lambda D)$, which best represents the actual one. For each distribution the values of the parameters D_o (median volume diameter) R and M were calculated.

4. RESULTS AND DISCUSSION

4.1 Drop size distributions and vertical air motions

From the study of the seven VIS sequences some general features were deduced. They are analysed hereafter with detailed illustration (fig. 4) and description for the first VIS sequence results. The vertical air motion is characterized by a weak downdraft under 1 800 m and an updraft increasing versus altitude up to 8 to 10 $m\ s^{-1}$ in the region of upward mean doppler velocity (see fig. 3). The values of N_o indicate a large variability (0.1 to 10 cm^{-4}) with a clear tendancy to increase with height, while the values of λ varies within a factor of 2, and are minimum ($\lambda < 30\ cm^{-1}$) -i.e. the width of the DSD's is maximum- in the region of maximum Ƶ. The height-time structures of D_o (0.5 to 2.3 mm), M (0.2 to 0.9 $g\ m^{-3}$) and R (1 to 25 $mm\ h^{-1}$) are well-organized and related to the reflectivity factor pattern with maximum values of all these parameters occurring in the same regions. Note that R is the rainfall rate calculated using the fall velocity of scatterers i.e. excluding the effects of the vertical air motions. These general features remain unchanged from one VIS to the other despite the high variability of all the parameters. Moreover, the more intense updrafts are observed during sequences evidencing the highest Ƶ values (VIS sequences T1 and T6).

Figure 5 illustrates the time averaged altitude profiles of the parameters w, V_D, λ, D_o, M, Ƶ for the first VIS. A balance level, corresponding to the level $V_D = 0$ as defined by ATLAS (1966) clearly occurs near an altitude of 4.8 km. It is located slightly under the level of maximum updraft (5.6 km) in agreement with ATLAS' analysis. An increase in the rain water content M is observed from the top of the cloud down to a maximum located under the balance level (3.6 km). In the same region there is a progressive increase in the DSD's width (increase in D_o in decrease of λ) with no particular feature when crossing the balance level. The same characteristics are observed for other VIS when a balance level exists (T2 and T6). The value of M decreases abruptly by a factor 2 from its maximum and then becomes almost constant in the lower altitude region (under 3 km) even though the DSD's exhibit a clear narrowing which could be related to the weak downdraft zone.

The actual shape of the DSD's was also studied by using a shape parameter s, as defined by JOSS and GORI (1976) and calculated here from median diameters involving the second and sixth moments of the DSD. This parameter characterizes the deviation of the shape of the DSD from an exponential one for which s = 1. A value of s greater (smaller) than unity indicates a concave (convex) shape of the size distribution on a semi-log plot. The values of s relative to the 7 VIS sequences indicate 49 % of convex type ($s < 0.9$), 22 % of exponential type ($0.9 \leqslant s \leqslant 1.1$) and 29 % of concave type DSD's. No clear organized height time structure of s was found in any of the studied VIS. In particular the balance level region is not associated with any local change in the shape of the DSD's even though it is generally thought to be a region of particles sorting owing to wind divergence effects. This is in agreement with the theoretical results of SRIVASTAVA and ATLAS (1969). In fig. 5 is also plotted the mean height profile of s, showing a majority of DSD's of convex type shape ($s < 1$) except for the lower region where a clear transition towards exponentially shaped ones is evidenced.

4.2 Ƶ - R, Ƶ - M, λ-R, N_o-R relationships

Some of the classical relationships between Ƶ, R, M and the parameters N_o and λ were determined each time adjusting the coefficients a and b of a $Y = aX^b$ law by a least square fitting. This method was successively applied to the 7 VIS data (limited to data under the 0°C isotherm level) showing a small spread in the studied relationships. Consequently only the mean results over the entire set of data (7 VIS or 463 samples) are presented. Table 1 indicates Ƶ - R, Ƶ - R* and Ƶ - M relationships and the corresponding values of the determination coefficient r^2. A weak correlation ($r^2 = 0.64$) is found between Ƶ and the rainfall rate R* not corrected for vertical air motions. Conversely, Ƶ and R (corrected for vertical air motion) are strongly correlated ($r^2 = 0.99$) as shown on fig. 6. This shows that the presence of vertical air motions can introduce strong distorsions in the relationship between Ƶ and the rainfall rate. When compared to the Ƶ - R relationship of MARSHALL and PALMER (1948) and of SEKHON and SRIVASTAVA (1971) the differences for R are within a range of 40 % for the 20-45 dBƵ range of Ƶ. The parameters Ƶ and M are also highly correlated ($r^2 = 0.97$) and the value 1.91 of

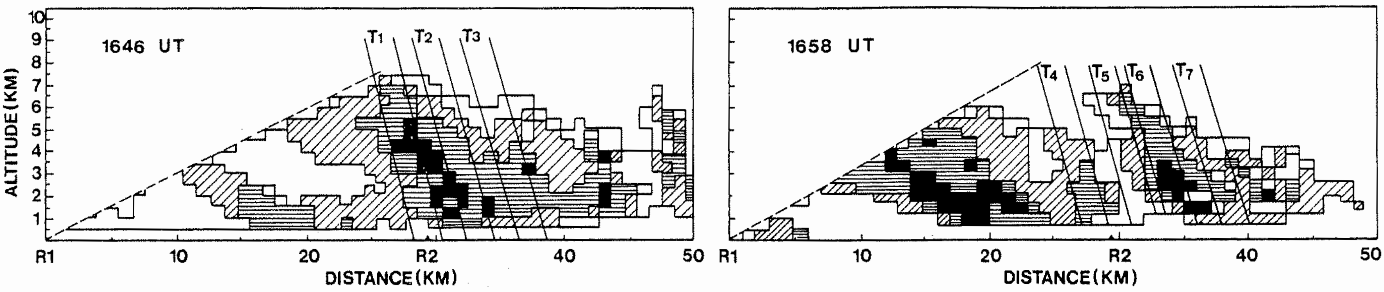

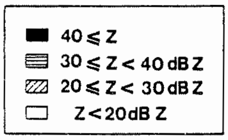

Fig. 1 : *Cross section of the reflectivity factor in the vertical plane including the radar baseline (R1-R2) as inferred from 2 sequences (starting at 1646 and 1658 UT) of radar R1, scanning at increasing elevation angles. The regions T1 to T7, drawn by taking into account the storm's advection, correspond to those sampled by radar R2 at vertical incidence.*

the exponent of M is in agreement with the observation of a majority of convex distributions since a value of 2 is expected for monodisperse distributions and a value of 1.75 for exponentially shaped ones. No correlation is found between N_0 and R. The direct λ - R relationship is characterized by a smaller determination coefficient ($r^2 = 0.85$) expected to result from the observed variability of N_0, as suggested by ULBRICH and ATLAS (1978). In order to take this N_0 variability into account, a λ - R/N_0 relationship was sought, and the result indicates a better determination coefficient ($r^2 = 0.96$). Furthermore the substitution of the MARSHALL and PALMER (1948) N_0 value in the λ - R/N_0 expression leads to $\lambda = 39\ R^{-0.20}$, which is very close to the expression $\lambda = 41\ R^{-0.21}$ obtained by the latter authors. This means that the obtained relationship between λ and the reduced parameter R/N_0 is implicitly in agreement with the M-P one. However, the value of N_0 must be known in order to relate uniquely the width of the DSD to the corresponding rainfall rate.

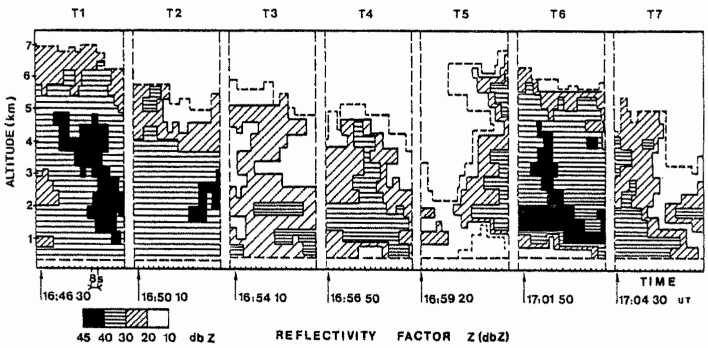

Fig. 2 : *Height-time patterns of Z as inferred from the 7 vertical incidence soundings of radar R2 (135 s duration each, starting times indicated by arrows). These patterns are obtained from data averaged over 8 sec periods in each range gate. Dashed lines indicate the limit of observations.*

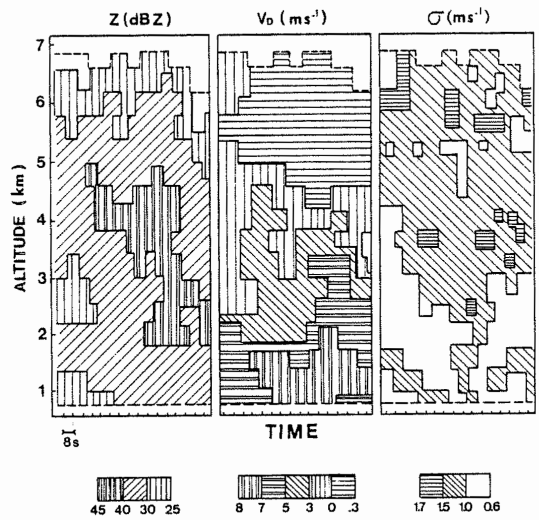

Fig. 3 : *Height-time patterns of the reflectivity factor Z, mean doppler velocity V_D (negative upward), and doppler velocity standard deviation σ, for the first VIS sequence T1 (164630 to 164845 UT). Same representation as in fig. 2.*

REFERENCES

ATLAS D. (1966), J. Atmos. Sci., 23, 635-651.
ATLAS D., R.C. SRIVASTAVA and R.S. SEKHON (1973), Rev. of Geoph. and Space Phys. 11, 1-35.
FOOTE G.B. and P.S. DU TOIT (1969), J. Appl. Met., 8, 249-253.
GUNN K.L.S. and G.D. KINZER (1948), J. Meteor., 6, 243-248.
HAUSER D. and P. AMAYENC (1980), Proc. of 19th Rad. Met. Conf., Miami (Fl.), AMS Boston Mass, to appear.
JOSS J. and WALDVOGEL A. (1970), Proc. of 14th Rad. Met. Conf., Tucson Ariz., AMS Boston Mass, 153-156.
JOSS J. and E. GORI (1976), Riv. Ital. Geofisica and Sci. Aff., III (5-6) 275-283.
MARSHALL J.S. and W.M.K. PALMER (1948), J. Meteor., 5, 165-166.
NUTTEN B., P. AMAYENC, M. CHONG, D. HAUSER, F. ROUX and J. TESTUD (1979), IEEE Trans. on Geos. Elec, GE-17 (4), 281-288.
SEKHON R.S. and R.C. SRIVASTAVA (1971), J. Atmos. Sci., 28, 983-994.
SRIVASTAVA R.C. and D. ATLAS (1969), J. Atmos. Sci., 26, 535-544.
ULBRICH C.W. and D. ATLAS (1978), J. Geoph. Res., 83, 1319-1325.

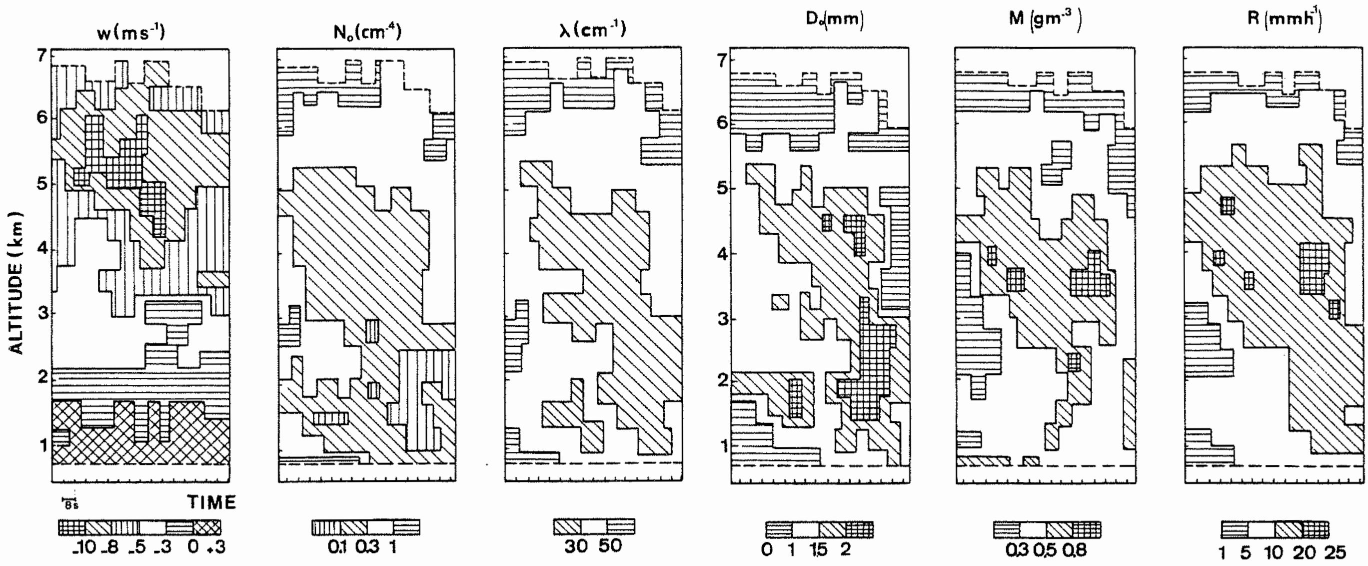

Fig. 4 : *Same as fig. 3, but for the vertical air velocity w (negative upward), N_0 and λ parameters of the drop-size distributions, mean volume diameter D_0, rain water content M and rainfall rate R.*

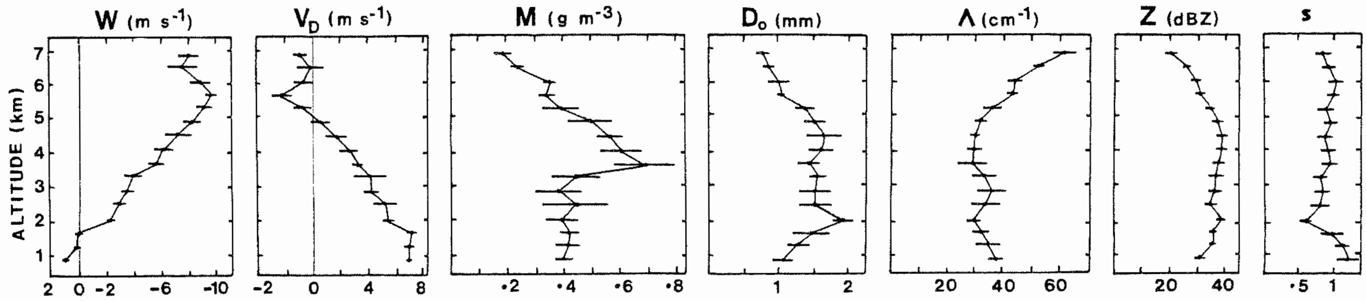

Fig. 5 : *Height profiles of the same parameters as shown in fig. 4, and of the shape parameter s of the drop-size distribution (see text), averaged in each range gate over the duration of the sequence (135 s). Bars indicate the standard deviation due to time variation of the parameters.*

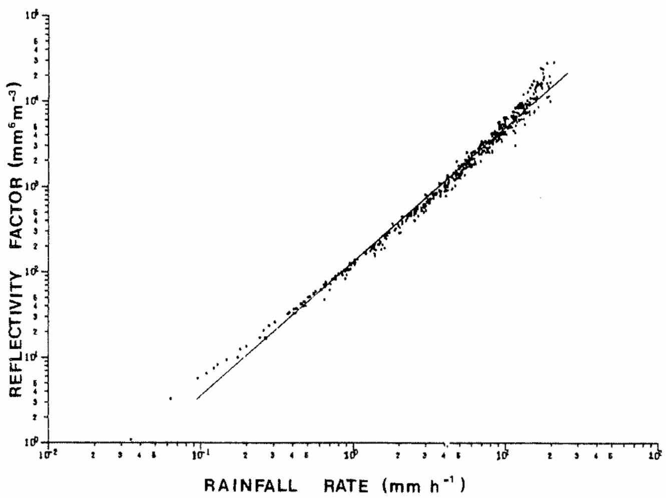

Fig. 6 : *Z versus R from the 7 VIS data limited to altitudes under the 0°C isotherm level (463 samples). The adjusted relationship $Z = 135\ R^{1.58}$ is indicated by a straight line.*

Table 1

Z - R	Z - R^*	Z - M
$Z = 135\ R^{1.58}$ $r^2 = 0.99$	$Z = 595\ R^{1.09}$ $r^2 = 0.64$	$Z = 2.7\ 10^4\ M^{1.91}$ $r^2 = 0.97$
λ - R	N_o - R	λ - (R/N_o)
$\lambda = 57\ R^{-0.24}$ $r^2 = 0.85$	$r^2 = 0.04$	$\lambda = 65(R/N_o)^{-0.20}$ $r^2 = 0.96$

Units : Z : mm^6m^{-3} ; R, R^*: $mm\ h^{-1}$; M : $g\ m^{-3}$;
λ : cm^{-1} ; N_o : cm^{-4}

A JOINT NUMERICAL AND OBSERVATIONAL STUDY OF CUMULONIMBUS CLOUDS

D.A.Bennetts and F.Rawlins

Meteorological Office, Bracknell, U.K.

1 Introduction

In order to investigate the interaction of cloud microphysics and dynamics a three dimensional numerical model of a cumulonimbus cloud has been developed. This is based on the non-hydrostatic, pressure co-ordinate model of Miller and Pearce (1974), with a grid resolution of 1 km x 1 km x 50 mb, and has been extended to include a parametrization of the ice phase.

Numerical results are compared with atmospheric data obtained from aircraft measurements over the sea in the region of the U.K. This allows an identification and adjustment of certain model parameters to give the best agreement with observations. Particular cases requiring further modification to reproduce observed behaviour can then be examined individually.

2 Moist parametrization

The water phase representation follows Kessler (1969) and includes water vapour (q), cloud water (l) and rain (l_r) mixing ratios as model variables. The processes described are: autoconversion of cloud water to rain, accretion of cloud water by rain and the evaporation of rain. Supersaturated water vapour is assumed to be instantly condensed.

The ice phase parametrization is similar to that of Wisner, Orville and Meyers (1972) and requires the bulk variables: hail (assumed to be all ice particles with radii greater than 300 μm) and three size classes of cloud ice in the ranges 0-100, 100-200, 200-300 μm radius. The ice phase is initiated by the activation of ice nuclei, assumed to be already in supercooled cloud drops, with the Fletcher (1962) expression $N=10^{-2}\exp(-0.6T)$ for the number activated per m^3 where $T^\circ C$ is the temperature. The cloud drops are considered to be distributed as in Mossop, Cottis and Bartlett (1972).

Ice phase calculations provide for the accretion of cloud water by hail, the freezing of rain by accretion of cloud ice, the accretion of cloud water by cloud ice, the melting of hail, the sublimation of water vapour by ice particles and the resultant transfer between the ice size classes. Contact nucleation and ice crystal multiplication processes are not included.

3 Route of precipitation

The present scheme allows two routes by which precipitation can form: namely cloud water-rain-hail and cloud water-cloud ice-hail. Preliminary integrations with an average mid-latitude sounding were performed in order to investigate the effect of the two routes. It was found that, for realistic ice nuclei activation rates, the route was predominantly controlled by the parameter α and l_{crit} in the autoconversion expression

$$\frac{dl_r}{dt} = \begin{cases} \alpha(l-l_{crit}) & l > l_{crit} \\ 0 & l \leqslant l_{crit} \end{cases}$$

The cloud water-rain-hail route was favoured in a typical mid-latitude cloud if lcrit was small (or α large). Then rain formed low and early in the clouds' lifetime leaving little cloud water to produce cloud ice or hail. The ground rainfall quickly decayed after reaching a quasi-steady maximum rate.

The cloud water-cloud ice-hail route was favoured if l_{crit} was large (or α small). This inhibited rain production and the precipitation occurred later in the clouds' lifetime. It was of longer duration but less intensive.

l_{crit} is mainly a function of the cloud condensation nuclei spectrum and updraught speed; a one-dimensional model indicated that its value should lie in the range 2.0 to 2.5 gm/kg for a wide variety of spectra in a typical maritime mid-latitude airmass. In physical terms it is closely related to the 'height of first echo'.

4 Measurements

The Met Research Flight C130 aircraft was used to obtain simultaneous visual and radar images throughout the chosen clouds' lifetime. The aircraft was flown in a racetrack figure with photographs being taken from a forward facing camera. The E290 X band radar scans 180° ahead of the aircraft and was elevated and depressed from +15° to -15° to enable a complete coverage of an area approximately 60x60 km by 10 km deep.

The photographs allowed the rate of rise of cloud top to be determined and the radar outlined the regions of precipitation, with a threshold estimated to be about ¼ mm/hr. A profile of thermodynamic measurements was made in the surrounding clear air and was supplemented with nearby radiosonde ascents to provide the initial sounding for the model.

Two such flights have been analysed: H182, 16th February 1977 and H320, 9th March 1979, both off the north west coast of Scotland. Two neighbouring but separate clouds were measured in the former flight; one a small single celled cloud and the other a large multicell cumulonimbus.

5 Parameter 'tuning'

The small cloud in H182 was used to determine those parameters not fully constrained theoretically. The vertical diffusion coefficient in the dynamical calculations was found from the rate of rise of cloud top. This cloud was observed early in its life-cycle and to account for the first echo height l_{crit} was required to be 2.0 gm/kg. In order to best reproduce the distribution and duration of the precipitation a value of $\alpha = 0.00025\ s^{-1}$ was used. The ice nuclei spectrum was found to play a secondary role, providing that realistic values were specified.

These adjustments produce a self-consistent framework which have sufficed for the limited range of clouds studied. Any large disparities from observations found in the future will point to limitations of the parametrization scheme.

6 Multicell cloud dynamics

The H182 single cell cloud was simulated with the sounding and hodograph given by Figure 1, with a surface temperature perturbation of $2^{\circ}C$; this gave a maximum cloud top at 4 km, as was observed. The H182 large cloud was initiated with a $2.75^{\circ}C$ perturbation, allowing agreement with the measured cloud top height of 7 km. The numerical results led to the following description of

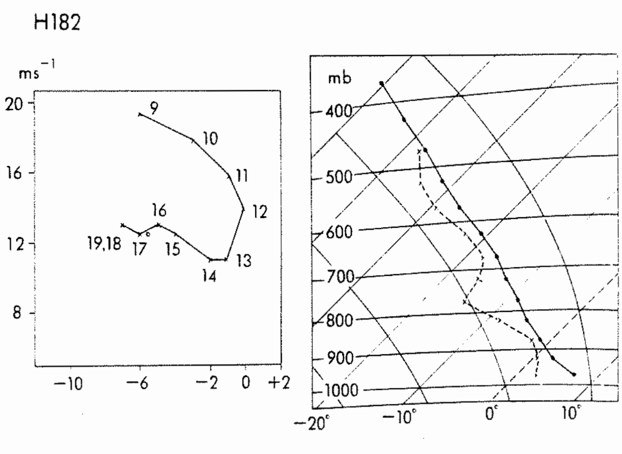

Figure 1 Sounding for H182 at pressure levels of model (50 mb intervals). The circle marks the simulated cell velocity in the hodograph

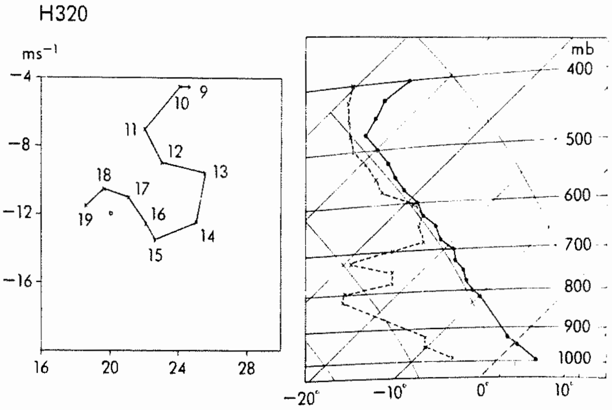

Figure 2 As for Figure 1 for case H320.

dynamical development.

The updraught, vertical in the early stages, had a downshear slope by the time that precipitation had reached the surface. The downdraught first formed at 700 mb downshear of the updraught and progressively extended downwards until it reached the surface, when the rainfall rate was at its maximum intensity of 25 mm/hr. The downdraught provides a frame of reference for the cloud since it is relative motion with respect to the cell which determines the storm evolution.

On reaching the surface the downdraught spread out in all directions, though more rapidly to the west, with the low level winds (relative to the cell). This produced a density current with a temperature deficit of $3^{\circ}C$, creating a gust front at the interface with the undisturbed air. This interruption to the supply of inflowing moist air caused a separation and weakening of the low level updraught, schematically indicated in Figure 3. The gust front created a ring of convergence around the downdraught with a near stationary region on the low level inflow flank i.e. the east. A second cell grew in this position, reaching a height of 7 km, and eventually supplanting the original cell. The rainfall rate and cell movement are shown in Figure 4 where the frame of reference is fixed and corresponds to the storm as a whole. The photographic and radar measurements confirm that the position and height of the daughter cell were correctly reproduced.

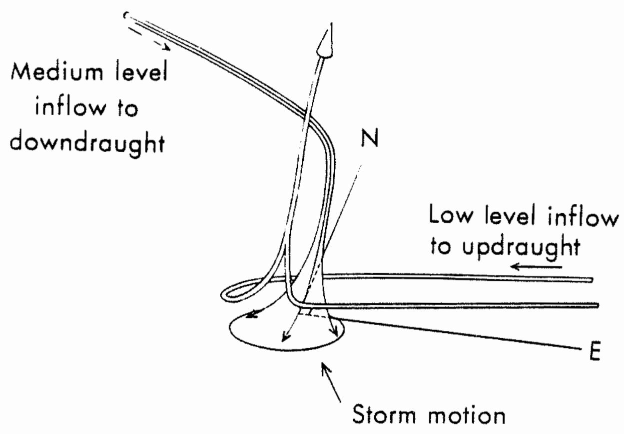

Figure 3 Schematic diagram of downdraught and inflow interaction for H182 cloud.

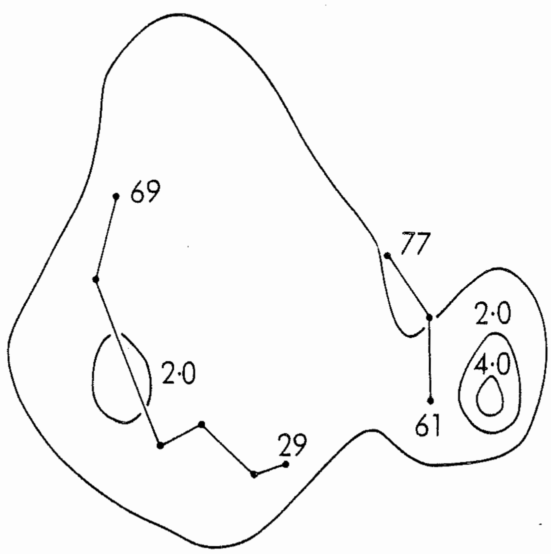

Figure 4 Rainfall intensity in mm/hr for H182 multicell cloud at time = 61 minutes (simulation). The cell tracks are also shown relative to the observation frame at times given in minutes.

The H320 storm was also multicellular and the hodograph, in Figure 2, was similar to the previous case. However the low level moisture in the clear air sounding (see Table 2) was insufficient to grow a cloud in the model; therefore 0.5 gms/kg was added to the two lowest layers for the integration. The cell produced was mostly glaciated and the precipitation route cloud water-cloud ice-hail was predominant, with a maximum rainfall rate of 15 mm/hr. A weaker downdraught was therefore created although the early behaviour was similar to that of H182 multicell cloud.

In this simulation the southern segment of the inflow branch was maintained - light precipitation fell directly on the northern branch due to the upper level winds. Two regions of low level convergence at the gust front were favoured to form incipient daughter cells on the south-west and east flanks. The atmospheric observations showed a number of daughter cells being formed all round the southern side of the main cell, though not being easily distinguishable as separate entities.

7 Discussion

The main features of both the large multicelled clouds were accurately reproduced without further tuning of the parameters. However it is instructive to consider how sensitive the numerical results are to these parameters.

The large cloud on flight H182 was relatively insensitive to change. The removal of the whole of the ice phase reduced the amount of precipitation and resulted in a weaker downdraught. A daughter cell still grew on the east flank; however it was weak and only attained half the observed height (7 km). Such a system can be considered to be strongly organised. Its basic structure is invariant and only the finer details are affected by changes to the parametrized microphysics.

The H320 multicell simulation displayed a greater variation. The location of the secondary growth varied with parametric changes. This cloud can be considered weakly organized.

Two reasons are advanced for this behaviour. For H320 the convection is weak, implying that the critical perturbation is a larger fraction of the total energy than for H182. (A basic assumption of the model is that advective processes dominate turbulent transfer.) Secondly H320 shows a large directional shear beneath cloud base whereas in H182 it was unidirectional. This implies that in the former cloud the interaction of the gust front with the low level winds is strongly dependent on height, a feature that is poorly resolved in the model.

8 Conclusions

The results presented indicate that once a matched parametrization scheme has been established the main features of the numerical simulations are robust to small changes in that scheme. Furthermore the atmospheric observations for this small sample of clouds can be reproduced without further parametric adjustment.

The incorporation of the ice phase is important for the accurate description of mid-latitude clouds both for the extra latent heat released and more importantly in the determination of the relative contributions of the two routes to produce hail. This allows accurate simulation of the downdraught and the development of secondary cells.

With the 'tuned' model it is possible to distinguish the different dynamics of the two storms H182 and H320. The former is strongly organized, its basic features being dynamically controlled and the microphysics only determining the finer details. The latter case is weakly organized with the position of the new cell being dependent on the details of the microphysical simulation.

9 References

Fletcher N.H., (1962) "The physics of rainclouds.", Cambridge University Press.

Miller M.J. and Pearce R.P., (1974) "A three-dimensional primitive equation model of cumulonimbus convection.", Quart.J.R.Met. Soc., 105, pp 833-848.

Mossop S.C., Cottis R.B. and Bartlett B.M., (1972) "Ice crystals concentration in cumulus and stratocumulus clouds.", Quart. J.R.Met.Soc., 98, pp 105-123.

Wisner C., Orville H.D. and Meyers C., (1972) "A numerical model of a hail bearing cloud.", J.Atmos.Sci., 29, pp 1160-1181.

DYNAMICS AND THERMODYNAMICAL STRUCTURE OF SUPERCELL HAILSTORM

N.Sh. Bibilashvili, G.S. Bartishvili,
A.N. Kovalchuk, T.N. Terskova

HIGH MOUNTAIN GEOPHYSICAL INSTITUTE,

NALCHIK, U.S.S.R.

The experimental results of investigations of dynamics and thermodynamical structure of hail clouds based on data analysis of radar, aerological and mesoscale networks which were made over 1972-1977 on research polygon / North Caucasus / are given.

Radar structure of hail clouds was investigated by radars with 3,2 and 10 cm wavelengths according to special program, making it possible to obtain series of horizontal sections of radar echo zones with 3-5mn intervals and altitude spacing of 1-2 km from the first radar echo appearance of the cloud before its dissipation / 1 /.

Thermodynamical parameters and air flow circulation in hail cloud region were studied by frequent radio-sounding and radar tracing of the sound and chaff movement which were sent to the cloud development zone / 2 /. Transformation of meteorological element fields was analyzed on the data of surface mesoscale network instrumented by meteorological recorders / 3,4 /.

The information about conditions of embryo hail formation and growth in studied clouds was obtained on the basis of analysis of hailstone crystal structure and deuterium concentration in water samples of ice bedding of hailstones / 6 /.

On the basis of common analysis of obtained data basic regularities and control mechanism of hail cell development were found out. The model of space-time evolution of mesoscale circulation and thermodynamical properties of updraft within severe hail cell was created.

As radar observations showed the convective processes in studied region are not differentiated unambiguously according to radar echo structure as it is typical for other regions of the world / 5 /.

In most cases hail clouds have multicell structure, sometimes transforming into one supercell and vice versa.

Interaction of cloud cells has compensative character and causes the process of cloud pulse regeneration related to formation and strengthening of mesofront, dividing the updrafts and downdrafts. The duration and intensity of pulses increases with development of process from 10 to 15 mn to 20-30 mn at initial period for severe hail cells.

Pulse development of the cloud is determined by accumulation of hydrometeors and is expressed in pulse change in time of cloud radar parameters. The upper boundary of radar echo and maximum reflectivity are the most quasi-steady parameters, while the volume zone of increased reflectivity of the supercooled part of the cloud is the least stable one. Transformation of the structure of the first radar echo shows the quickness of hail formation process. The first radar echo zone with $\eta = 10^{-12}$ - cm^{-1} / λ =3,2 cm / is formed firstly over the range 3-5 km above S.L. and with $\eta=10^{-7}$ cm^{-1} -6-9 km above S.L. The mean value to reach the ground by the radar echo from its appearance is 8-10 mn.

It was found out that the development of severe hail cells is determined by the disturbances of thermobaric fields of the same scale. The evolution of these mesoscale disturbancesin virture of feedback is the main control mechanism, transforming primary developed convective cell complex into organized, self-maintaining and surviving hail system.

Hydrostatic power is the main driving one at the initial period of the maximum cell development, but at the second period of their existence the hydrodynamic influence prevail due to disturbance of the baric gradient power.

The main role of the pressure field disturbances is underlined in organization and support of the closed vertical circulation / updraft and downdraft / inside severe hail cell at the period of its maximum development. Above mentioned mechanism leads to cloud and rain particle recirculation inside a cell and it is responsible for its sharp intensification and large hail growth.

Fig.1 shows the schematic model of air fluxes, thermobaric perturbation for the begining of maximum development of severe hail cell.

The begining of the formation of closed circulation system is related to low warm mesocyclone formation in the cell at the cloud base level.Its arising is mainly due to considerable heat release of condensation at warm

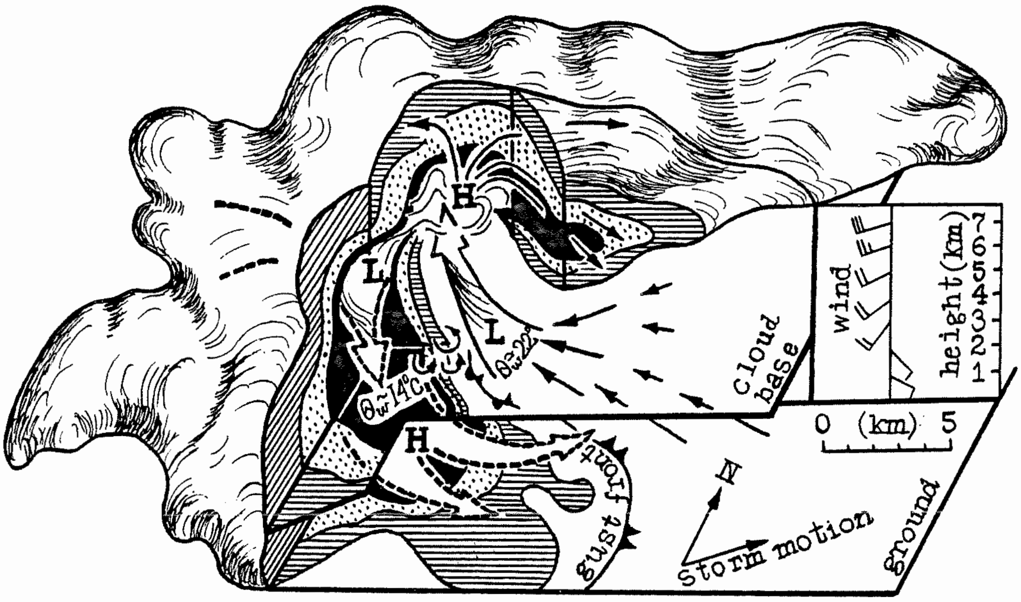

Fig.1 The schematic model of severe hail cell. Updraft is shown by solid arrows; downdraft is shown by dashed arrows.

wet air flow into the cell base.

In our cases the values of pressure deficit at low cwll levels changed mainly within 2-5 mb, the maximum observed value reached 10mb. The warm wet updraft is observed up to mean levels /appr. 500 mb / in central and northern mesocyclone parts. Because of heating, relative geopotential of isobaric surfaces inside updraft increases, the isobaric surface altitudes rise in its upper part and by the time it leads to the onset of the ageostrophic outflow in this region.

The resulting current distribution influenced by adaptation of wind field to pressure field corresponded with case of gradual filling up of low cyclone /mesoanticyclone / and its conversion into high mesoanticyclone / mesocyclone /.

During this period the titled cyclogenetic axis links low level convergence with the convergence at the mid levels in the cell.

The result of thermobaric perturbation evolution, adapting to its wind field disturbances and the main circulation branches - updrafts and downdrafts, respectively - low level cyclone cooling gradually and filling upwards, converts into the erect mid level cooled vortex to the second part of its maximum stage. During this period the inflow and outflow in the cell is due to disturbances of pressure gradient powers, influenced mainly by nonhydrostatic pressure. Distribution of pressure and wind field disturbances in the cell becomes opposite to initial distribution at the corresponding levels at the second part of its maximum stage.

It should be noted that the mid period of the maturity stage corresponded mostly to quasi-steady conception when there was the inflow balance at low /mid / levels and outflow at mid /low/ levels within the cell for updraft/ Downdraft/. Up to this period the intensification of updraft and accompaning downdraft is observed; the outflow at corresponding levels exceeds inflow. To the end of maximum development stage the above mentioned relation changed to opposite, resulting in gradual dissipation of flows. Gradual development periods followed by abrupt periods/cascade/ leading to the new growth impulses. Cyclogenetic axis becomes titled again but the link with new low level cyclone located ahead is realized where the greatest pressure deficite at the point of occlusion is observed.

The existence of well-organized, self-regenerating convection cell system is distroyed either by large-scale circulation changing or water supply depletion.

Thus, severe convective cell in its mature stage represents a stable system of two interacting well-organized air flows - updraft and downdraft - with absolute maximum vertical velocity up to 25-30 m/s. The most stable vertical velocity values in the moderate intense cells are 10-15 m/s, and for more severe sells - up to 20-25 m/s. Undeluted cores of these flows are located in close proximity to each other at mid cloud levels / appr. 3-6 km a.g.l. /. The maximum vertical velocities are observed in the adjacent sides of both flows at upper /low/ mentioned levels for updraft /downdraft/.

Updraft/downdraft/ region is the warmest/coldest/ part in the cell; virtual temperature differences between them may reach about 10°C. In the cores of strong updrafts /downdrafts/ air flow moves along wet adiabat, but air from weaker outlying flows is drawn rectilinear at some angle in the main flow core.

Intermediate layers of 1-2 km power at low and mid levels in the cell are the most important in hail growth process. An active air involving and mixing from the strongest updraft/downdraft/ into downdraft /updraft/ leading to rain particle recirculation and, as a result of this , to intensive and accelerating hail growth process, is observed. Significant turbulence occuring initially at these levels in intermediate zones at the updraft and downdraft boundary makes an additional influence on these processes. Cloud and fine rain particle recirculation from the cell front part descending at strengthening of low level convergence in mesocyclone is observed, In observing significant divergence in updraft at mid levels at environment produces a natural subseeding by rain particles ahead the cell.

In studied cases a similar distribution of vortex flows and radar echo structure was observed up to 30mn. A persistent hail fallout from individual cloud for 2-3 hours is the result of individual cell self-regeneration or new cell initiation. Both these processes occur in mesofront region and it is often difficult to differenciate them even at persistent radar echo observations since the inflow localization region supporting the cloud development is specified by mesofront localization in subcloud layer.

Fig.2 shows the transformation of flows and severe hail cell radar echo zone during hail fallout. Descending and enlarging of particles in front part form an overhang , spreading downward and gradually dissecting updraft and cutting its main part. Sharp particle descent occurs in cell rear, moreover, this process has always three-dimentional character. More intensive descent is observed in the right rear reginn, where sharp cyclonic / U /-turn of precipitation zone occurs causing mesofront displacement and warm wet inflow dislocation.

The crystal structure analysis of the samples of thin section hailstones shows that in the conditions of Northern Caucasus the hail embryos are usually formed in the range -4 - -10°C as a result of large droplet freezing /DIAM appr. 1-2 mm/. Measurement data of deuterium concentration in hailstone ice layers show that the large hailstones grow as a

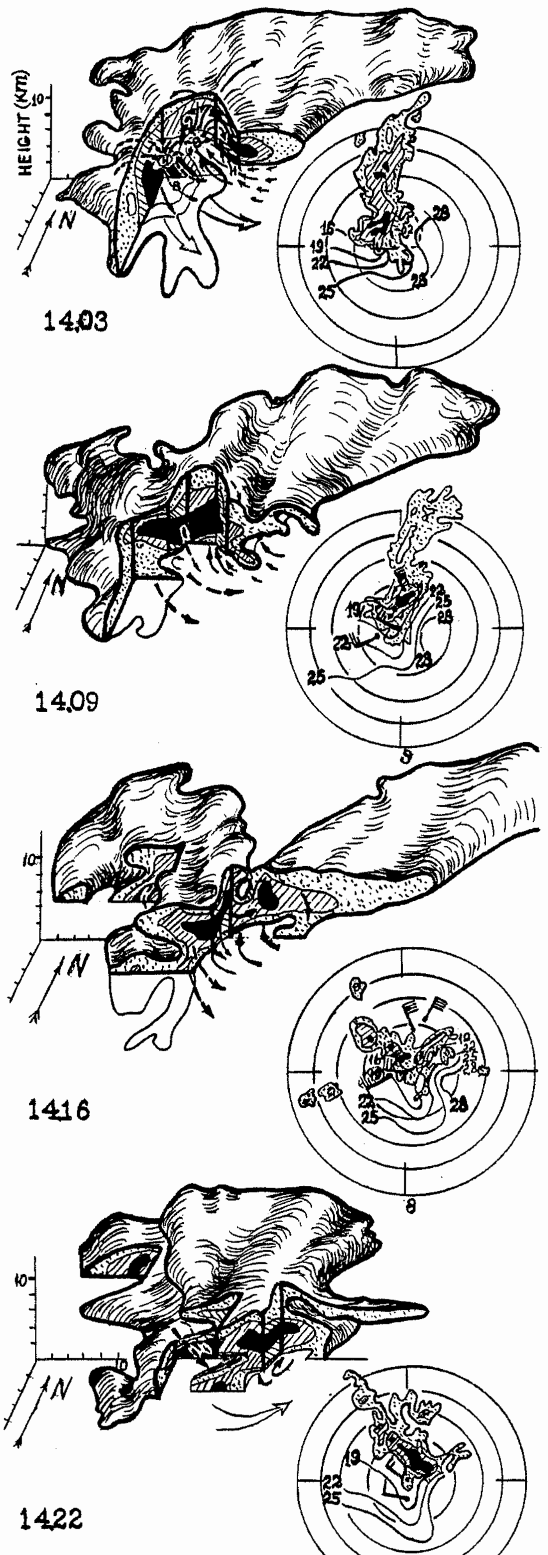

Fig.2 The transformation of three dimentional radar structure and air flows of severe hail cell at the second part of maturity stage. The three darker grades of stippled shading represent radar reflectivities of 10^{-12}, $2\cdot10^{-8}$ and $5\cdot10^{-7}$ cm^{-1}. Below, on the right side PPI echo at the ground level are shown . The solid lines represent isotherms at 3°C intervals, the wind arrows are shown also.

result of multiple /usually -2 / ascent and descent of hail stones in the cloud.

The obtained results are important for understanding of hail formation processes and may be used in hail suppression works.

REFERENCES

1. Bibilashvili N.Sh., Kovalchuk A.N. 1976, Study of cellular structure of Cumulonimbus. Trudy VGI, issue 33, p.92-99.
2. Bibilashvili N.Sh., Evstratov V.V., Kovalchuk A.N. 1974, Investigation results of airdraft structure in the vicinity of Cumulonimbus. Trudy VGI, issue 28, p.100-107.
3. Bibilashvili N.Sh., Terskova T.N. 1974, Study of updraft structure within Cumulonimbus. Trudy VGI, issue 28, p. 85-99.
4. Bibilashvili N.Sh., Terskova T.N. 1976, Vertical velocity profiles and thermodynamical features of updrafts in severe hail storms. Trudy VGI, issue 34, p.39-57.
5. Browning K.A. 1977, Structure and Mechanisms of Hailstorms. Met.Mon. Vol. 16, No. 38, p.1-39.
6. Bartishvili G.S., Kaviladze M.M., Solomko B.A. 1977, Study of Hail Growth Based on Isotopic Analysis. Trudy VGI, issue 38, p. 28-40.

THE RADAR CHARACTERISTICS AND THE IDENTIFICATION OF HAILSTORMS IN PINGLIANG REGION

Cai Qiming   Gong Naihu
The Lanzhou Institute of Plateau Atmospheric Physics, Chinese Academy of Sciences
Lanzhou, China

Pingliang region, being in the northwestern plateau of this country, is one of the regions with much hailfall in China. In 1972, a 3cm weather radar (JMA-133D) was installed there to coordinate the hail supression. Since then, the track observation to thunderstorms within the range of about 100 km, has been made in every summer. Our purpose is to find out the main radar characteristics of the thunderstorms and the rules of their development, motion and evolution, so as to suggest an indicator in identifying hailstorms among thunderstorms and provide a comparatively objective basis in hail suppression. In this paper the data of 182 thunderstorms obtained during 1972-1977 are analyzed with the emphasis on the relations between hailfall and thunderstorms echo height with reflectivity of 46, 36, 26,dbz and maximum echo height, also on vertical profiles of reflectivity in center of hailstorms and on the feature of PPI echo areas as well as the change of radar characteristics with time for hailstorms.

1. The maximum echo top height and the intense echo top height

The updraft in hailstorms is always very intense. It is one of the most important conditions for hail growth and is also the basic cause for hailstorms to become so immense. It is known that the hail growth needs not only intense updraft, but also sufficient supply and accumulation of water. It is generally considered that the important zone for hail growth is the supercooled zone in the upper-middle part of the cloud. That hails are able to grow up means that there exist a great deal of water content and large particles in the zone. On the basis of the calculation by Herman and Battan[1], for the wavelength of 3.2 cm when the diameter of a dry hailstone increases from 0.5 cm to 3 cm its back-scattering cross-section might be increased by the order of four. It can be, therefore, expected that though the maximum echo top height (i.e. the top height of an echo obtained from observation when radar gain is the maximum.) may indicate the strength of the updraft of a cloud, a better result could even be obtained if we use the top height of a more intense echo, responsive to the growth of large hails, which is in this paper known as the intense top height, as an indicator to identify hailstorms.

In 1972 - 1973, we have already noticed the point. Now we use the data of intense thunderstorms observed during 1972 - 1977 to discuss the issue in detail. The so-called intense thunderstorms here mean the clouds that their intense echo top height with reflectivity Z=36 dbz is larger than 5 km*. We did so because 99 % of the observed hailstorms in the period could be included in this criterion. During the years from 1972 to 1977, there were 182 thunderstorms that were observed satisfying the criterion. Among them 115 were reported to have produced hail on the ground, while the other 67 have not. The relation between the appearance frequency of hailstorms (or non-hailstorms) and their echo top height is shown in Fig. 1. This appearance frequency is the ratio of the number of hailstorms (or non-hailstorms) the top of which reaches a certain height interval, to the total number of intense thunderstorms reaching the same interval.

It can be seen from Fig. 1 that hailstorms have generally higher echo top than non-hailstorms, and for the great majority of hailstorms H_{46}= 5-8 km; H_{36} = 6-10 km; H_m = 7-13 km, the more intense the hailstorms are the higher their top will be. While for most of the non-hailstorms, $H_{46}<$ 5 km; $H_{36}<$ 7 km; $H_{26}<$ 8 km and $H_m<$ 11 km It can also be seen that in Fig. 1 a and b the peak zones of hailstorms and non-hailstorms do not overlap each other, while they do so in a certain degree in Fig. 1 c and d. This shows that in regard to the echo top height with less reflectivity there are more hailstorms and thunderstorms of the same height. Especially, although H_m of most of hailstorms is generally larger than 7 km, their appearance frequency will still be high enough, even until 10 - 13 km, yet many of thunderstorms with H_m= 7-11 km do not produce hailfalls. Hence, obviously it is better for us to use H_{46}

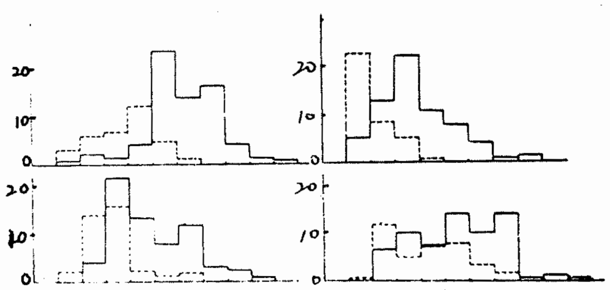

Fig. 1,   echo top height (km)

Fig. 1 Relation between occurence frequence and echo height for hailstorm and non-hailstorm
— hailstorm --- non-hailstorm

* The height in this paper denotes the one above the ground.

and H_{36} as indicators for the identification of hailstorms rather than H_m. The dot-diagram (Fig. 2) of H_{46} and H_{36} gives a clearer division.

According to the data of the 182 intense thunderstorms, if H_{46} = 5 km and H_{36} = 6 km are adopted as the criteria for identifying hailstorms, the accuracy rate might reach 88 %, the false and the omitted rate are 4 % and 8 % respectively.

The above mentioned phenomena show that the important zone for hail growth in a hailstorm is the layer at the height of 5-10 km over Pingliang region. According to the radiosonde data in the very region, it is the supercooled zone with the temperature of -15°C - -48°C.

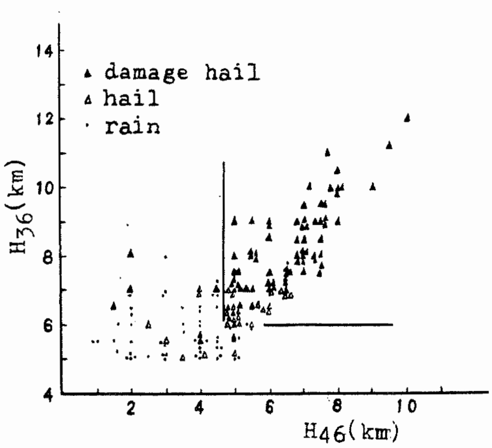

Fig. 2 Dot-diagram of hailstorm and non-hailstorm

2. The vertical reflectivity profile and the intense echo area

In 1972 and 1973 we detected the reflectivity profile in the centre of thunderstorms and obtained some significant characteristics. Fig. 3 and Fig. 4 are the typical examples. It can be seen from Fig. 3 that there are three types of profiles for hailstorms:

1) The profiles with maximum reflectivity at high level, as shown in curves (25) (31). Most of the maxima are at the height over 4 km. Their values are about 50 dbz. These are good agreement with Donaldson's results[2]. 2) The profiles with maxima at the lower part of clouds. Reflectivity value decreases monotonously with the increase of its height, as shown in curves (3) (18). 3) The profiles with reflectivity maintaining nearly a certain large value from the bottom of clouds to upper height. Above that height reflectivity value decreases quickly with the increase of its height, as shown in curves (10) (15).

However, whatever shapes of the curves may be, they have a common character, i.e. the intense reflectivity of hailstorms can stretch to greater height than that of the non-hailstorms. e.g. the 46 dbz and 36 dbz reflectivities for hailstorms respectively may stretch over the height of 4.5 and 6.0 km. Some severe hailstorms may reach over 9 km. The higher they stretch, the more intense the hailstorms would be and the bigger the hails. For example, we had two hailstorms on May 27 and June 12, 1973 (curves 15 and 3) which produced hails of the size of walnuts, even as big as eggs, and the accumulated depth on the ground was about 15 cm. Fig. 4 gives examples of the profiles of non-hailstorms. A number of the curves of them show that the reflectivity decreases monotonously with the increase of its height, though the reflectivity value at the bottom of clouds may approach 50 dbz. A few of them show that there is a maximum of reflectivity at the high level (curves 23,24). However, the maximum values are comparatively small and the layer with great reflectivity is rather thin. Hence, the main difference of vertical reflectivity profiles between hailstorms and non-hailstorms is not determined by reflectivity value at the lower part of the clouds or by the fact that there is obvious maximum at high level, but is determined by the fact that the layer with large reflectivity is rather thick.

By further careful analysis of PPI echo areas of 46 dbz at low angle of elevation (near 3°), it is found that many of non-hailstorms do not appear echo of 46 dbz in their low part, and even if some of them do so, their areas are relatively small (generally<9 km^2). But nearly all of the hailstorms appear the echo of 46 dbz, their areas are 2-30 km^2, even 50 km^2. Furthermore, the hailfall has a strengthening tendency with the increase of the area.

3 Probability of hailfall

We use the concept of probability of hailfall mentioned by Douglas and Hishfeld (1959)[3]. The probability is the ratio of the number of hailstorms which reach to a certain height interval to the total number of thunderstorms which reach to the same interval. The result derived from the data of the 182 intense thunderstorms in the years of 1972 - 1977 is shown in Fig. 5. It is shown that when the probability reaches 50 %, various echo top heights are respectively as follows: H_{46} = 5 km; H_{36} = 6 km; H_{26} = 7 km; and H_m= 9 km. But in the case of H_{46}= 5.5 km; H_{36} = 7 km; H_{26} = 8 km and H_m= 11 km, the probability would reach 70 %. This result is quite similar to that obtained in Johamesburg and Pretoria region in South-African Highveld[4].

4. The evolution of echo characteristics with time

As having already mentioned above, RHI intense echo height can be used as the

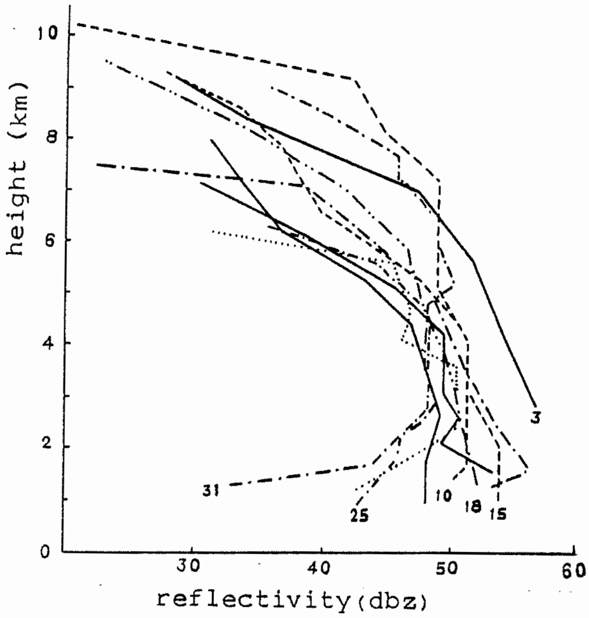

Fig. 3 Vertical reflectivity profiles of hailstorms

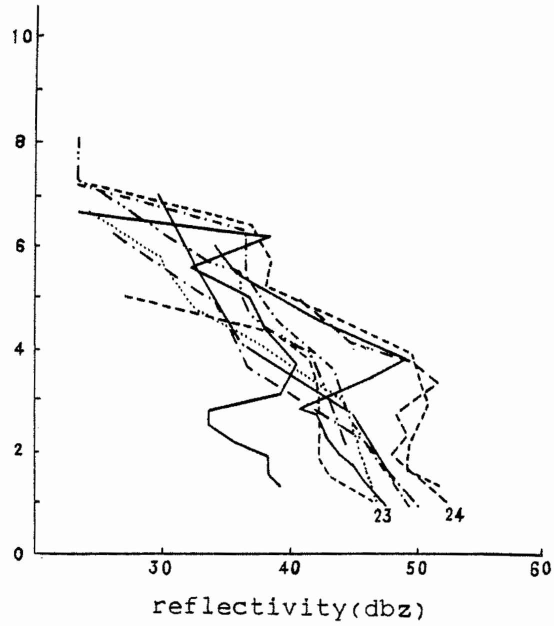

Fig. 4 Vertical reflectivity profiles of non-hailstorms

indicator for identifying hailstorms. It is, therefore, quite natural to link that its evolution with time will denote the variation of the characteristics of hailstorms. Since 1975, we have intentionally made some successive track observations to hailstorms and obtained more than ten series of the data of the evolution. Fig. 6 gives some examples. It can be seen from Fig. 6 that:

(1) The evolution curves of the various reflectivity have some similar tendency ,but the variation of the curves of 36, 46 dbz are the most evident, their amplitudes of variation are also the largest.

(2) Before a hailfall or a severe hailfall the intense echo top appears growing violently, the time necessary for the growth is generally not longer than 30 min, but the increment amplitude is rather large, especially for the curves of Z = 46 dbz and 36 dbz. For example, in Fig. 6 a the hailstorm rapidly grew during 18:19 - 18:42, taking about 23 min., with an amplitude of 7.8 km and 6.4 km for 46 dbz and 36 dbz respectively. This shows that there is a process of violent growth of hailstorms within a period of less than half an hour. It may also be regarded as a sign of hailfall.

(3) Following the violent growth, the echo top height will maintain a large value for a period of time about 40 min. to an hour in general. And correspondingly the hailfall takes place on the ground in succession or in intermittence. For example, in Fig. 6a the period is about one hour. This clarifies that the hailstorms are quasi-stable during this period and retains the basic conditions for forming hails.

(4) During this quasi-stable period some small fluctuation will still take place in the echo height. The fluctuation amplitudes are 1 - 1.5 km for the curves of 46 dbz and 36 dbz, and the fluctuation period is about 20-40 min. They are probably related to the formation and the fall of hailstones.

(5) The maximum echo top height has some similar variation but its amplitude is comparatively small and the period is not so obvious.

(6) The more violently the intense echo top height increases before a hailfall and the higher it will reach, the more intense the hailstorm will be. For example, the height of the reflectivity 46 dbz rapidly reaches 12 km in Fig. 6b. The curves of this type reflect a special intensity of hailstorms. In fact, a hailfall with large range and long duration occurred. The hailstones were as big as hen's eggs. and the hail depth on the ground was mere than 30 cm somewhere on the day, which caused a disastrous damage to crops.

5. Summary

In Pingliang region the difference of radar characteristics between hailstorms and ordinary thunderstorms, between weak hailstorms and tense hailstorms are very noticeable.

Firstly, the difference in the intense echo height of 46 dbz and 36 dbz is obvious. When echo top height of H_{46} and H_{36} are larger than 5 km and 6 km respectively, the thunderstorms can be regarded as hailstorms. Furthermore, when the height $H_{36}>7$ km, they can be considered as damaging hailstorms. When H_{46} and H_{36} are larger than 5.5 km and 7 km respectively, the probability of hailfall will

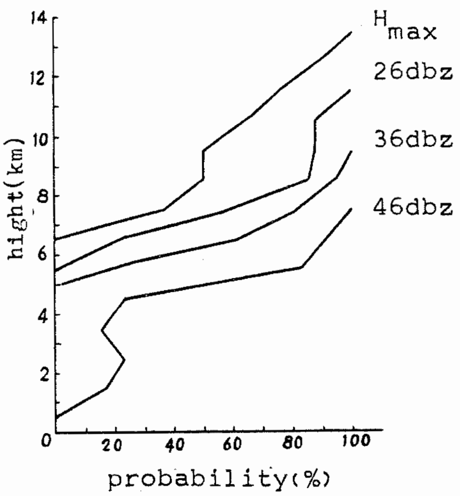

Fig. 7 Relation between hailfall probability and echo height

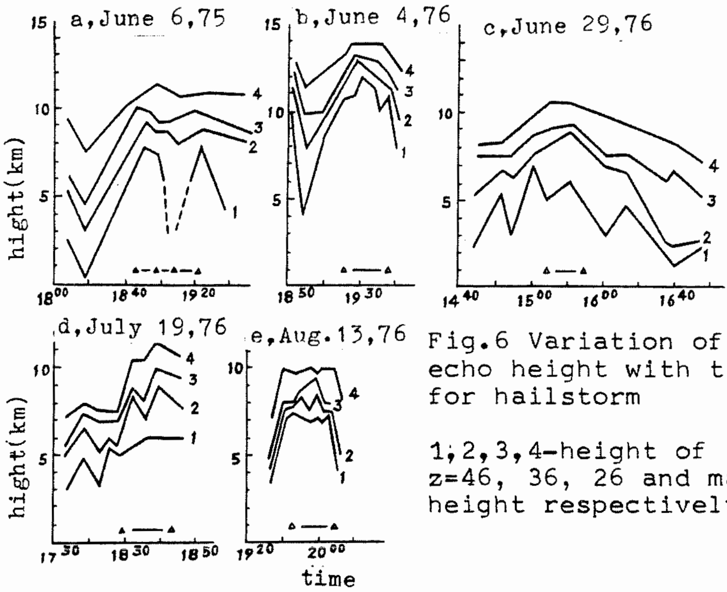

Fig.6 Variation of echo height with time for hailstorm

1,2,3,4-height of z=46, 36, 26 and max. height respectively

reach 70 %. Since H_{46} and H_{36} can be easily obtained and in real time by conventional weather radar, so the use of the previous indicators is rather simple and practical. In addition, it is either helpful for the choice of operating objects or useful for evaluating the effect in hail-suppression.

Secondly, the vertical reflectivity profiles and PPI intense echo area at low elevation angle of hailstorms are also different from those of ordinary thunderstorms. The most important difference is that the layer with large reflectivity is rather thick and the PPI area is larger for hailstorms. With the expansion of the layer depth and the area, the destructiveness of hailfall will show a strengthening tendency.

Finally, there is still difference between hailstorms and ordinary thunderstorms in the evolution of their radar characteristics.

References

(1) Herman, B. M. and L. J. Battan, 1961: Calculation of Mie backscattering of microwaves from ice spheres. Quart. J. R. Met. Soc. 87, 223-230.

(2) Donaldson, R. J. 1961: Radar reflectivity profiles in thunderstorms. J. Met. 18, 292-305.

(3) Douglas, R. H. and W. Hischfeld, 1959: Patterns of Railstorms in Alberta. Quart. J. R. Met. Soc., 85, 105-119.

(4) G. Held, 1978: The probability of hail in relation to radar echo heights on the South African Highveld. J. of Appl. Met., 17, 6, 755-762.

SOME COMPARISONS BETWEEN HAILSTORMS ON THE TRANSVAAL HIGHVELD AND THOSE ELSEWHERE

A.E. Carte

National Physical Research Laboratory
Pretoria SOUTH AFRICA

1. INTRODUCTION

The point hail frequency in the Transvaal Highveld is about five days per year and the thunderstorm frequency is 75 (Schulze, 1965). Hail occurs mainly during the summer months and the annual average number of days when hail falls within an area of about 2700 km^2 that includes Pretoria and Johannesburg is 69, with hailstones exceeding 3 cm in diameter on an average of three days per year. Aspects of the hail climatology derived from many years of investigations of hailstone structures, observations of surface patterns of hailfalls and radar studies were summarised by Carte and Held (1978). These results and many from elsewhere have revealed certain conditions that favour formation of hail but by no means can all the necessary conditions be specified. It is, for example, not known why adjacent contemporaneous storms may behave differently, with the lesser storm perhaps being the more severe one, or why one of two apparently similar storms at the same locality has produced a flood but not hail while the other was a destructive hailstorm. The use of airborne instruments and Doppler radars will contribute to providing explanations for such differences. In the meantime, further insight into hail growth can be gleaned from comparisons of hailstorms in various geographical regions.

2. SUSTAINED STORMS

The Highveld has a high frequency of thunderstorms but long-lived ones are uncommon. Practically all of the sustained storms have proved to be multicellular or to have had other characteristics indicating unsteadiness of airflow (Carte, 1979). The first storms to be identified as supercells occurred on 16/17 October 1978, after seven years of radar observations. Supercells are not too common in the northern hemisphere but they occur much oftener than here, especially in Oklahoma, USA (Nelson and Young, 1979). The lack of sustained steady-state storms on the Highveld has been ascribed to the relatively weak upper winds that are usual (Carte, 1979).

One storm (Storm H) on 16/17 October 1978 travelled 275 km in six hours. It traversed a hail-reporting network where hailstones up to 5 cm in diameter were recorded although there were not many of this size nor was there a large amount of hail at any point. This storm was classified as a left-moving, weakly-

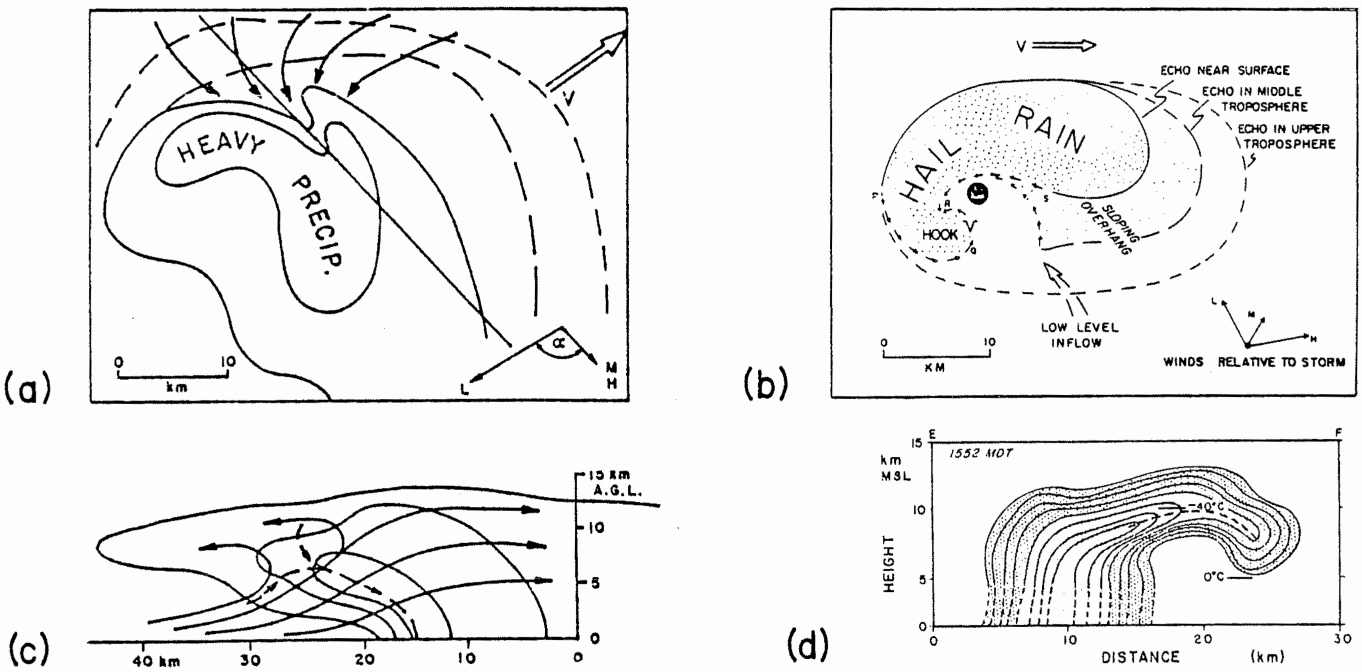

Fig. 1. Schematic sections: (a) horizontally through Storm H, with echo overhang and winds relative to the storm indicated as in (b); (b) horizontally through a supercell according to Browning (1964); (c) vertically through Storm H along the line indicated in (a), showing inferred airflow and hailstone trajectories (broken lines); and (d) vertically through the Fleming supercell (Browning and Foote, 1976).

vaulted supercell. Its structure is shown schematically in Fig. 1. Compare the overhang above the inflow region with that for the Fleming supercell (Figs 1a and c). Certain aspects of it were unusual compared with supercells elsewhere:

(a) Winds. Its occurrence was attributed partly to unusually strong sub-cloud and opposing upper winds but these were not as strong as those associated with multicells and supercells in the northern hemisphere as shown in Fig. 2. Furthermore there was no appreciable in-cloud shear. The occurrence of supercells is favoured by strong wind shear in speed and direction and by strong subcloud winds according to Marwitz (1972). Some but not all of these conditions were met by Storm H. Strength of winds and shear certainly are important factors in controlling the severity and persistence of storms but evidently not in a simple manner.

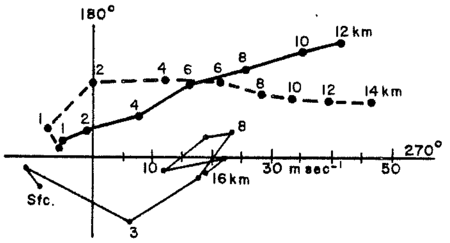

Fig. 2. Hodographs showing upper winds characteristic of multicells (solid line) supercells (broken line) according to Chisholm and Renick (1972). Lowest hodograph applies to Storm H.

(b) Hook echo. Marwitz (1972) suggested that a hook in the PPI echo at cloud base level is probably a sufficient condition to identify a storm as a supercell. Storm H had a persistent notch or hook-shaped weak-echo region (WER) which showed in scans at low altitude. It was located in the inferred region of low-level inflow but it was small and ill-defined and not always present at cloud-base level. The hook criterion may therefore be more applicable to supercells with vaults than those without.

(c) Crescent-shaped core. The echo core of Storm H had a pronounced concavity on the side remote from the inflow, whereas in the supercell as described by Browning (1964) such a concavity forms the lower boundary of the WER (see Fig. 1b). This crescent-shape in Storm H was, however, not a static feature as would appear from viewing occasional PPIs but was constantly evolving. The northern limb developed and then drifted southwards relative to the storm (following the direction of the cloud-level environmental winds) to become the southern limb. This behaviour suggested a periodic subsidiary region of inflow occurred at the left rear of the storm. The hailfall pattern confirmed that such discontinuities occurred, as did changes in the magnitude of the overhanging echo above the inferred inflow region.

The most important feature of Storm H was the steadiness of its airflow, maintained for many hours. There must have been fluctuations of the main inflow superimposed on the steady flow and furthermore there was a subsidiary and discontinuous inflow towards the rear. Hail growth may have been limited by lack of in-cloud shear, a strong tilt to the updraught and a simpler trajectory followed by the growing hailstones than the spiral path inferred for the archetypal supercell, e.g. Browning and Foote (1976).

3. AREAL FREQUENCY OF HAIL

Dense hail-reporting networks enable the average area of hailfalls to be determined. This can be derived from curves that relate hail frequency to observational area (or from the point-areal frequency relationship). Nelson and Young (1979) showed from such results that Oklahoma experiences a larger mean hailfall area than either the Transvaal, South Africa or Illinois, USA. Also, the mean hailstone per occurrence was larger in Oklahoma than in the Transvaal. The point frequencies of hail in these two localities are one and five days, respectively, while their thunderstorm frequencies differ by only 35 %. Hail production therefore seems to be relatively efficient in the Transvaal but the few hailstorms in Oklahoma are on average larger and more severe. The reason for these differences is attributed by Nelson and Young (1979) to the high proportion (25 %) of the storms in Oklahoma being supercells - the Transvaal, in contrast, has practically no supercell storms as mentioned earlier.

4. EMBRYOS

Knight and Knight (1978) have compared the proportion of two types of embryos (viz. graupel and frozen drops) which have been found in hailstones from a number of different geographical localities. These included the northern Caucasus, Switzerland, two regions in South Africa and five regions in the USA. Their conclusion was that embryo formation is significantly different in different regions. The findings in many instances were based on studies of relatively large numbers of hailstones (>1000) from many storm days and one would therefore expect their average values to be significant. However, there appear to be too many discrepancies for this to be the case: List (see Knight and Knight, 1978) found 80 % of the hailstones from more than 40 hailfalls had centres composed of graupel whereas later results from Switzerland (Federer and Waldvogel, 1978) found only 37 % of the embryos to be graupel; Knight and Knight report having found a relationship between embryo type and cloud base temperature but this was not substantiated by later results; and the tendency for large Highveld hailstones to have a higher proportion of graupel embryos than smaller ones does not agree with results from the South African Lowveld, where cloud bases have nearly the same average temperature as on the Highveld although terrain altitude differs considerably in these two regions.

It is well established that individual storms in one region may differ as regards type of embryo, e.g. in the Transvaal, practically all embryos of several hundred hailstones from three storms on one day were found to be rime (Carte and Mader, 1977) whereas on other days the embryos from adjacent hailstreaks produced by apparently similar storm cells differed, and variations related to storm stage were found (Roos, 1978). Federer and Waldvogel (1978) collected time-resolved specimens in Switzerland and found a general tendency for rimed embryos to occur at the beginning of hailswaths and for fewer to be found at later stages.

The conclusion that must be reached is that type of embryo is more dependent on dynamical effects than on other characteristics. Differences from storm to storm and within one storm make it doubtful whether any of the geographical differences so far found are significant. Many more results are needed. The best approach to understanding the factors that govern embryo type would seem to be detailed studies of the kinematic and reflectivity structures of individual cells in relation to hailstone structures rather than accumulation of further climatological data (although this too is important).

5. HAILSTONE TRAJECTORIES

Structural analyses of hailstones have provided estimates of displacements in the vertical which they experienced during growth. Results have been reported for hailstones from North America, Europe and Australia, but relatively few hailstones were examined (Macklin, 1977, Macklin *et al*, 1976 and Federer *et al*, 1978). Some were concluded to have made multiple ascents while others remained balanced at approximately the same altitude during growth from small to large dimensions. Similar results were found for the Transvaal Highveld (Roos *et al*, 1976 and 1977). From three storms on one day 34 hailstones were analysed. The updraught encountered by some apparently increased with time, while for others it pulsated or there were multiple updraughts. Hailstones from only a few kilometres apart in one storm evidently encountered very different conditions. One finding in general conformity with results for elsewhere was that large hailstones tended to acquire practically all their mass at ambient temperatures between -20 and -25 °C (7 to 8 km above ground level). Hailstones of all sizes mostly grew between these limits during the early (and vigorous) stages of severe storms. During later stages growth was during descent but then only small hailstones were produced. Complexity and unsteadiness of internal airflow is indicated by the variety of trajectories in some storms. This variability and inadequate sampling may explain why no definite geographical differences have been revealed. However, an important result is that in many regions hailstones require a time-varying updraught to maintain them within a rather narrow temperature regime if they are to grow large. Whether the updraught increases with time or the hailstones move horizontally towards the core of a steady updraught cannot be inferred from hailstone structures. The structure of the Fleming supercell led Browning and Foote (1976) to conclude that hailstones ultimately of 8 cm in diameter grew by following a path around a steady updraught. A two-dimensional up and down path seems more likely for the large hailstones (5 cm) that formed in Storm H (Section 2).

6. RADAR CHARACTERISTICS

Curves that relate probability of hail on the Transvaal Highveld to the maximum height reached by various iso-echo contours have been presented by Held (1978). He compared the data with similar results for the Lowveld and Alberta, Canada. The results shown in Fig. 3 show remarkably good agreement between those for Alberta and the Highveld in spite of geographical, topographical and other differences such as the height of the tropopause (about 16 km MSL over the Highveld and about 11 km for Alberta). In contrast, to have the same probability for hail, echo tops must extend to progressively greater heights as one moves southwards from Alberta to New England to Texas (Douglas, 1963). This suggests that there might be a latitude effect in North America, perhaps linked to the height of the tropopause.

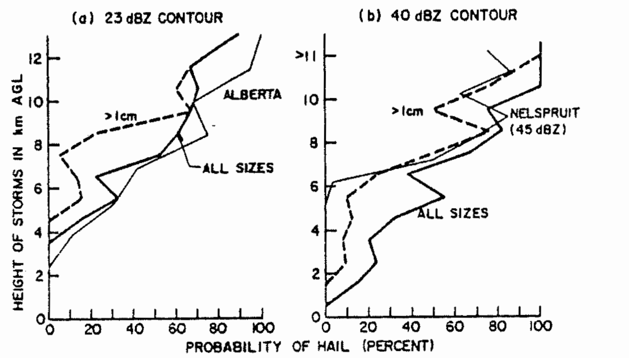

Fig. 3. The probability of hail as a function of echo heights on the South African Highveld (a) for the 23 dBZ contour and (b) for the 40 dBZ contour. Separate graphs are shown for cells producing hailstones >1 cm in diameter (from Held, 1978).

A curious feature of the results shown in Fig. 3 is that all curves have a point of inflection, i.e. above a certain height the probability for hail becomes less with increasing height, at least within a restricted height interval. This result holds for the Transvaal Highveld even when the data were stratified according to hailstone size or subdivided into relatively small samples.

7. CONCLUSIONS

Many other comparisons can be made that reveal conditions conducive to hail growth. To mention two: urban/orographic effects have been found to stimulate hail formation on the Highveld (Held, 1974) and in Illinois (Changnon, 1977); frontal storms are common in northern Italy where prodigious amounts of hail and large hailstones are not unusual and on the Highveld the most severe storms are often associated with fronts (which occur rather seldom) and the commoner air mass storms are less severe (see Carte and Held, 1978). To summarise other results:

(a) conditions favouring the occurrence of severe and sustained storms are strong upper winds and wind shear but these do not act in a fully predictable manner;

(b) essentially steady-state storms are rare on the Highveld because upper winds are usually rather weak;

(c) not all supercells have readily distinguishable morphological characteristics, especially when there is superimposed unsteadiness of the airflow;

(d) evidence that hailstone embryos differ with geographical region is inconclusive, but significant differences related to dynamical effects certainly occur;

(e) large hailstones seem to require critical conditions that maintain them in a narrow horizontal zone during growth;

(f) the internal airflow of storms needs to be known in detail for quantitative explanations of the variety of hailstone structures often found, the relatively large areas of hail produced by supercells and probability of hail/radar characteristics.

REFERENCES

Browning, K.A., 1964: Airflow and precipitation trajectories within severe local storms which travel to the right of the winds, J. Atmos. Sci. 21, 634-639.

Browning, K.A. and G.B. Foote, 1976: Airflow and hail growth in supercell storms and some implications for hail suppression, Quart. J. Roy. Meteor. Soc. 102, 499-533.

Carte, A.E., 1979: Sustained storms on the Transvaal Highveld, S. Afr. Geogr. J. 61, 39-56.

Carte, A.E. and G. Held, 1978: Variability of hailstorms on the South African plateau, J. Appl. Meteor. 17, 365-373.

Carte, A.E. and G.N. Mader, 1977: Hailstorms in the Transvaal on 29 November 1972, Quart. J. Roy. Meteor. Soc. 103, 731-749.

Changnon, S.A. Jr., 1977: The climatology of hail in North America. Hail: a review of hail science and hail suppression, Meteor. Monogr. 16, No 38, Amer. Meteor. Soc. 107-128.

Chisholm, A.J. and J.H. Renick, 1972: The kinematics of multicell and supercell Alberta hailstorms, Alberta Hail Studies, Research Council of Alberta Hail Studies Rep. No 72-2, 24-31.

Douglas, R.H., 1963: Recent hail research: a review, Severe local storms, Meteor. Monogr. 5, No 27, Amer. Meteor. Soc. 157-167.

Federer, B., J. Jouzel and A. Waldvogel, 1978: Hailstone trajectories determined from crystallography, deuterium content and radar backscattering, Pure Appl. Geophys. 116, 112-129.

Federer, B. and A. Waldvogel, 1978: Time-resolved hailstone analyses and radar structure of Swiss storms, Quart. J. Roy. Meteor. Soc. 104, 69-90.

Held, G., 1974: Hail frequency in the Pretoria-Witwatersrand area during 1962 to 1972, Pure Appl. Geophys. 112, 765-776.

Held, G., 1978: The probability of hail in relation to radar echo heights on the South African Highveld, J. Appl. Meteor. 17, 755-762.

Knight, N.C. and C.A. Knight, 1978: South African Lowveld hailstone embryos, Preprints Conf. on Cloud Physics and Atmos. Elec., Issaquah, Washington, 1-4.

Macklin, W.C., 1977: The characteristics of natural hailstones and their interpretation, Hail: a review of hail science and hail suppression, Meteor. Monogr. 16, No 38, Amer. Meteor. Soc. 65-88.

Macklin, W.C., J.N. Carras and P.J. Rye, 1976: The interpretation of the crystalline and air bubble structures of hailstones, Quart. J. Roy. Meteor. Soc. 102, 25-44.

Marwitz, J.D., 1972: The structure and motion of severe hailstorms. Pt. 1: Supercell storms, J. Appl. Meteor. 11, 166-179.

Nelson, S.P. and S.K. Young, 1979: Characteristics of Oklahoma hailfalls and hailstorms, J. Appl. Met. 18, 339-347.

Roos, D. v.d. S., 1978: Aspekte van die groei en dinamika van haelstene, Ph.D. thesis, Univ. of S. Africa, 1-189.

Roos, D. v.d. S., J.C. Vogel and A.E. Carte, 1976: Hailstone growth, Preprint Int. Conf. on Cloud Physics, Boulder, Colorado, 240-245.

Roos, D. v.d. S., H. Schooling and J.C. Vogel, 1977: Deuterium in hailstones collected on 29 November 1972, Quart. J. Roy. Meteor. Soc. 103, 751-767.

Schulze, B.R., 1965: Hail and thunderstorm frequency in South Africa, Notos 14, S. Afr. Weather Bureau, 67-71.

ELECTRICAL AND DYNAMICAL DESCRIPTION OF A FRONTAL STORM DEDUCED FROM LANDES 79 EXPERIMENT

S. Chauzy, P. Raizonville

Laboratoire de Physique de l'Atmosphère
Toulouse, FRANCE

D. Hauser, F. Roux

Centre de Recherches en Physique de l'Environnement
Issy-les-Moulineaux, FRANCE

1. INTRODUCTION

The electrical features of a thunderstorm are obviously related to its microphysical and dynamical evolution. In order to point out such a complex relationship, various experiments have been carried out for several years including in situ electric field measurements associated with radar observations. Winn et al. (1978) and Few et al. (1978) published important papers dealing with this subject.

A balloon-borne sensor for measuring both horizontal and vertical components of the electric field has been developed and made it possible to initiate in France a long term experiment on electric charge localization within thunderstorms. This system as well as the RONSARD system (dual-Doppler radars) participated in the LANDES 79 summer experiment performed by several french research organisms (C.E.A., C.E.S.T.A., C.N.E.T., D.R.E.T., D.R.S.W., E.E.R.M., L.M.D., L.P.A., O.N.E.R.A.)[x].

2. THE EQUIPMENT

2.1 The RONSARD radars

The RONSARD system is a dual radars system, operating at $\lambda = 5.3$ cm wavelength. Owing to this wavelength, only the precipitating part of the clouds (diameters of hydrometeors larger than 100 μm) can be observed. Detailed characteristics of the RONSARD radars may be found elsewhere (Nutten et al., 1979).

Three main operating sequences are used:

- the mapping of the precipitating field within the maximum scanning domain (200 km) and the restitution of the mean three dimensional motions and convergences with respect to altitude are obtained through VAD sequences, principally used for the study of frontal systems (Testud et al., 1979).

- the restitution of the three dimensional reflectivity and wind fields on the mesoscale (1 to 50 km) is obtained through COPLAN sequences, principally used for the study of convection (Lhong et al., 1979).

- the determination of microphysical characteristics of the precipitations (fall speed and granulometry) is obtained through Vertical Incidence Soundings (Hauser and Amayenc, 1979).

2.2 The electric field measurement system

It consists in a dropsonde type intrument carried by free balloon. The collected data are telemetered via 1680 MHz to a receiver (RD 65 model) which provides, at the same time, tracking of the balloon.

The sensing instrument is an improved version of the autorotating dropsonde first developed by Chauzy (1975). The body is a cylindrical field-mill with vertical axis (Fig. 1) providing the horizontal component of the external electric field. Two shutter field-mills, one at the top, the other one at the bottom of the cylinder ensure the measurement of the vertical component of the external electric field, excluding the influence of the proper charge. The sense of the vertical component (upward or downward) is obtained by making special shape apertures on the rotating screens and electrodes. As Winn and Moore (1971) previously did, the horizontal component of the terrestrial magnetic field is also detected by a small coil delivering a reference signal which is used to determine the direction of the electric field horizontal component.

In addition, atmospheric pressure is measured in order to provide the altitude of the sensor. The necessary autorotation is carried out by two counter-gyrating rotors attached, one to the body, the other one to the

[x]- C.E.A.: Commissariat à l'Energie Atomique
- C.E.S.T.A.: Centre d'Etudes Scientifiques et Techniques d'Aquitaine
- C.N.E.T.: Centre National d'Etude des Télécommunications
- D.R.E.T.: Direction des Recherches Etudes et Techniques
- D.R.S.W.: Direction Régionale du Sud-Ouest (Météorologie, Bordeaux)
- E.E.R.M.: Etablissement d'Etudes et de Recherches Météorologiques
- L.M.D.: Laboratoire de Météorologie Dynamique (Paris)
- L.P.A.: Laboratoire de Physique de l'Atmosphère (Toulouse)
- O.N.E.R.A.: Office National d'Etudes et de Recherches Aéronautiques

upper grounded shield (Fig. 1).

3. METEOROLOGICAL ENVIRONMENT

A cold front, associated with a depression centered on the north of England, begins to traverse France since the morning of August 14. Its motion is slowed down owing to the presence of a thalweg at the altitude of 5000 m. The cold front reaches Aquitaine during the following night, associated with weak showers. During the afternoon, a weak stormy activity develops southwest of the experimental zone, close to mountainous regions.

The present results concern 15:00 to 18:00 (local time) observations. The 16:24 local sounding (Fig. 2) shows a quite stable situation from ground level up to altitude 4500 m. Weak convective motions can develop between 4500 and 6000 m. This situation is confirmed by radar observations showing quite stratiform clouds without appreciable vertical motions.

4. PRELIMINARY RESULTS

Two electric field soundings have been performed during the afternoon: the first one started at 15:02, the second one at 17:17. Figures 3 and 4 display the variation with altitude and time of the vertical and horizontal components, E_v and E_h, of the external electric field. Since the electrical activity was rather weak (no close lightnings detected) and the temporal evolution very slow, we assume that the recorded electric field variations along the path of the balloon are primarily due to spacial changes, i.e. to vertical ascent of the sensor in relation to the charge distribution.

The first sounding (15:02) exhibits, at 5500 m above sea level, a typical reversal of the electric field vertical component. This component is upward below the reversal, downward above it and reaches respectively + 36 kV/m and - 39 kV/m (maximum values). The rapid change in polarity as well as the stratiform structure of the radar echoes suggest that the balloon flew through a negatively charged shallow layer situated at 5500 m above sea level. According to the slope variation of the sounding, the vertical extension of the layer is about 150 m. Now, if we want to deduce the approximate value of the charge density ρ responsible for the measured electric field variation from POISSON equation: $\operatorname{div} \vec{E} = \rho/\varepsilon_0$, it is necessary to neglect the variations of the horizontal component along a horizontal path . This approximation is justified if the horizontal extension of the layer is much larger than its vertical depth, which we assume here. Under these conditions,

$$\operatorname{div} \vec{E} \sim \partial E_v/\partial z \quad \text{and} \quad \rho \sim \varepsilon_0 \, \Delta E_v/\Delta z \ .$$

The electric field values at the lower and upper boundaries of the layer are respectively + 28 kV/m and - 30 kV/m. ΔE_v = -58 kV/m and the charge density: $\rho \sim -3.4$ nC/m.

The reflectivity mapping in the first plan (elevation angle $\alpha = 0.5°$) of the 15:13 COPLAN sequence (Fig. 5) shows that, at lower altitude (up to 3000 m), the balloon passed by the high reflectivity region without penetrating it. A vertical cross section along the trajectory (Fig. 6) shows that, above this altitude, the balloon flew through a horizontal extent of the cloud (reflectivity between 30 and 35 dBZ within the layer 5000-5500 m).

The second electric field sounding displays a different structure, since two layers have been flown through by the balloon. The lower layer (2300 m) is negatively charged, the upper one (3500 m) positively. The depths are respectively 250 m and 200 m corresponding to electric field variations ΔE_v: - 86 and + 67 kV/m. In consideration of the steepness of these field variations, the preceding treatment has been applied here. The deduced values of the charge density are then - 3.0 nC/m^3 for the lower layer and + 2.9 nC/m^3 for the upper one.

During this sounding, replaced in 17:28 reflectivity mapping (Fig. 7), the balloon passed through a horizontally extended cloudy mass. A vertical cross section along the trajectory (Fig. 8) shows, in particular, that it crossed a bright band (reflectivity factor greater than 40 dBZ) between altitudes 1500 and 2500 m, probably generated by the melting of ice crystals (16:24 meteorological sounding shows that 0°C isotherm was located at altitude 3000 m).

5. DISCUSSION OF RESULTS

Preliminary radar data reductions (COPLAN sequences and Vertical Incidence Soundings) suggest that the studied situation exhibits mainly stratiform features. The weakness of vertical motions could then explain the good connection between charged zones and reflectivity patterns for both electric field soundings.

The 15:02-15:30 sounding displays a charged zone at about 5500 m. At this altitude, the measured temperature (at 16:24) is - 15°C showing that the hydrometeor population consists of ice crystals. Charging process by freezing could then play an important part during the growing stage of crystals. A similar situation in altitude has previously been found (Chauzy et al., 1979).

As for the 17:17-17:43 electric field sounding, a quite different structure is observed. Two oppositely charged layers are located right below and above 0°C isotherm. The lower one tops the bright band observed with the radars. Since both phases coexist in such a region the charge separation process the most likely to be active here can be collisions between ice crystals and drops. As Gaskell et al.(1978) reported, electric charges and precipitations are closely connected.

6. CONCLUSION

Interesting informations can be obtained from the comparison between electric field in situ measurements and radar observations. It has been shown in previous paper (Waldteufel et al., 1979) that, during convective situations, there is no systematic coincidence between charge centers and radar echoes. In the case studied here, the rather stratiform stucture leads to a much better correlation between both features.

More detailed studies will be carried out in this direction on LANDES 79 data, using more elaborate radar results: Vertical Incidence Soundings data providing microphysical description of the precipitations and COPLAN data leading to a kinematic analysis of the observed events.

7. ACKNOWLEDGEMENTS

The authors wish to thank the Saint-Privat-d'Allier Research Group and the Météorologie Nationale for their helpfull contribution. The major part of this work has been sponsored by the Direction des Recherches Etudes et Techniques.

8. REFERENCES

Chauzy, S., 1975: Une méthode de mesure de la composante horizontale du champ électrique à l'intérieur des nuages. J. Rech. Atmos., IX n°3, 127-133.

Chauzy, S., P. Metzger, P. Raizonville and P. Waldteufel, 1979: Une observation du champ électrique au sein d'une zone orageuse. J. Rech. Atmos., XIII n°3, 127-133.

Chong, M., F. Roux and J. Testud, 1980: A new filtering and interpolating method for processing dual-Doppler radar data: performance in three dimensional wind restitution, ability to derive pressure and temperature fields. To appear in Preprints 19th Radar Meteor. Conf., Miami, Fl., Amer. Meteor. Soc..

Few, A.A., M.E. Weber and H.J. Christian, 1978: Vector electric field structure in thunderstorms. Conf. on Clouds Physics and Atmospheric Electricity, Issaquah Wash., A.M.S. 601-604.

Gaskell, W., A.J. Illingworth, J. Latham and C.B. Moore, 1978: Airborne studies of electric fields and the charge and size of precipitation elements in thunderstorms. Quart. J. R. Met. Soc., 104, 447-460.

Hauser, D. and P. Amayenc, 1980: A new method for deducing hydrometeor size distributions and vertical air motions from Doppler radar measurements at vertical incidence: first results in a warm frontal stratiform precipitation. To appear in Preprints, 19th Radar Meteor. Conf., Miami, Fl., A.M.S..

Nutten, B., P. Amayenc, M. Chong, D. Hauser, F. Roux and J. Testud, 1979: The RONSARD radars: a versatile C. Band dual-Doppler facility. IEEE Trans. Geosci. Electron., GE-17, 281-288.

Testud, J., G. Breger, P. Amayenc, M. Chong, B. Nutten and A. Sauvaget, 1980: A Doppler radar observation of a cold front: three-dimensional air circulation, related precipitation system and associated wave like motion. J. Atmos. Sci., 37, 78-98.

Waldteufel, P., P. Metzger, J.L. Boulay, P. Laroche and P. Hubert, 1979: Triggered lightning strokes originating in clear air. Conf. of Europ. Geophys. Soc.,Munich. To appear in J. Geophys. Res..

Winn, W.P. and C.B. Moore, 1971: Electric field measurements in thunderclouds using intrumented rockets. J. Geophys. Res., 76, 835-842.

Winn, W.P., C.B. Moore, C.R. Holmes and L.G. Byerley III, 1978: Thunderstorm on July 16, 1975, over Langmuir Laboratory: a case study. J. Geophys. Res., 83, 3079-3092.

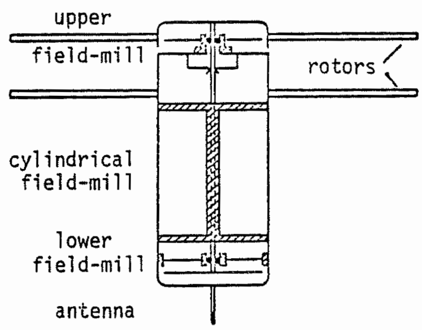

Fig. 1. Electric field measuring device

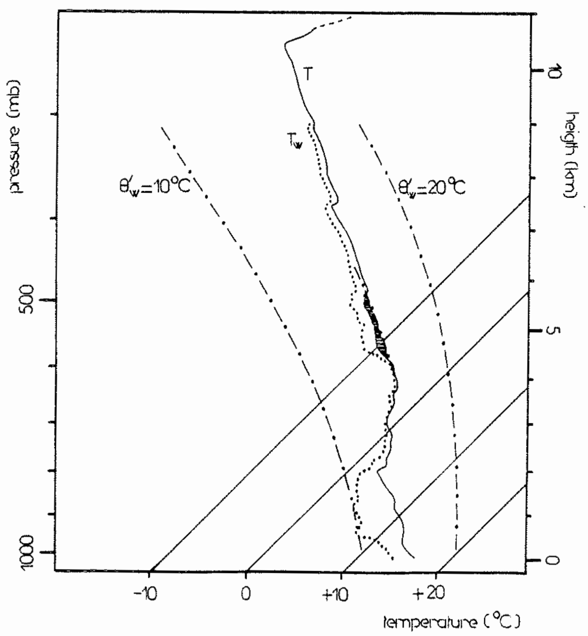

Fig. 2. Pressure, temperature and humidity sounding: August 15, 1979 at 16:24 (local time). Solid line represents temperature, dotted line wet bulb temperature. 10°C and 20°C wet adiabatic curves are plotted in dashed line

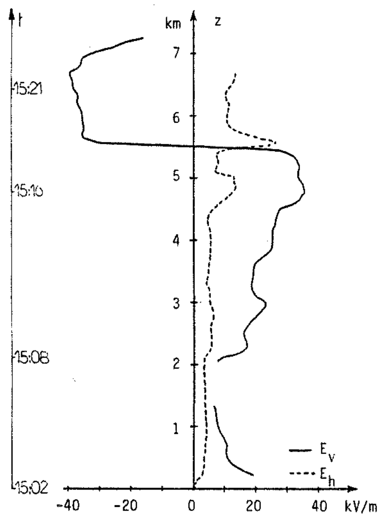

Fig. 3. Electric field sounding: August 15, 1979, from 15:02 to 15:30. Solid line represents the vertical component and dashed line the horizontal one.

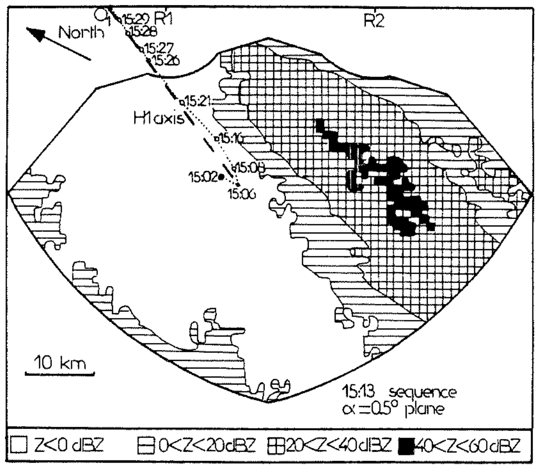

Fig. 5. Reflectivity mapping: elevation angle 0.5 °. R_1 and R_2 are radars locations. Dotted line represents the horizontal projection of the balloon trajectory (15:02 sounding). H_1 dashed axis is the straight line closest to this trajectory.

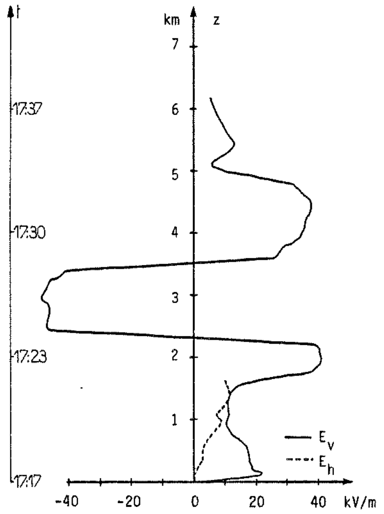

Fig. 4. Same as Fig. 3 except for sounding time: here from 17:17 to 17:43.

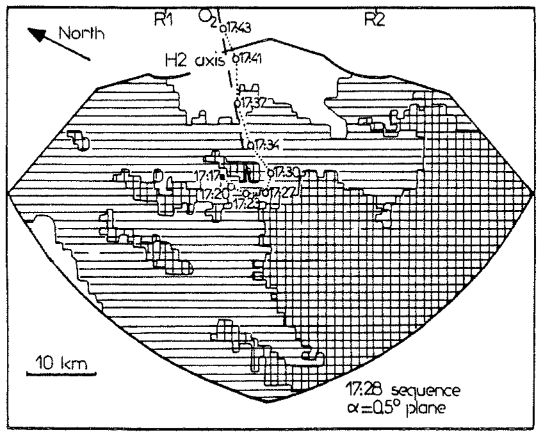

Fig. 7. Same as Fig. 5 except for sounding time: here 17:17.

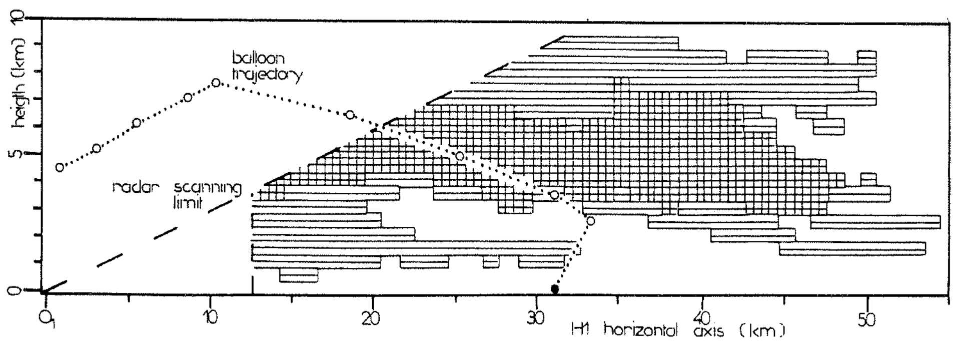

Fig. 6. Vertical cross-section reflectivity mapping along H_1 axis showing the balloon trajectory and the radar scanning limit. Sounding time: 15:02.

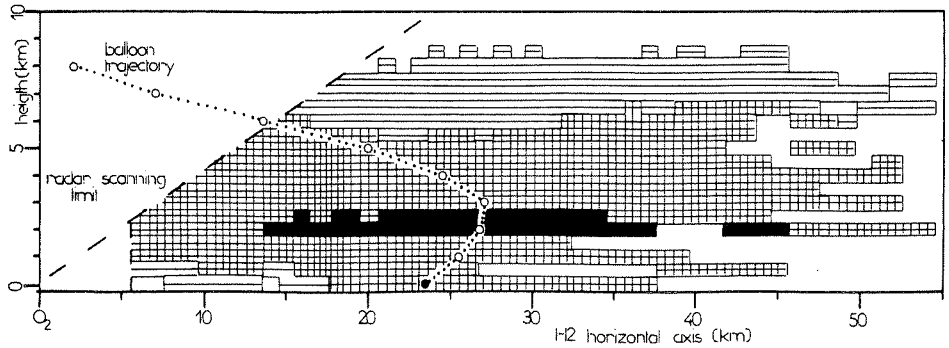

Fig. 8. Same as Fig. 6 except for sounding time: here 17:17.

THE INVESTIGATIONS OF WIND FIELD AND TURBULENCE IN CUMULONIMBUS CLOUDS USING RADAR EQUIPMENT

A.A. Chernikov, A.A. Ivanov, Yu.V. Melnichuk, A.K. Morgoev

Central Aerological Observatory
Dolgoprudny USSR

The last decade saw tangible progress in investigation of air motion in clouds by meteorological radars. These investigations are called for by the need to have a deeper insight into the process of cloud formation and development. Even though many other physical processes play a significant role in the life of a cloud the contribution of air motion is very large. If we knew the structure of air velocity field in each cloud the forecasting of dangerous phenomena and their modification would be much easier to accomplish. This is especially relevant because airflow variability strongly influences the microphysical processes which result, in particular, in rain- and snowfalls.

The air motions in a cloud are best described in terms of distribution of the air velocity vector in the entire cloud or in its most characteristic cross-sections. Very few investigations of wind fields in clouds have been completed because the available radar methods for observation of air motion inside clouds are not fast enough to obtain extensive and detailed data on the dynamics of Cb.

A major technique of observing the field of absolute velocities in clouds is observation by two separated Doppler radars which scan simultaneously in common planes with the computer processing of the radar data /1/. Unfortunately, acquiring the data on radial velocity components in the entire three-dimensional volume of the cloud takes too much time, up to five minutes if the measurements are to be accurate enough. Furthermore, even in coordinated plane measurements of two velocity components in some points are separated by a finite time intervals leading to significant errors in computing the absolute velocity vector from two components.

For these reasons methods seem to be helpful whereby one radar is employed and even though some deterioration of measurement accuracy may occur the rate of observation is increased to enable storm warning and use in weather modification.

To increase the rate of observation measuring the field of velocity differences with a scale of about 500m rather than the field of absolute radial velocities have been suggested /2/. The measurements and indication are performed in real time with a standard antenna scanning rate. As a result, what is displayed is the spatial structure of zones where the wind field is especially inhomogeneous in terms of differences of radial velocities with a scale of 500 m. It is very important that conventional non-Doppler meteorological radars are used.

Knowledge of spatial distribution of wind field inhomogeneities was found useful in studying the evolution of cumulonimbus clouds. Investigation of models which describe turbulence and mesoscale updrafts in clouds revealed that the zones of increased turbulence are seen as random points over radar echo pattern while the vertical flows are detected as vertically stretched structures of high velocity differences connected with flow boundaries and convergence or divergence zones which accompany the flows. Horizontal stripes are observed if there are large wind shears in clouds or precipitation.

The spatial structure of wind inhomogeneity was studied in vertical cross-sections of Cb at different stages of their evolution /3/. In the development stage the lower part of clouds displays in most cases vertically stretched stripes of increased velocity differences. The upper half of clouds invariably shows intensive turbulence. To locate clouds or cells at the stages of development on PPI, small elevation angles are used which insure observation of the lower part of cloud where vertical flows are stable.

At the mature stage the continuous zone of turbulence in the upper part divides into separate areas. The vertical stripes cease to exist. These features indicate cessation of cloud development and start of the dissipation stage.

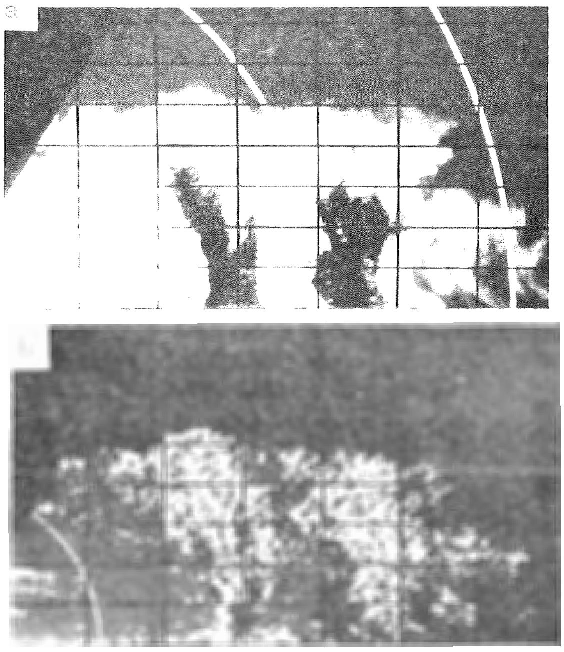

Fig.1. Range-height pictures of reflectivity (a) and wind field inhomogeneity (b) in Cb at the stationary stage.

At the stationary stage where the main cloud parameters are maintained for a long time (an hour or more) wind field mesoscale inhomogeneities are uniformly distributed over the entire vertical cross-section (Fig. 1). This structure of the velocity differences is the evidence of ascending and descending flows at all altitudes and their significant horizontal inhomogeneity.

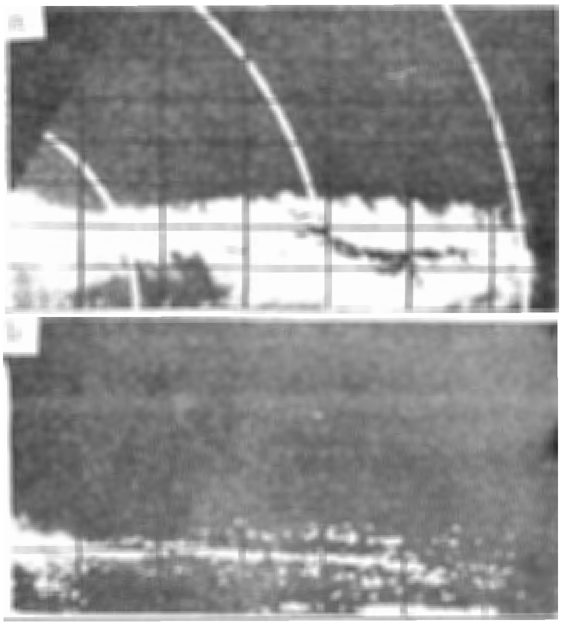

Fig.2. Range-height pictures of reflectivity (a) and wind field inhomogeneity (b) in dissipating convective cloud.

The dissipation stage is clearly revealed in the spatial structure of velocity differences. First, the differences generally reduce from 2 to 3 m/sec to 1 to 1,5 m/sec; also, vertical flows are replaced by stable horizontal flows and so the range-altitude display shows horizontal stripes of radial velocity gradients (Fig. 2).

Real-time determination of the cloud development stage is important for experiments on cloud seeding as well as for studying the life cycle of storms. Incoherent radars do not insure now the determination of the velocity sign, so the separation of updrafts and downdrafts is hindered. In addition to the direction of motion the knowledge, even approximate, of the airflow velocity would be useful and can be provided by a Doppler radar which takes a vertical cross-sections.

In this method /4/, the field of radial velocities is measured by a single Doppler radar and the vertical velocities of airflows in cumulonimbus are computed with an accuracy sufficient for many real tasks. The measurements proceed as folows. With the azimuth angle fixed the antenna elevation angle is varied in steps of two or three degrees. For each value of elevation angle the data on the average echo power and Doppler frequency shift are recorded for twenty range bins along the radar beam. The bins are spaced at 300 - 500 m.

In data processing all the quantities are transformed into appropriate absolute units from relative units; the power is corrected by range; radar reflectivity is computed; from the measured radial velocities the component is subtracted that is introduced by the terminal fall speed (estimated from the experimental ratio of the fall speed and the radar reflectivity), in this way the mean scatterer velocities are replaced by airflow velocities; the values of velocity and radar reflectivity are interpolated into the nodes of a Cartesian grid points. Then integration over the altitude of horizontal wind velocities defined through finite differences of velocities in the grid nodes leads to vertical velocities of air motion. The boundary condition is that the vertical velocities at the lower altitude level are zero.

The well-known continuity equation for an incompressible fluid has the form

$$\frac{\partial V_x}{\partial x} + \frac{\partial V_y}{\partial y} + \frac{\partial V_z}{\partial z} = 0 \quad (1)$$

In this approach the measured values of the horizontal velocity component leads to the first addend in equation (1), or the one-dimensional horizontal velocity divergence in the cross-section plane. However, to integrate the continuity equations over the altitude Z, allowance should also be made for the horizontal one-dimensional velocity divergence in a direction normal to the cross-section plane, or the second addend in equation (1).

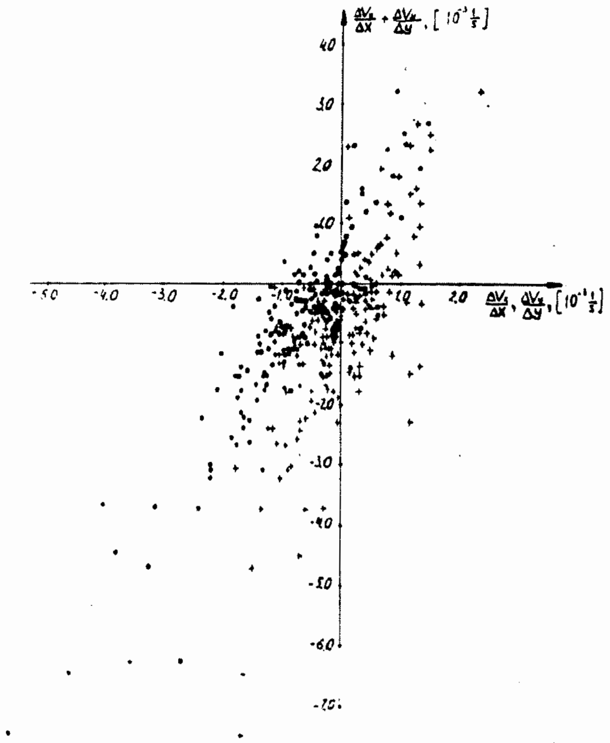

Fig. 3. Experimental results on relation of two-dimensional and one-dimensional horizontal velocity divergence in Cb.

Experiments have been carried out to study the statistical relations of the horizontal one-dimensional divergence components $\partial V_x/\partial X$ and $\partial V_y/\partial y$ in Cb. Two Doppler radars at a distance of 24.2 km from each other simultaneously sounded, with small elevation angles, the same region of space crossed by clouds. The sounding directions made an angle of 90° ± 30°. The results are shown in Fig. 3. The ordinate-axis representes the two-dimensional horizontal divergence $\mathcal{D} = \Delta V_x/\Delta X + \Delta V_y/\Delta y$ and the abscissa is the one-dimensional horizontal divergence $\Delta V_x/\Delta X$ or $\Delta V_y/\Delta y$.

The most important finding is that the experimental points of Fig.3 with rare exceptions lay in the first and third quadrants of the plot, which is evidence in favor of positive correlation between the two-dimensional divergence of horizontal wind and its one-dimensional components.

From Fig. 3 it follows that in this range of divergence values the experimental results can be approximated by equation

$$\mathcal{D} = a\mathcal{D}_1 \qquad (2)$$

where $\mathcal{D}$ is the divergence of the horizontal wind component and $\mathcal{D}_1$ is the one-dimensional component of this divergance. In the case where $\mathcal{D}_1$ is measured along a direction making an arbitrary angle with the average wind the dependence (2) can be represented as

$$\mathcal{D} = 1.2\mathcal{D}_1 \ [1/sec] \qquad (3)$$

and the r.m.s. deviation of the experimental points from the straight line (3) amounts to 9×10^{-4} 1/sec.

Thus the relation (2) provides an estimate of the two-dimensional horizontal divergence of the wind field in Cb from the data of a single Doppler radar. From invariance of point scattering with increasing divergence in Fig. 3 it follows that the absolute error in determining the two-dimensional horizontal divergence from the one-dimensional one is independent of the magnitude of divergence and so the relative error in computing the two-dimensional divergence decreases while the magnitude of one-dimensional divergence increases. Experiments with two Doppler radars which simultaneously take the vertical cross-section of Cb also showed that the error in computing the vertical velocity of airflows by integrating the values of one-dimensional divergence over altitude with the use of the relation (2) does not differ much from that given by

$$\sigma_{V_z} = \Delta h / 2\sigma\sqrt{i}, \qquad (4)$$

where σ_{V_z} is the r.m.s. error in computing the vertical velocity through (1) and (2); σ is the r.m.s. error in computing the two-dimensional velocity from one-dimensional data through (2); Δh is the integration step; and i is the ordinal number of the horizontal level with respect to the ground level.

The single Doppler radar was used in studying the structure of Cb over Moldavia in August 1979. An example of wind field structure in a vertical cross-section of Cb is presented by Fig. 4.

In most these clouds there was an intensive sloping updraft with horizontal dimension from one to three kilometers and the vertical velocities up to 15 m/sec. The updraft was most often to be fould in the region of high gradient of the radar reflectivity.

The updrafts and downdrafts at fixed altitudes were periodic in the entire cross-section of the cloud.

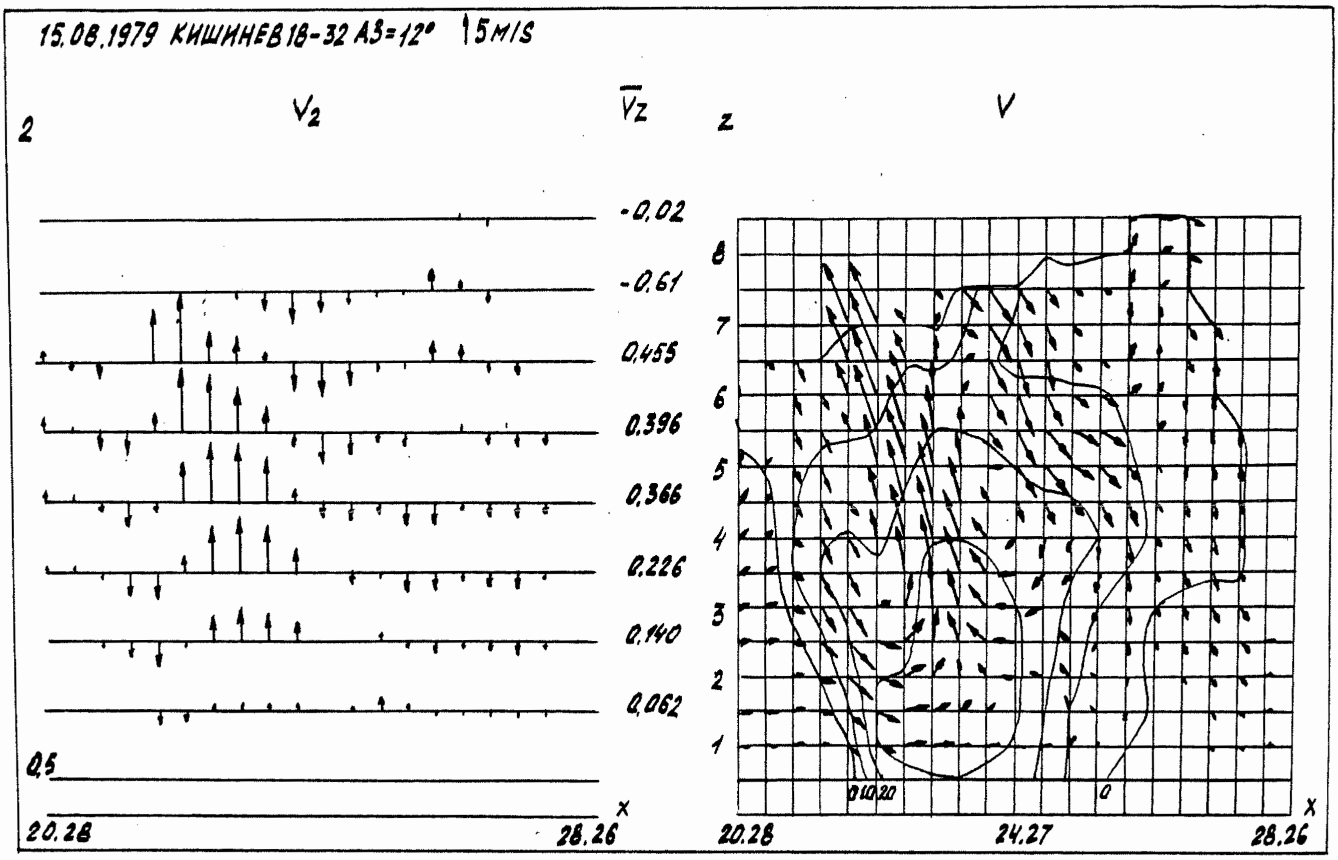

Fig. 4. Wind field structure in vertical cross-section of Cb: vertical velocities along the horizontal levels (left); velocity vector field (right). Velocity scale is marked at the top.

However, distribution of absolute velocities in the cloud cross-section indicates that in some regions the vertical flows are caused by mesoscale circulation and are not detected at all altitudes.

An air inflow into the updraft which increases the vertical velocity occurs mainly in the lower three to four kilometer layer. The ascending flow in a cloud interacts in a complex way with the wind field in the environmental troposphere. The downdrafts are less intensive and observed mainly in the peripherial part of clouds. The structure of the wind field in a cloud maintains its most important features during the active stage of the cloud life.

The preliminary results of wind field mesostructure investigations in Cb with both conventional and Doppler radars suggest that the observation methods reported here will lead to new data on the effect of the wind field in clouds during their evolution in natural conditions and/or as a result of cloud seeding.

REFERENCES

1. Lhermitte R.M., and L.J. Miller, 1970: Doppler radar methodology for the observation of convective storms. Proc. 14th Radar Meteorol. Conf., Tucson, Ariz., 133-138.

2. Melnichuk, Yu.V. and A.A.Chernikov, 1973: A radar method for turbulence detection in clouds and precipitation. Proc. of Central Aerological Observatory, 110, 3-11 (in Russ.).

3. Chernikov A.A., Ivanov A.A., and Yu.V. Melnichuk, 1975: The turbulence structure in cumulonimbus clouds. Proc. 16th Radar Meteorol. Conf., Houston, Texas, 134-137.

4. Ivanov A.A., Melnichuk Yu.V., and A.K. Morgoev, 1979: The evaluation technique of vertical air motion velocities in convective clouds with a help of Doppler radar. Proc. of Central Aerological Observatory, 135, 3-13 (in Russ.).

A THREE-DIMENSIONAL NUMERICAL SIMULATION AND OBSERVATIONAL ANALYSIS OF AN INTENSE, QUASI-STEADY THUNDERSTORM OVER MOUNTAINOUS TERRAIN

W.R. Cotton, G.J. Tripoli, K.R. Knupp

Department of Atmospheric Science
Colorado State University
Fort Collins, USA

1. Introduction

On 19 July, 1977, an intense, quasi-steady thunderstorm was observed by three Doppler radars, rawinsondes, and the NCAR Portable Automated Mesonet (PAM) over South Park, Colorado, during the Colorado State University, 1977 South Park Area Cumulus Experiment (SPACE-77).

In this paper, we summarize the salient mesoscale features leading to the formation of the quasi-steady thunderstorm and the observed structure of the storm. The results of numerical experiments with the three-dimensional cloud model reported by Cotton and Tripoli (1978), Tripoli and Cotton (1980) and Cotton, et al. (1980) attempting to simulate the formation and structure of the observed storm are discussed.

2. Observations

2.1 Mesoscale environment and general echo characteristics

The 19 July regional synoptic environment was characterized by relatively weak-shear 5-10 m s^{-1} southerly flow at mid to high levels. Throughout the day, the NE transport of low-level moisture over Colorado resulted in early deep convection over NW Colorado and midafternoon deep convection over South Park. An analysis of the evolution of the 19 July South Park mesoscale features by George (1979) revealed a relatively complex, time-evolving pattern. During the initial stages, a north-south line of echoes was induced by a corresponding north-south line of low-level convergence, with 5-7 m s^{-1} westerly winds to the west, and 5-7 m s^{-1} easterly winds to the east. New convective cells 6-8 km in diameter typically formed periodically (10-20 min) on the line's southern (upshear) end and moved northward at 6-8 m s^{-1} through the line while slowly weakening.

The low-level flow and echo patterns at 1742 MDT (approximately 90 min after the line's formation) are portrayed in Fig. 1. At this time, airflow behind a southward-advancing meso-cold front was characterized by relatively strong northerly surface winds (especially to the west of the line). The vertical structure of this post-frontal air mass exhibited significantly greater low-level shear of the horizontal wind ($\sim 10^{-2}$ s^{-1}) and relatively large low-level mixing ratios ($\sim$9g kg^{-1}). The total buoyancy of a parcel lifted from the surface was similar on each side of the front, although greater low-level negative buoyancy existed in the cooler air. The post-frontal northerly flow remained over the western half of South Park for the ensuing 90 min. The increased low-level shear of the relatively shallow ($\lesssim$1 km) airmass apparently altered subsequent storm structure and motion. One preexisting cell within the echo line's interior spawned a secondary cell which split and exhibited a diverging trajectory. Another storm, discussed in greater detail in the following section, rapidly intensified upon encountering the moist, northerly flow.

2.2 Observed characteristics of a quasi-steady storm (C11)

The most significant change in post-frontal storm behavior was the rapid intensification and organization of a relatively weak, multicellular cluster located on the southern end of the echo line. Prior to the arrival of the meso-cold front, this cell group exhibited a transient behavior in echo characteristics. Contrastingly, after the front's passage, the cell cluster rapidly intensified and consolidated within 30 min to become a heavy precipitating, quasi-steady storm which traveled $\sim 40^{o}$ to the left of the mean environmental cloud-level winds for the next 60 min.

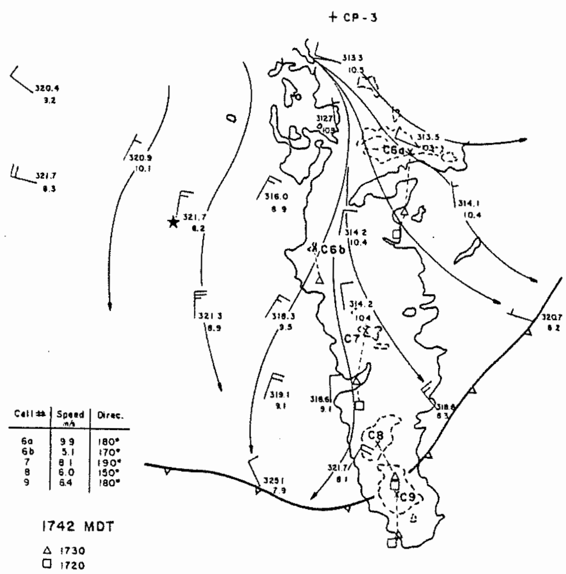

Fig. 1 Surface flow streamlines, mesonet parameters, and 5.5° CP-3 PPI echo contours (25 dBZ and 40 dBZ) at 1742 MDT. Trajectories of echo centroids are depicted. The 1710 vertical sounding location is denoted by star. (From George, 1979).

The salient features of the flow patterns within and adjacent to C11 during its steady period are portrayed in Fig. 2. Storm motion was directed towards the NW in response to continuous regeneration of precipitation within the propagating updraft U1, located above the gust front in the NW storm quadrant. The steadiness of storm circulation patterns is attributed to the constructive interaction of the NW-moving gust front with opposing low-level flow. The observed behavior is consistent with previous numerical experiments (eg., Klemp and Wilhelmson, 1978; Thorpe and Miller, 1978) which have elucidated the importance of wind shear profiles on storm motion and organization. Airflow at midlevels was characterized by accelerated flow around the updrafts and a weak flow wake region extending downstream. Anticyclonic vorticity peaking at midlevels ($1.2 \times 10^{-2}\ s^{-1}$) was associated with updraft U1, while cyclonic vorticity was associated with flow around the updraft U2. Tilting of vortex tubes was a primary contributor to these patterns. High turbulence (Doppler radar inferred) was especially pronounced and persistent at midlevels along the southern and western storm quadrants. Estimated turbulent kinetic energy dissipation rates exceeded $0.4\ m^2\ s^{-3}$ within a highly sheared region separating an updraft and downdraft. Less intense turbulence was associated with midlevel relative storm inflow along the southern storm quadrant.

Doppler-derived draft patterns (Fig. 2) exhibited more complexity than corresponding reflectivity patterns. Updraft U1 had roots ahead of the gust front in the NW (downshear) and exhibited a reversal in tilt from lower to upper levels. Continuous northwestward propagation of U1 apparently goverened storm movement. Analyzed maximum updraft speeds attained peak magnitudes of 20-30 m s^{-1} at upper midlevels (708 km AGL). A secondary, less intesnse and extensive updraft, with peak speeds of 10-20 m s^{-1}, was analyzed in the southern storm quadrant. Its forcing mechanism could not be resolved from the Doppler data or surface mesonet data. Diverging of low-level flow around the west side of the gust front and subsequent

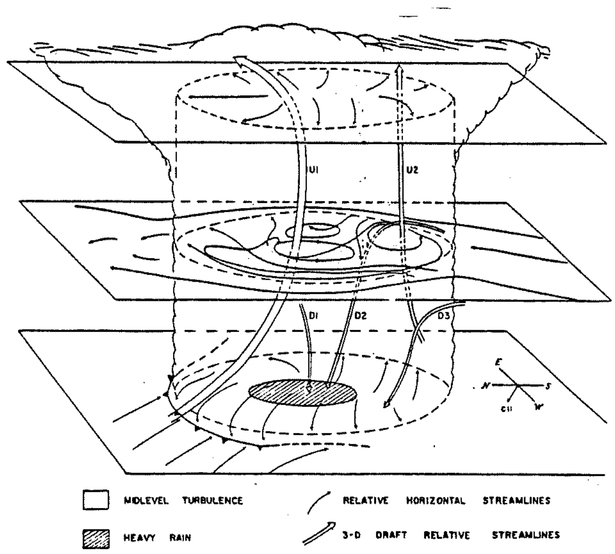

Fig. 2 Conceptual model of C11's flow patterns during its intense, organized storm stage.

convergence along the southern flank, similar to what has been modeled by Tripoli and Cotton (1980) may have played a role. The analyzed downdraft circulations consisted of three cells or source regions which coalesced near the surface to produce a coherent cold air mass and associated gust front. Inferred downdraft initiating and maintenance mechanisms consisted of precipitation drag (D1) and evaporational cooling (D2 and D3). Flow around U2 was instrumental in producing downdraft D2.

One of the most striking characteristics of C11 was its copious production of precipitation. Of the 12 primary storm cells observed during a 4½-hour period within South Park, C11 contributed ∿30% of the total precipitation. Such a large fraction was attributed to C11's quasi-steady organized circulation and relatively long lifetime. The peak measured rainfall rate (1855 MDT) was 190 mm hr^{-1}, corresponding to a maximum low-level reflectivity of less than 50 dBZ. Even higher rainfall rates may have existed after 1900 MDT since low-level reflectivity factors exhibited an increasing trend until 1937. Analysis of C11's radar echo characteristics revealed that areas of 40 dBZ and 45 dBZ echoes at 1 km AGL, as well as volumes enclosed by 40 dBZ and 45 dBZ echo surfaces attained maximum values at 1930. In contrast, updraft (and mass flux) magnitudes decreased slowly after attaining peak strength at 1900 MDT. Such a relationship implies that C11's precipitation efficiency increased with time.

Despite C11's dynamic vigor and organization, large hail was inferred absent because of the lack of significantly high reflectivity (55 dBZ maximum). However, small hail and/or graupel may have reached the surface. The absence of large hail, together with the presence of high rainfall rates, implies that precipitation processes within C11 were extremely efficient. Analyzed airflow and reflectivity patterns suggest that such a high precipitation efficiency resulted from an organized recirculation of precipitation from the updraft at midlevels to that at low levels. Recirculating tranjectories were made possible by the large angle (∿140°) between the midlevel and low-level wind vectors. Therefore, airflow and turbulent motions adjacent to the midlevel updraft would have transported precipitation from the updraft northward over the low-level inflow. The high precipitation efficiency also implies that the liquid water depletion concept advanced by Foote (1979) was occurring naturally with C11, where numerous particles reentered the downshear updraft (U1) in both liquid and solid form (this is substantiated by visual observations of a nebulous inflow sector). Thus, recirculation of precipitation elements explains (a) high rainfall rates, (b) lack of large hail, and (c) absence of a radar echo vault.

In summary, the change in low-level airflow affected storm-scale processes in two ways: (1) it altered storm dynamical processes by producing a quasi-steady updraft which governed storm movement; (2) the low to midlevel level directional wind shear promoted an organized recirculation of precipitation elements into the low-level updraft, thus modifying precipitation growth processes.

3.0 Numerical Experiments

In order to gain a greater understanding of the dynamics responsible for the production and maintenance of C11, a three-dimensional numerical simulation of cumulus development in the observed 17 July, 1977 environment was performed. The improved CSU multidimensional cloud model summarized by Cotton et al. (1980) was used. This model utilizes an ice phase parameterization developed by Stephens (1979) in which mixing ratios of ice crystals and larger graupel particles are explicitly predicted.

Because the ultimate objective of this study is to use the model to gain further insight into the dynamical structure of C11, the basic state temperature, moisture and wind fields were specified initially from a late afternoon post-frontal sounding. A domain of 35 km square by 17 km high was selected with a uniform 750 m grid spacing. A convective circulation was initiated by the introduction of a low-level focused convergence field (see Tripoli and Cotton, 1980) producing a strong induced uplifting within an 8 km radius of the domain center. Surface moisture and potential temperatures were initially perturbed upward to the level of free convection in the region of maximum convergence so that downward acceleration produced by negative buoyancy would not destroy the perturbation before the cloud became self-sustaining. As a result, an intense cumulus circulation developed reaching 14.5 km MSL. The updraft, with a peak magnitude of 14 m s^{-1}, evolved from the initial upward motion and migrated to the southern quadrant of the storm. This migration can be explained by the findings of Tripoli and Cotton (1980; hereafter referred to as T-C), which showed that in the presence of strong initial low-level convergence, the perturbation updraft may become long-lived. Associated with vigorous well-rooted, initial disturbances was a surface pressure low. In some cases, T-C found that the pressure anomaly was intense enough to divert downdraft air beneath the updraft in a direction opposite to the downward transport of horizontal momentum. Thus the downdraft reinforced the initial updraft which in this case was located in the southern quadrant of the storm.

Because the updraft in C11 was, in fact, observed in the northern quadrant of the storm, it was decided to try a different approach to storm initialization. Storm C11 was observed to first develop in the prefrontal environment before taking on the characteristics of a steady state circulation subsequent to frontal passage. This earlier development took place along the southern flank of a convective line formed in conjunction with a preexisting mesoscale convergence zone. In addition, the low-level wind shear was opposite to that encountered later on. It was decided, therefore, to simulate convection first in the prefrontal environment and then artificially induce a frontal passage in the presence of mature convective cells.

To accomplish this, a new domain 45 km long in the north-south direction, and 30 km wide in the east-west direction and 15 km high (18 km MSL) was used. A uniform grid spacing of 750 m was again taken. Initially, a uniform surface mesoscale convergence of 0.27 x 10^{-3} s^{-1} (similar to observed) was imposed. A region of more vigorous vertical motion was imposed in the center of the southern 2/3 of the domain within a diameter of 8 km. The focusing function was slightly different than that of T-C in order to contain all compensating subsidence within a radius of 15 km, instead of over the entire domain. This was necessary because the perturbation is not centered in the domain. It was anticipated that with this initialization method, convection will develop in conjunction with the focusing, drift northward and develop new cells to the south as observed. The results show that indeed convection developed, drifted northward and some new convection was produced to the south. The initial forced cell reached 14.5 km MSL which can be compared to 15 km MSL observed in the prefrontal environment. Peak updrafts of 24 m s^{-1} were produced. No prefrontal estimates of vertical velocity were made from observations, however values of 25 m s^{-1} were observed in C11 after frontal passage. Precipitation of over 1.5 cm over a 3.5 km^2 area occurred primarily in the form of graupel. This is compared to observed values of 1.0 cm, although sampling stations may not have been located in the maximum zone. Fig. 3 shows the cloud water field at 2250 m above the ground level after 50 min simulation time. A loosely organized north-south pattern of convective cells can be seen.

Numerical experiments in progress at the time of this writing include an altered initialization algorithm designed to tighten up the

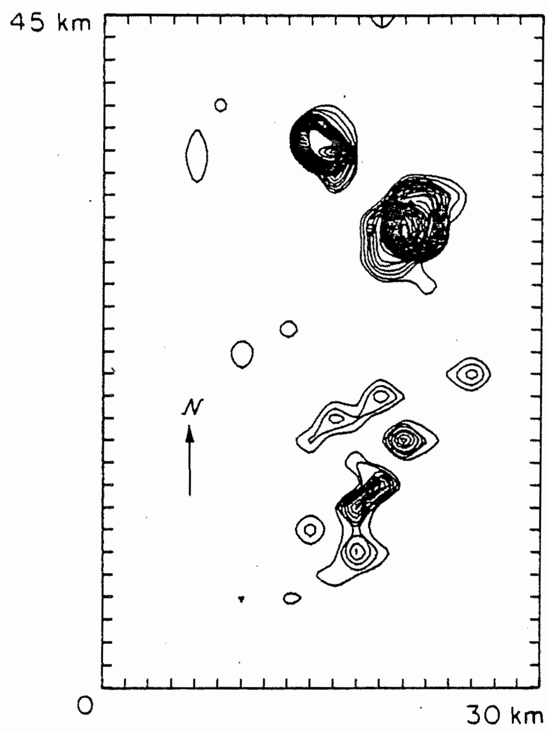

Fig. 3 Horizontal cross section at 2.25 km above ground with cloud water field contoured at intervals of .01 g kg^{-1}.

organization of the north-south line of cells. In addition, the passage of the meso-cold front through the line of mature convective cells will be induced. The results of these numerical experiments will be described in the oral presentations.

4.0 Acknowledgments

Ms. Polly Cletcher graciously typed the manuscript. This research was supported under NSF Grant ATM7908297. The numerical experiments were performed on the National Center for Atmospheric Research CRAY-1 computer; the NCAR is sponsored by the National Science Foundation.

5.0 References

Cotton, W.R., and G.J. Tripoli, 1978: Cumulus convection in shear flow - three-dimensional numerical experiments. J. Atmos. Sci., 35, 1503-1521.

Cotton, W.R., T. Nehrkorn, G.J. Tripoli and J.B. Cunning, 1980: A three dimensional simulation of the dynamic response of a Florida cumulus to seeding. Preprints to the Third WMO Scientific Conference on Weather Modification.

Foote, G.B., 1979: Further aspects of the hail suppression problem. Preprint to Seventh Conference on Inadvertent and Planned Weather Modification, 180-181.

George, R.L., 1979: Evolution of mesoscale convective systems over mountainous terrain. M.S. Thesis, Colorado State University, Fort Collins, Colo., 160 pp.

Klemp, J.B., and R.B. Wilhelmson, 1978: The simulation of three-dimensional convective storm dynamics. J. Atmos. Sci., 35, 1070-1096.

Stephens, M.A., 1979: A simple ice phase parameterization. M.S. Thesis, Colorado State University, Fort Collins, Colo., 122 pp.

Thorpe, A.J., and M.J. Miller, 1978: Numerical simulations showing the role of the downdraft in cumulonimbus motion and splitting. Quart. J. Roy. Met. Soc., 104, 873-893.

Tripoli, G.J., and W.R. Cotton, 1980: A numerical investigation of several factors contributing to the observed variable intensity of deep convection over South Florida. Under revision for J. Appl. Meteor.

CALCULATIONS ON THE SENSITIVITY OF SEVERE STORM DYNAMICS TO THE DETAIL OF MICROPHYSICS AND DOMAIN SIZE

W. D. Hall and T. L. Clark

National Center for Atmospheric Research*
Boulder, Colorado USA

1. Introduction

Clark (1979) demonstrated that lateral boundary conditions which consider only extrapolation from the domain interior outwards can lead to an ill-posed problem when simulating severe convection. Such schemes, when applied to the normal velocities resulted in a runaway situation for the horizontally averaged vertical velocity, <w>. Values of <w> as large as 3 m s^{-1} over a 60 x 60 km domain size were obtained using one such scheme. Further simulations using the NHRE 22 June 1976 case study environmental soundings were presented by Clark and Hall (1981) but this time a relaxation in time to specification at inflow for the normal velocities resulted in much better behaved profiles of <w>. Figure 1 shows profiles of <w> for three experiments from Clark and Hall (1981) where all experiments use $\Delta x = \Delta y = 1$ km for the horizontal grid increments, $\Delta z = .5$ km for the vertical grid size in the numerical model. All experiments used identical initialization and a warm rain parameterization based on the Kessler (1969) scheme. The only difference in these three experiments is horizontal domain size. We see in Fig. 1 three time levels of <w> versus z where the horizontal averaging has been performed over both the original model domain size as well as the reduced domain size of 40 x 40 km. Two points are evident in this figure. Firstly, for the original domain size $\langle w\rangle_{max}$ values are systematically decreasing with increasing domain size. Secondly, the 40 x 40 km averaged values of <w> are very similar for all three experiments. The values at t = 5760 s or 96 min for Exp. 25 and 23 are due to slight phase differences since when these models were continued for another 960 s the <w> profiles on the 40 x 40 km domain retreated back to near the t = 4800 s values. Thus, by using the relaxed type of inflow specification described in Clark and Hall (1981) well-behaved solutions are obtained which are not overly sensitive to the lateral boundary conditions. Thus, we are now at a stage to study the sensitivity of the model to physical processes without having to be overly concerned with ill-posedness of the problem being the main contributor to any observed sensitivity. To further demonstrate the reproducibility of results, Fig. 2 displays fields of vertical velocity at z = 6.5 km AGL for five experiments from Clark and Hall (1981). Only domain size and horizontal resolution differ between any of these experiments. We see one main cell with a minor cell to the northeast in each case. The structure and intensity are similar in all cases. As demonstrated by Clark and Hall (1981) if we eliminate the specification at inflow for the normal velocity then dramatic differences in both w and <w> result.

As a first test on the sensitivity of the dynamics and thermodynamics to the cloud physical processes one experiment was performed in which auto-conversion to rain water described by the Kessler parameterization was prohibited to occur. This results in $q_R = 0$ with no trace of a gust front. This experiment is referred to as 3D3 again taken from Clark and Hall (1981). A second experiment was performed using a modified version of the Koenig and Murray (1976) parameterization which considers the ice phase. This experiment produced some interesting results but was in fact a failure when compared with the observations. Due to deficiencies in the parameterization, as employed, the anvil precipitated instead of the main cells precipitating out in the northwest flank. This resulted in extremely weak gust fronts with $\Delta\theta = -4$K instead of the observed -16K. The gust front structure was similarly in poor agreement with observations. The warm rain Kessler experiments such as Exp. 21R, 23, 25, 26 and 27 were much closer to the observed producing $\Delta\theta = -9$K and a structure similar to the observations. This difference in simulations is attributed to the region of precipitation and subsequent evaporation being closer to those observed for the Kessler scheme than for the current version of the Koenig and Murray scheme. Improvement of the latter scheme for ice phase clouds is currently under study. The clouds considered are primarily ice phase clouds.

2. Sensitivity Between the No Rain (Exp. 3D3) and Warm Rain (Exp. 25) Case

The cell structures for 3D3 were rather close to those of 25 despite the fact that no gust front developed for the first experiment. Apparently the gust front was not sufficiently strong in Exp. 25 to be strongly coupled with cell evolution as had been earlier believed in Clark (1979). Figure 3 displays a vertically averaged correlation coefficient $C_{w\zeta}$ between vertical velocity and vertical vorticity for the two experiments. The averaging depth was taken as the first 5 km AGL. We see one effect of precipitation is to weaken the correlation between these variables where with $q_R = 0$ we reach $C_{w\zeta}$ values of .65 whereas $q_R \neq 0$ we reach values of only .38. This dramatic reduction is thought to be due to source/sink regions being decoupled due to sedimentation of the rain. The open triangles are taken from the observations and are again even smaller than Exp. 25

*The National Center for Atmospheric Research is sponsored by the National Science Foundation.

results suggesting even stronger sedimentation effects are present in the natural cloud than in the simulation. Figure 4 displays volume-integrated perturbation kinetic energies for the two experiments. Here we see that the effect of precipitation is to increase the eddy kinetic energy by a substantial amount. Figure 5 shows a similar result for volume-integrated values of the square of ζ.

3. A Koenig-Murray Parameterization Experiment

Along with the two categories of liquid phase, cloud water and rain water, introduced by Kessler, the ice phase is assumed to be represented by two types of ice. Type A originates from sorption nuclei and type B originates by type A ice contact with the rain. Each category contains the two field variables of number concentration and mass mixing ratio.

Figure 6 shows the model-simulated vertical velocity at t = 96 min in cross-sectional view with an east-west orientation. Maximum values of w are about 28 m s^{-1} in this plane. Figure 7 shows the type A ice mixing ratio for the same plane as in Fig. 6. We see $q_{ice,A}$ values as large as 9 gr kg^{-1}. The vault region is the result of particles being nucleated within the updraft and having no time to grow to large sizes until carried out of the main updraft.

4. Conclusions

It has been shown that two effects of precipitation are to reduce the correlation between vertical velocity and vertical vorticity as well as to increase the eddy kinetic energy.

The experiment with ice physics produces the expected vault in the updraft region but is deficient as an overall parameterization because problems associated primarily with the treatments of riming rate, melting and the subsequent sedimentation of raindrops.

5. References

Clark, T. L., 1979: "Numerical simulations with a three-dimensional cloud model: Lateral boundary condition experiments and multicellular severe storm simulations", *J. Atmos. Sci.*, *36*, 2191-2215.

Clark, T. L. and W. D. Hall, 1981: Section 8.1.1 of Chapter 8, "Cloud Modeling in Three Spatial Dimensions", of NHRE Final Report.

Koenig, L. R., and F. W. Murray, 1976: "Ice-bearing cumulus cloud evolution: Numerical simulation and general comparison against observations", *J. Appl. Meteor.*, *15*, 747-762.

Kessler, Edwin, 1969: "On the distribution and continuity of water substance in atmospheric circulation", Meteorological Monographs, Vol. 10, No. 32, 84 pp.

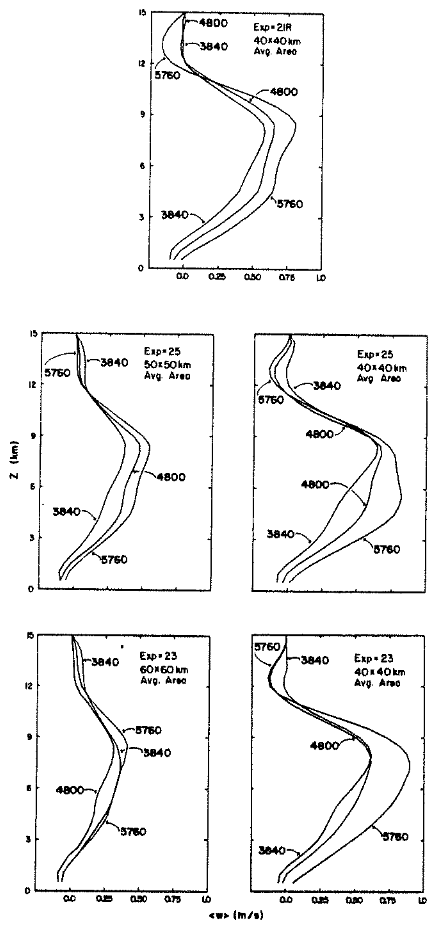

Figure 1. Horizontally-averaged vertical velocity, <w>, versus height, z, for three experiments using a warm rain parameterization. Time is in seconds. Note the two averaging domains used for Exp. 25 and 23. The reduced domain is equivalent to that of Exp. 21R.

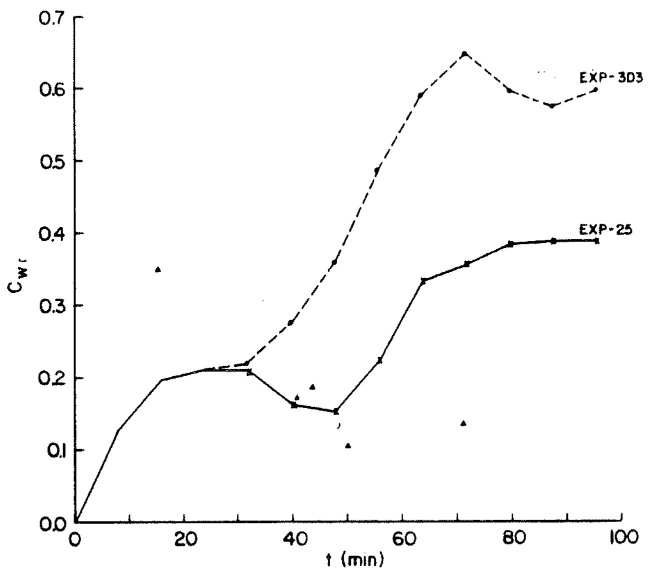

Figure 3. Correlation coefficient $C_{w\zeta}$ between vertical velocity and vertical vorticity for experiments, ---- Exp. 3D3, —— Exp. 25, and Δ observations. The absolute time of observation point is not meaningful, only the relative spacing in time is correct.

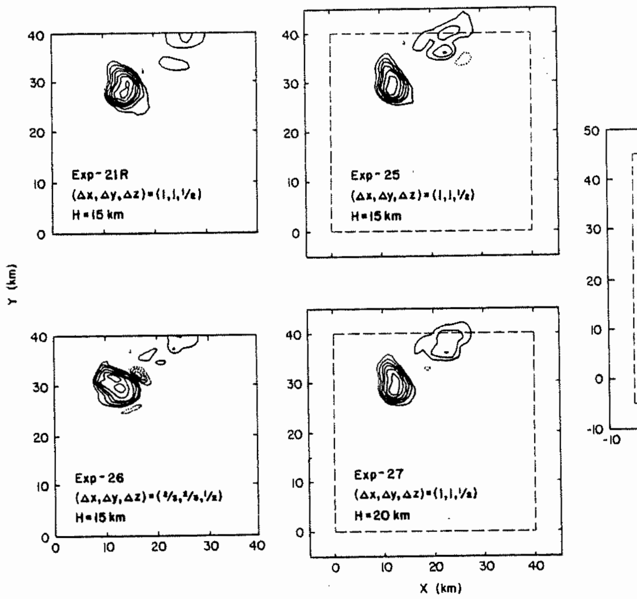

Figure 2. Vertical velocity at z = 6.5 km AGL at time = 96 min for five experiments with warm rain parameterization. Δx, Δy, Δz grid interval (km) used in x, y, and z direction, H, total domain height are shown. Contour interval is 4 m s^{-1} for positive values (solid) and 2 m s^{-1} for negative values (dashed).

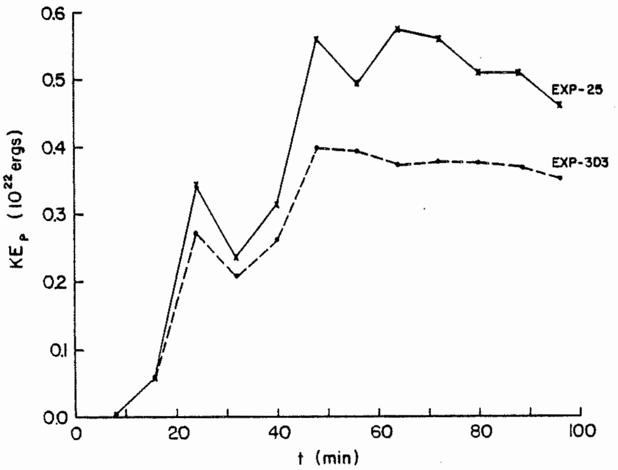

Figure 4. Volume-integrated perturbation kinetic energy. —— Exp. 25, ---- Exp. 3D3.

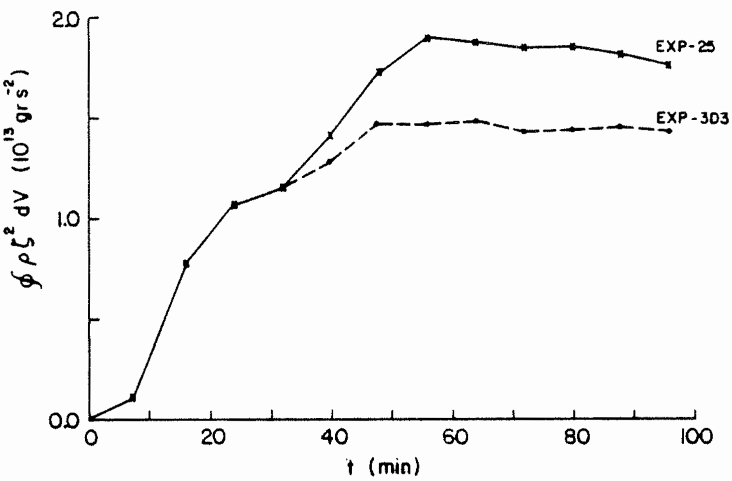

Figure 5. Volume-integrated square of the vertical vorticity. —— Exp. 25, ---- Exp. 3D3.

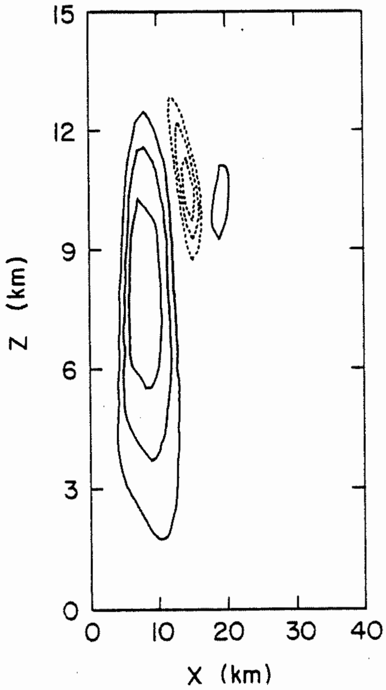

Figure 6. East-west cross-sectional of vertical velocity with Koenig and Murray ice parameterization at time = 96 min. Positive contour interval is 8 m/sec (solid lines). Negative contour interval is 4 m/sec (dashed lines).

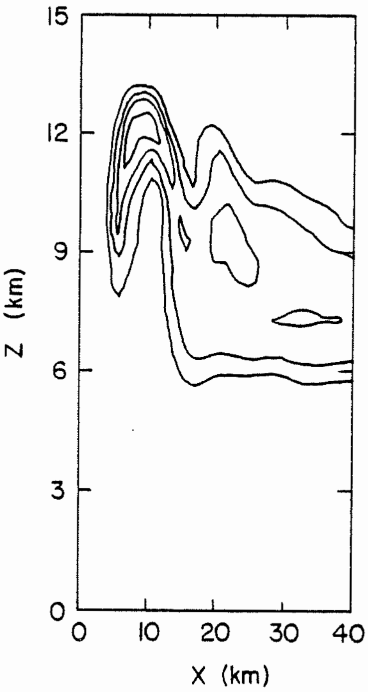

Figure 7. East-west cross-section of type A ice mixing ratio for same time and location as Fig. 6. Contour interval is 2 gm/kg.

PRECIPITATION AND HAIL FORMATION MECHANISMS IN A COLORADO STORM

Andrew J. Heymsfield

National Center for Atmospheric Research*
Boulder, Colorado 80307 USA

1. Introduction

The mechanisms of hailstone growth in clouds have been a topic of intrinsic scientific interest for many years. The present understanding of hail formation processes is incomplete, in part because the complete data sets that would be required to investigate the complex formation mechanisms do not exist. Previous hailstorm studies have relied extensively on radar reflectivity data and idealized hail growth trajectories to develop conceptual models of the hail formation process. Unlike earlier studies, the present study of a multicellular hailstorm which occurred on 22 July 1976 in NE Colorado identifies the locations of graupel and hail within the storm through use of the dual-wavelength technique described by Jameson and Heymsfield (1980; hereafter referred to as JH). This information, in conjunction with the triple-Doppler radar analysis of Hal Frank of NCAR, with simplified calculations of particle trajectories and *in situ* aircraft observations led to the identification in this storm of what appear to be the dominant hail growth mechanisms.

2. Description of the Data Set

The storm was characterized as a relatively intense hailstorm prior to the Doppler radar observations, but had declined to a moderate level during the period under investigation. Peak reflectivities of 70 dBZ were found at the earlier, intense period, but had declined to 60-65 dBZ during the period under investigation. The period from 1626-1718 MDT was chosen for the present analysis because of the simultaneity of the aircraft and triple-Doppler radar measurements. Unfortunately, hail collections during this period were sparse because of the lack of roads along the path of the storm. Hail collections were made only at two locations, but the storm was likely to have produced hail during a significant portion of the observational period, as described by JH. During the observational period, the storm was characterized by a cloud top height of approximately 14.5 km MSL. The 0°C and -40°C isotherms within the updraft were at approximately 4.7 and 10 km, respectively.

The triple-Doppler radar data was crucial to the present analysis. The time required for a complete scan of the storm volume ranged from 3.5 to 4 min and six complete scans were analyzed for the observational period. Integration of the equation of mass continuity proceeded from near the cloud top to the surface. The spatial resolution was 1-2 km in the horizontal and the vertical, and the accuracy was estimated to be generally better than ±2 m s^{-1} in the horizontal and ±6 m s^{-1} in the vertical.

In the study by JH, it was shown that dual-wavelength radar measurements can be used to discriminate particle sizes for the 22 July 1976 case study. In that study, the hail signal (Y') was defined as the logarithm of the ratio of the reflectivity at 10 cm (Z_{10}) to that at 3 cm. Values of $Y' \geq 3$ dB were found to be correlated with hailstones larger than 1 cm which had a fairly high density. Values of $Y' \leq -3$ dB were found to be correlated with rimed particles or graupel with a fairly low density over the size range 5 to 10 mm. Whenever -3 dB $< Y' <$ 3 dB, particles are presumed to be between graupel and hail in density and size or were less than 5 mm in size. A complete dual-wavelength scan of the storm took 1.5 min.

In addition to an extensive set of radar data, measurements were made with the South Dakota School of Mines & Technology T-28 aircraft during six penetrations through high reflectivity regions of the storm over the time period 1630-1720 MDT. These penetrations spanned an altitude range of 6.0 to 7.5 km MSL (2.4 to 3.9 km above cloud base) and a temperature range of -10 to -19°C. The measurements were supplemented by data below cloud base obtained from 15 passes with the NCAR Queen Air 306D. The altitude and temperature at the cloud base was found to be approximately 3.6 km MSL and +7.5°C, respectively.

3. Locations of Hail and Graupel Within the Storm Complex

Information on hail and graupel locations according to dual-wavelength measurements were compared with wind field data to provide a basis for investigating the hail production process. Six sets of dual-wavelength measurements were analyzed in detail. A pulsating hail production process was noted during the observational period. The periods during which Doppler data were collected (MDT) and the corresponding volume over which hail was measured above the melting level were: 1626 (82 km^3), 1632 (42 km^3), 1640 (12 km^3), 1708 (46 km^3), 1712 (123 km^3), and 1718 (145 km^3).

The processes leading to the pulsations in hail production were more fully investigated by combining the dual-wavelength radar data with the derived wind fields for the six times investigated in detail, and some of the general features of the synthesis will be discussed here. Figure 1a shows data on graupel and hail locations, the storm relative wind field and the measured reflectivity at 1640 MDT on a vertical section oriented from north to south through the main updraft region. This section was oriented approximately along the inflow direction. This figure illustrates one component of the hail production mechanism, in which particles are introduced into the main updraft

* The National Center for Atmospheric Research is sponsored by the National Science Foundation.

region from the forward overhang and some grow into hail when they reach the upper levels of the updraft region. The lack of appreciable hail noted at 1640 MDT indicates that the hail production mechanism was not efficient at this time. The dominant mechanism for hail production over the period 1626-1640 MDT was found to result from the advection of hailstones in the divergent wind field from a feeder cell located west of the main updraft region into the main updraft region where they continued to grow.

An illustration of the transfer of embryos from a feeder cell into the main updraft region at 1708 MDT appears in Fig. 1B in a vertical section oriented from west to east. An extensive region of graupel was observed at 6 km within the feeder cell located to the west of the main updraft region (Fig. 1B). These embryos were apparently advected in the divergent wind field into the main updraft region, where hail was produced. These transferred embryos were responsible for the production of copious amounts of hail within the storm several minutes later. A vertical section oriented from south to north through the storm at 1712 MDT appears in Fig. 1C. A continuous region of hail was noted to form within the updraft region at the low levels. A large band of graupel was noted downwind of the main updraft region and was a consequence of "size-sorting."

A three-dimensional-type diagram indicating the hail locations at 1712 MDT appears in Fig. 2. The outer contour in the figure represents a "smoothed" version of the locations where the hail signal (Y') $\geq$ 3 dBZ. The three-dimensional form representing the hail locations appears near the top of the figure, and a fully sliced view of the hail locations appears in the

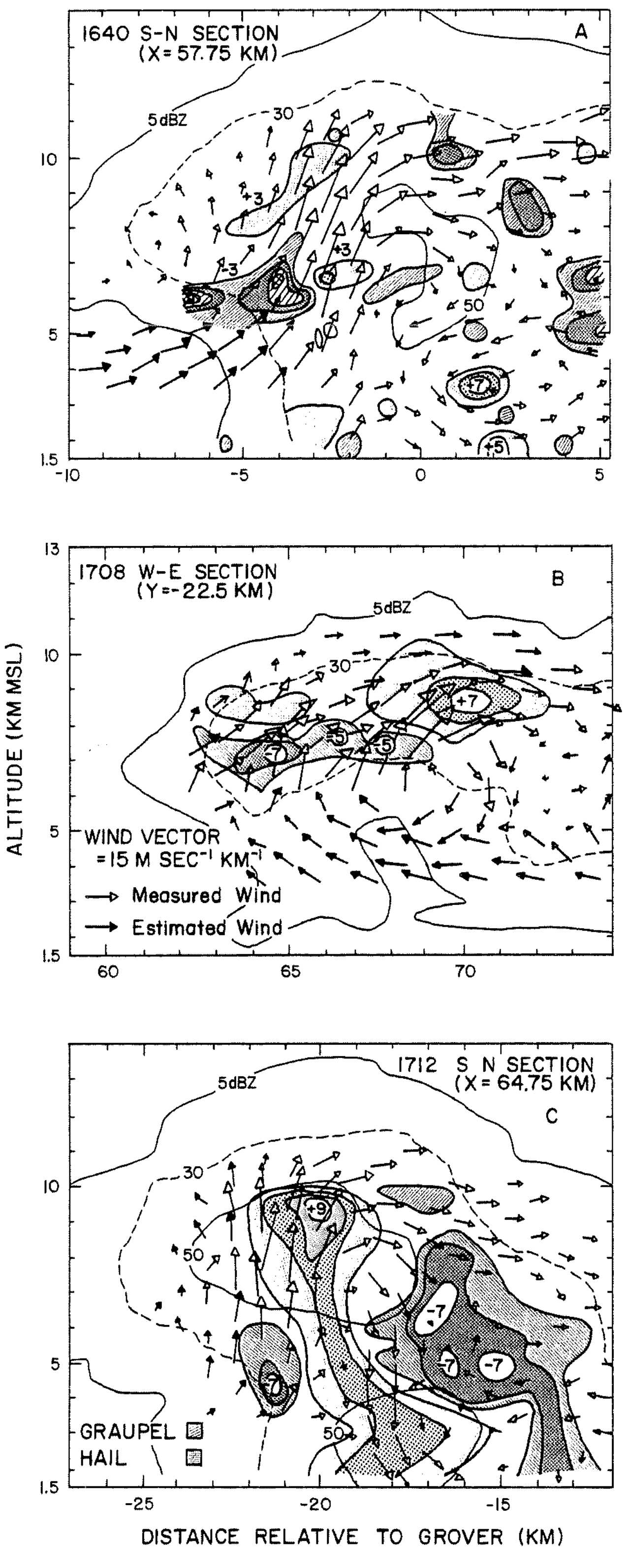

Fig. 1. Vertical sections through the updraft region showing the reflectivities, the graupel locations (indicated with negative hail signal in dB) and hail locations (indicated with positive hail signal in dB), and the wind field data.

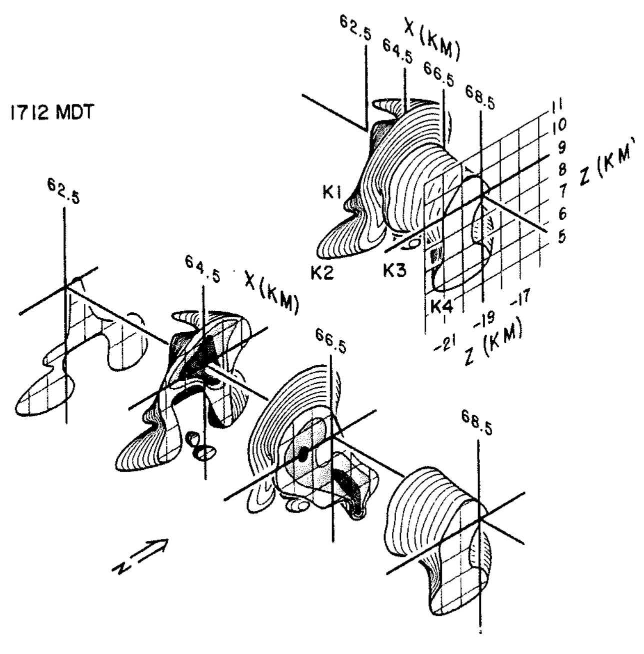

Fig. 2. Hail locations at 1712 MDT, with composite three-dimensional drawing at upper portion of figure and sliced view of three-dimensional form drawn on five planes which are oriented from north to south in lower portion of figure. Outer contours: dual-wavelength signal = +3 dB, increment of successive contours = +2 dB. Cell locations are indicated in upper portion of figure. Dark horizontal line oriented north to south: altitude (Z) = 9 km. Dark vertical line: Y = 19 km with respect to Grover coordinates. Position of north-south (X) planes are indicated in lower portion of figure. The separation between vertical lines and horizontal lines = 1 km.

bottom of the figure. Figure 2 indicates that at 1712 MDT, a well-defined region of hail was located near the top of the storm, at the upper levels of the strong updraft region. The individual cells associated with the hail are indicated in Fig. 2.

4. Trajectory Calculations

To provide insight into the dominant mechanisms responsible for hail growth, particle growth trajectories, computed from the three-dimensional wind field, were compared with the locations of hail within the storm which were obtained from the dual-wavelength data. The particle trajectories were computed backwards in time using the observed three-dimensional wind field and a simplified particle growth model. Average lineal growth rates (dD/dt) and velocity growth rates (dV/dt) as a function of particle size were computed from the T-28 aircraft measurements of the drop size distribution and the liquid water content, whenever the liquid water content exceeded 1 g m^{-3}. A 20 s timestep and the appropriate triple-Doppler wind field were also used in the calculations.

The calculations revealed two dominant trajectories existed for the growth of hail. The largest and most wide-spread hail resulted when graupel particles and hailstones were advected in the divergent wind field from a feeder cell into the main updraft region where they continued to grow. Smaller hail and graupel particles resulted when a feeder cell developed within a region of precipitation debris. The particles entrained into the developing cell had a "head-start" over those particles nucleated within the cell.

5. Discussion

A fundamental requirement for the growth of a hail embryo into a hailstone is the provision of sufficient time for the particle to grow within the liquid water region. In this study, particles which grew into hailstones achieved this sufficient growth time by starting in a feeder cell and then subsequently being carried by the diverging flow near the top of the feeder cell updraft into the main updraft region where the growth into hail was completed. The dominant modes of hail growth over the period are indicated in Fig. 3, for the period 1626-1640. A schematic for the period 1708 to 1718 is shown in Fig. 4. The particle transfer mechanism seems to be critically dependent upon the position of the feeder cell relative to the main updraft core, the presence of strong divergence at the mid- and upper levels of the storm and the magnitude of the vertical velocity within the divergent regions of the feeder cell, which must be sufficient to keep particles aloft. In the storm investigated in the present study, feeder cells often formed along the gust front generated by the storm. Specific characteristics of the environmental flow field may be important, as for example, cyclonic wind vorticity which may enable particles to advect around the forward side of the storm.

As noted in the previous section, many of the trajectories which ultimately became hail initiated within a region of "precipitation-debris." In order to understand the origin and composition of hail embryos, it was useful to trace the development of several of the main feeder cells in this region. The radar measurements indicated that the radar reflectivity developed rapidly within these feeder cells. The T-28 measurements indicated that the particles ingested from the precipitation debris region by the feeder cells were primarily aggregates of dendrites up to 7 mm in size (Fig. 5). Rapid growth of these large aggregates into hail is anticipated.

To assess the potential importance of aggregates in the hail formation process for this storm, a computer model was developed to determine the comparative rates of growth of various ice crystal forms. The calculations used the heat balance equations for determining the particle temperature, the accreted density based on the particle temperature and drop size distributions, and the most appropriate collection efficiencies and Best Number (X) Reynolds number (Re) relationships for terminal velocity calculations. One measure of the suitability of an embryo to grow into a

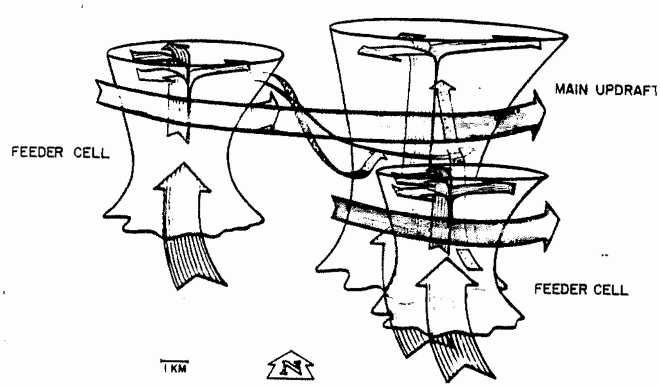

Fig. 3. Schematic representation of the hail formation process for the period 1626-1640 MDT. Arrows: No shading --environmental winds; vertical shading --updraft air; stipled shading--particle trajectories producing hail.

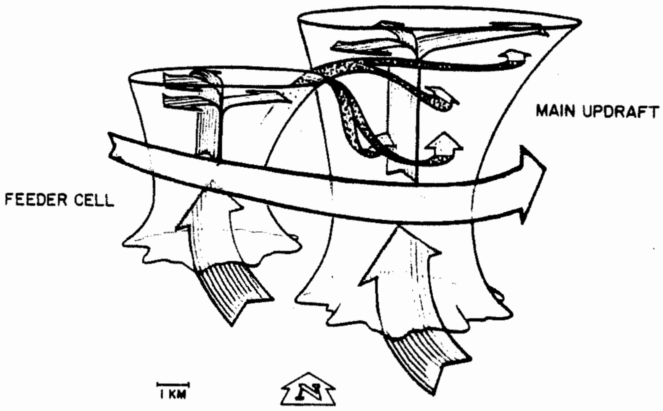

Fig. 4. Same as Fig. 3, except for 1708-1718 MDT.

hailstone is the time required for it to achieve a terminal velocity of 10 m s^{-1} (Fig. 6). The calculations indicated that frozen drops are the most suitable hail embryos, and large graupel particles and aggregates are less so, and, dendrites make rather poor embryos.

Within the newly developing feeder cells, the observed particle types were aggregates up to 5 mm and single dendrites up to 1 mm. It is apparent from Fig. 5 that aggregates are the preferable ice particle form for growth into graupel in the storm investigated. However, within the mature updraft regions, graupel particles can more rapidly increase their terminal velocities, and therefore are preferable forms of hail embryos within the intense updraft regions. These calculations are consistent with the observations of hail growth mechanisms described previously.

6. Conclusions

In the present study, a two-stage hail growth model is proposed in which 1) hail embryos originate in feeder cells and then 2) are transferred into the main updraft region where they continue to grow. The growth of hail embryos is accelerated if the feeder cell can ingest large aggregates from the precipitation debris region. The storm investigated in this study was a typical, moderate-intensity hailstorm in northeast Colorado, as indicated by the maximum hailstone sizes (approximately 2.2 cm) and radar reflectivities. Since the reflectivity patterns found in the storm were similar to that exhibited by many other hailstorms in that area, it seems likely that this two-stage hail growth model is applicable to other hailstorms in northeast Colorado. Future research is needed to define the importance of and determine the applicability of the particle transfer mechanism in hail and precipitation formation.

7. Acknowledgments

The author wishes to thank Hal Frank and Brant Foote for their helpful comments during the course of this study. The diligent efforts of John Murino are greatly appreciated. Drafting support from Howard Crosslen and the NCAR drafting group were invaluable, as were the excellent reproductions from the NCAR photography group and print shop. Discussions with David Johnson, Chuck Wade, Charlie Knight, and Nancy Knight were valuable. The manuscript was reviewed by Marian Heymsfield and typed by Carol Brown.

8. Reference

Jameson, A. R., and A. J. Heymsfield, 1980: Hail growth mechanisms in a Colorado storm: Part I. Dual-wavelength radar observations. Accepted for publication in *J. Atmos. Sci.*

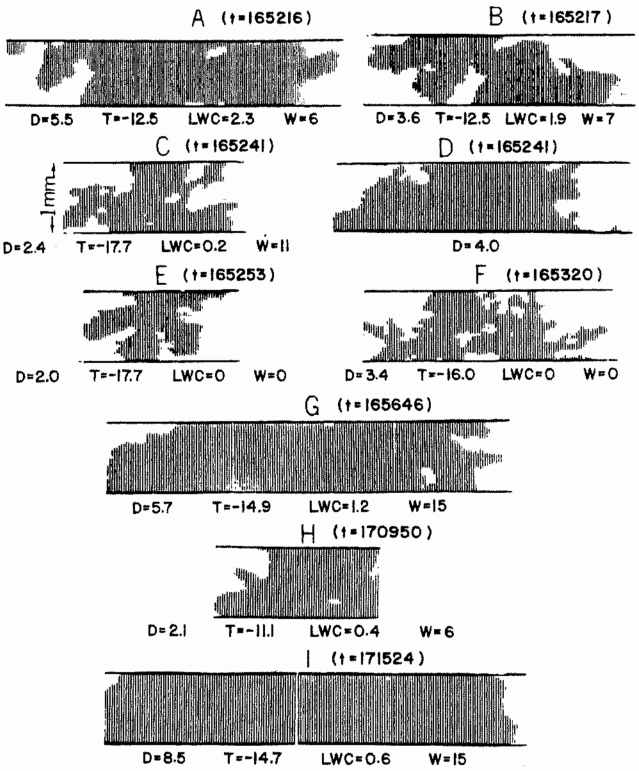

Fig. 5. Two-dimensional (2-D) images of particles sampled with the T-28 on 22 July 1976. The symbols in the figure are: t (time, MDT); D = maximum dimension (mm); T = temperature (°C); LWC = liquid water content (g m^{-3}); W = vertical velocity (m s^{-1}). All particles collected in feeder cells or upwind of feeder cells.

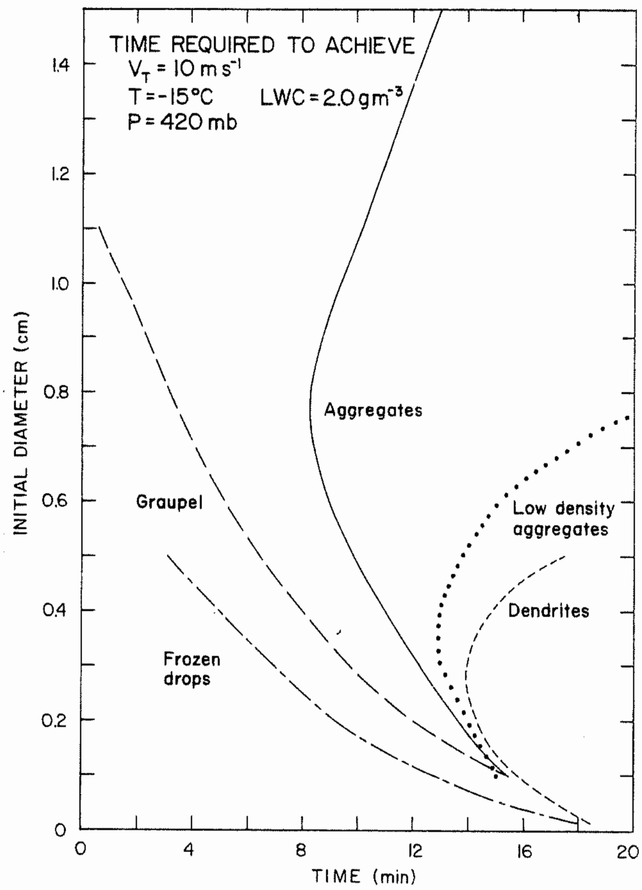

Fig. 6. Calculated times required for particles to achieve a terminal velocity of 10 m s^{-1}.

LIQUID WATER CONTENT VERSUS VERTICAL VELOCITY IN TROPICAL CUMULONIMBUS*

H. Isaka, M. Fodé[1] and G. Andraud[2]

L.A.M.P., University of Clermont-Fd, FRANCE

1. Introduction

Recent development of airborne microphysical probes has enabled to observe 'in situ' the entire size range of droplets and hydrometeors inside the clouds. However, such observations remain relatively scarce (Musil et al., 1978 ; Houze et al., 1978), while their importance to studies of the growth of precipitation and to cloud modellings is quite obvious.

The purpose of the present paper is to report some results of analyses of the tropical cumulonimbus penetrations made by a DC 7 of French Air Forces in October 1977 over Ivory Coast. One of these penetrations was already briefly described by Gayet et al. (1978). In this paper, we will be interested in some average features of microphysical parameters inside this kind of clouds and in their variations with the updraught intensity. Some of the implications of such observations will also be considered with respect to precipitation processes and cloud modellings.

2. Data and data processing

The data in this study were obtained during two (Nos. 2 and 7) of the 8 flights made by the DC 7 over Ivory Coast. These two flights totalizing 20 penetrations through continental tropical cumulonimbus, were selected for the present analysis, because almost all of their cloud penetrations were made through convectively active zones of cumulonimbus, characterized by moderate to strong updraughts. The penetration levels varied between 600 mb and 480 mb, corresponding to a temperature range of 0°C to - 10°C.

The DC 7 was instrumented for measurements of microphysical, thermodynamical and dynamical parameters. Characteristics of these instruments were previously described in detail by Lescure and Lejeune (1975) for thermodynamical and dynamical measurements and by Gayet (1976) for microphysical measurements. All analog data were digitalized and recorded with a sampling rate of 10 per second, except those supplied by an inertial navigation system, Litton 51 (4 per second) and by the Particle Measuring Systems ASSP, CDP and PSP probes (1 every 2 seconds). The output signals from the Ruskin probe for measurement of the total water content were recorded in analog form on magnetic tapes and later digitalized at an adequate samplig rate.

The three components of air velocity were computed according to the method previously described (Guillemet et al., 1977). This method includes a calibration scheme to minimize the effect of instrument biases in the estimated air velocity. The vertical velocity of aircraft was computed according to the Lenschow's scheme in which the pressure altitude is used to stabilize the altitude calculated by a twofold integration of the vertical acceleration of aircraft (Lenschow, 1972). This acceleration was measured with an accelerometer strapped down to the aircraft structure instead of a vertically aligned accelerometer of the Litton 51 inertial platform. This means that the accelerometer is sensitive not only to the vertical acceleration of aircraft, but also to other forces. Hence, we will only consider the vertical velocity computed on quasi-straight flight pathes. Furthermore, the vertical velocity was smoothed with a Gaussian low-pass filter to retain its variations of horizontal scales longer than 500 m.

The liquid water content of cloud was estimated by integrating size spectra of cloud and precipitation droplets obtained by the ASSP, CDP and PSP probes. In doing so, we assumed that all the particles detected by these probes were of liquid phase, although the negative temperature recorded at the penetration levels should allow the presence of some solid particles. In fact, the impact of solid elements, probably graupels and small hailstones, onto the cockpit window was reported for some of the penetrations. This implies that the estimate of liquid water content has to be considered cautiously. In this study, we did not refer to the liquid water content which could be estimated from the total liquid water contents measured by the Ruskin probe, because the difficulty in estimating the water content in vapour phase have not yet been overcome completely (Pinty et al., 1978).

3. Results and discussions

3.1 Typical observations

Figure 1 represents variations of some microphysical parameters and the vertical air velocity observed during one of the 20 cumulonimbus penetrations analyzed in this paper. This example may illustrate several interesting features of cloud penetration observations.

In order to replace this penetration with respect to the entire masses of cloud as observed by the airborne meteorological radar, we plotted the corresponding flight path of the DC 7 on an image of radar echoes photographed just before the cloud entry ; we reproduced it schematically in Figure 2. This figure shows

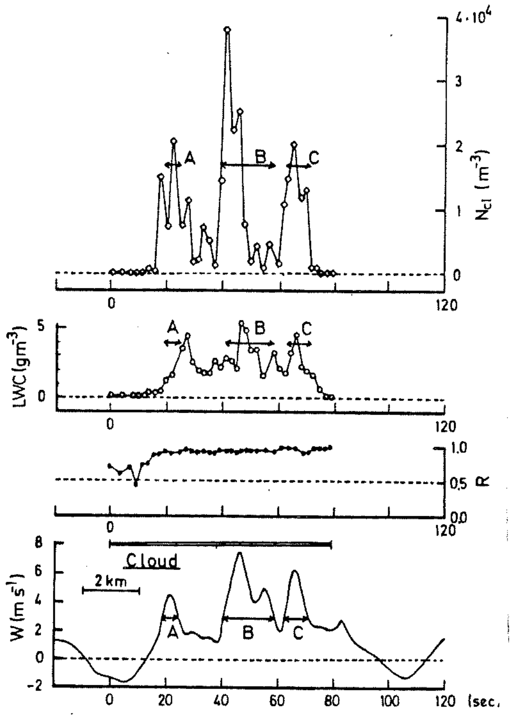

Fig. 1 : Example of Variations of Some Microphysical Parameters and Vertical Air Velocity during a Cumulonimbus Penetration (15 h 00 Penetration of Flight No. 2)

N_{cl} : Number concentration of cloud droplets (diameter < 300 μm) per litre ;
LWC : Liquid water content (g m^{-3})
R : Ratio between the precipitation water content and the liquid water content;
W : Vertical air velocity (m sec^{-1})

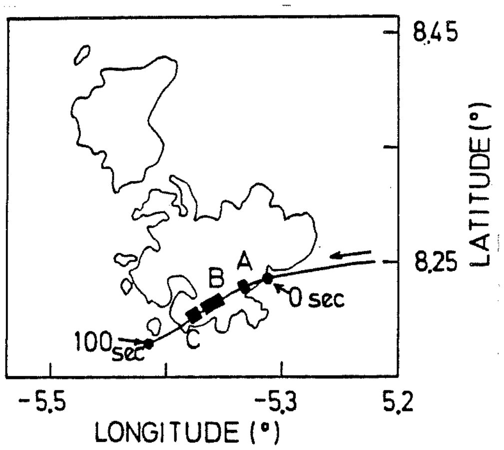

Fig. 2 : Horizontal Projection of the Flight Path of the DC 7 (15 h 00 penetration of Flight No. 2) and Radar Echoes observed by the Airborne Meteorological Radar (3 cm). Two solid cercles represent the locations of the DC 7 respectively at the cloud entry and after 100 seconds. The letters A, B and C indicate the three updraught regions identified in Fig. 1.

that the DC 7 was flown through an edge of cumulonimbus which covered an area of about 12 km x 10 km. It was reported that this part of the cumulonimbus was in developing phase with multiple visible convective towers.

The four curves in Fig. 1 display, from the top to the bottom, the number concentration of cloud droplets with a diameter less than 300 μm (litre-1), the liquid water content (g m^{-3}), the ratio between the precipitation water content and the liquid water content, and the vertical air velocity (m sec^{-1}). The precipitation water content is defined as the part of liquid water content due to the particles in the PSP size range. The abscissa is the elapsed time with its origin taken at the instant of cloud entry determined by the ASSP probe.

During this penetration of 7 km in length, the DC 7 crossed three distinct zones of weak to moderate updraughts, designated respectively by A, B, and C in Fig. 1. No downdraught was observed in this penetration, except at both edges of the cloud where weak subsidences of 2 m sec^{-1} were found. The horizontal extent of the draught zone is of about 1 km for both A and C regions, and 2 km for the B region. The updraughts, observed during other penetrations, also have similar values of the horizontal extent, except in a few cases where the updraught occupied a region exceeding 4 km in length.

Both the number concentration of cloud droplets and the liquid water content also exhibit three distinct zones of high values. Their locations suggest clearly a close relationship of these high cloud droplet concentration and the liquid water content with the existence of updraught. The number concentration reaches peak values of 2 to 4 10^4 per litre in these updraught regions. Its value drops by a factor of 5 to 10 outside. These peak values are quite moderate ; higher number concentrations in the range of 1 to 2 10^5 per litre were sometimes observed in much stronger updraughts.

The liquid water content varies between 2 and 5 g m^{-3}, except near the edges of the cloud where its values drop much less than 0.5 g m^{-3}. The ratio R remains close to unity throughout the entire length of the penetration, except in the zone located between the first edge of the A updraught region. This means that the liquid water content is mainly due to precipitation particles without any significant contribution from cloud droplets.

The location of peak liquid water content sometimes coincides with that of the peak vertical air velocity, as it can be seen in the B and C regions in Fig. 1, while it also occurs that these two locations are slightly separated from each others so that the peak water content may be observed near the edge of updraught regions. A similar observation was reported by Musil et al. (1978) in their analyses of thunderstorm penetrations. The A updraught region is one of these cases, though it is not the best example we can offer.

3.2 Liquid water content vs Updraught Velocity

The above example suggests that a fairly good correlation may be found between liquid water content and updraught velocity within developing convective cells in which a strong downdraft has not yet been produced. Many of

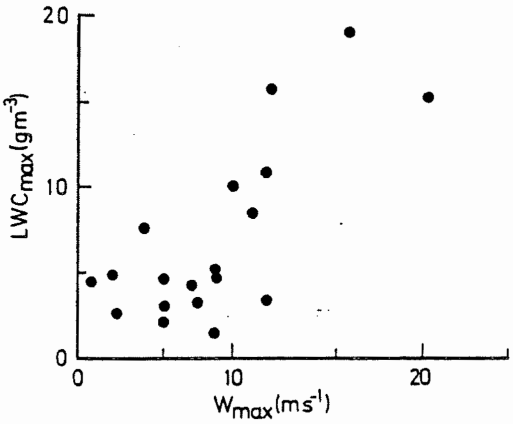

Fig. 3 : Peak Liquid Water Content within a Convective Cell as a Function of Corresponding Peak Updraught Velocity (Flight Nos. 2 and 7).

LWC_{max} : Peak liquid water content (g m^{-3})
W_{max} : Peak updraught velocity (m sec^{-1})

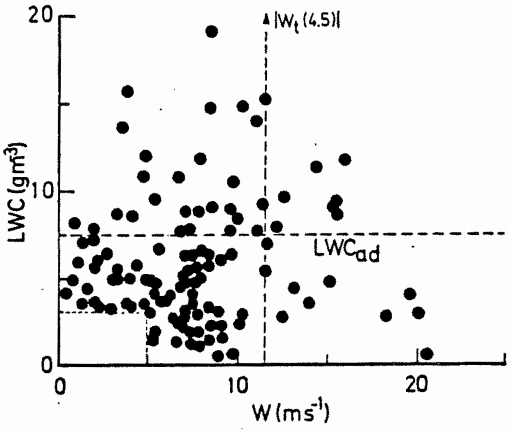

Fig. 4 : Liquid Water Content as a Function of Vertical Air Velocity (Flights Nos. 2 and 7). Each point represents these quantities averaged over a distance of 200 m.

$W_t(4.5)$: Absolute value of the terminal velocity for the largest drop measurable with the PSP probe (at 500 mb and - 10°C)

LWC_{ad} : Adiabatic value of liquid water content for an air parcel raised from the ground to 6 km ; the value is computed from upper air sounding data at Yamoussoukro (Ivory Coast).

the cloud penetrations analyzed here belong to these kind of data. Hence, without looking for an exact coincidence between the locations of peak water content and peak updraught velocity, we plotted in Figure 3 the peak liquid water content as a function of the peak updraught velocity for each of the well-defined and isolated convective cells we encountered during Flights Nos. 2 and 7. This figure shows that the peak liquid water content within a developing cell increases with the peak updraught velocity in the same cell. A liquid water content larger than 10 g m^{-3} may occur within a cell in which the updraught velocity exceeds 10 m sec^{-1}. The highest liquid water content in Fig. 3 approaches a value close to 20 g m^{-3}, while the adiabatic value of liquid water content for an air parcel raised from the ground to 6 km, average altitude of the cloud penetrations, is merely 7 g m^{-3}. This value is estimated from data of upper air sounding at Yamoussoukro, nearest upper sounding station in Ivory Coast during our field experiments.

These superadiabatic liquid water contents raise some questions :

- whether they are due to hydrometeors drifting downwards from higher altitudes or not ;
- what kind of size spectra they correspond to, etc...

In order to look into these problems, we need to analyze the liquid water content, the size spectrum and the updraught velocity in a much smaller horizontal scale than that of an entire convective cell. We plotted the liquid water content as a function of updraught velocity in Figure 4, where each point corresponds to both quantities averaged over 200 m. of flight path. We did not reproduce points in the hatched rectangular box, because too many points exist. The adiabatic liquid water content is indicated by an horizontal dashed line. The terminal velocity of a drop with a diameter of 4.5 mm, the largest drop detectable by the PSP probe, is about 12 m sec^{-1} at 500 mb and - 10°C according to the estimation made by Beard (1976). This means that all the drops measured by the PSP probe still continue to drift upwards within an updraught whose velocity exceeds 12 m sec^{-1}. Fig. 4 shows that a few of observed superadiabatic liquid water contents occurred with updraught velocities in this range. Furthermore, the relative displacement of drops, with respect to air parcels, may be comparatively small, as long as the relative drift velocity of drops remains small. This leads us to a conclusion that these superadiabatic liquid water contents, corresponding to updraught velocities greater than 10 m sec^{-1}, are not due to a massive downwards drift of precipitation water from higher altitudes. These findings suggest that an intense process of accumulation is going on within tropical cumulonimbus.

3.3 Size spectra for superadiabatic liquid water contents and large updraught velocity

'Specific' ASSP, CDP and PSP size spectra, within intense updraught ($W > 9$ m sec^{-1}) are divided into three categories according to the liquid water content and then averaged. Results based on the data of Flight No. 7, are presented in Figure 5. The 'specific' size spectrum is defined by dividing the ordinary spectrum by the corresponding liquid water content, in order to facilitate a comparison between size spectra belonging to different values of the liquid water content.

Figure 5 represents average 'specific' size spectra, over the size range of 10 µm to

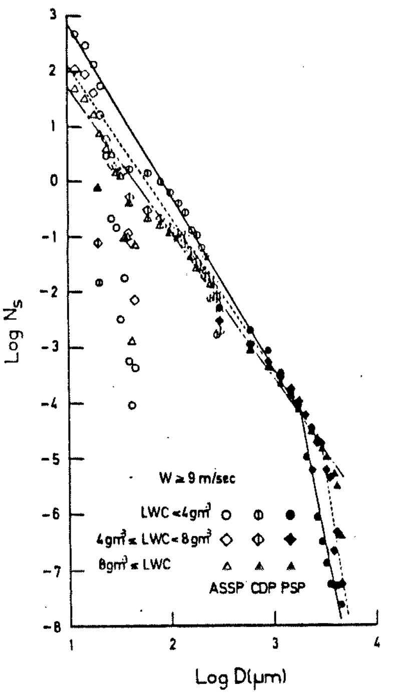

Fig. 5 : 'Specific' ASSP, CDP and PSP Size Spectra within Intense Updraught Velocity. The unit of N_S in this figure is the number of drops per litre per μm per 1 g m^{-3}.

4.5 mm, estimated for three categories of liquid water content, when the updraught velocity exceeds 9 m sec^{-1}. We immediately notice an abnormal underestimate of cloud droplet concentration by the ASSP probe in its highest 8 channels, the reason for which is not clear. Another underestimate with a smaller degree may also be noticed in the overlapping range of the CDP and PSP probes. If we neglect these dispersions of measurements in both the overlapping ranges, all the points, belonging to one category of the liquid water content, are aligned fairly well along a straight line in log-log plot up to a critical size situated in the PSP range. Beyond this size, another straight line may be adjusted, but with a different value of slope. These three spectra suggest a certain degree of coupling between the cloud droplets spectra and the precipitation spectra. The liquid water content less than the adiabatic value implies that the air parcel in the updraught has experienced an intense entrainment and this results in a size spectrum with fewer number of large drops. Hence, these drops are less efficient to deplet smaller cloud droplets, from which results a higher concentration in cloud droplets. As the liquid water content increases (as a result of either the accumulation processes or the smaller entrainment experienced by an air parcel with a greater updraught velocity), larger drops appear in the updraught and their concentration increases. This leads to a much more efficient depletion of cloud droplets and to a gentler slope of the cloud droplets size spectrum. A further increase of the liquid water content leads to a further increase of hydrometeors, so that the Marshall-Palmer distribution might be satisfied in the entire range of hydrometeors and that the size spectrum tend to an equilibrium state in its whole size range.

4. Conclusions

The following conclusions were drawn from the present investigation :

a) a fairly good correlation exists between the locations of high liquid water contents and of updraught within convective cells in developing phase.

b) The locations of peak values of both parameters do not always coincide with each others, but the peak value of liquid water content within an updraught increases with the peak value of updraught velocity.

c) The superadiabatic liquid water content may occur, while all the particles are still drifted upwards, suggesting the existence of efficient accumulation mechanisms in tropical cumulonimbus.

d) Some evidence suggest that the Marshall-Palmer distribution may not be valid in the entire range of hydrometeors. The extent to which this distribution is valid seems to depend on both the updraught velocity and the liquid water content.

e) The cloud droplet size spectrum seems to change within the intense updraught with the precipitation water content suggesting that the size spectra of cloud and precipitation droplets need to be considered as an entity, and not as two distinct entities without interaction.

These conclusions are tentative at the present state of our data analysis. Further observations and analyses are needed in order to reach to a comprehensive picture of the precipitation processes and its interaction with the dynamical processes in tropical cumulonimbus.

5. References

1) Beard, K.V., 1976 : Terminal velocity and shape of cloud and precipitation drops aloft. J. Atmos. Sci., 33, pp. 851-864.
2) Gayet, J.F., 1976 : Physique de la mesure du spectre dimensionnel de gouttes de nuages au moyen des capteurs de Knollenberg, Thèse 3ème cycle (1ère partie), Université de Clermont.
3) Gayet, J.F., Janmuzynski, M. and Soulage, R.G., 1978 : Microstructure of an accumulation zone on a tropical Cb cloud. Proc. of the Confer. on Cloud Phys. and Atmos. Elec., Issaquah, pp. 318-323.
4) Guillemet, B., Mascart, P. and Isaka, H., 1977 : Calibrage autonome et correction d'un système aéroporté pour la mesure du vent horizontal, J. Rech. Atmos., 11, pp. 9-37.
5) Houze, R.A., Hobbs, P.V., Herzegh, P.H. and Parsons, D.B., 1978 : Airborne Measurements of the size distributions of precipitation particles in frontal clouds, Proc. of the Conf. on Cloud Phys. and Atmos. Elec., Issaquah, pp. 168-172.
6) Lenshow, D.M., 1972 : The measurement of air velocity and temperature using the N.C.A.R. Buffalo aircraft measuring system, N.C. A.R., TN 74.
7) Lescure, B. and Lejeune, M., 1975 : Possibilités du DC 7 en matière de mesures météorologiques - Méthodologie des mesures aériennes en météorologie, Journées d'étude de Clermont-Fd, pp. 1-10.
8) Musil, D.J., Smith, P.L. and Heymsfield, A.J., 1978 : Total hydrometeor spectra in a hailstorm and implication for precipitation growth processes, Proc. of the Conf. on Cloud Phys. and Atmos. Elec., Issaquah, pp. 173-177.
9) Pinty, J.P. and Gayet, J.F., 1978 : Récapitulation préliminaire sur les caractéristiques microphysiques des cumulonimbus tropicaux givrants. Rapport "Moussafrica No. 3".

(*) This research was funded by :
D.R.E.T., Contract No. 77.34.380

(1) Present affiliation : University of Niamey (Republic of Niger)
(2) On leave from l'Ecole de Météorologie-Météorologie Nationale (France).

CONVECTIVE STORM DEVELOPMENT AND ELECTRIFICATION

Roger M. Lhermitte

Rosenstiel School of Marine and Atmospheric Science
Division of Meteorology and Physical Oceanography
University of Miami
Miami, Florida
33149

During the summers of 1977 and 1978, the convective storms in the vicinity of the NASA Kennedy Space Center, Florida developing under the triggering effect of a sea breeze convergence regime were observed by a network of three Doppler radars assisted by other instruments. The purpose of the experiments conducted within the Thunderstorm Research International Program (TRIP) was to assess the conditions for which these convective storms develop and reach the thunderstorm stage indicated by the onset and growth of electrical activity. The Doppler radar network acquired three dimensional observations of the velocity of precipitation particles and also radar reflectivity indicative of precipitation intensity. The electrical activity of the storms was monitored by visual observation of lightning and a network of radar receivers named LDAR (Light Detection and Ranging), operating at a 40 MHz center frequency and capable of locating the position of the electrical electrical radiation sources in the thunderstorm so that they can be compared with the radar data. The LDAR system, which was presented by Lennon (1975), is composed of seven receivers installed at different locations and a computer which evaluates the time of arrival differences of the same signal reaching different receiver sites. These data are then interpreted by the same computer to obtain the x, y,z origins of the received signal.

The data pertaining to only a few storms have been selected and analyzed at the present time with the results reported in several papers (Lhermitte, Conte, Pasqualucci, Lennon, and Serafin, 1977; Lhermitte, 1978; Lhermitte and Poor, 1979; Lhermitte and Krehbiel, 1979). The main concern in the data analysis was to present and discuss the joint radar and LDAR observations so that a descriptive model outlining possible mechanisms for storm electrification could be derived from the interpretation of the results. Two storm systems were more thoroughly studied: Storm I, observed on August 1, 1977 and Storm II, observed on August 13, 1978. Since they were observed approximately one year apart, these storms are unrelated, but they were both observed in the same geographical region, in the summer and in the same part (early afternoon hours) of the diurnal cycle of convection. The two storms show amazingly similar conditions in their dynamical, physical and electrical development which may serve as a basis for a more general understanding of the typical behavior of a thunderstorm. The purpose of this paper is thus to examine these similarities in an effort to report the typical or general conditions leading to the onset and development thunderstorm electrification.

Both storms evolved in a very strong wind shear environment which provided the conditions for quasi steady state circulation and precipitation without appreciable translation of the storm. However, environmental wind shear conditions for the two storms were different. Storm I evolved in an environment characterized by a southwest low level flow and northeast upper flow. These conditions produced a multicell storm in the form of a small squall line aligned with the wind shear. The mean shear conditions for Storm II were a southeast low level flow and northwest upper flow; the storm system was composed of only two cells which developed almost sequentially.

Both storms became electrically active when their vertical development reached approximately 7 to 8 kms, although intense precipitation was observed earlier originating in the storm low altitude levels. In both storms the regions where electrical radiation sources were observed were always in the 7 to 10 kms altitude range and in the vicinity of or above a strong updraft. In the Storm I case three cells, aligned with the wind shear, were active simultaneously with the cell in the storm center associated with a much more vigorous updraft. Although electrical activity was observed in the vicinity of each of the updrafts, it was much more intense in the vicinity of the stronger cell, where updraft velocity reached more than 20 ms^{-1}. In Storm II the cells developed sequentially and triggered well identified bursts of electrical activity correlated in space and time with updraft development. The altitude variation of the LDAR radiation sources followed similar behavior of the updraft. The updrafts always develop in the vicinity of or above the freezing level and exhibit a velocity maximum rising systematically towards the storm top; when that updraft maximum approaches the storm top, the updraft disappears which results in a strong divergence in this region. There is some question as to the steadiness and vertical continuity of the updrafts observed in these storms since their lifetime (less than 4 to 10 minutes) is comparable to the time necessary for an air parcel to rise from a few kilometers above the freezing level to the storm top. The updraft may appear in the form of a bubble fed by entrainment due to massive freezing occurring at a critical stage of the storm development.

Note that in these stationary Coastal Florida storms, there is no substantial low altitude downdraft except in the final stages of a large storm system. Indeed, there is never much divergence/convergence in the storm low levels where the dominant feature is heavy precipitation mostly located below the freezing level and not necessarily related to the development of storm electrification.

It is important to note that an updraft is always associated with high altitude downdrafts occurring upshear from it. This is not surprising since this is a region where evaporative cooling may be important thereby providing a mechanism for accelerating the downdraft.

Detailed inspection of the motion fields shows that the downdraft merges with the updraft in a region near the high reflectivity core. These conditions suggest a possible explanation for thunderstorm electrification which was proposed and discussed in detail for Storm II. (Lhermitte, Krehbiel, 1979). It is assumed that the separation of charges takes place in the vicinity of the updraft at an altitude where the downdraft meets that updraft. The high radar reflectivity observed in this part of the storm indicates that large, frozen particles must be present there which may be suspended on the upshear side of the updraft maximum where their downward terminal velocity might equal the upward air velocity. Since the updraft extends from below the freezing level, it carries liquid water droplets which become supercooled at higher altitudes. Some of these supercooled droplets collide with the heavy particles suspended in the updraft and therefore produce riming - and warming - of these large particles. The high altitude downdraft which accelerates by cooling, brings colder ice particles in contact with the large particles where it meets the updraft. Some of these particles, which come in temporary contact with the larger particles, bounce off carrying a positive charge resulting from a charge transfer process based on the temperature difference between the large particles and the ice crystals. The light, positively charged ice crystals are carried to the storm anvil by combination of the updraft velocity and the wind shear, leaving the high radar reflectivity core with a negative charge. The fact that LDAR activity is found on the edge of the high reflectivity core (essentially above it) may indicate that breakdown events tend to concentrate on the periphery of the negatively charged region.

In both storms, the electrical activity varies periodically with a maximum of intensity occurring every 4 to 6 minutes for Storm I and approximately 8 minutes for Storm II. These variations are correlated in space and time with updraft development. A possible explanation for the difference between the periods of variation of electrical activity for the two storms is that Storm I (shorter period) appears subdivided into smaller cells compared with Storm II, which exhibits only two cells developing sequentially. Note that the mean altitude of LDAR radiation always follows the vertical rise of the updraft maximum so that the variation of electrical activity is really associated with the pulsating nature of these updrafts. When the updraft maximum reaches the storm top, it disappears by divergence and the electrical radiation decreases in intensity and becomes more diffusel

The analysis of data pertaining to more storms must be included in this survey so that the hypothesis on thunderstorm electrification formulated in this report be consolidated. The data collected during the two summers of TRIP should provide such a data base.

Acknowledgements

This work was supported by NSF Grant No. ATM77-07982 and ONR Contract No. N00014-75-C-0321.

References

Lennon, C., 1975: Aerospace and Flight Test Radio Coordinating Council. Minutes. Vol. 62, October 1975, Appendix H.

Lhermitte, R., 1978: Doppler radar and electrical radiation observations of thunderstorms. Preprint, Conference on Cloud Physics and Atmospheric Electricity, American Meteorological Society, Boston, Mass.

Lhermitte, R. and M. Gilet, 1976: Acquisition and processing of Tri-Doppler radar data. Preprint, 17th Conference on Radar Meteorology of the American Meteorological Society, Boston, Mass.

Lhermitte, R., D. Conte, F. Pasqualucci, C. Lennon and R. Serafin, 1978: Doppler radar observation of thunderstorm circulation in the 1977 TRIP program. Preprint, 18th Conference on Radar Meteorology of the American Meteorological Society, Boston, Mass.

Lhermitte, R., and F. Poor, 1979: On the development of thunderstorms kinematics and electrification. Preprint, 11th Conference on Severe Storms of the American Meteorological Society, Boston, Mass.

Lhermitte, R., 1979: Doppler radar and radio observation thunderstorms, submitted to Special Issue on Radiometeorology, IEEE.

NUMERICAL SIMULATION OF SELF-INDUCED RAINOUT USING A DYNAMIC CONVECTIVE CLOUD MODEL

Charles R. Molenkamp

Lawrence Livermore Laboratory, University of California
Livermore, California 94550, U.S.A.

1. INTRODUCTION

Fallout of radioactivity from the atmospheric detonation of a nuclear weapon can produce a severe collateral damage hazard. This hazard can be mitigated by detonating the weapon as a free-air burst, i.e., far enough above the ground that the fireball does not contact the surface. For a free-air burst primary damage is inflicted by blast and thermal effects; the radioactive debris, which forms as submicron particles, is widely dispersed by atmospheric motion before falling to the ground.

If precipitation is falling in the vicinity of a nuclear burst, the radioactive debris particles can be entrained by the clouds and rapidly scavenged and deposited on the ground producing a severe collateral damage hazard. We have expended considerable effort at LLL trying to assess this hazard looking at microphysical, dynamic, and climatological aspects, and have concluded that a significant hazard would occur if the debris encounters precipitation before it is dispersed.[1] Because precipitation scavenging can occur only when it is raining, there is an upper limit on the probability of natural rainout of about 0.2.

The probability of a rainout collateral damage hazard could be considerably enhanced if the cloud produced by the nuclear detonation develops precipitation. We call the phenomenon of rapid deposition of nuclear weapons debris by a cloud caused directly by the explosion self-induced rainout. Several years ago we investigated this possibility using a dynamic convective cloud model to simulate the life cycle of a nuclear cloud with the result that precipitation occurred and a significant amount of radioactive debris was deposited.[2] On the basis of this simulation we surveyed the U.S. nuclear test data for evidence of self-induced rainout, but we did not find any. This was not particularly surprising for the Nevada tests because of the arid climate and the criterion to avoid precipitation. For the Pacific tests, where self-induced rainout would be more likely, the observers were situated 10 or more miles upwind of the detonation point and would not have seen precipitation falling from the base of the nuclear cloud if it occurred.

2. OBSERVATIONS AT HIROSHIMA AND NAGASAKI

About the time we completed our survey of the test data, we were told about the "black rain" that accompanied the nuclear events at Hiroshima and Nagasaki, Japan. "There has always been concern by survivors who were exposed to the so-called 'black rain' . . . The updraft caused by the nuclear explosions drew much debris and dust into the atmosphere. The ensuing turbulence generated rain showers in both cities beginning about half an hour after the blast. The first rain that fell was described as black, probably because it washed the dust and smoke from the burning cities out of the air. A number of survivors who had not been near enough to the explosion to receive significant initial exposures were caught in the black rain; they reported radiation-inducible symptoms."[3] Concern about exposure to "black rain" was great enough that one of the items in the survivor reports, which were compiled for thousands of survivors, dealt specifically with this phenomenon.

Evidence of radioactivity on the ground in the suburbs of Hiroshima was obtained by the Second Japanese Investigation on 13-14 August 1945. "Samples found in the area 3.5 km northwest of the hypocenter demonstrated considerably intense radiation. This is believed to be due to the fall of bomb fragments as a result of meteorological conditions at the time of the explosion."[4] "At that time [3-4 September 1945], in addition to the maximum residual gamma rays about twice as intensive as the background in the vicinity of the hypocenter, we detected on the Sanyo National Highway between Koi and Kusatsu [$\sim$3 km west of the hypocenter], gamma rays of about the same intensity as in the vicinity of the hypocenter, . . . The cause of this radiation is considered to be different from that in the vicinity at the hypocenter and for the following reasons it is felt that uranium nuclear fission products of the A-bomb explosion had fallen. That is, at the time of the explosion, an east wind was blowing in this area and there was much rain in this area about 30 minutes after the explosion. This rain is reported to have been black and dirty. Furthermore, evidence that this was due to fallout is that especially intensive radiation was found in mud which had collected in an eaves trough of a house . . . Chemical analysis was conducted on a part of it (mud collected from eaves trough of a small house below the Ueno Garden where the intensity of radiation was greatest) . . . and uranium nuclear fission products were confirmed to be present."[5]

"Radioactivity in the vicinity of Nishiyama Reservoir in Nagasaki City [Nishiyama Reservoir is 3 km east of the hypocenter] was measured and found to be far greater than that of the hypocenter area . . . In the latter area [Nishiyama], radioactivity was found over a wide area covering more than 10 km^2, . . . at some places being as high as over 25 times as strong as that in the hypocenter area [on 1 October 1945]. Since Nishiyama area was downwind from the hypocenter — a wind of 3 meters per second was blowing then — the rain which fell about 20 minutes later must have washed down radioactive substances with the dust blown up over Nagasaki City . . . The vicinity of Nishiyama being a hilly area, heavy rains which fell several times following the A-bomb detonation before the measurements were started washed away almost all the radioactive substances on the road. Therefore, grassy areas along the roadside were chosen for measurement and strong radioactivity was usually found in such places."[6]

Some of the details of the "black rain" are given in The Report of the Atomic Bomb Damage in Hiroshima.[7] "20 to 30 minutes after the blast, the black clouds nimbostratus moved towards the north-northwest and it distinctly caused to produce the phenomena of rain shower. The showers occurred between the hours of 0900-1600 . . . Fire became widespread from about 0900 hours, was at its height between 1000 and 1400 hours and slackened in the evening . . . This [motion of clouds and smoke to the NW] shows that a southeastern wind was blowing in the upper region at an altitude ranging from 500 to several thousand meters. Its estimated velocity is 1 to 3 m sec^{-1}. We regret that we are unable to make a study on actual observations as we do not have in hand the observation reports on the upper air currents of that day. [As far as I can determine, they have never been found.] The rainfall on this occasion came of two-fold influences, one being the direct influence of upward air current caused by the explosion itself and the other being the indirect influence of the upward air current caused by the fire after bombing.

"The hour of initial rainfall ranges from 15 minutes to 4 hours after observation of the flash of the explosion, but in most places it began raining from 20 minutes to an hour after . . . The rain stopped between 0900 and 0930 hours at the earliest points and between 1500 and 1600 hours at the latest . . . It may be concluded that the dust and soot in the air were for the most part washed down to be left on the ground during the first 1 to 2 hours of rainfall . . . I regret that we cannot give a definite figure of the amount of rainfall in the present case as there was not a single meteorological observation unit established in this area of rainfall. But judging from the fact that there appeared almost the same rise in water level in the same short hours in the mountain streams in Koi as well as in the Yasu River . . . as on the occasion of the typhoon experienced on 17 and 18 September [1945]; it is estimated that the rainfall in the area of downpour amounted to 50-100 mm within 1 to 3 hours of rain."

"In Nagasaki . . ., there was a shower phenomena far smaller in scale as compared with that of Hiroshima. This is probably due to reasons of the absence of frontier air current zones as was seen in Hiroshima and the far smaller scale of the fire at the former city, which became additional influential factors to the rain-forming conditions."[7]

Isodose contours for Nagasaki as measured with Geiger counters by the U.S. First Technical Group of the Manhatten Engineering District are shown in Fig. 1. These data were taken $\sim$60 days after the events and after 2 typhoons had swept through Southern Japan, but they appear generally consistent with the crude Japanese measurements obtained pre-typhoon. Arakawa[8] estimates the external integrated gamma dose at about 100 rads in Nishiyama compared to several rads in the western suburbs at Hiroshima.

My conclusions are that deposition of radioactive debris by precipitation occurred at both Hiroshima and Nagasaki, and that the precipitation was initiated by the explosion itself and by the ensuing fires. Additional meteorological data and films of these detonations suggest that precipitation would not have occurred naturally. The deposited radioactivity was a small fraction of the debris produced by the nuclear detonation, but the contours presented are subject to considerable uncertainty due to questions regarding the mix of radioactive decay products and changing decay rates and because of weathering during the time between deposition and measurement.

3. SIMULATION OF NAGASAKI EVENT

During our rainout reseach we developed a two-dimensional axisymmetric convective cloud model of precipitation scavenging. The cloud dynamics and microphysics were taken from the Rand Cumulus Dynamics Model.[9] We developed a representation for scavenging of sub-micron aerosols for this model that is compatible with the Kessler microphysics parameterization. We have used this model to simulate the scavenging and deposition of radioactive weapons debris by natural convective clouds.

Since we had this model available, we used it in an attempt to simulate self-induced rainout.[2] This was done with the realization that this application of the model violates one of the basic dynamic assumptions, that the density perturbation of the atmosphere is small. Nevertheless, the simulation produces an acceptable simulation of nuclear cloud rise and is considered reasonably realistic.

The major difference between a simulation of self-induced rainout and natural convection is the initial perturbation. For the simulation of the Nagasaki event, we used a weapons yield of 22 kT, and extracted data on initial temperature (3000°C) and fireball radius (230 m) from Ref. 10. We further assumed this thermal energy had a $\cos^2(R)$ distribution from a maximum at the center to ambient at a radius of twice the fireball size. The radioactivity was assumed to have a similar distribution.

The simulation was started from rest with this assumed perturbation and run with an initial grid spacing of 100 m from 0-30 sec. At this point the grid spacing was changed to 300 m and the model restarted using the motion field, temperature and debris distributions at 30 sec. No condensation had occurred at this time. With a 300 m grid spacing the domain of the model was height 13.5 km, radius 9 km.

The development of the cloud clearly depends on the vertical structure of the atmosphere. We have not been able to find any upper air data taken in Japan at this time, apparently it has been destroyed. We did find data from a series of weather reconnaissance missions flow by USAF over Japan from Guam. As planes approached the Japanese Islands from the east they ascended from about 2000 ft altitude to 30,000 ft and took measurements of temperature at 1000 ft intervals. Only one of these flights recorded humidity data, a flight on the morning of 9 August (the day of

Nagasaki bombing); we used the sounding from this flight in the simulation for Nagasaki. Since the data ends at 30,000 ft, we placed the tropopause at that altitude although it was probably quite a bit higher since there was a high pressure region centered just east of Japan at this time. In the simulation the nuclear cloud rises to this tropopause in about 4 minutes, after which the buoyancy term becomes negative and the upward velocity decreases. The cloud is also approaching the top boundary of the model. In the streamfunction-vorticity formulation, the upward velocity tends to be deviated to radially outward, but this is a minor effect in this particular simulation.

Sub-grid motions are represented in our model by a Fickian diffusion term. We have used a diffusion coefficient of 400 m^2 sec^{-1}, a very high value even for convective clouds but perhaps not unrealistic for nuclear weapons clouds particularly at early times. The model results are fairly dependent upon the value of this parameter.

An axi-symmetric model cannot represent the horizontal motion of the external atmosphere and particularly wind shear. Even a relatively small horizontal wind shear can dramatically affect the development of the cloud. Films of the Nagasaki event suggest that the wind shear was small, but not insignificant, and the distribution of deposited radioactivity suggest downwind transport of the debris at about 3 m sec^{-1}. We assumed in plotting our simulated deposition patterns that the cloud moved as a whole with a velocity of 5 m sec^{-1}.

The scavenging parameterization envisions a two-step removal process. Sub-micron debris particles are assumed to become attached to or incorporated in cloud droplets at a rate of 10^{-4} sec^{-1}. These debris-laden droplets can be inertially captured by raindrops, which transport the debris to the ground. Total evaporation of droplets and raindrops before they reach the ground leads to resuspension of radioactivity in the atmosphere. In the simulation there was no scavenging of debris by nucleation or direct attachment to raindrops.

Of the radioactivity entrained into the cloud in the simulation of the Nagasaki event only 14 percent is captured by droplets and only 3 percent is deposited on the ground by raindrops. The remainder is left suspended in the atmosphere after precipitation stops and the cloud dissipates.

In the simulation initial condensention occurs at $\sim$2 minutes after burst, and rain starts falling at 5 minutes. The cloud base is 1.2 km and maximum cloud top is 13.2 km. Rain continues for 30 minutes with maximum accumulation, assuming no cloud motion, of 8.5 mm. Maximum rain rate at cloud center of 31 mm/hr occurs at 18 minutes.

The surface distribution pattern of deposited radioactivity, assuming a 5 m sec^{-1} wind, is given in Fig. 2. This pattern can be compared with the measured patterns given in Fig. 1. We feel these patterns compare very favorably given the uncertainties in both the simulation and the observations. The greater downwind displacement in the simulation is due primarily to an overestimate of the mean wind.

4. CONCLUSIONS

The hypothesis that self-induced rainout can occur is supported by observations in Hiroshima and Nagasaki, where deposition of weapons debris with precipitation occurred several km downwind of the burst point. This precipitation was initiated either directly by the nuclear weapons or by the ensuing fires.

Simulation of the Nagasaki event with a convection cloud precipitation scavenging model, although fraught with many questionable assumptions, agrees surprisingly well with the observations and supports the hypothesis that self-induced rainout can occur.

5. ACKNOWLEDGMENT

This work was performed under the auspices of the U. S. Department of Energy by the Lawrence Livermore Laboratory under contract No. W-7405-Eng-48.

6. REFERENCES

1. Knox, J. B., et al., 1975, "Progress in Rainout Research at Lawrence Livermore Laboratory: Fiscal 1975," Lawrence Livermore Laboratory Report UCRL-51625-75.

2. Molenkamp, C. R., 1979, "An Introduction to Self-Induced Rainout," Lawrence Livermore Laboratory Report UCRL-52669.

3. Auxier, J. A., 1977, "ICHIBAN: Radiation Dosimetry for the Survivors of the Bombings of Hiroshima and Nagasaki," U. S. Energy Research and Development Administration (now Department of Energy) Report TID-27080.

References 4-7 are from the English Translation of <u>Collection of Investigation Reports on Atomic Bomb Disaster</u>. These papers by Japanese authors were compiled in 1953, but most of the papers date from 1946-1950. The English translation of these papers is not generally available. I am very grateful to Dr. John A. Auxier of Oak Ridge National Laboratory for making his copy available to me.

4. Arakatsu, B., 1953, "Report on Radiological Investigation of Hiroshima City Conducted for Several Days after the Bombing."

5. Yamasaki, F., 1953, "On Residual Radiation in West Hiroshima Following the A-Bomb Explosion."

6. Shinohara, K., et al., 1953, "Radioactivity on the Ground in Nagasaki City and Vicinity. Part II. Radioactivity Near the Nishiyama Reservoir."

7. Uda, M, 1947, "The Report on the Atomic Bomb Damage in Hiroshima, Meteorological Conditions Related to the Atomic Explosion in Hiroshima City."

8. Arakawa, E. T., 1959, "Radiation Dosimetry in Hiroshima and Nagasaki Atomic Bomb Survivors," Atomic Bomb Casulty Commission, Technical Report 14-59.

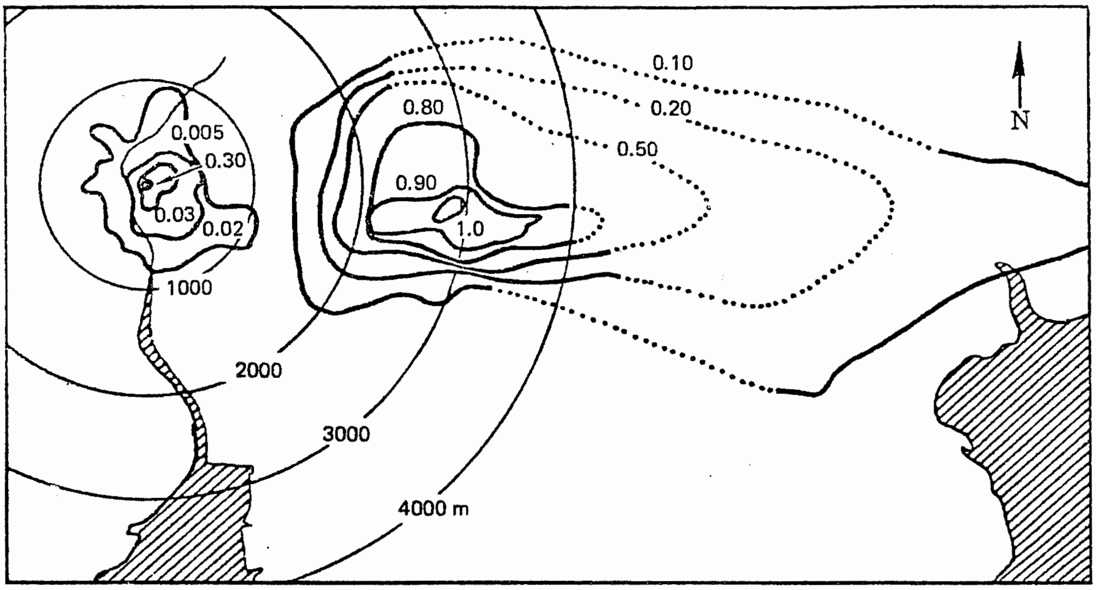

FIGURE 1. Isodose contours evaluated in milliroentgens per hour for October 3-7, 1945, at Nagasaki. Figure reproduced from Ref. 8.

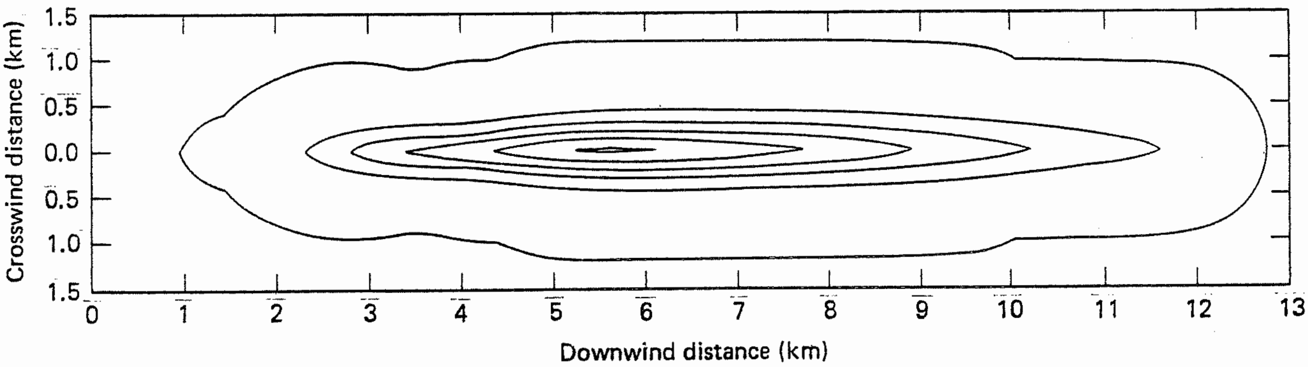

FIGURE 2. Isodose contours calculated by the scavenging model for Nagasaki assuming 5 m sec^{-1} wind. Contour levels are 500, 400, 300, 200, 100, 0 rad hr^{-1} at H+1 hour. The maximum dose rate is ∿25 times the comparable measured dose rate.

9. Murray, F. W., 1970, "Numerical Models of a Tropical Cumulus Cloud with Bilateral and Axial Symmetry," Mon. Wea. Rev., 98(1), 14-28.

10. Glasstone, S. and P. J. Dolan, 1977, The Effects of Nuclear Weapons, prepared and published by the U. S. Department of Defense and the U. S. Department of Energy.

KS:FLW/1134z

CHARACTERIZATION OF THUNDERSTORM CLOUDS FROM DIGITAL RADAR DATA RECORDED IN THE NORTH-WEST OF ITALY IN THE 1979 SUMMER

G.E. Perona[1], F. Canavero[1], O. Ghigo[2], L. Ordano[2]

[1]Istituto di Elettronica e Telecomunicazioni, Politecnico, Torino ITALY
[2]Ente di Sviluppo Agricolo del Piemonte (ESAP), Torino ITALY

1. INTRODUCTION

During the 1979 summer, digital reflectivity data have been collected using a C-band EEC radar placed at the top of the hill near Turin. The radar operates at a wavelength of 5.3 cm, with pulse length of 2 μsec, 259 Hz PRF, and 250 kW peak power. All data presented have been collected on digital tape, after processing by the DVIP section of the radar; the device provides 8-bit digitized data, that represent averages over 15 pulses and 1 km in range.

The radar observations have been carried on in the afternoon and evening hours (usually from 12.00 to 24.00), in the period 1 June - 9 September.

Fig. 1 shows the region under observation, namely the Piemonte and its immediate surroundings. In this region a few hail suppression campaign have been carried on in the past, without sufficient control. A comprehensive review of scientific studies concerning this same area is due to Morgan (1973). Just a few other papers have been published in the scientific literature (e.g. Prodi, 1974 and 1976; Federer, 1978; Vento, 1972); Bossolasco, 1949).

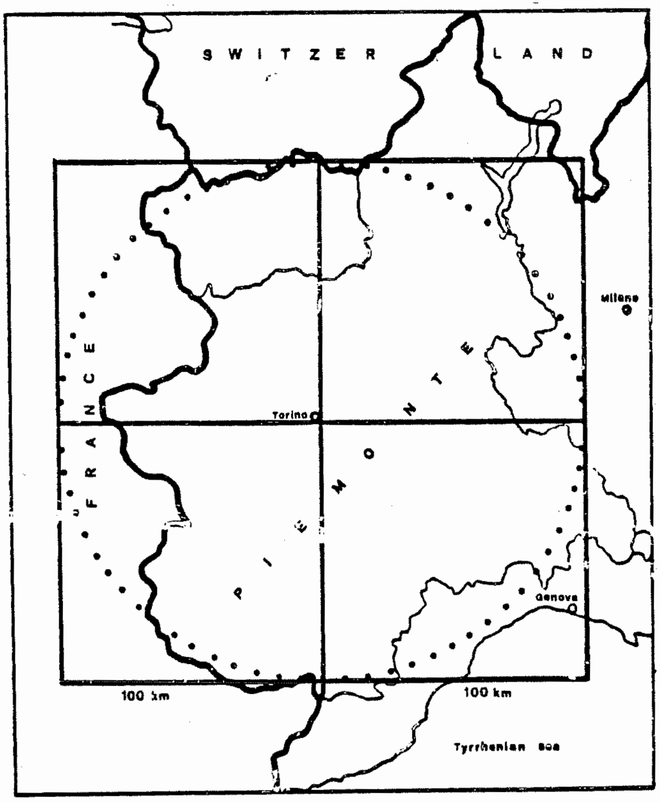

Fig. 1. Outline of the area under radar observation (N-W of Italy). The radar was usually operating with 100 km range (dotted circle). The squares represent the four quadrants covered by the computer maps (Fig. 3).

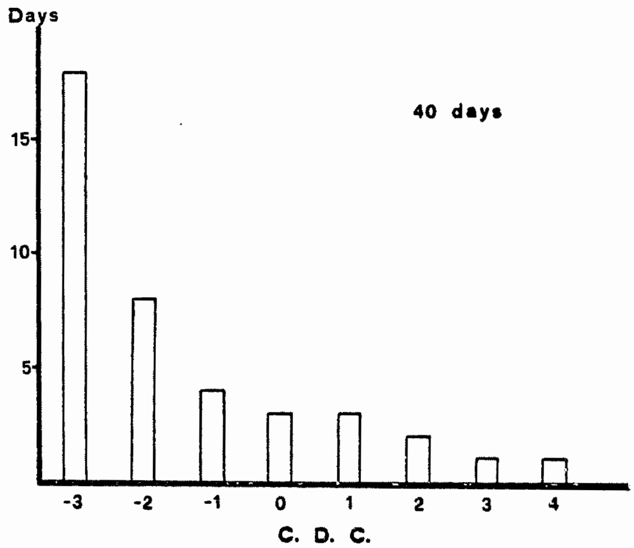

Fig. 2. Distribution of Convective Day Categories for the period 1 Aug. - 9 Sept. 1979.

During the 1979 campaign, the radar operators were asked to report all interesting phenomena in the 100 km radius region limited by the dotted circle in Fig. 1; at the same time they recorded on digital tape the observations for future analysis. The radar observations during the month of June and July have not been systematic and regular for organizational reasons; therefore some of the analysis presented will be limited to the period 1 August-9 September. Furthermore no hail pads data were available. Consequently, the results described in this paper may just represent a beginning of systematic and thorough studies that, we hope, will be conducted in the future.

Fig. 2 shows a statistical distribution of the day categories, classified according to the criteria adopted in the Alberta Hail Project (Strong, 1979). Of course, the attribution of a specific category to each day has been performed without the possibility of using completely objective criteria, due to the limitations stated before.

2. RADAR DATA ANALYSIS

The data stored on magnetic tape have been analyzed in order to study and classify the storms with particular emphasis to the hail-bearing ones. During the 1979 summer hail damages have been at an average level.

The data analysis has been performed using both the operators' reports, and computer maps. For this purpose a numerical program has been prepared: it searches the tapes and maps the maximum reflectivity projections of the scanned volume on three orthogonal planes, one of which represents the ground and the others are two vertical planes. The covered area is subdivided in four squares, 100 km wide, as shown by the heavy lines of Fig. 1.

Fig. 3 shows an example of two computer maps of the North-East quadrant, at different times (the projection on the eastern vertical plane is omitted). It is to be emphasized that only the events showing reflectivity values higher than 40 dBZ (DVIP level ranging from 3 to 6) are considered in the statistics to be presented.

3. RESULTS

Fig. 4 shows the distribution of the thunderstorm events versus the observation hours. The outlined cases correspond to the hail-bearing storms: they are certainly not enough to represent a statistically significant set. The top of the cells detected during the summer campaign (in 1 km height intervals) and the maximum intensity of their echo (expressed as DVIP levels) are collected in Fig. 5. The relative frequencies of top and reflectivity-level occurrences are drawn on the corresponding axis. Fig. 5 shows a correlation between the top of the cloud and the maximum reflectivity: the straight line represents the least square fit. Black boxes identify cases related to the hailstorms: hail-bearing cells appear to have high reflectivity values (maximum 50 dBZ or more) and cloud top exceeding sometimes the tropopause.

On the basis of computer maps and PPI photographs a classification of the cells and storms, detected in the period 1 August - 9 September, has been attempted. First, the cells have been classified as ordinary (or single) ones and supercells, following the criteria used by Chisholm and Renick (1972). We defined as single cell, one having horizontal and vertical scale length of less than 10 km, with maximum DVIP level corresponding to 5 or less, and evolution time of approximately 30 min. A supercell presents longer dimensions: 20-30 km horizontally and 12-15 km in height, with a maximum activity period of 1 hour, or more. The second step was to verify if the storms were constituted by a unique cell (unicellular), by a dominant cell and some satellites that grow to become dominant while the previous dissipate (multicellular), or by more cells laterally aligned (squall line): this classification follows the criteria stated by Browning (1977). The results of this double classification are represented in Table 1, for all storms, and in Table 2, only for hailstorms. During 1979 summer 49 cells in 28 storms were detected: the first classification identifies 43% of ordinary cells and 41% of supercells (16% of cells have not been classified). For what concern hailstorms, 10 are ordinary cells, 2 are supercells and 2 remain unclassified. This statistic of storms can be compared with the data available for the events collected in Oklahoma (USA) during the 1974-77 period (Nelson and Young, 1979): the hailstorms occurred in the North-Western part of Italy seem to be formed by a greater percentage of ordinary cells than the Oklahoma

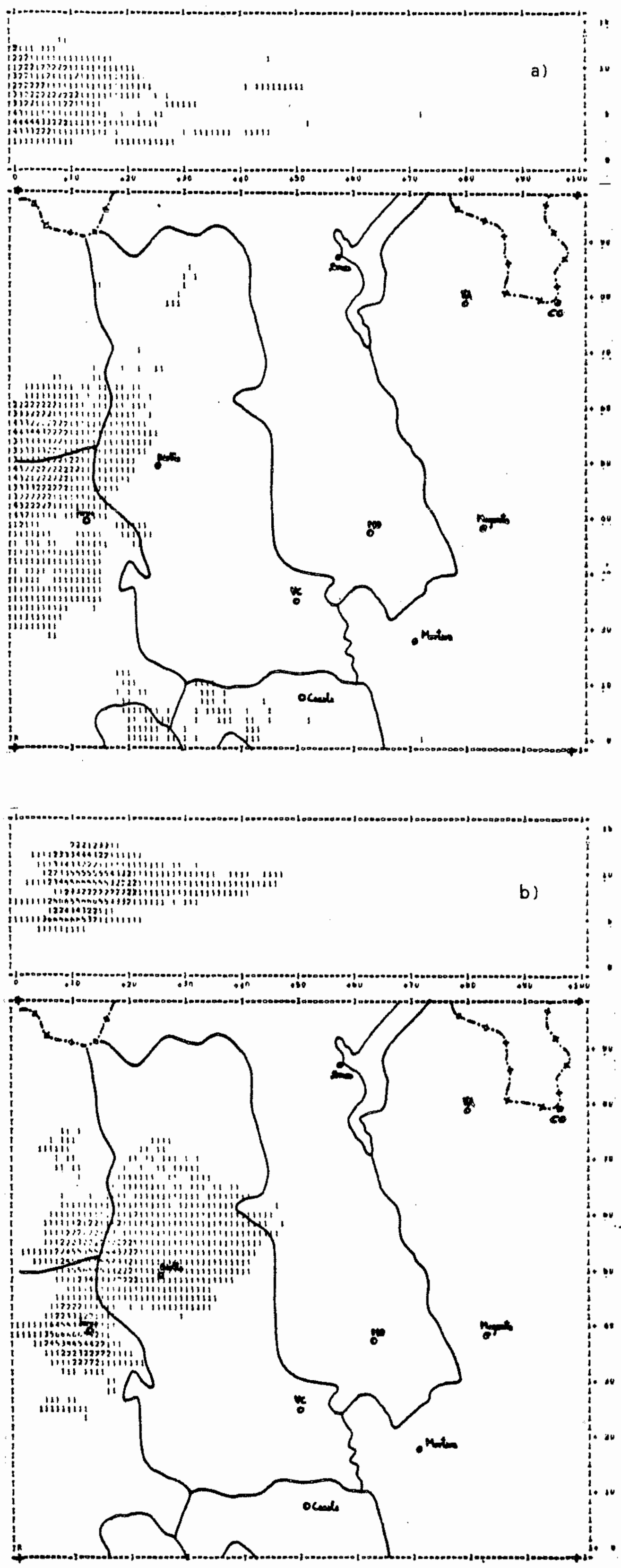

Fig. 3. An example of computer maps. Each picture represents the maximum reflectivity projection of the volume scanned by the radar,on the horizontal and vertical planes; the N-E quadrant is displaied. Evolution of a storm of the 2 Aug. 1979 is showed: a) time: 16.35; b) time: 17.18.

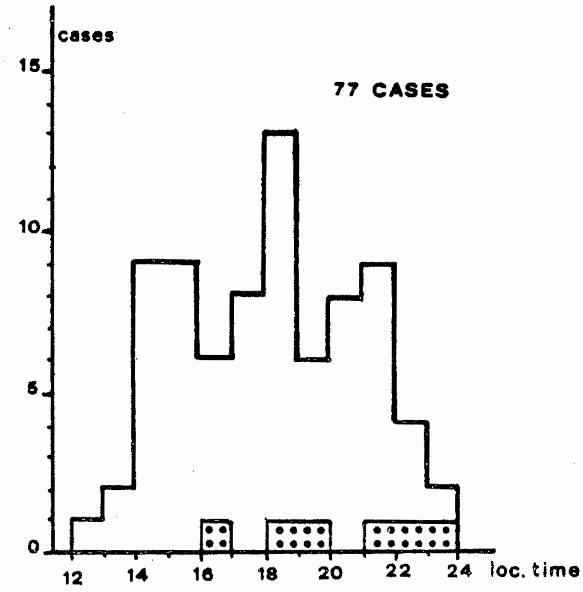

Fig. 4. Distribution of the thunderstorm events observed during 1979 summer (1 June - 9 September). The outlined cases correspond to the hail-bearing storms.

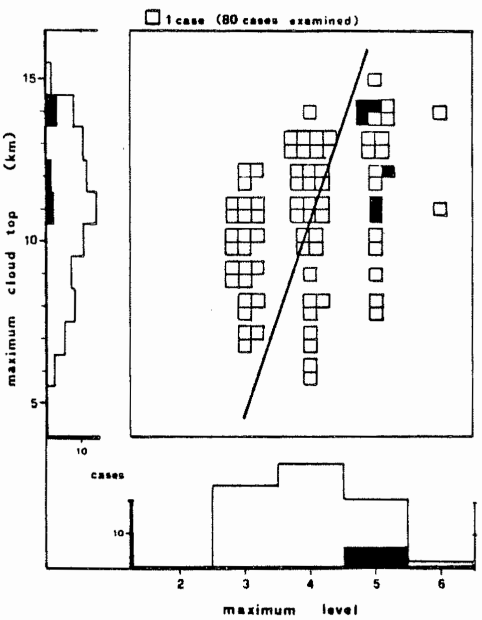

Fig. 5. Correlation between the maximum cluod top and the maximum reflectivity (as DVIP level). The straight line represents the least square fit and black boxes identify cases related to the hailstorms.

storms (72% instead of 55.9%), but, of course, no significance can be given at this result at this moment.

Fig.s 3a and 3b show an example of the evolution of an hailstorm that presents a typical multicellular behaviour: in the first map a growing cell appears; in the second picture

Table 1. Classification of all the thunderstorms observed in Piemonte, during the period 1 Aug. - 9 Sept. 1979. For secondary classification: U, unicellular storm; M, multicellular storm; L, squall line; in parenthesis the number of attributed storms.

Secondary classifications		Primary classifications Supercell	Ordinary cell	Missing data
U	(7)	3	4	-
M	(6)	7	6	-
L	(1)	3	11	-
Missing data	(14)	7	0	8
Total		20(41%)	21(43%)	8(16%)

Table 2. Classification of the hailstorms observed in Piemonte, during the period 1 Aug. - 9 Sept. 1979. For secondary classification: see Table 1.

Secondary classifications		Primary classifications Supercell	Ordinary cell	Missing data
U	(0)	0	0	-
M	(1)	0	2	-
L	(1)	2	8	-
Missing data	(2)	0	0	2
Total		2	10	2

(45 min after) the storm moved in the N-E direction, the dominant cell is mature and a new one is growing on the right hand side of the complex (Chisholm and Renick, 1972).

The meteorological radar is frequently used to detect the possible hail-bearing storms in an early stage of development: a few criteria have been used for this purpose (Battan, 1969; Federer et al., 1979). Our 1979 radar data have been analyzed "a posteriori" in an attempt to verify the fitting of two commonly used criteria (Waldvogel et al., 1979):

i) $H_{35} \geq H_{-5}$

ii) $H_{45} \geq H_0 + 1.4$ km

where H_{35} and H_{45} are the heights of the 35dBZ and 45 dBZ reflectivity contour, measured by the radar; H_{-5} and H_0 are the heights of the -5 C and 0 C isotherms, determined by the radio

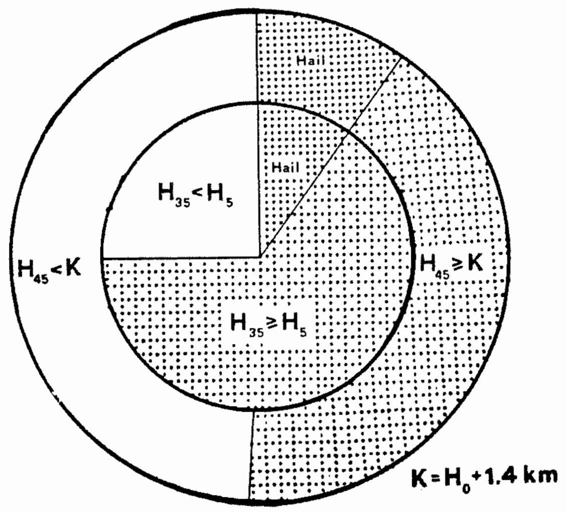

Fig. 6. Comparison between two hailstorm detection criteria. Dotted area represents the fitted condition. See the text for symbols explanation.

sounding of Milano. Fig. 6 shows the percentage of storms satisfying and not satisfying each criterion: it is to be noted that the two criteria were always satisfied in the occasion of hailstorms, but there is a relevant number of cases fitting the criterion in absence of hail. A reason for the result can be the use of midnight data provided by the Milano radiosonde, the nearest to Torino, but probably not sufficiently representative of the meteorological situation at the time and place of the hailstorms.

4. CONCLUSIONS

Radar data collected during the 1979 summer in the North-West part of Italy have been analyzed in order to study the main features of the thunderstorms.

A correlation between the cloud top and the maximum reflectivity of the core has been found (Fig. 5). The storms and the cells detected during the period 1 August - 9 September have been classified (Tables 1 and 2) and their distribution has been compared with the distribution obtained in Oklahoma.

An analysis of the validity of two hailstorm detection criteria has been performed. The best criterion appears to be the one comparing the height of the 45 dBZ reflectivity contour with the 0 C isotherm, although the number of false alarm is still relevant.

ACKNOWLEDGMENT

This research has been supported by the Ente di Sviluppo Agricolo del Piemonte.

REFERENCES

Battan,L.J.,1969. Weather Modification in the USSR. Bull. Amer. Meteor. Soc., 50, 924-945.

Bossolasco, M., 1949. La distribuzione dei temporali in Italia. L'Energia Elettrica (Nov.-Dic. 1949), 717-729.

Browning, K.A.,1977. Hail:the Structure and Mechanisms of Hailstorms. A Review of Hail Science and Hail Suppression, Meteor. Monogr. n. 38, G.B. Foote and C.A. Knight, Eds., Amer. Meteor. Soc., 1-39.

Chisholm,A.J. and J.H. Renick, 1972. Supercell and Multicell Alberta Hailstorms. Reprints Int. Cloud Physics Conf., London, Aug. 1972.

Federer, B., 1978. Methods and Results of Hail Suppression in Europe and in the USSR. Am. Meterol. Soc. Monograph no. 38, 215-223.

Federer,B., A. Waldvogel, W. Schmid, F. Hampel, E. Rosini, D. Vento, P. Admirat and J.F. Mezeix, 1979. Plan for the Swiss Randomized Hail Suppression Experiment. Design of Grossversuch IV. Pure and Appl. Geophys., 117, 548-571.

Morgan, G.M. jr., 1973. A General Description of the Hail Problem in the Po Valley of Northern Italy. J. Appl. Meteorol., 12, no. 2, 338-353.

Nelson, S.P. and Sondra K. Young, 1979. Characteristics of Oklahoma Hailfall and Hailstorms. J. Appl. Meteorol.,18, 339-347.

Prodi,F.,1974. Climatologia della grandine nella valle padana (1968-1972). Riv. Ital. Geofis.,XXIII, n.5/6,283-290.

Prodi,F.,1976. Hailstorms in the Po Valley of Northern Italy (1972-2973). Riv. Ital. Geofis. III, n.1/2,21-31.

Strong,G.S.,1979. Convective Weather Predictions Based on Synoptic Parameters. Preprints 11th Conf. Severe Local Storms, Amer. Metero. Soc. Kansas City, Oct. 1979.

Vento,D.,1972. La determinazione della energia di impatto della grandine. Riv. Ital. Geofis. XXI, 73-77.

Waldvogel,A., B. Federer and P. Grimm, 1979. Criteria for the Detection of Hail Cells. J. Appl. Meteor., in press.

THREE-DIMENSIONAL MOTIONS, PRESSURE AND TEMPERATURE FIELDS WITHIN A CONVECTIVE CELL, FROM DUAL DOPPLER OBSERVATION

F. ROUX, M. CHONG and J. TESTUD

Centre de Recherches en Physique de l'Environnement, Issy-les-Moulineaux, FRANCE

1. INTRODUCTION

Three-dimensional wind fields obtained from multiple Doppler radar data have proved of great interest for mesoscale meteorology. The main characteristic of this observation method consists in the restitution of detailed information concerning cloud internal structure within regions where other measurements are impossible or very partial.

Beyond the kinematic description of the flow, the thermodynamic parameters may be inferred from the computed wind field. A possible way consists in determining the flow accelerations, which are related, through the equation of motion, to the pressure and temperature fluctuations and to the water loading. It is important to notice that such a study needs an accurate restitution of first order derivatives of the three-dimensional wind field. This condition is fulfilled by an original data processing method, developed by Chong et al.(1980).

This paper presents the observation of a convective cell using the RONSARD system, C-band dual Doppler radar system (Nutten et al., 1979) first operated during the "FRONTS 77" experiment. As a matter of fact, the observed event is not a severe one, leading to results that may be quite different from those obtained for most violent events, as previously observed with multiple Doppler radar systems (for example, see Ray et al., 1975).

2. METEOROLOGICAL ENVIRONMENT

During the night October 5^{th} to 6^{th}, 1977, a depression had formed in the chops of the Channel. It caused an inflow of unstable and strongly sheared air from South-West associated with the blocking of a frontal system on the Atlantic coast during the morning.

A weak convective with cell (maximum altitude 6 km) has been observed at about 06:30 UT at 30 km from Magny les Hameaux (Site of Radar 1, 25 km SW from Paris). The 06:00 UT sounding (fig. 1) shows a potentially unstable layer between altitudes 1.6 and 4 km.

It may be noticed that the present situation is not a classical case of diurnal convection, with vertical motions starting from the bottom atmosphere, since here upward motions can only develop from 1 600 m altitude.

3. KINEMATIC STRUCTURE

The described cell was sampled with three successive COPLAN sequences starting at 06:28, 06:33 and 06:38 TU respectively, each one lasting 3 mn. Here, we only present results concerning the 06:38 sequence, other ones showing quite similar characteristics.

This cell has been shown to move identically whatever the altitude although horizontal wind shear, deduced from the 06:00 sounding was rather high ($5.10^{-3}s^{-1}$). Thus, this allowed to define, without any ambiguity, an advection speed for the whole cell ; horizontal motions are presented here with respect to cell displacement.

A first representation of the computed three-dimensional wind field is obtained through horizontal projections, allowing to define inflow and outflow during cell motion. Two distinct flows are present : the first one (fig. 2a), in lower altitudes (500 to 2 000 m), comes from East, with a mean speed of 10 ms^{-1} (it is named E flow subsequently) the second one (fig. 2b), above 1 500 m, is a westerly flow with a mean speed of 15 ms^{-1} that increases with respect to height (referred to as w flow).

Fig. 3a represents vertical cross section, parallel to X'X axis (Radars Axis), thus quite parallel to cell displacement and elongation, and shows internal motions. Large vertical motions (5 to 10 ms^{-1}) can be seen in the middle of the cell, in particular a vortex whose horizontal and vertical extent are respectively of about 4 km and 2 km, and on each side two updrafts, hereafter referred to as U1 and U2. In front of the cell, air circulation shows little vertical motions, with an inflow below a height of 2 000 m associated with E flow and a top outflow associated with the W flow. Behind the cell, the situation is more complicated, vertical motions exist but are less organized than in the middle, the vortex and inflow, alike those observed in U1, are present but seem not so clearly defined.

Vertical cross sections, parallel to the Y'Y Axis (perpendicular to Radar Axis), thus substantially parallel to direction of inflows, show quite different structures for U1 and U2. In U1 (fig. 3b), motions seem to be due to instability of the W flow which rises from 1 500-3 000 m to 3 500-5 000 m (similar to the 06:00 sounding forecast). In U2 (fig. 3c), E and W flows both seem to participate to vertical motions, which are less intense than in U1.

4. THERMODYNAMICAL PARAMETERS RETRIEVAL FROM THE THREE-DIMENSIONAL WIND FIELD

The proposed method for deducing pressure and temperature gradients is quite similar to that proposed by Gal-Chen (1978). Following Wilhelmson and Ogura (1972), air motions, expressed on grid points within the cell, are described by the equation :

$$\vec{\Gamma} = \frac{D\vec{V}}{Dt} = \frac{\partial \vec{V}}{\partial v} + (\vec{V}\vec{\nabla})\vec{V} = -Cp\theta_{vo}\vec{\nabla}\pi' + g\left(\frac{\theta'v}{\theta_{vo}} - ql\right)\vec{k} + \vec{F}$$

where $\vec{\Gamma}$ is the flow acceleration, $\vec{V}$ the velocity, $\vec{\nabla}$ the three-dimensional del operator, Cp the specific heat of satured wet air at constant pressure, θ_v the virtual potential temperature, defined as $\theta_v = (1 + 0.61\ qv)\ \theta$ where qv is the satured mixing ratio of water vapor and θ the potential temperature, $g\vec{k}$ is the gravity acceleration, ql the mixing ratio of liquid water, $\pi = (\frac{P}{Po})^K$ the non dimensional pressure where p is the dimensional pressure, Po a reference pressure taken to be 1 000 mb and $K = R/Cp$ where R is the gas constant for wet air, $\vec{F}$ denotes the subgrid scale turbulent force. Subscript o refers to an unperturbated state of the atmosphere and ' to perturbation.

The purpose of this study is to retrieve thermodynamical parameters, pressure and temperature fluctuations since radar data allow the other terms to be computed or estimated. Accelerations are deduced from three-dimensional velocities and their first order derivatives (Advection term : $(\vec{V}\vec{\nabla})\vec{V}$) and from differences between values obtained at the same points for successive sequences, taking cell motion into account (time derivative : $\frac{\partial \vec{V}}{\partial t}$). The mixing ratio of liquid water can be estimated from reflectivity factor values through adequate empirical relations, however the obtained values don't take non-precipitating cloud droplets into account. Owing to an error during data acquisition it was only possible to restore an estimation of reflectivity values allowing no exact calculation of the mixing ratio of liquid water. At last, the subgrid scale turbulent force $\vec{F}$ can be deduced from a parametrization following Gal-Chan we have used that defined by Deardorff (1979). $\vec{F}$ is proportional to the space derivative of the tensor $(\frac{\partial Uj}{\partial Xi} + \frac{\partial Ui}{\partial Xj})$ through turbulent energy on a scale smaller than the grid, requiring values for standard deviations from three-dimensional velocity components $(\langle u'^2_x\rangle, \langle v'^2_y\rangle, \langle w'^2_z\rangle)$. As these values are unavalaible we have estimated them in each mesh with standard deviations from mean radial velocities, thus leading to a rough estimation of the subgrid scale turbulent force. The applied forces are shown to have typical relative amplitudes.

$$|g\ ql\ \vec{k}| \sim |\vec{F}| \quad < \quad \left|\frac{\partial \vec{V}}{\partial t}\right| \quad < \quad |(\vec{V}\vec{\nabla})\vec{V}|$$

$$(10^{-4} \text{ to } 10^{-3}) \quad (10^{-3} \text{ to } 10^{-2}) \quad (10^{-2} \text{ to } 10^{-1})\ ms^{-2}$$

As we cannot obtain precise values for each grid point, water loading $(gql\vec{k})$ and subgrid phenomena $(\vec{F})$ will subsequently be neglected.

5. PRESSURE PERTURBATIONS HORIZONTAL GRADIENTS

The horizontal accelerations (subscript H) can be written as :

$$\vec{\Gamma}_H = -Cp\ \theta_{vo}\vec{\nabla}_H\pi' + \vec{\varepsilon}_H$$

where $\vec{\varepsilon}_H$ represents a noise added to the calculated accelerations $\vec{\Gamma}_H$, due to the radar error, to the data processing method and to the fact that the other terms in the equation of motion have been neglected. We have developed an iterative method for filtering the non-divergent part of $\vec{\varepsilon}_H$ (the divergent part is undiscernable from the real pressure gradient $\vec{\nabla}_H\pi'$) ; this filtering allows a 6 dB gain in the signal to noise ratio. Fig. 4 shows an example non-hydrostatic pressure gradient restitution, at a height 3 000 m. Similar features can be deduced from the 06:28, 06:33 and 06:38 sequences (the 06:38 sequence is the only one presented here).

Intensity increases with height, but always remains smaller than 07 mb/km.

In front and in the middle of the cell, gradients are nearly westward and behind the cell they are nearly eastward.

Comparison with vertical motions at the same altitude allows a better understanding of these features. Quite good correlation may be found between intense gradients and U1 and U2 updrafts regions, likewise, eastward gradients seem connected with intense downdraft. This structure may be explained in terms of interaction between horizontal wind shear and vertical motions. Horizontal accelerations $\vec{\Gamma}_H$ are expressed as,

$$\vec{\Gamma}_H = \left(\frac{\partial \vec{V}_H}{\partial t}\right) + Ux\frac{\partial \vec{V}_H}{\partial x} + v_y\frac{\partial \vec{V}_H}{\partial y} + w_z\frac{\partial \vec{V}_H}{\partial z}$$

Horizontal wind shear $\left(\frac{\partial \vec{V}_H}{\partial z} \sim 5.10^{-3}s^{-1}\right)$ is always greater than purely horizontal terms $\left(\frac{\partial \vec{V}_H}{\partial x} \sim \frac{\partial \vec{V}_H}{\partial y} \sim 10^{-3}s^{-1}\right)$, so pressure perturbations may be produced by horizontal flow acceleration into updrafts through parcels elevation in a strongly sheared environment. An additional proof may be found by comparing pressure gradients and wind shear directions.

6. VERTICAL FORCES RESTITUTION

The calculated horizontal pressure gradients also allow the restitution of vertical pressure gradients. Since $\oint_{\mathcal{C}} \vec{\nabla}\pi'.\vec{ds} = 0$

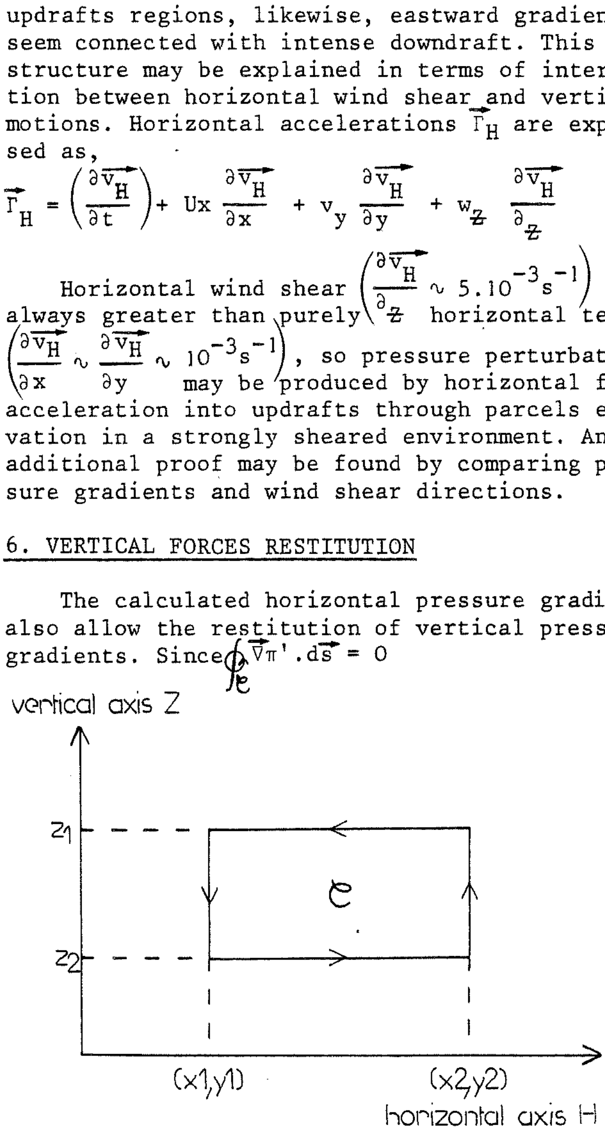

It follows that :

$$\int_{z_1}^{z_2}\left[\frac{\partial\pi'}{\partial z}(h_2)-\frac{\partial\pi'}{\partial z}(h_1)\right]dz=\int_{h_1}^{h_2}\left[\frac{\partial\pi'}{\partial h}(z_1)-\frac{\partial\pi'}{\partial h}(z_2)\right]dh$$

where h can be expressed in terms of (x,y), horizontal coordinates.
The left part of this equation may be expressed as the horizontal gradient of the vertical pressure gradient, integrated between altitudes z_1 and z_2 : $< \vec{\nabla}_h\left(\frac{\partial\pi'}{\partial z}\right) >_{z_1,z_2}$. A similar calculation for vertical acceleration Γ_z then allows the contribution of buoyancy in the vertical component of the equation of the motion to be separated :

$$< \vec{\nabla}_h \theta'_v >_{z_1,z_2} = \frac{\theta_{vo}}{g} < \vec{\nabla}_h \Gamma_z >_{z_1,z_2} + Cp\,\frac{\theta_{vo}^2}{g} < \vec{\nabla}_h\left(\frac{\partial\pi'}{\partial z}\right) >_{z_1,z_2}$$

The presented results were obtained between altitudes 2 000 and 3 000 m (fig. 5), which is the most active part of the cell. Alike in the case of horizontal pressure gradients, direction of the horizontal wind shear may be considered as a preferential one, showing that wind shear certainly plays a prominent part in the orientation of the dynamical structures within convective cells.

Horizontal gradients of vertical acceleration (fig. 5a) show two maxima of vertical acceleration that are associated with U1 and U2 updrafts.

Horizontal gradients of pressure force and buoyancy (fig. 5b and 5c) show opposite features. That situation may be explained through the principle of action and reaction : a vertical (upward or downward) motion, generated by one of the two phenomena will indice a vertical motion, in the opposite direction, generated by the other phenomena. The dynamical processes, associated with vertical motions, are quite different for U1 and U2 updrafts : in U1 buoyancy is greater than non-hydrostatic pressure strength, in U2 an opposite situation is observed.

These features can be explained through a circulation scheme within the precipitating part of the cell : the W flow enters into the cell from a height of 1 500 m and rises upwards owing the thermal instability (U1 updraft), interaction between vertical motions and horizontal wind shear causes an horizontal non-hydrostatic pressure gradient, inducing a pressure decrease in the internal part of the cell.

Thus, the E flow, entering into the cell at a lower altitude, is subjected to a vertical non-hydrostatic pressure gradient, that forces it upwards counteracting the effect of negative buoyancy.

This study shows the importance of non-hydrostatic pressure in the development of convection. The first effect leads to an attenuation of vertical motions due to thermal instability, owing to the counter-reactive role of pressure perturbation ; the second effect, associated with feeding of the cell at high levels, may induce vertical motions for thermally stable air.

7. CONCLUSION

The study of a weak convective cell, as observed with the RONSARD dual Doppler radar system using the COPLAN methodology, allowed to show some of the possibilities of this kind of observation. The coherence of results with respect to the expectation from sounding and the stability of restitutions for independant sequences show the reliability of the developped data processing method.

Beyond a kinematic analysis of air circulation within the cell, using of the ability to provide three-dimensional wind fields stable with respect to first order differentiation, we processed acceleration data to infer thermodynamical parameters by means of the equation of motion. Likewise, coherence of the results enhances the confidence in these restitutions, showing the production of horizontal pressure gradients through the interaction of vertical motions and horizontal wind shear, and displaying the importance of non-hydrostatic pressure in the development of convective cells.

REFERENCES

Chong, M., F. Roux and J. Testud, 1980 : A new filtering and interpolating method for processing dual Doppler data : performance in three-dimensional wind restitution, ability to derive pressure and temperature fields, to appear in Preprints 19th Radar Meteor. Conf., Miami, Florida, Amer. Meteor. Soc.

Deardorff J.W., 1975 : The development of boundary layer turbulence models for use in studying the severe storms environment, Proc. SESAME open meeting, Sept. 4-6 1974, published by NOAA/ERL, Boulder, Col., edited by D.K. Lilly, 251-264.

Gal-Chen, T., 1978 : Deduction of pressure and density fluctuations using Doppler radars observations : a feasibility study, Preprints 18th Radar Meteor. Conf., Atlanta, Georgia, Amer. Meteor. Soc., 194-11.

Nutten, B., P. Amayenc, M. Chong, D. Hauser, F. Roux and J. Testud, 1979 : The RONSARD Radars : a versatile C-Band dual Doppler facility, IEEE Trans. Geosci. Electron., GE-17, 281-288.

Ray, P.S., R.I. Doviak, G.B. Walker, D. Sirmans, J. Carter and B. Bumgarner, 1975 : Dual-Doppler observation of a tornadic storm, J. Appl. Meteor., 14, 1521-1530.

Wilhelmson, R. and Y. Ogura, 1979 : The pressure perturbation and the numerical modeling of a cloud, J. Atmos. Sci., 29, 1295-1307.

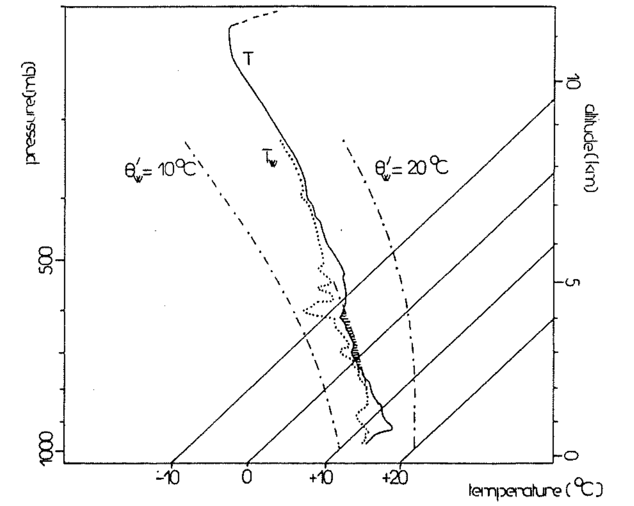

Fig. 1 : Pressure, temperature and moisture sounding on October 6[th] 1977 at 06:00 UT. Solid line represents temperature T, dotted line wet-bulb temperature Tw, 10°C and 20°C wet adiabats are plotted in dashed line.

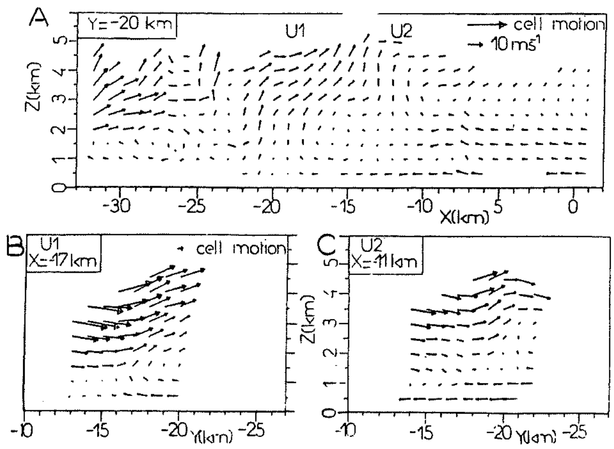

Fig. 3 : Vertical cross sections displaying internal vertical motions, a : in a plane parallel to radars axis, b : in a plane perpendicular to radars axis and into U1 updraft, c : same as b into U2 updraft.

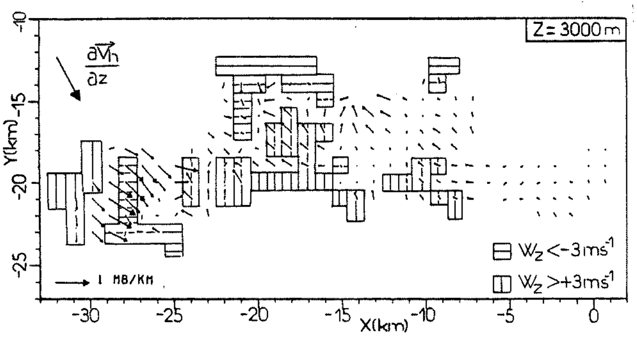

Fig. 4 : Horizontal pressure perturbation gradients at 3 000 m altitude. Hatched zones represent region where vertical velocity is greater than + 3 ms^{-1} or less than - 3 ms^{-1}. Direction of the horizontal wind shear $\frac{\partial v_H}{\partial z}$ is also indicated.

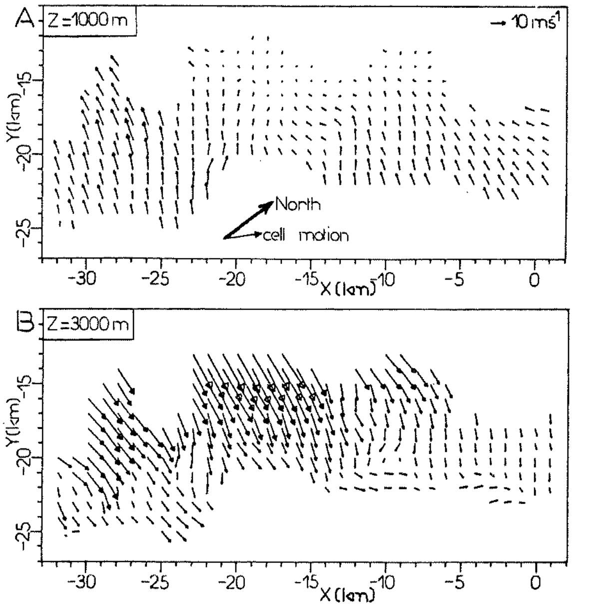

Fig. 2 : Horizontal projections of the three-dimensional wind field, a : at 1 000 m altitude showing E flow, b : at 3 000 m altitude showing W flow. Cell motion (27 ms^{-1}) and North direction are also indicated.

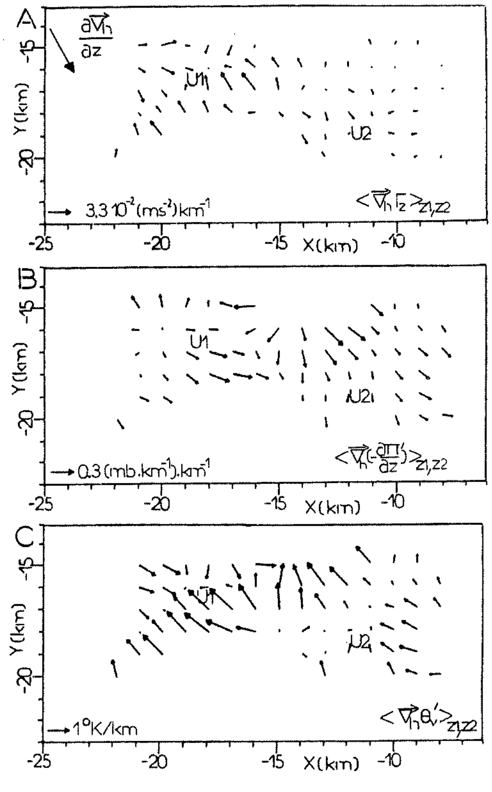

Fig. 5 : Horizontal gradients of the vertical forces, integrated between 2 000 and 3 000 m altitudes. a : vertical accelerations showing two maxima that are associated with U1 and U2 updrafts. b : pressure strength. c : buoyancy. Units are choised in order the various strengths to be comparated. Direction of the horizontal wind shear is also indicated.

CONDITIONS OF OCCURRENCE OF SEVERE CONVECTIVE STORMS LEWARDS OF THE ANDES, IN MENDOZA

M.E. Saluzzi

National Commission on Space Research, Buenos Aires, ARGENTINA

I. Introduction

The northern zone of the Province of Mendoza (Argentina), where an extended observational programme of severe convection has been developed, is situated inmediately leewards of the Andes. The orography then appears as one of the most important determinant factors of the behaviour of the convection. The ground relief is, however, so complicated and singular that the study of its influence may be undertaken in a direct and simple way.

Its most evident climatological effect is proved observing the trace of the isohyet. The 350 mm. annual isohyet shows a trace (in the zone) which is almost parallel to the Andes and located at some 200 km. from them. (Hoffmann, WMO, 1975).

That is to say, leewards of the Andes there is a quasi-desertic zone which is a natural consequence of the heating and intense drying undergone by the downward air. The zones where crops are intensive and valuable, artificially irrigated with water from thawing are true oasis.

For that reason, the consequences of sever convection (strong winds and hailstone) cause a great deal of damage and have originated the observational studies which are summarized since, in spite that the regimen conditions would seem not favourable to great convective developments, these occur frequently and with a considerable magnitude in summer.

Undoubtedly, at these times the regimen conditions must be altered noticeably. And likewise, some of these conditions must be, in spite of it all, favourable to the development of the process.

One of them is undoubtedly the strong heating undergone by air, which is the result of the strong isolation added to the descent effect, and enables it to hold huge amounts of humidity. Another condition is some dry macroturbulence which is undoubtedly produced when the descending air strikes the ground. This permanent effect is, according to our judgment, responsible for the zones of cumulus genesis observed in the region when the atmospheric conditions favourable to convective processes appear in phase.

2. Atmospheric conditions which are favourable to convective development

From the aforementioned it may be inferred that the permanent regimen in the zone, in spite of certain circumstances which might be considered favourable, does not really make possible the growth of big clouds. In fact, these do not develop if the regimen situation is not overcome.

The modifications which must take place are:

a) The surface thermodynamic parameters must change. Fundamentally there is no convective developments without the presence of the necessary surface humidity ($T_d \geqslant 10°C$). This enters the zone advected by the local circulation with a strong East component. The humidity must come, however, from the NE region of the country and will only reach the zone under study if a surface anticyclon is located to the ENE of the region. This basic configuration is the result of a second condition which must be situated in phase:

b) There must be a forward difluent region of an upper trough affecting the zone. This trough, at the same time that it determines the baric surface configuration (since it must have been preceeded by a ridge), modifies the temperature gradients in the vertical, causing the conditional instability which is characteristic of the zone radiosoundings for storm occurrence. Another effect is undoubtedly added movements resulting from the surface convergency and divergency fields aloft, characteristic of the forward trough zone. These vertical movements appear as the agents of the interaction between two different scales of atmospheric movements: those in synoptic scale and those in mesoscale. The localized convective phenomen appears as the result of this interaction. If the trough is associted to a frontal surface this synoptic mechanism can also operate as a trigger for convection, provided the prefrontal air mass fulfill the necessary thermodynamic conditions and the front affect the zone at evening and night hours (when the thermodynamic conditions are favourable to the development of the big clouds).

The Table shows the average values of certain synoptic thermodinamic param eters (and their variability) recorded during the occurrence of storms for 80 cases of severe convection in the zone.

Hour		12Z	σ	18Z	σ
$\bar{T}_{sup}$ (°C)	Máx	25,4		36,2	
		20.6	2.27	28.6	3.66
	Min.	16,8		21,0	
$\bar{T}_{d\,sup}$ (°C)	Máx	19.6		19.6	
		13.6	3.16	16.1	2.18
	Min	6.8		10.0	
$\bar{T}_{850}$ (°C)	Máx	23.0		29.0	
		16.5	3.34	21.2	3.58
	Min	10.8		13.4	
$\bar{T}_{d\,850}$	Máx	17.0		17.0	
		10.8	3.12	13.1	3.06
	Min	4.6		4.4	
$\bar{T}_{700}$ (°C)	Máx	15.6		15.6	
		7,8	3.46	10.0	3.0
	Min	3.4		2.6	
$\bar{T}_{d700}$ (°C)	Máx	9.0		10.2	
		0.84	4.11	2.4	4.2
	Min	-5.0		- 90	
$\bar{T}_{500}$ (°C)	Máx	-6.4		-4.5	
		-9.9	5.9	-8.8	6.1
	Min	-17.1		-15.1	
Melting Level (m)		4967		5416	
		4172		4339	
		2940		3260	
Factor "K" (whiting)		38.9		46.3	
		30.4	3.1	34.96	2.85
		20.3		24.0	

3. Radioechoes, precipitation and related parameters

A cloud from the storm of 22 December, 1976 is studied. This cloud was responsible for an intense hailfall and therefore was representative of a severe convection case. Its development is sufficiently unusual as to typify the behaviour of a "pulsating" echo, different from others with simpler evolution and which characterize the more frequent storms in the zone although they may all be hail storms.

Echo C-22 December 1976. Hailstorm

The C echo was first recorded by the FPS-18 Radar when it was at a distance of almost 50 km to the SE of its location, already on the plain. It had therefore emerged from the genesis zone and the first displacements which led it away from the mountains. It followed a SW-NE route to reach the city of San Martín at the end of its history. It always behaved as a mature echo and was observed for a very short time before the beginning of solid precipitation.

The observation took place between 22:29 and 23:50 LT, that is, it lasted for 1h.40 minutes; the last observation indicates the echo decay.

It is interesting to verify its pulsating behaviour. According to the observations of hailfall in the mesonetwork, hail fall was verified at 22:39; 22:43; 23:06; 23:20; 23:29 and 23:48 LT. All these times correspond to radar observations where a 50 dbz closed area was present in the PPI, at level oscillating between hights of 5 and 10 km in the cloud, exhibiting 3 maxima: two at 7 and 7.5 km and a stationary one during 10 min at 10 km. For the remaining observations (at 23:14; 23:25; 23:35; 23:44 and 23:56 LT). The maximun value observed in the PPI was 40 dbz (whitout an area of 50 dbz).

These islands with lower reflectivity correspond to the times of recovery of the cloud when, added to the precipitation, there was a process of feed back and formation of new hydrometeors. The last observation recorded marks the final decay of the echo.

The 50 dbz measured areas mark the patterns of the process culminanting times with their variations. Their total development may be seen in Fig. Nº 1.

The focus of the cloud activity is always observed in the left region according to the sense of its displacement. It was never stationary, but it had low velocity; during the whole observational period it covered a distance of the order of 40 km following the already mentioned general direction although the focus of high reflectivity was more erratic within the cloud with a marked vertical motility. This was emphasized by the pulsating character of the echo.

The evolution of the parameters read in the RHI shows another singularity

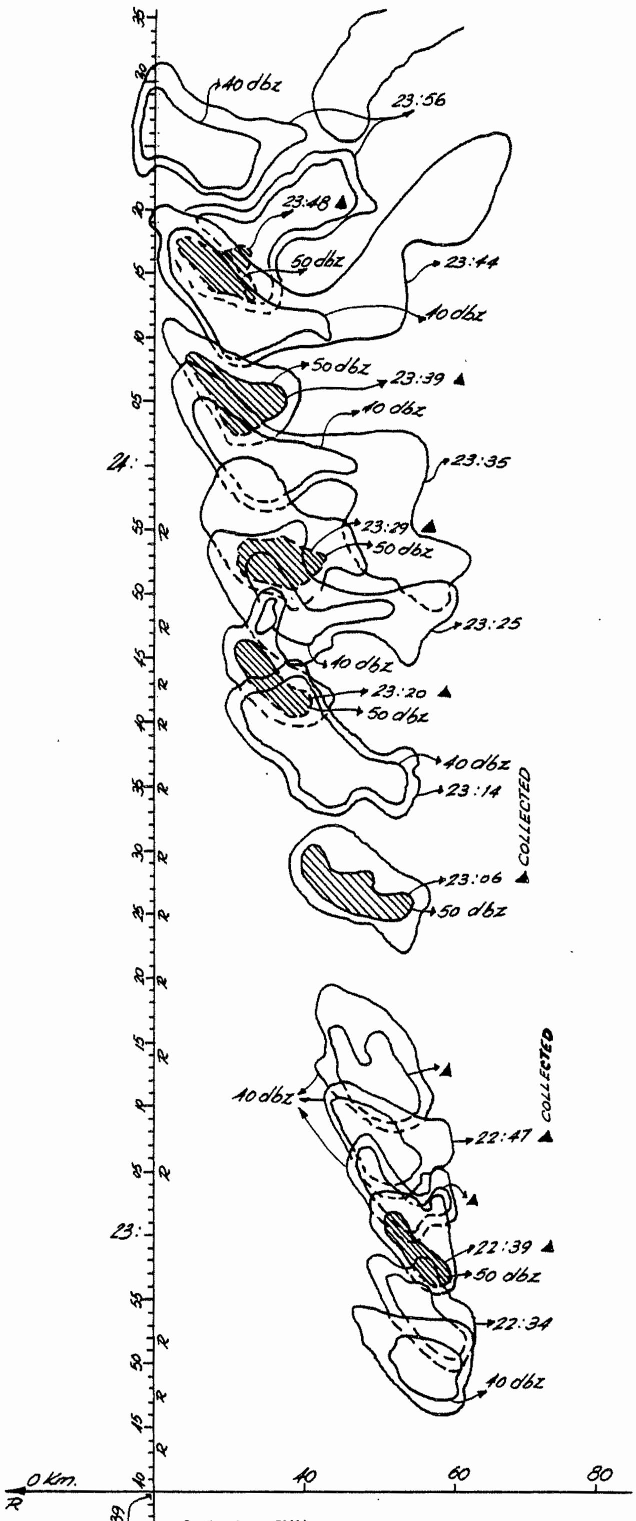

C ECHO- THUNDERSTORM 12 DEC 1976 Fig. 1

in the echo behaviour. Its development shows two periods. The first one lasts until 22.55, when the values of its parameters (except for the top one which was always very high) are comparable to the usual ones in the zone. The second period starts at 23:06 (marked by the discontinuity in the observations); from that time on, the permanence and the values of the parameters are extraordinary until the time of decay. Their development follows the aforementioned accurately, according to the PPI observations. However, the exceptional height of the top (indicating a strong upwards current) as well as that of the reflectivity area 30 dbz (indicating abundant liquid hydrometeors) are remarkable.

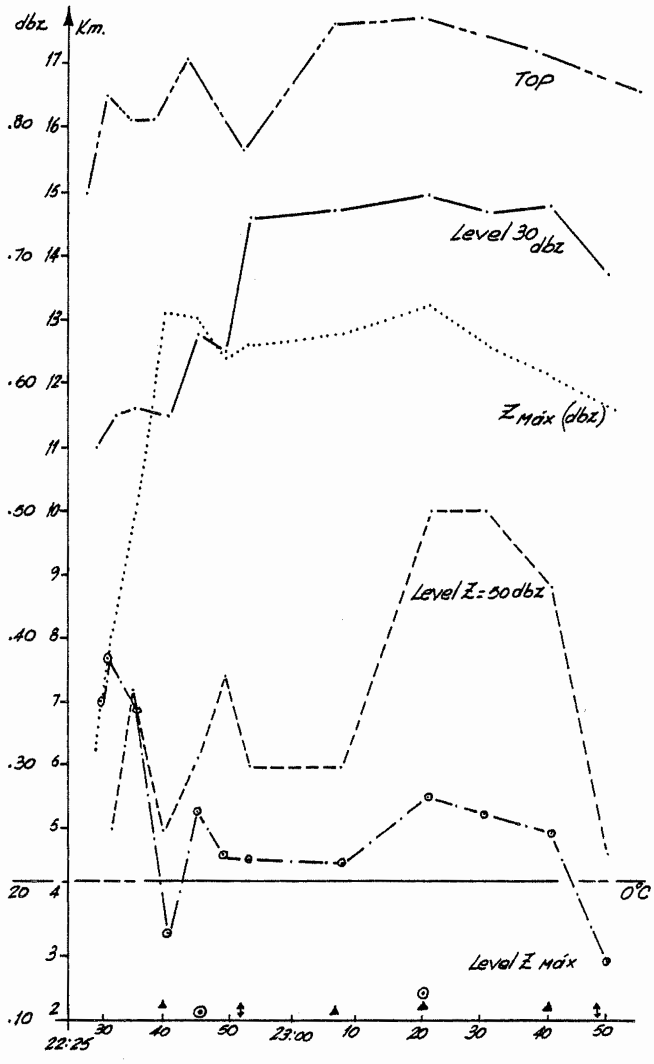

C ECHO - THUNDERSTORM 12 DEC 1976
⊙ STONE COLLECTION
FIG 2

The echo produced hail in both periods and samples were collected in both of them. The samples were analysed at the Instituto de Física de la Atmósfera of the Servicio Meteorológico Nacional; the results are presented in this Congress (Levi, Prodi et al). The hailstones were collected at mesonetwork posts 2148 and 3152, distant 10.35 km from each other, and they correspond to radar observations of 22:47 and 23:20 LT. Fig. 3 shows the location of the echoes on the mesonetwork for those times as well as an intermediate location corresponding to the maximum intensity of the hailfall at post 2645.

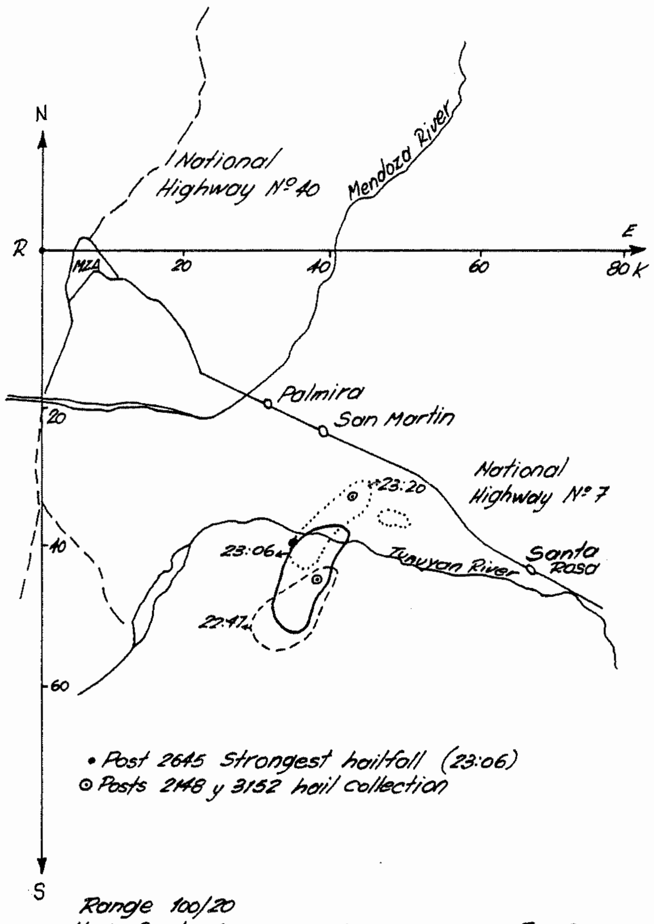

Range 100/20
Horiz. Scale 1mm - 0.69 Km.

Fig 3

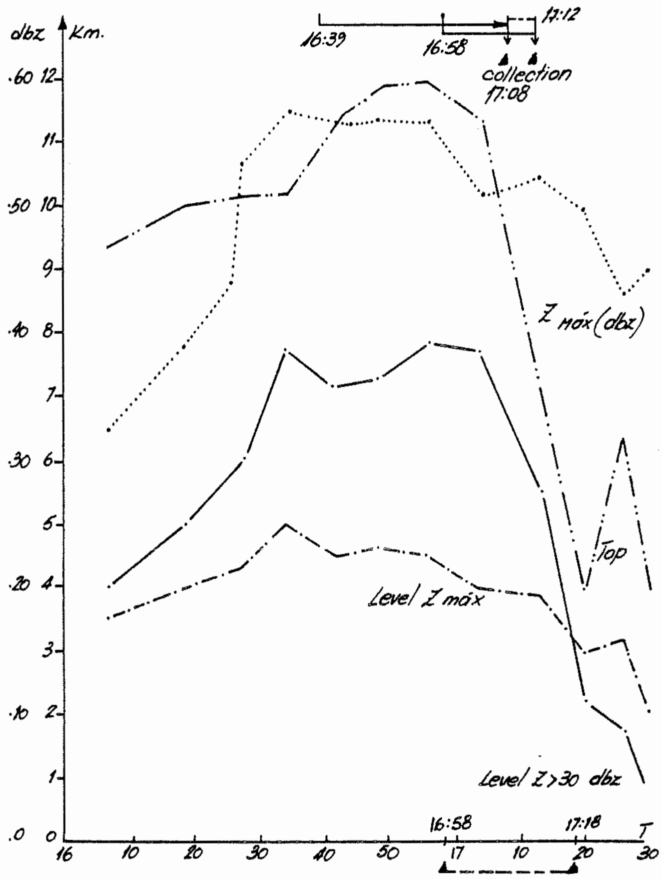

C ECHO-THUNDERSTORM OF 18 Jan 1977

Fig 4

During the 1st. period of the cloud, the precipitation was continuous from 22:39 on until 22:52 (13 min) whitout the appearance being recorded in the cloud of a reactivation of the 50dbz in the PPI's; a pulsation in the parameters read in the RHI is recorded. In the 2nd. period, between maximum activity and recovery periods, the lapse is of the order of 10 to 15 min. This seems to be, then, the hailstone growth time.

For the storm of 18 January, 1977, whose behaviour is significatively representative of the one most frequently observed radioechoes displayed by the FPS-18 radar for the region, hailstone samples were collected by means of guided interception. The exact collection times are plotted in the graph. From the structure studies their possible growth period was derived; this is also shown in the graph.

It may be seen that in general it coincides with the values inferred approximately for the preceeding case. Therefore, in spite of the different behaviour of the echoes, it seems to be true that the growth mechanism of the stones has worked similarly in both cases, taking similar times also.

CONCLUSIONS

The behaviour of severe convection in the northern region of Mendoza is sufficiently typified. The values and the behaviour of the synoptic and termodynamic parameters of clear air which are favourable for the great convective developments are known. In addition, the FPS-18 radar observations have enabled the study of many storm echoes which are thus related to the life and growth of the hailstones originating in them. To sum up, the macrobehaviour of storms, the behaviour of radioechoes and the characteristics of their products may be correlated. All this contributes some objective knowledge on the microphysics and the dynamics of great convective clouds.

REFERENCES

- José A. Hoffmann - 1975. Atlas Climático de América del Sur. WMO. UNESCO. Cartografía Hungría.
- Federer B. and Waldvogel A. 1978. Time-resolved haistone analysis and radar structure of Swiss storms. quart. 104.439.69
- Waldvogel A. Federer B. and Schmid W. 1978. The kinetic energy of hailfalls. Part II: Radar and Hailpads. J. Ap. Met. 17 1680
- Saluzzi M.E. Núñez J.M Lubart L. Ghidella M. y Levi L. 1977. Objetiva historia de un proceso granicero. Congremet Bs.As. 1979.

ON THE CHARACTERISTICS OF THE PHYSICAL PROCESSES OF HAIL CLOUD

Wang Ang-sheng, Xu Nai-zhang, Huang Mei-yun et al.
Institute of Atmospheric Physics, Academia Sinica
Beijing, The People's Republic of China

Since hail cloud is a kind of convective clouds which causes damages, hail cloud is an object that many scientists attentively study[1-4]. Today, it is necessary for us to understand the physical processes of hail cloud. So that we can improve theorems and methods of hail suppression. Hence, observations and researches for hail cloud are carried out in many countries during recent years[1,2,5,6], and lot of exciting progresses have been got[1,2,7,8]. But, only little complete data has been obtained because of difficulties in observations of hail cloud. It is necessary to conduct more extensive research from various fields and more cases[7,9,10]. Some of our results in the research during recent years are presented.

1. Some characteristics in the lifecycle of cell of hailcloud

Some characteristics in the lifecycle of cell of hail cloud are obtained by the observations during the years 1972-1978 over Xiyang.

(1) Leap increase

When differences between hail cloud and other convective clouds were studied, we found that parameters characterizing hail clouds increase rapidly. In the appearance the hail cloud extended rapidly, then the lightning frequency increased abruptly in short time interval before the drop of hail. The increase of lightning frequency is the most obvious[11,12]. The detailed observations by radar show that top height of different strength of echo grow rapidly before the drop of hail[13]. We define rapid increase of cloud parameters of hail cloud in short time interval as "leap increase".

Lightning frequency N (strokes/5 min) in hail cloud (top) and transit thunder cloud (below) over Xiyang during past years as a function of time T are shown in Fig.1, but it is drawn only obvious "leap increase" part for hail cloud. We see from Fig.1 that the parameter "leap increase" is a little in thunder cloud. This characteristic of lightning, therefore, had been used as one of important method to distinguish hail cloud[7,12].

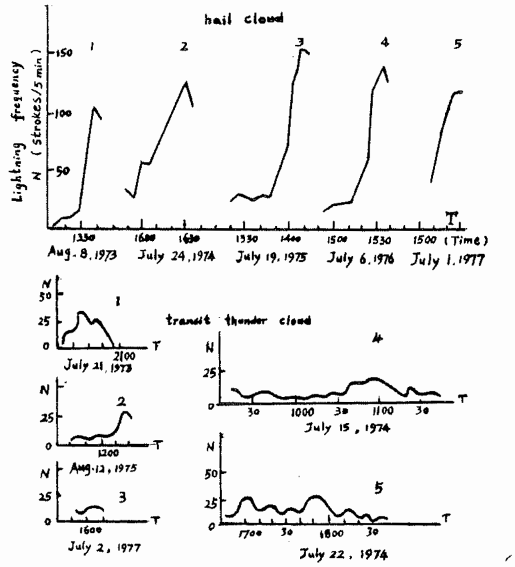

Fig.1. Lightning frequency N as a function of time T in hailcloud (top) and transit thunder cloud (below) over Xiyang.

We find a rapid increase in short time interval about cloud tower and top height of echo of different strength for hail cloud in the observation designed specially, an observational result is shown in Fig.2[13]. We can see that the cloud tower and echo top on July 14, 1977 increase obviously, and tend to be very consistent. Alike observations show that this phenomenon of cloud before the drop of hail is related closely to the hail formation. Rapid increase curves of radar reflectivity of each cells in a propagational hail cloud was obtained by J.P.Chalon et al[14], it is seldom in thunder clouds. The leap increase represents rapid growth of the above parameters at some degrees in hailcloud.

(2) Brew

We called the stage as "brew" from the stronger echo ($Ze = 5\times10^3\ mm^6/m^3$) top of hail cloud into natural ice forming layer (-20°C) to the appearance of hailstone on the ground (include growing, melting and subtimating processes along its drop path). This stage is an important stage in which hailstone growed up. The observations in Xiyang show that the "brew" stage was about twenty minutes.

The observations indicate that leap increase continues to inital term of brew stage. Obtained data show that the leap increase of lightning frequency somewhat later about ten minutes than that of echo (particularly strong echo)[12,15]. It is indicated that leap increase of hydrometeor field in cloud may be the precursor of the

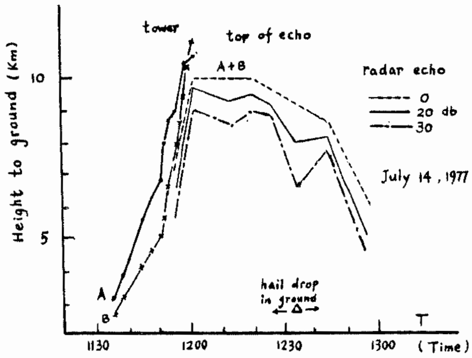

Fig.2. The top of cloud and its echo top height of different strength as a function of time T in hailcloud.

lightning leap increase[12] which is similar with the results of case research from abroad in recent years[16]. Cloud grow slowly and reach a relatively stable stage because of obstruction from top of troposphere and affect of concentration of cloud hydrometeor, which are important feature in brew stage[17]. The strong updraft supports quite rich hydrometeor in cloud and carries them into the most favourable stage for the growth of hailstone during lifecycle of a cell. In addition, echo strength increase obviously in the brew stage.

According to the view point about rapid growth of hailstone in accumulation zone[18], it requires not only rather short time for hail suppression (i.e. two minutes to complete all works from the finding of hail source to shooting), but over $20g/m^3$ of water content. It couldn't conform with practice. If the "brew" stage holds, hailstones could grew up in a few gram per cube meter of water content which can be observed in hail clouds. It conforms to reality in most clouds. Therefore the existence of "brew" period about twenty minutes proved reasonable time for hail cloud identification and hail suppression.

(3) Hail fall

We have seen from voluminous observations that echo top height of different strength of hail cloud descend obviously after or before hailstones appear on the ground, as shown in Fig.2. From some other examples such as 13,15, 17 and other, we could find that the top height descent 3-5 Km during 10-20 minutes, and meanwhile the lightning frequency also decreases obviously, as shown in Fig.3. All these show that falling of hailstone in hail clouds always dynamically lead to dissipation of cloud, and precipitation drag play an important role in collapse of cloud.

(4) The lifecycle of cells

We divide lifecycle of cell of hail cloud as five stages from the research on hail cloud over Xiyang, as Fig.4. It is quite obvious, there is a peak part in the figure, it consists of three stage, i.e. leap increase, brew and hail fall, as above. The front and rear of the peak show rapid increase of parameters during leap increase and rapid decrease during hail fall, relative stables part in the peak shows brew stage, which is a key period for forming hailstone. In addition, the stage before leap increase had been called the "emerging" of cloud, and the stage after hail fall had been called the "decay". Although the cells of hail cloud change complexly with different strength and scale, they always possess the above general characters. Convective cloud such as thundercloud, in general, couldn't reach to the condition about hail formation with the obvious peak, and particularly the condition of brew stage when stronger echo region ($Z_e = 5 \times 10^3 mm^6/m^3$) interjects -20°C level[13,17].

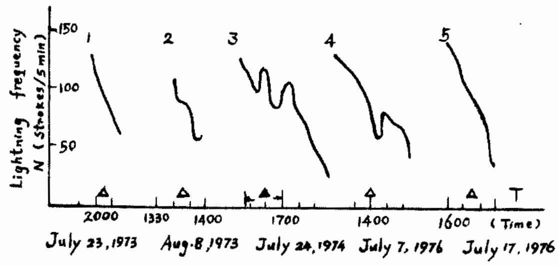

Fig.3. The lightning frequency decreases obviously when hail fall.

Division of lifecycle about cell of hail cloud into five stage, as above, generally is suitable for weak cell, multi cell and propagational hail cloud[19], except for severe cell, because of special structure in its life and it makes to sustation brew and continuous hail fall slightly late. The leap increase and brew stages above mentioned are very significant, the former is an important evolutional stage that facilitate to reach condition of hail formation, and the later is the most favourable stage for hailstone formation in the lifecycle. They are key term to identification, particularly, modification of hail cloud, and show that men identify and suppress hail cloud with certain physical basis[1,7].

2. The merging of cells and the formation of hailcloud

A lot of observational results in Xiyang show that merging of cells is one of important causes of the leap increase, particularly in severe hail cloud. These observations show that merging of new cells with growing cells promote their dynamic growth, whereas the mergings of mature or dissipative cloud, generally, promote to develop only slowly. Preliminary research shows that there are four classifications usually in the manner of mergings.

(1) Jet merging

When a jet updraft (characterized by weak echo region) exists between cells, because of thermodynamics and dynamics, it lead to merging of cells A and B with jet and facilitates leap increase and formation of hailstone in hail cloud.

(2) Pursuing merging

When the cell B with faster velocity caught up with gradually slow one (cell A), because of some causes (e.g. affect of topography), outflux from cell A could converge with influx of cell B to form circulation, so lead to merging of two clouds[15].

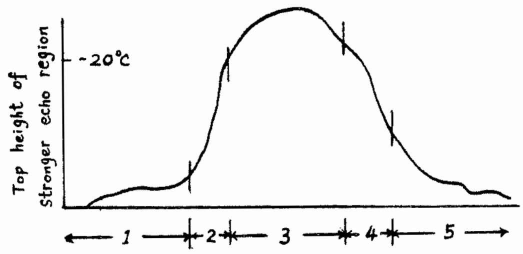

Fig.4. Schematic diagram of lifecycle of cell. 1 - emerging, 2 - leap increase, 3 - brew, 4 - hail fall, 5 - decay.

(3) Fingerlike merging

When a new cell grows rapidly in a favourable condition (such as updraft) on a flank of cloud and merges with the primary part of mother's cloud, they could form a obviously fingerlike echo[20].

(4) Convergence merging

In meso scale weather, the convergence mergings often occure in convergence region of airflow, in where convective clouds are close by each other, when clouds move with airflow, and sometime lead to the formation of hail cloud.

3. Some relations between hailcloud and environmental conditions

(1) Relations between hailcloud and environmental temperature

A high drop in temperature caused by cold advection in upper altitude is always one of important condition for hail damages. A typical case in 1977 is shown in Fig.5. In this year hail fall occurred in every day of six (August 9-14) which results from the continual descent of -20°C level about 100 mb during nine days (August 7-15), and severe hail damage occurs just while decreasing quickly in temperature. The correlation obtained from 87 hail fall days during June 15 to August 25 in 1970-1977 has been shown in Fig.6, in which indicates the strength of hail fall to ground (▲, △, o and × stand for damaged area (mu, a unit of area = 0.0667 hectares) over 10000, 1000, 100 and nondamage respectively). -20°C level descends obviously, as seen in Fig.6, in severe damaged days, but is higher in nondamaged days. It shows that environmental temperature may be an important factor of hail formation.

On the other hand, disposition of cloud with its enviroment is also important factor. We, as mentioned, emphasized[12,13,21] that the interjecting of stronger echo region with high water content in cloud to natural ice forming region (-20°C) is an important condition for hail formation. Works of our researchs indicated that 95 % hail cloud of 83 storms could come to the condition, but 84 % of thundercloud failed to it[13]. One example is shown in Fig.7, from which the leap increase of lightning frequency could be seen about ten minutes after the top of echo (T_1) interjected to -20°C layer[12].

(2) Relations between hailcloud and environmental wind shear

Our analyses from 42 hailstorms over Xiyang point out[19] that more moderate hail cloud appeared in weaker wind shear enviroment with mean wind shear 2.2 m/s·km in cloud region, whereas strong,severe hail cloud appeared in stronger wind shear environment with 3.4 m/s·km. It conforms with results from other scientists during recent years[22]. A most severe wind damage occured in one of the most severe wind shear enviroment with 6.4 m/s·km on August 11, 1977, but only light hail damage was suffered. There are analogous examples in U.S.A.[22] It may imply that excessive severe wind shear environment,probably, isn't favourable for formation of hailstone, as shown in Fig.8.[15]

4. The classification research on hailcloud physics

Like the division of cumulonimbus into thundercloud and hailcloud at the begining of research on hail process and hail suppression, it has been recognized at present that different mechanisms of hail formation exsist in hail cloud itself based on its physical and structural differences[1]. It is necessary to correctly know the characteristic and structure of hail cloud of different categories, if you hope modificate effectly and suppress it successfully on purpose. In view of the failure results of modification in different hail clouds by means of the same method, we must pay more attention to the classification research on it. J.D.Marwitz[22] and A.J.Chisholm[4] have developed preliminary view point about hail cloud classification, but unsophisticated yet.

Therefore, we have studied physical feature and structure of 42 hail clouds over Xiyang during 1975-1977, and divided them into four categories as follows[16,19]:

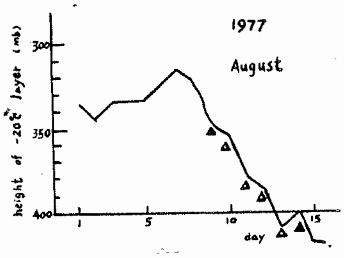

Fig.5. A severe descent of temperature in high altitude and appearence of hail in Aug.

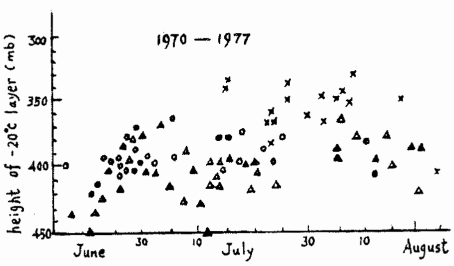

Fig.6. Correlation between damaged area and environmental height of -20°C layer.

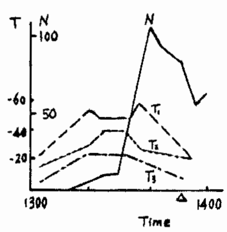

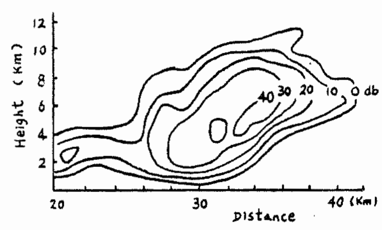

Left: Fig.7. The temperature of echo top, lightning frequency and hail fall as a function of time on Aug. 8, 1973.

Right: Fig.8. A strong convective cloud of obvious tilting in strong wind shear environment.

(1) Hailcloud of strong cell

The hailcloud, basically, is characterized by a great cell with an extending "overhang echo", below which is a "weak echo region" formed by strong updraft; near closely to main body of echo is almost vetical "echo wall"[1,5], when it is in vigorous stage. It always consists of a pair framework which formed by updraft and downdraft each other stand facing and shear, and maintains its quasisteady structure for long time, so that severe hail damage may occur .

(2) Hailcloud of weak cell

It consists of a main cell which controls the development of cloud with column shape more likely. Since weak cell always appears and decays in local area, it is correlated obviously with local thermodynamical and topographic behavior. It moves slow, hailstones fall in short time, therefore hail damage occured lightly in small area. Also the cloud is small scale in short lifetime.

(3) Propagational hailcloud

It consists of more than two cells which each one often undergoes emerging, leap increase, brew, hail fall and decay etc. New cell appears in front of hail cloud in motion. Whereas old cell decays in rear of it. Every cells are highly corrected to each other and in different developing stages at a moment. The cloud travels by propagational mode. Since its propagational feature is related to inducement of systematic updraft, it usually occures severely for long time.

(4) Hailcloud of multi cell

It consists of several small cells which exsist altogether and each one changes independently without propagational feather. Small hailstones probably fall to the ground from at least one of them with weak damage and short time.

Our research works at hail clouds over Xiyang indicate[15,19] that most of them are multi cell (about 47.6 %), next to it is weak cell (about 33.3 %) and then strong cell and propagational hail clouds (12.0 % and 7.1 %, respectively). It is inappropriate that only the later two categories in classifying was paid attention at present, but multi cell and weak cell which occur more frequently. We can see from our studies that though hail clouds of strong cell occurred lower frequent (only 12 %), but lead to the severest damage (over 80 %), their damage is ten -times as more as weak cell or multi cells once. As far as mean time of a hail fall process, strong cell and propagational hail cloud always continue for long time, especially strong cell damage most heavily.

The classification research on hailcloud shows that, to suppress hail damage on purpose, we must engage in classification research on hail clouds, no matter cloud seeding[1-3] or explosion method of cloud modification[1,7] are applied, and develop different means of hail suppression, we can resolve question usefully, otherwise the effects of hail suppression are limited.

References

1. Wang Ang-sheng and Huang Mei-yun; 1978: A review of the researches on hail and hail suppression. Scientia Atmospherica Sinica. Vol.2, NO.1, 76-84. China.
2. G.B.Foote and C.A.Knight; 1977: Hail: A review of hail science and hail suppression. Met. Monog. NO.38, AMS.
3. G.K.Sulakvelidze; 1967: Rainstorms and hail. Gidrometeoizdat. Leningrad, USSR.
4. A.J.Chisholm and M.English; 1973: Alberta hailstorms. Met. Monog. NO.36. AMS.
5. Staffmenbers and Participants NHRE; 1975: 9th Conf. on Severe Local Storm. 436-443.
6. M.T.Abshaev et al; 1973: Proc. of the WMO/ IAMAP Sci. Conf. on Wea. Modif. WMO. NO.399, 343-351.
7. Huang Mei-yun, Wang Ang-sheng et al; Write. Base of hail suppression. Scientific Press (send to the press). Beijing, China.
8. W.N.Hess; 1974: Weather and Climate Modification. A Wiley-interscience Publication.
9. D.Atlas; 1976: The present and future of hail suppression. WMO. NO.443, 207-216.
10. I.L.Burtsev; 1976: Hail Suppression. WMO Sci. Conf. on Wea. Modif. WMO. NO.443, 217-222.
11. Wang Ang-sheng and Huang Mei-yun; 1975: Hail and hail suppression. Physics. Vol.4, NO.1, 14-20. China.
12. Wang Ang-sheng et al; 1976: Lightning observation of the identification of hailcloud and thundercloud in hail suppression. Science Bulletin. NO.12, 546-549. China.
13. Wang Ang-sheng et al; 1980: Some characteristics of formative processes of hailcloud in Xiyang. Sci. Atmos. Sini. Vol.4, NO.2.
14. J.P.Chalon et al; 1976: Structure of an evolving hailstorm. Mon. Wea. Rev. Vol.104, 564-575.
15. Wang Ang-sheng et al; 1980: Some researches on hailcloud physics and hail suppression. Acta Meteorologica Sinica. Vol.38, NO.1, 78-86.
16. H.H.Medaliev et al; 1976: Atmosphric Electricity. 107-114. Gidrometeoizdat. L. USSR.
17. Wang Ang-sheng et al; 1980: The research on "brew" stage of hailcloud. Sci. Atmos. Sini. (in press).
18. G.K.Sulakvelidze et al; 1969: Trudi VGI NO.13.
19. Wang Ang-sheng et al; 1978: The research on hailcloud physics in Xiyang. The National Conf. on Wea. Modif. Nanning, China.
20. Wang Ang-sheng et al; An observation and analysis of finger echo. Sci. Atmos. Sini. (in press).
21. Xia Yu-ren, Wang Ang-sheng et al; 1980: Lightning characteristics of cumulonibus and application in hail suppression research. The 3rd W.M.O.Sci. Conf. on Wea. modif. France.
22. J.D.Marwitz; 1972: The structure and motion of severe hailstorm. J. Appl. Met. Vol.11, NO.1, 166-201.

<u>SESSION IV</u> : INTERACTIONS ENTRE ECHELLES

Scale Interactions

IV.1 - Interaction "Nuage-Environnement"

"Cloud-Environment" Interaction

ON COMPUTING AVERAGE CLOUD-WATER QUANTITIES IN A PARTIALLY-CLOUDY REGION

R. Banta and W.R. Cotton

Colorado State University
Fort Collins, USA

In numerical cloud models condensation is traditionally assumed to occur when the specific humidity of water, averaged over some region or volume, exceeds its mean saturation value. The mean saturation specific humidity is determined from temperature and pressure values that are also averaged over the region of concern. [The "averaging region" has normally been interpreted as a grid-volume average; see Cotton et al. (1978).] Thus within a volume, no "parcel" may become saturated until the moisture averaged over all parcels in the volume indicates saturation. At that time, however, all parcels within the region are assumed to become immediately saturated. This means first of all that initial condensation within a region is delayed until the entire region is saturated, and secondly, that a relatively large amount of latent heat is added impulsively to the model when this occurs. These produce unrealistic dynamic consequences in the model, as Sommeria and Deardorff (1977) have described.

As an alternative to these traditional "all or nothing" condensation schemes, several authors have proposed "partial" or "subgrid condensation schemes", which allow cloud-water quantities to be computed as though the region were partly-cloudy (Fig. 1). These schemes are formulated by assuming a probability distribution for (or a relationship between) certain temperature and moisture variables. Functions of the probability densities can then be integrated to obtain the cloud-water quantities of interest, namely the cloud fraction, the mean cloud-water specific humidity, and the cloud-water variance.

For three of the proposed partial-condensation schemes, the assumed temperature-moisture relationships are as follows: Manton and Cotton (1976, 1977, referred to hereafter as MC) assumed a normal distribution for the quantity q_t-q_s, where q_t is the total-water specific humidity and q_s is the saturation specific humidity. Sommeria and Deardorff (1977, referred to as SD) and Mellor (1977) assumed a bivariate normal distribution between q_t and the liquid-water potential temperature, θ_L. Finally, Oliver, et al. (1978) assumed that a volume is partly cloudy when the mean value $\overline{q}_t-\overline{q}_s$ lies within a "transition regime" defined in terms of the variances $\overline{q_t''^2}$ and $\overline{q_s''^2}$. Banta (1979) presented some preliminary analyses of aircraft data taken in clear air which tended to support MC's physical hypothesis over that of SD.

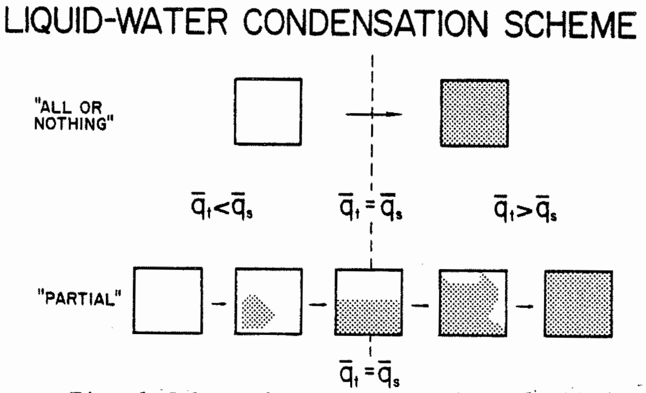

Fig. 1 Schematic representation of cloudiness for traditional condensation scheme (top) and partial condensation scheme (bottom) with moisture increasing from left to right.

The present paper discusses the partial-condensation scheme of MC. Their equations for the normal probability density, p(x), the cloud fraction h, the mean cloud water $\overline{q}_c$, and the cloud-water variance $\overline{q_c''^2}$ are given in Table Ia. Obviously these expressions, involving exponentials, are computationally expensive to evaluate, especially since their solution involves iteration. It is desirable, therefore, to find simpler expressions. This was done by assuming a simpler probability density for q_t-q_s, then integrating to find the other cloud-water variables. Banta (1979) proposed a parabolic approximation; these equations are presented in Table Ib. Assuming a uniform distribution results in an even simpler set of expressions, as shown in Table Ic.

The expressions for all three distributions are shown graphically in Fig. 2. Also shown are the corresponding functions for the traditional "all or nothing" condensation scheme. Note that in this case, the degenerate "probability density" has to be represented by a Dirac δ-function.

Also note that, unlike the functions of the normal probability density, which are valid for all values of $\overline{q}_t-\overline{q}_s$, the uniform and parabolic schemes divide the abscissa into three regimes: a regime of no cloudiness, a partly-cloudy regime, and a totally-cloudy regime. The width of these distributions is determined by a constant, c, and a parameter, σ_c, which is a computed quantity.

The cloud fraction for all three distributions is equal to 0.5 when $\overline{q}_t-\overline{q}_s = 0$. For the uniform and parabolic distributions the cloud fraction is zero for $\overline{q}_t-\overline{q}_s$ less than $-c\sigma_c$, and unity whenever $\overline{q}_t-\overline{q}_s$ is greater than $c\sigma_c$ --the half-width of the probability density. The mean cloud water given by the uniform and parabolic distributions is a good approximation to the

TABLE I

Expressions for Cloud-Water Quantities in the Partly-Cloudy Regime

$$\bar{x} = (\bar{q}_t - \bar{q}_s)/\sigma_c$$

a. NORMAL DISTRIBUTION

$$h = \tfrac{1}{2}\,(1 + \mathrm{erf}[\bar{x}]) \quad \text{where } \mathrm{erf}(z) = (2/\sqrt{\pi}) \int_0^z \exp(-u^2)\,du$$

$$\bar{q}_c/\sigma_c = \bar{x}h + \exp(-\bar{x}^2/2)/\sqrt{2\pi}$$

$$\overline{q_c''^2}/\sigma_c{}^2 = (\bar{x}^2 + 1)h + \bar{x}\,\exp(-\bar{x}^2/2)/\sqrt{2\pi} - \bar{q}_c{}^2/\sigma_c{}^2$$

b. PARABOLIC DISTRIBUTION, for $-\sqrt{5} < \bar{x} < +\sqrt{5}$

$$h = \tfrac{1}{2} + 3\bar{x}/4\sqrt{5} - \bar{x}^3/20\sqrt{5}$$

$$\bar{q}_c/\sigma_c = 3\sqrt{5}/16 + \bar{x}/2 + 3\bar{x}^2/8\sqrt{5} - \bar{x}^4/80\sqrt{5}$$

$$\overline{q_c''^2}/\sigma_c{}^2 = \tfrac{1}{2} + 3\sqrt{5}\,\bar{x}/8 + \bar{x}^2/2 + \bar{x}^3/4\sqrt{5} - \bar{x}^5/200\sqrt{5} - \bar{q}_c{}^2/\sigma_c{}^2$$

c. UNIFORM DISTRIBUTION, for $-\sqrt{3} < \bar{x} < +\sqrt{3}$

$$h = (\bar{x} + \sqrt{3})/2\sqrt{3} \qquad \bar{q}_c/\sigma_c = \sqrt{3}\,h^2 \qquad \overline{q_c''^2}/\sigma_c{}^2 = h^3(4-3h)$$

normal for the partly-cloudy regime, while for values of $\bar{q}_t - \bar{q}_s$ exceeding $c\sigma_c$ (ie., in the totally-cloudy regime), $\bar{q}_c$ is the same as the cloud water diagnosed by the "all or nothing" scheme. The cloud-water variance computed from the normal probability density approaches a value of $\sigma_c{}^2$ as $\bar{q}_t - \bar{q}_s$ gets large. In the case of the uniform and parabolic distributions, $\overline{q_c''^2}$ levels off at a value proportional to $\sigma_c{}^2$ as total cloudiness is approached. The proportionality factors, ν_1 and ν_2, however, are determined by the width of the distribution. Thus, if one requires that $\nu_1 = \nu_2 = 1$, one can calculate the numerical coefficient c in the half-width of the probability density expression. This is how the numerical coefficients in Table Ib and Ic were evaluated.

Fig. 2 shows the cloud-water-quantity functions in order of increasing mathematical complexity from bottom to top. The biggest jump between the simple "all or nothing" scheme at the bottom and MC's normal scheme at the top is between the "all or nothing" and the uniform schemes. The behavior of the cloud-water quantities for the uniform, parabolic, and normal equation sets are very similar. Thus, substituting the uniform scheme for MC's normal scheme

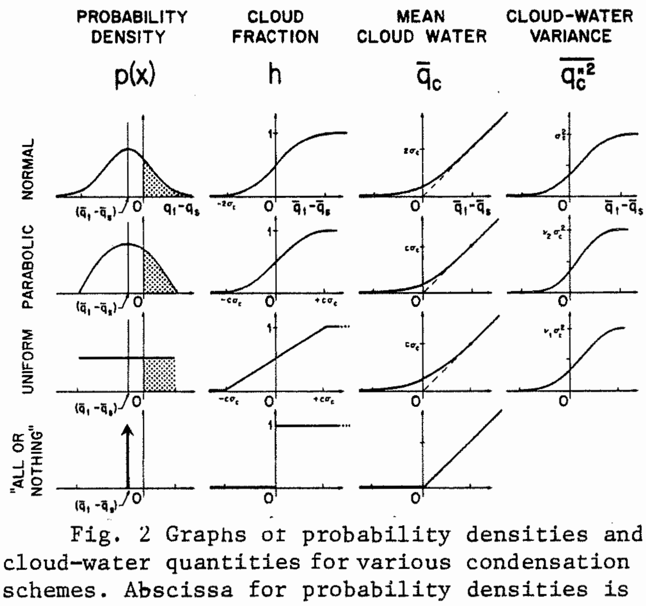

Fig. 2 Graphs of probability densities and cloud-water quantities for various condensation schemes. Abscissa for probability densities is the variable $q_t - q_s$, while for other cloud-water quantities, abscissa is the mean value $\bar{q}_t - \bar{q}_s$. Scale of the abscissa for each distribution is indicated on the graph of the cloud fraction, h.

should produce reasonable values of the cloud-water quantities at a substantial savings in computational expense.

Another advantage of the uniform scheme is that much of the mathematical complexity of solving the equations is reduced. MC's scheme results in a complicated, implicit relationship between the parameter σ_c and the cloud-fraction, h. The uniform scheme produces a fourth-order polynomial in h, which can be solved directly. Furthermore, if the cloud water variance can be reasonably approximated by a polynomial of lower order than fourth, then the uniform scheme yields a cubic equation - which has the advantage that it always has a real root.

As mentioned above, some observational evidence suggests that MC's physical assumption is more realistic than SD's. However, MC's scheme leads to a complex and implicit set of equations. Substituting a simpler probability density function for MC's assumed normal density reduces the mathematical complexity of MC's set, yet the simpler derived functions behave similarly to those from the normal.

The solutions to the various equation sets as a function of meteorological variables are currently being investigated. Additionally, a version of the uniform scheme is being incorporated into a numerical model of shallow cumulus cloud formation over complex topography.

Acknowledgments

The authors wish to thank Polly Cletcher for typing the manuscript, Lucy McCall for drafting the figures, and Duayne Barnhart for producing the photographic reductions. This research was sponsored by the U.S. National Science Foundation under Grant ATM-7908297.

References

Banta, R., 1979: Subgrid condensation in a cumulus cloud model. Preprint volume, Sixth Conf. on Probability and Statistics in Atmos. Sci., Banff, Alta., Can., 197-202. Boston: AMS.

Cotton, W.R., D.C. Hahn, and R. Banta, 1978: Air turbulence measurements in and below cumulus congestus over mountainous terrain. Preprints volume, Conf. on Cloud Physics and Atmos. Electricity, Issaquah, Wash., USA, 408-415. Boston: AMS.

Manton, M.J., and W.R. Cotton, 1976: A consistent set of approximate equations for moist deep convection in the atmosphere. Part II. Submitted to J. Atmos. Sci.

__________, and __________, 1977: Formulation of approximate equations for modeling moist deep convection on the mesoscale. Atmos. Sci. Paper No. 266, Dept. of Atmos. Sci., Colo. St. Univ., Ft. Collins, NSF Grant DES 7513310, 62 pp.

Mellor, G.L., 1977: The Gaussian cloud model relations. J. Atmos. Sci., 34, 356-358.

Oliver, D.A., W.S. Lewellen, and G.G. Williamson, 1978: The interaction between turbulent and radiative transport in the development of fog and low-level stratus. J. Atmos. Sci., 35, 301-316.

Sommeria, G., and J.W. Deardorff, 1977: Subgrid condensation in models of nonprecipitating clouds. J. Atmos. Sci., 34, 344-355.

TWO CASE STUDIES OF THE EFFECT OF ENTRAINMENT UPON THE MICROPHYSICAL STRUCTURE OF CLOUDS AT GREAT DUN FELL

A M Blyth, D J Carruthers, T W Choularton, M J Gay, J Latham, C S Mill, M H Smith and I M Stromberg

Physics Department, UMIST, Manchester

S J Caughey and B J Conway

Meteorological Office, Bracknell
ENGLAND

INTRODUCTION

This paper describes two case studies designed principally to examine the influence of entrainment upon the droplet spectra within natural clouds. The experiments were performed on Great Dun Fell, a high point of 847m on a long ridge running north-west to south-east in Cumbria, England. Measurements in cloud were made a few metres above ground level. At the summit of the hill drop spectral data were obtained using a Keily Probe (KP)(Corbin et al 1978) and a PMS Axially Scattering Spectrometer Probe (ASSP)(Ryder 1976). In addition, occasional measurements of drop concentration and size distribution were made using a Laser Photography System. An acoustic sounder was employed to monitor cloud top height and observations of cloud condensation nucleus spectra (CCN) were made just below cloud base using a modified Mee CCN counter. Profiles of wind speed, direction and temperature were made at approximately 2m above the local surface from just below cloud base to the mountain top. When the ASSP and KP were operated together reasonable agreement was found in the spectral properties and also in total drop concentration. These drop concentrations were supported by holographic measurements.

A microphysical model of the cloud has been developed in which droplets are grown on a CCN spectrum deduced from the measurements of the Mee counter in updraughts estimated from the observed wind profile. The predicted spectral properties of the adiabatic cloud have been compared with spectra measured at the mountain top. The model has also been used to estimate crudely the effects of dry air entrainment into the cloud for case study I. In addition the eddy diffusion equation has been solved to estimate the effect of depletion of the cloud by loss to ground. The results suggest that with U_*=1m s-1 and for clouds of vertical depth $\lesssim$200m depletion may be significant. Hence absolute values of drop concentration and liquid water content must be treated with some caution; subadiabatic liquid water contents may not be due to entrainment alone.

CASE I: 14 May 1979

The cap cloud formed in a weakly convective boundary layer capped by a strong subsidence inversion, which was generally at around 600m over lowland areas but was forced to rise in the vicinity of the hill, and was observed by the acoustic sounder to be between 50 and 100m above the mountain top. The 10m wind at the summit was from 210^o with a speed of ~10m s^{-1}. The CCN distribution was much more maritime than in Case II. Curve P of Figure 1 shows the percentage of 3-second drop counts which satisfy the conditions

$$N > \overline{N} + 2\sqrt{\overline{N}} \quad \text{or} \quad N < N - 2\sqrt{\overline{N}} \qquad (1)$$

where $\overline{N}$ is the fifteen minute average of drop concentration. Although the mean liquid water content was substantially subadiabatic, especially early in the period (Fig.2) the regions of highest drop count had liquid water contents which approached the adiabatic value and drop concentrations similar to those predicted by the model. Further, the droplet spectrum observed for these regions agrees well with the calculated adiabatic spectrum, especially early in the day (Fig.3). The spectra in the high and low drop concentration regions (defined by (1)) are shown in Fig.4. The shape of these spectra, taken with the proximity of the dry air source, suggests that the inhomogeneities in the cloud were produced by dry air entrainment and this is supported by the acoustic sounder traces.

In order to investigate the effect of this entrainment the model was used in calculations of the evaporation of the high count spectrum in two different ways until its liquid water content equalled that of the low count spectrum. The first was classical homogeneous evaporation and the second was a mixture of classical and extreme inhomogeneous evaporation (Baker & Latham, 1979)
1) Air was entrained into the cloud such that all droplets were subject to an initial undersaturation of 20%. The result is shown in Curve C, Figure 4.
2) Initially the entrained air totally evaporated an equal fraction of drops from all size categories. The evaporation of the remaining drops then proceeded as in (1). The length of the first stage was adjusted so that the final drop concentration was approximately equal to that in the low count spectrum. The result is shown in

curve D, Figure 4.

Curve C shows good agreement for radii greater than 8μm but seriously overestimates the number of small drops Curve D gives better overall agreement but underestimates the number of drops around the spectral peak of 8μm suggesting that too many drops of around this size have been removed. This tends to suggest a process closer to that of method 2 but in which a higher fraction of smaller drops suffered total evaporation.

Examination of curve P, Fig.1, shows that there is a mixing maximum around 11.00 after which a continual decrease occurs until near the end of the period. Despite this the form of the mixing remains as described above. The inhomogeneity at the end of the period was due to patchy cloud as the base rose above the mountain top.

The large rise in drop concentration towards the end of the period was partly reproduced by the model due to higher updraught speeds near cloud base as this moved up the hill, producing higher peak supersaturations and so activating more drops. However, the narrowing of the spectrum was greater than predicted and this suggests a change to a more continental CCN. Measurements with the Mee device were unavailable to test this possibility.

CASE II: 15 May 1979

The day was characterized by light SW winds, (less than 4m s^{-1} at the mountain top). A general cover of stratus and stratocumulus cloud enveloped the mountain. There was a weak subsidence inversion (much weaker than in case I) about 150m above the mountain top.

During the period up to 14.30 the adiabatic liquid water content fell as cloud base rose (Fig.5). Initially a rise in the observed liquid water content and drop concentrations also occurred. These were associated with increasing convective activity and were presumably due to upward transport of moisture and CCN in the boundary layer. After 12.00 the acoustic sounder showed entrainment into the cloud through the capping inversion on scales of several tens of metres (Fig.7). A large fall in mean drop count occurred as the cloud became very inhomogeneous (Fig.6) but the peak drop concentrations observed in the patches of thickest cloud remained unchanged until about 13.10. During this time the high and low count spectra became very similar in shape, (Fig.8), suggesting that the mixing was extremely inhomogeneous (Baker & Latham). At the same time the observed spectrum became appreciably broader (Fig.9). However, it was no broader than the adiabatic spectrum calculated for the same time using CCN measurements made at 11.40.

During the remainder of the experiment cloud base remained near the mountain top. The curve of the number of histograms outside the $2/\sqrt{N}$ criterion shows a marked lull in mixing around 16.10 BST (confirmed by the acoustic sounder) and this is a period with a narrower spectrum (Fig.9).

DISCUSSION

The microphysical data suggests than in case II the mixing is extremely inhomogeneous whereas in case I the mixing is of a form intermediate between the classical homogeneous and extreme inhomogeneous descriptions. For extreme inhomogeneous mixing the ratio of the time constants for eddy dissipation and droplet evaporation

$$\tau_\epsilon/\tau_d \to \infty.$$

The larger entrainment scales and lower windspeeds for case II suggest that the ratio is significantly higher than for case I.

In case II the highest concentrations of large drops tend to be associated with periods of greatest mixing. Due to the complex nature of the cloud dynamics and evolution in this study it is not possible to say whether this confirms the predictions made by Baker & Latham of enhanced growth rates of the largest drops resulting from inhomogeneous mixing.

REFERENCES

Blyth A M, Choularton T W, Carruthers D J Fullarton G, Gay M J, Latham J, Mill C S Smith M H & Stromberg I M 1980 Three case studies of the effect of entrainment upon the microphysical structure of clouds at Great Dun Fell. (submitted Quart.J.Roy.Met.Soc.)

Baker M B & Latham J 1979 The evolution of droplet spectra and the rate of production of embryonic raindrops in small cumulus clouds. (in press, J. Atmos.Sci.)

Corbin R G, Latham J, Mill C S and Stromberg I M 1978 An assessment of the Keily probe for the ground-based measurement of drop size distribution in clouds. Quart.J.Roy.Met.Soc., 104, 729-736

Ryder P 1976 The measurement of cloud droplet spectra. Int. Conf.Cloud Phys., Boulder, Colorado. 576-580

ACKNOWLEDGEMENTS The research described herein was supported by the Natural Environment Research Council and the European Research Office.

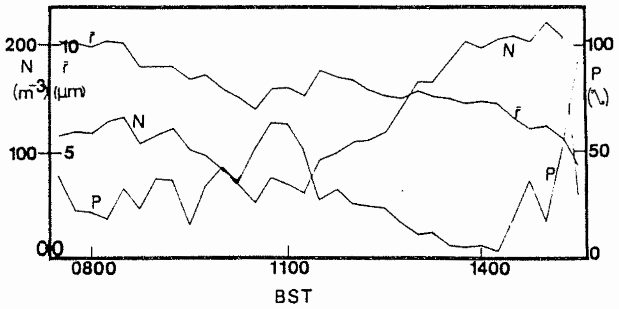

Figure 1. Drop concentration N, percentage P of histograms outside $\overline{N} \pm 2\sqrt{\overline{N}}$ and mean radius $\overline{r}$ during the period covered by case I.

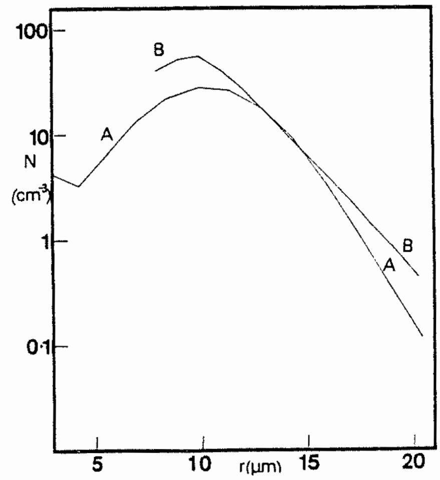

Figure 3. Case I. A, measured size distribution for the period 0830 to 0845 BST, $\overline{N}=132cm^{-3}$; B, calculated adiabatic spectrum $N = 212cm^{-3}$.

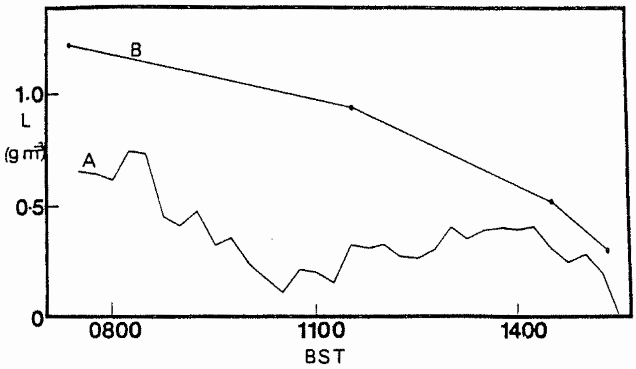

Figure 2. Observed (A) and calculated adiabatic (B) liquid water contents L during period covered by case I.

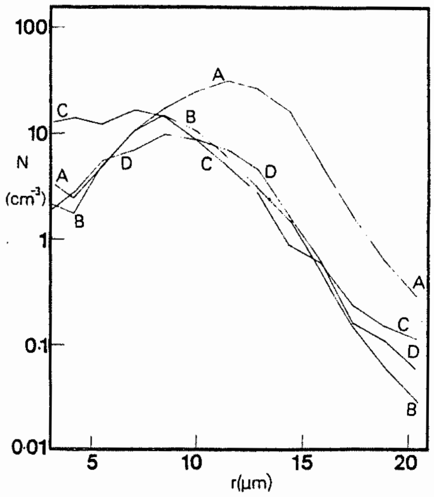

Figure 4. Case I. Size distributions.
A, observed high count spectrum;
B, observed low count spectrum;
C, calculated, method (1);
D, calculated, method (2).

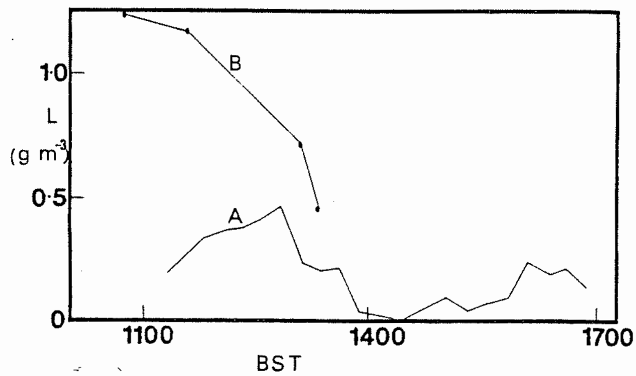

Figure 5. Observed (A) and calculated (B) liquid water contents during the period covered by case II.

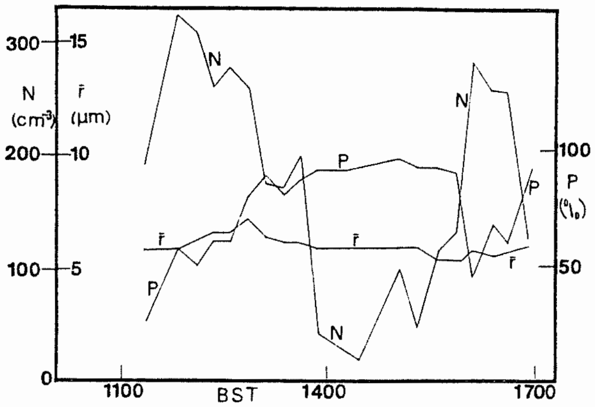

Figure 6. Drop concentration N, percentage P of histograms outside $\bar{N}\pm2\sqrt{\bar{N}}$ and mean radius $\bar{r}$ during the period covered by case II

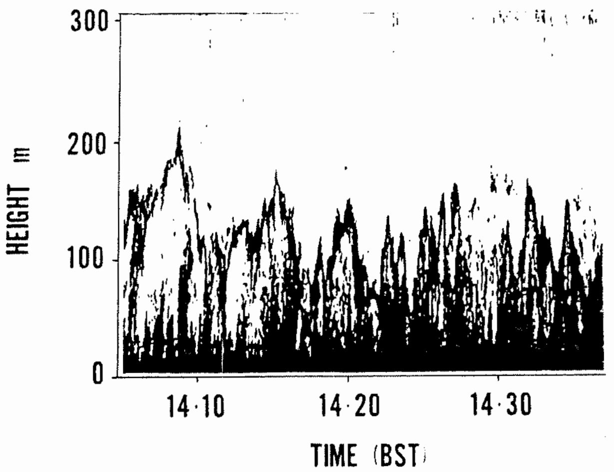

Figure 7. Case II. Acoustic sounder trace.

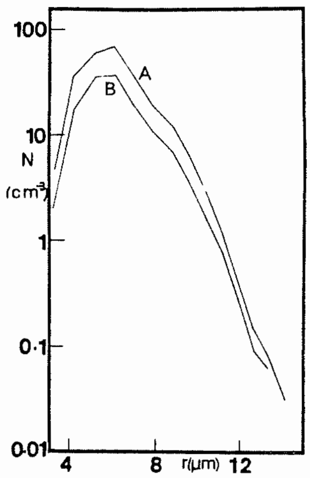

Figure 8. Case II. Measured size distributions for the period 1336-1351 BST. A, high count spectrum; B, low count spectrum.

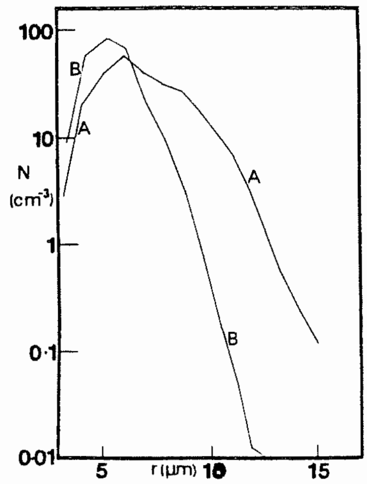

Figure 9. Case II. A, measured size distributions for the period 1251-1306 BST. $\bar{N}$=258cm^{-3}, $\bar{L}$=0.47gm^{-3}; B, measured size distribution for the period 1622-1637 BST. $\bar{N}$-256cm^{-3}, $\bar{L}$=0.20gm^{-3}

ENTRAINMENT OF ENVIRONMENTAL AIR BY CUMULUS CLOUDS

by

Joey F. Boatman and August H. Auer, Jr.

University of Wyoming, Department of Atmospheric Science
P.O. Box 3038, University Station, Laramie, Wyoming 82071 U.S.A.

I. Introduction

Entrainment of environmental air into cumulus clouds has been treated theoretically by Stommel (1947, 1951), Scorer and Ludlam (1953), Morton (1957), Levine (1959) and Townsend (1966). Alternatively, Squires (1958) has envisioned the mixing of environmental air into cumuli as a process whereby a parcel of dry air becomes immersed in the cloud top with subsequent mixing to produce a penetrative downdraft. Telford (1975) has proposed a mechanism whereby parcels of environmental air are entrained by cumulus clouds at their top. Recently, Paluch (1979) used temperature and liquid water content data collected within Colorado cumulus congestus clouds to conclude that the penetrative downdraft mechanism of Squires (1958) was most plausible in explaining the observed cloud behaviour.

To test the theories proposed, our work utilized measured cloudy and clear air properties in cumulus congestus clouds to determine where the entrained air within them originated.

The data were collected using the University of Wyomings'' King Air research aircraft and by rawinsondes during the summer, 1978 HIgh PLains EXperiment (HIPLEX) in Kansas and Montana. The King Air instrumentation, data acquisition and quality are discussed by Cooper (1977).

II. Entrainment Thermodynamics

The thermodynamics for the entrainment process in Cumuli have been concisely formulated by Dufour (1956) with essential assumptions as follows:

1) the cloud is initially composed of saturated air and liquid water;

2) the surrounding environmental air is composed of humid non-saturated air;

3) the mixed parcels of environmental and cloudy air form a closed system; and

4) the transformations within the closed systems are reversible and adiabatic.

Assumption 1) precludes the existence of ice within the model clouds. Assumptions 3) and 4) exclude precipitation size drops within the cloud since such drops could add or remove mass and sensible heat from the closed cloud-entrained air system.

With these assumptions the adiabatic temperature and liquid water content at any pressure level within an initially undilute model cloud are given by:

$$(c_{pd}+(r_w+r_v)c)\ln T - R_d\ln P_d + r_v\frac{Lv}{T} = \text{constant}$$

(Iribarne and Godsen, 1973) (1)

where,

r_w = liquid water mixing ratio within cloud
c_w = specific heat capacity of liquid water
L_v = latent heat of vaporization. $L_v = 597.3(\frac{273.15}{T})^{\gamma}, \gamma = 0.667 + 3.67 \times 10^{-4}T$ from Pruppacher and Klett (1978);
and the remaining terms have their common usage.

The constant in eqn. 1) is determined by fixing a cloud base pressure and temperature.

The mixing of different portions of environmental air into the initially undilute cloud at any pressure level will serve to dilute the adiabatic temperature (T) and liquid water content (r_w). This process was accomplished in the following way. A hypothetical entrainment parcel outside the model cloud with pressure, temperature and vapor mixing ratio P', T' and r', respectively, was chosen. The entrainment parcel was then moved reversibly and adiabatically to a sampling level P. In this process the vapor mixing ratio of the entrainment parcel remained constant while the parcel temperature changed according to the Poisson relation.

$$T_p' = T'\left(\frac{P}{P'}\right)^{\alpha}, \quad \alpha = \frac{R_d}{C_{pd}} \quad (2)$$

The entrainment parcel was then proportionately mixed with undilute cloud air at the sampling level P. The result was:

$$\overline{T} = \left(\frac{T + kT_p'}{1 + k}\right) \quad (3)$$

$$\overline{q} = \left[\frac{r_v + r_w}{1 + r_v + r_w} + K\frac{r'}{1 + r'}\right] / (1 + k) \quad (4)$$

where k is a non-dimensional mixing constant. If k = 0 no mixing of environmental air is allowed. If k = ∞ replacement of the model cloud by environmental air will occur.

Next, a reversible wet-bulb process was performed at constant pressure to evaporate any excess liquid water in the following way:

$$T_{wb} = \overline{T} + \left(\frac{L_v}{C_{pd}}\right)\left(\frac{\overline{q}}{1 - \overline{q}} - r_v(T_{wb})\right) \quad (5)$$

where;

T_{wb} = the wet bulb temperature; and
$r_v(T_{wb})$ = the saturation vapor mixing ratio at the wet bulb temperature.

The wet bulb temperature (T_{wb}) and vapor mixing ratio ($r_v(T_{wb})$) at the sampling pressure were found by iteration.

The amount of liquid water remaining in the entrained parcel may be found by recalling that the amount of liquid water plus vapor in the parcel must be conserved. This gives:

$$\frac{\bar{q}}{1-\bar{q}} + \frac{r_w}{1+k} = r_t = r_v(T_{wb}) + r_f \qquad (6)$$

where,

r_t = the sum of vapor and liquid water mixing ratio at pressure P, first before then after the wet bulb process; and
r_f = the final liquid water mixing ratio after completion of the wet bulb process at pressure P.

This yields:

$$r_f = \frac{\bar{q}}{1-\bar{q}} + \frac{r_w}{1+k} - r_v(T_{wb}) \qquad (7)$$

The effect on temperature and liquid water content at any sampling level due to entrainment of portions of environmental air from some other level may now be predicted.

III. Downdraft Generation

When subsaturated environmental air is entrained into cumuli it will be evaporatively cooled. This process may leave the initially neutrally buoyant entrained air parcel negatively buoyant relative to air outside the cloud.

The same assumptions used in formulating the entrainment model discussed above were again employed in exploring the generation of penetrative downdrafts in cumuli. In addition the environment was assumed quiescent so that dynamically induced vertical motions were not allowed. Initially, a fixed rate of mixing, α, between cloud and any previously entrained parcel was assumed.

With these stipulations, a reversible adiabatic mixing between the cloud and environment at initial pressure level P' was performed. The mixed parcel was then allowed to move to a new pressure level in density equilibrium with its new temperature and liquid water content. This pressure level was determined from the following equation given by Squires (1958).

$$\frac{dW}{dt} = \left[\frac{\bar{T}_v - T_v'}{T_v'} - r_f\right]g + \alpha(W) \qquad (8)$$

where,

$\bar{T}_v$ = virtual temperature of the entrained parcel after mixing at pressure P'
T_v' = virtual temperature in the environment at pressure P'

The remaining symbols have their common uses.

Using the hydrostatic equation the new pressure of the mixed parcel after any given time was found.

Employing a second by second integration of eqn. (9) with additional mixing between the entrained air and the undilute cloud at each new pressure level the vertical velocity and pressure of the entrained parcel were calculated for a 20 minute period.

IV. Case Study Results

Using the University of Wyoming King Air research aircraft, temperature liquid water content and vertical motion data were gathered in and near 16 large cumulus clouds.

On May 21, 1978 the atmosphere was characterized as convectively unstable, moist near the surface and dry aloft above Goodland, Kansas. Cumulus clouds with bases at 750 mb and a temperature of 10 C formed about 2100 Coordinated Universal Time (CUT; Coordinated Universal Time will be used throughout this work) and grew rapidly. The King Air research aircraft was used to study these clouds beginning about 2230.

Figure 1 depicts the pressure at the visual cloud top versus time for the first cloud studied on this day. The times and pressure level of each cloud penetration are also shown.

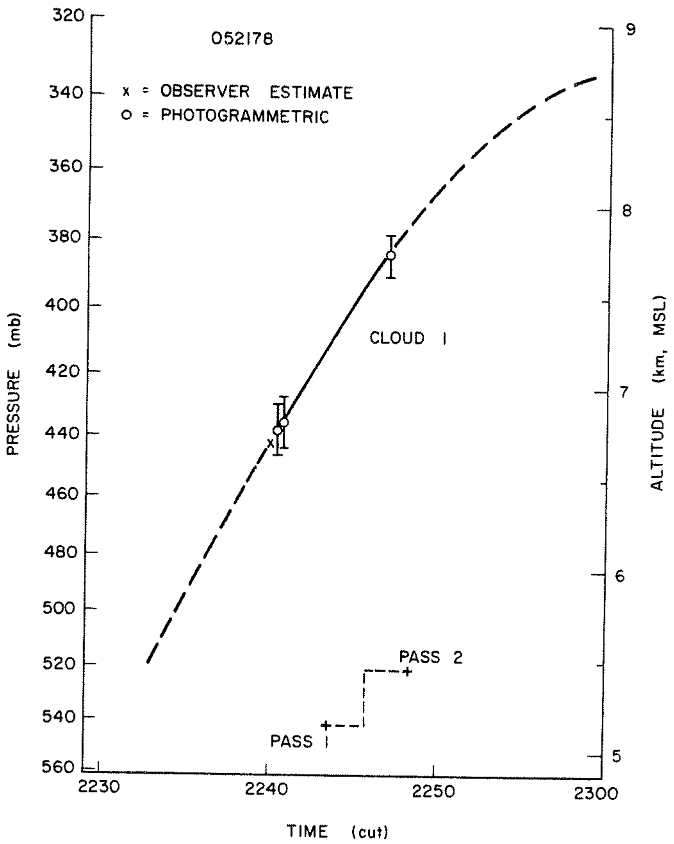

Figure 1. The visual cloud top observed on May 21, 1978.

The visual cloud top was measured photogrammetrically from the aircraft and these measurements supplemented by observer estimates when possible. An estimate of the error associated with each photographic measurement is also shown and is based on the physics of the simple photogrammetric technique used.

Figure 2 is a plot of liquid water content versus temperature. Thin lines represent the predicted depletion of cloud liquid water and temperature from the adiabatic values as the model cloud ingests increasingly large amounts of dry environmental air. Each thin line depicts the depletion process due to ingestion of environmental air from a different pressure level.

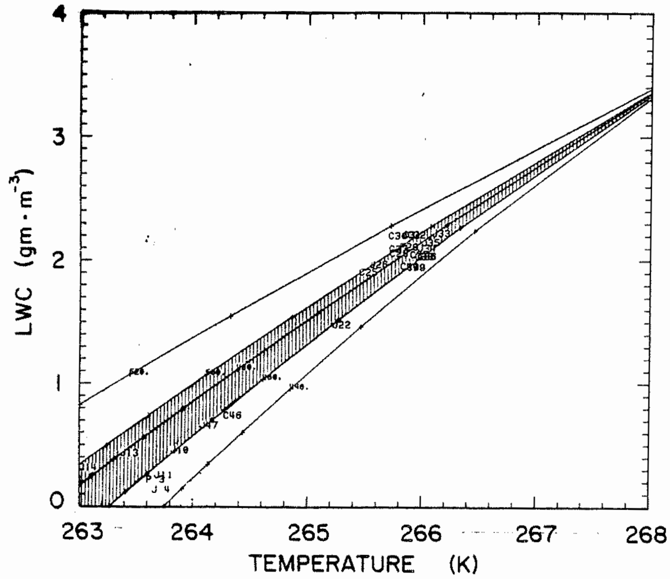

Figure 2. Liquid water content vs. temperature. Thin lines are modelled depletions due to entrainment from different pressures. Data points are cloud observations.

Also plotted on this figure are the observed cloud liquid water content and temperature during each second of the cloud penetration ast 525 mb. The liquid water content measurements were made with a Johnson-Williams device considered accurate within ±20%. The temperature measurements were made using a reverse flow sensor precise with ±0.2 C. Numbers associated with each data point refer to sampling time in seconds after entrance into the cloud. Letters associated with each data point refer to the following:

J - normal data point, no ice present;
C - Knollenberg probe detected small ice particles (50-600 μm) in concentrations greater than zero in this cloud volume;
P - Knollenberg probe detected large ice particles (800-2000 μm) in concentrations greater than zero in this cloud volume.

It is seen in Figure 2 that the majority of the data points fall within the range 460-500 mb. Thus, the model predicts that entrained air in this portion of cloud originated between 460-500 mb at some earlier time.

Figure 3 is a plot of pressure versus time. Thin lines represent the modelled time history of entrained air parcels originating at different pressure levels. Parcels entrained between 460-500 mb are seen to descend through the model cloud driven by evaporative cooling to the sampling level in 4.6 - 8.3 minutes.

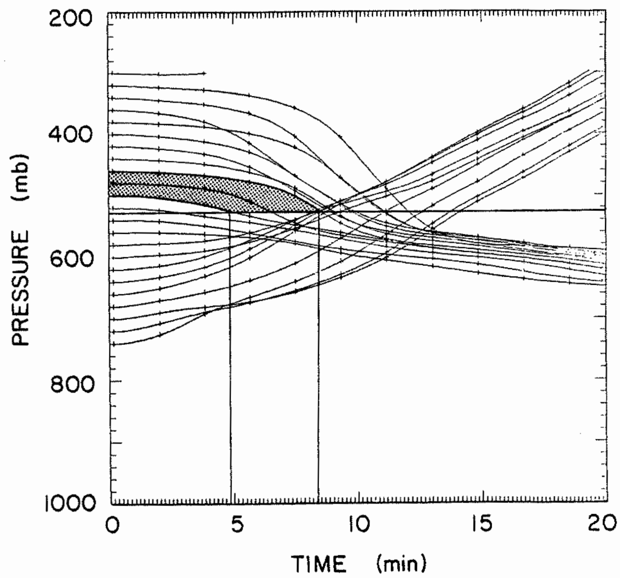

Figure 3. Modelled time for parcels entrained between 460-500 mb to reach 525 mb.

Using Figure 1 to project backward in time 4.8 - 8.3 minutes from the time of penetration two it is seen that the visual cloud top was between 420-450 mb during those times. In this case the model predicts that entrained air originating in the 460-500 mb range would have entered the observed cloud slightly below its visual top.

Figure 4 is a plot of pressure versus vertical wind. Thin lines represent the vertical velocity attained by air parcels entrained into the model cloud at different pressure levels as they descend through the cloud. Air entrained by the model cloud between 460-500 mb have a vertical velocity in the range -2.5 to -6.2 m/sec when it reaches 525 mb.

Figure 5 is a plot of observed vertical wind versus time during this cloud penetration. The observed downdraft has an average velocity of -2.6 m/sec and maximum of -5.8 m/sec. The prediction of -2.6 to -6.2 m/sec downdrafts presented in Figure 4 is in good agreement with the observed values.

In addition to the observations presented in detail an additional 25 useful cloud penetrations were made over a total of 5 days. A summary of these penetrations is presented in Table 1. In all cases the predicted entrainment region is seen to correspond well with the cloud top pressure at the time of entrainment. As well, the predicted and observed downdraft speeds are in agreement except in the May 23

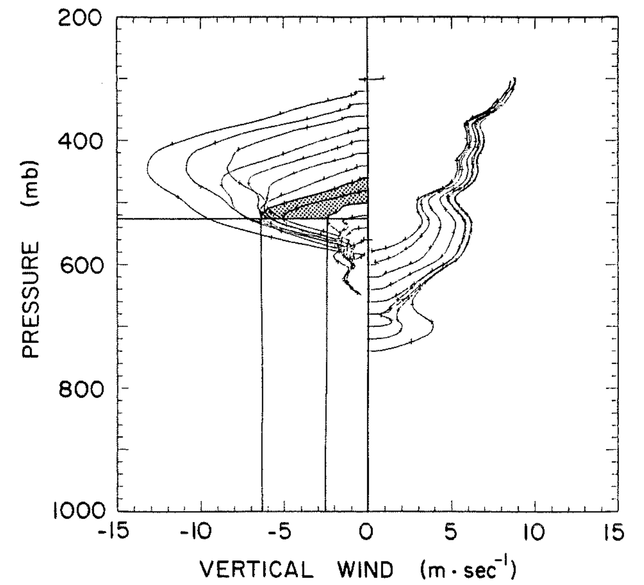

Figure 4. Modelled downdraft speed attained at 525 mb by sustained air originating between 460-500 mb.

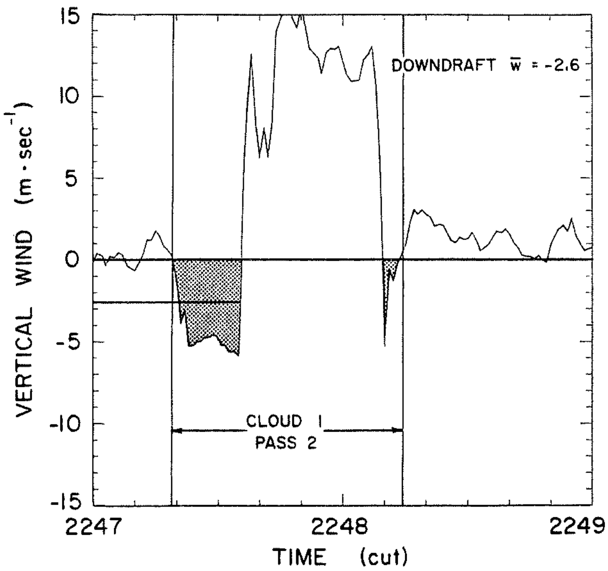

Figure 5. Observed vertical wind during passage through cloud 2 at 525 mb.

Table I. Cloud entrainment parameters Observed on 5 days during 1978

Date Cloud(Pass)	Pressure Level(mb)	Predicted Entrainment Region(mb)	Subsidence Time(min)	Cloud Top Pressure(mb)	Predicted Downdraft Speed(m/s)	Observed Downdraft Speed(m/s) Avg(Max)	Depletion of LWC by ice
05/21/79							
1(1)	543	480-520	5.3-7.3	460-490	1.4-4.4	2.1(4.5)	small
1(2)	525	460-500	4.8-8.3	420-450	2.5-6.2	2.6(5.8)	small
2(2)	508	460-500	3.7-7.7	465-500	1.5-5.6	1.5(6.6)	moderate
05/23/78							
1(2)	498	380-460	>20	———	0.3	2.1(7.0)	Large
1(3)	480	380-460	11.2-14.7	420-460	0.7	2.1(10.7)	Large
1(5)	463	360-400	10.7-13.0	380-390	2.2-2.9	1.9(8.1)	Large
5(1)	445	400-440	3.0-8.5	430	1.0-2.0	2.0(8.0)	Large
06/02/78							
4(1)	596	540-580	3.5-5.5	570-580	1.3-5.2	———	small
5(1)	574	540-580	0.0-4.5	540-560	0.0-3.9	———	small
5(2)	562	540-560	0.0-3.7	540-545	0.0-2.8	———	small
5(3)	598	540-560	4.0-5.5	540	4.2-5.1	———	moderate
06/15/78							
4(1)	458	270-320	12.2-13.3	———	2.0	———	small
4(2)	475	270-320	12.5-13.8	≈300	8.9-16.2	———	small
4(3)	500	250-320	13.0-14.3	≈300	5.7-13.3	———	moderate
4(4)	534	320-360	10.5-13.0	320-340	1.9-2.1	———	Large
4(5)	539	270-340	12.5-15.0	300-330	1.0-4.0	———	moderate
07/08/78							
5(2)	551	480-520	5.7-13.5	480	1.3-2.2	0	small
5(3)	588	500-540	8.3-11.5	490	1.9	0.8(3.2)	moderate
6(4)	585	500-540	7.8-11.0	500-530	1.9	1.1(2.2)	small
7(4)	585	480-520	9.8-13.0	470-500	1.9	0.5(1.8)	small
8(4)	589	480-540	8.3-13.5	470-510	1.9	0.1(1.0)	small
10(3)	550	460-480	8.8-9.3	≈470	2.1	1.1(2.2)	small
11(2)	550	480-500	6.8-8.7	———	2.1	0.1(0.5)	small
11(3)	583	500-520	9.5-11.0	≈520	1.9	0.4(1.2)	small
12(3)	510	460-480	4.5-5.5	460-470	2.2-5.0	1.5(4.0)	moderate
12(4)	551	460-480	8.8	450	1.9-2.1	1.1(2.1)	small

1978 case when ice concentrations were large. In this case ice loading of the downdrafts apparently added to the downdraft speed.

V. Discussion and Conclusions

Data from five different days of the 1978 HIPLEX season in Kansas and Montana have been examined. A thermodynamic model for the entrainment process was presented. By comparing the model predictions with the observed temperature and liquid water content during a cloud penetration a predicted entrainment region resulted. A model for penetrative downdraft formation via evaporative cooling was also used. It allowed estimation of the time necessary for air parcels from a predicted entrainment region to reach the sampling level and the downdraft speed attained by these parcels.

From an examination of the data it seems that 1) the predicted sources for entrained air were at or near the visual cloud top and 2) the predicted downdrafts produced by evaporative cooling agreed well with the downdrafts observed.

A possible consequence of this process is that the evaporation and cooling of cloud droplets near the entrainment region could produce contact or immersion freezing of these droplets via nuclei inactive at warmer temperatures.

ACKNOWLEDGMENTS

This research was sponsored by the U.S. Water and Power Resources Service, DAWRM, Department of the Interior, under contract 7-07-93-V0001.

REFERENCES

Cooper, W. A., 1977. Cloud Physics Investigations by the University of Wyoming in HIPLEX 1977. Report #AS119, Univ. of Wyo., Dept. of Atmos. Sci., Laramie, Wyo.

Dufour, L., 1956. Thermodynamical Study of the Entrainment of Air into a Cumulus. Tellus, VIII (2), p. 202-205.

Iribarne, J. V. and W. L. Godsen, 1973. Atmosperic Thermodynamics, Vol. 6, D. Reidel Publishing Co., Boston, Mass. 222 pp.

Levine, J., 1959. Spherical Vortex Theory of Bubble-like Motion in Cumulus Cloud., J. Meteor., Vol. 16, p. 653-662.

Morton, B. R., 1957. Buoyant Plumes in a Moist Atmosphere. J. Fluid Mech., 2, p. 127-144.

Paluch, I. R., 1979. The Entrainment Mechanism in Colorado Cumuli. J. Atmos. Sci., Vol. 36, p. 2467-2478.

Priestley, C.H.B., 1953. Buoyant Motion in a Turbulent Environment. Aust. J. Phys., Vol. 6, p. 279-290.

Prauppacher, H. R. and J. D. Klett, 1978. Microphysics of Clouds and Precipitation, D. Reidel Publishing Co., Boston, Mass., 714 pp.

Scorer, R. S., and F. H. Ludlam, 1953. Bubble Theory of Penetrative Convection. Quart. J. Roy. Meteor. Soc., Vol. 79, p. 94-103.

Squires, P., 1958. Penetrative Downdraughts in Cumuli. Tellus, Vol. 10, p. 381-389.

Stommel, H., 1947. Entrainment of Air into a Cumulus Cloud. J. Meteor., Vol. 4, p. 91-94.

_____, 1941. Entrainment of Air into a Cumulus Cloud II. J. Meteor., Vol. 8, p. 127-129.

Telford, J. W., 1975. Turbulence, Entrainment and Mixing in Cloud Dynamics. Pure Appl. Geophys., Vol. 113, p. 1067-1084.

Townsend, A. A., 1966. The Mechanism of Entrainment in Free Turbulent Flows. J. Fluid Mech., Vol. 26, No. 4, p. 689-715.

MODELISATION UNIDIMENSIONNELLE DE LA CONVECTION NUAGEUSE DANS LA CLP

Ph.Bougeault

Direction de la Météorologie
Boulogne FRANCE

I - INTRODUCTION

Plusieurs types de modèles numériques ont été proposés depuis quelques années pour la simulation de phénomènes dynamiques turbulents dans la couche limite planétaire (CLP), sous la seule restriction de l'homogénéité horizontale. Des modèles à points de grille résolvent explicitement les équations de la mécanique des fluides discrétisées sur une grille bidimensionnelle ou même tridimensionnelle (3D) (Deardorff, 1974). Des modèles unidimensionnels (1D) utilisent une discrétisation verticale et des équations d'évolution, dérivées des précédentes, pour les moments de variables fondamentales. Parmi les plus efficaces citons ceux de Wingaard et Coté (1974), Mellor et Yamada (1974), André et al. (1978). Les principaux succès concernent la simulation de couches convectives sèches et l'accent est porté maintenant sur l'enrichissement physique et la diversification de l'emploi de ces outils qui permettraient notament d'établir des paramétrisations de la CLP dans un plus grand nombre de situations réelles.

L'incorporation du cycle thermodynamique de l'eau dans les modèles, afin de prendre en compte le rôle dynamique des nuages, et ultérieurement leur rôle radiatif se fait sans difficulté conceptuelle, pour les modèles à points de grille (Sommeria, 1976), où l'on peut considérer que l'unité élémentaire saturée est une maille du modèle, ou même paramétrer la condensation à l'échelle inférieure à la maille (Sommeria et Deardorff, 1977) par une théorie statistique simple. Il faut toutefois inclure des mécanismes d'ajustement pour tenir compte des constantes de temps différentes de la condensation et de la dynamique, ce que l'on peut schématiser simplement en imposant à q la limite qs (T, p), où qs (T, p) est le contenu spécifique d'humidité saturante, calculé par une formule standart, négligant ainsi tous les phénomènes microphysiques. Des succès ont ainsi été obtenus dans la simulation de l'expérience Porto Rico (1972) du NCAR(*) (Sommeria et Le Mone 1978), qui reproduit assez fidèlement une couche convective marine surmontée d'une couche stable où se développent de petits cumulus des alizés.

Parallèlement, des modèles unidimensionnels ont été utilisés pour simuler des nuages bas stratiformes, mais il faut alors tenir compte d'une influence prépondérante des processus radiatifs et microphysiques. Récemment, des schémas de paramétrisations ont été proposés pour permettre à ces modèles de reproduire des nuages non stratiformes (Manton, 1978, Mellor, 1977) et une simulation de 4 journées de l'expérience BOMEX (Holland et Rasmusson, 1973) a été réalisée par Yamada et Mellor (1979). On propose ici une contribution dans cette direction.

(*) National Center for Atmospheric Research Boulder, Colorado

II - VARIABLES CONSERVATIVES ET SCHEMA DE PARAMETRISATION

Un modèle unidimensionnel de couche limite se présente traditionnellement sous la forme d'une hiérarchie d'équations pour les moments turbulents des variables fondamentales u, v, w, θ, q. La description d'une couche nuageuse impose les variables supplémentaires ql, contenu spécifique d'eau liquide et R (fraction condensée en volume pour chaque niveau). La rapidité relative des phénomènes de condensation conduit à traiter ces variables de manière diagnostique: on réalise ce filtrage en utilisant des variables conservatives

$$qw = q + ql, \quad \theta l = \theta - \frac{L}{C_p}\frac{\bar{\theta}}{\bar{T}}\, ql$$

On obtient des équations d'évolution simples (diffusion) pour θl et qw sous des hypothèses assez restrictives : - schéma de diffusion simple de la vapeur d'eau dans l'air,
- diffusion des gouttelettes négligée
- faibles variations du facteur L/C_p. La fermeture des équations nécessite alors d'exprimer les moments de la variable ql, qui intervient dans la température virtuelle

$$\theta_v = \theta_\ell + 0.61\, T_0\, q_w + \left\{\left(\frac{p_0}{p}\right)^{R/C_p}\frac{L}{C_p} - 1.61\, T_0\right\} q_\ell$$

C'est le problème de la paramétrisation de la condensation aux échelles non résolues. Une théorie générale simple a été développée par Mellor (1977) sur une idée de Sommeria et Deardorff (1977). En négligeant l'influence des fluctuations de pression sur qs, on obtient, par un développement au premier ordre qui utilise la formule de Clapeyron, R, ql, et tous ses moments, en fonction des moments des variables conservatives et de la distribution adimensionnée G(s) de la variable s, combinaison linéaire de qw et θl. Le problème est alors de trouver la distribution G(s) la plus simple qui permet de rendre compte correctement des phénomènes. La loi normale a été proposée par Sommeria Dearforff et utilisée par Yamada et Mellor pour la simulation de BOMEX, mais sans possibilité de contrôler la qualité des résultats. Il parait intéressant de tester sur des résultats la validité de cette hypothèse pour divers types de loi G(s). C'est de qui a été entrepris.

III - RESULTATS DE SIMULATION POUR G(s) NORMALE

Devant l'absence de données réelles, on est conduit à utiliser les résultats d'un modèle 3D (Sommeria, 76) pour tester ceux du modèle 1D. Une simulation de l'expérience Porto Rico a donc été réalisée. Le modèle 1D choisi est le modèle COLT de l'EERM, qui décrit l'évolution des moments des variables conservatives jusqu'à l'ordre 3. G(s) est la distribution normale. On compare le résultat des deux modèles dans les figures.

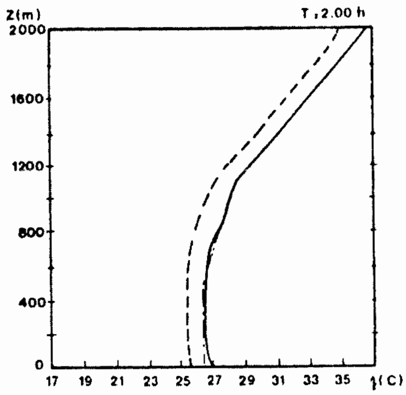

FIG. 1. — Profils comparés de $\overline{\theta_l}$. Le décalage provient d'une définition différente de la pression de référence. Pour toutes les figures, trait continu : modèle 1-D ; trait interrompu : modèle 3-D ; trait mixte : conditions initiales.

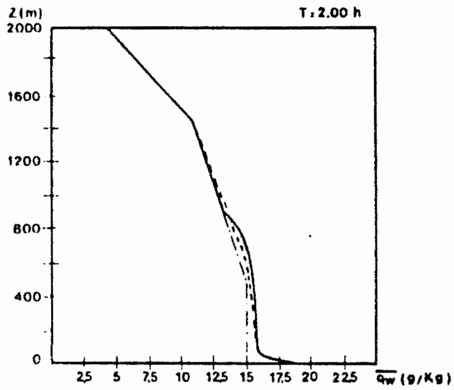

FIG. 2. — Profils comparés de $\overline{q_w}$.

Ces profils moyens initiaux font apparaitre trois couches superposées (fig. 1 et 2). Une couche mélangée, une couche légèrement stable qui devient nuageuse, une couche stable supérieure. Les flux inférieurs sont obtenus par des relations flux-gradients, la valeur des paramètres moyens étant fixée au niveau de la mer. Le reste de l'information est reconstitué par les modèles. Pendant 3 heures de simulation (durée totale disponible pour le modèle 3D) les ordres de grandeur des résultats sont comparables.

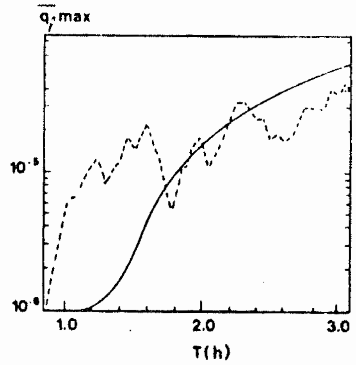

FIG. 3. — Evolution du contenu maximal d'eau liquide de 1 à 3 heures de simulation.

La figure 3 montre que le développement nuageux est retardé puis surestimé par le modèle 1D. Deux explications sont proposées :

1) Inadéquation de la distribution Gaussienne, qui représente mal l'asymétrie et l'élargissement liés aux excursions nuageuses (particulièrement au voisinage de la 2è inversion). Il conviendrait donc d'employer des distributions comportant plus d'élargissement ou même incluant l'asymétrie, ce qui alourdirait le schéma de paramétrisation.

2) Mauvaise représentation de la couche stable : En effet, la plupart des modèles 1D ne représentent pas le transport d'énergie dû aux presso-corrélations c'est-à-dire aux ondes internes libres. La couche stable se comporte alors comme une zone de blocage et la vapeur d'eau s'accumule sous l'inversion, ce qui conduit à un contenu nuageux trop important.

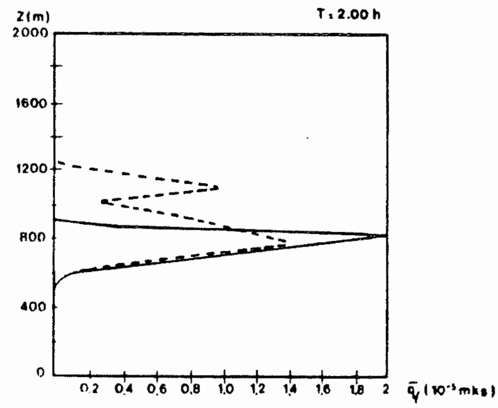

FIG. 4. — Profils comparés de $\overline{q_l}$.

La fig. 4 donne une idée du profil d'eau liquide : elle confirme que l'eau liquide est mal répartie dans le modèle 1D ; néanmoins la base des nuages est bien représentée.

En conclusion, ce type de théorie semble efficace, on peut attendre des améliorations dans deux directions : ditribution G(s) optimale, meilleure modélisation des presso-corrélations $\overline{\theta p}$, $\overline{wp}$; ces recherches sont actuellement en cours à l'EERM, à partir de l'analyse des résultats du modèle 3D. Cette utilisation de modèles élaborés, comme laboratoires numériques, qui ne remplace pas les mesures in situ, mais les complète, se révèle très fructueuse.

BIBLIOGRAPHIE

André, J. C., G. de Moor, P. Lacarrère, G. Therry, and R. du Vachat, 1978 : Modeling the 24 h evolution of the mean and turbulent structures of the planetary boundary layer. J. Atmos. Sci., 35, 1861-1883.

Deardorff, J. W., 1974 : Three dimensional numerical study of the height and mean structure of a heated planetary boundary layer. Bound. - Layer Meteor., 7, 81-106.

Holland, J. Z. and Ramusson, E. M., 1973 : Measurements of the atmospheric mass, energy, and momentum budgets over a 500-kilometer square of tropical ocean. Mon. Weath. Rev., 102, 44-55.

Manton, M. J., 1978 : A finite element model of a moist atmospheric boundary layer. Part. I : Model equations. Tellus, 30, 219-228.

Mellor, G. L., et T. Yamada, 1974 : A hierarchy of turbulence closure models for Planetary Boundary Layer. J. Atmos. Sci., 31, 1791-1806.

Mellor, G. L., 1977 : The gaussian cloud model relations. J. Atmos. Sci. 34, 356-358.

Sommeria, G. and J. W. Deardorff, 1977 : Subgrid scale condensation in models of non precipitating clouds. J. Atmos. Sci., 34 , 345-355.

Wyngaard, J. C., et O. R. Coté, 1974 : The evolution of a convective planetary boundary layer. A Higher Order - Closure model study. Bound. - Layer Meteor., 7, 289-308.

Yamada, T., and G. L. Mellor, 1979 : A numerical simulation of BOMEX data using a turbulence Closure model coupled with ensemble cloud relations. Quart. J. R. Met. Soc., 105, 915-944.

Bougeault Ph., G. Sommeria, et J. C. André, 1979 : Méthode de modélisation unidimensionelle de la couche limite planétaire nuageuse. J. Rech. Atmos. 13, 249 - 259.

A SYSTEM OF SELF-AMPLIFICATION FOR THE GROWTH OF ORGANIZED CLOUD STRUCTURES

G. Chimonas
Wave Propagation Laboratory, Boulder, Colorado

F. Einaudi
Georgia Institute of Technology, Atlanta, Georgia

D. P. Lalas
Wayne State University, Detroit, Michigan

Abundant evidence can be found in the literature for the existence of organization in the flow fields of condensation, precipitation and storms. This organization manifests itself as both time periodicity and spatial coherence of motion. For example, Chalon et al. (1976) found that new cells of hailstorms appear at intervals of 13 to 16 minutes and at locations 10 km apart. The list of spatially organized phenomena is long and includes rain bands (Browning, 1974; Houze et al., 1976a, b), cloud clusters in the tropics (Reed and Recker, 1971), travelling disturbances (Uccellini, 1975), and the familiar striations in mid-latitude cloud forms.

The range of wavelengths and periods of the organized activity is such that internal gravity waves seem to be the most likely agents. This has already been noted by several investigators, notably Matsumoto and Ninomiya (1969), Raymond (1976) and, for CISK in the tropics, Stevens and Lindzen (1978).

In attempting to develop a model for this interaction between gravity waves and condensation, two main problems have to be resolved. One is the mechanism of gravity wave generation from the background temperature and wind profiles, and the second is the interaction between saturation, latent heat release and the wave itself. One usually bypasses the first obstacle by simply assuming a gravity wave has been generated by some unspecified mechanism; the second hurdle is overcome by parameterizing the latent heat release through the introduction of a phenomenological but ad hoc relation between the induced velocity component and the amount of condensation. Partial objections to these solutions have been raised on predictable grounds. Yet the evidence of periodicity is compelling enough that the hypothesis of gravity waves being an important mechanism of cloud and precipitation organization, and storm generation, cannot be discarded. In this study we look anew at the problem and try to develop a consistent approach for the initial stage of the triggering of condensation cells by gravity waves.

Explicitly we consider a pre-condensation atmosphere in which the wind and temperature profiles give rise to a shear instability gravity wave mode. Initially the amplitude of this wave may be small, and its effect on the atmosphere is nothing more than a perturbation of velocity and temperature fields. But after some time its amplitude will exponentiate to the stage where it disturbs the conditions enough to initiate saturation in a localized 'most favored' region. And associated with the water substance condensation there will be a latent heat release that is communicated to the other atmospheric components.

If this latent heat occurs in the right fraction of the wave cycle it can feed back into the dynamics of the atmosphere to enhance the growth of the wave disturbance. This in turn will force further condensation, and a feedback instability occurs in which periodic cloud cells and the atmospheric wave grow together.

We have formulated the dynamics and thermodynamics of this process in a fully self-consistent fashion using a forwards propagating Green's function technique. A stepwise integrating routine allows us to accurately follow the space-time distribution of water substance, the heat transfers accompanying liquid-vapor transitions and the dynamic-thermodynamic behavior of the atmospheric gas. Applying the routine to any specific combination of mean atmospheric state and initial excitation of shear modes, we can trace the development of the system to see if the feedback is positive, negative or in quadrature.

The method has been applied to wind, temperature and moisture profiles that are typical of certain pre-storm conditions. The temperature contains a strong inversion that acts as a lid to plentiful moisture in the lower atmosphere. The wind forms a low level jet with shears that are strong enough to produce the subcritical ($< 1/4$) Richardson numbers needed for linear instability.

Not all modes show positive feedback when condensation occurs. In fact positive feedback is the exception rather than the rule, and occurs only over a narrow band of the spectrum of linear instabilities. However, where it does occur, substantial enhancement of the growth of the wave-cloud system is discovered. This suggests that there is a natural tendency of the atmosphere to form quasi-periodic cloud bands, rather than broadband quasi-random patches of condensation.

The critical levels of the linear stability theory are found to play a major role in the condensation dynamics. Strong positive feedback seems to require a near coincidence of the wave critical level and the cloud condensation height. This seems plausible from various physical considerations, and serves to emphasize the intimate coupling between the thermodynamics and neutral dynamics of the atmospheric system.

Conclusions

It appears from this study that gravity waves generated by background shear instability in a realistic atmosphere near saturation constitute a viable mechanism for inducing condensation and sustaining it by the utilization of the resultant heat release to amplify themselves. Further, it is shown that this process of self-amplification is tractable without the use of parameterization, and the system's early characteristics, growth rates, height of saturation, etc. can be calculated via this consistent approach.

References

Browning, K. A., 1974: Mesoscale structure of rain systems in the British Isles. J. Met. Soc. Japan, 52, 314-327.

Chalon, J. P., J. C. Fankhauser and P. J. Eccles, 1976: Structure of an evolving hailstorm, part I: General characteristics and cellular structure. Mon. Wea. Rev., 104, 564-575.

Houze, R. A. Jr., P. V. Hobbs, K. R. Biswas and W. M. Davis, 1976a: Mesoscale rainbands in extratropical cyclones. Mon. Wea. Rev., 104, 868-878.

Houze, R. A. Jr., J. D. Locatelli and P. V. Hobbs, 1976b: Dynamics and cloud microphysics of the rainbands in an occluded frontal system. J. Atmos. Sci., 33, 1921-1936.

Matsumoto, S. and K. Ninomiya, 1969: On the role of convective momentum exchange in the mesoscale gravity wave. J. Meteor. Soc. Japan, 47, 75-85.

Raymond, D., 1976: Wave-CISK and convective mesoscales. J. Atmos. Sci., 33, 2392-2398.

Reed, R. J. and E. E. Recker, 1971: Structure and properties of synoptic-scale wave disturbances in the equatorial western Pacific. J. Atmos. Sci., 28, 1117-1133.

Stevens, P. I. and R. Lindzen, 1978: Tropical wave CISK with a moisture budget and cumulus friction. J. Atmos. Sci., 35, 940-961.

Uccellini, L., 1975: A case study of apparent gravity wave initiation of severe convective storms. Mon. Wea. Rev., 103, 497-513.

OBSERVATIONS OF THE SCALE AND DURATION OF CUMULUS CLOUD INITIATION

C.E. Coulman

Division of Cloud Physics, CSIRO
Sydney, Australia

1. Introduction

This paper is concerned with observations which throw some light on the question of whether or not cumulus clouds are initiated by a pulse-like fluctuation in properties of the sub-cloud layer which is short when compared with the average lifetime of a cloud. There is an extensive literature on numerical modelling of individual cumulus clouds, well reviewed by Cotton (1975), which contains evidence that the nature, magnitude and duration of cloud-initiating phenomena are somewhat arbitrarily chosen because of the paucity of observational information.

In a previous paper Coulman and Warner (1977) examined thermodynamic properties of the sub-cloud layer on scales of the order of cloud-size and larger; more recently Coulman (1980) directed attention towards both thermodynamic and dynamic variables on horizontal scales from cloud-size down to 15 m. The expedition described in the latter reference provided the data used in this paper and a detailed description of the observational procedure used and the conditions encountered was given there. Briefly, the data were obtained by an instrumented aircraft which flew level measurement runs at about 50 to 100 m below the base of cumulus cloud fields which formed over flat terrain in north-western NSW, Australia.

2. Observed Cloud Base and Calculated Condensation Level

In Figures 1 and 2 the observed variation of cloud-base height with time of day is shown for two days of the expedition. By flying just beneath cloud base the natural variability of this level was assessed to be as small as ±20 m over tens of kilometres during the period 1200 hrs to 1430 hrs local time. Later than this each afternoon this figure increased to about ±40 m.

The aircraft made runs of about 10 km length at 50 to 100 m below cloud base during which high-frequency dynamic and thermodynamic data were recorded and the presence of cloud above the aircraft was detected by an upward-facing photoelectric instrument. To distinguish between sections of each run made beneath cloudy and clear areas the recorded signal for any variable has been multiplied by an indicator function I(t). This function is the output of the upward-facing cloud detector and,

$$I(t) = \begin{cases} 1 & \text{under cloud} \\ 0 & \text{under clear} \end{cases} . \qquad (1)$$

This conditional sampling technique has been more completely described in Coulman (1978).

The adiabatic lifting condensation level z_a has been calculated from observed data by numerical solution of the following equations

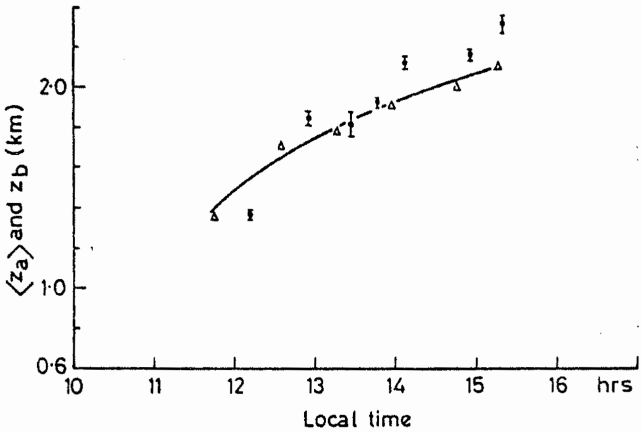

Fig. 1 - Observed cloud base (Δ), z_b, as a function of time on 2 April 1976. Calculated lifting condensation level, $\langle z_a \rangle$, averaged in each run beneath clouds and its standard deviation are shown by (Ī).

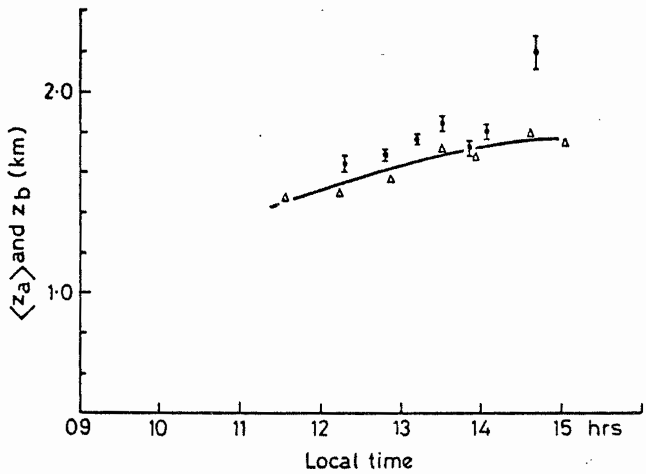

Fig. 2 - As Figure 1, but for 5 April 1976.

$$p_a = \left|\frac{622}{q} + 1\right| \exp\left|\frac{\alpha\{\theta(p_a/1000)^{0.288} - \beta\} + \gamma}{\theta(p_a/1000) - \delta}\right| \quad \text{(mb)}, \tag{2}$$

$$z_a = 44.308\left|1 - \left(\frac{p_a}{1013.2}\right)^{0.19028}\right| \quad \text{(m)}. \tag{3}$$

Here p_a is the pressure at adiabatic lifting condensation level, z_a the equivalent (ICAN) height, q and θ the ambient mixing ratio and potential temperature respectively, and α; β, γ, δ are constants (see List, 1951).

The average lifting condensation level of air beneath clouds, denoted by $\langle z_a \rangle$, has been calculated for each run and is shown in Figures 1 and 2 for comparison with the observed cloud base height z_b. The standard deviation $\langle \sigma_a \rangle$ is shown by vertical bars; it is important to note that $\langle \sigma_a \rangle$ is generally smaller than the hourly increment in cloud base height except in the decaying phase of the cloud field from about 1500 h onwards. Lifting condensation level is a sensitive function of q and θ; if we calculate the average value for each run $\langle\langle z_a \rangle\rangle$ under clear areas we may compare the difference $\langle\langle z_a \rangle\rangle - \langle z_a \rangle$ with $\langle \sigma_a \rangle$ and, as shown in Figure 3, $\langle \sigma_a \rangle$ is generally smaller than this quantity.

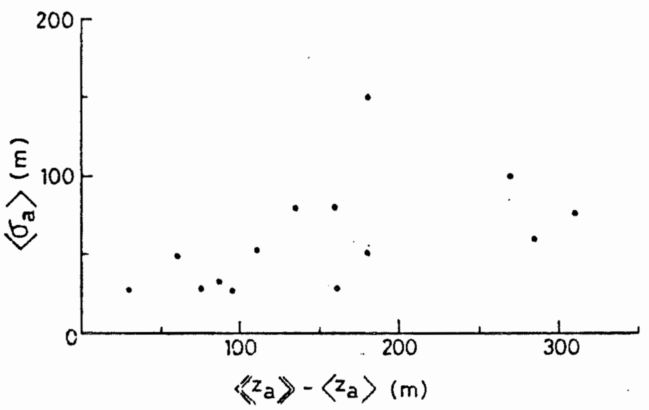

Fig. 3 - Standard deviation of lifting condensation level beneath cloud in each run is smaller than the difference between average L.C.L. beneath clear $\langle\langle z_a \rangle\rangle$ and beneath cloud $\langle z_a \rangle$.

The measurement flights were made on predetermined headings for specified times and so the cloud field was randomly sampled without intentional bias. It is therefore likely that clouds at most stages of their evolution were encountered and from cine-film records taken from the ground the average lifetime of these clouds was about 20 min. The above results therefore suggest that only small changes in θ and q, and hence z_a, occur in the air beneath a cloud during its lifetime.

3. Temperature, Humidity and Velocity Structure beneath Cloudy and Clear Areas

To facilitate comparison of results from various days the conditionally sampled data have been normalized; normalized fluctuations are denoted by double-primed symbols such as,

$$\theta'' = \frac{\theta'}{\sigma_\theta}, \tag{4}$$

where θ' is the fluctuation from a run mean $\overline{\theta}$ and σ_θ^2 is the run variance. Sharp brackets $\langle\ \rangle$ denote an average under cloud and $\langle\langle\ \rangle\rangle$ an average under a clear region.

Under cloud the mixing ratio $\langle q'' \rangle$ exhibits in Figure 4 an excess over the value in the

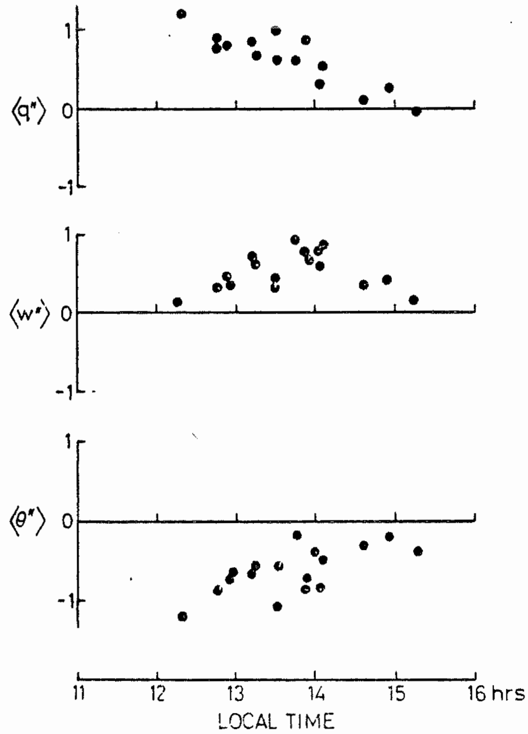

Fig. 4 - Conditionally sampled, normalized and averaged under-cloud fluctuations in q, w and θ show a well-marked maximum in $\langle w'' \rangle$ around 1330 hrs and a strong tendency for $\langle q'' \rangle$ to decrease with increasing time. A less pronounced trend is evident in $\langle \theta'' \rangle$. Since the clouds were sampled randomly these results presumably characterize clouds at any stage of their individual lifetimes.

surroundings and this excess diminishes as the afternoon advances; $\langle \theta'' \rangle$ exhibits a deficit beneath cloud (see Coulman and Warner, 1977) which also tends toward zero with increasing time after cloud formation. Vertical velocity $\langle w'' \rangle$ has a fairly well-marked peak at about 2 h after cloud formation in this collection of data; it is always positive (upward). In Figure 5 the normalized fluctuations averaged under clear areas exhibit very weak dependence on time of day; there is, perhaps, a suggestion of a peak in $\langle\langle w''\rangle\rangle$ at about 1400 hrs and a weak trend in $\langle\langle q''\rangle\rangle$. However, all show opposite signs to the corresponding variables in Figure 4.

4. Conclusions

In cumulus models which employ a brief pulse-like change in properties to initiate cloud it is common to find a rate of increase in the height of cloud base during the individual cloud lifetime which is markedly larger than the observed values, such as are shown in Figures 1 and 2. In the observations referred to in Figures 4 and 5 more than 50 clouds were studied. It seems reasonable to assume that clouds at most stages of their individual lifetimes will have been encountered during the observing period of several hours each day. Hence the general deductions from Figure 4 are presumably applicable to most of the lifetime of these cumulus clouds; for example, it appears that $\langle w''\rangle$, the velocity beneath cloud, is positive for much of a cloud's existence.

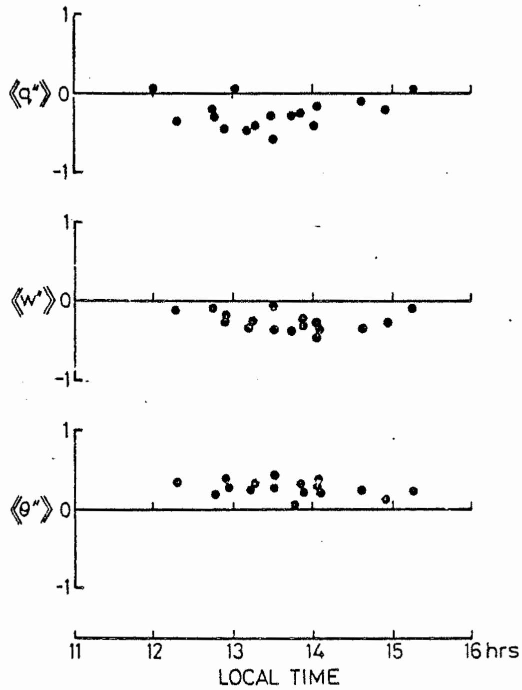

Fig. 5 - As for Figure 4, but relating to fluctuations under clear areas. The signs of the normalized fluctuations are opposite to those under cloud but show insignificant dependence on time of day.

If $\langle w''\rangle$ were, in fact, positive only at the moment of incipient cloud formation and thereafter zero, as assumed in some numerical models, the distribution seen in Figure 4 would be most unlikely to eventuate from an examination of over 50 clouds taken at random. Similar arguments may be followed in respect of the other variables. It is, of course, not implied that these properties in the sub-cloud layer remain unchanged throughout the lifetime of a cloud, but the present observations do not provide any direct information on that matter.

It will be noted in Figures 1 and 2 that z_a for air just beneath clouds is usually slightly higher than observed cloud base; this is consistent with Coulman and Warner (1977) and with the postulate that some comparatively dry air from above the top of the convection layer is mixed with sub-cloud air. The horizontal scale of these parcels of air beneath cloud is known from Coulman and Warner (1977) and Coulman (1980) to be of cloud scale or larger. Hence it is not improbable that once condensation has occurred as a result of the arrival of a parcel of air from the well-mixed convection layer at condensation level the resultant cloud continues to "feed" from a substantial reservoir of warm, moist air. The volume of such a reservoir and the degree of mixing it experiences will determine the cloud's growth and lifetime, provided it remains a fair-weather cumulus. Should it become a cumulo-nimbus with properties dominated by dynamic processes (Miller, 1978) these arguments become invalid.

REFERENCES

Cotton, W.R., 1975. Theoretical cumulus dynamics, Rev. Geophys. Space Phys., 13, 419-448.

Coulman, C.E., 1978. Boundary-layer evolution and nocturnal inversion dispersal - Pt. II, Boundary-Layer Meteorol., 14, 493-513.

Coulman, C.E., 1980. Diurnal evolution of properties of the sub-cloud layer over land, Boundary-Layer Meteorol. (in press).

Coulman, C.E. and J. Warner, 1977. Temperature and humidity structure of the sub-cloud layer over land, Boundary-Layer Meteorol., 11, 467-484.

List, R.J., 1951. Smithsonian Meteorological Tables. Smithsonian Institution, Washington, D.C.

Miller, M.J., 1978. The Hampstead storm: A numerical simulation of a quasi-stationary cumulonimbus system, Q. J. R. Meteorol. Soc., 104, 413-427.

DYNAMICS OF A COLD AIR OUTFLOW FROM THE BASE OF A THUNDERSTORM. A SIMPLE MODEL

M. Ćurić

Institute for Meteorology, University of Belgrade
Belgrade, YUGOSLAVIA

1. Introduction

The thunderstorm has been characterising with extremely complicated dynamic, thermodynamic and microphysical process. This process is complicated in the cloud as well as below its base. For this purpose a different models have been developed to describe this process in a simpler form (Fujity and Grandoso, 1968; Thorpe and Miller, 1978).

Due to the evaporation and melting of hydrometeors the cooling of air occurs below the cloud base. The motion of such cooled air is one of the important factors in the formation of new Cumulonimbus (Newton, 1966). The cooled air has been descending and spreading out in the form of the funnel over the surface. This spreading out is known as the gust front. The process of descending and spreading of cooled air causes supstantial energetic changes in the air below the base of Cumulonimbus. On the base of the energetic changes we shall find out a horizontal speed of gust front as one of the most important parameter of the dynamics of a cooled air outflow from the base of a Cumulonimbus.

2. Energetic Changes Due to the Descending and Spreading out the Cooled Air

In order to find out energetic changes and to express quantitatively a model has been formulated similar to the model developed by Margules (1906). Let the height of the Cumulonimbus base is h and radius of the base r. Between the Cumulonimbus base and the surface the vertical column of cooled air is considered with the same radius and the height. Around the cooled air the shell of warmer air with external radius R is considered. The cooled air is indicated by index 1 and warmer by index 2. The characteristic elements of this system of air, S, at the initial state are not supplied with an apostrophe and in the later stage they are supplied with an apostrophe.

The cooled and warmer air has to change the position under the influence of the horizontal pressure gradient force, effective gravity and viscosity force. First, we shall consider the energetic changes when the system S is composed of incompressible fluids with densities ρ_1 and ρ_2 and after that, when the system is composed of compressible fluids.

In the initial stage the considered system has potential energy

$$P = g\,\frac{h^2}{2}\,(\rho_1\sigma_1 + \rho_2\sigma_2) \qquad (1)$$

where $\sigma_1 = r^2\pi$ and $\sigma_2 = (R^2-r^2)\pi$.

After the change of position the system has a potential energy

$$P' = g\frac{h^2}{2}\,\frac{\sigma_1}{\sigma}\left[\rho_1\sigma_1+\rho_2\sigma_2\,\frac{2\sigma_1+\sigma_2}{\sigma_1}\right] \qquad (2)$$

where $\sigma = R^2\pi$.

The difference of the potential energies of the system at the beginning and at the end of the process described above, $p-p'$, is the available kinetic energy

$$K = g\frac{h^2}{2}\,\rho_1\sigma_1 - P\frac{\sigma_1}{\sigma} \qquad (3)$$

It can be seen that system of mass $m = m_1+m_2$ in the case when $\sigma \gg \sigma_1$ $(m \to m_2)$ has at the end kinetic energy

$$K = g\,\frac{m_1 h}{2}\,\frac{\rho_1-\rho_2}{\rho_1} \qquad (4)$$

where $m_1 = \rho_1\,\sigma h$.

When $\sigma_1 \gg \sigma_2$, i.e., $\sigma \gg \sigma_2$,

than

$$K = g\,\frac{m_2 h}{2}\,\frac{\rho_1-\rho_2}{\rho_1} \qquad (5)$$

where $m_2 = \rho_2\sigma_2 h$.

If the considered system is composed of the two air masses, cold and warm, then we can estimate of the amount of the kinetic energy as Margules did. For this reason we shall assume that the potential temperature of all parcels of the cooled air at initial stage is the same and does not change when the air masses change position. The same assumption is applied to the parcels of the wormer air mass.

The sum of internal and potential energy of the whole system S at the initial stage is in this case

$$E = U+P = \frac{c_p \pi}{g(1+\chi)} (R^2-r^2) r^2 \left(\frac{T_{o1}p_{o1} - T_{h1}p_h}{r^2} + \frac{T_{o2}p_{o2} - T_{h2}p_h}{R^2 - r^2} \right) \qquad (6)$$

where $\chi = c_p/c_v$. Index o and h referred to the surface values and to the cloud base values.

When the air masses change the position adiabaticaly, the sum of these two energies of the considered system is

$$E' \equiv (U+P)' = \frac{c_p \pi R^2}{g(1+\chi)} \left[T_{o1}' p_o' - T_{g1}' p_g' + T_{g2}' p_g' - T_{h2} p_h \right] \qquad (7)$$

where

$$p_g' = p_h + \frac{R^2-r^2}{R^2} (p_{o2} - p_h) \qquad (8)$$

$$p_o' = p_h + \frac{R^2-r^2}{R^2} (p_{o2} - p_h) + \frac{r^2}{R^2} (p_{o1} - p_h). \qquad (9)$$

The difference of the (6) and (7), $K' = E - E' = 1/2\ mv^2$, is equal to the kinetic energy of the system which is available when the masses change position under the conditions the system is considered.

From the Poisson equation we have approximately

$$T_1' = T_1 \left(1 + \frac{R^2-r^2}{R^2} \frac{p_{o2} - p_1}{p_1}\right)\chi \qquad (11)$$

$$T_2' = T_2 \left(1 - \frac{r^2}{R^2} \frac{p_1 - p_h}{p_2}\right) \qquad (12)$$

Internal energy of the considered air masses at the initial and in the finale state can be expressed in the following way:

$$U = \frac{c_v \pi r^2}{g} \int_{p_h}^{p_{o1}} T_1 dp_1 + c_v \pi \frac{R^2-r^2}{g} \int_{p_h}^{p_{o2}} T_2 dp_2 \qquad (13)$$

$$U' = \frac{c_v \pi R^2}{g} \left[\int_{p_g}^{p_o'} T_1' dp_1' + \int_{p_h}^{p_g} T_2' dp_2' \right]. \qquad (14)$$

After substitution (11) and (12) in (14) we have

$$V' = \frac{c_v \pi}{g} \left[\int_{p_h}^{p_{o1}} r^2 T_1 \left(1 + \frac{\chi}{R^2} (R^2-r^2) \frac{p_{o2} - p_1}{p_1}\right) dp + \int_{p_h}^{p_{o2}} (R^2-r^2) T_2 \left(1 - \chi \frac{r^2}{R^2} \frac{p_2 - p_h}{p_2}\right) dp_2 \right]. \qquad (15)$$

From

$$K' = \frac{c_p}{c_v} (U - U') \qquad (16)$$

and (13) as well as (14) we have

$$K' = \frac{R_s \pi}{g} \frac{r^2}{R^2} (R^2 - r^2) \left[\int_{p_h}^{p_{o2}} T_2 \frac{T_2 - p_h}{p_2} dp_2 - \int_{p_h}^{p_{o1}} T_1 \frac{p_{o2} - p_1}{p_1} dp_1 \right]. \qquad (17)$$

By integration we get

$$K' = \frac{R_s \pi}{g} \frac{R^2 - r^2}{R^2} \left[\bar{T}_1 (p_{o1} - p_h) + \bar{T}_2 (p_{o2} - p_h) - \frac{g}{R_s} h (p_{o2} - p_h) \right]$$

where $\bar{T}_1$ and $\bar{T}_2$ are the mean temperatures with height in cold and warm air.

After some rearangement the kinetic energy should be as it follows

$$K' = \frac{g h^2 p_h}{2 R_s} \left(\frac{r}{R}\right)^2 (R^2 - r^2) \pi \frac{\bar{T}_2 - \bar{T}_1}{\bar{T}_1\ \bar{T}_2}. \qquad (18)$$

It is obvious that kinetic energy has increased after the air masses has changed the position.

3. The Velocity of the Gust Front

Velocity v, as a measure of the kinetic energy, can be obtained in the following way: The air mass m, of which system S is composed, may be expressed in the form

$$m = \frac{r^2\pi}{g}(p_{o1}-p_h) + \frac{(R^2-r^2)\pi}{g}$$

$$(p_{o2}-p_h) \ . \qquad (19)$$

Expressing p_{o1} and p_{o2} by p_h that mass can be described as

$$m = \frac{\pi h p_h}{R_s} \ \frac{\bar{T}_2 \ r^2 + \bar{T}_1 (R^2-r^2)}{\bar{T}_1 \ \bar{T}_2} \qquad (20)$$

From the definition of the kinetic energy, as well as (18) and (20), when the difference between $\bar{T}_1$ and $\bar{T}_2$ is not so large, follows

$$v = \frac{r}{R^2} \left[g \ h(R^2-r^2) \ \frac{\bar{T}_2-\bar{T}_1}{\bar{T}_1}\right]^{1/2} \qquad (21)$$

In the case of the incompressible fluid velocity v is

$$v = \frac{r}{R} \left[gh(R^2-r^2)\right.$$

$$\left.\frac{\rho_1 - \rho_2}{\rho_1 r^2 + \rho_2 (R^2-r^2)}\right]^{1/2} . \qquad (22)$$

If the whole considered air mass is in the motion than it should obtain aditional velocity v. The following example ilustrates the mentioned velocity. Let the height is h=500 m, the mean temperature $\bar{T}_1 = 285^oK$, the difference of the mean air temperatures $\bar{T}_2-\bar{T}_1 = 5^oK$, the ration of considered surfaces, $\sigma_2/\sigma_1 = 2$ than v is equal 7 m/s. The importance of this velocity is bigger if we know that this new generated kinetic energy does not exite in whole considered mass and in some volumen of the air it can be supstantionaly bigger. In the case of the incompressible fluid, for example water, with densities $\rho_1 = 10^3$ and $\rho_2 = 991 \ kg/m^3$, velocity is about 3^2 m/s.

If the cold air should be obtained this aditional kinetic energy only, that velocity should be bigger. From the definition of the kinetic energy we have

$$v^2 = \frac{2K'}{m_1+m_2} , \qquad (23)$$

where m_1 and m_2 are the masses of cooled and warmer air. Science we wish that is

$$v_1^2 = \frac{2K'}{m_1} \qquad (24)$$

it follows

$$v_1 = \frac{R}{r} \ v \qquad (25)$$

where v_1 is velocity of cooled air.

Velocity v_1 which have cooled air is significantly greater than v. The main part of this energy is realy horizontal velocity by which cooled air folow over surface. It moves under the wormer air. Spreading of the cold air which flowout from the Cumulonimbus base has been happening along the vally in the mountain regions. On this way the gust front produces forced lifting of the warmer air in the head of it. This forced vertical velocity may be about 1 m/s (Ćurić, 1977) what is sufficient to produce new Cumulonimbus cell.

The dynamics of the spreading out of outflowing cold air from the base of a thunderstorm is simulated in the laboratory. In the center of the tank which is filled in with a slightly lighter fluid (fresh water) the tube is vertically situated. It is filled with a denser fluid (aqueous solution, water plus potassium permanganate, $KMnO_4$). Carefully taking out of a tube the denser dyed water start to spread out. The head part of this denser fluid changes it shape with time. This motion is actually a density carent which is, among the other, laboratory simulated Simpson (1969). As a consequent of the change in shape of the head part the slope of gust front has been changing. The forced lifting of warmer air has been favoring on this places.

Acknowledgement

The author wish to express his thanks to Prof.M.Čadež for valuable discussions during preparing this paper and Lj. Radoja for typing.

References

Ćurić, M., 1977: A model for the calculation of the appearance of the frontal profiles and of the vertical velocity of air at a front, Arch.Met.Geoph., Ser.A, 26, 13-19.

Fujita, T.T. and Grandoso, H., 1968: Split of a thunderstorm into anticyclonic and cyclonic storms and their motions as determined from numerical model experiments, J. Atmos. Sci., 25, 416-439.

Margules, M., 1906: Zur Sturmtheorie, Met.Zeit., 23, 481-497.

Newton.C.W., 1966: Circulation in large sheared Cumulonimbus, Tellus, 18, 699-713.

Simpson, J.E., 1969: A comparation between laboratory and atmospheric density currents. Quart J. R.Met.Soc., 95, 758-765.

Thorpe, A.J. and Miller, M.J., 1978: Numerical simulations showing the role of the down draught in Cumulonimbus motion and splitting, Quart. J.R. Met.Soc., 104, 873-893.

A PARAMETERIZED CLOUD MODEL FOR MESOSCALE SIMULATIONS WITH OROGRAPHY

G.U. Dorwarth

Meteorologisches Institut
Universität Karlsruhe (TH)
Karlsruhe GERMANY

1. INTRODUCTION

As orography exercises a large influence on mean isohyets, it is of great interest to study in mesoscale models orographically induced cloud systems like those connected with the stable upgliding of air on a mountain ridge. Such motions can produce high precipitation rates (Colton 1976)because of their occurence in the lower troposphere where the condensation rate is high, although the vertical velocities are small compared to the convective case.

In contrast to microphysical studies dynamical simulations allow only a highly parameterized representation of the precipitation process. This paper intends to introduce a parameterized kinematic cloud model for the mass balance of hydrometeors and to show first results for the simulation of orographic clouds. This model is one part in the development of a complete dynamical mesoscale model.

2. MODELING THE WARM CLOUD

For the calculation of the warm rain process the parameterization scheme after Kessler (1969) is used. Liquid water density is divided into two categories. While cloud droplets are in suspense, raindrops fall with their mass weighted terminal velocity. They are distributed with an exponential size spectrum

$$f(r) = f_0 \exp(-\lambda r) \qquad (1)$$

Droplets are initiated when air reaches the saturation point. Raindrops develop by autoconversion and grow by collection of droplets and loose mass by evaporating outside the cloud.

3. MODELING THE ICE CLOUD

In order to save computer time the ice phase is treated in only one additional density class so that the mass fluxes in the whole scheme can be described as illustrated by figure 1. It is assumed that rainwater densities develop above the melting layer in only small amounts so that the freezing of raindrops may be neglected.

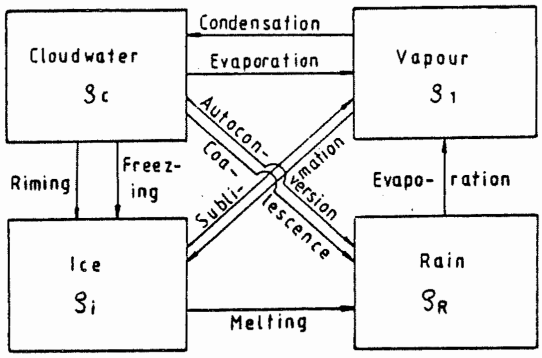

Fig. 1 Mass fluxes in the model of an ice cloud

For the computation of the mass fluxes and terminal celocities of ice, the number, size, and shape of ice particles must be known. In an Eulerian framework it is difficult to determine these parameters because there is no information about the history of particles. Therefore only hypotheses are possible, which limits the model to situations where the basic suppositions are valid. The following case is assumed:

a. In the initial stage of glaciation the ice phase is considered to consist of hexagonal plates. They are monodispersely distributed, their number being parameterized by the average ice nuclei number (Fletcher 1962)

$$n = 10^{-2} \exp(0{,}6\,(273 - T_C)) \quad m^{-3} \qquad (2)$$

and by an enhancement factor α. T_C is the cloud top temperature. The crystal mass-size-relationship is formulated after Pruppacher and Klett (1978).

b. It is assumed that neither riming nor diffusional growth is negligible. Therefore we postulate the ice particles to be graupel with a low density, if the plates exceed a critical size. This requires a sufficient quantity of liquid water for riming to occur. The particles are distributed exponentially where the parameter f_0 depends on temperature and ice concentration (Houze et al.1979).

The freezing of cloud droplets treated by the theory of Bigg (1953) is used as the ice nucleation process at temperatures below 263 K. The collision efficiency of plates for collisions with droplets depends on the particle size (Pitter 1977). For graupel a constant value is used. The melting equation assumes the shedding of all liquid water. The terminal velocities are formulated after Locatelli and Hobbs (1974) and Davis and Auer (1974).

4. BOUNDARY CONDITIONS AND OROGRAPHY

At the ground the atmospheric vapour field is coupled with the soil moisture, which is computed by a two layer model for the moisture fluxes in the soil. An irregular lower boundary is avoided by the transformation of z into a new coordinate

$$\eta = \frac{z - H}{h - H} \tag{3}$$

H represents the model height and h the height of the orography.

5. INPUT PARAMETERS

Although designed for combining with a dynamical model, first tests are conducted kinematically. So only the mass balance equations are solved. The steady state wind and temperature fields are taken from a hydrostatic dryadiabatic boundary layer model (Tangermann-Dlugi 1979) for the twodimensional airflow over a mountain ridge. The temperature gradient was modified in order to represent quasi moistadiabatic conditions. The values at the inflow boundary are shown in figure 2.

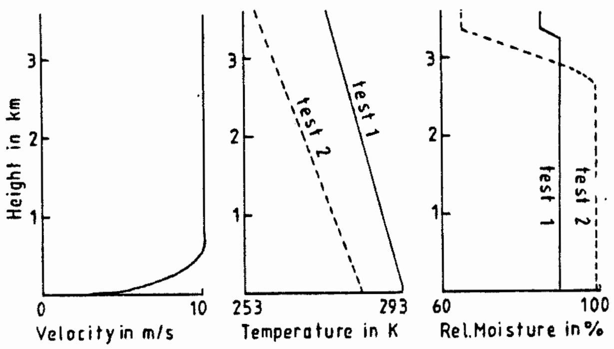

Fig. 2 Inflow boundary values

6. WARM CLOUD RESULTS

Here only the role of autoconversion is noteworthy. Autoconversion will initiate rain only in case of high liquid water contents. Two formulas are tested for a warm cloud development: the autoconversion of Kessler (1969) depending linearly on cloud water content, and the nonlinear formulation of Orville and Kopp (1977). As a remarkable difference between the two cases the linear formula produces a smooth cloud water profile with one maximum while the nonlinear formulation results in two liquid water maxima. This result is illustrated in figure 3 by the autoconversion rate itself, which is also a measure for the cloud water content.

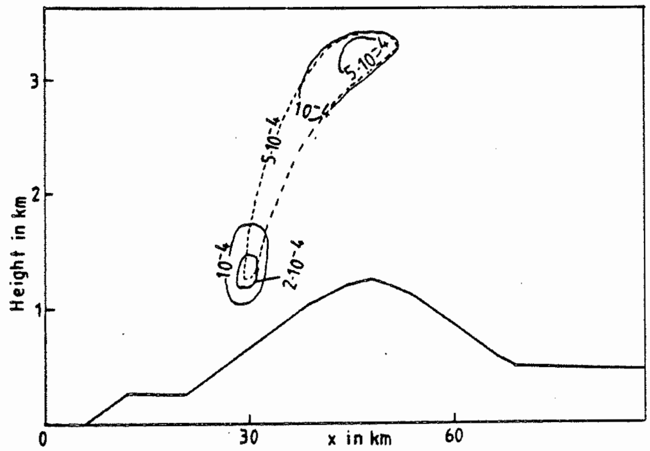

Fig. 3 Autoconversion rates of test 1 in g m^{-3} s^{-1} ---linear, — nonlinear formulation

7. ICE CLOUD RESULTS

For the comparison of the model results with microphysical experiments zero dimensional simulations for a parcel with impermeable boundaries were carried out. For $T=T_c=255$ K figure 4 shows the glaciation behaviour of the model cloud. The increase of ice density ρ_i and the decrease of cloud water density ρ_c depend mainly on the enhancement factor α. This fact and the shape of the graphs are well confirmed in literature, although the total glaciation times differ somewhat.

Twodimensional simulations are also sensitive to the number of ice crystals. Figure 5 shows the ice and rainwater content for test 2. The cloud water in figure 6 is characterized by two maxima. This result agrees quantitatively with observations by Hobbs et al. (1972). The

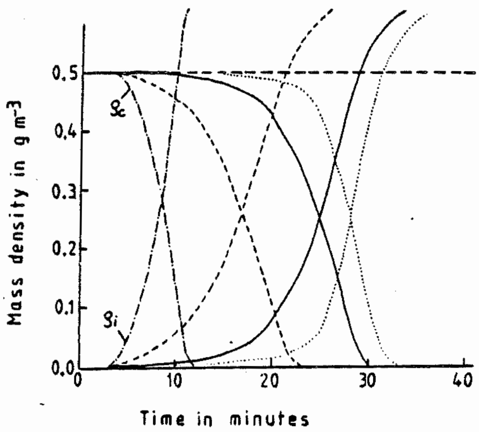

Fig. 4 The glaciation process. -·-·- α = 1000, --- α = 100, —— α = 10, ... α = 1

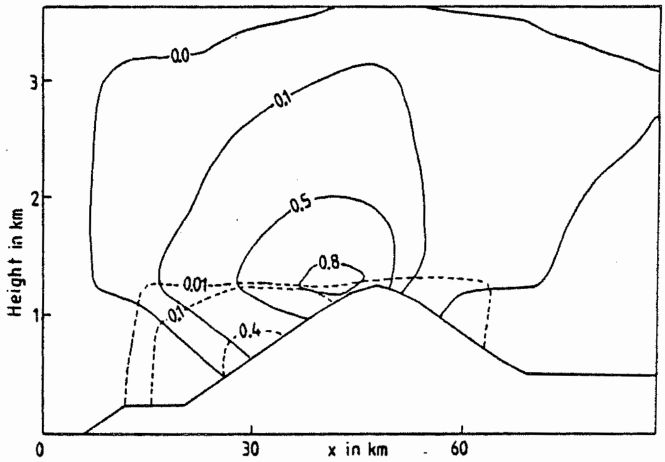

Fig. 5 ——ice content in g m^{-3}, ---rainwater content in test 2

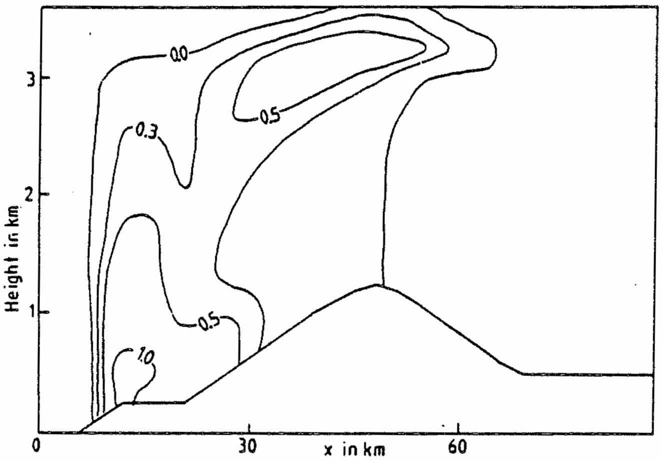

Fig. 6 Cloud water content for α = 10

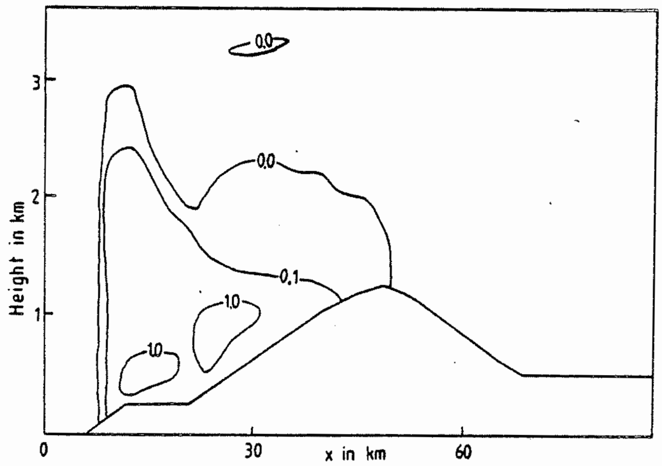

Fig. 7 Cloud water content for α = 1000.

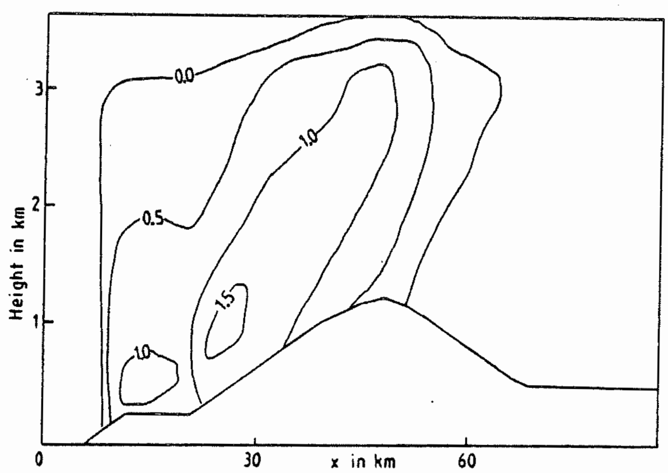

Fig. 8 The cloud water content for β = 0,25 and α = 10.

secondary liquid water maximum over the crest depends on the enhancement factor. In this case it was α = 10. The maximum diminishes for α = 1000 (see figure 7). In this last case however not all of the model assumptions are valid as there is only a small amount of liquid water above the melting layer.

Another important factor is the radius of rimed crystals. Above it was assumed that crystals have the radius of unrimed crystals. A reduced lateral growth can be simulated by introducing

$$r = \beta r_u + (1 - \beta) r_o \qquad (4)$$

into the continuous coalescence equation. r_u represents the radius of unrimed crystals and r_o the radius at which riming starts. Further simulations show that the cloud water content rises with a sinking β . The result for an extreme case β= 0.25 is shown in figure 8.

8. CONCLUSIONS

For dynamical simulations it is necessary to reproduce the result of microphysical models in a parameterized form. It was shown that even a simple model can simulate several important features.

Such models also can help to facilitate the understanding of complicated processes. So an increased degree of riming under the diffusional growth region reduces the water content and produces the relative liquid water maximum at greater heights. An increased crystal number reduces the water content already in the diffusional growth region.

9. REFERENCES

Bigg, E.K.,(1953) The supercooling of water. Proc.Phys.Soc. B 66, 688 - 694

Colton, D.E.,(1976) Numerical simulation of the orographically induced precipitation distribution for use in hydrologic analysis. J. Appl.Meteor.15, 1241 - 1251

Davis, C.I., Auer jr. A.H. (1974) Use of isolated orographic clouds to establish the accuracy of diffusional ice crystal growth equations. Conf. on Cloud Physics, Tucson, Arizona

Fletcher, P.V., Radke, L.F., Locatelli, J.D., Atkinson, D.G., Robertson, C.E., Weiss, R.R., Turner, F.M., Brown, R.R. (1972) Field observations and theoretical studies of clouds and precipitation over the cascade mountains and their modifications by artificial seeding. (Contributions from the Cloud Physics Group) Res.Rept. No.7, Dept. of Atmospheric Sciences, University of Washington, Seattle, Washington.

Houze, R.A. jr., Hobbs, P.V., Herzegh, P.H., Parsons, D.B. (1979) Size distributions of precipitation particles in frontal clouds. J. Atmos. Sci. 36, 156 - 162

Kessler, E. (1969) On the distribution and continuity of water substance in atmospheric circulations. Meteor. Monograph 10, No. 32, Am Meteor. Soc., Boston, Mass.

Locatelli, J.D., Hobbs, P.V. (1974) Fall speeds and masses of solid precipation particles. J. Geophys. Res. 79, 2185 - 2197.

Orville, H.D., Kopp, F.J. (1977) Numerical simulation of the life history of a hailstorm. J. Atmos. Sci. 34, 1596 - 1618

Pitter, R.L. (1977) A reexamination of riming on thin ice plates. J. Atmos. Sci. 34, 684 - 685

Pruppacher, H.R., Klett, J.D. (1978)Microphysics of clouds and precipitation. D. Reidel-Verlag.

Tangermann-Dlugi, G. (1979) Mesoskalige Modellentwicklung und erste Ergebnisse. Fortbildungstag des Zweigvereins Frankfurt der Deutschen Meteorologischen Gesellschaft am 9.November 1979.

ON THE SUPERSATURATION PRODUCED BY MIXING

J.T. Hallett

Department of Mathematics
University of Nevada,
Reno, Nevada, U.S.A.

J. Hallett

Desert Research Institute,
Reno, Nevada, U.S.A.

When two volumes of moist air of different vapor density and temperature, are uniformly mixed the final equilibrium condition may or may not be supersaturated. When a supersaturation is produced, the straight line joining the initial conditions of the two volumes on a vapor density-temperature plot crosses the saturation density curve at two points. If the initial conditions were saturated, all mixing volume proportions represented by points on the straight line joining the initial condition are supersaturated (a, Fig. 1); if the initial conditions were under saturated, only those where the proportion to the left of the saturation curve are supersaturated, (b, Fig. 1), if the straight line lies entirely to the right of the saturation curve, no supersaturation is produced (c, Fig. 1).

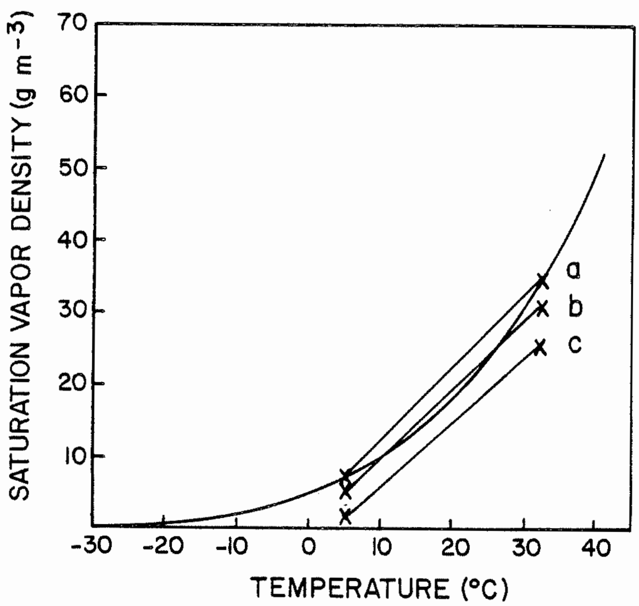

Figure 1. Conditions for supersaturation by uniform mixing of two moist air volumes; the position on each line is in proportion to the volumes mixed, (50% is in the center).

This analysis represents two equilibrium situations and in any realistic mixing process, parcels of fluid having different characteristics are brought into juxtaposition by complex flow patterns, whereupon equilibrium is established by molecular transport of both heat and moisture over the spatial scale of the mixing process. During this non steady state situation, transient supersaturations occur which may lead, locally, to quite different supersaturations that result from the equilibrium mixing of two volumes indicated in Fig. 1. The detail of the frequency spectra of such occurrences evidently relates to the detail of the mixing process itself.

One idealization is to take two air parcels in juxtaposition, initially thermally and mechanically isolated and at initial time to permit moisture and heat to diffuse by molecular processes. Both temperature and vapor density relax, to be described analytically by solutions of the time dependent Laplace equation (Carslaw & Jaeger 1959). Fig. 2 shows how the temperature of two 0.5 cm air slabs relaxes as they are brought into contact; a similar process takes place for the vapor density with a time enhancement of the ratio by the molecular diffusivity to the thermometric conductivity ($\sim$ 1.2 at 0°C).

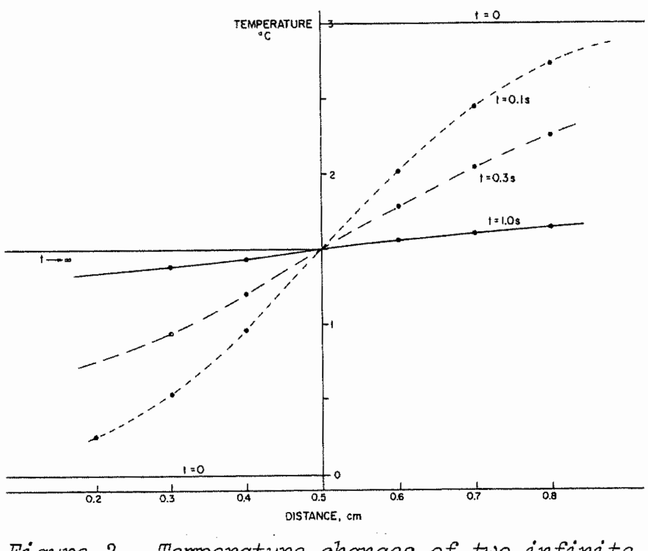

Figure 2. Temperature changes of two infinite slabs of air temperature 0°C, 3°C brought into contact at t=0.

The overall result is that a supersaturation pulse spreads from the interface, with a maximum in the warm air. This reaches the warm air boundary (impervious in this model) and falls to overall equilibrium in $\sim$ 5 sec. (Fig. 3). The peak of the supersaturation in the example shown, air saturated at 0°C and +3°C, increases with time as the pulse spreads

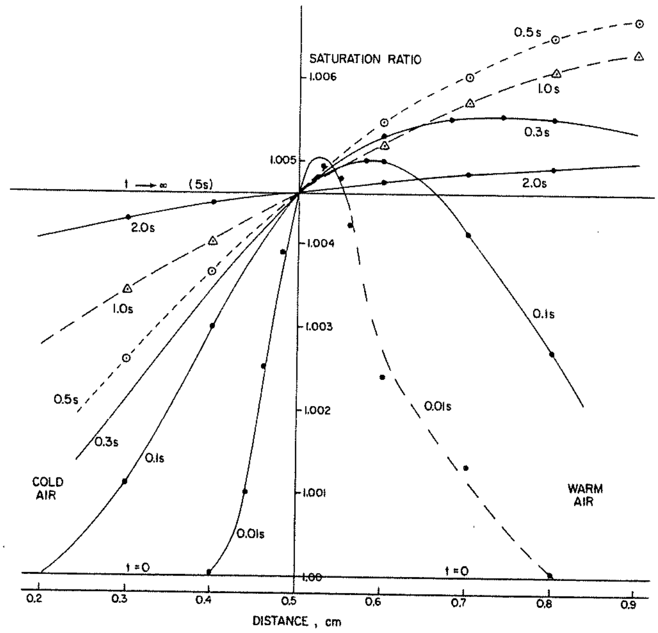

Figure 3. Supersaturation produced in two air slabs, salurated at 0°C and 3°C, brought into contact at t=0.

to the edge of the volume to reach a maximum of 0.6%, it then decays to the equilibrium volume, in ∿ 5 seconds.

The realism of this model in any atmospheric situation lies in an understanding of the detail of the mixing process. Mixing in a shear flow between fluids of differing properties is conventionally depicted as a series of vortices which wind up until destroyed by viscous dissipation, with simultaneous transport of heat and moisture. This process is conceptually more appropriate for horizontally stratified layers with shear giving Kelvin-Helmholtz Waves. In the more turbulent situation of the convective process an important question is the mechanism whereby air of different properties are brought together and the magnitude of the resulting supersaturation.

A process for transport of a fluid property with little interaction with its surroundings is by a vortex ring. The coherence of such a phenomenum is demonstrated in simple laboratory demonstrations, where rings of dimension centimeter to meter propagate considerable distances in still air. Recent experiments in water by Hallett & Christensen, relevant to cloud drop interactions, inspired by an earlier paper of Reynolds (1875) have shown how vortex rings of water with a specific characteristic (temperature, density) propagate and come to rest, relaxing first in motion, then in temperature and finally in density. This provides a mechanism for injection of a slightly different fluid over a considerable distance; cm vortex rings propagate in water some 20 to 20 cm. A solution vortex ring saturated at one temperature can propagate into fluid saturated at another temperature, and become supersaturated as it relaxes.

It is suggested that in a turbulent field of motion as produced in the convective environment, that such vortex ring motion is initiated on a random basis to be conceptualised by the successive occurrence of two normal stresses of different magnitude and size - to produce, in effect the mechanics of a vortex ring formation of a typical laboratory set up. Once formed, the ring propagates, to be distorted by other motion; but nevertheless carrying its initial characteristics undiluted, some 10 to 50 diameters distance. Here, moisture and thermal relaxation occur to produce a supersaturation, comparable to Fig. 3, but in cylindrical or more realistically toroidal symmetry. Those stresses which do not happen to be appropriate for producing a propagating ring will evidently not influece the process, and fail to lead to any transport; it is only those stresses which happen to give propagation which dominate the long range transport.

CONCLUSION

In the cloud environment, propagation of vortex rings of varying degrees of distortion have the capability of transporting air of one temperature and moisture characteristic into regions of a different characteristic and giving rise to transient supersaturation in excess ∿ 0.5%.

ACKNOWLEDGEMENT

This work was supported in part by the Universities Space Research Association, and the National Sciences Division, Grant No. (ATM 77-07995).

REFERENCES

Carslaw,H.S. & Jaeger,J.C., 1957. Conduction of heat in solids. 2nd Edition, Oxford, Clarendon Press.

Hallett,J. & Christensen,L. An experimental study of the interaction of cloud and rain size drops with a water surface. In preparation.

Reynolds,O. 1875. On the actions of rain to calm the sea. Proc.Lit. & Phil.Soc., Manchester, 14, 72-74.

DYNAMICAL CHARACTERISTICS OF THE SUB-CLOUD LAYER IN A MARITIME ENVIRONMENT

A. Mary Selvam, B.K. Bandyopadhyay, K.G. Vernekar, Brij Mohan, R. Vijayakumar, A.S. Ramachandra Murty and Bh.V. Ramana Murty

Indian Institute of Tropical Meteorology, Poona-411005, India.

1. INTRODUCTION

Knowledge of the spatial power spectrum of temperature is valuable for the understanding of the dynamical characteristics of the atmospheric boundary layer. The clear air temperature spectra in an isotropic atmosphere follow the -5/3 power law (Berman, 1976). Fluctuations in the turbulent air affect the characteristics of the temperature spectra.

High resolution dry- and wet-bulb temperature observations across the wind were made, along the aircraft flight legs of about 30 km at 14 levels, over the Arabian sea on a clear day during the summer monsoon of 1979. The characteristics of the horizontal temperature spectra and the vertical temperature structure of the ABL in the region were investigated. Also during the above flights, measurements on cloud condensation nuclei (CCN) were made at 8 levels. The variations noticed in the concentration of CCN were studied in relation to the thermal stratification of the atmospheric boundary layer (ABL). The results are presented below.

2.0 MEASUREMENTS AND ANALYSIS

Measurements were made using an instrumented DC-3 aircraft on 8 September 1979 during the afternoon hours. On the above day weak monsoon conditions existed in the region and no clouds were present during the period of observations.

The height of the cloud base in the region during the summer monsoon is between 2 and 3 kft (Mary Selvam et al., 1980). The details of the monsoon circulation and monsoon rainfall were reviewed (Ananthakrishnan, 1977). The location of the measurements was over the Arabian sea, about 40 km off the coast at Bombay (18° 51'N, 72° 49'E, 11 m ASL). The flight altitudes chosen for horizontal temperature measurements were 1.0, 1.5, 2.0, 2.5, 3.0, 3.5, 4.0, 4.5, 5.0, 6.0, 7.0, 8.0, 9.0 and 10.0 kft ASL. CCN measurements were made only at 8 of the above levels.

Temperatures were measured using vortex (dry- and wet-bulb) thermometers (Vernekar and Mohan, 1975). The data at 3 second intervals, which give a resolution of 150 metres were utilised for the spectral analysis. The vertical temperature structure of the ABL was obtained using the measurements made with a Weston (USA) make aircraft thermometer (dry-bulb). The accuracy of the temperature measurements were discussed elsewhere (Mary Selvam et al., 1980). The CCN were measured using a chemical diffusion chamber (Twomey, 1959) and the details of the measurements were described (Ramachandra Murty et al., 1978).

The spectral analysis technique used in the present study is that of Jenkinson (1975).

3.0 RESULTS AND DISCUSSION

3.1 Vertical Temperature Structure

The vertical temperature distributions obtained during the aircraft ascent and descent in the ABL are shown in Figure 1. The concentrations of CCN obtained at 0.1 per cent supersaturation are also shown in the Figure.

The ABL consisted of near isothermal layers of thickness up to 1000 ft with alternating layers having dry adiabatic lapse rate. The concentrations of CCN in general, decreased

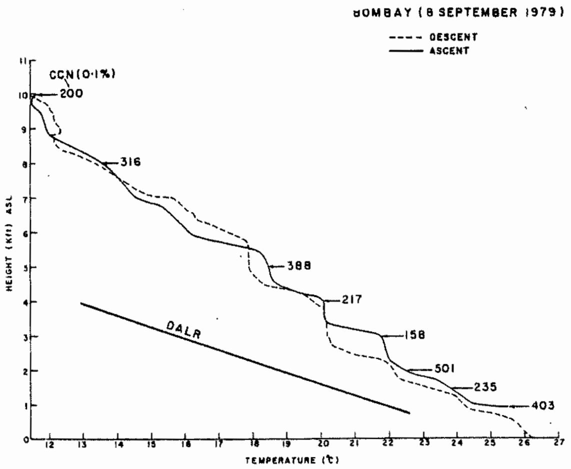

Figure 1 : Vertical distributions of dry-bulb temperature obtained during the aircraft ascent and descent. Dry adiabatic lapse rate (DALR) distribution is also shown. Figures indicate the concentration of cloud condensation nuclei (CCN) at the respective levels.

with height. However, in the regions of isothermal layers the concentrations were higher up to about 100 per cent than those in the respective preceding levels (Figure 1).

3.2 Horizontal Temperature Spectra (Dry- and Wet-bulb)

The spectra of the dry- and wet-bulb temperatures at 1, 2, 3, 5, 7 and 9 kft levels are shown as representative sample data in Figures 2-4. Both the dry- and wet-bulb temperature spectra at all the levels suggested that the wavelengths 2 km and above are significant above the white noise level (95 per cent). These wavelengths may correspond to gravity waves (see Vinnichenko et al., 1973).

Also, Grant (1965) observed moist patches of air from 1 to 3 km in horizontal extent in a sub-cloud layer and radar observations (Konrad, 1970) have suggested structure in the temperature and humidity fields on kilometre scales. The results of the present study are in agreement with those of the above studies.

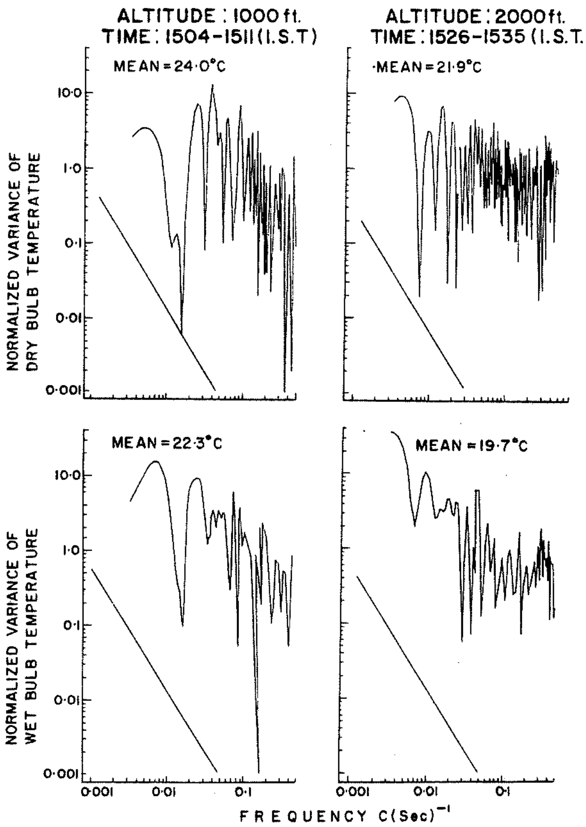

Figure 2 : Dry- and Wet-bulb temperature spectra.

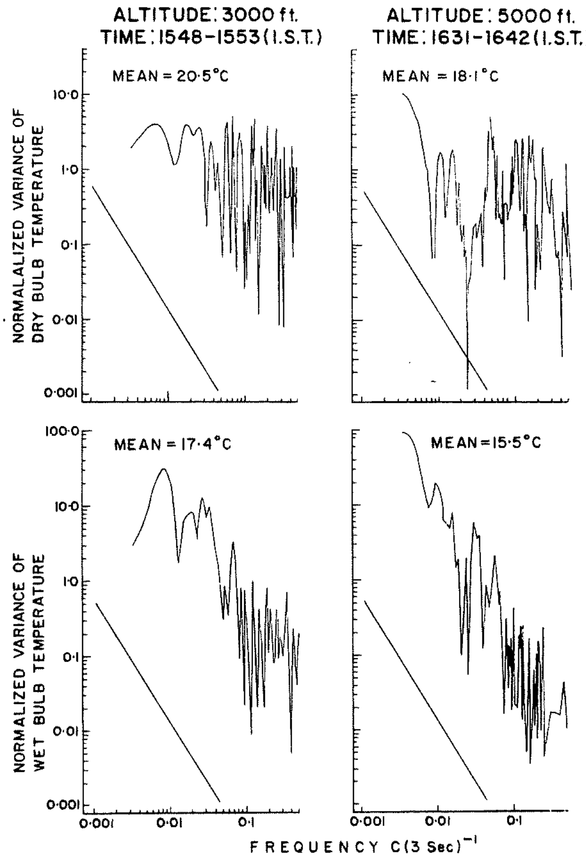

Figure 3 : Same as Figure 2.

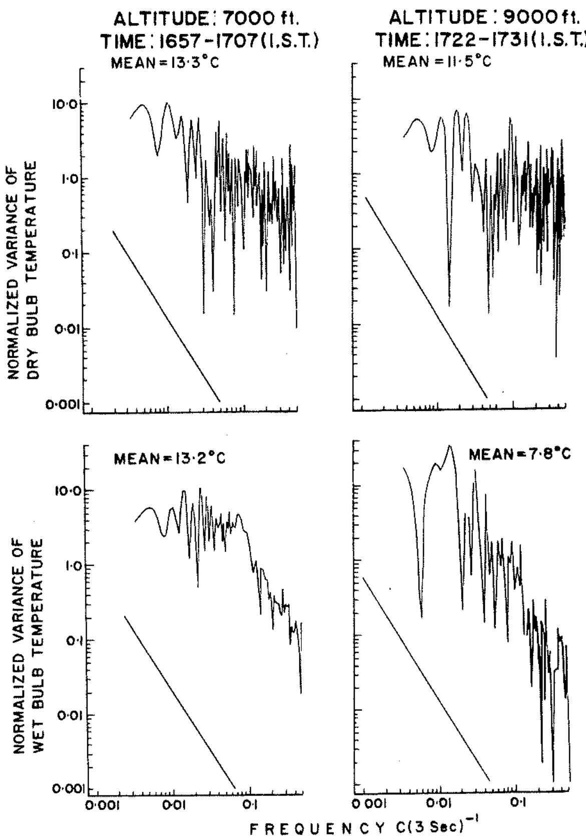

Figure 4 : Same as Figure 2.

Table 1 : Values of dry- and wet-bulb temperatures and specific humidity at different levels.

Altitude ft ASL	Dry-bulb temperature		Wet-bulb temperature		Specific humidity
	Mean °C	Variance	Mean °C	Variance	gm kgm^{-1}
1000	24.0	2.7	22.3	0.4	16.45
2000	21.9	6.7	19.7	1.8	15.14
3000	20.5	8.7	17.4	0.7	12.38
5000	18.1	2.8	15.5	0.2	11.07
7000	13.3	1.9	13.2	0.6	12.06
9000	11.5	1.0	7.8	0.2	6.50

The energy input and dissipation in the atmosphere can be studied from the slope of the temperature spectra. When the atmosphere is isotropic the energy input rate in the longer wavelength will be equal to the energy dissipation rate in the shorter wavelength and the slope of the spectrum tends to follow the -5/3 power law (Kolmogorov, 1941).

The slope of the dry-bulb temperature spectra was less than -5/3 at all the levels of observation which indicates that the dissipation of energy in the shorter wavelengths was less. The slope of the wet-bulb temperature spectra was less than -5/3 up to 3 kft (sub-cloud layer). The slope of the spectra increased with altitude above 3 kft and approached the -5/3 power law at higher levels (above 5 kft). This feature may be associated with the decrease in specific humidity with height in the atmosphere (Table 1). The slopes of the wet-bulb temperature spectra were more than those of the dry-bulb temperature spectra at all levels which may be attributed to the differences in the diffusivity of water vapour and heat in the atmosphere. The diffusivity of water vapour is slightly more than that of heat in the atmosphere (Hill, 1978).

The longer wavelengths of the temperature spectra contained more energy in the case of wet-bulb than that of dry-bulb at all levels of observation (Figures 2-4). The energy dissipation rates were less in the case of dry-bulb temperature spectra, in the air layers having near isothermal stratification (5 and 9 kft) than those observed in the air layers having dry adiabatic lapse rates (2 and 3 kft). This could be due to the stagnation of air in the isothermal layers, when vertical transport of heat flux will be inhibited. The trend is opposite in the case of wet-bulb temperature spectra. This feature was particularly marked in the shorter wavelength portion of the spectra. The opposite trends noticed in the case of dry-bulb and wet-bulb temperature spectra are consistent since mixing ratio and temperature are negatively correlated in clear air conditions (Jensen and Lenschow, 1978). As seen from the above discussion the larger variance in the dry-bulb temperature and smaller variance in the wet-bulb temperature observed in the smaller wavelengths of spectra relating to the regions of the isothermal layers (Figure 2 and Table 1) is consistent. Also, the variance of the dry-bulb temperatures was more than that of the wet-bulb temperature at all the levels (Table 1). The variance of the dry-bulb temperature was maximum at 3 kft while that of wet-bulb temperature was maximum at 2 kft (Table 1). As already mentioned, the cloud base height varies between 2 kft and 3 kft in the region. During the aircraft flight turbulence was experienced at 2 kft which was the level where the combined variance of dry- and wet-bulb temperatures was maximum (Table 1). Also, the energy level of the temperature spectra of the dry-bulb and wet-bulb in the shorter wavelength was noticed to be maximum at 2 kft (Figure 3) which is consistent with the turbulence encountered.

4.0 CONCLUSIONS

High resolution temperature observations were made in the clear air at 14 levels along aircraft flight legs of 30 km in the atmospheric boundary layer (up to 10 kft ASL) over the Arabian sea during the summer monsoon of 1979. Cloud condensation nuclei (CCN) were also measured at 8 levels. The results of the study suggested the following.

The atmospheric boundary layer consisted of near isothermal layers of thickness up to 1000 ft with alternating layers having dry adiabatic lapse rate.

The concentration of CCN decreased in general with height. In the region of isothermal layers the concentrations were higher up to about 100 per cent than those in the respective preceding levels.

All wavelengths exceeding 2 km of the dry- and wet-bulb temperature spectra at all the levels of observation are significant. These wavelengths may correspond to the gravity waves.

The slope of the wet-bulb temperature spectra increased with height and tends to -5/3 at higher levels. The slope of the dry-bulb temperature spectra was less than -5/3 at all levels. The slopes of the wet-bulb temperature spectra were more than those of the dry-bulb temperature spectra at all levels which was attributed to the differences in the diffusivity of water vapour and heat in atmosphere.

The variance of the temperature spectra of dry-bulb was higher than that of the wet-bulb and the maximum values were found at 2 to 3 kft (cloud base levels).

The longer wavelengths of the temperature spectra contain more energy in case of wet-bulb than that in the case of dry-bulb. The energy dissipation rate from the longer to the shorter wavelengths of the temperature spectra is more in the case of wet-bulb than that in the case of dry-bulb.

The slope of the dry-bulb temperature spectra in isothermal layers was less than in layers with dry adiabatic lapse rate. The slope of the wet-bulb temperature spectra showed an opposite trend to that of the dry-bulb. In isothermal layers the energy dissipation rates are less in the case of dry-bulb temperature spectra and more in the case of wet-bulb temperature spectra. This feature is more markedly seen in the shorter wavelength region of the spectra. The above result was attributed to the negative correlation which exists between the water vapour mixing ratio and temperature in clear air conditions.

REFERENCES

Ananthakrishnan, R., 1977 : Some aspects of the monsoon circulation and monsoon rainfall, PAGEOPH, 115, 1209-1249.

Berman, E.A., 1976 : Measurement of temperature and downwind spectra in the buoyant subrange, J. Atmos. Sci., 33, 495-498.

Grant, D.R., 1965 : Some aspects of convection as measured from aircraft, QJRMS, 91, 268-281.

Hill, R.J., 1978 : Spectra of fluctuations in refractivity, temperature humidity and the temperature humidity co-spectrum in the inertial and dissipation ranges, Radio Science, 13, 953-961.

Jenkinson, A.F., 1975 : Some quasi-periodic changes in rainfall in Africa and Europe, Proc. WMO/IAMAP Symp. on Long Term Climatic Fluctuations, Norwich, 18-23 August, 1975, Geneva, 453-460.

Jenson, N.O. and D.H. Lenschow, 1978 : An observational investigation of penetrative convection, J. Atmos. Sci., 35, 1924-1933.

Kolmogorov, A.N., 1941 : The local structure of turbulence in incompressible viscous fluid for very large Reynolds numbers, Doklady Akad. Nauk, SSR, 30, 301-335.

Konrad, T.C., 1970 : Dynamics of convective process in clean air as seen by radar, J. Atmos. Sci., 27, 1138-1147.

Mary Selvam et al., 1980 : Some thermodynamical and microphysical aspects of monsoon clouds, Proc. Indian Academy Sciences, A. (submitted)

Ramachandra Murty, A.S., A.M. Selvam, R. Vijayakumar and Bh.V. Ramana Murty, 1978 : Aircraft measurements on cloud condensation nuclei in maritime and continental environments "Some Problems of Cloud Physics", Academy of Sciences of the USSR.

Twomey, S., 1959 : The nuclei of natural cloud formation I : The chemical diffusion method and its application to atmospheric nuclei, Geofis. Pure Appl., 43, 227-242.

Vernekar, K.G. and B. Mohan, 1975 : Temperature measurements from aircraft using vortex thermometer, Indian J. Meteor. Hydrol. Geophys., 26, 253-258.

Vinnichauko, N.K., N.Z. Pinus, S.M. Shmeter and G.N. Shur, 1973 : Turbulence in the Free Atmosphere, Translated from Russian Consultants Bureau, New York, 264 pp.

A NUMERICAL SIMULATION OF WARM RAIN OVER HAWAII

E. C. Nickerson and D. R. Smith*

National Oceanic and Atmospheric Administration
Atmospheric Physics and Chemistry Laboratory
Boulder, Colorado

1. Introduction

Warm rain microphysical processes have been incorporated into a three-dimensional mesoscale model designed to predict airflow and clouds over complex terrain (Nickerson, 1979). The model makes use of stability dependent surface layer and planetary boundary layer formulations for the vertical fluxes of sensible heat, latent heat, and momentum. At the lower boundary the temperature, vapor mixing ratio, and surface roughness vary with position but do not change during the course of the model run.

There are 15 computational levels in the terrain following (modified sigma) coordinate system which extends through the entire depth of the atmosphere. The lowest grid level is approximately 18 meters above the lower boundary, and there are four computational levels within the lowest kilometer. The horizontal grid length is 10 km and the model domain covers an area 250 km x 250 km. Centered differences are used to represent the time derivative, except that every eighth time step a Time and Space Uncentered Matsuno procedure is introduced. The time increment has been set equal to 15 seconds.

2. Rain Water

Prediction equations for rain water mixing ratio and rain drop concentration have been derived and include the following processes: autoconversion, accretion, sedimentation, self collection, advection, and turbulent transport.

Rain water is assumed to be distributed log-normally with diameter; that is, the droplet concentration in the size range D to D + δD is given

$$\delta N_r = \frac{N_r}{\sqrt{2\pi}\,\sigma D} \exp\left[-\frac{1}{2\sigma^2}\left(\ln\frac{D}{D_o}\right)^2\right]\delta D \qquad (1)$$

where N_r is the total number concentration of droplets and σ and D_o are distribution parameters. From (1) we may derive the following expression for rain water mixing ratio:

$$q_r = \frac{N_r}{\sqrt{2\pi}\,\sigma\rho_a}\int_{D_{min}}^{D_{max}}\left(\frac{\pi D^3\rho_L}{6}\right)\exp\left[-\frac{1}{2\sigma^2}\left(\ln\frac{D}{D_o}\right)^2\right]\frac{dD}{D}, \qquad (2)$$

where ρ_a and ρ_L represent the density of air and liquid water, respectively. If D_o is sufficiently large there should be very few drops in the distribution of cloud drop size. We therefore take the limits in (2) from zero to infinity and obtain

$$q_r = \frac{N_r}{\rho}\left(\frac{\pi}{6}D_o^3\,\rho_L\right)\exp\left(\frac{9}{2}\sigma^2\right) \qquad (3)$$

Equation (3) states that q_r consists of N_r drops of diameter D_o multiplied by a factor exp $(9\,\sigma^2/2)$, where σ represents the dispersion of the distribution. It will be convenient, however, to define a mean diameter by $q_r\,\rho_a = N_r\left(\frac{\pi}{6}\bar{D}_r^{\,3}\,\rho_L\right)$, which from (3) gives

$$\bar{D}_r = D_o \exp\left(\frac{3}{2}\sigma\right) \qquad (4)$$

This diameter $\bar{D}_r$ is the diameter the rain drops would have if they were all the same size.

From (3) we see that there are two independent distribution parameters, only one of which can be diagnosed from (3) given q_r and N_r. To close the system of equations we assume σ is constant and compute $\bar{D}_r$. For the model run reported on here σ = .5, although model sensitivity studies have been carried out using other values in the range .25 to 1.0.

*Present Affiliation is the
Naval Arctic Research Laboratory
Barrow, Alaska

We have made extensive use of the work of Berry and Reinhardt (1973) in developing parameterizations for autoconversion, accretion, and self collection processes appropriate to the log-normal rain drop distribution. Because the bulk cloud water formulation to be discussed in the following section does not allow supersaturation with respect to water, we assume that diffusional growth of rain drops can be neglected. In the case of evaporation, the necessary amount of rain water to maintain water saturation is evaporated after prediction, and the rain drop concentration reduced accordingly.

3. Cloud Water

Cloud water mixing ratio q_{cw} is diagnosed from the predicted values of $W = q_v + q_{cw}$ (q_v = vapor mixing ratio) according to

$$\left.\begin{aligned} q_v &= q_{vs} \\ q_{cw} &= W - q_{vs} \end{aligned}\right\} \quad \text{if } W > q_{vs}$$

or

$$\left.\begin{aligned} q_v &= W \\ q_{cw} &= 0 \end{aligned}\right\} \quad \text{if } W \le q_{vs}$$

where q_{vs} is the saturation mixing ratio. The prediction equation for W includes the rate of conversion of cloud water to rain water by stochastic coalescence, as well as the rate of accretion of cloud water by rain water.

We assume that the average mass of the cloud droplets is constant. This seemingly crude assumption is, however, consistent with the autoconversion and accretion parameterizations of Berry and Reinhardt used in this model. They found in their numerical experiments that the average cloud droplet mass tended to remain constant throughout the formation of hydrometeors by stochastic coalescence. This assumption also saves computer time and storage.

4. Initial Conditions

The island of Hawaii (Fig. 1) has been selected as the site of this mesoscale modeling study. The twin peaks of Mauna Loa and Mauna Kea extend from sea level to 4.2 kilometers and exert a dominant influence on local rainfall patterns. The model was initialized with a single sounding in which a moist, well mixed layer is capped by a 2^oC inversion at a height of 2 kilometers. Low level winds are initially from the east at 5 m sec^{-1} changing to westerlies aloft. The low level air is close to saturation, but no clouds are present at the start of the model run.

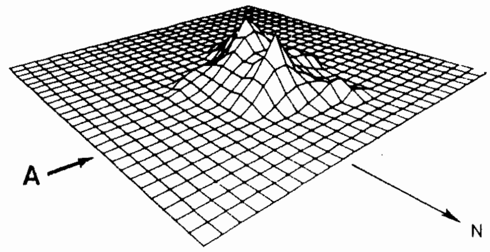

Fig. 1. Perspective view of Hawaii terrain. Locations of individual grid points coincide with the intersections of north-south and east-west lines. The letter "A" identifies the location of the vertical cross sections shown in Figs. 3 to 5 which traverse the saddle region on a west-east plane.

5. Model Results

As the moist trade wind air is forced up the mountain slopes condensation occurs and clouds first form over those areas which receive the heaviest annual rainfall. Fig. 2 shows the areal distribution of vertically integrated cloud water defined by

$$\overline{q}_{cw} = \int_0^\infty \rho_a \, q_{cw} \, dz. \tag{5}$$

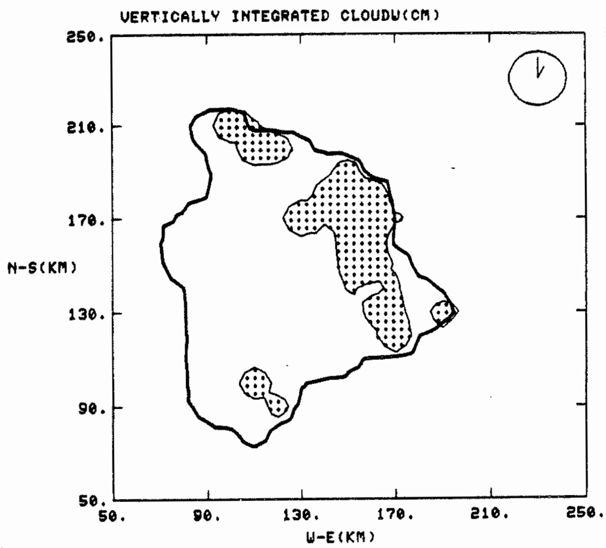

Fig. 2. Vertically integrated cloud water after one hour of model time. Shaded areas indicate values in excess of 1 cm. The maximum value is 4.1 cm.

Maxima in $\overline{q}_{cw}$ occur over the Kohala mountains in the northwest, over the windward Hilo area, and over the Kau forest area on the southeast slope of Mauna Loa. As time progresses the clouds increase in areal coverage and extend up over the saddle region between the two peaks. In addition to the above mentioned primary areas of cloudiness, smaller transient cloud masses appear which have a typical life cycle of 15 to 30 minutes.

Fig. 3 shows a vertical cross section of cloud water mixing ratio after 4 hours of model time along the west-east line denoted "A" in Fig. 1. The shaded areas indicate values in excess of 0.1 gm kgm^{-1}; however, in some portions of the cloud nearly 0.3 gm kgm^{-1} are found.

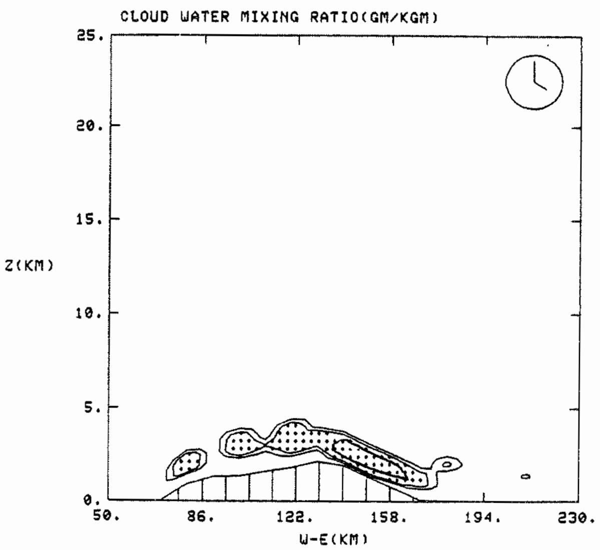

Fig. 3. Vertical cross section of cloud water mixing ratio along (A) after 4 hours of model time. The shaded areas indicate values in excess of 0.1 gm kgm^{-1}. The inner contour has a value of 0.2 gm kgm^{-1} while the outer contour has a value of 0.05 gm kgm^{-1}. The maximum value is .29 gm kgm^{-1}.

The corresponding cross sections of rain water mixing ratio and number concentration are shown in Figs. 4 and 5, where values as high as .79 gm kgm^{-1} and 365 ℓ^{-1} are found. The maximum value of $\overline{D}_r$ for this cross section is 0.27 mm. These values are consistent with observations made within the upslope orographic cloud (Fujiwara, 1967),

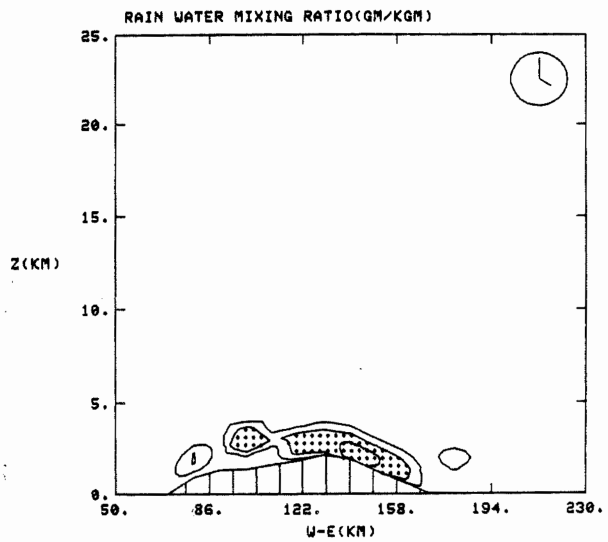

Fig. 4. Vertical cross section of rain water mixing ratio corresponding to Fig.3. The shaded areas indicate values in excess of 0.5 gm kgm^{-1}. The inner contour has a value of 0.6 gm kgm^{-1} while the outer contour has a value of 0.1 gm kgm^{-1}. The maximum value is 0.79 gm kgm^{-1}.

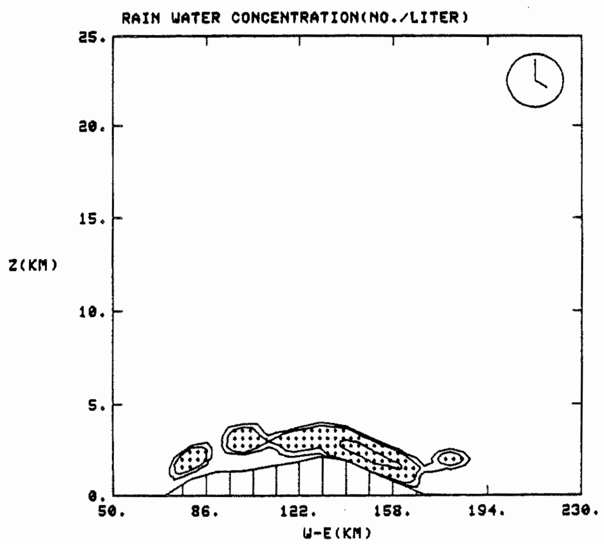

Fig. 5. Vertical cross section of rain water concentration corresponding to Fig.3. The shaded areas indicate values in excess of 100 ℓ^{-1}. The inner contour has a value of 300 ℓ^{-1} while the outer contour has a value of 50 ℓ^{-1}. The maximum value is 365 ℓ^{-1}.

The predicted rainfall distribution after 4 hours of model time is shown in Fig. 6. The maximum rainfall rates of 4 to 6 mm hr^{-1} observed during the model run are relatively light but are quite consistent with the high frequency of such events actually observed (Fullerton, 1972).

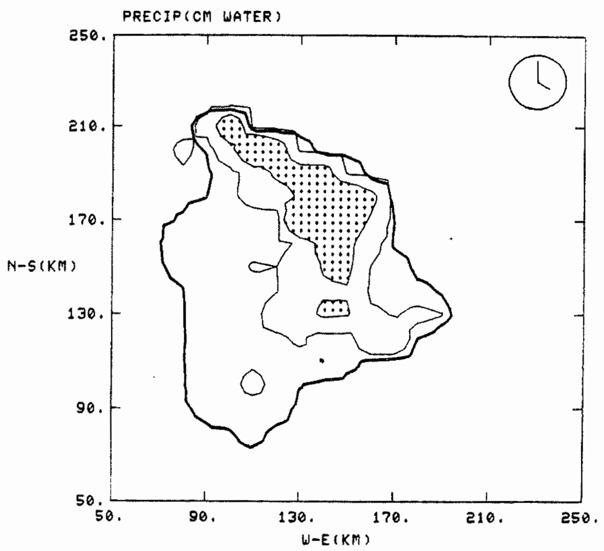

Fig. 6. Model predicted rainfall after 4 hours. The shaded areas indicate values in excess of 0.5 cm, while the outer contour has a value of 0.1 cm. The maximum value is 1.6 cm.

6. Discussion

A mesoscale model has been developed to predict rainfall from warm clouds over complex terrain. Preliminary results are encouraging, but a much more complete data set is needed to initialize and validate the model. Data gathered aboard a NOAA P3-D aircraft during the June, 1980 Hawaii Mesoscale Energy and Climate Project (HAMEC) will permit a more accurate specification of initial conditions and the subsequent assessment of model results.

7. Acknowledgements

The authors gratefully acknowledge the support and encouragement of H. K. Weickmann, C. F. Chappell, and C. S. Ramage during the course of this study.

8. References:

Berry, E. X., and R. L. Reinhardt, 1973: Modeling of Condensation and Collection within clouds, Desert Research Inst. Phys. Sci., Pub. No. 16, U. of Nevada.

Fujiwara, M., 1967: Raindrop Size Distribution in Warm Rain as measured in Hawaii. Tellus, 19, 392-401.

Fullerton, C. M., 1972: A Rainfall Climatology of Hilo, Hawaii. U. of Hawaii Tech. Rept. No. 61. UHMET 72-03.

Nickerson, E. C., 1979: On the Numerical Simulation of Airflow and Clouds over Mountainous Terrain. Beit. Zur Physik der Atmos., 52, 161-177.

THE EFFECT OF MELTING PARTICLES ON THE THERMODYNAMIC AND MICROPHYSICAL CHARACTERISTICS OF SIERRA NEVADA WINTER STORMS

J. C. Pace and R. E. Stewart

Department of Atmospheric Science
University of Wyoming
Laramie, Wyoming, U.S.A.

1. INTRODUCTION

Widespread stratiform-like storms often occur in the wintertime in the vicinity of the Sierra Nevada Mountains. Observations made within the Sierra Cooperative Pilot Project (SCPP), have indicated that isothermal or near isothermal layers near 0°C are often present within such storms. These layers are generally caused by melting particles.

The objective of this paper is to elucidate a few of the thermodynamic and microphysical effects associated with the evolution and presence of this melting-produced feature. Features discussed in the paper were measured with instruments on board the University of Wyoming's King Air (Cooper, 1978; Marwitz et al., 1978) during the last three field seasons of the SCPP.

2. TYPICAL TEMPERATURE PROFILE

Fig. 1 shows an ascent sounding in a stratiform storm on March 2, 1978. Features of the sounding are very typical for such situations. Precipitation was falling at 2-4 mm per hour and had been doing so for several hours previous to the aircraft's ascent. The atmosphere was saturated with respect to water from the surface to 690 mb, and cloud top was colder than -15°C.

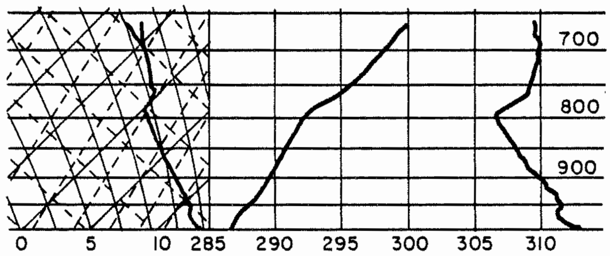

Fig. 1 Ascent sounding made on 2 March 1978. Isopleths shown, left to right, are dewpoint temperature (°C), temperature (°C), potential temperature (°K), and equivalent potential temperature (°K). Vertical axis is pressure (mb).

A near isothermal layer existed between about 785 and 765 mb (∿ 200 m) at a temperature very close to 0°C. As shown in the temperature and equivalent potential temperature (θ_e) profiles, a dramatic alteration of the environmental lapse rate had occurred in the vicinity of the 0°C layer. The minimum value of θ_e occurred near the base of the 0°C isothermal layer, and the associated maximum θ_e depression, relative to the atmosphere above the melting layer, was 2-3°K. Similar observations have been made numerous times in soundings attained in this type of widespread precipitation (Marwitz et al., 1978).

It is believed that melting particles were mainly responsible for the observed lapse rate alterations near the 0°C layer. Melting is a diabatic process which cools air toward 0°C and decreases θ_e values in proportion to the temperature change. As seen in Fig. 1, the effect of this is to increase convective stability ($\frac{d\theta_e}{dz} > 0$) above the 0°C layer and to increase convective instability ($\frac{d\theta_e}{dz} \leq 0$) below this layer. This fact was originally recognized by Findeisen (1940) and the pressure perturbations accompanying melting were the main thrust of an excellent article by Atlas et al. (1969).

3. THEORETICAL DEVELOPMENT

A simple model has been developed to examine the evolution of the melting layer. The model equates the energy absorbed by a flux of melting particles as they fall into air warmer than 0°C to the amount of energy required to cool the surrounding air. It is assumed that particles melt as soon as they encounter air warmer than 0°C. Account is made as to whether the air is initially saturated or not. Condensation of water vapor in saturated air involves release of latent heat of vaporization, which reduces the cooling effect of melting by about 50%. Evaporation of melted snow in unsaturated air involves absorption of latent heat of vaporization. This can cause additional cooling and increase the depth of the isothermal layer. However, evaporation of melting snow is usually not a consideration in Sierra Nevada storms since the atmosphere is typically saturated through the 0°C layer (Marwitz and Stewart, 1979).

The depth of the isothermal layer as a function of the amount of melted snow for unsaturated, just saturated, and saturated environments is shown in Fig. 2. In constructing the figure, initial lapse rates of 6°C/km were assumed for all cases in order to isolate and examine the effects of varying the saturation. In the just saturated example, it was assumed that the air in the melting layer was being saturated by the cooling so that condensation of water vapor and evaporation of melting snow were not considered (Atlas et al., 1969). In the unsaturated case, the unrealistic assumption was made that all the melted snow evaporated within the final depth of the isothermal layer. Thus, this case serves as an upper limit to the layer thickness that can be produced by melting snow.

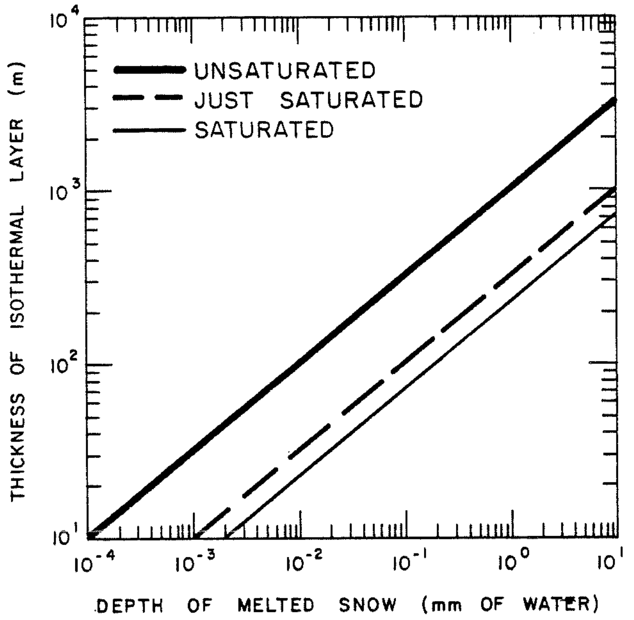

Fig. 2 Thickness of the 0°C isothermal layer vs. accumulated depth of melted snow for three atmospheric conditions.

Several insights into the effects of melting particles on the vertical structure near the 0°C layer can be gleaned from Fig. 2. First, very small amounts of ice can produce significant isothermal layers. In just saturated air, a 100 m deep isothermal layer is produced by only 0.1 mm of water. Second, for a given mass of melted ice, the isothermal layer is much deeper if melting occurs in unsaturated air. For example, with 1 mm of water, the isothermal depth in unsaturated air is 1000 m while in saturated air it is only about 230 m. Third, the figure also implies that significant isothermal layers can be produced within extremely short time periods. At a rainfall rate of 1 mm per hour (relatively low for many stratiform storms), a 100 m deep isothermal layer would be produced in 6 minutes in just saturated air and in 12 minutes in saturated air. At a rainfall rate of 10 mm per hour, the computed times would only be a tenth as large. Fourth, comparison of the just saturated and saturated cases illustrates that the inclusion of the latent heat of vaporization significantly reduces the rate at which the isothermal layer is produced. For example, 1 mm of water produces a 320 m isothermal layer in a just saturated environment and one only 70% as deep within a saturated environment. Fifth, in steady precipitation, the rate at which the 0°C layer is produced decreases with time. For example, with a constant rainfall rate of 1 mm per hour in just saturated air, a 100 m thick isothermal layer will be produced in only 6 minutes, whereas a layer twice as deep requires four times as long to be developed.

4. DISCUSSION

Isothermal layers up to 200-300 m thick have commonly been observed in Sierra Nevada widespread storms, although the model has predicted that much thicker layers could be produced within minutes in moderate precipitation. As first suggested by Findeisen (1940), this discrepency can be at least partially explained by the development of convection at the melting layer. This counteracts the cooling effect of melting and erodes the isothermal layer from below. This convection must obviously be initiated very soon after melting commences. Such convection has often been observed in the SCPP, and it rarely extends above the -5°C level (Marwitz et al., 1978). It is not known why 200-300 m is generally the upper limit to isothermal depths as opposed to much deeper layers.

Several microphysical characteristics appear to be affected by the melting layer. First, significant amounts of supercooled liquid water ($\gtrsim$ 0.1 g m^{-3}) are often only found within these stratiform storms in the convection tied to the destabilization caused by melting. Second, the largest ice crystal concentrations within the storms (sometimes up to 100 ℓ^{-1}) are also typically found just above the melting layer in connection with this convection whereas concentrations of ice crystals higher in the cloud are usually about 20 ℓ^{-1}. Large numbers of warm temperature columnar crystals are responsible for the increase in concentration, but it is not known how this apparent ice crystal multiplication process operates. Third, aggregational growth is occurring in the vicinity of the melting layer. Although speculative at this time, it may be that very large aggregates ($\gtrsim$ 1-2 cm) are only produced when a substantial melting layer is present.

In summary, this preliminary analysis has shown that melting particles affect the thermodynamic and microphysical aspects of Sierra Nevada stratiform storms. As discussed by Marwitz and Stewart (1979), melting can also affect the dynamics of these clouds. Further research will lead to a better understanding of the implications of melting particles on each of these areas.

5. ACKNOWLEDGMENTS

The authors gladly acknowledge the many helpful discussions with John Marwitz. This research was funded by the Division of Atmospheric Water Resources Management, Water and Power Resources Services, Department of the Interior. Contract 7-07-83-V0001.

REFERENCES

Atlas, D., R. Tatehira, R. C. Srivastava, W. Marker, and R. E. Carborne, 1969: Precipitation-induced mesoscale wind perturbations in the melting layer. Quart. J. Roy. Meteor. Soc., 95, 544-560.

Cooper, W. A., 1978: Cloud physics invistigations by the University of Wyoming in HIPLEX 1977. Report No. AS119 to Div. Atmos. Water Res. Mgmt., Bur. of Rec., Dept. of Int. Contract No. 7-07-93-V0001, August, 1978.

Findeisen, W., 1940: The formation of the 0°C isothermal layer and fracto-cumulus under nimbostratus. Met. Zeit., 57, 49-54.

Marwitz, J. D., R. E. Stewart, T. S. Karacostas, and B. E. Martner, 1978: Cloud Physics Studies in SCPP During 1977-78. Report No. AS121 to Div. of Atmos. Res. Mgmt., Bur. of Rec., Dept. of Int. Contract No. 7-07-93-V0001, September, 1978.

Marwitz, J. D., R. E. Stewart, 1979: Description of cloud types in Sierra Nevada winter storms. Seventh Conf. on Inadv. and Planned Wea. Modif., Banff, Canada, October, 1979.

CHARACTERISTICS OF TEMPERATURE SPECTRA IN THE ATMOSPHERIC BOUNDARY LAYER

S.S. Parasnis, A. Mary Selvam, K.G. Vernekar, Brij Mohan,
A.S. Ramachandra Murty and Bh.V. Ramana Murty

Indian Institute of Tropical Meteorology, Poona - 411005, India.

1. INTRODUCTION

Study of the horizontal temperature spectra in the atmospheric boundary layer would be valuable for the understanding of the dynamical characteristics of the atmosphere. It is known that one-dimensional spectra of clear air temperature obey the -5/3 power law in the inertial subrange (Kolmogorov, 1941). Weinstock (1978) attributed the slopes of the spectra higher than -5/3 to the decay of turbulence and the slopes lower than -5/3 to the growth of turbulence.

Temperature observations in clear air were obtained in the horizontal during continuous aircraft flights made over the Arabian sea, across the Western Ghats and the Deccan Plateau in the summer monsoons of 1973, 1974 and 1976. The characteristics of the horizontal temperature spectra over the above three locations showed differences. Observations were also made of the vertical temperature structure over the Deccan Plateau. The results of the study are presented below.

2. MEASUREMENTS AND ANALYSIS

Observations were made in the regions over (i) Arabian sea, 50 km off the coast at Alibag, (ii) Alibag (18° 38'N, 72° 52'E, 7 m ASL), (iii) Pali (18° 35'N, 73° 25'E, $\simeq$ 150 m ASL), about 50 km inland on the windward side of the Western Ghats, (iv) Mulshi (18° 32'N, 73° 37'E 662 m ASL), crest of the Western Ghats, and (v) east of Poona (18° 32'N, 73° 51'E, 559 m ASL) in the Deccan Plateau. The locations are shown in Figure 1.

The air flow in the region during the period of observations was westerly in the lower troposphere. The average heights of cloud bases over the Arabian sea, Western Ghats and the Deccan Plateau are respectively 2 kft, 8 kft and 7 kft (Mary Selvam et al., 1980; Parasnis et al., 1980a). The characteristics of the monsoon circulation and the monsoon rainfall were discussed (Ananthakrishnan, 1977). The effects of orography in the region on certain meteorological parameters were studied (Sarker, 1966).

The details of the vortex thermometer which was used for temperature measurements in the horizontal were described (Vernekar and Mohan, 1975). The data points extracted at 3 seconds interval, which correspond to a resolution of 150 m, were considered in the study. A Weston (USA) make aircraft thermometer was used for the measurement of temperature in the vertical. Details were given of the accuracy of temperature measurement (Mary Selvam et al., 1980) and the power spectral analysis technique (Sadani et al., 1979; Parasnis et al., 1980b) adopted in the study.

3.0 RESULTS AND DISCUSSION

3.1 Horizontal Temperature Structure

The horizontal temperature spectra obtained at different levels over the Arabian sea and across the Western Ghats are shown in Figures 2-7. The flight altitudes are also shown in the figures. All the spectra suggested that the wavelength of 2 km is significant at the white noise level (95 per cent) which may be attributed to the internal gravity waves (see Gossard et al., 1970; Stilke, 1973). The characteristics of the spectra obtained at different locations are discussed below.

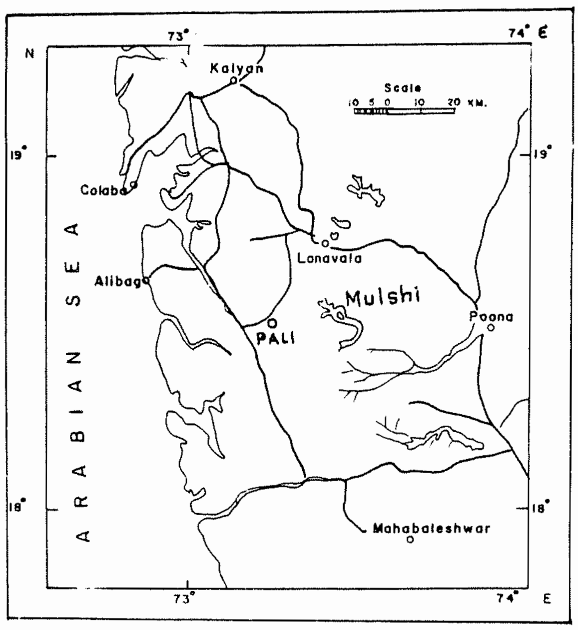

Figure 1 : Location of places of observations

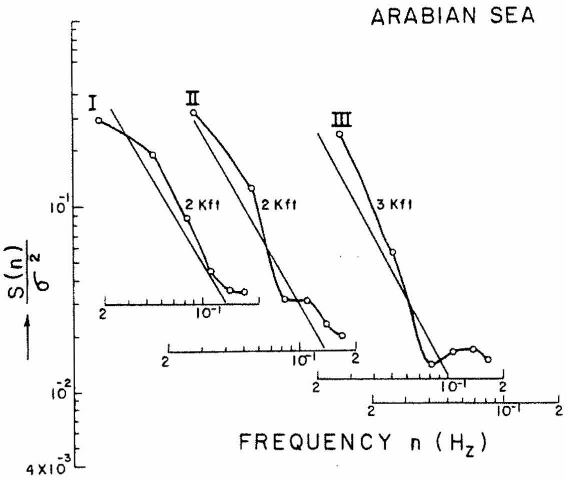

Figure 2 : Temperature spectra. The lines correspond to -5/3 power law.

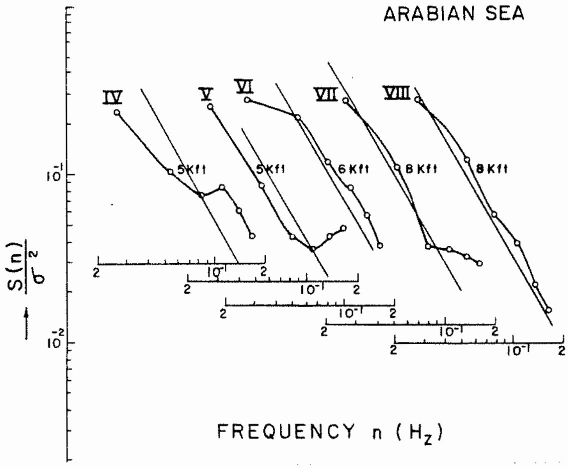

Figure 3 : Same as Figure 2.

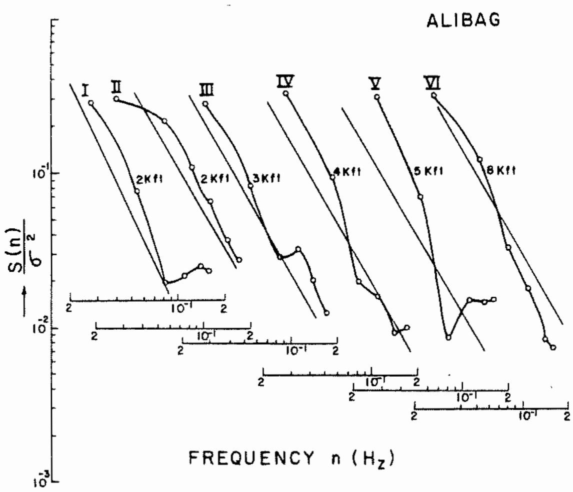

Figure 4 : Same as Figure 2.

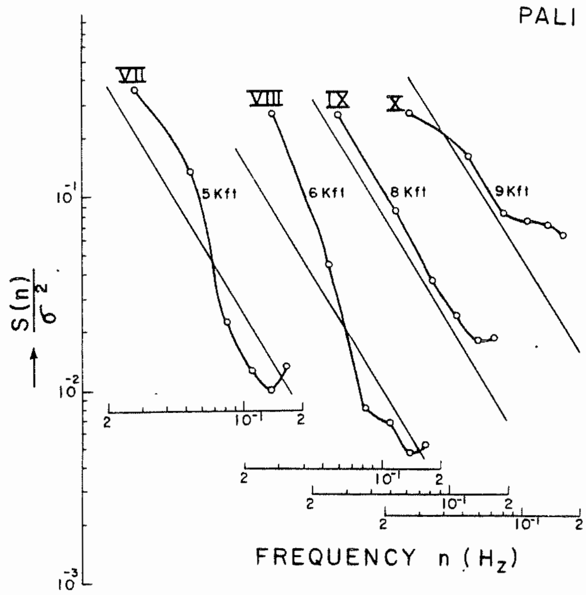

Figure 5 : Same as Figure 2.

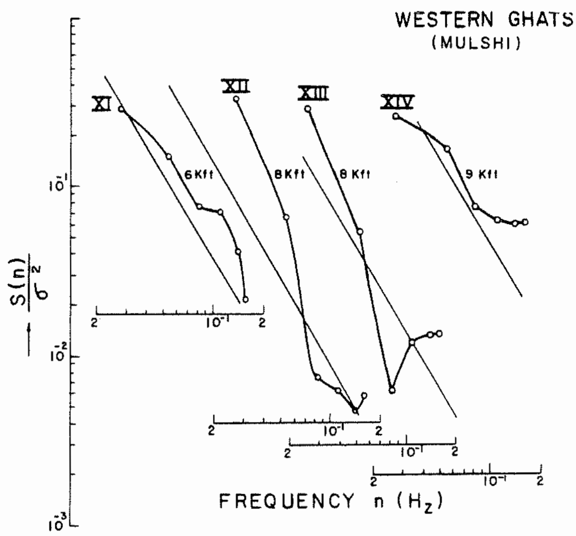

Figure 6 : Same as Figure 2.

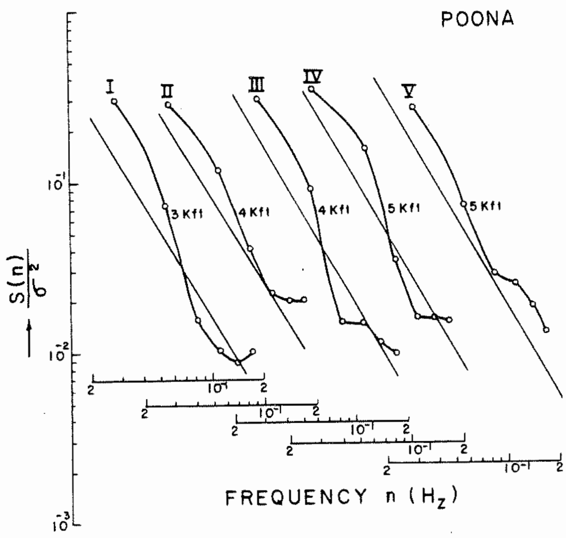

Figure 7 : Same as Figure 2.

3.1.1 Arabian Sea

The spectra are shown in Figures 2 and 3. The spectra at 2 kft (I and II) and 3 kft (III) showed steeper slopes than -5/3 power law in the wavelength range 1 km-540 m. The slope was lower than -5/3 in case of the spectra at 5 kft (IV) in the wavelength range 1 km-540 m. A feeble secondary peak was observed in the spectra at 2 kft (II), 3 kft (III) and 5 kft (IV), in the wave-length range 540 m-350 m, but it was not present at higher levels. The secondary peak may represent the thermal bubble which gives rise to clouds (Jensen and Lenschow, 1978). The spectra at 6 and 8 kft (VI to VIII) followed the -5/3 power law in the wavelength range 1 km-350 m. The steeper slope of the spectra exceeding -5/3 at the lower levels (below the cloud base levels) indicates higher energy dissipation rate leading to the decay of turbulence. At higher levels (6 and 8 kft) the slope almost approached the -5/3, which indicates that there is a balance between the energy input and dissipation.

3.1.2 Alibag

The spectra are shown in Figure 4. The slope was steepest at 5 kft. The spectra exhibited a secondary peak at 2 kft (I), 3 kft (III) and 5 kft (V). The slope was nearly equal to -5/3 at 8 kft.

3.1.3 Pali

The spectra are shown in Figure 5. The slopes were steeper than -5/3 in case of the spectra at 5 kft (VII) and 6 kft (VIII) in the wavelength range 1 km-540 m. The slope was nearly equal to -5/3 in case of the spectra at 8 kft and 9 kft. The secondary peak was absent.

3.1.4 Western Ghats (Mulshi)

The spectra are shown in Figure 6. The characteristics of the spectra are different from those observed at other locations, which may be due to the effect of orography. The slope was steeper than -5/3 in case of the spectra at 8 kft (XII and XIII) in the wavelength range 1 km - 540 m. A feeble secondary peak was noticed at 6 kft (XI) in the wave-length range 540 m-350 m. The slope of the spectra at 9 kft is nearly equal to -5/3.

3.1.5 Poona

The spectra are shown in Figure 7. In general, the slope of the spectra were steeper than -5/3 in the wavelength range 1 km-540 m at all the levels.

3.2 Vertical Temperature Structure

The temperature profiles obtained over the Deccan Plateau (east of Poona) during the aircraft ascents and descents in the atmospheric boundary layer (up to 10,000 ft ASL) are shown in Figures 8 and 9.

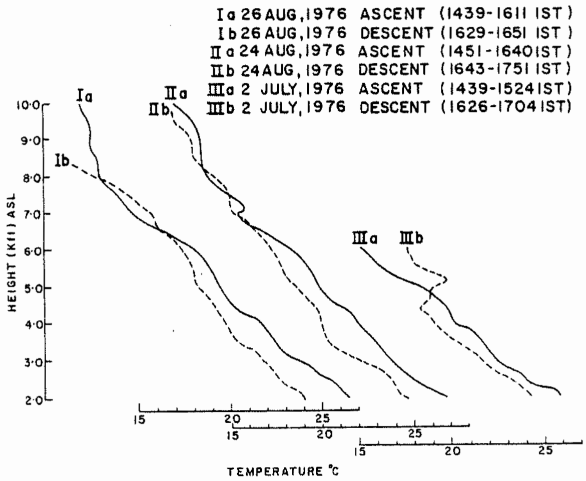

Figure 8 : Vertical temperature profiles

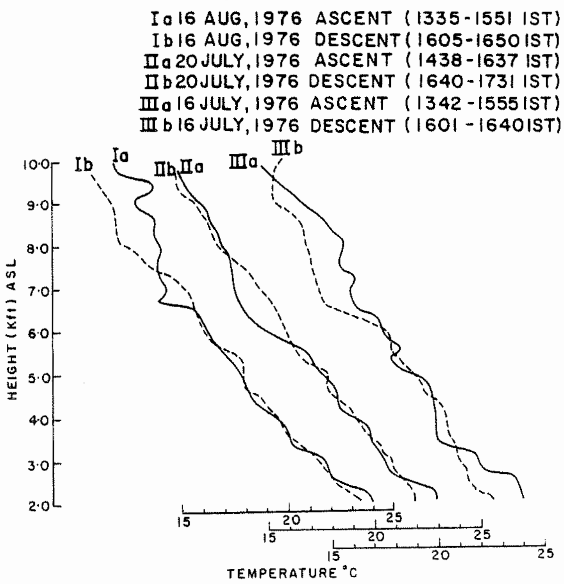

Figure 9 : Same as Figure 8

In general the ABL consisted of nearly isothermal layers of about 1500 ft thickness with alternating layers of saturated adiabatic lapse rate when the monsoon was active in the region of observations. The locations of the near isothermal layer did not show marked change in their altitude on different days of observation. This feature is attributed to the nearly similar meteorological conditions prevailed on those days.

4.0 CONCLUSIONS

Temperature measurements were made from aircraft up to 10,000 ft over the regions of Arabian sea, Western Ghats and Deccan Plateau. The horizontal and vertical temperature structures of the atmospheric boundary layer were investigated. The study suggested the following.

i) The horizontal temperature spectra suggested that the wavelength of 2 km is highly significant which may be attributed to the gravity waves.

ii) A secondary peak was observed in the spectra in the wavelength range 540 m-350 m at levels lower than the cloud base level which may represent the thermals in the atmosphere.

iii) Over the Arabian Sea the slopes of the temperature spectra were steeper than -5/3 at levels lower than the cloud base level. At higher levels the slope nearly tends to the -5/3 power law. Over the Deccan Plateau the slopes were steeper than -5/3 at all levels.

iv) During the active monsoon conditions the ABL over the Deccan Plateau consisted of nearly isothermal layers of about 1500 ft thickness with alternating layers of saturated adiabatic lapse rate.

ACKNOWLEDGEMENT

The above observations were carried out as a part of one of the research programmes of the Institute for which Dr. K. Krishna was the Project Leader.

REFERENCES

Ananthakrishnan, R., 1977 : Some aspects of the monsoon circulation and monsoon rainfall, PAGEOPH, 115, 1209-1249.

Gossard, E.E., J.H. Richter and D. Atlas, 1970 : Internal waves in the atmosphere from high resolution radar measurements, J. Geophys. Res., 75, 3523-3536.

Jensen, N.O. and D.H. Lenschow, 1978: An observational investigation of penetrative convection, J. Atmos. Sci., 35, 1924-1933.

Kolmogorov, A.N., 1941 : The local structure of turbulence in incompressible viscous fluid for very large Reynolds numbers, Dokl. Akad. Nauk SSSR, 30,301-335.

Mary Selvam, et al., 1980 : Some thermodynamical and microphysical aspects of monsoon clouds, Proc. Indian Academy Sciences, A, (submitted).

Parasnis, S.S., A. Mary Selvam, C.S. Bhosale and Bh.V. Ramana Murty, 1980(a) : Some thermodynamical aspects of the atmospheric boundary layer in the Arabian sea region during the summer monsoon, National Space Sci.Symp. Jan 22-25, 1980, Varanasi, India.

Parasnis, S.S., K. Krishna and B. Mohan, 1980(b) : Temperature stratification of the atmospheric boundary layer over the Deccan Plateau, India, during the summer monsoon, Boundary Layer, Meteor., 18 (in press).

Sadani, L.K., K. Krishna, K.G.Vernekar C.P. Kulkarni and S.S. Parasnis, 1979 : Temperature fluctuations in a cloud laden air over a hill station, Boundary Layer Meteor., 17, 203-212.

Sarker, R.P., 1966 : A dynamical model of orographic rainfall, Mon. Wea. Rev., 94(9), 555-572.

Stilke, G., 1973 : Occurrence and features of ducted modes of internal gravity waves over Western Europe and their influence on microwave propagation, Boundary Layer Meteor., 4, 493-509.

Vernekar, K.G. and B. Mohan, 1975 : Temperature measurements from aircraft using vortex thermometer, Ind. J. Meteor. Hydrol. Geophys., 26, 253-258.

Weinstock, J., 1978 : On the theory of turbulence in the buoyancy subrange of stably stratified flows, J. Atmos. Sci., 35,634-649.

WARM RAIN STUDY IN HAWAII

T. TAKAHASHI

Cloud Physics Observatory
Hawaii U.S.A.

1. Introduction

The ease with which rain forms and falls from shallow clouds over oceanic tropical regions has intrigued many investigators. Squires (1958) found a low concentration and broad size distribution of cloud droplets in the air over tropical oceans. Juisto (1967) and Twomey and Wojciechowski (1969) measured a low concentration of cloud nuclei in the maritime air mass. Brown and Braham (1959) measured drizzle size distributions in clouds above the Carribean Sea, while Blanchard (1953) observed raindrop size distributions beneath the cloud base at the ground in Hawaii. Recently, Takahashi (1977) used aircraft to sample rainfall just beneath the cloud base and found major differences in the rainfall pattern between isolated clouds and band clouds. While past studies have contributed to our understanding of the characteristics of warm rain, these studies have been fragmentary insofar as they concentrated on only a portion of the drop size range and life cycle during rain development.

The purpose of the present work was to study the mechanism of warm rain development, from cloud droplet to raindrop, by measuring a wide range of drop sizes at critical locations and stages of the cloud life cycle. These measurements are then compared with the results derived from the author's three dimensional warm rain model (Takahashi, 1980).

2. Aircraft Operation

To define the initial state of droplets it was necessary first to measure the distribution of cloud droplet size near the cloud base. To verify the cloud model result (Takahashi, 1973, 1974, 1975, and 1976) that major drop growth occurs near the cloud top, drop observations were taken at the cloud top throughout the entire cell life. When the cloud cell dissipated, the aircraft quickly descended to the cloud base and made successive traverses beneath the base to measure the amount of rainwater (Fig. 1).

All observations were made over the ocean upwind of Hilo, Hawaii. The cloud base was typically 600 m; the cloud top 3 km (10°C).

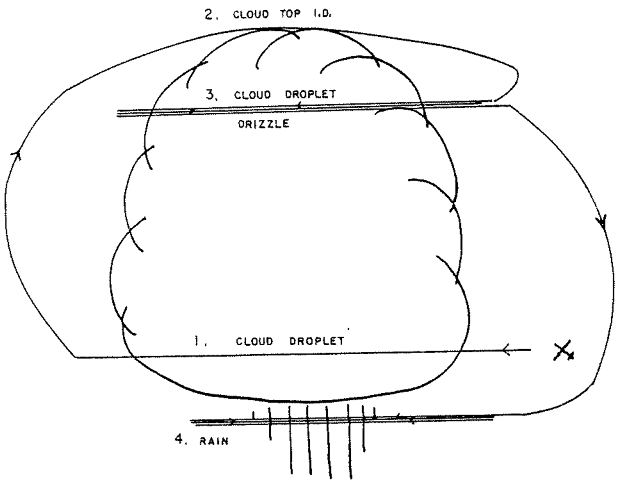

Fig. 1: Flight path during operation:
1. cloud droplet sampling near cloud base (100 m above the base).
2. cloud top identification.
3. successive traverses near cloud top (200 m below cloud top) to measure both cloud droplets and drizzle during entire cloud top cell life.
4. successive traverses beneath cloud base to observe maximum rainfall intensity.

3. Instruments (Photo 1A-C)

The major instruments employed were a cloud droplet sampler, a drizzle sampler, and a rainwater collector.

The cloud droplet sampler has forty thin glass plates (3 mm long, 35 mm wide) coated with a carbon film (Neiburger, 1949). Each plate is attached to an alluminum slide (50 mm x 50 mm) on the lower end of an open frame (11 mm long, 33 mm wide). They were inserted into a modified commercial slide projector. Each slide was exposed for a short time to air flowing through a 50 mm square intake.

The drizzle sampler also contains forty slides (25 mm wide, 50 mm long) coated with a thin layer of vegetable oil (Crisco shortening). As drizzle strikes the coated surface, clear circular traces form with drops larger than 200 μm. At no time did cloud droplets activate the oil surface.

The rainwater collector contains a copper plate angled low in the direction of incoming air. The intake section is 10 cm deep and 25 cm wide. As raindrops strike the plate, a thin layer of water forms. This layer of water flows up and over the plate and drains into a tube where it is measured by the capacitance method (Takahashi, 1977).

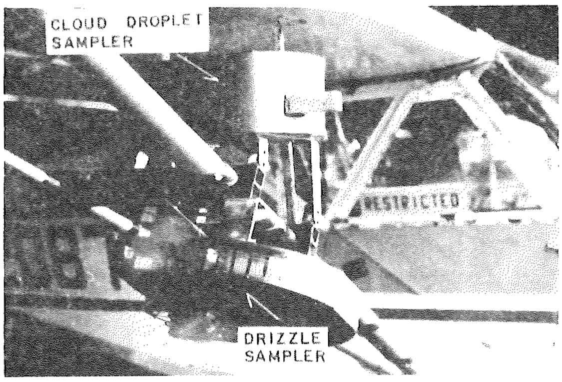

IA

IB

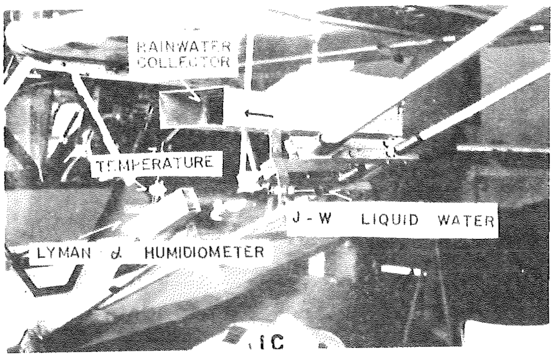

Photo 1A: *Cloud droplet sampler (soot method) and drizzle sampler (Crisco shortening).*
Photo 1B: *Drizzle traces on the glass plate.*
Photo 1C: *Rain-collector, temperature and humidity instruments. Cloud size was identified by the Johnson-Williams hot wire instrument.*

Other airborne instruments used include a variometer to measure the rate of aircraft climb, a Johnson-Williams heated-wire instrument to measure the cloud droplet water content and to identify the cloud size, a back flow type temperature measuring instrument and a Lyman-α humidiometer. All these instruments were installed on the strut of the aircraft (Stensen L-5 or Cessna 182).

4. Results

Cloud droplet size distributions near the cloud base generally are similar even at different locations. Large droplets at very low concentration were occasionally observed. In all probability these large droplets grew on giant nuclei. At higher altitudes, the condensation-collection growth of smaller cloud droplets results in a greater number of large cloud droplets; consequently, the contribution of the few large cloud droplets formed earlier on giant nuclei is negligible for drizzle growth. This result was suggested by the author's cloud model (Takahashi, 1976; Takahashi and Lee, 1978). Cloud droplets exhibit broader spectra as the peak droplet size exceeded 30 μm in diameter during upward movement.

Near the cloud top, a bimodal distribution of cloud droplets is commonly observed (Warner, 1969). Except at the extreme edges of the cloud, where large cloud droplets are abundant, cloud droplet size distributions near the cloud top resemble one another, even at different times and locations.

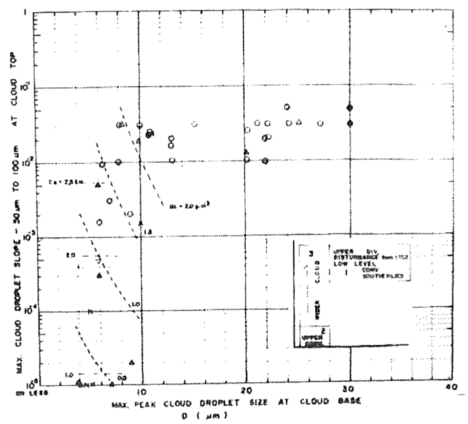

Fig. 2: *Maximum broadening of cloud droplet size distribution near the cloud top (ratio of number concentration of 100 μm to 50 μm cloud droplet) and maximum peak cloud droplet size near cloud base. Maximum cloud droplet water contents (Qc) were also shown. The value 3.3 g m^{-3} was observed when maximum peak droplet size at cloud base was 27 μm in diameter (April 11, 1979). Cloud size at cloud base of isolated cloud was shown by Cs.*

The cloud droplet size distribution near the cloud top, however, is largely determined by the cloud droplet size distribution near the cloud base. Large droplets near the cloud base induced large droplet broadening near the cloud top. Large cloud droplets at the cloud base were observed during particular synoptic patterns. When the upper cyclone is located northwest of the Hawaiian Islands and the upper level southwesterlies from the near-equatorial ridge blow strongly from the southern edge of the island chain, upper air divergence forms upwind of the islands. During this process the inversion layer lifts, allowing moist air to fill the trade wind layer. Large cloud droplets form near the cloud base (Fig. 2).

Two other processes may cause the formation of large cloud droplets near the cloud base. With low level convergence, formed by the sea breeze-land breeze interaction, the cloud base is lowered a few hundred meters. Large cloud droplets form because of the deeper cloud depth. In the second case, when southerlies prevail, cloud droplets grow large during horizontal movement through clouds developed along the wind direction.

When upper level convergence is formed by the combination of the polar westerlies, from the mid-latitudes, and the upper southwesterlies, from the near-equatorial ridge, the inversion layer lowers and the trade wind layer dries. In this case, only small droplets are observed near the cloud base.

Drizzle size drops were observed in the updraft column during the developing stage, when the cloud base droplets were large and cloud droplet broadening was pronounced near the cloud top (Fig. 3).

Within such a shallow layer (about 200 m), the drizzle-raindrop water content is increased by one order of magnitude during the cell life. Raindrops are commonly observed near the cloud top when the drizzle water content is greater than 0.1 gm $^{-3}$. The sudden increase in rainwater probably is due to the interaction of drop growth and the airflow pattern. The drizzle water content must be high enough to permit the development of large drops (formation of secondary peak raindrops) which can float against the updraft. Otherwise, the drops would be expelled from the cloud top. (Fig. 4-5).

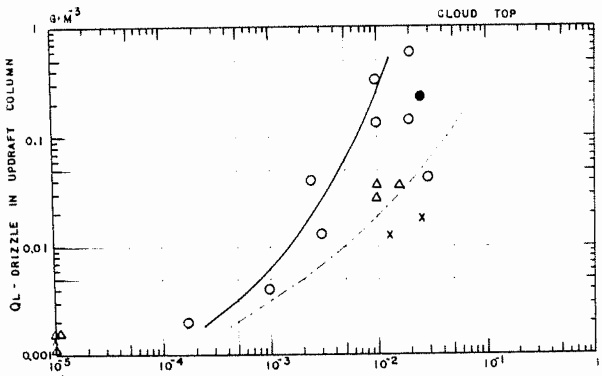

Fig. 3: Maximum value of broadening of cloud droplets and maximum drizzle water content in updraft column at the developing stage near cloud top. Solid line shows the results by 3D model.

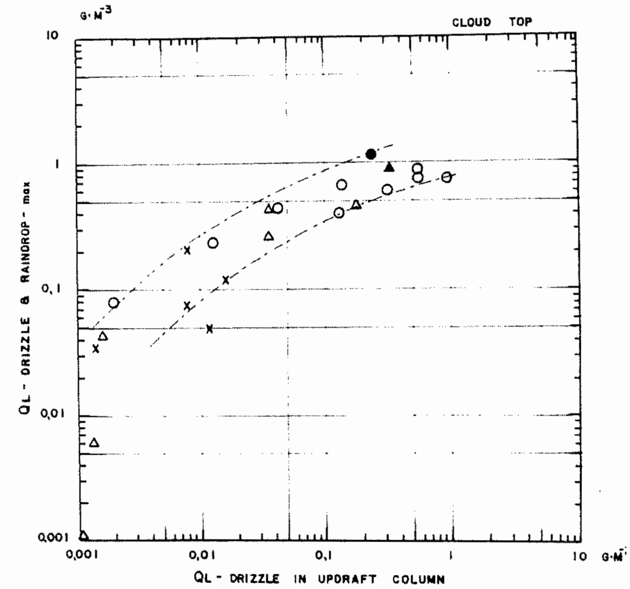

Fig. 4: Maximum drizzle water content in updraft column at developing stage and maximum water content of drops larger than drizzle size near the cloud top during entire cell life.

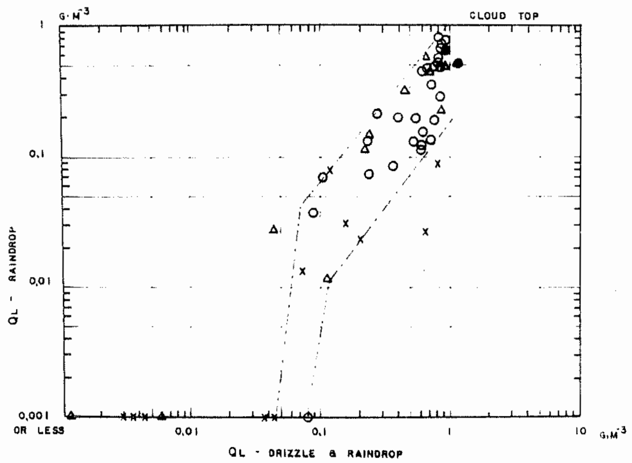

Fig. 5: Maximum raindrop water content and maximum drizzle-raindrop water content near the cloud top.

Rainfall occurs when the raindrop water content at the cloud top exceeds 0.1 gm^{-3}. The amount of rain depends on the cloud type. For example, tilted clouds produce little or no rain. In general, rain from band clouds is heavier than rain from isolated cumuli. Findings were compared with the output of the three dimensional, shallow-anelastic cloud model where drops are classified into 59 groups (Fig. 6-7).

The general pattern, such as the growth rate of peak cloud droplets during upward movement, droplet broadening when the peak droplet size becomes larger than 30 μm in diameter and the high accumulation rate of drops near the cloud top, was well simulated. However, the observed raindrop size distribution is much sharper than the model-predicted distribution, probably because the collision-breakup process

(McTaggart-Cowan and List, 1975; Takahashi, 1978) is neglected in the model.

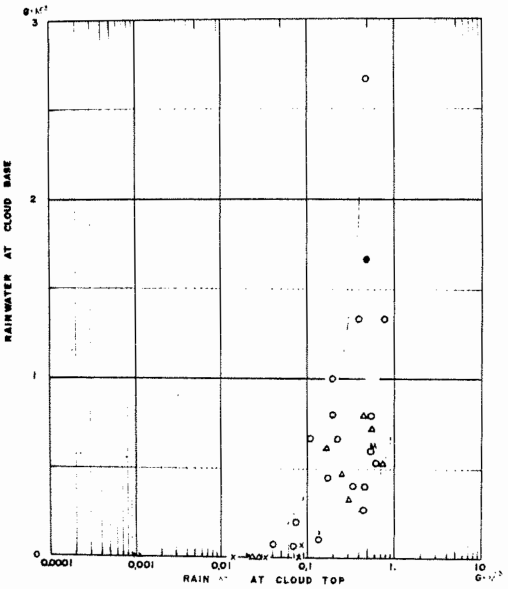

Fig. 6: Maximum rainwater contents near the cloud top and beneath the cloud base.

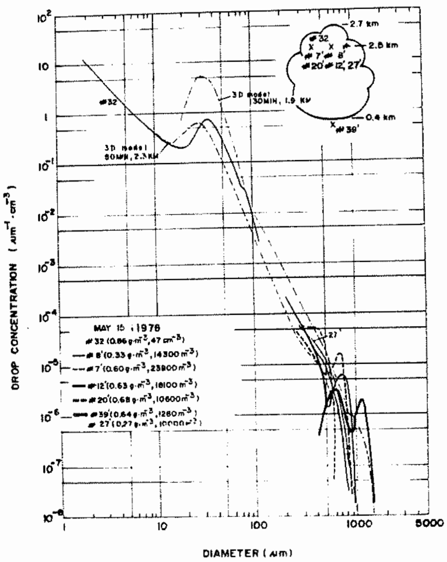

Fig. 7: Cloud droplet size distribution near the cloud top (#32) and drizzle size distribution at various locations and at different times in a cell. Thin dash-dotted lines indicate size distribution calculated in 3D model. Since #32 sample was measured at dissipating stage, this cloud droplet size distribution is closer to the T = 50 min droplet distribution in the model.

Heavier rainfall than predicted by the model was observed from band clouds. This result is probably due to less dilution of liquid water in band clouds and the existence of strong inflow at the lower cloud layer due to local convergence.

References

Blanchard, D. C., 1953: Raindrop size-distribution in Hawaiian rains. *J. Meteor.*, 10, 457-473.

Brown, E. N., and R. R. Braham, Jr., 1959: Precipitation-particle measurements in trade wind cumuli. *J. Meteor.*, 16, 609-616.

Jiusto, J. E., 1967: Aerosol and cloud microphysics measurements in Hawaii. *Tellus*, 14, 359-368.

McTaggart-Cowan, J. D., and R. List, 1975: Collision and breakup of water drops at terminal velocity. *J. Atmos. Sci.*, 32, 1401-1411.

Neiburger, M., 1959: Reflection, absorption and transmission of isolation stratus cloud. *J. Met.*, 6, 98-104.

Squires, P., 1958: The microstructure and colloidal stability of warm clouds. *Tellus*, 10, 257-261.

Takahashi, T., 1973: Numerical simualtion of tropical showers. *J. Geophys. Res.*, 78, 6233-6247.

______, 1974: Numerical simulation of tropical showers. *J. Atmos. Sci.*, 31, 219-232.

______, 1975: Tropical showers in axi-symmetric cloud model. *J. Atmos. Sci.*, 32, 1318-1330.

______, 1976: Warm rain, giant nuclei and chemical balance - a numerical model. *J. Atmos. Sci.*, 33, 269-286.

______, 1977: A study of Hawaiian warm rain showers based on aircraft observation. *J. Atmos. Sci.*, 34, 1773-1790.

______, 1978: Raindrop size distribution with collision breakup in an axi-symmetric warm cloud model. *J. Atmos. Sci.*, 35, 1549-1553.

______, 1980: Warm rain in three dimensional cloud model. (To be published.)

______, and S. M. Lee, 1978: The nuclei mass range most efficient for the initiation of warm cloud showers. *J. Atmos. Sci.*, 35, 1934-1946.

Twomey, S. and T. A. Wojciechowski, 1969: Observations of the geographical variation of cloud nuclei. *J. Atmos. Sci.*, 26, 684-688.

Warner, J., 1969: The microstructure of cumulus cloud. Part 1. General features of the droplet spectrum. *J. Atmos. Sci.*, 26, 1049-1059.

NUMERICAL STUDY OF THE EFFECTS OF AEROSOL-COMPOSITIONS ON THE MICROSTRUCTURE OF CLOUDS

T. Takeda and N. Harada

Water Research Institute, Nagoya University
Nagoya, JAPAN

1. Introduction

There have been very few models by which the effects of aerosol-compositions on the microstructure of clouds and the mechanism of precipitation formation can be studied, though the numerical studies of the effects of condensation nuclei on the size distribution of cloud droplets or the effects of initial size distribution of droplets on precipitation formation have been made (Fitzgerald, 1974; Hjelmfelt, et al., 1978; Kornfeld, 1970; Lee and Pruppacher, 1977; Mordy, 1959; Ogura and Takahashi, 1973; Takeda, 1975; Warner, 1969 and 1973). In this paper the influence of aerosol-compositions on the microstructure of clouds will be studied. Aerosols composed of NaCl, H_2SO_4 or $(NH_4)_2SO_4$ are adopted as cloud condensation nuclei, taking into account internally and externally mixed nuclei.

2. Numerical model

i) Dynamical framework

A time-dependent cumulus model adopted here is axially symmetric. For the simplification of dynamical framework, the atmosphere is divided into three regions —— an inner region of cloud (I), an outer region of cloud (II) and an environment (III) (Fig.1). The sizes of regions are constant with time. Two cloud regions are made so as to describe the difference between the trajectories of large and small precipitation particles in cloud and the weak intrusion of an entrained environmental air into the center of the cloud, because these processes could not be represented in one-dimensional model. A compensating current occurs in the region III. The detail of the model is described in the paper of the author (Takeda, 1975).

The time variation of vertical air-velocity (w), potential temperature (θ) and the mixing ratio of water vapor (q) are given for each region as follows :

$$\begin{aligned}\frac{\partial \bar{A}_J}{\partial t} = &-\bar{w}_J \frac{\partial \bar{A}_J}{\partial z} + \nu \frac{\partial^2 \bar{A}_J}{\partial z^2} + \bar{F}_J \\ &- \frac{2}{r_{j+1}^2 - r_j^2}\Big\{ r_{j+1}\tilde{u}(r_{j+1})\big[\tilde{A}(r_{j+1}) - \bar{A}_J\big] \\ &- r_j \tilde{u}(r_j)\big[\tilde{A}(r_j) - \bar{A}_J\big] \\ &+ \alpha^2\Big[r_{j+1}(\bar{A}_J - \bar{A}_{J+1})\cdot|\bar{w}_J - \bar{w}_{J+1}| \\ &- r_j(\bar{A}_{J-1} - \bar{A}_J)\cdot|\bar{w}_{J-1} - \bar{w}_J|\Big]\Big\}\end{aligned} \qquad (1)$$

$$F_w = \left(\frac{\theta_v - \theta_{vo}}{\theta_{vo}} - \ell\right) g$$

$$F_\theta = \frac{\theta}{c_p T} L C_d$$

$$F_q = -C_d \qquad (2)$$

A = w, θ or q

j = 1, 2 or 3 when J = I, II or III

Here A_J, $A(r_j)$, A'_J and $A''(r_j)$ are defined by

$$\bar{A}_J = \frac{1}{\pi r_{j+1}^2 - \pi r_j^2}\int_0^{2\pi}\int_{r_j}^{r_{j+1}} A_J \, r\, dr\, d\lambda$$

$$\tilde{A}(r_j) = \frac{1}{2\pi}\int_0^{2\pi} A(r_j)\, d\lambda$$

$$A'_J = A_J - \bar{A}_J$$

$$A''(r_j) = A(r_j) - \tilde{A}(r_j) \qquad (3)$$

The time variation of the mixing ratio of liquid water (ℓ) or the number density of drops of each size (n(R)dR) is given by the modified form of eq.(1) in which the growth of drops due to condensation- and coagulation-processes and their falling are taken into account.

The first half of the fourth term in eq.(1) indicates the mixing by the organized motion between neighboring regions under the condition of

$$\begin{aligned} &\tilde{A}(r_{j+1}) = A_J && \text{if } u(r_{j+1}) \geq 0 \\ &\tilde{A}(r_{j+1}) = A_{J+1} && \text{if } u(r_{j+1}) < 0 \\ &\tilde{A}(r_j) = A_{J-1} && \text{if } u(r_j) \geq 0 \\ &\tilde{A}(r_j) = A_J && \text{if } u(r_j) < 0 \end{aligned} \qquad (4)$$

The second half of the fourth term is the modification of lateral eddy mixing $\overline{u''(r_j)A''(r_j)}$.

$u(r_2)$ and $u(r_3)$ are determined from the following equation derived from continuity equation of air, using boundary conditions at z = 0 and Z_H and r = r_1 and r_4.

$$2\big[r_{j+1}\tilde{u}(r_{j+1}) - r_j\tilde{u}(r_j)\big] + (r_{j+1}^2 - r_j^2)\frac{1}{\rho_0}\cdot\frac{\partial}{\partial z}(\rho_0 \bar{w}_J) = 0 \qquad (5)$$

w_{III} is given as the compensating current of w_I and w_{II}.

ii) Growth of drops due to condensation process

Cloud droplets are assumed to form on a specified population of cloud condensation nuclei in which internally mixed nuclei (hygroscopic aerosols containing insoluble matter) are also included. As pointed out by Hjelmfelt et al. (1978), the dispersion coefficient of computed cloud-droplet size-distribution is critically dependent upon what size classes nuclei are discretized into. In this paper 96 size classes are adopted in describing the size distribution of nuclei. The number of nuclei contained in each class is nearly the same.

3. Some results of computation

Before the effects of aerosol-compositions on the microstructure of cloud are studied in axially symmetric cumulus model, their fundamental effects on the size distribution of cloud droplets were studied in the model of a closed air parcel with constant vertical velocity. The results of numerical computation are summarized as follows :

a) If the size distribution of nuclei is the same, the nuclei composed of matter which can be activated at lower super-saturation produce a broader size spectrum of droplets (Table 1).

b) If the substance of nuclei is the same, a population of nuclei in which a greater number of small nuclei are contained produces a broader size spectrum of droplets (Figs. 2a and 2b). The difference in the number of large nuclei has hardly an influence on the value of dispersion coefficient, because the extent of super-saturation in the air parcel is not so much affected by their growth. It is to be noted that the growth rate of droplets formed on small nuclei is much affected by the extent of realized super-saturation, while the growth of droplets originated from large nuclei continues to be influenced by the amount of soluble matter for a longer time than droplets from small nuclei.

c) If the size distribution of nuclei is the same, a population of mixed nuclei which contain insoluble matter internally produces a narrow size spectrum of droplets. However, if the mass spectrum of soluble matter is the same, a population of mixed nuclei causes nearly the same size spectrum of droplets as not-mixed nuclei (Tables 2 and 3).

Fig. 3b shows the size distribution of droplets obtained in cumulus model under the assumption that in case b a great number of small nuclei composed of H_2SO_4 were added to a population of nuclei composed of $(NH_4)_2SO_4$ in case a (Fig. 3a). It can be seen in Fig. 3b that the size distribution of droplets is broader and their mean radius is smaller in case b than in case a, since the extent of super-saturation is reduced near cloud base because of the supply of a great number of small nuclei and so the growth rate of small droplets is not so large as in case a.

The effects of aerosol-compositions on the microstructure of cumulus cloud will be described on the basis of the results of computation in which coagulation process and sedimentation of drops are taken into account in the time variation of the size distribution of drops. The conversion rate of cloud water into rainwater in cloud will be also discussed in relation to the difference in aerosol-compositions.

References

Fitzgerald, J. W., 1974 : Effect of aerosol composition on cloud droplet size distribution : a numerical study. J. Atmos. Sci., 31, 1358 - 1367.

Hjelmfelt, M. R., R. D. Farley and P. C. S. Chen, 1978 : A preliminary numerical study into the effects of coal development on cloud and precipitation processes in the Northern Great Plains. J. Appl. Meteor., 17, 846 - 857.

Kornfeld, P., 1970 : Numerical solution for condensation of atmospheric vapor on soluble and insoluble nuclei. J. Atmos. Sci., 27, 256 - 263.

Lee, In-Young, and H. R. Pruppacher, 1977 : A comparative study on the growth of cloud drops by condensation using an air parcel model with and without entrainment. Pageoph, 115, 523 - 545.

Mordy, W., 1959 : Computations of the growth by condensation of a population of cloud droplets. Tellus, 11, 16 - 44.

Ogura, Y., T. Takahashi, 1973 : The development of warm rain in a cumulus model. J. Atmos. Sci., 30, 262 - 276.

Takeda, T., 1975 : Evolution of a precipitating cloud and cloud droplets. Pageoph, 113, 891 - 907.

Warner, J., 1969 : The microstructure of cumulus cloud. Part II. The effect on droplet size distribution of the cloud nucleus spectrum and updraft velocity. J. Atmos. Sci., 26, 1272 - 1282.

_____, 1973 : The microstructure of cumulus cloud : Part IV. The effect on the droplet spectrum of mixing between cloud and environment. J. Atmos. Sci., 30, 256 - 261.

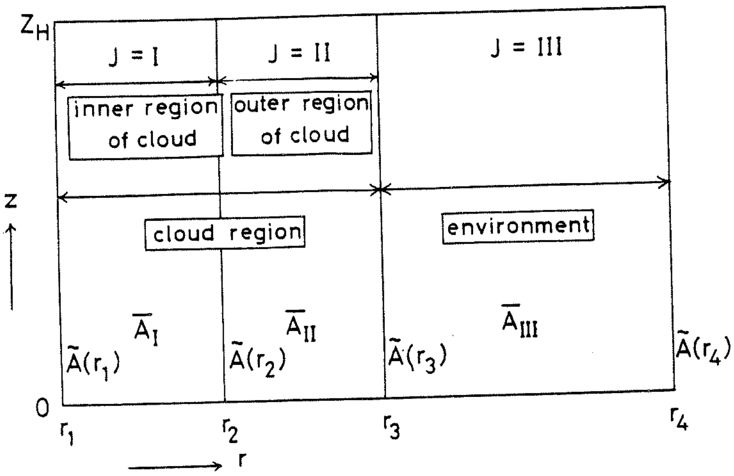

Fig. 1 Domain and regions used in numerical model

NaCl	$(NH_4)_2SO_4$
Total number of cloud droplets in dry air of 1 g.	
1.97×10^5	1.57×10^5
Maximum value of super-saturation	
0.89%	0.96%
Dispersion coefficient σ at 250 m level above cloud base	
$\sigma_{(NH_4)_2SO_4} / \sigma_{NaCl} = 0.8$	

Table 1 Results of computation for populations of nuclei NaCl and nuclei $(NH_4)_2SO_4$. Size distribution of type B in Fig.2a is used.

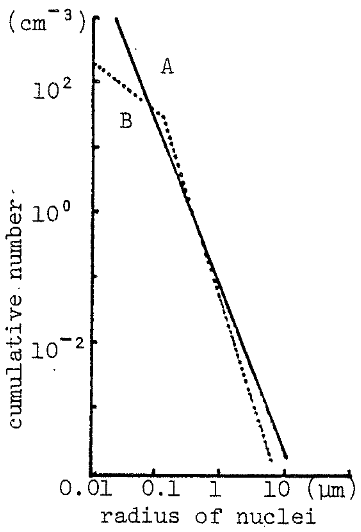

Fig. 2a Size distribution of nuclei of types A and B.

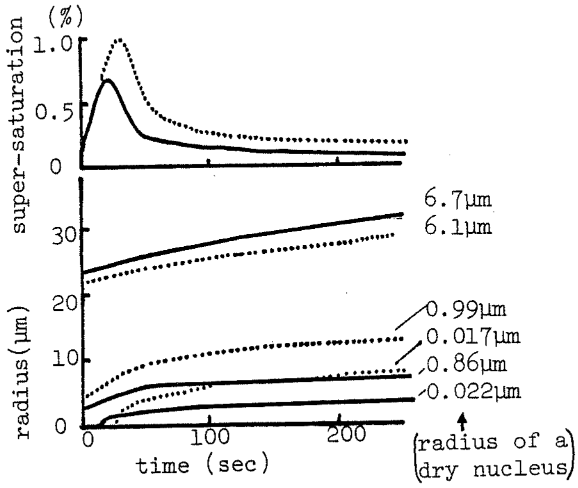

Type A	Type B
Total number of cloud droplets in dry air of 1 g.	
1.38×10^6	1.57×10^5
Maximum value of super-saturation	
0.63 %	0.96 %
Dispersion coefficient σ at 250 m level above cloud base	
$\sigma_{Type\ B} / \sigma_{Type\ A} = 0.3$	

Fig.2b Results of computation for size distributions of types A(solid line) and B(dashed line) . The substance of nuclei is $(NH_4)_2SO_4$ in both cases.

Pure	$\varepsilon = 0.8$	$\varepsilon = 0.2$
Total number of cloud droplets in dry air of 1 g.		
1.38×10^6	1.22×10^6	4.94×10^5
Maximum value of super-saturation		
0.63 %	0.65 %	0.88 %
Dispersion coefficient σ at 250 m level above cloud base		
$\sigma_{0.8} / \sigma_{Pure} = 0.7$ $\sigma_{0.2} / \sigma_{Pure} = 0.4$		

Table 2 Results of computation for not-mixed nuclei and mixed nuclei. The same size distribution of nuclei is used. ε is a fraction of soluble matter in the nucleus.

Pure	ε = 0.2
Total number of cloud droplets in dry air of 1 g.	
1.38×10^6	1.40×10^6
Maximum value of super-saturation	
0.63 %	0.62 %
Dispersion coefficient σ at 250 m level above cloud base	
$\sigma_{0.2} / \sigma_{Pure} \simeq 1$	

Table 3 Results of computation for not-mixed nuclei and mixed nuclei. The same mass spectrum of soluble matter is used in both cases.

Case a	Case b
Mean radius	
3.7 μm	2.5 μm
Dispersion coefficient	
0.12	0.25

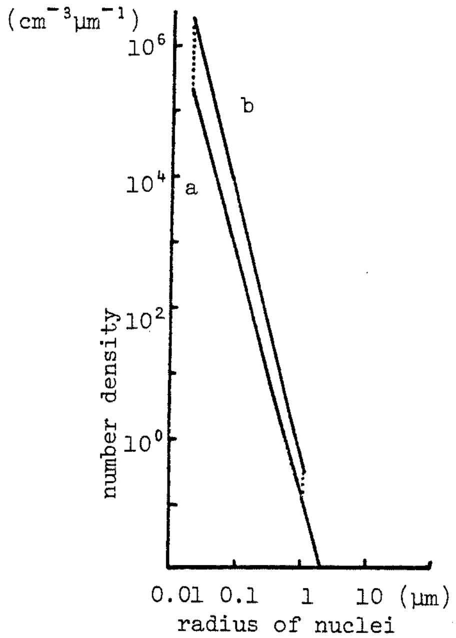

Fig. 3a Size distributions of case a (only $(NH_4)_2SO_4$) and case b ($(NH_4)_2SO_4$ + H_2SO_4) .

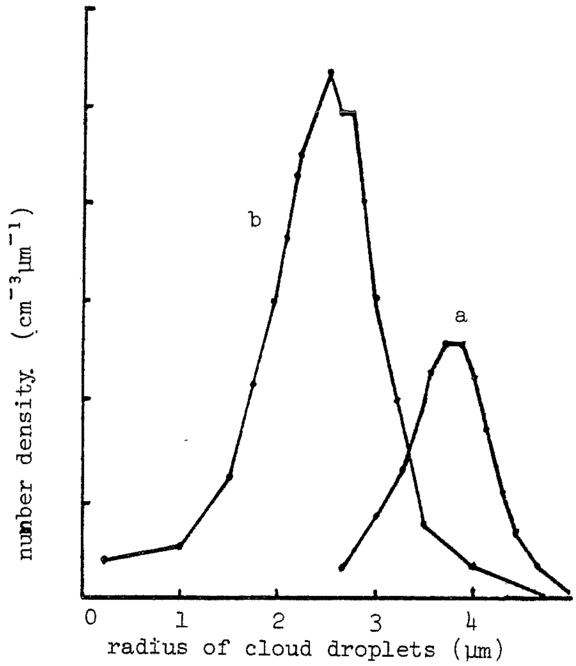

Fig. 3b Size distribution of cloud droplets in cases a and b at 150 m level above cloud base.

ON THE BOUNDARY CONDITIONS FOR CONVECTION

I. Zawadzki

Université du Québec à Montréal, CANADA

1. Introduction

The interaction between convective storms and their larger scale environment has been a challenging problem for many years. A large number of attempts have been made to identify the dynamic and thermodynamic mesoscale parameters which determine the triggering, development and organization of convective systems. The dynamical interaction between large scale convective clouds and their environment was described by Newton and Newton (1959). More recently and from a different perspective Ogura (1976) gives an account of the influence of large scale convergence on convective cloud initiation and development. Koch (1975) studied the effect of the mesoscale fields of pressure disturbances, wind convergence and equivalent potential temperature on the development of new cells. The effect of the wind shear on the storm efficiency was reported by Marwitz (1972). This list is by no means exhaustive and a large number of references can be found in the works mentioned.

The present paper describes an attempt at a systematic evaluation of the relative importance of the thermodynamic conditions of the environment for the development of precipitating systems. For this purpose a large number of storm systems was studied and consequently standard network observations were used. Rainfall rate, being the only parameter of the convection that was observed systematically, was used as a mesure of convective activity. Of the environmental factors, surface temperature and humidity as well as the upper air temperature profile were considered both individually and combined into a single parameter (positive area on a tephigram). A similar analysis was performed in detail for three cases using radar data.

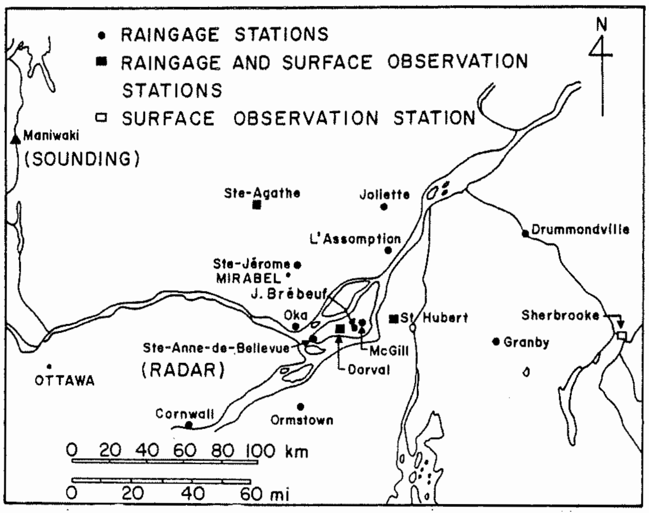

Fig. 1. - Geographical distribution of the observation stations.

We will see in sections 2 and 3 that there is a strong relationship between the maximum and mean rain rates observed in a storm and the thermodynamic variables of the environment on the day in which the storm occurred. This relationship appears to hold on an hour by hour basis as indicated by a detailed analysis of a few storm cases (section 4). However, no attempt is made here to establish a one to one connection between a particular rain rate event and the thermodynamic conditions at the same time or the same place. The point of view adopted here is that the convection-precipitation process is represented by the solutions of a set of differential equations; these solutions depend entirely on the initial and boundary conditions (IBC). The fact that there could be a direct relationship between the IBC and precipitation does not imply that the relationship is physically simple. In fact it is as complex as the set of equations which govern the phenomenon.

2. Maximum rain rate

The present section complements the results reported by Zawadzki and Ro (1978), henceforth to be referred as (I). Therefore the description given here is rather brief.

We will now examine the correlations between the thermodynamic variables and the maximum rain rate observed during a rain day. Precipitation data were obtained from a network of 14 tipping bucket raingages and only cases for which the strongest radar echo for the day passed over one of the gages are considered in this section.

Four ground stations in the Montreal region (Fig. 1) provided hourly values of temperature and humidity while the vertical temperature profile was given twice a day by the Maniwaki sounding. For each hour and station the adiabatic parcel energy (positive area) was calculated for the parcel having the surface temperature and humidity and using the nearest (in time) sounding* from Maniwaki. Parcel energies for unstable points in the soundings (upper air energies) were also calculated.

Fig. 2 shows the correlogram of the maximum rain rate, R_{max}, observed during a storm, and the maximum parcel energy, E_{max} detected during the day in which the storm occurred. The population was divided in two: the cases for which the strongest instabilities are related to the surface conditions and those for which the upper air instabilities seem to be dominant. Since for the latter 6 cases the

* In (I), the previous instead of the closest sounding was used. This explains the minor differences between the results given in this section and those presented in (I).

relevant thermodynamic parameters are sampled only twice a day, the possibility of establishing their relationship to rain rates is rather slim. We will only take notice of the fact that there is an indication of two types of storm systems: those for which the surface condition are directly related to precipitation and those for which they are not. The thermodynamic distinction between the two groups would depend on the relative importance of the surface and upper air parcel energies.

The correlation coefficients between R_{max} and surface conditions, namely the surface maximum wet bulb potential temperature, θ_{wmax} and the maximum mixing ratio, r_{max} are $\rho = 0.74$ and $\rho = 0.75$ respectively. Since E_{max}, θ_{wmax} and r_{max} are not independent variables, a partial correlation analysis was performed to find the degree to which each of these variables determines the variability of R_{max}.

The partial correlation coefficient between R_{max} and E_{max} when their dependence on surface conditions is eliminated (therefore only the vertical temperature profile is variable) is $\rho = 0.47$. Thus 22% of the storm to storm variability of R_{max} is explained by the vertical thermal structure. In the same way 46% of the variance of R_{max} is explained by the variance of r_{max} and a non significant contribution to the explained variance of R_{max} is given by the variance of the surface temperature. However, the two last results have a low statistical significance since they require the introduction of the sounding temperature at every level, thus reducing appreciably the degrees of freedom.

It appeared from (I) that the ambient upper air humidity is of relatively small importance in determining the rate of precipitation. This result could be attributed in part of the data used: although the Maniwaki sounding may represents well the vertical structure of temperature in the region under study, it could fail to do so for the more variable humidity profile. Since the humidity aloft is well determined by the surface humidity (Bolsenga, 1965), it seems sufficient to relate the latter with precipitation. The multiple correlation coefficient between E_{max}, r_{max} and R_{max} is $\rho = 0.82$, about the same as obtained in (I) by introducing the upper air mixing ratio.

3. Mean rain rate

While the maximum value of rain rate is unique, the mean value can be defined in many ways: over a fixed area and over the total time of precipitation; over the area of precipitation and the actual time of precipitation at each point; and so on. From our point of view the most significative mean rain rate is the one we call the "system mean" defined at the sum of all observed values of rain rate divided by the number of observations. If precipitation is observed at N uniformly spaced rain-gages with R_i the rain rate at the i^{th} gage, starting at time t_i^o and finishing at time t_i^f, the total rainfall is

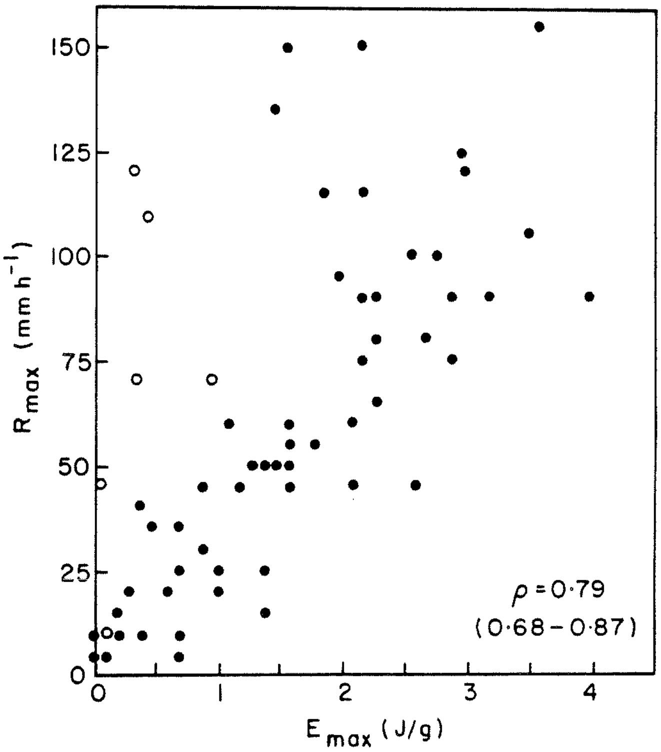

Fig. 2. - Maximum rain rate vs. maximum parcel energy for 67 storms days of the summer seasons of 1969/1970. The indicated energies correspond to surface parcel or upper air parcel whichever was greater. Open circles indicate cases for which upper air energy was greater than surface energy. The correlation coefficient for the 61 remaining cases (full circles) and the confidence limits, to the 5% significance level (in brackets) are indicated.

$$\sum_{i=1}^{N} \int_{t_i^o}^{t_i^f} R_i \, dt.$$

The total lenght of record is $\sum_{i=1}^{N} (t_i^f - t_i^o)$.

Thus, the system mean is

$$\bar{R} = \frac{1}{\sum_{i=1}^{N}(t_i^f - t_i^o)} \sum_{i=1}^{N} \int_{t_i^o}^{t_i^f} R_i dt = \frac{1}{(t_i^f - t_i^o)\ N} \sum_{i=1}^{N} \int_{t_i^o}^{t_i^f} R_i dt \qquad (1)$$

If the gages are not uniformly spaced, the integral in (1) has to be multiplied by some weighting factors a_i.

Daily totals of precipitation were available from 74 gages distributed over the area under consideration. The weighting factors were obtained by the Thiessen's polygon method (a standard hydrological technique). Each factor a_i is then the polygon area over which the measurement by the i^{th} gage is considered representative. Thus (1) is transformed into

$$\bar{R} = \frac{1}{(t_i^f - t_i^o)\ S} \iint_S \int_{t_i^o}^{t_i^f} R_i dt \qquad (2)$$

where $S = \sum_{i=1}^{N} a_i$ is the area of precipitation.

The chart records of the tipping bucket gages were inspected and the actual times of precipitation at every gage were added to obtain the mean time of precipitation $(t_i^f - t_i^o)$.

Surface and upper air parcel energies were calculated for each stations and at every hour of each day for which there was not more than one storm in the same 24h period. For the surface energy, the maximum of the four hourly values of θ_w was calculated from the four ground stations and was applied to the closest in time Maniwaki sounding. The time sequences of energy thus obtained were averaged over a time period including the precipitation time - from the first to the last detection of rain by any of the 14 tipping bucket gages - and a time interval Δt, taken from one to four hours before the onset of precipitation was added in an attempt to include values of energy affecting the clouds at the formation stage. The scattergram of $\bar{R}$ versus the mean energy $\bar{E}$ is shown in Fig. 3 for 80 cases for which the surface energy was greater than the upper air energy (100 out of 106 cases) and more than one tipping bucket gage detected precipitation. The highest value of ρ corresponds to Δt = 2h, that is, for $\bar{E}$ including values of energy two hours previous to the detection of precipitation.

The correlation between $\bar{R}$ and $\bar{E}$ can be easily improved. For cases for which at least four tipping bucket gages recorded precipitation (70 cases) - thus a better estimation of the mean time of precipitation could be expected - the correlation coefficient goes up to $\rho = 0.78$. Separating the 70 cases in air mass (21 cases) and frontal (49 cases) gives $\rho = 0.821$ and $\rho = 0.764$ respectively.

The fact that the energy is averaged over a time period which includes two hours previous to the detection of rain is of minor importance. The variation of ρ with Δt is small and the conclusions to be drawn from the correlations should not be affected by the choice of Δt. Fourteen raingages are not sufficient to determine accurately the onset time of precipitation which could have started earlier than the time of first detection. Therefore the value of Δt = -2h should be taken only as part of the description of the procedure followed, although it is physically reasonable to expect that ambient conditions present in the formation stage are relevant.

Correlation coefficients between $\bar{\theta}_w$, $\bar{r}$ and $\bar{R}$ are $\rho = 0.55$ and $\rho = 0.58$ respectively. As they are quite a bit lower than the ones obtained for the maximum values, the importance of the sounding is greater in this case. In effet the partial correlation between $\bar{R}$ and $\bar{E}$ when the dependence on surface conditions is eliminated is $\rho = 0.62$. Thus, while $\bar{R}$ and R_{max} are both equally determined by parcel energy the surface conditions appear to be dominant in determining R_{max} while upper air conditions are of greater importance for $\bar{R}$.

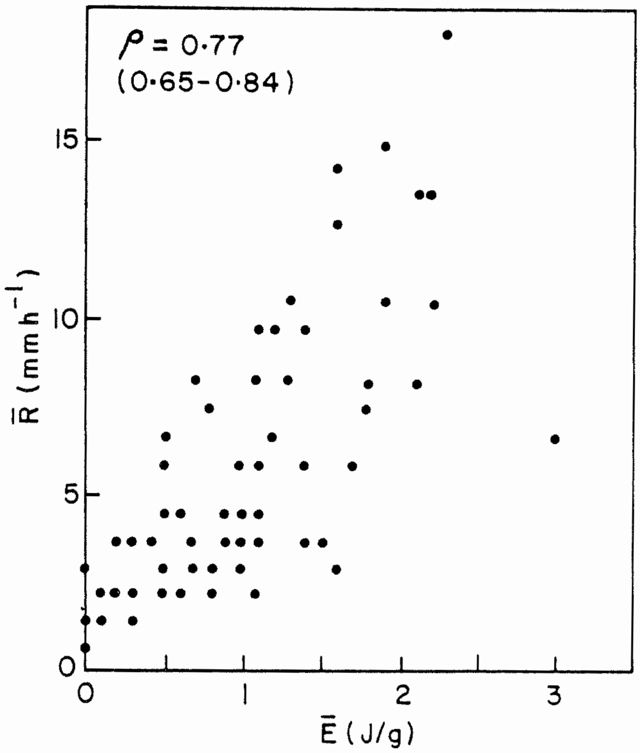

Fig. 3. - Daily mean rain rates and daily mean surface parcel energies for 80 storm cases for which the entire precipitation occurred in a 24h period.

4. Case analysis

Three storm cases were studied in detail using the McGill Weather Radar Observatory data in the form of 3 Km altitude CAPPI maps. These maps have a time resolution of five minutes and a space resolution of (4.8 x 7.5) Km^2. Rain rate data are given in intervals increasing by a factor of ~ 1.5 and a geometric mean of the extremes of each interval is used in this study. Only the precipitation within a range of 180 Km is considered here.

Surface data of the Ottawa and Mirabel stations were used in addition to the previous four. Surface parcel energies were calculated for every hour at every station as described previously. The time sequences of the hourly maxima and the hourly means over the area of the parcel energies (E_m and $\langle E \rangle$ respectively) are shown in Fig. 4.

The other curves of Fig. 4 represent: R_m, the maximum rain rate over the area and during an hour interval centered around the time of the surface observations; $\langle R \rangle$, the mean rain rate over the hour and the area; $\langle R_m \rangle$, the hour average of the area maximum of each CAPPI.

Given the low density of surface observations the correlations between the precipitation and the thermodynamic parameters is remarkable. On the 1st of June, with the lowest correlations, the radar echoes passed south of all the six ground stations.

These correlations indicate that the close relationship between daily means and maxima of rain rates and energies holds hour by hour. Observation of the development of individual echo cells confirms results of other authors: cells tend to develop when approaching zones of instability. However, this spacial relationship is not clear cut, particularly with cells forming part of large clusters or a frontal system. An easily identifiable spacial correspondence between the boundary conditions and precipitation may not be present for the highly interactive convective clusters.

5. Conclusions

The results presented here show that the development of storms appears to be strongly related to the thermodynamic variables. In particular the surface conditions are of critical importance. It remains questionable whether the 6 cases discussed in section 2, for which the surface conditions appeared to be irrelevant, were actually an upper air phenomenon or there was a question of inadequate measurements. In any case their inclusion in the statistical analysis does not affect appreciably the results.

It should be mentioned that although ~ 60% of storm to storm variability of R_{max} and $\bar{R}$ is explained by the variability of the thermodynamic variables, the latter do not necessarily initiate the precipitation. It was seen in (I) that parcel energy could be present and no precipitation observed. There is enough evidence that larger scale convergence plays an important role in the initiation and the organization of precipitation systems. However, only a study of a large number of cases will determine to what extent and in which types of storms this convergence is the result of convection or vice versa.

The existence of the correlations reported here and in (I) should not necessarily be interpreted as an expression of any simple physical process. Taken strictly as its face value the reported relationships imply that for the storms studied, at least 60% of storm to storm variability of rainfall rate characteristics was determined by the sounding and the time evolution of surface values of temperature and humidity. We would like to stress, however, the importance of this fact: it reveals a strong regularity in the storm systems behaviour notwithstanding the complexity of the convection and precipitation formation processes. It is encouraging to see that a standard observation network, as the one used in this study, is sufficient to establish the relationships described. This indicates a certain stability in the convection-precipitation process so that the outcome of the process is not too sensitive to the fine scale details of the IBC.

The importance of the surface condition is particularly relevant in relation to cloud modeling. If indicates the important role played by the boundary layer in the development of convection.

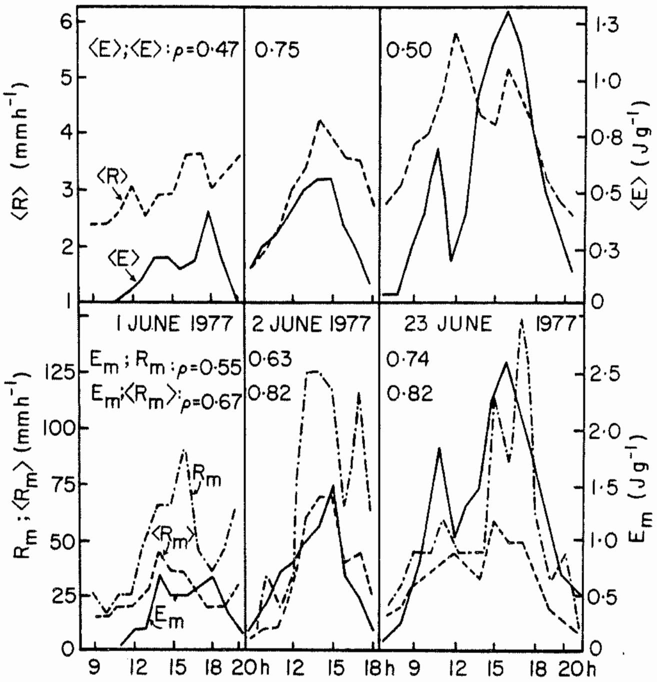

Fig. 4. - Time sequences of the parameters defined in text, for three storms. The correlation coefficients between pairs of the indicated parameters are shown.

References

Bolsenga, S.J., 1965. The relationship between total Atmospheric water vapor and surface dew point on a mean daily and hourly bases. J. Appl. Meteor. 4, 430-432.

Koch, E.S. (1975) Mesoscale influences upon the intensity of new cells in two severe local storms. Proceeding of the 9th Conference on Severe Local Storms. American Meteor. Soc., 105-112.

Marwitz, J.D. (1972), Precipitation efficiency of thunderstorms on the high plains. Journal de Rech. Atmosph. 1-2-3, 367-370.

Newton, C.W., Newton HR (1959) Dynamical interactions between large scale convective clouds and environment with vertical shear. J. Meteorol. 16, 483-496.

Ogura, Y. 1976. On the interaction between cumulus clouds and the larger-scale environment. Cloud Dynamics (H.R. Pruppacher, Editor) Birkhäuser Verloug Basel and Stuttgart, 869-890.

Zawadzki, I., and Ro, C.U., 1978. Correlations between maximum rate of precipitation and mesoscale parameters. J. Appl. Meteor. 17, 1327-1334.

IV.2 - Interaction "Environnement de nuages-Mésoéchelle"

"Cloud Environment-Mesoscale" Interaction

DEUX ETUDES DE PARAMETRISATION DE LA COUCHE LIMITE CONVECTIVE

J.C. André[(1)], M.A. Artaz[(1)], P. Lacarrère[(1)] et L.J. Mahrt[(2)]

(1) Direction de la Météorologie, Boulogne, FRANCE
(2) Oregon State University, Corvallis, U.S.A.

1. Motivations et cadre général :

La prévision du déclenchement des phénomènes nuageux nécessite une bonne connaissance de la structure et de l'évolution de la couche limite. Ceci est plus particulièrement vrai dans le cas des brouillards d'évaporation (cf. par exemple Wessels, 1979) mais s'applique aussi au cas de la convection très développée (cf. par exemple Mahrt, 1977). Le niveau de condensation dépend en effet de façon cruciale de la hauteur h de la couche mélangée convective et de la répartition verticale $\overline{q}(z)$ de l'humidité spécifique moyenne dans cette couche.

Depuis quelques années, la couche limite convective a été étudiée en détails à la fois aux plans expérimentaux et théoriques. Sa dynamique et ses propriétés sont maitenant assez bien comprises et il existe de nombreux modèles, de complexités très variables, pour en effectuer la simulation (voir par exemple Artaz et André, 1980, pour une liste de ces différents modèles).

Le présent travail a pour objectif d'utiliser au mieux cet ensemble de résultats expérimentaux et d'études théoriques pour tester, modifier ou proposer des paramétrisations simples du taux d'épaississement dh/dt de la couche convective et du gradient vertical d'humidité spécifique $\partial\overline{q}/\partial z$ dans cette couche. Un formalisme basé sur la théorie de similitude a été développé à cet effet, plus particulièrement pour faciliter la normalisation puis la comparaison de toutes les données théoriques et expérimentales. Ces données que nous utiliserons proviennent soit d'expériences en laboratoire (Deardorff et al., 1969 ; Willis et Deardorff, 1974 ; Heidt, 1977), soit des campagnes de mesures WANGARA-1967 (Clarke et al., 1971), LIMAGNE-1974 (Jouvenaux, 1978), AMTEX-1975 (Lenschow et Agee, 1976), HASWELL-1975, PHITIVIERS-1976 et VOVES-1977, soit enfin de simulations numériques réalisées à l'aide du modèle de couche limite d'André et al. (1978) basé sur une théorie d'ordre élevé de la turbulence.

Les résultats présentés ici sont extraits de deux publications récentes auxquelles le lecteur intéressé pourra se reporter : Artaz et André (1980) en ce qui concerne le taux d'épaississement dh/dt et André, Laccarrère et Mahrt (1979) pour l'étude de la structure verticale de l'humidité.

2. Théorie de similitude de la couche convective :

Nous schématisons la structure de la couche limite convective de la façon, maintenant classique, représentée à la figure 1. Les paramètres fondamentaux qui gouvernent l'évolution et la structure de cette couche limite sont :

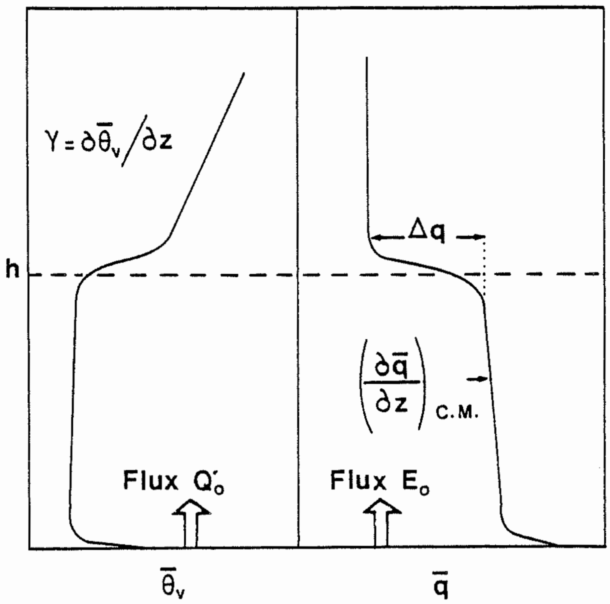

Figure 1 : Profils moyens verticaux schématiques de la température potentielle $\overline{\theta}_v$ et de l'humidité spécifique $\overline{q}$ dans la couche limite convective.

- le flux cinématique vertical de chaleur virtuelle au sol Q'_o :

- le flux cinématique vertical d'humidité au sol E_o ;

- le gradient de température potentielle virtuelle γ dans la couche stable supérieure ;

- la discontinuité d'humidité spécifique Δq au sommet de la couche convective ;

- le paramètre de flottabilité $\beta = g/T_o$;

- la hauteur h de la couche convective.

A l'aide de ces six paramètres dépendant de quatre dimensions physiques "indépendantes" (longueur, temps, température et humidité) il est donc possible de construire deux nombres sans dimension indépendants, par exemple un nombre x mesurant l'intensité de la convection

(1) $x = Q'_0 / \gamma h w_*$

[où $w_* = (\beta Q'_0 h)^{1/3}$ est l'échelle de vitesse convective] et un nombre y égal au rapport des flux turbulents d'humidité à l'inversion h et au sol

(2) $y = (\Delta q / E_0)(Q'_0 / \gamma h)$

L'influence de l'humidité sur la croissance de la couche convective étant prise en compte par l'introduction de la température virtuelle, on aura alors simplement

(3) $\dfrac{dh}{dt} = w_* \Psi_h(x)$

où $\Psi_h(x)$ est une fonction universelle du nombre x qui reste à déterminer. Le gradient vertical moyen de l'humidité spécifique $(\partial \bar{q}/\partial z)_{C.M.}$ dans la couche de mélange devrait, quant à lui, dépendre de x et y :

(4) $(\partial \bar{q}/\partial z)_{C.M.} = (E_0/w_* h)\, \varphi(x, y)$

mais un raisonnement simple permet de passer d'une fonction φ de 2 variables x et y à une fonction de la seule variable y. En effet, l'apparition, puis la permanence, de ce gradient vertical résulte d'une compétition entre le mélange (qui se fait avec une vitesse de l'ordre de w_*) et l'entrainement d'air d'humidités spécifiques différentes depuis le haut et le bas (dont les valeurs caractéristiques sont respectivement Δq dh/dt et E_0) :

$$\left(\frac{\partial \bar{q}}{\partial z}\right)_{C.M.} \sim \frac{\Delta q \, dh/dt - E_0}{h w_*}$$

L'utilisation de (3) conduit alors à :

$$\left(\frac{\partial \bar{q}}{\partial z}\right)_{C.M.} = \frac{E_0}{w_* h}\left[\alpha' y \frac{\Psi_h(x)}{x} - \beta\right]$$

et, puisqu'il sera montré plus bas que Ψ_h est linéaire, cette dépendance se réduit donc à :

(5a) $\left(\dfrac{\partial \bar{q}}{\partial z}\right)_{C.M.} = \dfrac{E_0}{w_* h} \Psi_q(y)$

(5b) $\Psi_q(y) = \alpha y - \beta$

Il faut maintenant faire appel aux données expérimentales et numériques pour, d'une part, tester la validité des formulations (3) et (5) et, d'autre part, déterminer la forme précise des fonctions universelles Ψ_h et Ψ_q.

3. Détermination des fonctions universelles et paramétrisations :

Sur la figure 2 ont été reportées les données relatives au taux d'épaississement de la couche convective. Il faut tout d'abord noter que les données atmosphériques (□, WANGARA ; O, LIMAGNE et PHITIVIERS ; △, AMTEX et HASWELL ; ◇, VOVES) sont beaucoup plus dispersées que les données provenant du laboratoire (●, Deardorff et al. ; ■, Willis et Deardorff ; ▲, Heidt) et d'études de la thermocline lacustre (◆, Farmer 1975), sans qu'il soit toutefois possible de déceler de différences systèmatiques entre ces diverses données. Les résultats du modèle numérique (•, André et al.), qui, en premier lieu, sont compatibles avec les résultats expérimentaux, permettent d'autre part de mettre en évidence une loi universelle pour la montée de

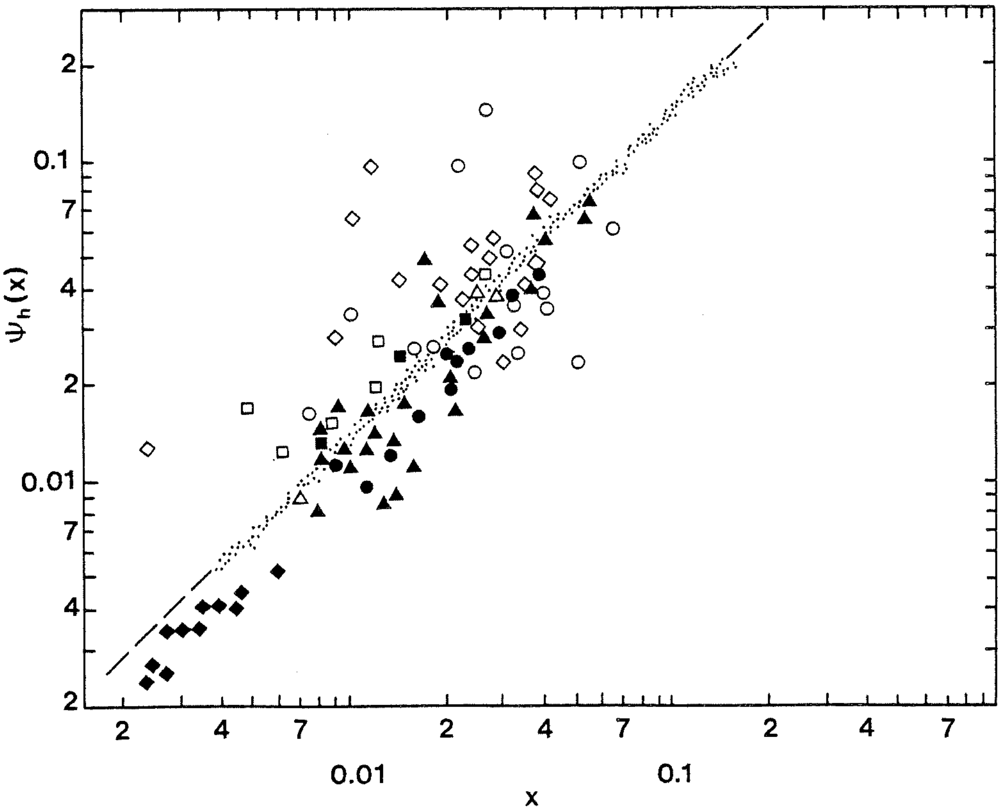

Figure 2 Taux d'épaississement normalisé de la couche limite en fonction de l'intensité de la convection ; ., données numériques ; symboles pleins (●, ■, ▲, ◆), données de laboratoire ; symboles évidés (□, O, △, ◇), données atmosphériques. La courbe en tireté représente l'équation (6a) $\Psi_h(x) = 1,4\, x$.

l'inversion ; cette loi est représentée très simplement par la relation linéaire (indiquée en tireté) :

(6a) $\Psi_h(x) = 1{,}4\ x$

ou de façon équivalente, en termes de variables dimensionnelles,

(6b) $\frac{dh}{dt} = 1{,}4\ \frac{Q'_o}{\gamma h}$

Il semble donc que le modèle simplifié de Tennekes (1973), équivalent à (5b), soit le mieux adapté pour la paramétrisation de l'épaississement de la couche convective et qu'il soit peu utile de chercher à le développer en le complexifiant.

Sur la figure 3 ont été reportées les données relatives au gradient vertical d'humidité spécifique dans la couche convective. Les données expérimentales (□, WANGARA ; △, AMTEX ; ○, HASWELL ; ◇, VOVES) et numériques (•, André et al.) sont affectées d'une dispersion relativement faible qui justifie donc le passage de la description (4) à deux paramètres à la description (5a) à un seul paramètre. Ces deux types de données sont d'autre part en très bon accord et permettent de déterminer les constantes de la loi (5b)

(7a) $\Psi_q(y) = 13\ y - 1{,}7$

ou encore, en fonction des variables dimensionnelles

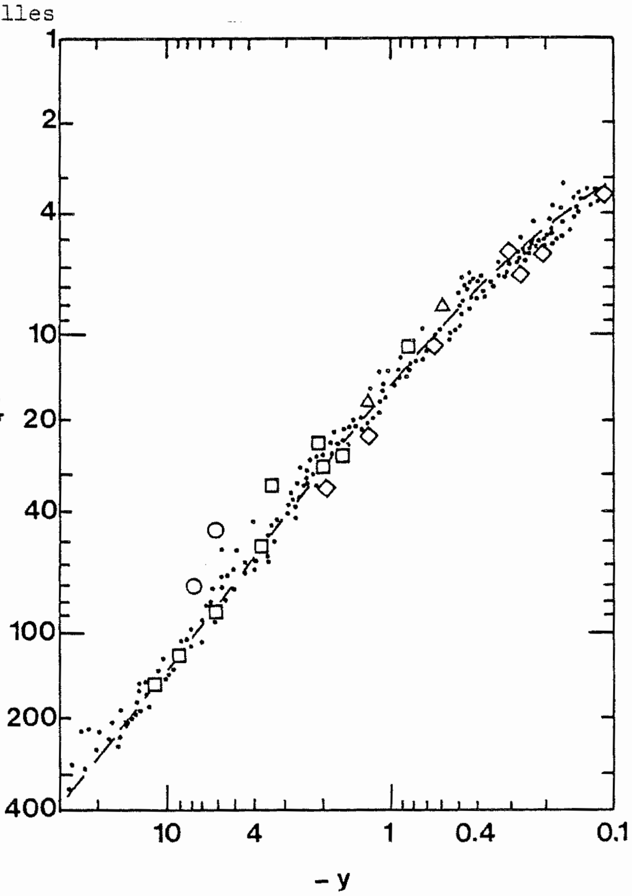

Figure 3 Gradient normalisé de l'humidité spécifique dans la couche limite convective : ., données numériques ; (□, △, 0, ◇), données atmosphériques. La courbe en tireté représente l'équation (7a) $\Psi_q(y) = 13\ y - 1{,}7$

(7b) $\left(\frac{\partial \bar{q}}{\partial z}\right)_{c.m.} = 13\ \frac{Q'_o}{\gamma h}\ \frac{\Delta q}{w_* h} - 1{,}7\ \frac{E_o}{w_* h}$

Il faut enfin noter que dans un grand nombre de situations la paramétrisation (7b) pourra être simplifiée en négligeant le second terme du membre de droite, ce qui correspond au cas où le flux d'assèchement au sommet de la couche convective est beaucoup plus efficace que le flux d'humidification au sol.

Références blibliographiques

André, De Moor, Lacarrère, Therry et du Vachat, 1978 : Modeling the 24-hour evolution of the mean and turbulent structures of the planetary boundary layer, J. Atmos. Sci. 35, 1861-1883.

André, Lacarrère et Mahrt, 1979 : Sur la distribution verticale de l'humidité dans une couche limite convective, J. Rech. Atmos. 13, 135-146.

Artaz et André, 1980 : Similarity studies of entrainment in convective mixed layers, Bound.-Layer Meteor., à paraître.

Clarke, Dyer, Brook, Reid et Troup, 1971 : The Wangara experiment-Boundary layer data. Paper N° 19, Division Meteorological Physics, CSIRO, Australia.

Deardorff, Willis et Lilly, 1969 : Laboratory investigation of non steady penetrative convection, J. Fluid Mech. 35, 7-31.

Farmer, 1975 : Penetrative convection in the absence of mean shear, Quart. J.R. Meteor. Soc. 101, 869-891.

Heidt, 1977 : The growth of the mixed layer in a stratified fluid due to penetrative convection, Bound.-Layer Meteor. 12, 439-461.

Jouveneaux, 1978 : Etude expérimentale de la structure turbulente de la couche de mélange convective, Thèse de 3ème cycle de l'Université de Clermont-Ferrand, 125 pp.

Lenschow et Agee, 1976 : Preliminary results for the Air Mass Transformation Experiment (AMTEX) , Bull. Amer. Meteor. Soc. 57, 1346-1355.

Mahrt, 1977 : Influence of low-level environment on severity of high-plains moist-convection, Mon. Wea. Rev. 105, 1315-1329.

Tennekes, 1973 : A model for the dynamics of the inversion above a convective boundary layer, J. Atmos. Sci. 30, 558-567.

Wessels, 1979 : Growth and disappearance of evaporation fog during the transformation of a cold air mass, Quart. J.R. Meteor. Soc. 105, 963-977.

Willis et Deardorff, 1974 : A laboratory model for the unstable planetary boundary layer, J. Atmos. Sci. 31, 1297-1307.

ETUDE DE LA COUCHE LIMITE TROPICALE MARITIME PAR SONDAGES ACOUSTIQUES : ASPECT CONVECTIF

C. Asselin de Beauville
Centre Universitaire Antilles-Guyane
et
H. Oger
Ingénieur de la Météorologie
Sous-Région Guadeloupe

Introduction : Cette étude de la couche limite planétaire tropicale a débuté en 1979, par l'utilisation conjointe d'un radar acoustique (C.U.A.G.-Fouillole - Pointe-à-Pitre) et des sondages classiques du Centre Local de Météorologie (Aéroport du Raizet à Pointe-à-Pitre). Les sondages du Raizet sont dépouillés automatiquement par une calculatrice HP 9825 (système ETAROM).

But de cette étude :

Le but de cette recherche est multiple. Précisons tout d'abord que ce travail est effectué dans le cadre de l'A.T.P. Recherches Atmosphériques. Le premier objectif est de réaliser une étude suivie de la basse atmosphère tropicale par sondages acoustiques.
Le deuxième est de déterminer les corrélations pouvant exister entre les résultats de ces sondages, les conditions climatiques propres et certains paramètres de nature à caractériser le régime convectif local.
Il convient enfin, de déterminer si, malgré son caractère qualitatif, le sodar peut être ou non, en milieu tropical humide, un instrument qui peut apporter une amélioration à l'aspect prévisionnel.

Réalisation des travaux :

Cette réalisation comporte trois étapes :

a) La première, qui a débuté en 1979, a visé principalement à mettre en oeuvre et à analyser les sondages acoustiques obtenus. Cette première étude permet de mettre en évidence 5 types principaux de sondages acoustiques. Ceci confirme le classement fait par K. BETTS (1974) en fonction de la température potentielle équivalente ainsi que celui d'ASPLIDEN (1976).
Les échos de type 1, relatifs au régime diurne (thermiques) représentent environ 36 % des cas analysés.
Les échos de type 2, relatifs au régime nocturne avec présence d'inversion de rayonnement au voisinage du sol soit 29 % des cas analysés.
Les échos de type 3, relatifs également au régime nocturne mais présentant par rapport au type 2 la disparition de l'inversion de rayonnement au sol. L'influence de l'évolution saisonnière est très nette. Cette catégorie représente environ 10 % des cas étudiés.
Les échos de type 4. Ce type de sondage est relatif à la fois au régime diurne et au régime nocturne. Il montre des variations ondulatoires à ondes multiples. Il concerne environ 6 % des cas analysés.
Les échos de type 5 couvrent à la fois le régime diurne et le régime nocturne et concernent les passages de perturbations. Leur pourcentage représente environ 19 % des cas analysés.

- Il n'a pas été possible jusqu'à maintenant, de mettre en évidence la présence d'une inversion thermique entre 500 et 1000 m (la portée maximale du sodar est de 1000 mètres).
- L'étude des situations météorologiques permet de situer l'apparition des échos de type 4 en présence de convergence préfrontale au niveau de l'Archipel des Petites Antilles jointe à une forte humidité dans les basses couches. (80 à 100 %).
- Les échos sodar semblent particulièrement sensibles aux variations d'humidité.

b) La deuxième étape a consisté, grâce au calculateur de la Météorologie précédemment cité, à tracer toutes les courbes, en fonction de l'altitude, relatives à l'énergie statique de l'air humide (1) et celles de l'air saturé (2) pour les différents types sodar rencontrés. En effet, différentes études du G.A.R.P. et autres travaux (FAL'KOVICH A.I. (1977), ALBRECHT B.A. (1979))montrent que ce paramètre caractérise bien l'évolution de la convection et est assez sensible en milieu tropical humide pour permettre l'interprétation des phénomènes par des considérations énergétiques et l'élaboration de modèles représentatifs. Rappelons son expression mathématique :

(1) $Q = Cp\ T + gz + Lq$

(2) $Q^* = Cp\ T + gz + Lq^*$

Les courbes ont été tracées d'après les sondages météorologiques de ooH et 12 HTU pour les journées et les différents cas de la campagne d'enregistrement sodar.

c) La troisième étape de ce travail de recherche consiste à déterminer à l'aide des courbes précédemment citées, l'épaisseur des couches de blocage, celle des couches en instabilité convective ainsi que leurs niveaux. Ces dernières jouent en effet un rôle déterminant dans le déclenchement des processus convectifs. Il convient également, de calculer l'énergie que doit avoir une particule prise au niveau de la mer (température de l'eau relevée à la Désirade à 7 H le matin, évolution + 1°C dans la journée, avec une humidité moyenne de 80 %) pour vaincre la couche de blocage et arriver jusqu'à son niveau de convection libre (N C L). L'utilisation des données sodar principalement celles relatives au type 1 doivent permettre de déterminer le début de l'apparition des thermiques, leur intensité et éventuellement le moment où une particule peut dépasser son niveau de convection libre. Tout ceci devrait conduire à l'élaboration d'un modèle simple d'évolution et de prévision quant à la répartition des nébulosités (altitude, étendue) avec tous les effets qui leur sont directement liés.

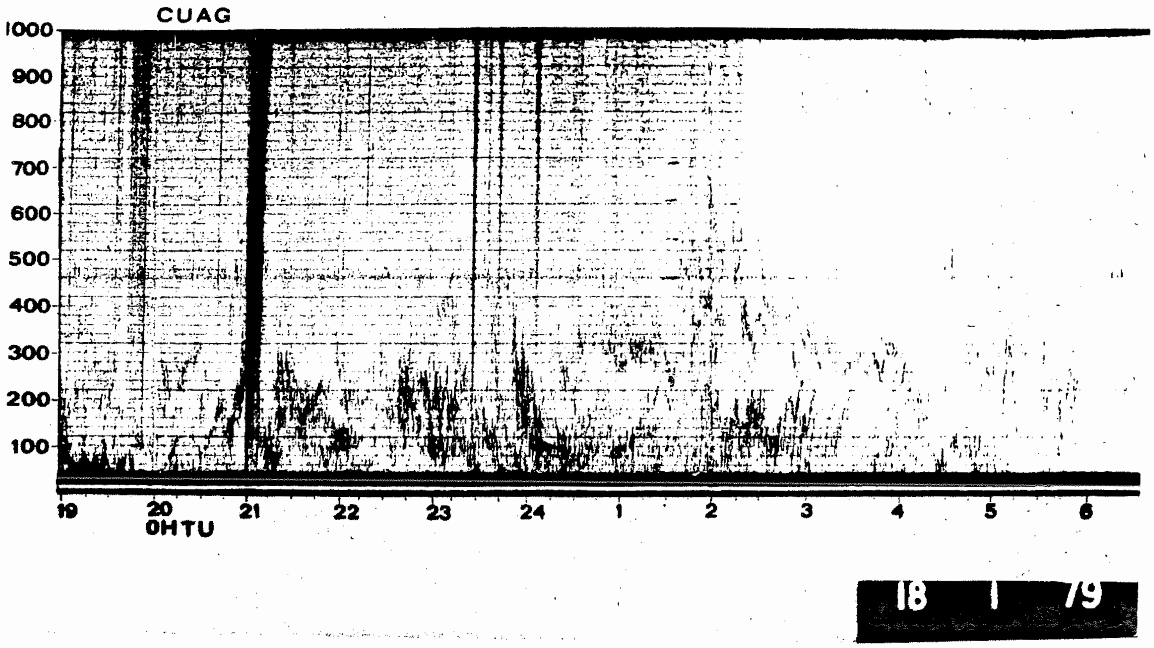

Photographie illustrant les sondages de type 4

Conclusion

Il semble que l'intérêt de ce travail de recherche réside à la fois, dans l'association d'un sondage acoustique avec un autre procédé de sondage classique, ainsi que par le fait qu'il s'appuie sur des données expérimentales réelles dans un milieu où il n'y a pas souvent de mesures faites.
Cette étude en milieu tropical maritime humide devrait rendre possible l'élaboration de modèles théoriques plus élaborés. Précisons à ce sujet, pour ceux qui souhaiteraient apporter leur aide dans l'élaboration de ces modèles, que le C.U.A.G. dispose d'un ordinateur C 6-36 Honeywell Bull et d'une table traçante.

Note à propos des formules (1) et (2)

L = chaleur latente de condensation
q = humidité spécifique de l'air non saturé
q* = humidité spécifique de l'air saturé

Références bibliographiques

1) ALBRECHT B.A. (1979) "A Model of the Thermodynamic structure of the Trade-Wind Boundary Layer : Part I. Theoretical Formulation and Sensivity Tests"
Atmosph. Sciences vol. 36 n° 1 pp 73-89.

2) ALBRECHT B.A. (1979) "A Model of the Thermodynamic Structure of the Trade-Wind Boundary Layer : Part II. Applications.
Atmosph. Sciences vol. 36 n° 1 pp 90-98

3) ASPLIDEN C.I. (1976) "A Classification of the Structure of the Tropical Atmosphere and Related Energy Fluxes".
Applied Meteorology vol. 15 pp 692-697

4) BETTS A.K. (1974) "Thermodynamic Classification of Tropical Convective Soundings"
Weather vol.102 pp 759-764.

5) FAL'KOVICH (1977) "Thermodynamic Parameters and Convective Instability of the Tropical Atmosphere"
Note of G.A.R.P. Meteorolgiya i Gidrologiya n° 9 pp 70-78.

AN INVESTIGATION OF A FRONTAL ZONE

D A Bennetts and P Ryder

Meteorological Office, Bracknell, U.K.

Introduction

Following successful attempts to study the fine structure and dynamics of certain weather systems (Hardman et al, 1972 Browning et al, 1973), the Meteorological Office began to develop an aircraft dropsonde capable of measuring ambient temperature, humidity, pressure and wind. The sondes were to be used to obtain a sequence of atmospheric soundings at a set of grid points in a chosen weather system, anywhere within a large operational area over the North Atlantic. This replaced the previous approach, which required a suitable system at an appropriate state of development to pass a specially manned and instrumented, land based field site. The design requirements were set by the desire to use the sonde with other airborne instrumentation, whilst achieving an effective independence of special ground based facilities.

Since that time the design, development and production of a suitable sonde has been achieved in parallel with that of necessary instrumentation and a safe, effective sonde ejector for the Meteorological Research Flight Hercules aircraft. Evaluation trials of the complete system were conducted in 1978. The first pilot study of frontal structure took place over the North Atlantic in March 1979. Some of the results are reported below. Further investigations are planned.

The dropsonde facility

A sketch of the sonde is shown in figure 1. It is in the form of a cylinder of length 84cm and diameter 12.5cm. The total weight is 3.5kg. A spring loaded drogue is used to pull out the main guide-surface parasheet beneath which the sonde descends at a terminal velocity of about 12 ms^{-1}.

The transducers for measuring temperature and humidity are located within a small duct at the downward facing end of the sonde. These are a fast response thermistor and carbon hygristor respectively. The latter is of the type used on the VIZ*radiosonde. Laboratory and field trials suggest that temperature is measured to better than 0.5°C and humidity to ± 5% RH in the range 30 to 95% RH.

The pressure transducer is a proprietary integrated circuit device, the National LX1602A. Trials in which the pressure altitude of the sonde has been derived from the surface pressure, radar height and sonde observed air temperature have demonstrated that an operational accuracy of ± 1 to 2mb is possible, provided

*VIZ Manufacturing Co., Philadelphia, USA

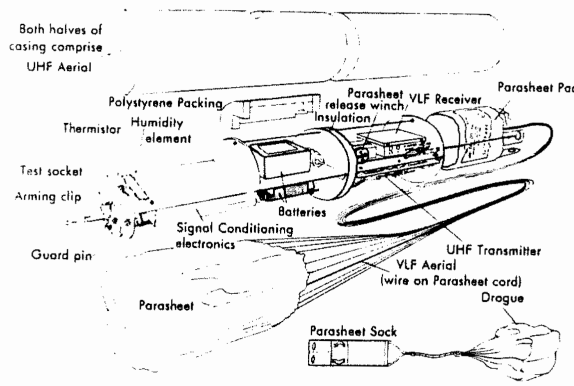

Figure 1. The Meteorological Office windfinding dropsonde.

that the transfer characteristics of each device are determined in the laboratory and a calibration at aircraft cabin pressure is made shortly before use.

The ability to measure the magnitude and direction of the wind from the horizontal movement of the sonde is an important requirement. Such information from a sequence of sondes allows inferrence of regions of vertical motion through the equation of continuity, for example. The expected scale and magnitude of such motion fields - a few cm per sec on scales of a few tens of kilometres in frontal studies - demands measurement of horizontal winds, averaged over 600m or so, to ± 0.5 ms^{-1} or better.

A guide surface parasheet was chosen as a result of comparative tests to establish wind following characteristics. Unlike some conventional parachutes this type possesses positive stability and is not prone to 'fly' relative to the air. Given that the sonde responds to and moves with the local wind, the problem is one of measuring the rate of change of its position. Conventionally such position finding has been achieved by radar or optical tracking. Unfortunately these techniques require a very stable reference platform and are essentially short range (≤ 100 km) methods. Such characteristics are not compatible with the desire to carry out self contained aircraft experiments over the North Atlantic. As a result sonde tracking through the re-transmission of the long range navigation aid, 'Loran C', was chosen after a careful assessment of its potential accuracy - see Beukers (1968) and Ryder et al (1972) for example. Loran C consists of a set of powerful transmitters which emit pulses of 100 kHz signal on a common and closely controlled time-base. The difference in time of arrival of signals from two separate but coherent transmitters defines a locus or 'line of position'. In practice this is a vertical plane except close to either transmitter. Two such time differences obtained from signals from at least three transmitters create intersecting lines of position and hence effectively define a unique plan position. The advantage of this technique for sonde wind finding arises from the fact that positions can be established provided only that time or phase differences are preserved without distortion. In particular, any common and varying signal path such as that between a moving aircraft and sonde is unimportant.

The accuracy with which the wind vector can be defined by this method is a function of the relative position of the transmitters and sonde, and upon received signal strength and stability. Loran C is operated by the US Coastguard in co-operation with host nations and has been set up to provide an accurate navigation aid in various parts of the world, including the North Atlantic. The predicted wind finding accuracy for that region is shown in figure 2, taken from Ryder et al (1972). These data are based upon ground based measurements of received signal stability and known transmitter locations. However the predictions have been confirmed in trials at test ranges in UK where sondes have been tracked by both radar and Loran C.

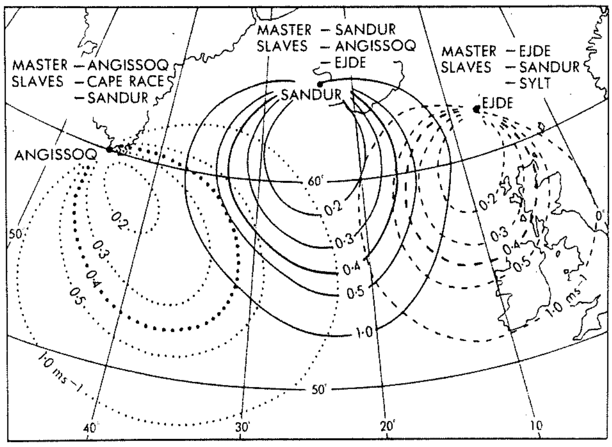

Figure 2. Predicted RMS 1 minute wind errors for daytime using the indicated Loran C transmitters.

The sonde Loran C receiving aerial is formed from a thin wire attached to a parasheet shroud line. The received signal is used to frequency modulate a UHF crystal controlled transmitter which feeds a dipole antenna formed from the two halves of the sonde - see figure 1. The output signals from the pressure temperature and humidity transducers also modulate the same transmissions.

Equipment on the Hercules aircraft is capable of receiving these transmissions at any one of five crystal controlled frequencies in the 400 MHz band. Thus information from up to five sondes can be received and processed simultaneously. Individual sonde data in the form of a time series of temperature, humidity and pressure measurements and Loran C time differences are stored on magnetic tape for post flight analysis. The results of one such analysis of data from one of the sondes released in the experiment described below, is shown in figure 3.

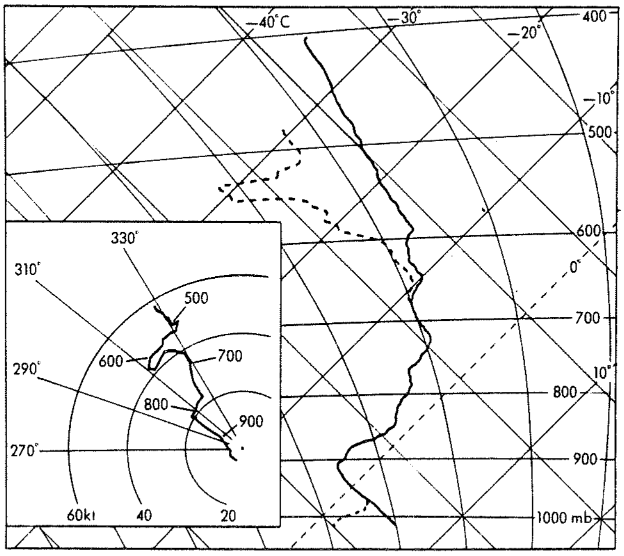

Figure 3. Temperature/dew point profile and wind hodograph measured by a sonde released at $57^{\circ}50'$N $15^{\circ}21'$W, 1145 GMT on 29 March 1979.

The aircraft is also equipped with an Ecko E290 3cm weather radar. The antenna, which has a beam width of 3°, is programmed to scan the 180° sector ahead of the aircraft at one of a number of angles of tilt to the horizontal. This facility combined with the forward motion of the aircraft allows a three dimensional view of the precipitation echo to be constructed. The radar has range compensation and an experimentally determined threshold equivalent to a rainfall rate of about 0.25 to 0.5 mm hr^{-1} out to ranges of 40 km. The radar display is photographed at regular intervals to allow detection of areas of rainfall exceeding this threshold.

A pilot study of an Atlantic front

The surface analysis for 1200 GMT 29 March 1979 as produced by the Meteorological Office is shown in figure 4. Although rather a weak feature with little thermal contrast and producing only light rain and drizzle, the occluded/warm front S was chosen as the subject of a pilot study. The objectives were primarily to test some operational procedures for locating and studying such fronts but a number of results were obtained which augur well for future investigations.

Measurements were made between 1100 and 1300 GMT by sondes dropped along an East-West line centred at $57^{\circ}50'$N, 17°W. Nine sondes were released in two groups from an altitude of 7.3km in the vicinity of the front. Although wind data were obtained from only five of these and one parachute failed to deploy correctly so that temperature and humidity data are suspect from

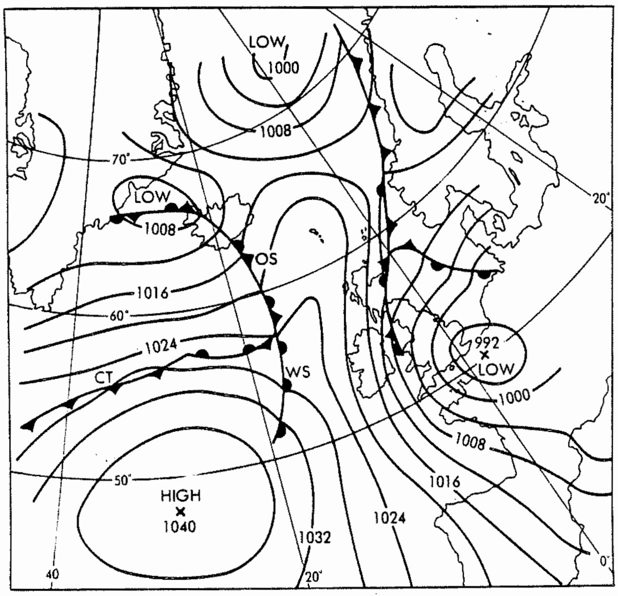

Figure 4. Surface analysis for 1200 GMT 29 March 1979.

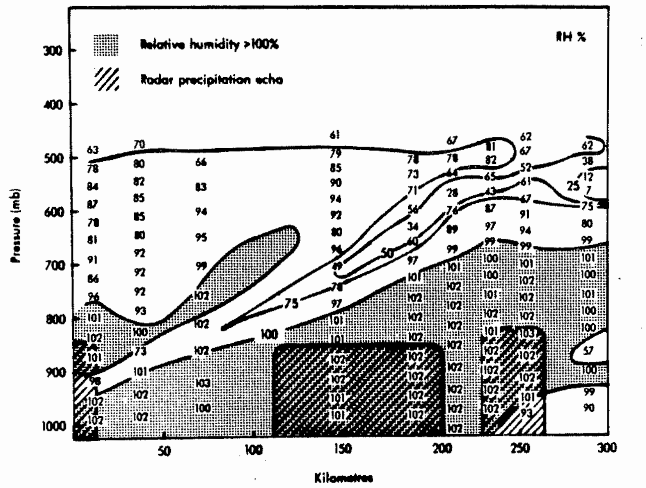

Figure 5. East-West cross section of relative humidity and radar echo.

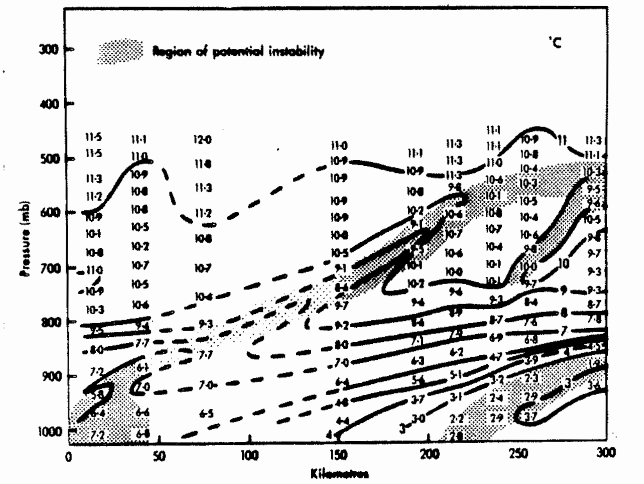

Figure 6. East-West cross section of wet bulb potential temperature.

this sonde also, a number of E-W cross-sections of interest have been derived.

Data are presented in a (p,x-st) frame of reference where p is pressure and s is the component of the system velocity vector in the x direction; west to east in this case. Normally a sequence of sondes would be dropped both to test the validity of the system velocity concept (which assumes a non-developing system being advected at some constant velocity $\underline{s}$) and where appropriate to define the vector. This was not done on the 29 March. However the synoptic scale observations suggest that the front was moving eastwards at between 10 and 15 ms^{-1} and the 700 mb westerly wind measured by all the sondes was close to 12.5 ms^{-1}. Accordingly this value has been assumed to be the system velocity. Because the time between sonde ejections is short the resulting fields are not very sensitive to this assumption. The origin of the x co-ordinate is arbitrarily set to the west of the most upstream observations.

Figure 5 shows the variation of relative humidity in this frame of reference. The major feature is the layer of saturated air in the lower half of the figure with a long sloping tongue of dry air overlaying it. Above the dry zone the air is moist again. The location of the radar echo above the threshold is superimposed on the diagram. The same echo structure was observed throughout the area 20 km to the north and south of the section but the extent to which the echoes represent bands of precipitations beyond that range is unknown.

The field of wet bulb potential temperature, figure 6, exhibits the expected strong gradient in what is assumed to be the frontal zone extending from the surface, at 150 km, to 850 mb at 300 km, and weaker gradients elsewhere. Of special interest are the hatched regions denoting air which is potentially unstable. The two zones below 900 mb are saturated and represent regions where the measured lapse rate is at or greater than the moist adiabatic. Precipitation echoes are observed in the vicinity in both cases. The band of potentially unstable air above the frontal surface mainly corresponds to the dry tongue of air identified in figure 5. It is conceivable that the implied instability there may have been realised subsequently following saturation by moistening/lifting. The potentially unstable air at 250 to 300 km is partially within a saturated region and moist convective overturning in that area is again compatible with the observed precipitation echo and air motion field discussed below. The identified zones exhibit an interesting mesoscale structure, if not periodicity, which is readily resolved by the pattern of sondes. In this context, it is particularly unfortunate that further data were not obtained between 50 and 150 km; the observations at 75 km were made from an unretarded sonde.

Figure 7 shows the u component of velocity relative to the system. Although perhaps distorted by the choice of system velocity, as expected air above the front is moving to the east and over-running that beneath the front. The v component (not shown) is broadly compat-

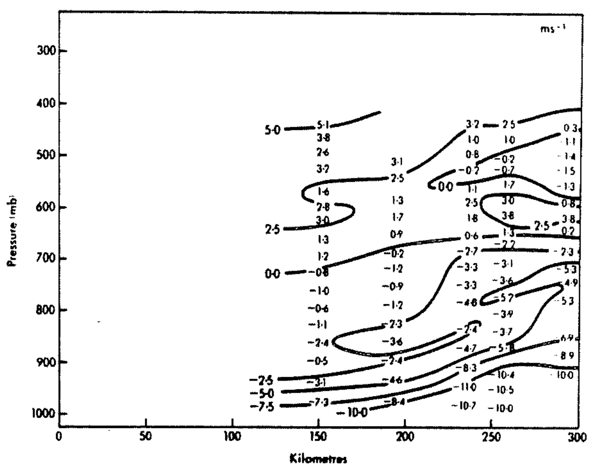

Figure 7. East-West cross section of westerly component of wind relative to the system, assumed to be moving at $270^{\circ}/12.5\ ms^{-1}$.

ible with the thermal wind equation producing an upper level jet parallel to the front. Because divergence perpendicular to the section is unknown, it is not possible to derive the vertical motion field rigorously from the horizontal field and the equation of continuity. However within a frontal zone it is reasonable to expect that locally $\partial u/\partial x > \partial v/\partial y$. Accordingly it is sensible to expect changes in vertical motion where $|\partial u/\partial x|$ is a maximum. In particular ascent is likely where $\partial u/\partial x$ is large and negative, implying convergence and descent is probable where $\partial u/\partial x$ is large and positive. The field of $\partial u/\partial x$ shown in figure 8 is then compatible with ascent near 240 km, 600 mb just below the cusp in the dry zone (figure 5) and descent at the same level at 200 and 275 km, which correlates well with the two humidity minima. There is also a strong correlation with the precipitation echo at 250 km (figure 5) as well as the regions of potential instability at 250 km, 700 mb (figure 6) already referred to. The analogous region of implied descent at 230 km, 900 mb is closely related to the break in the radar echo.

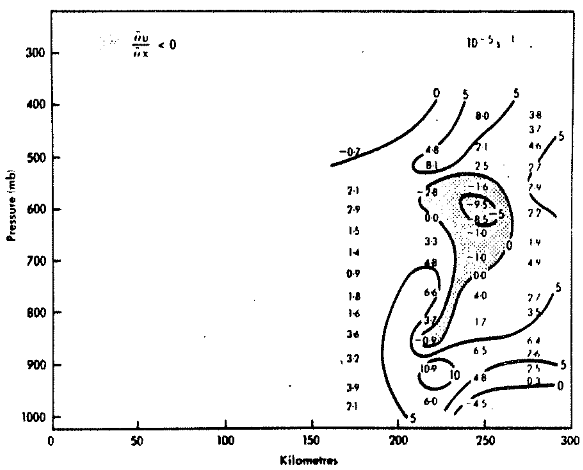

Figure 8. East-West cross section of $\partial u/\partial x$

Discussion

This first use of a new facility has highlighted its potential for the study of the mesoscale structure and dynamics of the atmosphere. In particular the ability to define thermal and moisture fields together with the coexisting air motions, in two dimensions here and eventually in three, has been shown to provide a self consistent and mutually supportive data set.

At the moment the results are rather limited in extent. Nevertheless in the example described above, a number of interesting features have been identified and a coherent if tentative picture of the airflow, cloud and precipitation has emerged.

References

Browning K.A., Hardman M.E., Harrold T.W., and Pardoe C.W. 1973. "The structure of rainbands within a mid-latitude depression". Quart.J.R.Met.Soc. 99, pp 215-231.

Beukers J.M. 1968. "Windfinding using the Loran C and Omega Long Range Navigational Systems". IEEE Transactions on Geoscience Electronics, GE-6, pp 143-151.

Hardman M.E., James D.G. and Goldsmith, P. 1972 "The measurement of mesoscale vertical motions in the atmosphere". Quart.J.R. Met Soc. 98, pp 38-47.

Ryder P., Hardman M.E. and Goldsmith P. 1972. "The development and use of dropsondes for Meteorological Research". Met O 15 Internal Report No. 18. Meteorological Office, Bracknell.

A SEVERE WINTER SQUALL LINE

R. E. Carbone and R. J. Serafin
National Center for Atmospheric Research*
Boulder, CO, U.S.A.

and

J. A. Moore
Water and Power Resources Service
Denver, CO, U.S.A.

EXTENDED ABSTRACT

I. INTRODUCTION

The kinematic structure of cold-front zones rarely has been observed on the cloud scale. Triple-Doppler radar measurements permit detailed resolution of this structure. The Sierra Cooperative Pilot Project, sponsored by the U.S. Bureau of Reclamation, conducted such observations in cooperation with NCAR and the University of Wyoming. The case considered herein occurred on 5 February 1978 in the Central Valley of California, 100-150 km northeast of San Francisco and, kinematically, was the most intense event of the winter. The authors believe it to be a severe version of an important class of cold frontal events which have been reported by Browning and Harrold (1970), Browning and Pardoe (1973), and James and Browning (1979). Hobbs et al (1980) have also reported a similar event. This class of cold fronts is accompanied by a thin line of intense, two-dimensional convection referred to by Browning et al as "line convection" and by Hobbs et al as "narrow cold frontal bands." The results of this case study identify a kinematic structure similar to that proposed by Newton (1963) for a squall line. Given that this event was accompanied by intense electrical activity as well as torrential rainfall rates the term "squall line" seems most appropriate despite the season and relatively shallow nature of convection compared to summertime events.

There are two conditions which are common to at least some narrow cold frontal lines of precipitation. The pre-frontal atmosphere is nearly neutral with respect to a moist lifting process. In the Browning and Harrold (1970) case, as well as the case presented herein, a negligible amount of positive buoyancy is generated (over a very thin layer) when the pre-frontal boundary layer air is mechanically forced upward by the cold front. The second condition, which is of great importance, is the presence of a low-level jet, typically 25-30 m/s, immediately ahead of the front. Strong wind shear and convergence across the narrow frontal zone creates the potential for severe hydrodynamic instability in the presence of what is essentially a hydrostatically stable environment.

This particular case study resulted from the passage of a cold front which was directly associated with a strong short wave trough in advance of a long wave trough located west of California. Satellite imagery revealed that the cold front progressed northeastward at an average speed of 30 m/s across the Pacific Ocean. The convection was identified by satellite imagery approximately three hours prior to Doppler observations over Northern California. The squall line was approximately 500 km in length. Figure 1 shows the detailed radar reflectivity structure along a representative section of the front as observed by Doppler radar. Peak radar reflectivity factor values were typically 50-60 dBZ (where dBZ is defined as 10 log Z and where Z is in units mm^6/m^3). The quasi two-dimensional structure is apparent along with the narrow (5 km) zone of high reflectivity values. On a scale larger than shown in Figure 1 the reflectivity band was composed of several wave-like arcs, each approximately 75 km long.

II. KINEMATIC STRUCTURE

Three Doppler radars scanned a major portion of the region in Figure 1. Data were interpolated and filtered to Cartesian space, and horizontal

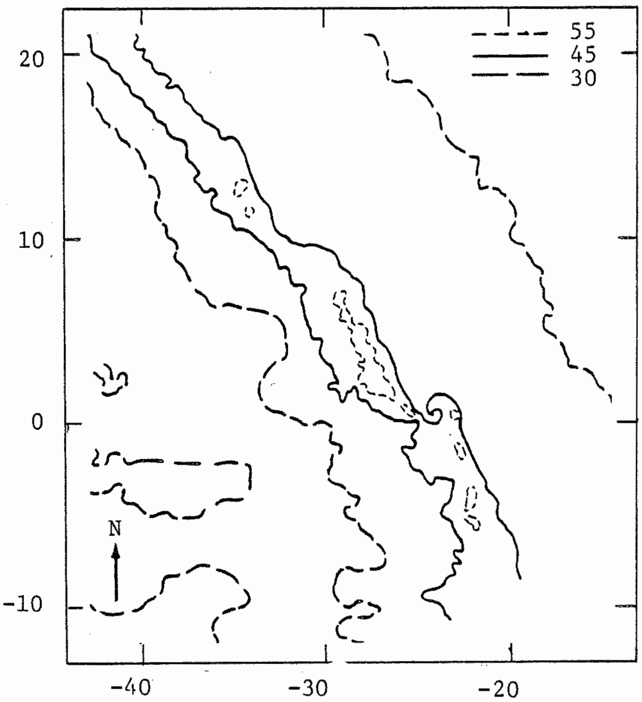

Fig. 1. Reflectivity factor, 30, 45, 55 dBZ_e from 1.5° PPI scan, NCAR CP-3 radar.

* The National Center for Atmospheric Research is sponsored by the National Science Foundation.

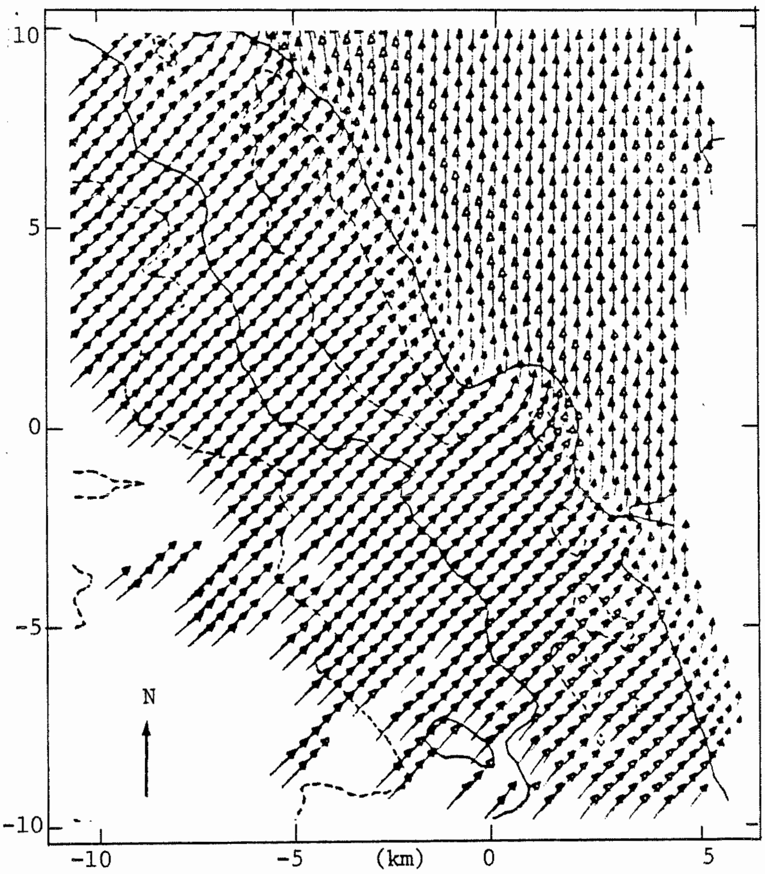

Fig. 2. Total wind.

Fig. 2. Total horizontal wind field at 1.2 km level and radar reflectivity contours at 10 dB increments (40 dBZ, solid). Note sharp wind shear at leading edge of reflectivity line. Prefrontal flow below 0.7 km is essentially parallel to front as measured by single Doppler radar.

Fig. 3. Same as Fig. 2 except storm motion removed. Storm advection from 205° at 28 m/s. Note position of vortex in shear/convergence zone at leading edge of reflectivity line. All derivative motion field parameters average 10^{-2}/s.

Fig. 4. Expanded view of vortex which is the parent circulation of a small tornado. Note classical hook echo and weak echo inflow region. Reflectivity contours every 5 dB, 40 dBZ solid. Lowest level of triple Doppler data shown. Vertical component of vorticity maximizes in center of vortex (4×10^{-2}/s).

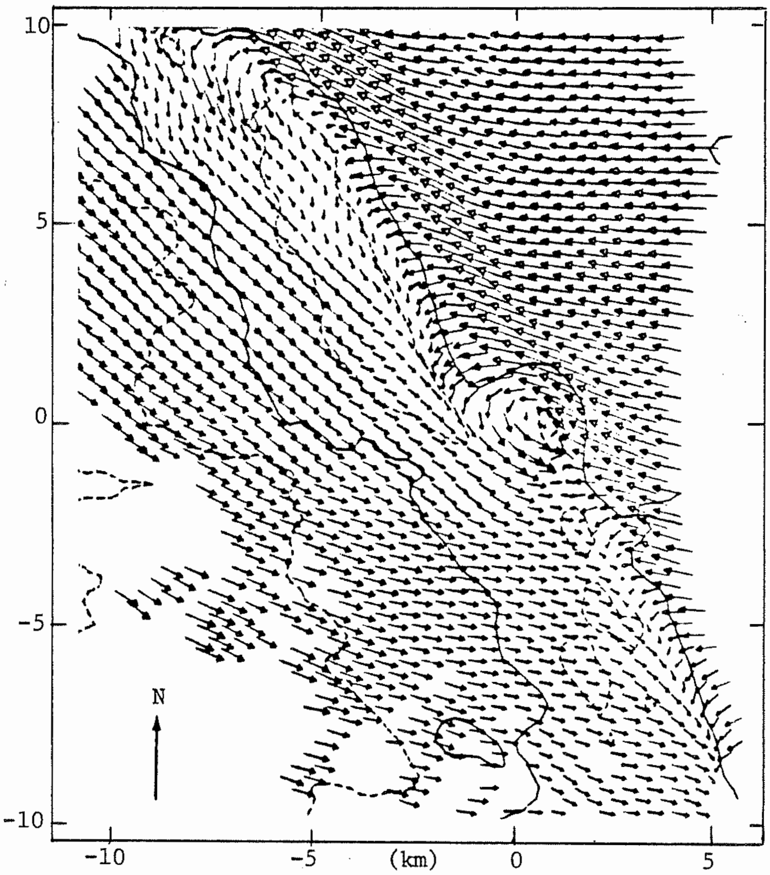

Fig. 3. Storm-relative wind.

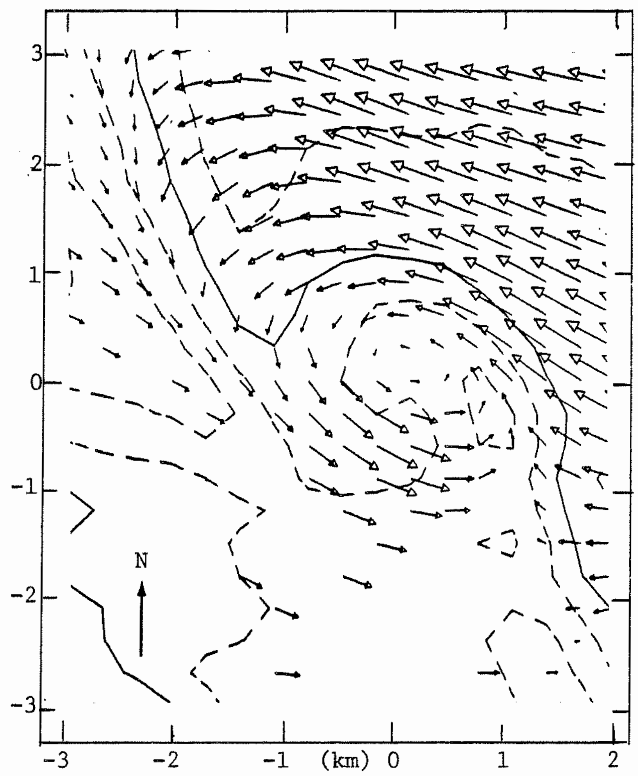

Fig. 4. Vortex circulation.

air motions were calculated. Horizontal planes of data were shifted to compensate for storm advection which occurred during the radar scan time. Vertical air motion was obtained indirectly by means of mass continuity. An upper boundary condition of $w = 0$ at $z = 6.3$ km was assumed. Downward integration of the anelastic mass continuity equation was the final step. The upper boundary condition is vulnerable to significant error; however, homogeneity of the reflectivity field aloft suggests that it is satisfactory for this case.

Figure 2 shows the 1.2 km total horizontal wind field with contours of radar reflectivity factor superimposed (40 dBZ, solid). Note the sharp wind shift line at the leading edge of the band. Winds ahead of the front are south-southeasterly at 25-30 m/s. Single Doppler observations confirm a pre-frontal flow nearly parallel to the wind shear line below 0.7 km. Triple Doppler data were not available so close to the lower boundary. Winds behind the front are southwesterly at 30-35 m/s. The transition zone between pre- and post-frontal flow is only a few hundred meters wide. This is due to the fact that hydrostatic stability is able to maintain both flow regimes up to the narrow zone of forced ascent along the surface cold front.

An illustrative way to examine the horizontal air flow is to vectorially subtract storm motion and see air motion relative to the storm. Figure 3 shows the storm-relative horizontal air flow at 1.2 km with radar reflectivity factor superimposed as in Figure 2. Figure 3 dramatically illustrates the strong cyclonic shear zone along the leading edge of the high reflectivity zone. Horizontal shear of the horizontal wind averages 10^{-2}/s throughout the zone with peak values in excess of 3×10^{-2}/s. It is also obvious that breakdown of the shear zone has created a small vortex. The vortex has been directly associated with tornadic damage near Sacramento Metropolitan Airport (Carbone and Serafin, 1980). Close examination of Figure 1 reveals a "hook echo" which is also coincident with the vortex. The average value of the vertical component of vorticity along the frontal shear zone is roughly 10^{-2}/s with a maximum value of 4×10^{-2}/s in the vortex circulation. Horizontal divergence values along the shear zone also average -1×10^{-2}/s with maxima in excess of 3×10^{-2}/s at the leading edge of the high reflectivity zone. Figure 4 shows an expanded view of the vortex circulation at the lowest level of triple Doppler data. The reflectivity hook echo and shear-induced folding of the frontal zone are obvious features. Such vortex circulations are, in all likelihood, similar to the "corrugations" reported by Browning and Harrold (1970). In the dissipation stage the vortex region appears as a step discontinuity in the line with minimum wind shear in the mixed zone.

Figure 5 shows a typical vertical cross-section oriented orthogonal to the squall line (WSW-ENE), where into the page is north-northwestward. The figure shows vertical air motion together with the storm-relative cold front-orthogonal component of horizontal air motion. Radar reflectivity factor contours are also shown at 10 dBZ intervals with the 40 dBZ contour solid. Pre-frontal low-level inflow of 20 m/s is seen to be mechanically forced upward over the westerly momentum cold air below 2 km. Maximum updraft speed is typically 15-20 m/s at 2.1 km. Inertial ascent above 2.1 km continues for some of the updraft air to a level of 6 km or greater. The updraft is divergent above 2.1 km with maximum divergence typically between 3 and 4 km. Soundings indicate that updraft parcels should be slightly negatively buoyant above 2.1 km which agrees well with the deduced kinematic structure shown in Figure 5. Most of the air emanating from the updraft aloft diverges toward the rear of the squall line and rapidly subsides. A very small fraction of updraft

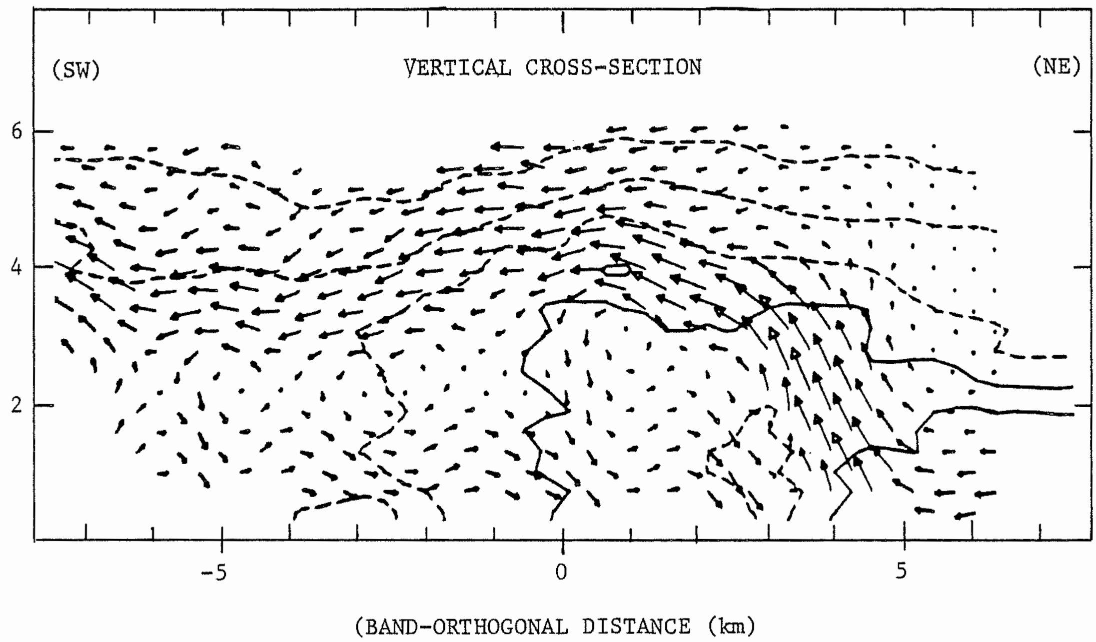

Fig. 5. Typical squall line cross-section. Reflectivity contours at 10 dB increments, 40 dBZ solid. Storm-relative horizontal wind and vertical air velocity. See text for explanation.

air diverges ahead of the band at an outflow rate of 1 m/s. Hydrometeors which exit the updraft via this forward branch of the outflow invariably re-enter the updraft at lower levels subsequent to sedimentation. The pre-frontal environment above 2 km is strongly subsident (~ 1 m/s) for a distance of at least 12 km ahead of the squall line.

Post-frontal cellular convection is also evident in Figure 5. Vertical shear of the horizontal wind to the rear of the surface front (combined with shallow destabilization caused by melting hydrometeors) drives the post-frontal convection. Typical updraft values are 2-3 m/s; however, isolated cells sometimes exceed 5 m/s. The post-frontal convection is three-dimensional as opposed to the highly two-dimensional structure of the main pre-frontal updraft. Close correspondence between air motion vectors and reflectivity contours suggests transport of hydrometeors with relatively small terminal fallspeed (rather than growth of large particles) in the post-frontal convection. No hail was observed at the surface in connection with this storm. It is felt that the residence time of hydrometeors in the main updraft was much too small to permit hail production despite the fact that at least a few particles were recycled. Downdrafts, which averaged approximately 5 m/s, were commonly present in the heaviest precipitation and also along the rear flank. Local values occasionally exceeded 15 m/s.

III. PRECIPITATION EFFICIENCY

The squall line kinematic and radar reflectivity structure were observed to be in a quasi-steady state for a period of approximately one hour. For example, the line-averaged maximum updraft speed was 17 m/s $\pm$ 1.5 m/s during the entire period of triple Doppler observations. When a quasi-steady two-dimensional storm advects through a region, cumulative rainfall amounts are quite uniform. In this case, all eight rain gauges were within $\pm$ 35 percent of the 10.7 mm average cumulative rainfall amount. Peak rainfall rates were well in excess of 100 mm/hr.

One may calculate the total condensate production rate at each point in the storm from the vertical air motion field. Provided that a quasi-steady state is maintained over the whole region, then condensate production may be interpreted as rainwater flux given by:

$$R = \int_{Z_1}^{Z_2} \rho(z) \frac{dM}{dz} w(z)\, dz$$

where ρ is air density, M is saturation mixing ratio, w is vertical air velocity (wherever $w > o$) and z is the vertical space dimension. Our preliminary calculation assumes a gradual transition from water saturation (at 0°C) to ice saturation (at -25°C) at the storm top. Cloud base was measured at 0.7 km (8°C). This calculation has been performed for all horizontal space and $\langle R \rangle$ has been computed where $\langle R \rangle$ is the ensemble average over the horizontal domain. Knowing the speed and direction of storm advection (28 m/s, 205°), it is straightforward to compute the total rainfall which would result from a 100 percent efficient storm. In this case $\langle R \rangle$ is 70 mm/hr. (equivalent rainfall/rate) and effective storm residence time is 11.66 min. It follows that a 100 percent efficient storm would have produced 13.6 mm precipitation as compared to the 10.7 mm measured. The calculations imply a 79 percent average efficiency over the entire frontal precipitation band. It is concluded that this squall line is highly efficient in spite of very short residence time in the main updraft. Hydrometeor recycling in post-frontal cells together with low potential for evaporative losses are likely to be the principle reasons for high efficiency.

Topographical effects in the Central Valley of California are likely to have contributed to the severity of this case. These considerations will be discussed in detail in a formal publication.

REFERENCES

Browning, K.A. and T.W. Harrold, 1970: Air Motion and Precipitation Growth at a Cold Front. Quart. J. Roy. Meteor. Soc., 96, 371-382.

Browning, K.A. and C.W. Pardoe, 1973: Structure of Low-level Jet Streams Ahead of Mid-latitude Cold Fronts. Quart. J. Roy. Meteor. Soc., 99, 619-638.

Carbone, R.E. and R. Serafin, 1980: A Severe Winter Squall Line Part II: Kinematic Structure Deduced from Triple Doppler Radar Observations. Preprints, 19th Conference on Radar Meteorology, AMS, Boston, Mass.

Hobbs, P.V., T.J. Matejka, P.H. Herzegh, J.D. Locatelli, and R.A. Houze, 1980: The Mesoscale and Microscale Structure and Organization of Clouds and Precipitation in Mid-Latitude Cyclones, Part I: A Case Study of a Cold Front. J. Atmos. Sci., in press.

James, P.K. and K.A. Browning, 1979: Mesoscale Structure of Line Convection at Surface Cold Fronts. Quart. J. Roy. Meteor. Soc., 105, 371-382.

Newton, C.W., 1963: Dynamics of Severe Convective Storms. Meteorol. Monogr., 5(27), 33-55.

ATMOSPHERIC POLLUTION BY PARTICULATE MATTER AND WEEKLY REGIME OF RAIN IN MADRID

J. Catalá, M.C. Martínez, M.T. Rico

Cátedra de Física del Aire
Madrid ESPAÑA

ABSTRACT

A comparative study between the evolution of the P.M. atmospheric pollution vs. the average daily measured precipitation for every day on the week within the last ten years, in Madrid city, shows a clear and strong correlation between both phenomena, with minimum values for both during the weekends.

These results are corroborated by the same weekly pluviometric evolution along the 30's (1931-1940), where that minimun over the weekends does not appear, but the other round.

INTRODUCTION

As it is well known not all the aerosols or Particulate Matter (P.M.) suspended in the atmosphere are able to act as Condensation Nuclei (CN), because this phenomenon depends not only on the size and nature of the P.M. but also on the degree of supersaturation of the atmosphere.

In order to became a real "cloud drop" the droplet fixed on the P.M. has to grow up over a critic radius which is related to the saturation ratio by the Kohler equation (Mason 1971). According to this equation, for the different atmospheric conditions, the radii of the particles acting as condensation nuclei are between 10^{-2} and 1μ. (Stern et al. 1973).

Those nuclei generate cloud droplets that after different microphysical processes reach enough size to became a rain drop, origin of the different kinds of precipitations.

In those regions in which atmospheric pollution is high because there is a great number of P.M. there will be also many CN, and that bring us to suppose that there might be a possible modification of the pluviometric regime.

In order to known this possible modification, in the case of Madrid, we have compared the weekly pluviometric regime of the last ten years (1969-78) with that of the decade of "the thirties" (1931-40) looking for the possible influence of the growing up atmospheric pollution since 1970.

As we have not sufficient measurements of CN, we have been obliged to use as a reference the P.M. data having into account that those data included particles with r ⩾ 0.5μ (Navarro 1975) and some of them are really what one calls CN.

DATA

The weekly pluviometric regime corresponding to the years 1969-78 and 1931-40 has been studied considering the daily values registered at the Retiro Observatory (Madrid).

The P.M. concentrations have been obtained with an equipment "Dust Impactor" (Martínez 1976), and belong to observations made during a five years period (1974-78) in the Campus of the University of Madrid.

RESULTS

The average rainfall for every day of the week during the last ten years (1969-78) on the area of Madrid has been computed, compared with the average rainfall in the same area for every day of the week during the decade (1931-40) when the pollution was practically none. Those evolutions are given respectively in figs.1 and 2.

Fig.1(a) shows a clear maximun in the middle of the week and a minimun on Sundays. The average rainfall during the working days is 1.45 mm. and the average rainfall during the weekends is only 1.12 mm. which means a 30% less (fig.1(b)). This situation is quite different to the one we can see in the fig. 2 where the average rainfall during the working days (1.08 mm.) is a 15% smaller than the average (1.25 mm.) of the weekends rainfall (fig.2 (b)).

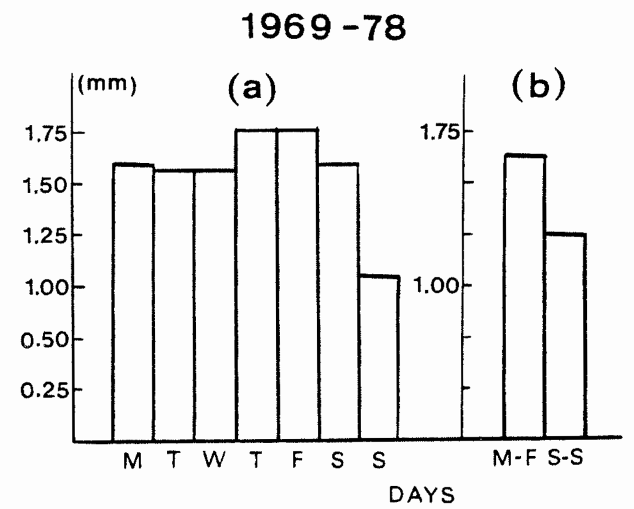

Fig.1. Average weekly variation of regime pluviometric (M-F: working days S-S: weekend).

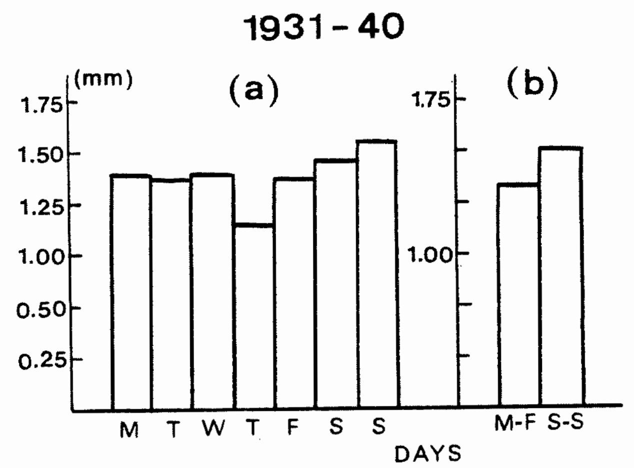

Fig.2. Average weekly variation of regime pluviometric (M-F: working days S-S: weekend).

By spectral analysis (Catalá and Martínez 1976), it has been proved that the atmospheric pollution by P.M. has a 7 days periodicity. If we compare the weekly evolution of the P.M. concentration (fig.3) with the pluviometric regime obtained from fig.1 we may observe a great concordance, being both evolutions practically parallel, with a maximun in the middle of the week and a sharp minimun over the weekend, specially on Sundays. These facts enhance the evidence of the change that the pluviometric regime has suffered from the years with no atmospheric pollution to those in which this pollution is high. The good agreement between the grafic of the rainfall and the one of the atmospheric pollution by P.M. shows that those P.M. acted as additional CN.

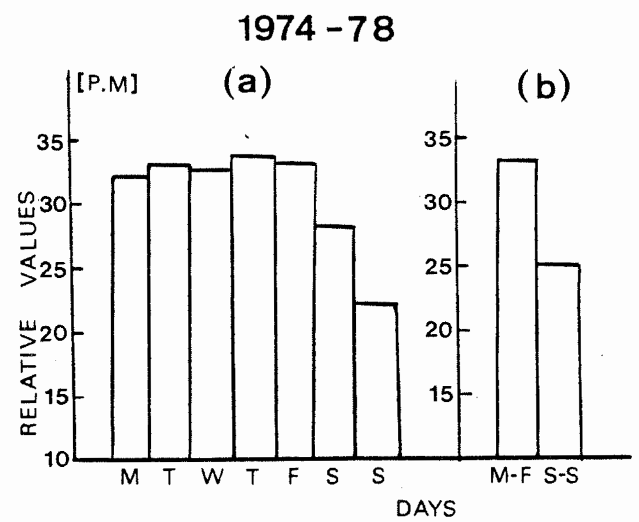

Fig.3. Average weekly variation of P.M. concentrations (M-F: working days S-S: weekend).

These results are similar to those found by Detwiller (1970) for the city of Paris. This author found also similar results in other four cities of the north of France where the values obtained for the rainfall during the weekend are between 14 and 32% less to those of the rest of the week; he considered data from the period 1960-67.

REFERENCES

Catalá, J. and Martínez, M.C., 1976. Espectro de potencias de las concentraciones medias de partículas materiales. Proceedings, II Asamblea Nacional de Geodesia y Geofísica. Inst. Geográfico y Catastral, Vol.II, Spain pp 1039-1046.

Detwiller, J., 1970. Incidence possible de l'activité industielle sur les precipitations a Paris. Urban Climates, Vol.I, No.254, TP.141, Technical Note No.108, W.M.O. Geneva, Switzerland.

Martínez, M.C., 1976. La contaminación por partículas materiales: sus variaciones, análisis de frecuencias y relación con diversas variables y fenómenos meteorológicos. Doctoral Thesis. Univ. Complutense, Madrid, Spain.

Mason,B.J., 1971. The physics of clouds Oxford Univ. Press 671 pp.

Navarro, E., 1975. Estudio de la contaminación ambiental en Valencia. Doctoral Thesis. Univ. de Valencia. Spain.

Stern, A.C., et al., 1973. Fundamentals of air pollution. Academic Press, New York, p.25.

STRUCTURE A MOYENNE ECHELLE D'UN FRONT FROID

Jean-Pierre CHALON et Marc GILET

Etablissement d'Etudes et de Recherches Météorologiques

78470 Magny-les-Hameaux FRANCE

1 - INTRODUCTION

Aux échelles synoptique et subsynoptique, le front froid apparaît comme un phénomène bi-dimensionnel. La plupart des études de petite échelle effectuées jusqu'à présent se sont appuyées sur cette hypothèse pour décrire la structure des systèmes frontaux (voir par exemple Browning et Harrold, 1970). L'un des objectifs de la campagne Fronts 77 était de parvenir à une description tridimensionnelle à petite et moyenne échelle des fronts passant sur la région parisienne, afin de vérifier la validité de l'hypothèse de bidimensionnalité.

Trois laboratoires français participaient à la campagne, l'Etablissement d'Etudes et de Recherches Météorologiques de la Météorologie Nationale (EERM), le Centre de Recherches sur la Physique de l'Environnement (CRPE) et l'Institut et Observatoire de Physique du Globe du Puy de Dôme (IOPG).

L'expérience qui s'est déroulée pendant l'automne 1977 et le printemps 1978 mettait en oeuvre en particulier, trois stations de radiosondage dont deux équipées de radar-vent et disposées en triangle (Magny-les-Hameaux, Orléans, Rouen), un système de deux radars Doppler (Ronsard) et un avion instrumenté Aerocommander.

Nous présentons ici les principaux résultats d'une étude du front froid qui est passé sur la région parisienne le 3 Novembre 1977 (Chalon et al. 1980). L'analyse détaillée de cette situation montre que si la structure de ce front peut être présentée comme bi-dimensionnelle à l'échelle subsynoptique, cette interprétation n'est pas applicable à petite échelle.

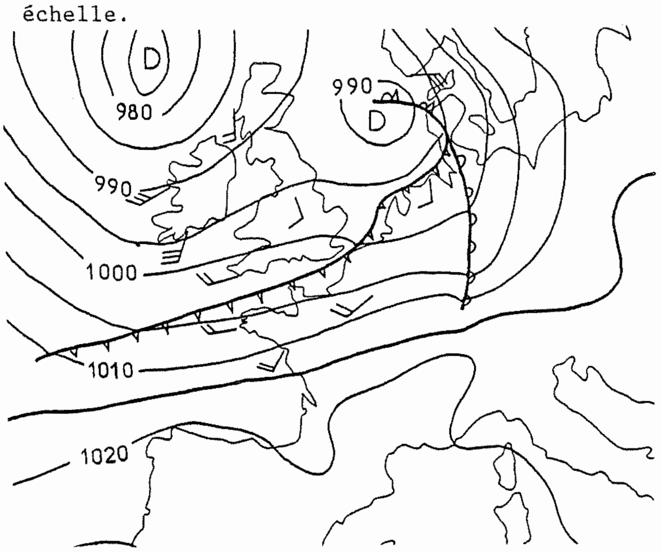

Figure 1. Situation météorologique en surface le 3 Novembre 1977 à 00 TU.

2 - SITUATION SYNOPTIQUE

La situation en altitude le 3 Novembre à 00.TU est caractérisée par une vaste zone dépressionnaire entre l'Islande et le Groenland. Cette zone qui se déplace vers l'Est est associée à un thalweg thermique orienté Nord-Sud dont l'axe passe au-dessus de la Bretagne. La Figure 1 montre la situation au sol à 00.00 TU. Elle met en évidence un système frontal associé à une dépression secondaire qui est centrée sur la mer du Nord. Le front chaud est passé sur Paris le 2 à 7.00 TU. Le front froid visible sur la Manche se déplace à 50 km/h vers le SSE. Sa progression sera ralentie à 15 km/h à son arrivée sur les terres et il atteindra Magny-les-Hameaux vers 15.00 TU. Dans le secteur chaud, l'air a un caractère cinématique de mélange. A l'arrière du front, l'air froid a un caractère convectif et donne lieu à de nombreuses averses.

La limite entre les deux masses d'air est sensiblement parallèle au flux, ce qui amène le front à onduler. Il s'atténuera progressivement dans la journée du 4, et ne produira plus que des averses éparses en arrivant sur la Provence.

3 - ANALYSE SUB-SYNOPTIQUE

Une série de radiosondages (PTU) et de mesures de vent en altitude a été effectuée à partir de Magny-les-Hameaux et d'Orléans entre le 2 Novembre à 9.00 TU et le 4 Novembre à 10.00 TU. Au voisinage du front, les radio-sondages étaient espacés de 2 heures. Les profils de température pseudo-adiabatique potentielle du thermomètre mouillé (θ'_W - Figure 2) mettent en évidence une surface frontale correspondant sensiblement à l'iso - θ_W 14°C et la présence en altitude de plusieurs gouttes froides de dimensions variées, notées C1 à C5. Les précipitations les plus importantes se trouvent le long d'une bande de convection préfrontale associée à de l'instabilité en altitude et au niveau d'une bande de convection ancrée sur la trace du front au sol. On observe des averses dans le secteur froid.

L'analyse des vents parallèles au front montre la présence de vents légèrement plus forts à 850 mb à l'avant du front (jet de basses couches) et de deux jets à 300 mb. Cette répartition des vents est similaire à celle décrite par Browning et Pardoe (1973 - Situation du 6 Février 1969). Ces auteurs ont montré que ce genre de structure est associé à une circulation hélicoïdale de l'air à l'avant du front. Le maximum de vitesse correspondant au jet de basses couches augmente la convergence au niveau de la surface frontale par effet de frottement au sol. A cause de la convection, la pente du front est pratiquement verticale dans

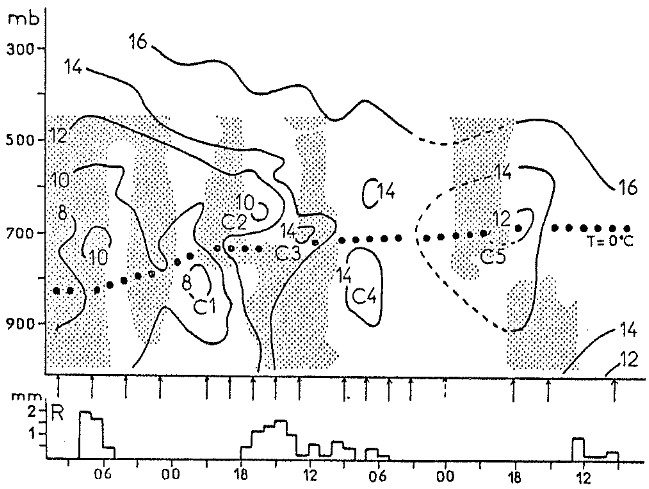

Figure 2. Coupe spatio-temporelle de θ'_W déduite des radiosondages effectués à Magny-les-Hameaux entre le 2 et le 4 Novembre. Les flèches sous la Figure indiquent les heures des sondages. L'altitude de l'isotherme 0°C est représentée en pointillés. La hauteur de pluie mesurée au sol est représentée sous la Figure (en mm) Les zones grisées correspondent aux vitesses verticales ascendantes (déduites des données de radar vent).

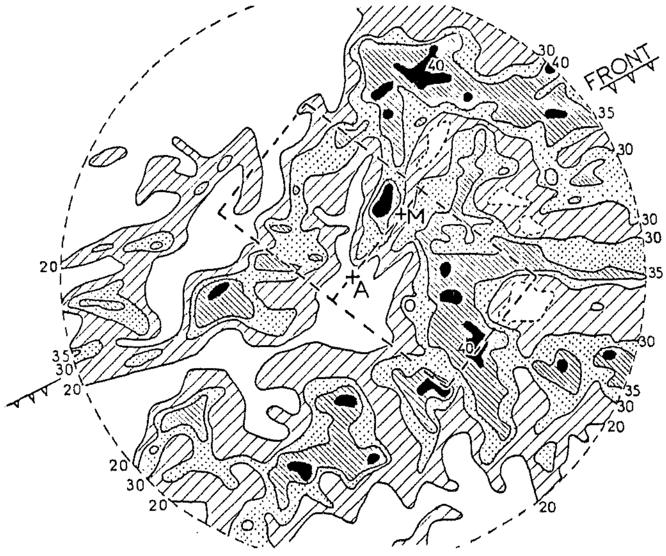

Figure 3. Organisation des échos radar (en dB non étalonnés) observés à 14.39 TU par le radar d'Ablis. Le deuxième radar Doppler situé à Magny-les-Hameaux est représenté par le point M. Le rectangle délimite les deux zones de restitution des champs de vent à partir des données Coplan. La position du front froid est indiquée à la même heure.

les 3000 premiers mètres. Au-dessus de 4500 m, l'air chaud subit une ascension plus lente, au-dessus de l'air froid, suivant une pente plus douce (environ 1%).

La convection frontale prenant naissance au niveau du sol est atténuée à 650 mb. Ceci peut être attribué à un mélange de l'air convectif avec de l'air sec subsident (θ'_W = 10°C) provenant de la masse d'air froid. Une partie de cet air froid semble parvenir à déferler au-dessus de l'air chaud pour se retrouver à l'avant du front sous forme de gouttes froides en altitude. La présence de ces gouttes froides (en θ'_W) au-dessus d'air plus chaud crée des zones d'instabilité potentielle. Cette situation ressemble à celle décrite par Kreitzberg et Brown (1970) pour une occlusion. La goutte froide C 3 correspond à une ligne de convection préfrontale. Une partie de l'air associé à cette goutte a été humidifié par mélange avec l'ascendance frontale et contient probablement des cristaux de glace (présence d'altocumulus). La présence de la goutte C 3 dans l'air chaud crée une instabilité potentielle et le déclenchement de la convection peut être attribué à la fonte des cristaux au passage de l'isotherme 0°C. L'examen des humidités (non représentées ici) et des vitesses verticales ascendantes estimées à partir des données de radar vent en intégrant l'équation de continuité avec une hypothèse de bi-dimensionnalité (Figure 2) confirme cette description.

4 - DONNEES RADAR

Les données radar obtenues avec le système RONSARD mis en oeuvre par le CRPE et analysées à l'EERM ont permis de préciser la structure à petite échelle du front. Le système RONSARD, composé de deux radars DOPPLER identiques, fonctionnant en bande C, a été décrit par Waldteufel et al. (1975). Les radars étaient installés à Magny-les-Hameaux et Ablis (voir Figure 3) et espacés de 29 km.

La Figure 3 montre la position des échos dans un rayon de 100 km autour d'Ablis à 14.31 TU. Ces échos peuvent être classés en fonction de leur position par rapport à la surface frontale (Hobbs et al., 1978). On constate que les précipitations associées à la trace du front au sol sont organisées en cellules et sont assez dispersées. Leur déplacement suit sensiblement l'axe du front (60° par rapport au Nord) à une vitesse de 28 m/s. Une telle cellule est passée quelques kilomètres au Nord de Magny-les-Hameaux un peu avant 15 heures et les précipitations enregistrées au passage du front y ont été relativement importantes. Ces précipitations précédaient très légèrement le passage du front au sol qui a été marqué de façon nette par des variations peu élevées mais rapides de température (-1.5°C), température du point de rosée (-1.5°C) pression (+0.5 mb), direction (+40 degrés) et vitesse du vent (-4 m/s).

Les précipitations les plus étendues sont situées à l'avant du front et peuvent être attribuées aux phénomènes de convection préfrontale mentionnés plus haut. Elles se déplacent à peu près à la même vitesse que les cellules frontales mais en suivant un axe de 75° par rapport au Nord, ce qui leur donne une composante perpendiculaire au front, dont elles s'éloignent de 7 à 8 m/s.

L'analyse des données du système RONSARD a permis d'obtenir une description tri-dimensionnelle des champs de vent dans ces précipitations. La méthode de restitution des vents a été décrite par GILET et al. (1979).

Le principe consiste à rééchantillonner les données de vitesse radiale pour chaque radar dans un domaine décrit en coordonnées cartésiennes, à évaluer en chaque point de grille la composante du vent dans le plan défini par ce point et les deux radars, puis à intégrer l'équation de continuité anélastique pour obtenir les vitesses verticales, en tenant compte de la contribution des vitesses de chute des particules. La Figure 4 montre une coupe verticale obtenue perpendiculairement à la surface frontale. La convection préfrontale située 35 km à l'avant du front est très développée. La cellule observée culmine à plus de 6000 mètres avec des vitesses verticales ascendantes supérieures à 5 ms-1.

Aux environs de l'altitude 3 km, l'air situé au-dessus du front suit une trajectoire qui l'éloigne du front au-dessus de la masse d'air chaud. C'est probablement l'arrivée de cet air potentiellement instable et subsident sur l'isotherme 0°C qui déclenche la convection par absorption de chaleur latente accompagnant la fonte des cristaux de glace.

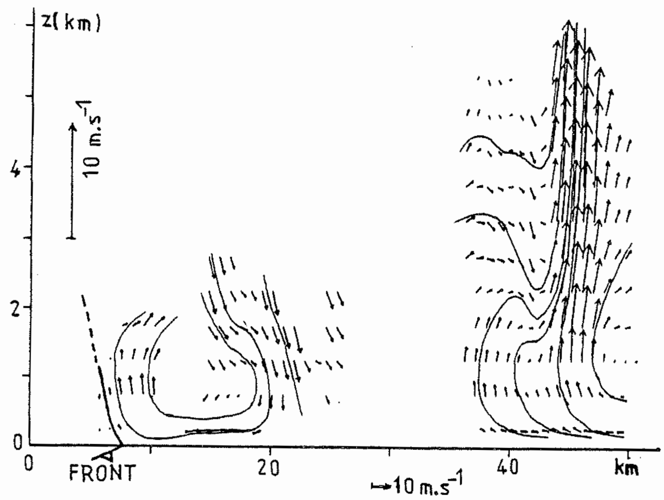

Figure 4. Représentation des vitesses Doppler dans un plan vertical perpendiculaire au front à 15.29 TU. Les échelles des vitesses horizontales et verticales sont représentées le long des axes correspondants.

La Figure 5 représente les perturbations du champ de vent horizontal à 250 mètres dans le front. Les lignes de courant déduites de ce résultat sont présentées sur la Figure 6. Elles mettent en évidence une ligne de cisaillement de vent correspondant au front (FF') et une ligne de cisaillement CC' le long de laquelle la convergence est maximale ; ces deux lignes se rejoignent en T qui correspond à une région de fort tourbillon cyclonique. Dans la région NE, derrière le front, on remarque une région de divergence correspondant à un tourbillon anticyclonique. La Figure 6 montre également la répartition de la vitesse verticale ascendante obtenue avec le système DOPPLER. Bien que le front soit bien marqué par un cisaillement de vent, les vitesses verticales le long de FF' sont faibles. Les maxima de vitesse ascendante sont situés le long de CC' qui correspond par ailleurs à une zone de réflec-

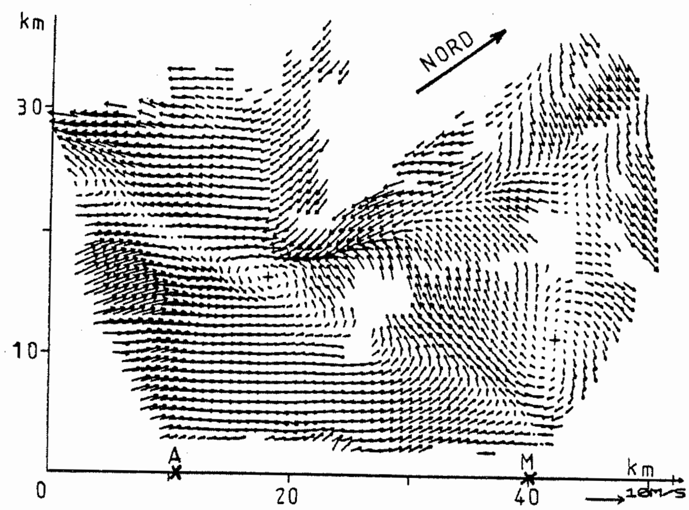

Figure 5. Champ de vent Doppler horizontal à 250 mètres d'altitude à 14.25 TU. La vitesse moyenne du vent à ce niveau a été retranchée pour faire ressortir les perturbations du champ. Les positions des radars d'Ablis et de Magny-les-Hameaux sont indiquées (A et M).

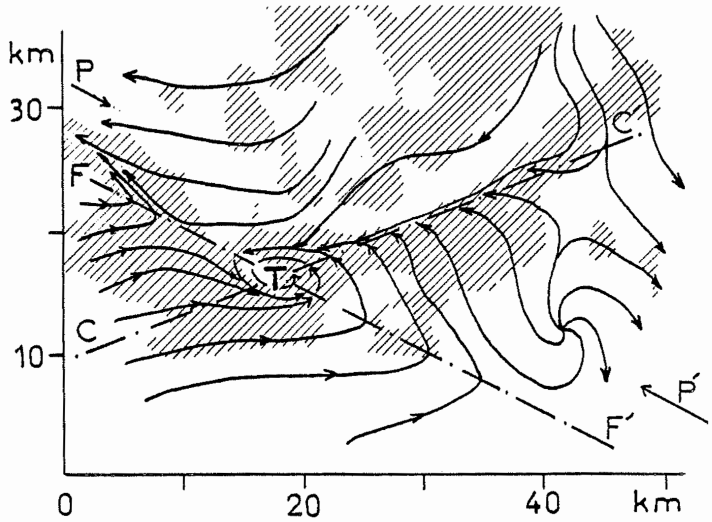

Figure 6. Lignes de courant déduites de la Figure 5. Les zones en grisé correspondent aux vitesses verticales ascendantes obtenues à partir des données Doppler.

tivité maximum. Des coupes verticales ont été effectuées au niveau des noyaux de plus forte ascendance.

La Figure 7 représente une telle coupe effectuée dans la région d'ascendance maximale qui est associée au tourbillon T. Sous le vent de la zone d'ascendance, on remarque deux zones de subsidence. Celle qui est proche de l'ascendance est la plus active et correspond aux réflectivités maximales qui sont associées à la cellule. L'autre région de subsidence, plus étendue horizontalement correspond à de plus faibles réflectivités.

5 - SYNTHESE ET CONCLUSION

L'analyse comparée des données aérologiques et

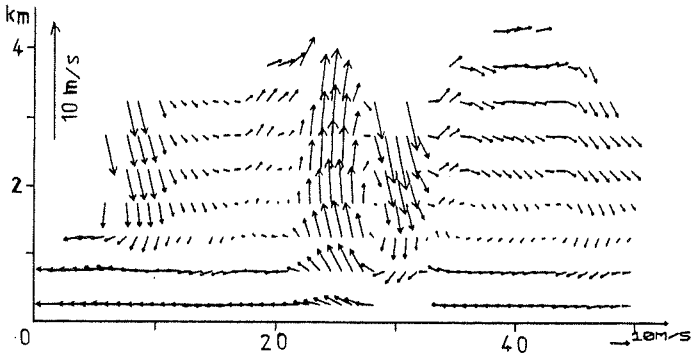

Figure 7. Représentation des vitesses Doppler dans un plan vertical dont la position PP' est indiquée sur la Figure 6. La vitesse de déplacement de la cellule (28 m/s) a été retranchée afin d'obtenir une circulation relative. Les échelles de vitesses horizontales et verticales sont représentées le long des axes correspondants.

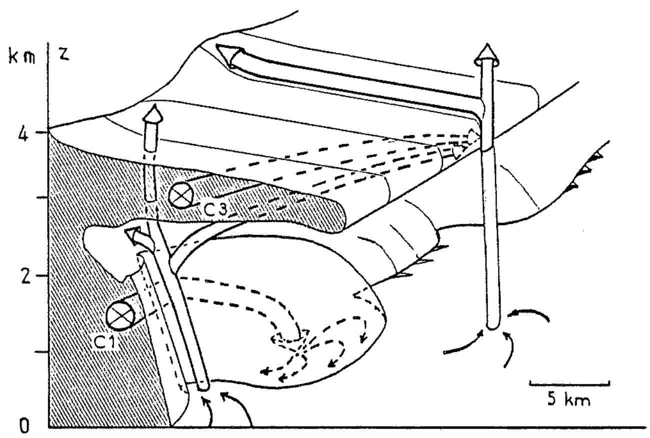

Figure 8. Schéma de synthèse mettant en évidence le mécanisme de déclenchement de la convection préfrontale et les déformations de petite échelle de la surface frontale.

des données radar permet d'aboutir à un schéma possible de la circulation de l'air à moyenne échelle dans la zone active du front. Le front présentait aux échelles synoptiques et subsynoptique une structure assez homogène et se déplaçait suivant une translation régulière. Cependant, la circulation de l'air paraît plus complexe que celle qui est décrite dans les schémas maintenant classiques de Browning et Pardoe (1973).

A moyenne échelle, son mouvement semble plutôt provenir de la combinaison d'une translation lente et régulière et d'une propagation discrète associée aux cellules de précipitation. Les zones de convergence et de tourbillon observées par les radars correspondent à des ascendances bien localisées et de dimensions limitées. Les ascendances provoquent des précipitations qui entraînent de l'air froid dans leur chute (air provenant de la masse d'air froid aux environs de 3000 mètres). Cet air, plus rapide que la progression de la cellule, tombe à l'avant de celle-ci et s'étale en arrivant sur le sol (création de zones de divergence horizontale et de tourbillon anticyclonique). Ayant une composante horizontale plus rapide que l'air chaud, il permet alors la formation de nouvelles régions de convergence sous le vent des précipitations et contribue à plus long terme à l'isolement des ascendances qui lui avaient donné naissance et à leur destruction. De nouvelles ascendances peuvent prendre naissance plus loin dans les nouvelles régions de convergence. Dans notre cas, ces descentes d'air froid semblent être l'élément moteur de l'entretien du contraste thermique et de la progression de la surface frontale.

Au-dessus de 3000 mètres, l'ascendance humidifie une partie de l'air froid (C 3 sur la Figure 2) qui passe au-dessus de l'air chaud. On est en présence d'une instabilité convective potentielle. Cette instabilité qui se traduit à l'avant du front par une zone de convection est probablement déclenchée par la fonte des cristaux de glace à l'isotherme 0°C qui se trouve à une altitude de 2800 mètres. Cette convection s'étend alors aux niveaux inférieurs où se situe la source principale d'humidité.

6 - REMERCIEMENTS

L'expérience Fronts 77 a été effectuée dans le cadre de l'Action Thématique Programmée (ATP) Recherches Atmosphériques de l'Institut National d'Astronomie et de Géophysique. Les données RONSARD nous ont été communiquées par le CRPE. L'IOPG et l'équipe de l'EERM/GMA/4M ont effectué les radiosondages. Nous tenons aussi à remercier Messieurs Gaillard et Klaus qui ont participé à la mise au point des programmes d'analyse des données radar.

7 - BIBLIOGRAPHIE

BROWNING K.A. and T.W. HARROLD, 1970- Air motion and precipitation growth at a cold front - Quart J.R. Met Soc., 96, 369-389.

BROWNING K.A. and C.W. PARDOE, 1973- Structure of low-level jet streams ahead of mid-latitude cold fronts - Quart. J.R. Met.Soc.99,619-638.

CHALON J-P, M.GILET, L. BEAUVAIS, M. ROCHARD 1980 - Structure d'un front froid : Situation du 3 Novembre 1977. Document non publié.

GILET, AMAT, AMAYENC, CAMPISTRON, CHALON, LE BERRE, PASTRE, TESTUD, WALDTEUFEL - 1978 Campagne de mesures "FRONTS 77". Compte rendu des opérations. Note EERM N°407 - Direction de la Météorologie - PARIS.

HOBBS P.V., J.D. LOCATELLI, T.J. MATEJKA, R.A. HOUZE Jr. - 1978 - Air motions, Mesoscale Structure and cloud microphysics associated with a cold front. Reprints - Conference on cloud physics and Atmospheric Electricity -1978 - ISSAQUAH. WASHINGTON. American Meteorological Society.

KREITZBERG C.W. et H.A. BROWN - 1970 - Mesoscale weather Systems within an Occlusion. J. Appl. Meteor, 9, 417 - 432.

WALDTEUFEL P.,B. NUTTEN et A. SAUVAGET - 1975 Les radars RONSARD, Document d'information. Note Technique CRPE/1003, CNET, ISSY-LES-MOULINEAUX.

MESOSCALE FLOW, SMALL SCALE MOTIONS, AND MICROPHYSICS OF PRECIPITATIONS WITHIN A WARM FRONT : A DUAL-DOPPLER RADAR OBSERVATION

M. CHONG, P. AMAYENC, D. HAUSER, G. SCIALOM, J. TESTUD

Centre de Recherches en Physique de l'Environnement, Issy-les-Moulineaux, FRANCE

1 - INTRODUCTION

During the night of November, 2 1977 the dual Doppler Radars of the "Ronsard" system involved in an experiment in association with a meteorological network, observed a wide-spread precipitation area, ahead of a surface warm front. The present paper deals with a description of the mesoscale motion, thermal structure and of the small scale motions deduced from the observations. Both classical VAD (Browning and Wexler, 1968) and COPLAN (Lhermitte, 1970) scannings were used in order to infer the air motions. Also vertical incidence soundings were operated in order to obtain results about the hydrometeor size distributions and vertical motions.

2 - METEOROLOGICAL SITUATION

The warm front (associated with a low pressure zone centered over the Irish Sea at OUT) was oriented approximately N-S and was travelling eastward over France at a speed of 45 km h^{-1} (fig. 1). The two Doppler radars were located at Magny-les-Hameaux and Ablis (see fig. 1). The surface warm front passed over the radar sites at about 7.30 UT. The nearest soundings at Orléans (fig. 2), 70 km South of Ablis, indicate that the frontal zone is located in the layers 1.8 - 4.4 km at 1 UT and .2 - 2.6 km at 4.50 UT.

At 1 UT the atmosphere was conditionally unstable between 1.4 and 2 km and stable in the frontal zone and above. The equivalent potential temperature jump, deduced from temperature profiles in Fig. 2, is about 7°K.

3 - DATA ACQUISITION AND PROCESSING

Doppler radar data were collected during 6 consecutive hours between 1 and 7 UT, by operating various classical scannings : COPLAN, VAD and vertical incidence soundings. They provide a description of the frontal system at various scales. Three methods were used for processing the velocity data obtained by each scanning type :

- For the coplanar scanning, a method based upon a technique of least square fit under constraints (Chong et al., 1980) is used. It allows to interpolate the radial velocities in cartesian grid points 1 km spaced and to filter the turbulent motions with scales less than the grid mesh. When integrating the continuity equation, this method also takes into account the speed of advection of the convective structure. Finally it provides a three-dimensional wind field in cartesian grid points.

- For the conical scanning (VAD), an analysis similar to that of Browning and Wexler (1968) is used (Testud et al., 1980), assuming that the horizontal wind field, in stratiform precipitation, can be represented at scales of a few tens of km by its first order expansion. This method based upon a least square fit, allows to define the mean horizontal wind and divergence height profiles. Then, using the air mass continuity equation, the vertical velocity profile can be calculated.

- From the doppler spectra obtained at vertical incidence, it was possible to deduced the hydrometeor size distributions n(D) and the vertical air velocity w by means of a new method (Hauser and Amayenc, 1980). This method allows to determine simultaneously the three parameters w, N_O, λ where N_O and λ are the two classical parameters of an exponential shaped size distribution $n(D) = N_O \exp(-\lambda D)$.

4 - MESOSCALE CIRCULATION AND THERMAL STRUCTURE

During the period 1 to 7 UT, 11 of the available radar volume sequences were analysed : 8 VAD sequences and 2 COPLAN sequences. Radar echoes were observed up to 6 km before 3.30 UT. After 5 UT only those between 0 and 2 km were available for the analysis.

4-1 The mean horizontal wind fields deduced from the VAD and COPLAN scannings, and their characteristics

In Fig. 3 (a) and (b), we have represented the two components U and V of the mean horizontal wind along X and Y axis pointing respectively to 108° and 18° East of North (directions respectively perpendicular and parallel to the surface warm front, near the radar sites). Two profiles are obtained from the VAD analysis (Magny site) at 3.16 and 3.41 UT. The mean horizontal wind profile deduced from the COPLAN analysis at 2.20 UT (corresponding to 2.50 UT when referring to Magny and taking into account the advection), is assumed to be represented by its first order expansion. From the analysis of Fig. 3, the following comments can be made :

i) we notice a good agreement between the profiles, which confirms the consistency of each method for processing Doppler radar data ;

ii) the flow parallel to the surface warm front is characterized by an intense shear separating a low layer with large velocity (22 to 24 ms^{-1}) from an upper layer with weak velocity (2 to 4 ms^{-1}). In addition, the shearing zone is displaced downwards as time increases, with a speed of 360 mh^{-1}.

iii) with respect to the speed of the front ($Uo = 12.5\ ms^{-1}$) the cross front velocity profiles exhibit a flow which is directed in opposite to the front motion, below 1.5 km. Above 3 km the flow appears homogeneous in altitude with a large velocity (18 to 22 ms^{-1}).

4-2 Thermal structure and mesoscale circulation

In order to describe the characteristics of the thermal structure and of the mesoscale circulation within the warm front, we use the analysis developed in Testud et al. (1980). For that matter, we assume that the flow within the front is two-dimensional (depending only on X and h) and quasi-stationary with respect to a reference frame moving along X axis at the front speed Uo. Thus, the height-time representation of the components U, V, W, and of the horizontal divergence (fig. 4) is equivalent to that of vertical cross section perpendicular to the front (the origin along X axis corresponds to 7.30 UT).

From the equation of the thermal wind, it can be shown (Testud et al. 1980) that the jump in long front velocity ΔV is expressed as a function of the jump in potential temperature $\Delta\theta'$ accross the front :

$$\Delta V = gs\Delta\theta'/f\theta_o \qquad (1)$$

where s is the slope of the shearing zone ($s \sim .8$ % in our case), θ_o is the large scale mean of potential temperature ($\theta_o = 283°K$). Some results corresponding to the height profiles shown in Fig. 3 are summarized in the following table.

Time (UT)	ΔV (ms^{-1})	$\Delta\theta'$ (°K)
2.20	20	7.2
3.16	21	7.6
3.46	20	7.2

The obtained values of $\Delta\theta'$ are in perfect agreement with the value 7°K deduced from rawinsond data.
Going now in more details on the analysis and using again the hypothesis that the wind field is time and Y independent, the equations of motion in the Xoh plane can be written (Testud et al., 1980) :

$$\overline{U}_\perp.\overline{\nabla}_\perp U + \partial\phi/\partial x - fV = 0 \qquad (2)$$

$$\overline{U}_\perp.\overline{\nabla}_\perp V + fU = 0 \qquad (3)$$

where $\overline{U}_\perp = \begin{cases} U \\ W \end{cases} \qquad \overline{\nabla}_\perp = \begin{cases} \partial/\partial x \\ \partial/\partial h \end{cases}$

with the function $\phi = Cp\ \theta_o(p/p_o)^{R/Cp} + gh_o$.
Let us consider equation (3). It states that the isocontours of the long front velocity V allow to determine the cross front circulation which are indicated by dark arrows on Fig. 4a. Then the cross front circulation corresponds to vertical ascents in the frontal zone. Below this zone it is characterized by a descent of cold air ahead of the front.

Above the frontal zone (in the warm sector for X > 180 km and h > 3 km) no information on $\overline{U}_\perp$ is gained from equation (3) since $|\overline{\nabla}_\perp V|$ is negligible. Then, let us consider equation (2) in that region. The term $fV < 0.5\ 10^{-3}\ ms^{-2}$ is negligible when compared to the $\overline{U}_\perp.\overline{\nabla}_\perp U$ term which is of the order of 2 and 3 $10^{-3}\ ms^{-2}$. Moreover, since the air is homogeneous above 3 km with $\partial\theta'/\partial X \sim 0.1°K\ km^{-1}$ (a value deduced from rawinsond data), the term $\partial\phi/\partial X$ can be considered as uniform horizontally and of the same order of magnitude as fV. Neglecting $\partial\phi/\partial X$ in the same time as fV, equation (2) can be approximately rewritten as :

$$\overline{U}_\perp\ \overline{\nabla}_\perp U \simeq 0 \qquad (4)$$

which indicates that $\overline{U}_\perp$ is parallel to the U isocontours (fig. 4b), and implies the existence of a roll centered near X = 270 km and h = 6 km.

Figs. 4(c) and 4(d) represent respectively the corresponding cross sections of the vertical velocity W and of the horizontal divergence. We observe two cores of convergence, one in the shearing zone and the other in the warm sector. This is in agreement with the results inferred independently by considering the balance of the various terms of the equations of motion as done previously.

The structure of the obtained mesoscale wind field is very similar to that observed by Browning and Harrold (1969), using a Doppler radar in a warm front at middle latitude.

5 - SMALL SCALE MOTIONS

This section deals with the fluctuations of the horizontal wind field which are characterized by the residual signals δU_i and δV_i obtained after removing the mean horizontal wind field (U_i, V_i) at each grid point i. On fig. 5 are shown the height profiles of the velocity standard-deviation σ_u and σ_v obtained from the coplanar sequence at 2.20 UT.

The non-negligible values of σ_u and σ_v in the shearing zone (between 1.5 and 3 km) show the existence of small scale motions. A preliminary analysis of the perturbation wind field indicates a tendancy to present organized patterns with a typical horizontal scale of the order of 10 km. However, a detailed study presently under progress, is necessary in order to confirm this picture. Moreover, in the shearing zone, it is possible to calculate the Richardson number R_i of the flow at 2.20 UT, expressed as :

$$R_i = (g/\theta_E)\ (\partial\theta_E/\partial h)/|\partial\overline{U}_H/\partial h|^2 \qquad (5)$$

where θ_E is the equivalent potential temperature and U_H is the horizontal wind.
By using for this evaluation the rawinsond data

at 3.00 UT, in the shearing zone which is statically stable, it is found $R_i = 0.3$, a value very close to the theoretical critical value of 0.25. This indicates that the small scale motions could result from conditions close to dynamical instability.

6 - VERTICAL INCIDENCE SOUNDINGS

The vertical velocity structures deduced from vertical incidence soundings at 1.20, 1.30 and 1.51 UT (see Hauser and Amayenc, 1980, for details) are in agreement with those observed by conical scannings with a maximum updraft around 5 km. The order of magnitude of the deduced vertical air motions (within $\pm$ 1 ms^{-1}) is quantitatively coherent with the existence of the previously mentioned small scale motion. The analysis of the deduced hydrometeor size distributions led to identify three regions versus height :

i) a region of formation and important growth of ice particles above 5 km altitude (i.e. above the -10°C isotherm level).

ii) a region of relatively slower growth of ice crystals between 2 and 5 km altitude.

iii) a lower region (0.8 - 2 km) characterized by a pronounced bright band revealing the melting of ice crystals to form raindrops under the 0°C isotherm level.

7 - CONCLUSION

In this paper, we have examined the mesoscale circulation within a warm front, as inferred from Doppler Radar data. It is characterized by an intense shear flow in the warm frontal zone with a lower parallel flow and an upper cross flow. The behaviour of the streamlines in a cross section as deduced from the isocontours of U and V are coherent with the vertical velocity field.

The shearing zone corresponding to the frontal zone is close to dynamical instability conditions ($R_i = 0.3$) which can probably be related with the observed local increase in the small scale motions amplitude. However a more detailed study is necessary in order to characterize the space structure of the small scale motions.

In addition, we have summarized some results inferred from vertical incidence soundings. The detailed description can be found elsewhere (Hauser and Amayenc, 1980).

REFERENCES

Browning K.A., T.W. Harrold, 1969 : Air motion and precipitation growth in a wave depression. Quart. J.R. Met. Soc., 95, 288-309.

Browning K.A., R. Wexler, 1968 : The determination of kinematic properties of a wind field using Doppler Radar. J. App. Met., 7, 105-113.

Chong M., F. Roux, J. Testud, 1980 : A new filtering and interpolating method for processing Dual-Doppler Radar data : Performance in three-dimensional wind restitution, ability to derive pressure and temperature fields. To appear in Preprints of 19th Radar Meteor. Conf., Miami, Florida, Amer. Meteor. Soc.

Hauser D., P. Amayenc, 1980 : A new method for deducing hydrometeor-size distributions and vertical air motions from Doppler Radar measurements at vertical incidence : first results in a warm frontal stratiform precipitation. To appear in Preprints of 19th Radar Meteor. Conf., Miami, Florida, Amer. Meteor. Soc.

Lhermitte R., 1970 : Doppler Radar observation of convective storm circulation. Preprints 14th Radar Meteor. Conf., Tucson, Ariz., 153-156.

Testud J., G. Breger, P. Amayenc, M. Chong, B. Nutten, A. Sauvaget, 1980 : A Doppler Radar observation of a cold front : three-dimensional air circulation, related precipitation system and associated wave-like motions. J. Atmos. Sci., 37, 78-98.

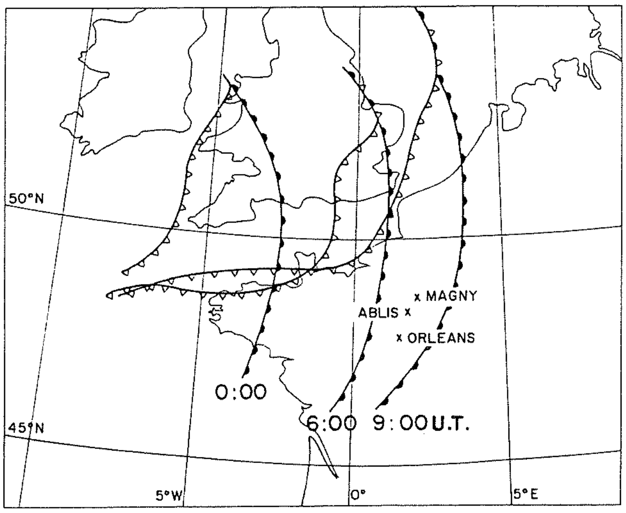

Fig. 1 : Traces of the front observed at ground at different times on November, 2 1977

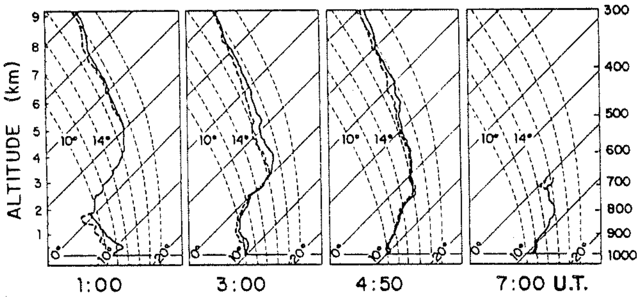

Fig. 2 : Temperature (——) and wet-bulb temperature (---) profiles from Orléans soundings at different times. Light continuous and dotted lines respectively represent isotherms and pseudo-adiabatics.

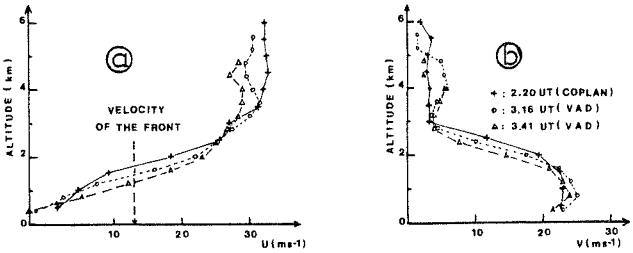

Fig. 3 : Cross front velocity (U) and long front velocity (V) profiles deduced from Doppler Radar data.

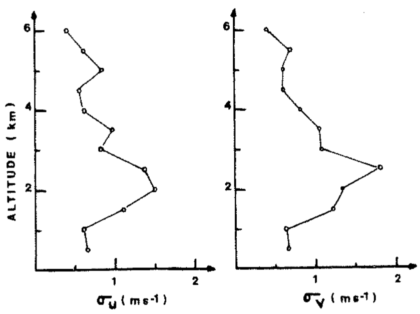

Fig. 5 : Standard-deviation profiles of cross front velocity (σ_U) and long front velocity (σ_V) at 2.20 UT.

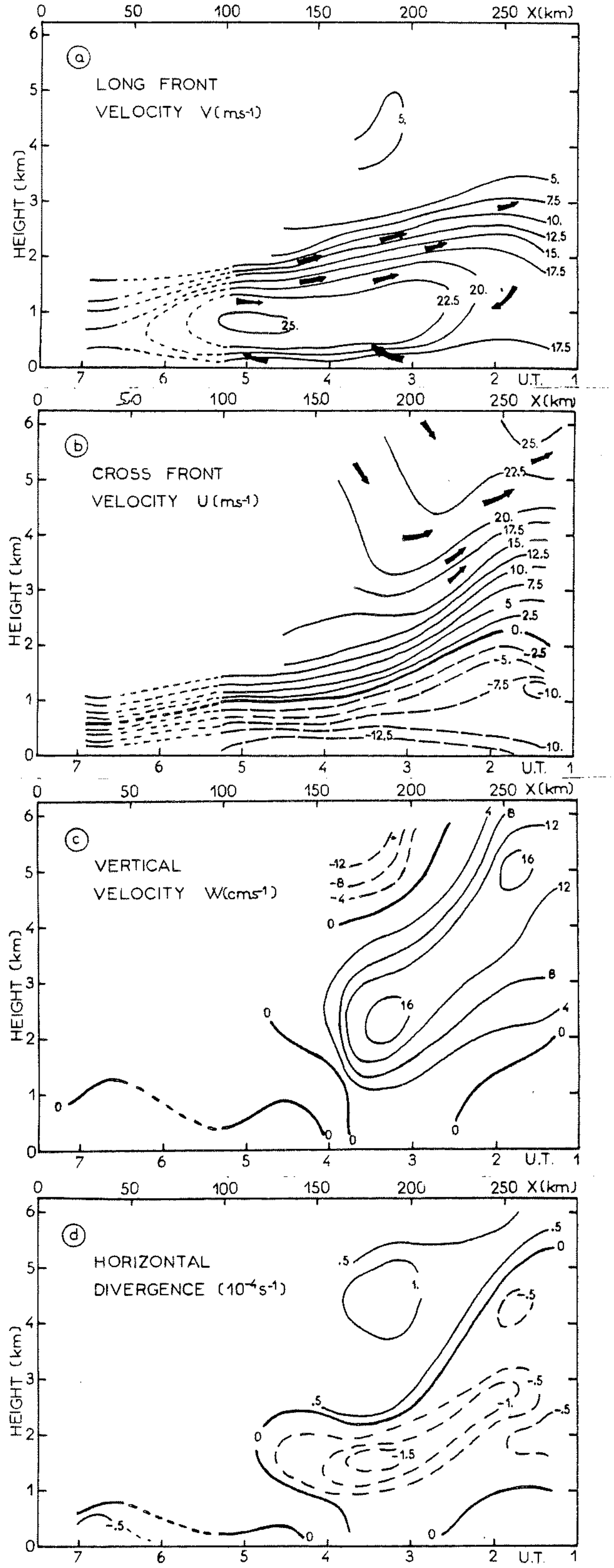

Fig. 4 : Height-time cross sections of the long front velocity V(a), cross front velocity U(b), vertical velocity W(c) and horizontal divergence (d). Time axis also represents X axis. Dark arrows in (a) and (b) indicate the schematic behaviour of the streamlines.

AIRFLOW SIMULATIONS OVER ELK MOUNTAIN

Terry L. CLARK
National Center for Atmospheric Research*
Boulder, Colorado USA

and

Robert GALL
University of Arizona
Tucson, Arizona USA

1. Introduction

In recent years, considerable progress has been made in the numerical simulation of both the dynamics and microphysics of precipitating cloud systems. The literature is of course filled with examples of such simulations [e.g. Whiz (1980)]. However, most of the interesting precipitating systems that have been the subject of these simulations, such as convective clouds, are rather complex dynamically and strongly influenced by small-scale processes. A proper initialization would require complete data of temperature and winds on spatial scales ∿1 km. Currently there is no way to precisely know the initial state of these systems and therefore it is impossible to make exact comparisons between subsequent evolution of the simulation and the real system. The best that can be hoped for is a reasonable comparison between various statistical parameters and a similarity between certain large-scale features.

Ultimately we would like to use the numerical simulation models to assess various proposed precipitation modification methods. However, before we can be certain of the ability of the numerical models to assess a modification process, we must be certain of its ability to simulate the details of both the dynamics and microphysics of the unmodified cloud. This of course is accomplished by comparing details of the simulation with detailed observations.

To do this it is necessary to at least start with a very simple precipitating system, one in which turbulent processes play only a very minor role and where the forcing is steady state and clearly defined. An example of such a system is the stable steady state winter orographic cap cloud. In such a system there is little turbulence, the forcing is clearly defined (the topography) and diabatic processes (such as solar heating of the ground) are negligible. Furthermore, since precipitation is light, the feedback from the cloud microphysics is minimal. It is the purpose of the research, described in part here, to use up-to-date numerical and physical parameterization methods to simulate first the flow field over a mountain during a period when a stable cap cloud formed and then use this flow field in a microphysical model to simulate the microphysical processes going on inside the cloud. Only preliminary results from the simulation of the flow field will be discussed here. This will include a comparison of the generated flow fields with aircraft observations. Some discussion of the sensitivity of the flow over the peak to surrounding topography and the location of the upstream boundary will also be presented.

2. The Model

The dynamical model used in these simulations is discussed in detail by Clark (1977). It is nonhydrostatic, uses the anelastic approximation to eliminate sound waves, and employs a terrain-following vertical coordinate system to treat the lower boundary condition. In all simulations described here, horizontal resolution was 1 km while vertical resolution was 1/2 km. Initial conditions consisted of a sounding, assumed to apply initially everywhere in the integration domain, and specified in the lower levels (up to 3 km MSL) by an aircraft sounding taken about 10 km upstream from the mountain and above 3 km MSL by a rawinsonde sounding taken about 100 km upstream. The model was then integrated in time until the flow over the mountain became slowly varying. For all runs this took about 1 hr real time.

3. The Case Studies

Two cases of flow over Elk Mountain, Wyoming were studied. In the first case, shown in Fig. 1, no cap cloud formed over the mountain since the air at all levels was very dry. Aircraft data of the wind field in the vicinity of Elk Mountain, however, were taken by the University of Wyoming (Karacostas, 1978) allowing at least some verification of the simulation. A cap cloud did form in the second case (not shown), but only microphysical data within the cloud were taken - no wind data - and therefore no direct verification of the model-generated flow field is possible. Only the first case will be described here.

Figure 2 shows the topography in the vicinity of Elk Mountain which is located at the center of the diagram. The topography was generated from terrain data tapes obtained from the National Cartographic Information Center. On the original tapes terrain data were available at 200 foot intervals. The data were then interpolated to the grid points used in the model followed by a very weak smoothing.

4. Comparison with Real Data

Figure 3 shows streamline and isotachs

*The National Center for Atmospheric Research is sponsored by the National Science Foundation.

produced by the model at 2550 m and 3310 m above sea level. These are compared with similar fields subjectively prepared from the aircraft data (Karacostas, 1978). For reference, the aircraft tracks relative to the mountain are indicated.

The main features found by the aircraft are present in the numerical simulation. These include the area of decreased velocity downstream from the mountain, and higher velocities both north or southeast of the mountain at the two levels. Generally the streamlines produced by the model agree well with those determined by the aircraft. The main discrepancies between the simulations and the observations are in the magnitude of the maximum and minimum velocities. The model produced winds that were about 4 m/sec slower in the maximum northeast of the mountain at the 2550 m level. Similar error was found at 3310 m. At 2550 m, the aircraft found easterly winds just east of the mountain while the model produced westerly winds with a minimum velocity of only 8 m/sec. Thus the model appears to be able to reproduce the main features of the flow field although significant quantitative errors are present.

These errors appear to be due in part to specification of the upstream sounding. The aircraft sounding showed considerable vertical structure in the upstream wind field which could not be resolved by the model. This structure was removed by subjective smoothing. Some of this detail may have been due to transients in the upstream flow but regardless of its origin, it must necessarily lead to some discrepancy between the model and the aircraft data. By modifying the upstream sounding we were able to produce significant changes in the generated flow fields and the one shown is our best simulation.

Figure 4 shows the vertical velocity field at 3310 m in three different runs. In Fig. 4a and 4b, the real topography surrounding Elk Mountain was used but in 4a the western boundary (the upstream boundary for the low level flow) was 40 km from the mountain while in 4b it was only 20 km. These runs show the sensitivity of the flow over Elk Mountain to the location of the upstream boundary. The vertical velocity fields in both runs were quite similar indicating that at 20 km the upstream boundary is sufficiently far away to not influence the flow over the mountain.

Figure 4c shows the vertical velocity field at 3310 m over an elliptical mountain defined by:

$$h(x,y) = \frac{h_o}{x^2/a^2 + y^2/b^2 + 1}$$

where $a = 3$ km, $b = 4$ km and $h_o = 1.4$ km. Such a mountain is of course much smoother than Elk Mountain but has a very similar overall shape. In addition, the surrounding topography is removed. The model run depicted in 4c used the same upstream flow field as 4b. Note that there are large differences well to the northeast and south of Elk Mountain but that in the vicinity of the mountain itself the differences are slight. In fact the magnitude of the first minimum and maximum vertical velocities downstream from the mountain are the same in 4b and 4c. Most of the differences are in the vicinity of the downstream mountains southeast of Elk, where of course one would expect them. The flow over Elk Mountain appears to be only very slightly influenced by the downstream topography for low level flows from the west.

Even though the general flow over Elk Mountain is not strongly influenced by downstream topography, there can be some significant effects. In particular, there was a region of strong southwest flow east of Elk Mountain for the real topography case. This effect is essentially absent using the elliptical topography where the downstream topography has been removed. When air flows over a mountain an excess of pressure develops at the surface upstream in order to force the flow upward, while the surface pressure is reduced downstream under the descending current. Thus in the case without downstream topography, broad areas of relatively high pressure develop southwest of the mountain and low pressure northeast. When downstream topography was included the ridge southeast of Elk Mountain produced similar pressure patterns superimposed on the pressure fields forced by Elk. This reduces the area of negative pressure perturbation southeast of Elk that would exist without this downstream ridge and increases the pressure gradients east of Elk. These increased pressure gradients deflect the flow toward the northeast of Elk much more than they would be without the downstream topography. Clearly, therefore, the downstream topography can exert some significant influence on the flow in the vicinity of even a relatively isolated peak such as Elk Mountain.

5. Conclusions

These preliminary results indicate that reasonably accurate simulations of the flow field over a mountain are possible with the model developed by Clark (1977). The results seem to be relatively insensitive to the detail of the surrounding topography. In fact virtually the same results can be obtained in the vicinity of Elk Mountain when a smooth elliptical mountain is used instead of the real topography. Even the details of topography over the mountain itself seem relatively unimportant. Errors due to incomplete specification of the small-scale detail in the topography of the mountain and removal of the surrounding topography are no larger than errors due to inaccurate specification in the upstream sounding.

6. References

Clark, T. L., 1977: "A small-scale dynamic model using a terrain-following coordinate tranformation". *J. Comp. Phys.*, *24*, 186-215.

Karacostas, T. R., Transport and Turbulent Diffusion Over Mountainous Terrain. M.S. Thesis, Dept. of Atmos. Sci., Univ. of Wyoming, July, 1978.

Whiz, G., 1980: "Theoretical and practical aspects of comparing simulations and observations". *J.G.W.R.*, *2000*, 14-212.

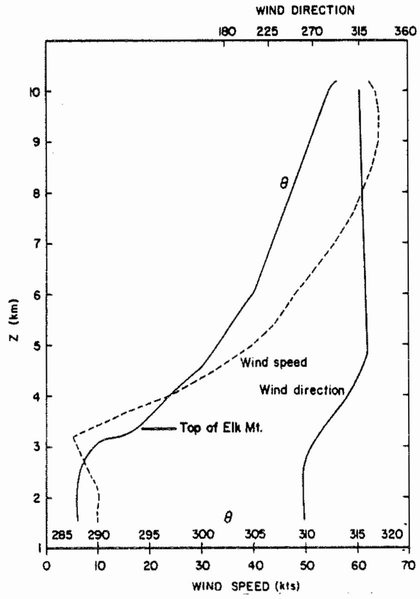

Figure 1. Environmental sounding for 22 December 1976 from aircraft observations and Lander, Wyoming rawinsonde.

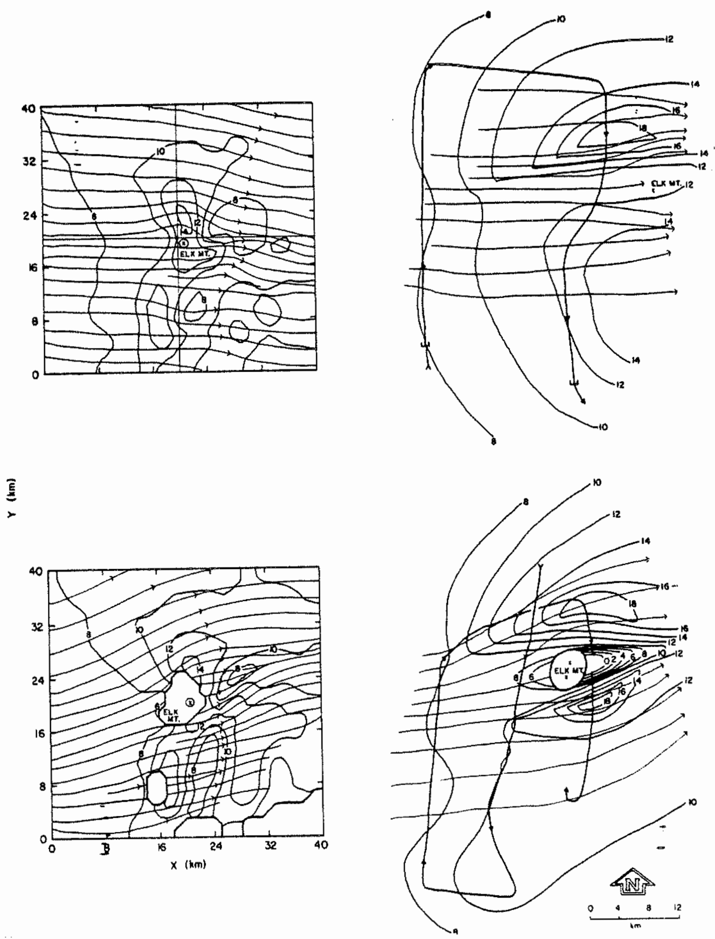

Figure 3. Streamlines and isotachs ($m\,s^{-1}$) for 3.31 km MSL in upper two plates and for 2.55 km MSL in lower two plates. Aircraft tracks for observational data are shown with heavy lines. The right-hand panels are from Karacostas (1978).

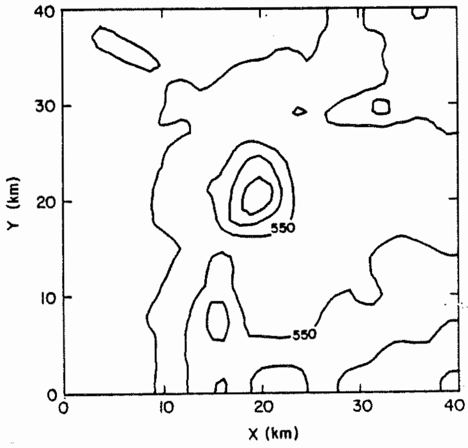

Figure 2. Topography of Elk Mountain region. Contour interval is 275 m with base level taken as 1950 m MSL.

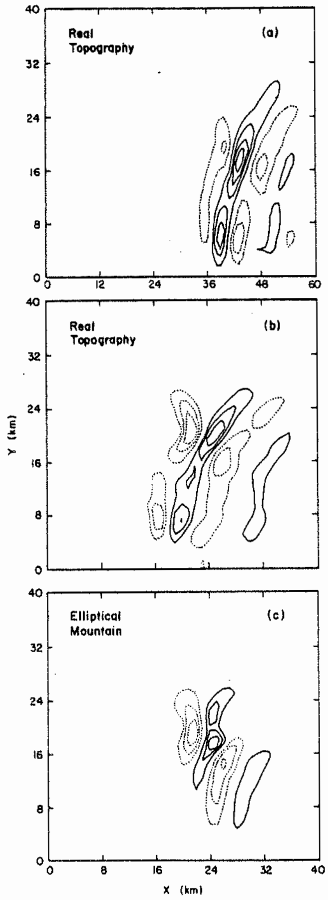

Figure 4. Vertical velocity contours at z = 4.45 km MSL. Contour interval is $1\ m\,s^{-1}$ with solid contours indicating updrafts and dashed contours indicating downdrafts. a) Real topography with 40 x 60 km horizontal domain size; b) Real topography with 40 x 40 km horizontal domain size; c) Elliptical mountain case with 40 x 40 km domain size.

OBSERVATION A L'AIDE D'UN SYSTEME DE DEUX RADARS DOPPLER D'UN TOURBILLON DE MOYENNE ECHELLE ASSOCIE A UN FRONT FROID

C. Gaillard M. Gilet

Etablissement d'Etudes et de Recherches Météorologiques
78470 - Magny-les-Hameaux FRANCE

1. INTRODUCTION

La plupart des campagnes de mesures récentes destinées à l'étude de la dynamique des fronts à moyenne et petite échelle (e.g. Browning et Harrold, 1969, Kreitzberg et Brown, 1970,...) ont abouti à décrire le front froid comme un phénomène bi-dimensionnel, i.e. invariant dans la direction parallèle à sa trace au sol. Au vu des cartes d'échelle synoptique, les fronts sont généralement conformes à cette représentation, dans le cas de systèmes actifs associés à un flux zonal. Cependant, pour des fronts liés à un flux méridien, on observe souvent à l'échelle synoptique le phénomène d'ondulation. L'ondulation est caractérisée par l'apparition d'un minimum de pression au niveau du front, associé à un tourbillon cyclonique, et peut dans certains cas donner lieu à l'apparition de dépressions secondaires, voire de cyclogenèse. Faute de moyens expérimentaux permettant d'accéder à une description tri-dimensionnelle on connait encore mal la dynamique de ce type de phénomène. C'est ce qui a pu être observé lors du passage du front froid du 16 mars 1978.

Ces observations ont été faites à l'occasion d'une campagne de mesures sur les fronts associant trois laboratoires français, l'Etablissement d'Etudes et de Recherches Météorologiques de la Météorologie Nationale, le Centre de Recherches sur la Physique de l'Environnement et l'Institut et Observatoire de Physique du Globe du Puy-de-Dôme. Cette campagne, décrite ailleurs par Gilet et al. (1978),était conçue de façon à obtenir un maximum d'information sur la structure tri-dimensionnelle des phénomènes observés, grâce en particulier à trois stations de radio-sondage et de mesure du vent en altitude disposées selon un triangle, et d'un ensemble de deux radars Doppler, le système Ronsard.

2. LA SITUATION METEOROLOGIQUE

La figure 1 indique les positions au sol des interfaces entre masses d'air le 16 mars 1978 à 18:00 TU ainsi que l'emplacement des zones nuageuses d'après la photographie infrarouge prise du satellite Météosat à la même heure. La situation est caractérisée en altitude par la présence d'un profond thalweg, s'étendant de la Norvège à la Bretagne, qui gouverne le flux au-dessus de la France.

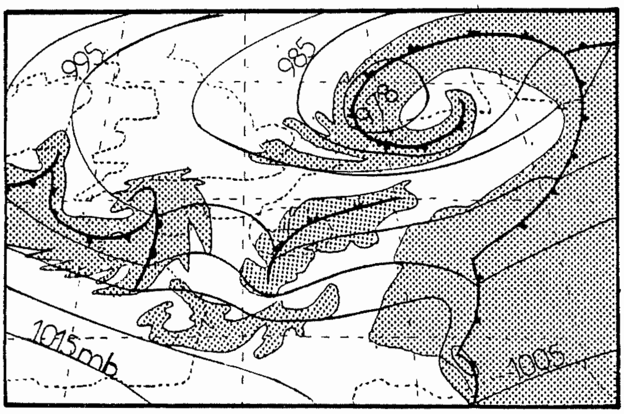

fig. 1 : situation synoptique à 18 H TU le 16.3.78. Les zones en grisé représentent les masses nuageuses associées aux systèmes frontaux.

Le front froid situé sur les Alpes est passé sur Paris le même jour à 5:00 TU. Le front présent sur la région parisienne à 18:00 TU est dessiné comme une occlusion sur la figure 1, à cause de la présence d'une petite vallée chaude contrastant avec deux masses d'air froid situées à l'Est et à l'Ouest. Ce front se déplace vers 140° à 55 km/h lors de son passage sur Paris. Sa trace au sol subit un fort mouvement de rotation cyclonique, de sorte que sa vitesse croît en se déplaçant vers le Sud.

La figure 2 montre les isolignes de la température pseudo-adiabatique potentielle de thermomètre mouillé ($\theta'w$) et les vents en fonction du temps et de l'altitude. Les sondages ont été effectués depuis Magny-les-Hameaux. On constate que le front froid, situé à gauche de l'air chaud W, est bien délimité du point de vue des vents et des $\theta'w$. Il passe à Magny-les-Hameaux à 17:45 TU.

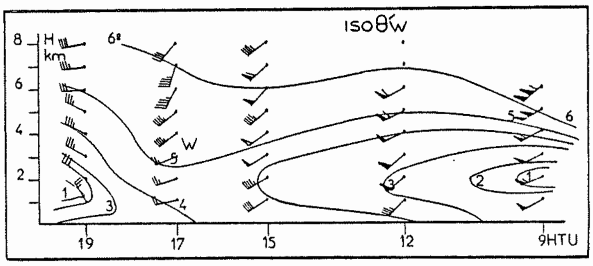

fig. 2 : Isolignes de θ'w et vents en altitude en fonction du temps. Les heures en abscisse correspondent aux sondages.

Une analyse du champ de pression au sol a été faite à partir des données horaires du réseau climatologique de la région parisienne. Le résultat est porté sur la figure 3. On constate la présence d'un minimum de pression associé à l'air chaud W de la figure précédente.

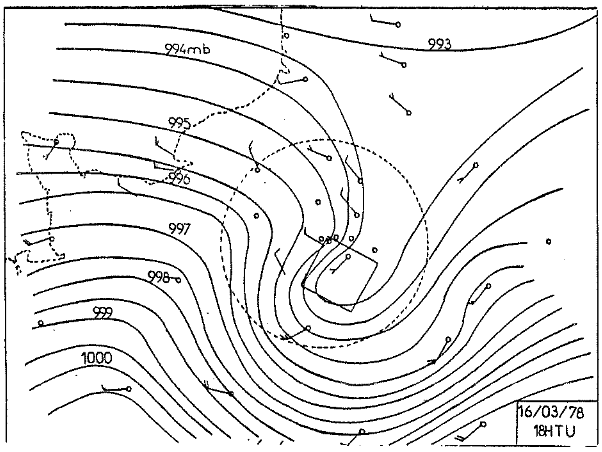

fig. 3 : champ de pression au sol sur la région Nord à 18 h TU. Le cercle en pointillés est centré sur Magny et a un rayon de 100 km.

3. LES DONNEES RADAR

On a pu obtenir des champs de réflectivité radar et de vitesse de vent au moment du passage du front, à l'aide du système Doppler Ronsard. Ces radars, qui sont mis en oeuvre par la CRPE, ont été décrits précédemment par Waldteufel et al. (1975). La méthode de restitution des champs de vent développée à l'EERM est proche de celle qui a été employée par Lhermitte et Gilet (1975) et a été décrite en détail par Gilet et al. (1979). Nous nous attacherons ici essentiellement aux résultats.

Les radars étaient situés à Ablis et à Magny-les-Hameaux, et se trouvaient donc espacés de 29 km dans la direction 38°. Les balayages choisis variaient entre le Coplan, le PPI et le tir vertical.

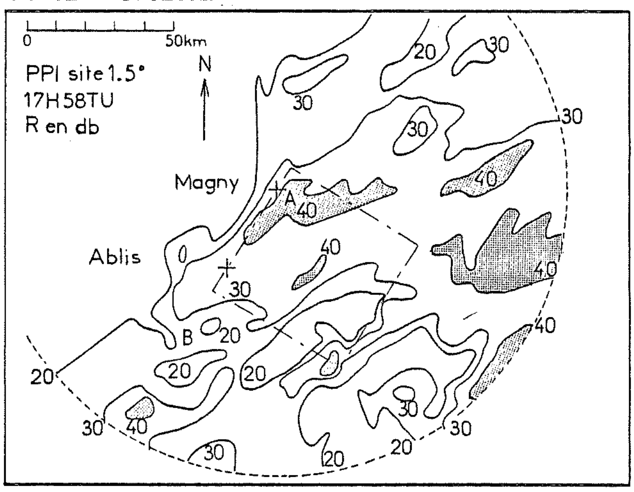

fig. 4 : champ de réflectivité relative (radar non étalonné) EN DB. Les zones en grisé correspondent aux échos supérieurs à 40 DB. Le carré délimite l'aire de restitution des champs de vent (figures suivantes).

La figure 4 montre la situation d'ensemble à 17:58 TU vue de Magny-les-Hameaux. La portée du radar (100 km) est matérialisée sur la figure 3 par un cercle en pointillés. On constate l'absence d'échos à l'arrière du front. La cellule la plus intense (A) est située au niveau du front près de Magny-les-Hameaux. Le sommet des échos plafonnait à 6000 m. Au SW d'Ablis (B), on note une zone de faible réflectivité. Sur les PPI suivants, non représentés ici, on remarque que cette zone d'échos faibles a tendance à s'allonger vers l'Est en se courbant vers le Nord. On verra plus loin que ceci est certainement lié à une avancée d'air froid.

La figure 5 représente en coupes horizontales les perturbations des champs de vent Doppler observées à 18:16 TU. Les vitesses ont été calculées à l'intérieur du domaine carré porté sur les figures 3 et 4, au SE de la ligne Ablis-Magny-les-Hameaux. Ses dimensions sont de 51,2 x 51,2 km2 horizontalement, les altitudes variant entre 250 m et 8750 m. Les vitesses radiales Doppler ont d'abord été rééchantillonnées sur une grille de pas 800 x 800 x 500 m3. Avant de calculer les composantes cartésiennes de la vitesse du vent, on a lissé les vitesses radiales fournies par chaque radar selon une

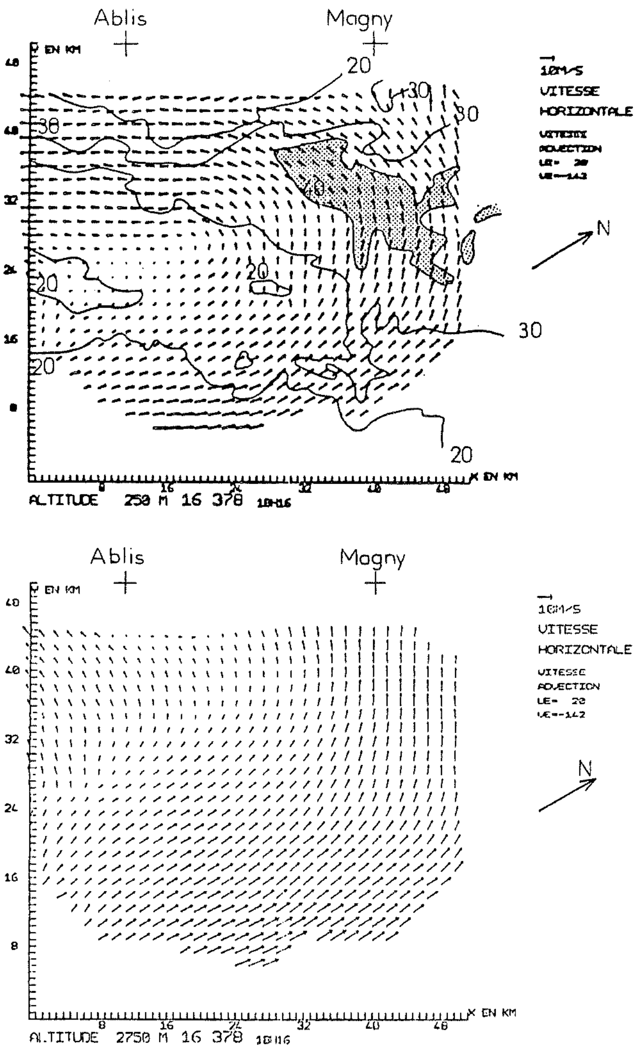

fig. 5 : Champs de perturbations de vitesse par rapport au déplacement du front à deux niveaux à 18:16 TU. Les réflectivités relatives à un seuil arbitraire sont superposées au champ à 250 m (de 10 en 10 db)

pondération Gaussienne portant sur deux points de grille de part et d'autre horizontalement et un point verticalement (voir Gilet et al. 1979).

Le passage du front est marqué par un fort tourbillon cyclonique (jusqu'à $10^{-3}s^{-1}$) superposé au cisaillement horizontal que l'on attendait. L'examen des vitesses Doppler obtenues à 18:30 TU (non représentées ici) confirme la présence de ce tourbillon, qui se trouve advecté en son centre du déplacement du front, alors que la zone de cisaillement subit une rotation cyclonique. La comparaison des coupes horizontales de vent à différentes altitudes montre par ailleurs que la zone de cisaillement se décale vers le NW avec des altitudes croissantes ; ceci est bien en accord avec la correspondance entre le vent thermique et la forme attendue pour une surface frontale froide.

4. ESTIMATION DES CHAMPS DE PRESSION ET DE TEMPERATURE

Il est théoriquement possible, moyennant certaines approximations, d'accéder à une estimation des champs de pression et de température à partir des données cinématiques Doppler (voir Leise, 1978 et Gal Chen, 1978). C'est ce qui a été tenté sur le champ de vent de 18:16 TU.

L'équation du mouvement horizontal s'écrit :

$$\frac{D\vec{V}_H}{Dt} + \frac{1}{\rho}\vec{\nabla}_H p + f\,\vec{k}\wedge\vec{V}_H = 0 \quad (1)$$

Les forces de frottement et les flux turbulents ont été négligés. $\vec{V}_H$ et $\vec{\nabla}_H$ sont les vecteurs vitesse et opérateur gradient horizontaux. D/Dt représente la différenciation totale, ρ la densité, p la pression, $\vec{k}$ le vecteur unitaire vertical et f le paramètre de Coriolis. Conformément à l'approximation de Boussinesq, on admet que les variations de ρ par rapport à sa moyenne horizontale (estimée à l'aide des données de radiosondage) ont une contribution négligeable. Par ailleurs, les champs de vent disponibles (18:16 TU et 18:30 TU) sont trop espacés pour procéder à la différenciation temporelle nécessaire à une estimation rigoureuse de la différentielle totale. On a donc recours à une hypothèse de stationnarité, confirmée qualitativement par la similitude des champs aux deux instants. La vitesse d'advection retenue est celle de la trace du front au sol, en tenant compte de sa rotation d'ensemble.

La figure 6 montre le champ de pression obtenu après intégration horizontale, près du sol et en altitude. A 250 m, on note une bonne concordance avec les données du réseau (fig. 3) autant pour l'orientation des isobares que pour la variation globale de pression. La figure 6b montre que par rapport au champ au sol, les isobares en altitude subissent une rotation cyclonique et un décalage vers l'arrière du front.

Connaissant le gradient horizontal de pression, il est possible d'accéder au champ de température, en utilisant l'équation du mouvement vertical et la relation fondamentale de la thermodynamique :

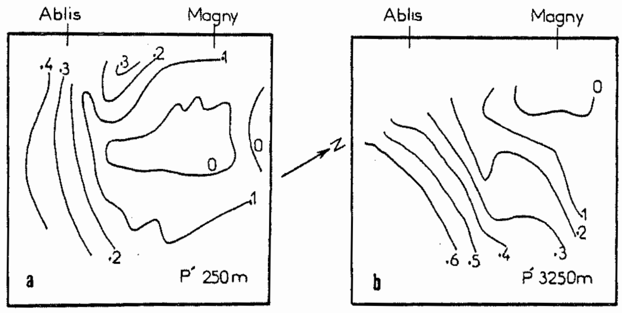

fig. 6 : champs de pression relative à 250 m et 3250 m à 18:16 TU (dixièmes de MB)

$$\frac{DW}{Dt} + \frac{1}{\rho}\frac{\partial p}{\partial z} + g = 0 \quad (2)$$

$$p = \rho RT \quad (3)$$

On néglige dans (2) les forces de frottement et les effets liés à la présence d'eau. En différenciant (1) et (2) et en tenant compte de (3) on obtient :

$$\vec{\nabla}_H T = \frac{T}{p}\vec{\nabla}_H p + \frac{RT^2}{p\left(g+\frac{DW}{Dt}\right)}\left[\frac{\partial \vec{\nabla}_H p}{\partial z} + \frac{p}{RT}\vec{\nabla}_H\left(\frac{DW}{Dt}\right)\right]$$

Cette équation est intégrée après quelques simplifications applicables à notre cas :

- T et p sont remplacés par leur moyenne horizontale
- Dw/Dt est négligé par rapport à g
- $\vec{\nabla}_H$ (Dw/Dt) est négligé.

Les deux dernières approximations se justifient au vu de la faiblesse des vitesses verticales et de leurs gradients obtenus expérimentalement (les w sont inférieurs à 2 ms^{-1}). Ceci équivaut à une hypothèse d'équilibre hydrostatique, et ne saurait s'appliquer à un cas de convection développée.

La figure 7 représente le résultat obtenu près du sol et en altitude. On remarque à 250 m un réchauffement de l'air quand on se déplace le long du front d'Ablis vers Magny-les-Hameaux. En altitude, on observe au contraire un refroidissement. Il semble que l'on assiste à une pénétration de l'air chaud sous l'air froid aux niveaux inférieurs, ou que l'air froid arrive à surplomber l'air chaud dans la partie de la figure située du côté de Magny-les-Hameaux.

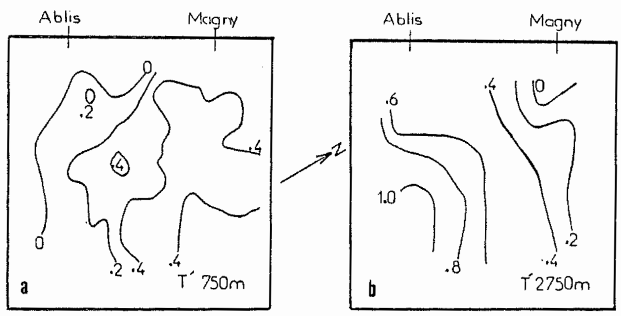

fig. 7 : champs de température relative à 750 m et 2750 m (unités 10^{-1}° C)

5. SYNTHESE ET CONCLUSION

La figure 8 est une image synthétique et simplifiée de la façon dont on peut se représenter le front au moment de son passage dans la zone observée par les radars. D'après le chapitre précédent, la partie NE du tourbillon correspond à une zone où l'air froid provenant de l'arrière du front surplombe la vallée chaude, ce qui peut être interprété comme une sorte de déferlement. Au SW du tourbillon, le front a une allure plus classique, l'air chaud se trouvant au-dessus de l'air froid. Cette analyse se trouve confirmée par les champs de réflectivité, puisqu'on observe un maximum d'activité convective au NE de Magny-les-Hameaux, et une zone d'échos faibles au SW, qui a tendance à s'agrandir et à se recourber dans le sens cyclonique (voir figure 4 en A et B). L'interprétation est également confirmée par les données au sol (figure 3) et par l'analyse de l'organisation des nuages vus par Météosat.

La présence d'un tourbillon de moyenne échelle sur une surface frontale n'est somme toute pas surprenante quand on sait que le phénomène d'ondulation des fronts froids soumis à un flux méridien se rencontre couramment en météorologie synoptique. L'analyse d'un autre front froid observé lors de la même campagne (voir Chalon et Gilet, 1980) révèle aussi la présence d'un tourbillon (de plus petite dimension) au niveau de la surface frontale. Le mécanisme d'instabilité donnant lieu à ces perturbations de petite et moyenne échelle ne semble pas connu actuellement, et mérite certainement d'être étudié. Le phénomène de déferlement du front, plus surprenant pour le météorologiste, mérite également d'être confirmé par d'autres études de cas et analysé d'un point de vue théorique. Des travaux s'engagent actuellement dans ce sens à l'EERM.

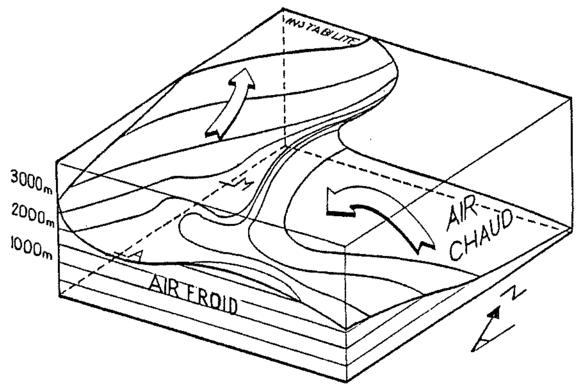

fig. 8 : représentation simplifiée de la position relative des deux masses d'air dans la zone de reconstitution des champs de vent. Les flèches indiquent le mouvement de l'air chaud près du sol et en altitude (relativement au front).

6. REMERCIEMENTS

Les données Ronsard nous ont été communiquées par le CRPE, que nous tenons à remercier vivement. Nous sommes également reconnaissants envers l'équipe de l'EERM/GMA/4M/ME qui a effectué les radiosondages, et M. KLAUS (EERM/GMI) qui a participé à la mise au point des programmes d'analyse des données radar.

7. BIBLIOGRAPHIE

Browning, K.A. et T.W. Harrold, 1969. Air motion and precipitation in a wave depression. Quart. J.R. Met. Soc., 95, 288-309.

Chalon, J.P. et M. GILET, 1980. Structure à moyenne échelle d'un front froid. VIII Conf. Int. Phys. des nuages - Clermont Ferrand, F.

Gal Chen, T., 1978. Deduction of pressure and density fluctuations using Doppler radars observations : a feasibility study. AMS 18th Conf. on radar Meteor., 104-111.

Gilet, M., A. Amat, P. Amayenc, B. Campistron, J.P. Chalon, P. Le Berre, C. Pastre, J. Testud et P. Waldteufel, 1978. Campagne de mesures Fronts 77. Note EERM n° 407 - Direction de la Météorologie - Paris.

Gilet, M., V. Klaus et C. Gaillard, 1979. Analyse des données du système de deux radars Doppler Ronsard. Reconstitution des champs de vent. Note EERM n° 29 nouvelle série - Direction de la Météorologie. Paris.

Kreitzberg, C.W. et H.A. Brown, 1970. Mesoscale weather systems within an occlusion. J. Appl. Meteor., 9, 417-432.

Leise, J.A., 1978, Temperature retrieval from Dual Doppler wind field data. AMS 18th Conf. on Radar Meteor., 94-99.

Lhermitte, R.M. et M. Gilet, 1976. Acquisition and processing of tri Doppler radar data. AMS 17th Conf. on radar Meteor., 1-6.

Waldteufel, P., B. Nutten et A. Sauvaget, 1975. Les radars Ronsard. Document d'information. Note technique CRPE.1003. CNET Issy-les-Moulineaux.

THE MESOSTRUCTURE AND MICROSTRUCTURE OF EXTRATROPICAL CYCLONES

Peter V. Hobbs

Atmospheric Sciences Department, University of Washington
Seattle, Washington, 98195 USA

1. INTRODUCTION

At the last International Conference on Cloud Physics I reviewed the progress that had been made in the CYCLES (CYCLonic Extratropical Storms) PROJECT during the period 1973-1976 in increasing our understanding of the mesoscale and microscale processes associated with rain and precipitation in extratropical cyclones (Hobbs and Houze, 1976). The purpose of the present paper is to provide a brief review of CYCLES findings during the period 1976-1980.

2. FACILITIES AND MODES OF OPERATION

The measuring facilities and the ways in which they are employed have played a crucial role in the CYCLES PROJECT. Details are given in Hobbs (1978) and Hobbs et al. (1980).

The facilities include quantitative reflectivity and Doppler radars, several instrumented aircraft, rawinsondes, dropsondes, and ground stations. These facilities, together with synoptic data and satellite photographs, permit study of phenomena ranging from the synoptic-scale, through the mesoscale, down to the microscale. As much data as possible is relayed in real-time to a Control Center. The aircraft are directed by the Control Center into specific features of the storms that appear interesting and these features are then tracked by the aircraft as they move across the observational network (Lagrangian-type measurements). Alternatively, the aircraft make a series of horizontal flight tracks at different altitudes above the radar as mesoscale features pass over the radar (Eulerian-type measurements). The color-displayed Doppler radar data are particularly useful in identifying mesoscale features (Baynton et al., 1977).

3. CLASSIFICATION OF MESOSCALE RAINBANDS

Hobbs and Houze (1976) identified six types of mesoscale rainbands in extratropical cyclones. Shown in Fig. 1 is a slightly refined version of their classification of rainbands. In addition to some renumbering of the types of rainbands, the new classification incorporates the following changes: warm-frontal rainbands (Types 1a and 1b) are now differentiated by the positions ahead of or coincident with the surface warm front. The surge rainband (Type 4a) which occurs in advance of the cold front in an occlusion, has been added. the rainbands (Type 4b) that follow the surge rainband are an example of the small wavelike rainbands described by Houze et al. (1976).

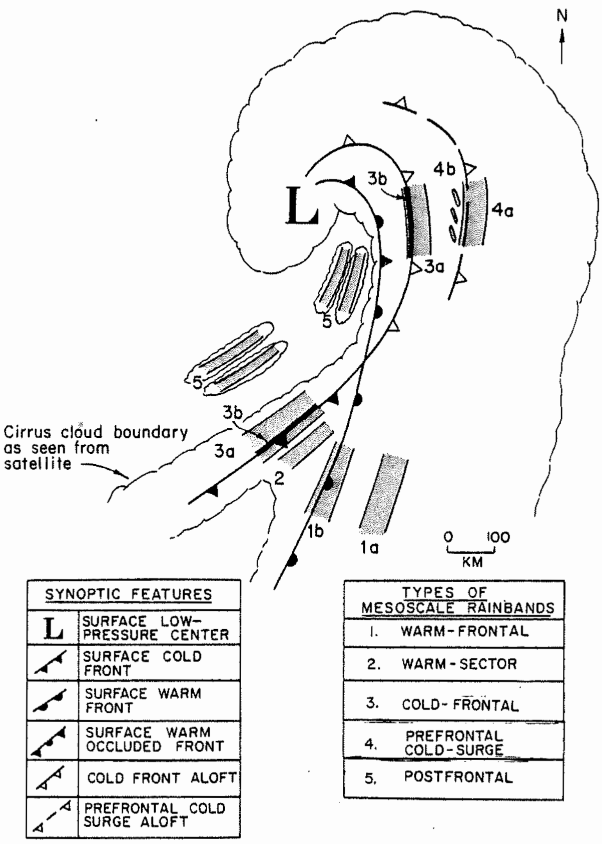

Fig. 1 Schematic depiction in horizontal cross-section of the types of mesoscale rainbands (stippled areas) observed in extratropical cyclones. (From Hobbs, 1978.)

4. STRUCTURES OF THE RAINBANDS

Simultaneous airborne and radar measurements have revealed important aspects of the structures of the clouds and the processes acting to produce precipitation in the different types of rainbands (Hobbs et al., 1980; Herzegh and Hobbs, 1980; Matejka et al., 1980). The results are summarized below, with illustrations and schematics based on CYCLES case studies.

Warm-frontal rainbands arise when precipitation is enhanced in a mesoscale region embedded within the widespread area of lighter precipitation associated with warm-frontal lifting. Natural "seeding" of the cloud layers below the warm front by ice particles from shallow convective "generating" cells located above the warm front is an important mechanism

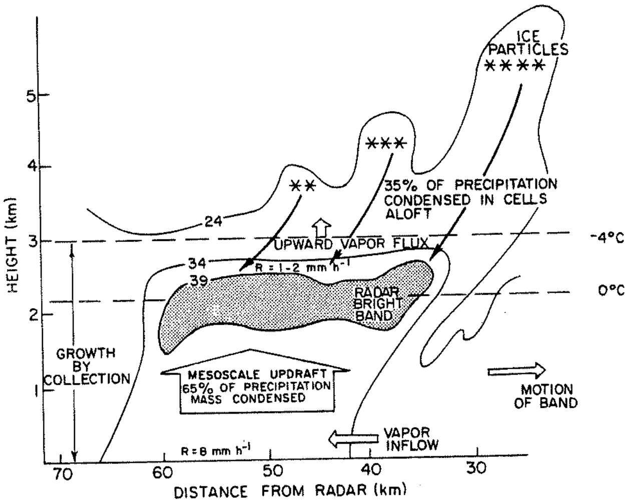

Fig. 2 Schematic depiction in a vertical cross-section of the dynamical and microphysical processes associated with a warm-frontal rainband. Contours show radar reflectivity pattern in units of dBZ). (From Houze et al., 1980.)

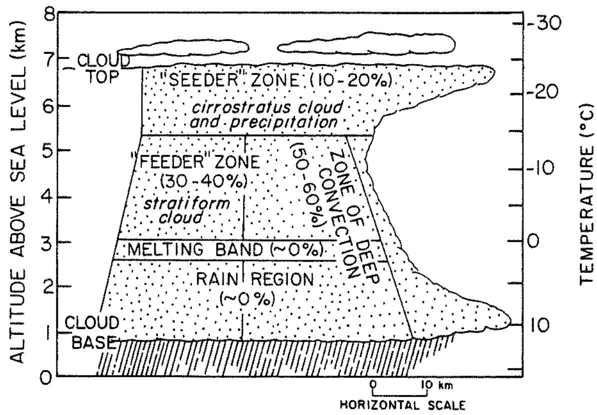

Fig. 3 Schematic vertical cross-section of a warm-sector rainband showing approximate fractions of the total mass of the precipitation that was produced in various regions of the rainband. The motion of the rainband is from left to right. (From Hobbs et al., 1980.)

in the production of precipitation in these rainbands. Fig. 2 summarizes the results from one of the CYCLES case studies. In this case, the low stratiform cloud layer was entirely below the -4°C level and was enhanced by non-convective, mesoscale lifting. Associated with this lifting was water vapor convergence in the lowest 1.4 km. The mesoscale lifting below the -4°C level led to the condensation of enough of the converged moisture to explain 65% of the precipitation. The remaining 35% of the precipitation was due to condensation aloft of vapor converged at low levels but transported upward across the -4°C level by the mesoscale vertical motion. Above the -4°C level this moisture was condensed in the convective generating cells. The condensation below the -4°C level was in the form of liquid droplets. The removal of the main mass of the condensate below the -4°C level as precipitation was due to its collection by ice particles falling from the generating cells. The pronounced radar "bright band" confirmed that considerable numbers of ice particles were drifting down into the lower layer. The snowfall rates just above the melting layer were <1-2 mm hr^{-1}. Since surface rainfall rates were ~8 mm hr^{-1}, collection of cloud water by the precipitation particles below the -4°C level was obviously substantial. A "seeder-feeder" mechanism, such as that described above, results in precipitation efficiencies approaching 100% (Hobbs et al., 1980; Hobbs and Matejka, 1980).

Some warm-sector rainbands in extratropical cyclones resemble intense squall lines. Even the more benign warm-sector rainbands appear to be dynamically similar to squall lines, with younger more active convective elements, containing relatively large amounts of liquid water, being followed by older glaciated clouds. Fig. 3 indicates the precipitation growth processes in a warm-sector rainband. Both the "seeder-feeder" process and deep convection played important roles. The top of the warm-sector band, which consisted of heavy cirrostratus cloud containing light precipitation and generating cells, functioned as a "seeder" zone. 10-20% of the mass of the precipitation in the rainband originated in the "seeder" zone. The remaining 80-90% of the precipitation growth occurred in two distinct regions below this level. One of these regions was a zone of deep, vigorous convection; 50-60% of the mass of the precipitation in the main warm-sector rainband developed in this zone. The convection in this region produced a region of water-saturated cloud in which "seed" ice particles from above grew rapidly by deposition, riming and aggregation. The other region consisted of stratiform cloud in which "seed" ice crystals from above grew by deposition and aggregation to account for ~30-40% of the total mass of precipitation from the rainband. The precipitation efficiencies in the convective and stratiform regions were ~40% and ~80%, respectively.

Narrow cold-frontal rainbands occur at the advancing noses of cold fronts, where convergence of air in the boundary layer produces a narrow (~5 km) convective updraft of a few meters per second. Hobbs and Biswas (1979) observed that on the small mesoscale a narrow cold-frontal rainband consists of ellipsoidal areas of heavy precipitation oriented at an angle of ~35° to the surface cold front. A schematic of the airflow associated with a narrow cold-frontal rainband is shown on the right-hand side of Fig. 4. The young clouds that form in the strong updrafts have relatively high liquid water contents (~1 g m^{-3}) and relatively low concentrations of small ice

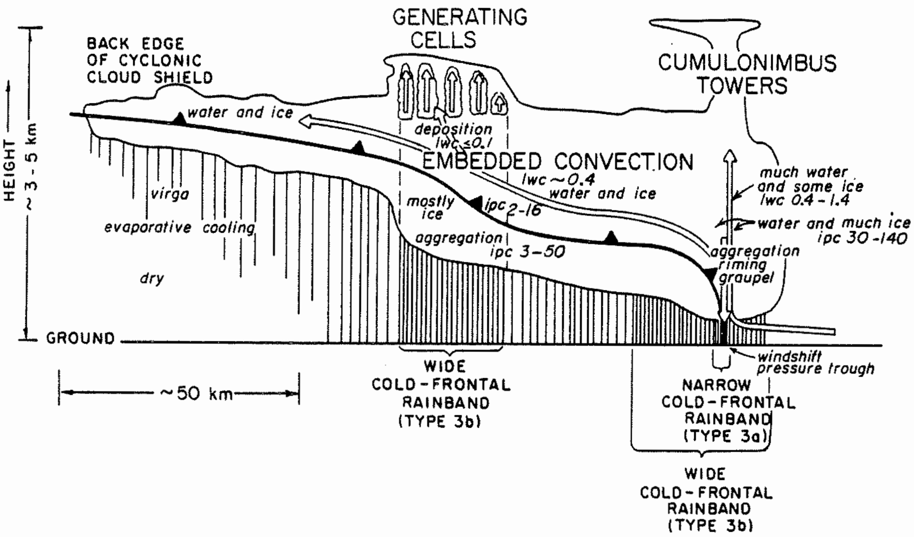

Fig. 4 Schematic depiction in vertical cross-section of the clouds associated with a cold front showing narrow and wide cold-frontal rainbands. Open arrows depict airflow relative to the front. Ice particle concentrations (ipc) are given in numbers per liter and cloud liquid water contents (lwc) in g m^{-3}. The motion of the rainband is from left to right. (From Matejka et al., 1980.)

particles. Rimed ice particles, graupel and aggregates are common in these clouds. Alongside the updraft is a downdraft in which are found much higher ice particle concentrations and less liquid water than in the updraft. The heaviest precipitation in the narrow cold-frontal rainband (and generally in the whole cyclone) is contained in this downdraft.

Wide cold-frontal rainbands occur when lifting over the cold front is enhanced by several tens of centimeters per second over horizontal distances of several tens of kilometers in width (see center of Fig. 4). Below the cold front, the clouds associated with wide cold-frontal rainbands contain high concentrations of ice particles, many of which are aggregates. Above the cold front, the clouds are more turbulent, have more cloud liquid water, and may contain convective generating cells that provide "seed" crystals to the clouds below.

Postfrontal rainbands form in the cold airmass behind the zone of strong subsidence that immediately follows the passage of a cold front. They resemble organized convective systems and sometimes appear to be related to secondary cold fronts. The clouds in these rainbands have the structures of convective elements in various stages of development.

In the occluded portions of a cyclone, the cold air that advances over the warm front may move in a series of pulses. The strongest pulse is associated with the cold front itself; associated with the cold front aloft are narrow and wide cold-frontal rainbands (Fig. 1) similar to those previously described. Ahead of the cold front aloft may be weaker pulses of cold air which are referred to as prefrontal cold surges (Fig. 5). Two types of mesoscale rainbands may be associated with the prefrontal cold surge aloft: a deep band of cloud and precipitation that precedes or straddles the leading edge of the prefrontal cold surge (Type 4a in Fig. 1), and sharply defined small-scale (sometimes wavelike) rainbands (Type 4b in Fig. 1). The passage of a prefrontal cold

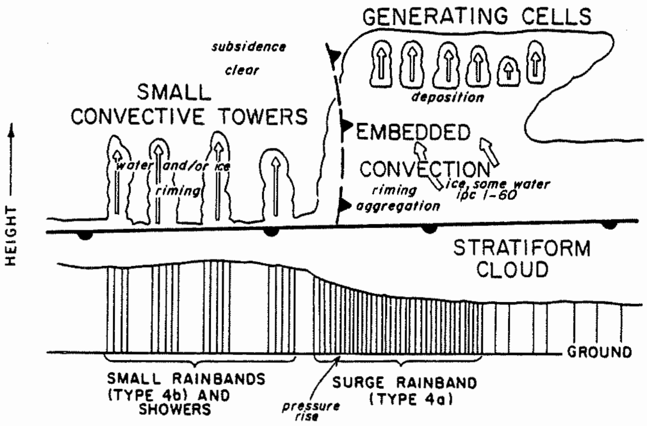

Fig. 5 Schematic depiction in vertical cross-section of mesoscale rainbands associated with a prefrontal surge of cold air aloft, ahead of an occluded front. The broken cold-frontal symbol indicates the leading edge of the surge (the primary cold front aloft is off the picture to the left). Open arrows depict airflow relative to the cold surge and convective ascent. Ice particle concentrations (ipc) are given in numbers per liter. The motion of the cold surge and the rainbands is from left to right. (From Matejka et al., 1980.)

surge rainband is marked at the surface by a temporary slight rise in pressure. As in wide cold-frontal rainbands, warm-sector air ascends ahead of the advancing cold air, the potential instability is released to produce convection and generating cells in the prefrontal cold surge rainbands. The clouds in this type of rainband are composed of both ice particles and liquid water, and precipitable particles grow by riming and aggregation. The wavelike rainbands consist of a field of small convective towers extending upward from the cloud layer associated with the warm front below. These towers occur in various stages of development, and range from young towers, containing mostly supercooled liquid water, to old glaciated towers, with high concentratons of ice particles.

5. CONCLUSIONS

The 1970's have seen significant advances in our understanding of the mesoscale and microscale structures of extratropical cyclones and the processes involved in the formation of precipitation in these systems. Subjects for future investigation include studies of the evolution on meso- and micro-scales of cyclones, the effects of orography on storm structures and precipitation processes, the development of diagnostic and prognostic numerical models that incorporate the principal features of the meso- and micro-processes, and applications of this growing body of knowledge to the forecasting and artificial modification of precipitation in extratropical cyclones.

Acknowledgments. I am indebted to all the members of my research group who have contributed to the success of the CYCLES PROJECT. The CYCLES PROJECT is supported by the Experimental Meteorology and Weather Modification Program, Division of Atmospheric Sciences, National Science Foundation (Grant ATM-77-01344), the U.S. Air Force Office of Scientific Research (Contract F49620-77-01344), the U.S. Army Research Office (Grant DAAG29-79-G-0005), and the National Oceanic and Atmospheric Administration (Grant 04-7-022-44033).

REFERENCES

Baynton, H. W., R. J. Serafin, C. L. Frush, G. R. Gray, P. V. Hobbs, R. A. Houze, Jr., and J. D. Locatelli, 1977: Real-time wind measurements in extratropical cyclones by means of Doppler radar. J. Appl. Meteor., 16, 1022-1028.

Herzegh, P. H., and P. V. Hobbs, 1980: The mesoscale and microscale structure and organization of clouds and precipitation in midlatitude cyclones. II: Warm-frontal clouds. J. Atmos. Sci., 37 (March issue - in press).

Hobbs, P. V., 1978: Organization and structure of clouds and precipitation on the mesoscale and microscale in cyclonic storms. Rev. Geophys. and Space Phys., 16, 741-755.

______, and T. J. Matejka, 1980: Precipitation efficiencies and the potential for artificially modifying extratropical cyclones. Preprint Volume WMO Conference on Weather Modification, Clermont-Ferrand, France, July, 1980.

______, and K. R. Biswas, 1979: The cellular structure of narrow cold-frontal rainbands. Quart. J. Roy. Meteor. Soc., 105, 723-729.

______, and R. A. Houze, Jr., 1976: Mesoscale structure of precipitation in extratropical cyclones. Preprint Volume, International Conference on Cloud Physics, Boulder, Colorado, 488-493.

______, T. J. Matejka, P. H. Herzegh, J. D. Locatelli and R. A. Houze, Jr., 1980: The mesoscale and microscale structure and organization of clouds and precipitation in midlatitude cyclones. I: A case study of a cold front. J. Atmos. Sci., 37 (March issue - in press).

Houze, R. A., Jr., P. V. Hobbs, K. R. Biswas and W. M. Davis, 1976: Mesoscale rainbands in extratropical cyclones. Mon. Wea. Rev., 104, 868-878.

______, S. A. Rutledge, T. J. Matejka and P. V. Hobbs, 1980: Air motions and water budget of a warm-frontal rainband. Preprint Volume Amer. Meteor. Soc. 19th Conference on Radar Meteor., Miami Beach, Florida, 23-29.

Matejka, T. J., R. A. Houze, Jr. and P. V. Hobbs, 1980: Microphysics and dynamics of the clouds associated with mesoscale rainbands in extratropical cyclones. Quart. J. Roy. Meteor. Soc., 106, 29-56.

OBSERVATIONS OF WINTER MONSOON CLOUDS AND PRECIPITATION IN THE VICINITY OF NORTH BORNEO

R. A. Houze, Jr.[1], S. G. Geotis[2], F. D. Marks, Jr.[2], and A. K. West[1]

[1]Department of Atmospheric Sciences
University of Washington
Seattle, U.S.A.

[2]Department of Meteorology
Massachusetts Institute of Technology
Cambridge, U.S.A.

1. Introduction

The clouds and precipitation of the winter monsoon occur over the complex of islands and peninsulas of Malaysia and Indonesia, called the "maritime continent" (Ramage, 1968). As low-level northeasterly flow from the cold Asian continent arrives in this region, convergence at low levels and upward motion occur, while in the upper levels of the troposphere, the strongest divergence in the wintertime global circulation is observed (Krishnamurti et al., 1973; Murakami and Unninayar, 1977). The latent heat release over the maritime continent is immense, constituting one of the primary sources of energy for the whole atmosphere (Ramage, 1968; Webster, 1972). Yet winter monsoon rains have been described only in the most general terms. Ramage (1971) categorizes monsoon precipitation into "showers", from towering cumulus and cumulonimbus, and "rains", from deep nimbostratus with embedded cumulonimbus. He notes that both stratiform and convective air motions can occur in association with monsoon clouds and that the precipitation may be either widespread or localized.

The question arises as to whether the stratiform component of the clouds and precipitation is in any way similar to the widespread stratiform precipitation associated with synoptic-scale disturbances in mid-latitudes, or whether it develops in association with deep convection, in a manner more similar to that of the widespread precipitation that falls from the anvils of cloud clusters over the equatorial oceans (Zipser, 1969, 1977; Houze, 1977; Leary and Houze, 1979a, b; Cheng and Houze, 1979).

Though the clouds and precipitation over the maritime continent are primarily forced by the nearly steady monsoonal convergence, they may fluctuate in intensity in response to synoptic-scale disturbances, such as "cold surges" over the South China Sea (Ramage, 1971) and westward-propagating near-equatorial disturbances (Cheang, 1977; Chang et al., 1979). Moreover, the clouds and precipitation are modulated on subsynoptic time and space scales by land-sea contrasts, orography and the diurnal cycle of radiative heating (Ramage, 1971).

In this paper, we use radar and satellite observations obtained in MONEX[3] to examine: (1) the diurnal variation of winter monsoon clouds and precipitation; and (2) the relative extent to which the clouds and precipitation are stratiform and convective.

[3]The International Winter Monsoon Experiment conducted in December 1978 (Greenfield and Krishnamurti, 1979)

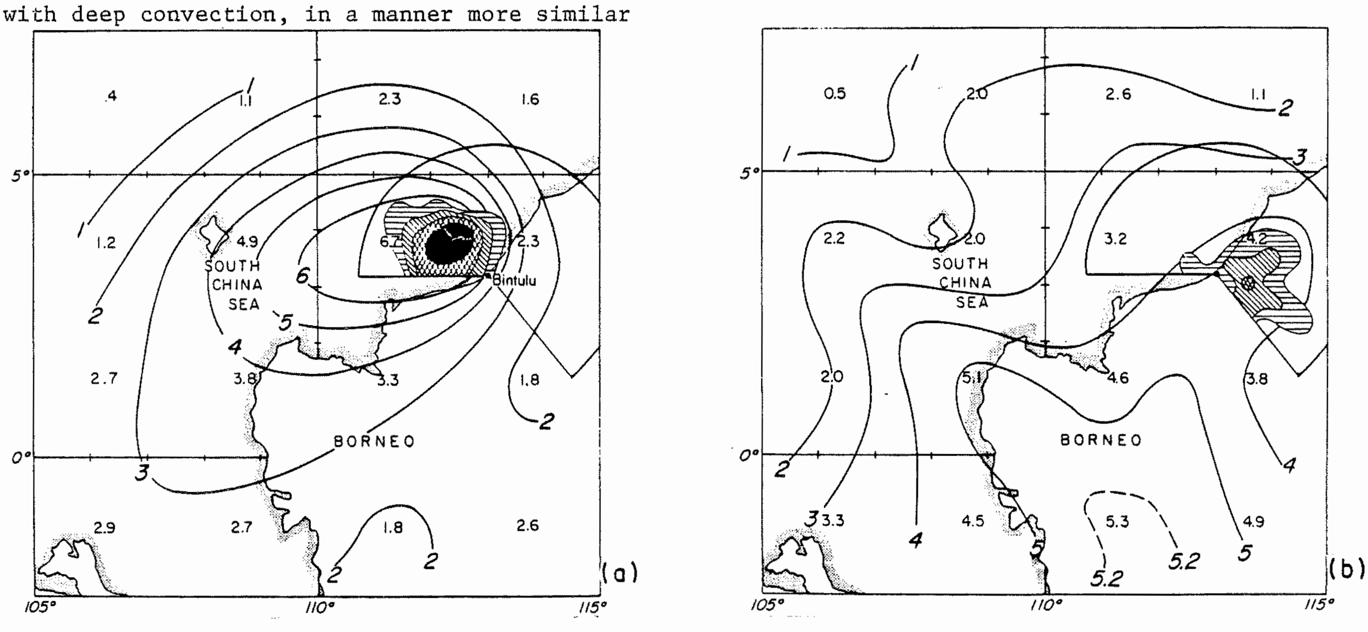

Fig. 1 Contours and grid point values of the December 1978 average high cloud coverage in tenths for (a) 0800 LST and (b) 2000 LST as determined from infrared geosynchronous satellite imagery. Partial circle shows area of radar observation. Shading within the radar circle shows contours of the 8-31 December 1978 average areal precipitation coverage in contours of 0.1, 0.2, 0.3 and 0.4.

2. Diurnal Variation of the Clouds and Precipitation

The upper-level cloud cover, determined from infrared images from the Japanese geosynchronous satellite, and the area covered by precipitation measured with the Massachusetts Institute of Technology's WR-73 Weather Radar, which was located on the north coast of Borneo, have been averaged for two times of day (Fig. 1). At 0800[4], the precipitation and upper-level clouds were centered over the South China Sea, just west northwest of the radar site (Fig. 1a). At 2000, the clouds and precipitation were centered over land (Fig. 1b). The precipitation observed by radar at this time occurred under an extension of the area of maximum cloud cover, which was centered southwest of the region of radar observations.

The diurnal variation of the radar echo pattern is further seen by dividing the radar region into offshore and onshore sectors and plotting the mean fractional areas covered by rain in the two sectors (Fig. 2). The offshore feature reaching its peak coverage at 0600, and the onshore feature reaching its peak at 2100.

The regularity of the diurnal cycle of cloudiness and precipitation is illustrated by Fig. 3, which shows that the offshore peak occurred every single morning, while the onshore peak, midway between the offshore peaks, was just about as regular, being absent on only 2 or 3 days. Thus, the diurnal cycle is evident in each day's observations; the data do not have to be composited or filtered to see it. Rather, the diurnal periodicity dominates the time series. Synoptic-scale modulations of the cloudiness and precipitation are more difficult to discern. We are currently investigating the extent to which variations in the intensity of the diurnal peaks in Fig. 3 can be related to cold surges or westward propagating disturbances.

That the diurnal variation of clouds and precipitation is associated with a land-sea circulation is confirmed by pilot balloon measurements at the radar site, which show that

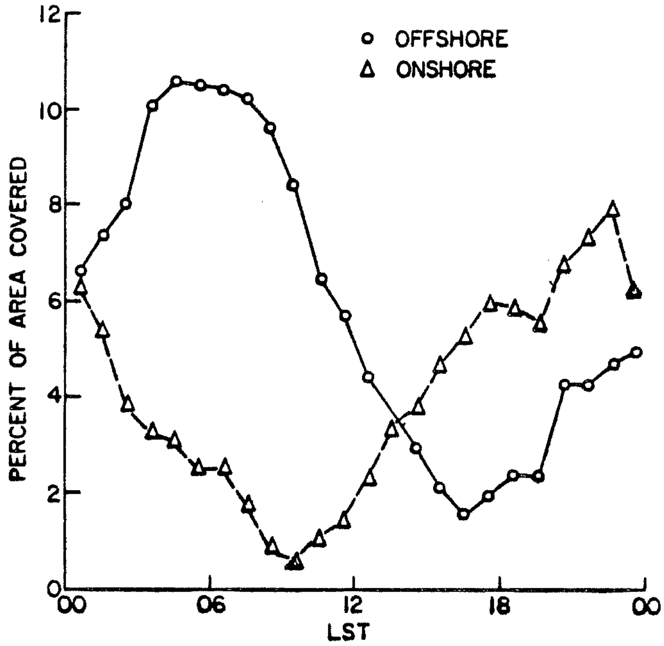

Fig. 2 Diurnal cycles of the area covered by precipitation onshore and offshore as shown by the radar on the North Borneo coast.

[4]All times are in LST for Borneo (8h later than GMT).

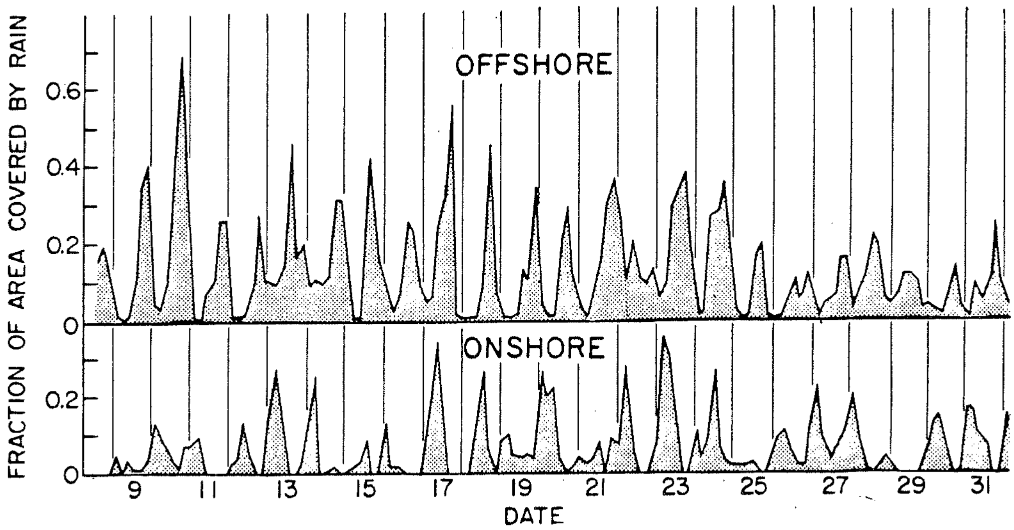

Fig. 3 December 1978 time series of area covered by precipitation detected by the radar on the North Borneo Coast.

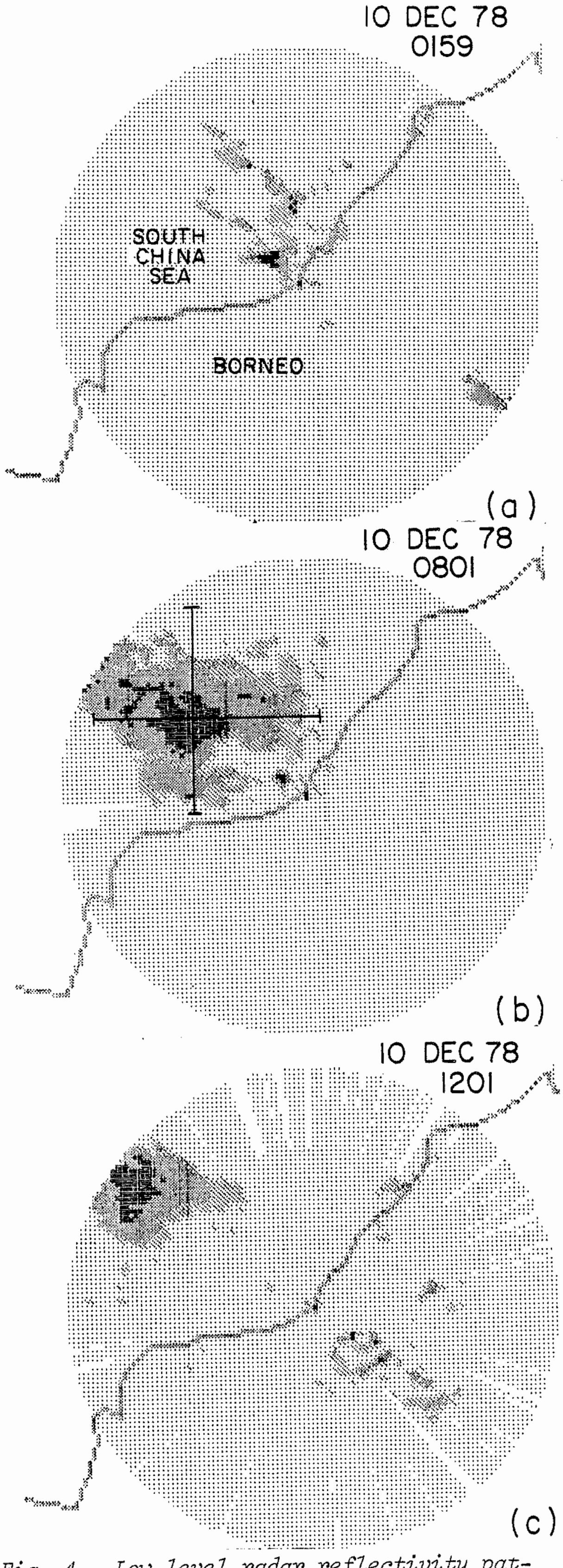

Fig. 4 Low-level radar reflectivity patterns showing the development and dissipation of the offshore rain area on 10 December 1978. Reflectivity is indicated by gray shades with thresholds of 12, 24 and 36 dBZ. Cross hairs in b show positions of cross sections in Fig. 5.

from 1400-2000, the period of active clouds and rain over land, the winds in the lowest 1.5 km were directed onshore, while for the next 12 h, when the clouds and precipitation were active over the water, the winds were offshore.

3. Development and Structure of the Offshore Precipitation

Since the offshore precipitation that reached its peak activity in the morning was so well sampled by radar (Fig. 1), its development and structure could be studied in detail. An example of the offshore precipitation feature on 10 December is shown in Fig. 4. Although the cloud system that developed on this day was a particularly well defined example, the offshore cloud systems on all other days tended toward and often closely approached the same structure.

Around 0200, the offshore precipitation began as a group of convective cells (Fig. 4a). By 0800, it had developed into a large region of continuous precipitation over 200 km in dimension centered over the water just northwest of the radar site (Fig. 4b). Later, the portion of the rain nearest the shore began to decay and the radar echo moved toward the northwest. By noon, the echo was dissipating and moving past the northwest edge of the region of radar observations (Fig. 4c).

Vertical cross sections through the offshore precipitation show that at the time of its maximum size (around 0800) the echo was almost completely horizontally stratified (Fig. 5). These sections are typical of the early morning echo. A bright band at the melting level extended continuously over 150-200 km, accentuating the stratiform character of the precipitation and indicating a near absence of convective scale updrafts and downdrafts. Convective cells, such as the one near S in Fig. 5a occupied only a small fraction of the area of rain at this stage of its development.

Satellite data show that this primarily stratiform rain was falling from a large anvil cloud, which had expanded from an initially small entity associated with the convective cells seen just offshore in Fig. 4a. Thus, the diurnally generated offshore cloud system developed in a manner similar to that of cloud clusters over the equatorial oceans (Zipser, 1969, 1977; Houze, 1977; Leary and Houze, 1979a, b; Cheng and Houze, 1979). Those clusters are also characterized in satellite data by large cirrus canopies and in radar data by mesoscale regions of stratiform precipitation with well defined melting layers, and the stratiform rain areas in the clusters also evolve from groups (usually lines) of convective cells. These structural similarities suggest that the diurnally generated monsoonal cloud systems are similar in their dynamics and cloud microphysical processes to the cloud clusters.

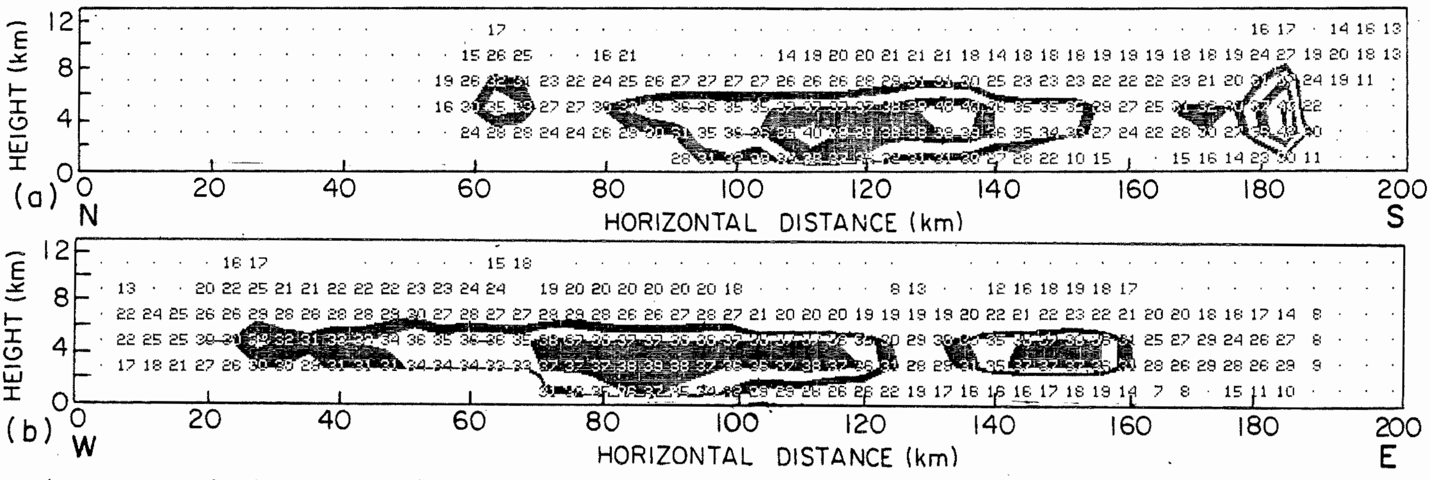

Fig. 5 *Vertical cross sections of radar reflectivity through the offshore rain area on 10 December 1978. Sections are taken along the (a) north-south, and (b) west-east cross hairs in Fig. 4b.*

4. Conclusions

The winter monsoonal clouds and precipitation that occur over north Borneo are strongly modulated diurnally, with the peak cloud and precipitation coverage occuring at 0600 offshore and at 2100 onshore. Synoptic-scale time variations in the cloud and precipitation amounts, on the other hand, were more subtle and difficult to discern. It its mature stages, the regularly recurring offshore cloud feature consisted of primarily stratiform precipitation falling from a widespread anvil cloud. Its development, structure and probably its internal dynamics and microphysics, resembled those of cloud clusters over the equatorial oceans.

Acknowledgments

The cooperation and assistance of Malaysian Meteorological Office personnel are gratefully acknowledged, in particular, Mr. Lim Yit Sen and his staff at the Bintulu airport were most helpful at the radar site. This research was supported by the Global Atmospheric Research Program, Division of Atmospheric Sciences, National Science Foundation, under grant ATM 78-00232.

References

Chang, C.-P., J. E. Erickson and K. M. Lau, 1979: Northeasterly cold surges and near-equatorial disturbances over the Winter MONEX area during December 1974. Part I: Synoptic aspects. Mon. Wea. Rev., 107, 812-829.

Cheang, B. K., 1977: Synoptic features and structures of some equatorial vortices over the South China Sea in the Malaysian region during the Winter Monsoon, December, 1973. Pure Appl. Geophys., 115, 1303-1333.

Cheng, C.-P., and R. A. Houze, Jr., 1979: The distribution of convective and mesoscale precipitation in GATE radar echo patterns. Mon. Wea. Rev., 107, 1370-1381.

Greenfield, R. S., and T. N. Krishnamurti, 1979: The Winter Monsoon Experiment--Report of December 1978 field phase. Bull. Amer. Meteor. Soc., 54, 439-444.

Houze, R. A., Jr., 1977: Structure and dynamics of a tropical squall line system. Mon. Wea. Rev., 105, 1540-1567.

Krishnamurti, T. N., M. Kanamitsu, W. J. Koss and J. D. Lee, 1973: Tropical east-west circulations during the northern winter. J. Atmos. Sci., 30, 780-787.

Leary, C. A., and R. A. Houze, Jr., 1979a: The structure and evolution of convection in a tropical cloud cluster. J. Atmos. Sci., 36, 437-457.

_____ and _____, 1979b: Melting and evaporation of hydrometeors in precipitation from the anvil clouds of deep tropical convection. J. Atmos. Sci., 36, 669-679.

Murakami, T., and M. S. Unninayar, 1977: Atmospheric circulation during December 1970 through February 1971. Mon. Wea. Rev., 105, 1024-1038.

Ramage, C. S., 1968: Role of a tropical "maritime continent" in the atmospheric circulation. Mon. Wea. Rev., 96, 365-370.

__________, 1971: Monsoon Meteorology, Academic Press, New York, 271 pp.

Webster, P. J., 1972: Response of the tropical atmosphere to local, steady forcing. Mon. Wea. Rev., 100, 518-541.

Zipser, E. J., 1969: The role of organized unsaturated convective downdrafts in the structure and decay of an equatorial disturbance. J. Appl. Meteor., 8, 799-815.

__________, 1977: Mesoscale and convective-scale downdrafts as distinct components of squall-line circulation. Mon. Wea. Rev., 105, 1568-1589.

COMPUTATION OF INSTABILITY IN OROGRAPHIC CLOUDS

J. D. Marwitz

Department of Atmospheric Science
University of Wyoming
Laramie, Wyoming 82071
U.S.A.

1. INTRODUCTION

It is becoming increasingly evident that a seeding potential exists only in orographic storms which contain convection. Specifically it appears that the higher condensation rates associated with embedded and individual convective elements produce clouds which sometimes contain significant quantities of supercooled water (> 0.5 gm^{-3}) and a dearth of natural ice crystals (< 10 ℓ^{-1}). Aircraft observations by our group lend support to this contention. We have flown a number of orographic storms over the San Juan Mountains of southern Colorado (Marwitz, 1974 and 1980; Cooper and Saunders, 1980 and Marwitz and Cooper, 1980); over the Central Sierras of California (Marwitz et al., 1978 and 1979), and over the Wasatch Mountains of Utah (Marwitz and Stewart, 1979). The observations and analysis by Hill (1979a & b) over the Bridger Range in Utah also indicate that supercooled water is primarily restricted to orographic clouds containing convective elements.

2. THERMODYNAMIC INSTABILITY

There are two classic measures of thermodynamic instability, namely convective or potential instability and static or hydrostatic instability. Convective instability is the state of a column or layer of air and is measured by the vertical profile of wet-bulb potential temperature, θ_ω (or equivalent potential temperature, θ_e). Static instability is the state of the buoyancy restoring force on a parcel of air with respect to its environment and is measured by density differences or in the case of parcel theory by thermal differences assuming hydrostatic equilibrium (Huschke, 1959).

The presence of convective instability is determined by examination of the vertical profile of θ_ω or θ_e. Only three states can be specified; unstable, $(\frac{\partial\theta_\omega}{\partial Z} < 0)$; neutral $(\frac{\partial\theta_\omega}{\partial Z} = 0)$; or stable $(\frac{\partial\theta_\omega}{\partial Z} > 0)$. The magnitude of the convective instability is not directly related to whether the instability will be released or if released, what will be the intensity of the convection. The convective instability is released only after the layer is vertically displaced to or above the lifted condensation levels in the layer.

The use of parcel theory to determine static instability assumes hydrostatic pressures exist. Lifting individual parcels and noting their thermal differences and/or accumulated positive and negative energy areas is the traditional and valid measure of static instability. The release of static instability only requires that an unstable parcel be vertically displaced above its level of free convection. This is typically produced in the atmosphere by small hills, thermals or turbulence.

Fig. 1 contains an aircraft measured sounding upwind of the Central Sierra Mountains of California. Parcel theory applied to parcels below 900 mb indicates negative thermal buoyancy exists below 700 mb and hence no convective clouds would develop. Using parcel theory on a parcel near 850 mb also predicts negative thermal buoyancy and hence no convective cloud below 700 mb. A thin stratocumulus cloud layer with tops near 880 mb was present over the California Valley. The winds within and below the stratocumulus layer were light and variable, i.e. no upslope flow. The winds above the 850 mb layer were upslope. The crest of the Sierras is ∿ 3 km or 700 mb. Towering cumulus were present over the barrier above the 1.8 km (829 mb) contour with bases at +2°C. If the layer from 850 mb to 600 mb was lifted ∿ 150 mb (850-700 mb), then the observed convective clouds were readily explained.

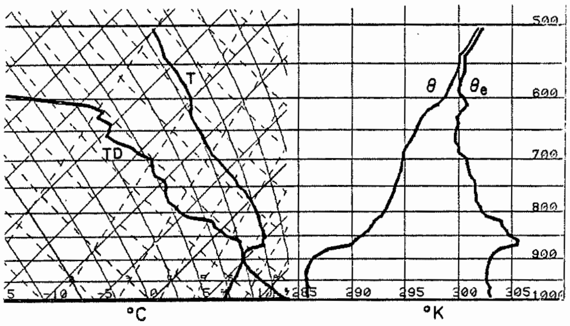

Fig. 1 Sounding on March 21, 1979 during takeoff and climbout. The temperature (T) and dewpoint (DP) are plotted on a Skew-T, log-p diagram. Potential temperature (θ) and equivalent potential temperature (θ_e) are plotted on the right side of the diagram. (From Marwitz 35 al., 1979).

Fig. 2 contains another example of an aircraft sounding upwind of the Sierras. Using parcel theory below 930 mb, negative thermal buoyancy was present below 800 mb. Stratiform clouds with embedded convection (stratocumulus) were observed over the barrier. The winds were upslope above 930 mb. Examination of the sounding indicates that if each level above 930 mb were vertically displaced only 50 mb (which must occur with the upslope flow), then the convective instability would be released in the form of embedded convection.

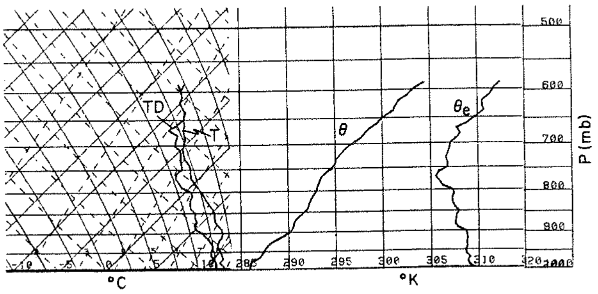

Fig. 2 Same as Fig. 1 except for January 9, 1978. (From Marwitz et al., 1978).

3. RECOMMENDED PROCEDURE

We have developed a reliable technique for evaluating the thermodynamic instability in orographic clouds from soundings taken upwind of of the barrier. If the sounding evaluated by this technique indicated convection should have been present, then indications of convection were observed. Conversely if the sounding indicated convection should not be present, then it was not observed.

The procedure is as follows:

- Examine only those atmospheric layers which are moving upslope as indicated by the winds.
- Vertically displace all layers an equal Δp amount corresponding to the pressure difference between the crest and the lowest upslope level.
- Use parcel theory on the modified sounding to quantify the magnitude of the resultant instability.

This technique attempts to simulate the method whereby thermodynamic instability is released in orographic clouds. It uses the convective/potential instability procedure whereby the layers of upslope air are vertically displaced, then the resultant sounding is examined for static/hydrostatic instability using the parcel method. If the parcel method indicates convection should be present, then our experience indicates it will be present.

4. REFERENCES

Cooper, W. A. and C.P.R. Saunders, 1980: Winter storms over the San Juan Mountains, Part II. Microphysical processes. Accepted by the J. Appl. Meteor.

Hill, G. E., 1979a: Analysis of randomized winter orographic cloud seeding experiments in Utah. J. Appl. Meteor., 18, 413-448.

Hill, G. E., 1979b: Reassessment of cloud seeding concepts for winter orographic storms. Paper presented at 7th Conf on Inadv. & Planned Wea. Modif., Banff, Amer. Meteor. Soc., 71-73.

Huschke, R. E., 1959: Glossary of Meteorology, Amer. Meteor. Soc., Boston, 638 pp.

Marwitz, J. D., R. E. Stewart, T. Karacostas and B. Martner, 1978: Cloud physics studies in SCPP during 1977-78. Report No. AS 121. Dept. Atmos. Sci., Univ. of Wyo., Laramie, Wyo., 202 pp.

Marwitz, J. D. and R. E. Stewart, 1978: Cloud physics studies in Utah during 1978. Report No. AS 122. Dept. of Atmos. Sci., Univ. of Wyo., Laramie, Wyo., 162 pp.

Marwitz, J. D., R. E. Stewart, B. Martner, and T. Karacostas, 1979: Cloud physics studies in SCPP during 1978-79. Report No. AS 123. Dept. of Atmos. Sci., Univ. of Wyo., 154 pp.

Marwitz, J. D., 1980: Winter storms over the San Juan Mountains, Part I, Dynamic processes. Accepted by J. Appl. Meteor.

Marwitz, J. D. and W. A. Cooper, 1980: Winter storms over the San Juan Mountains, Part III: Seeding potential. Accepted by J. Appl. Meteor.

UTILISATION CONJOINTE DE DONNEES RADAR ET DE "METEOSAT" POUR L'ETUDE DE LA CONVECTION TROPICALE EN VUE DE LA PREPARATION DE L'EXPERIENCE "COPT"

Paul Olory-Togbé

Laboratoire de Météorologie Dynamique du C.N.R.S.
Ecole Polytechnique - 91128 Palaiseau Cedex - France

Les nuages précipitants associés à 12 perturbations tropicales d'échelles synoptiques sont observés simultanément à l'aide d'un radar au sol et de photographies du satellite Météosat.

On fait une étude de la morphologie des nuages à l'échelle convective et on essaie de faire un lien entre leur organisation, la stratification et l'écoulement atmosphérique à grande échelle.

Les données de base sont :

- les photos du scope PPI du radar 5 cm (WRS-100 Entreprise Electronic) de l'Aéroport de Niamey, et du radar 3 cm (Ramo) de la Météorologie Nationale française, installé à Khorogo (Côte d'Ivoire) ;

- les photographies du satellite Météosat dans les trois canaux : visible (0,4 - 1,1 µm) ; infrarouge (5,7 - 7,1 µm) ; vapeur d'eau (10,5 - 12,5 µm).

Ces photographies ont été obtenues par l'intermédiaire de l'E.S.A. sous forme de transparents positifs et de bandes magnétiques des valeurs vidéo mesurées par le radiomètre du satellite.

On a également des données de radiosondages, ainsi que les rapports des stations météorologiques régionales de l'Afrique de l'Ouest fournis par l'A.S.E.C.N.A.

Deux pluviomètres enregistreurs installés sur un rayon de 30 km autour du radar permettent de calibrer l'intensité des échos des radars.

Les observations ont eu lieu du 2 au 31 juillet 1978 à Niamey, et du 15 mai au 15 juin à Khorogo.

Les systèmes observés à l'aide du radar apparaissent organisés en cellules de forme elliptique, de dimensions variables, le plus souvent alignées.

Un tableau donnant la distance moyenne séparant les cellules, leurs dimensions, et leur durée de vie a été établi.

Ce tableau met en évidence un lien entre les dimensions des cellules et, d'une part, la distance qui les sépare, et, d'autre part, leur durée de vie : plus les dimensions des cellules sont grandes, plus la distance qui les sépare est faible et plus grande est la durée de vie. Et inversement.

Les systèmes nuageux diffèrent les uns des autres par le nombre de cellules présentes, leur degré d'alignement, ainsi que par leurs dimensions.

On calcule actuellement la variation en fonction du temps, du taux précipitant moyen des perturbations observées, et on essaie de faire le lien entre le bilan en eau des perturbations et la distribution des différentes classes de nuages présents.

La Figure 1 présente la variation en fonction du temps, du volume moyen d'eau précipitée par heure, de la ligne de grains observée le 22.07.78 à Niamey, dont la durée de vie a été de 4 heures.

L'observation à l'aide du satellite permet d'étudier le développement de la convection à grande et à petite échelle :

a) A grande échelle, les séries chronologiques des photographies de Météosat permettent d'associer le développement des nuages convectifs aux passages d'ondes planétaires de périodes de 3 à 4 jours.

b) L'observation de la structure des nuages à l'échelle de la résolution spatiale du satellite permet de calculer le nombre de zones d'ascendance présent dans un amas nuageux par l'observation de la photo prise dans le canal vapeur d'eau, la surface relative couverte par les nuages hauts et leur taux de croissance dans le canal infrarouge. Ces résultats sont comparés aux caractéristiques des cellules précipitantes observées par le radar (ce travail est en cours).

On a calculé les profils moyens du vent, d'humidité et de température potentielle équivalente (θ_e) du jour qui précède une perturbation, considéré comme favorable au développement de la convection, et du jour qui suit une perturbation, considéré comme défavorable au développement de la convection.

La Figure 2 présente la différence entre les profils moyens d'humidité pour 6 perturbations observées à Niamey. Elle montre que, avant la perturbation, le profil vertical est plus uniforme et l'humidité plus importante dans les hautes couches au-dessus de 800 mb.

La Figure 3 présente la différence entre les profils moyens du vent. Elle montre que, avant la perturbation, il y a un accroissement de la force du courant d'est à 700 mb et 100 mb, ainsi que du cisaillement vertical entre 950 et 700 mb.

Tableau 1

CARACTERISTIQUES DES NOYAUX PRECIPITANTS
DES PERTURBATIONS OBSERVEES AU NIGER

	Largeur moyenne du noyau B (km)	Longueur moyenne du noyau L (km)	Distance moyenne entre les noyaux D (km)
8.07.78	7	14	21
14.07.78	9	17	15
18.07.78	10	16	14
22.07.78	4	9	4
25.07.78	9	18	5
26.07.78	17	38	9
29.07.78	11	22	10

FIG 1

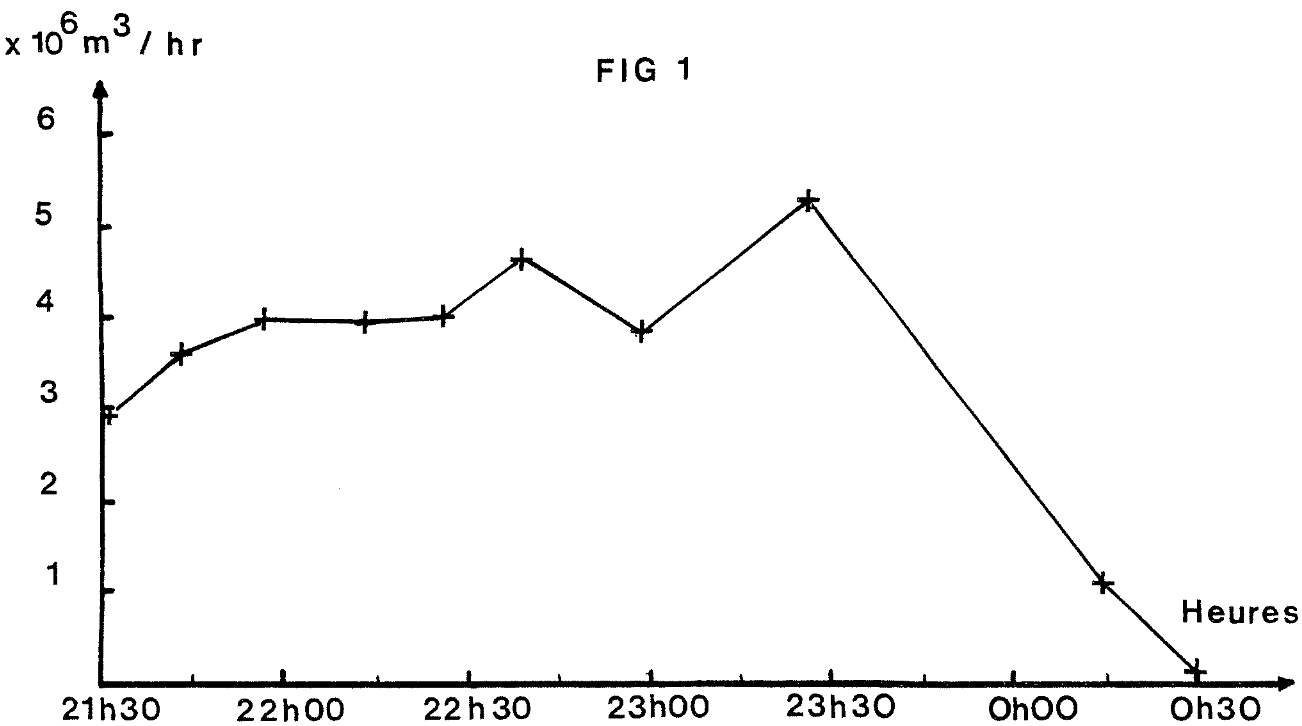

Taux Précipitant / Temps

(perturbation du 22/07/78 durée de vie = 4heures)

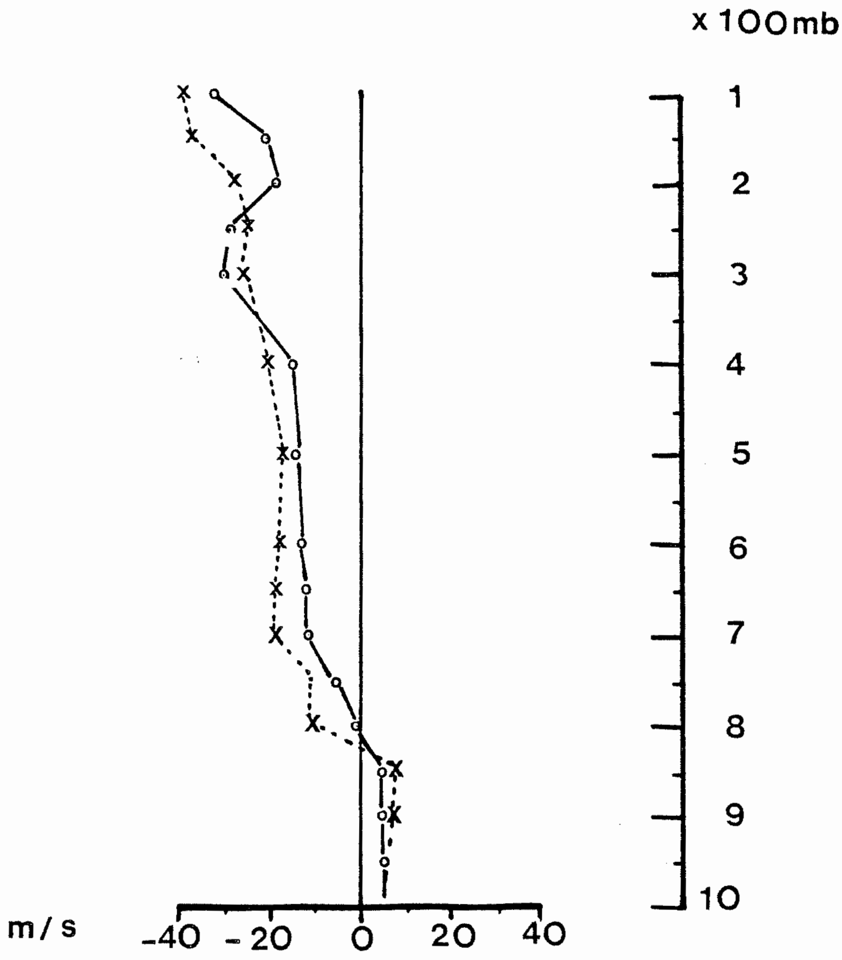

FIGURE 3

U Composante
Zonale
du vent

o—o—o Profil après passage de la perturbation
x- - -x- - -x " avant " "

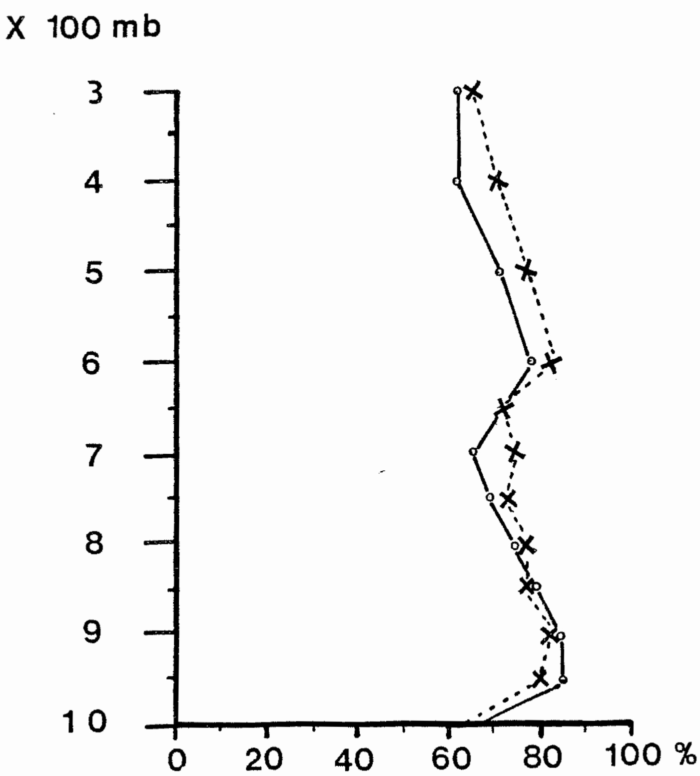

FIGURE 2

HUMIDITE

NUMERICAL SIMULATION OF CLOUD INTERACTIONS

Harold D. Orville, Ying-Hwa Kuo,
and Richard D. Farley

South Dakota School of Mines and Technology
Rapid City, South Dakota, USA 57701

A two-dimensional, time-dependent cloud model has been used to investigate factors controlling the merging of cumulus clouds (more precisely the merging of lines of cumulus clouds, because of the geometry of the model). The model predicts the evolution of the air flow, the water vapor field, the cloud liquid, cloud ice, rain, and precipitating ice (graupel/hail), temperature, and pressure fields (Orville and Kopp, 1977).

Pairs of clouds were triggered by specified temperature perturbations. Spacing, timing, and intensity of the two perturbations were varied to simulate cloud interactions under various conditions. Also closed, periodic, and open boundary conditions were used to simulate different physical situations. Edge-to-edge spacing between the two initial perturbations (within the model domain) varied from 1.2 km to 4.8 km (the corresponding center-to-center spacing varied from 6.0 km to 9.6 km). With closed boundary conditions, the model clouds have image clouds outside the domain. Thus, the interaction of the clouds (of equal intensity) is perfectly symmetric only in the 4.8 km spacing case. It is in that case that the center axes of the image and domain clouds (in a 19.2 km wide domain, 200 m grid interval model) are all 9.6 km apart. All other spacings lead to asymmetric clouds.

Two other factors can cause asymmetries and have been tested. First, the timing differences for the cloud initiation were varied from 0 to 9 min at 3 min intervals. Second, the "intensity" of the clouds (maximum excess temperature of the initial perturbation) was varied from 1°C to 3°C.

Figure 1 shows a case with perfect symmetry. This is Case C4.8L3R3 where C stands for closed boundary condition, 4.8 for the edge-to-edge spacing (in km), and L3R3 indicates that both the left cell and right cell have 3°C initial temperature perturbations. The two clouds in this case have only "destructive" interaction with each other (and their images), and both clouds together produce about as much precipitation as a single cell initiated along the central axis of the domain (at 9.6 km in from the left boundary) [see Table 1].

TABLE 1

Precipitation Results From Cases With Closed Boundary Conditions

Unit: Dm^3 (per 1 km)

Cases	Rain	Hail	Total Precip.	Merger
A. Different Spacing Cases:				
Group a:				
CSINGLE3	41.0	1.6	42.6	no
C4.8L3R3	43.1	0.4	43.5	no
C1.2L3R3	39.5	3.6	43.1	no
Group b:				
C4.8L3R1	40.2	1.9	42.1	no
C3.6L3R1	40.9	1.6	42.5	no
C2.4L3R1	45.7	0.5	46.2	no
C1.2L3R1	59.3	1.0	60.3	yes
B. Different Intensity Cases:				
C1.2L3R1	59.3	1.0	60.3	yes
C1.2L3R1.5	43.1	0.9	44.0	no
C1.2L3R2	42.2	1.6	43.8	no
C1.2L3R3	39.5	3.6	43.1	no
C. Different Timing Cases:				
C1.2L3R3DT0	39.5	3.6	43.1	no
C1.2L3R3DT3	48.4	1.0	49.4	no
C1.2L3R3DT6	71.1	2.6	73.7	yes
C1.2L3R3DT9	55.1	3.2	58.3	no

Figure 2 shows an example of cloud merger, which is caused by initiating one cloud 6 min later than the first. The basic force causing merger is the horizontal pressure gradient, which is maximized in this case due to the positive pressure perturbation region above

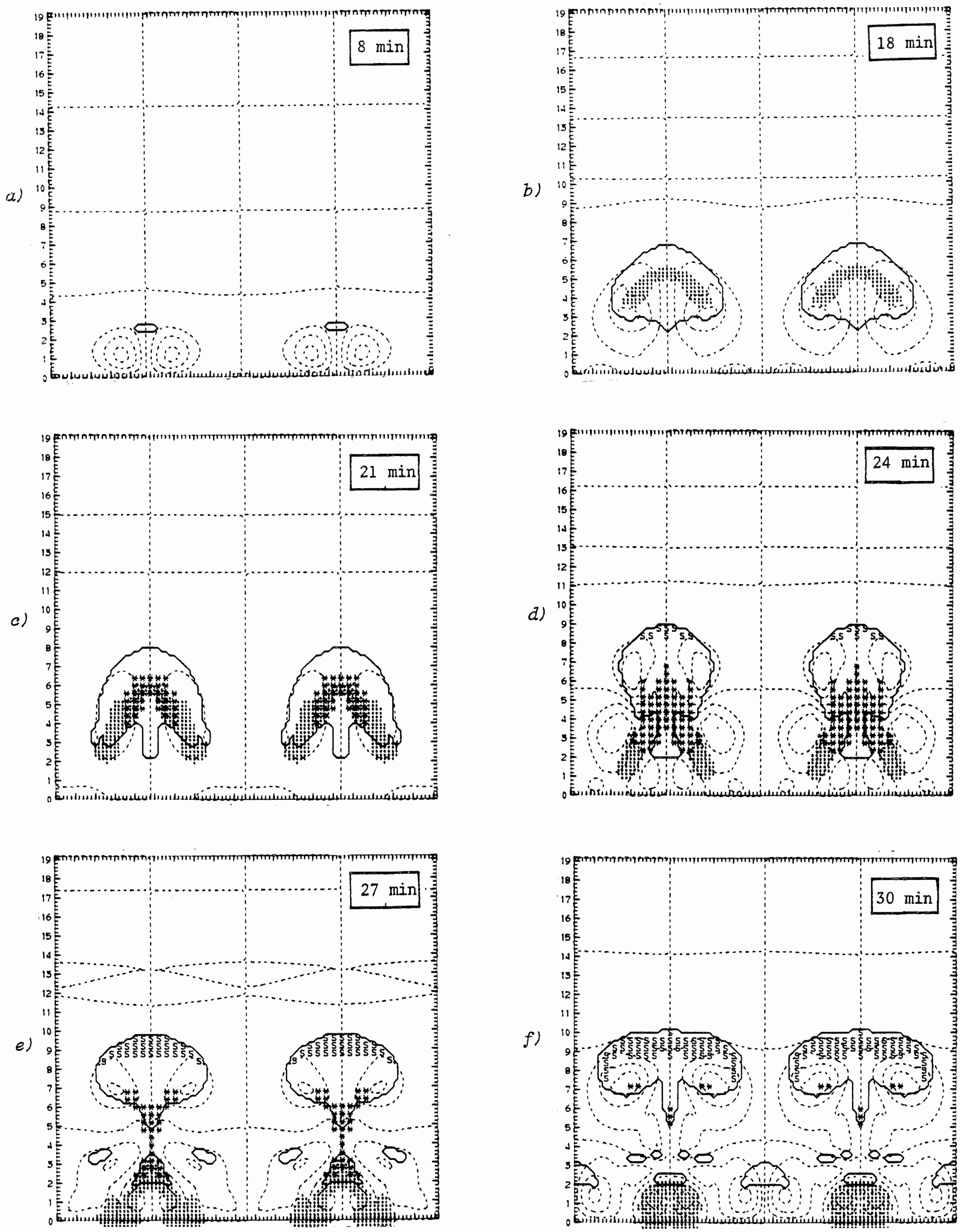

Fig. 1: Simulation of two perfectly symmetric clouds, Case C4.8L3R3. Cloud areas (100% R.H.) are outlined by a solid line; streamlines are dashed lines. Small solid circles and asterisks indicate rain and hail greater than 1 g kg^{-1}, respectively; and the S's indicate cloud ice greater than 0.1 g kg^{-1}.

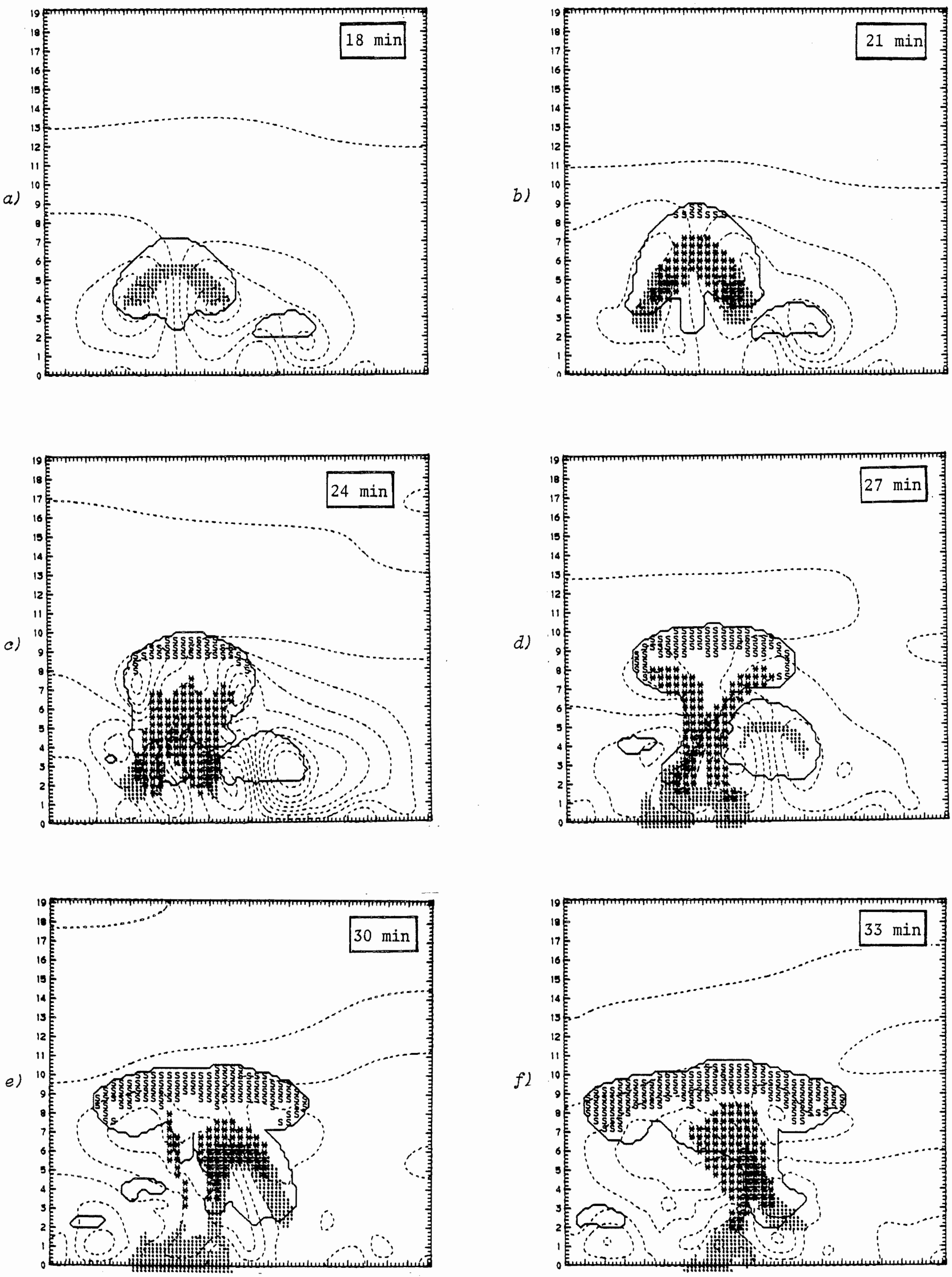

Fig. 2: Simulation of two clouds with 6 min difference in cloud initiations, Case C1.2L3R3DT6. The symbols are the same as those in Fig. 1.

the cloud on the right, and the negative pressure perturbation region in the strong updraft of the cloud on the left (the pressure perturbation centers occurring at about the same elevation).

Many more cases have been run. Table 1 summarizes the results regarding total precipitation and merger occurrence. The mnemonic for the cases is the same as described above with the addition that "single" stands for the single cloud case. Merger occurs if clouds are relatively close, or if one is stronger (more vigorous) than the other, or if one is initiated earlier than another of equal strength. Merger produces an increase in total precipitation by a factor of about 1.5.

Quite possibly, the addition of mesoscale convergence in the lower levels would increase the number of merger cases, because the effect of the convergence is to move cells closer together (see Chen and Orville, 1980). Further tests need to be made.

Acknowledgments. This material is based upon work supported by the Division of Atmospheric Sciences, National Science Foundation, under Grant ATM 77-05187 and Grant ATM 79-16147. The computations were performed at the Computing Facility of the National Center for Atmospheric Research, which is sponsored by the National Science Foundation.

We thank Mrs. Joie Robinson for the preparation of this paper.

REFERENCES

Chen, C-H., and H. D. Orville, 1980: Effects of mesoscale convergence on cloud convection. (March issue), J. Appl. Meteor.

Orville, H. D., and F. J. Kopp, 1977: Numerical simulation of the life history of a hailstorm. J. Atmos. Sci., 34, 1596-1618.

MESOSCALE INTERACTION BETWEEN CONVECTIVE CELLS AND THE ENVIRONMENT : AN EFFICIENT NUMERICAL MODEL

Y. POINTIN

L.A.M.P., University of Clermont II, FRANCE

I. Introduction

The aim of the proposed model is to study the influence of a deep convective cell on its neighboring environment and the modification that the resulting local variations of the thermodynamic and dynamic fields induce on the life cycle of the clouds. The time and space scales of the convective vertical transport of heat, humidity and momentum are of the order of one minute and a few kilometers respectively and can hardly be assumed to be smaller than the characteristic time and space scales of an isolated cumulonimbus cloud adopted by other works (Kuo, 1974 ; Kreitzberg and Perkey, 1976 ; Anthes, 1977). Active and convective cells concern a relatively small volume of the atmosphere which is otherwise stratified with very weak vertical transfers. The basic principle of this numerical model is to use a simplified description of the evolution of each convective cell in order to evaluate the vertical transports (convective fluxes) and to simulate their effects on the mesoscale flow with a simplified mesoscale model. This is realized by the imbrication of a one-dimensional time-dependent cumulus cloud in a three-dimensional non-hydrostatic mesoscale model.

II. General description of the model

The equations of the mesoscale model, similar to Tapp and White's (1976), simulate the dynamics and thermodynamics of the flow which is mainly quasi-barotropic and quasi-isentropic. Theses equations cannot take into account the internal structure of the convective cells but include their effects by mean of convective fluxes induced by each cell (Fig. 1). The dynamic and thermodynamic fields are modified in a consistent way over the whole domain and at every instant through the mesoscale equations and their deformation indicate clearly the position of each convective cell. The integration time step Δt is of the order of 40s and the grid cells have mean dimensions of the order of 5 km x 5 km x 1 km.

The cloud model is based on existing models (Ogura and Takahashi, 1973) but several features have been added to permit the imbrication.

Each cloud is visualized as three axisymmetric coaxial cylinders vertically erected and topped by an hemispheric dome. The innermost cylinder represents the active part of the cell which is usually simulated by other models. The middle cylinder represents the close neighborhood of the cell in which a

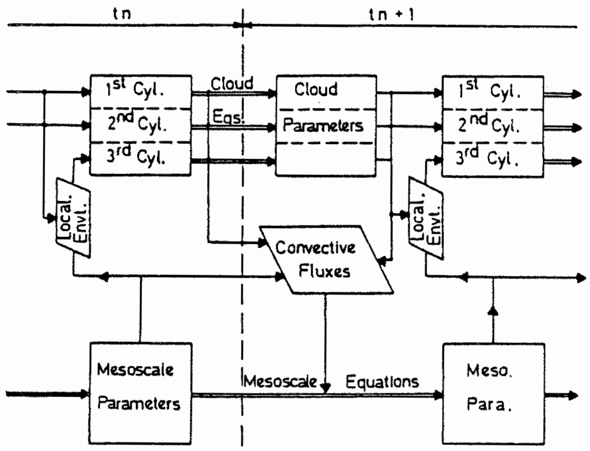

Fig. 1 : Block diagram of the imbrication of the cloud model in the mesoscale model (⟹ evolution following the equations, ⟶ data transmission, ▭ parameters, ▱ Evaluation of the imbrication terms).

localized downdraft can occur. The outermost cylinder represents the environment of the cloud which is modified both by the cloud and by the mesoscale flow. The top dome has the structure of a Hill vortex, raises like an air bubble and is pushed up or pulled down by the underlying turbulent jet. The air and the water substances pass from one cylinder to another through the lateral surface by means of turbulent motions induced by shear and thermal instabilities. The important effects of the boundary layer are partially simulated by the continuity equation, applied to the lowest layer of the cloud, from which a non zero velocity value for the bottom of the innermost cylinder is deduced. The microphysical phenomena are parameterized according to Kessler's formulation. The turbulent field evolves under equations obtained following Lopez (1973) for the innermost and middle cylinders and is deduced from the mesoscale flow fields by the diagnostic equations of Sommeria (1974) for the external cylinder. The vertical spacing between grid points of the axisymmetric one dimensional cloud model is 350 m and the variable time step is of the order of 10 s.

The consistency of the description of the physical variables by two sets of parameters, one set in the mesoscale model, the other in the cloud model, requires that, for each altitude, the surface integral over the horizontal cross section of the external cylinder should be the same in the two models. According to this requirement, the values of the parameters in the external cylinder of the cloud model are computed from the values of the parameters in the mesoscale model every time these latter are modified ($tn = n\Delta t$)(Fig. 1). Then, the cloud parameters evolve during a time internal Δt and the differences between the new values and the old ones are used to define the convective fluxes which modify the values of the mesoscale parameters during the same time internal Δt (Fig.1). This computing method for the fluxes is different from the methods previously proposed (Kuo, 74 ; Kreitzberg and Perkey, 1976 ; Anthes, 1977) in the fact that the time evolution of the cloud parameters is essential. The fluxes are functions of time and space and closely reflect the evolution of the cloud. When the external cylinders of several clouds are intersecting, the fluxes over the common area are computed from the evolution of the values of the cloud parameters in each cell.

The interaction between several cells is simulated by the direct influence that each cell has on the mesoscale surrounding of all the others. Furthermore, each cell competes in proportion to its radius, for the air supply provided by the mesoscale convergence in the boundary layer. The modifications of the value of the mesoscale parameters, either by other cells or by itself, influence the life cycle of the cell. This model permits a more realistic and not too expensive simulation of the evolution of a convective cell.

III. Imbrication of the two models

The effects of the convective fluxes in the mesoscale vertical momentum equations, in the energy equation and in the humidity equation are similar to the effects of an internal body force, of a heat source and of a humidity source respectively. For example, the momentum equation reads :

$$\frac{\partial \vec{U}}{\partial t} + \vec{U}.\nabla\vec{U} = -\frac{1}{\rho}\nabla P' + \nabla(\nu_T \quad \nabla\vec{U} - \hat{f} \times \vec{U}$$

$$- \nabla P' \left[\rho^{-1} - \overline{\rho}^{-1}\right] + \vec{F}_c$$

where $\overline{P}$, $\overline{\rho}$ are the pressure and density of a reference hydrostatic state and P' is the pressure perturbation with respect to this mean state. The internal body force F_{cw} is computed between the time t_n and t_{n+1} as :

$$F_{cw} = (Wi\overset{*}{j}k - Wi\overset{n}{j}k) / \Delta t$$

where $Wi\overset{n}{j}k$ is the value of the vertical velocity in the grid cell centered at ($i\Delta x$, $j\Delta y$, Zk) at time t_n and $W_{i\overset{*}{j}k}$ is the mean value of the vertical velocities of the various volumes of all the parts of the clouds which intersect this grid cell. These modified vertical velocities are the result of the time integration of the cloud equations (Fig. 1) between t_n and t_{n+1}. The other fluxes are computed in the same way but, so far, no convectively induced body force has been introduced in the horizontal momentum equations and this explains the axisymmetric aspect of the perturbation pressure, temperature and vertical velocity fields in the mesoscale model.

At every time step of the mesoscale model, the local environment of each cell is characterized by some parameters whose values are computed from the values of the mesoscale parameters (Fig. 1) and which are used in the time integration of the differential equations of each cloud as initial or boundary values. These local environment parameters include the temperature, the vapor (or small droplet) water content, the vertical velocity, the mean horizontal wind and its divergence at the ground and the perturbation pressure. This latter parameter is needed in order to transmit the effect of mesoscale divergence to the vertical velocity equation of the cloud and to enable a non-zero vertical velocity at the "ground" in the inner cylinder which represents the dynamical forcing of the convective cell by the local environment. Holton (1973) has shown that the reactions of the surrounding of the cell, through the effect of the perturbation pressure, drastically influence the life cycle of the cell. This imbrication procedure takes in account such effects which become important for the organized convection.

IV. Case study

A numerical simulation has been carried out, starting with hydrostatic and horizontally uniform mesoscale fields with the temperature, dew point temperature and horizontal wind profiles shown in fig. 2.

A cloud has been created near the center of the domain with an arbitrary vertical velocity of 2 m/s, an humidity of 95 % and a radius or 1700 m. The time-height cross section of the

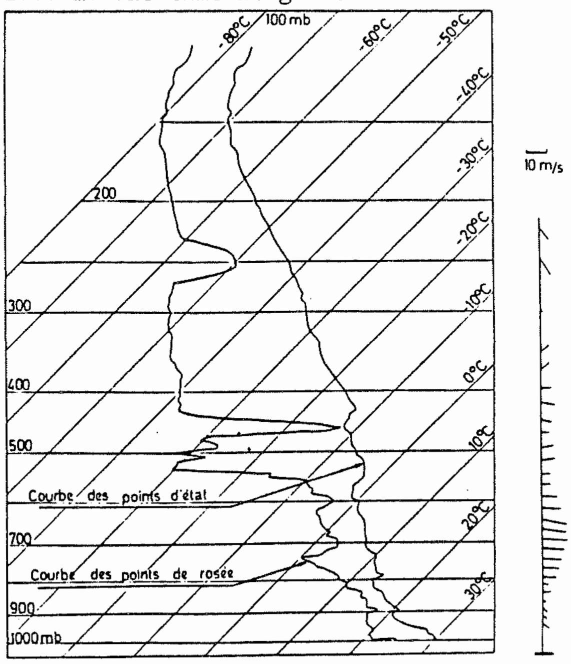

Figure 2 : Initial sounding of temperature, dew point temperature and horizontal wind profile.

vertical velocity (WC) and of the temperature difference (DT) between the inner cylinder and the third cylinder (local environment of the cell) are shown in fig. 3 and 4 respectively.

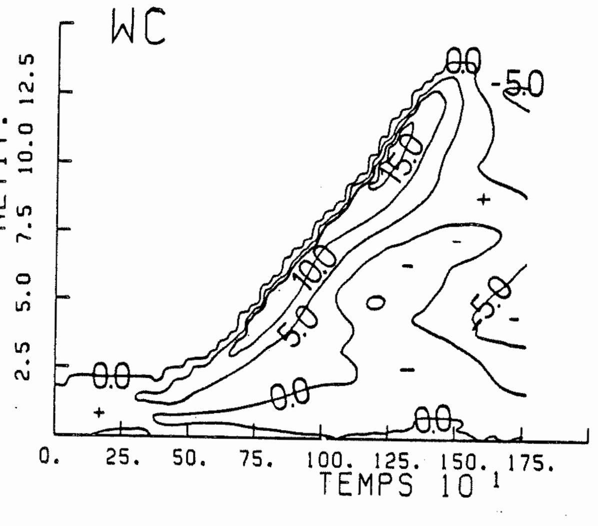

Fig. 3 : Time-height cross section of the vertical velocity in the innermost core of the cloud (altitude in km, time in second).

The cloud top reaches 13.5 km in 24 mn with a maximum vertical velocity of the order of 16.2 m/s. As the cloud reaches 5 km (540 mb), it penetrates into dryer layer where the small droplets in the updraft rapidly evaporate in the entrained dry air. By 1000 s of simulation, the temperature in the updraft becomes lower than the external temperature in the 5 km layers and induces a negative vertical velocity later on. By reaching the freezing level, the cloud top resumes its activity and the vertical velocity reaches its maximum value just below the cloud top. In the dryer 5 km layers, the negative vertical velocity contributes to the heating of the air, the small droplets soon disappear and the evaporation decreases, leading to a positive temperature difference by 1200 s of simulation. After 1300 s, the cloud top reaches 12 km where the

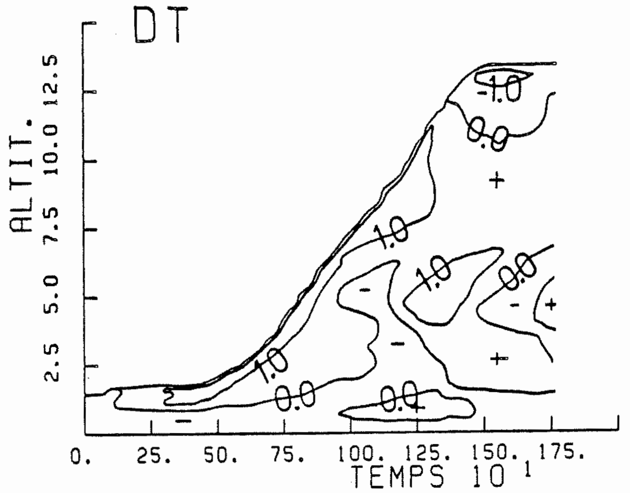

Fig. 4 : Same as fig. 3 for the temperature difference between the innermost cylinder and the outermost one (local environment).

saturated vapor water content is low, the condensation heating is small and the temperature difference becomes negative. After 1600 s of simulation, the vertical velocity and the temperature difference becomes small taking positive and negative values and the liquid water content decreases by precipitation and evaporation respectively. The impact of this convective cell on its mesoscale surroundings is visualized by the time evolution of various parameters at the mesoscale grid point closest to the center of the cloud on the figures 5-6-7. The general features of these graphs is that the value of the mesoscale variables at the various altitudes are strongly affected by the cloud after various simulation times corresponding to those at which the cloud top reaches each altitude. These figures also show the influence that the cloud has on the mesoscale field namely that the cloud heats and dries its neighborhood below 4 km (curbes labelled 1), cools and humidifies the dry layer between 5 km and 7 km (curves labelled 2) and heats the layer between 8 km and 12 km after 1200 s of simulation (curve labelled 3). The vertical

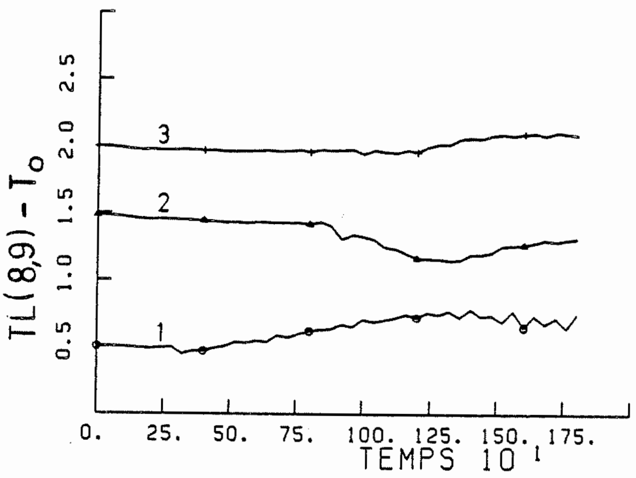

Fig. 5 : Time evolution of the mesoscale temperature at the closest point to the cloud position for three different altitudes. Curve labelled 1 = 880 m, 2 = 5372 m, 3 = 8349 m. A constant value has been substracted

velocity is also strongly affected but the perturbation pressure redistributes the effects of the momentum convective fluxes implying that the vertical velocity is downward at 8349 m by 1200 s before the penetration of the cloud in this layer. The other important influence of the cloud is the appearance of a convergence maximum near the cloud position in the ground layer as shown in fig. 8, convergence which contributes to the non-zero vertical velocity in the cloud model (Fig. 3).

The horizontal extent of these perturbation fields is of the order of 15 km increasing with time while the amplitude of these perturbations decrease (Fig. 9).

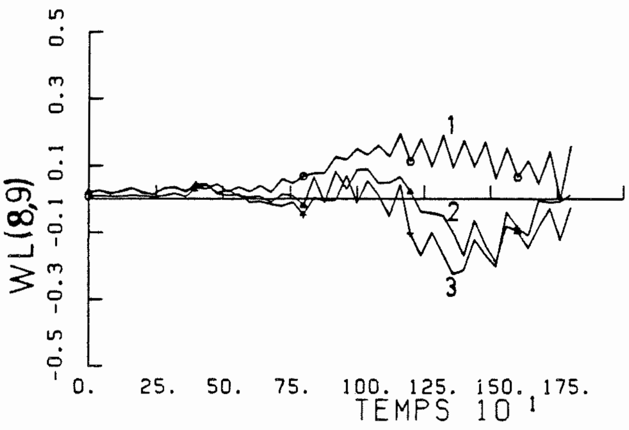

Fig. 6 : Same as fig. 5 for the vertical velocity.

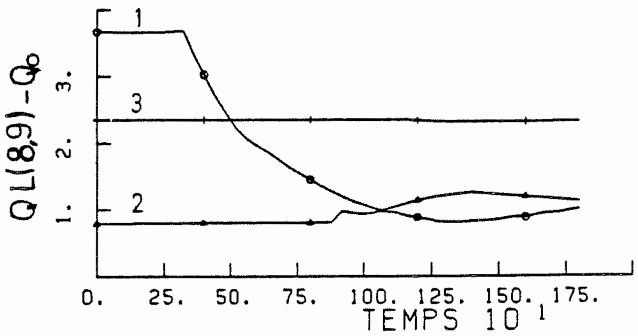

Fig. 7 : Same as Fig. 5 for the vapor water content.

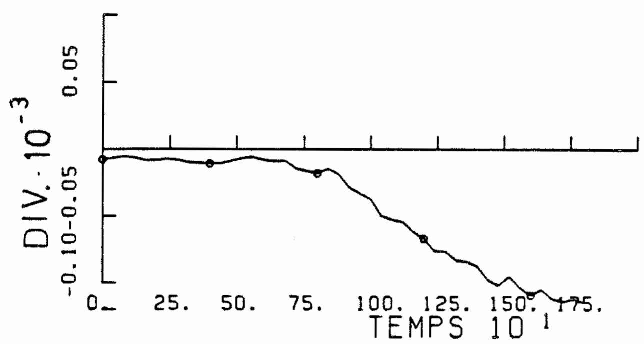

Fig. 8 : Time evolution of the horizontal wind divergence in the ground layer.

V. Conclusions

This simulation has shown that this cloud significantly modifies its environment and acts as a heat source in the layers between the ground and 5 km and between 8 km and 12 km but has a cooling effect on the layers between 5 km and 7 km and above 12 km. This heating pattern is strongly dependent upon the time evolution of the cloud parameters and some processes like precipitation are important in this respect.

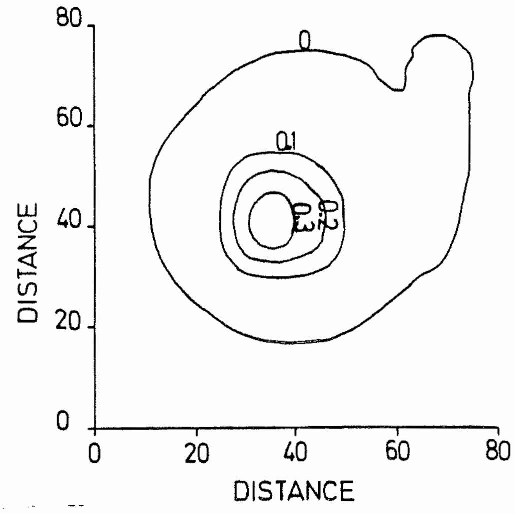

Fig. 9 : Horizontal cross section of the virtual temperature in the mesoscale domain after 1200 s of simulation for an altitude of 880 m.

VI. Acknowledgments

The author is indebted to Professor R.G. Soulage, to Doctor H. Isaka and R. Rosset for their encouragements, supports and guidance in developing the model and to Doctor Mascart and Mr. Pejoux for the graphic software.

VII. References

Anthes, R.A., 1977 : A Cumulus Parameterization Scheme Utilising a One-dimensional Cloud Model : Mon. Wea. Rev. 105, 270-286.

Holton, J.R., 1973 : A One-dimensional Cumulus Model Including Pressure Perturbation. Mon. Wea. Rev. 101, 201-205.

Kreitzberg, C.W. and Perkey, D.J. : Release of Potential Instability, Part I : A sequential Plume Model within a Hydrostatic Primitive Equation Model. J. Atmos. Sci. 33, 456-475.

Kuo, H.L., 1974 : Further Studies of the Parameterization of the Influence of Cumulus Convection on Large Scale Flow. J. Atmos. Sci. 31, 1232-1240.

Lopez, R.E., 1970 : A Parametric Model of Cumulus Convection. J. Atmos. Sci. 30, 1354-1373

Marwitz, J.D., 1972 : Trajectories within the Week Echo Regions of Hailstorms. J. Appl. Meteor. 12, 1174-1182.

Ogura, Y. and Takahashi, T., 1971 : Numerical Simulation of the Life Cycle of a Thunderstorm Cell. Mon. Wea. Rev. 99, 895-911.

Sommeria, G., 1976 : Three dimensional Simulation of Turbulent Processes in an Undisturbed Trade Wind. J. Atmos. Sci. 33, 216-241.

Tapp, M.C. and White, P.W., 1976 : A non-hydrostatic Mesoscale Model. Quart. J.R. Met. Soc. 102, 277-296.

Animated 3-D Depiction of a Summer Shower

Gary R. White and Harry C. Vaughan
Iowa State University
Ames, Iowa U.S.A.

Introduction

The application of a series of isoplethic analyses to summer showers provides some insight into the complex composition of precipitation patterns. However, it is difficult for the observer to visualize the many contributing events which build to a total area rain accumulation. In an attempt to better document the sub-cellular composition within a single rain event, a time dependent series of three-dimensional surfaces were plotted, based on real data from a symmetrical matrix of 25 rain gauges.

To provide maximum insight into the development, movement and longevity of a shower a time lapse movie of the accumulation of precipitation over a 41 km^2 area has been assembled.

Collection of Data

The data used for this study were collected over a 41 km^2 area of gently rolling farmland in central Iowa. A square matrix of 25 recording rain gauges with a linear spacing of 1.6 km was used. These gauges have a depth resolution of 0.025 mm and a time resolution of one minute. The data collected consists of summer (June, July, August) showers and thunderstorms. The gauges were serviced before and after each separate rain event. The charts were hand read and corrected for errors such as time clock and weighing mechanism inaccuracies. These results were then tabulated to give the minute-by-minute rain accumulation.

Description of Program

The computer program used to plot the rainfall data was translated from a FORTRAN version written by Steven L. Watkins (Watkins, 1974) into scientific BASIC used on Tektronix 4050 series graphics computers. This three-dimensional program has the capability of changing the viewing angle (degree of rotation), the elevation angle (above or below horizontal), and the spacing between plotted lines. A cubic spline interpolation routine (Johnson and Wiess, 1977) was developed for use with the plot program. This consisted of two steps: 1) interpolating points along each row of the rain gauge matrix and 2) interpolating along each of the columns (including interpolated points of step 1). This results in a smooth data field to be used by the three-dimensional plot program.

Each minute of rain gauge data from the 25 gauges are entered into this interpolation program by means of a 5 x 5 matrix. This program interpolates a 50 x 50 array (from the original 5 x 5 matrix) and prepares the result for storage onto magnetic tape. The three-dimensional plot program reads this interpolated array off the tape and begins the plotting process. The masking of hidden lines involved in this plot process requires that the foreground data to be plotted before data in the background.

Uses of Displays

The output of the three-dimensional plot program can be seen in Figures 1-4. These four plots represent the life cycle of the rainfall pattern from thunderstorms the morning of August 16, 1976. These thunderstorms were triggered by an approaching warm front to the west. The first figure (Figure 1) describes the rainfall accumulated as of 1132 CST (four minutes after the rain began). The reader is viewing from southeast to northwest at an elevation of 45°. The vertical scale is exaggerated, with a vertical measurement of 1 cm equalling 5.7 mm of rainfall.

In Figure 1 it appears that the most rainfall has occurred in a narrow band (2 km wide) from the west central edge of the rain gauge matrix to the north central side. The rest of the area generally has received very little or no precipitation by this time (1132 CST).

Figure 2 (1137) contains several changes that took place in the preceding five minutes. First, all areas of the matrix have received additional, more general rainfall, except for the east central and extreme west central sides which are still near zero total precipitation. It also appears that the far northwest corner has received more rain than the rest of the gauges.

Figure 3 (1203 CST) shows only two major differences from Figure 2: a) the general, matrix-wide rainfall continuing to raise the surface and b) a much higher rainfall area located at the northwest corner.

The final figure (Figure 4) represents the total accumulation for this particular rain which lasted 77 minutes, ending at 1245 CST. The only change that occurred between 1203 and 1245 was relatively uniform rainfall over the area, thereby raising the entire surface.

Conclusion

These three-dimensional figures have some interesting attributes. With these figures the small scale variability of rainfall is much easier to visualize, as in the 2 km wide band of rain seen in Figure 1. Because variability of area rainfall is a value that is difficult to document, this type of plot helps the changes in accumulation over a small area become visible.

It is hoped a time-lapse movie of a complete rain's minute-by-minute accumulation will accentuate the above mentioned qualities and show the movement associated with small scale events.

References

Johnson, L. and R. D. Wiess, 1977. Numerical Analysis, Addison Wesley Pub. Co.

Watkins, S. 1974. Masked Three-Dimensional Plot Program with Rotations, Comm. of the ACM. Vol. 17:9:520-523.

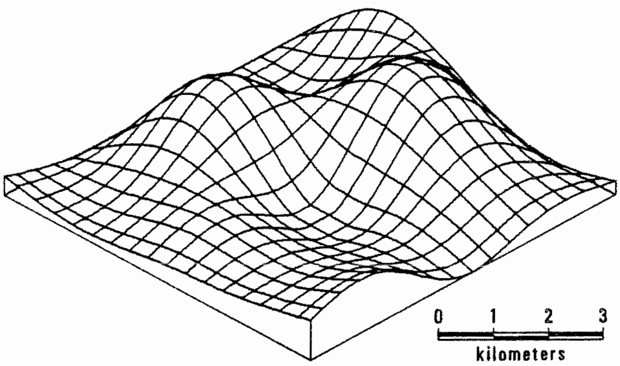

Figure 1. Three-dimensional representation of accumulated precipitation for August 16, 1976. Precipitation began at 1128 CST. This figure represents 1132 CST, viewing southeast to northwest.

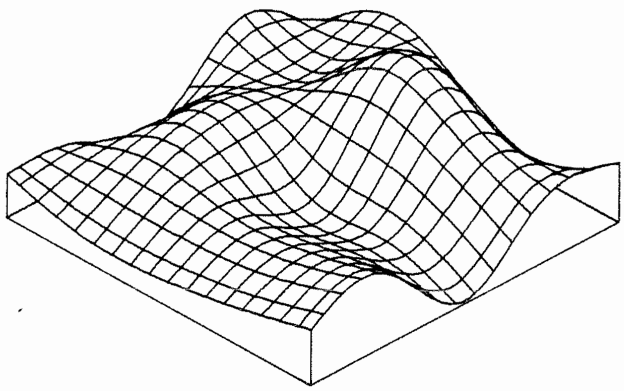

Figure 2. Three-dimensional representation of accumulated precipitation for 1137 CST August 16, 1976.

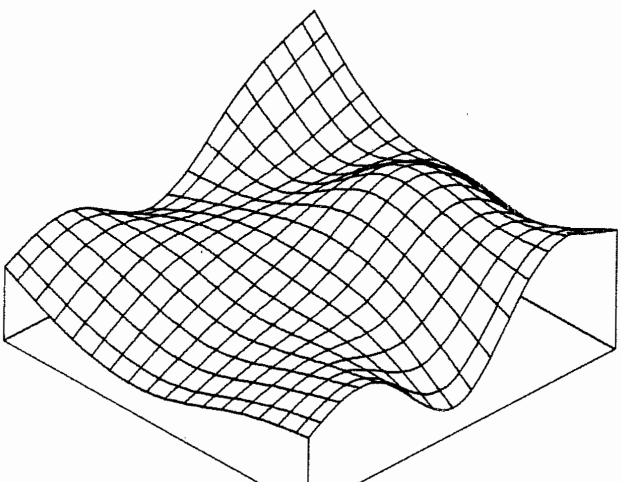

Figure 3. Three-dimensional representation of accumulated precipitation for 1203 CST August 16, 1976.

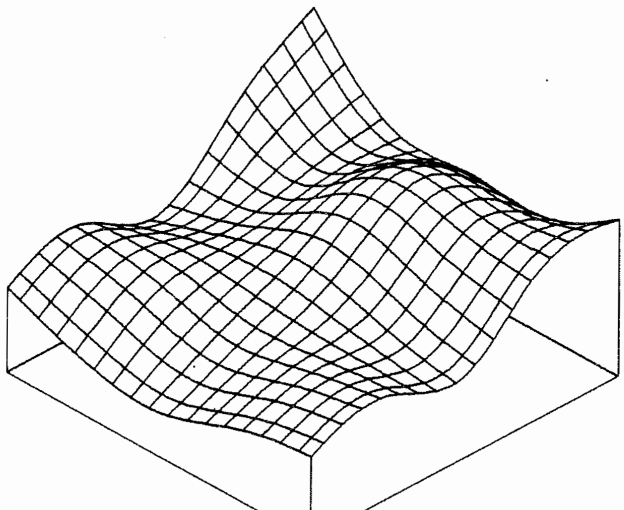

Figure 4. This figure represents the final accumulation for August 16, 1976 occurring at 1245 CST.

SESSION V : INSTRUMENTATION

Instrumentation

BACKSCATTERING OF MICROWAVES BY SPONGY ICE SPHERES

Louis J. Battan and Craig F. Bohren*

University of Arizona
Tucson, Arizona USA

1. Introduction

Radar plays a crucial role in hailstorm seeding programs in many countries. Decisions on whether or not to seed and evaluation of the result of seeding are made on the basis of radar backscatter measurements. The radar cross sections of hailstones depend on their shape, size, and composition as well as on the wavelength of the radiation. Various authors have calculated the scattering cross sections of uniform ice spheres and of ice spheres coated with a shell of water. Theoretical calculations of the radar cross sections of inhomogeneous spheres, large with respect to the wavelength, have been limited, in part because of uncertainties in specifying the dielectric properties of ice-water mixtures (sometimes called "spongy ice").

A number of authors starting with Ryde (1946) have used an expression derived by Debye (1929) to calculate the refractive indices of mixtures of ice with air or with water. Battan and Herman (1962) having obtained the refractive indices in this way, calculated scattering cross sections of spheres composed of spongy ice and of spheres having a core of ice surrounded with shells of spongy ice. Subsequently, Atlas, Hardy, and Joss (1946) found that the latter calculations did not correlate at all with measurements of the backscattering from ice spheres having spongy ice shells. Instead, as shown in Fig. 1 the measurements corresponded quite well with the backscattering from ice spheres having water shells containing the same amount of water as was contained in the spongy ice. These results verified early concerns that the Debye formulation was not appropriate for calculating the refractive indices of ice-water mixtures.

2. Dielectric function of mixtures

In a recent paper, Bohren and Battan (1980) have discussed several other formulas for calculating the dielectric function (or refractive index) of a mixture of two substances, when the subunits of the mixture are small with respect to the wavelength. This report is largely a condensed version of the Bohren-Battan paper.

Maxwell Garnet (1904), treating the mixture as spherical inclusions embedded in a homogeneous matrix, derived the following expression:

$$\varepsilon_{MG} = \varepsilon_m \left[1 + \frac{3f\left(\dfrac{\varepsilon - \varepsilon_m}{\varepsilon + 2\varepsilon_m}\right)}{1 - f\left(\dfrac{\varepsilon - \varepsilon_m}{\varepsilon + 2\varepsilon_m}\right)} \right], \quad (1)$$

where ε_{MG}, ε and ε_m are the dielectric functions of the mixture, of the inclusions and of the matrix, respectively. The factor f is the volume fraction of the inclusions. It is easily seen that the values of ε_{MG} of an ice-water mixture depend on whether ice is the inclusion or the matrix.

Another formula for calculating the dielectric function of a mixture, called the effective-medium dielectric function, was first derived by Bruggeman (1935):

$$f\left(\frac{\varepsilon - \varepsilon_{EM}}{\varepsilon + 2\varepsilon_{EM}}\right) + (1 - f)\left(\frac{\varepsilon_m - \varepsilon_{EM}}{\varepsilon_m + 2\varepsilon_{EM}}\right) = 0. \quad (2)$$

These can be compared with Debye's (1929) function:

$$\frac{\varepsilon_D - 1}{\varepsilon_D + 2} = f\left(\frac{\varepsilon - 1}{\varepsilon + 2}\right) + (1 - f)\left(\frac{\varepsilon_m - 1}{\varepsilon_m + 2}\right). \quad (3)$$

Bohren and Battan (1980) show that if the values of ε of the two components of a mixture are not too different,

*Present affiliation of Craig F. Bohren is Department of Meteorology, The Pennsylvania State University, University Park, Pennsylvania USA.

any one of the three equations above give about the same results. This is the case when air ($\varepsilon \approx 1$) and ice ($\varepsilon \approx 3$) are mixed to give low density ice.

When the components of a mixture have dielectric functions that differ appreciably, the three equations can yield very large differences. This is the case for mixtures of water ($\varepsilon \approx 80$) and ice ($\varepsilon \approx 3$) as shown in Fig. 2.

3. Backscattering cross sections

Calculations have been made of the radar cross sections of ice spheres having overall diameters of 2 cm and composed of ice cores with shells of spongy ice. Figure 3 shows that the values of refractive index yielded by the Maxwell-Garnet function for ice inclusions in a water matrix yield backscattering cross sections in good agreement with the measurements shown in Fig. 1. It was found, but not shown here, that the correspondence between theory and measurements is poor when the refractive index is calculated for a mixture with water in an ice matrix.

Figure 4 shows, as would have been anticipated from Fig. 2 that when f, the fraction of water, is high, the refractive indices obtained by the effective-medium function yield backscattering cross sections in good agreement with the measurements. The correspondence changes markedly as f decreases.

At first glance, it appears to be more reasonable to assume that spongy ice more nearly resembles water in an ice matrix. Nevertheless in view of the results to date, we would be inclined to use the Maxwell-Garnet equation with ice in a water mixture to calculate the refractive indices of ice-water mixtures. Future research should help resolve some of the existing uncertainities.

4. References

Atlas, D., K. R. Hardy, and J. Joss, 1964: Radar reflectivity of storms containing spongy hail. *J. Geophys. Res.*, 69, 1955-1961.

Battan, L. J. and B. M. Herman, 1962: The radar cross sections of 'spongy' ice spheres. *J. Geophys. Res.*, 67, 5139-5145.

Bohren, C. F. and L. J. Battan, 1980: Radar backscattering by inhomogeneous precipitation particles. Submitted to *Journal of Atmospheric Sciences*.

Bruggeman, D. A. G., 1935: Berechnung verschiedener physikalischer Konstanten von heterogenen Substanzen. I. Dielektriztätskonstanten und Leitfähigkeiten der Mischkörper aus isotropen Substanzen. *Ann. Phys.* (Leipzig), 24, 636-679.

Debye, P., 1929: *Polar Molecules*. The Chemical Catalog Company, New York.

Maxwell Garnet, J. C., 1904: Colors in metal glasses and in metallic films. *Phil. Trans. Roy. Soc.*, A203, 385-420.

Ryde, J. W., 1946: The attenuation and radar echoes produced at centimeter wavelengths by various meteorological phenomena. *Meteor. Factors in Radio Wave Prop.*, Physical Soc., London, 169-188.

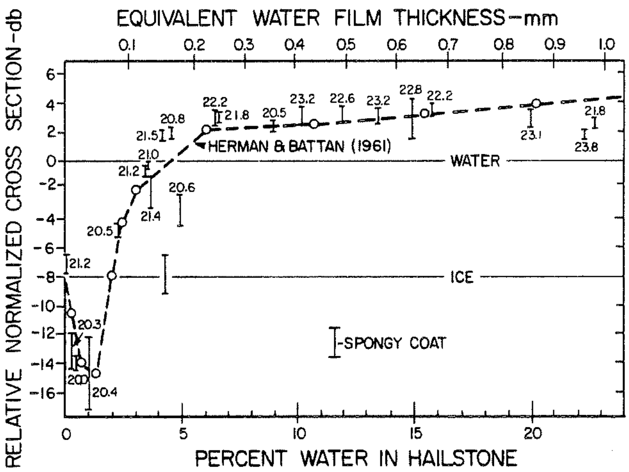

Fig. 1 Normalized backscattering cross sections (in decibels) of ice spheres (diameters in mm given by numerals) obtained at 5.05 cm wavelength. The spheres were composed of solid ice cores and having outer shells of spongy ice between 0.4 and 2 mm thick and various water contents. The upper abscissa is the thickness of a water shell of the same water mass as in the ice-water shell. Each vertical line represents the range of measurements as each sphere was rotated. The all-water and all-ice values are shown as horizontal lines, taking the former at 0 db. From Atlas, Hardy, and Joss (1964).

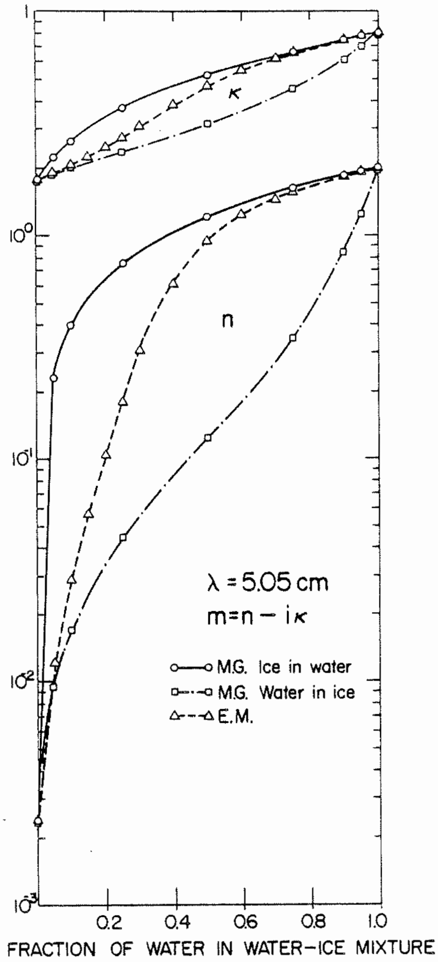

Fig. 2 Calculations of refractive index $m = n - i\kappa$ from the Maxwell-Garnet (MG) and the effective-medium (EM) dielectric functions.

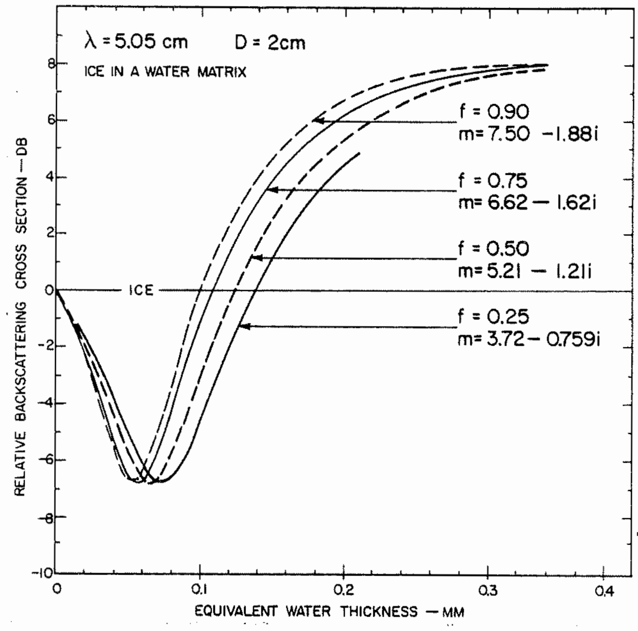

Fig. 3 Calculated normalized backscattering cross sections of spheres (in decibels with respect to the cross sections of all-ice spheres) composed of solid ice cores with shells of spongy ice. The fraction of water in the mixture is given by f. The refractive indices were obtained by means of the Maxwell-Garnet function for water included in an ice matrix.

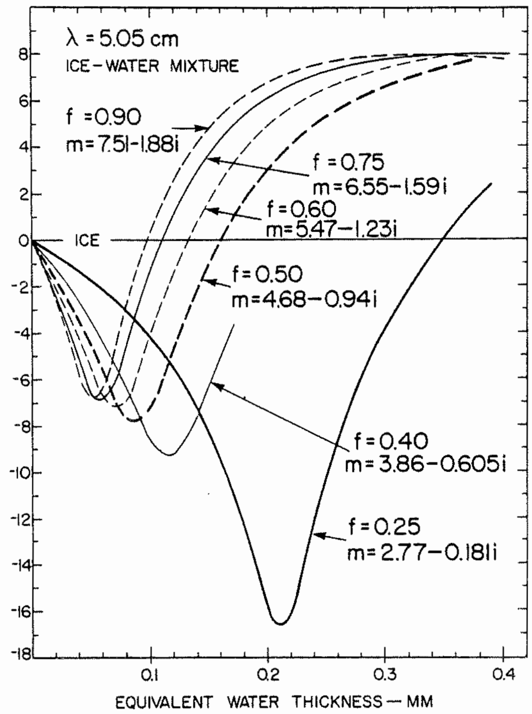

Fig. 4 Same as Fig. 3 except that the refractive indices were obtained by means of the effective-medium function.

ACCURACY AND LIMITATION OF SOME CLOUD PHYSICS PROBES

J.L. Brenguier, J.F. Gayet, P. Personne, J.P. Pinty, Y. Pointin, D. Rousset

L.A.M.P., University of Clermont II, France

I. Introduction

These last few years, the LAMP has been using several probes in order to determine the microphysical characteristics of natural (airborne measurements) and artificial (wind tunnel measurements) clouds. These probes have been tested in laboratory in order to know their range of suitability and their respective limitations. However, it is not easy to reproduce in laboratory the natural conditions of the airborne measurements, especially the relative speed of the particles (100 m/s), neither to know the spectral characteristics of the droplet distribution with enough accuracy. Therefore, we have studied these probes "a posteriori" by comparing their respective measurements in the very different kinds of clouds studied during several experimental programs of the LAMP. An example of such comparisons concerning the small droplets liquid water content is given here mainly based on measurements made during the PEP 79 experiment.

II. Microphysical probes

a) Measurement of the droplet spectra

- The FSSP probe of Particle Measuring System (Knollenberg, 1976) is based on the measurement of the light intensity of the laser beam scattered by each droplet. All the droplets having a diameter between 3 μm and 45 μm are sized and counted into 15 classes of 3 μm width every 1 s by the electronic circuitry. The liquid water content is computed over the spectrum using the following relation :

$$LWC_F = \frac{\Pi}{6} \sum_{i=1}^{15} \rho Ni\ Di^3 \ / \ (V.A.T.)$$

where Ni is the number of droplets in the ith class of mean diameter Di, V the relative velocity of particles and T is the sampling time. The edge effect rejection circuitry and the depth of field limitation give a sampling area A of 0.35 mm^2.

b) Direct measurement of the liquid water content (LWC)

- The Johnson-Williams probe of Bacharach Instrument Company (sampling area ≃ 10 mm^2). It is based on the measurement of the power dissipated by a hot wire impacted by the droplets under a constant intensity current. The liquid water content is computed from the variation of the wire resistance (Spyers - Duran, 1968).

c) Measurement of the total water content (TWC)

- The Ruskin probe of General Eastern Corp. (sampling area = 75 mm^2) is based on the measurement of the attenuation of the Lyman-α ray by water vapor after evaporation of the droplets and ice crystals by heated grids. The liquid water content can be estimated by substracting the water vapor content deduced from the dew point temperature.

III. Response of the Probes

a) Dynamical response of the probes

Fig 1 shows two ratios of power spectra of water content deduced from the measurements of the different probes made during a 20 mn flight in a stratocumulus layer. The upper curve is relative to the FSSP liquid water content compared to the Ruskin total water content and shows that the Ruskin cut-off frequency is at least equal to the FSSP's one (5 Hz). The lower curve is relative to the JW liquid water content. It shows that the JW probe has a cut-off frequency close to 0.4 Hz above which the signal has an attenuation of 20 dB per decade. This is further corroborated by the curve on Fig. 2 where the phase angle of the cross power spectrum of the JW liquid water content and of the Ruskin total water content is drawn and which show that a phase lag of 45° is reached

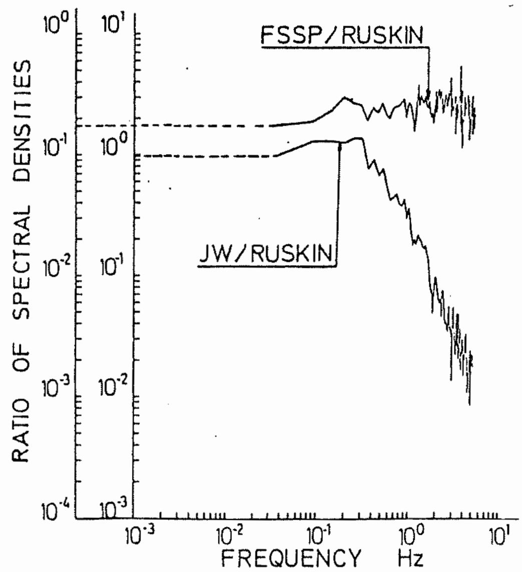

Fig. 1 : Ratios of the power spectra of the water content as functions of frequency

at the cut-off frequency and which implies that the JW can be compared to a first order filter.

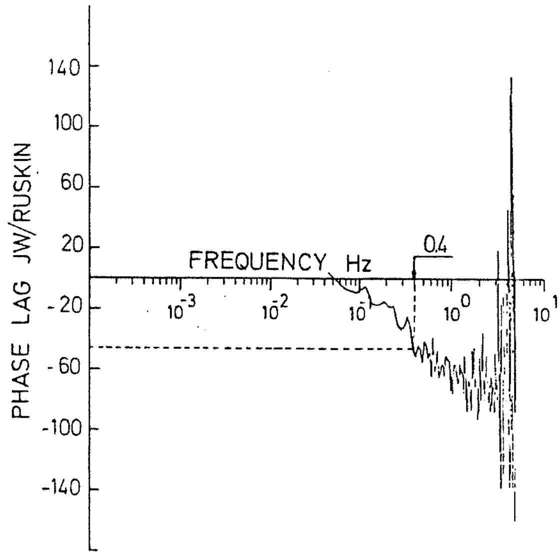

Fig. 2 : Phase lag of the power spectra ratio of the JW LWC to the Ruskin TWC.

b) Amplitude response of the probes

- Fig. 3a and b show the Ruskin total water content as a function of the Johnson-Williams and of the FSSP liquid water content respectively. Each dot corresponds to a one second (∿ 100 m) averaged value during a constant level flight (700 mb, - 10°C) in a stratocumulus cloud (PEP experiment). The points corresponding to a liquid water content greater than 0.05 g/m^3 are distributed along a line which has a slope of 0.82 on fig 3a and a slope of 1.66 on fig 3 b. The intersection values of these lines with the y-axis are close to the water vapor content computed from the dew point temperature (2.4 g/m^3). These figures reveal that the JW and Ruskin estimations of the liquid water content are equivalent whereas the FSSP values are underestimated by as much as 40 %.

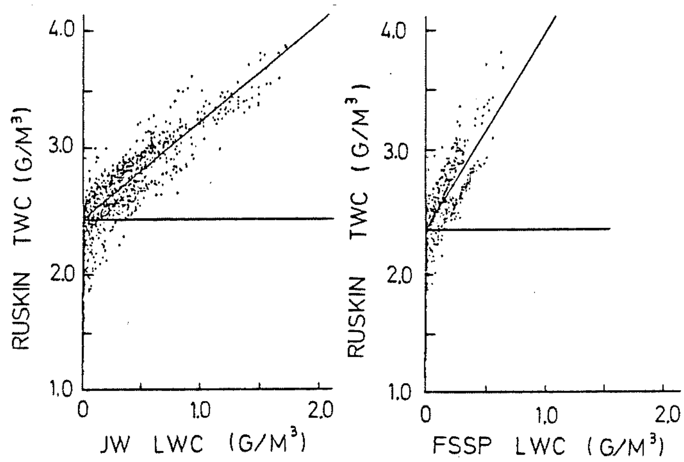

Fig. 3a *Fig. 3b*

Fig. 3 : One second averaged values of the Ruskin TWC as a function of the corresponding one-second averaged values of (a) the JW LWC and (b) the FSSP LWC.

IV. Analysis of the comparison

a) The Cooper Formulation

The previous part has shown that the JW probe gives a good estimate of the liquid water content in steady state measurements but has a time lag of 2.5 s in transient measurements. In order to refine the amplitude comparison, the Ruskin and FSSP values recorded every .1 s have been smoothed by a recursive first order filter ($\overline{Yn}$ = .2 Yn + 0.8 $\overline{Yn-1}$) and averaged over 1 s in order to be compared to the 1 s averaged JW values. Figs. 4a and 4 b give an example of the FSSP LWC as a function of the JW LWC during a stratocumulus cloud penetration in a layer near 700 mb, - 10 C without and with smoothing of the FSSP values respectively showing that the dispersion is reduced by the filtering of the FSSP values.

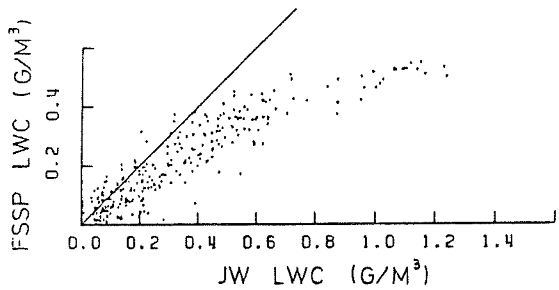

Fig. 4 a

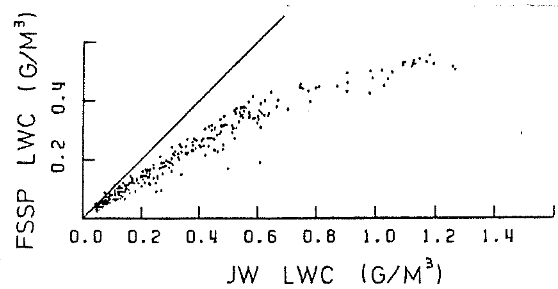

Fig. 4 b

Fig. 4 : Same as Fig. 3 for (a) the unsmoothed and (b) the time-filtered FSSP LWC as a function of the JW LWC.

The dots on Fig. 4b are distributed along a curve which has been described analytically by Cooper (Breed, 1978) under the relation

(1) $Nm = No \exp(-\Lambda\, No)$

where No is the true number of particles per unit volume and Nm is the corresponding number measured by the FSSP. This relation is a consequence of the electronic behaviour of the probe. Any droplet crossing the laser beam and scattering enough light triggers a one shot circuitry which stays active during the time τ = 16 µs and which prevents any subsequent particle to be counted if it crosses the beam during this time. If the mean time lag between droplets is less than τ, only the first one is counted. This implies that the measured concentration reaches a maximum value and then decreases as the real concentration increases. In this above relation, the coefficient $\Lambda = V.\tau.d.L$ is the reciprocal of the true concentration for which the measured concentration is maximum ; V is the air speed, τ the time lag, d the beam width and L the beam length along which a droplet gives a high enough scattered light. $\frac{Nm}{No}$ represents the probability that a drop is counted by the FSSP probe and is independent of the radius. Assuming that the JW gives a reasonable estimate of the smoothed liquid water content, this probability is equal to FS/JW where FS represents the smoothed liquid water content deduced from the droplet spectrum measured by the FSSP probe and JW the liquid water content measured by the JW probe. The above relation can be written :

$$(2) \qquad FS \ln(FS/JW) = - \Lambda \; JW \; Nm$$

and is illustrated by Fig. 5 where the left hand side is drawn as a function of the product $JW.Nm.V.d.\tau$ every second during several cloud penetrations. The slope of the regression line gives an estimate of the effective beam length L = 4.6 mm leading to a coefficient Λ =1.5 10-3

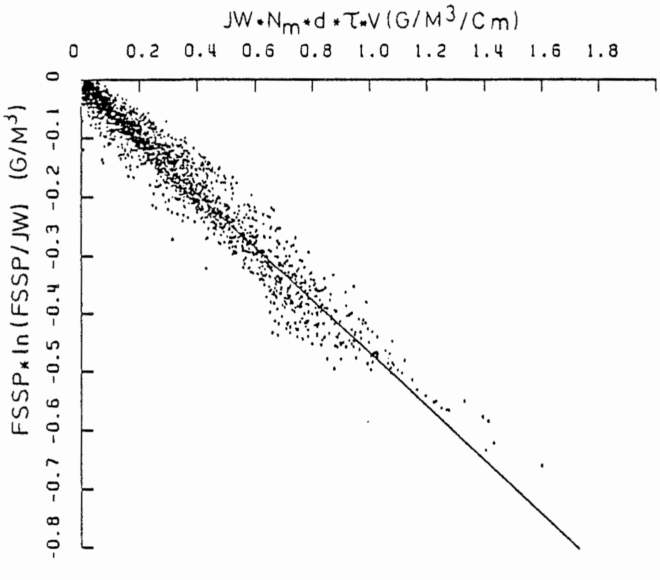

Fig. 5 : The left hand side of Eq. 2 as a function of the right hand side divided by L.

This value of L is greater than the depth of field of the probe (2.85 mm) in which a particle is effectively counted into one of the 15 classes. Fig. 5 shows that the formulation proposed by Cooper is suitable.

However, some penetrations give dots which are significantly away from the Cooper curve as shown in Fig. 4b. Two different behaviours, which are strongly inconsistent with the above relation are observed. On the one hand, Nm measured by the FSSP can be greater than the JW value, as for example during flight 9 in a cumulus congestus cloud. On the other hand, Nm measured by the FSSP can be much larger ($Nm > 400\ cm^{-3}$) than the maximum value allowed by equation 1, namely $(\Lambda\ e)^{-1}$ = 245 cm-3 with the adjusted value of Λ, as for example during flight 10 in a stratocumulus cloud.

b) Underestimation of the JW probe for the large droplets

One explanation of the first behaviour may be found in the fact that, as shown on Fig. 6, the JW liquid water content is also underestimated with respect to the Ruskin values for the same flight in a cumulus cloud (compare with Fig. 3a). This suggests that the JW probe cannot properly take into account the water content of the larger droplets.

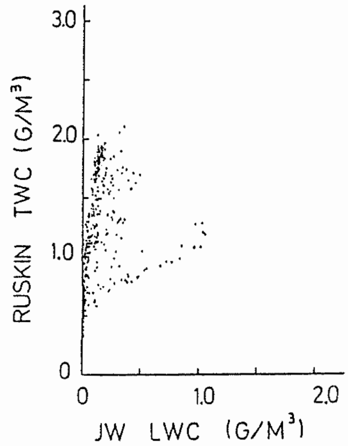

Fig. 6 : Same as Fig. 3a during a cumulus penetration in flight 9.

For a cumulus cloud penetration at the level 620 mb, - 20 C, the JW liquid water content is compared to the FSSP values computed by integration over the whole droplet spectra (3.5 µm < D < 45 µm) on Fig. 7a and to the FSSP values computed by integration over the nine first classes on Fig. 7b (3.5 µm < D < 30 µm). The cut-off value of 30 µm has been roughly adjusted in order to decrease the dispersion.

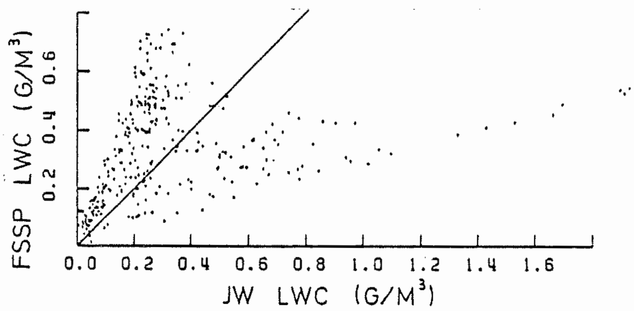

Fig. 7 a

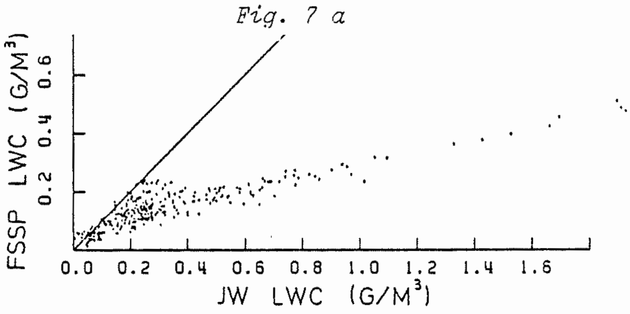

Fig. 7 b

Fig. 7 : Same as Fig. 4b during a cumulus penetration in flight 9 for the FSSP LWC computed over (a) the whole spectrum (3.5 µm < D < 45 µm), (b) the first nine classes (3.5 µm < D < 30 µm).

The comparison between these two graphs shows that some dots are unaffected by the spectra truncation while others which were away from the Cooper curve on Fig 7a have been brought closer to this curve on Fig. 7b. This implies clearly that the JW probe underestimates strongly the water content of the droplets with a diameter greater than 30 µm. It remains to estimate how the attenuation depends upon the diameter of the droplet and upon the water phase (ice or liquid).

c) Diameter dependence of Λ

In this discussion of Cooper formula (1), L was the beam length along which a droplet gives a threshold level of scattered light. The laser beam is focussed by optical lenses and the scattered light intensity decreases as the distance x between the droplet and the focus plane increases. The scattered intensity behaves like :

$$i \simeq A\, D^2\, e^{-x^2/L_o^2} \quad \text{(Gayet, 1976)}$$

The beam length inside which a particle of diameter D gives a scattered intensity greater than the threshold value depends upon the diameter as :

$$(3)\quad L(D) = 2\, Lo \sqrt{2 \ln D + B}$$

This implies that, amongst the droplets outside the depth of field, large droplets have a higher probability to trigger the electronic circuitry than smaller ones, leading the FSSP to count a smaller number of droplets when large droplets are present. Taking into account the probability that a particle crossing the beam has a diameter D and assuming that the time lag between subsequent particles has an exponential distribution, the following formula can be derived

$$(4)\quad Nm = No \exp\left(- \sum_i \Lambda i\ Ni\right)$$

where Ni is the true particle concentration in class i, $No = \Sigma\, Ni$ is the total particle concentration, $\Lambda i = V d\tau\ L(Di)\ d$ and Nm is the total particle concentration measured by the FSSP. This formulation explains the second inconsistent behaviour previously discussed namely that a high concentration can be observed ($Nm \simeq 500\ cm^{-3}$) in cloud containing only small particles. Preliminary results clearly indicate that the Λ coefficient of the Cooper formula (1) depends upon the spectrum shape as suggested by equation (4) and that the deviations of the instantaneous measures from the equation (4) is smaller that the deviations from equation (1).

V. Conclusions

The Ruskin probe has a cut-off frequency greater than 5 Hz and gives a good estimate of the total water content but without a fast response probe measuring the vapor water content, one cannot deduce the LWC with a good accuracy. The JW probe has a frequency cut-off at around 0.4 Hz and measures only the small droplets (D < 30 µm) water content. The FSSP probe undercounts the particles in a ratio which depends on the total concentration and on the distribution shape.

A formula has been suggested which can give a better estimate of the real spectrum from the measured spectrum.

References

Breed, D.W., 1978 : "Case studies on convective storms : 22 June 1976 : First Echo Case, NCAR, Technical note, NCAR/TN - 130 + STR.

Gayet, J.F., 1976 : "Sur les Performances de l'ASSP-100 de Knollenberg pour la granulométrie des nuages, J. Rech. Atmos., 2, pp. 105-118.

Knollenberg, R.G., 1976 : "Three new instruments for Cloud Physics Measurements : The 2-D Spectrometer, the Forward Scattering Spectrometer Probe, and the Active Scattering Aerosol Spectrometer. Preprint volume, International Conference on Cloud Physics, July 26-30 30 1976, Boulder, Colo.

Spyers-Duran, P.A., 1958 : "Comparative Measurements of Cloud Liquid Water using Heated Wire and Cloud Repricating Devices, J. Appl. Meteor., 3, pp. 450-460.

APPLICATIONS OF THE DIFFERENTIAL REFLECTIVITY RADAR TECHNIQUE IN CLOUD PHYSICS

V. N. Bringi and T. A. Seliga

Atmospheric Sciences Program and Department of Electrical Engineering
The Ohio State University
Columbus, Ohio, U.S.A.

Introduction

The shapes of falling hydrometeors in the atmosphere are usually nonspherical resulting in polarization dependent backscattering properties of distributions of such scatterers. In particular, raindrops tend to be oblate spheroidal in shape and fall with their symmetry axis nearly vertical. The combined effect of nonsphericity and preferred orientation of raindrops forms the basis of the Differential Reflectivity (Z_{DR}) radar technique for rainfall measurement. Z_{DR}(dB) is defined as $10\log(Z_H/Z_V)$ where $Z_{H,V}$(mm^6m^{-3}) are the radar reflectivity factors at horizontal (H) and vertical (V) polarizations, respectively. Z_{DR} in rain typically ranges between 0 - 5dB and can be measured very accurately [Bringi et al., 1978, 1980]. Seliga and Bringi (1976) first demonstrated that improved estimates of rainfall rate could be obtained by combining measurements of Z_H and Z_{DR} over conventional Z-R relationships. Experiments performed using the University of Chicago and Illinois State Water Survey (CHILL) radar and the Chilbolton radar operated by the Rutherford and Appleton Laboratories have demonstrated the usefulness of this technique in radar meteorology [Seliga et al. (1979, 1980a,b), Bringi et al. (1978, 1980), and Cherry et al. (1979, 1980)]. This paper outlines the theory and reviews some of the results of experiments performed using the CHILL radar, and cites possible applications of this remote measurement capability in cloud physics research.

Theory

Raindrops are assumed to be distributed exponentially with parameters N_o and λ such that

$$N(D_e) = N_o \exp(-\lambda D_e) \qquad 0 < D_e \leq D_m \qquad (1)$$

where D_e is the equivalent spherical diameter of the assumed oblate spheroidal drop and D_m is the maximum expected drop size. We define D_o as the median volume diameter corresponding to the distribution $N(D_e)$ in (1) so that $D_o = 3.67/\lambda$ for $D_o << D_m$.

Z_{DR}(dB) is defined as $10\log(Z_H/Z_V)$ where $Z_{H,V}$ is given by

$$Z_{H,V} = \frac{\lambda^4}{\pi^5|K|^2}\int_0^{D_m} \sigma_{H,V}(D_e)\, N(D_e)\, dD_e \qquad (2)$$

where λ is the radar wavelength, $|K|^2 = |(m^2-1)/(m^2+2)|$, m is the refractive index of water and $\sigma_{H,V}$ are the radar cross sections of the oblate spheroidal raindrops at horizontal (aligned along the major axis) and vertical (aligned along the minor axis) polarizations, respectively. From (1) and (2) it is clear that Z_{DR} is a function of D_o or λ. These functional relationships are given in Figure 1, assuming D_m = 0.8cm. Hence, by combining measurements of Z_{DR} and Z_H it should be possible to estimate N_o and λ and, hence, rainfall rate (R) or water content (W).

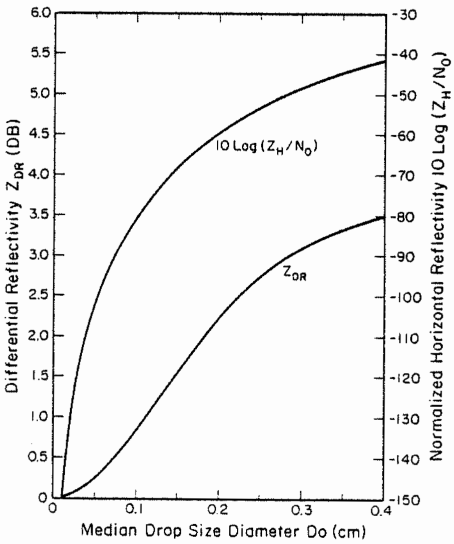

Fig. 1. Variations of Z_{DR} and normalized horizontal reflectivity $10\log(Z_H/N_o)$ with D_o.

Experimental Results

As an example of the use of the Z_{DR} technique in the accurate measurement of rainfall rate, we compare radar derived rates with disdrometer derived rates at the surface. Details of the experiment which used the CHILL radar located near Chicago are given in Seliga et al. (1980b). A disdrometer was operating at the radar site automatically measuring the raindrop size spectra at 30s intervals. Simultaneously, the radar operated in an RHI mode in the direction of the approaching storm. This enabled us to compare radar-derived, range-dependent rainfall rates obtained at the lowest elevation angles of the RHI scan with the disdrometer results translated from a time to a range dependency by assuming the storm approached the radar at a speed of 11mph. This comparison is meaningful only if the storm can be assumed to be in steady state between the times of the radar and disdrometer measurements; the radar scan which preceded the results given here by 4m produced a similar rainfall rate profile, thus supporting this assumption. Figure 2 gives Z_H

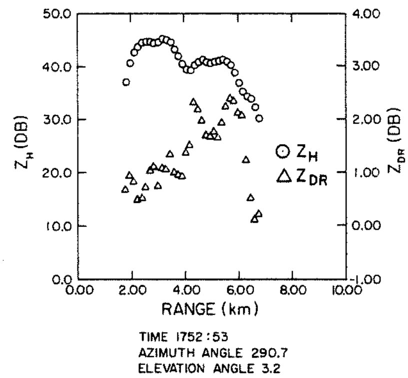

Figure 2. Z_{DR} and Z_H as a function of range.

and Z_{DR} as a function of range along the radar beam just before the storm reached the radar site. These values were used to calculate (N_o, D_o) and, hence, rainfall rate as outlined in the previous section. The radar-derived rainfall rate is shown in Figure 3 along with the disdrometer results. The comparison is remarkably good, including the overall shape of the curves, the magnitude of the maximum rainrate (~150mm hr^{-1}) at range 3km and the secondary maximum (~10 mm hr^{-1}) at range 5km.

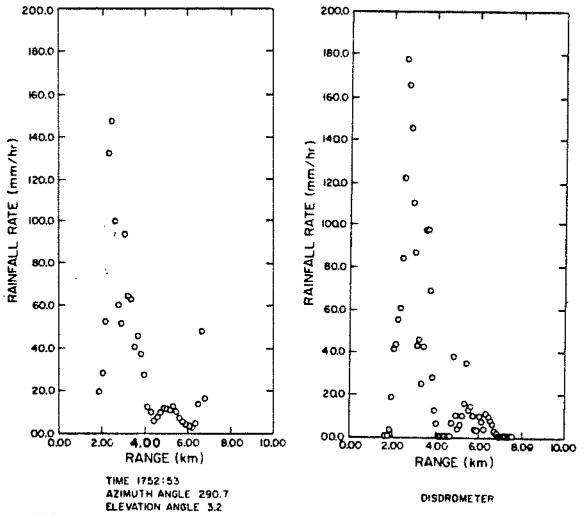

(a) (b)

Figure 3. Comparison of radar and disdrometer rainfall rates.

The Z_{DR} technique in rain can be used to estimate the parameters N_o and D_o as well as rainfall rate as shown in Figures 4 - 8. Figures 4 and 5 depict profiles of Z_H and Z_{DR} as a function of range along the radar beam at an elevation of 0.5^o using the CHILL radar located in Oklahoma. The derived values of D_o, N_o and rainfall rate are shown in Figures 5, 6 and 7, respectively. Note the wide variability in the values of N_o and D_o clearly showing the inapplicability of the constant Marshall-Palmer (1948) value of N_o = 80,000 m^{-3}cm^{-1}. These profiles illustrate the type of data available using scanning radars equipped to measure Z_{DR} and Z_H as opposed to measuring reflectivity alone.

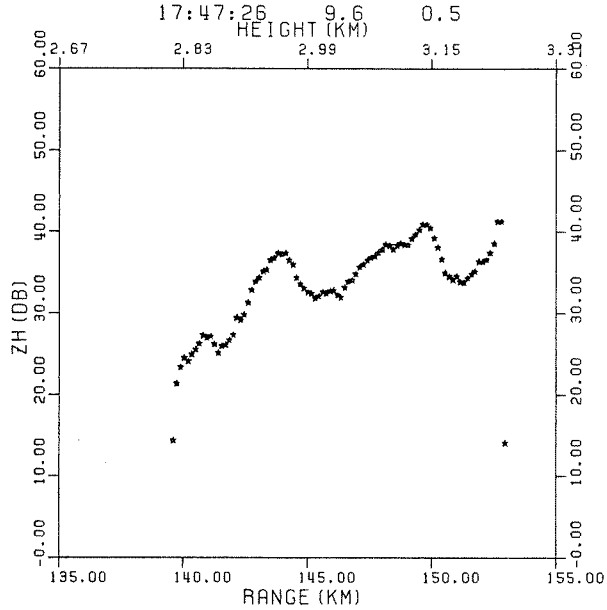

Figure 4. Z_H versus radar range.

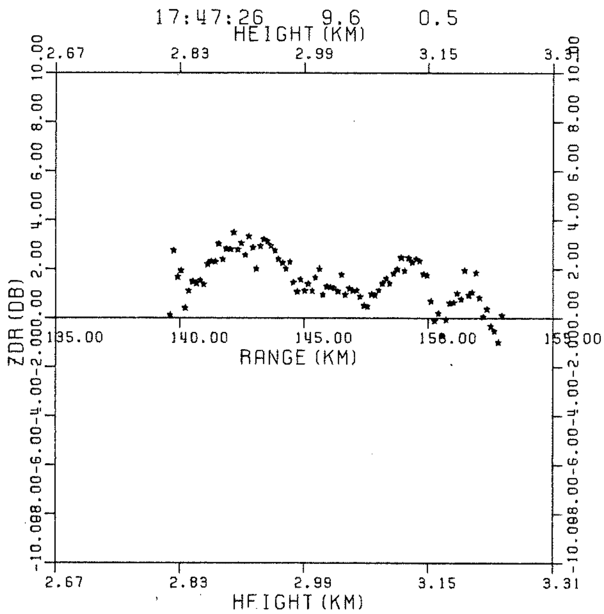

Figure 5. Z_{DR} versus radar range.

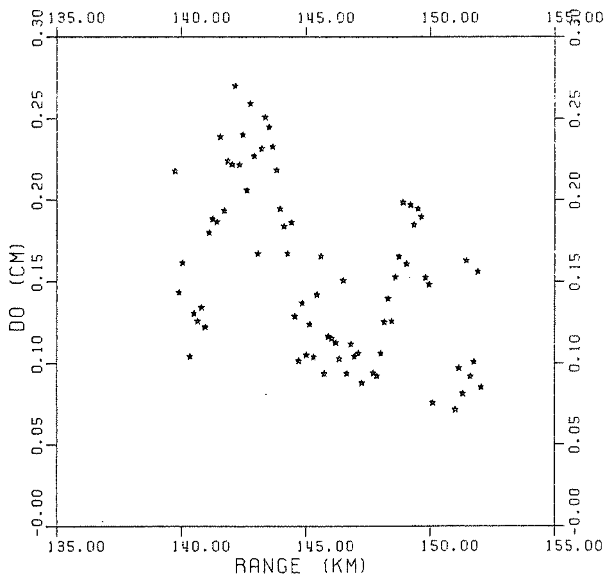

Figure 6. Radar-derived values of D_o corresponding to Z_{DR} in Fig. 5.

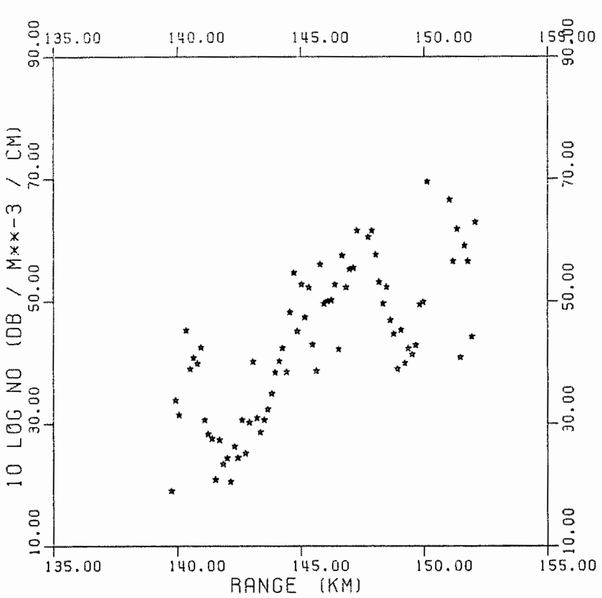

Figure 7. Radar derived values of N_o corresponding to Z_H and Z_{DR} profile of Figs. 4 and 5.

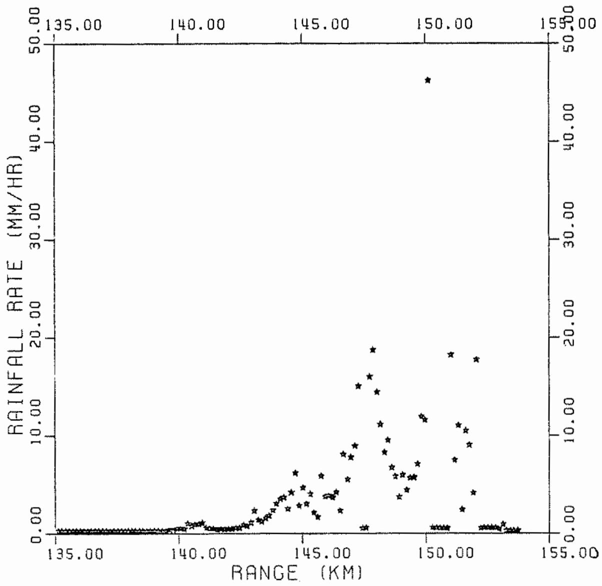

Figure 8. Radar derived rainfall rates computed from (D_o, N_o) profiles of Figs. 6 and 7.

The accurate estimate of spatial and time averaged rainfall rate is an important objective in cloud physics. We review rainfall rate measurements obtained with the CHILL radar operating near Chicago for comparison with a dense raingauge network. Experimental details can be found in Seliga et al. (1980a). Figure 9 shows the location of the radar site and the raingauge network. Also shown are subareas S_{1i} and S_{2i}, i = 1,7, and areas S_1 and S_2 (~550 km^2) over which areal rainfall rate estimates are obtained over a period of about 1 hr. Table 1 gives comparative statistics of radar derived rainfall rate and raingauge (R_G) derived rainfall rates using the subareas S_{1i}, S_{2i}, i = 1,7. Radar derived rainfall rates were obtained using the Z_{DR} technique, R_{ZDR}, the Z-R relationship, R_{ZR}, and a calibrated Z-R relationship, R^C_{ZR}. Note the excellent agreement between the Z_{DR} technique and the raingauge network including substantially lower values of the average difference between the two estimates as opposed to using either average Z-R ($Z = 486R^{1.37}$) or calibrated Z-R relationships ($Z = 187R^{1.27}$).

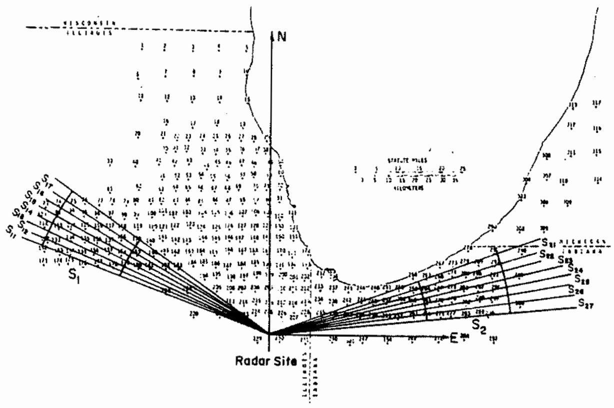

Figure 9. Radar and raingauge locations near Chicago and areas S_1 and S_2 (see Table 1).

TABLE 1

Comparative Statistics of Rainfall Data

Ratio Estimates	S_1	S_2	Average
$\langle R_{ZDR}\rangle / \langle R_G\rangle$	0.86	1.17	1.02
$\langle R^C_{ZR}\rangle / \langle R_G\rangle$	1.36	1.33	1.35
$\langle R_{ZR}\rangle / \langle R_G\rangle$	0.57	0.66	0.62
$\langle R_{ZDR}/R_G\rangle$	0.77	1.16	0.965
$\langle R^C_{ZR}/R_G\rangle$	1.28	1.37	1.32
$\langle R_{ZR}/R_G\rangle$	0.52	0.64	0.58
Average difference*			
$R_i = R_{ZDRi}$	24%	20%	22%
$R_i = R^C_{ZRi}$	40%	43%	41.8%
$R_i = R_{ZRi}$	56%	38%	47%
Fractional Standard Deviation**			
$R = R_{ZDR}$	20%	11.5%	15.8%
$R = R^C_{ZR}$	26%	12.5%	19.3%
$R = R_{ZR}$	24.8%	14%	19.4%

* $\frac{1}{N}\sum_{i=1}^{N}\frac{|R_{G_i} - R_i|}{R_{G_i}}$ N = 7

** FSD = Standard Deviation of $(R/R_G)/\langle R/R_G\rangle$ where $R = R_{ZDR}$, R^C_{ZR} or R_{ZR}.

Conclusions

The Z_{DR} technique appears to be an important radar measurement in cloud physics research. The experimental results reviewed here have shown that this technique can yield (a) accurate, high resolution rainfall rate estimates below cloud base, (b) spatial and temporal variations of (N_o, D_o) of an assumed exponential drop size distribution, and (c) accurate areal estimates of rainfall. In addition, the Z_{DR} signature has been found (Cherry et al., 1979) to discriminate uniquely between water and ice phase hydrometeors due to the differences in the polarization dependent backscattering properties of distributions of such scatterers.

Acknowledgments

This research was supported by the Atmospheric Research Section, National Science Foundation, under Grant Numbers ATM-7683648 and ATM-7908666. The CHILL radar was provided by the Illinois State Water Survey (ISWS), and the disdrometer system by the Air Force Geophysics Laboratory, Hanscom Air Force Base, Massachusetts. We are particularly grateful to Dr. E. A. Mueller for his assistance and expertise in operating the radar.

References

Bringi, V. N., S. M. Cherry, M. P. M. Hall and T. A. Seliga, 1978: A new accuracy in determining rainfall rates and attenuation due to rain by means of dual-polarization radar measurements. *IEE Conf. Proc., No. 169, Part II, Antennas and Propagation,* London, England, 28-30 November, 120-124.

Bringi, V. N., T. A. Seliga and M. G. SriRam, 1980: Statistical characteristics of the differential reflectivity radar signal. *Preprints 19th AMS Conf. on Radar Meteor.,* 15-18 April, Miami Beach, Florida.

Cherry, S. M., J. W. F. Goddard, M. P. M. Hall and G. R. Kennedy, 1979: Measurement of raindrop size distributions using dual polarization radar. *Proc. 5th Int'l. Conf. on Erosion by Solid and Liquid Impact,* Cambridge, England, 3-6 September.

Cherry, S. M., J. W. F. Goddard and M. P. M. Hall, 1980: Examination of raindrop sizes using a dual polarization radar. *Preprints 19th AMS Conf. on Radar Meteor.,* 15-18 April, Miami Beach, Florida.

Seliga, T. A. and V. N. Bringi, 1976: Potential use of radar differential reflectivity measurements at orthogonal polarizations for measuring precipitation. *J. Appl. Meteor., 15, No. 1,* 69-76.

Seliga, T. A., V. N. Bringi and H. H. Al-Khatib, 1979: Differential reflectivity measurements in rain: First experiments. *Trans. IEEE, GE-17, No. 4,* 240-244.

Seliga, T. A., 1980a: Differential reflectivity measurements of rainfall rate: Raingauge comparisons. *Preprints 19th AMS Conf. on Radar Meteor.,* 15-18 April, Miami Beach, Florida.

Seliga, T. A., V. N. Bringi and E. A. Mueller, 1980b: Comparison of rainfall rates derived from differential reflectivity and disdrometer measurements. *Preprints 19th AMS Conf. on Radar Meteor.,* 15-18 April, Miami Beach, Florida.

A DOPPLER RADAR HAIL SENSOR

A.E. Carte

National Physical Research Laboratory
Pretoria SOUTH AFRICA

1. INTRODUCTION

Recent comprehensive reviews of methods for measurement of hailfalls have shown that a great variety of instruments has been developed (Towery *et al*, 1976 and Nicholas, 1977). In practice, however, only the hailpad is extensively used, despite its well-known limitations. This is because studies of hailfall patterns on the ground have revealed fine-scale structures in time and space, which imply that to characterize a hailfall fully a dense network of instruments spread over a relatively large area is required. Economic considerations have up to now ruled out instruments other than the hailpad for such networks. Improved hailpads have been developed (Roos, 1978) which are hardly affected by wind or weathering. These pads can be evaluated rapidly and objectively and have been incorporated into recorders to provide time resolution. Even so, an automatic method would have obvious advantages. For this reason, the use as hail recorders of small, simple Doppler radars of the type used in communications systems, proximity alarms and speed traps was investigated.

2. APPARATUS AND METHODS

The radar that was selected for testing was a varactor-tuned Gunnplexer with a 17 dB horn antenna giving a half-power beamwidth in both planes of 30°. It comprised little more than a resonant cavity with a Gunn diode which acted as both transmitter and local oscillator, a Schottky diode mixer and a 10 volt power supply. The radar operated in the continuous wave mode and its output was the Doppler shift frequency, $f_d = 2\ v/\lambda$ where v is the radial velocity of the target and λ is the wavelength of the transmitted radiation. The amplitude of the received signal was dependent upon range and back-scattering properties of the target. The power output of the unit was 15 mW and the operating frequency was 10·250 GHz (wavelength ≅3 cm). The choice of this frequency meant that the Doppler shift from hailstones of 5 to 50 mm in diameter falling at terminal velocity would be in the audio frequency range. The output could therefore be recorded with an inexpensive audio cassette recorder.

Laboratory tests were carried out with falling spheres to check the frequency response and to determine the beam pattern. It was necessary to add an auxiliary amplifier in order to increase the sensitivity sufficiently to detect 5 mm spheres of ice satisfactorily at a range of 50 cm. On the basis of these tests, various configurations of the equipment were then tried to establish the best method for the detection of hailstones (Fig. 1). The radar was pointed vertically upwards for measuring only the vertical component of the velocity of falling hydrometeors, i.e. their terminal velocities would be determined even when there was a wind. The concentration of large particles would be overestimated if they entered a diverging beam, as shown schematically by Fig. 1a, since they would be detected at longer ranges than smaller particles. Use of a parallel beam would overcome this unless there was a horizontal wind, when again larger objects would be overestimated (Fig. 1b). Thus a sensing platform, transparent to microwaves and located directly above the radar, was used. It was 30 x 30 cm at a distance of about 40 cm, such that it was illuminated reasonably uniformly. This platform defined the sensing area provided that only impacting hailstones were counted. A horizontal surface, as in Fig. 1c, was abandoned in favour of a sloping surface, as in Fig. 1d, to allow rainwater to drain away readily and to ensure that hailstones would tend to bounce out of the beam and not undergo multiple impacts.

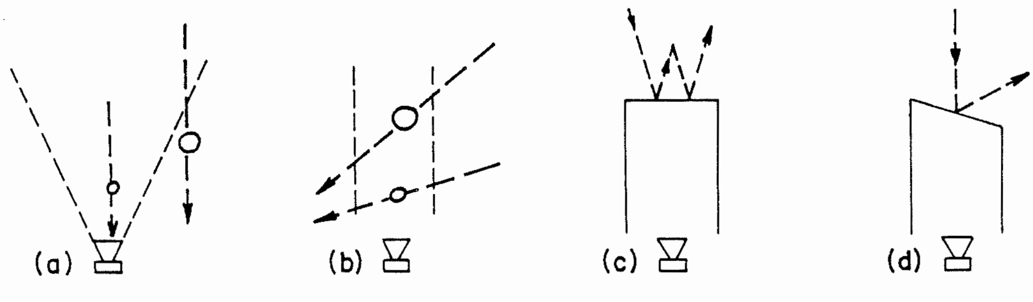

Fig. 1. Radar system with: (a) conical beam; (b) parallel beam; (c) sensing surface horizontal; and (d) sensing surface inclined.

3. RESULTS

(a) Test objects

The output waveforms for various falling objects were recorded by a storage oscilloscope. Some results are shown in Fig. 2. Impacts on a resilient surface gave rise to low frequency oscillations that could persist for many tens of milliseconds, as in Fig. 2c, and these modulated the signal from objects that arrived shortly after an impact (Fig. 2d). Thick rigid surfaces caused too much attenuation of the microwave radiation, thus a compromise was necessary. Surfaces of Perspex, 6 mm thick, were used for the first instruments that were tested in the field. Another effect of surfaces that were not completely transparent to the wavelength used was to cause interference which gave rise to fluctuations in amplitude of the signals as targets approached the surface. Also, amplitude at the instant of impact varied with distance of the target from the beam axis, so that amplitude could be used to give only a rough indication of size, even if the effects of Mie scattering could be disregarded.

simply by playing back the audio record. However, to enable quantitative measurements of frequency to be made and to detect small hailstones, the record was digitised (with sampling done at 20 kHz) followed by a Fourier analysis by computer. The record was divided into blocks of 40 ms in duration and both the analogue results (amplitude versus time) and the results of the Fourier analysis (amplitude versus frequency) were plotted.

Five radar hail sensors were tested in the field during the summer of 1979/80. A few hailfalls were recorded. They mostly comprised small hailstones but one had hailstones with fallspeeds of up to 20 m/s. Four short sections of the record taken during a 5-minute hailfall are shown in Fig. 3. One section includes the signal from a hailstone with a fallspeed of 20 m/s. Its record extended partly across two 40 ms blocks so that its corresponding frequency peak also appears on two adjacent records, but with a high amplitude, low frequency signal from the impact being present only on the second one. The signals in the bottom line peak at a frequency that

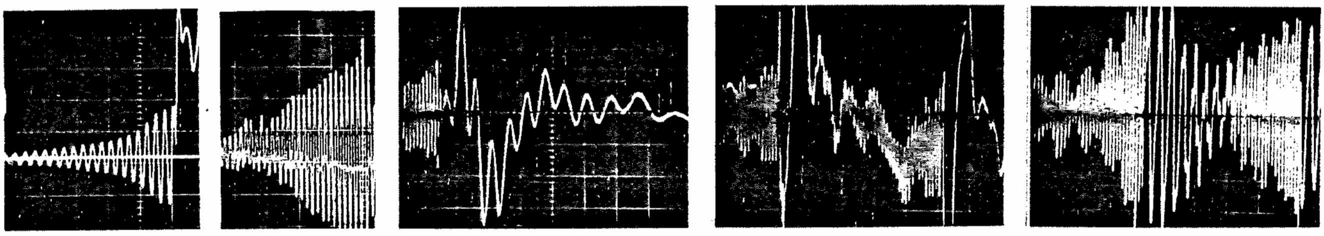

(a) (b) (c) (d) (e)

Fig. 2. Output waveforms: (a) water drop, 5.5 m/s; (b) sphere, 9 m/s; (c) sphere impacting on resilient surface; (d) two spheres in rapid succession on a resilient surface; and (e) two spheres in rapid succession on a firm surface, showing the low frequency signal from a non-vertical rebound. (Vertical grid lines are at 10 ms intervals in (a) and (b) and 20 ms in (c), (d) and (e).

(b) Rain and hail

The measurement of the Doppler frequency shift of an individual hailstone is quite straightforward. This gives fallspeed, which can then be related to size (Carte and Roos, 1973). The areal concentration of hailstones can be determined by counting only those that struck the known area, and the spatial concentration can also be derived when the duration of the hailfall has been recorded. However, in actuality hailstones are usually accompanied by heavy rain. This produces two complications: (i) there may be a number of hydrometeors in the beam simultaneously, producing complex, fluctuating signals; and (ii) the sensing surface tends to become covered with water which flows away discontinuously in "blobs" that produce low frequency signals of large amplitude. Inexpensive audio tape recorders have poor response to low frequencies and therefore filter out much of the background noise produced by movement of water.

The signals from large hailstones that strike the surface can be recognised readily

gives a speed of 9 m/s, and were probably produced by large raindrops as this frequency was found throughout much of the record and when there was rain without hail.

The results have also been displayed in a more compact manner by plotting the frequency of peaks against time. This, however, does not enable impacting hailstones to be distinguished from those that missed the sensing surface. A more sophisticated method of analysis should enable such discrimination to be achieved.

4. CONCLUSIONS

A small Doppler radar has shown promise as a relatively inexpensive hail recorder. It provides a straightforward and accurate method for measuring the speed of free-falling hailstones. Time-resolved size distributions and measurements of hailfall intensity such as areal concentration and kinetic energy density can also be obtained. These all require that only those hailstones that are intercepted by a known area are counted. The technique of detecting impacts on a sensing

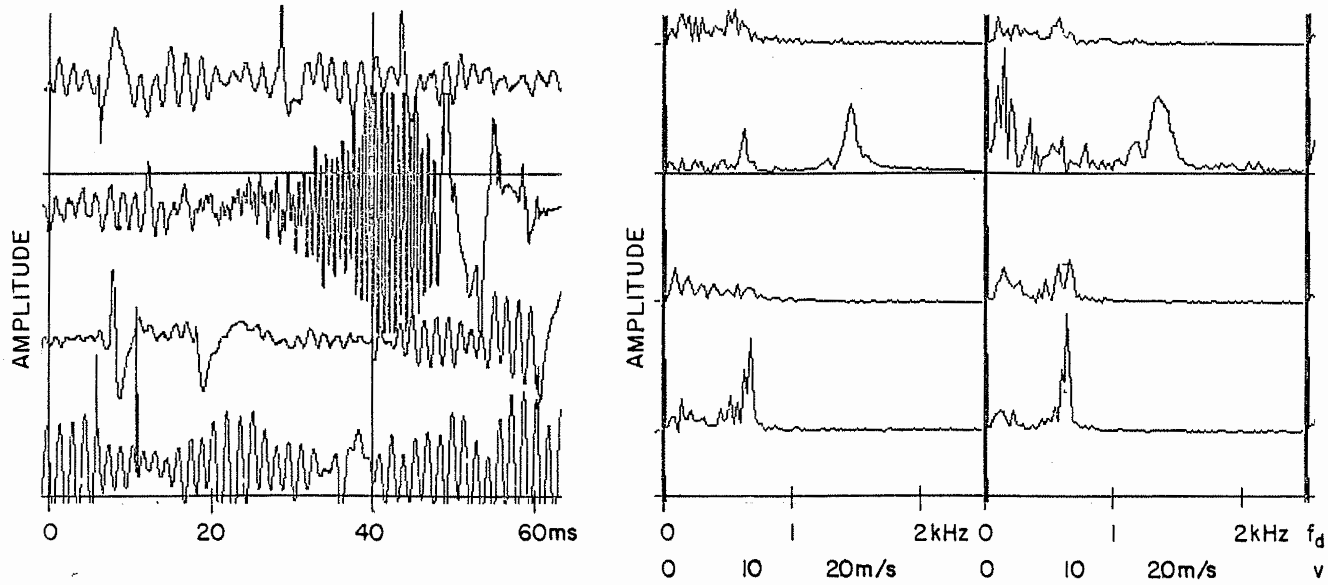

Fig. 3. Analogue and Fourier results as plotted by computer from a digitised record of the radar output during a hailfall accompanied by rain. Four sections of the record, every one of 60 ms duration, are shown.

platform is feasible for large hailstones but has limitations for smaller ones. Run-off of rainwater from this surface introduces complications. Other methods of delineating the area of interception are being investigated.

ACKNOWLEDGEMENTS

Many persons have been involved in this project and their contributions are gratefully acknowledged. They include Dr F. Pasqualucci and Mr M.C. Hodson from whose ideas the work originated, Mr G. Mader who was responsible for the Fourier analysis, Mr J. de Jager, Mr D. Dicks and various student assistants.

REFERENCES

Nicholas, T.R., 1977: A review of surface hail measurement. Hail: a review of hail science and hail suppression, *Meteor. Monogr.* 16, No 38, 257-267.

Roos, D. v.d. S., 1978: Hailstone size inferred from dents in cold-rolled aluminum sheet, *J. appl. Meteor.* 17, 1234-1239.

Roos, D. v.d. S. and A.E. Carte, 1973: The falling behaviour of oblate and spiky hailstones, *J. de Rech. Atmos.* 7, No 1, 39-52.

Towery, N.C., S.A. Changnon, Jr. and G.M. Morgan, Jr., 1976: A review of hail-measuring instruments, *Bull. Amer. Meteor. Soc.* 57, 1132-1140.

L'AQUASONDE, SONDE DONNANT LE SPECTRE DIMENSIONNEL DES GOUTTES DE NUAGE SUIVANT LA VERTICALE

J-L. Champeaux

Etablissement d'Etudes et de Recherches Météorologiques
Magny-les-Hameaux FRANCE

Jusqu'à présent, la mesure in situ de particules était effectuée par des instruments de mesure aéroportés : impacteurs, appareils photographiques, procédés optiques (Knollenberg).

La variation des paramètres microphysiques suivant la verticale étant un élément important dans les divers processus de genèse des précipitations, il nous est apparu utile de développer une sonde, largable d'avion, qui donne en continu la structure verticale du nuage et son évolution temporelle. La gamme de mesure de l'Aquasonde va de 8 à 200 microns.

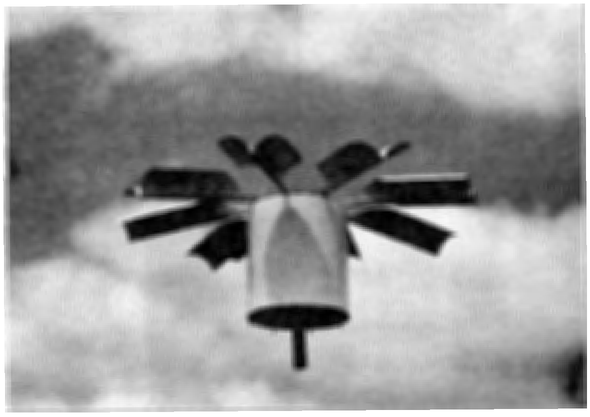

PHOTO N° 1

1 - CONCEPTION MECANIQUE

Le corps de la sonde (photos 1,2), en polyuréthane, se présente sous la forme d'un cylindre (diamètre 200 mm, hauteur 300 mm) traversé de part en part par le tube de mesure (diamètre 2 mm). Son poids est de 2,5 kg. L'Aquasonde peut actuellement être équipée de deux versions de ralentisseurs :

- un ralentisseur à huit ailettes concaves étudié en soufflerie qui confère à la sonde une très bonne stabilité (vitesse de chute 11 m/s) (photo N°1)

- un parachute à fentes, qui réduit la vitesse de chute à 3 m/s tout en conservant une bonne stabilité à la sonde.

Des études en soufflerie ont permis de définir un écoulement peu perturbé au niveau du volume de mesure en prolongeant de 10 cm le tube de mesure par rapport à la face avant de la sonde.

PHOTO N° 2

2 - PRINCIPE OPTIQUE (Figure 1)

Le principe de la mesure consiste à recevoir sur un détecteur photoélectrique, placé à 30° par rapport au flux incident, une partie de l'énergie réfractée par la goutte d'eau lorsque celle-ci traverse le volume éclairé. Le volume d'échantillonnage est un parallélipipède droit à bords nets de 2 mm^3 de volume ; la surface d'échantillonnage étant de 4 mm^2, la hauteur de 500 microns (Figure 2). La fluctuation moyenne de l'éclairement dans tout le champ est de 6%, ce qui donne une erreur de 3% sur le diamètre.

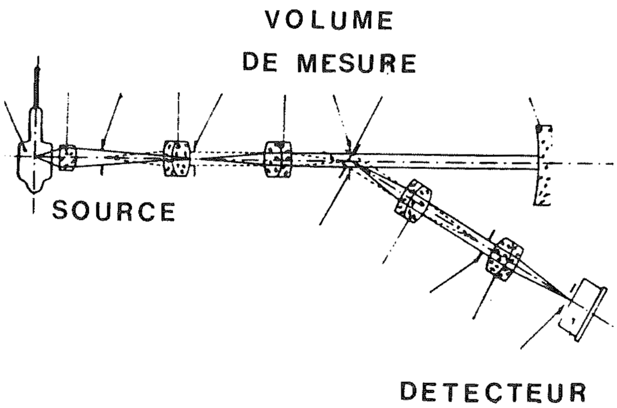

Figure 1 : Schéma optique

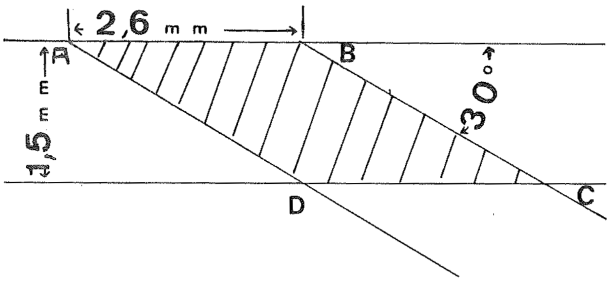

FIGURE 2 : zone de captation : vue de dessus

Pour des raisons d'homogénéité de la zone d'épreuve, d'encombrement et de luminance, la source lumineuse est une lampe à filament de tungstène aux halogènes (6V, 10W) fonctionnant en surtension (8V). L'élément sensible est une photodiode PIN 5 D de 2,5 mm de diamètre.

Les blocs optiques sont montés sur une galette en nid d'abeille.

3 - PARTIE ELECTRONIQUE

La photodiode transforme l'énergie reçue en courant ; 2 amplificateurs successifs délivrent un signal rectangulaire dont l'amplitude est proportionnelle au diamètre de la goutte d'eau. Les signaux, après avoir subi une compression, modulent un émetteur en 400 MHz. Parallèlement une information pression, délivrée sous la forme d'une fréquence, permet de donner l'altitude de la sonde dans le nuage. Le récepteur multi-fréquence permet d'effectuer des lâchers de plusieurs sondes simultanément. La réception s'effectue à bord de l'avion ; les informations peuvent être traitées en temps réel, ou bien enregistrées sur bande magnétique.

Un système de localisation monté sur avion et sur un véhicule au sol permet de récupérer une grande partie des sondes.

4 - TRAITEMENT DU SIGNAL

Les impulsions démodulées issues du récepteur sont comptées et simultanément classées par comparaison instantanée à différentes valeurs de seuil (30 classes) réglables et définies dans la gamme de mesure de l'Aquasonde. La valeur de l'amplitude crête du signal est prise en mémoire et validée sur le flanc de descente (ΔV de quelques mV). Ces informations sont enregistrées sur cassette et traitées sur calculateur.

5 - ERREURS DE MESURE

Les erreurs de mesure sont de deux types : d'une part, les effets dûs au passage de gouttes sur le bord de la zone sensible ; dans ce cas, la goutte est comptée dans une classe inférieure. Ces effets sont minimes. D'autre part, les effets de coïncidence : le problème se pose lorsque deux ou plusieurs gouttes se présentent en même temps dans le volume de mesure.

Plusieurs cas peuvent se produire

a)

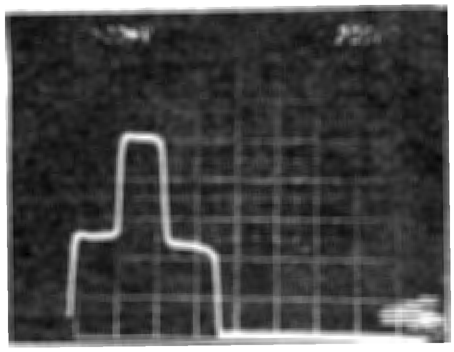

Deux gouttes se trouvent simultanément dans le volume éclairé. Electroniquement, on compte une goutte plus grosse au lieu de deux plus petites ; on commet alors une erreur sur le nombre et le spectre dimensionnel.

b)

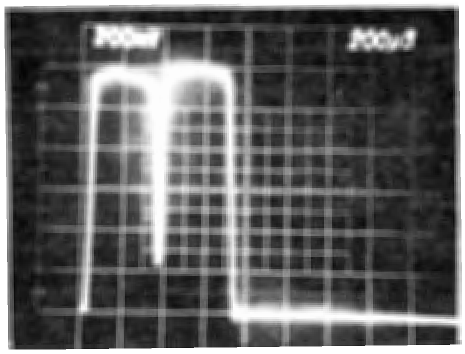

Ce cas est un cas limite ; il est traité de manière correcte au niveau de la chaîne d'acquisition. Ce type de signal se présente cependant fréquemment, car dans certaines configurations de passage des gouttes le "cas a" devient "cas b".

Pour améliorer le système de comptage, on peut analyser le signal plus finement par échantillonnage. Une diminution de la surface d'échantillonnage réduirait considérablement le nombre de coïncidence.

Un programme de correction des erreurs de mesure (effets de bord, coïncidence) a été mis au point, ce qui permet à l'Aquasonde de mesurer des concentrations de l'ordre de 200 gouttes/cm^3 avec une bonne précision.

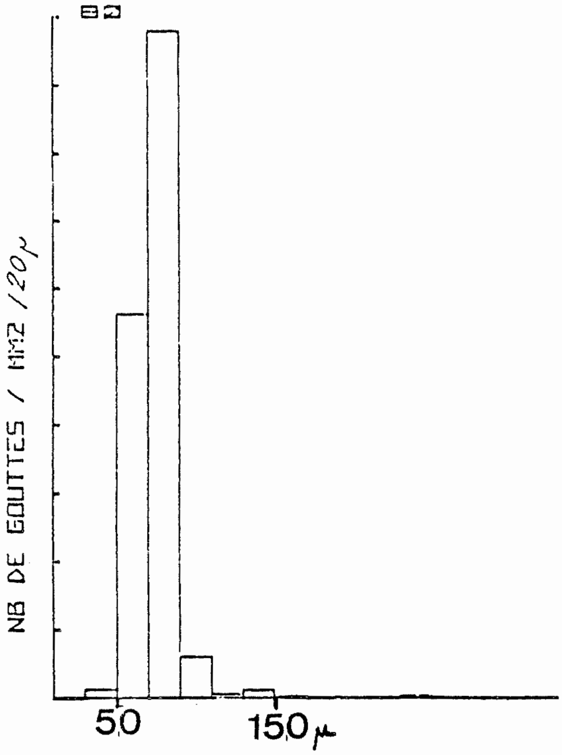

SPECTRE		CDP
DIMENSION		NOMBRE
CANAL	TAILLE	
1	20	0
2	40	1
3	60	45
4	80	76
5	100	5
6	120	0
7	140	1
8	160	0
9	180	0
10	200	0
11	220	0
12	240	0
13	260	0
14	280	0
15	300	0

FIGURE 3.a : Spectre dimensionnel mesuré par le CDP - Billes de latex de 70 microns.

SPECTRE AQUASONDE

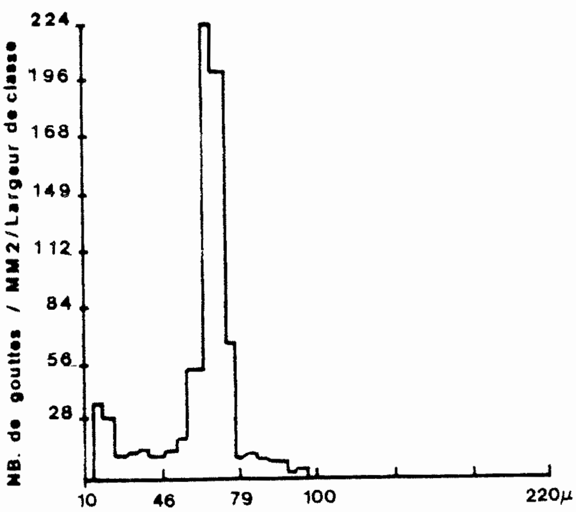

CLASSE	DIAMETRE (μ)	NBRE DE GOUTTES
0	10	
1	14	39
2	18	32
3	24	11
4	29	13
5	35	15
6	39	11
7	46	14
8	52	20
9	57	55
10	65	227
11	69	204
12	75	68
13	79	10
14	83	13
15	88	11
16	94	10
17	101	4
18	105	5
19	111	3
20	116	1
21	121	1
22	132	0
23	146	0
24	161	0
25	172	0
26	185	0
27	197	0
28	210	0
29	220	1

FIGURE 3.b : Spectre dimensionnel mesuré par l'Aquasonde - Billes de latex de 70 microns.

6 - COMPARAISON AQUASONDE-KNOLLENBERG

Une comparaison a été effectuée entre les appareils de Knollenberg (FSSP et CDP) et l'Aquasonde à l'aide de particules de latex calibrées, et par pulvérisation de gouttelettes d'eau. Les surfaces d'échantillonnage avaient été positionnées le plus près possible l'une de l'autre.

L'examen des résultats montre une bonne concordance entre les diamètres mesurés par l'Aquasonde et les appareils de Knollenberg. (Figures 3 a et 3 b).

Le comptage de particules dans les premiers canaux est certainement dû à la présence de poussières dans le jet de latex.

BIBLIOGRAPHIE

J-F. GAYET, J-L. CHAMPEAUX, - 1979 -
Comparaison des résultats de l'Aquasonde et des appareils de Knollenberg pour la mesure du spectre dimensionnel des gouttes de nuage.
Note technique de l'EERM.

J-F. GAYET, - 1976 -
Physique de la mesure des appareils de Knollenberg.
Université de Clermont Ferrand

V. KLAUS, J-L. CHAMPEAUX - 1977 -
L'Aquasonde.
La Météorologie, VIème Série, N°10 pp 61-75.

J. SIMON, A. ROUSSEL - 1976 -
Etude et essais de la partie optique de l'Aquasonde.
Institut d'Optique théorique et appliquée.

RESULTS FROM THE METEOROLOGICAL OFFICE AIRBORNE HOLOGRAPHIC PARTICLE-MEASURING INSTRUMENT

B.J. Conway, A.N. Bentley, M. Kitchen and S.J. Caughey

Meteorological Office
Bracknell U.K.

Introduction

The UK Meteorological Office has developed a holographic instrument for ground and aircraft - based measurements in cloud and precipitation (Ryder, 1976). Its characteristics complement those of the ASSP-100 and 2D instruments, made by Particle Measuring Systems Inc, which are also in use. Thus each hologram is a virtually instantaneous (20 ns exposure) record of a localised volume of about 0.5 litre whereas the ASSP-100 sample is less than 1mm^2 in cross-section and tens or hundreds of metres in length. The holographic instrument can be used to measure ice particles and water drops from around 10 μm radius up to large precipitation elements, and is able to show particle-shape down to about 100 μm diameter at which size the 2D cloud droplet probe images are poorly resolved. The ASSP-100 and 2D instruments have the great advantage of presenting results in real time and hence one of their functions will be to enable selection of holograms for detailed analysis.

The holographic system has been test-flown on the Meteorological Research Flight Hercules aircraft and used in ground-based measurements in cloud. This paper briefly describes the instrument and presents some results from recent trials.

Technical Description

The instrument uses the in-line geometry which is generally favoured for particle holography since it minimises the laser coherence requirements and eliminates the need for a separate reference beam. Fig 1 shows the recording and reconstruction arrangements in schematic form.

The laser employed for recording is a Ferranti Nd:Yag type, designed for airborne use, which produces some 50 mj of radiation at 1.06 μm wavelength in each 20 ns pulse. A lithium iodate crystal converts about 10% of this radiation to the second harmonic at 0.53 μm, which is a good match to the spectral sensitivity peak of the Agfa 10E56AH holographic film. The unconverted infra-red light plays no part in hologram formation.

A Vinten reconnaissance camera (without lens) is loaded with enough 70 mm film to record some 300 holograms in a single flight. A roller-blind shutter, which limits exposure

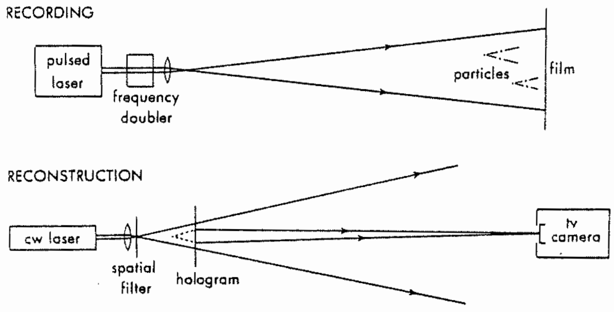

Figure 1. Holographic recording and reconstruction arrangements showing geometry and all essential components.

of the film to background light, opens to a maximum aperture of 5 x 5 cm, whereupon the hologram is exposed by a synchronised laser pulse. The present system can operate at 2 frames/sec; minor modifications will allow operation at up to 8 frames/sec.

The optimum film-processing procedure is still being investigated, following results obtained at Loughborough University (Dunn and Walls, 1979). At present absorption holograms are produced by development in Kodak D19 to an overall density of about 1.5, followed by use of a rapid fixer such as Super Amfix. Absorption holograms are preferred, having been found to be much less noisy in reconstruction than phase holograms produced by bleaching out the silver image. For reconstruction it is found that holograms are held sufficiently flat when supported at their edges only, in a sprocketed frame mounted on micropositioners. A helium-neon laser provides the reconstruction beam.

No imaging lenses are used in recording or reconstruction. The curved wavefronts associated with the use of diverging beams (Fig 1) result in the production of magnified real images (Collier et al, 1971) which are allowed to fall directly onto the face of the TV camera's vidicon tube. The magnification varies with the distance of the droplet from the film at recording time and is typically 30 or less for a recording length of 1-2 m. Movement of the hologram towards or away from the TV camera brings different planes into

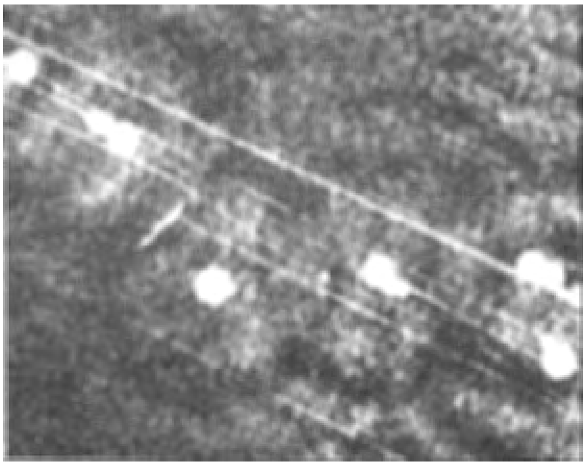

Figure 2. Reconstruction of ballotini on perspex fibres. Radius of largest particle = 65 μm.

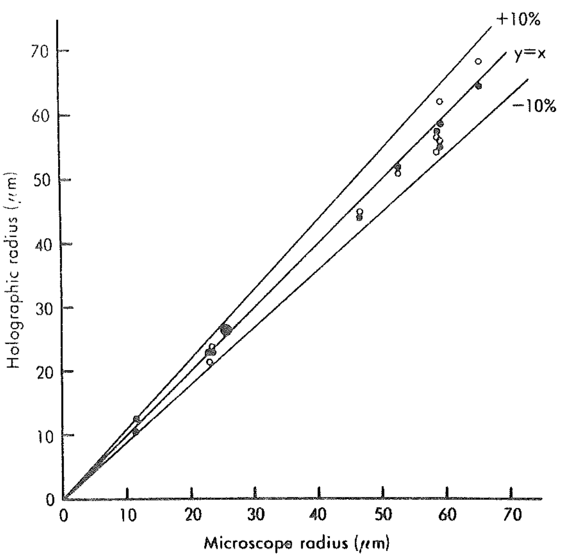

Figure 3. Holographic vs microscope size measurements for the particles in Fig 2.
● Particles recorded 12 cm from film.
○ Same particles recorded 30 cm from film.

focus and allows the entire recorded volume to be scanned.

Laboratory Tests

Test-recordings were made of ballotini (small glass beads) supported on perspex fibres as well as of water droplet sprays. Reconstructions of holograms recorded on film were not noticeably worse than those from holograms on glass plates.

Fig 2 shows a typical reconstruction, from a film hologram, of ballotini supported on fine threads, the thinnest of which are 2 to 3 μm in diameter. Threads of this size are clearly distinguishable in reconstruction although they cannot be sized accurately, but particles of such small dimensions are difficult to pick out. The ballotini range from 11 to 65 μm in radius. Their radii deduced from the holographic reconstruction are plotted in fig 3 against corresponding values measured directly by microscope. The comparison is made for two cases: in one the particles were recorded 12 cm from the film and in the other the distance was 30 cm, ie opposite ends of a recording volume of some 350 cm^3. Agreement with microscope measurements is within ± 10% in both cases.

In other tests, recordings were made of beads in the precipitation size-range (several mm diameter) and found to give clear, well-defined reconstructions.

Ground-based field trials

In May 1979, the complete instrument was field-tested during an experimental study of entrainment effects in clouds (Blyth et al, 1980). The experimental site was at the top of Great Dun Fell in Cumbria, 847 m a.m.s.l. The laser and camera were enclosed in weather-proof aluminium boxes about 1 m apart on a framework platform 4 m high. An ASSP-100 droplet-sizing probe was mounted about 1 m from the holographic instrument.

Fig 4 shows typical reconstructions of cloud droplets in the range 5-10 μm radius recorded on 14th May in non-precipitating cap cloud. The mean ASSP droplet size spectrum (averaged over 10 seconds around the hologram recording time) appears in fig 5(a). For comparison the holographic size spectrum (mean of 3 scans each of 400 drops) is shown in fig 5(b).

Direct comparison of the results is complicated by the difference in sample volumes. The holographic sample was about 25 cm in maximum extent while the ASSP ten-second sample stretched over some 100 m alongwind (wind speed was ~10 m sec^{-1}).

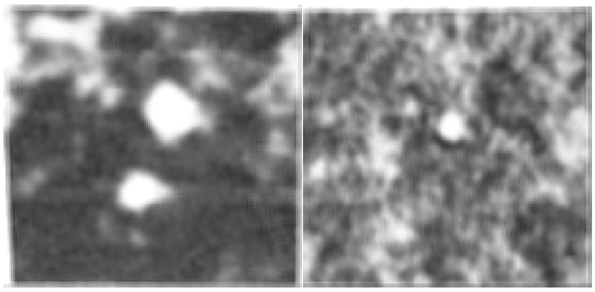

(a) (b)

Figure 4. Reconstructions of droplets recorded during ground-based trials in natural cloud. In 4(a) a second, out of focus, droplet is also visible. Droplet radii: (a) 6.5 μm (larger droplet); (b) 9.0 μm (Image size depends on magnification which varies with the position of the particle at recording time).

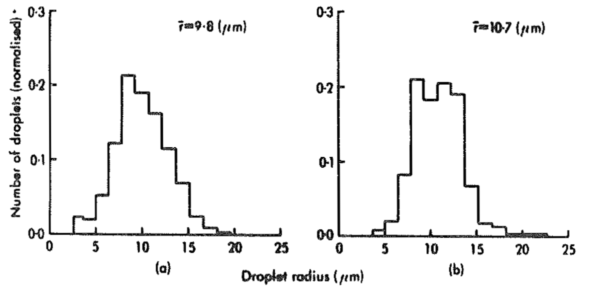

Figure 5. Droplet size spectra measured by ASSP-100 and holographic instrument. (Ground-based trials on 14th May 1979).
(a) Mean ASSP spectrum, 10-second sample.
(b) Holographic spectrum.

The maximum ASSP sampling rate was 1 spectrum per second, ie an average over approximately 10 m. Much shorter ASSP sampling periods would result in unreliable spectra containing very few droplets.

Mean droplet radii from the ASSP 10-second spectrum and from the holographic spectrum are 9.8 μm and 10.7 μm respectively. However, the mean radii of individual 1-second ASSP spectra from within the 10-second sample of fig 5(a) range from 9.1 μm to 10.5 μm, the spread of values encountered within 15 seconds either side of the holographic exposure being even greater: 8.0 to 12.2 μm. Since even these 1-second spectra, being 10 m averages, smooth out any fluctuations on the scale of the holographic sample volume, the holographic sizing is clearly consistent with the available ASSP data.

Such attempts to compare measurements from the two instruments highlight the ability of the holographic system to permit investigations on length-scales inaccessible by other means.

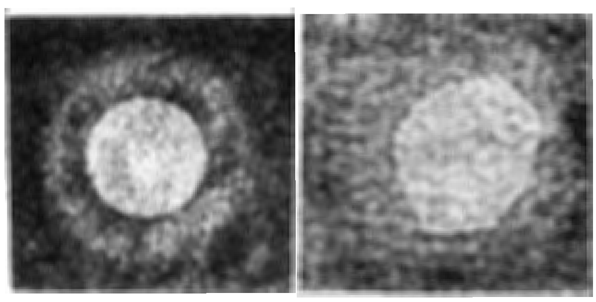

(a) (b)

Figure 6. Reconstructions of precipitation particles recorded during ground-based trials.
(a) Drizzle drop, radius 110 μm.
(b) Hail pellet, max chord 750 μm.

Thus we can obtain three-dimensional spatial information on statistically significant numbers of particles within the sample volume of an individual hologram, and have similar, localised samples at spatial intervals governed by the period between consecutive exposures and the speed of the instrument relative to the surrounding air.

Recordings made at other times during the trials at Great Dun Fell showed larger hydrometeors well outside the size range of the ASSP-100. Examples are shown in figs 6(a) and 6(b). The former shows a drizzle drop of radius 110 μm. The spherical shape of the particle is immediately apparent and measurements of perpendicular diameters agree to within 2%. In contrast, fig 6(b) shows a clearly non-spherical particle, of maximum chord 750 μm, considered to be a small, partially melted, hail pellet.

Aircraft-based measurements

More recently, the holographic equipment was installed in wing-pods on the MRF Hercules aircraft, and on 4th October 1979, penetrations were made of small, scattered, maritime cumulus clouds in an area a few miles north of the Scilly Isles. Cloud bases were at about 2300 ft with tops extending to 4700 ft. Holograms were exposed in cloud and ASSP-100 spectra were recorded at 1-second intervals (corresponding to a path length of about 100 m).

On this occasion a minor camera fault resulted in some fogging of the holograms by background light. Nevertheless, it was found possible to recover information by partially

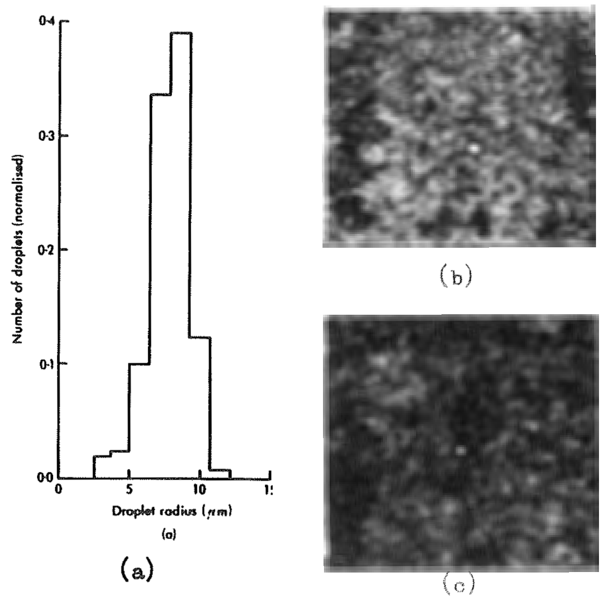

(a) (b) (c)

Figure 7. Small maritime cumulus. Aircraft penetration at 3400 ft (mid-point of cloud).
(a) ASSP-100 size spectrum.
(b) and (c) Reconstructions of droplets, radii 11 μm and 6.5 μm respectively.

bleaching them down to the usual density.

Fig 7(a) shows the mean ASSP drop-size spectrum from a typical cloud penetration at 3400 ft. The spectrum is a mean of the six one-second spectra obtained during that penetration. No droplets above about 12 μm radius were found so the sample was at the small-size end of the holographic instrument's range. Images of droplets were readily found however and typical examples are shown in figs 7(b) and 7(c). All the droplets reconstructed were found to fall within the size range of the ASSP distribution in fig 7(a), those in figs 7(b) and 7(c) being of radius 11 μm and 6.5 μm respectively.

Conclusion

Recordings of cloud and precipitation particles have been made under a variety of conditions in ground and aircraft-based trials, and the resulting drop-size measurements found to compare well with values obtained in other ways. Successful reconstructions have been made of droplets down to about 6 μm radius, ie at the small-size end of the instrument's range, recorded during aircraft penetrations of cumulus clouds, and these provide considerable encouragement for airborne use of the instrument in its other obvious area of application: the precipitation size regime.

The unique sampling characteristics of the instrument have been contrasted with those of single-particle scattering instruments such as the ASSP-100, in connection with ground-based measurements at Great Dun Fell, and suggest a major role for the holographic system in future studies of inhomogeneities and entrainment effects in clouds.

Work continues in the Meteorological Office on improving reconstruction quality by optimising the chemical processing of holograms. It is planned to transfer, in the near future, much of the analysis task to the automatic analysis system described by Bexon et al (1976), as the holographic technique becomes routinely used in cloud physics research programmes.

Acknowledgements

The authors wish to thank colleagues past and present who have contributed to this work, and particularly Messrs J D Turton and J R Leighton for their work on the hologram analyses presented.

References

Bexon, R., Gibbs, J. and Bishop, G.D., 1976, "Automatic assessment of aerosol holograms", J. Aerosol Sci., 7, pp 397 - 407.

Blyth, A., Choularton, T., Fullerton, T., Latham J., Mill, C.S., Smith, M.H., Stromberg, I,M., Caughey, S.J., and Conway, B.J., 1980, "Two case studies of the effect of entrainment upon the microphysical structure of clouds at Great Dun Fell". Proc. VIIIth International Cloud Physics Conference - Clermont Ferrand.

Collier, R.J., Burckhardt, C.B., and Lin, L.H., 1971, "Optical Holography", Academic Press.

Dunn, P., and Walls, J.M., 1979, "Improved microimages from in-line absorption holograms" Appl. Opt., 18, pp 263-264.

Ryder, P., 1976, "The measurement of cloud droplet spectra", Proc: VIIth Int. Conf. on Cloud Physics, Boulder, pp 576-580.

A METHOD OF DETECTING CONTACT ICE NUCLEI USING FILTER SAMPLES

W. A. Cooper

University of Wyoming
Laramie, Wyoming, U.S.A.

1. INTRODUCTION

Membrane filters are used widely for the detection of ice nuclei. The method introduced by Bigg et al. (1961), and modified by Stevenson (1968), provides convenience and reproducibility. However, the ice nuclei detected in Stevenson's method are primarily deposition nuclei; the method is not sensitive to most immersion nuclei or to contact nuclei. The purpose of this paper is to describe a technique for processing filter samples to determine the separate contributions of deposition, immersion, and contact nuclei. Three processing instruments are used, each sensitive to different nucleation modes.

2. FILTER PROCESSING METHODS

a. Settling chamber. To simulate contact nucleation, droplets were sprayed into the top of a cold chamber and allowed to settle onto filters placed near the bottom of the chamber. A Berglund-Liu monodisperse droplet generator (Berglund and Liu, 1973) was used to generate droplets of about 70 μm diameter, a size chosen to insure thermal relaxation to the chamber temperature before the droplets contact the filters. The thermal relaxation time for droplets of this size is about 0.05 s, and several seconds are required for the droplets to fall through the chamber.

The settling chamber used for these studies was 20 cm in diameter and 75 cm high. The walls were coated with circulating glycol to prevent frost. Filters were placed on a thin coating of microscope immersion oil on a brass plate, and this plate was placed into the chamber and allowed to cool to the temperature of the chamber. Droplets of distilled water were then sprayed into the chamber, while both the temperature of the plate and of the air just above the plate were monitored by thin thermocouples. The droplet exposure was timed to produce about 25% coverage of the filter surface; this required 60 s. The fraction of the surface covered by droplets was determined by microscopic examination of the filter, and was also monitored by counting and sizing craters produced in gelatin-coated slides exposed next to the filters.

After exposure to the falling droplets, the filter was covered for 10 min to allow time for the nucleated ice particles to grow to visible ice patches. Since most of the filter remained coated with supercooled droplets during this time, those droplets provided the required vapor source for growth of the ice. After 10 min the filter was removed from the chamber and the ice patches were counted and photographed.

The use of microscope immersion oil was not necessary for the detection of ice, but it made the processing more convenient. It reduced the background and made the ice patches easier to see, and it also reduced the rate at which the ice would melt during examination and photography. STP, often used for filter processing, was also tried, but produced ice patches which were not as compact and which were more difficult to count. Petrolatum jelly was less suitable because of a tendency for frost to propagate over the droplet-coated surface.

All three nucleation modes (deposition, immersion, and contact) would be activated by this processing technique. The entire filter surface is exposed to a humidity near water saturation, which could activate deposition nuclei. Immersion nuclei would be a subset of the contact nuclei, and both would be activated only on that portion (typically 25%) of the filter covered by droplets.

b. Drop freezing. The technique used to detect immersion-freezing nuclei is an adaptation of that of Schnell (1979). Distilled water drops were placed on the filter surface and then the filter and drops were slowly cooled. To insure good thermal contact and reduce background freezing events, the filters were placed on a thin coating of microscope immersion oil. The filters were cooled on a copper stage, and the number of droplets that froze was observed as a function of temperature. Normally, 30 drops with a 3-mm diameter area of contact with the filter were used on each filter, and filters were processed in tandem with blanks to monitor the background. The spectra to be presented are all well above the background concentrations. Cooling was at a rate of 0.5°C/min, and the number of frozen drops was recorded in 1 min or 2 min intervals.

The analysis for the ice nucleus spectrum is an adaptation of that used by Vali (1971). If the fraction of drops that remain unfrozen at temperature T is f, then the concentration of nuclei active at temperature T or warmer is

$$N(T) = -\frac{\ln(f)}{S\ (a/A)}$$

where S is the sample volume drawn through the filter, a is the area covered by each drop, and A is the total area of the filter.

c. Thermal diffusion processor. A conventional filter processor was also used. The Wyoming filter processor has been described by Gordon and Vali (1976), and has been compared with a number of similar instruments (Vali, 1976). The measurements to be reported in this paper were made at relative humidities between 99-100% relative to water saturation, and will be interpreted as measurements of nuclei active in the deposition mode. There are some indications that measurements from chambers such as this depend on the CCN content of the air (Vali, 1975), but the results should still provide an upper limit to the concentrations of deposition nuclei. Gagin (1972) and Huffman (1973) have shown that the concentrations from such chambers depend primarily on supersaturation relative to ice, and are not functions of relative humidity with respect to water saturation or of temperature except as those measures affect supersaturation relative to ice. This dependence argues for the deposition mode as the primary mode of activation in thermal diffusion processors.

3. MEASUREMENTS OF NUCLEUS CONCENTRATIONS

Sets of filter samples were collected on Sartorius hydrophobic filters (0.45 µm pore size, 45 mm diameter), and the filters were processed by the three methods described in section 2. The concentration detected in each processor represents a different combination of nucleation modes. The concentrations measured by the thermal diffusion processor and by the drop freezing technique will be interpreted as concentrations of deposition and immersion-freezing nuclei, respectively. To determine concentrations from the settling chamber, the corresponding concentrations of deposition nuclei (at water saturation) were subtracted from the number of ice patches on the filter surface, and then the remaining number was multiplied by a factor of typically 4 to account for the probability of a particle being covered by a droplet. The resulting concentrations are assumed to represent contact-nucleus concentrations in the following discussion. As used here, the contact-nucleus concentrations will include the immersion-freezing nucleus concentrations as a subset.

Fig. 1 shows a representative result. The filter samples used to determine these concentrations were collected near the surface in Wyoming in wintertime. Sample volumes used were 50-200 liters. The samples processed in the settling chamber yielded substantially higher concentrations, even before correction for droplet coverage, than did the other two techniques. Concentrations of 1/liter were common at temperatures of -11°C to -13°C.

A similar test using an AgI aerosol is shown in Fig. 2. The AgI particles were generated by heating a flask of AgI and then blowing nitrogen through the flask. The concentration detected in the settling chamber was by far the highest, and the threshhold was the warmest, of the three techniques.

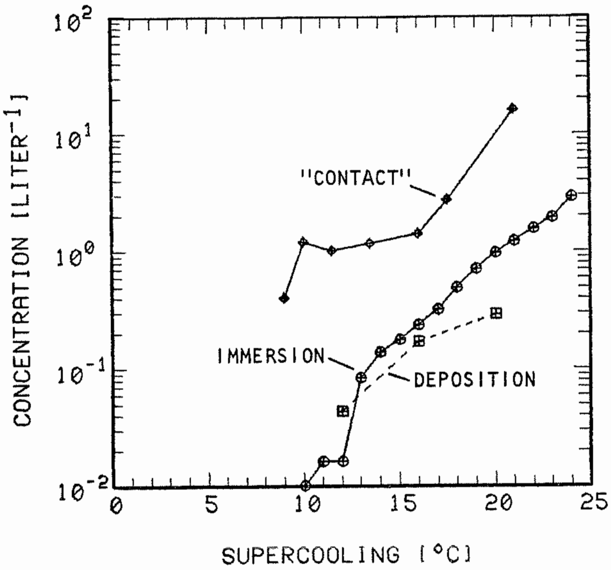

Figure 1: Concentrations of ice nuclei as a function of supercooling. These results are based on filter samples collected near the surface in Wyoming in wintertime. In the case of deposition nuclei, the filters were processed at water saturation at the indicated temperature.

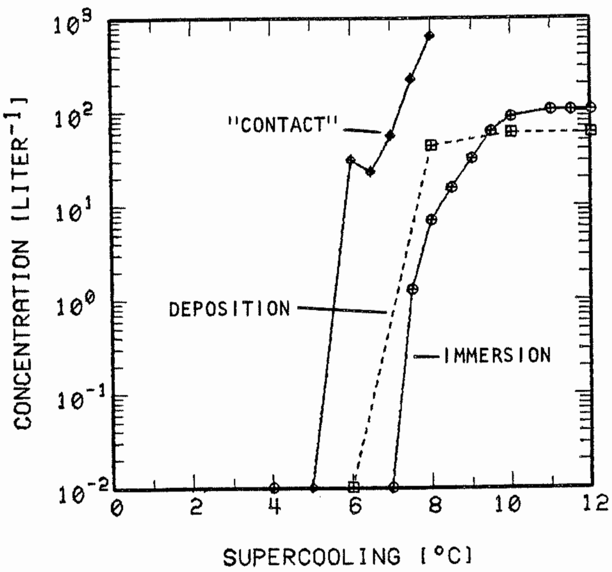

Figure 2: Concentrations of ice nuclei as a function of supercooling, for an AgI sample.

Fig. 3 shows some concentrations determined by processing filters collected on Elk Mountain in Wyoming, at an elevation of about 3400 m MSL. Typical ice crystal concentrations in this cloud have been discussed in Cooper and Vali (1976); they are similar to the concentrations determined by the settling chamber method, although a more extensive and direct comparison is needed. Cooper and Vali (1976) suggested that nucleation in the cap cloud was not in agreement with predictions from filter measurements, and that the development of ice in the cloud seemed to require either a condensation-freezing or a contact nucleation

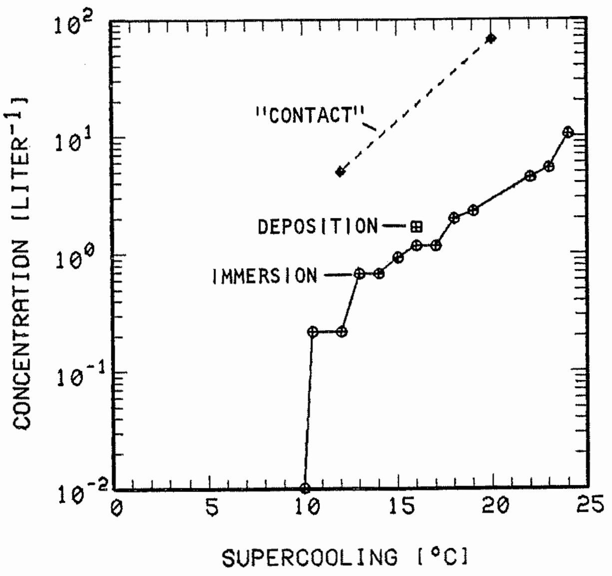

Figure 3: Ice nucleus concentration as a function of supercooling for filter samples collected on Elk Mountain, Wyoming, in wintertime.

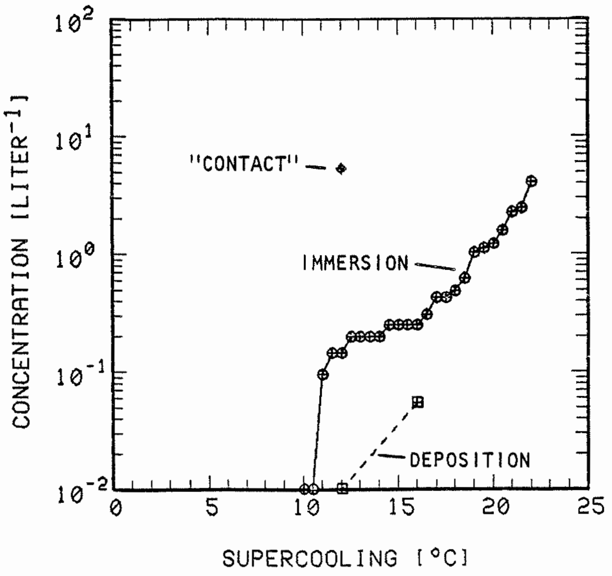

Figure 4: Ice nucleus concentration as a function of supercooling for samples collected near the -10°C level in Montana in summertime.

process. The present results seem to favor the contact nucleation process; results to be presented in section 4 indicate that the nucleation process in the settling chamber is not a condensation-freezing process.

Fig. 4 shows some results from the HIPLEX Montana area during summer 1979. Again, the contact nucleus concentrations are well in excess of deposition or immersion concentrations, and are in a range that is similar to ice concentrations in new turrets of this region.

In the preceding examples and in all other samples processed to date, the concentrations detected in the settling chamber were well above those detected using the other methods.

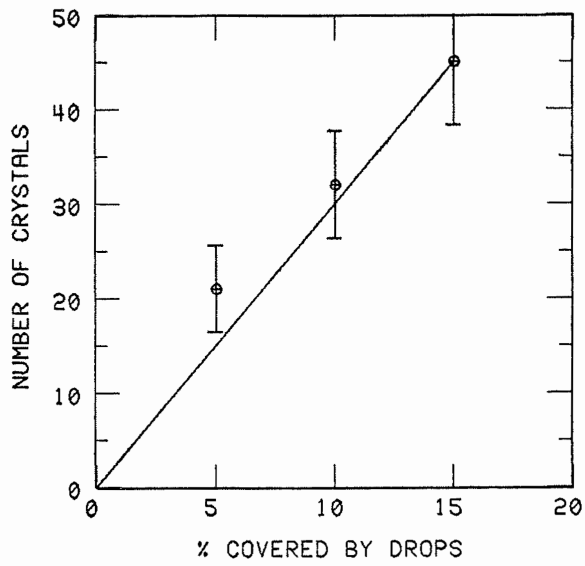

Figure 5: Number of ice crystals appearing on similar filters exposed to the settling droplets for different periods of time.

4. TESTS OF THE SETTLING-CHAMBER TECHNIQUE

a. Dependence on area covered. If the process responsible for nucleation in the settling-chamber is a contact nucleation process, the number of ice patches appearing on the filter should be proportional to the fraction of the filter covered by droplets. To test this proportionality, filters from the same aerosol sample were exposed to the droplet spray for different lengths of time. Fig. 5 shows that the resulting number of ice crystals was proportional to the fraction of the filter covered by ice. (Corresponding blank filters yielded counts of 1-2/filter.)

b. Refreeze tests. If the nucleation process in the settling chamber is a contact nucleation process, the activity should be substantially less when the sample is melted after processing and is then refrozen. To test this, processed filters were warmed until the ice melted (without evaporating the water droplets) and were then cooled to the initial processing temperature. The resulting concentrations of ice patches were generally less than 10% of the initial concentrations.

c. Warm-contact tests. To check if the drops must be supercooled before contact in order to activate the ice nuclei, warm droplets were sprayed on filters and the filters were then cooled. Ice concentrations were generally less than 10% of the concentrations obtained using supercooled droplets, and generally agreed with the concentrations obtained from the drop freezing tests.

d. Blank tests. Blank filters yielded concentrations of <1, 1-5, and ∿10 at temperatures of -12, -16, and -20°C, respectively. Blank filters were processed with all filter samples to monitor the background counts. The concentrations in Figs. 1-4 were well above background concentrations, and include corrections for the background obtained by blanks.

5. SOME REMAINING DIFFICULTIES

The results reported here are preliminary, and several difficulties are still being investigated. One problem which prevented a more extensive report of field measurements in this paper is that the concentrations detected in the settling chamber decay with time: samples processed several months after collection yield concentrations an order of magnitude lower than samples processed within days of collection. This behavior is unlike that of conventional filter processing, and is not understood.

Another uncertainty involves the relative humidity to which the filter and droplets are exposed in the settling chamber. The correction for deposition nucleation used in this paper is based on an assumed relative humidity of 100%, an assumption that seems reasonable because of the high concentration of droplets injected into the chamber. If the supersaturation is actually higher, this correction would be invalid, but supersaturations in excess of 5% would be required to account for the observed concentrations by deposition nucleation alone. Because the chamber walls were coated with glycol, the chamber was initially subsaturated, and there was an initial cooling of the chamber at the start of processing because of the evaporation of droplets. (The temperature used to characterize the nucleation, and plotted in Figs. 1-4, was the coldest temperature observed using a thin thermocouple placed just above the filter surface.)

Also needing investigation is the size of the particles responsible for the nucleation in the settling chamber, and the location of those particles within or on the surface of the filters.

6. CONCLUSIONS

A set of three measurements provided the possibility of detecting the deposition, immersion-freezing, and contact nucleation modes separately using only filter samples. The technique yielded contact nucleus concentrations that were typically an order of magnitude higher than deposition or immersion nucleus concentrations, and the values were similar to ice concentrations found in newly-formed clouds of the regions in which the samples were collected.

ACKNOWLEDGEMENTS

This research was sponsored by the U. S. Water and Power Resources Service, DAWRM, Department of the Interior, under contract 7-07-93-V0001, and by the National Science Foundation under Grant ATM75-02515.

REFERENCES

Berglund, R.N. and B.Y.H. Liu, 1973: Generation of monodisperse aerosol standards. Environmental Science and Technology, 7, 147-153.

Bigg, E.K., C.T. Miles and K.J. Heffernan, 1961: Stratospheric ice nuclei. J. Meteor., 18, 804-806.

Cooper, W.A. and G. Vali, 1976: Ice crystal concentrations in wintertime clouds. Preprints, International Conference on Cloud Physics, Boulder, Colorado, pp. 91-96.

Gagin, A., 1972: The effect of supersaturation on the ice crystal production by natural aerosols. J. Rech. Atmos., 6, 175-185.

Gordon, G. and G. Vali, 1976: University of Wyoming thermal diffusion chamber. The Third International Workshop on Ice Nucleus Measurements, Laramie, WY, pp. 91-98.

Huffman, P. J., 1973: Supersaturation spectra of AgI and natural ice nuclei. J. Appl. Meteor., 12, 1080-1082.

Schnell, R.C., 1979: A new technique for measuring atmospheric ice nuclei active at temperatures from -20°C to approaching 0°C, with results. Seventh Conference on Inadvertent and Planned Weather Modification, Banff, pp. 110-111.

Stevenson, C.M., 1968: An improved Millipore filter technique for measuring the concentrations of freezing nuclei in the atmosphere. Quart. J. Roy. Meteor. Soc., 94, 35-43.

Vali, G., 1971: Quantitative evaluation of experimental results on the heterogeneous freezing nucleation of supercooled liquids. J. Atmos. Sci., 28, 402-409.

Vali, 1975: Workshop summary -- Ice nucleation workshop. Bull. Amer. Meteor. Soc., 56, 1180-1184.

Vali, 1976. The Third International Workshop on Ice Nucleus Measurements, Laramie, 186 pp.

COMPARAISON DE CHAMBRES A DIFFUSION THERMIQUE A PLAQUES PARALLELES

F. Desalmand et R. Serpolay

I.O.P.G. du Puy de Dôme, L.A.M.P. Clermont-Fd, FRANCE

On dispose de trois chambres à diffusion thermique du modèle décrit par TWOMEY (1963). Ce sont des cylindres plats, creux, à axe vertical. On mesure la concentration des noyaux de condensation nuageuse dans le plan médian de la chambre où la sursaturation est maximale.

I. DESCRIPTION DES APPAREILS

I.1 Caractéristiques géométriques des chambres

La valeur du rapport D/H entre le diamètre intérieur D du cylindre et sa hauteur H permet de classer les chambres en "chambres hautes" (2 et 3bis) et "chambres plates" (1 et 3). On tient compte également du rapport h/H, où h est le diamètre du faisceau laser qui sert à éclairer les gouttelettes formées sur les noyaux.

VARIABLES	CHAMBRE 1	CHAMBRE 2	CHAMBRE 3	CHAMBRE 3 bis
D cm	8,8	7,6	7,5	6,9
H cm	1,0	2,6	0,9	1,7
h cm	0,118	0,125	0,125	0,125
D/H	8,8	2,9	8,3	4,1
h/H	12%	5 %	14%	7 %

TABLEAU 1 - CARACTERISTIQUES GEOMETRIQUES DES CHAMBRES

I-2 Obtention de la sursaturation

Dans la chambre 1, on peut refroidir la plaque inférieure ou chauffer la plaque supérieure à l'aide de plaques à effet Peltier. Dans les autres chambres, un fil résistant impose le chauffage de la plaque supérieure.

I-3 Admission de l'air dans la chambre

Elle est effectuée d'une manière discontinue par aspiration a travers deux orifices diamétralement opposés. Sur la chambre 1, ces orifices sont situés au milieu de la paroi latérale de la chambre. Sur les chambres 2, 3 et 3bis, ils se trouvent sur la périphérie de la plaque inférieure.

I-4 Enregistrement des gouttelettes formées sur les noyaux

Le faisceau laser utilisé pour éclairer les gouttelettes se propage selon un diamètre situé dans le plan médian. Pour les chambres 1 et 2, les gouttelettes sont visualisées à l'aide d'un dispositif photographique ; pour les chambres 3 et 3 bis, elles sont visualisées par l'intermédiaire d'un ensemble améra-vidéo - magnétoscope dont on analyse la bande enregistrée.

I-5 Mode opératoire

Pour chaque valeur de la sursaturation S, on réalise quatre fois le cycle suivant : admission de l'air, formation des gouttelettes, prise de vue, évacuation de l'air. On détermine le nombre maximal de gouttelettes avec un microlecteur, dans le cas de photographies sur film, ou par l'intermédiaire d'un moniteur, dans le cas de l'enregistrement sur bande. Le nombre n de gouttelettes est alors la moyenne arithmétique des gouttelettes formées au cours des quatre cycles précédents. V étant le volume du champ photographié ou enregistré, la concentration N par cm^3 vaut alors :

$\boxed{N = \frac{n}{V}}$ où n est déterminé à 30% près et V à 20% près.

II. RESULTATS EXPERIMENTAUX

II-1 Chauffage de la plaque supérieure et refroidissement de la plaque inférieure de la chambre 1

On détermine le spectre des noyaux en fonction de la sursaturation, de S = 0,25% à S=1,25%, en prenant cinq valeurs de S. On opère d'abord en refroidissant la plaque inférieure (chambre 1) puis, immédiatement après, en chauffant la plaque supérieure (chambre 1bis). Cette expérience a été réalisée quatre fois ; elle donne donc vingt couples (N_1, N'_1) des concentrations des noyaux actifs à la sursaturation S, N_1 étant obtenues par refroidissement de la plaque inférieure et N'_1 par réchauffement de la plaque supérieure.

La concentration des noyaux de condensation nuageuse actifs à la sursaturation S étant une fonction puissance de S :

(1) $N_1 = C_1 S^{k_1}$ (2) $N'_1 = C'_1 S^{k'_1}$

on voit qu'en éliminant S entre (1) et (2), N'_1 est aussi une fonction puissance de N :

(3) $N'_1 = C'_1 C_1^{-k'_1/k_1} N_1^{k'_1/k_1}$

Le tableau 2 donne les résultats des calculs effectués à partir des vingt couples (N_1, N'_1). r désigne ici le rapport de corrélation linéaire de la méthode des moindres carrés.

(4) $\boxed{N'_1 = 0{,}59\ N_1^{1{,}08}}$ avec un rapport de corrélation r = 0,92

(5) $\boxed{N'_3 = 1{,}84\ N_3^{0{,}96}}$ avec un rapport de corrélation r = 0,93

7.3.77	C_1	k_1	r	C'_1	k'_1	r
7h	3810	0,98	0,990	4300	1,05	0,980
11h	2630	0,67	0,990	3890	0,79	0,950
14h	2180	0,39	0,990	2560	0,45	0,989
17h	1850	0,64	0,990	1740	0,73	0,990

TABLEAU 2 - PARAMETRES C ET k DE LA RELATION $N = CS^k$ OBTENUS A L'AIDE DE LA CHAMBRE 1 :
a) EN REFROIDISSANT LA PLAQUE INFERIEURE (moitié gauche du tableau)
b) EN CHAUFFANT LA PLAQUE SUPERIEURE (moitié droite du tableau)

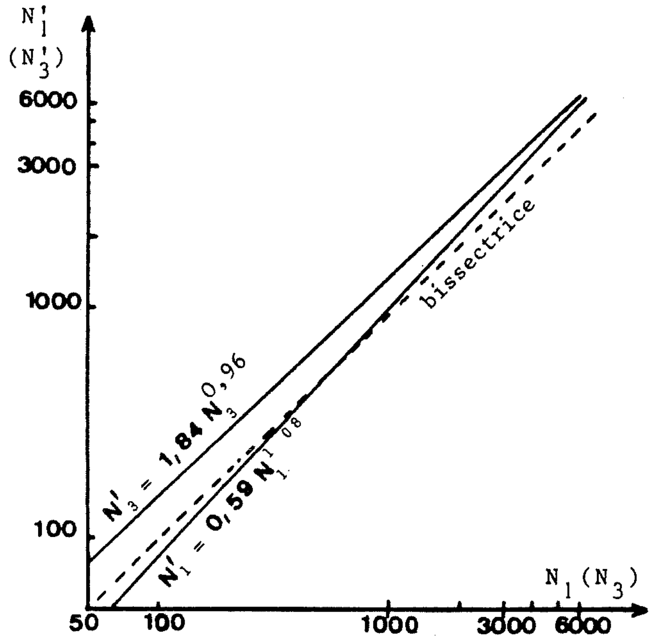

FIGURE 1 - DROITES CORRELANT :
a) Les mesures de la chambre 1bis à celles de la chambre 1
b) Les mesures de la chambre 3bis à celles de la chambre 3

II-2 Influence de la hauteur de la paroi verticale de la chambre

La chambre 3 peut être équipée alternativement de deux parois verticales de hauteur différente, ce qui permet de réaliser deux chambres selon la formule "chambre 3 - plate" ou "chambre 3bis - haute" (cf. Tableau 1). On opère selon la méthode décrite en II-1 en utilisant d'abord la paroi la moins haute, puis, immédiatement après, la paroi la plus haute. Cette expérience, réalisée dix fois, donne 50 couples de valeurs (N_3 , N'_3) que l'on exploite selon la même démarche qu'en II-1.

Le tableau 3 donne les paramètres C et k de la loi caractéristique $N = CS^k$ et la relation puissance entre N_3 et N'_3 s'écrit :

septembre 79		N_3	k_3	r	N'_3	k'_3	r
le 18	16h	1290	1,03	0,997	2200	1,29	0,980
le 19	11h	1970	0,87	0,990	3160	0,58	0,995
le 20	9h	1150	1,02	0,992	1860	1,34	0,970
le 20	14h	1420	1,59	0,992	1340	1,11	0,958
le 21	10h	3570	0,94	0,988	3180	1,03	0,995
le 24	19h	2000	0,54	0,994	3730	0,43	0,911
le 25	11h	3100	0,74	0,972	5140	1,07	0,996
le 26	9h	5050	0,78	0,991	5760	0,39	0,964
le 26	17h	2670	0,86	0,995	5740	0,86	0,947
le 27	9h	8300	0,69	0,985	8650	1,16	0,987

TABLEAU 3 - PARAMETRES C ET k DE LA RELATION $N = CS^k$ OBTENUS
a) A L'AIDE DE LA CHAMBRE 3 (plate)
b) A L'AIDE DE LA CHAMBRE 3bis (haute)

La droite correlant N'_3 et N_3 est représentée sur la figue 1 ; on remarque que $N'_3 > N_3$. Pour une même sursaturation, la chambre haute active un nombre plus grand de noyaux que la chambre plate.

II-3 Influence de la turbulence dans les chambres 1 et 2

La chambre 1 est plate et les deux orifices réservés au passage de l'air se trouvent dans la paroi latérale. La chambre 2 est haute et le passage de l'air se fait par la plaque inférieure. Les plaques supérieures sont chauffées.

Les deux chambres fonctionnent d'une manière indépendante avec des lasers, des appareils photographiques et des volumes photographiés différents.

A l'aide de ces chambres, on procède simultanément à la mesure des concentrations N_1 et N_2 des noyaux actifs à la même sursaturation (14 mesures à 0,25% et 15 mesures à 0,50%).

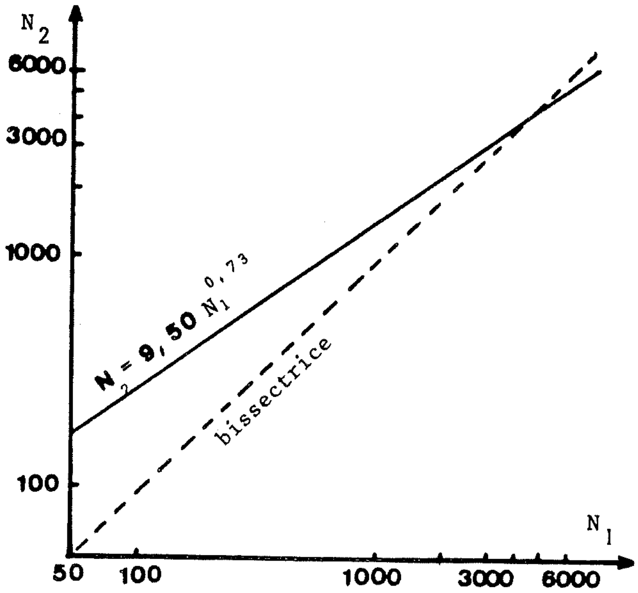

FIGURE 2 - DROITE DE CORRELATION ENTRE N_2 ET N_1

La recherche d'une fonction puissance entre vingt neuf couples de valeurs (N_1, N_2) aboutit à la relation :

$$N_2 = 9{,}50\ N_1^{0{,}73} \qquad r = 0{,}92 \tag{6}$$

La figure 2 illustre cette relation.

Vers 4.200 noyaux/cm^3, les deux chambres donnent la même concentration.

II-4 Conclusion

Ces séries de comparaisons permettent d'obtenir des indications sur l'influence desdivers paramètres envisagés.

A partir des relations (4), (5) et (6), on a calculé les rapports des concentrations N'_1/N_1, N'_3/N_3 et N_2/N_1 pour des valeurs extrêmes et moyennes des concentrations N_1 , N_3 et N_2 correspondant à différentes sursaturations et différentes masses d'air. Il en résulte le tableau 4.

Dans le premier cas, le rapport des concentrations N'_1/N_1 reste voisin de 1 : pour une même chambre, le chauffage de la plaque supérieure ou le refroidissement de la plaque inférieure aboutissent à des concentrations voisines (tableau 4, partie gauche).

Dans le deuxième cas, pour une même chambre, le nombre de noyaux activés augmente avec la hauteur de la paroi verticale (tableau 4, partie centrale).

La troisième série de comparaisons est établie avec les deux chambres les plus différentes. L'écart entre celles-ci est maximal aux faibles sursaturations pour des populations de gros noyaux ; il décroit quand les concentrations augmentent et, au-dessus de 4200/cm3, les réponses sont voisines. Au-dessous de 4200/cm3, la chambre 2, où l'air entre avec la plus grande turbulence, active plus de noyaux que la chambre 1 (tableau 4 - partie droite).

N_1	N'_1	N'_1/N_1	N_3	N'_3	N'_3/N_3	N_1	N_2	N_2/N_1
50	40	0,81	50	80	1,57	50	165	3,30
730	730	1				4180	4180	1
6000	7100	1,18	6000	7800	1,30	6000	5440	0,91

TABLEAU 4 - RAPPORTS DES CONCENTRATIONS DEDUITS DES RELATIONS PUISSANCE POUR DES VALEURS EXTREMES ET MOYENNES DES CONCENTRATIONS

III. INTERPRETATION PHYSIQUE

On mesure la concentration des noyaux actifs à la sursaturation S théoriquement égale à la valeur maximale qui règne à l'équilibre, au centre de la chambre, entre les 2 plaques supérieure et inférieure, respectivement à température T_s et T_i

$$S = S(T_i,\ T_s - T_i) \tag{7}$$

Mais deux faits contrarient cette prévision:

- l'étendue du volume photographié ou enregistré ;
- la turbulence consécutive à l'admission de l'air dans la chambre.

III-1 Etendue du volume photographié ou enregistré

La sursaturation décroit à partir du centre de la chambre selon la verticale et selon l'horizontale. La décroissance verticale augmente avec le rapport h/H entre le diamètre du laser et la hauteur de la chambre, tandis que la décroissance horizontale varie en sens inverse du rapport D/H (tableau 1).

Ainsi, si la décroissance horizontale de la sursaturation dans une chambre plate à partir du centre est faible, la décroissance verticale peut y être importante, ce qui reviendrait à sous-estimer les valeurs des concentrations N_3 à la sursaturation calculée prévalant dans le plan médian de la chambre.

Cependant, en étudiant les enregistrements effectués avec les chambres 3 et 3bis, on ne discerne pas de différences dans les répartitions horizontale et verticale des gouttelettes; et, si ces différences se manifestent, il est peu probable qu'elles atteignent les 30% parfois constatées au cours de deux prélèvements successifs effectués sur un même échantillon d'air et avec une même chambre.

III-2 Hauteur de la chambre

Dans les deux chambres plates 1 et 3, toutes les gouttelettes tombent. Par contre, dans les deux autres chambres hautes 2 et 3bis, de nombreuses gouttelettes sont prises dans des courants ascendants, particulièrement bien visibles sur les enregistrements pris avec la chambre 3bis. Lorsque l'air humide ascendant s'approche de la surface humide et plus chaude de la plaque supérieure, il peut y avoir formation de sursaturations élevées qui activent un nombre plus grand de noyaux et l'on a toujours $N'_3 > N_3$ (tableau 4).

III-3 Turbulence

Elle résulte de l'entrée discontinue de l'air. Elle est très importante dans les chambres hautes où le passage de l'air se fait par la plaque inférieure (chambre 2 et 3bis). Elle est moindre dans la chambre 1 : paroi basse munie des orifices réservés au passage de l'air. Le cas le plus défavorable est donc celui de la chambre 2 comparée à la chambre 1 ; le rapport des concentrations, très variable, diminue de 3,30 à 1 lorsque N_1 passe de 50 à 4.200 noyaux par cm3 (tableau 4, droite). La turbulence produit donc des sursaturations dont les effets sont particulièrement nets pour des populations de gros noyaux peu nombreux, actifs aux faibles valeurs de S. Ces effets diminuent pour des populations plus nombreuses nécessitant des valeurs de S plus élevées et dépendent de l'humidité de l'air introduit. L'évaluation des sursaturations transitoires d'origine turbulente est difficile (SAXENA, BURFORD et KASSNER, 1970).

III-4 Importance de l'instant choisi pour la prise de vue ou le comptage

Si, à partir d'un enregistrement sur magnétoscope, nous effectuons des déterminations de la concentration N à intervalles rapprochés, de l'ordre de la seconde par exemple, nous constatons que les valeurs de N fluctuent et passent par un ou plusieurs maximums. Ce comportement à l'intérieur des chambres est d'autant plus net que celles-ci ont un faible rapport D/H. De plus, il semble que l'instant du premier maximum soit d'autant plus rapproché de l'instant où l'échantillon d'air a été isolé dans la chambre que le gradient de température entre les plaques est plus important (mesures à sursaturations S élevées). Les sursaturations transitoires d'origine thermique et turbulente, en produisant des gouttelettes qui emportent noyaux et vapeur d'eau, peuvent expliquer ce maximum. Après s'être stabilisé, l'air dans la chambre présente une population en noyaux plus pauvre et une humidité plus faible. Une procédure satisfaisante serait d'effectuer la prise de vue ou la mesure à l'instant de ce maximum, c'est-à-dire au moment où les noyaux présents ont été activés à une sursaturation inconnue et non mesurable, mais sans doute supérieure à la valeur théorique (7).

IV. CONCLUSION

Les concentrations des noyaux de condensation nuageuse mesurées à l'aide de deux chambres à diffusion thermique à plaques parallèles sont du même ordre de grandeur. Il existe entre elles une relation puissance, en accord avec la loi caractéristique des noyaux de condensation nuageuse :

$$N = CS^k$$

où N est la concentration des noyaux actifs à la sursaturation S, C et k sont des paramètres qui dépendent de la masse d'air et de l'appareil utilisé. Les concentrations augmentent avec la hauteur de la chambre. La turbulence, inévitable, produit des sursaturations particulièrement importantes aux concentrations faibles. Vers 3.500 à 4.200 noyaux/cm3, toutes les chambres donnent des concentrations sensiblement équivalentes.

REFERENCES

V.K. SAXENA, J.N. BURDFORD and J.L. KASSNER,Jr, 1970, *Operation of a thermal diffusion chamber for measurements on cloud condensation nuclei,* J. Atmos. Sci., 27, pp. 73-80

S. TWOMEY, 1963, *Measurements of natural cloud nuclei,* J. Rech. Atmos., 1, pp. 101-105

REMERCIEMENTS

Une partie de cette recherche a été réalisée avec une chambre à diffusion thermique prêtée par le Graduate Center for Cloud Physics Research (laboratoire du Prof. J.L. KASSNER) de l'Université de Missouri-Rolla. Elle a aussi grandement bénéficié d'un financement accordé au titre du Fond d'Aide à la Coopération.

A NEW HORIZONTAL GRADIENT, CONTINUOUS FLOW, ICE THERMAL DIFFUSION CHAMBER AND DETAILED OBSERVATION OF CONDENSATION-FREEZING AND DEPOSITION NUCLEATIONS

N. Fukuta and E.M. Tomlinson

Department of Meteorology, University of Utah
Salt Lake City, Utah, U.S.A.

1. INTRODUCTION

For studying ice nucleating behaviors of aerosol particles in the atmosphere, deposition and condensation-freezing nucleations in particular, accurate control of both temperature and supersaturation is essential (Schaller and Fukuta, 1979). In addition, the aerosol particles for ice nucleation studies should be freely suspended in this controlled environment so that they are devoid of any substrate effects. Thermal diffusion chambers can meet these requirements. The continuous flow-type thermal diffusion chambers for cloud condensation nucleus (CCN) study are advantageous for sampling a large volume of air (Hudson and Squires, 1973; Sinnarwalla and Alofs, 1973; Fukuta and Saxena, 1979). In the thermal diffusion chamber developed by Fukuta and Saxena, a temperature gradient across one or both plates is also maintained so that a range of temperature and/or supersaturation is sustained, and effects of temperature and/or supersaturation can be studied in a single sampling. For ice nucleation studies this concept of varying temperature and/or supersaturation was already demonstrated in the wedge-shaped ice thermal diffusion chamber, and although the chamber operation was static (without flow), its operation resulted in a number of new findings as we reported in the last conference (Schaller and Fukuta, 1979).

Starting from concept of the wedge-shaped ice thermal diffusion chamber and that of the Fukuta-Saxena CCN spectrometer, we have developed a horizontal gradient continuous flow ice thermal diffusion chamber, incorporating a new integration scheme of nucleated ice crystals. The new chamber allows for the continual treatment of the sample air under a range of accurately controlled supersaturations and the integtation of nucleated ice crystals for analysis. This paper reports the design, operation principle and testing of the chamber as well as results of detailed studies on pure silver iodide nuclei and some preliminary measurements of natural nuclei.

2. THE HORIZONTAL GRADIENT, CONTINUOUS FLOW, ICE THERMAL DIFFUSION CHAMBER

2.1 Design and Operation of the Chamber

The Chamber consists of three sections (see Fig. 1); the preprocessing (referred to as the prechamber), main activation (main chamber), and crystal settling section (postchamber), which have lengths of 15, 20, and 40 centimeters respectively. The interior width of the chamber is 15 centimeters and the height 6 millimeters except in the crystal settling section where it expands to 11 millimeters. All the thermally conducting parts are made of copper while plexiglass is used for the thermally insulating portions. All three sections have a common top plate which is coated with a 1 millimeter layer of ice and is held isothermal using a circulating refrigerated bath. The bottom plates are coated with ice except in the crystal collection region of the post chamber. The walls are continuous through the chamber and are made of thermal insulators.

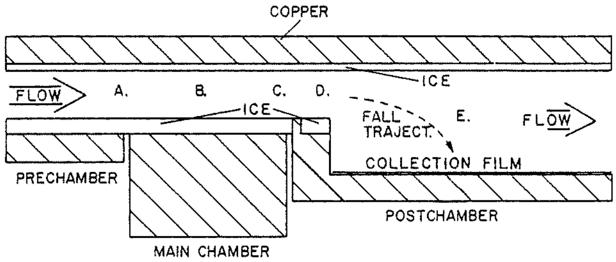

Fig. 1. Design of the chamber. The height scale is expanded by a factor of 10. Typical values for positions A through E are presented in Table 1.

The pre-chamber is held nearly isothermal with the bottom plate slightly colder than the top. The incoming air is preconditioned in this section before entering into the main chamber to avoid transient supersaturations (Saxena, et al, 1970). The prechamber is sufficiently long to allow steady state to be reached for the temperature and vapor fields before the air moves into the main chamber.

The main chamber provides a range of conditions for the activation of ice nuclei. The top plate is isothermal while a temperature gradient is maintained across the bottom plate. This configuration results in a nearly constant temperature horizontally across the sample flow and produces a reage of supersaturations. The use of a thick copper plate on the bottom enables a nearly linear temperature gradient to be maintained across it. The temperature of the bottom plate is controlled using thermoelectric modules on each edge. Rectangular heat pipes are adopted to insure uniformity of temperature along the direction of flow. The top surfaces of the heat pipes are cooled with the thermoelectric modules with the help of coolant from the circulating bath. The cooling is regulated by adjusting the current through the modules. A heating wire is adhered to the warmer side for use when heating is required to maintain a steady temperature profile. The design and flow of the main chamber allow steady state of the supersaturation field to be reached in the first half of the chamber so that a sufficient time at the final level of supersaturation is secured for ice nuclei activation. The nucleated crystals are then carried out of the main chamber by the flow into the postchamber.

The postchamber serves as a collector for the nucleated ice crystals. The collection scheme requires the postchamber to be operated at warmer temperatures than the main chamber, and therefore special precautions must be taken to prevent transient supersaturation development. This is achieved by delaying vapor diffusion while allowing thermal conduction to proceed at the beginning of the postchamber. A copper plate substitutes for the first 1 centimeter of the ice surface on the bottom of the postchamber to achieve the delay of the vapor diffusion. After this delay device, the air passes over a 4 centimeter length of ice surface held at the temperature of the postchamber so that the vapor pressure saturated at the postchamber temperature can be achieved before the sample air moves over the ice crystal collection film. This configuration insures that ice-supersaturated conditions are maintained at all times in the postchamber, thereby eliminating the possibility of ice crystal loss by sublimation. A photograph of the chamber is presented in Fig. 2.

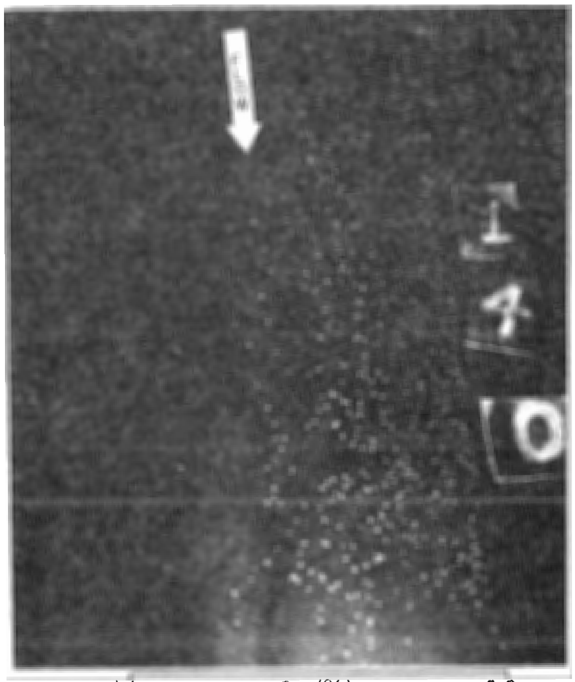

Fig. 3. Example of collected crystals on the mylar film. Sample; AgI.

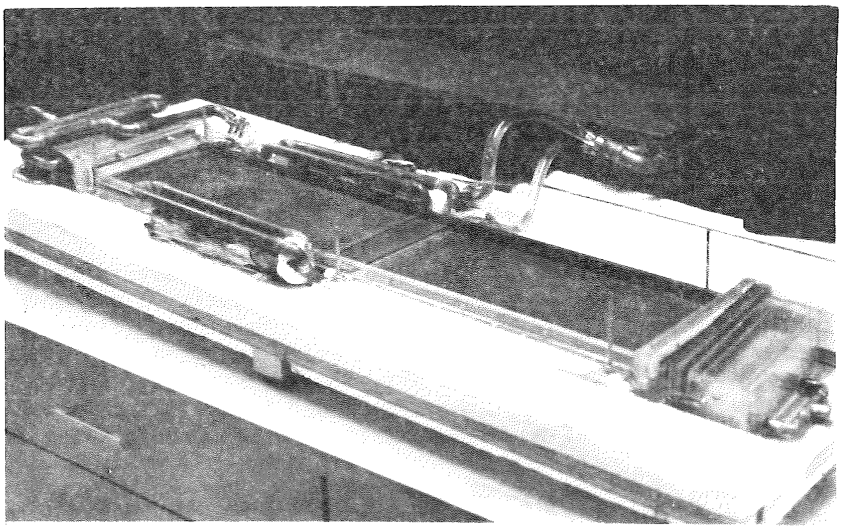

Fig. 2. The entire chamber with the top plate removed.

Ice crystal detection and counting in ice thermal diffusion chambers has been a well-known problem, so we have developed a new method. Mylar copy film (carbon paper) holding condensed water droplets is placed in the postchamber where the temperature is kept warmer than that of the main chamber. Ice crystals nucleated in the main chamber fall on the film and grow to visible size in the presence of the droplets. The positions of the ice crystals across the flow direction give the supersaturation and temperature at which they nucleated. After sampling is completed, the film is moved into a freezer and photographed under low angle illumination. An example is shown in Fig. 3. The sample is confined to the middle 10 centimeters of the chamber width leaving a 2.5 centimeter crystal free region along each edge to avoid flow instability zones near the walls. An overlay which divides the sample into ten regions or lanes across the flow is placed over the photograph, and the crystals in each lane are counted. For the pure AgI studies, active number of ice nuclei is compared with the acutal number of smoke particles in the sample air as determined by the ultramicroscope method.

The emtire chamber has been modeled numerically considering vapor diffusion and heat conduction as well as advection by the shear (Poiseuille) flow.

The equations used for heat and vapor transport respectively are

$$\frac{dT}{dt} = \kappa\nabla^2 T + V(z)\frac{\delta T}{\delta y} \quad \text{and}$$

$$\frac{de}{dt} = D\nabla^2 e + V(z)\frac{\delta e}{\delta y} \, ,$$

where T is the temperature, κ the thermal diffusivity of air, D the vapor diffusivity, V(z) the shear flow velocity, and e the water vapor pressure. The z direction is taken in the vertical between the plates and the y in the direction of the flow. These equations were integrated numerically. Table 1 gives values for the temperatures and supersaturations at the positions indicated in Fig. 1. The model is used to determine the positions in the chamber when a steady state is reached in the sample layer as well as to confirm that the transient supersaturations are properly suppressed.

Table 1

Values for locations A through E as shown in Fig. 1. The top plate temperature is -10.0°C and the bottom plate temperature of the main chamber is -24.6°C.

	A	B.	C.	D.	E.
Temperature (°C)	-10.4	-17.3	-17.3	-10.6	-10.4
Ice-supersaturation (%)	0.0	22.0	22.1	1.3	5.3
Water-supersaturation (%)	-9.5	3.1	3.2	-8.6	-4.7

Copper-constantan thermocouples with ice bath reference junctions are used for temperature measurements. The temperature is measured at nine locations in the chamber. Temperature recording is automated and controlled by a Terak mimicomputer. Each temperature is recorded every 25 seconds on a magnetic disk and also displayed on a video screen for monitoring. The high accuracy voltmeter used enables an accuracy of 0.01°C at -10°C.

2.2 Positioning of the Sample

The near linear temperature and vapor pressure profiles between the plates of a thermal diffusion chamber produces a supersaturation maximum near the center. For ice thermal diffusion chambers, a sufficiently large temperature difference between the plates produces a region of supersaturation with respect to water with a maximum near but not necessarily colocated with the ice supersaturation maximum. For a continuous flow chamber, the parabolic velocity profile of flow is symmetric about the chamber center. Therefore, if we can position a thin sample layer near the center of the chamber, being sandwiched between filtered air layers, the flow velocity and the supersaturations with respect to ice as well as water will be close to their maxima. Furthermore, use of a thin sample layer in the linear temperature profile makes the sample temperature nearly constant. Fig. 4 illustrates an example of top and bottom plate temperatures of -10.0°C and -24.6°C respectively. The sample thickness is 0.2H and is centered around 0.45H where H is the chamber height. Air filtered through glass wool is used to properly position the sample layer. The correct sandwiching of the sample between the layers of filtered air is achieved with the intake device (see Fig. 5.). This device introduces the layers into the chamber while maintaining a laminar flow. The height of the sample layer is controlled by adjusting the ratio of the thicknesses of the upper and lower layers of filtered air.

Wall effects can be a significant factor in the operation of thermal diffusion chambers (Tomlinson and Fukuta, 1979). Our chamber has been numerically modeled and the extent of the wall effects precisely determined. Laminar flow is required throughout the chamber in order that the temperature and supersaturation fields can be adequately controlled. Thermal convection tends to develop along the walls, and caution must be taken to avoid any effect on the sample air. By keeping the chamber height small, these effects can be minimized and confined to the immediate vicinity of the walls. Filtered air is used to separate the sample from the walls in order to avoid wall effects. Smoke tests were performed to verify the correct positioning as well as the laminar flow of the sample air through the chamber. A photograph of one of these smoke tests is presented in Fig. 6.

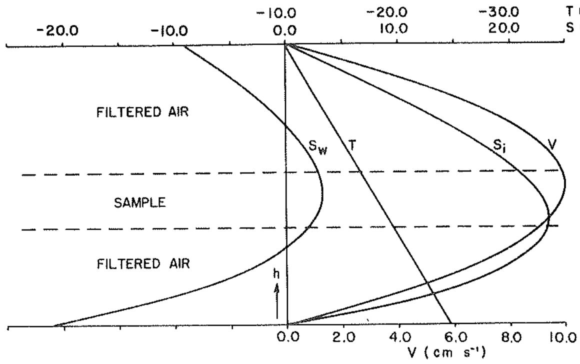

Fig. 4. Profiles of the temperature (T), water supersaturation (S_w), ice supersaturation (S_i), and shear velocity (V) between plates of an ice thermal diffusion chamber.

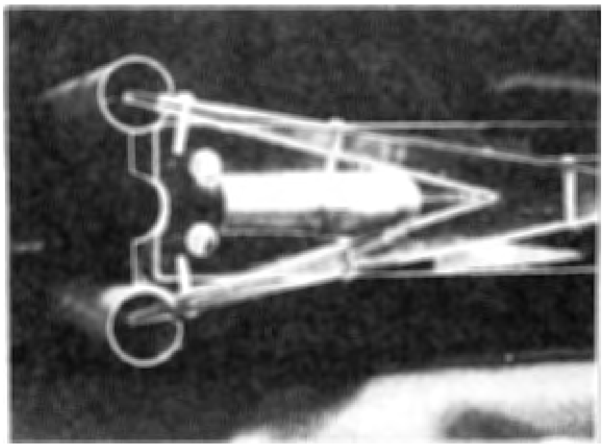

Fig. 5. The intake device before final assembly

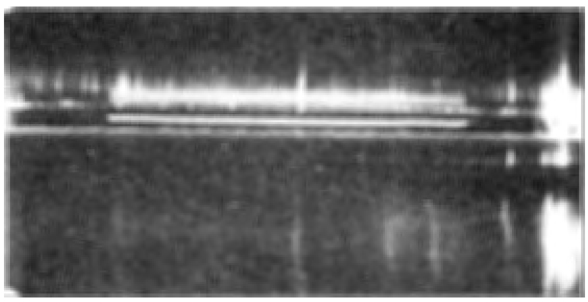

Fig. 6. A typical smoke test where the smoke is introduced into the sample layer and illuminated through the transparent chamber wall.

3. RESULTS OF MEASUREMENTS AND DISCUSSIONS

Silver Iodide. This compound was selected because its ice nucleating characteristics have been most extensively investigated in the past. Smoke particles of AgI were prepared by heating the compound on a platinum wire. The average size of the smoke particles was 0.04 μm. Although tests were made with AgI smoke particles generated in the room air, their behaviors did not differ appreciably from those generated in filtered air. Fig. 7 shows the results of nucleation tests with AgI nuclei. The mechanism of ice nucleation under these conditions is apparently condensation-freezing. From the figure, it is clear that more supersaturation with respect to water (S_W) is needed for the ice nucleation to take place as T increases.

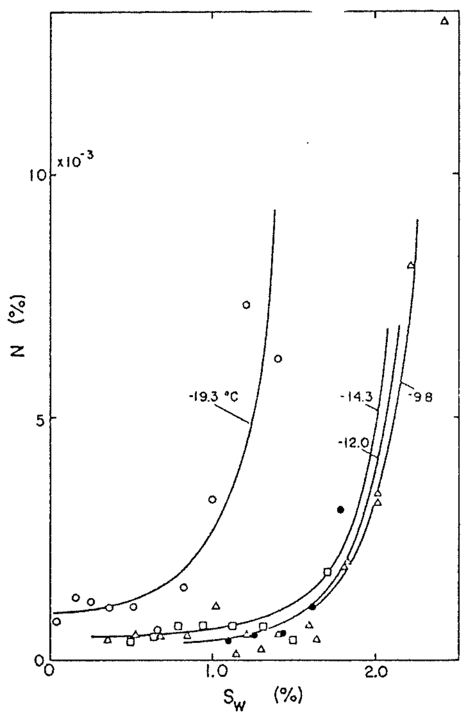

Fig. 7. Fraction of activated AgI particles plotted as a function of supersaturation with respect to water under different temperatures.

At temperatures above -15°C, significant increase in number of nucleation occurs as S_W exceeds 1.5%. Since it is rare for S_W to exceed 1% level in natural clouds, majority of AgI particles are likely to remain unactivated in seeded clouds unless other ice nucleation mechanisms are activated. This in turn suggests the danger of transient S_W for testing AgI nuclei in the laboratory.

Natural ice nuclei. Preliminary investigation of natural ice nuclei at temperatures between -16 and -21°C showed that they are scarcely dependent on supersaturation within the range between -1% and 1% S_W. The reason is not yet clear. However, it is possible that due to the long period of time the natural ice nuclei have existed in the atmosphere, many of them must have coagulated with hygroscopic particles or the like, so that they absorb a substantial amount of water at around water saturation, providing the necessary supercooled water for freezing nucleation to take place.

On March 4, 1980, the outdoor air was sampled before and during a snow shower. The chamber was operated with the sample air temperature at -20.0°C and S_W ranging from 0.0% to 2.8%. Shortly before the arrival of the shower, an ice nucleus concentration of 10 ℓ^{-1} was recorded, but when the precipitation arrived, the count went down to below 1 ℓ^{-1}. Again, we observed little supersaturation dependency with the sample natural nuclei.

Research on natural and artificial ice nuclei using this chamber is continuing in our laboratory.

REFERENCES

Fukuta, N., and V. K. Saxena, 1979: A horizontal thermal gradient cloud condensation nucleus spectrometer. J. Appl. Meteor., 18, 1352-1362.

Hudson, J. G., and P. Squires, 1973: Evaluation of a recording continuous cloud nucleus counter. J. Appl. Meteor., 12, 175-183.

Saxena, V. K., J. N. Burford and J. L. Kassner, 1970: Operation of a thermal diffusion chamber for measurements on cloud condensation nuclei. J. Atmos. Sci., 27, 73-80.

Schaller, R. C., and N. Fukuta, 1979: Ice nucleation by aerosol particles: Experimental studies using a wedge-shaped ice thermal diffusion chamber. J. Atmos. Sci., 36, 1788-1802.

Sinnarwalla, A. M., and D. J. Alofs, 1973: A cloud nucleus counter with long available growth time. J. Appl. Meteor., 12, 831-835.

Tomlinson, E. M., and N. Fukuta, 1979: Aspect ratio of thermal diffusion chambers. J. Atmos. Sci., 36, 1362-1365.

CALIBRATION AND APPLICATION OF TWO KNOLLENBERG OPTICAL PARTICLE COUNTERS

D. M. Garvey*
R. G. Pinnick
and
C. W. Bruce

US Army Atmospheric Sciences Laboratory
White Sands Missile Range, New Mexico, USA

1. Introduction

Pinnick and Auvermann (1979) have provided detailed response characteristics for two Particle Measuring Systems (PMS) light-scattering aerosol counters. They have pointed out that determination of particle size from the instrument response is indirect because of the dependence of the response on other properties of the particles, namely particle shape and complex index of refraction. Even for particles of shperical shape and known index of refraction the size resolution of the counters is reduced because in the region where particles have sizes comparable to the radiation wavelength, resonance effects can produce a multivalued response.

The purpose of this paper is to describe the response characteristics of two other PMS light scattering counters, the Active Scattering Aerosol Spectrometer Probe (ASASP-X) and the Forward Scattering Spectrometer Probe (FSSP 100). The work was motivated by a desire to use the counters to characterize the smokes and resultant fogs produced by pyrotechnics designed to generate large quantities of cloud condensation nuclei. Preliminary results of measurements with the ASASP-X on dry smoke particles are described.

2. The Particle Counters

A description of each of the PMS optical counters has been given by Knollenberg (1976). The ASASP-X is specified by the manufacturer to size particles from 0.09 to 3.00μm diameter. It differs from other PMS optical scattering counters in that it hydrodynamically focuses the particle stream through the central portion of a laser beam. All of the particles passing through the instrument are counted; no attempt is made to further define an active sampling cross-section by means of a masked slit and depth-of-field or time-of-flight considerations. The absolute concentrations measured by the ASASP-X are therefore as accurate as the measurement of the flow rate through the instrument. Because the size range of the ASASP-X is limited to particles with diameters less than 3.0μm, distortions of the aerosol size spectrum caused by anisokinetic sampling and/or sedimentation are minimal. There may be a potential problem of partially or even completely clogging the sample jet, however, if large particles should find their way into it.

It was found that proper allignment of the sample jet with respect to the laser was quite critical. Moreover, because of the design of the jet and its allignment mechanism, there was some danger of inadvertently bending the jet and causing the true allignment to change from that set by the manufacturer. Improper allignment causes particles of a given size to result in scattered light of reduced intensity because they either do not pass through the central portion of the laser beam or through the focal point of the parabolic mirror. The response to a monodispersed aerosol is then a spectrum of sizes exhibiting a "plateau" in the channels below that corresponding to the acutal size. With proper allignment a sharp peak is obtained.

The FSSP-100 is specified by the manufacturer to size particles from 0.5 to 47μm diameter. In the FSSP the depth of field over which particles are counted is determined by comparing paired signals from scattered light passing through a circular aperture and an annular aperture created using a circular mask. In our instrument the depth of field is defined to be 3.07mm by the relative gain ratios between these two signals. Particles passing through the edge of the laser beam, which would result in pulse amplitudes less than that resulting from the same particle passing through the center of the beam, are rejected using a transit-time analysis scheme. For our instrument the actual beam width is reduced from 0.193mm to an effective beam width of 0.112mm. Distortions of the aerosol size spectrum caused by anisokinetic or other sampling errors are dependent on the manner in which the instrument is used; they are not addressed in this paper.

3. Theoretical Response Calculations

The response calculations, based on Mie theory, employ the same methods as those outlined by Pinnick and Auvermann (1979). For a polarized plane wave having wave-number $\underline{k}$ $\underline{k}$ $(=\frac{2\pi}{\lambda})$ incident on a sphere with radius $\underline{r}$, the scattering cross-section for radiation scattered into a solid angle having axial symmetry with respect to the incident beam is:

$$R = \frac{\pi}{k^2} \int_\alpha^\beta \{|S_1|^2 + |S_2|^2\} \sin\theta d\theta,$$

where S_1 (x, m, θ) and S_2 (x, m, θ) are the Mie scattering amplitude functions corresponding to

*National Research Council Senior Research Associate on leave from Colorado State University, Fort Collins, Colorado.

light polarized with electric vector perpendicular and parallel, respectively, to the plane of scattering. They depend on the particle size parameter $\underline{x} = \underline{kr}$, the refractive index $\underline{m}$, and the scattering angle $\underline{\theta}$. For the FSSP the integration is from $\alpha = 3^0$ to $\beta = 13^0$.

Because the scattering for the ASASP-X is for a particle in the standing wave within the active cavity of a laser tube, the scattering amplitude S' is calculated by adding the Mie scattering amplitudes for plane waves traveling in opposite directions: $S'(\theta) = S(\theta) + S(\pi-\theta)$. The response is then

$$R = \frac{\pi}{k^2} \int_\alpha^\beta \{|S_1(\theta) + S_1(\pi-\theta)|^2 + |S_2(\theta) + S_2(\pi-\theta)|^2 \sin\theta d\theta.$$

For the ASASP-X the integration is from $\alpha = 35^0$ to $\beta=120^0$. It should be noted that no correction has been made for the fact that the inlet and outlet sample jets protrude into the collecting optics and reduce in a small but complicated fashion the solid angle over which scattered light is detected.

4. Calibration Results

Response characteristics for the ASASP-X have been calculated for spherical particles of non-absorbing substances having indices of refraction from 1.33 to 1.74. Calculations have also been made for highly absorbing nigrosin dye particles having a complex index of refraction (m = 1.67-0.26i). Response characteristics have been measured for monodispersed latex particles (m = 1.59) and for nigrosin dye particles generated using a Bergland-Liu vibrating orifice device.

The measured responses of the ASASP-X for latex particles of 23 different sizes are superimposed on the theoretical response curve for polystyrene (m = 1.592) in Fig. 1. The particle sizes are those provided by Dow Chemical or Particle Information Services. All were generated by nebulizing hydrosol samples diluted with distilled water using a Royco Model 256 Aerosol Generator. Some of the particles were actually polyvinyltoluene or styrene/vinyl toluene, which have indices of refraction slightly different from that of polystyrene. Theoretical response curves were determined for these substances, but the differences from the curve of Fig. 1 were so slight as to be experimentally indistinguishable. The response voltages were determined from the measured peak channel readings, the relative gain ratio for each of the four size ranges, and the manufacturer's discriminator levels for each range provided with the instrument manual. They were calculated relative to a reference level of 10 volts corresponding to the upper limit of the highest channel in Range 0. Each experimental value given in Fig. 1 is based on the estimated center of size-frequency histogram. The upper and lower bounds for each measurement were determined from the breadth of the size-frequency histograms. The differences between the upper and lower bounds correspond to as many as 5 channels

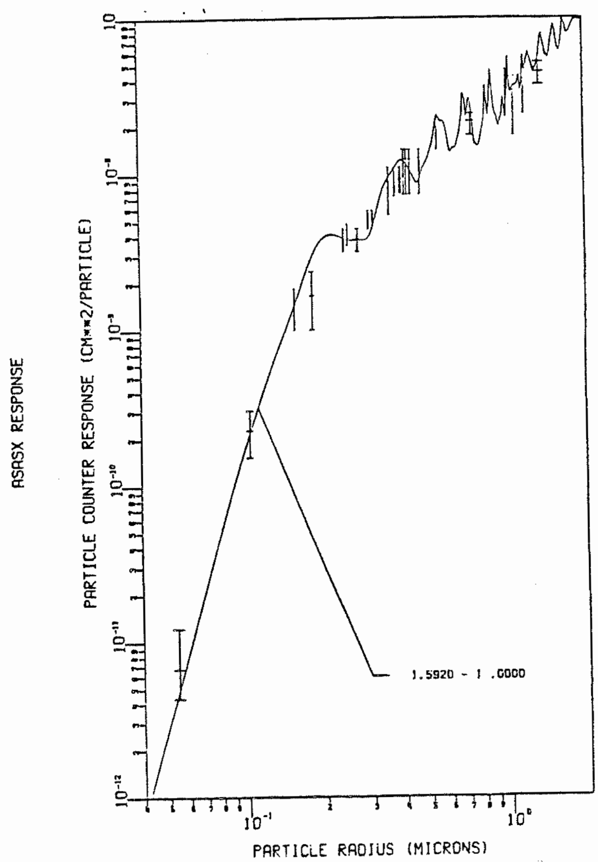

Figure 1. Comparison of theoretical ASASP-X response curve for polystyrene spheres with measured response for monodispersed latex particles of 23 different sizes. Normalization constant is $5.2 \times 10^{-9} cm^2/volt$ (See text).

and as few as 1. In cases where the size-frequency histogram overlapped two ranges, the lower bound was determined from the more sensitive range and the upper bound from the less sensitive range.

In general the experimental results for latex particles bear out the theoretical prediction quite well. The theoretical resonance peaks, however, are not resolved experimentally. In only two cases did a particle of a given size clearly result in a response less than that of particles of a smaller size. The normalization constant employed in fitting the experimental data to the theoretical response curve of Fig. 1 is: 1 volt $= 5.2 \times 10^{-9} cm^2$. Instrument response to aerosols of other materials, not all of which were spherical, was determined relative to this normalization.

Both the theoretical calculations and the experimental results for nigrosin dye indicate that the ASASP-X will considerably undersize highly absorbing particles of radii greater than 0.15μm. For example, the theoretical prediction indicates that a 1μm nigrosin dye particle will produce the same response as a polystyrene latex particle of radius just slightly greater than 0.3μm. Experimentally, the ASASP-X has a very limited resolution capability for nigrosin particles with radii from ∿0.15 to ∿0.50μm. All particles with radii in this range produce a pulse which falls in one of three channels, (4, 5, or 6 of Range 1). Again there is no experimental evidence that the resonance peaks evident in the theoretical response curve can, in fact, be resolved by the instrument.

At the time of this writing, calibration of the FSSP with monodispersed glass beads and latex spheres has not yet been completed. So the question remains open as to whether the resonance peaks predicted theoretically for particles of radius near 1μm (Fig. 2) will be evident. Particularly important for our purposes are the differences in response for particles having an index of refraction of 1.33 (water) as opposed to that for particles having indices near 1.50 (NaCl, KCl, and phosphoric acid) because as these hygroscopic particles absorb water and become solution drops, their indices of refraction will approach that of water and alter the response of the FSSP. For example, it can be seen that a water droplet 0.8μm in radius should

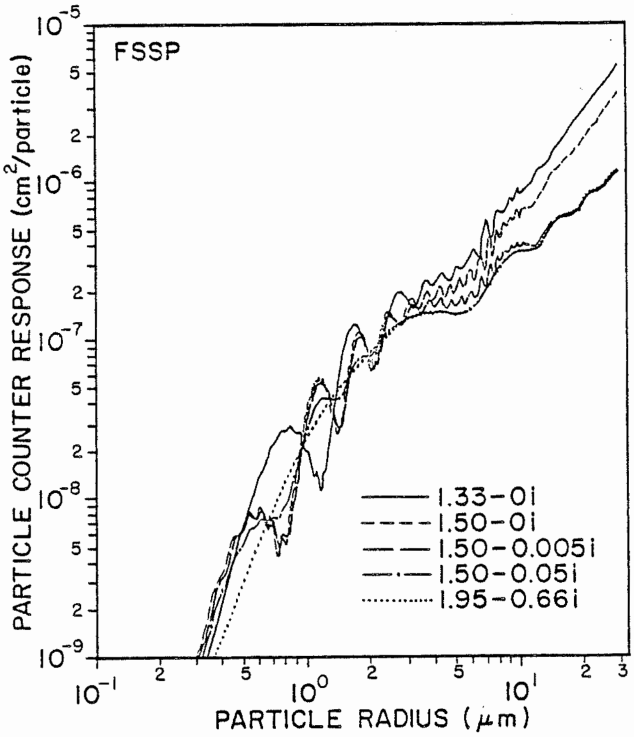

Figure 2. Theoretical FSSP response curves for spherical particles having specified indices of refraction (from Pinnick and Auvermann, 1979).

exhibit a response about 5 times greater than the same size particle of KCl (m = 1.49) while a water droplet 1.2μm in radius should exhibit a response about 5 times less than the same size particle of KCl. The calibration results of Pinnick and Auvermann (1979) for the PMS Classical Scattering Aerosol Spectrometer Probe (CSASP) suggest that such effects will be experimentally resolvable.

5. Dry Particle Measurements

Preliminary measurements using the ASASP-X have been made of the smoke particles produced by Salty Dog (predominantly KCl and NaCl) and White Phosphorus pyrotechnics. Following the manufacturer's calibration, the peaks in the particle size distributions (dN/dD) for laboratory measurements have been found to be between 0.25 and 0.45μm diameter. Field measurements of phosphorus smoke have yielded greater variability, the peaks in the number versus size distributions ranging from less than 0.2μm to greater than 0.5μm diameter. It is evident that as these particles are exposed to environments of varying humidities and grow by condensation they will pass through the size range for which the FSSP demonstrates pronounced theoretical resonance effects. Until the results of the FSSP calibration are known, it would appear prudent to use the ASASP-X to size haze-fog particles up to 3.0μm diameter and to employ the FSSP only for larger sizes.

References:

Knollenberg, R. G., 1976: Three new instruments for cloud physics measurements: The 2-D Spectrometer, the Forward Scattering Spectrometer Probe and the Active Scattering Aerosol Spectrometer. Preprints International Cloud Physics Conf, Boulder, CO, 544-561.

Pinnick, R. G., and J. J. Auvermann, 1979. Response Characteristics of Knollenberg Light-Scattering Aerosol Counters. J. Aerosol Sci., 10, 1, 55-74.

MEASUREMENTS OF RELATIVE HUMIDITY IN FOGS AND CLOUDS

H.E. Gerber

Naval Research Laboratory
Washington, D.C. 20375, U.S.A.

1. INTRODUCTION

A new instrument, a saturation hygrometer, has been developed to measure relative humidity (RH) between 95% and 105%. The purpose of this paper is to present results of the first measurements with the hygrometer which were made in radiation fog. These measurements demonstrate the unique capabilities of the hygrometer, and they provide new insights into the microphysics of such fogs. A brief description of the hygrometer is given first, details are found elsewhere (Gerber, 1980). Also given are some results of modelling the performance of the hygrometer in cumulus clouds.

2. INSTRUMENTATION

The saturation hygrometer shares some characteristics with the well-known dew-point hygrometer: A droplet deposit on a mirror responds to the ambient RH, and a thermo-optical servo system regulates the deposit. However, the new instrument differs in two important aspects: The deposit of droplets is regulated by heating the mirror instead of cooling it, and the exchange of water vapor with the mirror is carefully controlled to occur only on predetermined condensation sites instead of relying on an uncontrolled formation of dew. The latter aspect is critical, since uncontrolled dew formation causes about a 0.2C uncertainty in dew-point hygrometer measurements (Wylie et al. 1965). Controlled condensation permits the temperature of the new hygrometer to be established to within about 0.005C which corresponds to the supersaturations S (a few hundredths of 1%) thought to exist in fogs.

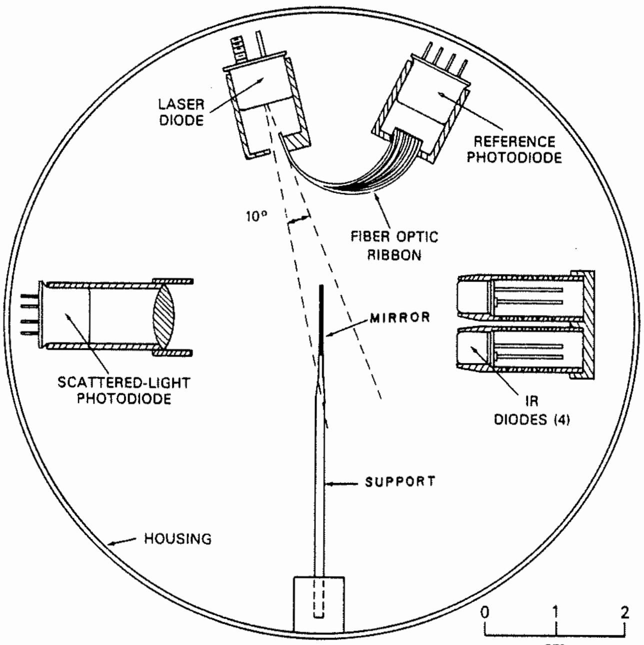

FIGURE 1. Head-on view of the hygrometer sensor head.

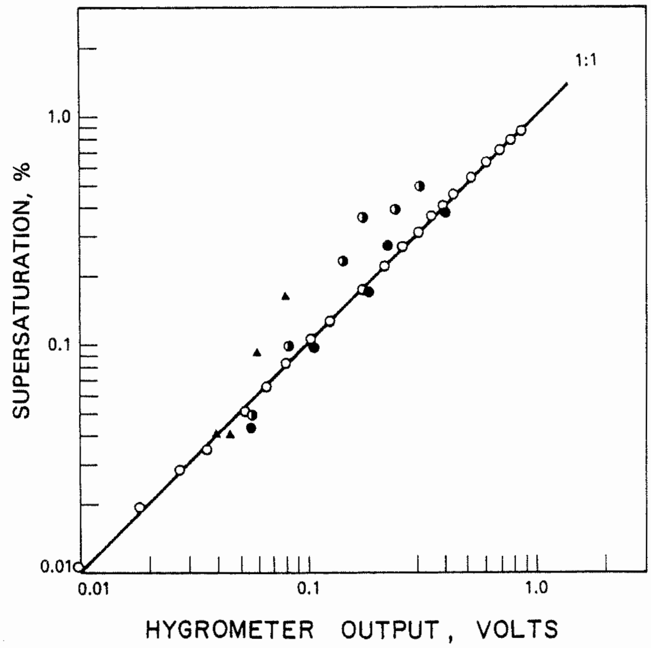

FIGURE 2. Results of laboratory calibration of the hygrometer for supersaturations.

The droplet deposit of the new hygrometer is controlled by first coating the mirror with a hydrophobic film and then coating the film with presized salt condensation nuclei. For ambient RH greater than the deliquescent point of the salt, the nuclei grow into salt-solution droplets; and due to the energy barrier imposed by the Kelvin effect, little water vapor exchange occurs between the atmosphere and the hydrophobic mirror surface between the droplets.

The hygrometer is calibrated by exposing it to a precise and constant value of RH. This done by placing the hygrometer into a "wet" box which consists of an insulated container with inner walls wetted with distilled water. After enough time has elapsed, the RH in the box closely approaches 100%. During use of the hygrometer in the atmosphere, the mirror is heated whenever RH ≥ 100%. The heat, controlled by a servo loop, is supplied in an amount which causes the droplets on the mirror to remain at their calibration size (their size at 100% RH). The temperature increase of the mirror is then related directly to the value of the ambient S through saturation-water-vapor tables. (This technique enhances the stability of the mirror droplet deposit, since the salt-solution droplets cannot become "activated" and must remain at a "haze-droplet"size, and the scavenging of

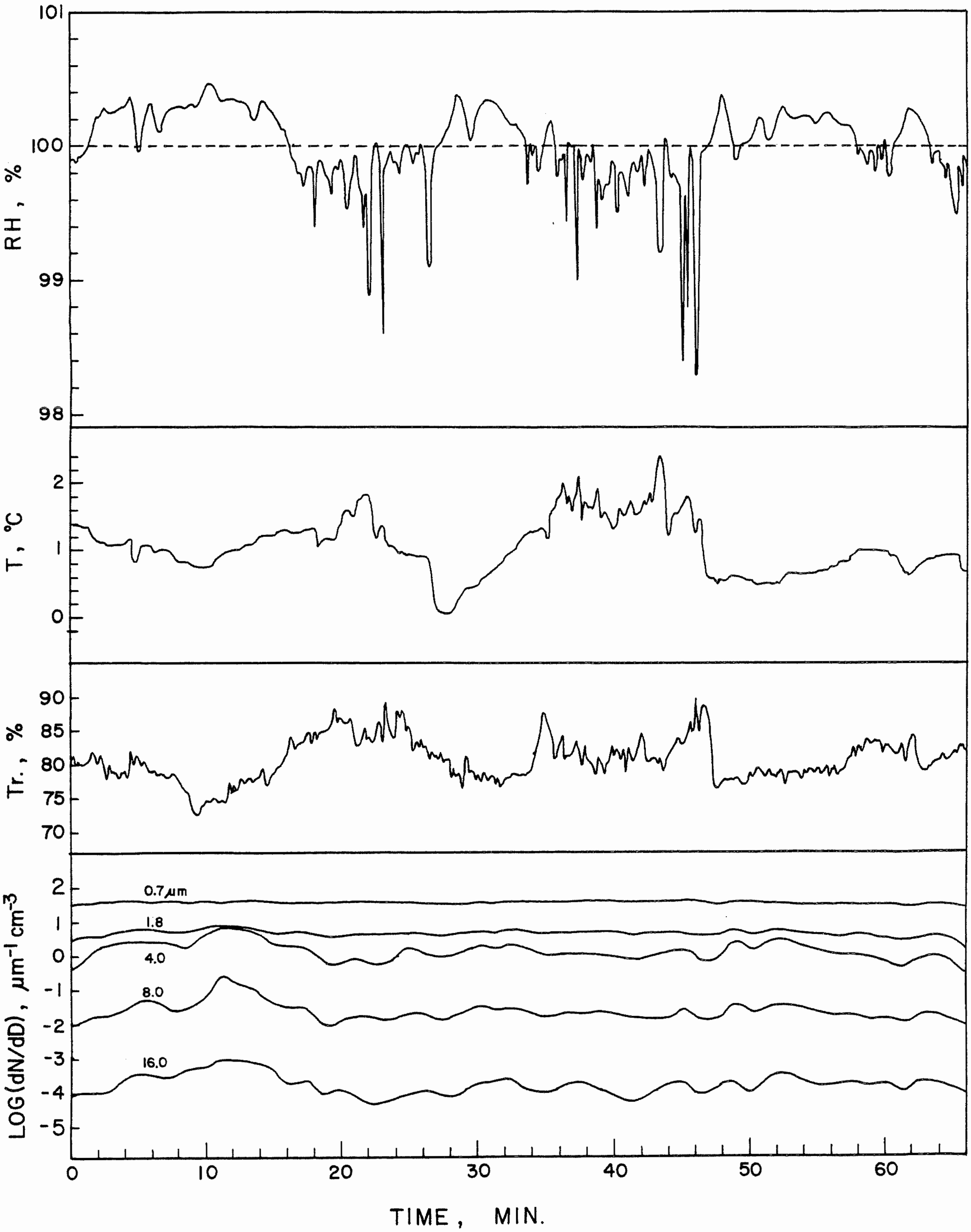

FIGURE 3. The time dependence of the various quantities measured in radiation fog on 20 November, 1979. The time response of the hygrometer for the relative humidity (RH) measurements greater than 100% differs from the response for RH< 100% (explained in the text). The temperature (T) was measured with a thermistor with a still-air response of 10 sec. A transmissometer provided transmission (Tr.) values at a light wavelength of 632.8 nm. The droplet size distribution(dN/dD) was measured with a Royco particle counter which sampled for 60 sec before providing each set of 5 data points.The path for Tr. was 45-m long.

ambient aerosols by the mirror is minimized.) For measurements less than the calibration RH, the size of the droplets on the mirror must be sensed; it is possible with the "wet" box to precisely set the calibration point at a value of RH < 100%, e.g., at 98%.

The components of the hygrometer sensor head are shown in Fig. 1. The mirror consists of a thin square metal foil with its long dimension parallel to the direction in which the aspirated air is drawn into the cylindrical housing. The mirror is mounted on a support which has a low heat conductance, and a droplet guard (not shown) prevents the accumulation of fog or cloud droplets on the mirror's leading edge. Laser light scattered by the droplets is measured by a photodiode, and the mirror is heated on its other side with infrared diodes. The housing and mirror coatings are so designed to cause negligible errors from heat conductance and black-body radiation exchanges.

Figure 2 shows laboratory calibrations of the hygrometer. The open data points relate measured temperature increases of the mirror to S values determined from water-vapor tables, and the other points are measurements of S produced in a continuous-flow thermal-gradient diffusion chamber. The calibration for RH < 100% is not shown. The same hygrometer mirror was exposed for 4 hrs. to S in the laboratory, for 2 weeks to aerosols in room air, and for 7 hrs. during measurements in fog. Since the optical characteristics of this mirror's salt-solution droplet deposit did not change noticibly during this time, it can be concluded that the inevitable deterioration of the mirror deposit is longer than the time scale of useful measurements. If it does deteriorate, it can easily be replaced.

3. MEASUREMENTS IN RADIATION FOG

On 19 and 20 Nov. 1979 humidity measurements were made 1 m over a relatively flat and tree-less grassy area located near Reston, Virginia. Typical radiation fog (visual range, 200-800 m) formed on both those nights when the area was experiencing the low winds (mostly < 0.5 m sec^{-1}) and clear skies of a high pressure cell. Figure 3 shows the quantities measured in the fog during 0400-0506 on 20 Nov., this time period is typical of the behavior of the fogs during 7 hrs. of observation.

The most pronounced feature of Fig. 3 is the rapid and large fluctuations seen in the RH measurements. (The reader should not be misled by the smoother curves for RH > 100% as compared to RH < 100%; the response time of the instrument accounts for this difference, since this time was 5 sec for RH < 100% and 30 sec for RH > 100%. By increasing the gain of the servo system, the fine structure was also evident for RH > 100%, however this caused overshoot in the readings. Future measurements will show a 1-sec response for both RH ranges.) Excursions of RH into the supersaturation regime were brief and rapid (faster than shown here), with maximum values of several tenths of 1%. The mean RH over a 4 hr. period ending with the Fig.-3 data showed that conditions in the fog were subsaturated (99.83%) on the average. Figure 3 shows RH and temperature 180° out of phase; however, the specific humidity is in phase with the temperature. The latter holds when the heat and moisture fluxes are in the same direction (Schmitt et al. 1979), downward in this case. Clearly, turbulence plays a major role in this radiation fog. This gives credence to the "classical" theory of fog formation (e.g., see Rodhe, 1962) where the turbulence mixes nearly saturated air parcels at different temperatures. Another theory for radiation-fog formation (Brown and Roach, 1976; Roach, 1976a) where supersaturations of a few hundredths of 1% are formed near droplets cooling by black-body raddiation, appears not to apply here. Nor does it appear necessary, as required by the fog model of Roach and co-workers, for droplet sedimentation losses to the ground to play a major role, since RH in this fog remains on the average just below saturation so that an excessive water content does not develop. The fog of 20 Nov. showed persistent periodic oscillations which were also reported by Roach (1976b). The The oscillations are most evident in the RH record, and they have a mean period of 18 min.

To successfully model this type of fog it is not sufficient to only know CCN spectra at low supersaturations, as for example, measured with the Laktionov (1972)-type haze chambers. It is necessary to establish CN and CCN spectra from several % of RH < 100% to a S of several tenths of 1%. Further, these models must incorporate the influence of turbulence on the broadening of the fog-droplet size distribution which appears to play a very important role here. The transmissometer record which was resolved to 0.2 sec (not shown here; all data in Fig. 3 is resolved to 12 sec.) persistently showed changes which correspond to eddies as small as 10 cm. This granularity in the fog is probably due to small turbulent eddies, although the release of latent heat in areas of droplet "activation" and the accompanying changes in air buoyancy may contribute. The turbulence appears sufficiently strong and rapid that the "finite-phase-relaxation-time" droplet-broadening effect (e.g., Clark and Hall, 1979) may also be important.

It is of interest to continue these RH measurements to obtain results which are based on more than two occurrences of radiation fog, and to study other types of fogs including those where modelling has had reasonable successes (e.g., Fitzgerald, 1978; also Fitzgerald in these proceedings).

4. MEASUREMENTS IN CLOUDS

No direct measurements in clouds have yet been made with the new hygrometer. Instead, the performance of the hygrometer was modelled for the hypothetical case where the instrument is imbedded in an atmospheric updraft and is permitted to move through the base and lower portions of a cumulus cloud. The RH values given by the hygrometer are compared to the predicted variation of S with time, and the physical characteristics of the hygrometer are varied in the calculations to discover its optimum performance. The effects of salt-nucleus size, heat conduction to the mirror support, radiation energy exchanges, interactions with ambient cloud droplets, and mirror thermal properties were evaluated. The theoretical treatment will not be repeated here, since it

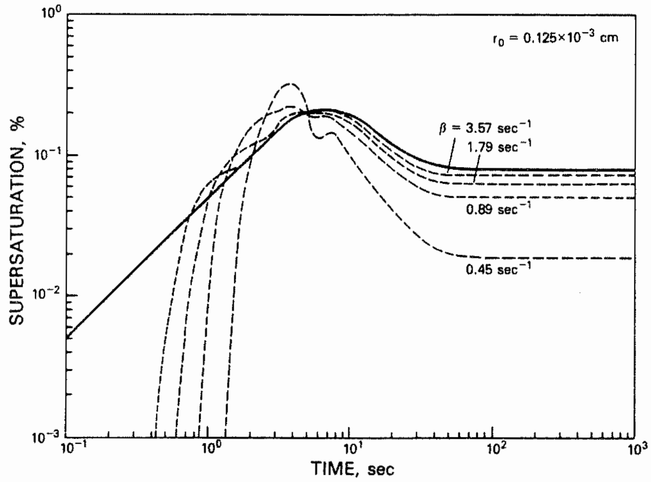

FIGURE 4. Calculated responses (dashed curves) of the hygrometer as it rises imbedded in an updraft of 1 m sec^{-1} through the base and lower portions of a continental cumulus cloud. The hygrometer reacts to the predicted supersaturations given by Fletcher (1966) (solid curve). The calculated curves are for the hygrometer mirror coated with salt nuclei which give droplets of size $r_o = 0.125 \times 10^{-3}$ at the calibration RH of 100%. The thermal properties of the mirror are combined in $\beta = 2h/\rho c\delta$, where h is the unit surface heat conductance, ρ is the density, c is the specific heat, and δ is the thickness of the mirror. Given that a tantalum mirror is used, the four values of β in the figure correspond to mirrors with four different values of δ: 1.27×10^{-3} cm, 2.54×10^{-3} cm, 5.08×10^{-3} cm, and 1.02×10^{-2} cm.

is given elsewhere (Gerber, 1980).

Figure 4 shows the hygrometer's predicted performance which indicates that a judicious choice of materials and dimensions in the construction of the hygrometer will permit balloon-borne in-cloud measurements of RH which do not excessively distort the actual RH values. The principal sources of error are the finite growth time of the solution droplets on the mirror, and the lag of the hygrometer-mirror temperature behind the ambient temperature which cools as the air and hygrometer move upward in the cloud. The latter error shows up primarily in the asymptotic region of Fig. 4 where time is large, the thickest mirror shows the greatest error.

Measurements from aircraft are also feasible if the compression heating of the air accelerated to aircraft speed can be adequately compensated.

5. REFERENCES

Brown, R., and W.T. Roach, 1976: The physics of radiation fog:II- a numerical study. Quart. J. R. Met. Soc., 102, 335-354.

Clark, T.L., and W.D. Hall, 1979: A numerical experiment on stochastic condensation theory. J. Atmos. Sci., 36, 470-483.

Fitzgerald, J.W., 1978: A numerical model of the formation of droplet spectra in advection fogs at sea and its applicability to fogs off Nova Scotia. J. Atmos. Sci., 35, 1522-1535.

Fletcher, N.H., 1966: The Physics of Rainclouds. Cambridge University Press. 390 pp.

Gerber, H.E., 1980: A saturation hygrometer for the measurement of relative humidity between 95% and 105%. J. Appl. Meteor., submitted.

Laktionov, A.C., 1972: A constant temperature method of determining the concentration of cloud condensation nuclei. Ivz. Atmos. Ocean. Phys., 8, 672-677.

Roach, W.T., 1976a: On the effect of radiative exchange on the growth by condensation of a cloud or fog droplet. Quart. J. R. Met. Soc., 102, 361-372.

Roach, W.T., 1976b: On some quasi-periodic oscillations observed during a field investigation of radiative fog. Quart. J. R. Met. Soc., 102, 355-359.

Rodhe, B., 1962: The effect of turbulence on fog formation. Tellus, 14, 49-86.

Schmitt, K. F., C.A. Friehe and C.H. Gibson, 1979: Structure of marine surface layer turbulence. J. Atmos. Sci., 36, 602-618.

Wylie, R.G., D.K. Davies and W.A. Caw, 1965: The basic process of the dew-point hygrometer. Humidity and Moisture , ed. R.E. Ruskin, Reinhold Pub. Co., 125-134.

INVESTIGATION OF SPATIAL DISTRIBUTION OF DROPLETS IN FOG BY HOLOGRAPHIC METHODS

K.E.Haman[1] and A.Kozikowska[2]

[1] Institute of Geophysics, University of Warsaw
[2] Institute of Geophysics, Polish Academy of Sciences
Warsaw, POLAND

1. Introduction

The assumption, that droplets of any size class in clouds or fogs are randomly distributed in the space is a basic one for the classical coalescence theory. However, various mechanism of droplet separation, selection and clustering, due to superimposed effects of air motion, gravity and electrical interactions, may make this assumption unvalid. The most straightforeward method of verification of this assumption is finding the positions of droplets in a sample of air and analysing them statistically. The only technique which seems suitable for that purpose is holography. The first device for making holograms of fog droplets was built in USA in 1966 (Thompson et al., 1966) and used for measuring droplets size spectra, but essential developement of holographic techniques since this time, has not improoved especially their applicability for small particles and droplets imaging. Holography of fog and cloud samples appears to be a very laborious and time consuming technique and it is very difficult to obtain images of quality suitable for fully automatic analysis.

In order to avoid numerous technical difficulties at the very beginning of the work, the authors decided to start their study from investigation of spatial distributions of droplets in radiative and advective fogs at Central Geophysical Observatory of the Polish Academy of Sciences in Belsk near Warsaw, where relatively good technical facilities were available. The authors are indebted to dr.S.Puchalski, the leader of the Atmospheric Optics Division at the Belsk Observatory, for his valuable support and assistance in realisation of this project.

2. Registration of holograms

The scheme of the device built for recording the holograms of fog samples is presenten in Fig.1. The light beam from a ruby laser (1) (single TEM_{00} mode pulse of about 0.5mJ energy and 20 ns duration) becomes slightly divergent (apex angle 0.05°) after passing throgh the lens (2) and a 67µm pinhole (3). The holograms have been recorded in a Gabor-type arrangement, which is the simplest and most frequently used for small particle holography. The beam is guided outside the cottage (4), where the laser (1) is located, through a 3 m long and 7 cm in diameter metall tube (5), closed at the end with a glass plate covered with dew-repealing substance. 7 cm from the end of the tube a holographic plate 6x9 cm is fixed

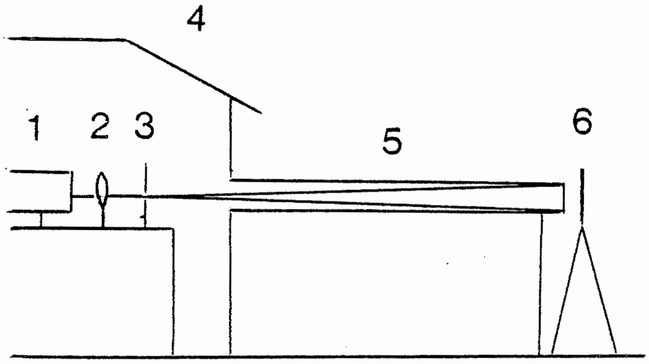

Fig.1. The scheme of recording device

casette (6). The holograms are made during foggy nights, preferably when the wind gusts are perpendicular to the tube, in order to minimize disturbances in the airflow through the sample volume located between the end of the tube and casette (6). After making a hologram of the fog, a second hologram of a system of mutually crossing 20µm tungsten wires is recorded on the same plate in order to get a fixed reference frame for determining positions of the droplets.

3. Reconstruction of the holograms

In the reconstruction process the Bexon's method (Bexon 1973) is applied. The hologram is reconstructed in a diverging beam and the magnification is attained by a purely holographic method, without using any optical elements, which may spoil the beam. The source of reconstruction beam and the image plane are fixed and the subsequent slices of the holographed sample are focused in the image plane by moving the hologram. This arrangement has the advantage of giving a good quality image, but also one important shortcoming consisting in the changes of magnification along the depth of examined sample.

The reconstruction and analysis device is schematically presented in Fig.2. It consists of a He-Ne laser (1), the beam of which passes through a microscope objective (2) and a 20µm pinhole to form a diverging beam. The holographic plate (4) is fastened to a micrometric table mounted on a havy chassis of a micrometric microscope with semiautomatic motion in both horizontal directions. Vertical motion of the plate is possible by means of a small, manually controlled micrometric table. The beam difracts on the hologram and magnified real

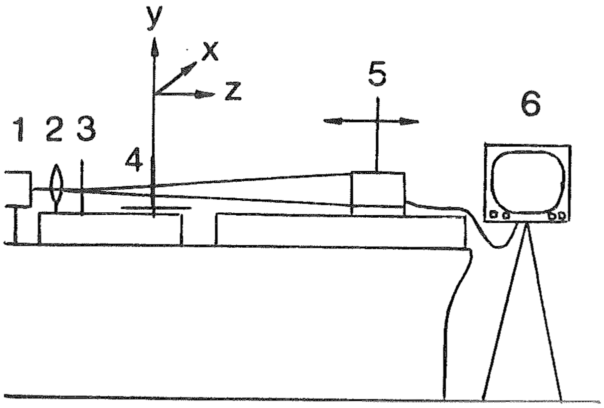

Fig.2.Scheme of the reconstruction and analysis device

images of droplets are focused on the vidicon of a high resolution,distortion-free TV camera (5) connected with the monitor (6).Analysing of the hologram consists in mooving the plate until a well focused picture of the droplet appears in the center of the monitor(6). The indications of the micrometers are then recorded,together with the diameter of the droplet estimated by means of the scale superimposed upon the screen of the monitor.The position of the vidicon is being changed few times during the scanning,in order to keep the variations of magnification smaller than 1:2. After any change in the system as well as few times during each scanning, the coordinates of holographic images of crossings of the reference wires are checked.The registered coordinates of the droplets,their sizes and coordinates of the reference points are then computer processed,in order to get the true spatial coordinates and sizes of the droplets.

Accuracy of positioning of droplet centres in x and y directions (perpendicular to the beam)depend on the quality of the micrometers and stability of the device.In our case this accuracy has been estimated about 10 μm. Positioning along the beam (z - coordinate) depends upon the sharpness of focusing and its accuracy varies in the range 50 - 100μm.Six size classes (0 < 10 < 20 < 30 < 40 < 70 <) are presently used in preliminary analyses.

4.Program of statistical analysis

The first two problems which are going to be solved are: 1) - testing,by taking and analysing a random sample of partial volumes of the hologram,whether and with what confidence level the hypothesis on the Poisson spatial distribution in given size classes can be rejected; 2) - testing,whether there exists any preference for the droplet of a partioular size to have the closest neibourgh also in a certain particular size class.

During the cold season 1979/80, 40 holograms of about 5x5x5 cm fog samples, containing 100 - 1000 droplets each, have been taken,and very laborious analysis of them is going on.

At the time this paper is being written,definite numerical results are not yet available, though it seems that there are considerable inhomogeneities in the spatial distribution of fog droplets,even on the scale of relatively small volume of a fog sample.However,the authors are aware of the fact that this may be a result of particular conditions in which the holograms were made.

Further program consists in making a mobile recording device and taking samples of low stratus (from high buildings); eventually investigation of micromotions of the droplets by means of double exposure.

General view of the reconstruction and analysis device and pictures of droplets and re-ff ference points images on the monitor screen are presented in the Figs 3 - 5.

References

Bexon R.,1973.Magnification in aerosol sizing by holography,Journ.Phys.Ser.Sci.Instr.6, 245 - 248.

Thompson B.J.,Parrent G.B.,Ward J.H.,Just B.,1966, A readout technique forvthe laser fog disdrometer.Journ.Appl.Meteor,5,343 - 348.

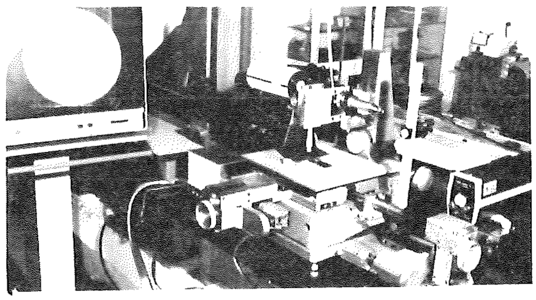

Fig.4 General view of the reconstruction and analysis device.

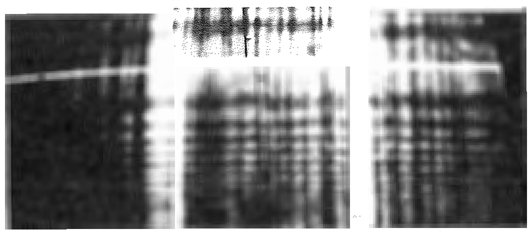

Fig.4. A reconstructed image of refernce wi- on the sreen of the monitor

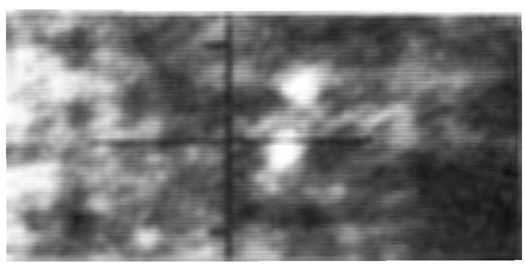

Fig.5.A reconstruted image of a 15um droplet recorded in a double impulse

A NEW AIRBORNE, FAST-RESPONSE THERMO- AND PSYCHROMETER

K.E.Haman and A.Makulski

Institute of Geophysics, University of Warsaw
Warsaw, POLAND

1. Introduction

Despite of considerable progress in cloud physics airborne instrumentation achieved in recent years, there still exists need for relatively simple and cheap but yet precise and reliable instruments for measuring even so basic parameters like temperature and humidity, especially from small aircrafts. Particularily measurements of humidity yield some problems, since classical sensors like hair or Goldbeater skin are too slow and inacurate. From commonly used more modern solutions, automatic condensation hygrometer may be for certain purposes too slow, Lyman-α hygrometer, though virtually inertialess is relatively complicated and requires permanent check of reference level, while thin-film hygristors or capacitors are sensitive to temperature fluctuations and require individual calibration.

One of the methods which are sometimes considered as alternative, is psychrometry based upon fine thermistors or thermocouples. However, for airborne use such psychrometers have considerable drawbacks. Dry and wet sensors have usually different time constants and this difference varies with pressure and temperature, making such measurements difficult for interpretation. Their accuracy falls down with temperature and the wet sensor is usually sensitive to contamination.

In this paper a new method of adopting the psychrometry to fast response humidometers, suitable for small aircraft or truck-based mobile units, is proposed.

The principle of psychrometer based upon thermocouples (if time constant of decyseconds is required) or thermistors (if few seconds are sufficient) is retained, but the air is first suitably processed by passing through a heater, which rises (if necessary) its temperature to a level more suitable for psychrometric measurements and then through a "heat filter", which smoothes out fluctuations of dry-bulb temperature, leaving only components with periods much longer than the time constant of the dry thermometer. The heat filter is simply a fast heat exchanger with relatively large heat capacity - for instance a thick bundle of fine copper wire.

In this system the time constant of the dry thermometer does not affect the measurements; they depend now only upon the wet-bulb time constant, which is usually about 3 times smaller than that of a dry bulb of similar size. The filter helps also to reduce contamination of the wetting wick. The ambient air temperature, if needed, must of course be measured with a separate sensor.

It is easy to see, that the same principle of "heat filtering" can be applied to thin-film hygristors or capacitors, which also suffer from dry-bulb temperature variations and which for certain purposes may be more suitable than the thermocouples.

At the University of Warsaw few such instruments were built, both for small aircraft (Yak-12, "Rallye") or truck-based mobile units.

The airborne instruments were based upon thermocouples, with separate thermocouple for ambient air temperature. Allthough slightly more inert than resistance thermometers, the thermocouple has the advantage, that with point-like sensor it is less sensitive to the thermal influences of the support and can be easier protected against impact of cloud droplets. On the other hand, it is less inert and mechanically stronger than fine-bead thermistors.

The reference junctions in early models were kept in ice-water thermostate, which prooved to be operationally inconvenient and not too reliable. On the other hand the "filtered" dry-bulb temperature prooved to be so smooth, that it can be measured with a relatively slow but precise thermistor and used as a reference for the ambient air thermocouple sensor. Additionally, this thermistor can be easily built into a feedback with a small heater, which keeps the dry-bulb temperature perfectly constant, what essentially facilitates interpretation of the results if recorded in an analogue form.

These improovements were introduced into the new model of thermo-psychrometer ATP-4, designed for the 2-seater motor-glider "Ogar" or 4-seater "Rallye" aircraft.

2. ATP-4 airborne thermo-psychrometer

The general scheme of the ATP-4 instrument is presented in Fig.1. The air enters the psychrometer through the inlet (1) which is exposed directly to the speed of the aircraft (90 - 150 km/h). The housing of the inlet contains a preheater with transistors BD-176 as heating elements and a simple stabilizer with thermistor (2) inside. The preheater protects the inlet against dew and rime and roughly stabilizes the the air temperature at a certain preset level, with accuracy of few K. With small effort, this heater be turned to evaporator for total water content measurements. After leaving the inlet, the air enters the filter-stabilizer through the plastic pipe (3). The filter-stabilizer (4), is made of 300 g of enameled copper wire, 0.2mm diameter, with four BD-176 embedded in it as heaters, controlled by a feedback system with

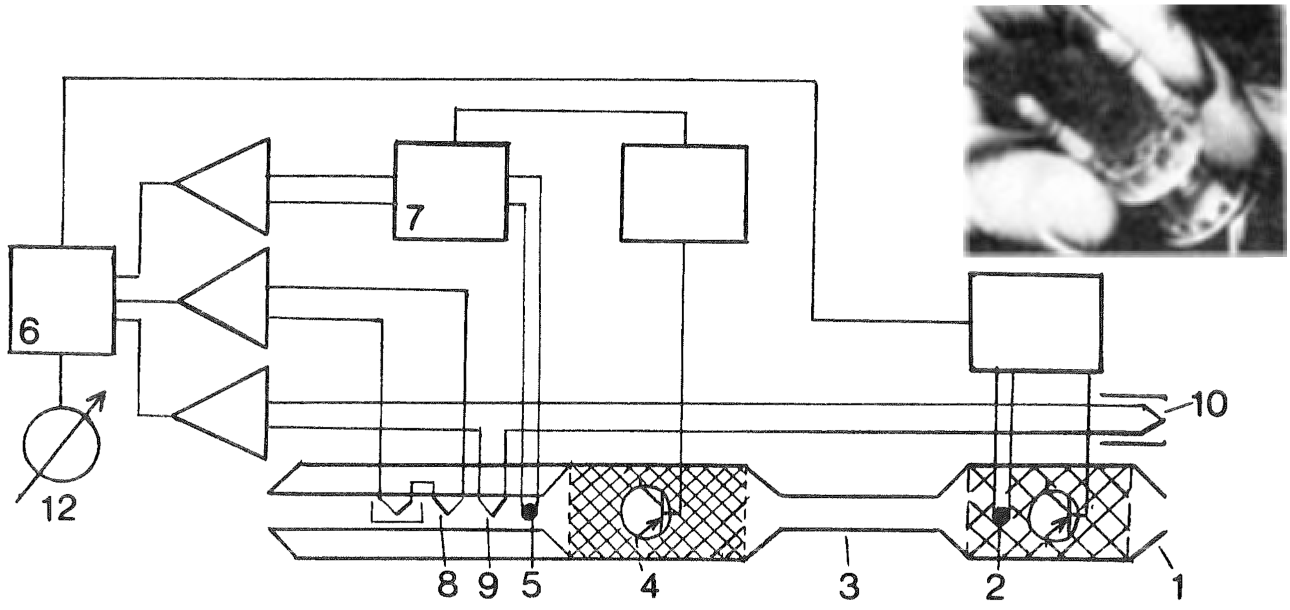

Fig.1. Scheme of the ATP-4 airborne thermo-psychrometer.In the right upper corner a picture of the exchangeable segment with thermocouples and wetting device.

thermistor (5).Direct use of transistors as heating elements essentially simplifies the design.The temperature of the heaters can be adjusted from the operator's board (6).If it is set at a level few K above the average of the preheater,the temperature of the air flowing out from the filter-stabilizer is kept constant with accuracy to 0.05K. As a passive heat filter (with heaters switched off),it has thermal time constant about 400s (for airflow rate about 300 mg/s) and smoothes out short period fluctuations of temperature practically independently of changes of ventilation caused by variable flight conditions.The thermistor (5),placed within easily exchangable plexiglass segment has time constant less than 3s.Its output is used to control the heaters and indicate the dry-bulb temperature.Resistance-voltage converter (7) of original design,permitts keeping the power dissipation of the thermistor below 10 µW.The differential dry-wet thermocouple (8) made of chromel-constantan 0.07mm wire has the wet point in a fine viscose wool wick,wetted withna pressure-controlled device. Its time constant is lessthan 0.5s.Another thermocouple (9) placed within one exchangeable segment with (8) is used as a reference for the ambient air temperature sensor (10).Sensors (5) (8) and (9) are ventilated with speed of about 5 m/s, what makes the wet-bulb depression practically insensitive to ventilation variations possible during flight.The thermocouples are connected to high-quality solid-state preamplifiers,well protected agains ambient electromagnetic disturbances (11).Their output signal is about 100mV/K and can be measured by means of any suitable recording voltmeter (12).The ambient air temperature sensor (10) consists of a 0.07 mm chromel-constantan thermocouple,connected with the reference point (9) by means of a doubly screened 0.7mm extension.In the new model of the sensor (10),the thermocouple is fixed 5 mm behind a 0.7 mm metall rod.It is believed,that this should create a fairly good protection against wetting the sensing point (and its close vicinity)by the cloud droplets with relatively little disturbance to the temperature indications,at least in suffiently smooth flight conditions.Tests made in a small wind tunnel were encouraging - flight tests have not been made till the time this paper is being written.

The accuracy of the instrument is not worse than 0.1K for the thermocouples and 0.05 for the thermistor (5) disregarding external sources of errors.Accuracy for humidity follows then from the psychrometric relation and should be about 0.1 - 0.2 g/kg of mixing ratio for typical summer conditions.Both the accuracy and response times of the instrument(0.5s for humidity,0.1 s for temperature) might be subjects to certain further improovements.Correction for the time needed for the air to pass through the instrument (0.1 - 0.2s) can be eventually applied.

The variant of ATP-4 instrument,which was recently built has filter-stabilizer,sensors (5),(8) and (9) mounted together in a sequence inside a duraluminum tube 480x60 mm.It can be fixed at the end of the wing ("Rallye") or inside the cabin ("Ogar"); in the latter case the ambient temperature sensor (10) and the preheated inlet (1) are fixed separately outside the fuselage and are connected with the main unit by means of flexible electrical and pneumatical extensions.However,dimensions and arrangement of various parts of the instrument can be adjusted to particular technological and operational demands.

TECHNIQUES FOR MEASURING ICE FORMING NUCLEI IN ROCKET EXHAUST CLOUDS

Edward E. Hindman II
Department of Atmospheric Science
Colorado State University
Fort Collins, Colorado 80523, USA

INTRODUCTION

The combustion aerosol from unpressured burns of Space Shuttle solid-rocket-motor propellant contains about 5 x 10^{10} ice nuclei (IN) per gram of propellant active at -20C (1,2). This measurement was made by burning slabs of propellant in a vertical wind tunnel and injecting aerosol samples into a large, isothermal cloud chamber (3). The Shuttle will burn about 5 x 10^8 g of solid propellant from the surface to approximately 3 km above the ground. Consequently, up to 10^{19} IN active at -20C could be released into the atmosphere each launch ($5x10^{10}g^{-1}x\ 5x10^8g$). For this calculation, the laboratory figure is assumed representative of IN activity in rocket exhaust clouds.

In order to test the laboratory figure, field measurements were made in the exhaust clouds from Titan III rockets and Super-HIPPO motor firings using airborne ice nucleus counters and filters (these rocket motors use solid cast-composite propellant similar to Shuttle propellant which contains primarily aluminum and ammonium perchlorate). The exhaust clouds contain high concentrations of Al_2O_3 particles, HCl gas (4), water vapor and cloud condensation nuclei (CCN) (5). This environment is foreign to the normal function of the counters and filters. The behavior of the counters and filters in solid rocket exhaust clouds is summarized in this paper. The counters measure IN values within about an order of magnitude of values expected from the laboratory measurements. Further, the filters cannot be used to characterize the IN content of the clouds.

ICE NUCLEUS COUNTERS

The first IN measurements in Titan III exhaust clouds, obtained with Mee Industries counters, demonstrated the presence of IN. Absolute values were not obtained because of instrument difficulties (6). A properly operating Mee IN counter detected a maximum of 850 ℓ^{-1} (active at -25C) in an exhaust cloud from a nozzle-up Super-HIPPO motor firing (6). According to laboratory findings from the Shuttle propellant combustion aerosol (2), the Mee IN counter and a NCAR IN counter (7) detected up to 10^3 fewer IN than the standard, isothermal cloud chamber. This result was due to larger quantities of HCl in the counters than in the chamber and shorter residence times in the counters. Consequently, the maximum IN concentration active at -25C in the Super-HIPPO cloud was approximately $8.5x10^5\ell^{-1}$ (850 ℓ^{-1} x 10^3). Using the $5x10^{10}$ g^{-1} figure for activity at -20C from the laboratory (a conservative figure for IN activity at -25C), the expected concentration of IN in the Super-HIPPO cloud is $6.0x10^5$ ℓ^{-1} ($1.2x10^7$ g propellant burned x 10^{-12} ℓ^{-1} (cloud volume)$^{-1}$ x $5x10^{10}$ g^{-1}). The measured concentration is a factor of 1.4 greater than the expected concentration. This difference is considered negligible because of the order-of-magnitude nature of the calculations.

A second set of IN measurements has been obtained in the exhaust cloud from a Titan III launch (5). A maximum of 200 ℓ^{-1} active at -20C was measured with a NCAR IN counter two hours after launch. The maximum concentrations were not detected shortly after launch because of the high concentrations of interfering HCl and CCN in the cloud. The higher the concentration of combustion aerosol, the fewer IN the NCAR counter detects as demonstrated in a laboratory test (see the table). As the Titan III exhaust cloud diluted with ambient air, its IN activity increased, a phenomenon also present in the earlier Titan III data (6). Applying the 10^3 calibration factor to the 200 ℓ^{-1} measurement produces a worst case concentration of $2x10^5$ ℓ^{-1}. The expected IN concentration in the exhaust cloud is $6.8x10^6$ ℓ^{-1} ($2.5x10^8$ g propellant burned x $5.5x10^{-13}$ ℓ^{-1} (cloud volume)$^{-1}$ x $5x10^{10}$ g^{-1}). The measured concentration is a factor of 34 less than the expected concentration.

TABLE

IN (ℓ^{-1}) Detected with NCAR IN Counter (-20C) in Combustion Aerosol from Burning Two Pieces of Shuttle Propellant

Mass of Propellant (g)	Time From Ignition (min)									
	0	1	2	3	4	5	6	7	8	9
0.1	1	4	28	4	16	24	720	600	40	1
0.003	1	240	720	Too Numerous To count	372	28	1	1	1	1

The measured and expected IN concentrations were in a reasonable agreement in the Super-HIPPO exhaust cloud and differed by a factor of 34 in the Titan III exhaust cloud. These results illustrate the imprecise state of IN measurements with portable IN counters in rocket exhaust clouds. Nevertheless, it is concluded that order-of-magnitude IN measurements can be made in exhaust clouds using the counters if the laboratory calibration factor is employed and the cloud is sufficiently dilute. Further laboratory tests are necessary to determine the required amount of dilution.

FILTERS

Filter samples have been obtained from two Titan III exhaust clouds (1,8). The filters were cut in half; one half was processed by Parungo and Allee (1) and the other half at the State University of New York at Albany (8). Parungo and Allee report detecting high concentrations of IN early in the life of both clouds and a decrease to ambient values after 3 hours. Hindman and Lala (8) report this result is consistent with their result before correcting for the sample-volume-effect (large sample volumes yielded low IN concentrations and vice versa). After correcting the data from both flights and both processes (4 data sets), the high IN concentrations decreased to background values in three of the four data sets. Consequently, this result suggests the filters might not be able to detect the IN in the exhaust clouds due to interfering HCl gas and high CCN concentrations.

Subsequent to these measurements, the filters were calibrated in the laboratory with Shuttle propellant combustion aerosol (2). It was found that the filters detected 10 to 1000 times fewer IN than did simultaneously operating IN counters. The IN counters also underestimated the numbers of IN in the combustion aerosol (2). Consequently, the laboratory results, that the filters are much less sensitive to the IN in the combustion aerosol than the counters, indicate that the filters may not be able to detect IN in rocket exhaust clouds.

The most recent filter samples obtained in the exhaust cloud from a Titan III launch (5) were collected at the same volumes following the recommendation of Parungo and Allee (1). The filters also were processed using the same apparatus as Parungo and Allee and were corrected for the sample-volume-effect. The filters detected IN concentrations in the cloud below background values shortly after launch. Concentrations slightly greater than background values were detected with the filters when the simultaneously operating IN counter detected 200 ℓ^{-1} in the dilute cloud two hours after launch. These results are consistent with the earlier Titan III filter results (8) and the laboratory findings (2). Consequently, the use of the filter technique is not an effective method for detecting IN in concentrated exhaust clouds. However, when the HCl concentrations are sufficiently low in dilute clouds, the filters should be able to detect the IN.

CONCLUSIONS

Concentrated solid rocket motor exhaust clouds should be diluted with clean ambient air in order to obtain order-of-magnitude IN measurements with portable counters. The IN concentrations measured with the counters are underestimated by a factor of about 10^3 because of interfering HCl and CCN. Filters are unable to detect IN in concentrated clouds significantly above background values due to interfering HCl and CCN. Filters have detected IN in dilute clouds, but useful numbers were not obtained because of a significant sample-volume-effect.

ACKNOWLEDGEMENTS

This work was supported with funds from the Environmental Effects Office, NASA, Johnson Space Center, Houston, Texas.

REFERENCES

1. Parungo, F.P. and P.A. Allee, 1978: Rocket effluent: its ice nucleation activity and related properties. J. Appl. Meteor., 17, 1856-1863.

2. Hindman, E.E., II, D.M. Garvey, G. Langer, F.K. Odencrantz and G.L. Gregory, 1980: Laboratory investigations of cloud nuclei from combustion of Space Shuttle propellant. J. Appl. Meteor., in press.

3. Garvey, D.M., 1975: Testing of cloud seeding materials at the Cloud Simulation and Aerosol Laboratory, 1971-1973. J. Appl. Meteor., 14, 883-890.

4. Gregory, G.L., R.J. Bendura and D.C. Woods, 1979: Launch vehicle effluent measurements during the May 12, 1977, Titan III launch at Air Force Eastern Test Range. NASA Technical Memorandum 78753, 65 pp.

5. Hindman, E.E.,II and L.F. Radke, 1979: Cloud nuclei from launches of liquid- and solid-fueled rockets. Extended Abstracts 7th Conf. on Inadvertent and Planned Weather Modification, Am. Meteor. Soc., Boston, 18-19.

6. Hindman, E.E., II, F.K. Odencrantz and W.G. Finnegan, 1980: Cloud nuclei from launches and firings of solid rocket boosters. J. Wea. Modif., in press.

7. Langer, G., 1973: Evaluation of NCAR ice nucleus counter, Part I: basic operations. J. Appl. Meteor., 12, 1000-1011.

8. Hindman, E.E., II and G.G. Lala, 1980: Comments on "Rocket effluent: its ice nucleation activity and related properties". J. Appl. Meteor., in press.

TWO NEW CCN SPECTROMETERS

James G. Hudson, Gary Keyser, and C. Fred Rogers

Desert Research Institute
University of Nevada System
Reno, Nevada, U.S.A.

1. INTRODUCTION

Two new CCN instruments which have evolved from the DRI continuous flow diffusion chamber (CFD) (Hudson and Squires, 1973, 1976) are presented. Both instruments can accurately monitor the concentration of CCN over the conventional supersaturation range between 0.1% and 1%. The first instrument accomplishes this by rapidly changing the supersaturation level within the chamber so that an entire spectrum can be obtained in a short time. The second instrument derives CCN spectra by passing the sample aerosol through a series of supersaturation zones which creates a dispersion in drop sizes which can be used to deduce the critical supersaturation of the nuclei. This second instrument then yields instantaneous spectra.

2. RAPID CYCLE CCN SPECTROMETER

The first instrument was built as a prototype for the NASA low gravity cloud physics laboratory. Rapid changes in supersaturation are accomplished by injecting a surge of fluid into the temperature-controlled plates. This displacement of fluid is at a temperature different from the original plate temperature. Thus the change in temperature of the plates is accomplished by proper mixing of an appropriate amount of fluid from a reservoir at an extreme temperature. A hot and a cold reservoir are on hand for this purpose. Microprocessor control is used to inject the fluid into the plates so that a smooth cycle of supersaturations can be obtained. Thus four or five supersaturations can be examined within a period of 5 to 10 minutes, depending upon the desired accuracy and the particle concentration. This same period of time is required just to make one change in supersaturation with the original CFD's.

Figure 1 is a schematic diagram of the rapid cycle CCN spectrometer. It is quite similar even in dimensions to the earlier versions of the CFD's. A notable exception to this is the elimination of the flow around the back sides of each plate. In this version, the carrier flow enters the chamber at the opposite end of the chamber from the optical bench (Royco 225) unlike the previous CFD's, where the carrier flow entered at the optical bench end of the chamber behind both plates only to flow toward the other end of the chamber around the plates and back between the plates. The laminar flow so accomplished is obtained in the spectrometer by the use of a diffuser screen. A stainless steel wicking surface is used instead of filter paper.

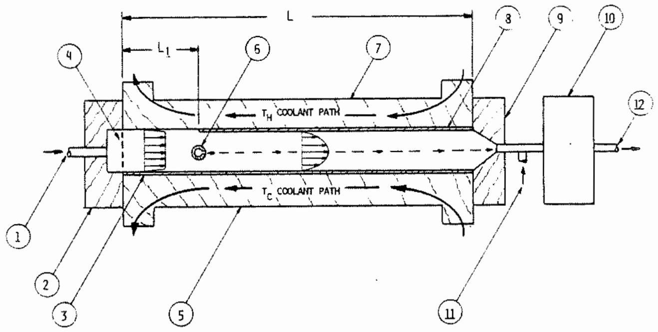

Figure 1. Physical Schematic of the Rapid Cycle CCN Spectrometer

Legend:

1. *Carrier flow entrance*
2. *Entrance manifold*
3. *Cold plate wicking surface*
4. *Diffuser screen*
5. *Cold thermal plate*
6. *Sample injection tube*
7. *Warm thermal plate*
8. *Warm plate wicking surface*
9. *Exhaust manifold*
10. *Optical particle counter*
11. *Sheath flow entrance*
12. *OPC exhaust*

Dimensions: $L = 44.45$ cm
$L_1 = 10$ cm
Width $= 29$ cm
Plate spacing $= 1.6$ cm

A hypothetical experiment is shown in Fig.2. Each supersaturation can be maintained as long as desired; each subsequent supersaturation can be established and stable within about 30 seconds.

Each thermal plate is accurately controlled in temperature such that the temperature difference between the two plates is stable and known to within about $\pm 0.01°C$ for each supersaturation. Figure 3 is schematic of the hydraulic circuit for the warm thermal plate. A centrifugal pump circulates water through the thermal plate and a housing containing four electrically resistive emersion heaters in a coolant flow of about 60 cm^3/sec. The coolant is also circulated over a small glass bead thermistor just downstream of the pump; this method of temperature measurement provides an accurate estimate of the average temperature because of the thorough mixing present at the pump exit. The thermal plate consists of a covered channeled metal surface with large distribution manifolds at both ends. The large manifolds assure that flow through each of the 18 water channels is uniform. Placing the exit and entrance ports

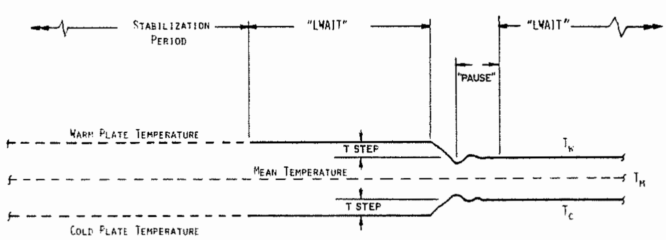

EVENT SEQUENCE

1. *Stabilization: ∿15-20 min. is required to allow the CFD to become equilibrated at the initial temperature settings.*
2. *"LWAIT" Period: The experiment is initiated by a manual command at the start of "LWAIT". This period is long enough to allow sufficient time for counting particles in the OPC.*
3. *"TSTEP": Counting stops at the end of the "LWAIT" period. TSTEP is a temp. parameter required for reaching the next supersaturation level in the experiment protocol. The computer control servos around the value Tw defined by this variable. Time required for this step is ∿2-5 sec.*
4. *"PAUSE": Allows time for system to stabilize at new temp. settings. This has been a period of ∿30 sec. in preliminary experiments. The end of "PAUSE" initiates another "LWAIT" period at a new supersaturation. The instrument continues to sequence until ΔT reaches a predetermined minimum.*

Figure 2. Temperature control of the thermal plates of the rapid cycle CCN spectrometer is programmed to follow the sequence shown above.

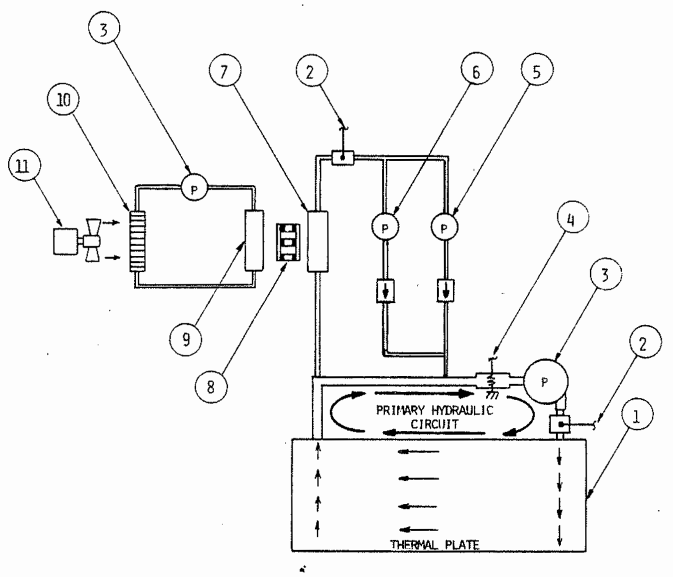

Figure 3. Schematic representation of hydraulic circuit of the rapid cycle CCN spectrometer

Legend:
1. *Thermal plate*
2. *Thermistor*
3. *Centrifugal pump*
4. *Servo heater*
5. *Trickle pump*
6. *Surge pump*
7. *Cold source heat exchanger*
8. *Thermoelectric module*
9. *Water jacket*
10. *Waste heat radiator*
11. *Fan*

on the same side of the thermal plate assures kinematic mixing of the water in the primary circuit. The time required for a parcel of water to flow completely around the primary circuit is one to two seconds.

Temperature control is provided by a secondary hydraulic circuit consisting of a thermoelectric module (TEM) powered "cold source" heat exchanger and a small gear pump. Since this is a closed hydraulic system, operation of the gear pump (trickle pump) displaces cold water into the primary circuit and returns warmer water to the cold source heat exchanger. By correctly metering the proper water flow, any equilibrium temperature of the thermal plate above the cold source temperature can be maintained. Very fine temperature control can be achieved by metering slightly more cold water than is required (slightly overcooling the primary circuit) and adding electrical energy with the use of the immersion heater. Both immersion heater output and flow of water through the trickle pump are under servo control of the control computer.

A second pump is included in the secondary hydraulic circuit in order to provide rapid changes of thermal plate temperature during the "TSTEP" period shown in Fig. 2. The surge pump is operated full on for a period ranging from about 1 to 7 seconds, depending upon the magnitude of the desired temperature decrease in the warm plate. A relatively large parcel of cold water is displaced into the primary circuit during this period, causing a rapid drop in temperature. A period of about 10-30 seconds is required for temperature equilibrium. The surge pump is not used again until another change in plate temperature is desired. The hydraulic circuit for the cold plate is similar to that described above except that the surge pump for the cold plate is attached to a separate TEM-powered heat exchanger (Hot Source), controlling temperature of water above the mean temperature of the experiment. Operation of the surge pump for the cold circuit raises the temperature of the cold plate, such that the temperature difference between the plates is reduced in steps as the experiment progresses.

The ΔT measurement is accomplished with the use of a ten-element thermopile mounted on the back surface of each thermal plate. The thermocouple junctions are chromel-constantan and are potted in good thermal contact with an aluminum base with thermally conductive epoxy. The thermopile is assembled in the form of a yoke; the thin thermocouple leads are sandwiched between two layers of grounded copper foil tape for support and electrical shielding. The entire bundle is mounted on a thin (0.04 cm x 2.5 cm) strip of fiberglass that forms a yoke around the two thermal plates. The base of the yoke mounts on the thermopile amplifier, located at the bottom edge of the CFD chamber, reducing the lead length of the thermocouples to a minimum. The resolution of measurement is 0.0024°C.

Carrier flow and sample flow rates are similar to those used in the earlier model CFD's. The high degree of precision and accuracy achieved with the earlier models is preserved in the spectrometer. In fact, the increased temperature uniformity and measurement sensitivity allows for increased accuracy. Moreover, this accuracy holds true during the supersaturation cycles of the spectrometer. Thus, the entire spectrum can be monitored with precision and accuracy limited primarily by statistics.

Figure 4 displays an example of an F-plateau in the rapid cycle CCN spectrometer. This shows that the nculeus concentration is independent of the time the sample is exposed to the supersaturation. Thus all particles are allowed to activate but not fall out. This is more fully explained in Hudson and Squires (1976). Fig. 4 also displays a comparison in particle concentration between the rapid cycle spectrometer and the earlier model CFD's. Agreement was within 3% which is about the same as the experimental uncertainty. Figure 5 is an example of a spectrum obtained with this instrument within a 10-minute period. Cycles such as this can be preprogrammed for any set of supersaturations or time spans.

3. INSTANTANEOUS SPECTROMETER

The second instrument is still being tested at the time of this writing. However, early tests of the device show that the basic operating principle is sound. This instrument is a more radical departure from the original DRI CFD, as it uses the sizes of the drops detected by the optical counter to deduce the supersaturation of the nculei. The principle that larger drops grow on larger nuclei has been used in the isothermal haze chamber (IHC) first presented by Laktionov (1972) and used by Hudson (1976), Alofs (1978), and Hoppell (1979). In the isothermal haze chamber (IHC) the drops are in equilibrium sizes below cloud drop activation. Thus the sizes are fixed and should not depend upon growth time as long as sufficient time was allowed for growth to the equilibrium haze drop sizes. The idea of using the drop sizes to determine nucleus size or Sc in a supersaturated chamber (S = 0) originated with Hudson(1976). It was found that drop size was inversely related to Sc as anticipated. However, the application of this process depended on nearly continuous monitoring with a second CFD. Droplet size was extremely sensitive to small changes in flow rate, temperature, etc. Since the drop distribution was continuous there was no way to detect these small shifts which would lead to changes in nucleus concentrations. Although two CFD's could be used in this manner to obtain 4 or 5 supersaturations, the procedure required very careful monitoring and did not seem practical.

The new method presented here employs a series of supersaturation steps.The device,Fig.6,is essentially a series of three CFD's inside one chamber. Thus it is a series of three sets of temperature controlled plates so that a sample aerosol is exposed to three supersaturations in ascending order (S_1, S_2, S_3). This means that in the first zone only the largest nuclei become activated drops. That is only those nuclei with Sc's below S_1 grow into droplets while the remaining nuclei remain as unactivated haze drops. After being exposed to this constant

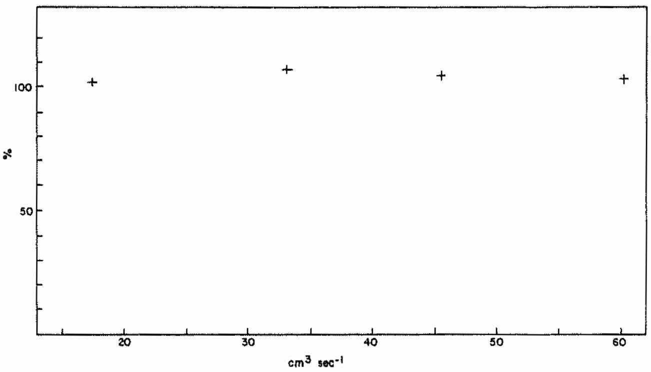

Figure 4. Relative concentration of CCN detected by the rapid cycle spectrometer vs. carrier (main) flow through the chamber. Here the count is normalized to the deduced concentration in a conventional CFD operating side-by-side. The supersaturation in both instruments was fixed at 0.80%.

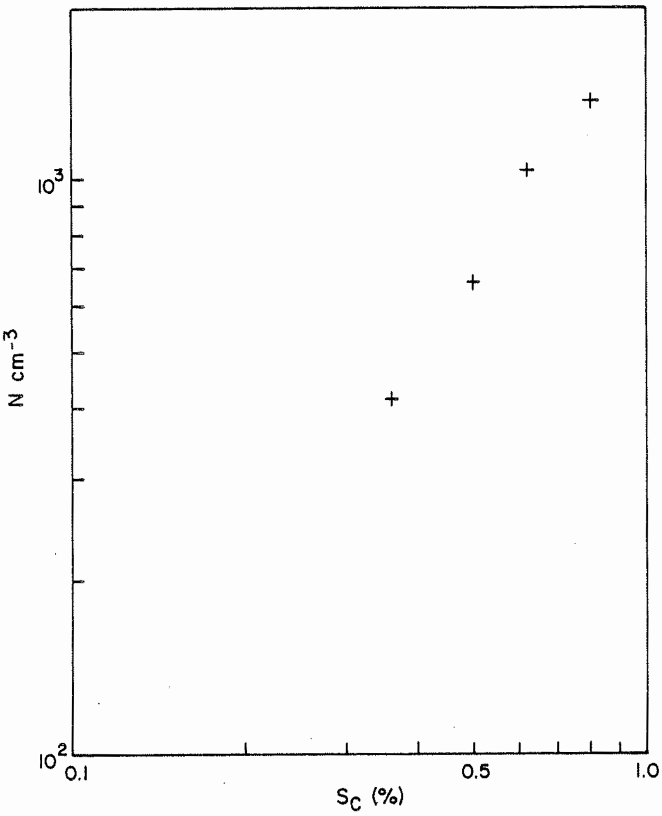

Figure 5. CCN spectrum obtained with the rapid cycle spectrometer in a 10-minute interval, Dec. 27, 1979.

supersaturation, these drops eventually take on a monodisperse distribution in agreement with classical theory.

In the next zone nuclei with $S_1 < S_c < S_2$ become activated and grow into cloud droplets. In the meantime the drops which were already activated in the first zone continue to grow in the second zone. In fact, their growth rate is speeded up due to the higher supersaturation. Thus, the nuclei with $S_c < S_1$ grow even larger and become perhaps even more monodisperse. Nuclei with $S_1 < S_c < S_2$ activate, grow, and begin to form a monodisperse distribution which is much smaller than the first group of drops. Thus at the end of the second zone a bimodal drop distribution should exist. Finally, the third zone activates the drops with $S_2 < S_c < S_3$ and a trimodal distribution is obtained. Then if voltage thresholds are set at levels which correspond to sizes between these drop size modes, the appropriate discrimination can be obtained to determine N vs. S_c and an instantaneous CCN spectrum results.

A computer model was developed in order to design the instrument for optimal operation. The model predicts the radius of a cloud droplet grown upon a nucleus of known critical supersaturation Sc, after the droplet has passed through the spectrometer on a path along the long axis of the chamber. Therefore, the cloud droplet size spectrum at the exit of the chamber may be approximately predicted by repeated runs of the model, varying for each run the Sc of the entering cloud condensation nucleus.

The component computer programs of the model are first, a finite-difference computation of the supersaturation field within the instantaneous spectrometer, and second, a numerical integration of the Carstens theory (Carstens, et al., 1974) of cloud droplet growth. The supersaturation program solves the diffusion equations for heat and mass transfer, including the axial diffusion term in the presence of laminar flow, in a manner similar to that described by Rogers and Squires (1977). The supersaturation field is then calculated and stored on disc file to be used as input by the cloud droplet growth program.

The model revealed that the first zone with the lowest supersaturation should be the largest while the last stage needs to be relatively short because activation and growth are much faster at higher supersaturations. The Royco optical counter was again used as the detecting device. However, the five channels of the Royco are not sufficient to determine if monodisperse distributions exist. For this purpose a 512 channel multichannel analyzer (MCA) (Northern Scientific, Inc.) was interfaced to the Royco. This greatly increases particle size resolution so that the monodispersity of the cloud drop spectrum can be seen on the CRT display. When three supersaturations are applied to the two sections of the spectrometer, a distinctly separated trimodal distribution is observed. When the upstream lower supersaturation, S_1, is increased, the larger sized droplet peak increases and becomes larger as it should. When the higher downstream supersaturation, S_3, is increased, the magnitude of the smaller sized peak is increased and there is an increase in its size. The larger sized peak is only shifted to a slightly larger size. These observations are all in keeping with the operating principles. Thus, sizes which allow separations between the peaks can be chosen. Moreover, the Royco voltage thresholds can be set so that certain size channels can be used to monitor the concentration at specific supersaturations. The size channels can be adjusted so that an individual drop size plateau can be obtained for each supersaturation (see Hudson and Squires, 1976). This assures that all drops which should have been activated at a certain supersaturation were activated and counted.

Changes in the downstream supersaturation, S_3, do not affect the detected concentration active for instance at S_1 or S_2. Extensive tests will be conducted to see if the instrument continues to perform under a variety of conditions and with a variety of aerosols.

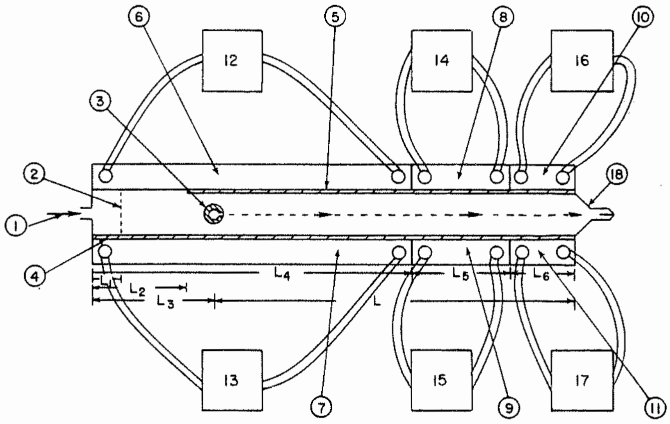

Figure 6. Schematic of the instantaneous CCN spectrometer.

Legend: L = 60 cm; L_1 = 1.3 cm; L_2 = 10 cm; L_3 = 12 cm; L_4 = 40 cm (1st supersaturation zone - S_1, T_3, T_4); L_5 = 12 cm (2nd supersaturation zone - S_2, T_2, T_5); L_6 = 8 cm (3rd supersaturation zone - S_3, T_1, T_6).

Supersaturation: $S_1 < S_2 < S_3$; Plate Temp: $T_1 < T_2 < T_3 < T_4 < T_5 < T_6$

(1) Carrier flow entrance; (2) Diffuser screen; (3) Sample injection tube; (4) Cold plate diffuser screen; (5) Warm plate diffuser screen; (6) First warm section, T_4; (7) First cold section, T_3; (8) Second warm section, T_5; (9) Second cold section, T_2; (10) Third warm section, T_6; (11) Third cold section, T_1; (12) Temperature bath at T_4; (13) Temperature bath at T_3; (14) Temperature bath at T_5; (15) Temperature bath at T_2; (16) Temperature bath at T_6; (17) Temperature bath at T_1; (18) Exhaust to OPC.

4. ACKNOWLEDGEMENTS

Development of the rapid cycle CCN spectrometer was supported by the NASA Marshall Space Flight Center, under Contract NAS8-31470. Principal Investigators for this contract were Patrick Squires and Warren Kocmond. The contributions of Sam Keck, Peter Wagner, and Darrel Reid to this project are gratefully acknowledged.

5. REFERENCES

Alofs, D.J., 1978: Performance of a dual-range cloud nucleus counter. J. Appl. Meteor., 17, 1286-1297.

Hoppel, W.A., 1979: Measurement of the size distribution and CCN supersaturation spectrum of submicron aerosols over the ocean. J. Atmos. Sci., 36, 2006-2015.

Laktionov, A.G., 1972: A constant-temperature method of determining the concentrations of cloud condensation nuclei. Atmos. Oceanic Phys., 8, 382-385.

Hudson, J.G. and P. Squires, 1976: An improved continuous flow diffusion cloud chamber. J. Appl. Meteor., 15, 776-782.

Hudson, J.G., 1976: A CCN spectrometer. Preprints International Conf. on Cloud Physics, Boulder, CO, July 26-30, 613-617.

Hudson, J.G. and P. Squires, 1973: Evaluation of a recording continuous cloud nucleus counter. J. Appl. Meteor., 12, 175-183.

Carstens, J.C., J. Podzimek, and A.N. Saad, 1974: On the analysis of the condensational growth of a stationary cloud droplet in the vicinity of activation. J. Atmos. Sci., 31, 592-596.

Rogers, C.F., and P. Squires, 1977: A new device for studies of cloud condensation nuclei active at low supersaturations. Proceedings, Ninth International Conf. on Atmospheric Aerosols, Condensation and Ice Nuclei, Galway, Ireland, 21-27 September, 1977.

DIRECT MEASUREMENT OF RAINDROP CONCENTRATIONS AT THE GROUND

A J Illingworth
UMIST, Manchester
ENGLAND

1. INTRODUCTION

Existing commercial ground based instruments for measuring raindrop sizes and concentrations detect the raindrop flux incident upon a horizontal surface, and derive the concentration from a knowledge of the drop velocity. The Joss disdrometer (Joss and Waldvogel 1967) senses the momentum of individual raindrops incident upon a horizontal plate of 50cm^2 area, whereas the Knollenberg precipitation probe (Heymsfield 1976) measures the diameter of shadows cast by raindrops on a linear photodiode array as they pass through a 60cm^2 sample area. In both cases the drop concentrations are calculated assuming the drops to be falling with terminal velocity.

In many field situations wind will result in raindrops falling at considerable angles to the vertical, consequently the projected sample area will decrease. This change in sample area will also be different for different drop sizes. The instrument described in this paper overcomes this problem.

2. THE DISDROMETER

The device operates on the shadowgraph principle, but, whereas the PMS device has a horizontal rectangular sample area, this instrument detects drops as they enter and leave a cylindrical volume. This cylindrical volume presents an equal area to any drops which, due to high winds, are not falling vertically.

Figure 1 shows the optical arrangement. The device is very simple so that operation in hazardous field environments will be reliable. The use of coherent radiation has been avoided because of interference problems arising from dust particles and the expensive optical elements which would be required. None of the lenses need to be very precisely positioned thus no accurate adjustments are required in the field.

A quartz-halogen filament light source of diameter 1mm at the focus of a lens of focal length 1m provides a parallel beam of light. After this light has crossed the sample volume (in this example a distance of 17cm) it is normally incident upon a mask which only transmits light falling upon an annulus of diameter 3cm and width 100μm, thus defining the boundary of the sample volume. The light passing through the annulus is then focussed on a large area photodiode. When a drop enters and leaves the volume it should give rise to two equally sized pulses from the photodiode amplifier as it obscures first one side of the annulus and then the other. Provided that the drop is larger than 100μm diameter the amplitude of the pulses should be proportional to the drop diameter. Single pulses resulting from drops passing through the edge of the annulus are rejected in subsequent computer analysis. (Figure 2).

3. DIFFRACTION LIMITS AND SAMPLING VOLUME

Knollenberg (1970) shows that a raindrop acts as an opaque sphere and refraction can be neglected but the smallest detectable drop size is limited by diffraction. It can be seen from Knollenberg's isodensitometer traces of diffraction patterns of particles in white light that, at a distance equal to $(3d^2)/(4\lambda)$ (where d is diameter and

FIGURE 1:

Optical set-up.

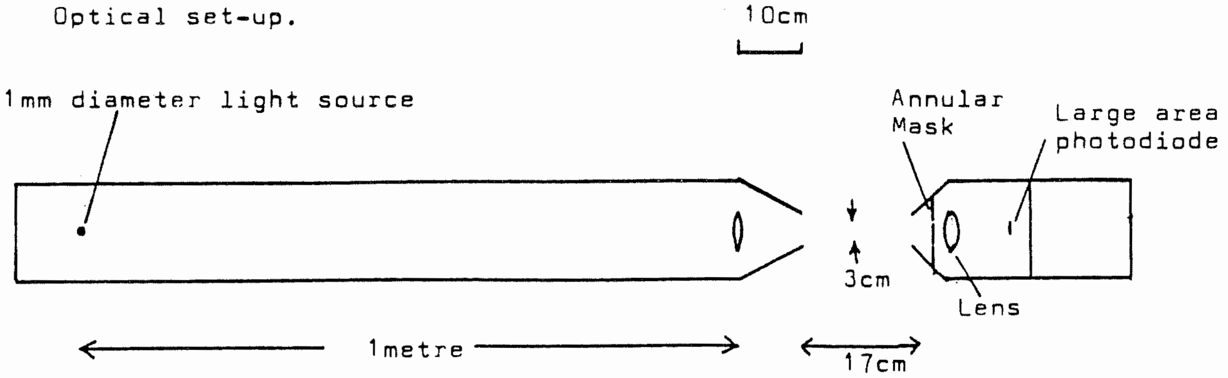

λ is the wavelength of light) the total intensity of light measured along a narrow slice through the diffraction pattern has fallen to 75% of its value for a perfect geometric shadow. For a sample cylinder of length 17cm this corresponds to a particle of diameter 300μm being measured to an accuracy of 100μm. Laboratory calibration of the disdrometer with artificially produced drops confirms this limit.

The 17cm sample length, giving a sample area of 51cm^2, was chosen as a compromise so that a reasonable number of large drops would be sampled without having too high a minimum detectable drop size. If it were considered important to build up a statistically significant number of both very small and very large drops in the minimum time then two instruments with differing lengths of sampling cylinder would be operated simultaneously. The disdrometer is constructed so that this is a trivial mechanical adjustment.

4. DATA ANALYSIS

The photodiode output as a drop enters and leaves the sample volume(V) is shown in Figure 2. Computer analysis enables pulse pairs of the same amplitude to be identified and interpreted as the passage of a drop of a particular size, having a transit time through the sample volulme of τ. If, during a total observation time (T), the sum of the transit times for a given drop size is $\Sigma\tau$, then the concentration of these drops is given directly as $\Sigma\tau/T$ per volume V. The measurement needs no correction for wind speeds or droplet terminal velocity, and the cylindrical sample volume presents the same incident area to any non-vertically falling raindrops.

Figure 2.

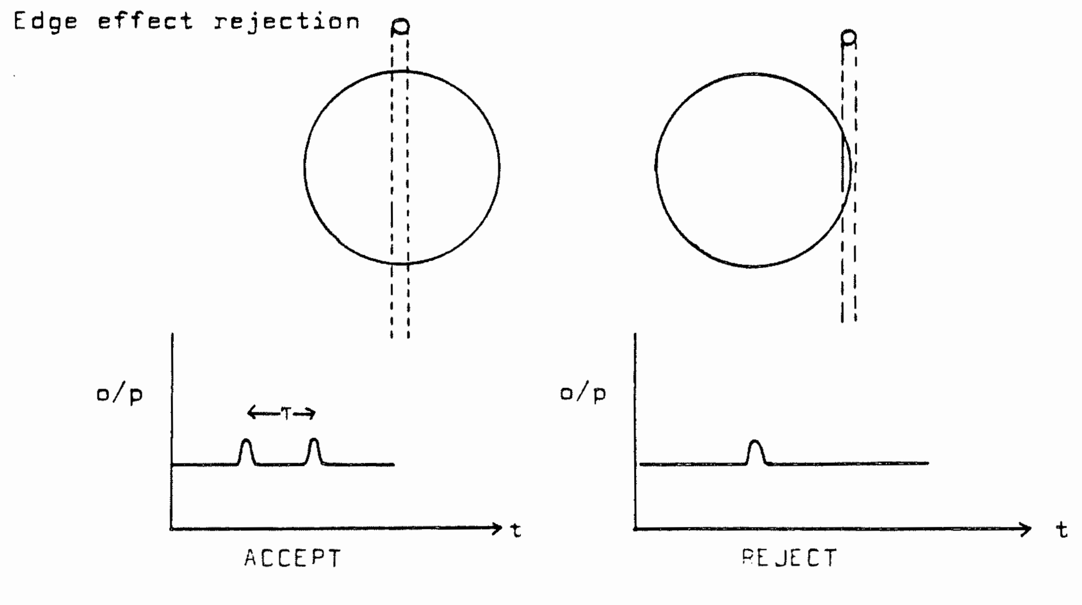

In theory the rise and fall timesof the individual pulses shown in Figure 2 give an independent check of the drop velocity as it crosses the 100μm annulus. However, diffraction effects, especially important for small drops some distance from the mask, will tend to superimpose a broadening of the pulse.

REFERENCES

Heymsfield A J 1976 Particle size distribution measurement: An evaluation of the Knollenberg optical array probes. Atmos.Tech. No 8, 17-24

Joss J and Waldvogel A 1967 Ein spektrograph für Niederschlagstropfen mit automatischer Auswertung. Pure & Appl. Geophys., 68, 161-167

Knollenberg R G 1970 The optical array: an alternative to extinction and scattering for particle size measurements. J.Appl.Met.,9,86-103

ACKNOWLEDGEMENT The research described herein was supported by the Natural Environment Research Council. Dr J A Crabb has made a valuable contribution to this work.

A DROPLET IMPACTOR TO COLLECT LIQUID WATER FROM LABORATORY CLOUDS FOR CHEMICAL ANALYSIS

Ulrich Katz

Desert Research Institute
University of Nevada System
Reno, Nevada, U.S.A.

1. INTRODUCTION

The study of interactions between clouds and atmospheric trace constituents (aerosols and gases) frequently requires the ability to obtain bulk samples of cloud water for chemical analysis. Thereby it is essential that the sampling device rejects aerosols other than cloud droplets, since chemical processes in the dilute cloud droplets are likely to be different from those associated with other particles such as the concentrated solutions of deliquesced but unactivated CCN.

In the course of a laboratory investigation on effects of aerosols and cloud droplets on nighttime transformations of sulfur oxides being carried out in the DRI's 7 m^3 dynamic cloud chamber, a cloud water collector (CWC) was designed and built which has, in addition to the above-mentioned separation characteristics, the capability to extract nearly quantitatively and virtually free of contamination the liquid water from 2.5 m^3 of cloud in two minutes.

2. BASIC DESIGN CONCEPTS

Since cloud droplets differ mostly by their size from the other aerosol particles, the strongly size discriminating process of impaction was selected for the CWC droplet collecting operation. Several types of impaction devices were considered: (1) whirling arm samplers have been used successfully by Mack, et al. (1973) in field studies; however, in a cloud chamber, the stirring action of that device causes the cloud to dissipate prematurely; (2) cyclones have a less well defined size cut-off than (3) jet impactors which thus offer the best overall potential for meeting all requirements for a CWC.

A key element in the present impactor design is the application of slowly rotating Teflon cylinders as impaction surfaces thereby providing solutions to three separate problems: (1) While collection of solid particles in jet impactors generally requires that the impaction surface be coated with a sticky substance to prevent reentrainment of the deposited particles into the airstream, a different approach has to be found for the case of liquid deposits where reentrainment occurs after the accumulation has reached a certain critical size. Thus, rotation of the Teflon cylinders removes the deposit from the impact area where air velocities are high, and transports the sample to a sheltered position. (The earliest version of the CWC utilized a stationary coarsely ground glass cylinder as impaction surface which had the disadvantage that it was (a) difficult to clean and (b) withheld too much sample - see Katz (1977).
(2) Unlike samples of low mass which are usually kept on the impact surface or on filters (e.g., as in the currently often-used dichotomous impactor), the cloud water sample, being in the range of 0.5 to 5 ml, has to be brought into bulk form by forcing it to converge into a container. This is accomplished by addition of a second (collection) Teflon cylinder parallel to and in contact with the impaction cylinder which causes the deposited water to accrue at the contact line of the two counter-rotating cylinders due to the Teflon's hydrophobicity. Vertical orientation of the cylinders provides continuous run-off along the contact line into a collection vessel.
(3) The described system provides for the sample to contact no other material but an inert, smooth Teflon surface prior to collection in a container. Thus, contamination is kept to a minimum.

3. DESCRIPTION OF DESIGN

Figure 1 shows schematically how the above described concept was applied in the actual design. By arranging three impaction cylinders around a thin central collection cylinder (or roller), it was possible to obtain a mechanically stable system while, at the same time, minimizing the surface area contacted by the collected water.

The particular shape of the impaction surfaces practically mandated the use of high aspect ratio rectangular jets (one per impaction cylinder). The jet nozzles as well as the exhaust ducting are incorporated in a one-piece acrylic housing; as Fig. 1 indicates, two concentric tubes at the underside of the CWC penetrate the bottom of the cloud chamber, whereby the outer tube serves as exhaust duct connecting with a suction pump, while the inner tube provides a means to insert and retrieve 6 ml pyrex sample vials from the outside of the chamber. A drive shaft located in the exhaust tube connects the Teflon cylinders to an external 10 rpm motor. The Teflon roller assembly can easily be removed from the housing for maintenance. An overall view of the CWC is provided in Figure 2.

In order to determine the critical dimensions of the CWC, the given values (sampling rate F = 20 ℓs^{-1}, 50% collection for 5 µm

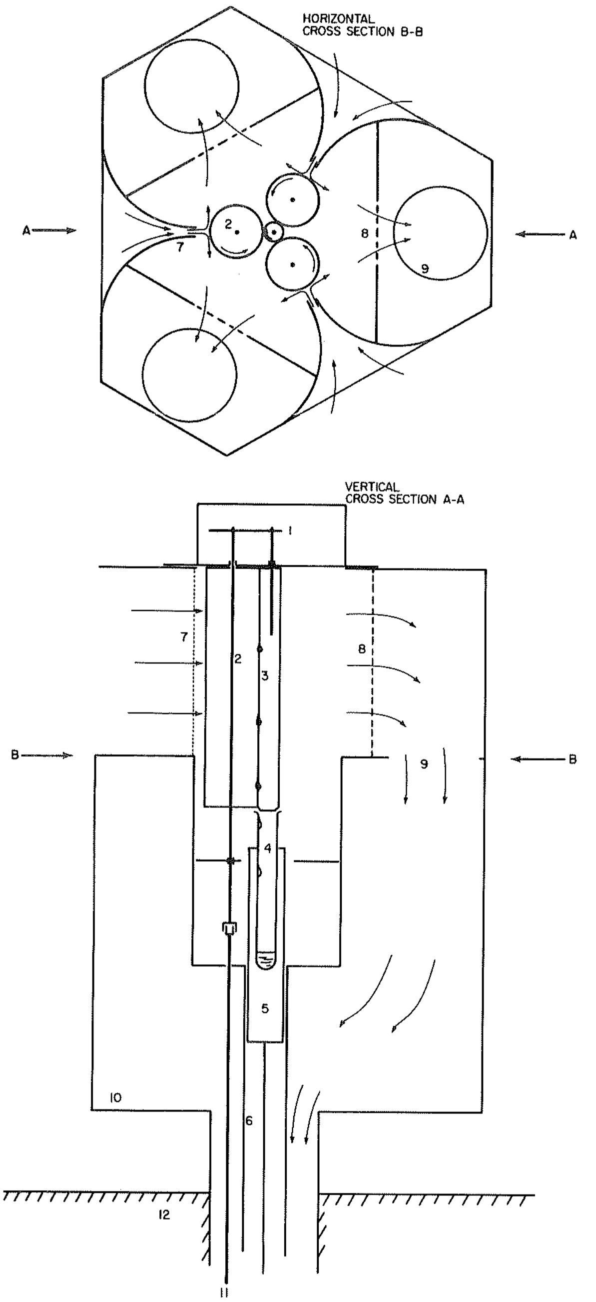

Figure 1. Schematic cross-section of Cloud Water Collector. (1) gears for control of Teflon roller rotation; (2) one of three Teflon rollers (2.5 cm diameter) serving as droplet impaction surface; (3) small central Teflon roller guiding collected water into (4) sample water receptacle (test tube); (5) holder to guide test tube through (6) sample entry/exit tube which connects to outside of chamber; (7) slot shaped nozzle to form cloud air jet, width W = 0.4 cm, length L = 8.3 cm; (8) diffusor to distribute air flow evenly over length of nozzle: (9) suction ports; (10) plenum; (11) shaft connecting one Teflon roller with motor outside of chamber; and (12) chamber bottom.

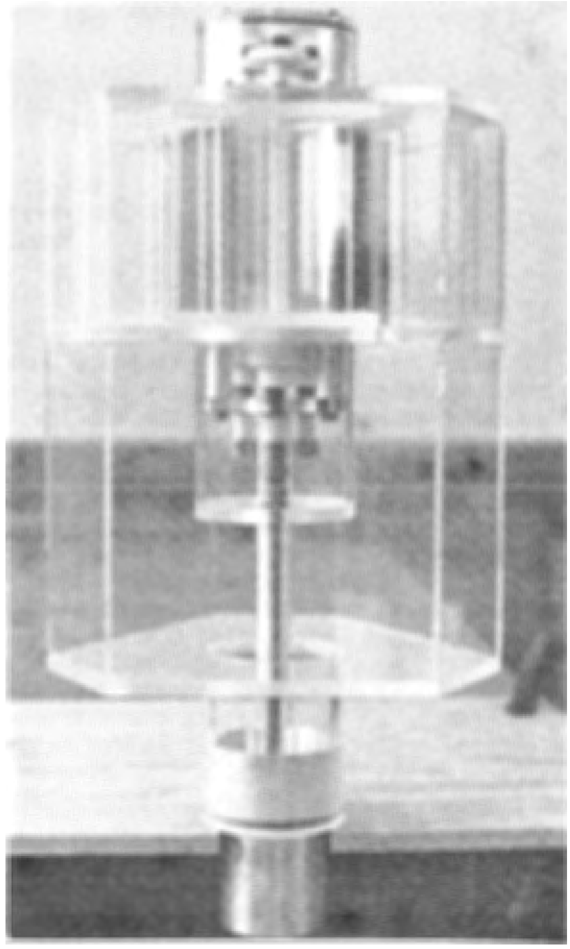

Figure 2. Photograph of Cloud Water Collector.

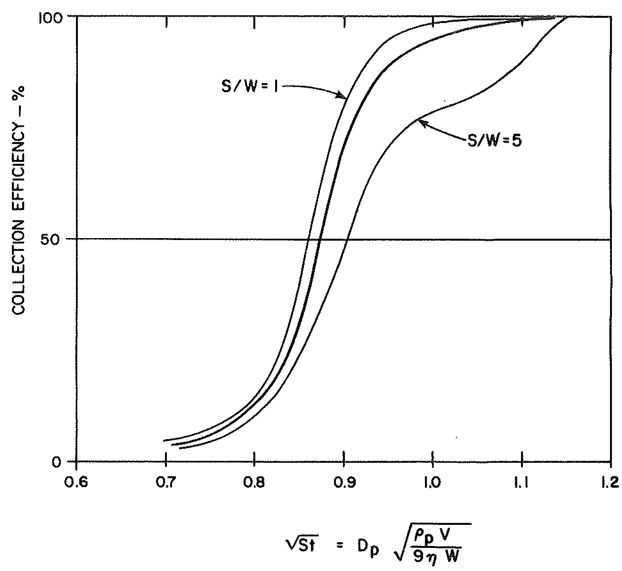

Figure 3. Collection efficiency of rectangular jet impactors as a function of the Stokes number. (After Mercer and Chow, 1968). D_p, droplet diameter; ρ_p, droplet density; η, air viscosity; V, jet velocity; W, jet width.

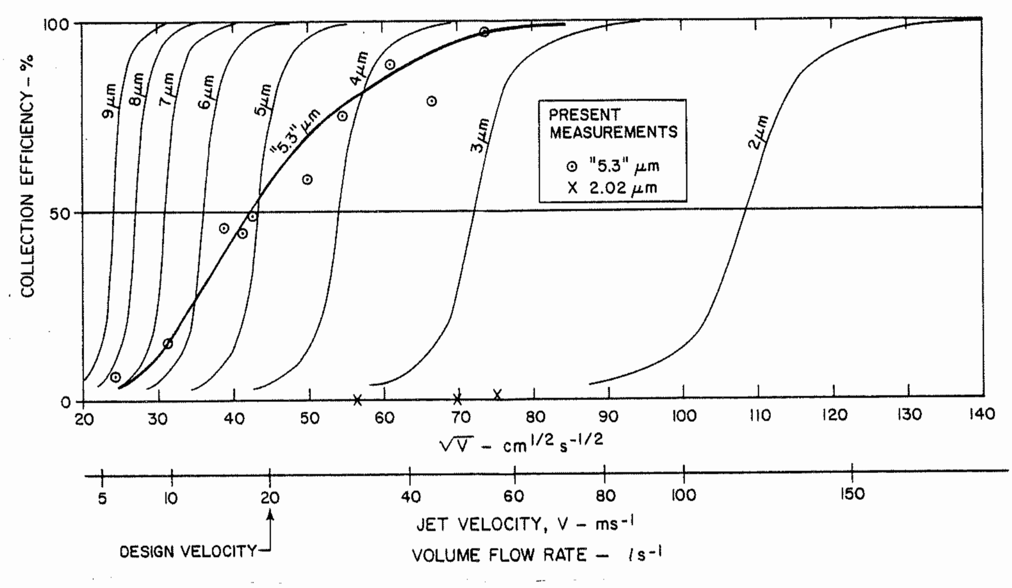

Figure 4. Collection efficiency vs. jet velocity for Cloud Water Collector. Curves derived from Fig. 3 for droplets at indicated sizes. See text for details.

diameter droplets) were combined with experimental data of Mercer and Chow (1968) for the collection efficiency of rectangular jet impactors. Two of their curves are shown in Figure 3, labelled S/W = 1 and 5, where S denotes the jet to impaction plate distance and W the jet width. The unlabelled curve in the middle represents the estimate for S/W = 1.75 which was selected for the present design. This determines the Stokes number for the 50% cut-off and, consequently, the ratio V/W. Since the only other condition relates the flow rate, F = VWL (where L denotes the total length of the nozzle) one of the jet parameters could be chosen for convenience. Thus, W was set at 0.4 cm, small enough for the cylindrical impaction surface to appear to the jet as flat. The remaining jet parameters can then be calculated: $V = 20\ m\ s^{-1}$ and L = 25 cm (or 3 nozzles each 8.3 cm long).

4. PERFORMANCE TESTS

While routine operation of the CWC in the cloud chamber showed that, without any problem, sufficient water was collected for chemical analysis, separate tests were conducted to confirm the size dependency of the collection efficiency. Two sizes of Dow Chemical latex spheres were aerosolized and collected over a wide range of jet velocities, whereby the Teflon surface of the impaction cylinder was replaced by a vaseline coat to prevent particle bounce-off. Microscopic evaluation of the deposits provided the data shown in Figure 4. Less than 1% of 2.02 μm particles (X) were collected even at speeds three times the design velocity. The measurements for the "5.3 μm" particles (⊙) show a gradual increase of the collection efficiency over a wide range of velocities which is due to the broad size distribution (σ = 1.5 μm). On the basis of Fig. 3 the collection efficiency curves for droplets of indicated sizes were obtained and served as basis for calculating the bold curve for the polydisperse "5.3 μm" particles. Since the measurements agree reasonably well with the calculated curve, the collection efficiency of the CWC can be assumed to be well represented by the curves of Figure 4.

Various tests with clouds of known composition showed that the CWC does not represent a source of contamination and that small amounts of sample remaining on the Teflon surfaces after an experiment can be best washed off by collecting the water from two subsequent "clean" clouds (i.e., clouds formed on nuclei which do not interfere with the chemistry under investigation).

5. SUMMARY AND CONCLUSIONS

Cloud chamber studies of the interaction of clouds with air pollutants require a device that can collect and coalesce cloud droplets into a bulk water sample, while rejecting smaller interstitial particles. To achieve this objective, the DRI cloud water collector was designed utilizing the jet impactor principle. Through use of slowly rotating Teflon cylinders as impaction surfaces, reentrainment of deposited water is prevented while the sample is forced to converge into a receptacle. This design also serves to minimize sample contamination.

Tests with the cloud water collector have shown its collection efficiency to be near unity for 5 μm diameter drops and near zero for 2 μm particles (of unit density) at typical sampling rates of $2.5 \times 10^4 cm^3 s^{-1}$. Chemical analyses confirmed the excellent discrimination between cloud droplets and interstitial particles.

6. ACKNOWLEDGEMENTS

The author gratefully acknowledges the Electric Power Research Institute who provided much of the support for this work.

7. REFERENCES

Katz, U., 1977: Report No. CG-5742-M-1, Calspan Corp., Buffalo, NY. "Development of Technology for Collecting Cloud Water for Chemical Analysis."

Mack, E.J., R.J. Pilié, and W.C. Kocmond, 1973: "An Investigation of the Microphysical and Micrometeorological Properties of Sea Fog." Report No. CJ-5237-M-1, Calspan Corp., Buffalo, NY.

Mercer, T.T., and H.Y. Chow, 1968: "Impaction from Rectangular Jets." J. Colloid Interface Sci., 27, p. 75-83.

AIRCRAFT CLOUD WATER CONTENT METER

A.N. Nevzorov

Central Aerological Observatory
Moscow, USSR

I. Introduction. The modern solution of the problem of precise cloud water content measurement from aircraft seems to be closely connected with the development of thermal measuring techniques [I] . The most common thermal instrument uses electrically heated water-exposed sensor ("hot wire") with temperature being a function of water content. Limitations of this constant-power mode was repeatedly discussed [I-3] . The alternative idea of constant-temperature mode with power monitored has been suggested in [2,3] and constant-temperature instruments have been reported in [3,4] . However, the instruments cited have no considerable advantages in accuracy and sensitivity since provide no operation to eliminate the drift problem. Besides, the streamlined form of sensor like a cylinder is not favourable in regard to particle breakup problem as it results in undesirable dependence of collected water evaporation efficiency on cloud phase and disperse composition and flight speed. This effect limits the representability of empiric calibration of NHRL instrument [3] as well as of calculated calibration used for CSIRO instrument [4] . The two reasons make the instruments insensitive to ice clouds.

A new constant-temperature cloud water content meter IVO-CAO reported here is rather free of above limitations. It has a sensitivity of about 0.002 gm^{-3} and allows more reliable calculated calibration. The instrument is available for operating in extended (stratiform) clouds including ice ones.

2. Operating principle. To maintain the sensor at constant temperature T_S the total power is required $P_S = P_c + P_W$, where P_c is convective heat emission from the sensor and P_W is heat losses associated with the precipitating cloud water warming and evaporation. The device contains auxiliary water-shadowed (reference) sensor maintained at the same temperature T_S by the power P_R . It may be assumed that P_c is proportional to P_R , i.e. $P_c = kP_R$ (k = const) at least for limited range of air flow parameters variations.

Further, the method of direct determination of P_W is based on the principle of independence of partial powers of incoherent currents via the same load. The main sensor is maintained at operating temperature by DC control voltage and in parallel is feeded by AC voltage proportional to the control output of separate reference sensor circuit, so that in dry air its temperature is kept T_S by AC alone. Then, under cloud conditions the "dry" term P_c is compensated by AC and the "wet" term P_W by control DC voltage. We have

$$e^2/R(T_S) = \varepsilon W \sigma v L^*, \qquad (I)$$

where e is DC component voltage across the main sensor, $R(T_S)$ is its resistance at T_S , W is cloud water content, σ is the sensor sampling area, v is true air speed, ε = collection efficiency $\times$ evaporation efficiency. The value of L^* is a specific heat required to warm the water from air temperature T_A to effective evaporation temperature T_E (including if necessary ice melting heat) and to evaporate it at T_E . The value of T_E is found from the known equation of stationary water collection/evaporation equilibrium:

$$\varepsilon W v = 0.622 \alpha_\sigma (p C_p)^{-1} [E(T_E) - E(T_A)]. \qquad (2)$$

Here p and C_p are air pressure and specific heat, $E(T)$ is saturated vapour pressure at T , α_σ is heat transfer coefficient per unit σ area.

3. Probe design (see fig.I). The IVO-CAO probe consists of two sensors placed on the same cylinder base directed with its axis along the airstream. Both sensors are made of isolated nickel wire closely wound in a single layer. The main (water-exposed) sensor is cone-shaped and glued within the base butt-end cone hollow. The reference one is wound on the cylinder side. The cylinder diameter is 8 mm. The estimated collection efficiency of the main sensor is close to one of stream-cross cylinder with dia of 2 to 2.5 mm. The concave sensor collection surface contributes to more effective evaporation of particles even if splashing, especially of ice crystals.

The frontal heating of the probe and of its holder provides ideal conditions for long normal operating in supercooled cloud.

4. Circuitry (see fig.2). Every sensor is connected to a separate control loop of self-balancing by electrical heating a bridge with temperature-dependent resistance of a leg which is the sensor itself. Both bridges are balanced at the same sensor temperature (80 to I00°C). The main sensor bridge is feeded by DC control voltage as well as by rectangular voltage from control output of reference sensor circuit. The rheostat R allows manual balance adjusting in dry air with zero DC output.

The instrument output is taken directly from the main sensor terminals via the AC filter with time constant of 0.I sec or another desired.

5. Flight tests. Since I975 the instrument was thoroughly tested in various ambient and flight conditions. The real sensitivity was established in clean air flights by the output zero drift. Under steady flight conditions, the equivalent water content drift as a rule did not exceed 0.002 gm^{-3}, and at variable flight altitude reaches 0.005 to 0.0I gm^{-3}. The drift is prove to be associated mainly with variations in plane angle of attack.

The preliminary experimental test of measurement accuracy was carried out by comparing of IVO-CAO calculated data with simultaneous data obtained from filter paper LWC meter in Cu clouds. The mean relative discrepancy of the data was 6% with correlation coefficient of 0.92. That is, the comparison result lies within the error of fitter paper device.

The flight tests showed that the instrument responds to even weakest cirrus with their ice content less than 0.0I gm^{-3}.

6. Accuracy. The formula (I) is used for calculated calibration of the instrument. The value of ε is estimated for most stratiform water clouds by $\varepsilon = 0.9 \pm 0.I$. In principle, it is possible to correct value of ε using, for instance, simultaneous extinction coefficient measurement [5]. To simplify data processing we use the calculated values of L^* averaged for reasonable range of variability of W and T_A in stratiform clouds, commiting the error up to 5% for purely water and purely ice clouds and II% for clouds of mixed or uncertain phase state. Other accumulated errors are estimated by 5%. Thus, excepting particular cases, the overall maximum error in determining cloud water content amounts to the order of (0.002 gm^{-3} + 20%). The relative item is expected to be reduced 2 to 3 times by introducing ε and L^* correction.

7. Conclusion. The described improvements of the constant temperature technique results in arising of sensitivity, calculated calibration reliability and responsability to ice cloud. The new instrument seems to be quite useful for investigation of stratiform, particularly of ice clouds. Since I977 the IVO-CAO instrument is regularly used in cloud physics experimental studies.

References

I. Ruskin R.E., I976: Liquid water content devices. Atm. Techn., N0.8, 38-42.

2. Nevzorov A.N., Tolkachev V.K., I974: On the interpretation of output of a flow LWC meter with a heated thermosensitive probe. Proc. of Main Geoph. Obs., is. 309, I06-II3.

3. Merceret F.J., Shricker T.L., I975: A new hot wire liquid water content meter. J. Appl. Met., v.I4, No.3, 3I9-326.

4. King W.D., Parkin D.A., Handsworth R.J., I978: A hot-wire liquid water device having fully calculable response characteristics. J. Appl. Met., v.I7, No.I2, I809-I8I3.

5. Nevzorov A.N., Shugaev V.F., I972: Using of integral parameters in studying microstructure of water clouds. Proc. of Central Aerolog. Obs., is. I0I, 32-47.

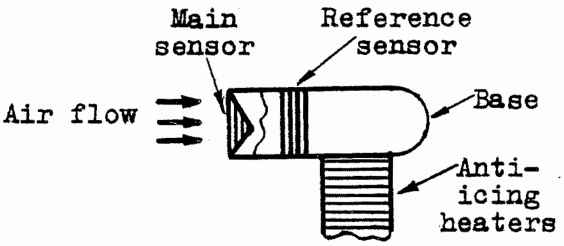

Fig.1.
IVO-CAO probe

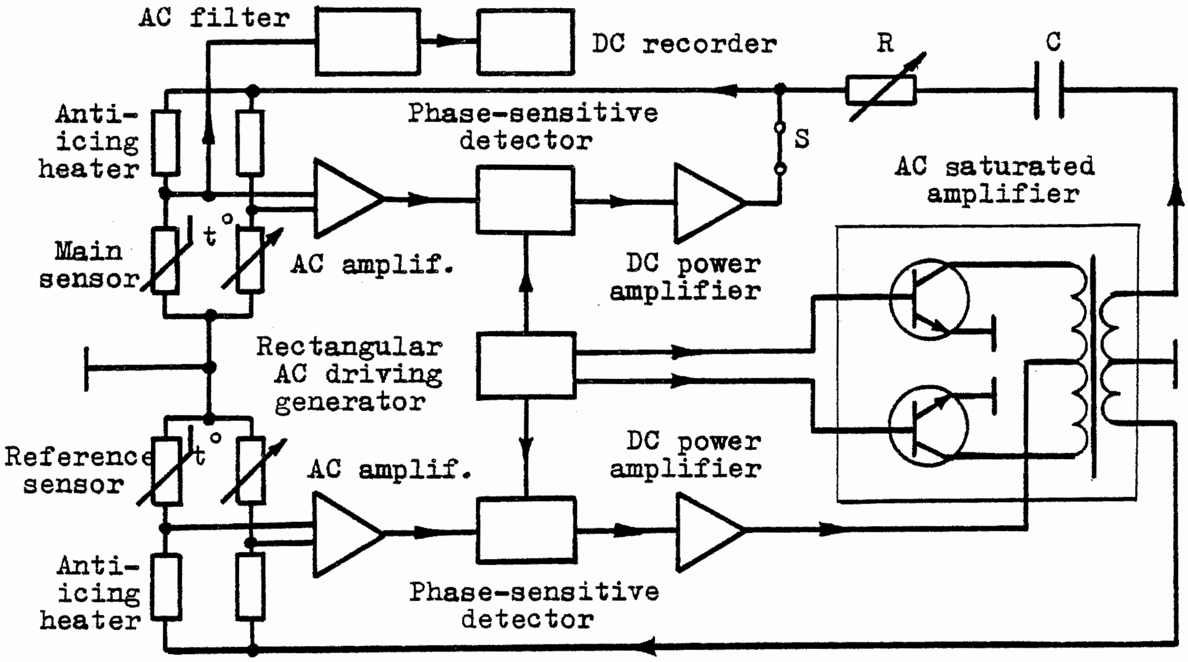

Fig.2. A block diagram of IVO-CAO circuitry

MILLIMETER RADAR OBSERVATIONS OF VERTICAL VELOCITIES IN NONPRECIPITATING CUMULUS CLOUDS

Fausto Pasqualucci
NOAA/ERL/Wave Propagation Laboratory
Boulder, Colorado 80303

Introduction

The understanding of cloud development and evolution necessitates a knowledge of the entrainment of environmental air and its effects on cumulus convection. Environmental entrainment causes convective overturning of the cloud interior, and this instability is in general independent of the gross overturning of the cloud as a whole. The cloud top mixes with the dry air above it; this causes cooling of the upper regions of the cloud by evaporation with an increase of the instability in the mixing air. This phenomenon will increase convective turbulence in the cloud and thus increase mixing. The cloud will then act as a device taking in air from the upper and lower levels and ejecting a mixture of air and cloud particles at mid-levels (Fraser, 1968; Telford, 1975). The mixed air will usually be in buoyancy equilibrium, relative to the environment, between cloud base and cloud top.

The above discussion shows the importance of vertical mixing as suggested by Warner (1955) and Squires (1958a and b); actual aircraft measurements discussed by Telford and Wagner (1974) have shown a net divergent flow near the middle of small cumulus clouds. The vertical mixing near the top of the cloud will generate downdrafts when the overlying dry air is entrained and descends because of evaporative cooling of the mixed-in cloud water. Doppler radar measurement at vertical incidence should be able to detect these downdrafts. Such detection is the purpose of the experiments discussed here.

A pseudo-noise (P-N) coded 35 GHz Doppler radar was used in the vertically pointing mode to measure the profiles of vertical air velocity in growing cumulus clouds in Johannesburg, South Africa.

The radar system operates in the continuous wave mode and uses two separate 6 ft antennas for the transmitter and the receiver (Pasqualucci, 1972).

The short wavelength of the radar (0.86 cm) allows the study of clouds at their earliest stage of formation and evolution when standard weather radars operating at longer wavelengths (5 cm to 10 cm) fail to detect them.

Experimental Observations and Data Processing

On the 16th of February 1973, cumulus clouds started to develop near the radar station at Johannesburg. At $12^h 45'$ the radar started to take data on a growing cumulus cloud. The P-N code clock rate was 2.5 MHz, giving the radar a range resolution of 60 m. Four complete scans were taken between the ground and 5.4 km AGL. The time interval between consecutive scans was 4 min, and the cloud moved relatively slowly (3 to 6 km/h) over the vertically pointing radar during the measurement period. The true vertical velocity component is measured in the center of the scattering volume common to the two antennas although slight variations appear at the edge of that scattering region. The contamination of the Doppler by the presence of the horizontal wind can therefore be considered negligible and will not affect the computation of the spectral first moment. The observed vertical velocities will involve only the terminal speed of the cloud particles and the vertical air velocity. In our case the diameter of the cloud particles is typically less than about 100 µ. The terminal velocity of the cloud particles can be considered negligible. and therefore the Doppler frequency shift gives a direct estimate of the vertical air velocity.

It is found from the radar measurements that enough particles of different kinds (seeds, pollution particles etc.) exist between ground and cloud base to give echoes of the same order of magnitude as the backscattering from cloud particles ($Z \approx -20$ dBZ). The signal dwell time is 1.6 s. At a sampling rate of 10 kHz, 128 Doppler spectra are averaged to obtain one Doppler spectrum of 128 points at each range gate. The mean Doppler velocity $\bar{v}$ is then computed from this averaged Doppler spectrum. When the effects of turbulence in the small scattering region are neglected, the variance σ_s of the individual estimates $\bar{v}$ is dependent on the dwell time and the standard deviation of the Doppler spectrum σ_v. For a signal dwell time of 1.6 s and a standard deviation of 1.2 m s^{-1}, a value of σ_s = 0.03 m s^{-1} is obtained. This will give a maximum uncertainty (95% confidence limit) of $\pm$ 0.06 m s^{-1} in the estimate of the spectrum first moment $\bar{v}$.

Discussion and Conclusion

The height profiles of the vertical air velocity are shown in Figs. 1 and 2. Three of the four profiles clearly show the presence of a penetrative downdraft near the top of the cloud, as detected by the radar. Between $12^h 45'$ and $12^h 49'$ the cloud top height increased from 4.32 to 4.8 km at an average velocity of 2 m s^{-1}. This speed is very close to 1.8 m s^{-1} which is half the maximum updraft of 3.6 m s^{-1}. Between $12^h\ 49'$ and $12^h\ 53'$ the average velocity of the cloud top height increase is 1.75 m s^{-1} which again is very close to the value of half the maximum updraft or 1.6 m s^{-1}.

It is interesting to note the change in the vertical air velocity profile between $12^h\ 53'$ and $12^h\ 57'$ which indicates the limited spatial extent of the penetrative downdraft. Unfortunately the lack of knowledge of the time changes in the structure of the air flow inside the cloud makes it very difficult to estimate the horizontal dimension of the downdraft. However, assuming an air flow that does not change over the total measurement time, and using an estimated advection velocity of 3 to 6 km/h, we obtain a minimum estimate of the horizontal dimension of the penetrative downdraft between 400 and 800 m.

A good check of the accuracy of the vertical velocity estimates is provided by the very small values of $\bar{v}$ at the cloud top and near the ground.

The results discussed above, showing the presence of downdrafts near the top of the cloud, clearly demonstrate the usefulness of short wavelength Doppler radars in the study of the early stages of cloud development and evolution. A system of multiple short wavelength Doppler radar should be able to monitor the time variation of the three-dimensional wind field and provide new insights into the processes involved in the formation and evolution of clouds. This should tremendously benefit cloud modelers and cloud physicists and should be of great help in weather modification experiments.

Acknowledgment

The author gratefully acknowledges the help and cooperation of the Director and staff of the Council for Scientific and Industrial Research, National Institute for Telecommunications Research, Johannesburg, South Africa.

References

Fraser, A. B., 1968: The white box: The mean mechanics of the cumulus cycle. Quart. J. Roy. Meteor. Soc., 94, 71-87.

Pasqualucci, F., 1972: Measurements of dropsize distributions using a 35 GHz Doppler radar. Preprints of the 15th Radar Meteorology Conference, Champaign-Urbana, Illinois, AMS, Boston, Mass.

Squires, P., 1958a: The spatial variation of liquid water and droplet concentration in cumuli. Tellus, 10, 372-380.

Squires, P., 1958b: Penetrative downdraughts in cumuli. Tellus, 10, 381-389.

Telford, J. W., 1975: Turbulence, entrainment and mixing in cloud dynamics. Pure Appl. Geophys., 113, 1067-1084.

Telford, J. W., and P. B. Wagner, 1974: The measurement of horizontal air motion near clouds from aircraft. J. Atmos. Sci., 31, 2066-2080.

Warner, J., 1955: The water content of cumuliform cloud. Tellus, 7, 449-457.

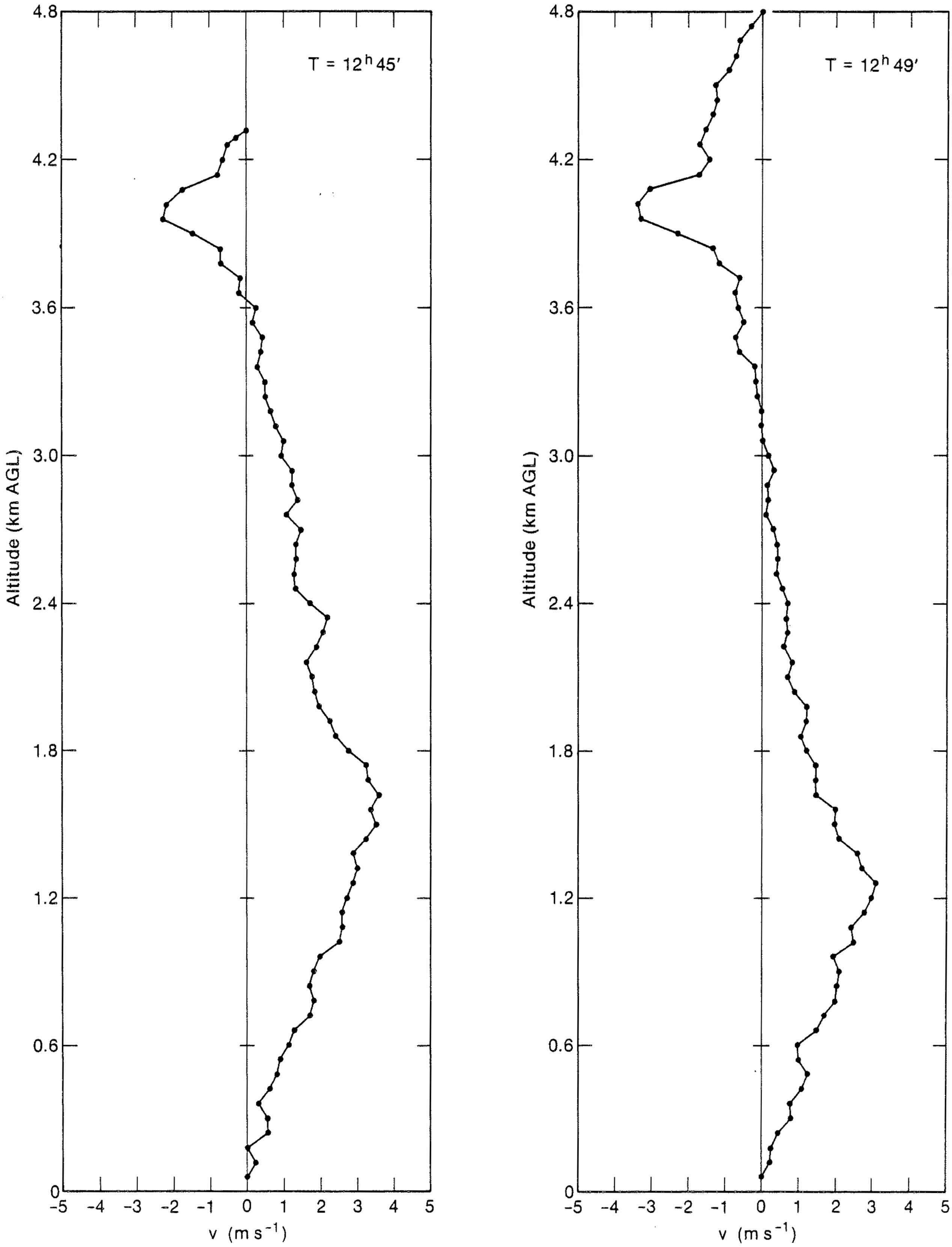

Figure 1. Height profiles of vertical air velocity measured with the vertically pointing 35 GHz Doppler radar. Note the presence of penetrative downdraft between 3.6 km and cloud top at $12^h\,45'$ and between 3 km and 4.8 km at $12^h\,49'$.

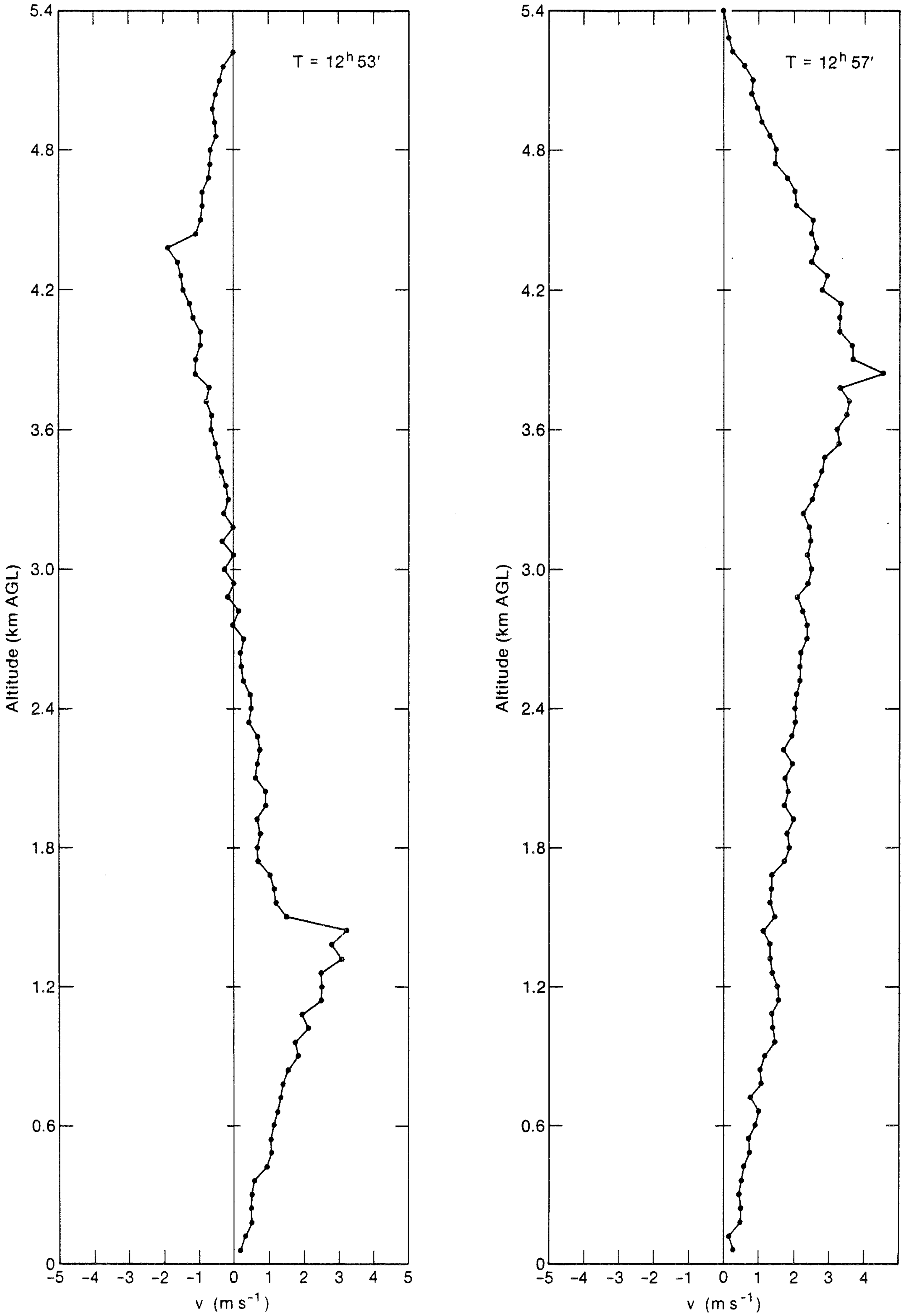

Figure 2. Height profiles of vertical air velocity measured with the vertically pointing 35 GHz Doppler radar. At $12^h\ 53'$ the data show the presence of a penetrative downdraft between 3 km and 5.2 km while at $12^h\ 57'$ there is only updraft throughout the cloud.

ICE NUCLEUS CONCENTRATIONS

C P R Saunders and K Hussain

University of Manchester Institute of Science and Technology
ENGLAND

1) INTRODUCTION

Field observations of ice crystal concentrations and sizes in winter-time clouds in the San Juan Mountains (Cooper & Saunders 1976) and in cap clouds over Elk Mountain (Cooper & Vali 1976) revealed the presence of ice crystals very close to the cloud edges. The inference drawn was that these crystals may have been formed near the edge of the cloud in association with the initial condensation process upon condensation-freezing nuclei or, less likely, by the process of Brownian capture of contact nuclei smaller than 0.02μm by water dropets. Ice nucleus measurements, by Millipore filters and subsequent diffusion chamber processing gave nuclei concentrations of around $0.1 l^{-1}$ whereas the crystal concentrations were around 3 or $4 l^{-1}$ over Elk Mountain at -18°C and exceeded $100 l^{-1}$ at -19°C and $50 l^{-1}$ at -13°C over the San Juan Mountains. The rapid development of the high crystal concentrations near the cloud edges and the absence of further increase inside the cloud suggested that ice multiplication was not the cause of the high crystal concentrations. In particular, the requirements for the Hallett-Mossop mechanism to operate were not met. The discrepancy between crystal and nucleus concentrations may therefore be due to the inability of the filter process to detect condensation-freezing nuclei. In order to test this possibility, a continuous flow chamber was developed by Cooper, Rogers & Vali at the University of Wyoming and a second chamber has been built at UMIST. The continuous flow chamber permits nuclei to be activated while they flow between two ice coated, temperature controlled plates which provide the required supersaturation. In this way the activation process is close to the natural cloud process and supersaturations both above and below water saturation can be experimented with in order to activate different modes of ice nucleation. Below water saturation, but above ice saturation, deposition (sublimation) nuclei are activated while above water saturation, both deposition and condensation-freezing nuclei will be activated. The filter processor technique suffers from the volume effect in which the number of nuclei detected is not proportional to the volume of air sampled due to vapour depletion by activated nuclei. It also has the drawback that during processing at humidities close to 100% hygroscopic nuclei sampled on the filter nucleate small water droplets which may contact ice nuclei and cause spurious freezing. These disadvantages are not present in the continuous flow chamber.

2) APPARATUS

The UMIST continuous flow chamber (CFC) is shown in Fig.1. The CFC consists of two parallel, horizontal, plates with a separation of 1cm.through which a flow of clean, dry, filtered air may be drawn at a rate of around $20 l \min^{-1}$. This flow draws in, via a row of jets at the inlet to the chamber, the air sample to be examined. The sample is introduced mid-way between the top and bottom plates and maintains itself in a laminar layer through the apparatus. This behaviour has been verified using smoke as an air tracer. During the passage between the plates, which are covered in a layer of ice, ice nuclei are activated and the resulting ice crystal embryos grow by vapour diffusion. Calculations of the growth rate for the appropriate values of the controlling growth parameters show that the crystals can be expected to grow to around 10μm in size during the passage time and will fall through approximately 1cm in the same time. The crystals may be detected in a supercooled sugar bath placed at the output of the chamber where they can be counted visually. Occasionally, a Royco particle counter has been available in place of the sugar solution. The plates of the chamber are cooled by means of chilled methanol from two subsidiary coolers. The temperature of the ice surfaces are monitored with a series of thermocouples and the coolers are capable of maintaining the methanol temperature steady to within $\pm$0.03°C. The supersaturation in the chamber can be determined from the plate temperature. The chamber was designed so that access between the plates could be readily obtained by using hinges on one side and suitcase clasps on the other. An airtight seal is maintained by tightly compressed rubber strips between the side walls and the plates. This ready access is useful for polishing the ice surfaces flat and for introducing water onto the plates before cool-down. The plates have been covered with a strong fabric attached by a water and low temperature resistant adhesive; this has proved better than the conventional blotting paper which can rot, tear and peel off. The fabric is water absorbent and so can hold a layer of water on the plate during cool-down.

The non-steady-state solutions of the vapour pressure and temperature equations have been used to find the times for equilibrium to occur when air is introduced at one end of the CFC. Vapour equilibrium is attained before temperature equilibrium which results in a separation between these equilibrium points of about only 1cm. In general, for the air velocities used in these experiments, equilibrium occurs at about 20cm from the input end of the CFC leaving about 100cm for the activated ice nuclei to grow at the required supersaturation. Transient supersaturations greater than the final equilibrium value do not occur in this chamber because the incoming air sample is warmer than the top plate temperature.

The sugar both at the chamber exit is maintained at its threshold of nucleation and is able to detect crystals for about 10 minutes or so before the crystals grow to completely cover the bath.. There is a background ice crystal count, due to fibres blown from the growth on the ice walls of the chamber. This background count is noted between data runs when filtered air alone is drawn into the chamber. When the number of background crystals detected approaches the same number of activated nuclei detected in the same time then the chamber is opened up and the ice walls are polished.

A static diffusion chamber (SDC) was built in addition which allows 4 47mm diameter millipore filters to be processed at a required temperature and supersaturation. The two horizontal plates are cooled by chilled methanol solution while the top ice-coated plate is warmed by thermoelectric modules embedded in it. The filter samples are usually gathered close to the times that the CFC is running in order to permit comparisons of the results. Normally 100l of sample air are drawn through each filter. The filters rest on brass discs on the lower plate and good thermal contact is ensured by soaking the back of each filter in petroleum jelly. The effect of chamber height (separation between the filter surface and the ice surface above it) has been investigated and agreement with other workers noted in that increased height leads to a reduced number of crystals activated on the filter; a value of 0.5cm has been adopted for the present measurements. The volume effect has also been investigated. The volume effect relationship $N=AV^{-k}$ was found to hold with k=0.63 and A=3.54 at T=-15.5°C and S_i=1.15 for Manchester laboratory air with sample volumes between 50 and 1000l. Filter samples of over 500l were found to be coloured by dust. The mean value of k for Albany (USA) is 0.9 and Laramie (US) is 0.86 (Jiusto & Lala 1976). Futher comparisons with the present results can be made from Figure 2.

3) RESULTS

In Summer 1979 measurements were made with the CFC at the UMIST Great Dun Fell field station. Some of these data are shown in Table 1. Filter samples were taken simultaneously and were processed later in the SDC. The concentration of crystals from the CFC has been corrected for the background count measured with filtered air. The SDC data is corrected for an average background count found on processed but unused filters. The deposition nuclei results for both chambers showed some agreement although the CFC results will be an underestimate of the nucleus concentration because of large crystal fall-out before the sugar bath and small crystal carry-over to miss the sugar bath. In general the CFC detected more ice nuclei than did the SDC.

TABLE 1

CFC DATA			SDC DATA		
$\bar{T}$°C	SSI%	Conc. no l^{-1}	T_2°C	SSI%	Conc. no l^{-1}
-19.57	18.86	0.996	-16.89	16.7	1.6
-19.55	18.65	0.875	-16.86	16.8	0.8
-19.55	18.65	0.75			
-15.31	13.38	0.375	-16.50	16.8	0.3
-15.54	15.21	0.833	-17.2	17.9	0.2
-15.56	15.20	0.5	-17.2	17.6	0.5
-13.99	13.91	0.22			
-15.38	14.34	0.53	-16.9	17.2	0.13

Subsequent measurements in the laboratory have shown that the average concentration of ice nuclei detected with the CFC at a mid-plane temperature of -16°C with SSI≃15% is $0.8l^{-1}$. Corresponding values of ice nucleus concentration in Manchester laboratory air, determined with the SDC, are shown on Figure 3 where at -16°C the concentration is $\simeq 0.5l^{-1}$. Also shown are values from other workers. All the data fits the power law $N_i=bS_i^a$ and the values of a and b are shown on the figure. The present results have a=2.3 and b=7.7 x 10^{-4} at -16°C; Huffman obtained at -20°C, a=2.6 to 3.2 for Northeast Colorado (Summer) and a=4.1 to 5.1 for Laramie (Winter).

When a Royco optical particle counter was available it was connected to the output of the CFC and counted particles which were too small to have fallen in the sugar bath. A preliminary experiment was conducted to check whether natural aerosol would be present which would swamp the ice particle count. With the CFC plates above 0°C, filtered and sample air was drawn through in the normal way. The Royco counted no particles in the >3.0μm size range; these particles were obviously falling out during passage through the CFC. When in the mode for detecting deposition nuclei, the counter detected no particles >5μm, these fell out during transit. However in the 3.0 to 5.0μm range, particles which had been activated late and had not grown large enough to fall out were detected. The average concentration detected over 29 runs taking background concentration into account is $6.5 l^{-1}$. Taking the average value counted with the sugar technique together with the Royco value leads to a typical crystal count of around $7 l^{-1}$. This is still an underestimate because of the fallout of large crystals inside the CFC. Nevertheless the CFC data is indicating the presence of a larger concentration of ice nuclei than does the SDC data by a factor of≃10.

Measurements above and below water saturation have been made with the CFC in order to determine whether condensation freezing nuclei are present. For several hundred 20l samples taken from Manchester city air, the average increase in crystal count for measurements made above water saturation is 324% compared with measurements made below water saturation. The increases range from 53% to 1767%. Thus the average nucleus concentration measured with the Royco and sugar bath together is $22.7 l^{-1}$ when detecting both condensation freezing nuclei and deposition nuclei above water saturation. Such high values are not obtained from the filters in the static diffusion chamber when processed at the same supersaturation.

Measurements are continuing to compare further the two techniques of ice nucleus detection and to learn more about the presence of condensation freezing nuclei in natural aerosol.

4)ACKNOWLEDGEMENTS
This work was supported by the Natural Environment Research Council.

Fig 1 The Continuous Flow Chamber

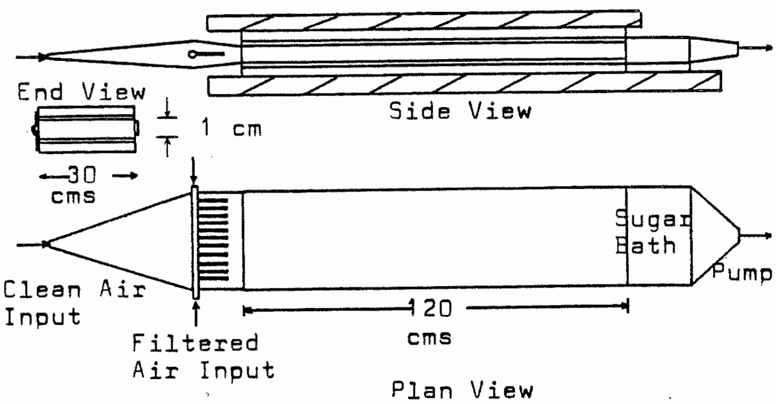

REFERENCES
Cooper W A & Saunders C P R 1976 Microphysical observations in San Juan storms. Proc. Weather Mod. Conf. Boulder, pp93-98
Cooper W A & Vali G 1976 Ice crystal concentrations in wintertime clouds Proc.Cloud Physics Conf.Boulder, p91-96
Gagin A 1973 Studies of the size and supersaturation spectra of ice nuclei. Proc.8th Int.Conf. Nucleation, Leningrad, 294-307
Huffman P J & Vali G 1973 The effect of vapor depletion on ice nucleus measurements with membrane filters. J.Appl. Met.12, 1018-1024.
Jiusto J E & Lala G G 1976 SUNYA diffusion chamber measurements and related analysis. Proc 1975 Int.Ice Nuclei Measurements Workshop. Laramie, Wyo.
Mossop S C & Thorndike N S C 1966 The use of membrane filters in measurements of ice nucleus concentration 1. Effect of sampled air volume. J.ApplMet.5, 474-480

Fig 2 The Volume Effect

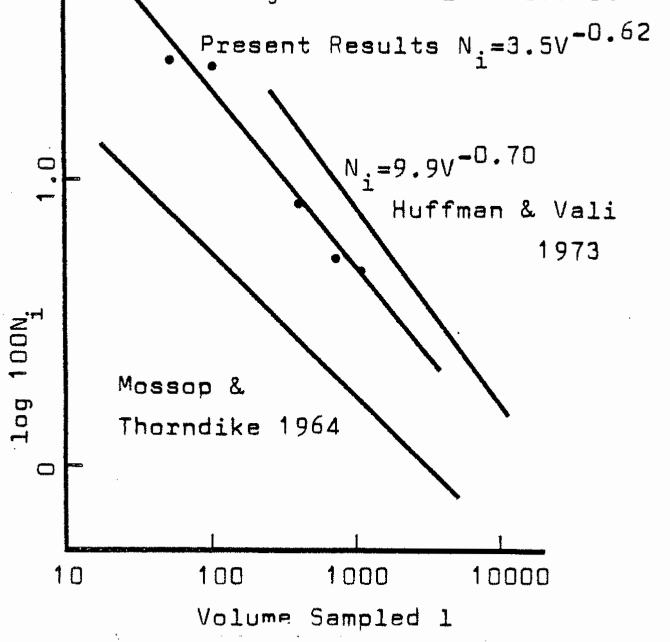

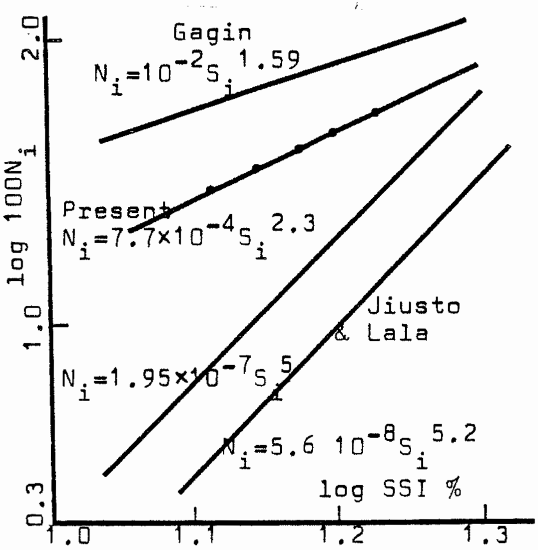

Fig 3 SDC Spectra

A METHOD FOR DEDUCING THERMODYNAMICAL INFORMATION FROM DOPPLER RADARS OBSERVATIONS

Tzvi Gal-Chen

National Center for Atmospheric Research
Boulder, Colorado, U.S.A.

Carl E. Hane

National Severe Storms Laboratory
Norman, Oklahoma, U.S.A.

1. INTRODUCTION AND GOALS

Doppler radars can provide a detailed and reasonably accurate estimation of the horizontal wind components of a convective system. It is recognized, however, that "directly derived" estimates of vertical velocities and liquid water content are subject to great uncertainties. In this paper we briefly outline a procedure, whereby, from the observed two dimensional wind and the anelastic momentum and continuity equations, the vertical velocity, liquid water content, temperature and pressure are evaluated. The method is an extension and modification of previous methods developed by the authors (Hane and Scott, 1978; Gal-Chen, 1978). In order to assess the viability of the method we have conducted several simulations with simulated radar data generated by numerical models (Deardorff, 1974; Klemp and Wilhelmson, 1978). Some of these results are presented in Section 3. Encouraged by the results of the simulations we are now experimenting with real radar data from projects PHOENIX (boundary layer observations) and SESAME (severe storms observations).

2. PRINCIPLES OF THE MODEL

2.1 Governing Equations

A special form of the Navier-Stokes equations for low Mach number flows is the so-called "anelastic" approximation (Batchelor, 1953; Ogura and Charney, 1962; Ogura and Phillips, 1962). The continuity and momentum equations of the "anelastic" set may be written in Cartesian coordinates as follows: Continuity equation,

$$\partial/\partial x_i(\rho_{o_a} u^i) = 0 \tag{2.1}$$

Momentum equations,

$$\begin{aligned}\partial/\partial t(\rho_{o_a} u^i)+\partial/\partial x_j(\rho_{o_a} u^i u^j) \\ = -\partial p'/\partial x_i-\delta^{i3}\rho' g+\partial\tau^{ij}/\partial x_j+f^i\end{aligned} \tag{2.2}$$

δ^{i3} is the Kronecker delta, g is the constant of gravity. Here the tensorial notation with the summation convention has been used. u^i is the velocity in x_i direction averaged over a grid of volume $\Delta x\Delta y\Delta z$, where Δx, Δy, Δz are the grid resolution in the x, y, z direction, respectively (i, j, k run from 1 to 3 $x_1 \to x$, $x_2 \to y$, $x_3 \to z$ which is the vertical direction). τ^{ij} is the i, j turbulent stress component. ρ' and p' are density and pressure deviations from their "basic" hydrostatic values given by

$$u = v = w = 0, \tag{2.3a}$$

$$\partial p_o/\partial z = \rho_o g,\ p_o = p_o(z),\ \rho_o = \rho_o(z) \tag{2.3b}$$

$$p_o = \rho_o R T_o,\ T_o = T_o(z). \tag{2.3c}$$

(2.3c) is the equation of state for ideal gases, R is the gas constant for dry air (= 2.8704 × 10^6 cm^2 sec^{-2} deg^{-1}). $T_o(z)$ is the environmental stratification and is measured by conventional radiosondes. $\rho_{o_a}(z)$ is the density which corresponds to hydrostatic adiabatic atmosphere and is given by

$$\rho_{o_a} = \rho_{oo}(1-z/H_i)^{C_v/R}, \tag{2.4a}$$

$$H_i = c_p\theta_o/g. \tag{2.4b}$$

Where ρ_{oo} is the density at z = 0, θ_o is the potential temperature (constant for adiabatic atmosphere). C_p and C_v are the specific heats at constant pressure and volume, respectively; for an ideal gas, their values are: $C_p = (7/2)R$, $C_v = (5/2)R$. f^i is a general representation for body forces other than gravity (e.g. Coriolis force).

Following Deardorff (1975) we assume

$$\tau^{ij} = \rho_{o_a} K_m(\partial u^i/\partial x_j+\partial u^i/\partial x_i), \tag{2.5a}$$

$$K_m = .12\Delta E^{\frac{1}{2}} \tag{2.5b}$$

$$\Delta = (\Delta x\cdot\Delta y\cdot\Delta z)^{1/3}, \tag{2.5c}$$

$$E \equiv \tfrac{1}{2}(\overline{u'^2}+\overline{v'^2}+\overline{w'^2}), \tag{2.5d}$$

$$\varepsilon = D(z)0.70E^{3/2}/\Delta. \tag{2.5e}$$

Where K_m is the sub-grid eddy viscosity coefficient, Δ is the average grid resolution, Δx, Δy, Δz are the grid resolutions in the x, y, z directions respectively, E is the turbulent energy on scale smaller than the grid resolution, $\overline{u'^2}$, $\overline{v'^2}$, $\overline{w'^2}$ are the standard deviations from u, v, w respectively. Where the ($\overline{\quad}$)

indicate an average over the interval

$$(-\underset{\sim}{a},\underset{\sim}{a}),\ \underset{\sim}{a} = (\Delta x/2,\ \Delta y/2,\ \Delta z/2). \qquad (2.6)$$

2.2 Outline of the algorithm

The first step consists of casting the continuity and momentum equations in a non-orthogonal non-Cartesian radar coordinates (Gal-Chen and Somerville, 1975). In doing so two potential sources of errors are minimized. The first are the errors introduced by interpolating the radar data (measured in radar coordinates) from irregularly spaced points to a regularly spaced grid. The interpolation, does not take into account the non-linearity of the governing equations and, therefore, lead to loss of information about smaller scales (Gal-Chen, 1978). In the transformed coordinates the radar measurements are regular. The only interpolations needed are those which, made the centers of two (or more) pulse volumes coincide. The second one are errors introduced by inverting the radial velocities into Cartesian u, v, w components. To do so one solves a matrix equation of the form

$$\hat{A}(\vec{x}) \cdot \vec{u} = \vec{v}_r. \qquad (2.7)$$

Here $\hat{A}(\vec{x})$ is a position matrix, where the elements are the cosines of the angles between the radial directions and the rectangular x, y, z coordinates, $\vec{x}$-position vector, $\vec{u} = (u, v, w)$, $\vec{v}_r$ - radial components. In practice, the radars do not measure $\vec{v}_r$ but $\bar{\vec{v}}_r$-some volume average and since $\hat{A}\cdot\vec{u} \neq \hat{\bar{A}}\cdot\bar{\vec{u}}$, an error is introduced (Miller, personal communication). Even more seriously, however, the noise of two radial velocities measured by two radars is uncorrelated, but by virtue of Eq. (2.7) the noise of two orthogonal components (say u and v) is correlated. This affects both the integration of the continuity Eq. (2.1) and the calculations of velocity products (Eq. 2.2). Since in the transformed coordinates the governing Eqs. are expressed in terms of $\vec{v}_r$ rather than $\vec{u}$ the above mentioned errors are eliminated.

The second step is the estimation of the vertical velocity. If four (or more) radars are used and the elevation angle is sufficiently high than, one can measure directly w; in practice, four radars are not always available and in a substantial portion of a remotely sensed cloud the elevation angle is low. Under those circumstances, in order to obtain vertical velocities, one still has to integrate the continuity Eq. (2.1) either, upward or downward. For the integration of the continuity Eq. one needs either lower or upper boundary condition for w. Unless one can manage to have horizontal wind measurements very close to the surface ($\sim$ 50 m above ground and less) the assumption of zero vertical motion at the lowest observational level is questionable. Recently, it has been demonstrated (Gal-Chen, 1979) that, the vertical velocity at the lower (upper) boundary can be inferred from the vertical vorticity (i.e. $\partial u/\partial y - \partial v/\partial x$) equation. Unfortunately, the method requires calculations of second derivatives, the most crucial are $\partial/\partial y(\partial u/\partial t)$ and $\partial/\partial x(\partial v/\partial t)$. Because derivatives are powerful amplifiers of noise, the method works only with very smooth data. To overcome this limitation we are now using the integral form of the vorticity Eq. which, requires only calculation of first derivatives, therefore, less smooth data is also accpeted. The integral form of the vertical vorticity Eqs. turns out to be

$$\int[\vec{A}(\vec{x}')\times\nabla G(\vec{x},\vec{x}')]\cdot\vec{k}d\vec{x}' = H(\vec{x}) \qquad (2.8a)$$

$$\vec{A}(\vec{x}') = [w_o\partial u/\partial z-(\partial w_o/\partial x)(\partial K_m/\partial z)]\vec{i} + [w_o\partial v/\partial z-(\partial w_o/\partial y)(\partial K_m/\partial z)]\vec{\partial} \qquad (2.8b)$$

Here w_o is the unknown lower (or upper) boundary conditions. $\vec{i}$, $\vec{\partial}$, $\vec{k}$ are unit vectors in the x, y, z directions respectively, G is a Green function (see e.g. Courant and Hilbert, 1953; Courant and Hilbert, 1962 for its definition and use), $H(\vec{x})$ is a known function of the horizontal velocities and is given by,

$$H(x) = \int\{[(d\tilde{u}/dt-\partial\tilde{\tau}^{1\partial}/\partial x_\partial)\vec{i} \quad (d\tilde{v}/dt-\partial\tau^{2\partial}/\partial x_\partial)\vec{\partial}] \times \nabla G\}\cdot\vec{k}d\vec{x} \quad .$$

Here $d\tilde{u}/dt$ and $d\tilde{v}/dt$ are the horizontal accelerations that the u and v components would have had if the lower (upper) boundary conditions were zero. Similarly, $\tilde{\tau}^{1\partial}$ and $\tilde{\tau}^{2\partial}$ are the turbulent stress terms obtained assuming zero vertical velocities at the lower (upper) boundary. The method of solution of the integral Eq. (2.8a, b) is involved and its description will be given elsewhere.

The next step is the determination of liquid water content. This can be done only in places where the elevation angle is sufficiently high so that, one can measure directly $w + v_T$, v_T - terminal fall velocity. Since w is deduced in the previous step it follows that v_T can be measured. Z-- the radar reflectivity factor is also a measurable quantity. Assuming a generalized Marshall and Palmer distribution given by

$$N_D(D) = N_o\exp(-\Lambda D),$$

where $N_D(D)$ = number concentration per unit volume per unit size interval of particle diameter D. N_o, Λ are empirical constants to be determined from the data. Following Atlas, Srivastava and Sekhon (1973) it may be shown that,

$$V_T = 965\text{-}1030[\Lambda/(\Lambda+6)]^7,\ Z=720N_o/\Lambda^7.$$

Thus, from the inferred v_T and Z, Λ and N_o may be estimated. The liquid water content M is given by

$$M = (\pi\rho N_o/\Lambda^4) \times 10^3\text{kg/m}^3.$$

It is noteworthy that traditional estimates of liquid water content use only one parameter, the radar reflectivity, and are therefore subject to great uncertainties (Atlas, Srivastava and Sekhon, 1973). Since we are using two parameters (v_T and Z) it is hoped that, a better estimation of the liquid water content is obtained.

The fourth and last step is the retrieval of buoyancy and pressure fluctuations. The buoyancy is defined as the density fluctuation of the medium. For the case of boundary layer observations the medium is a dry air. In the case of clouds the medium is the moist air and the solid and liquid water. The buoyancy and the pressure are evaluated using Gal-Chen (1978) method.

3. RESULTS

The viability of the method is tested with data generated by numerical models. To simulate boundary layer observations we have used Deardorff (1974) model. For severe storm simulations we have used the Klemp-Wilhelmson (1978) cloud model. With no errors added our procedure recovers exactly the vertical velocities, buoyancy and pressure. To test the sensitivity of the procedure to observational errors we have contaminated the data as follows: (a) addition of random noise to the "observed" horizontal velocities $\pm$ 15 cm/sec for the boundary layer case and $\pm$ 50 cm/sec for the severe storm case. (b) We have taken "observations" which are 2 min apart in the boundary layer case and 4 min apart for the severe storm case. This simulates the fact that, radar measurements are non-simultaneous. In both models the actual time step (i.e. interval between successive time integration) is the order of 10 sec. Thus the models generate data every 10 sec, but we "observed" it every 2 or 4 minutes. The results for the boundary layer case are summarized in Fig. 1 and for the severe storm case in Fig. 2. In Fig. 1 four curves are plotted as a function of z: 1) $\langle|\theta'|\rangle$ here θ' is the potential temperature deviation from the horizontal average, $|\;|$ is a symbol for absolute value and $\langle\;\rangle$ is a symbol for horizontal average; 2) $\langle(|\theta'| - \langle|\theta'|\rangle)^2\rangle^{\frac{1}{2}}$ i.e. the standard deviation associated with $\langle|\theta'|\rangle$; 3) $\langle|\Delta\theta'|\rangle \equiv \langle|\theta' - \theta'_{obs}|\rangle$ where θ'_{obs} is the "observed" potential temperature deviation, $|\Delta\theta'|$ is the "observed" absolute value of the "error"; and 4) $\langle(|\Delta\theta'| - \langle|\Delta\theta'|\rangle)^2\rangle^{\frac{1}{2}}$, the standard deviation of the absolute value of the error. In Fig. 2 we have also plotted the temperature statistics as a function of Z. Solid line is the retrieved temperature, broken line is the standard deviation of the temperature. Short dashed lines (near axis) is the measure of the error (average and standard deviation). From these simulations we have concluded that our procedure may be a viable one. We are now testing it with real data.

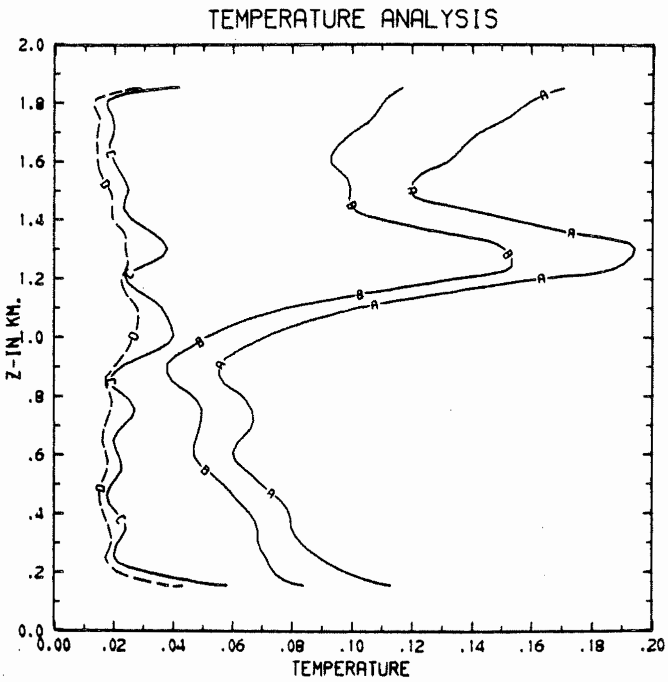

Figure 1. Statistical analysis of the calculated virtual potential temperature deviations $\theta' = \theta - \langle\theta\rangle$ for the boundary layer simulation. Curve A is a vertical profile of $\langle|\theta'|\rangle$; curve B is $\langle(|\theta'| - \langle|\theta'|\rangle)^2\rangle^{\frac{1}{2}}$, i.e. the standard deviation associated with A; curve C is the average "observation error" $\langle|\Delta\theta'|\rangle$; curve D is the standard deviation associated with C.

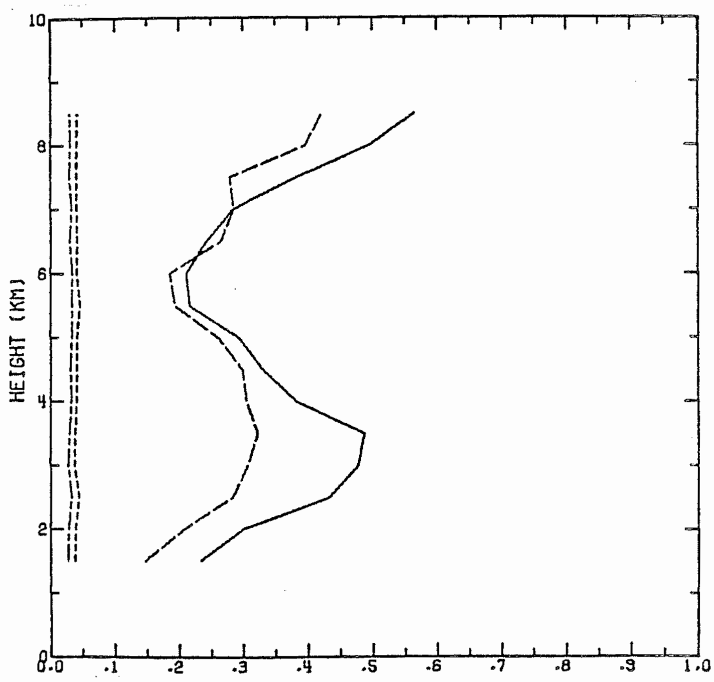

Figure 2. Same as Figure 1 but for the severe storm simulations. Solid line is for the retrieval temperature, broken line is the standard deviation of the temperature, and short dashed lines (near axis) is the measure of the error.

REFERENCES

Atlas, D., R. C. Srivastava, and R. S. Sekhon, 1973: Doppler radar characteristics of precipitation at vertical incidence. Rev. Geophys. and Space Phys., 11, 1-35.

Batchelor, G. K., 1953: The conditions for dynamical similarity of frictionless perfect-gas atmosphere. Quart. J. Roy. Meteor. Soc., 29, 224-235.

Courant, R. and D. Hilbert, 1953: Methods of Mathematical Physics, Vol. 1, Interscience Publishers, 561 pp.

_____ and _____, 1962: Methods of Matheamtical Physics, Vol. 2. Interscience Publishers, 830 pp.

Deardorff, J. W., 1974: Three-dimensional numerical study of the height and mean structure of a heated planetary boundary layer. Bound.-Layer Meteor., 7, 81-106.

_____, 1975: The development of boundary layer turbulence models for use in studying the severe storm environment. Proc. SESAME Open Meeting, D. K. Lilly, ed., Boulder, NOAA Environmental Research Laboratories, 251-264.

Gal-Chen, T., 1978: A method for the initialization of the anelastic equations: Implications for matching models with observations. Mon. Wea. Rev., 106, 587-606.

_____, 1979: A method for calculating temperature pressure and vertical velocities from Doppler radar observations. Preprints 9th Severe Storms Conference, Kansas City, Amer. Meteor. Soc., 492-496.

_____, and R.C.J. Somerville, 1975: Numerical solution of the Navier-Stokes equations with topography. J. Comput. Phys., 17, 276-310.

Hane, C.E. and B.C. Scott, 1978: Temperature and pressure perturbations within convective clouds derived from detailed air motion information: Preliminary testing. Mon. Wea. Rev., 106, 654-661.

Klemp, J. B. and R. B. Wilhelmson, 1978: The simulation of three dimensional convective storm dynamics. J. Atmos. Sci., 35, 1070-1096.

Ogura, Y. and J. C. Charney, 1962: A numerical model of thermal convection in the atmosphere. Proc. Intern. Symp. Numerical Weather Prediction, Tokyo, Japan Meteor. Soc., 431-451.

_____, and N. W. Phillips, 1962: Scale analysis of deep and shallow convection in the atmosphere. J. Atmos. Sci., 19, 173-179.

A D D E N D U M

SATELLITE OBSERVATIONS OF LIGHTNING IN CLOUD SYSTEMS OVER LAND AND OVER OCEANS

R. E. Orville

State University of New York at Albany
Albany, New York, UNITED STATES OF AMERICA

Introduction

The launch of several satellites in the Defense Meteorological Satellite Program (DMSP) has produced a series of papers on lightning observations from satellites. Results published to-date, however, have failed to give a complete picture of global lightning for any time and date. The research reported in this paper is on a detailed effort that is analyzing all global midnight lightning recorded by a DMSP satellite for 365 consecutive days, beginning in September 1977.

Data Source

The data consist of photographs recorded by the high-resolution scanner on the DMSP midnight-noon satellite. It is important to understand the basic characteristics of the satellite before examining the initial results of our analyses.

The DMSP satellite is in a sun-synchronous orbit around the earth; that is, the orbit precesses around the earth once a year and passes overhead near the same local time each day. The orbit is circular with an altitude of 830 km and inclined 98.7° to the equator on the northbound pass. The orbital period is 101.56 min and the highest latitude reached by the subpoint track is 81.3°.

The satellite's high-resolution detector is a silicon PN photodiode with a response curve that peaks at 800 nm with the 0.5 response points at 570 and 970 nm. Gain controls allow the satellite to photograph the surface under illuminations from full daylight to one-quarter moonlight. A change in gain changes the saturation threshold of the system. At night the threshold is low enough so that cities, gas and brush fires, and lightning flashes saturate the system. T. A. Croft has studied these images and determined that the DMSP sensor responds to bright sources from an area extending 92.5 km (50 n mi) above and below the path being scanned by the sensor. Thus the area from which the satellite sensor can respond to lightning is defined by a vertical rectangle with dimensions 3.8 km x 185 km. The sensor's characteristic response to lightning produces a horizontal streak on the negative. The differential sensitivity, if any, to cloud-to-ground or intracloud lightning is unknown.

Data Reduction and Discussion

The lightning data consist of a series of photographs taken by the high-resolution scanner on the DMSP satellite. The entire globe between 60°S and 60°N is covered in these data and some areas receive more coverage than others. Areas at higher latitudes are generally of poor image quality because the satellite is passing through a daylight-night transition period. Consequently, lightning at latitudes higher than 60° is neglected.

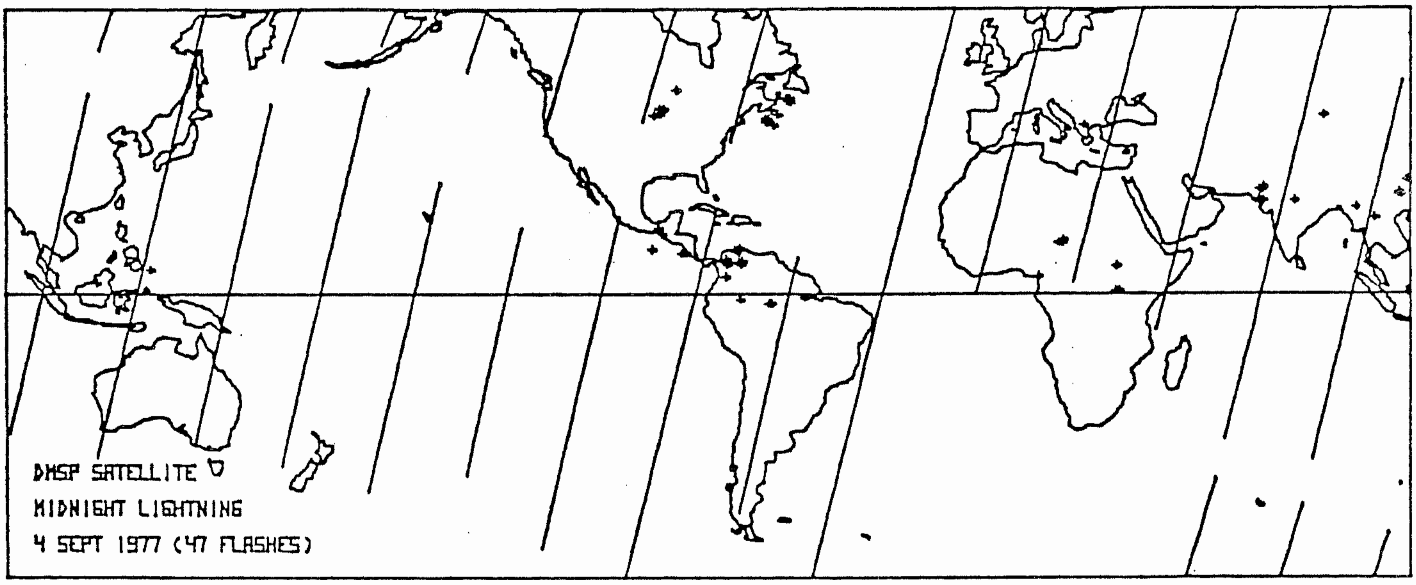

Fig. 1 : Satellite orbital paths and lightning flash locations are plotted for one twenty-four hour period. Gaps in the orbital path indicate that data were not obtained over these areas on September 4, 1977. Lightning locations are marked with a "+" sign.

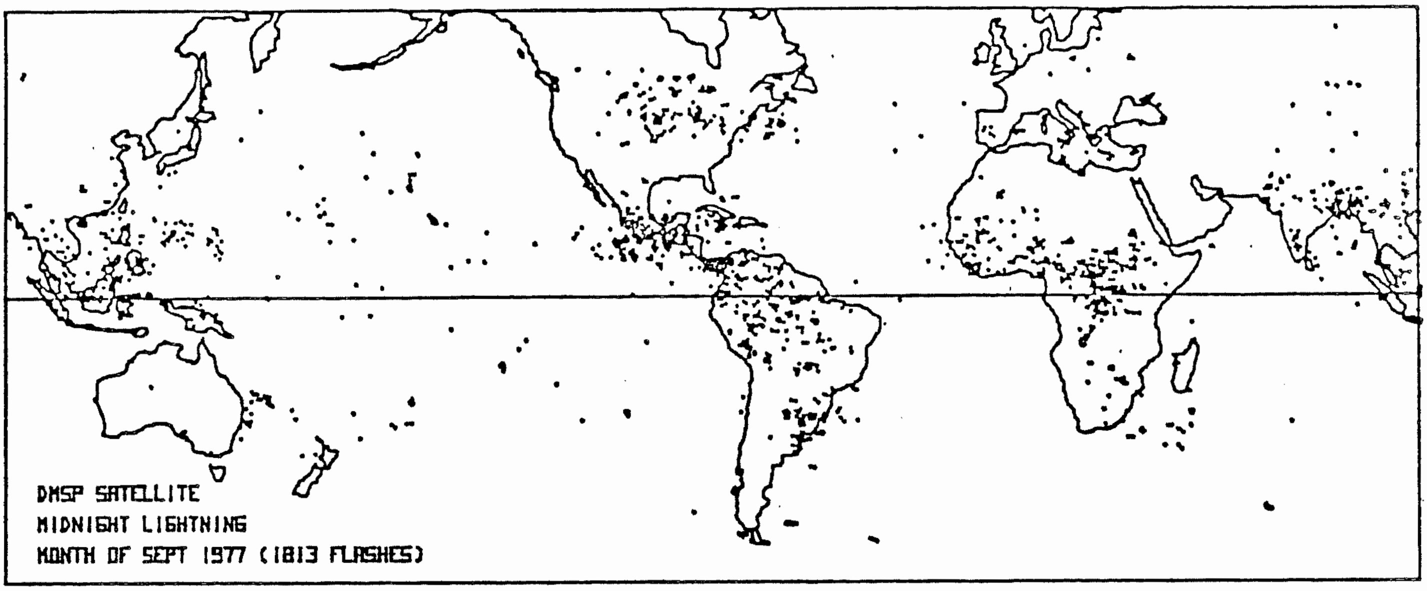

Fig. 2 : Midnight lightning flash locations for the month of September 1977 are plotted with a dot. A total of 1813 flashes show concentrations over Indonesia, South America, and Africa. There appear to be very few lightning flashes occurring over the oceans.

The data set under analysis consists of photographs which are archived at the University of Wisconsin-Madison Space Science and Engineering Center. Our analysis begins with the photographs collected on September 1, 1977 and continues for 365 days.

The lightning flashes are easy to differentiate from other bright areas such as cities, and gas and brush fires. These latter events are several scan lines thick while lightning is only one line thick, and is always associated with clouds.

Our analysis requires that each lightning streak on a DMSP photograph be marked on a map as near as possible to the location where it occurred. On the same map, we plot the path of the orbit subpoint when the high resolution scanner was on. The maps are then mounted on a digitizer board and the coordinate of the lightning flashes and orbital path entered into a minicomputer. The resulting data can then be plotted for one day or any number of days under software control.

One example is shown in Fig. 1 for September 4, 1977. The world is plotted as a mercator projection from 60°S to 60°N. The diagonal lines represent the approximate paths of the DMSP satellite over the earth near local midnight. Small plus marks are plotted to show the location of each flash recorded by the DMSP satellite - a total of 47 flashes for this 24 hour period. Where several flashes are in proximity to each other, the plotting marks overlap. A plot of the local midnight data for one 24 hour period, however, is of little use except to check the accuracy of the digitization process. Only a small percentage of the flashes occurring near local midnight are recorded in one day. Consequently, significant plots can be generated only by summing the data for one month and plotting the result.

Our initial analysis has been completed for the month of September 1977 and the results are presented in Fig. 2. The location of 1,813 lightning flashes are shown in respect to the major land areas. Satellite orbit paths have been omitted.

We note the obvious concentration of lightning in Indonesia, Central and South America and Africa. An apparent lack of lightning over the oceans is a curious result. For example, lightning is concentrated in central Africa in a pattern which appears to represent the intertropical convergence zone. This lightning pattern, however, does not continue to the west over the Atlantic Ocean where the intertropical convergence zone is observed. Other lightning concentrations appear in eastern India and Bangladesh in association with the monsoon and in Uruguay and off the east coast of Australia in association with areas of cyclogenesis. Note that no lightning flashes are recorded over Florida, but frequent midnight lightning is recorded over the midwestern part of the United States. This result is consistent with the diurnal variability of convection over Florida which reaches a maximum in the afternoon, more than six hours before the DMSP satellite passes overhead. Our observations are also consistent with the maximum frequency of thunderstorms over the midwest around midnight which has been studied by J. M. Wallace.

These data are only the first results of a detailed study of the global lightning frequency near local midnight. Monthly maps are now being generated for the remaining eleven months and will result in the cataloging of over 20,000 flash locations. Quantitative analyses are also in progress to determine the land-ocean midnight flash ratio which is the order of 10 and the global lightning frequency which is thought to range from 40 per sec to 150 per sec.

NOTE: References and acknowledgments have been omitted to conserve space.

COMPARAISON DES CONCENTRATIONS EN NOYAUX GLAÇOGENES OBTENUES PAR UNE CHAMBRE A NUAGE ET PAR UNE CHAMBRE A DIFFUSION THERMIQUE

J.J. BERTRAND, P. BOULARD
Faculté des Sciences
Abidjan COTE D'IVOIRE

Des mesures systématiques de concentration en noyaux glaçogènes ont été faites à Abidjan (Côte d'Ivoire) à l'aide d'une chambre à nuage d'une part, de l'analyse sur filtres dans une chambre à diffusion thermique d'autre part.

I.- TECHNIQUES DE MESURE

I.1. La chambre à nuage. Un volume d'air de deux litres est introduit dans une cuve et refroidi uniformément à -20°C. On crée par évaporation un nuage d'eau surfondu. Ces noyaux glaçogènes donnent naissance à des cristaux qui se développent et tombent dans une solution surfondue où ils sont comptés lorsqu'ils atteignent une taille suffisante.

I.2. Méthode des Filtres. Un volume d'air est prélevé entre 6 et 20 m au-dessus du sol et filtré avec un débit de 15 à 20 l/mn sur Filtres Millipores ; les filtres sont exposés 30 mn à -20°C et saturation nominale par rapport à l'eau dans une chambre à diffusion thermique de Gagin avant le dénombrement des cristaux développés sur le Filtre.

II.- RESULTATS

2.1.- Comparaison de valeurs ponctuelles (décembre 1971-mai 1972)

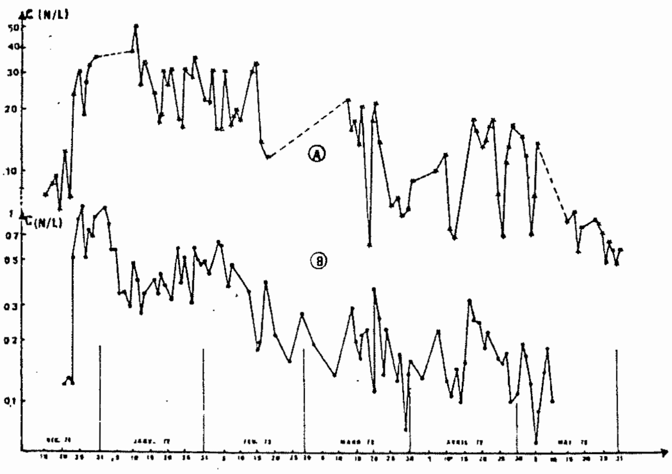

FIGURE 1.- Concentration en noyaux glaçogènes à Abidjan

A. Analyse sur filtre
B. Analyse par la cuve à nuage.

La figure 1 présente des résultats obtenus de décembre 1971 à mai 1972. Les deux méthodes permettent de mettre en évidence une même évolution générale de l'activité glaçogène. On assiste en décembre 1971 à une brusque et importante augmentation du nombre de noyaux glaçogènes. Les valeurs trouvées se maintiennent à un niveau élevé en janvier, puis décroissent en moyenne progressivement de février à mai.

Il apparaît clairement que les deux méthodes permettent de suivre avec des ordres de grandeurs différents les mêmes variations de l'activité glaçogène.

On a tracé (Fig. 2) les courbes de régression entre les résultats obtenus par les deux méthodes, à partir de cinquante sept jours où les prélèvements sur filtres ont été faits, immédiatement après les comptages par la cuve.

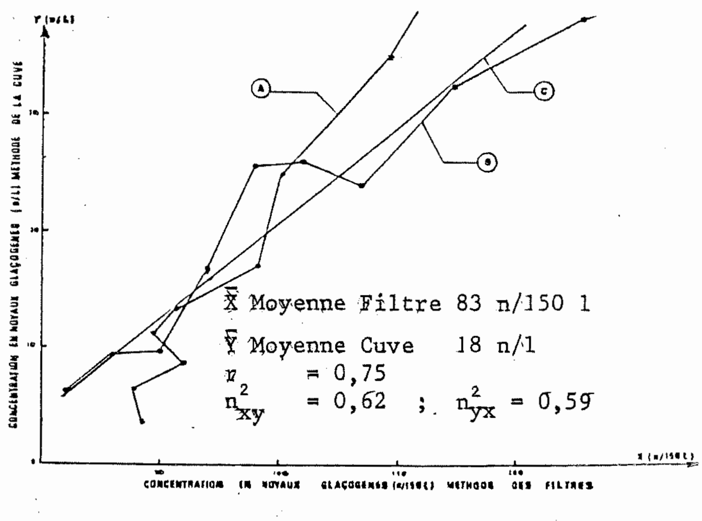

FIGURE 2.- Courbes de régression entre les concentrations en noyaux glaçogènes mesurées sur filtre dans la chambre à diffusion thermique et par la cuve à nuage (A et B).

Droite des Moindres Carrés (C).

Les variations importantes du pouvoir glaçogène sont perçues de la même façon par les deux méthodes. Un coefficient de corrélation linéaire de 0,75 et des rapports de corrélation, tous deux voisins de 0,60 attestent d'une liaison certaine et réciproque entre les deux méthodes.

2.2.- Comparaison de Moyennes mensuelles (1973-1974)

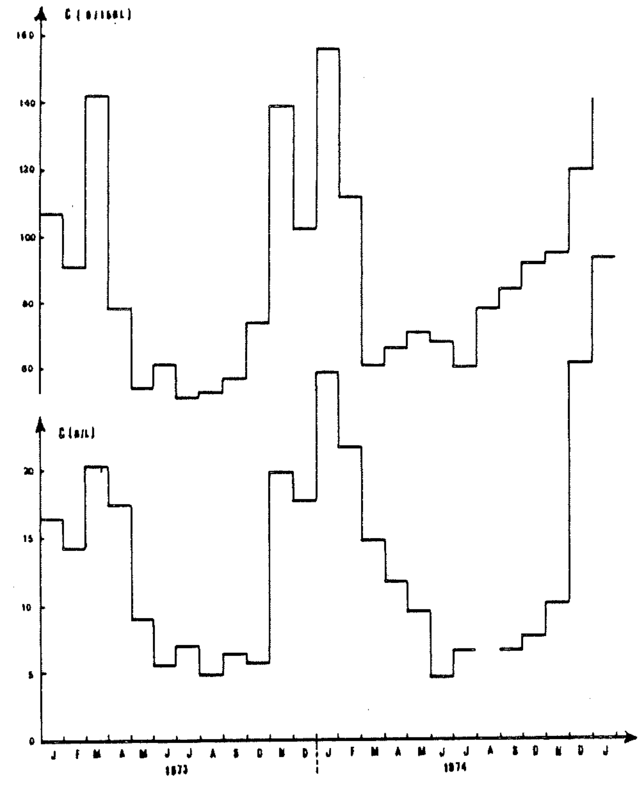

FIGURE 3.- Concentrations mensuelles moyennes en noyaux glaçogènes mesurées :

A. sur filtres

B. par la cuve à nuage.

Les mesures systématiques du pouvoir glaçogène de l'air réalisées à Abidjan en 1973 et 1974 par la méthode de la cuve peuvent être utilement comparées à celles faites par la méthode des filtres (150 l d'air prélevés sur des filtres de pores 0,22 µm) à Abidjan en 1973 et à Adiopodoumé (15 km d'Abidjan) en 1974. Les dates et heures de prélèvement ne se correspondant pas exactement, nous avons comparé les moyennes mensuelles (Fig. 3).

Les deux méthodes donnent des variations généralement bien corrélées, mais les rapports entre les valeurs extrêmes sont de deux à trois fois plus importants par la méthode de la cuve que par la méthode des filtres (4,3 contre 2,6 en 1973 ; 6,1 contre 2,6 en 1974. Les concentrations en noyaux glaçogènes sur filtre sont de dix à trente cinq fois plus faibles que celles obtenues par la méthode de la cuve. Le rapport moyen entre le nombre de noyaux glaçogènes dénombrés par litre dans la cuve et sur les filtres est de 20,7 en 1973 et 20,8 en 1974.

Il est intéressant de noter que ce rapport subit une évolution saisonnière très marquée comme la figure 4 permet de le constater.

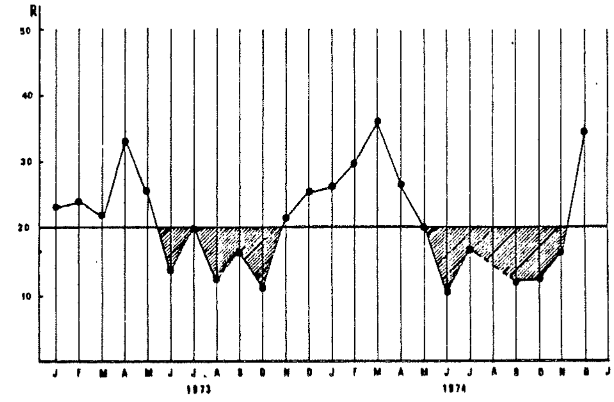

FIGURE 4.- Evolution saisonnière du rapport R entre les concentrations en noyaux glaçogènes mesurées dans la cuve à nuage et sur filtres dans la chambre à diffusion.

Les plus faibles valeurs de ce rapport sont observées de mai à octobre aux époques où l'activité glaçogène est la plus faible. Ceci peut être attribué à une moindre importance de l'effet de volume sur les filtres qui est d'autant plus réduit que le nombre de particules activables est plus faible (2)

Inversement, lorsque le nombre de noyaux glaçogènes est important, le nombre de noyaux dénombrés par la cuve croît plus vite que le nombre de noyaux dénombrés sur filtres et le rapport entre les deux a tendance à augmenter.

Un facteur différent de l'effet de volume doit cependant intervenir pour expliquer que les maxima du rapport représenté sur la figure 4 se situent, non pas en janvier, où la concentration en noyaux glaçogènes est la plus forte, mais en avril 1973 et mars 1974. Cela signifie que, dans ce cas, le nombre de noyaux détectés dans la cuve diminue moins vite que le nombre de noyaux détectés par la méthode des filtres. Cette différence est imputable, semble t-il, à l'élimination des particules glaçogènes les plus grosses qui sont aussi les plus actives par la méthode des filtres, au fur et à mesure que le Front Intertropical s'éloigne d'Abidjan (1).

III.- CONCLUSION

L'activité glaçogène est une donnée qui dépend de multiples paramètres et chaque méthode de mesure ne permet que d'en donner un aspect. Les deux méthodes de mesure utilisées permettent d'apprécier de deux façons différentes les variations importantes du pouvoir glaçogène de l'air. Elles fournissent des réponses relatives mais cohérentes et manifestent un accord satisfaisant. D'une façon générale, la méthode de la cuve est beaucoup plus sensible que la méthode des filtres et les valeurs obtenues se rapprochent, semble-t-il, plus des valeurs réelles. La méthode des filtres, en raison de l'uniformité des conditions d'analyse, permet par contre une analyse plus objective, lorsque les caractéristiques physiques de l'air analysé, en particulier l'humidité, varient de façon importante. Mais la pénétration des particules à l'intérieur des filtres et leur interaction sur sa surface (effet de volume) diminuent considérablement le nombre de particules glaçogènes détectées.

BIBLIOGRAPHIE

1.- BERTRAND, J., 1977,
Action des poussières sub-sahariennes sur le pouvoir glaçogène de l'air en Afrique de l'ouest.
Thèse d'Etat, n° d'ordre 253, Clermont-Ferrand.

2.- LANGER, G., and ROGERS, J., 1975,
An experimental study of the Detection of the nuclei on membrane Filters and other substrata.
J. Appl. Meteor., 14, 4, 560-570.

3.- GAGIN, A. and AROYO, M., 1969,
A thermal diffusion Chamber for the measurement of ice nuclei concentrations.
J. Rech. Atm., 4, 115-122.

REAL TIME PROCESSING OF CLOUD PARTICLE IMAGE DATA

Philip G. Stickel and D. Ray Booker
Aeromet, Inc.
P.O. Box 45447
Tulsa, Oklahoma 74145

1.0 INTRODUCTION

Aeromet, Inc. is currently under contract with the United States Army Ballistic Missile Defense Systems Command (BMDSCOM) to furnish in real time; descriptions of cloud particle habits, liquid water contents, and cloud particle spectra information. The aircraft collected cloud particle data are collated with radar "S" band and "C" band data. The particle data are used to determine Z-M equations in real time so the radars can be used to define liquid water content profiles in real time. There was a need to improve aircraft cloud particle information through the use of a real time program for two dimensional (2-D) Particle Measuring Systems (PMS) probe data. The following paper describes the method Aeromet accomplishes this requirement.

2.0 DATA SOURCE

The cloud particle data are measured and recorded by means of a Learjet at altitude ranges from the surface to 15 km and at sampling speeds near 180 ms^{-1}. The majority of the measurements are in a tropical environment, however, data are also collected in continental air masses at the middle latitudes, near Tulsa, Oklahoma.

The aircraft is equipped with a full set of Particle Measuring Systems (PMS) Optical Array Spectrometer one dimensional and two dimensional probes, two Omega navigation systems, a TACAN system and state parameter measuring equipment such as altitude, static air temperature, etc. A minicomputer system, two magnetic tape drives and a dual floppy disk drive process and record the data in real time.

3.0 PMS PROBES

The release of the two dimensional (2-D) Optical Array Spectrometer Probes (Knollenberg, 1976) provided an additional means of measuring cloud and precipitation droplets in an undisturbed air flow. Numerious authors (Cunningham, 1978; Heymsfield, 1972, 1976; Cannon, 1976) have described and reviewed the PMS probes. Due to the abundance of reading material available, a discussion of the 2-D probes will be included only to enhance the topic presented.

The 2-D system uses a linear array of 32 photodiodes illuminated by a 1.5 mW helium-neon laser. The laser beam is reflected from the laser source by optical mirrors to provide a vertical beam in the free airstream before illuminating the photodiodes. Cloud particles passing through the beam cast a shadow on the photodiodes. If 50% or more of the light is occulted, then the photodiode is considered shadowed, Fig. 1. The probe hardware checks the status of the 32 photodiodes, at a rate of up to 4 MHz for the 2-D cloud probe and 1 MHz for the precipitation probe. Once a photodiode is shadowed, the status of each of the photodiodes is recorded into a 32 bit binary word and stored into a 1024 word buffer. Data are stored at the status sampling rate until no photodiodes are shadowed, at which time a series of 2 to 3 blank words are recorded during the clock shutdown, and two words containing sync information and 24 bits of elapsed time information are recorded. When the buffer is full, the data are dumped through a Data Acquisition System (DAS) to magnetic tape. The important items of note are that the data are already compressed by the recording technique, and that there are 2 to 3 blank scans immediately after the image and before the time information. However, the amount of data recorded is still tremendous with a 1200 foot reel of magnetic computer tape only archiving ten minutes of data at the maximum sampling rate.

Fig. 1. Rosette ice particle passing across the optical array of PMS 2-D probe is imaged as a matrix of ones and zeros.

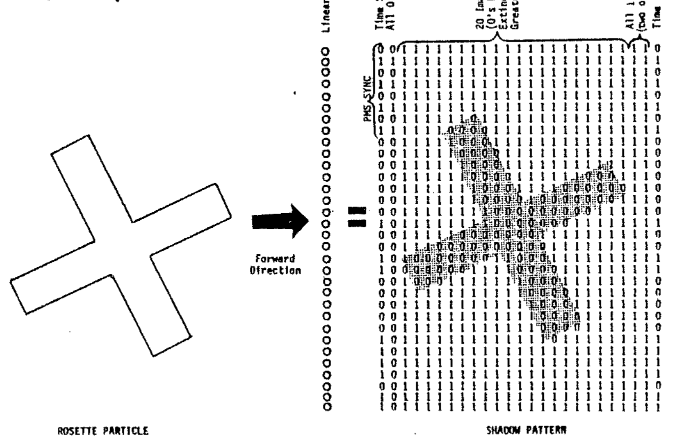

The only means by which PMS supplied to use the 2-D data in real time was through the viewing of the data on a Particle Image Detector (PID) CRT. The data are displayed as a shadow pictograph where one picture element (pixel) corresponds to one bit of each 32 bit scan word. During in cloud sampling the update rate is typically too fast to visually digest the information.

The processing time required of the copious amounts of data by a computer is typically a factor of 1.5 to 2 times longer than to collect. This puts a serious crimp into real time processing of the data.

4.0 ADVANTAGES OF 2-D DATA ANALYSIS TECHNIQUES

The use of 2-D data have many advantages to aid in the definition of a "cloudy" environment. A list of advantages may be as follows.

1. The ability to define the actual image area instead of a predicted area based on a one dimensional measurement.

2. The ability to see the shadow image of the particle, which aids in the understanding the crystal type and growth process.

3. The ability to distinguish between valid images and image artifacts.

Many papers have been released on the analysis techniques used to glean useful information from the data (Cunningham, 1978; Cooper, 1978; Heymsfield, and Parrish, 1978). Each of these authors and data users are interested in, but not limited to the following.

1) Defining techniques which use measurable image characteristics to convert from physical size to equivalent melted diameter, (EMD). These characteristics are sometimes referred to as roughness parameters i) aspect ratio, ii) equivalent circle ratio, iii) average projection ratio, and iv) bulk area ratio.

2) Defining techniques to eliminate image artifacts.

3) Defining techniques to reconstruct particles lying partially within the sampling volume in order to improve sampling statistics.

4) Developing techniques to speed up the processing of 2-D data.

The following section is a method by which item 4 can be achieved to the level of real time processing of 2-D data.

5.0 REAL TIME IMAGE PROCESSOR

The 2-D data is needed for real time decisions, but the abundance of data is too great to process by a computer in real time. It also becomes evident from the support material referenced, that there exists a preferred group of image characterizing parameters which are required to derive needed spectral information.

Under a contract to the Air Force Geophysics Laboratory, Aeromet designed, built, and currently uses operationally a Real Time Image Processor (RTIP), to calculate by hardware in real time, image characterizing parameters. The RTIP system, which consists of 16 printed circuit cards, is installed in the spare card slots of the DAS and intercepts the incoming eight bit byte bursts of one MHz bit data rate from each probe at the input of the DAS. The image data are then routed through the RTIP where several image characteristics are computed. The data are delayed by 64 bits so the PMS sync byte can be recognized and used as an indication of the end of the image data. The flow of data is shown in Fig. 2.

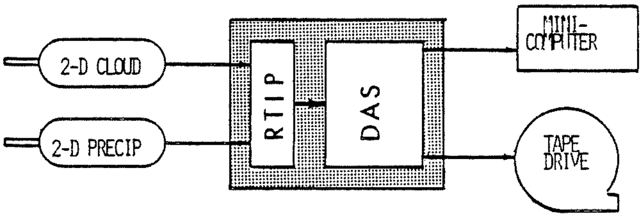

Fig. 2. Flow diagram of the Real Time Image Processor (RTIP) interface to the Data Acquisition System (DAS).

The RTIP data are then inserted into the data stream just ahead of the PMS word containing the sync byte and elapsed time word. Thus, it is written over the blank data after the end of each image and before the elapsed time word. This format allows the RTIP information to be inserted into the normal PMS record without changing the length of the record or altering any of the information normally used for processing 2-D data. The resulting format of an image is shown in Fig. 3. An RTIP sync byte is written so post flight computer processing can easily identify the RTIP data.

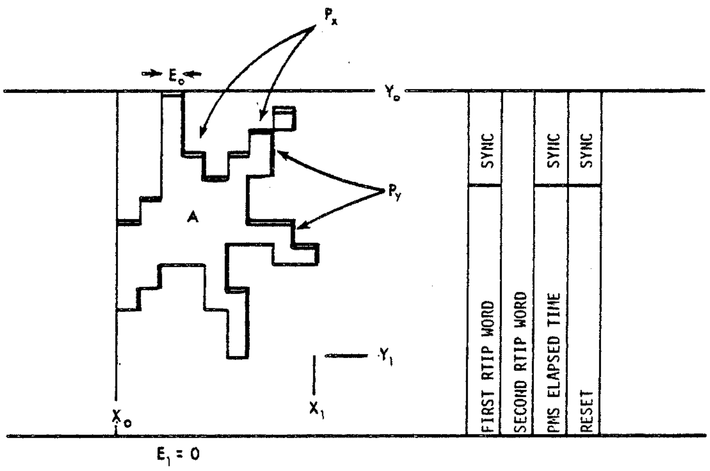

Fig. 3. Example of the Real Time Image Processing (RTIP) information recorded with the PMS image data. The length of the image record is unchanged.

The RTIP contains several counters which accumulate the; 1) area, 2) length, 3) perimeter and other characteristics discussed below as the image data are passed through the RTIP. The contents of these counters are sequentially dumped as two 32 bit words when the PMS sync byte is recognized.

The RTIP data contained in the two words can be output to a computer in real time in addition to being written onto the magnetic tape. The real time computer program can then use the RTIP data to compute particle size spectra, equivalent water content and other information that may be needed for real time purposes.

To further discuss the recorded RTIP variables, a conventional notation must be defined to simplify the discussion. If one views the image printouts as shown in Fig. 3, the particle images are displayed as if the aircraft was sampling from the left side of the page eastbound towards the right side of the page. Tops of the images can, therefore, be referred to as the north side and so forth around the compass. Use of this orientation allows one to define "x" to be increasing in the easterly direction, agreeing with the direction of flight. However, "y" will be defined to increase from north to south to agree with PMS documentation manuals. An image element is defined to correspond to a shadowed diode during sampling. The characterizing parameters defined by the RTIP, making reference to Fig. 3 are as follows.

1. XMAX - a flag set when the number of image elements in the "x" direction equals or exceeds 64, (1 bit of RTIP data).

2. North end element count (E_0) - the total number of image elements along the north edge, (6 bits of RTIP data).

3. South end element count (E_1) - the total number of image elements along the south edge, (6 bits of RTIP data).

4. Area (A) - the total number of image elements contained within the image (11 bits of RTIP data).

5. Probe identification flag - written as a binary "01" for the 2-D cloud probe and a "10" for the 2-D precipitation probe (2 bits of RTIP data).

6. North facing perimeter (P_x) - the total number of image elements with a northern exposure, which also equals the southern exposure, (7 bits of RTIP data).

7. East facing perimeter (P_y) - the total number of image elements with an eastern exposure, which equals the western exposure, (7 bits of RTIP data).

8. Maximum x address (X_1) - the address of the eastern most image elements (6 bits of RTIP data). Minimum x address is always zero.

9. Maximum y address (Y_1) - the image element number counting from the north end element to the southern most image element, (5 bits of RTIP data).

10. Minimum y address (Y_0) - the image element number counting from the north end element to the northern most image element, (5 bits of RTIP data).

11. Sync byte - written as the compliment of the PMS sync byte (8 bits of RTIP data).

The eleven characterizing parameters produced by the RTIP provide all the information needed to properly size and categorize the 2-D image data on a particle by particle basis which can then be converted to spectral information.

6.0 2-D REAL TIME PROGRAM

Aeromet, Inc. is in the process of developing a 2-D real time program, using the RTIP information, to replace the present 1-D real time program. The RTIP data are being recorded on the 2-D flight tapes and used as a real time input to the software development. A brief description follows to illustrate the point of how RTIP data can be used.

The processing of the 2-D data is illustrated in Fig. 4 through the use of a Warnier-Orr diagram common to structure design. The program is being developed to allow freedom in many areas of the calculations based on modifications to the decision constraints. The first of these areas is in the image artifact rejection criteria section. A second area of the software decision making which is also on muddy ground is the classifying of data into bin types (EMD, area, maximum length), while a third area is in the conversion from physical dimensions of ice crystals to equivalent melted diameters. Experience with the use of 2-D data in spectral form along with intercomparison with radar data will define a more rigid processing technique.

Real-Time Process of 2-D
- 1. Convert slow data to engineer units
- 2. Read entire buffer of image data (process image by image)
  - 1. Find RTIP sync byte
  - 2. Correct area
    - 1. For 1½ initial missing scans
    - 2. For true airspeed overdrive
  - 3. Calculate roughness parameters
    - 1. Aspect ratio
    - 2. Equivalent circle ratio
    - 3. Average project ratio
    - 4. Bulk area ratio
  - 4. Apply rejection criteria
    - 1. Raw area $\geq$ 50% of 32 x 64 image element field
    - 2. North end element > 0
    - 3. South end element > 0
    - 4. XMAX $\geq$ 64
    - 5. Aspect ratio $\geq$ 6
    - 6. Bulk area ratio < 40%
  - 5. Accumulate the accepted particles into 30 bins
- 3. Convert to spectral information (in development phase)

Fig. 4. Warnier-Orr diagram illustrating the design structure of the Aeromet 2-D Real Time Program.

PART NUM	REC ELAPS SECONDS	TIME MILSEC	XTAL-TM MICSEC	ID	YMAX CNT	YMIN CNT	XMAX CNT	XFLG	NEE CNT	SEE CNT	SPER CNT	EPER CNT	PERIM MIC	LY MIC	LX MIC	LMAX MIC	AREA R-CNT	AREA A-CNT	AREA MM**2	ECR	APR	ASR	TST REJ
31	1989.	362.	131.	CL	10	8	8	0	0	0	8	3	240	120	0	120	19	0	0.0000	0.00	1.00	0.00	0
32	1989.	362.	17705.	CL	32	23	7	0	0	6	9	10	800	400	0	400	47	0	0.0000	0.00	1.00	0.00	4
33	1989.	362.	8298.	CL	0	31	0	0	0	0	0	0	0	0	0	0	0	0	0.0000	0.00	0.00	0.00	32
34	1989.	362.	2270.	CL	32	1	37	0	7	7	56	49	3920	1200	0	1200	516	0	0.0000	0.00	1.53	0.00	6
35	1989.	362.	2230.	CL	29	27	2	0	0	0	4	2	160	120	0	120	4	0	0.0000	0.00	.67	0.00	0
36	1989.	362.	2188.	CL	8	3	4	0	0	0	5	6	480	240	0	240	22	0	0.0000	0.00	1.00	0.00	0
37	1989.	362.	2560.	CL	32	25	9	0	0	7	9	9	720	320	0	320	56	0	0.0000	0.00	1.13	0.00	4
38	1989.	362.	4121.	CL	32	16	23	0	0	10	26	18	1440	680	0	680	202	0	0.0000	0.00	1.06	0.00	4
39	1989.	362.	1222.	CL	32	31	3	0	0	2	3	2	160	80	0	80	4	0	0.0000	0.00	1.00	0.00	4
40	1989.	362.	16465.	CL	32	31	3	0	0	3	3	2	160	80	0	80	6	0	0.0000	0.00	1.00	0.00	4
41	1989.	362.	5273.	CL	32	10	16	0	0	12	27	23	1840	920	0	920	185	0	0.0000	0.00	1.00	0.00	4
42	1989.	362.	8684.	CL	18	9	8	0	0	0	8	10	800	400	0	400	57	0	0.0000	0.00	1.00	0.00	0
43	1989.	362.	3670.	CL	10	1	7	0	6	0	8	10	800	400	0	400	60	0	0.0000	0.00	1.00	0.00	2
44	1989.	362.	1055.	CL	23	22	1	0	0	0	1	2	160	80	0	80	2	0	0.0000	0.00	1.00	0.00	0

REJECT TOTALS:[AREA.GE.50%	N.DIODE	S.DIODE	X.GE.64	ASPR.GT.6	RCNT.EQ.0	A/XY.LT..4	NO. REJ.	% REJECT]	X CORR.F
0	10	16	0	0	2	3	27	61.	0.0000

Fig. 5. Partial computer generated listing of the characterizing parameters generated for each image. The rightmost column is the test rejection code. A summary of the total percent rejection for the image scan is given directly above the scan.

A more indepth description of the 2-D real time program will be available in a subsequent publication. An example of some of the current computer generated output is given in Figs. 5 and 6 to illustrate the versatility and usefulness of RTIP data.

2-D CLOUD PROBE
Y-DIMENSION TO EMD
START= 212920. END= 212950. CRYSTAL TYPE=BULLET ROSETTES

CHAN	ADJ.CHAN DIODE	AREA MM**2	EMD MM	RAW CLSS SIZE	COUNT
1	1.33	4.80	12.95	40.	5.
2	2.48	18.56	22.34	80.	2.
3	3.63	40.32	31.17	120.	2.
4	4.78	65.88	39.66	160.	1.
5	5.93	63.44	47.89	200.	3.
6	7.08	61.00	55.93	240.	1.
7	8.23	58.56	63.80	280.	2.
8	9.38	56.12	71.54	320.	1.
9	10.53	53.68	79.16	360.	0.
10	11.68	51.24	86.67	400.	0.
11	12.83	48.80	94.09	440.	1.
12	13.98	46.36	101.43	480.	0.
13	15.13	43.92	108.70	520.	0.
14	16.28	41.48	115.89	560.	0.
15	17.43	39.04	123.03	600.	0.
16	18.58	36.60	130.10	640.	0.
17	19.73	34.16	137.12	680.	0.
18	20.88	31.72	144.09	720.	1.
19	22.03	29.28	151.01	760.	1.
20	23.16	26.84	157.88	800.	0.
21	24.33	24.40	164.72	840.	0.
22	25.48	21.96	171.51	880.	0.
23	26.63	19.52	178.28	920.	0.
24	27.78	17.08	184.98	960.	0.
25	28.93	14.64	191.66	1000.	0.
26	30.08	12.20	198.31	1040.	0.
27	31.23	9.76	204.93	1080.	0.
28	32.38	7.32	211.52	1120.	0.
29	33.53	4.88	218.08	1160.	0.
30	34.68	2.44	224.61	1200.	0.

Fig. 6. An example of the preliminary results of the Aeromet Real Time Program using the RTIP input.

7.0 SUMMARY

The use of 2-D data has many advantages over 1-D data, especially when used in making real time decisions. Some of these advantages are known to be: 1. better crystal habit definition; 2. increased accuracy of the data base; and 3. better size range.

The 2-D data in its present form was seen to be too much for real time processing. The development of the Real Time Image Processor (RTIP) by Aeromet, Inc. has provided the avenue to achieve real time processing of 2-D data on a minicomputer. The means for this achievement is through hardware circuitry consisting of several counters which interpret the image data at the leading edge of the Data Acquisitions System (DAS) and accumulate known parameters which characterize the image. The output of the counter buffers are overlayed as two 32 bit words between the image data and corresponding PMS sync and elapsed time information. No additional space on the magnetic tape is required. An additional port from the RTIP can provide the information directly into a minicomputer for real time processing. The operational use of the RTIP coupled with its accuracy and reliablity has permitted Aeromet to develop a real time program on a minicomputer using 2-D RTIP data.

8.0 ACKNOWLEDGMENTS

The authors wish to thank the Army Ballistic Missile Defense Systems Command and the Air Force Geophysics Laboratory for their continued support of technology development in conjunction with operational testing.

9.0 REFERENCES

Cannon, T.W., 1976: Imaging devices. Atmos. Technology, No. 8, pp 32-37.

Cooper, W.A., 1978: Cloud physics investigations by the University of Wyoming in HIPLEX 1977. Report No. AS119, Dept. of Atmos. Science, Univ. of Wyoming. August, 1978, pp 320.

Cunningham, R.M., 1978: Analysis of particle spectra data from optical array (PMS) 1D and 2D sensors. Fourth Symposium on Meteorological Observations and Instrumentation. Denver, Amer. Meteor. Soc., Boston, pp 345-350.

Heymsfield, A.J., 1976: Particle Size Distribution Measurement: An Evaluation of the Knollenberg Optical Array Probes. Atmospheric Technology, No. 8, pp 17-24.

________________, and J.L. Parrish, 1978: A computational technique for increasing the effective sampling volume of the PMS two dimensional particle size spectrometer. J. Appl. Meteor., Vol. 17, pp 1566 - 1572.

Knollenberg, R.G., 1976: Three new instruments for cloud physics measurements. International Conference on Cloud Physics, Boulder, Amer. Meteor. Soc., Boston, pp 554 - 561.

MISE EN EVIDENCE DE L'EFFICACITE GLAÇOGENE DES AEROSOLS AU CONTACT D'UNE MASSE D'AIR OCEANIQUE

J. Bertrand

Laboratoire de Physique Atmosphérique
Abidjan COTE D'IVOIRE

1.- Introduction.

Les concentrations en noyaux glaçogènes (NG) mesurées en Afrique de l'ouest à différentes latitudes, Abidjan (5°15'N), Lamto (6°13'N), Bobo-Dioulasso (11°10'N) sont caractérisées par des variations annuelles similaires et bien marquées dont la figure 1 donne un exemple.

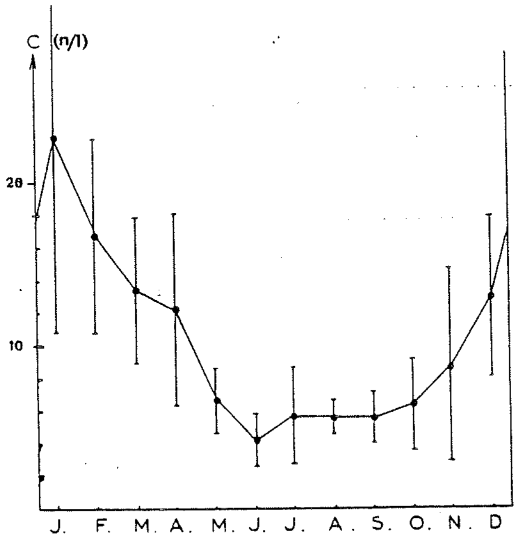

FIGURE 1 : Moyennes mensuelles (1968-1974) des concentrations en noyaux glaçogènes à Abidjan mesurées par la méthode de la Chambre à nuage.

Ces variations sont liées d'une part au mouvement des masses d'air représentées par le déplacement du Front Intertropical (F.I.T.) limite entre l'air océanique au Sud et l'Alizé continental au Nord (Fig. 2), d'autre part à la génération et au déplacement de brumes de poussière ayant pour origine la bordure Sud du Sahara (1).

En été, lorsque le FIT est haut en latitude et que la mousson pénètre profondément sur le continent, les concentrations en N.G. sont faibles. En hiver par contre, époque privilégiée des brumes sèches, ces concentrations sont élevées.

Ainsi le pouvoir glaçogène dépend essentiellement de la présence d'aérosols continentaux dont l'efficacité peut être expliquée par la présence constante d'une fraction argileuse.

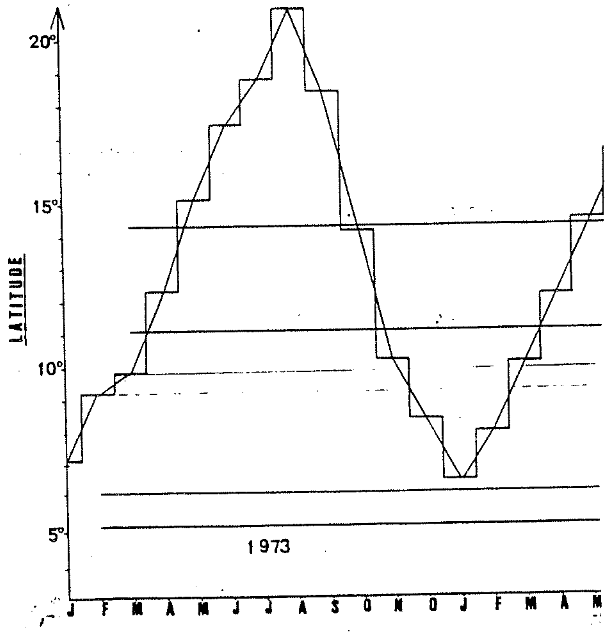

FIGURE 2 : Position de la trace au sol du FIT en latitude à 5°W, de janvier 1973 à avril 1974.

Cependant, de nombreuses observations montrent qu'il est nécessaire de distinguer soigneusement entre concentrations en noyaux glaçogènes et concentrations en aérosols. (2) D'une façon générale, la décroissance de la concentration en noyaux glaçogènes, tant dans la variation annuelle que pour des situations particulières, est moins rapide que la décroissance des concentrations en aérosols. Par ailleurs, on peut, dans certains cas, obtenir des pouvoirs glaçogènes aussi ou plus élevés avec une faible masse d'aérosols continentaux que dans des situations caractérisées de brumes de poussière.

Nous avons essayé d'interprêter ces anomalies sur la base d'une augmentation de l'efficacité glaçogène des aérosols continentaux lorsqu'ils pénètrent dans la masse d'air océanique.

2.- Collecte des données

Des échantillons d'aérosols atmosphériques ont été collectés d'août à décembre 1974, à la fois sur filtres MILLIPORE HSWP et sur filtres WHATMAN 41, à Adiopodoumé, Lamto et Bobo-Dioulasso. Cette période de prélèvement correspond à un déplacement du FIT de sa position la plus au Nord en août, à la position la plus au Sud en décembre. Les prélèvements de 150 litres sur filtres MILLIPORE ont servi à déterminer le pouvoir glaçogène à -20°C dans une chambre à diffusion thermique de GAGIN (3). Les prélèvements sur filtres WHATMAN, correspondant à une moyenne de 900 m^3 d'air filtré en trois ou quatre jours, ont servi à analyser les principaux constituants élémentaires de l'aérosol atmosphérique exceptée la Silice (Na, K, Ca, Mg, Al, Fe) sous leur forme soluble (s) et insoluble (i), par la méthode d'adsorption atomique (4).

A chaque prélèvement sur filtre WHATMAN, nous avons fait correspondre la valeur moyenne du pouvoir glaçogène. Les données sont constituées de 88 échantillons à 24 variables obtenues en considérant, en plus du pouvoir glaçogène et des concentrations des éléments sous leur forme soluble et insoluble, la concentration en masse de l'aérosol atmosphérique, la position et la vitesse moyenne du FIT au cours du prélèvement et la position du FIT quatre jours avant le prélèvement.

3.- Analyse des données

Un programme d'analyse en composantes principales a été appliqué à quatre groupes d'échantillons en utilisant les critères de la position et des mouvements du FIT pour stratifier les données.

a) Ce groupe inclue l'ensemble des échantillons (88)
b) On a sélectionné tous les cas où la trace au sol du FIT se trouvait entre 4° de latitude au Nord et 2° de latitude au Sud de la Station où était prélevé l'échantillon (36 cas)
c) Parmi les échantillons de (b), on a retenu les cas où le FIT se trouvait au Nord de la station, quatre jours avant le prélèvement (21 cas)
d) Echantillons de (b) pour lesquels le FIT se trouvait au Sud de la Station, quatre jours avant le prélèvement (15 cas).

4.- Résultats

Nous ne présenterons ici que la position dans le plan principal des vecteurs correspondant aux cinq variables les plus significatives pour la discussion : noyaux glaçogènes (N.S.), position du FIT (F.I.T.), masse d'aérosols (M.P.), sodium soluble Na_S et Aluminium (Al), ainsi que les matrices de corrélation de ces variables entre elles.

4.1. Premier cas incluant l'ensemble des observations

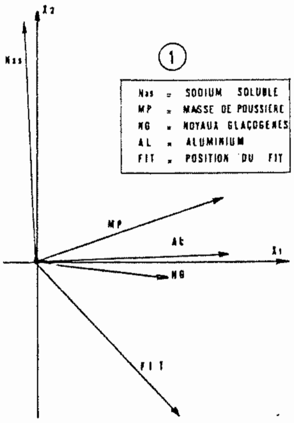

	N.G.	M.P.	AL	NaS	P. F.I.T
N.G.	1	0,604	0,542	0,006	0,555
M.P.	0,604	1	0,830	0,141	0,516
AL	0,542	0,830	1	- 0,106	0,618
NaS	0,006	0,141	- 0,106	1	- 0,449
P. F.I.T.	0,555	0,516	0,613	-0,449	1

FIGURE 3 : Position des vecteurs variables dans le plan principal et Matrice de correlation.

La corrélation positive de la position du FIT en latitude avec l'aluminium et négative avec le sodium soluble montre que l'aluminium est un élément d'origine continentale et le sodium soluble un élément surtout d'origine océanique. Al et Na(s) sont ainsi d'une façon générale anticorrélés. Les valeurs relativement faibles des rapports de corrélation s'expliquent aisément si l'on considère que la concentration en aérosols continentaux n'est pas nécessairement une fonction croissante de la latitude et dépend en particulier, de la trajectoire des poussières à partir des zones de génération et qu'une fraction du sodium soluble est d'origine continentale.

La corrélation forte existant entre la concentration en masse des aérosols et l'aluminium montre que les aérosols présents sur l'Afrique de l'ouest sont essentiellement d'origine continentale. Le pouvoir glaçogène est corrélé avec la concentration en masse (0,604), et avec les aérosols continentaux représentés par Al (0,542). Il n'est par contre pas lié à Na_S (0,006).

4.2. Second cas regroupant les Echantillons prélevés au voisinage du FIT

Le champ de variation du FIT autour de chaque station de prélèvement étant réduit, sa position devient alors moins significative. La concentration en masse reste fortement liée à Al, c'est-à-dire aux aérosols continentaux. Mais la corrélation entre ces aérosols et le pouvoir glaçogène diminue par rapport au cas précédent. On constate simultanément une corrélation positive entre pouvoir glaçogène et sodium soluble. Si le sodium soluble était

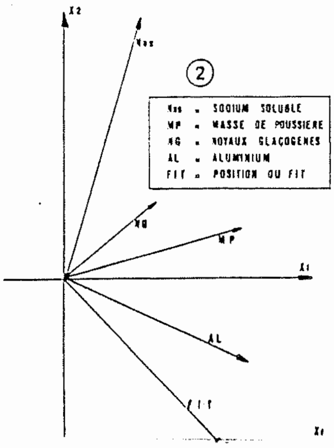

	N.G.	M.P.	Al	NaS	P. FIT
N.G.	1	0,435	0,283	0,373	0,319
M.P.	0,435	1	0 721	0,497	0,143
Al	0,283	0,721	1	0,162	0,353
NAS	0,373	0,497	0,162	1	0,407
P. F.I.T	0,319	0,143	0,353	0,407	1

FIGURE 4 : Matrice de corrélation et position des vecteurs variables dans le plan principal.

uniquement d'origine océanique, on pourrait y voir une preuve de l'influence d'aérosols marins sur le pouvoir glaçogène. Mais la corrélation entre Al et Na(s) qui, de négative devient positive, manifeste que dans ce cas la majeure partie du sodium soluble est d'origine continentale. On ne peut donc conclure. Pour le faire, nous avons dû considérer les mouvements du FIT en nous référant à sa position quatre jours avant le prélèvement.

4.3. Troisième cas : les prélèvements ont lieu à proximité du FIT et celui-ci se trouvait au Nord des stations, quatre jours avant.

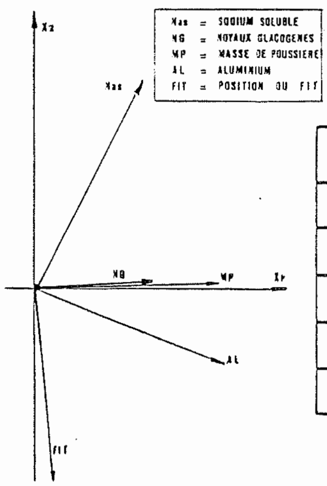

	N.G.	M.P.	Al	NaS	P. F.I.T
N.G.	1	0,671	0,573	0,478	0,434
M.P.	0,671.	1	0,932	0,581	0,124
AL	0,573	0,932	1	0,367	0,259
NaS	0,478	0,581	0, 367	1	-0,455
P. F.I.T	0,434	0,124	0,367	-0,455	1

FIGURE 5 : Position des vecteurs variables dans le plan principal.

Il y a donc eu en moyenne une descente du FIT et un apport d'aérosols typiquement continentaux. C'est ce que marque la très forte corrélation (0,932) existant entre la masse d'aérosols et l'aluminium. C'est dans ce cas que le lien existant entre le pouvoir glaçogène et la masse de poussières est le plus fort. La bonne corrélation existant entre le pouvoir glaçogène et le sodium soluble n'est pas une preuve d'action des aérosols marins, puisque la corrélation positive entre Al et Na(s) montre, qu'ici encore, le sodium soluble est surtout d'origine continentale.

4.4. Quatrième cas : les prélèvements ont lieu à proximité du FIT qui se trouvait au Sud des stations, quatre jours avant.

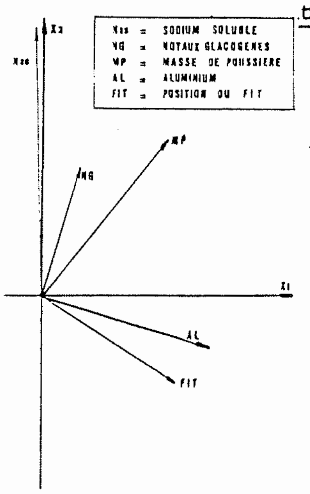

	N.G.	M.P.	Al	NaS	P. FIT.
N.G.	1	0,061	0,014	0,361	0,102
M.P.	0,061	1	0,321	0,492	0,071
Al	0,014	0,321	1	-0,077	0, 571
NaS	0,361	0,492	-0,077	1	-0,330
P. F.I.T	0,102	-0,071	0,571	-0,330	1

FIGURE 7 : Position des vecteurs variables dans le plan principal.

Ceci indique en moyenne une remontée du FIT dans les jours qui ont précédé la prise d'échantillon.

On constate, à l'inverse des trois cas précédents qu'il n'existe pas de corrélation entre le pouvoir glaçogène et la masse d'aérosols ou la concentration en aluminium. Par contre, une corrélation faible mais positive existe avec le sodium soluble dont l'origine est principalement océanique, puisque cet élément est anticorrélé avec l'aluminium. L'activité glaçogène augmente donc ici avec un élément d'origine océanique qui n'est pas actif par lui-même puisque toutes les mesures montrent que l'activité glaçogène d'une masse d'air typiquement océanique est très faible. Cet élément agit donc par son interaction avec les aérosols continentaux. L'absence de corrélation entre le pouvoir glaçogène et la masse d'aérosol dans ce quatrième cas s'explique par l'effet de cette activation.

Lorsque le FIT remonte, entraînant une diminution de la masse de poussière, l'activation des aérosols continentaux qui, en raison de la structure verticale du FIT, restent présents dans la couche de mousson, maintient le pouvoir glaçogène à un niveau élevé. On peut même, comme nous l'avons montré dans plusieurs cas particuliers, obtenir avec une concentration en poussières faible, un pouvoir glaçogène plus élevé qu'en période de brume sèche dense. Dans ces conditions, la corrélation entre masse de poussière et activité glaçogène ne peut être que faible. Elle sera par contre, relativement élevée, si, comme dans le cas précédent, le mélange des aérosols continentaux et océaniques est faible.

5.- Discussion

L'activation de particules au contact d'une masse d'air océanique avait été suggérée par Soulage dès 1959 (5). Elle est en bon accord avec la théorie des sites de nucléation développée par Fletcher (6) et avec de nombreux résultats expérimentaux. Ainsi, une des principales conclusions du Workshop de Laramie sur les techniques de mesure des N.G. présentée par Vali (7) est que le nombre de noyaux glaçogènes détectés augmente de façon considérable avec la concentration en noyaux de condensation. Dans le même sens Rosinski et Langer (8), analysant la composition chimique des N.G. naturels, ont montré qu'ils sont pour la plupart des particules mixtes, c'est-à-dire contenant une fraction soluble.

L'action des particules hygroscopiques serait de créer des sites de nucléation en favorisant la formation à sous saturation par rapport à l'eau, d'eau liquide ou adsorbée à partir de laquelle se développe la phase solide (2).

5.- Conclusion

L'analyse des différents cas envisagés permet une mise en évidence les facteurs dont dépend le pouvoir glaçogène en Afrique de l'ouest : présence d'aérosols continentaux et augmentation de leur efficacité glaçogène au contact d'une masse d'air océanique.

Les aérosols marins hygroscopiques non glaçogènes peuvent ainsi jouer indirectement un rôle important sur le pouvoir glaçogène.

Bibliographie

(1) Bertrand J., Cerf A., Domergue J.L., 1979
Répartition in space and time of dust haze south of the Sahara.
W.M.O. Symposium on Long Range Transport. Sofia 1-5 oct.

(2) Bertrand J., 1977
Action des poussières sub sahariennes sur le pouvoir glaçogène de l'air en Afrique de l'ouest.
Thèse d'Etat n° 253 Clermont-Ferrand p. 158

(3) Gagin A. and Aroyo M., 1969
A thermal diffusion chamber for the measurement of ice nuclei concentrations.
J. Rech. Atm., 4, 115-122.

(4) Domergue J.L., 1980
Contribution à l'étude de l'aérosol atmosphérique en région tropicale.
Thèse d'Etat. Toulouse n° 911.

(5) Soulage G., 1959
Hauts pouvoirs glaçogènes dus à la concentration de fumées sidérurgiques au-dessus de l'océan.
Ann. Géoph., 15, 4, 461-480.

(6) Fletcher N.H., 1959
Active sites and Ice crystal nucleation.
J. Atm. Sci., 26, 1266-1271.

(7) Vali G., 1976
Int. Workshop on Ice Nucleus Measurements
Univ. Wyoming. Laramie 7-15.

(8) Rosinski J., Langer G...., 1976
Chemical composition of surfaces of Natural Ice forming nuclei.
J. Rech. Atm., 10, 4, 201-210.

EFFECT OF METEOROLOGICAL FLUCTUATIONS ON HAIL GROWTH

J. L. Xu

Lanzhou University, P.R.C

Gu et al. (1962) and Zhou (1964) have made theoretical calculations of the mechanisms of precipitation in warm clouds using a monodispersed size spectrum for the initial particle and fluctuations in the meteorological factors. In this paper we consider the radii of growth particles as a function of random variables (initial particle radius and different meteorological factors). Here we use a polydispersed size spectrum for the initial particle radii and fluctuating water content and turbulent acceleration. We derive and calculate the equation and compare with other, more simple models. The results show that convective storm may produce moderately sized hail in a relatively short time.

We specify quantitatively the effects of increasing or decreasing fluctuations in the meteorological factors as well as changing hail size distributions on the hail spectra.

1. HAIL GROWTH IN AVERAGE METEOROLOGICAL CONDITIONS

The growth rate equation is

$$\frac{dr}{dt} = \frac{E}{4\rho_i} qv \qquad (1)$$

where E = collection efficiency, q the cloud water content, ρ_i the hailstone density and v the hailstone terminal velocity, a semi-empirical formula

$$v = \alpha\sqrt{r}, \quad \alpha = 2.04 \times 10^3 \ \mathrm{cm}^{1/2}\ \mathrm{sec}^{-1} \qquad (2)$$

Integrating (1) we obtain

$$r = (Aq + \sqrt{r_o})^2$$

where $A = \frac{E\alpha}{8\rho_i} t$, t is time from r_o to r.

The radius, r_o, of the hail embryo is the random variable from observation, its probability distribution is

$$\phi_o(r_o) = \begin{cases} \frac{1}{\sqrt{2\pi}\sigma_{r_o}} e^{-\frac{[r_o - \bar{r}_o]^2}{2\sigma_{r_o}^2}} & r_o \geq 0.05 \text{ cm} \\ 0 & r_o < 0.05 \text{ cm} \end{cases}$$

From these equations we obtain

$$\phi(r) = \frac{1}{\sqrt{2\pi}\sigma_{r_o}} \left(1 - \frac{A}{\sqrt{r}} q\right) e^{\frac{-[(\sqrt{r} - Aq)^2 - \bar{r}_o]^2}{2\sigma_{r_o}^2}} \qquad (3)$$

If q = 2grms/m^3; t=540 sec; the minimum embryo radius = 0.05 cm and the maximum 0.3 cm with a mean radius of 0.15 cm and mean square deviation, σ_{r_o}=0.05 cm, then the result is curve A in Fig. 1.

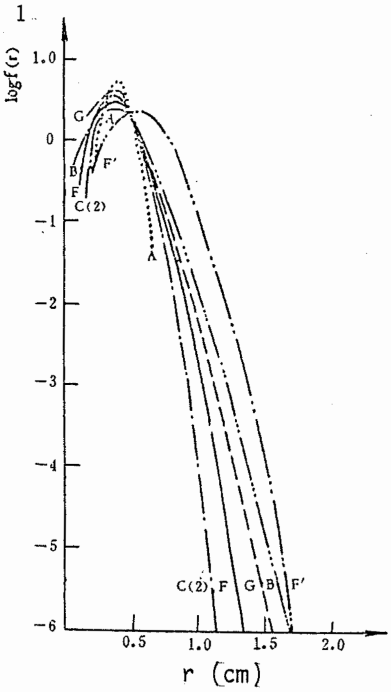

Fig. 1 - Hail size distributions for different conditions.

2. HAIL GROWTH WITH POLYDISPERSED EMBRYO SPECTRUM, FLUCTUATING WATER CONTENT AND FLUCTUATING TURBULENT ACCELERATION

The condition of turbulent acceleration, we obtain the semi-empirical formula for terminal velocity $v = \beta\sqrt{w}\sqrt{r}$ where w is the vertical acceleration of a hailstone with respect to the air, β = 65.27, and w is ≥ 0.

The distributions of q and w are assumed as

$$\phi_1(q) = \begin{cases} \frac{1}{\sqrt{2\pi}\sigma_q} e^{\frac{-(q-\bar{q})^2}{2\sigma_q^2}} & q \geq 0 \\ 0 & q > 0 \end{cases} \qquad (4)$$

and

$$\phi_2(w) = \begin{cases} \frac{1}{\sqrt{2\pi}\sigma_w} e^{\frac{-(w-g)^2}{2\sigma_w^2}} & w \geq 0 \\ 0 & w < 0 \end{cases} \quad (5)$$

where $\bar{q}$ is the mean value, σ_q and σ_w the mean square deviations. Integrating (1) we obtain

$$r=(B\sqrt{wq} + \sqrt{r_o})^2 = \phi\ (w,\ q,\ r_o) \quad (6)$$

$$B = \frac{E\beta}{8\rho_i}t$$

because r_o, q and w are random variables, r is also a random variable. For a given time, t, and assuming E and ρ_1 are constant, B is also constant, and we obtain the distribution function of r as

$$F(r) = P[r_o \leq \phi\ (r_o,\ q,\ w) \leq r] \quad (7)$$

in the domain where $r_o \leq \phi(r_o,\ q,\ w) \leq r$, the probability of r may be expressed as a triple integration

$$F(r) = \iiint_V \psi(r_o,\ q,\ w)dr_o dqdw \quad (8)$$

assuming

$$\psi(r_o,\ q,\ w) = \phi_o(r_o)\phi_1(q)\phi_2(w) \quad (9)$$

Making the transformation $(B\sqrt{wq}+\sqrt{r_o})^2 = z$ and differentiating for r, we obtain the probability density of r as

$$\phi(r)= \frac{1}{2\sqrt{8\pi^3}\ B\sigma_{r_o}\sigma_q\sigma_w\ \sqrt{r}}\int_{r_{om}}^{r_{oM}} dr_o \int_{g-2\sigma_w}^{g+3\sigma_w} \frac{1}{\sqrt{w}} \quad (10)$$

$$.e^{-\left\{\frac{(r_o-\bar{r}_o)^2}{2\sigma_{r_o}^2}+\frac{(w-g)^2}{2\sigma_w^2}+\frac{\left[\frac{1}{\sqrt{w}}(\sqrt{r}-\sqrt{r_o})-B\bar{q}\right]^2}{2\sigma_q^2B^2}\right\}} .dw$$

If $\bar{r}_o$ = 0.15 cm; σ_{r_o} = 0.05 cm; the minimum hail embryo radius ≅ 0.05 cm, the maximum = 0.30; $\bar{q}$ = 2 grms/m^3; σ_q = 0.3 $\bar{q}$; σ_w =]/3 g; t = 545 sec, from (10) we obtain the curve B in Figs. 1 and 2.

The result obtained are in good agreement with observations by Douglas (1963)(curve (2) in Fig. 2) and Xu et al (1965) (curve (1) in Fig. 2.

3. MORE SIMPLE MODELS

a. Hail growth with a monodispersed hail embryo spectrum and a fluctuating water content: The distribution density of r is

$$\phi(r) = \frac{1}{2\sqrt{r}} \cdot \frac{1}{\sqrt{2\pi}\sigma_q A} e^{-\frac{(\sqrt{r}-\sqrt{\bar{r}})^2}{2\sigma_q^2A^2}} \quad (11)$$

and in the domaine where $r_1 \leq r \leq r_2$ the probability of hailstone radii size is

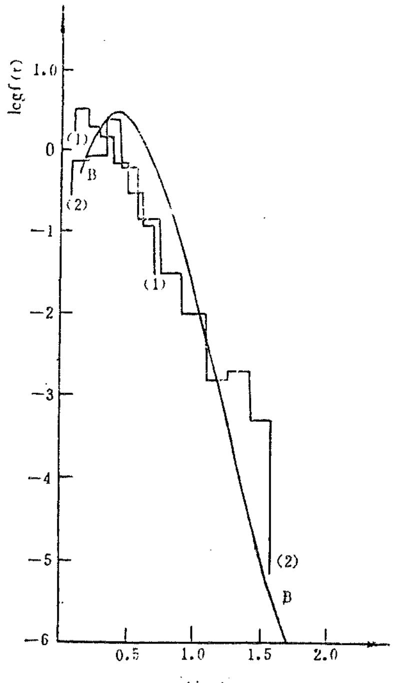

Fig. 2 - Hail size distribution - polydispersed hail embryos, water content and turbulent acceleration fluctuation.

$$P(r_1 \leq r \leq r_2) = \frac{1}{2}\ [\Phi(y_2) - \Phi(y_1)] \quad (12)$$

where $\Phi(y) = \frac{2}{\sqrt{2\pi}}\int_0^y e^{-\frac{\xi^2}{2}} d\xi$, $\xi = \frac{\sqrt{r}-\sqrt{\bar{r}}}{\sigma_r}$.

If $\bar{q}$ = 2 gm/m^3, σ_q = 0.3 $\bar{q}$; r_o = 0.15 cm; t = 540 sec, we obtain the curves C_2 in Figs 1 and 3.

In Fig. 3, curves C_1 and C_3 show the probability densities of hailstone radii where σ_q = 0.15 $\bar{q}$ (C_1) and 0.45 $\bar{q}$ (C_3) when r_o = 0.05 cm. In Fig. 4, curves D and E give the probability densities for hailstone radii where σ_q = 0.15 $\bar{q}$ and 0.45 $\bar{q}$ respectively when r_o = 0.25 cm. The probability of hailstone radii $\geq$ 0.5 cm and $\geq$ 0.75 cm was calculated from (12) and the results are given in Table I.

Table I
Probability of Hailstone Radii

	C(1)	C(2)	C(3)	D	E
$P(r \geq 0.5)$	0.063	0.22	0.31	2.3×10^{-3}	0.75
$P(r \geq 0.75)$	$<10^{-8}$	2.6×10^{-3}	0.031	3.3×10^{-7}	0.087

b. Hail growth with a polydispersed embryo spectrum and fluctuating water content: The distribution density for r is

$$\phi(r) = \frac{1}{4A\pi\sigma_{r_o}\sigma_q\sqrt{r}}\int_{r_{om}}^{r_{oM}} e^{-\Big\{}$$

$$\left.\frac{(r_o-\bar{r}_o)^2}{2\sigma_{r_o}^2} + \frac{[(\sqrt{r}-\sqrt{\bar{r}})-(\sqrt{r_o}-\sqrt{\bar{r}_o})]^2}{2\sigma_q^2 A^2}\right\} \cdot dr_o \qquad (13)$$

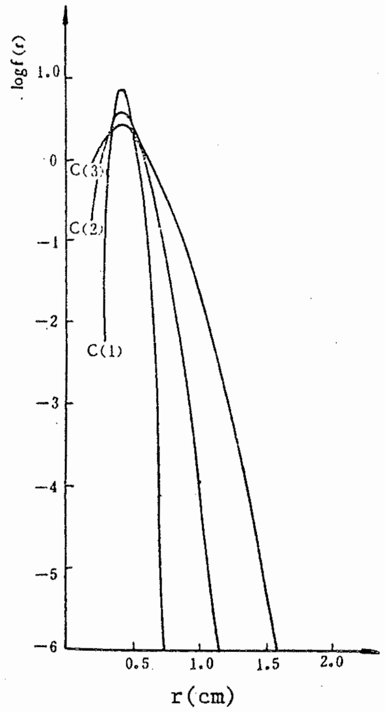

Fig. 3 - Hail size distribution - monodispersed hail embryo, fluctuating water content for different fluctuation amplitudes.

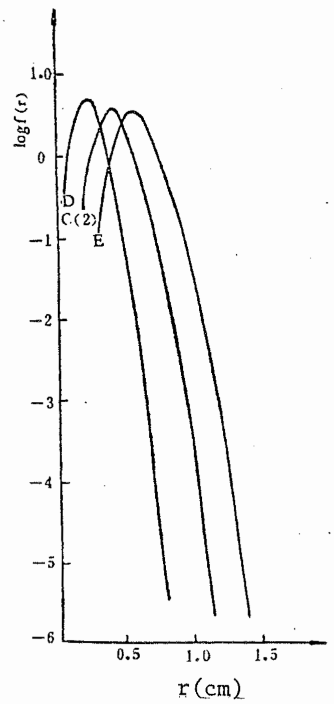

Fig. 4 - Hail size distribution - polodispersed hail embryo, fluctuating water content for different hail embryo size.

The results of the calculations are shown in curves F and F' in Fig. 1. for F, t and q are the same as in curve C_2 in the same figure and the other parameters are the same as in curves A and B. For F', the parameters are the same as F except r_{om}=0.5 cm; $\bar{r}_o$=0.25 cm; and $\sigma_{r_o} = \frac{1}{3}\bar{r}_o$.

c. Hail growth with a monodispersed hail embryo spectrum, fluctuating water content and fluctuating turbulent acceleration:

$$\phi(r) = \frac{1}{4B\pi\sigma_q\sigma_w\sqrt{r}} \int_{g-2\sigma_w}^{g+3\sigma_w} \frac{1}{\sqrt{w}}\, e^{-\left\{\frac{(w-g)^2}{2\sigma_w^2} + \frac{\left[\frac{1}{\sqrt{w}}(\sqrt{r}-\sqrt{r_o})-B\bar{q}\right]^2}{2\sigma_q^2 B^2}\right\}} \cdot dw \qquad (14)$$

The results are shown in curve G, Fig. 1 where the parameters are the same as curve B except r_o=0.15 cm.

4. SUMMARY

If average meteorological factors are used and the hail embryo size spectrum is monodispersed, the resulting hail size spectrum is also monodispersed. If the meteorological factors are allowed to fluctuate, however, the resulting hail size spectrum is polydispersed.

Increasing or decreasing the magnitude of the fluctuations seriously affects the hail size distributions.

Hail size distributions are also affected by whether the hail embryo size spectrum is mono or polydispersed.

The effect of the size of the hail embryo radius or mean radius are striking.

The results show that a relatively weak convective storm ($\bar{q}$ = 2 gms/m^3), with moderate fluctuations in meteorological parameters (σ_q=0.3$\bar{q}$) may produce hailstones 2 to 3 cm in diameter in a relatively short time (9 min.) which can damage crops.

ACKNOWLEDGMENT

The author appreciates the assistance given by Dr. Nancy Knight in her interpretation, and for the accurate typing of the manuscript by Ms. Barbara Franklin and Ms. Mickey Tyo.

REFERENCES

(1) Douglas, R. H., 1963, Recent Hail Research: A review, Meteorol. Monograph, vol. 5, no. 27.

(2) Gu, Z. C. and L. S. Zan, 1962, Fluctuating Growth of Precipitation in Warm Clouds, Acta. Meteorol. Sinica, vol. 32, no. 4.

(3) Xu, J.L., M.L. Wang, Z.L. Liu and Z.J. Duan, 1965, Analysis of hail sections and hail size distributions in Min District, Acta Meteorol. Sinica, vol. 35, n°2.

(4) Zhou, X.J., 1964, Microphysical Mechanisms of Precipitation in warm clouds, Science Press, Beijing.

ANALYSIS OF THE RADAR ECHOES AND THE HAILSTONE MICROSTRUCTURE OF A MULTICELL HAILSTORM

Naihu Gong, Tangfu Liu, Songxi Yang
Lanzhou Institute of Plateau Atmospheric Physics
Chinese Academy of Sciences

Jialiu Xu
Department of Geology and Geography, Lanzhou University
Lanzhou, China

A multicell hailstorm was for the first time well observed at the pingliang hail suppression base, Gansu, China, from 17:07 to 19:50 on June 25, 1977. In the process of motion and propagation, the hailstorm hailfall shot on the ground hailstones of various sizes as big as broad beans and apricots. The hail accumulation was about 15 cm in thickness in some regions. At the same time, strong thunder shower was accompanied. The precipitation at the central region amounted to 16 mm within 15 minutes. In order to make clear the structure of the hailstorm and its physical process of formation so as to conduct more effective operation to suppress hail artificially, we have analysed the radar echo and the hailstone microstructure of the multicell hailstorm.

1. The radar echo character

a) The developing and evolving process. The radar (Type JMA-133d made in Japan) echo evolving process of the this hailstorm is shown in figure which shows

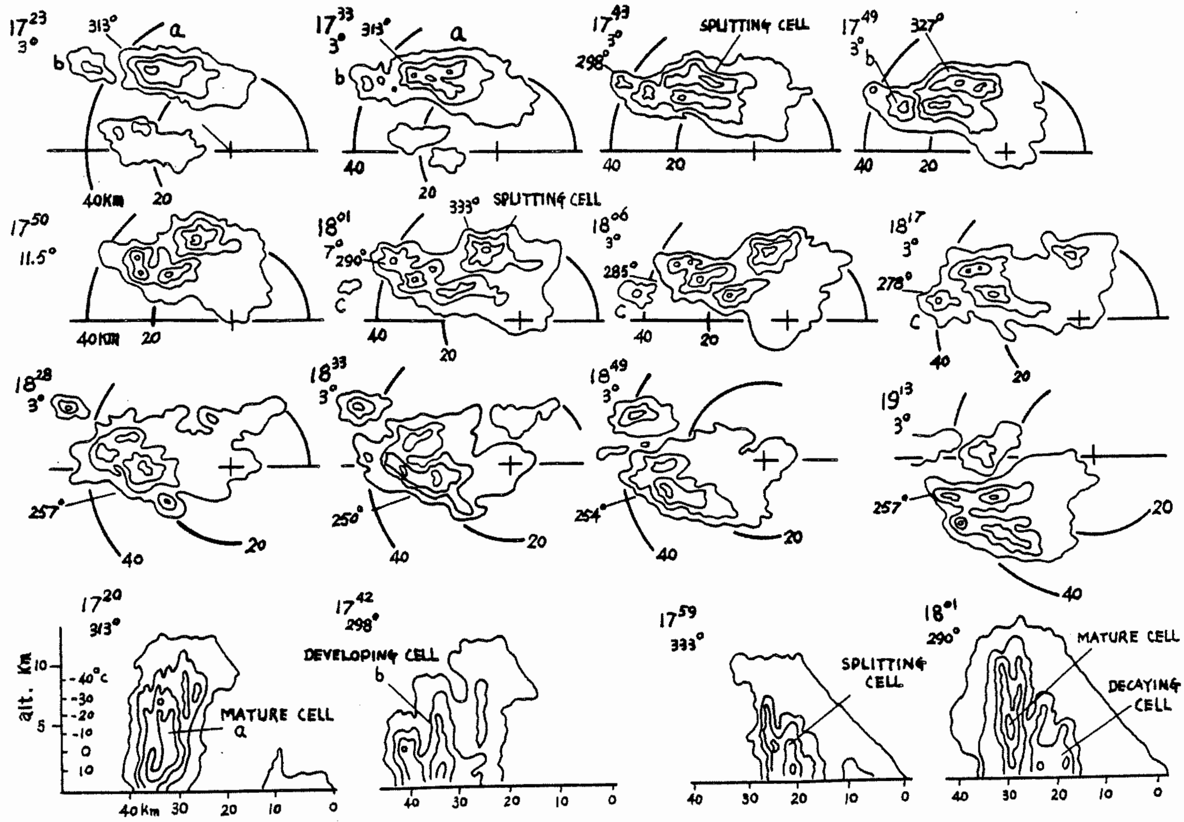

Fig. 2. Echo charts of reflectivity contours (dbZ) in PPI. RHI at some main time. (reflectivity contours from outside oo, 26, 36, 46, 56 dbZ respectively)

the complete process of how the multicell hailstorm generated, developed, matured and dissipated. The b cloud echo generated just at 17:23 was very small and weak and was in the initial stage, situated at the right front flank of the hailstorm, but developed rapidly during its moving process and combined into the compound body of hailstorm at 17:33. The developing stage was represented at 17:42. The height of the top of b cloud from RHI was about 7 km, with corresponding temperature of -10° — -25°c. This is the right place where hail-embryos formed and grew into the small hail ($\leqslant$5mm). It grew rapidly in a further step and became the main center of original cell group at about 18:01, ie. the mature stage. The cloud body was then high and intensive. The reflectivity region of $\geqslant$46dbZ stretched to the height of 5-9 km with the corresponding temperature of -15° — -40°c. It is main growing regions of hailstone. It turned into the decaying stage at about 18:30. During the b cloud developing, the original primary cloud a dissipated gradually. Another cloud c was formed at the right front flank of hailstorm. The cloud c repeated again the same process afterwards, ie. 18:01 being the initial stage, 18:17 developing stage, 18:33 mature stage and decaying stage at 19:00 about. The radar echo evolution showed a sequence of developing cells at the right front flank of hailstorm. Each of cells proceeds though a similar life cycle and at the same time the old cells dissipated gradually at the left rear flank of hailstorm.

b) The life cycle of the cells. Tracking cells motion and discontinuity propagation of hailstorm in our example, it was found that the life cycle of cell at its initiating and developing stages was 15±5 minutes respectively, and that at the mature and decaying stages was each about 30 minutes, thus the whole life cycle of the cell was not more than 1.5 hours.

c) The moving direction of cell and hailstorm. Observing that the individual echo moved continuously toward 30° left of the environmental wind and the echo group of hailstorm propagated discontinuously toward 30° right of the environmental wind, the deviative angle between the moving direction of the cell and the hailstorm was then about 60°. Inspecting the splitting cell, the deviative angle was even 90°.

d) The splitting phenomenon. There was a splitting phenomenon in the intensive region of the cell in mature stage. Figure shows that splitting occurred at 17:43 in the intensive region of radar echo. The phenomenon of the high elevation angle of PPI was also the same. The cross-section of elevation angle 11.5 at 17:50 shows the splitting of a thicker layer of cloud too. After splitting, the two mature cells moved at the same time in different direction and caused hailfalls respectively with the area of coverage being enlarged. The cell splits from the intensive region weakened and dissipated gradually after the hailfall and didn't go through the regular life-cycle as the multicell did.

2. The microstructure character of hailstones

a) The feature of the shapes of hailstones. Analysis of 120 hailstones collected from the ground shows that the diameters of the hailstones produced by the multicell hailstorm were small, the hailstones had more identical shapes, mainly the spheres and the spheroids. The spheric shape was the major 83.6%. It denotes that the environmental disturbance was much serious.

b) The inner structure of the hailstone. Cross-sectional observation on the 108 hailstones collected from the field has been made. The major shape of the hail-embryos was sphere and the secondary one was spheroid. The hail-embryos of 64.8 percent were transparent and semitransparent and their diameter were small, the distribution was biased.

From the analyses of the selected 130 pieces of hailstones it could be seen that in spite of it was not so large size (the maximum diameter was not more than 2 cm) the hailstone consisted of many layers, the number of which was rather divergent. Pieces with 2-5 layers were in the majority, amounting to 67.6% and the secondary were that of 6-9 layers, amounting to 30.8%. This illustrates the great fluctuation of the air current and the water content in the cloud, and also the feature of hailstone growth through different stages of cells in a multicell hailstorm.

c) The character of hailstone spectrum. looking through the spectral distribution of 1557 hailstones collected at random two hours after the hailfall, the relationship between its relative concentration and diameters was unsymmetrical distribution with single peak. The mode diameter was 7mm, and could be expressed as

$$f(d)=1.08d^{5.12}e^{-0.89d} \quad (\%)$$

Besides, during the former period of hailfall (17:43'-17:44'39''), the hailstone spectral distribution of the absolute concentration was also observed. Its mode diameter was 6-7mm. The total concentration of the hail was $0.136/m^3$ (being somewhat too little).

3. The operating portion on the hail suppression

For different hailstorm we propose to use different methods of hail suppression. For the multicell hailstorm, basing upon the analysis of the radar echo we consider that it is not only necessary to bombard to the front part of the main cell and to the region of intense echo, but also to bombard to those where the little cloud mass formed in the right front flank of the moving hailstorm, the site of b. c initial echo with height of 3-5 km and the site of developing b. c echo after combined with the main cloud with the height of 5-7km (the forming and growing region of hailembryos). Because the cells have the similar developing evolving process in the multicell hailstorm, it is better to make several repetitions to the operating portion as above mentioned in hail-suppression work.

REFERENCES

1.NHRE, 1975: Air motion and radar echo evolution in a multicell hailstorm. Preprints 9th Severe Local Storms Conf., PP. 436-443.

2. Marwitz, J. D., 1972 b: The structure and motion of severe hailstorms. Part II: Multicell Storms. J. Appl. Meteor., Vol. 11, PP. 180-188.

3. B. J. Mason, 1971: The Physics of Clouds. Oxford University Press.

ERRATUM

- Les articles II-1.5 et II-1.6 sont les mêmes.

  The papers II-1.5 et II-1.6 are the same.

- La classification a été légèrement modifiée entre l'impression des Proceedings et l'établissement du Programme Scientifique.

  The classification has been slightly changed between the Proceedings and the Scientific Program.

Imp Sciences . 24 , avenue des Landais - 63170 - Aubière . Dépôt Légal .

3e trimestre 1980